



# Understanding risk factors of a new variant outburst through global analysis of Omicron transmissibility

Marko Djordjevic<sup>a,\*</sup>, Sofija Markovic<sup>a</sup>, Igor Salom<sup>b</sup>, Magdalena Djordjevic<sup>b</sup>

<sup>a</sup> Quantitative Biology Group, Institute of Physiology and Biochemistry, Faculty of Biology, University of Belgrade, Serbia

<sup>b</sup> Institute of Physics Belgrade, National Institute of the Republic of Serbia, University of Belgrade, Serbia

## ARTICLE INFO

### Keywords:

Omicron transmissibility  
Outburst risk factors  
Effective reproduction number  
Ecological regressions  
Machine learning

## ABSTRACT

The emergence of a new virus variant is generally recognized by its usually sudden and rapid spread (outburst) in a certain world region. Due to the near-exponential rate of initial expansion, the new strain may not be detected at its true geographical origin but in the area with the most favorable conditions leading to the fastest exponential growth. Therefore, it is crucial to understand better the factors that promote such outbursts, which we address in the example of analyzing global Omicron transmissibility during its global emergence/outburst in November 2021–February 2022. As predictors, we assemble a number of potentially relevant factors: vaccinations (both full and boosters), different measures of population mobility (provided by Google), estimated stringency of measures, the prevalence of chronic diseases, population age, the timing of the outburst, and several other socio-demographic variables. As a proxy for natural immunity (prevalence of prior infections in population), we use cumulative numbers of COVID-19 deaths. As a response variable (transmissibility measure), we use the estimated effective reproduction number ( $R_e$ ) averaged in the vicinity of the outburst maxima. To select significant predictors of  $R_e$ , we use machine learning regressions that employ feature selection, including methods based on ensembles of decision trees (Random Forest and Gradient Boosting). We identify the young population, earlier infection onset, higher mobility, low natural immunity, and low booster prevalence as likely direct risk factors. Interestingly, we find that all these risk factors were significantly higher for Africa, though curiously somewhat lower in Southern African countries (where the outburst emerged) compared to other African countries. Therefore, while the risk factors related to the virus transmissibility clearly promote the outburst of a new virus variant, specific regions/countries where the outburst actually happens may be related to less evident factors, possibly random in nature.

## 1. Introduction

The new strain of SARS-CoV-2 (which appeared in November 2022) was designated as a “variant of concern” by the World Health Organization. This title echoed through worldwide media both as a “variant of fear” and a “variant of hope”. Namely, the new Omicron variant started to spread at rates previously unseen (indicating that its contagiousness was paralleled only by measles (Gerke et al., 2022; Rozsa and Karlis, 2022)) while seemingly, ignoring prior individual immunity and vaccination status (Gao et al., 2022; Khandia et al., 2022). The news prompted many world countries to (re)introduce travel bans and lockdowns to postpone local epidemics (Güvendik and Kavak, 2021). On the other hand, the preliminary data hinted at significantly reduced disease severity (Abdullah et al., 2022; Khandia et al., 2022; Ulloa et al., 2022),

raising hopes that we might be witnessing a transition to the endemic phase and a more peaceful coexistence with the virus (Mattiuzzi et al., 2022; Picheta, 2022).

Nevertheless, the mounting data were difficult to interpret unambiguously. The new variant was spreading through an unevenly vaccinated population, with different prevalences of prior exposure to the virus, different mobility patterns, and potential significant differences in other socio-demographic and medical factors, which may complicate every Omicron study. For example, it is unclear to what extent Omicron’s rapid expansion is due to its shortened incubation period (Jansen et al., 2021) and inherently increased basic transmissibility or due to immune evasiveness in combination with the waning immunity of the population (Lyngse et al., 2021b). While it was quickly apparent that the new strain is suddenly causing a substantial number of reinfections

\* Corresponding author.

E-mail address: [dmarko@bio.bg.ac.rs](mailto:dmarko@bio.bg.ac.rs) (M. Djordjevic).

(Bastard et al., 2022; Pulliam et al., 2022) and that the effects of the full (double) vaccination in spread prevention are marginal (if any) (Accorsi et al., 2022; Ferguson et al., 2021; Hansen et al., 2021), the effects of booster vaccines were more challenging to understand. Most studies thus far show that boosters confer certain protection from Omicron infection (Accorsi et al., 2022; Ferguson et al., 2021; Lustig et al., 2021). However, it is unclear if this is a qualitatively new increase in immunity (e.g., due to affinity maturation (Schmidt et al., 2021) or some other mechanism (Willyard, 2022)) or merely a restoration of the immunity produced by the second dose, which is again rapidly waning (to 25–40% protection after 15 weeks (Rigby, 2022)). Moreover, if the booster protection is generally short-lived, it is disappointing and surprising that the introduction of the fourth dose provides hardly any remedy (Regev-Yochay et al., 2022), which raises doubts about the proper timing of the booster shots and long-term strategies. On the other hand, while the influence of booster doses on disease transmission appears limited, their effect on the prevention of hospitalization is quite significant (Tenforde et al., 2022). Unfortunately, it also seems to be quickly waning (Rigby, 2022). However, the large-scale impact of the boosting efforts remains unclear, since the disease severity seems to be already heavily reduced by widespread prior COVID-19 infections and/or the full vaccination. The prior COVID-19 immunity (rather than the inherent characteristics of the strain) might be the leading underlying cause of the reduced Omicron severity (Nealon and Cowling, 2022) - which is a potentially serious problem for countries that so far had low SARS-CoV-2 exposure, such as China. Therefore, there are many open questions due to many competing effects and their interactions, which are hard to disentangle yet essential to understand, especially since the Omicron variant might be here to stay. Moreover, even Omicron's geographical origin is disputed: while its detection and the first major outburst occurred in southern Africa, it is unclear whether this region was the variant's actual origin or merely a fertile soil for its transmission and a place where it finally reached a genome sequencing laboratory (Ellyatt, 2021; Mallapaty, 2022). Consequently, analyzing factors that promote Omicron transmissibility is also needed to objectively assess arguments on the disease origin. Previous research demonstrated the utility of analyzing global patterns of SARS-CoV-2 spread (see, e.g. (Dankulov et al., 2021; Magdalena Djordjevic et al., 2021; Sarkar et al., 2020; Vilar and Saiz, 2021a)).

In this light, we intend to complement the existing studies (dominantly of cohort and case-control type) with an ecological study design systematically comparing the Omicron epidemic's evolution in more than a hundred world countries. We emphasize the influence of full vaccination, boosters, and natural immunity (taking the cumulative number of COVID-19 deaths as the proxy for the prevalence of prior infections in the population) on the virus transmission in the population, but also considering the effects of some other likely important factors: population age and density, prevalence of diabetes and cardiovascular diseases, time until the epidemic onset, and human development index. Additionally, we consider the estimated measure stringency and, more importantly, the actual (observed) human mobility data. As the response variable, we consider the effective reproduction number  $R_e$ , averaged (for each country) in the vicinity of the Omicron outbreak peak ( $R_{avg}$ ). Apart from analyzing direct (univariate) correlations, we apply linear regression methods that employ feature selection and state-of-the-art (nonlinear) machine learning techniques. This approach allows controlling for multiple factors that influence transmissibility while excluding those (initially considered) variables that do not influence the response. Additionally, more advanced machine learning techniques, which we also employ in this work, account for possible nonlinear effects and interactions among the predictors.

In this way, we provide insights on the Omicron expansion complementary to other studies' conclusions, emphasizing global (i.e., country-level) epidemical tendencies and effects of implemented (vaccination and social) policies. After identifying the main factors that promote the virus transmission, we show that all of them were highly

elevated in African countries during the Omicron outburst, suggesting that it is not surprising that the variant was first recognized on this continent. This, together with negative correlations between the perceived time of the outburst and the reproduction number, argues against inclinations to equate the place where the virus originated with the place where it initiated the first outburst. In particular, this casts further doubts that this new strain has necessarily originated in Africa.

Instead, we suggest that the local medical, socio-demographic, or mobility patterns that modulate the  $R_e$  value may substantially affect the onset of the local epidemic, potentially misleading about the actual location of virus origin. In extreme cases, the local modulation can keep the reproduction number below the threshold necessary to transition to the exponential phase of the epidemic, which can be exacerbated by stochastic effects (particularly at a low number of infected) and by population and spatial heterogeneities (e.g., social bubbles) (Britton et al., 2020; Hellewell et al., 2020; Leng et al., 2021). This can preclude any observable local outburst (Kochańczyk et al., 2020) (or significantly delay its onset) in regions with lower transmissibility, despite the appearance of a new virus (or variant) in this region. In such cases, the new virus/strain will show up only when and if it, in the stochastic regime, manages to reach some other, possibly distant region, with more favorable conditions for its transmission. Therefore, we argue that a new strain is likely to be first observed and sequenced in the regions with the most favorable conditions for its transmission, irrespective of its actual location of origin (but assuming a reasonably high level of interconnectedness of populations across the globe). Therefore, the risk factors that we identified (which tend to intensify the reproduction number of Omicron and similar future strains/viruses) can point to world regions that should be closely monitored for the appearance of new variants. Finally, we compare our results with the data analysis from the initial pandemic wave (Marko Djordjevic et al., 2021), revealing some similarities and reversed trends.

## 2. Methods

### 2.1. Data acquisition

Complete Our World in Data COVID-19 dataset was retrieved from (Dong et al., 2020; Ritchie et al., 2020), where it was aggregated from several external sources (see below). All rows that do not belong to countries, i.e., correspond to larger regions such as continents (recognized by OWID in iso code), were filtered out. Rows from Nov. 20th, 2021, to Feb. 14th, 2022, were selected for each country. Nov. 20th was taken as the initial date since the new Omicron variant was first reported to the WHO from South Africa on Nov. 24th (CDC COVID-19 Response Team, 2021; Tian et al., 2022). Columns were extracted that correspond to iso code (three-letter), continent, country, date, total deaths per million, reproduction rate ( $R_e$ ), fully vaccinated per hundred (fully vaccinated), boosters per hundred (boosters), stringency index (stringency), population density (pop. density), median age, aged 65 or older (older population), cardiovascular death rate (cardiovasc), diabetes prevalence (diabetes), and human development index (HDI). Here, the cardiovascular death rate and diabetes prevalence were chosen as readily available measures of two known COVID-19 comorbidities (Liu et al., 2020; Sanyaolu et al., 2020). The inferred reproduction rates come from (Arroyo-Marioli et al., 2021), while the other direct data sources are listed in (Hasell et al., 2020; Mathieu et al., 2021). We take total COVID-19 deaths per million as proportional to the prevalence of prior COVID-19 infections in the population, i.e., natural immunity in a country (immunity proxy). This measure is taken as a reasonable immunity proxy, as the number of deaths is proportional to the number of infections while being much less dependent on the testing coverage (which significantly varies between countries).

Global mobility data, provided by Google LLC, were retrieved from (Google, 2022). The data are aggregated in six categories, represented as percent change from baseline: retail and recreation; grocery and



pharmacy; parks; transit stations; workplaces; residential. Countries were selected from this dataset, i.e., smaller territorial units were filtered out. The same range of dates as for OWID data was then selected. Also, to facilitate joining with the OWID dataset, a two-letter country code was substituted by a three-letter code, and the two datasets were joined by their standard country code and date. An integrated (filtered) dataset consisting of selected OWID variables and Global mobility categories is provided in [Supplement Table 1](#) and was used in further analysis.

## 2.2. Data processing

A maximum of  $Re(t)$  was found for each country in the considered time interval (Nov. 20th, 2021–Feb. 14th, 2022). The Onset was defined as the number of days between the first date (Nov. 20th, 2021) and the maximum. As the maximum of  $Re(t)$  is based on a single date, to more robustly estimate the response variable (transmissibility), we calculated an average value  $R_{avg}$  for a 21 days time window centered around the maximum for each country.  $R_{avg}$  was used as the response variable in further analysis. The countries were included in the study if *i*) The 21 days time window is within the interval considered in the analysis. This ensures that peaks unrelated to Omicron are likely to be excluded (for a too early maximum) and that  $Re(t)$  had a chance to reach its maxima within this time interval (satisfied for a large majority of countries). *ii*) The maximum of  $Re(t)$  was at least 1.2 to ensure that there was indeed a peak (outburst) adequately reflected in the data. *iii*)  $Re(t)$  values are available for at least 50% of the dates in the considered interval. Note that many  $Re(t)$  values will be missing for countries with irregular case count measurements.

With the criteria above, i.e., the three conditions and availability of OWID and Global Mobility data, 104 countries were included in the further analysis. For these countries, total death per million (used as immunity proxy) was calculated at the beginning of the time window (ten days before maximum). The vaccination data (full vaccinations and boosters) are reported at larger time intervals than days for some countries. Consequently, we used the available value closest to the date of  $Re(t)$  maxima. Stringency has been calculated as an average during the 20-day time window. Equivalently, all mobility categories are included as the window averages. The socio-demographic and medical data (prevalence of chronic diseases) that do not change during the considered interval were included as is in the dataset. The complete dataset used in further analysis, with the response  $R_{avg}$  and the predictor variables for each country, is provided in [Supplement Table 2](#).

## 2.3. Variable transformations

Variables were transformed before further analysis, as reduction of the data skewness (and the corresponding reduction of the outliers associated with heavy asymmetric tails of non-transformed distributions) is needed for implementing Lasso and Elastic Net regressions ([Hastie et al., 2009](#)). The variable transformations are similar to Box-Cox transformations ([Box and Cox, 1964](#)). We wrote a custom script, where for each variable the transformation was selected so that the skewness of the data was as close to zero as possible, with the minimal number of remaining outliers (subsequently substituted by the median value of the transformed variable). The list of the applied transformations is provided in [Table 1](#).

## 2.4. Machine learning regressions

Statistical analysis was performed following the previously implemented methodology ([Markovic et al., 2021](#)). Two regularization-based regression methods, Lasso ([Hastie et al., 2009](#); [Tibshirani, 1996](#)) and Elastic net ([Hastie et al., 2009](#); [Zou and Hastie, 2005](#)) were implemented as “Relaxed” ([Hastie et al., 2009](#); [Meinshausen, 2007](#)), i.e., two rounds of regression were performed, where only predictors selected in the first

**Table 1**  
Variable transformation.

Variable	Description	Transformation
immunity proxy	Number of deaths per million people as the proxy for population immunity	$x^{1/3}$
fully vaccinated	Percentage of the fully vaccinated population	$-\sqrt{\max(x) - x}$
boosters	Vaccine boosters administered per 100 people	$x^{1/3}$
stringency	Government response stringency index	None
pop. density	Population density	$\log(x)$
median age	Population median age	$x^2$
older population	Percentage of population over 65 years	$x^{1/3}$
cardiovasc	Prevalence of cardiovascular diseases	$\log(x)$
diabetes	Prevalence of diabetes	$x^{1/3}$
HDI	Human development index	$-\sqrt{\max(x) - x}$
mobility retail	Changes in mobility trends for retail and recreation	$\log(x - \min(x))$
mobility grocery	Changes in mobility trends for grocery and pharmacy	$\log(x - \min(x))$
mobility parks	Changes in mobility trends for parks	$(x - \min(x))^{1/3}$
mobility transit	Changes in mobility trends for public transport	$(x - \min(x))^{1/3}$
mobility workplace	Changes in mobility trends for places of work	$\sqrt{x - \min(x)}$
mobility residential	Changes in mobility trends for places of residence	$-(\max(x) - x)^{1/3}$
onset	Delay of the Omicron wave onset (time from Nov. 20th, 2021, until the peak of $R_e$ )	None
$R_{avg}$	Average effective reproductive number of the virus	$\log(x)$

round were used as input for the second round of regression. In both rounds, the optimal model was selected through 5-fold cross-validation, with the data repartitioned 40 times, as the sparsest model among those with mean squared error (MSE) within one standard error from the minimal MSE.

Decision tree-based machine learning algorithms, Random Forest ([Breiman, 2001](#); [Hastie et al., 2009](#)) and Gradient Boosting ([Breiman, 1996](#); [Hastie et al., 2009](#)), were also implemented in the “Relaxed” settings, where only variables with the importance above the mean importance threshold of the minimal MSE model (selected through cross-validation, same as in Lasso and Elastic Net) in the first round of regression were kept in the second round. In the second round, a model with the minimal MSE was selected as optimal. Partial dependence plots ([Hastie et al., 2009](#)) were then used to examine further the contribution of features with the highest estimated importance in the minimal MSE model. In these plots, the effect of a given feature on the average prediction (i.e., taking the average effects of the remaining model features) is estimated. This allows confirmation of the model results and determining the direction of the association, as the importance estimate does not imply it.

## 3. Results

### 3.1. Exploratory data analysis and $R_{avg}$ inference

We start with exploratory data analysis, where  $R_e(t)$  patterns were analyzed for different countries, grouped by continents, allowing us to assess the progression of the Omicron variant. Here we specifically emphasize South African countries for which the data are available (South Africa, Mozambique, Namibia, Zimbabwe), where the initial outburst happened. Consequently, in [Fig. 1A](#), we showed each country’s  $R_e(t)$  dependences. In [Fig. 1B](#), average  $R_e(t)$  profiles for six continents are shown. By observing patterns in [Fig. 1A](#) and [B](#), we see the same general  $R_e(t)$  pattern, first increasing, reaching a maximal value, and then decreasing. Such a pattern is consistent with our definition of the response variable (see Methods), where  $R_{avg}$  in a 21-day window centered at maximum is calculated and used as a response. The

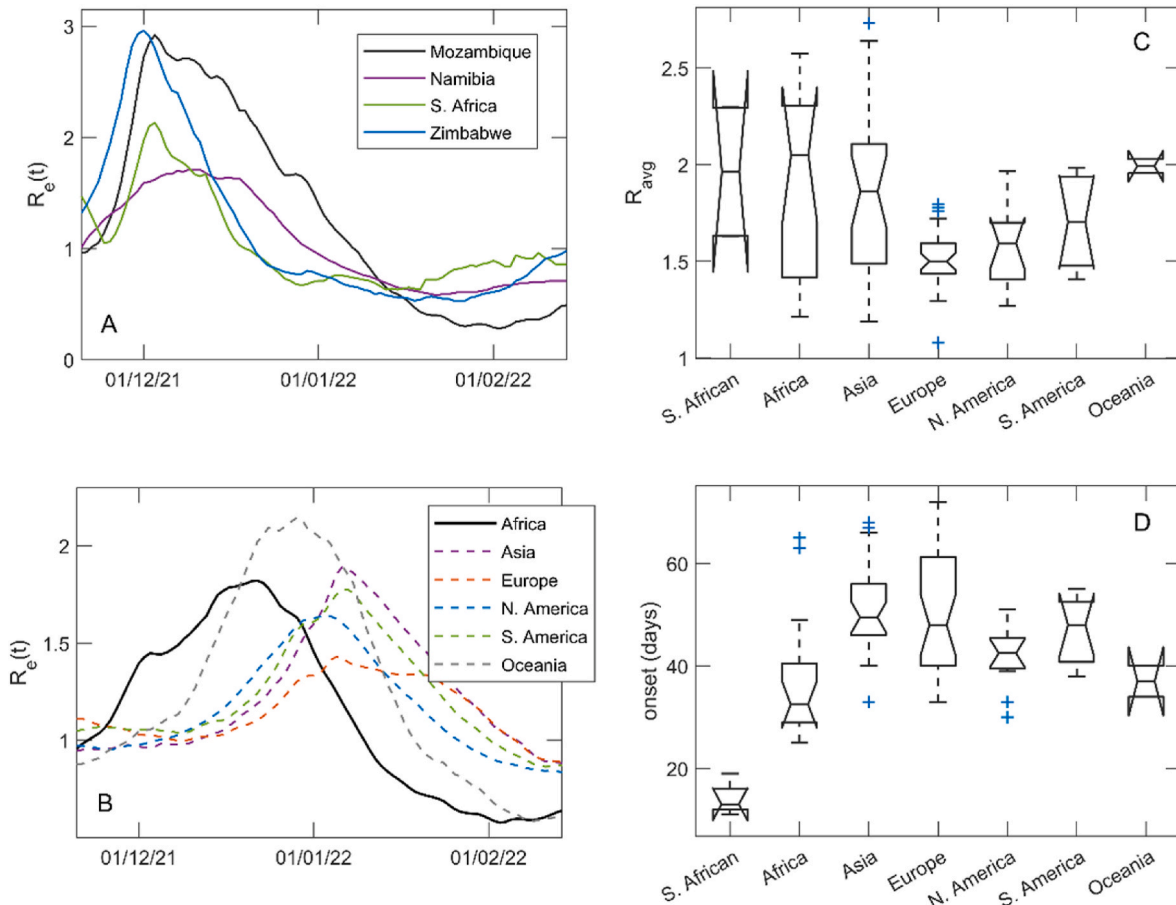


**Fig. 1. Exploratory data analysis.** A)  $R_e(t)$  dependences for four South African countries during Omicron outburst. B) Averaged  $R_e(t)$  profiles for the six continents. C) Box plots of  $R_{avg}$  for South African countries and six continents (South African countries excluded from Africa). D) Box plots of the delay of the epidemic's onset, relative to Nov. 20th, 2021, for South African countries and six continents; In Figs. C and D, the outliers are represented by blue plus marks ("+").  $R_e$  – effective reproductive number of the virus.  $R_{avg}$  –  $R_e$  averaged in 21 day window around maxima. (For interpretation of the references to color in this figure legend, the reader is referred to the Web version of this article.)

emergence of this time pattern of  $R_e(t)$  is discussed in the next section.

By comparing Fig. 1A and B, we see that the curves for South African countries are shifted to the left, corresponding to an earlier outburst in these countries. This is also clear from Fig. 1D, where onsets are compared, with the onset for South African countries happening significantly earlier than for the other countries. The onset for South African countries is clearly (and significantly) separated from other African countries. The onset in the other African countries also happens earlier than for the other continents; however, it is not nearly as clearly separated as the South African countries from the rest of the regions. This is a nontrivial result, as  $R_e(t)$  is inferred only from the case counts, i. e., it does not a priori take into account that the first outburst happened in South African countries but is independently reproduced/obtained from our analysis. Fig. 1C shows  $R_{avg}$  again for South African countries and continents. One can see that  $R_{avg}$  shows significant variability both within and in-between continents. For example, Europe has a significantly smaller  $R_{avg}$  than the other continents. Our next goal is to explore what factors (i.e., assembled predictors) contribute to this variability. Also, African countries have the largest  $R_{avg}$ , though interestingly, the South African countries have a somewhat smaller value than the rest of the African countries. We will come back to this at the end of our analysis.

Finally, note that the maxima values of the peaks in Fig. 1B should not be directly compared with Fig. 1A and C. The curves in Fig. 1B correspond to averages over many countries, where peaks for individual countries happen asynchronously (at different dates), which effectively

lowers the maxima of the averaged curves. Nevertheless, the utility of average profiles is to clearly show the same pattern of  $R_e(t)$  (initial increase, reaching maxima, and then decrease). Also, Fig. 1A and B additionally support the conclusion from Fig. 1D that the outburst in South African countries happened much earlier than in the rest of the world, followed (with significant delay) by the outbursts in the rest of Africa.

3.2. Univariate data analysis

Pearson correlation coefficients between all the considered variables and the response variable  $R_{avg}$  were determined after appropriately transforming variables (see Table 1) and presented in Fig. 2. As an alternative to calculating Person correlations for the transformed data, we could have used Spearman or Kendall coefficients, for which normally distributed data is not needed. However, in our previous work with COVID-19 data (Salom et al., 2021) we did not get much difference in obtained results when using these different correlations.

Fig. 2 shows that  $R_{avg}$  exhibits the highest negative correlation with the delay of the epidemic onset, percentage of the older population, median age, immunity proxy, boosters, and HDI, and the highest positive correlation with transit (longer range) mobility. Scatter plots of  $R_{avg}$  with these variables are presented in Fig. 3.

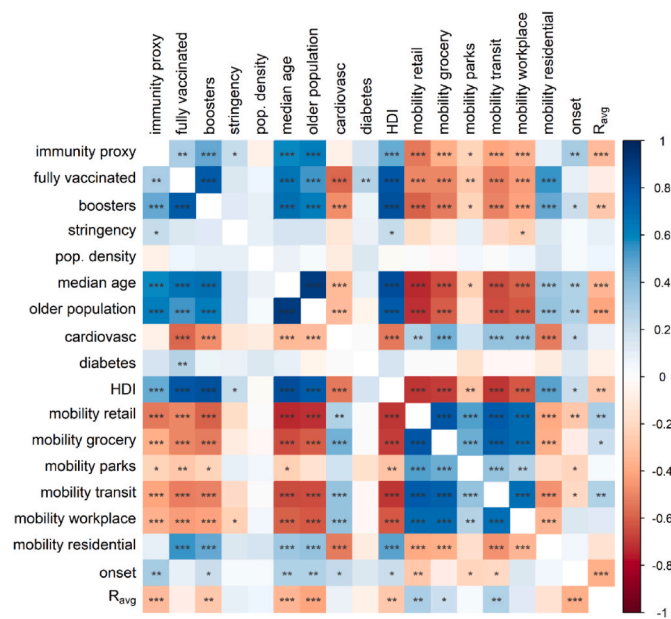


**Fig. 2. Correlation matrix for the predictors and the response.** Colors correspond to the value of Person correlation coefficients, as specified by the color bar on the right, while asterisks correspond to the statistical significance of the results ( ' ' -  $P > 0.05$ , ' \* ' -  $0.05 > P > 0.01$ , ' \*\*\* ' -  $0.01 > P > 0.001$ , ' \*\*\*\* ' -  $P < 0.001$ ); HDI – human development index,  $R_{avg}$  - average effective reproductive number of the virus; see Table 1 for more detailed variable descriptions. The figure was created using the R (R Core Team, 2021) corplot package (Wei and Simko, 2021). (For interpretation of the references to color in this figure legend, the reader is referred to the Web version of this article.)

### 3.3. Feature selection by machine learning regressions

Relaxed Lasso and Elastic net regressions were first performed on the entire set of variables, yielding results presented in Fig. 4A and C, respectively. These regressions selected the percentage of an older population and the delay of epidemic onset (relative to the approximate time of the first diagnosed Omicron case), both negatively associated with  $R_{avg}$ . Since the direct causal impact of these variables on transmissibility is unlikely, to further analyze the effect of other predictors (potentially masked by these selected variables), the regressions were repeated, excluding age-related variables (median age and older population) and onset. From this reduced set of variables, immunity proxy, boosters, mobility retail, and mobility transit are robustly selected by both methods (Fig. 4B and D). While immunity proxy and boosters are negatively associated with  $R_{avg}$ , long-range transit mobility and, to some extent, retail mobility are positively associated with the transmissibility measure.

The importance estimates from Relaxed Random Forest and Gradient Boosting regressions, performed on the reduced set of variables, are presented in Fig. 5A and D. While Random Forest and Gradient Boosting are generally robust to data transformations, for consistency we apply them to the same (transformed) dataset as used in Lasso and Elastic Net. From Fig. 5A, only immunity proxy is above the mean importance threshold in the second (relaxed) round of Random Forest regression, while mobility transit has the second-highest importance estimate value, which is consistent with Lasso and Elastic Net results. Interestingly, the rest of the variables previously selected by these two methods – boosters and mobility retail were not included in the second round of Random Forest (i.e., their importance was not above the importance threshold in the first round of Random Forest regression). On the other hand, some other variables, e.g., percentage of the fully vaccinated population, were included, with the importance estimate close to the threshold. However, the impact of these predictors on  $R_{avg}$ , examined by Partial Dependence Plots, was negligible (not shown). On the other hand, the effects of immunity proxy and transit mobility can be seen from the partial

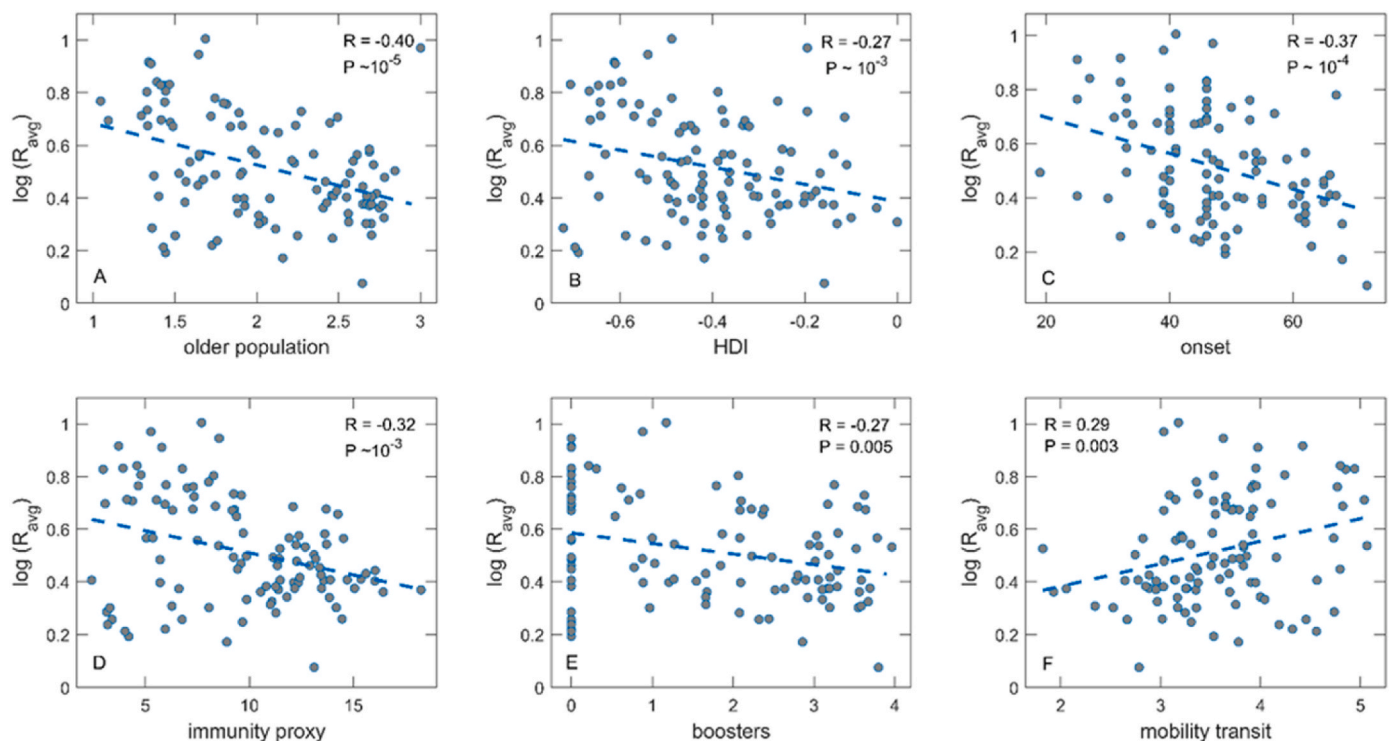


**Fig. 3. Scatterplots of  $R_{avg}$  vs. six predictors with the highest (positive or negative) Pearson’s correlation coefficients.** Values of the transformed variables (see Table 1) are presented on the horizontal axes; HDI – human development index,  $R_{avg}$  - average effective reproductive number.

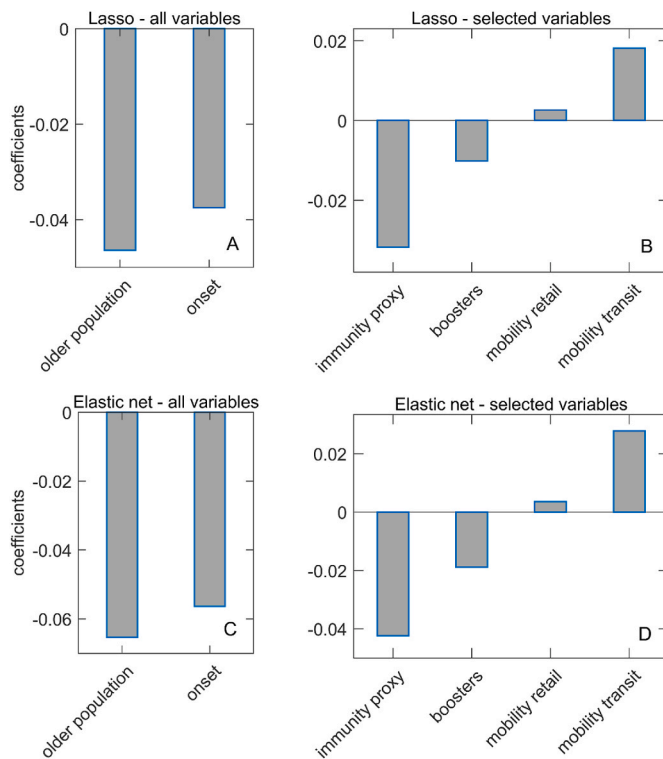


**Fig. 4. Relaxed Lasso and Elastic net regression coefficients.** A) Relaxed Lasso with all variables included in the first round of regression, B) Relaxed Lasso without onset and two age-related variables, C) Relaxed Elastic net with all variables, D) Relaxed Elastic net without onset and two age-related variables.

dependence plots in Fig. 5B and C, respectively.

Gradient Boosting results confirm the findings from previous regressions regarding the importance of immunity proxy and mobility transit variables in explaining  $R_{avg}$ , which can also be observed from the partial dependence plots in Fig. 5E and F, which resemble those obtained from the Random Forest. In Fig. 5C and F, a positive association between mobility transit and  $R_{avg}$  can be observed, while Fig. 5B and E shows step-like dependence between immunity proxy and  $R_{avg}$ . Several other predictors were selected to enter the second round of Gradient Boosting regression. However, similarly to Random Forest results, Partial Dependence Plots showed that their contribution to Omicron variant transmissibility is insignificant.

### 3.4. Analyzing risk factors

We next go backward, asking what the values of identified risk factors for different countries across continents are, specifically for South African countries. We obtain that these risk factors are indeed significantly elevated for African countries: The fraction of the older population is significantly lower (Fig. 6A); Mobility has been significantly elevated compared to the baseline (in contrast to, e.g., Europe where it has been significantly lowered from baseline); Natural immunity (proxy immunity) has also likely been significantly smaller in Africa. Finally, the booster vaccinations were very low in Africa and significantly lower than in other regions.

On the other hand, while risk factors for South African countries were clearly higher than in other continents, they were not distinct from other African countries (and are, in fact, even somewhat smaller). Consequently, while African countries are optimal for Omicron progression, South African countries were not specifically distinct from the rest of Africa. Overall, we obtain an interesting result that the continent/region where the Omicron wave has initiated is also a 'fertile ground' in

terms of the disease transmissibility. This is a highly nontrivial observation, as nothing in our analysis a priori uses information on where the outburst initiated. (Note that, even if we had not treated South African countries separately, the African continent would stand out as the one with the most favorable conditions for the outburst: the values for the overall African continent would be somewhere in between the nearby values for South Africa and Africa in Fig. 6, clearly singling out this continent as the riskiest one according to the relevant factors identified by our analysis.) It is also interesting that South African countries do not have distinctly optimal conditions among the other African countries. We will further discuss these findings below.

## 4. Discussion

### 4.1. Change of the effective reproduction number with time

We find that the dependence of the effective reproduction number on time has the same global pattern in the observed interval: increases, reaches a maximum, and afterward decreases (reaching a value below one for the majority of countries, indicating the end of the outburst (Khajanchi et al., 2021)). The increase in  $R_e$  is likely due to introducing the much more virulent Omicron strain, which was found to have more than two times higher effective reproduction number than Delta (Ito et al., 2022a, 2022b). An increase in the number of infected by Omicron leads to a rapid dominance of Omicron over the other (much less transmissible) SARS-CoV-2 variants in the population (Ito et al., 2022a), which is observed as an increase in  $R_e$  in Fig. 1A and B. The smoothing by the Kalman filter used for  $R_e$  extraction (Arroyo-Marioli et al., 2021) and the gradual transition from the stochastic phase (due to an increase in the number of infected by Omicron) may also be behind the gradual increase of  $R_e$ . Therefore, the maximum of  $R_e$  (averaged in a window around the maxima to evade the dependence on a single number) likely reflects an instance where Omicron dominates over other strains and where the other artifacts can be neglected. It thus provides a reasonable measure of Omicron transmissibility (effective reproduction number) for different countries. The start of the phase where  $R_e$  drops is likely due to a decrease in susceptibility numbers or a ramp-up in social measures. We here assume that the outburst in November 2021–February 2022 (and the consequent surge in  $R_e$  values) for the countries analyzed is indeed due to Omicron. There is no direct (genetic) evidence for this assumption (at least not at the level of all countries analyzed). However, the outburst in this interval is widely attributed to Omicron (Chassalevris et al., 2022; del Rio et al., 2022). Since the rapid increase in  $R_e$  is also consistent with the introduction of a highly transmissible variant (a pronounced Omicron property), we believe that our assumption is reasonable.

### 4.2. Influence of the population age and onset

Our preliminary analysis, performed on all independent variables, identified only two variables as dominant (and important) predictors of the effective reproduction number: the percentage of older people and epidemic onset, Fig. 4A and C. For both variables, the correlation is negative - a higher percentage of the older population and the longer interval to the epidemic onset are related to lower  $R_{avg}$  values. However, for either of the two, it is evident that we cannot presume a direct causal influence in the literal sense: assuming that older individuals have, per se (i.e., inherently biologically), a lower chance of catching and transmitting the virus, or that the potency of the virus has somehow decreased within the observed weeks, does not seem plausible. For example, a study in Danish households actually found increased transmissibility of SARS-CoV-2 in the older population (though the study does not concern Omicron) (Lynge et al., 2021a).

Instead, there are clear arguments for the strong indirect influence of the two factors. In the case of population age, it is reasonable to assume that the older population was, due to higher risks, on average, better



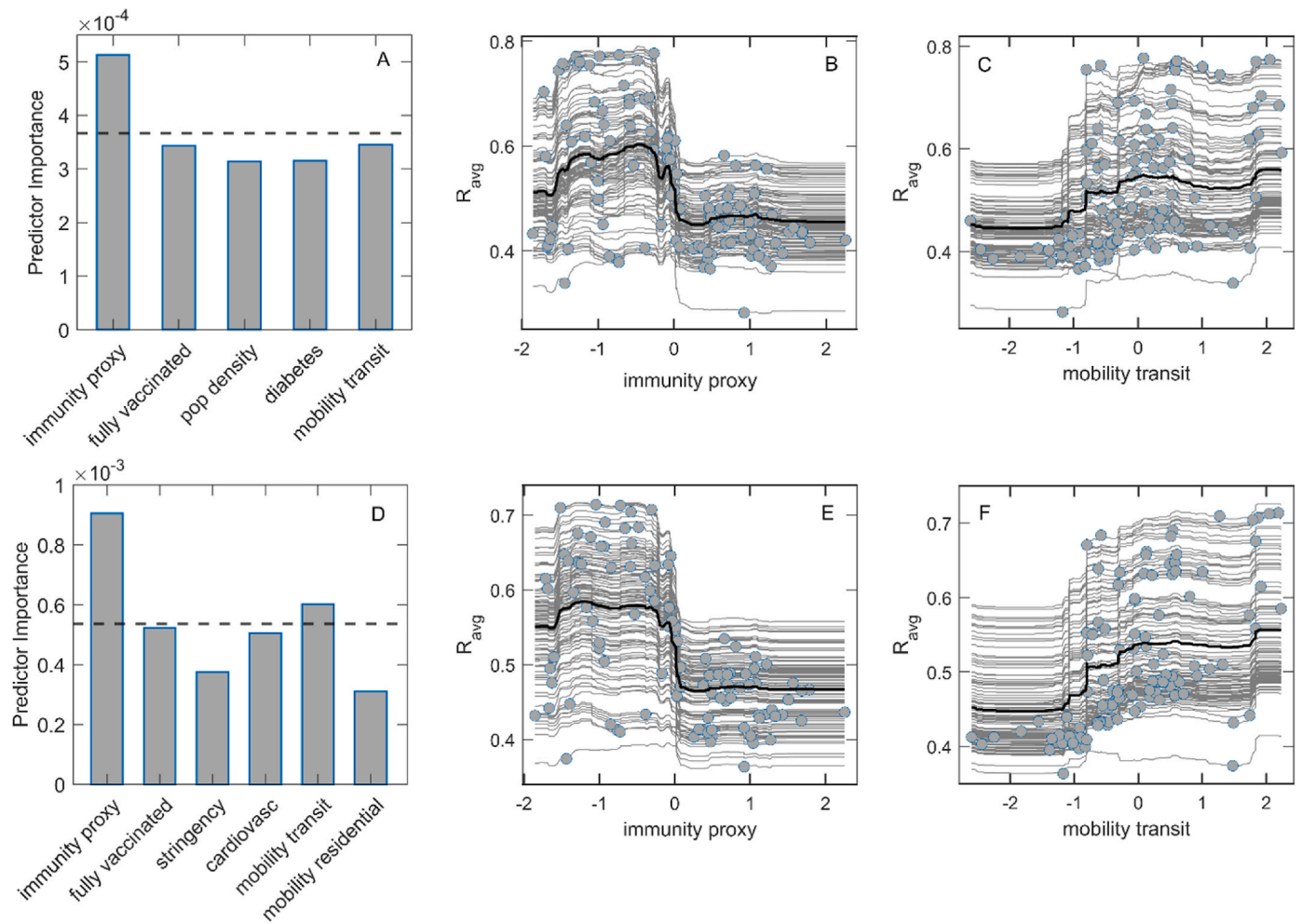


**Fig. 5. Random Forest and Gradient Boosting machine learning algorithms and partial dependence (PD) plots for variables with the highest importance.** A) Relaxed Random Forest predictor importance estimates, B–C) PD plots for Random Forest, D) Relaxed Gradient Boosting predictor importance estimates, E–F) PD plots for Gradient Boosting, Dashed line in A and D correspond to the mean variable importance in a given model.

observing social measures and taking more care to avoid the infection (as supported by a number of studies (Lin et al., 2021; Wright et al., 2022):). This is consistent with the obtained negative correlation between age-related variables and mobility measures, showing higher drop-in activities (work, shopping, transit) where the population was older (the correlation with mobility residential variable is positive, translating to longer stay-at-home time). Furthermore, vaccination, including booster shots, was generally more prevalent in the older population, both as a result of prioritizing population at higher risks and due to vaccine hesitancy in younger population (Diesel et al., 2021; Ritchie et al., 2020; Rzymiski et al., 2021; Sønderkov et al., 2021). This trend, also indicated by correlations shown in Fig. 2, likely contributes to lower infection and transmission rates in older population.

Age-related variables are also strongly positively correlated with the human development index, further connecting this variable to other influences. Namely, richer countries had higher overall vaccination percentages (among the older and younger populations), lowering  $R_{avg}$  values. Besides, more developed countries were also harder hit by COVID-19 in the first waves of the pandemic (Dalglish, 2020; Marko Djordjevic et al., 2021; Stribling et al., 2020). This led to higher values of natural immunity proxy (which in later analysis turned out to be a highly important predictor) and may explain why social measures were now stronger and more obeyed in these countries (as especially indicated by the strong negative correlation of HDI with mobility variables). Indeed, we note the inverted trend for the HDI variable for the Omicron

phase compared to the first wave of the pandemic. I.e., while, in the first wave, HDI was the dominant predictor of fast epidemic progression (Marko Djordjevic et al., 2021), now it is negatively correlated with  $R_{avg}$  values. This suggests that high HDI countries were better prepared and took more resolute actions in the later stages of the pandemic (learning from their own prior mistakes and having more resources to implement actions such as vaccination). Overall, age is highly correlated with almost all of our significant predictors of transmissibility. Therefore, we repeated the analysis after removing the age-related variables from the list of potential predictors to investigate which of these variables genuinely influence Omicron spread.

On the other hand, the cause behind the relatively strong influence of the onset variable on the transmissibility is much more intriguing, since this variable only loosely correlates with other predictors - mostly with population age, immunity proxy, and HDI (positive correlation), and somewhat with mobility measures (negative correlation). The mere sign of these correlations is, indeed, consistent with the observed connection of onset and reproduction number, because age, immunity proxy and HDI all negatively correlate with  $R_e$ , while mobility measures correlate positively. However, these correlations appear too weak to explain the magnitude and robustness of the effect, and seem more likely to merely reflect the fact that the first apparent outburst of the Omicron variant occurred in South Africa, while the waves in western countries (with old population, strong measures, high values of HDI, and immunity proxy) followed with a delay visible in Fig. 1B and D. Alternatively, it might

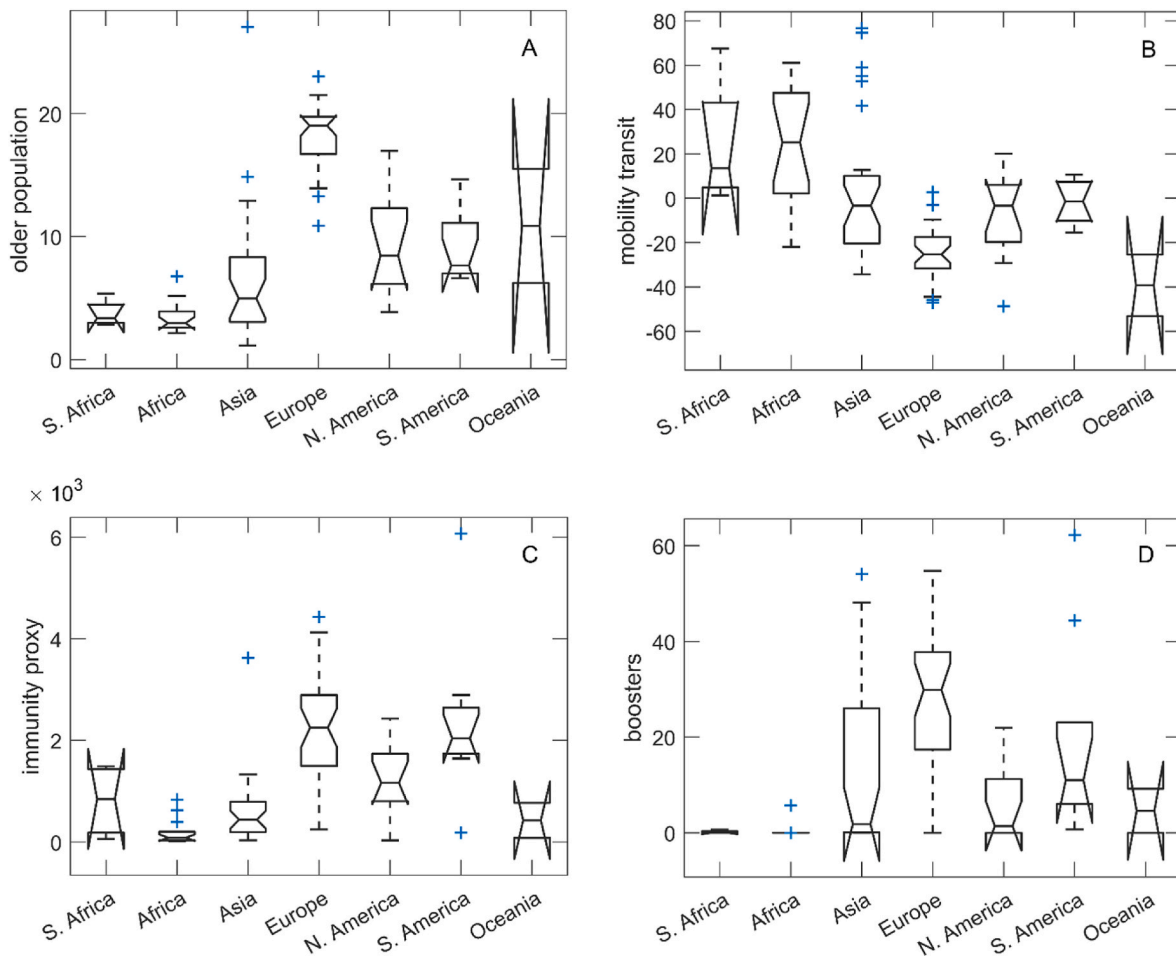


**Fig. 6. Risk factors for continents** Values of four identified risk factors are shown as box plots for South African countries and six continents: A) older population, B) mobility transit, C) immunity proxy, D) boosters; blue plus marks (“+”) represent the outliers. (For interpretation of the references to color in this figure legend, the reader is referred to the Web version of this article.)

seem relevant that a number of countries have quickly introduced travel bans from the initially affected African countries (Güvendik and Kavak, 2021), in attempts to postpone the Omicron epidemic. It is likely that the same countries, apart from the travel bans, have also (re)introduced stronger social measures (later leading to lower  $R_e$  values). However, this effect does not seem to be sufficiently large either - otherwise, a stronger correlation between onset and mobility variables (and/or stringency index) should be expected. On the contrary, weak correlations of this kind dismiss (at least as a complete answer) a simple explanation that the additional time to outburst provides more opportunity to introduce significantly stronger control measures and appropriately modify behavior (thus consequently lowering the reproductive number) (Rai et al., 2022).

The effects considered so far do not seem to offer sufficient explanation for the obtained significance of the onset variable as a predictor. Mainly since this connection is unusually robust, i.e., the onset variable was similarly strongly negatively correlated with the reproduction number in the first wave of the pandemic (Marko Djordjevic et al., 2021); however, low values of the onset variables were then tied to high HDI western nations.

Instead of looking only for indirect influences of this sort (i.e., via common confounders), we point to a potential connection of mathematical nature, which, to a certain extent, directly correlates the onset variable with the reproduction number. Namely, the effective reproduction number crucially determines the shapes of epidemic curves, affecting not only the evolution of case numbers but, consequently, also how quickly will the number of (effectively) susceptible individuals be

sufficiently depleted so that the reproductive number value begins to decline. Higher transmissibility of the virus in the given environment also leads to a shorter initial phase of stochastic epidemic evolution (as higher numbers of infected will be reached sooner). Consequently, the  $R_e$  value may strongly determine the epidemic peak time – the higher the virus’s transmissibility, the sooner the new epidemic wave becomes apparent and attracts attention. (However, due to the stochastic nature of the early epidemic’s evolution and interplay of various parameters, including variation in the initial number of introduced cases, we cannot expect any strict proportionality but merely a probabilistic correlation.) Therefore, the larger  $R_e$  values will (statistically) directly lead to shorter observed onset times.

Importantly, this conclusion can be expected to hold irrespective of the exact definition of the “onset time” that we adopt: whether we assume that the local epidemic has started when daily case numbers reach a certain threshold and it becomes apparent in the population, or we consider the timing of the peak in the effective reproduction number as in this paper, or even if we define the onset as the moment when the epidemic definitively enters the phase of exponential growth (Marko Djordjevic et al., 2021). We chose the maximum position as the measure of the outburst timing (the onset time), as the switching time from decay/fluctuations to growth is generally harder to estimate and associated with uncertainties due to the low number of infected (Vilar and Saiz, 2021b). Evidently, the daily detected cases threshold will be reached sooner if the transmission is faster. In the case of onset as the peak time of the effective reproduction number, we note that the maximal  $R_e$  value is reached just before its values begin to decline either

due to depletion of susceptibility numbers or increased efforts to stop the new wave – and both occur sooner if the number of cases is larger (as is also the case with the transition from the stochastic into the exponential phase). In the last case, i.e., if we associate onset with the start of the exponential phase, the negative correlation of the transmissibility and the onset can be expected due to the  $R_e$ -dependent duration of the stochastic phase (Kochańczyk et al., 2020; Leng et al., 2021).

The relation of the  $R_e$  value and the onset variable is best illustrated in a hypothetical scenario in which the new virus or strain appears simultaneously in different world regions but with different effective reproductive numbers (due to characteristics of the local population and/or environment). It will take some time to notice the new pandemic – until case numbers sufficiently increase to attract attention – but this threshold will be reached sooner in regions of higher  $R_e$  value. In turn, we would tend to falsely conclude that the virus “originated” from the region where it was first observed, in spite that it (in this hypothetical scenario) started everywhere simultaneously. Such an example illustrates that the location of the first outburst does not, necessarily, reveal much about the place of true mutation origin. Note that the effect is more pronounced in the case of a new virus strain appearing during an already raging epidemic – in this case, it will take a higher threshold for the new strain to be noticed in the background of existing infections.

#### 4.3. Identified risk factors

Our data thus suggest that a significant part of the onset influence on  $R_{avg}$  value could be of this “mathematical” nature – implying that, to some extent, the onset variable can be seen as a proxy for transmissibility, making it less meaningful to consider it as an independent variable. The observed correlations of the onset value with other variables, indicating indirect connection with  $R_{avg}$  via different confounders, also contribute to this conclusion. Therefore, to gain better insight into other predictor variables’ influences, we removed the onset variable (together with age variables) from the initial set and repeated the analysis. Among the remaining variables, both linear regression methods (relaxed Lasso and Elastic net) selected the same important predictors of Omicron transmissibility: immunity proxy and booster prevalence as negatively influencing, and mobility variables (mainly transit mobility and less pronounced mobility retail) as positively influencing  $R_{avg}$  values (Fig. 4B and D). Similar, though somewhat more restrictive results were obtained by machine learning methods with ensembles of decision trees, with the Random Forest leaving only the immunity proxy variable above the importance threshold and Gradient Boosting attributing some significance also to the mobility transit variable, Fig. 5. Interestingly, none of the methods assigned importance to the full vaccination.

These results should be interpreted with care. The much stronger significance assigned to the immunity proxy than to the booster vaccines should not be, per se, interpreted as stronger Omicron protection provided by prior COVID-19 infection than by the booster vaccine. Whether this is the case or not simply cannot be addressed by our analysis. Namely, the effect of booster vaccination on the effective transmission rate of Omicron in the population crucially depends on the percentage of boosted individuals: even if the booster vaccine provides total immunity, this would hardly affect the population-measured  $R_{avg}$  value if the booster coverage is negligible.

However, our results indicate that, on a larger population level, the influence of past COVID-19 infections on Omicron epidemic evolution seems stronger than the achieved influence of the booster policies. This is likely to be mostly the effect of insufficient booster coverages. However, it could also be related to the relatively rapid waning of the vaccine-produced immunity (Lyngse et al., 2021b; Mahase, 2022). In any case, it is interesting that the importance of our immunity proxy is so consistently obtained. The most natural and direct way to interpret this result is that the prior COVID-19 exposure reduces the Omicron transmission rate. Namely, even if this protection is not high on an individual

basis, it might play an important role in slowing down the epidemic on the population level, if the prevalence of individuals with a prior infection is sufficient (note that Fig. 5 shows the highly nonlinear influence of immunity proxy on  $R_{avg}$ , suggesting the existence of a certain threshold value above which the effect of natural immunity becomes significant). Especially since there are indications that the immunity conferred by prior infection by any SARS-CoV-2 strain, albeit not strong, could be longer-lasting: a national database study in Qatar found that this protection against Omicron strain remains at the level of 56 percent (which is, however, substantially lower than against other variants) even after 10 months (median) from the initial infection (Altarawneh et al., 2022). Roughly, our result can be seen as consistent with these findings.

Moreover, suppose there is a substantial influence of the natural immunity already on the virus transmission. In that case, its significance for the disease severity is likely much higher, and it might be responsible for prevalently mild forms of Omicron infections (Altarawneh et al., 2022; Nealon and Cowling, 2022; Pilz et al., 2022). It is suggested that T-cells (which last longer and are less strain-specific) developed in the initial infection can prevent severe forms of the disease, despite being unable to stop virus transmission or symptomatic infection (Ledford, 2022). In turn, this might have ramifications for populations that have, so far, experienced low COVID-19 exposures, such as China, due to its “zero Covid” policy (and could be related to the current outburst in Shanghai and its severity) (Burki, 2022; Taylor, 2022).

Of course, the above interpretations and discussion hinge on our assumption that cumulative COVID-19 mortality can be used as the immunity proxy. While the number of deaths is much less affected by insufficient testing policies than the number of confirmed cases (e.g., asymptomatic or mild COVID-19 cases will much more easily remain undetected than a virus fatality), it is also true that the number of COVID-19-induced deaths is not simply a function of the number of COVID-19 cases alone. The case-fatality ratio is influenced by the quality of medical care, while the COVID-19 deaths can also be misattributed to other causes, often still due to low testing capabilities or inadequate policies (alternatively, we could have considered total cumulative excess of deaths, but neither this number was available for a large number of countries nor all excess deaths in a region can be directly attributed to SARS-CoV-2 infections).

Nevertheless, we believe our assumption is still fairly reasonable, especially in the absence of any more precise measure. Namely, two main effects that can influence the relation between COVID-19 mortality and natural immunity tend to cancel each other: in highly developed countries, advanced medical care leads to lower COVID-19 mortality (i.e., case fatality ratio), but, on the other hand, better reporting in these countries results in fewer deaths being misattributed to other causes (e.g., due to stricter medical protocols and larger availability of testing kits). Conversely, in underdeveloped areas, weaker medical care leads to more COVID-19 casualties, but, at the same time, COVID-19 deaths are more often under-reported (e.g., due to lower testing rates). Our recent quantitative analysis (Markovic et al., 2022) shows that these two effects are either small or approximately cancel each other, rendering the number of COVID-19-induced deaths a reasonably good measure for the total cumulative number of infected individuals (i.e., of the natural immunity).

Alternatively, the obtained importance of the immunity proxy could, in principle, be also a failure of the used methods to identify our immunity proxy as a confounder, ascribing it instead importance due to its strong correlation to other factors, such as population age, booster vaccines or social measures (represented by mobility variables). These correlations are not surprising from a psychological perspective since more severe initial waves of COVID-19 could influence the population (especially the older population) to better practice social distancing and opt for booster vaccines in greater numbers.

Independently of the interpretation of the importance of immunity proxy, we note the lack of any relevance assigned to full vaccination.

This is especially evident when contrasted with the relevance of the booster doses we obtained, despite the much higher prevalence of full vaccination. This supports the findings of many studies (Andrews et al., 2022; Gao et al., 2022; Gardner and Kilpatrick, 2021; Lyngse et al., 2021b) that the effects of full vaccination on Omicron transmission are effectively negligible, possibly since the Omicron outburst happened substantially later than the full vaccination. Our results regarding the importance of mobility variables are straightforward to interpret: it is expected that the decrease in interpersonal contacts and activities potentially leading to virus transmission should consequently lead to lower  $R_{avg}$  values. Note that the measures of this activity, obtained by aggregating geolocation data from mobile phones, seem to reflect the actual situation and true level of adherence to social measures much better than the stringency index (Arroyo-Marioli et al., 2021), based on formally enacted policies. In our study, the latter neither significantly correlated with any variable (including  $R_{avg}$  values and mobility variables) nor was selected as an important predictor of the effective reproduction number.

#### 4.4. Ramifications for the strain origin

The insights that Fig. 6 provides about the regional distribution of the identified risk factors directly relate to our prior conclusions about the relevance of the onset variable. The risk factors promoting high transmission were higher in Africa than on other continents. Incidentally, the first Omicron outburst occurred in Africa (and while these risk factors were slightly milder at the very place of the outburst in southern Africa than in Africa on average, Fig. 1 reveals that  $R_{avg}$  values were nevertheless above-average in this region). A priori, this connection was not expected: a new strain need not appear in regions where its transmissibility is high.

Of course, this might have been a coincidence. Alternatively, we note that such coincidence is in line with our discussion on the relation of the onset variable and the reproduction number: had the Omicron mutations occurred basically anywhere in the world, there would still have been an increased probability for the first outburst to be observed precisely in Africa, simply since the virus effects on the population-scale would be there sooner detectable (due to optimal local conditions for high  $R_e$ ). In other words, our analysis further argues that Omicron's true origin was not necessarily in Africa. While others have already contemplated this possibility (Ellyatt, 2021; Mallapaty, 2022), we now provided more concrete analytical and mathematical reasons for this doubt by identifying the risk factors leading to high  $R_e$  (and showing that it was precisely Africa where the fastest virus spread could have been expected) and by pointing to the relation of the effective reproduction number and the time to the epidemic onset.

However, we must also note that, while showing that it is premature to judge the origin of the virus mutation only based on the location of the first observed outburst, our results neither prove that the true origin of the mutations could not be in Africa (it might have been in South Africa, but – as generally overlooked – it might also be somewhere else). The location of the initial mutations does not play absolutely any role only if we assume that the strain is instantly spread around the globe – which is far from the truth. In reality, we have two relevant time scales: *i*) for the virus to arrive from its true origin to the considered region, and *ii*) for the epidemic of the new variant to sufficiently grow locally to be noticed and the new strain recognized. And what matters is the sum of these two time durations. It is hard to estimate the orders of magnitude of the two scales, but in the contemporary civilization heavily interconnected by international flights, the first scale might be even significantly shorter than the second – in which case the country of the first outburst would be primarily determined by the favorable conditions for the transmission of the new variant.

From the practical side, an implication should be that the regions expected to exhibit high values of the effective reproductive number should be more closely monitored for new strains. Of course, an obvious

problem is how to know in advance which regions are more favorable for transmitting a strain that is yet to appear? However, consideration of the Omicron risk factors that we identified reveals that, even generally, it might be possible to obtain certain hints sufficient to form an educated guess. Namely, it might be generally expected that prior infection will, at least to some extent, affect the transmissions of the new strains where the prevalence of past infections at the population level is high. Similarly, it is reasonable to assume that subpopulations under higher inherent risk from the current variant (the older population in this case) will be more cautious and better exercising social measures (or even less mobile in general), thus being less prone to a fast spread of any new strain epidemic. This information should complement the real-world data on mobility trends – associating higher risks with regions where the mobility is higher (especially where it has increased during the pandemic, instead of being stifled by the measures). Clearly, the prevalence of the vaccinated population is also expected to have a significant impact. Only the booster vaccination turned out to be relevant in the Omicron case, but this is not entirely surprising due to generally quickly waning SARS-CoV-2 immunity (Gardner and Kilpatrick, 2021; Lauring et al., 2022). Overall, all these arguments jointly point to a higher risk of regions that were less affected in the earlier course of the pandemic. And while it was impossible to foresee that the new variant would have such capacity for immune escape as the Omicron exhibited, note that the potential relevance of this reasoning should be only stronger if the prior immunity/vaccination has more impact on the new strain.

We remark that, in principle, it could also be argued that Omicron appeared in southern Africa precisely because higher transmissibility in the local environment promoted the evolutionary chances of the strain. This reasoning certainly plays a major role for viruses with comparatively low values of the reproductive number, for which unfavorable conditions can reduce the transmissibility below the threshold necessary for igniting a local epidemic and cause them to immediately disappear (unless they initially emerge on a fertile soil). For example, such appears to be the case with a very deadly and prolonged incubation of the Nipah virus in Southeastern Asia, which, despite its ability for human-to-human transmission (with bats as its natural reservoir), seems to have an insufficient effective reproduction number to cause the epidemic and consequently survive in the long term in the human population (Luby, 2013). Interestingly, many more infections are being recorded in Bangladesh than in the rest of the region, which has been attributed to modulation of its transmissibility due to local conditions (Cappelle et al., 2020; Hughes et al., 2009) – it is not inconceivable that with even-more favorable local conditions, Nipah transmissibility might reach the point of causing an outburst. However, for a strain of Omicron type, with a potential to cause epidemic outbursts anywhere on the planet, local variations in the  $R_e$  value are unlikely to have such a strong selective impact (i.e., deciding if the virus will propagate through the population or not). Nonetheless, even that possibility is still congruent with the implication that regions with anticipated higher effective reproduction numbers should be more closely monitored and where the above guidelines for recognizing higher risk areas could be useful.

## 5. Conclusion and outlook

Our goal in this study was to investigate factors that influenced the transmission of the Omicron SARS-CoV-2 variant. Our data analysis revealed that a younger population, increased mobility, low natural immunity, and low booster prevalence are associated with higher average Omicron effective reproduction number values. In line with most other studies, we have not obtained that full vaccination played any significant role. However, our analysis indicates that – on the country level – natural immunity had more influence on the intensity of the Omicron outburst than the booster vaccination (probably due to much lower prevalences of the latter).

Additionally, we obtained that the Omicron transmission depended quite significantly upon the time of the outburst: countries where the



infection peaked earlier also had a tendency toward higher  $R_{avg}$  values. We argue that this connection is primarily mathematical, reflecting a faster transition to the exponential phase of the epidemic and more rapid depletion of effectively susceptible individuals in regions with higher local transmissibility. In addition to the relation between  $R_{avg}$  and onset, this conclusion is supported by the significantly elevated risk factors for the African countries compared to the other continents. If so, we pointed out that this conclusion has profound general implications. Under the assumption of highly interconnected populations, it implies that the country where the first outburst of a new strain will be observed might be more strongly determined by the presence or the absence of favorable local conditions for the virus transmission than by the true whereabouts of the initial mutations (however, in most of the real-world scenarios, both factors are expected to play important roles). Furthermore, this means that regions expected to potentially exhibit higher  $R_e$  values in future outbursts should be more on the alert for the appearance of new variants. Moreover, based on the insights into risk factors for Omicron transmission, we suggested that regardless of the genetic details of the new variant, high  $R_e$  values may be expected in countries/regions that were previously spared from the severe impact of the pandemic. Therefore, in addition to other important considerations relevant to the emergence of novel viral agents/variants (Coccia, 2022; Domingo, 2021a, 2021b), factors that modulate transmissibility in the initial outburst should also be carefully considered.

Several limitations of the present study can be identified. In the absence of precise and reliable epidemiological data, we used the cumulative number of reported COVID-19 deaths (per capita) as the proxy for the natural immunity since the two clearly must be highly correlated. While these data are less dependent on the testing policies than the COVID-19 case numbers, they still can depend on the uneven mortality and varying definitions of what constitutes a death attributable to COVID-19 infection (as we discussed in more detail above). And even if the cumulative number of deaths fairly represents true natural immunity, we cannot dismiss the possibility that it primarily affected the course of the outburst not by immunological means but due to the psychological effect that the population severely struck by the previous pandemic waves will more strongly uphold social measures. Furthermore, many of our variables are highly mutually correlated, so even the most advanced data analysis techniques could, in principle, fail to identify the main drivers of the response variable correctly. And our suggestion that the first outburst can easily show up in a high  $R_e$  value country (rather than near the true origin of the initial mutation) strongly depends on the ratio of the two time scales (i.e., of the characteristic time for the spread of a pathogen across countries and of the duration of the stochastic/pre-exponential phase of the epidemic) - but we could not reliably estimate this ratio, and it has to be yet investigated.

Despite these limitations, we believe that these results can be a valuable contribution to the growing body of knowledge on Omicron and COVID-19 and potentially valuable for the possible future outbursts of new strains or in the context of an entirely new pandemic.

#### Author contributions

MarD and MagD conceived the research with the help of IS. Data acquisition and processing, exploratory data analysis, and mapping of risk factors to geographic locations was done by MarD with the help of MagD. Data transformation, correlation, and machine learning analysis was done by SM. Figures and tables made by SM and MagD, with the help of MarD. A literature search by SM and IS. Result interpretation by MarD, MagD, and IS. The manuscript was written by IS, SM, MarD, and MagD.

#### Funding

This work was partially supported by the Ministry of Education, Science, and Technological Development of the Republic of Serbia.

#### Declaration of competing interest

The authors declare that they have no known competing financial interests or personal relationships that could have appeared to influence the work reported in this paper.

#### Data availability

Data will be made available on request.

#### Appendix A. Supplementary data

Supplementary data to this article can be found online at <https://doi.org/10.1016/j.envres.2022.114446>.

#### References

- Abdullah, F., Myers, J., Basu, D., Tintinger, G., Ueckermann, V., Mathebula, M., Ramlall, R., Spoor, S., de Villiers, T., Van der Walt, Z., Cloete, J., Soma-Pillay, P., Rheeder, P., Paruk, F., Engelbrecht, A., Lalloo, V., Myburg, M., Kistan, J., van Hougenhouck-Tulleken, W., Boswell, M.T., Gray, G., Welch, R., Blumberg, L., Jassat, W., 2022. Decreased severity of disease during the first global omicron variant covid-19 outbreak in a large hospital in tshwane, South Africa. *Int. J. Infect. Dis.* 116, 38–42. <https://doi.org/10.1016/j.ijid.2021.12.357>.
- Accorsi, E.K., Britton, A., Fleming-Dutra, K.E., Smith, Z.R., Shang, N., Derado, G., Miller, J., Schrag, S.J., Verani, J.R., 2022. Association between 3 doses of mRNA COVID-19 vaccine and symptomatic infection caused by the SARS-CoV-2 omicron and Delta variants. *JAMA* 327, 639–651. <https://doi.org/10.1001/jama.2022.0470>.
- Altarawneh, H.N., Chemaitelly, H., Hasan, M.R., Ayoub, H.H., Qassim, S., AlMukdad, S., Coyle, P., Yassine, H.M., Al-Khatib, H.A., Benslimane, F.M., Al-Kanaani, Z., Al-Kuwari, E., Jeremijenko, A., Kaleeckal, A.H., Latif, A.N., Shaik, R.M., Abdul-Rahim, H.F., Nasrallah, G.K., Al-Kuwari, M.G., Butt, A.A., Al-Romaihi, H.E., Al-Thani, M.H., Al-Khal, A., Bertollini, R., Tang, P., Abu-Raddad, L.J., 2022. Protection against the omicron variant from previous SARS-CoV-2 infection. *N. Engl. J. Med.* 386, 1288–1290. <https://doi.org/10.1056/NEJMc2200133>.
- Andrews, N., Stowe, J., Kirsebom, T., Toffa, S., Rickeard, T., Gallagher, E., Gower, C., Kall, M., Groves, N., O'Connell, A.-M., Simons, D., Blomquist, P.B., Zaidi, A., Nash, S., Iwani Binti Abdul Aziz, N., Thelwall, S., Dabrera, G., Myers, R., Amirhalingam, G., Gharbia, S., Barrett, J.C., Elson, R., Ladhani, S.N., Ferguson, N., Zambon, M., Campbell, C.N.J., Brown, K., Hopkins, S., Chand, M., Ramsay, M., Lopez Bernal, J., 2022. Covid-19 vaccine effectiveness against the omicron (B.1.1.529) variant. *N. Engl. J. Med.* 386, 1532–1546. <https://doi.org/10.1056/NEJMoa2119451>.
- Arroyo-Marioli, F., Bullano, F., Kucinskas, S., Rondón-Moreno, C., 2021. Tracking R of COVID-19: a new real-time estimation using the Kalman filter. *PLoS One* 16, e0244474. <https://doi.org/10.1371/journal.pone.0244474>.
- Bastard, J., Taisne, B., Figoni, J., Mailles, A., Durand, J., Fayad, M., Josset, L., Maisa, A., van der Werf, S., Parent du Châtelet, I., Bernard-Stoecklin, S., 2022. Impact of the omicron variant on SARS-CoV-2 reinfections in France, march 2021 to february 2022. *Euro Surveill.* 27, 2200247. <https://doi.org/10.2807/1560-7917.ES.2022.27.13.2200247>.
- Box, G.E.P., Cox, D.R., 1964. An analysis of transformations. *J. Roy. Stat. Soc. B* 26, 211–252.
- Breiman, L., 1996. Bagging predictors. *Mach. Learn.* 24, 123–140. <https://doi.org/10.1007/BF00058655>.
- Breiman, L., 2001. Random forests. *Mach. Learn.* 45, 5–32. <https://doi.org/10.1023/A:1010933404324>.
- Britton, T., Ball, F., Trapman, P., 2020. A mathematical model reveals the influence of population heterogeneity on herd immunity to SARS-CoV-2. *Science* 369, 846–849. <https://doi.org/10.1126/science.abc6810>.
- Burki, T., 2022. Dynamic Zero COVID Policy in the Fight against COVID. *The Lancet Respiratory Medicine*. [https://doi.org/10.1016/S2213-2600\(22\)00142-4](https://doi.org/10.1016/S2213-2600(22)00142-4), 0.
- Cappelle, J., Hoem, T., Hul, V., Furey, N., Nguon, K., Prigent, S., Dupon, L., Ken, S., Neung, C., Hok, V., Pring, L., Lim, T., Bumrungrsri, S., Duboz, R., Buchy, P., Ly, S., Duong, V., Tarantola, A., Binot, A., Dussart, P., 2020. Nipah virus circulation at human–bat interfaces, Cambodia. *Bull. World Health Organ.* 98, 539–547. <https://doi.org/10.2471/BLT.20.254227>.
- CDC COVID-19 Response Team, 2021. SARS-CoV-2 B.1.1.529 (omicron) variant - United States, december 1-8, 2021. *MMWR. Morbidity and mortality weekly report* 70, 1731–1734. <https://doi.org/10.15585/mmwr.mm7050e1>.
- Chassalevris, T., Chaintoutis, S.C., Koureas, M., Petala, M., Moutou, E., Beta, C., Kyritsi, M., Hadjichristodoulou, C., Kostoglou, M., Karapantsios, T., Papadopoulos, A., Papaioannou, N., Dovas, C.I., 2022. Wastewater Monitoring Using a Novel, Cost-Effective PCR-Based Method that Rapidly Captures the Transition Patterns of SARS-CoV-2 Variant Prevalence (From Delta to Omicron) in the Absence of Conventional Surveillance Evidence (Preprint). *Epidemiology*. <https://doi.org/10.1101/2022.01.28.21268186>.
- Coccia, M., 2022. Meta-analysis to explain unknown causes of the origins of SARS-COV-2. *Environ. Res.* 211, 113062. <https://doi.org/10.1016/j.envres.2022.113062>.
- Dalglish, S.L., 2020. COVID-19 gives the lie to global health expertise. *Lancet* 395, 1189. [https://doi.org/10.1016/S0140-6736\(20\)30739-X](https://doi.org/10.1016/S0140-6736(20)30739-X).

- Dankulov, M.M., Tadić, B., Melnik, R., 2021. Worldwide Clustering and Infection Cycles as Universal Features of Multiscale Stochastic Processes in the SARS-CoV-2 Pandemic (Preprint). *Epidemiology*. <https://doi.org/10.1101/2021.12.20.21268095>.
- del Rio, C., Omer, S.B., Malani, P.N., 2022. Winter of omicron—the evolving COVID-19 pandemic. *JAMA* 327, 319. <https://doi.org/10.1001/jama.2021.24315>.
- Diesel, J., Sterrett, N., Dasgupta, S., Kriss, J.L., Barry, V., Vanden Esschert, K., Whiteman, A., Cadwell, B.L., Weller, D., Qualters, J.R., Harris, L., Bhatt, A., Williams, C., Fox, L.M., Meaney Delman, D., Black, C.L., Barbour, K.E., 2021. COVID-19 vaccination coverage among adults — United States, december 14, 2020–may 22, 2021. *MMWR Morb. Mortal. Wkly. Rep.* 70, 922–927. <https://doi.org/10.15585/mmwr.mm7025e1>.
- Djordjevic, Magdalena, Djordjevic, Marko, Ilic, B., Stojku, S., Salom, I., 2021. Understanding infection progression under strong control measures through universal COVID-19 growth signatures. *Global Challenges* 5, 2000101. <https://doi.org/10.1002/gch2.202000101>.
- Djordjevic, Marko, Salom, I., Markovic, S., Rodic, A., Milicevic, O., Djordjevic, Magdalena, 2021. Inferring the main drivers of SARS-CoV-2 global transmissibility by feature selection methods. *GeoHealth* 5, e2021GH000432. <https://doi.org/10.1029/2021GH000432>.
- Domingo, J.L., 2021a. What we know and what we need to know about the origin of SARS-CoV-2. *Environ. Res.* 200, 111785. <https://doi.org/10.1016/j.envres.2021.111785>.
- Domingo, J.L., 2021b. Scientific evidence on the origin of SARS-CoV-2. *Environ. Res.* 201, 111542. <https://doi.org/10.1016/j.envres.2021.111542>.
- Dong, E., Du, H., Gardner, L., 2020. An interactive web-based dashboard to track COVID-19 in real time. *Lancet Infect. Dis.* 20, 533–534. [https://doi.org/10.1016/S1473-3099\(20\)30120-1](https://doi.org/10.1016/S1473-3099(20)30120-1).
- Ellyatt, H., 2021. Omicron Covid Variant Likely Circulating for Longer — and More Widely — than Thought, Experts Say. CNBC. <https://www.cnbc.com/2021/12/02/where-did-omicron-covid-variant-come-from-and-where-is-it-circulating.html>.
- Ferguson, N., Ghani, A., Cori, A., Hogan, A., Hinsley, W., Volz, E., 2021. Growth, Population Distribution and Immune Escape of Omicron in England (Report 49). WHO Collaborating Centre for Infectious Disease Modelling, MRC Centre for Global Infectious Disease Analysis, Jameel Institute, Imperial College London. <https://www.imperial.ac.uk/medicine/departments/school-public-health/infectious-disease-epidemiology/mrc-global-infectious-disease-analysis/covid-19/report-49-omicron/>.
- Gao, S.-J., Guo, H., Luo, G., 2022. Omicron variant (B.1.1.529) of SARS-CoV-2, a global urgent public health alert. *J. Med. Virol.* 94, 1255–1256. <https://doi.org/10.1002/jmv.27491>.
- Gardner, B.J., Kilpatrick, A.M., 2021. Estimates of Reduced Vaccine Effectiveness against Hospitalization, Infection, Transmission and Symptomatic Disease of a New SARS-CoV-2 Variant, Omicron (B.1.1.529), Using Neutralizing Antibody Titers. <https://doi.org/10.1101/2021.12.10.21267594> [Preprint] medRxiv 2021.12.10.21267594.
- Gerke, C., Pulverer, B., Sansonetti, P., 2022. COVID-19 vaccination, time for a second breath? *EMBO Mol. Med.* 14, e15810. <https://doi.org/10.15252/emmm.202215810>.
- Google, L.L.C., 2022. Google COVID-19 Community Mobility Reports [WWW Document] (accessed 2.14.22). <https://www.google.com/covid19/mobility/>.
- Güvendik, M.O., Kavak, G., 2021. World Closing its Doors to African Countries Due to Omicron. *Anadolu Agency*. <https://www.aa.com.tr/en/americas/world-closing-its-doors-to-african-countries-due-to-omicron/2434131>.
- Hansen, C.H., Schelde, A.B., Moustsen-Helm, I.R., Emborg, H.-D., Krause, T.G., Mølbak, K., Valentiner-Brant, P., 2021. Vaccine Effectiveness against SARS-CoV-2 Infection with the Omicron or Delta Variants Following a Two-Dose or Booster BNT162b2 or mRNA-1273 Vaccination Series: A Danish Cohort Study. <https://doi.org/10.1101/2021.12.20.21267966> [Preprint] medRxiv 2021.12.20.21267966.
- Hasell, J., Mathieu, E., Beltekian, D., Macdonald, B., Giattino, C., Ortiz-Ospina, E., Roser, M., Ritchie, H., 2020. A cross-country database of COVID-19 testing. *Sci. Data* 7, 345. <https://doi.org/10.1038/s41597-020-00688-8>.
- Hastie, T., Tibshirani, R., Friedman, J., 2009. *The Elements of Statistical Learning*, second ed. Springer, New York.
- Hellewell, J., Abbott, S., Gimma, A., Bosse, N.I., Jarvis, C.I., Russell, T.W., Munday, J.D., Kucharski, A.J., Edmunds, W.J., Sun, F., Flasche, S., Quilty, B.J., Davies, N., Liu, Y., Clifford, S., Klepac, P., Jit, M., Diamond, C., Gibbs, H., van Zandvoort, K., Funk, S., Eggo, R.M., 2020. Feasibility of controlling COVID-19 outbreaks by isolation of cases and contacts. *Lancet Global Health* 2020, e488–e496.
- Hughes, J.M., Wilson, M.E., Luby, S.P., Gurley, E.S., Hossain, M.J., 2009. Transmission of human infection with Nipah virus. *Clin. Infect. Dis.* 49, 1743–1748. <https://doi.org/10.1086/647951>.
- Ito, K., Piantham, C., Nishiura, H., 2022a. Estimating Relative Generation Times and Relative Reproduction Numbers of Omicron BA.1 and BA.2 with Respect to Delta in Denmark. <https://doi.org/10.1101/2022.03.02.22271767>.
- Ito, K., Piantham, C., Nishiura, H., 2022b. Relative instantaneous reproduction number of Omicron SARS-CoV-2 variant with respect to the Delta variant in Denmark. *J. Med. Virol.* 94, 2265–2268. <https://doi.org/10.1002/jmv.27560>.
- Jansen, L., Tegomoh, B., Lange, K., Showalter, K., Figliomeni, J., Abdalhamid, B., Iwen, P.C., Fauver, J., Buss, B., Donahue, M., 2021. Investigation of a SARS-CoV-2 B.1.1.529 (omicron) variant cluster — Nebraska, november–december 2021. *MMWR Morbidity and Mortality Weekly Report* 70, 1782–1784. <https://doi.org/10.15585/mmwr.mm705152e3>.
- Khajanchi, S., Bera, S., Roy, T.K., 2021. Mathematical analysis of the global dynamics of a HTLV-I infection model, considering the role of cytotoxic T-lymphocytes. *Math. Comput. Simulat.* 180, 354–378. <https://doi.org/10.1016/j.matcom.2020.09.009>.
- Khandia, R., Singhal, S., Alqahtani, T., Kamal, M.A., El-Shall, N.A., Nainu, F., Desingu, P. A., Dhama, K., 2022. Emergence of SARS-CoV-2 Omicron (B.1.1.529) variant, salient features, high global health concerns and strategies to counter it amid ongoing COVID-19 pandemic. *Environ. Res.* 209, 112816. <https://doi.org/10.1016/j.envres.2022.112816>.
- Kochańczyk, M., Grabowski, F., Lipniacki, T., 2020. Super-spreading events initiated the exponential growth phase of COVID-19 with R0 higher than initially estimated. *R. Soc. Open Sci.* 7, 200786. <https://doi.org/10.1098/rsos.200786>.
- Lauring, A.S., Tenforde, M.W., Chappell, J.D., Gaglani, M., Ginde, A.A., McNeal, T., Ghamande, S., Douin, D.J., Talbot, H.K., Casey, J.D., Mohr, N.M., Zepeski, A., Shapiro, N.I., Gibbs, K.W., Files, D.C., Hager, D.N., Shehu, A., Prekker, M.E., Erickson, H.L., Exline, M.C., Gong, M.N., Mohamed, A., Johnson, N.J., Srinivasan, V., Steingrub, J.S., Peltan, I.D., Brown, S.M., Martin, E.T., Monto, A.S., Khan, A., Hough, C.L., Busse, L.W., ten Lohuis, C.C., Duggal, A., Wilson, J.G., Gordon, A.J., Qadir, N., Chang, S.Y., Mallow, C., Rivas, C., Babcock, H.M., Kwon, J. H., Halasa, N., Grijalva, C.G., Rice, T.W., Stubblefield, W.B., Baughman, A., Womack, K.N., Rhoads, J.P., Lindsell, C.J., Hart, K.W., Zhu, Y., Adams, K., Schrag, S. J., Olson, S.M., Kobayashi, M., Verani, J.R., Patel, M.M., Self, W.H., 2022. Clinical Severity and mRNA Vaccine Effectiveness for Omicron, Delta, and Alpha SARS-CoV-2 Variants in the United States: A Prospective Observational Study. <https://doi.org/10.1101/2022.02.06.22270558> [Preprint] medRxiv 2022.02.06.22270558.
- Ledford, H., 2022. 'Killer' immune cells still recognize Omicron variant. *Nature* 601, 307. <https://doi.org/10.1038/d41586-022-00063-0>, 307.
- Leng, T., White, C., Hilton, J., Kucharski, A., Pellis, L., Stage, H., Davies, N.G., Group, C. for M.M. of I.D. 2019 nCoV W., Keeling, M.J., Flasche, S., 2021. The Effectiveness of Social Bubbles as Part of a Covid-19 Lockdown Exit Strategy, a Modelling Study [version 2; Peer Review: 2 Approved]. *Wellcome Open Research*. <https://doi.org/10.12688/wellcomeopenres.16164.2>.
- Lin, T., Harris, E.A., Heemskerck, A., Van Bavel, J.J., Ebner, N.C., 2021. A multi-national test on self-reported compliance with COVID-19 public health measures: the role of individual age and gender demographics and countries' developmental status. *Soc. Sci. Med.* 286, 114335. <https://doi.org/10.1016/j.socscimed.2021.114335>.
- Liu, H., Chen, S., Liu, M., Nie, H., Lu, H., 2020. Comorbidity chronic diseases are strongly correlated with disease severity among COVID-19 patients: a systematic review and meta-analysis. *Aging and disease* 11, 668. <https://doi.org/10.14336/AD.2020.0502>.
- Luby, S.P., 2013. The pandemic potential of Nipah virus. *Antivir. Res.* 100, 38–43. <https://doi.org/10.1016/j.antiviral.2013.07.011>.
- Lustig, Y., Gonen, T., Melzer, L., Gilboa, M., Indenbaum, V., Cohen, E., Amit, S., Jaber, H., Doolman, R., Asraf, K., Rubin, C., Fluss, R., Mendelson, E., Freedman, L., Regev-Yochay, G., Kreiss, Y., 2021. Superior Immunogenicity and Effectiveness of the 3rd BNT162b2 Vaccine Dose. <https://doi.org/10.1101/2021.12.19.21268037> [Preprint] medRxiv 2021.12.19.21268037.
- Lynsge, F.P., Mølbak, K., Skov, R.L., Christiansen, L.E., Mortensen, L.H., Albertsen, M., Møller, C.H., Krause, T.G., Rasmussen, M., Michaelsen, T.Y., Voldstedlund, M., Fonager, J., Steenhard, N., Kirkeby, C.T., 2021a. Increased transmissibility of SARS-CoV-2 lineage B.1.1.7 by age and viral load. *Nat. Commun.* 12, 1–8. <https://doi.org/10.1038/s41467-021-27202-x>.
- Lynsge, F.P., Mortensen, L.H., Denwood, M.J., Christiansen, L.E., Møller, C.H., Skov, R.L., Spiess, K., Fomsgaard, A., Lassaunière, M.M., Rasmussen, M., Stegger, M., Nielsen, C., Sieber, R.N., Cohen, A.S., Møller, F.T., Overvad, M., Mølbak, K., Krause, T.G., Kirkeby, C.T., 2021b. SARS-CoV-2 Omicron VOC Transmission in Danish Households. <https://doi.org/10.1101/2021.12.27.21268278> [Preprint] medRxiv.
- Mahase, E., 2022. Covid-19: is the UK heading for another omicron wave? *BMJ* 376, o738. <https://doi.org/10.1136/bmj.o738>.
- Mallapaty, S., 2022. Where did Omicron come from? Three key theories. *Nature* 602, 26–28. <https://doi.org/10.1038/d41586-022-00215-2>.
- Markovic, S., Rodic, A., Salom, I., Milicevic, O., Djordjevic, Magdalena, Djordjevic, Marko, 2021. COVID-19 severity determinants inferred through ecological and epidemiological modeling. *One Health* 13, 100355. <https://doi.org/10.1016/j.onehlt.2021.100355>.
- Markovic, S., Salom, I., Rodic, A., Djordjevic, M., 2022. GHSI COVID-19 puzzle: did highly developed countries indeed fare worse? [Preprint] medRxiv. <https://doi.org/10.1101/2022.08.28.22279258>.
- Mathieu, E., Ritchie, H., Ortiz-Ospina, E., Roser, M., Hasell, J., Appel, C., Giattino, C., Rodés-Guirao, L., 2021. A global database of COVID-19 vaccinations. *Nat. Human Behav.* 5, 947–953. <https://doi.org/10.1038/s41562-021-01122-8>.
- Mattuzzi, C., Henry, B.M., Lippi, G., 2022. SARS-CoV-2 pandemic: on its way to becoming an endemic disease? [Preprint] Research Square. <https://doi.org/10.21203/rs.3.rs-1262987/v1>.
- Meinshausen, N., 2007. Relaxed Lasso. *Comput. Stat. Data Anal.* 52, 374–393. <https://doi.org/10.1016/j.csda.2006.12.019>.
- Nealon, J., Cowling, B.J., 2022. Omicron severity: milder but not mild. *Lancet* 399, 412–413. [https://doi.org/10.1016/S0140-6736\(22\)00056-3](https://doi.org/10.1016/S0140-6736(22)00056-3).
- Picheta, R., 2022. Omicron Has Changed the Shape of the Pandemic. Will it End it for Good? CNN. <https://www.cnn.com/2022/01/22/world/omicron-changed-pandemic-intl-cmd/index.html>.
- Pilz, S., Theiler-Schwetz, V., Trummer, C., Krause, R., Ioannidis, J.P.A., 2022. SARS-CoV-2 reinfections: overview of efficacy and duration of natural and hybrid immunity. *Environ. Res.* 209, 112911. <https://doi.org/10.1016/j.envres.2022.112911>.
- Pulliam, J.R.C., van Schalkwyk, C., Govender, N., von Gottberg, A., Cohen, C., Groome, M.J., Dushoff, J., Mlisana, K., Moultrie, H., 2022. Increased risk of SARS-CoV-2 reinfection associated with emergence of Omicron in South Africa. *Science* 376, eabn4947. <https://doi.org/10.1126/science.abn4947>.
- R Core Team, 2021. *R: A Language and Environment for Statistical Computing*.
- Rai, R.K., Khajanchi, S., Tiwari, P.K., Venturino, E., Misra, A.K., 2022. Impact of social media advertisements on the transmission dynamics of COVID-19 pandemic in India. *J. Appl. Math. Comput.* 68, 19–44. <https://doi.org/10.1007/s12190-021-01507-y>.

- Regev-Yochay, G., Gonen, T., Gilboa, M., Mandelboim, M., Indenbaum, V., Amit, S., Meltzer, L., Asraf, K., Cohen, C., Fluss, R., Biber, A., Nemet, I., Kliker, L., Joseph, G., Doolman, R., Mendelson, E., Freedman, L.S., Harats, D., Kreiss, Y., Lustig, Y., 2022. Efficacy of a fourth dose of covid-19 mRNA vaccine against omicron. *N. Engl. J. Med.* 386, 1377–1380. <https://doi.org/10.1056/NEJMc2202542>.
- Rigby, J., 2022. COVID Booster Provides Protection for Over-65s after 15 Weeks -UK Data. Reuters. <https://www.reuters.com/business/healthcare-pharmaceuticals/covid-booster-provides-protection-over-65s-after-15-weeks-uk-data-2022-03-24/>.
- Ritchie, H., Mathieu, E., Rod s-Guirao, L., Appel, C., Giattino, C., Ortiz-Ospina, E., Hasell, J., Macdonald, B., Beltekian, D., Roser, M., 2020. Coronavirus Pandemic (COVID-19) [WWW Document]. Our World in Data (accessed 5.4.22). <https://ourworldindata.org/coronavirus>.
- Rozsa, M., Karlis, N., 2022. Omicron Variant of COVID-19 May Be the Most Contagious Virus to Ever Exist. Salon. <https://www.salon.com/2022/01/27/omicron-variant-of-may-be-the-most-contagious-to-ever-exist-scientists-say/>.
- Rzymiski, P., Poniedzia ek, B., Fal, A., 2021. Willingness to receive the booster COVID-19 vaccine dose in Poland. *Vaccines* 9, 1286. <https://doi.org/10.3390/vaccines9111286>.
- Salom, I., Rodic, A., Milicevic, O., Zigic, D., Djordjevic, Magdalena, Djordjevic, Marko, 2021. Effects of demographic and weather parameters on COVID-19 basic reproduction number. *Front. Ecol. Evol.* 8.
- Sanyaolu, A., Okorie, C., Marinkovic, A., Patidar, R., Younis, K., Desai, P., Hosein, Z., Padda, I., Mangat, J., Altaf, M., 2020. Comorbidity and its impact on patients with COVID-19. *SN Compr. Clin. Med.* 2, 1069–1076. <https://doi.org/10.1007/s42399-020-00363-4>.
- Sarkar, K., Khajanchi, S., Nieto, J.J., 2020. Modeling and forecasting the COVID-19 pandemic in India. *Chaos, Solit. Fractals* 139, 110049. <https://doi.org/10.1016/j.chaos.2020.110049>.
- Schmidt, F., Muecksch, F., Weisblum, Y., Silva, J.D., Bednarski, E., Cho, A., Wang, Z., Gaebler, C., Caskey, M., Nussenzweig, M.C., Hatzioannou, T., Bieniasz, P.D., 2021. Plasma Neutralization Properties of the SARS-CoV-2 Omicron Variant. <https://doi.org/10.1101/2021.12.12.21267646> [Preprint] medRxiv 2021.12.12.21267646.
- S nderskov, K.M., Vistisen, H.T., Dinesen, P.T., Østergaard, S.D., 2021. COVID-19 booster vaccine willingness. *Dan Med J* 69, A10210765.
- Stribling, J., Clifton, A., McGill, G., de Vries, K., 2020. Examining the UK Covid-19 mortality paradox: pandemic preparedness, healthcare expenditure, and the nursing workforce. *J. Adv. Nurs.* 76, 3218–3227. <https://doi.org/10.1111/jan.14562>.
- Taylor, L., 2022. Covid-19: Hong Kong reports world's highest death rate as zero covid strategy fails. *BMJ* 376, o707. <https://doi.org/10.1136/bmj.o707>.
- Tenforde, M.W., Self, W.H., Gaglani, M., et al., 2022. Effectiveness of mRNA vaccination in preventing COVID-19-associated invasive mechanical ventilation and death — United States, march 2021–january 2022. *MMWR. Morbidity and Mortality Weekly Report* 71, 459–465. <https://doi.org/10.15585/mmwr.mm7112e1>.
- Tian, D., Sun, Y., Xu, H., Ye, Q., 2022. The emergence and epidemic characteristics of the highly mutated SARS-CoV-2 Omicron variant. *J. Med. Virol.* 94, 2376–2383. <https://doi.org/10.1002/jmv.27643>.
- Tibshirani, R., 1996. Regression shrinkage and selection via the Lasso. *J. Roy. Stat. Soc. B* 58, 267–288. <https://doi.org/10.1111/j.2517-6161.1996.tb02080.x>.
- Ulloa, A.C., Buchan, S.A., Daneman, N., Brown, K.A., 2022. Estimates of SARS-CoV-2 omicron variant severity in ontario, Canada. *JAMA* 327, 1286–1288. <https://doi.org/10.1001/jama.2022.2274>.
- Vilar, J.M.G., Saiz, L., 2021a. Reliably quantifying the evolving worldwide dynamic state of the COVID-19 outbreak from death records, clinical parametrization, and demographic data. *Sci. Rep.* 11, 19952 <https://doi.org/10.1038/s41598-021-99273-1>.
- Vilar, J.M.G., Saiz, L., 2021b. Ascertainning the initiation of epidemic resurgences: an application to the COVID-19 second surges in Europe and the Northeast United States. *R. Soc. Open Sci.* 8, 210773 <https://doi.org/10.1098/rsos.210773>.
- Wei, T., Simko, V., 2021. R Package ‘corrplot’: Visualization of a Correlation Matrix, Version 0.92.
- Willyard, C., 2022. What the Omicron wave is revealing about human immunity. *Nature* 602, 22–25. <https://doi.org/10.1038/d41586-022-00214-3>.
- Wright, L., Steptoe, A., Fancourt, D., 2022. Patterns of compliance with COVID-19 preventive behaviours: a latent class analysis of 20 000 UK adults. *J. Epidemiol. Community Health* 76, 247–253. <https://doi.org/10.1136/jech-2021-216876>.
- Zou, H., Hastie, T., 2005. Regularization and variable selection via the elastic net. *J. Roy. Stat. Soc. B* 67, 301–320. <https://doi.org/10.1111/j.1467-9868.2005.00503.x>.



# COVID-19 severity determinants inferred through ecological and epidemiological modeling

Sofija Markovic<sup>a</sup>, Andjela Rodic<sup>a</sup>, Igor Salom<sup>b</sup>, Ognjen Milicevic<sup>c</sup>, Magdalena Djordjevic<sup>b</sup>, Marko Djordjevic<sup>a,\*</sup>

<sup>a</sup> Quantitative Biology Group, Faculty of Biology, University of Belgrade, Serbia

<sup>b</sup> Institute of Physics Belgrade, National Institute of the Republic of Serbia, University of Belgrade, Serbia

<sup>c</sup> Department for Medical Statistics and Informatics, School of Medicine, University of Belgrade, Serbia

## ARTICLE INFO

### Keywords:

COVID-19  
Disease severity  
Ecological regression analysis  
Epidemiological model  
Environmental factors  
Machine learning

## ABSTRACT

Understanding variations in the severity of infectious diseases is essential for planning proper mitigation strategies. Determinants of COVID-19 clinical severity are commonly assessed by transverse or longitudinal studies of the fatality counts. However, the fatality counts depend both on disease clinical severity and transmissibility, as more infected also lead to more deaths. Instead, we use epidemiological modeling to propose a disease severity measure that accounts for the underlying disease dynamics. The measure corresponds to the ratio of population-averaged mortality and recovery rates ( $m/r$ ), is independent of the disease transmission dynamics (i.e., the basic reproduction number), and has a direct mechanistic interpretation. We use this measure to assess demographic, medical, meteorological, and environmental factors associated with the disease severity. For this, we employ an ecological regression study design and analyze different US states during the first disease outbreak. Principal Component Analysis, followed by univariate, and multivariate analyses based on machine learning techniques, is used for selecting important predictors. The usefulness of the introduced severity measure and the validity of the approach are confirmed by the fact that, without using prior knowledge from clinical studies, we recover the main significant predictors known to influence disease severity, in particular age, chronic diseases, and racial factors. Additionally, we identify long-term pollution exposure and population density as not widely recognized (though for the pollution previously hypothesized) significant predictors. The proposed measure is applicable for inferring severity determinants not only of COVID-19 but also of other infectious diseases, and the obtained results may aid a better understanding of the present and future epidemics. Our holistic, systematic investigation of disease severity at the human-environment intersection by epidemiological dynamical modeling and machine learning ecological regressions is aligned with the One Health approach. The obtained results emphasize a syndemic nature of COVID-19 risks.

## 1. Introduction

COVID-19 has brought large changes to people's lives, including significant impacts on health and the economy. At the population level, the effects of the disease can be characterized through the disease transmissibility and clinical severity. Transmissibility relates to the number of infected people, which in epidemiological models (see e.g. [1]) is quantified by the reproduction number  $R(t)$  (corresponding to an average number of people infected by an individual during its infectious period). Clinical severity corresponds to the medical complications experienced by infected individuals, potentially also including death. In

the epidemic models, two population average rates relate with the disease severity (see e.g. [2]): i) Mortality rate ( $m$ ), corresponding to the probability per day for the detected case to result in death. ii) Recovery rate ( $r$ ), corresponding to the inverse time needed for a detected case to recover.

This study aims to quantify the generalized severity of the COVID-19 disease in a given population described with a set of demographic and environmental factors by proposing an easy-to-evaluate but plausible measure. Applying that measure to diverse countries, together with carefully designed multivariate regression analysis, allows identifying the severity predictors among the population-level factors. Knowing the

\* Corresponding author.

E-mail address: [dmarko@bio.bg.ac.rs](mailto:dmarko@bio.bg.ac.rs) (M. Djordjevic).

<https://doi.org/10.1016/j.onehlt.2021.100355>

Received 8 August 2021; Received in revised form 25 November 2021; Accepted 26 November 2021

Available online 27 November 2021

2352-7714/© 2021 The Authors. Published by Elsevier B.V. This is an open access article under the CC BY license (<http://creativecommons.org/licenses/by/4.0/>).



particular causes of a potentially higher fatality of the disease in a population can help plan efficient strategies for disease prevention, control, and treatment, specifically targeting the health vulnerabilities of the society.

COVID-19 transmissibility and severity are often assessed through the numbers of confirmed cases and fatalities, respectively [3–8]. Regarding severity, a major complication is that the fatalities are correlated with the number of infected, as more infections lead to more fatalities. Additional complications are related to nonlinearities and delays that inherently characterize the disease dynamics [9]. For example, the time from infection to death can be long and highly variable, while the number of fatalities in different regions (at a given time) may correspond to different points of the infected curve. Thus, equal-time comparisons of mortality numbers (or rates) would be inadequate. For these reasons, somewhat modified variables, such as delay-adjusted case fatality rate (aCFR), are sometimes used [10–12], but their mechanistic interpretation is unclear [13]. Alternatively, we propose a novel quantity for the disease severity measure. This quantity has a clear mechanistic interpretation, can be derived directly from epidemic modeling and inferred from publically available data. Specifically, we argue that the ratio of mortality and recovery rates ( $m/r$ ) is a highly plausible population-level measure of disease severity: higher mortality and lower recovery rates indicate a more severe disease leading to a larger  $m/r$ . We will also show (both theoretically and from empirical data) that this measure is a priori unrelated to  $R(t)$ , which is a result independent from the specific assumed transmission mechanism.

To assess how reasonable is the proposed measure, it is desirable to use it to infer significant predictors (and their importance) of COVID-19 severity. However, this entails certain methodological challenges [14]. Specifically, significant predictors have to be selected among a large number of potentially relevant variables. Moreover, these variables may be highly correlated [15,16], and mutual interactions (and nonlinear relations) may be relevant. To address this, we apply a novel approach that combines Principal Component Analysis (PCA) and machine learning regression methods [17].

## 2. Methods

There are many compartmental models used in epidemiology, obtained as extensions of the basic SIR or SEIR models [2] – a number of them recently developed in the context of COVID-19, e.g. to account for contact tracing and hospitalization strategies [18], media effects [19], unreported cases [1,20], infected but asymptomatic individuals [21], uninfected but quarantined population [22], seasonality effects [23],

etc. To extract the severity variable  $m/r$  directly from dynamical compartmental models, we used our SPEIRD modification [24] of the SEIR model, schematically represented in Fig. 1. Note that  $m/r$  derivation is independent of the transmission mechanism and (by construction) from  $R(t)$ . Consequently, the left rectangle (from which  $R(t)$  and its special case at the early stages of the epidemic, i.e., basic reproduction number ( $R_0$ ), is determined) is presented only for clarity and coherence. The relevant part of the model represents the transition of the active cases ( $A$ ) to healed ( $H$ ) at recovery rate  $r$ , or to fatalities ( $F$ ) at mortality rate  $m$ . Note that the cumulative (total) number of detected cases ( $D$ ) corresponds to the sum of  $A$ ,  $H$ , and  $F$ .

The system of differential equations, which mathematically represents the model in Fig. 1 is given in [24]. From eqs. (5–6) in [24], we obtain:

$$\frac{dH}{dt} = rA; \frac{dF}{dt} = mA \Rightarrow \frac{dF}{dt} = \frac{m}{r} \frac{dH}{dt} \tag{1}$$

We integrate the right side of Eq. (1) from the epidemics start ( $t = 0$ ) to the end ( $t = \infty$ ):

$$F(\infty) = \frac{m}{r} H(\infty) \tag{2}$$

Since  $D(t) = A(t) + F(t) + H(t)$ , and since there are no more active cases at  $t = \infty$ , while  $F(\infty)$  and  $H(\infty)$  reach constant values (see Fig. 2A), we obtain:

$$D(\infty) = F(\infty) + H(\infty) \tag{3}$$

Combining Eqs. (2) and (3) gives:

$$\frac{m}{r} = \frac{CFR(\infty)}{1 - CFR(\infty)}; CFR = \frac{F(\infty)}{D(\infty)} \tag{4}$$

where  $CFR(\infty)$  is the case fatality rate at the end of the epidemic (the “long COVID-19” cases, being detected but not dead, contribute to  $H(\infty)$  in Eq. (3)). As the COVID-19 pandemic is still ongoing, we use the end of the first peak, where the number of active cases can be approximately considered as zero.

For consistency and easier direct comparison with the COVID-19 transmissibility analysis, data collection, data processing, and machine learning techniques are similar to the one presented in [25]. For completeness, full information is provided in the Supplementary Methods, which also includes definitions for all variables and principal components (PCs) used in the analysis. Supplementary Methods also provide a complete dynamical model and derivations for both  $m/r$  and  $R_0$ . The Supplementary Table contains all input data.

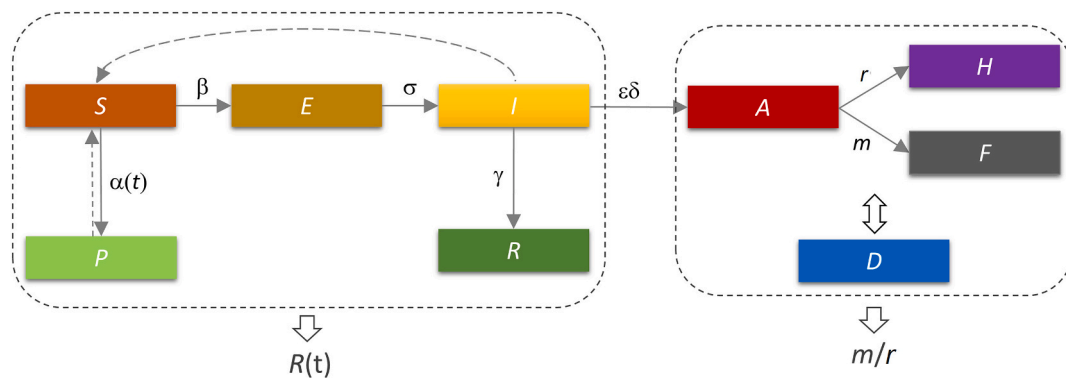


**Fig. 1.** Deriving the severity measure  $m/r$  from the epidemics compartmental model. SPEIRD model is schematically shown. Transitions between the compartments are denoted by solid arrows, with the transition rates indicated above arrows. The dashed arrow from I to S indicates the interaction of I and S (infections) leading to the transition to E. The dashed arrow from P to S indicates the potential (reverse) transition from P to S due to the easing of measures. The dashed rectangles indicate parts of the model corresponding to the disease transmission (the left rectangle) and the disease outcome for the detected cases (the right rectangle). The single arrows indicate parts of the model from which the reproduction number  $R(t)$  and the severity measure ( $m/r$ ) are, respectively, inferred. The total number of detected cases ( $D$ ) corresponds to the sum of  $A$ ,  $H$ , and  $F$  and is denoted by a double arrow. Compartments are S – susceptible, P – protected, E – exposed, I – infected, R – recovered, A – active, H – healed, F – fatalities, D – total number of detected cases.  $r$  and  $m$  represent recovery and mortality rates of active (detected) cases.

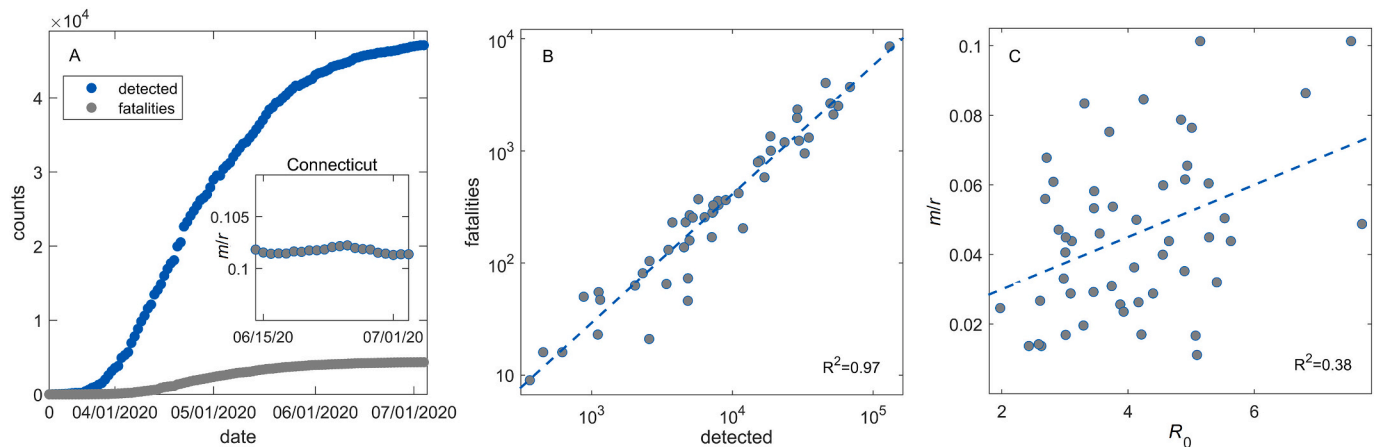


**Fig. 2.** Inferring  $m/r$  from data. A) Cumulative detected (D) and fatality (F) counts in Connecticut.  $m/r$  is inferred from the time period (enlarged in the inset) corresponding to saturation (end of the first peak). B) and C) Correlation plots of F vs. D and  $m/r$  vs.  $R_0$  with the Pearson correlation coefficients shown.

### 3. Results

Fig. 2A illustrates how  $m/r$  values are inferred from data. The cumulative number of detected cases and fatalities during the first peak of the epidemic is presented for one of the USA states (Connecticut).  $m/r$  is inferred once both classes of the case counts reach saturation, leading to constant  $m/r$  (inset in the figure). In Fig. 2B a very high positive correlation ( $R = 0.97$ ) is obtained between the cumulative number of fatalities and detected cases observed at fixed time cross-sections, quantitatively confirming the intuitive expectation that a higher number of infected is strongly related to higher fatality counts. This shows that fatality counts are strongly related to COVID-19 transmissibility, despite being often used as a measure of the disease severity [3–8]. On the other hand, the moderate correlation between  $m/r$  and  $R_0$  (Fig. 2C) is consistent with the a priori independence of these two variables. This correlation reflects a genuine similarity in COVID-19 transmissibility and severity determinants (e.g., air pollution or weak immunity can be associated with both increased transmissibility [25] and severity of the disease [26]).

Univariate analysis of  $m/r$  relation to the variables used in the study is presented in Fig. 3. Statistically significant correlations ( $P < 0.05$ ) of  $m/r$  with several variables/PCs are shown in Fig. 3A and scatterplots (Fig. 3B–E). The highest (positive) correlation was observed for NO PC1, Disease PC4, and Density PC1, while the percentage of the youth population showed the highest negative correlation with  $m/r$ . Several other predictors, specifically, Density PC2, Disease PC2,  $SO_2$ , and NO Insurance PC1, Black and  $PM_{2.5}$  also exhibit statistically significant correlations with  $m/r$ . As expected, chronic disease, pollution, population-density-related variables promote COVID-19 severity (positive correlations), as does the percentage of Afro-Americans (Black). Percentage of population under 18 (Youth) decreases the severity (negative correlation), also as expected. Sign of the correlation with No Insurance PC1 is opposite than expected, as people with health insurance should get better medical treatment (further analyzed below).

Fig. 4A–D provide interpretation of the relevant PCs through their correlations with the variables entering PCA. Density PC1 is comprised of all three parameters from the population density group (Fig. 4A), presenting a general measure of population density, while Density PC2 is significantly correlated only with population density (Fig. 4B). Disease PC2 and PC4 show, respectively, the highest positive correlation with the prevalence of cancer and cardiovascular diseases. Fig. 4E shows a high correlation of No Insurance PC1 with Youth and Density PC1. Signs of these correlations, and the effect of these two variables on  $m/r$ , indicate that the unintuitive sign of No Insurance PC1 correlation with  $m/r$  (noted above) is an artifact of its high correlations with Youth and Density PC1.

We next performed multivariate analyses, where the effect of each variable on  $m/r$  is controlled by the presence of all other variables. We used Lasso and Elastic net methods [17] that both perform feature selection by shrinking the coefficients of variables that do not affect  $m/r$  to zero, followed by, so-called, relaxed Lasso and Elastic net procedures (as described in Supplementary Methods).

Both methods robustly show similar results (Fig. 5A–B) and prediction accuracy (MSE indicated in figures). Disease PC4 appears in regressions as the most important predictor, followed by NO PC1 and Disease PC2. Other selected predictors are Density PC1 and PC2, No Insurance PC1,  $PM_{2.5}$ , and Youth. These results agree with pairwise correlations, except for  $SO_2$  and Black, which appeared significant in pairwise correlation but were not selected by either linear regression-based method.

We next apply Gradient Boost and Random Forest [17] (see Supplementary Methods), which are non-parametric machine learning methods, i.e., account for potentially highly non-linear relations and interactions between the predictors. For each of these methods, the predictor importance is presented in Fig. 5C–D, where the dashed lines indicate a standard threshold for distinguishing important predictors. Largely consistent results are obtained by both methods, where the predictors with the highest importance are Disease PC4, NO PC1, Disease PC2, No Insurance PC1, Black, and Youth. The only difference is in Density PC1, which appears as important in Random Forest but not in Gradient Boost. Results of Gradient Boost and Random Forest are also consistent with those of Lasso and Elastic Net, with an exception in Black (important in non-linear, but not linear, methods) and  $PM_{2.5}$  (vice versa). The effect of Black on  $m/r$  may therefore be nonlinear and/or based on interactions with other predictors (further discussed below).

To test our assumption that No Insurance PC1 appears in regressions due to its high correlation to other  $m/r$  predictors (mainly Youth and Density PC1), we next repeated the analysis, this time excluding No Insurance PC1. The results presented in Supplementary Fig. S1 show that removing No Insurance PC1, besides leading to an (expected) increase of importance of Youth and Density PC1 (which are highly correlated with No Insurance PC1), does not significantly alter previously obtained results – confirming our assumption.

Finally, in Fig. 6, we quantitatively estimate the influence of the five most important predictors determined above. For each of 51 states, we fix the values of all other predictors while changing the analyzed predictor's value within the range observed in all other states. The resulting distribution of the relative changes in  $m/r$  ( $\delta(m/r)$ ) due to the variation of Chronic disease is shown in Fig. 6A, where each data point in the distribution corresponds to a single USA state. We see that changing Chronic disease values in a realistic range leads to significant variations of  $m/r$ , with a median of  $\sim 30\%$  and going up to 40%. To increase

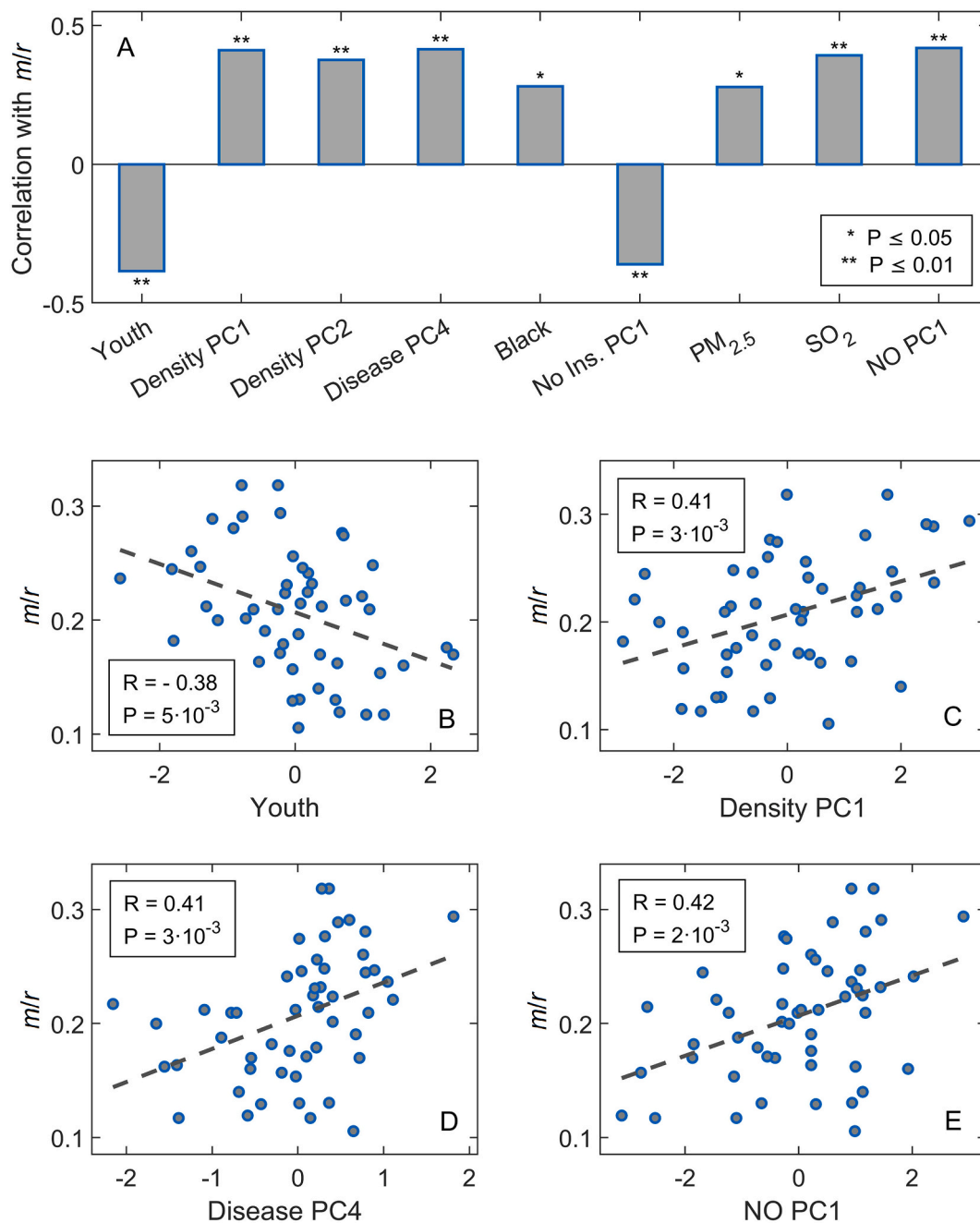


**Fig. 3.** Univariate correlation analysis. (A) Values of Pearson’s correlations for the variables significantly correlated ( $P < 0.05$ ) with  $m/r$ . Correlation plots of  $m/r$  with (B) Youth (percent of the population under 18), (C) density PC1, (D) disease PC4, (E) NO PC1.

robustness, the predictions are made by the consensus of all relevant models. For the remaining four predictors, the obtained median and maximal relative changes are shown in Fig. 6B. The obtained results confirm the importance of Chronic disease, Youth, Black, and Pollution, and, to a smaller extent, Population density.

#### 4. Discussion

While we have earlier studied the parameters that might affect  $R_0$  [25,27], the present goal was to investigate which demographic and environmental variables may influence the average disease severity as manifested in a population. The first step was to propose the response variable, which has to be causally independent of  $R_0$  [25,27], to allow understanding the effects of clinical severity alone. We showed that this

is indeed satisfied by our choice ( $m/r$ ). Additionally, this work allowed us to mechanistically interpret the standard (simple) measure of clinical severity (CFR), i.e., to relate its saturation value with the rate parameters in the epidemiological dynamical model. The relation is, however, non-linear (sigmoidal), which further underscores the non-triviality of the obtained result.

The proposed measure is practical to implement on a large scale (i.e., for diverse regions or countries, as we here demonstrated for 51 USA states), as only publicly available data are required, and calculation corresponds to a simple (though nonlinear) relation. Estimating the saturation (end of the peak) is straightforward in most cases, through both case counts and  $m/r$  reaching a saturation (nearly constant) value. We set the following aims for the selected significant predictors of  $m/r$ : i) test if we can recover clinically observed dependencies, ii) uncover

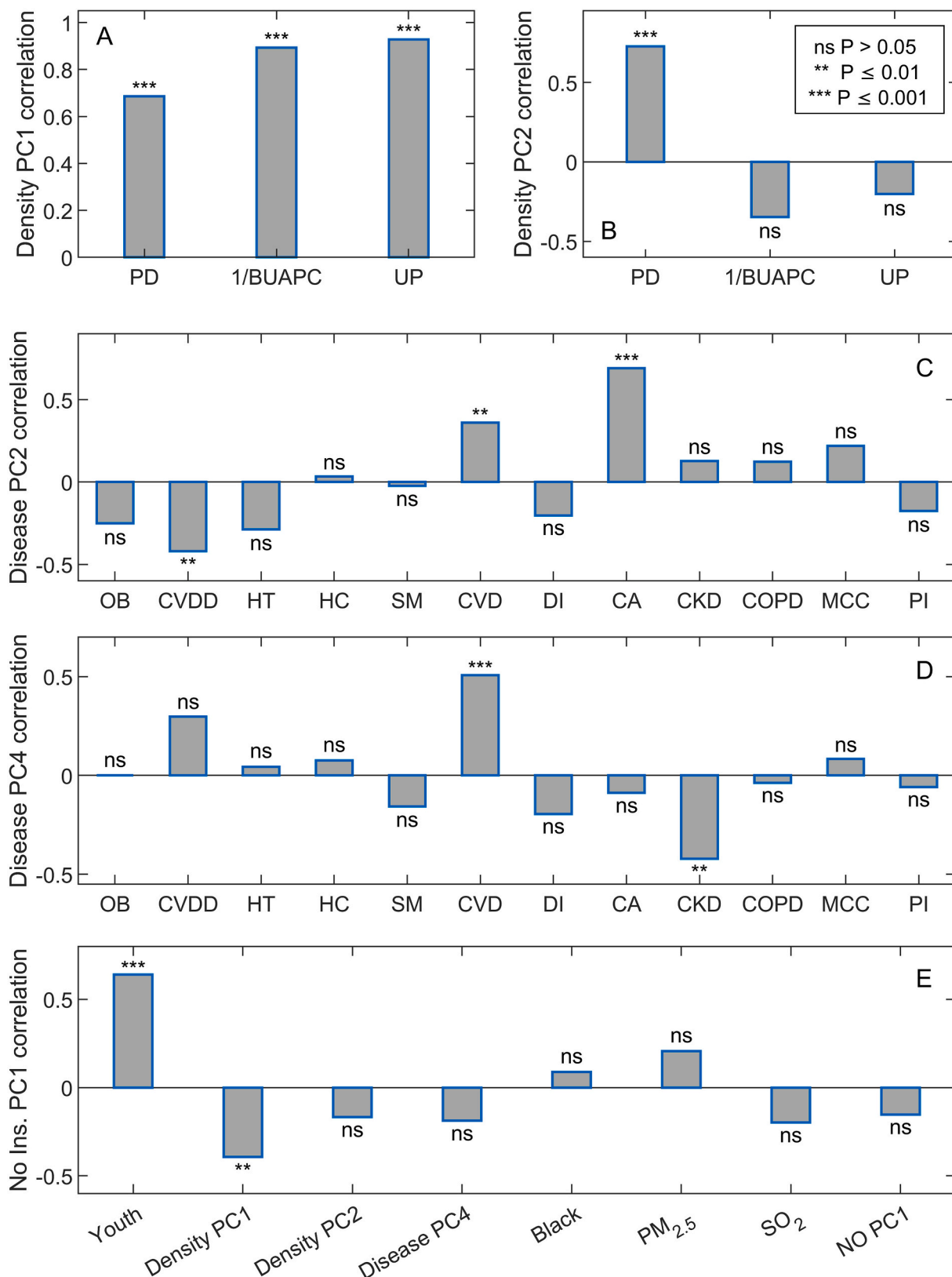


**Fig. 4.** Interpretation of the relevant PCs. Correlation of the relevant principal components with the independent variables is shown, where the height of bars corresponds to the value of Pearson's correlation coefficients. A) and B) Correlation of Density PC1 and Density PC2 with three population density variables. C) and D) Correlation of Disease PC2 and Disease PC4 with the variables from the chronic disease group. (E) Correlations of No Insurance PC1 with the variables from Fig. 3A. The abbreviations correspond to PD – population density, BUAPC – Built-Up Area Per Capita, UP – Urban Population, OB – obesity, CVDD – cardiovascular disease deaths, HT – hypertension, HC – high cholesterol, SM – smoking, CVD – cardiovascular disease, DI – diabetes, CA – cancer, CKD – chronic kidney disease, COPD – chronic obstructive pulmonary disease, MCC – multiple chronic conditions, PI – physical inactivity.



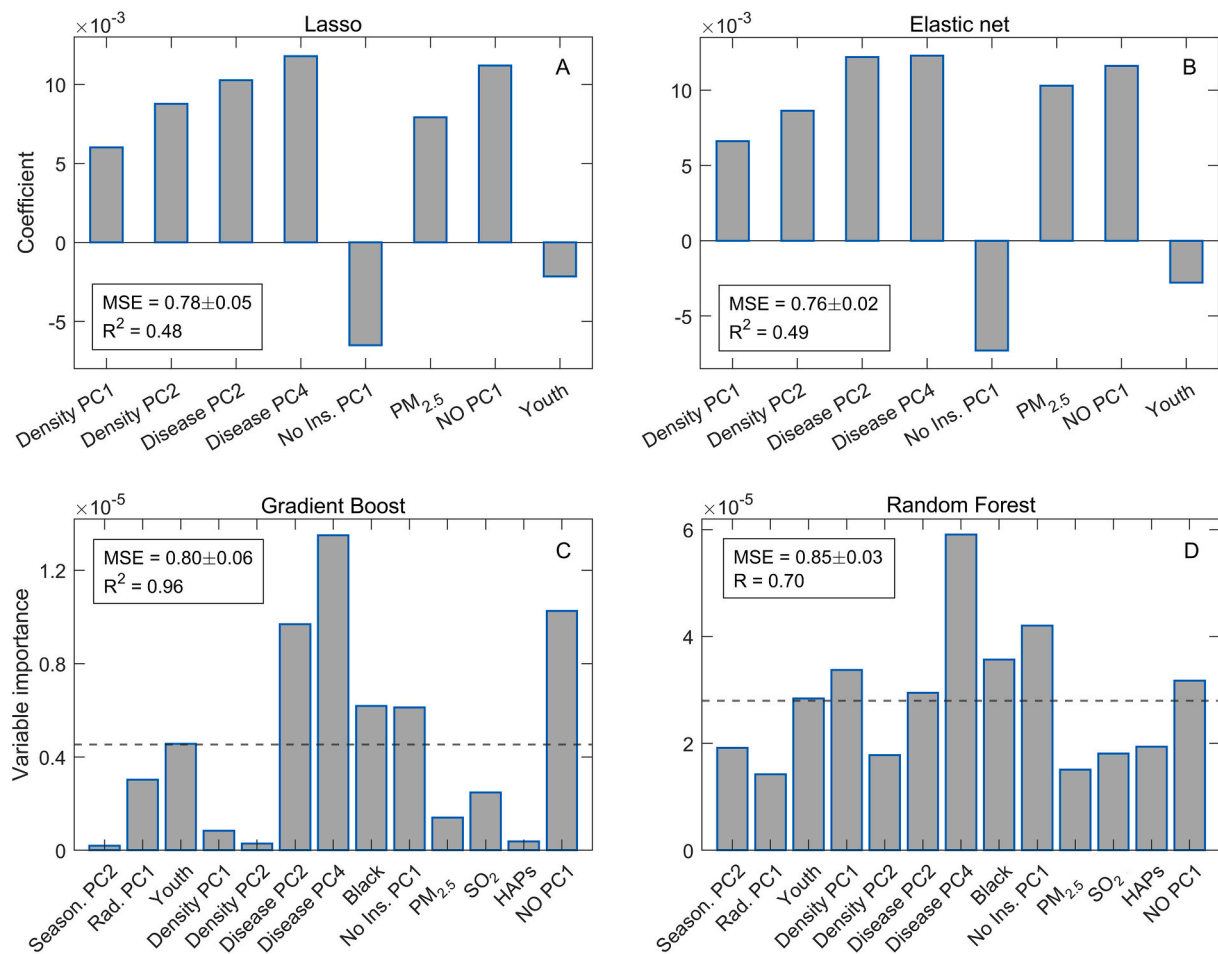


**Fig. 5.** Multivariate (machine learning) analysis. Values of regression coefficients in relaxed A) Lasso and B) Elastic Net regressions. Only the variables whose coefficients are not shrunk to zero by the regressions are shown. The height of bars corresponds to the value of coefficients. Variable importance in C) Gradient Boosting and D) Random Forest regressions, where the height of bars corresponds to estimated importance. Testing set MSE values with the standard errors are shown for each model, corresponding to 5-fold cross-validations with 40 repartitions. Coefficients of determination on the entire dataset ( $R^2$ ) are also shown for each model. Variable names are indicated on the horizontal axis.

additional risk factors for COVID-19 clinical severity, suitable to extract from ecological study design [28–30], *iii*) compare with significant predictors of COVID-19 transmissibility ( $R_0$ ) that we previously obtained [25,27]. We here indeed obtained different predictors for  $m/r$  compared to  $R_0$  [25,27]. There are also some similarities consistent with inherent connections in COVID-19 transmissibility and severity drivers, e.g., the role of pollution, unhealthy living conditions, and indoor population density [25]. We further discuss *i*) and *ii*).

We obtain that both the prevalence of chronic diseases and Youth significantly influence  $m/r$ . This is hardly surprising - though quite a non-trivial result - as we started from a large group of initial variables. The influence of Disease PC4, dominantly reflecting the prevalence of cardiovascular diseases, is well documented by clinical studies [31,32] together with some other ecological studies [11,15]. Other chronic conditions that are known COVID-19 comorbidities (i.e., hypertension, obesity, and diabetes) are significant risk factors for cardiovascular diseases [33], and it is not surprising that cardiovascular diseases dominate over other chronic conditions in our results. Disease PC2, dominantly reflecting the prevalence of cancer (though also related to cardiovascular diseases), agrees with CDC warning that people with a history of cancer may be at increased risk of getting severely ill from COVID-19 [34]. Regarding Youth, it is established that younger individuals are, on average, less severely affected by COVID-19, and that the disease severity increases with age [3,35,36].

We found that chronic pollution exposure, NO<sub>x</sub> levels in particular,

significantly promote COVID-19 severity. While difficult to assess through clinical studies, it has been suggested that pollution is associated with the severity of COVID-19 conditions through similar pathways by which it affects respiratory and cardiovascular mortality [37]. In particular, NO<sub>x</sub> may reduce lung activity and increase infection in the airway [38]. Similarly, the effect of population density (which here significantly affects  $m/r$ ) is hardly suited to detect through clinical studies, while some ecological regression studies also noticed this dependence [39]. An explanation might be that while medical facilities are, in general, more abundant in overcrowded areas [40], this effect becomes overshadowed by the highly increased rate of the COVID-19 spread in these areas. Therefore, population density probably acts as a proxy for smaller healthcare capacity per infected (as the infections increase with the population density, particularly in indoor areas). Additionally, it was also proposed that higher viral inoculum may lead to more severe COVID-19 symptoms [41,42], where overcrowded conditions might lead to higher initial viral doses.

The appearance of the variable Black among the important predictors (Fig. 5C-D) suggests that Afro-Americans are, on average, at higher risk of developing more severe COVID-19. While clinical evidence and several ecological meta-analyses [40,43] seem to confirm this, the underlying reasons are still a matter of debate (see e.g. [44]). Interestingly, this predictor appears only in non-parametric models, where interactions with other predictors are (implicitly) included. A posteriori, this result may not be surprising as it has been argued that

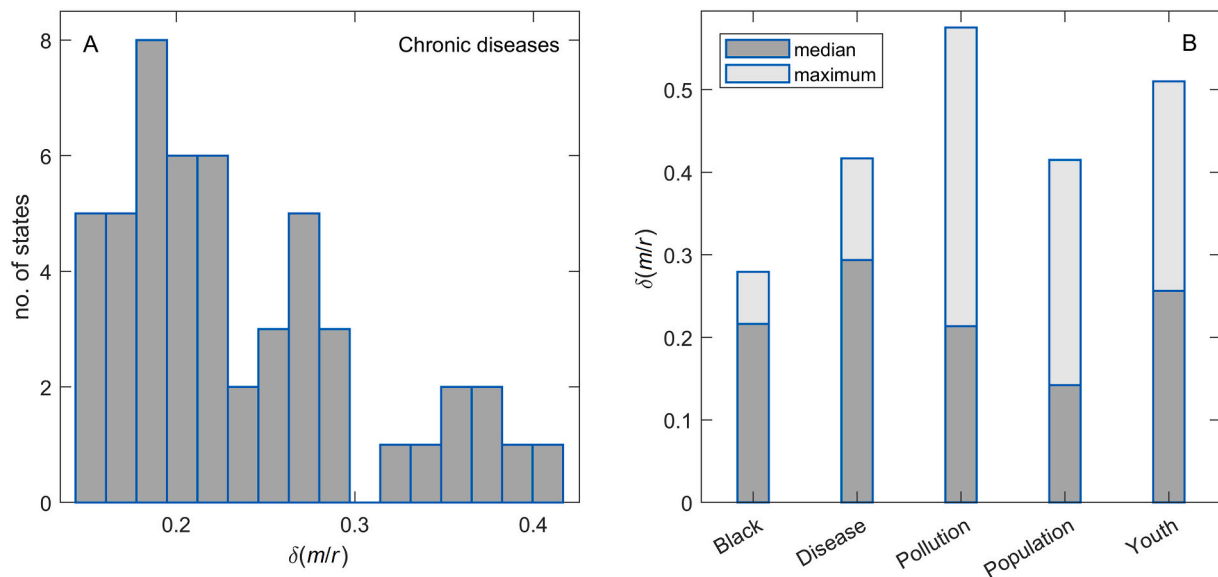


**Fig. 6.** Estimated change in  $m/r$  due to variations of important predictors. A) Distribution of relative changes in  $m/r$  ( $\delta(m/r)$ ) due to variations in prevalence of chronic diseases observed in USA states. For each state,  $m/r$  was predicted for the range of the disease prevalence values observed throughout all other states. B) The same as in A) is repeated, but for the groups of predictors indicated on the horizontal axis. For each group, the median and maximal value of  $\delta(m/r)$  is reported.  $\delta(m/r)$  values for each group of predictors are estimated as described in Supplement Methods.

higher clinical severity of COVID-19 for Black may be tightly related to other significant factors of COVID-19 severity (larger prevalence of chronic diseases, more crowded conditions, higher air pollution).

Our broad estimates of the magnitude of the effects on  $m/r$  are also consistent with all four groups of factors (disease, youth/age, pollution, race) being significant drivers of COVID-19 severity, where a somewhat smaller magnitude was obtained for the fifth group (population density). The immediate implications are that prevention of chronic diseases, reduction of pollution, and improving living conditions can indirectly also alleviate the harms of the pandemics.

#### 4.1. Limitations

To infer the  $m/r$  value, our method requires the existence of a well-defined end of an epidemic wave. While all US states met this criterion in the first COVID-19 wave, in general, this may show up as a limitation.

Some of the studied predictors exhibited limited variability across US states. E.g., this must be considered when interpreting the absence of meteorological variables from the set of significant predictors (despite their significant association with  $R_0$  [18,37]) and the presence of air pollution (occasionally hypothesized to contribute to COVID-19 severity [45]).

## 5. Conclusion

We employed a cross-disciplinary (One Health) approach [46–49], combining epidemiological modeling with advanced statistical (machine) learning approaches, to explore the relationship of environmental factors to COVID-19 clinical severity. From a large number of variables, we achieved a robust selection of a small number of significant factors, including those that are clinically known as determinants of COVID-19 severity. Our findings (performed in an unbiased manner directly from the data) are thus consistent with previous clinical studies – which may be interpreted as a kind of experimental validation of our method. Additionally, our results underscore a syndemic nature of COVID-19 risks [50] through a selection of variables related to pollution, population density, and racial factors (intertwined with the effects of other factors). These results might have important implications for both longer and shorter-term efforts to alleviate the effects of this and (likely) future

epidemics, in terms of longer-term policies to reduce these risks and shorter-term efforts to accordingly relocate medical resources. Our proposed measure (independent of disease transmissibility) originates from general considerations that are not limited to COVID-19. Thus, it may also be utilized in potential future outbreaks of infectious diseases, possibly also combined with other more traditional measures [9].

#### Conflict of interest statement

The authors declare that the research was conducted in the absence of any commercial or financial relationships that could be construed as a potential conflict of interest.

#### Acknowledgements

This work was partially supported by the Ministry of Education, Science and Technological Development of the Republic of Serbia.

#### Appendix A. Supplementary data

Supplementary data to this article can be found online at <https://doi.org/10.1016/j.onehlt.2021.100355>.

#### References

- [1] P. Samui, J. Mondal, S. Khajanchi, A mathematical model for COVID-19 transmission dynamics with a case study of India, *Chaos, Solitons Fractals* 140 (2020), 110173, <https://doi.org/10.1016/j.chaos.2020.110173>.
- [2] M.J. Keeling, P. Rohani, *Modeling Infectious Diseases in Humans and Animals*, Princeton University Press, Princeton, NJ, 2011.
- [3] N. Kapitsinis, The underlying factors of the COVID-19 spatially uneven spread. Initial evidence from regions in nine EU countries, *Reg. Sci. Policy Pract.* 12 (2020) 1027–1045, <https://doi.org/10.1111/rsp3.12340>.
- [4] T.A. Pana, S. Bhattacharya, D.T. Gamble, Z. Pasdar, W.A. Szlachetka, J. A. Perdomo-Lampignano, K.D. Ewers, D.J. McLernon, P.K. Myint, Country-level determinants of the severity of the first global wave of the COVID-19 pandemic: an ecological study, *BMJ Open* 11 (2021), e042034, <https://doi.org/10.1136/bmjopen-2020-042034>.
- [5] K. Allel, T. Tapia-Muñoz, W. Morris, Country-level factors associated with the early spread of COVID-19 cases at 5, 10 and 15 days since the onset, *Glob. Public Health.* 15 (2020) 1589–1602, <https://doi.org/10.1080/17441692.2020.1814835>.
- [6] A. Adhikari, J. Yin, Short-term effects of ambient ozone, PM<sub>2.5</sub>, and meteorological factors on COVID-19 confirmed cases and deaths in Queens, New

- York, *Int. J. Environ. Res. Public Health* 17 (2020) 4047, <https://doi.org/10.3390/ijerph17114047>.
- [7] G. Perone, The determinants of COVID-19 case fatality rate (CFR) in the Italian regions and provinces: an analysis of environmental, demographic, and healthcare factors, *Sci. Total Environ.* 755 (2021), 142523, <https://doi.org/10.1016/j.scitotenv.2020.142523>.
- [8] J. Pan, J.M. St Pierre, T.A. Pickering, N.L. Demirjian, B.K.K. Fields, B. Desai, A. Gholamrezaezhad, Coronavirus disease 2019 (COVID-19): a modeling study of factors driving variation in case fatality rate by country, *Int. J. Environ. Res. Public Health* 17 (2020) 8189, <https://doi.org/10.3390/ijerph17218189>.
- [9] C. Reed, M. Biggerstaff, L. Finelli, L.M. Koonin, D. Beauvais, A. Uzicanin, A. Plummer, J. Bresee, S.C. Redd, D.B. Jernigan, Novel framework for assessing epidemiologic effects of influenza epidemics and pandemics, *Emerg. Infect. Dis.* 19 (2013) 85–91, <https://doi.org/10.3201/eid1901.120124>.
- [10] E.K. Yeoh, K.C. Chong, C.J. Chiew, V.J. Lee, C.W. Ng, H. Hashimoto, S. Kwon, W. Wang, N.N.S. Chau, C.H.K. Yam, T.Y. Chow, C.T. Hung, Assessing the impact of non-pharmaceutical interventions on the transmissibility and severity of COVID-19 during the first five months in the Western Pacific region, *One Health.* 12 (2021), 100213, <https://doi.org/10.1016/j.onehlt.2021.100213>.
- [11] B.B. Singh, M.P. Ward, M. Lowerison, R.T. Lewinson, I.A. Vallerand, R. Deardon, J. P.S. Gill, B. Singh, H.W. Barkema, Meta-analysis and adjusted estimation of COVID-19 case fatality risk in India and its association with the underlying comorbidities, *One Health.* 13 (2021), 100283, <https://doi.org/10.1016/j.onehlt.2021.100283>.
- [12] K. Mizumoto, S. Dahal, G. Chowell, Spatial variability in the risk of death from COVID-19 in Italy, *Int. J. Tuberc. Lung D.* 24 (2020) 829–837, <https://doi.org/10.5588/ijtld.20.0262>.
- [13] L. Böttcher, M. Xia, T. Chou, Why case fatality ratios can be misleading: individual- and population-based mortality estimates and factors influencing them, *Phys. Biol.* 17 (2020), 065003, <https://doi.org/10.1088/1478-3975/ab9e59>.
- [14] B.F. Zaitchik, N. Sweijd, J. Shumake-Guillemot, A. Morse, C. Gordon, A. Marty, J. Trtanj, J. Luterbacher, J. Botai, S. Behera, Y. Lu, J. Olwoch, K. Takahashi, J. D. Stowell, X. Rodó, A framework for research linking weather, climate and COVID-19, *Nat. Commun.* 11 (2020) 5730, <https://doi.org/10.1038/s41467-020-19546-7>.
- [15] E.S. Asirvatham, J. Lakshmanan, C.J. Sarman, M. Joy, Demystifying the varying case fatality rates (CFR) of COVID-19 in India: lessons learned and future directions, *J. Infect. Dev. Countr.* 14 (2020) 1128–1135, <https://doi.org/10.3855/jidc.13340>.
- [16] K. Liu, M. He, Z. Zhuang, D. He, H. Li, Unexpected positive correlation between human development index and risk of infections and deaths of COVID-19 in Italy, *One Health.* 10 (2020), 100174, <https://doi.org/10.1016/j.onehlt.2020.100174>.
- [17] T. Hastie, R. Tibshirani, J. Friedman, *The Elements of Statistical Learning: Data Mining, Inference, and Prediction*, 2nd ed., Springer-Verlag, New York, 2009.
- [18] S. Khajanchi, K. Sarkar, J. Mondal, K.S. Nisar, S.F. Abdelwahab, Mathematical modeling of the COVID-19 pandemic with intervention strategies, *Results Phys.* 25 (2021), 104285, <https://doi.org/10.1016/j.rinp.2021.104285>.
- [19] R.K. Rai, S. Khajanchi, P.K. Tiwari, E. Venturino, A.K. Misra, Impact of social media advertisements on the transmission dynamics of COVID-19 pandemic in India, *J. Appl. Math. Comput.* (2021), <https://doi.org/10.1007/s12190-021-01507-y>.
- [20] S. Khajanchi, K. Sarkar, Forecasting the daily and cumulative number of cases for the COVID-19 pandemic in India, *Chaos.* 30 (2020), 071101, <https://doi.org/10.1063/5.0016240>.
- [21] J. Mondal, S. Khajanchi, Mathematical Modeling and Optimal Intervention Strategies of the COVID-19 Outbreak, 2021, <https://doi.org/10.21203/rs.3.rs-872671/v1>.
- [22] K. Sarkar, S. Khajanchi, J.J. Nieto, Modeling and forecasting the COVID-19 pandemic in India, *Chaos, Solitons Fractals* 139 (2020), 110049, <https://doi.org/10.1016/j.chaos.2020.110049>.
- [23] F.A. Engelbrecht, R.J. Scholes, Test for Covid-19 seasonality and the risk of second waves, *One Health.* 12 (2021), 100202, <https://doi.org/10.1016/j.onehlt.2020.100202>.
- [24] M. Djordjevic, A. Rodic, I. Salom, D. Zigic, O. Milicevic, B. Ilic, M. Djordjevic, A systems biology approach to COVID-19 progression in population, *Adv. Protein Chem. Struct. Biol.* 127 (2021) 291–314, <https://doi.org/10.1016/bs.apcsb.2021.03.003>.
- [25] O. Milicevic, I. Salom, A. Rodic, S. Markovic, M. Tumbas, D. Zigic, M. Djordjevic, M. Djordjevic, PM2.5 as a major predictor of COVID-19 basic reproduction number in the USA, *Environ. Res.* 201 (2021), 111526, <https://doi.org/10.1016/j.envres.2021.111526>.
- [26] X. Wu, R.C. Nethery, M.B. Sabath, D. Braun, F. Dominici, Air pollution and COVID-19 mortality in the United States: strengths and limitations of an ecological regression analysis, *Sci. Adv.* 6 (2020) eabd4049, <https://doi.org/10.1126/sciadv.abd4049>.
- [27] I. Salom, A. Rodic, O. Milicevic, D. Zigic, M. Djordjevic, M. Djordjevic, Effects of demographic and weather parameters on COVID-19 basic reproduction number, *Front. Ecol. Evol.* 8 (2021), 617841, <https://doi.org/10.3389/fevo.2020.617841>.
- [28] M.B. Araújo, B. Naimi, Spread of SARS-CoV-2 Coronavirus likely constrained by climate, *MedRxiv [Preprint]* (2020), <https://doi.org/10.1101/2020.03.12.20034728> (Accessed 6 August 2021).
- [29] F.H. Zakianis, S. Adzania, G.P. Fauzia, R. Mahkota Aryati, Sociodemographic and environmental health risk factor of COVID-19 in Jakarta, Indonesia: an ecological study, *One Health.* 13 (2021), 100303, <https://doi.org/10.1016/j.onehlt.2021.100303>.
- [30] J. Qiu, R. Li, D. Han, Q. Shao, Y. Han, X. Luo, Y. Wu, A multiplicity of environmental, economic and social factor analyses to understand COVID-19 diffusion, *One Health.* 13 (2021), 100335, <https://doi.org/10.1016/j.onehlt.2021.100335>.
- [31] B. de Almeida-Pititto, P.M. Dualib, L. Zajdenverg, J.R. Dantas, F.D. de Souza, M. Rodacki, M.C. Bertoluci, Severity and mortality of COVID 19 in patients with diabetes, hypertension and cardiovascular disease: a meta-analysis, *Diabetol. Metab. Syndr.* 12 (2020) 75, <https://doi.org/10.1186/s13098-020-00586-4>.
- [32] V. Chidambaram, N.L. Tun, W.Z. Haque, M.G. Majella, R.K. Sivakumar, A. Kumar, A.T.-W. Hsu, I.A. Ishak, A.A. Nur, S.K. Ayeh, E.L. Salia, A. Zil-E-Ali, M.A. Saeed, A. P.B. Sarena, B. Seth, M. Ahmadzada, E.F. Haque, P. Neupane, K.-H. Wang, T.-M. Pu, S.M.H. Ali, M.A. Arshad, L. Wang, S. Baksh, P.C. Karakousis, P. Galiatsatos, Factors associated with disease severity and mortality among patients with COVID-19: a systematic review and meta-analysis, *PLoS One* 15 (2020), e0241541, <https://doi.org/10.1371/journal.pone.0241541>.
- [33] A. Pozzer, F. Dominici, A. Haines, C. Witt, T. Münzel, J. Lelieveld, Regional and global contributions of air pollution to risk of death from COVID-19, *Cardiovasc. Res.* 116 (2020) 2247–2253, <https://doi.org/10.1093/cvr/cvaa288>.
- [34] CDC, Coronavirus Disease 2019 (COVID-19), Centers for Disease Control and Prevention. <https://www.cdc.gov/coronavirus/2019-ncov/index.html>, 2020. (Accessed 7 August 2021).
- [35] I.A. Moosa, I.N. Khatatbeh, Robust and fragile determinants of the infection and case fatality rates of Covid-19: international cross-sectional evidence, *Appl. Econ.* 53 (2021) 1225–1234, <https://doi.org/10.1080/00036846.2020.1827139>.
- [36] J.F. Shelton, A.J. Shastri, C. Ye, C.H. Weldon, T. Filstein-Sonmez, D. Coker, A. Symons, J. Esparza-Gordillo, S. Aslibekyan, A. Auton, Trans-ancestry analysis reveals genetic and nongenetic associations with COVID-19 susceptibility and severity, *Nat. Genet.* 53 (2021) 801–808, <https://doi.org/10.1038/s41588-021-00854-7>.
- [37] D. Liang, L. Shi, J. Zhao, P. Liu, J.A. Sarnat, S. Gao, J. Schwartz, Y. Liu, S.T. Ebel, N. Scovronick, H.H. Chang, Urban air pollution may enhance COVID-19 case-fatality and mortality rates in the United States, *Innovation (N. Y.)* 1 (2020), 100047, <https://doi.org/10.1016/j.xinn.2020.100047>.
- [38] US EPA, Basic Information About NO2. <https://www.epa.gov/no2-pollution/basic-information-about-no2>, 2016. (Accessed 7 August 2021).
- [39] S. Koderia, E.A. Rashed, A. Hirata, Correlation between COVID-19 morbidity and mortality rates in Japan and local population density, temperature, and absolute humidity, *Int. J. Environ. Res. Public Health* 17 (2020) 5477, <https://doi.org/10.3390/ijerph17155477>.
- [40] S. Hamidi, S. Sabouri, R. Ewing, Does density aggravate the COVID-19 pandemic? *J. Am. Plan. Assoc.* 86 (2020) 495–509, <https://doi.org/10.1080/01944363.2020.177891>.
- [41] W. Van Damme, R. Dahake, R. van de Pas, G. Vanham, Y. Assefa, COVID-19: does the infectious inoculum dose-response relationship contribute to understanding heterogeneity in disease severity and transmission dynamics? *Med. Hypotheses* 146 (2021), 110431 <https://doi.org/10.1016/j.mehy.2020.110431>.
- [42] M. Gandhi, C. Beyrer, E. Goosby, Masks do more than protect others during COVID-19: reducing the inoculum of SARS-CoV-2 to protect the wearer, *J. Gen. Intern. Med.* 35 (2020) 3063–3066, <https://doi.org/10.1007/s11606-020-06067-8>.
- [43] K. Desmet, R. Wacziarg, J.U.E. Insight, Understanding spatial variation in COVID-19 across the United States, *J. Urban Econ.* (2021), 103332, <https://doi.org/10.1016/j.jue.2021.103332>.
- [44] A. Moreira, K. Chorath, K. Rajasekaran, F. Burmeister, M. Ahmed, A. Moreira, Demographic predictors of hospitalization and mortality in US children with COVID-19, *Eur. J. Pediatr.* 180 (2021) 1659–1663, <https://doi.org/10.1007/s00431-021-03955-x>.
- [45] A.J. Smit, J.M. Fitchett, F.A. Engelbrecht, R.J. Scholes, G. Dzihvhuho, N.A. Sweijd, Winter is coming: a southern hemisphere perspective of the environmental drivers of SARS-CoV-2 and the potential seasonality of COVID-19, *Int. J. Environ. Res. Public Health* 17 (2020) 5634, <https://doi.org/10.3390/ijerph17165634>.
- [46] M.G. Hemida, M.M. Ba Abdulllah, The SARS-CoV-2 outbreak from a one health perspective, *One Health.* 10 (2020), 100127, <https://doi.org/10.1016/j.onehlt.2020.100127>.
- [47] D. Schmiege, A.M. Perez Arredondo, J. Ntajal, J. Minetto Gellert Paris, M.K. Savi, K. Patel, S. Yasobant, T. Falkenberg, One health in the context of coronavirus outbreaks: a systematic literature review, *One Health.* 10 (2020), 100170, <https://doi.org/10.1016/j.onehlt.2020.100170>.
- [48] J. Lebov, K. Grieger, D. Womack, D. Zaccaro, N. Whitehead, B. Kowalczyk, P.D. M. MacDonald, A framework for one health research, *One Health.* 3 (2017) 44–50, <https://doi.org/10.1016/j.onehlt.2017.03.004>.
- [49] C.A. Gallagher, J.R. Keehner, L.P. Hervé-Claude, C. Stephen, Health promotion and harm reduction attributes in one health literature: a scoping review, *One Health.* 13 (2021), 100284, <https://doi.org/10.1016/j.onehlt.2021.100284>.
- [50] I. Fronteira, M. Sidat, J.P. Magalhães, F.P.C. de Barros, A.P. Delgado, T. Correia, C. T. Daniel-Ribeiro, P. Ferrinho, The SARS-CoV-2 pandemic: a syndemic perspective, *One Health.* 12 (2021), 100228, <https://doi.org/10.1016/j.onehlt.2021.100228>.



# PM<sub>2.5</sub> as a major predictor of COVID-19 basic reproduction number in the USA

Ognjen Milicevic<sup>a</sup>, Igor Salom<sup>b</sup>, Andjela Rodic<sup>c</sup>, Sofija Markovic<sup>c</sup>, Marko Tumbas<sup>c</sup>, Dusan Zigic<sup>b</sup>, Magdalena Djordjevic<sup>b</sup>, Marko Djordjevic<sup>c,\*</sup>

<sup>a</sup> Department for Medical Statistics and Informatics, School of Medicine, University of Belgrade, Serbia

<sup>b</sup> Institute of Physics Belgrade, National Institute of the Republic of Serbia, University of Belgrade, Serbia

<sup>c</sup> Quantitative Biology Group, Institute of Physiology and Biochemistry, Faculty of Biology, University of Belgrade, Serbia

## ARTICLE INFO

### Keywords:

COVID-19 pollution dependence  
Outdoor air pollutants  
Basic reproduction number  
Principal component analysis  
Machine learning

## ABSTRACT

Many studies have proposed a relationship between COVID-19 transmissibility and ambient pollution levels. However, a major limitation in establishing such associations is to adequately account for complex disease dynamics, influenced by e.g. significant differences in control measures and testing policies. Another difficulty is appropriately controlling the effects of other potentially important factors, due to both their mutual correlations and a limited dataset. To overcome these difficulties, we will here use the basic reproduction number ( $R_0$ ) that we estimate for USA states using non-linear dynamics methods. To account for a large number of predictors (many of which are mutually strongly correlated), combined with a limited dataset, we employ machine-learning methods. Specifically, to reduce dimensionality without complicating the variable interpretation, we employ Principal Component Analysis on subsets of mutually related (and correlated) predictors. Methods that allow feature (predictor) selection, and ranking their importance, are then used, including both linear regressions with regularization and feature selection (Lasso and Elastic Net) and non-parametric methods based on ensembles of weak-learners (Random Forest and Gradient Boost). Through these substantially different approaches, we robustly obtain that PM<sub>2.5</sub> is a major predictor of  $R_0$  in USA states, with corrections from factors such as other pollutants, prosperity measures, population density, chronic disease levels, and possibly racial composition. As a rough magnitude estimate, we obtain that a relative change in  $R_0$ , with variations in pollution levels observed in the USA, is typically ~30%, which further underscores the importance of pollution in COVID-19 transmissibility.

## 1. Introduction

In the current era of globalization, the appearance of the new SARS-CoV-2 virus in 2019 has harshly reminded humanity of how easily an epidemic can also become a global issue. While essentially the entire world, already for more than a year, suffers from the COVID-19 disease, not all areas have been hit equally. Hence, scientists worldwide are struggling to find patterns in observable variations in the epidemic progression speed and/or its severity, and the present paper is a part of this international and interdisciplinary effort (Bontempi et al., 2020). More specifically, we aim to understand the possible effects of air pollution on the transmission of COVID-19.

Many previous studies have already provided arguments for the importance of pollution (primarily PM<sub>2.5</sub> and, to a lesser degree, PM<sub>10</sub> and NO<sub>2</sub>) in COVID-19 transmissibility and suggested mechanisms that

might explain this connection. It was argued that droplets with virus particles may bind to Particulate Matter (PM), which may promote the diffusion of virus droplets in the air (Chen et al., 2010; Comunian et al., 2020; Contini and Costabile, 2020). Furthermore, once the virus droplet bound to PM reaches a susceptible individual, it can penetrate deeper in alveolar and tracheobronchial regions – especially in the case of small (PM<sub>2.5</sub>) pollution particles (Copat et al., 2020; Qu et al., 2020). Besides these direct mechanical effects on transmission, pollution has a general effect on weakening the immune system making the organism more susceptible to infection (Domingo and Rovira, 2020; Paital and Agrawal, 2020; Qu et al., 2020). In addition, it promotes overexpression of ACE-2 receptors, which allows SARS-CoV-2 binding and entry into cells (Comunian et al., 2020; Paital and Agrawal, 2020; Sagawa et al., 2021).

While these arguments are compelling, and several studies pointed to correlations between pollutant levels and increased severity of COVID-

\* Corresponding author.

E-mail address: [dmarko@bio.bg.ac.rs](mailto:dmarko@bio.bg.ac.rs) (M. Djordjevic).

<https://doi.org/10.1016/j.envres.2021.111526>

Received 15 April 2021; Received in revised form 5 June 2021; Accepted 9 June 2021

Available online 24 June 2021

0013-9351/© 2021 Elsevier Inc. All rights reserved.



19 progression (De Angelis et al., 2021; Kolluru et al., 2021; Lorenzo et al., 2021; Tello-Leal and Macías-Hernández, 2020; Yao et al., 2021; Zhu et al., 2020), there are also prominent methodological difficulties in establishing this link, as discussed in (Anand et al., 2021; Bontempi, 2021; Bontempi et al., 2020; Villeneuve Paul J. and Goldberg Mark S., 2020). Specifically, comparing case counts (Adhikari and Yin, 2020; Suhaimi et al., 2020) in different geographical regions may be influenced by significant differences in the epidemic onsets (Villeneuve Paul J. and Goldberg Mark S., 2020), applied control (e.g., social distancing) measures (Bontempi, 2021), and testing methodologies (most significantly the number of performed tests). Consequently, adequately controlling for the infection dynamics, rather than relying on absolute case counts, is crucial. Secondly, due to a multitude of potential confounding factors, it is crucial to, jointly with pollution, consider possible influences of diverse sociodemographic, economic, medical, and meteorological factors on transmission (Bontempi, 2020b; Bontempi et al., 2020). Ideally, the scope of the study should be conceived to emphasize variability in pollution, while being relatively homogenous in these other factors. As another obstacle, the considered variables can be mutually highly correlated (Notari and Torrieri, 2021; Salom et al., 2021). Such high correlations realistically present a problem for any statistical inference method, though modern machine-learning approaches can partially account for this difficulty (Gupta and Gharhgozli, 2020). Additionally, the relationship of input variables to  $R_0$  might be (highly) non-linear, which can hardly be accounted for by linear regressions, but may be successfully addressed by e.g. ensembles of decision trees (Hastie et al., 2009). Finally, to obtain robust predictions that are not an artifact of the applied methodology and the underlying assumptions, it is crucial to perform analysis by several independent methods.

In our approach, we aim to address these general limitations. First of all, the USA dataset seems to be optimal for this analysis: while, in absolute figures, the pollution in the United States is not high, there is still sufficient variability in the pollution variables to extract reasonable conclusions, whereas heterogeneities in sociodemographic and weather parameters are not too large to overshadow the dependence on pollution. Next, as a measure of transmissibility, we use the basic reproduction number ( $R_0$ ).  $R_0$  is a measure of SARS-CoV-2 transmissibility in a completely susceptible (non-resistant) population and in the absence of social distancing (sometimes also referred to as  $R_{0,free}$  (Magdalena Djordjevic et al., 2021b; Maier and Brockmann, 2020)), which is insensitive to differences in specific testing policies and control measures. We here apply our previously developed methodology (Salom et al., 2021), which is based on observation of different dynamical regimes in COVID-19 infection counts during the disease outburst (Magdalena Djordjevic et al., 2021a). Our model is then applied to one of these growth regimes (the exponential one), to estimate  $R_0$  for individual USA states. These  $R_0$  estimates, instead of the disease counts (or other similar measures), are then used as the dependent (response) variable in further analysis. As independent (input) variables, we assemble a large set of available sociodemographic, medical, and weather variables. Importantly, to assess the pollution levels in detail, we assemble the data for ten different pollutants, with the levels determined in the time windows relevant for the analyzed exponential growth regimes. We gather the weather parameters in the same dynamically relevant manner. This results in a large number of predictors, many of which we group in sets of similar and mutually often highly correlated variables. Additionally, the number of assembled variables exceeds the total sample size, so it is necessary to reduce the number of predictors to a smaller and less correlated set. We achieve this through data preprocessing (feature engineering), which includes variable transformations, removing all outliers, and grouping mutually related and highly correlated variables into subsets (e.g., age-related, population prosperity measures, chronic diseases). Principal Component Analysis (PCA) is then applied within these subsets, resulting in dimensionality reduction (reducing the number of predictors) and

smaller overall correlations within this reduced predictor set. Finally, to go beyond establishing mere correlations between different variables/components with  $R_0$ , we use four established machine learning approaches: Lasso, Elastic net, Random Forest, and Gradient Boost. Our goal is to: i) select important variables and rank their relative importance in explaining  $R_0$ , ii) obtain an estimate of expected changes in  $R_0$  based on observed variability in pollution levels. While the estimates we get in this way are only rough (due to the inability to assemble all relevant factors in determining  $R_0$ ), the obtained results nevertheless provide a quantitative assessment of the importance of pollution in SARS-CoV-2 transmissibility.

## 2. Methods

### 2.1. $R_0$ extraction

As the proxy for the COVID-19 transmissibility, we used the basic reproduction number ( $R_0$ ). Basic reproduction number is a measure of SARS-CoV-2 transmissibility in a fully susceptible population and in the absence of intervention measures (social distancing, quarantine). For extraction of  $R_0$ , we used our previously published methodology, in particular analysis of widespread infection growth regimes (Magdalena Djordjevic et al., 2021a) and extraction of  $R_0$  from the exponential growth phase that we previously applied on a worldwide level (Salom et al., 2021). For the sake of completeness, we summarize this methodology below.

To describe the SARS-CoV-2 transmission in a population, we constructed an adapted version of an SEIR compartmental model (Maier and Brockmann, 2020; Maslov and Goldenfeld, 2020; Perkins and España, 2020; Tian et al., 2020; Weitz et al., 2020), which takes into account all the relevant features of this process, while being simple enough to be used for  $R_0$  estimation in a wide range of populations (Magdalena Djordjevic et al., 2021a; Salom et al., 2021). In the early stages of epidemics and before social distancing measures are introduced, the flow between the model compartments leads to the changes of the compartment member abundances  $S$  (susceptible),  $E$  (exposed),  $I$  (infected),  $R$  (recovered), and  $D$  (cumulative detected cases) which are described by the following system of ordinary differential equations:

$$\frac{dS}{dt} = -\frac{\beta SI}{N} \quad (1.1.)$$

$$\frac{dE}{dt} = \frac{\beta SI}{N} - \sigma E \quad (1.2.)$$

$$\frac{dI}{dt} = \sigma E - \gamma I \quad (1.3.)$$

$$\frac{dR}{dt} = \gamma I \quad (1.4.)$$

$$\frac{dD}{dt} = \varepsilon \delta I \quad (1.5.)$$

where  $N$  is the population size. Parameters represent:  $\beta$  - the rate of virus transmission from an infected to the encountered susceptible individual,  $\sigma$  - the inverse of the average incubation period ( $\sim 3$  days),  $\gamma$  - the inverse of the average period of infectiousness,  $\varepsilon$  - the detection efficiency (as not every infected individual becomes detected), and  $\delta$  - the detection rate.

We here applied the model to the relatively brief, initial epidemics period when only a small fraction of the population is resistant, and before social distancing interventions take effect. Note that, even after introducing the measures, there is  $\sim 10$  days delay in observing their effect in the confirmed case-counts curve, due to the incubation period and the time needed between the symptom onset and the infection detection/confirmation. During this period, the virus is spreading at a rate determined by its natural biological potential, modulated by the

characteristics of the given population and the environment. Therefore, the above parameter values of infection progression are considered constant in this period. The standard measure of the virus transmissibility in these conditions (not influenced by interventions or immunity) is the basic reproduction number,  $R_0$ , defined as the average number of secondary infections caused by a primary infected individual in a fully susceptible population ( $S/N \approx 1$ ), and in the absence of social distancing measures (also sometimes denoted as  $R_{0,free}$ ) (Maier and Brockmann, 2020). At the start of an epidemic,  $R_0 > 1$  and the number of infected individuals grows exponentially. The model can then be linearized by invoking  $S/N \approx 1$ , reducing the model to two linear differential Eqs. (1.2) and (1.3). Solving for the eigenvalues of this system,

$$\lambda_{\pm} = \frac{-(\gamma + \sigma) \pm \sqrt{(\gamma - \sigma)^2 + 4\beta\sigma}}{2}, \quad (1.6.)$$

provides the solution of the form  $I(t) = C_1 \cdot e^{\lambda_+ t} + C_2 \cdot e^{\lambda_- t}$ , which can be approximated by

$$I(t) = I(0) \cdot e^{\lambda_+ t} \quad (1.7.)$$

where the term containing the negative eigenvalue,  $\lambda_-$  can be neglected (see (Salom et al., 2021)). With  $R_0 = \beta/\gamma$  (Keeling and Rohani, 2011; Martcheva, 2015), the equation for the basic reproduction number,

$$R_0 = 1 + \frac{\lambda_+ \cdot (\gamma + \sigma) + \lambda_+^2}{\gamma \cdot \sigma}. \quad (1.8.)$$

can be obtained by expressing  $\beta$  from Eq. (1.6).

To estimate the  $R_0$  values for 46 US states, we collect the detected case counts for each state from online resources (Worldometer, 2020). The solution  $D(t) = \varepsilon \cdot \delta \cdot I(0) \cdot (e^{\lambda_+ t} - 1) / \lambda_+$  of Eq. (1.5) using Eq. (1.7) models the dependence of the cumulative number of detected with time. Taking its logarithm

$$\log(D(t)) = + \lambda_+ \cdot t, \quad (1.9.)$$

results in the equation of the straight line that can be fitted to the data on the semilogarithmic scale. Notably, the slope of that line is given by the positive eigenvalue of the system,  $\lambda_+$ . Once that  $\lambda_+$  is determined by fitting, the value of  $R_0$  for a particular state can be calculated from Eq. (1.8).

## 2.2. Pollution data collection

Air quality information was obtained from the US environmental protection agency (EPA) Air Data service (US Environmental Protection Agency, 2020). We used aggregated daily data for pollutant gases ( $O_3$ ,  $NO_2$ ,  $SO_2$ ,  $CO$ ), particulates ( $PM_{2.5}$  and  $PM_{10}$ ) and other available species, such as VOCs (Volatile Organic Compounds),  $NO_x$ , and HAPs (Hazardous Air Pollutants). For a given state, aggregation was done over all cities with available information. The populations of cities were obtained from the US Census Bureau (U.S. Census Bureau, 2020). All the variable values are averaged for each city over the identified time period, and the state average is calculated as the average of all included state cities weighted by the population.

## 2.3. Weather data collection

Weather parameters were downloaded in bulk using a custom Python script from the NASA POWER project service (NASA Langley Research Center, 2020). All the parameters were downloaded via the POWER API at the longitude and latitude coordinates matching the largest cities in each state that comprise above 10% of the state population. Variables include temperature at 2 m and 10 m, measures of humidity and precipitation (wet bulb temperature, relative humidity, total precipitation), insolation indices, wind speed, and pressure. The

maximum predicted UV index was downloaded from OpenUV (OpenUV, 2020). Geographical coordinates of the cities and populations of cities and states were adapted from Wikidata (Wikipedia, 2021a, b).

## 2.4. Socio-demographic data collection

Demographic data were collected from several sources. The demographic composition of the US population by gender, race, and percentage of the population under 18 and over 65 was taken from the Measure of America, a project of The Social Science Research Council website (Measure of America, 2018). Information about health insurance, GDP, life expectancy at birth, infant and child mortality was also taken from the Measure of America website. Medical parameters such as hypertension, cholesterol, cardiovascular disease, diabetes, cancer, obesity, inactivity, and chronic kidney and obstructive pulmonary disease were taken from America's Health Rankings website (America's Health Ranking, 2021) hosting Centers for Disease Control and Prevention (CDC) data (CDC, 2019). Percentages of the population that are actively smoking and consuming alcohol are taken from the same source. The percentage of the foreign population was taken from the Census Reporter website (U.S. Census Bureau, 2019). The subnational HDI was taken from the Global Data Lab website (2020) (Smits and Permanyer, 2019). Population density, urban population percentage, and median age were taken from the U.S. Census Bureau website (U.S. Census Bureau, Population Division, 2019).

## 2.5. Data processing

The initial analysis of the assembled data distributions and QQ plots revealed non-normal distributions in a majority of variables. To reduce the skewness of the data we applied a number of transforms with different strengths (square root, cubic root, or log), adjusted in sign to maintain the data ranking (Spearman correlation). Individual data values that remained more than three median absolute deviations from the new median were substituted by the said median value.

The main purpose of these transformations, and outliers' removal, was to account for more extreme variable values (such as heavy distribution tails), which may significantly affect some of the analysis methods that we further use (in particular, correlation analysis, Lasso and Elastic net regressions). On the other hand, methods based on the ensembles of decision trees (e.g., Random Forest and Gradient Boost) are fairly robust to outliers and non-normal variable distributions and provide a consistency check of the obtained conclusions.

The table with all applied transformations is provided below. Also, note that the entire dataset used in this analysis (variable values for all 46 states) is provided in Supplement Table 1. In addition to the transformations applied, the table below also links the variables to the dataset, by relating a variable abbreviation (used in Supplemental files) with its full name and units (see Table 1).

## 2.6. Feature engineering and principal components analysis

The total number of variables (74) is larger than the sample size (46 states). While the regressions with feature selection (Lasso and Elastic net) can handle the number of variables that is significantly larger than the sample size (as long as the number of selected features is smaller than the sample size), this large number of variables (some highly correlated) is a major risk for overfitting, particularly for Random Forest and Gradient Boost methods. To reduce the number of variables, we first divided them into groups by conceptual similarity and expected correlation, after which we performed Principal Component Analysis (PCA) on each group. This also partially reduced data correlation (Jolliffe, 2002). Variables were grouped according to two criteria: *i*) those that represent similar quantities so that, after PCA, the interpretation of the obtained PC remains unambiguous; *ii*) the correlations between the variables in the same group are high, so that in this way, after PCA, the

**Table 1**  
List of variables (with units) and the applied transformations. Variable shortcuts (first column) correspond to [Supplement Table 1](#).

Data	Name (units)	Transformation f (x)
T2M, T2M <sub>MAX</sub> , T2M <sub>MIN</sub> , T10M, T10M <sub>MAX</sub> , T10M <sub>MIN</sub> , TS, T2MWET	Temperatures (°C)	None
RH2M	Relative humidity at 2 m (%)	$-\log(\max(x) - x)$
QV2M	Specific humidity at 2 m (g/kg)	$\log(x)$
T2MDEW	Dew Point (°C)	None
PRECTOT	Precipitation (mm/day)	$x^{1/3}$
TQV	Total Column Precipitable Water (cm)	$\log(x)$
CLRSKY_SFC_SW_DWN	Clear Sky Insolation Incident on a Horizontal Surface (MJ/m <sup>2</sup> /day)	$-(\max(x) - x)^{1/3}$
ALLSKY_SFC_LW_DWN	Downward Thermal Infrared (Longwave) Radiative Flux (MJ/m <sup>2</sup> /day)	$\log(x)$
ALLSKY_SFC_SW_DWN	All Sky Insolation Incident on a Horizontal Surface (MJ/m <sup>2</sup> /day)	$\log(x)$
OpenUV <sub>max</sub>	UV radiation index	$x^{1/3}$
WS2M	Wind speed at 2 m	None
WS10M	Wind speed at 10 m	None
P	Pressure	$x^{1/2}$
Population over 65 (%)	Population over 65 (%)	None
Life Expectancy	Life Expectancy at Birth (years)	$-(\max(x) - x)^{1/2}$
Median age	Median age (years)	$-(\max(x) - x)^{1/2}$
Youth population	Population under 18 (%)	$\log(x)$
Population density	Population density (people/km <sup>2</sup> )	$\log(x)$
BUAPC	Built Up Area Per Capita (km <sup>2</sup> /people)	$\log(x)$
Urban Population	Urban Population (%)	$-(\max(x) - x)^{1/2}$
HDI	Human development index (0–1) Average of education, health and standard of living. (Mean years of schooling of adults aged 25+, Expected years of schooling of children aged 6 + Life expectancy at birth + GNIpc)/3	$-(\max(x) - x)^{1/2}$
GDPpc	Gross domestic product per capita	$\log(x)$
Infant mortality rate	Infant Mortality Rate (per 1000 live births)	$-\log(x)$
Child mortality	Child Mortality (age 1–4, per 1000 population)	$-\log(x)$
Alcohol consumption	Adults alcohol consumption binge drinking (%)	$\log(x)$
Foreign-born population	Foreign-born population (%)	$\log(x)$
Obesity	Obesity age 20 and older (%)	None
CVD deaths	Age 65+ Cardiovascular disease deaths per 100000 people	$\log(x)$
Hypertension	Adults with Hypertension (%)	$\log(x)$
High cholesterol	Population with high cholesterol (%)	None
Smoking	Population smoking (%)	None
Cardiovascular disease	Population with cardiovascular disease (%)	None
Diabetes	Population with diabetes (%)	$x^{1/3}$
Cancer	Population with cancer (%)	None
Chronic kidney disease	Population with chronic kidney disease (%)	$x^{1/2}$
Chronic obstructive pulmonary disease	Population with chronic obstructive pulmonary disease (%)	$\log(x)$
Multiple chronic conditions	Population with multiple chronic conditions (%)	None
Physical inactivity	Population physically inactive (%)	$x^{1/3}$

**Table 1 (continued)**

Data	Name (units)	Transformation f (x)
Male percent	Fraction of male in the population (%)	$\log(x)$
White percent	Fraction of white in the population (%)	$-\log(\max(x) - x)$
Black percent	Fraction of black in the population (%)	$x^{1/3}$
Native percent	Fraction of native in the population (%)	$\log(x)$
Asian percent	Fraction of Asian in the population (%)	$\log(x)$
Latino percent	Fraction of Latino in the population (%)	$\log(x)$
No health insurance children	No health insurance under 18 (%)	$x^{1/2}$
No health insurance adults	No health insurance 18–64 (%)	None
No health insurance all	No health insurance all population (%)	None
No insurance black	No health insurance black (%)	None
No insurance native	No health insurance native (%)	$x^{1/3}$
No insurance Asian	No health insurance Asian (%)	$x^{1/2}$
No insurance Latino	No health insurance Latino (%)	None
No insurance white	No health insurance white (%)	None
PM <sub>2.5</sub>	PM <sub>2.5</sub> concentration (µg/m <sup>3</sup> )	None
PM <sub>10</sub>	PM <sub>10</sub> concentration (µg/m <sup>3</sup> )	$x^{1/2}$
CO	CO concentration (ppm, 10 <sup>-6</sup> )	$x^{1/2}$
NO <sub>2</sub>	NO <sub>2</sub> concentration (ppb, 10 <sup>-9</sup> )	None
SO <sub>2</sub>	SO <sub>2</sub> concentration (ppb)	$\log(x - \min(x))$
O <sub>3</sub>	O <sub>3</sub> concentration (ppm)	None
VOC	Volatile organic compounds concentration (ppb Carbon)	$\log(x)$
Lead	Lead concentration (µg/m <sup>3</sup> )	$\log(x)$
HAPs	Hazardous air pollutants concentration (µg/m <sup>3</sup> )	$(x - \min(x))^{1/2}$
NONOxNOy	Nitrous oxides concentration (ppb)	$x^{1/3}$
R <sub>0</sub>	Estimated basic reproduction number	$\log(x)$

overall correlations in the new predictor set are substantially reduced. Grouping of variables and their relation to PCA is provided in [Table 2](#).

Since different variables are expressed in different units and correspond to diverse scales, each variable in the dataset was standardized (the mean subtracted and divided by the standard deviation) before PCA. For each dataset, we retained as many PCs (starting from the most dominant one) as needed to (cumulatively) explain >85% of the data variance. It was inspected that PCs reasonably follow a normal distribution (as expected, based on the transformation of the original variables). Note that some of the initial variables did not satisfy our grouping criteria and thus do not appear in [Table 2](#). They either have a distinct meaning from other variables (e.g., racial prevalence) or have a similar meaning, but do not exhibit a high correlation with the related variables (e.g., relative humidity RH2M, which does not correlate well with the other two humidity measures, QV2M and T2MDEW). These variables enter further analysis independently, i.e., together with PCs obtained after PCA on grouped variables.

### 2.7. LASSO regression

To complement the PCA feature selection, additional L1 regularization was done with Lasso ([Hastie et al., 2009](#); [Tibshirani, 1996](#)). All input variables were standardized. Hyperparameter  $\lambda$  (which controls the model complexity) was optimized through grid search on an

**Table 2**  
Grouping of variables and relation to PC.

PC components	Variables
PC1 temperature	T2M, T2M <sub>MAX</sub> , T2M <sub>MIN</sub> , T10M, T10M <sub>MAX</sub> , T10M <sub>MIN</sub> , TS
PC1 humidity	QV2M, T2MDEW
PC1 precipitation	PRECTOT, TQV
PC1 wind	WS2M, WS10M
PC1 - PC2 radiation	CLRSKY_SFC_SW_DWN, ALLSKY_SFC_SW_DWN, ALLSKY_SFC_LW_DWN
PC1 - PC2 seasonality	PC1 temperature, PC1 humidity, PC1 precipitation, PC1 radiation, PC2 radiation, RH2M, OpenUVmax
PC1 NO	NO <sub>2</sub> , NONOXNOy
PC1 - PC2 age	Population over 65, Youth population, Median age
PC1 - PC2 density	1/BUAPC, Urban population, Population density
PC1 - PC4 prosperity	Life expectancy, Infant mortality, GDP, HDI, Child mortality, Alcohol consumption, Foreign-born population
PC1 - PC4 disease	Obesity (% age 20 and older), Age 65+ CVD deaths, Adults with hypertension (%), Population with high cholesterol (%), Population smoking (%), Population with cardiovascular disease (%), Population with diabetes%, Population with cancer (%), Population chronic kidney disease (%), Population chronic obstructive pulmonary disease (%), Population multiple chronic conditions (%), Population physical inactivity (%)
PC1 - PC3 ins.	No health insurance (% of children under 18), No health insurance (% of adults ages 18–64), No health insurance total population (%), No health insurance black (%), No health insurance native (%), No health insurance Asian (%), No health insurance Latino (%), No health insurance white (%)

exponential scale from numerical zero (OLS regression) to the value yielding the intercept-only model. Mean Squared Error (MSE) on the cross-validation testing set (200 repeats, 80-20 split) was taken as the loss function, and we chose the  $\lambda_{1SE}$  as the simplest model still comparable to the optimal one (Krstajic et al., 2014). The final model was comprised of all the non-zero coefficients.

### 2.8. Elastic net regression

Elastic Net expands the Lasso regression with an L2 regularization and introduces a second hyperparameter  $\alpha$  (Friedman et al., 2010; Hastie et al., 2009; Zou and Hastie, 2005). The same preprocessing was done for the input variables, after which the 2-dimensional grid-search with the same  $\lambda$ -scale as in Lasso, and the  $\alpha$  linearly equidistant on the interval from 0 (Ridge regression) to 1 (Lasso regression) inclusive. Cross-validation was performed in the same way as for the Lasso regression, but each fold gave a distinct  $(\alpha, \lambda)$  pair of hyperparameters. The final chosen value was the pair closest to the centroid of all the folds, and these hyperparameters were used to retrain the model on the whole dataset. Again, the final model was comprised of all the non-zero coefficients.

### 2.9. Random forest and gradient boost

To avoid overfitting, the variables were preselected to exhibit significant correlations with  $R_0$  (with a liberal threshold of  $P < 0.1$ ) by either Pearson, Kendall, or Spearman correlations. Cross-validation and hyperparameter selection for Gradient Boost (GBoost) and Random Forest (Breiman, 1996, 2001; Freund and Schapire, 1997; Friedman, 2001; Hastie et al., 2009) was done equivalently as for Lasso and Elastic net. For Gradient Boost, maximal number of splits, minimal leaf size, and learning rate were chosen through grid search, with the respective values: {1, 2, 3, 4, 5, 8, 16}; {1, 2, 3, 4, 5, 8, 16, 18}; {0.1, 0.25, 0.5, 0.75, 1}. For Random Forest, the grid values for the maximal number of splits and minimal leaf size were, respectively: {6, 12, 18, 22, 24, 26, 30, 35}, {1, 2, ..., 7}. In the ensemble, the number of trained decision trees was chosen to minimize Mean Square Error (MSE) on the testing set, for both methods. The obtained hyperparameters were used to retrain the models on the whole dataset, and predictor importance was estimated

for both methods.

### 2.10. Model metrics

MSE for the testing data, averaged over all cross-validations, was used as a metric to compare the performance of different models. For easier interpretability, MSE values were scaled by those corresponding to the constant model (so that MSE of 1 corresponds to the constant model). To assess statistical significance with respect to the constant model, a  $t$ -test was applied to MSE values obtained through cross-validation.

## 3. Results

### 3.1. Extraction of $R_0$ and feature engineering

The  $\log(D(t))$  in the exponential growth regime for a subset of selected USA states is shown in Fig. 1. The linear dependence confirms that the progression of the epidemic in the early infection stage is almost perfectly exponential and is robustly observed for a wide range of USA states, while the same initial exponential growth was previously observed for a wide range of world countries (Notari and Torrieri, 2021; Salom et al., 2021). We exploited this exponential regime to infer  $R_0$  as described in Methods, which we further use as our independent (response) variable.

Next, we transformed the variables so that their distribution became as close as possible to normal, and removed the outliers, followed by a grouping of the variables into subsets and performing PCA on these subsets, as detailed in Methods. The results of PCA are shown in Table 2, where each group of variables is related to their corresponding PCs in that table. For each variable group, we retained as many PCs as needed to explain more than 85% of the variability in the subset (standard threshold). To each of the PCs listed in Table 2, we assigned an intuitive name (e.g., PC1 prosperity, PC1 age) according to the set of variables from which they are formed.

### 3.2. Feature extraction

We started from the basic assessment of the variable importance in explaining  $R_0$ , which are pairwise correlations. Note that these do not control for the presence of other potentially important variables but are a straightforward initial assessment of the relation with  $R_0$ . In Fig. 2A, we show the Pearson correlation constant of the variables with  $R_0$ , where predictors with statistically significant correlations ( $P < 0.05$ ) are shown together with their correlation constants (represented by bars' heights) and statistical significance levels (indicated by stars). Somewhat surprisingly, we found that the highest correlation was with  $PM_{2.5}$ , with  $R \sim 0.6$  and  $P \sim 10^{-4}$ . A large positive correlation between  $R_0$  and  $PM_{2.5}$  levels can also be observed from the scatter plot in Fig. 2B. Additionally, several other variables exhibit statistically significant correlations with  $R_0$ , as indicated in Fig. 2A. Note, however, that some of these variables are also significantly correlated with  $PM_{2.5}$ . Moreover, their correlation with  $R_0$  and  $PM_{2.5}$  is in the same direction (Fig. 2C). Consequently, their significant correlation with  $R_0$  may be, at least in part, due to their correlation with  $PM_{2.5}$ .

To partially address this, we performed an analysis that allows us to select the most important predictors from the set of correlated variables. Specifically, results of Lasso and Elastic net regressions are shown in Fig. 3A and B. Both of these methods provide both regularization and the ability to select significant predictors through shrinking other coefficients to zero. Moreover, we standardized all the variables before using them in regressions, so that the absolute values of the regression coefficients provide estimates of relative importance of the selected variables. For each of the two methods, we performed repeated cross-validations, together with optimizations of hyperparameters, so that methods have maximal predictive power (minimal MSE) on the training



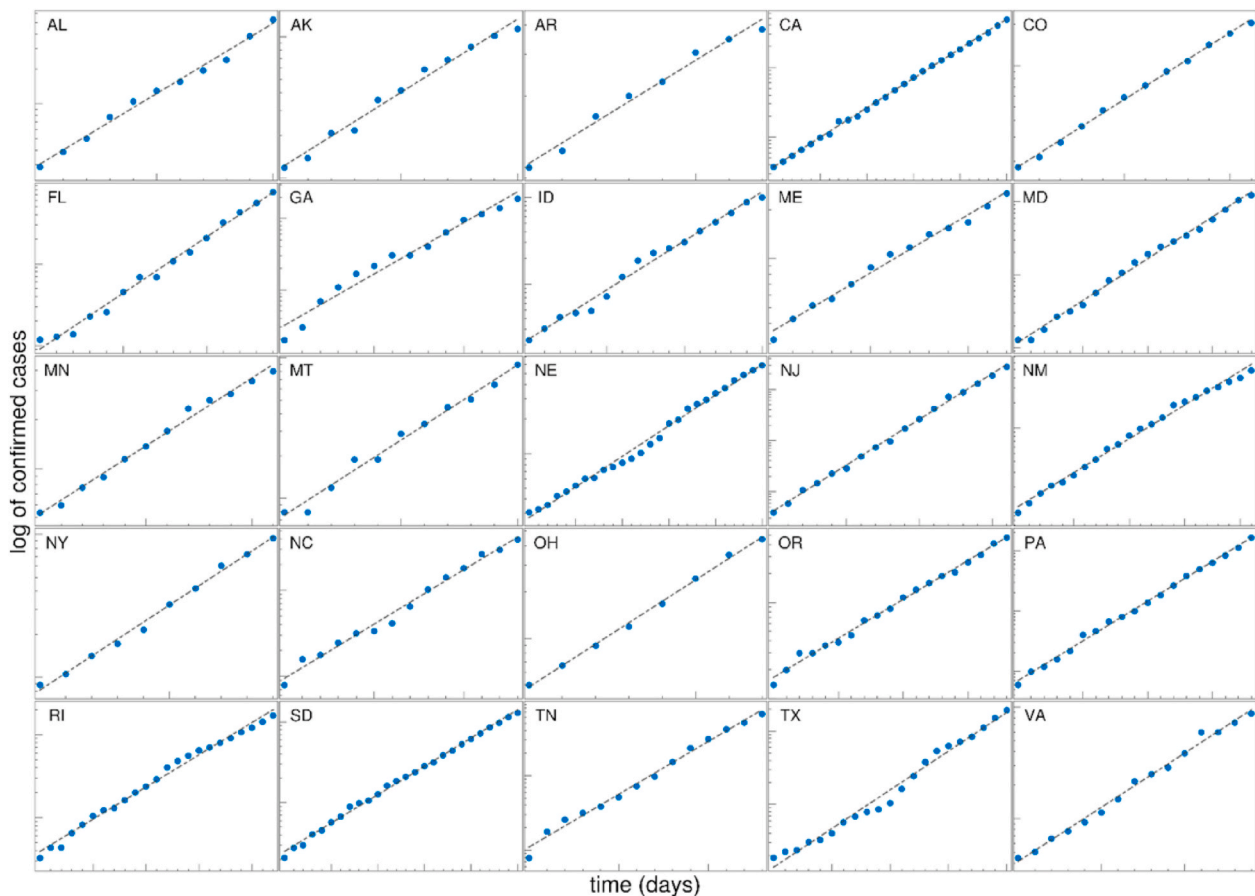


**Fig. 1.** The time dependence of the detected cases for the different US states during the initial period of the epidemic is shown on a log-linear scale. The linear fit of  $\log(D)$  shows that the spread of COVID-19 is well approximated by exponential growth in this phase. Values on axes are chosen differently for each state to emphasize the exponential growth phase. For each state, the start and end dates, the extracted slope  $\lambda_{+,s}$  of the exponential regime, are given in [Supplementary Table S1](#). AL – Alabama; AK – Arkansas; AR – Arizona; CA – California; CO – Colorado; FL – Florida; GA – Georgia; ID – Idaho; ME – Maine; MD – Maryland; MN – Montana; NE – Nebraska; NJ – New Jersey; NM – New Mexico; NY – New York; NC – North Carolina; OH – Ohio; OR – Oregon; PA – Pennsylvania; RI – Rhode Island; SD – South Dakota; TN – Tennessee; TX – Texas; VA – Virginia.

set (see Methods for details). We obtained that the two methods are statistically highly significant compared to the constant model ( $P \sim 10^{-19}$  and  $10^{-23}$ , for Lasso and Elastic net, respectively). The predictive power of these methods is, however, only moderate, as can be seen for the obtained MSE values (MSEs are scaled, so that MSE of 1 corresponds to the constant model, which is not a large difference from 0.79 to 0.76, obtained by Lasso and Elastic net, respectively). Note, however, that the main purpose of these models was in feature selection, while predictability was improved through models employed in the next subsection.

From both Lasso and Elastic net, we again obtained that  $PM_{2.5}$  was the most important predictor, positively affecting COVID-19 transmissibility (so that higher  $PM_{2.5}$  leads to higher transmissibility). A similar trend was obtained for CO and PC1 NO (formed from NO<sub>2</sub> and Nitrogen-oxides concentrations) – CO was also found to be significantly related with  $R_0$  through pairwise correlations. Additionally, the population density (PC2 density) appears as an important predictor through both Lasso and Elastic net, though with smaller importance (regression coefficient), but consistently with pairwise correlations and with a tendency to increase transmissibility. Also, through all three approaches employed so far (pairwise correlations, Lasso, and Elastic net), we obtained that the higher state prosperity (PC1 prosperity) negatively influences  $R_0$ . Also, chronic diseases significantly influence (increase)  $R_0$  as obtained by both pairwise correlations and Elastic net. Finally, PC2 ins., which is related to the fraction of the population (in particular Latinos) with medical insurance, also negatively correlates with  $R_0$

(through all three methods). Interpretation of these dependencies is further addressed in the Discussion section.

### 3.3. Variable importance estimates

Our next goal was to assess variable importance and achieve better model predictability through methods that are considered state-of-the-art in machine learning for these types of problems. We employed two methods based on ensembles of weak learners (decision trees), in particular Gradient Boost and Random Forest. They are substantially different from Lasso and Elastic net employed in the previous subsection, as they do not assume linear dependence of the response from input variables (so-called non-parametric models). Consequently, their employment provided an independent check for the importance of  $PM_{2.5}$  in explaining  $R_0$ . Our motivation was also to obtain better predictability of these models so that we can generate a quantitative estimate of pollution variation effects on  $R_0$ .

Two methods were implemented similarly to Lasso and Elastic net, i. e., model hyperparameters are optimized to achieve maximal predictability through repeated cross-validations (see Method for details). As these models (i.e., decision trees in general) are prone to overfitting, we performed a simple variable selection. That is, only variables with  $P < 0.1$  (according to either Pearson, Kendall, or Spearman correlations) were selected, resulting in 13 variables shown on the horizontal axes of [Fig. 3C and D](#), which were then used in further analysis. We obtained a much better predictive power for both Gradient Boost and Random

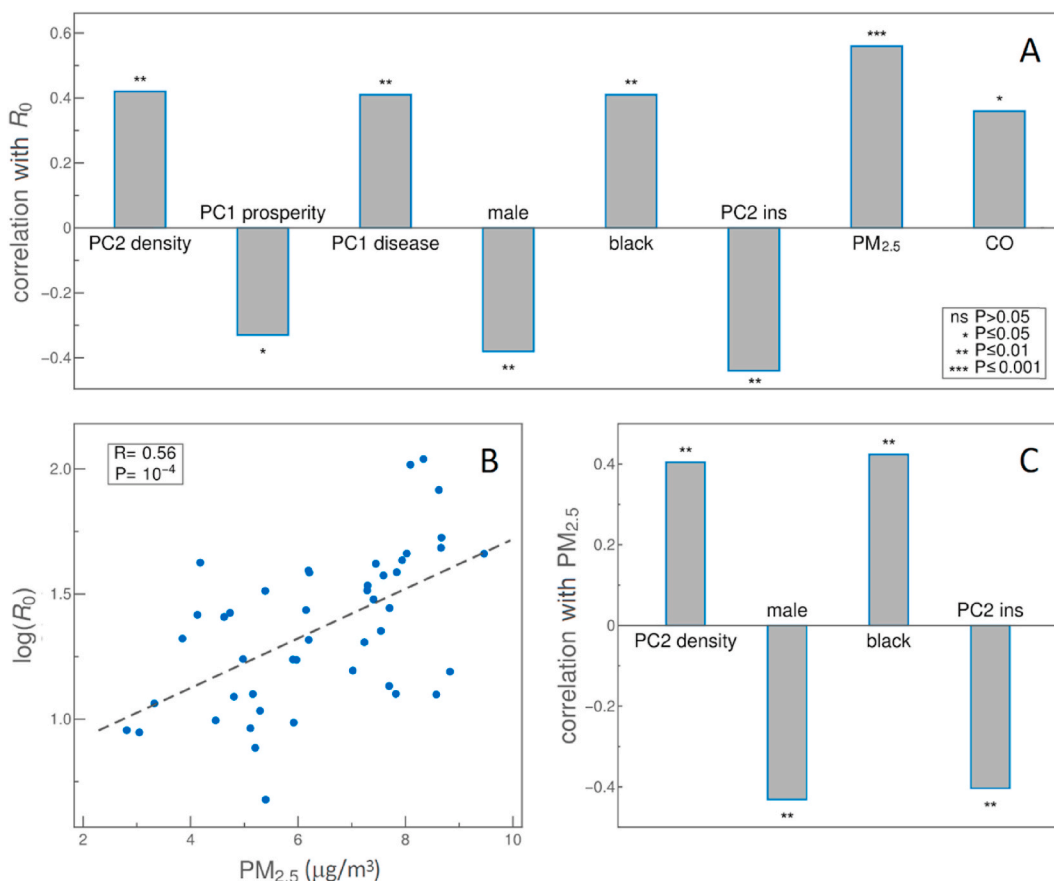


**Fig. 2.** Pearson's correlations for relevant variables. A) Variables significantly correlated ( $P < 0.05$ ) with the basic reproduction number  $R_0$  are shown. The bars' height indicates the value of Pearson's correlation coefficient ( $R$  on the y axis). B) Scatter plot of  $R_0$  vs.  $PM_{2.5}$ . The dashed line shows linear fit. C) Pearson's correlations of variables in A) with  $PM_{2.5}$ . Variable names are indicated on the horizontal axis. Stars in bar plots represent the level of statistical significance, as indicated in the figure legend.

Forest models (compared to regressions in the previous subsection) with MSE of 0.44 and 0.5, respectively, where these differences compared to the constant model (MSE = 1) are statistically highly significant ( $P \sim 10^{-83}$  and  $10^{-84}$ , respectively).

Estimates of variable importance for both of these models are shown in Fig. 3C and D. In both figures, the most prominent feature is  $PM_{2.5}$ , consistently with all other results obtained so far. Furthermore, PC1 disease and PC1 NO appear with moderate importance in both methods, where GBoost also emphasizes the importance of PC2 ins., which is all generally consistent with the analysis presented in the previous subsection. With respect to the pollution, the only difference is that  $PM_{10}$  appears as moderately important in GBoost, while not selected by other models. Also, CO was selected by Random Forest as moderately important (consistent with the previous analysis) but does not appear as such in GBoost. Finally, the racial factor (in particular, fraction of black population) was selected as important by Random Forest (and also appeared as significant through pairwise correlations) but does not appear as important in GBoost. A possible interpretation of these findings is addressed in the Discussion section.

### 3.4. Quantitative estimate of pollution influence on $R_0$

As we obtained a reasonable model accuracy through both GBoost and Random Forest, we were able to estimate how pollution variations (observed through different USA states) affect  $R_0$ . While we included a substantial number of variables (all that we managed to systematically assemble) in our analysis, these are of course not all the variables that can affect  $R_0$ , so we only aimed to provide rough estimates. Still, such an

estimate is useful, as it provides the magnitude by which reasonably realistic changes in the pollution levels can affect  $R_0$ . For example, the new SARS-CoV-2 strain that was first detected in Great Britain (known as B.1.1.7, or more recently Alpha (Callaway, 2021)), which has, at the time of writing, become dominant in many other parts of the world, is estimated to lead to up to 1.9 increase in  $R_0$  – this value can e.g. be compared with our estimated change due to pollution variations. To generate predictions for each of the analyzed states, we kept all other parameters fixed while changing the pollution values so that the changes corresponded to the actual values observed in all 46 states. In this way, the relative change in  $R_0$ , due to observed variations in pollution ( $\Delta R_0/R_0$ ), was estimated, where  $\Delta R_0$  corresponded to the difference between maximal and minimal estimated  $R_0$  values.

The obtained results for  $\Delta R_0/R_0$  for all analyzed states are shown as histograms in Fig. 4A (GBoost) and 4B (Random Forest). For GBoost, a somewhat larger  $\Delta R_0/R_0$ , corresponding to the median of  $\sim 40\%$  (and going up to  $\sim 70\%$ ), was obtained, while for Random Forest, smaller values with a median of  $\sim 25\%$  were estimated. This can e.g. be compared with  $\Delta R_0/R_0$  of up to 90% for the Alpha strain (Davies et al., 2021) so that estimated changes due to pollution variation are smaller but still substantial. Finally, as the two histograms are somewhat different, in Fig. 4C we directly test the consistency of their  $\Delta R_0/R_0$  predictions. It can be seen that they are well consistent, with reasonably high correlation ( $R = 0.73$  and  $P \sim 10^{-8}$ ). Note that these two methods are independent and substantially different (though both based on ensembles of decision trees), so differences in their predictions are expected.

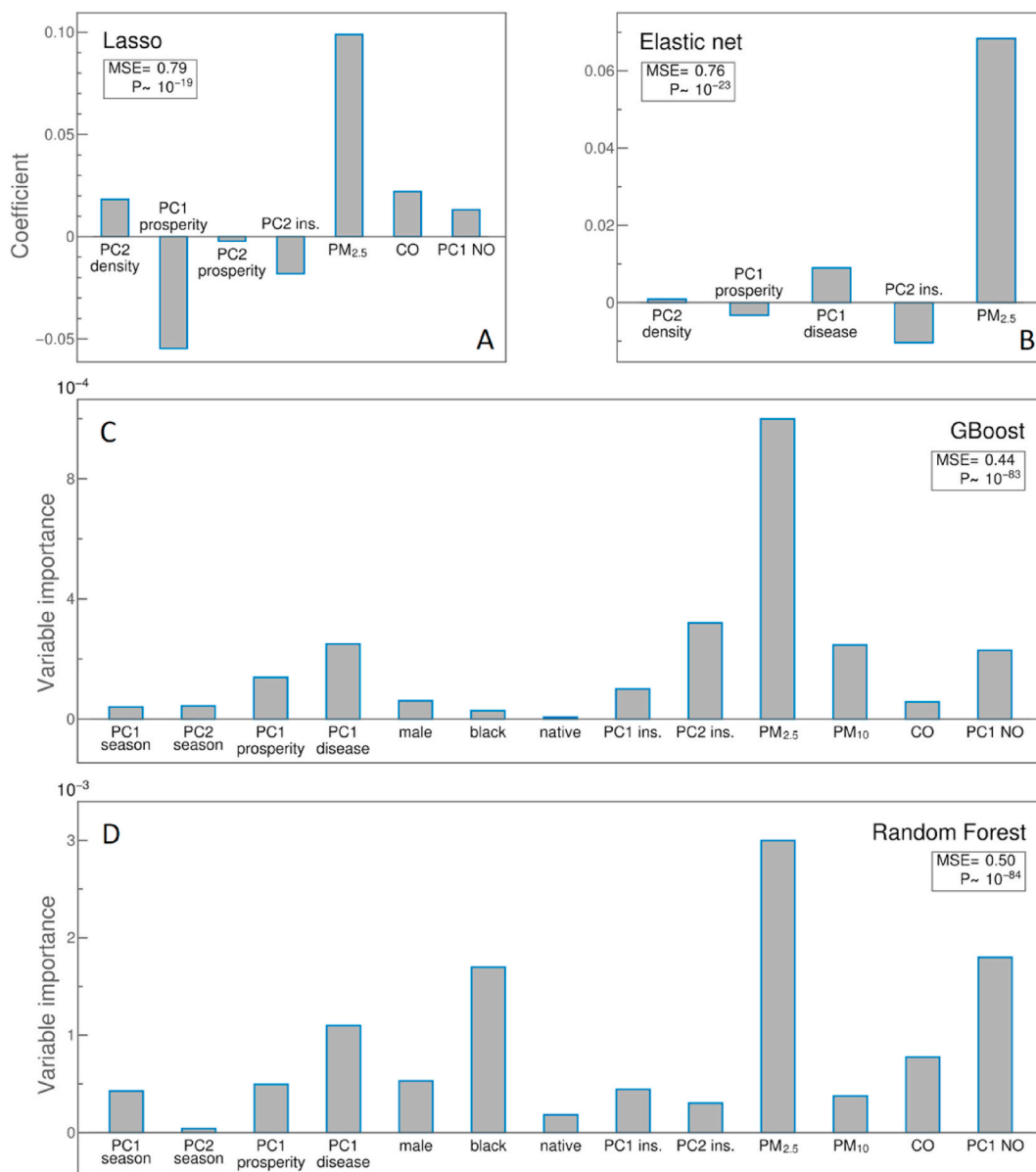


**Fig. 3.** Values of regression coefficients in A) Lasso and B) Elastic Net regressions, respectively, where the bars' height corresponds to the coefficients' values for selected variables. Coefficients of all other variables are shrunk to zero (not shown) by the regressions. Variable importance in C) Gradient Boosting (GBoost) and D) Random Forest (RF) regressions, with the bars' height corresponding to estimated importance. Only variables with  $P < 0.1$  (according to either Pearson, Kendall, or Spearman correlations with  $R_0$ ) are included in GBoost and RF regressions. MSE values are scaled to the constant value model and averaged over 200 cross-validations.  $P$ -values correspond to the statistical significance of obtained MSE's compared to the baseline model. Variable names are indicated on the horizontal axis.

**4. Discussion**

Figs. 2 and 3 reveal the main result of the paper:  $PM_{2.5}$  pollution is, throughout our analysis, consistently singled out as the main driver behind SARS-CoV-2 transmissibility in the US. This result was obtained through both pairwise correlations of variables with  $R_0$ , and by the applied machine learning approaches.

The association of the  $PM_{2.5}$  pollution with the rate of COVID-19 spread *per se* is not a novel result (Gujral and Sinha, 2021; Gupta and Gharehgozli, 2020; Kolluru et al., 2021; Lorenzo et al., 2021; Maleki et al., 2021; Stieb et al., 2020). However, the existing studies had several methodological limitations (Anand et al., 2021; Bontempi, 2021; Bontempi et al., 2020; Villeneuve Paul J. and Goldberg Mark S., 2020), outlined in the Introduction, that we here tried to address. Moreover, previous studies in the USA obtained non-consistent reports on pollution relevance, underlying the importance of more extensive modeling and

statistical learning approaches that we employed here (Allen et al., 2021; Gupta and Gharehgozli, 2020; Luo et al., 2021).

First of all, by explicitly taking into account the infection dynamics, i. e., the model-based estimate of  $R_0$  as SARS-CoV-2 transmissibility measure (instead of, for example, considering case counts) we addressed a number of common shortcomings of studies with a similar goal:  $R_0$  obtained in this way (as it depends only on the curve exponent and is thus scaling invariant) is prone neither to underreporting bias nor to errors due to differences in testing policies (Villeneuve Paul J. and Goldberg Mark S., 2020); since we concentrate only on the initial period of the local epidemic, our results do not suffer from the problem of comparing different stages on the epidemic curves, are not influenced by the existence of multiple epidemic peaks nor by the later appearance of multiple virus strains, and are unaffected by social measures which alter dynamic only later (Bontempi, 2021; Villeneuve Paul J. and Goldberg Mark S., 2020); our approach does not rely on time series and thus

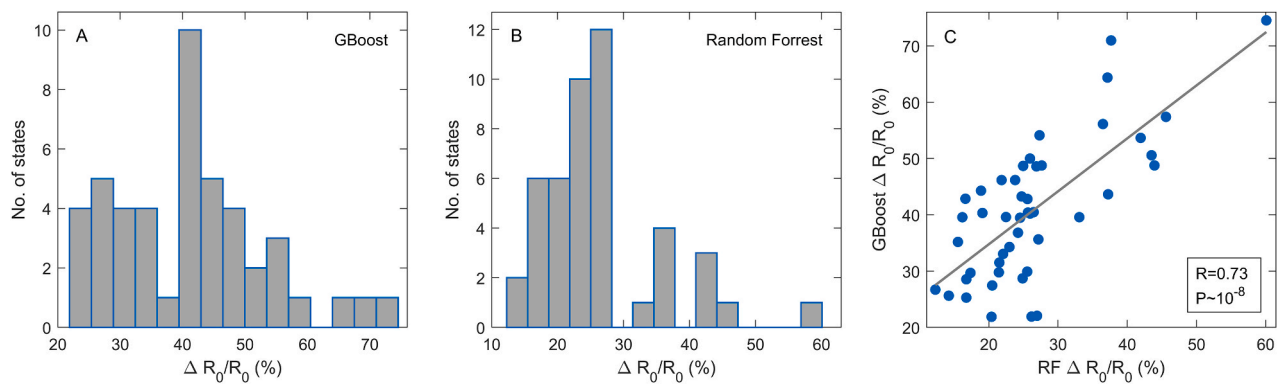


**Fig. 4.** Relative change in  $R_0$  due to pollution variations observed in USA states. For each state included in the analysis,  $R_0$  was predicted for the range of pollution values observed throughout all other states. Relative variation in  $R_0$  was estimated through both A) Gradient Boost (GBoost) and B) Random Forest (RF) regressions, with the models trained as in Fig. 3C) Scatter plot of  $\Delta R_0/R_0$  predictions for GBoost and RF, with indicated Pearson's correlation coefficient and  $P$ -value.

avoids the related methodological difficulties (Villeneuve Paul J. and Goldberg Mark S., 2020). Next, as our inferences are not based simply on mutual correlations of variables alone, but we also robustly obtain the same main conclusion by employing four different machine learning techniques, including those that can account for potentially highly non-linear dependences of  $R_0$  on predictors. Consequently, common objections to statistical methodology (Bontempi et al., 2020; Villeneuve Paul J. and Goldberg Mark S., 2020) do not apply here. Furthermore, by taking into account 74 diverse predictors covering a broad scope of potentially relevant factors, we avoid the lack of multidimensionality and a bias that may result from considering only a narrow class of variables – problems otherwise observed in many similar studies (Bontempi, 2020b; Bontempi et al., 2020). With regards to that, we note that our study was initially conceptualized to explore which parameters, from a large collected set, had the most influence on the spread of the SARS-CoV-2 virus in the USA (without initial bias towards pollution). As our preliminary results singled out air pollution as the major predictor of COVID-19 transmission speed, this motivated us to put the pollution variables in the spotlight of this research, trying also to differentiate which types of pollution mostly contribute to the transmission of COVID-19.

As several limitations still remain in our study, the observed association between  $PM_{2.5}$  pollution and COVID-19 cannot be yet taken to guarantee the existence of a causal relation. Even with the use of advanced statistical learning methods, it is difficult and not always possible to disentangle the effects of strongly correlated variables. As we will further discuss below, it is particularly problematic to differentiate between the independent effects of pollution and the indirect effects of factors related to economic and racial disparities, which often go hand in hand in the USA (Chakraborty, 2021). Another problem is to select a proper proxy (or proxies) for the frequency of human interactions in a given society, as there is little doubt that the human-to-human mode of transmission is most dominant in COVID-19. In this context, some authors (Bontempi, 2020b; Bontempi et al., 2020; Carteni et al., 2020; Guo et al., 2021) rightfully emphasize the importance of properly assessing the mobility of the considered population, and suggest possible proxies: from specific measures of economic relations and commercial exchanges to taking into account the number of job seekers/investors and analysis of public transportation statistics. Presently, we have taken into account only basic measures of economic prosperity that are expected to indirectly but highly correlate with mobility and frequency of human to human interactions: human development index, gross domestic product per capita, life expectancy, infant/child mortality, and foreign-born population. While it is not easy to identify and find further variables that could properly reflect these factors and yet be available, in a systematic and unified way, across all studied regions, there is certainly room for methodological improvement in this respect.

Another methodological limitation that cannot be easily overcome is the potential difference between indoor and outdoor air pollution. This is of obvious relevance since it is estimated that people, on average, spend 80–90 percent of their time indoors (Noorimotlagh et al., 2021b). In the absence of systematic data sources on indoor pollution, our conclusion must rely on a reasonable assumption that indoor and outdoor pollution are, in general, highly correlated, as is illustrated in (Harbizadeh et al., 2019). The unavoidable trade-off between choosing a scope of analysis that exhibits extreme levels (and variations) of air pollution on one side, and the need for uniformity of other parameters on the other side – that we settled by choosing the USA dataset – presents an additional limitation, considering that pollution values in the USA are generally not high, and certainly below serious health-hazard levels. (The values are far below the levels investigated in the COVID-19 context in some other locations: for example, in a study done in Bangkok (Sangkham et al., 2021) the authors reported much higher  $PM_{2.5}$  values but had to face severe methodological limitations of the sorts discussed above.) Despite these remaining limitations of our research, we believe that this work presents substantial progress in terms of methodology and reliability of the obtained results. It thus establishes the link of  $PM_{2.5}$  pollution with COVID-19 transmissibility much more firmly than the previous studies and provides further motivation for research in this direction.

Since this study suggested a direct relation between pollution and COVID-19 transmissibility, we finally provided a quantitative estimate of the established connection in Fig. 4. We estimated that varying the pollutant levels (specifically, levels of  $PM_{2.5}$ ,  $PM_{10}$ , CO, and  $NO_2$ , which enter Random Forest and Gradient Boost methods), where changes in  $PM_{2.5}$  levels are by far the most important, makes a difference of  $\sim 30\%$  in terms of the  $R_0$  values. While this is smaller compared to reproduction number changes due to the appearance of new highly infective strains (estimated to increase  $R_0$  for up to  $\sim 90\%$  higher) (Davies et al., 2021), it is still sizable, and clearly illustrates the potential importance of  $PM_{2.5}$  in modulating the virus transmissibility. For example, in an exponential regime of infection progression (c.f. Eq. (1.7) in Methods) lasting for  $\sim 10$  days (a typical period in which exponential growth is observed for the USA states), and with typical parameter values, such difference would lead to two times larger number of infected, and (at least) equal proportion of lost human lives. Aside from increasing transmissibility, an additional (and largely independent) effect of larger pollutant levels is the potentially increased COVID-19 mortality (due to health hazards of pollution), as suggested by several studies (Luo et al., 2021; Pozzer et al., 2020; Wu et al., 2020). Overall, this underscores the importance of reducing pollutant levels in the epidemiological context, along with other established non-pharmaceutical measures (Abboah-Offei et al., 2021; Anand et al., 2021; Bontempi, 2021).

While we obtain that  $PM_{2.5}$  pollution is the dominant predictor of



virus transmissibility, our results also identify the relevance of other factors. First, a few other pollutants are also selected through our analysis, most notably NO<sub>2</sub> and its related nitrogen oxide derivatives (where its particularly high importance was assigned by the Random Forest method, see Fig. 3D), and to some extent CO and PM<sub>10</sub>. These results are partially in line with findings that several pollutants, more precisely particulate matter (Comunian et al., 2020; Sagawa et al., 2021), but also NO<sub>2</sub> (Paital and Agrawal, 2020), cause overexpression of ACE-2 in respiratory cells, thus increasing the likelihood of infection. This is not the only potentially relevant mechanism, as some studies point to the prolonged exposure to pollutants as a cause of a general weakening of the immune system (Glencross et al., 2020; Qu et al., 2020). However, the relatively low importance of NO and CO pollutants that we obtained more speaks in favor of the hypothesis that PM pollution, by binding to virus droplets, mechanically facilitates SARS-CoV-2 spread through the air - both extending the range of virus diffusion and allowing its direct transport into deeper pulmonary regions (Qu et al., 2020). This suggested mechanism of the pollution-to-human mode of transmission should be seen in the light of substantial evidence for COVID-19 airborne transmission via aerosols (Anand et al., 2021; Kenarkoochi et al., 2020; Noorimotlagh et al., 2021a, b) and of established positive correlation between the concentration of certain pathogens in air and PM pollution (Chen et al., 2010; Harbizadeh et al., 2019). The fact that we were here considering short-term (acute) pollution values precisely in the initial days of the outbreak, and the fact that pollution levels in the US are well below serious health hazards, are also in favor of this mechanistic interpretation of the pollution-COVID-19 link, rather than of the explanation via general adverse effects of pollution on the immune system. On the other hand, the inferred large difference in the influence of PM<sub>2.5</sub> and PM<sub>10</sub> particles may be understood through the difficulty of particulate matter larger than 5 μm to reach ACE2 receptors located in type II alveolar cells (Copat et al., 2020; Zhu et al., 2020). It should be noted that our study is not the only one suggesting a substantial difference between the effect of PM<sub>2.5</sub> and PM<sub>10</sub> particles on the spread of COVID-19 (Copat et al., 2020; Lorenzo et al., 2021; Zhu et al., 2020).

Another factor (unsurprisingly) related to the susceptibility of an organism to infections, is the presence of different comorbidities and, in general, any diseases that could potentially compromise the immune system (Allel et al., 2020; Coccia, 2020; Liu et al., 2020). Indeed, all applied analysis methods except for Lasso find the prevalence of chronic diseases in the population (i.e., its dominant principal component PC1-disease) to be an important  $R_0$  predictor.

Additionally, our applied methods also identify a group of three mutually interrelated factors: the dominant PC reflecting the overall prosperity of the state (PC1 prosperity), the percentage of the black population, and the PC2 insurance component (this component effectively reflects the insurance coverage among the Hispanic population). Our recent study of the effects of various demographic and weather parameters on the spread of COVID-19 based on the data from 118 world countries (Marko Djordjevic et al., 2021) also pointed to the essential role of the country's prosperity, but we note a disagreement in the sign of the correlation: whereas, worldwide, the more developed countries suffered from higher COVID-19 expansion rates, data on US states show an opposite trend - wealthier and more developed areas of US on average seem to exhibit lower  $R_0$  values (Gupta and Gharehgozli, 2020). However, this difference may be expected: on the global level, there are substantial variations in the development level between countries, and this level effectively becomes a proxy for the frequency of social contacts (reflecting business and cultural activity, population mixing due to work/education, international travel, etc.) (Bontempi, 2020b; Bontempi et al., 2020; Gangemi et al., 2020). On the other hand, US states have highly developed societies and the dominant effect of these more subtle differences is likely different: within this prosperity range, the better off population has more means to prioritize and practice precautionary behavior (e.g., have professions that require less physical contacts,

fewer comorbidities, healthier lifestyle, higher awareness of the infection risks, etc.). Furthermore, compared to the global analysis, we note that air pollution also played a role in that study, though a less prominent one, via a principal component that turned out to encapsulate also other measures of unhealthy living conditions and lifestyle. While the influence of PM<sub>2.5</sub> on COVID-19 transmission should, of course, exist everywhere and cannot be effect unique to the territory of the USA, we note that this influence is much more difficult to observe when considering more diverse areas/populations, as it might be overshadowed by more dominant factors.

The COVID-19 pandemic has also emphasized a specific racial aspect of healthcare disparities. The correlation between the percentage of the black population and  $R_0$  observed in our data (Fig. 2A), as well as the results of the Random Forrest regression method (Fig. 3D), agree with the already established conclusion that the black minority is by far overrepresented not only among COVID-19 fatalities (Luo et al., 2021; Wu et al., 2020) but also among the total infected population (Chakraborty, 2021). Another relevant factor is the health insurance coverage (PC2 insurance), which consistently through our analysis shows that COVID-19 infection is spreading faster among people without medical insurance (Figs. 2 and 3). Both the percentage of the black population and the prevalence of insurance coverage are significantly correlated with pollution, in particular with PM<sub>2.5</sub>, as can be seen in Fig. 2C (curiously, our data do not show such correlation with the PC1 prosperity component). Further complicating this relation of poverty, pollution and COVID-19, are the findings that indicate the importance of high quality and well maintained artificial ventilation (which is not equally affordable to everyone) in reducing indoor pollution with possible consequent effects on COVID-19 transmission (Harbizadeh et al., 2019; Noorimotlagh et al., 2021b). It has been already argued that the influence of factors related to a more economically disadvantaged population (overrepresentation of minorities, absence of medical insurance...) is inherently hard to disentangle from the effects of pollution (Chakraborty, 2021). While this standpoint is also in part supported by our analysis, we also note that PM<sub>2.5</sub> consistently appeared with much larger importance through all analyses compared to these economically disadvantaged factors (Chakraborty, 2021; Stieb et al., 2020). In this sense, based on our results, it seems more plausible to associate PM<sub>2.5</sub> (rather than these other factors) with  $R_0$  changes.

It is also interesting to consider which parameters did not show up as important in our results. The absence of seasonal principal components from the final sets of significant predictors may indicate that the importance of the weather parameters such as temperature, UV radiation, and humidity on the SarS-CoV2 transmission is lesser than commonly assumed. While there are substantial arguments that high temperatures and humidity levels should suppress virus transmission (Byun et al., 2021; Fu et al., 2021; Noorimotlagh et al., 2021a; Notari, 2021; Sarkodie and Owusu, 2020), the literature is not fully unison on this conclusion, with some even reporting the opposite effects (Kolluru et al., 2021; Lorenzo et al., 2021; Sangkham et al., 2021). The results presented here seem to side with some authors who disagree that weather factors bear a significant influence on the course of the COVID-19 epidemic (Wang et al., 2021). One should however note that variations of meteorological factors are much larger on a global scale, where indeed we find out a larger significance of these factors (Salom et al., 2021). Another somewhat surprising conclusion is the moderate significance of the population density that we obtain. While there is a significant correlation of PC2 density component with  $R_0$ , it further appeared significant only in Lasso regression, and even there with not a quite high coefficient. While in disagreement with common expectation and some studies (Chakraborty, 2021), this is however in line with several other studies, that also didn't assign a high significance to population density (Carozzi et al., 2020; Hamidi et al., 2020; Pourghasemi et al., 2020; Rashed et al., 2020). Rather than interpreting such an outcome simply as the irrelevance of population density, we, as already argued in (Salom et al., 2021), see it as an indication that more

subtle measures of density (that would more accurately reflect effective proximity of individuals in everyday scenarios) are needed.

## 5. Conclusion and outlook

Starting from 74 initial parameters and by using five different analysis approaches, we obtained the results that robustly select PM<sub>2.5</sub> pollution as a major predictor of SARS-CoV-2 transmissibility in the USA. Using  $R_0$  as a transmissibility measure and non-linear dynamics to extract its values for different USA states, these results are largely insensitive to the differences in the state policies. The obtained large quantitative estimate of the magnitude of the PM<sub>2.5</sub> effect on virus transmissibility may be intuitively unexpected and is not that far from estimated differences in transmissibility caused by virus mutations.

The main issue to be addressed in future studies is that of causality, i. e., disentangling the effects of pollution from those of socio-demographic factors with which it is correlated. This clearly cannot be achieved through studies with low resolution, such as the one employed here, despite using sophisticated statistical (machine) learning methods and studiously taking into account the infection progression dynamics. Carefully crafted, and high-resolution, longitudinal epidemiological studies may be a way forward in this regard. The results obtained here, and by other similar studies, may provide a basis for these high-resolution studies, particularly in terms of factors that should be considered, their expected relative importance, and the magnitude of the effects that may be expected.

### Credit author statement

MarD, IS and MagD conceived the research. The work was supervised by MarD, IS and AR. Data acquisition and supplementary material by OM, MT and DZ. Code writing and data analysis by OM, MarD, DZ, SM. Figures and tables made by OM, DZ, MT and MagD. A literature search by AR and SM. Result interpretation by MarD, MagD, IS, AR and SM. Manuscript written by MarD, IS, AR, MagD, OM and MT.

### Data availability statement

Data is provided in the Supplementary material.

### Funding

This work was partially supported by the Ministry of Education, Science and Technological Development of the Republic of Serbia.

### Declaration of competing interest

The authors declare that they have no known competing financial interests or personal relationships that could have appeared to influence the work reported in this paper.

### Appendix A. Supplementary data

Supplementary data to this article can be found online at <https://doi.org/10.1016/j.envres.2021.111526>.

### References

- Abboah-Offei, M., Salifu, Y., Adewale, B., Bayuo, J., Ofori-Poku, R., Opare-Lokko, E.B.A., 2021. A rapid review of the use of face mask in preventing the spread of COVID-19. *Int. J. Nursing Stud. Adv.* 3, 100013 <https://doi.org/10.1016/j.ijnsa.2020.100013>.
- Adhikari, A., Yin, J., 2020. Short-term effects of ambient ozone, PM(2.5) and meteorological factors on COVID-19 confirmed cases and deaths in Queens, New York. *Int. J. Environ. Res. Publ. Health* 17, 4047. <https://doi.org/10.3390/ijerph17114047>.
- Allel, K., Tapia-Muñoz, T., Morris, W., 2020. Country-level factors associated with the early spread of COVID-19 cases at 5, 10 and 15 days since the onset. *Global Publ. Health* 15, 1589–1602. <https://doi.org/10.1080/17441692.2020.1814835>.

- Allen, O., Brown, A., Wang, E., 2021. Socioeconomic Disparities in the Effects of Pollution on Spread of Covid-19: Evidence from US Counties (MPRA Paper No. 105151). University Library of Munich, Germany.
- America's Health Ranking, 2021. America's Health Rankings Analysis of CDC, Behavioral Risk Factor Surveillance System [Online]. United Health Foundation. accessed 3.28.21. <https://www.americashealthrankings.org/>.
- Anand, U., Cabrerros, C., Mal, J., Ballesteros, F., Sillanpää, M., Tripathi, V., Bontempi, E., 2021. Novel coronavirus disease 2019 (COVID-19) pandemic: from transmission to control with an interdisciplinary vision. *Environ. Res.* 197, 111126 <https://doi.org/10.1016/j.envres.2021.111126>.
- Bontempi, E., 2020. Commercial exchanges instead of air pollution as possible origin of COVID-19 initial diffusion phase in Italy: more efforts are necessary to address interdisciplinary research. *Environ. Res.* 188, 109775 <https://doi.org/10.1016/j.envres.2020.109775>.
- Bontempi, E., 2021. The Europe second wave of COVID-19 infection and the Italy "strange" situation. *Environ. Res.* 193, 110476 <https://doi.org/10.1016/j.envres.2020.110476>.
- Bontempi, E., Vergalli, S., Squazzoni, F., 2020. Understanding COVID-19 diffusion requires an interdisciplinary, multi-dimensional approach. *Environ. Res.* 188, 109814 <https://doi.org/10.1016/j.envres.2020.109814>.
- Breiman, L., 1996. Bagging predictors. *Mach. Learn.* 24, 123–140. <https://doi.org/10.1007/BF00058655>.
- Breiman, L., 2001. Random forests. *Mach. Learn.* 45, 5–32. <https://doi.org/10.1023/A:1010933404324>.
- Byun, W.S., Heo, S.W., Jo, G., Kim, J.W., Kim, S., Lee, S., Park, H.E., Baek, J.-H., 2021. Is coronavirus disease (COVID-19) seasonal? A critical analysis of empirical and epidemiological studies at global and local scales. *Environ. Res.* 196, 110972 <https://doi.org/10.1016/j.envres.2021.110972>.
- Callaway, E., 2021. Coronavirus variants get Greek names — but will scientists use them? *Nature*. <https://doi.org/10.1038/d41586-021-01483-0>.
- Carozzi, F., Provenzano, S., Roth, S., 2020. Urban Density and COVID-19 (IZA Discussion Paper No. 13440). Institute of Labor Economics (IZA), Bonn.
- Carteni, A., Di Francesco, L., Martino, M., 2020. How mobility habits influenced the spread of the COVID-19 pandemic: results from the Italian case study. *Sci. Total Environ.* 741, 140489 <https://doi.org/10.1016/j.scitotenv.2020.140489>.
- CDC, 2019. CDC - Behavioral Risk Factor Surveillance System [Online]. accessed 3.28.2021. <https://www.cdc.gov/brfss/index.html>.
- Chakraborty, J., 2021. Convergence of COVID-19 and chronic air pollution risks: racial/ethnic and socioeconomic inequities in the U.S. *Environ. Res.* 193, 110586 <https://doi.org/10.1016/j.envres.2020.110586>.
- Chen, P.-S., Tsai, F.T., Lin, C.K., Yang, C.-Y., Chan, C.-C., Young, C.-Y., Lee, C.-H., 2010. Ambient influenza and avian influenza virus during dust storm days and background days. *Environ. Health Perspect.* 118, 1211–1216. <https://doi.org/10.1289/ehp.0901782>.
- Coccia, M., 2020. An index to quantify environmental risk of exposure to future epidemics of the COVID-19 and similar viral agents: theory and practice. *Environ. Res.* 191 <https://doi.org/10.1016/j.envres.2020.110155>, 110155–110155.
- Comunian, S., Dongo, D., Milani, C., Palestini, P., 2020. Air pollution and Covid-19: the role of particulate matter in the spread and increase of Covid-19's morbidity and mortality. *Int. J. Environ. Res. Publ. Health* 17, 4487. <https://doi.org/10.3390/ijerph17124487>.
- Contini, D., Costabile, F., 2020. Does air pollution influence COVID-19 outbreaks? *Atmosphere* 11. <https://doi.org/10.3390/atmos11040377>.
- Copat, C., Cristaldi, A., Fiore, M., Grasso, A., Zuccarello, P., Signorelli, S.S., Conti, G.O., Ferrante, M., 2020. The role of air pollution (PM and NO<sub>2</sub>) in COVID-19 spread and lethality: a systematic review. *Environ. Res.* 191, 110129 <https://doi.org/10.1016/j.envres.2020.110129>.
- Davies, N.G., Abbott, S., Barnard, R.C., Jarvis, C.I., Kucharski, A.J., Munday, J.D., Pearson, C.A.B., Russell, T.W., Tully, D.C., Washburne, A.D., Wenseleers, T., Gimma, A., Waites, W., Wong, K.L.M., van Zandvoort, K., Silverman, J.D., Diaz-Ordaz, K., Keogh, R., Eggo, R.M., Funk, S., Jit, M., Atkins, K.E., Edmunds, W.J., 2021. Estimated transmissibility and impact of SARS-CoV-2 lineage B.1.1.7 in England. *Science* 372. <https://doi.org/10.1126/science.abg3055>.
- De Angelis, E., Renzetti, S., Volta, M., Donato, F., Calza, S., Placidi, D., Lucchini, R.G., Rota, M., 2021. COVID-19 incidence and mortality in Lombardy, Italy: an ecological study on the role of air pollution, meteorological factors, demographic and socioeconomic variables. *Environ. Res.* 195, 110777 <https://doi.org/10.1016/j.envres.2021.110777>.
- U.S. Census Bureau, Population Division, 2019. Annual Estimates of the Resident Population by Single Year of Age and Sex for the United States, States, and Puerto Rico Commonwealth: April 1, 2010, to July 1, 2018 [Online]. accessed 3.28.2021. <https://www.census.gov/en.html>.
- Djordjevic, Marko, Salom, I., Markovic, S., Rodic, A., Milicevic, O., Djordjevic, Magdalena, 2021. Inferring the Main Drivers of SARS-CoV-2 Transmissibility arXiv [Preprint]. <https://arxiv.org/abs/2103.15123>.
- Djordjevic, Magdalena, Djordjevic, Marko, Ilic, B., Stojku, S., Salom, I., 2021a. Understanding Infection Progression under Strong Control Measures through Universal COVID-19 Growth Signatures. *Global Challenges*. <https://doi.org/10.1002/gch2.202000101>, 2000101.
- Djordjevic, Magdalena, Rodic, A., Salom, I., Zigic, D., Milicevic, O., Ilic, B., Djordjevic, Marko, 2021b. A systems biology approach to COVID-19 progression in population. *Adv. Protein Chem. Struct. Biol.* <https://doi.org/10.1016/bs.apcsb.2021.03.003>.
- Domingo, J.L., Rovira, J., 2020. Effects of air pollutants on the transmission and severity of respiratory viral infections. *Environ. Res.* 187, 109650 <https://doi.org/10.1016/j.envres.2020.109650>.

- Freund, Y., Schapire, R.E., 1997. A decision-theoretic generalization of on-line learning and an application to boosting. *J. Comput. Syst. Sci.* 55, 119–139. <https://doi.org/10.1006/jcss.1997.1504>.
- Friedman, J.H., 2001. Greedy function approximation: a gradient boosting machine. *Ann. Stat.* 29, 1189–1232.
- Friedman, J.H., Hastie, T., Tibshirani, R., 2010. Regularization paths for generalized linear models via coordinate descent. *J. Statist. Software* 33, 1–22. <https://doi.org/10.18637/jss.v033.i01>.
- Fu, S., Wang, B., Zhou, J., Xu, X., Liu, J., Ma, Y., Li, L., He, X., Li, S., Niu, J., Luo, B., Zhang, K., 2021. Meteorological factors, governmental responses and COVID-19: evidence from four European countries. *Environ. Res.* 194, 110596 <https://doi.org/10.1016/j.envres.2020.110596>.
- Gangemi, S., Billeci, L., Tonacci, A., 2020. Rich at risk: socio-economic drivers of COVID-19 pandemic spread. *Clin. Mol. Allergy* 18, 12. <https://doi.org/10.1186/s12948-020-00127-4>.
- Glencross, D.A., Ho, T.-R., Camiña, N., Hawrylowicz, C.M., Pfeffer, P.E., 2020. Air pollution and its effects on the immune system. *Free Radic. Biol. Med.* 151, 56–68. <https://doi.org/10.1016/j.freeradbiomed.2020.01.179>.
- Gujral, H., Sinha, A., 2021. Association between exposure to airborne pollutants and COVID-19 in Los Angeles, United States with ensemble-based dynamic emission model. *Environ. Res.* 194, 110704 <https://doi.org/10.1016/j.envres.2020.110704>.
- Guo, Y., Yu, H., Zhang, G., Ma, D.T., 2021. Exploring the impacts of travel-implied policy factors on COVID-19 spread within communities based on multi-source data interpretations. *Health Place* 69, 102538. <https://doi.org/10.1016/j.healthplace.2021.102538>.
- Gupta, A., Gharehgozli, A., 2020. Developing a Machine Learning Framework to Determine the Spread of COVID-19. <https://doi.org/10.2139/ssrn.3635211>.
- Hamidi, S., Sabouri, S., Ewing, R., 2020. Does density aggravate the COVID-19 pandemic? *J. Am. Plann. Assoc.* 86, 495–509. <https://doi.org/10.1080/01944363.2020.1777891>.
- Harbizadeh, A., Mirzaee, S.A., Khosravi, A.D., Shoushtari, F.S., Goodarzi, H., Alavi, N., Anjali, K.A., Rad, H.D., Maleki, H., Goudarzi, G., 2019. Indoor and outdoor airborne bacterial air quality in day-care centers (DCCs) in greater Ahvaz, Iran. *Atmos. Environ.* 216, 116927 <https://doi.org/10.1016/j.atmosenv.2019.116927>.
- Hastie, T., Tibshirani, R., Friedman, J., 2009. *The Elements of Statistical Learning, second ed.* Springer, New York.
- Jolliffe, I.T., 2002. *Principal Component Analysis*, 2nd ed. Springer Series in Statistics, Springer-Verlag, New York. <https://doi.org/10.1007/b98835>.
- Keeling, M.J., Rohani, P., 2011. *Modeling Infectious Diseases in Humans and Animals*. Princeton University Press, Princeton, NJ.
- Kenarkoobi, A., Noorimotlagh, Z., Falahi, S., Amarloei, A., Mirzaee, S.A., Pakzad, I., Bastani, E., 2020. Hospital indoor air quality monitoring for the detection of SARS-CoV-2 (COVID-19) virus. *Sci. Total Environ.* 748, 141324 <https://doi.org/10.1016/j.scitotenv.2020.141324>.
- Kolluru, S.S.R., Patra, A.K., Nazneen, Shiva Nagendra, S.M., 2021. Association of air pollution and meteorological variables with COVID-19 incidence: evidence from five megacities in India. *Environ. Res.* 195, 110854 <https://doi.org/10.1016/j.envres.2021.110854>.
- Krstajic, D., Buturovic, L.J., Leahy, D.E., Thomas, S., 2014. Cross-validation pitfalls when selecting and assessing regression and classification models. *J. Cheminf.* 6 <https://doi.org/10.1186/1758-2946-6-10>.
- Liu, H., Chen, S., Liu, M., Nie, H., Lu, H., 2020. Comorbid chronic diseases are strongly correlated with disease severity among COVID-19 patients: a systematic review and meta-analysis. *Aging Dis.* 11, 668–678. <https://doi.org/10.14336/AD.2020.0502>.
- Lorenzo, J.S.L., Tam, W.W.S., Seow, W.J., 2021. Association between air quality, meteorological factors and COVID-19 infection case numbers. *Environ. Res.* 197, 111024 <https://doi.org/10.1016/j.envres.2021.111024>.
- Luo, Y., Yan, J., McClure, S., 2021. Distribution of the environmental and socioeconomic risk factors on COVID-19 death rate across continental USA: a spatial nonlinear analysis. *Environ. Sci. Pollut. Res. Int.* 28, 6587–6599. <https://doi.org/10.1007/s11356-020-10962-2>.
- Maier, B.F., Brockmann, D., 2020. Effective containment explains subexponential growth in recent confirmed COVID-19 cases in China. *Science* 368, 742–746. <https://doi.org/10.1126/science.abb4557>.
- Maleki, M., Anvari, E., Hopke, P.K., Noorimotlagh, Z., Mirzaee, S.A., 2021. An updated systematic review on the association between atmospheric particulate matter pollution and prevalence of SARS-CoV-2. *Environ. Res.* 195, 110898 <https://doi.org/10.1016/j.envres.2021.110898>.
- Martcheva, M., 2015. *An Introduction to Mathematical Epidemiology*. Springer, Boston, MA.
- Maslov, S., Goldenfeld, N., 2020. Window of Opportunity for Mitigation to Prevent Overflow of ICU Capacity in Chicago by COVID-19. medRxiv. <https://doi.org/10.1101/2020.03.20.20040048> [Preprint].
- Measure of America, 2018. Mapping America: Demographic Indicators [Online]. accessed 3.28.2021. <http://measureofamerica.org/tools-old/>.
- NASA Langley Research Center, 2020. The Prediction of Worldwide Energy Resources (POWER) Project [Online]. accessed 3.28.2021. <https://power.larc.nasa.gov/>.
- Noorimotlagh, Z., Mirzaee, S.A., Jaafarzadeh, N., Maleki, M., Kalvandi, G., Karami, C., 2021a. A systematic review of emerging human coronavirus (SARS-CoV-2) outbreak: focus on disinfection methods, environmental survival, and control and prevention strategies. *Environ. Sci. Pollut. Res.* 28, 1–15. <https://doi.org/10.1007/s11356-020-11060-z>.
- Noorimotlagh, Z., Jaafarzadeh, N., Martínez, S.S., Mirzaee, S.A., 2021b. A systematic review of possible airborne transmission of the COVID-19 virus (SARS-CoV-2) in the indoor air environment. *Environ. Res.* 193, 110612 <https://doi.org/10.1016/j.envres.2020.110612>.
- Notari, A., 2021. Temperature dependence of COVID-19 transmission. *Sci. Total Environ.* 763, 144390 <https://doi.org/10.1016/j.scitotenv.2020.144390>.
- Notari, A., Torrieri, G., 2021. COVID-19 Transmission Risk Factors arXiv:2005.03651 [physics, q-bio, stat].
- OpenUV, 2020. Global UV Index API [Online]. accessed 7.30.2020. <https://www.openuv.io/>.
- Paital, B., Agrawal, P.K., 2020. Air pollution by NO<sub>2</sub> and PM<sub>2.5</sub> explains COVID-19 infection severity by overexpression of angiotensin-converting enzyme 2 in respiratory cells: a review. *Environ. Chem. Lett.* 1–18. <https://doi.org/10.1007/s10311-020-01091-w>.
- Perkins, T.A., España, G., 2020. Optimal control of the COVID-19 pandemic with non-pharmaceutical interventions. *Bull. Math. Biol.* 82, 118. <https://doi.org/10.1007/s11538-020-00795-y>.
- Pourghasemi, H.R., Pouyan, S., Heidari, B., Farajzadeh, Z., Fallah Shamsi, S.R., Babaei, S., Khosravi, R., Etemadi, M., Ghanbarian, G., Farhadi, A., Safaeian, R., Heidari, Z., Tarazkar, M.H., Tiefenbacher, J.P., Azmi, A., Sadeghian, F., 2020. Spatial modeling, risk mapping, change detection, and outbreak trend analysis of coronavirus (COVID-19) in Iran (days between February 19 and June 14, 2020). *Int. J. Infect. Dis.* 98 <https://doi.org/10.1016/j.ijid.2020.06.058>.
- Pozzer, A., Dominici, F., Haines, A., Witt, C., Münzel, T., Lelieveld, J., 2020. Regional and global contributions of air pollution to risk of death from COVID-19. *Cardiovasc. Res.* 116, 2247–2253. <https://doi.org/10.1093/cvr/cvaa288>.
- Qu, G., Li, X., Hu, L., Jiang, G., 2020. An imperative need for research on the role of environmental factors in transmission of novel coronavirus (COVID-19). *Environ. Sci. Technol.* 54, 3730–3732. <https://doi.org/10.1021/acs.est.0c01102>.
- Rashed, E.A., Kodera, S., Gomez-Tames, J., Hirata, A., 2020. Influence of absolute humidity, temperature and population density on COVID-19 spread and decay durations: multi-prefecture study in Japan. *Int. J. Environ. Res. Publ. Health* 17. <https://doi.org/10.3390/ijerph17155354>.
- Sagawa, T., Tsujikawa, T., Honda, A., Miyasaka, N., Tanaka, M., Kida, T., Hasegawa, K., Okuda, T., Kawahito, Y., Takano, H., 2021. Exposure to particulate matter upregulates ACE2 and TMPRSS2 expression in the murine lung. *Environ. Res.* 195, 110722 <https://doi.org/10.1016/j.envres.2021.110722>.
- Salom, I., Rodic, A., Milicevic, O., Zigic, D., Djordjevic, Magdalena, Djordjevic, Marko, 2021. Effects of demographic and weather parameters on COVID-19 basic reproduction number. *Front. Ecol. Evol.* 8, 524. <https://doi.org/10.3389/fevo.2020.617841>.
- Sangham, S., Thongtip, S., Vongruang, P., 2021. Influence of air pollution and meteorological factors on the spread of COVID-19 in the Bangkok Metropolitan Region and air quality during the outbreak. *Environ. Res.* 197, 111104 <https://doi.org/10.1016/j.envres.2021.111104>.
- Sarkodie, S.A., Owusu, P.A., 2020. Impact of meteorological factors on COVID-19 pandemic: evidence from top 20 countries with confirmed cases. *Environ. Res.* 191, 110101 <https://doi.org/10.1016/j.envres.2020.110101>.
- Smits, J., Permyer, I., 2019. The subnational human development database. *Sci. Data* 6, 190038. <https://doi.org/10.1038/sdata.2019.38>.
- Stieb, D.M., Evans, G.J., To, T.M., Brook, J.R., Burnett, R.T., 2020. An ecological analysis of long-term exposure to PM<sub>2.5</sub> and incidence of COVID-19 in Canadian health regions. *Environ. Res.* 191, 110052 <https://doi.org/10.1016/j.envres.2020.110052>.
- Suhaimi, N.F., Jalaludin, J., Latif, M.T., 2020. Demystifying a possible relationship between COVID-19, air quality and meteorological factors: evidence from Kuala Lumpur, Malaysia. *Aerosol Air Qual. Res.* 20, 1520–1529. <https://doi.org/10.4209/aaqr.2020.05.0218>.
- Tello-Leal, E., Macías-Hernández, B.A., 2020. Association of environmental and meteorological factors on the spread of COVID-19 in Victoria, Mexico, and air quality during the lockdown. *Environ. Res.* 110442 <https://doi.org/10.1016/j.envres.2020.110442>.
- Tian, H., Liu, Y., Li, Y., Wu, C.-H., Chen, B., Kraemer, M.U.G., Li, B., Cai, J., Xu, B., Yang, Q., Wang, B., Yang, P., Cui, Y., Song, Y., Zheng, P., Wang, Q., Bjornstad, O.N., Yang, R., Grenfell, B.T., Pybus, O.G., Dye, C., 2020. An investigation of transmission control measures during the first 50 days of the COVID-19 epidemic in China. *Science* 368, 638–642. <https://doi.org/10.1126/science.abb6105>.
- Tibshirani, R., 1996. Regression shrinkage and selection via the Lasso. *J. Roy. Stat. Soc. B* 58, 267–288. <https://doi.org/10.1111/j.2517-6161.1996.tb02080.x>.
- U.S. Census Bureau, 2019. Nativity in the United States American Community Survey 1-year Estimates [Online]. accessed 1.15.2021. <https://censusreporter.org/>.
- U.S. Census Bureau, 2020. U.S. Census Data [Online]. accessed 7.10.2020. <https://www.census.gov/en.html>.
- US Environmental Protection Agency, 2020. Air Quality System Data [Online]. US EPA. accessed 3.28.2021. <https://www.epa.gov/outdoor-air-quality-data>.
- Villeneuve Paul, J., Goldberg Mark, S., 2020. Methodological Considerations for epidemiological studies of air pollution and the SARS and COVID-19 coronavirus outbreaks. *Environ. Health Perspect.* 128, 095001 <https://doi.org/10.1289/EHP7411>.
- Wang, Q., Zhao, Yu, Zhang, Yajuan, Qiu, J., Li, J., Yan, N., Li, N., Zhang, J., Tian, D., Sha, X., Jing, J., Yang, C., Wang, K., Xu, R., Zhang, Yuhong, Yang, H., Zhao, S., Zhao, Yi, 2021. Could the ambient higher temperature decrease the transmissibility of COVID-19 in China? *Environ. Res.* 193, 110576 <https://doi.org/10.1016/j.envres.2020.110576>.
- Weitz, J.S., Beckett, S.J., Coenen, A.R., Demory, D., Dominguez-Mirazo, M., Dushoff, J., Leung, C.-Y., Li, G., Mägälne, A., Park, S.W., Rodriguez-Gonzalez, R., Shivam, S., Zhao, C.Y., 2020. Modeling shield immunity to reduce COVID-19 epidemic spread. *Nat. Med.* 26, 849–854. <https://doi.org/10.1038/s41591-020-0895-3>.
- Wikipedia, 2021a. List of States and Territories of the United States by Population [Online]. accessed 3.28.2021. [https://en.wikipedia.org/w/index.php?title=List\\_of\\_states\\_and\\_territories\\_of\\_the\\_United\\_States\\_by\\_population&oldid=1016990633](https://en.wikipedia.org/w/index.php?title=List_of_states_and_territories_of_the_United_States_by_population&oldid=1016990633).

- Wikipedia, 2021b. List of United States Cities by Population [Online]. accessed 3.28.2021. [https://en.wikipedia.org/w/index.php?title=List\\_of\\_United\\_States\\_cities\\_by\\_population&oldid=1017904123](https://en.wikipedia.org/w/index.php?title=List_of_United_States_cities_by_population&oldid=1017904123).
- Worldometer, 2020. COVID-19 Coronavirus Pandemic [Online]. accessed 1.14.2021. <https://www.worldometers.info/coronavirus/>.
- Wu, X., Nethery, R.C., Sabath, M.B., Braun, D., Dominici, F., 2020. Air pollution and COVID-19 mortality in the United States: strengths and limitations of an ecological regression analysis. *Sci. Adv.* 6 <https://doi.org/10.1126/sciadv.abd4049>.
- Yao, Y., Pan, J., Liu, Z., Meng, X., Wang, Weidong, Kan, H., Wang, Weibing, 2021. Ambient nitrogen dioxide pollution and spreadability of COVID-19 in Chinese cities. *Ecotoxicol. Environ. Saf.* 208, 111421 <https://doi.org/10.1016/j.ecoenv.2020.111421>.
- Zhu, Y., Xie, J., Huang, F., Cao, L., 2020. Association between short-term exposure to air pollution and COVID-19 infection: evidence from China. *Sci. Total Environ.* 727, 138704 <https://doi.org/10.1016/j.scitotenv.2020.138704>.
- Zou, H., Hastie, T., 2005. Regularization and variable selection via the elastic net. *J. Roy. Stat. Soc. B* 67, 301–320.





# An analytical framework for understanding infection progression under social mitigation measures

Bojana Ilic · Igor Salom · Marko Djordjevic ·  
Magdalena Djordjevic 

Received: 5 February 2022 / Accepted: 24 April 2023 / Published online: 1 August 2023  
© The Author(s), under exclusive licence to Springer Nature B.V. 2023

**Abstract** While there has been much computational work on the effect of intervention measures, such as vaccination or quarantine, the influence of social distancing on the epidemics' outbursts is not well understood. We present a realistic, analytically solvable, framework for COVID-19 dynamics in the presence of social distancing measures. The model is a generalization of the compartmental SEIR model that accounts for the effects of these measures. We derive a closed-form mathematical expressions for the time dependence of epidemiological observables, in particular, the detected cases and fatalities. These analytical solutions indicate simple quantitative relations between the model variables and epidemiological observables, which give insights into cause-effect connections that underlie the outburst dynamics but are obscured in more standard (numerical) approaches. While the obtained results and conclusions are based on the study of the COVID-19 pandemic, the presented analysis has general applicability to infection outbursts. Our findings are particularly important in the emergence of new pandemics when effective pharmaceutical treatments are unavail-

able, and one must rely on well-timed and appropriately chosen social mitigation measures.

**Keywords** SEIR model · Analytical solutions · Infection progression · Population dynamics · Epidemics peak · Infection tipping points

## 1 Introduction

Numerical computation methods and/or simulations are routinely used to study epidemiological dynamics. These tools can easily produce predictions of even very complex epidemiological models. Yet, in a certain sense, the numerical computation/simulation is comparable to a black-box system that converts given model parameters to the prediction outcomes, hardly facilitating any direct and deeper understanding of the influences of individual parameters on model observables. Additionally, inferring the parameter values from the observed data, analogous to reverse-engineering of the black-box functioning, often becomes a difficult task.

These problems have become additionally pronounced in the context of the current COVID-19 pandemic, which, since being unprecedented in many aspects, underlines the necessity to expand the commonly used epidemiological models. Progress has been made in various directions, e.g. by taking into account the effects of quarantine [1,2], temporary immunity [3], recurrent outbreaks [4], vaccination [5–8], different levels of population susceptibility [9], comorbidi-

---

B. Ilic · I. Salom · M. Djordjevic (✉)  
Institute of Physics Belgrade, National Institute of the Republic of Serbia, University of Belgrade, Pregrevica 118, Belgrade 11080, Serbia  
e-mail: magda@ipb.ac.rs

M. Djordjevic  
Quantitative Biology Group, Faculty of Biology, University of Belgrade, Studentski trg 3, Belgrade 11000, Serbia

ties [8, 10], stratification by age [11–13], competitive virus strains of different severity and/or transmissibility [14, 15], spatial diffusion [16], human mobility between different regions [17–19], availability of testing kits [20], hospital infrastructure [21] and media coverage [22, 23] to name a few. In particular, the attempts to combat the disease led to the introduction of social distancing measures on the scales hardly imaginable before [24].

While it is evident that social distancing measures seriously impact the epidemiological dynamic, their effects are not yet well understood [25–27], despite a lot of undergoing effort to incorporate the influence of these measures into the existing epidemiological models [4, 8, 22, 28–39]. These studies often use an analytical approach to analyze and reveal some of the system's characteristics—e.g., system equilibria, positivity and boundness of variables, stability, sensitivity and bifurcation analysis [8, 35–39]. Thus, they allowed insights into some important aspects of the system's behavior, and the role played by the social measures. For example, analytical calculations provided a better understanding of the interventions required to control the disease, such as the interplay between governmental actions and the public response [39], and quarantine [35]. However, to our knowledge, no attempts were made to analytically solve complex systems of nonlinear differential equations stemming from these extended epidemiological models (neither from the models aimed to include the effects of mitigation measures nor from those trying to incorporate other relevant factors). Instead, computer simulations and/or numerical solving of differential equations are commonly used to compute and analyze the time evolution of the epidemic (e.g., to make comparisons with the actual epidemiological data). Consequently, despite the ability to include intricate details of the models, these studies lacked the full analytical approach to establish direct functional relations between variables and outcomes, thus missing the advantages of having analytical formulas describing the entire time evolution of the system variables.

While the advantages of the analytical approach are clear, all of the studied models in epidemiology, including the very basic ones such as SIR (Susceptible-Infected-Removed [40]), are nonlinear and the corresponding differential equations cannot be solved in a straightforward manner [41]. Nevertheless, in the last two decades, there was significant progress in

the field. To our knowledge, the earliest advances in this direction appeared with the turn of the century and were related to the SIR model, on networks [42] and its stochastic variant [43], followed by solutions given in the forms of convergent series, for SIR [44] and then also for SIR and SIS (Susceptible-Infected-Susceptible) models [45]. Further progress was made by Harko et al. in 2014 [46], by providing the SIR model analytical solutions, albeit in parametric form and up to an integral inexpressible by elementary functions. COVID-19 pandemic has intensified the efforts in this direction, resulting in new forms of solutions for SIR model: as infinite series (using Asymptotic Approximants method) [47], as an inverse solution with an approximated integral [48], using integrals inexpressible in terms of elementary functions [49], and a direct approximated solution [50, 51]. Some of these approaches preserve (approximative) integrability even when constant model parameters (such as infection rate) are replaced by time-varying functions (though with certain constraints). Recently, there has been also some progress even with compartmental models more complex than the basic SIR variant. More precisely, papers [52] and [53] analytically treat SEIR (Susceptible-Exposed-Infected-Removed) model and find, respectively, a solution in the form of a well converging infinite series and as an exact solution to an approximative reduced model.

Along with the attempts to analytically solve the equations governing the epidemic dynamics, there was an ongoing effort to find useful analytical relations between the relevant epidemiological variables. One such simple but transcendental equation, relating the basic reproductive number with the final size of the susceptible compartment, was an immediate consequence of the SIR model [40], and a similar result was obtained for the SEIR model [53] (the robustness of such relations is discussed in [54]). Moreover, it often turns out to be possible to derive useful simple analytical expressions for the time of the infection peak and/or the fraction of immunized required to stop the epidemic [48, 50, 51, 53, 55, 56]. These formulas, obtained at a low cost of applying practically negligible approximations to the starting equations or intermediary expressions, turn out to be very accurate (when compared to precise numerical computations).

All these analytical results were obtained only in the context of SIR and SEIR models, and the presence of intervention measures likely renders them unus-

able. Therefore, this study aims, for the first time, to establish a realistic—analytically solvable—model of COVID-19 dynamics in the presence of social distancing measures and to demonstrate the benefits of such an approach. The model is a generalization of the compartmental SEIR model—so-called SPEIRD [57,58]—that accounts for the influence of social measures by mathematically representing them as an effect that removes susceptibles from the transmission process (and places them in a newly introduced Protected compartment). A similar approach to introduce the effects of distancing in compartmental models can be found in [32,34–37] and is in certain aspects advantageous over simply varying transmission coefficients in time, implemented in many models [4,8,22,33,38,39]. SPEIRD also introduces additional compartments that directly correspond to epidemiological observables: the number of detected cases and fatalities. The model was introduced in [57], but due to the complex system of nonlinear differential equations, no attempts were made to solve them analytically. However, it turned out that, despite complicated equations, it was possible to analytically compute the closed-form expression for the number of infected cases as a function of time. This partial result was published in [58] and presents a starting point in this study. However, due to its complexity, we were unable to make further progress toward computing other system variables. We only recently managed to analytically compute the time evolution of all relevant variables (i.e., the closed-form expressions for the full-time evolution of the number of confirmed (detected) cases and fatalities). These two variables have been used as crucial measures for tracking epidemic progression and its severity, and this manuscript presents the full analytical treatment of the equations by deriving their closed-form mathematical expressions.

The time evolutions derived here allow us to analytically investigate the effect of different model parameters on the infection outcome and to recognize particular interplays. Knowing explicitly the relations between input and output variables not only vastly simplifies our ability to extract model parameters from experimental data (e.g., by distinguishing special regimes in which equations have characteristic behavior [58]) but, more importantly, to straightforwardly draw conclusions that may simplify public policy decision making. In particular, the asymptotic expressions obtained here for the cumulative numbers of COVID-19 detected cases and fatalities, quantitatively reveal a simple interplay

between the basic reproduction number  $R_0$ , the strength of introduced social measures, and the timing of their introduction. Namely, it turns out, as we show in Sect. 4 and further elaborate in Sect. 5, that more flexible, i.e., relaxed measures can be easily afforded if they are timely introduced (to the same overall effect as with far more stringent measures introduced just a week or two later). Moreover, we provide simple analytical expressions for estimating the timing of the peak, the tipping points of the epidemic wave, as well as the maximum of detected cases per day. Providing an analytical framework to understand such epidemiological behavior may have a significant impact both on the economy and the quality of human lives.

While the obtained results and conclusions were based on the study of the COVID-19 pandemic (and tested on corresponding epidemiological data), the analysis presented here is of general validity and therefore directly applicable to any possible infection outbreak in the future. While at this stage of the COVID-19 pandemic, we already have additional tools to combat the disease (e.g., vaccines and mounting clinical experience), general conclusions drawn from the models like this one can be a particularly valuable aid in the initial stages of any new epidemic.

## 2 Methodology

To assess the dynamics of COVID-19 infection, we employ a mechanistic model SPEIRD, which we developed in Refs. [57,58]. More precisely, concerning the standard compartmental models in epidemiology [25–27], which comprise susceptible ( $S$ ), exposed ( $E$ ), infectious ( $I$ ), and undiagnosed recovered ( $R$ ) pools, we added a few additional compartments. These are introduced to take into account the available data (direct observable quantities), such as the total number of detected (confirmed and thereupon quarantined) cases ( $D$ ), active cases ( $A$ ), and fatalities ( $F$ ). It also accounts for the effects of the social protection measures by adding a compartment ( $P$ ) of protected individuals (denoting those effectively removed from susceptible category due to social distancing). The corresponding equations, describing the model dynamics, read:

$$\frac{dS}{dt} = -\frac{\beta SI}{N} - \frac{dP}{dt}, \quad (1)$$

$$\frac{dP}{dt} = \frac{\alpha S}{1 + (t_0/t)^n}, \tag{2}$$

$$\frac{dE}{dt} = \frac{\beta SI}{N} - \sigma E, \tag{3}$$

$$\frac{dI}{dt} = \sigma E - \gamma I - \epsilon \delta I, \tag{4}$$

$$\frac{dR}{dt} = \gamma I, \tag{5}$$

$$\frac{dD}{dt} = \epsilon \delta I, \tag{6}$$

$$\frac{dA}{dt} = \epsilon \delta I - hA - mA, \tag{7}$$

$$\frac{dF}{dt} = mA. \tag{8}$$

In the above equations,  $N$  stands for the total population number, while parameters have the following meaning:  $\beta$ — the transmission rate;  $\alpha$ — strength of the social measures;  $\sigma$ — the inverse of the latency period;  $\gamma$ — the inverse of the infectious period;  $\delta$ — the inverse of the infected detection period;  $\epsilon$ — the detection efficiency;  $h$  and  $m$ — the recovery and the mortality rate, respectively. According to [59–61], we assume  $\sigma = 1/3 \text{ day}^{-1}$  and  $\gamma = 1/4 \text{ day}^{-1}$ . The gradual effect of social measures is introduced through Eq. (2) where  $t_0$  denotes the time when the measures are enforced. In [58], it was shown that Hill function [62] can be reliably replaced by the step function of the form  $\alpha \theta(t - t_0)$ , which we further apply. We also assume that, after  $t_0$ , the 2<sup>nd</sup> term in Eq. (1) dominates over the 1<sup>st</sup> term, i.e.,  $S(t) \sim e^{-\alpha t}$ , which we previously numerically showed to hold well for a wide range of countries in the first COVID-19 wave [58].

In Fig. 1, we provide a schematic representation of the SPEIRD model (Eqs. (1)-(8)). Thus, Eq. (1) determines the rate of depletion of the susceptible population due to both the infection process and the social distancing measures. These measures result in a transition of the susceptible to the protected compartment, described by Eq. (2). In Eq. (3), the exposed pool increases due to the infection events. Simultaneously, it decreases due to a transition to the infectious compartment with the rate  $\sigma$ . Equation (4) describes how the number of infectious individuals grows due to the transition from exposed to the infectious category, while it decreases with the rate  $\gamma$  (recovery of undiagnosed infected to  $R$  compartment) or with rate  $\epsilon \delta$  (corresponding to their detection and subsequent quarantine, resulting in a transition to the detected compartment  $D$ ). Equation (7) fixes

the rate at which the active compartment is depleted through two channels – by being healed (rate  $h$ ) or by dying from the virus (rate  $m$ ). Equation (8) describes the growth of the fatalities.

The model corresponds to the infection phase, where social distancing measures are first introduced (in our case, the first COVID-19 wave), corresponding to the effective transition from  $S$  to  $P$  compartment. As the measures later got eased, there can also be a transition from  $P$  back to  $S$ . This is, for simplicity, not implemented in SPEIRD (and usually neither in similar models, see e.g. Refs. [32,34–37]), i.e., only the first phase of epidemics (and the social measure introduction) is considered. We implement our model deterministically, as publicly available COVID-19 counts [63] are very high in most countries, making the relative importance of fluctuations low, and the deterministic description appropriate [62]. The advantage of such an approach is the analytical tractability and more intuitive understanding of the obtained results.

Despite the complexity of the system of equations (1)-(8), we show that the model can be analytically treated. As a starting point in our calculation, we use the explicit expression for the number of infectious individuals as a function of time, obtained in [58]:

$$I(t) = \theta(t_0-t)I_0e^{\lambda+t} + \theta(t-t_0)I_0e^{\lambda+t_0}e^{-\frac{\gamma+\epsilon\delta+\sigma}{2}(t-t_0)} \times \frac{K\left(\frac{\gamma+\epsilon\delta-\sigma}{\alpha}, \frac{2\sqrt{e^{-\alpha(t-t_0)}\beta\sigma}}{\alpha}\right)}{K\left(\frac{\gamma+\epsilon\delta-\sigma}{\alpha}, \frac{2\sqrt{\beta\sigma}}{\alpha}\right)}, \tag{9}$$

where  $K(n, x)$  stands for the modified Bessel function of the second kind [64],  $\lambda_+ = \frac{\sqrt{(\gamma+\epsilon\delta-\sigma)^2+4\beta\sigma}-(\gamma+\epsilon\delta+\sigma)}{2}$ ,  $\theta(t)$  denotes Heaviside step function and  $I_0$  is the initial number of infectious individuals in population.

The main result of this paper is the derivation of the time-dependent expressions for the numbers of fatalities  $F(t)$  and detected cases  $D(t)$ , which are continuously tracked and publicly available quantities for a vast number of countries and regions [63]. The analytical derivations of these expressions are presented in Appendix A. Essentially, Eqs. (6)-(8) lead to two disentangled differential equations determining  $F(t)$  and  $D(t)$ :

$$\frac{d^2 F(t)}{dt^2} + (h + m) \frac{dF(t)}{dt} - m\epsilon\delta I(t) = 0, \tag{10}$$



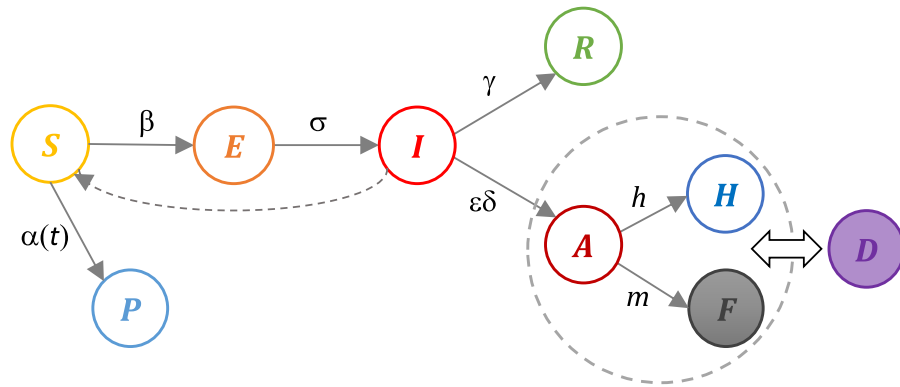


**Fig. 1** Scheme of the SPEIRD model. The compartments are represented with circles and named as indicated in the text. The transitions between different compartments are denoted by arrows, with labels corresponding to the appropriate transition rates, as explained in the text. The two main categories for our

study (also corresponding to widely tracked observable quantities) – fatalities (*F*) and detected cases (*D*) are denoted by the full gray and purple circles, respectively. The dashed circle indicates that *A*, *H*, and *F* compartments from the original model compose the detected cases *D*

$$D(t) = \epsilon\delta \int I(t) dt + C. \tag{11}$$

Here,  $I(t)$  is given by Eq. (9) and  $C$  stands for the constant of integration. All constants of integration are determined from the requirement of continuity of functions, their first derivatives, and/or the initial conditions:  $F(0) = 0$  and  $D(0) = D_0$ , where  $D_0$  is the initial number of detected cases at onset of infection progression in a population.

Solving these equations is highly nontrivial due to the complex form (see Eq. (9)) of the function  $I(t)$ . To accomplish this task, aside from commonly used methods for solving differential equations (i.e., known methods for second-order inhomogeneous Cauchy–Euler equation), we used a number of special properties of modified Bessel functions of the first and second kind, of upper incomplete gamma functions, and of regularized generalized hypergeometric functions, as detailed in Appendix A.

### 3 Analytical results

Using the methodology outlined in the previous section, in Appendix A, we derived closed-form expressions for the number of fatalities and the cumulative number of detected cases, as functions of time. The number of fatalities  $F(t)$  has the following form:

$$F(t) = \theta(t_0 - t) \frac{I_0 \epsilon \delta}{\lambda_+} \frac{m}{m + h} \left\{ -1 + \frac{\lambda_+}{h + m + \lambda_+} e^{-(h+m)t} + \frac{h + m}{h + m + \lambda_+} e^{\lambda_+ t} \right\} + \theta(t - t_0) \left\{ C_1 + C_2 e^{-(h+m)t} + C_1(t) + C_2(t) \left( \frac{2\sqrt{\beta\sigma}}{\alpha} \right)^{\frac{2(h+m)}{\alpha}} e^{-(h+m)t} \right\}, \tag{12}$$

where:

$$C_1(t) = C_0 \left[ \left( \frac{\sqrt{\beta\sigma}}{\alpha} \right)^{\frac{\gamma + \epsilon\delta - \sigma}{\alpha}} e^{-(\gamma + \epsilon\delta)t} \Gamma \left( \frac{\gamma + \epsilon\delta}{\alpha} \right) \times {}_1\tilde{F}_2 \left( \frac{\gamma + \epsilon\delta}{\alpha}; 1 + \frac{\gamma + \epsilon\delta}{\alpha}, 1 + \frac{\gamma + \epsilon\delta - \sigma}{\alpha}; \frac{e^{-\alpha t} \beta \sigma}{\alpha^2} \right) - \left( \frac{\sqrt{\beta\sigma}}{\alpha} \right)^{-\frac{\gamma + \epsilon\delta - \sigma}{\alpha}} e^{-\sigma t} \Gamma \left( \frac{\sigma}{\alpha} \right) \times {}_1\tilde{F}_2 \left( \frac{\sigma}{\alpha}; 1 + \frac{\sigma}{\alpha}, 1 + \frac{\sigma - \gamma - \epsilon\delta}{\alpha}; \frac{e^{-\alpha t} \beta \sigma}{\alpha^2} \right) \right]$$

$$\begin{aligned}
 C_2(t) = & -C_0 \left[ \left( \frac{\sqrt{\beta\sigma}}{\alpha} \right)^{\frac{\gamma+\epsilon\delta-\sigma}{\alpha}} \Gamma \left( \frac{\gamma+\epsilon\delta-h-m}{\alpha} \right) \right. \\
 & \times {}_1\tilde{F}_2 \left( \frac{\gamma+\epsilon\delta-h-m}{\alpha}; 1 + \frac{\gamma+\epsilon\delta-h-m}{\alpha}, 1 + \frac{\gamma+\epsilon\delta-\sigma}{\alpha}; \frac{e^{-\alpha t} \beta\sigma}{\alpha^2} \right) \\
 & - \left( \frac{\sqrt{\beta\sigma}}{\alpha} \right)^{-\frac{\gamma+\epsilon\delta-\sigma}{\alpha}} \Gamma \left( \frac{\sigma-h-m}{\alpha} \right) \\
 & \times {}_1\tilde{F}_2 \left( \frac{\sigma-h-m}{\alpha}; 1 + \frac{\sigma-h-m}{\alpha}, 1 + \frac{\sigma-\gamma-\epsilon\delta}{\alpha}; \frac{\beta\sigma}{\alpha^2} \right) \left. \right] \\
 & \times \frac{\pi}{2} \operatorname{csc} \left[ \frac{\pi(\gamma+\epsilon\delta-\sigma)}{\alpha} \right] \tag{13}
 \end{aligned}$$

$$\begin{aligned}
 C_1 = & I_0\epsilon\delta \frac{m}{(h+m)} \frac{e^{\lambda+t_0} - 1}{\lambda_+} - C_0 \\
 & \left[ \left( \frac{\sqrt{\beta\sigma}}{\alpha} \right)^{\frac{\gamma+\epsilon\delta-\sigma}{\alpha}} \Gamma \left( \frac{\gamma+\epsilon\delta}{\alpha} \right) \right. \\
 & \times {}_1\tilde{F}_2 \left( \frac{\gamma+\epsilon\delta}{\alpha}; 1 + \frac{\gamma+\epsilon\delta}{\alpha}, 1 + \frac{\gamma+\epsilon\delta-\sigma}{\alpha}; \frac{\beta\sigma}{\alpha^2} \right) \\
 & - \left( \frac{\sqrt{\beta\sigma}}{\alpha} \right)^{-\frac{\gamma+\epsilon\delta-\sigma}{\alpha}} \Gamma \left( \frac{\sigma}{\alpha} \right) \\
 & \times {}_1\tilde{F}_2 \left( \frac{\sigma}{\alpha}; 1 + \frac{\sigma}{\alpha}, 1 + \frac{\sigma-\gamma-\epsilon\delta}{\alpha}; \frac{\beta\sigma}{\alpha^2} \right) \left. \right] \\
 & \times \frac{\pi}{2} \operatorname{csc} \left[ \frac{\pi(\gamma+\epsilon\delta-\sigma)}{\alpha} \right] \tag{14}
 \end{aligned}$$

$$\begin{aligned}
 C_2 = & I_0\epsilon\delta \frac{m}{(h+m)} \frac{e^{-(h+m)t_0} - e^{\lambda+t_0}}{h+m+\lambda_+} \\
 & + C_0 \left[ \left( \frac{\sqrt{\beta\sigma}}{\alpha} \right)^{\frac{\gamma+\epsilon\delta-\sigma}{\alpha}} \Gamma \left( \frac{\gamma+\epsilon\delta-h-m}{\alpha} \right) \right. \\
 & \times {}_1\tilde{F}_2 \left( \frac{\gamma+\epsilon\delta-h-m}{\alpha}; 1 + \frac{\gamma+\epsilon\delta-h-m}{\alpha}, 1 + \frac{\gamma+\epsilon\delta-h-m}{\alpha} \right) \left. \right]
 \end{aligned}$$

In these formulas  $C_0 = \frac{I_0\epsilon\delta}{\alpha} \frac{m}{h+m} e^{\lambda+t_0} / K \left( \frac{\gamma+\epsilon\delta-\sigma}{\alpha}, \frac{2\sqrt{\beta\sigma}}{\alpha} \right)$ , while  ${}_p\tilde{F}_q(a_1, a_2, \dots, a_p; b_1, b_2, \dots, b_q; z)$  denotes regularized generalized hypergeometric function [65].

While these expressions jointly constitute the exact solution to the differential equations governing the dynamics of  $F(t)$ , their form is too complex to convey a useful conclusion about the epidemic dynamics. However, by applying a combination of appropriate mathematical transformations and by using Hankel’s asymptotic expression for Bessel functions (see Appendix A.1 for details), we arrive at the following approximate expression for  $F(t)$ :

$$\begin{aligned}
 F(t) = & I_0\epsilon\delta \frac{m}{h+m} \\
 & \left[ \theta(t_0 - t) \left( \frac{e^{\lambda+t} - 1}{\lambda_+} + \frac{e^{-(h+m)t} - e^{\lambda+t}}{h+m+\lambda_+} \right) \right. \\
 & + \theta(t - t_0) \\
 & \left( \frac{e^{\lambda+t_0} - 1}{\lambda_+} - e^{-(h+m)t} \frac{e^{(h+m+\lambda_+)t_0} - 1}{h+m+\lambda_+} \right. \\
 & \left. + \frac{2}{\alpha} \left( \frac{2\sqrt{\beta\sigma}}{\alpha} \right)^{-\frac{\gamma+\epsilon\delta+\sigma}{\alpha} + \frac{1}{2}} e^{\lambda+t_0 + \frac{2\sqrt{\beta\sigma}}{\alpha}} \right. \\
 & \times \left\{ \Gamma \left( \frac{\gamma+\epsilon\delta+\sigma}{\alpha} - \frac{1}{2}, \frac{2\sqrt{e^{-\alpha(t-t_0)}\beta\sigma}}{\alpha} \right) \right. \\
 & - \Gamma \left( \frac{\gamma+\epsilon\delta+\sigma}{\alpha} - \frac{1}{2}, \frac{2\sqrt{\beta\sigma}}{\alpha} \right) \\
 & + \left( \frac{2\sqrt{e^{-\alpha(t-t_0)}\beta\sigma}}{\alpha} \right)^{\frac{2(h+m)}{\alpha}} \\
 & \times \left[ \Gamma \left( \frac{\gamma+\epsilon\delta+\sigma-2(h+m)}{\alpha} - \frac{1}{2}, \frac{2\sqrt{\beta\sigma}}{\alpha} \right) \right. \\
 & - \Gamma \left( \frac{\gamma+\epsilon\delta+\sigma-2(h+m)}{\alpha} \right. \\
 & \left. \left. - \frac{1}{2}, \frac{2\sqrt{e^{-\alpha(t-t_0)}\beta\sigma}}{\alpha} \right) \right] \left. \right] \tag{16}
 \end{aligned}$$

This expression replaces expressions (12)-(15) while not significantly deviating from the full solution (the deviations are essentially negligible, having in mind the limited precision with which we know most of the COVID-19 epidemiological parameters).

As expected, the  $F(t)$  saturates at some maximal, asymptotic value as  $t \rightarrow \infty$  (for details see Appendices A.3 and A.4). This value corresponds to the total (final) number of COVID-19 fatalities  $F_{fin}$  in the observed epidemic outburst:

$$F_{fin} \approx \frac{2I_0\epsilon\delta}{\alpha} \frac{m}{h+m} \left(\frac{2\sqrt{\beta\sigma}}{\alpha}\right)^{-\frac{\gamma+\epsilon\delta+\sigma}{\alpha}+\frac{1}{2}} e^{\lambda_+t_0+\frac{2\sqrt{\beta\sigma}}{\alpha}} \times \Gamma\left(\frac{\gamma+\epsilon\delta+\sigma}{\alpha}-\frac{1}{2}\right). \tag{17}$$

Furthermore, due to the fact that for realistic values of epidemiological parameters [58]  $(\gamma + \epsilon\delta + \sigma)/\alpha - 1/2$  is high enough, we utilize Stirling’s formula [66] (for large  $n$ ):  $\Gamma(n + 1) \approx \sqrt{2\pi n} \left(\frac{n}{e}\right)^n$ . After making use of  $4\beta\sigma \gg (\gamma + \delta\epsilon - \sigma)^2$  (for multiple times) Eq. (17) reduces to:

$$F_{fin}^{approx} \approx 2D_0 \frac{m}{h+m} e^{\frac{3}{2}} \sqrt{\frac{2\pi/\alpha}{\gamma+\epsilon\delta+\sigma-\frac{3}{2}\alpha}} \lambda_+ \times \left(\frac{2\lambda_+ + \gamma + \epsilon\delta + \sigma}{\gamma + \epsilon\delta + \sigma - \frac{3}{2}\alpha}\right)^{\frac{1}{2}-\frac{\gamma+\epsilon\delta+\sigma}{\alpha}} e^{(t_0+\frac{2}{\alpha})\lambda_+}, \tag{18}$$

where  $D(0) = D_0 = I_0\epsilon\delta/\lambda_+$ .

By applying a similar procedure, we straightforwardly obtain the equivalent expressions for the time evolution of the number of detected cases (see Appendix A.2). For brevity, we here provide only the final results:

$$D(t) = \frac{I_0\epsilon\delta}{\lambda_+} \left( \theta(t_0 - t)e^{\lambda_+t} + \theta(t - t_0)e^{\lambda_+t_0} \times \left\{ 1 + \frac{2\lambda_+}{\alpha} \left(\frac{2\sqrt{\beta\sigma}}{\alpha}\right)^{-\frac{\gamma+\epsilon\delta+\sigma}{\alpha}+\frac{1}{2}} e^{\frac{2\sqrt{\beta\sigma}}{\alpha}} \times \left[ \Gamma\left(\frac{\gamma+\epsilon\delta+\sigma}{\alpha}-\frac{1}{2}, \frac{2\sqrt{e^{-\alpha}(t-t_0)}\beta\sigma}}{\alpha}\right) - \Gamma\left(\frac{\gamma+\epsilon\delta+\sigma}{\alpha}-\frac{1}{2}, \frac{2\sqrt{\beta\sigma}}{\alpha}\right) \right] \right\} \right) \tag{19}$$

and for the total number of detected cases at the end of the epidemic wave:

$$D_{fin} \approx \frac{2I_0\epsilon\delta}{\alpha} \left(\frac{2\sqrt{\beta\sigma}}{\alpha}\right)^{-\frac{\gamma+\epsilon\delta+\sigma}{\alpha}+\frac{1}{2}} e^{\lambda_+t_0+\frac{2\sqrt{\beta\sigma}}{\alpha}} \times \Gamma\left(\frac{\gamma+\epsilon\delta+\sigma}{\alpha}-\frac{1}{2}\right), \tag{20}$$

that can be again approximated to the form:

$$D_{fin}^{approx} \approx 2D_0 e^{\frac{3}{2}} \sqrt{\frac{2\pi/\alpha}{\gamma+\epsilon\delta+\sigma-\frac{3}{2}\alpha}} \lambda_+ \times \left(\frac{2\lambda_+ + \gamma + \epsilon\delta + \sigma}{\gamma + \epsilon\delta + \sigma - \frac{3}{2}\alpha}\right)^{\frac{1}{2}-\frac{\gamma+\epsilon\delta+\sigma}{\alpha}} e^{(t_0+\frac{2}{\alpha})\lambda_+}. \tag{21}$$

Consequently, the estimate for Case Fatality Rate (CFR), which is defined as the final number of fatalities per detected cases ( $CFR = F_{fin}/D_{fin}$ ), acquires a simple form [67], involving a ratio of mortality ( $m$ ) and healing ( $h$ ) rates:

$$CFR = \frac{m}{h+m}, \tag{22}$$

further supporting that our analytical derivation is plausible.

The explicit formulas (18) and (21) provide analogs—though now in the entirely different context with social distancing—of the final size (i.e. asymptotic value) relations for SIR [40,54] and SEIR models [53]. Based on our analytical solution, we can also provide a fairly simple relation for the timing of the epidemic peak (see Appendix A.5 for details), which is another quantity that has been previously analytically derived in simpler scenarios of SIR [48,50,51,55,56] and SEIR [53] models:

$$t_{max} = t_0 + \frac{1}{\alpha} \ln \left[ \frac{16\beta\sigma}{(2(\gamma + \epsilon\delta + \sigma) - \alpha)^2} \right]. \tag{23}$$

From Eq. (23), we can also obtain the maximal number of detected cases per day during the outburst:

$$\left(\frac{dD}{dt}\right)_{max} = D_0\lambda_+ e^{\lambda_+(t_0+\frac{2}{\alpha})+\frac{1}{2}} \left(\frac{4\sqrt{\beta\sigma}}{2(\gamma + \epsilon\delta + \sigma) - \alpha}\right)^{\frac{1}{2}-\frac{\gamma+\epsilon\delta+\sigma}{\alpha}} \tag{24}$$

which we will further analyze in the next section.

The infection tipping points (see Appendix A.5) correspond to the inflection points of the bell-shaped infected curve. We can explicitly express the two tipping points, from which we can obtain the duration of the epidemic peak (cf. Figure 1D in [58]), corresponding to the time interval between these two points:

$$\Delta t_{peak} = \frac{4}{\alpha} \ln \left( \frac{\gamma + \epsilon\delta + \sigma + \sqrt{\alpha(\gamma + \epsilon\delta + \sigma - \frac{\alpha}{4})}}{\gamma + \epsilon\delta + \sigma - \alpha/2} \right). \quad (25)$$

When  $\alpha \ll (\gamma + \sigma)$  this formula effectively simplifies to:

$$\Delta t_{peak} \approx \frac{4}{\sqrt{\alpha(\gamma + \epsilon\delta + \sigma)}}, \quad (26)$$

where we used [68]  $\ln(1+x) \approx x$  for  $x \ll 1$ . Note that  $\Delta t_{peak}$  is independent of the transmission rate  $\beta$ , which is a nontrivial result.  $\Delta t_{peak}$  provides an estimate of the time interval during which the infected are at a high level, and the chance of contracting the infection is the highest.

#### 4 Numerical analysis

To test the model reliability, we first compare our full-fledged predictions for case counts (detected cases and fatalities) with the observed data counts for three representative countries: Austria, Switzerland, and Israel. Figure 2 shows that we obtain an overall good agreement between our predictions and the data for all three countries. In particular, we see that the time delay, much discussed in interpreting COVID-19 case counts data [12, 61], is also well reproduced. This agreement provides confidence that the analytical expressions, which we derived from our model, indeed reasonably represent the observed case counts data.

The obtained results allow us to analyze the effect of each model parameter on  $D(t)$  and  $F(t)$  curves. For succinctly presenting the results in Figs. 3, 4, 5 and 6, we will further use the parameter values that were extracted for Israel in Fig. 2. We note that the obtained results are independent of the analyzed country, as long as the data are continuously tracked with moderate testing capacities and fairly transparent reporting policies. First, we will consider the influence of the  $\epsilon$  parameter—the fraction of the infections that are

detected and consequently quarantined. We here, and in the subsequent analysis, fix the initial (observed) number of detected cases  $D_0 = D(t=0)$ . The trivial (direct) proportionality dependence of  $D(t)$  on  $\epsilon$  in Eq. (6) then gets absorbed in  $D_0$ , so that we investigate the nontrivial effect of the quarantine ( $\epsilon$ ) on the case count dynamics from Eq. (4). For this, we opt for two limiting cases  $\epsilon = 0.1$  and  $\epsilon = 0.5$ , which respectively correspond to the low and high detection rates inferred from the observed data [58]. From Fig. 3, which represents the time evolution of detected cases and fatalities, we observe that a substantial change of this parameter leads to at most  $\sim 20\%$  change in saturation value of  $D$  and  $F$ . In comparison to changes due to variations of other parameters, see below, we will see that this is a minor effect. Expectedly, better detection efficacy (i.e., the higher  $\epsilon$  value) leads to lower overall numbers of case counts, simply because the larger part of infected individuals is timely quarantined. The value of  $\epsilon$  has practically no impact on the steepness of these time-evolution curves. Consequently, detected cases and fatalities are nearly independent of  $\epsilon$ , and, for simplicity, we will further set this value to be 0.1. (Note that, if not indicated otherwise, full-fledged expressions are used for generating predictions through the entire section.)

Next, we assess how sensitive case counts are on the initial slope (on a log scale) of the exponential growth of the infectious curve, quantified by  $\lambda_+$ . Indirectly, in this way, we also test the dependence of the curves on the closely related basic reproduction number  $R_0$  (quantifying inherent virus transmissibility in population [69]), which relates to  $\lambda_+$  by  $R_0 = \beta/\gamma = \frac{\lambda_+^2 + \lambda_+(\gamma + \epsilon\delta + \sigma) + (\gamma + \epsilon\delta)\sigma}{\sigma\gamma}$  [57, 70]. To this end, we vary  $\lambda_+$  in the range between 0.1/day and 0.4/day, based on our previously inferred  $\lambda_+$  values for a large number of analyzed countries [70, 71]. From the left plot in Fig. 4, we observe that  $D(t)$  is highly sensitive to this parameter, to the extent that the linear–linear plot is unable to adequately illustrate this dependency. The log–linear plot in the inset is much better suited for this: it clearly demonstrates that the greater the  $\lambda_+$  is, the  $D(t)$  curve is steeper, and the final saturation value becomes exponentially larger. The same tendency is preserved in the case of  $F(t)$  dependence on  $\lambda_+$  (see middle plot in Fig. 4), where we *ab initio* opt for log–linear display.

To gain some further insight on the influence of  $\lambda_+$  on case counts saturation values, we note that the dom-



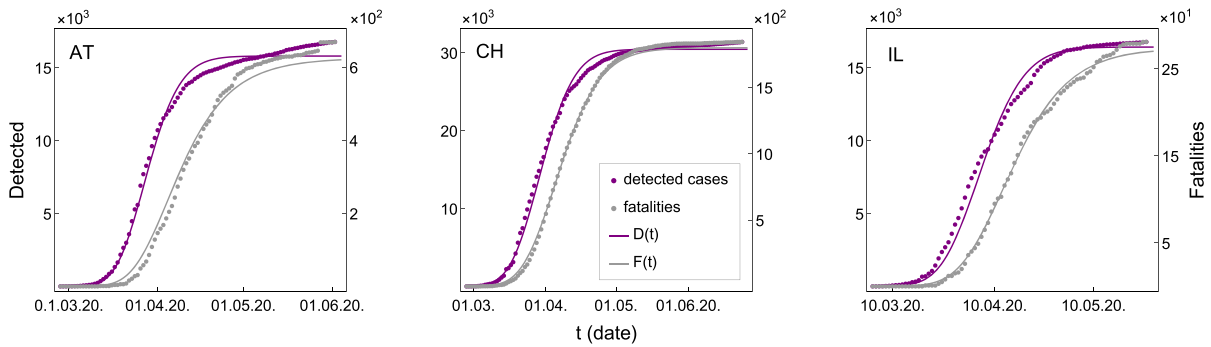
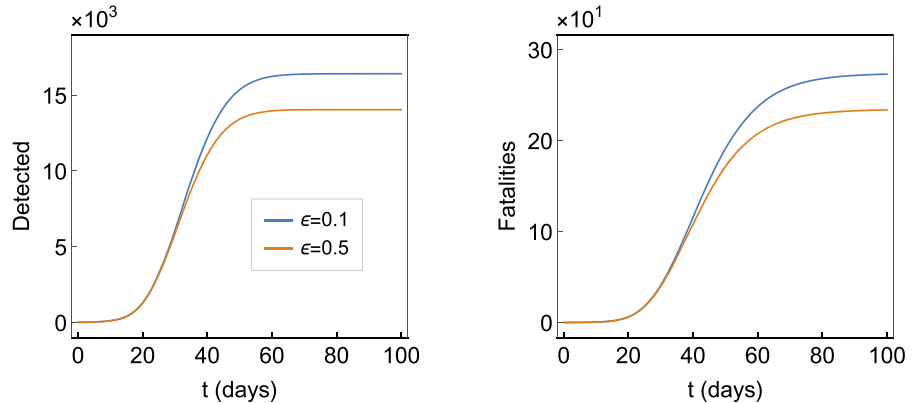


**Fig. 2** Comparison between model prediction and data for Austria (the left plot), Switzerland (the central plot), and Israel (the right plot), as indicated by abbreviations in the upper left corners. The predictions are generated for the evolution of detected cases (the purple curves) and fatalities (the gray curves). The observed detected counts are denoted as purple dots, while the

fatality counts are represented by gray dots. The left and the right y-axis of each plot corresponds to detected cases and fatalities, respectively, while the ticks on the x-axis denote the dates given in DD/MM/YY format. The data for detected cases and fatalities are taken from [63]

**Fig. 3** The dependence on the infection detection efficiency  $\epsilon$  of detected cases (the left plot) and fatalities (the right plot). The blue and the orange curves correspond to  $\epsilon = 0.1$  and  $\epsilon = 0.5$ , respectively



inant  $\lambda_+$  dependence in Eqs. (18) and (21) is exponential, of the form  $e^{(t_0 + \frac{2}{\alpha})\lambda_+}$ . However, it can be shown that  $\lambda_+$  terms outside of the exponent in Eqs. (18) and (21) still contribute by effectively lowering the exponent from  $e^{(t_0 + \frac{2}{\alpha})\lambda_+}$  to  $t_\alpha = t_0 + 1/\alpha$ . In Ref. [57], we introduced  $t_\alpha$  as the, so-called, protection time (the time at which  $\sim \frac{1}{2}$  of the population moves to the protected category), so that there is a simple, overall, dependence of the case counts on  $\lambda_+$  as  $\sim e^{t_\alpha \lambda_+}$ .

The  $\lambda_+$  dependence of three curves:  $D_{fin}$ ,  $D_{fin}^{approx}$  and our estimate  $\sim e^{(t_0 + \frac{1}{\alpha})\lambda_+}$ , is presented in the rightmost plot of Fig. 4. The practically overlapping  $D_{fin}$  and  $D_{fin}^{approx}$  curves confirm the adequacy of the approximation applied in Eqs. (18) and (21). Moreover, the fact that the simple exponential dependence  $e^{t_\alpha \lambda_+}$  very well qualitatively and quantitatively reproduces

$D(\lambda_+)$ , highlights usefulness of the protection time in assessing infection risks.

Finally, we concentrate on the effect of the social distancing strength  $\alpha$  on the case counts. We assume that  $\alpha$  lies in the range between 0.03 and 0.3, as inferred from the observed data by our previous numerical analysis [58]. All plots on Fig. 5 are again presented in log-linear scale. From the left and central plot in Fig. 5, we see that both  $D(t)$  and  $F(t)$  are strongly affected by the change of  $\alpha$ . As the epidemic progresses, the stronger social measures result in a significantly lower plateau of case counts. The effect of  $\alpha$  on these two observables is the opposite of the one of  $\lambda_+$ , as expected.

To further clarify the dependence of  $D$  and  $F$  on  $\alpha$ , we again use Eq. (21). After taking a logarithm, we obtain:

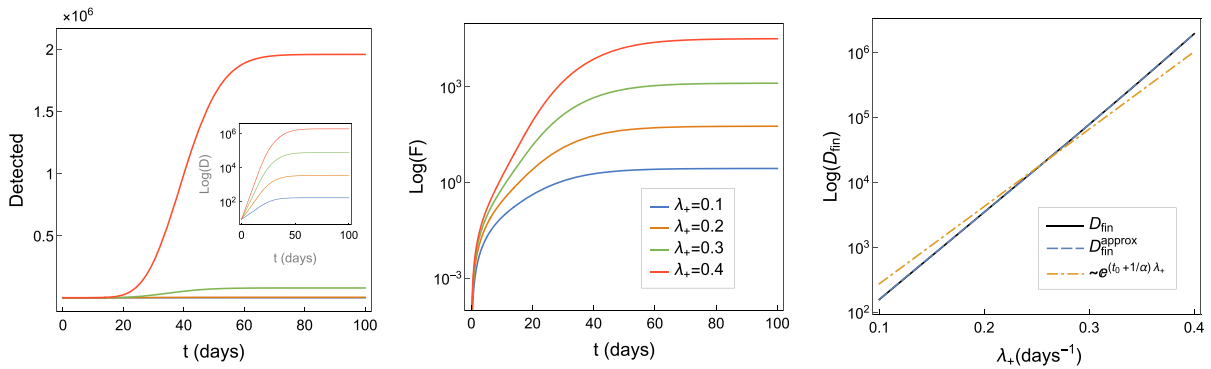


**Fig. 4** The effect of initial slope of infectious curve  $\lambda_+$  on the main observables. The time evolution of detected cases is presented in the left plot, with inset on a more pronounced log-linear plot. The central plot shows fatalities versus time on a log-linear scale.  $\lambda_+$  values are indicated in the legend. In the right plot,  $\lambda_+$

dependence of detected cases at saturation is displayed on a log-linear scale.  $D_{fin}$ ,  $D_{fin}^{approx}$  and  $e^{t_0 \lambda_+}$  are denoted by the solid black, the dashed blue and dot-dashed orange curves, respectively

$$\ln(D_{fin}^{approx}) \approx \kappa_1 + \frac{2\lambda_+}{\alpha} + \left(\frac{\kappa_2}{\alpha} - 1\right) \ln\left(\kappa_2 - \frac{3}{2}\alpha\right) - \frac{\ln(\alpha)}{2}, \tag{27}$$

where  $\kappa_1 = \ln(2D_0\lambda_+\sqrt{2\pi}) + \lambda_+t_0 + \frac{3}{2} + \left(\frac{1}{2} - \frac{\gamma+\epsilon\delta+\sigma}{\alpha}\right) \times \ln(\gamma + \epsilon\delta + \sigma + 2\lambda_+)$  and  $\kappa_2 = \gamma + \epsilon\delta + \sigma$ . The dominant term on the right-hand side of Eq. (27) is proportional to  $1/\alpha$ , i.e., the logarithmic terms could be neglected. To test this obtained simple dependence, in the rightmost plot of Fig. 5 we compare  $D_{fin}$ ,  $D_{fin}^{approx}$  and our estimate  $\sim e^{0.8\lambda_+/\alpha}$ , as functions of  $\alpha$ , on log-linear scale. The very good agreement between  $D_{fin}$  and  $D_{fin}^{approx}$  again confirms the validity of our approximations. Moreover, we demonstrate that the influence of the strength of social distancing on detected cases (and fatalities) can be reduced (at saturation) to a simple dependence of the form  $\sim e^{0.8\lambda_+/\alpha}$ .

From Figs. 4 and 5, we also see that  $\lambda_+$  has no significant effect on infection extinguishing time, i.e., the time for case counts to enter saturation. That is, its most prominent effect is on the total case counts. On the other hand, the strength of social distancing measures affects (i.e., diminish) both the total case counts and the time needed for extinguishing the infection.

Finally, in Fig. 6, we show how the maximal value of detected cases per day depend on  $\lambda_+$  and  $\alpha$ . For  $\lambda_+$ , we see that, similarly to  $D_{fin}$  and  $F_{fin}$ , simple exponential dependence  $e^{t_0 \lambda_+}$  well reproduces  $(\frac{dD}{dt})_{max}$ , further highlighting the importance of the lower protection

time for reducing the infection risks. For social distancing strength, we see that  $(\frac{dD}{dt})_{max}$  is also strongly affected by  $\alpha$ , where this dependence can be approximated by the simple expression  $\sim e^{0.6\lambda_+/\alpha}$ .

### 5 Discussion

The main goal of the present paper was to provide a fully-analytical treatment of our epidemiological model with introduced social distancing, which predicts observables that are readily accessible in a large-scale epidemic. We accomplished this task by calculating these observables as explicit functions of time, expressed in closed-form: Eqs. (16) and (19). Particularly useful are the derived (approximate) expressions (18) and (21) for the detected cases and fatalities at saturation (i.e., at the end of an epidemic wave). We tested the model predictions against the observed COVID-19 data, obtaining a very good agreement (as illustrated in Fig. 2).

The obtained analytical results facilitate a better understanding of the influence of individual epidemiological parameters on COVID-19 observables. In particular, the effect of varying the detection efficacy  $\epsilon$  (within reasonable boundaries) turned out to be exponentially smaller than the influence of the  $\lambda_+$  value, as illustrated in Figs. 3 and 4. Since the  $\lambda_+$  value is directly related to the basic reproduction number  $R_0$ , which characterizes the inherent biological transmission of the virus in an (initially) completely unprotected pop-

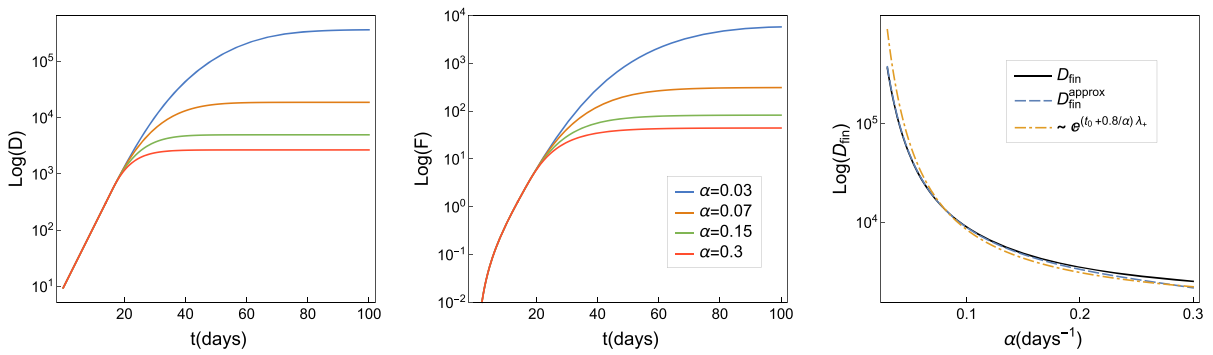
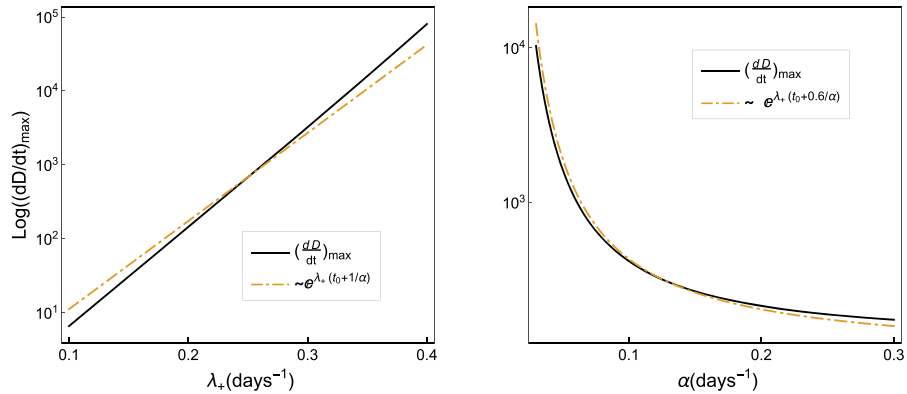


**Fig. 5** The effect of social distancing strength  $\alpha$  on the main observables. The time evolution of detected cases and fatalities are presented in the left and central plots, respectively.  $\alpha$  values are indicated in the legend. The  $\alpha$  dependence of detected

cases at saturation is assessed in the right plot.  $D_{fin}$ ,  $D_{fin}^{approx}$  and  $\sim e^{0.8\lambda_+/\alpha}$  are denoted by the solid black, the dashed blue and dot-dashed orange curves, respectively. All plots are on log-linear scale

**Fig. 6** The effect of initial slope of the infectious curve  $\lambda_+$  and social distancing strength  $\alpha$  on the maximum of detected cases per day  $(\frac{dD}{dt})_{max}$  is shown on the left and right plots, respectively.  $(\frac{dD}{dt})_{max}$  and approximate expressions are denoted by the solid black and dot-dashed orange curves, respectively. All plots are on a log-linear scale



ulation ( $\lambda_+$  and  $R_0$  are roughly proportional, in realistic parameter ranges) [57], this conclusion has a simple and yet important interpretation. Namely, it means that medical, demographic, and environmental predispositions (determining  $R_0$ ) [70, 71] should be expected to strongly influence the behavior of the considered observables (detected cases and fatalities attributed to the virus) [72–74]. On the other hand,  $R_0$  seems not to significantly impact the infection extinguishing time.

Our analysis has shown that the strength of the implemented social measures, quantified by  $\alpha$ , effectively appears in the denominator in the exponent of the number of total COVID-19 casualties, as follows from Eq. (27). The impact of the social measures is thus, unsurprisingly, highly significant— as illustrated in Figs. 5 and 6.

Even more interesting is the interplay between  $t_0$  (the timing of the introduction of measures) and  $\alpha$  values in the asymptotic behavior of the COVID-19 observables.

Careful analysis of the functions for COVID-19 fatalities (18) and detected cases (21) at saturation, as well as the maximum of detected cases per day (24), revealed that this dependence is, in all three cases, effectively of the form:  $e^{(t_0+\frac{1}{\alpha})\lambda_+}$  (see also Figs. 4 and 6). The significance of the value  $t_\alpha = t_0 + \frac{1}{\alpha}$  has already been numerically recognized in [57], where this combination of parameters was named “protection time”. Here we show that the total number of fatalities and detected COVID-19 cases for the entire infection wave does not depend on either  $t_0$  or  $\alpha$  individually, but only jointly, through the protection time  $t_\alpha$ . The implications of this analytical result are striking: introducing very strict (and economically debilitating) social measures can have precisely the same effect (infected case-wise and mortality-wise) as implementing much weaker measures somewhat earlier.

For example, consider a decision to introduce weak-to-moderate social measures, corresponding to  $\alpha =$

0.1, some  $t_0$  days from the epidemic onset. If this decision is only one week postponed (i.e., measures put into practice at  $t_0 + 7$ ), it would require far more restrictive policies, corresponding to  $\alpha = 0.3$ , to compensate for the delay and retain the same number of fatalities (according to our analysis [58] -  $\alpha = 0.3$  corresponds to the strongest social measures that had been imposed in practice, in the first wave of COVID-19 pandemic).

“The sooner the better” conclusion regarding the introduction of social measures is hardly surprising [28–30] and does not require such a sophisticated analysis to reach. However, the analysis presented here provides us with additional insight that was not so obvious: even reasonably weak measures introduced quickly and without prolonged preparations seem to have much stronger mitigation potential than very strong measures introduced with hesitation and delay.

Furthermore, since the numbers of COVID-19 fatalities and detected cases in saturation depend upon the protection time  $t_\alpha$  as  $e^{t_\alpha \lambda}$ , it is clear that the measures must be put into force sooner and/or be stronger (i.e.,  $t_\alpha$  lower) in populations with higher SARS-CoV-2 reproduction number  $R_0$ . While this conclusion is fairly natural, having this quantitative relation and combining it with machine learning techniques to estimate  $R_0$  dependence upon demographic and environmental parameters [71] may substantially aid the policymaking process, in multiple ways. For example, by estimating how much sooner the measures must be implemented in areas with greater median age, higher prevalence of comorbidities, or higher pollution [70, 71]. Also, to properly allocate medical resources according to this interplay of  $R_0$ ,  $t_0$ , and  $\alpha$ .

## 6 Conclusion

In this manuscript, we demonstrated that it is possible to carry out a full analytical treatment of a compartmental epidemiological model that takes into account the effects of social distancing measures. The model has shown a good agreement with publicly available data on COVID-19 case counts.

As a benefit of having analytical solutions to the model equations, we were able to point out simple quantitative relations between the model variables and epidemiological observables. Such relations provide insights into cause-effect connections that underlie the

epidemiological dynamics and are obscured in more standard, i.e., purely numerical, approaches.

Our analysis revealed a quantitatively expressible interplay between the strength of the social measures and the time of their introduction, showing that the two variables effectively combine into a single relevant parameter called protection time. This not only implies that stringent measures can be often substituted by more relaxed ones introduced at earlier times but provides a direct analytical expression to quantify this trade-off.

We emphasize that our model and its implications are not COVID-19 specific and should hold for any potential future epidemic. Many epidemiologists believe that outbursts of new infectious diseases (or even pandemics) are likely, possibly even in the near future [75]. Thus, our results might be even more useful in the future, i.e., in the early stages of some new pandemic, when vaccines or effective pharmaceutical treatments are still not at our disposal, but we can only count on well-timed and appropriately chosen control measures.

**Author contributions** Magdalena Djordjevic and Marko Djordjevic contributed to the study conception and design. Analytical calculations were performed by Magdalena Djordjevic, Bojana Ilic and Igor Salom. Numerical analysis was performed by Bojana Ilic, Magdalena Djordjevic and Marko Djordjevic. The first draft of the manuscript was written by Bojana Ilic and Igor Salom with the help of Magdalena Djordjevic and Marko Djordjevic. All authors read and approved the final manuscript.

**Funding** This work was supported by the Ministry of Education, Science and Technological Development of the Republic of Serbia.

## Declarations

**Competing Interests** The authors have no relevant financial or non-financial interests to disclose.

**Data Availability** All data used in the study are publically available through Ref. [62].

## A Appendix

### A.1 Analytical derivation of the number of fatalities

To assess the dynamics of COVID-19 infection, we employed the mechanistic model, defined by equations (1)–(8). In Ref. [58], we have already obtained the number of infectious individuals as a function of time (9).



Throughout the derivations, we will distinguish two-time regions: I)  $t \leq t_0$  and II)  $t > t_0$ , and will denote the variables in these two regions accordingly.

First, we concentrate on deriving the expression for the time evolution of the number of fatalities. To this end, we start from Eqs. (7)-(8), which lead to a single equation (10). In region I, this second-order inhomogeneous differential equation, after taking into account the first term of Eq. (9) (i.e.,  $I_I(t) = I_0 e^{\lambda_+ t}$ ), reduces to:

$$\frac{d^2 F_I(t)}{dt^2} + (h + m) \frac{dF_I(t)}{dt} - m\epsilon\delta I_0 e^{\lambda_+ t} = 0. \tag{28}$$

If we assume  $F_I(t = 0) = 0$  and  $F'_I(t = 0) = 0$ , the time-dependent fatalities for  $t \leq t_0$  are given by:

$$F_I(t) = \frac{I_0 \epsilon \delta}{\lambda_+} \frac{m}{m + h} \left\{ -1 + \frac{\lambda_+}{h + m + \lambda_+} e^{-(h+m)t} + \frac{h + m}{h + m + \lambda_+} e^{\lambda_+ t} \right\}. \tag{29}$$

In region II, for simplicity we shift  $t - t_0 \rightarrow t$ , and take into account that the expression for infectious now reads  $I_{II}(t) = I_0 e^{\lambda_+ t_0} e^{-\frac{\gamma + \epsilon \delta + \sigma}{2} t} K\left(\frac{\gamma + \epsilon \delta - \sigma}{\alpha}, \frac{2\sqrt{e^{-\alpha t} \beta \sigma}}{\alpha}\right) / K\left(\frac{\gamma + \epsilon \delta - \sigma}{\alpha}, \frac{2\sqrt{\beta \sigma}}{\alpha}\right)$  (the second term of Eq. (9)). Since  $I_{II}(t)$  has this complex form, the further derivations are quite demanding. By substituting  $t \rightarrow y = \frac{2\sqrt{e^{-\alpha t} \beta \sigma}}{\alpha}$ , it can easily be verified that Eq. (10) is in region II reduced to the well-known second-order inhomogeneous Cauchy–Euler equation [76,77]  $ax^2 y'' + bxy' + cy = g(x)$ . After dividing thus obtained differential equation by  $y^2$ , we obtain

$$\frac{d^2 F_{II}}{dy^2} + \left[ 1 - \frac{2(h + m)}{\alpha} \right] \frac{1}{y} \frac{dF_{II}}{dy} = C y^{\frac{\gamma + \epsilon \delta + \sigma}{\alpha} - 2} K\left(\frac{\gamma + \epsilon \delta - \sigma}{\alpha}, y\right), \tag{30}$$

where  $C = \frac{4I_0 \epsilon \delta m}{\alpha^2} (2\sqrt{\beta \sigma} / \alpha)^{-\frac{\gamma + \epsilon \delta + \sigma}{\alpha}} e^{\lambda_+ t_0} / K\left(\frac{\gamma + \epsilon \delta - \sigma}{\alpha}, \frac{2\sqrt{\beta \sigma}}{\alpha}\right)$ .

Next, we apply the standard procedure for solving inhomogeneous differential equation given by Eq. (30): the full solution equals homogeneous plus particular solution  $F_{II}(y) = F_{II,h}(y) + F_{II,p}(y)$ . It is straightforward to show that auxiliary/characteristic equation yields the following simple form of homo-

geneous solution  $F_{II,h}(y) = C_1 + C_2 y^{\frac{2(h+m)}{\alpha}}$  (where linearly independent solutions are  $F_{II,1}(y) = 1$  and  $F_{II,2}(y) = y^{\frac{2(h+m)}{\alpha}}$ ), while for obtaining particular solution  $F_{II,p}(y)$  we used the Lagrange’s method of variation of parameters [76]. More precisely, we assume that  $F_{II,p}(y) = C_1(y) + C_2(y) y^{\frac{2(h+m)}{\alpha}}$ , where again linearly independent solutions of the homogeneous equation are employed. The unknown functions  $C_i$  ( $i = 1, 2$ ) of variable  $y$  are sought for via the standard procedure

$$C_1(y) = - \int \frac{F_{II,2}(y) f(y)}{W} dy, \tag{31}$$

$$C_2(y) = \int \frac{F_{II,1}(y) f(y)}{W} dy,$$

where  $f(y)$  denotes the right-hand side of Eq. (30), while Wronskian [76,77] is given by  $W = F_{II,1} F'_{II,2} - F_{II,2} F'_{II,1} = \frac{2(h+m)}{\alpha} y^{\frac{2(h+m)}{\alpha} - 1}$ . This leads to:

$$C_1(t) = - \frac{C\alpha}{2(h+m)} \int_0^{\frac{2\sqrt{e^{-\alpha t} \beta \sigma}}{\alpha}} y^{\frac{\gamma + \epsilon \delta + \sigma}{\alpha} - 1} K\left(\frac{\gamma + \epsilon \delta - \sigma}{\alpha}, y\right) dy,$$

$$C_2(t) = \frac{C\alpha}{2(h+m)} \int_0^{\frac{2\sqrt{e^{-\alpha t} \beta \sigma}}{\alpha}} y^{\frac{\gamma + \epsilon \delta + \sigma - 2(h+m)}{\alpha} - 1} K\left(\frac{\gamma + \epsilon \delta - \sigma}{\alpha}, y\right) dy. \tag{32}$$

In spite that the above form of the result will be more useful in what follows, we nevertheless provide also its full-fledged form:

$$C_1(t) = C_0 \left[ \left(\frac{\sqrt{\beta \sigma}}{\alpha}\right)^{\frac{\gamma + \epsilon \delta - \sigma}{\alpha}} e^{-(\gamma + \epsilon \delta)t} \Gamma\left(\frac{\gamma + \epsilon \delta}{\alpha}\right) \times {}_1\tilde{F}_2\left(\frac{\gamma + \epsilon \delta}{\alpha}; 1 + \frac{\gamma + \epsilon \delta}{\alpha}, 1 + \frac{\gamma + \epsilon \delta - \sigma}{\alpha}; \frac{e^{-\alpha t} \beta \sigma}{\alpha^2}\right) - \left(\frac{\sqrt{\beta \sigma}}{\alpha}\right)^{-\frac{\gamma + \epsilon \delta - \sigma}{\alpha}} e^{-\sigma t} \Gamma\left(\frac{\sigma}{\alpha}\right) \times {}_1\tilde{F}_2\left(\frac{\sigma}{\alpha}; 1 + \frac{\sigma}{\alpha}, 1 + \frac{\sigma - \gamma - \epsilon \delta}{\alpha}; \frac{e^{-\alpha t} \beta \sigma}{\alpha^2}\right) \right] \frac{\pi}{2} \csc\left[\frac{\pi(\gamma + \epsilon \delta - \sigma)}{\alpha}\right]$$

$$C_2(t) = -C_0 \left[ \left(\frac{\sqrt{\beta \sigma}}{\alpha}\right)^{\frac{\gamma + \epsilon \delta - \sigma}{\alpha}} e^{-(\gamma + \epsilon \delta)t} \Gamma\left(\frac{\gamma + \epsilon \delta - h - m}{\alpha}\right) \right]$$

$$\begin{aligned}
 & \times {}_1\tilde{F}_2\left(\frac{\gamma + \epsilon\delta - h - m}{\alpha}; 1 + \frac{\gamma + \epsilon\delta - h - m}{\alpha}, 1\right. \\
 & \quad \left. + \frac{\gamma + \epsilon\delta - \sigma}{\alpha}; \frac{e^{-\alpha t} \beta\sigma}{\alpha^2}\right) \\
 & - \left(\frac{\sqrt{\beta\sigma}}{\alpha}\right)^{-\frac{\gamma + \epsilon\delta - \sigma}{\alpha}} e^{-\sigma t} \Gamma\left(\frac{\sigma - h - m}{\alpha}\right) \\
 & \times {}_1\tilde{F}_2\left(\frac{\sigma - h - m}{\alpha}; 1 + \frac{\sigma - h - m}{\alpha}, 1\right. \\
 & \quad \left. + \frac{\sigma - \gamma - \epsilon\delta}{\alpha}; \frac{e^{-\alpha t} \beta\sigma}{\alpha^2}\right) \Bigg] \\
 & \times \frac{\pi}{2} \operatorname{csc}\left[\frac{\pi(\gamma + \epsilon\delta - \sigma)}{\alpha}\right], \tag{33}
 \end{aligned}$$

where  $C_0 = \frac{I_0 \epsilon \delta}{\alpha} \frac{m}{h+m} e^{\lambda+t_0} / K\left(\frac{\gamma + \epsilon\delta - \sigma}{\alpha}, \frac{2\sqrt{\beta\sigma}}{\alpha}\right)$ , while  ${}_p\tilde{F}_q(a_1, a_2, \dots, a_p; b_1, b_2, \dots, b_q; z)$  denotes regularized generalized hypergeometric function [65]. The general solution of Eq. (30), when returned to variable  $t$ , has a form:

$$\begin{aligned}
 F_{II}(t) &= C_1 + C_2 e^{-(h+m)t} + C_1(t) \\
 & + C_2(t) \left(\frac{2\sqrt{\beta\sigma}}{\alpha}\right)^{\frac{2(h+m)}{\alpha}} e^{-(h+m)t}, \tag{34}
 \end{aligned}$$

where the only unknown parameters are  $C_1$  and  $C_2$ . In order to determine these constants we use the following boundary conditions:  $F_{II}(0) = F_I(t_0)$  and  $F'_{II}(0) = F'_I(t_0)$ . After some cumbersome calculation steps we obtain the following expressions:

$$\begin{aligned}
 C_1 &= I_0 \epsilon \delta \frac{m}{(h+m)} \frac{e^{\lambda+t_0} - 1}{\lambda_+} \\
 & - C_0 \left[ \left(\frac{\sqrt{\beta\sigma}}{\alpha}\right)^{\frac{\gamma + \epsilon\delta - \sigma}{\alpha}} \Gamma\left(\frac{\gamma + \epsilon\delta}{\alpha}\right) \right. \\
 & \times {}_1\tilde{F}_2\left(\frac{\gamma + \epsilon\delta}{\alpha}; 1 + \frac{\gamma + \epsilon\delta}{\alpha}, 1\right. \\
 & \quad \left. + \frac{\gamma + \epsilon\delta - \sigma}{\alpha}; \frac{\beta\sigma}{\alpha^2}\right) \\
 & - \left(\frac{\sqrt{\beta\sigma}}{\alpha}\right)^{-\frac{\gamma + \epsilon\delta - \sigma}{\alpha}} \Gamma\left(\frac{\sigma}{\alpha}\right) \\
 & \left. {}_1\tilde{F}_2\left(\frac{\sigma}{\alpha}; 1 + \frac{\sigma}{\alpha}, 1 + \frac{\sigma - \gamma - \epsilon\delta}{\alpha}; \frac{\beta\sigma}{\alpha^2}\right) \right] \frac{\pi}{2} \\
 & \times \operatorname{csc}\left[\frac{\pi(\gamma + \epsilon\delta - \sigma)}{\alpha}\right] \tag{35} \\
 C_2 &= I_0 \epsilon \delta \frac{m}{(h+m)} \frac{e^{-(h+m)t_0} - e^{\lambda+t_0}}{h+m+\lambda_+}
 \end{aligned}$$

$$\begin{aligned}
 & + C_0 \left[ \left(\frac{\sqrt{\beta\sigma}}{\alpha}\right)^{\frac{\gamma + \epsilon\delta - \sigma}{\alpha}} \Gamma\left(\frac{\gamma + \epsilon\delta - h - m}{\alpha}\right) \right. \\
 & \times {}_1\tilde{F}_2\left(\frac{\gamma + \epsilon\delta - h - m}{\alpha}; 1 + \frac{\gamma + \epsilon\delta - h - m}{\alpha}, 1\right. \\
 & \quad \left. + \frac{\gamma + \epsilon\delta - \sigma}{\alpha}; \frac{\beta\sigma}{\alpha^2}\right) \\
 & - \left(\frac{\sqrt{\beta\sigma}}{\alpha}\right)^{-\frac{\gamma + \epsilon\delta - \sigma}{\alpha}} \Gamma\left(\frac{\sigma - h - m}{\alpha}\right) \\
 & \times {}_1\tilde{F}_2\left(\frac{\sigma - h - m}{\alpha}; 1 + \frac{\sigma - h - m}{\alpha}, 1\right. \\
 & \quad \left. + \frac{\sigma - \gamma - \epsilon\delta}{\alpha}; \frac{\beta\sigma}{\alpha^2}\right) \Bigg] \frac{\pi}{2} \\
 & \times \operatorname{csc}\left[\frac{\pi(\gamma + \epsilon\delta - \sigma)}{\alpha}\right] \tag{36}
 \end{aligned}$$

Now, if we use the definition of regularized generalized hypergeometric functions, the above expressions can be significantly simplified and reduced to the form similar to Eq. (32). Namely [65]

$${}_1\tilde{F}_2(a_1; b_1, b_2; z) = \sum_{k=0}^{\infty} \frac{(a_1)_k z^k}{k! \Gamma(k + b_1) \Gamma(k + b_2)}, \tag{37}$$

where  $(a_1)_0 = 1$ , while for  $k \geq 1$

$$(a_1)_k = a(a + 1) \dots (a + k - 1). \tag{38}$$

Let us first concentrate on  $C_1$ , where from Eq. (35) it follows that  $z = \beta\sigma/\alpha^2$ . By denoting  $a_1 = (\gamma + \epsilon\delta)/\alpha$  and  $a_2 = \sigma/\alpha$ , it is straightforward to infer that the expression in the square brackets of Eq. (35) can be rewritten in a form:

$$\begin{aligned}
 \mathcal{I}_1 &= z^{\frac{a_1 - a_2}{2}} \Gamma(a_1) {}_1\tilde{F}_2(a_1; 1 + a_1, 1 + a_1 - a_2; z) \\
 & - z^{\frac{a_2 - a_1}{2}} \Gamma(a_2) {}_1\tilde{F}_2(a_2; 1 + a_2, 1 + a_2 - a_1; z). \tag{39}
 \end{aligned}$$

After multiplying the right-hand side by  $z^{\frac{a_1 + a_2}{2}} / z^{\frac{a_1 + a_2}{2}}$  we obtain:

$$\begin{aligned}
 \mathcal{I}_1 &= \frac{1}{z^{\frac{a_1 + a_2}{2}}} \sum_{k=0}^{\infty} \left[ \frac{z^{k+a_1}}{k!(k + a_1) \Gamma(k + 1 + a_1 - a_2)} \right. \\
 & \quad \left. - \frac{z^{k+a_2}}{k!(k + a_2) \Gamma(k + 1 + a_2 - a_1)} \right], \tag{40}
 \end{aligned}$$

where we made use of the fact that  $\Gamma(n + 1) = n\Gamma(n)$  and  $\Gamma(a)(a)_k = \Gamma(a + k)$  (see Eq. (38)). To further simplify Eq. (40), we adopt the following notation  $\mathcal{I}_1 = \sum_{k=0}^{\infty} \frac{z^{k+a_1}}{k!(k+a_1)\Gamma(k+1+a_1-a_2)}$  and differentiate it with respect to  $z$ :

$$\frac{d\mathcal{I}_1}{dz} = \sum_{k=0}^{\infty} \frac{(\sqrt{z})^{2k+2a_1-2}}{k!\Gamma(k+1+a_1-a_2)}. \tag{41}$$

As already mentioned, the main idea is to try to reduce Eq. (35) to a form similar to Eq. (32), i.e., to relate the above expression to modified Bessel functions, and the modified Bessel function of the first kind [64] is defined as:

$$I_n(x) = \sum_{k=0}^{\infty} \frac{\left(\frac{x}{2}\right)^{2k+n}}{k!\Gamma(k+n+1)}. \tag{42}$$

By comparing Eqs. (41) and (42), we observe that their right-hand sides are of a similar form, if  $x/2 \rightarrow \sqrt{z}$ ,  $n \rightarrow a_1 - a_2$ , that is:

$$\frac{d\mathcal{I}_1}{dz} = (\sqrt{z})^{a_1+a_2-2} I_{a_1-a_2}(2\sqrt{z}). \tag{43}$$

Proceeding in a similar manner in the case of the remaining term in Eq. (40)  $\mathcal{I}_2 = \sum_{k=0}^{\infty} \frac{z^{k+a_2}}{k!(k+a_2)\Gamma(k+1+a_2-a_1)}$  we arrive at:

$$\frac{d\mathcal{I}_2}{dz} = (\sqrt{z})^{a_1+a_2-2} I_{a_2-a_1}(2\sqrt{z}). \tag{44}$$

Note, from Eq. (40), that  $\mathcal{I} = z^{-\frac{a_1+a_2}{2}} (\mathcal{I}_1 - \mathcal{I}_2)$ .

By substituting integrated Eqs. (43) and (44) in Eq. (40), and thus obtained expression in Eq. (35), for  $C_1$  we finally obtain:

$$C_1 = I_0 \epsilon \delta \frac{m}{(h+m)} \frac{e^{\lambda+t_0} - 1}{\lambda_+} + 2C_0 \left(\frac{2\sqrt{\beta\sigma}}{\alpha}\right)^{-\frac{\gamma+\epsilon\delta+\sigma}{\alpha}} \times \int_0^{\frac{2\sqrt{\beta\sigma}}{\alpha}} y^{\frac{\gamma+\epsilon\delta+\sigma}{\alpha}-1} K\left(\frac{\gamma+\epsilon\delta-\sigma}{\alpha}, y\right) dy. \tag{45}$$

Note that, in obtaining the above expression the identity [66,68] relating modified Bessel function of the first and the second kind  $I_{-n}(x) - I_n(x) = \frac{2}{\pi} \sin(n\pi) K_n(x)$  was used.

The remaining constant  $C_2$  (see Eq. (36)) from fatality counts expression is simplified by applying the same procedure as in the case of  $C_1$ . To avoid redundant derivations (i.e., the repetition of the above calculations), we simply outline the final expression:

$$C_2 = I_0 \epsilon \delta \frac{m}{(h+m)} \frac{e^{-(h+m)t_0} - e^{\lambda+t_0}}{h+m+\lambda_+} - 2C_0 \left(\frac{2\sqrt{\beta\sigma}}{\alpha}\right)^{-\frac{\gamma+\epsilon\delta+\sigma-2(h+m)}{\alpha}} \times \int_0^{\frac{2\sqrt{\beta\sigma}}{\alpha}} y^{\frac{\gamma+\epsilon\delta+\sigma-2(h+m)}{\alpha}-1} K\left(\frac{\gamma+\epsilon\delta-\sigma}{\alpha}, y\right) dy, \tag{46}$$

with the only distinction that, in the process of simplification, parameters  $a_1$  and  $a_2$  now read  $(\gamma + \epsilon\delta - h - m)/\alpha$  and  $(\sigma - h - m)/\alpha$ , respectively.

Now that all terms of fatalities count (given by Eq. (34)) are determined, we note that all constants ( $C_1, C_2, C_1(t)$  and  $C_2(t)$ ) are still in their integral form. Since, for all countries that we consider it holds  $2\sqrt{\beta\sigma}/\alpha \gg 1$ , we may further simplify these integrals by utilizing Hankel’s asymptotic expression [66]:

$$K_n(x) \sim \sqrt{\frac{\pi}{2x}} e^{-x} \left(1 + \mathcal{O}\left(\frac{1}{x}\right)\right), \tag{47}$$

which holds for large  $x = 2\sqrt{\beta\sigma}/\alpha$ .

Along these lines, we rewrite Eqs. (32, 45, 46):

$$C_1 \approx I_0 \epsilon \delta \frac{m}{(h+m)} \left[ \frac{e^{\lambda+t_0} - 1}{\lambda_+} + \frac{2}{\alpha} \left(\frac{2\sqrt{\beta\sigma}}{\alpha}\right)^{-\frac{\gamma+\epsilon\delta+\sigma}{\alpha} + \frac{1}{2}} e^{\lambda+t_0 + \frac{2\sqrt{\beta\sigma}}{\alpha}} \times \int_0^{\frac{2\sqrt{\beta\sigma}}{\alpha}} y^{\frac{\gamma+\epsilon\delta+\sigma}{\alpha} - \frac{3}{2}} e^{-y} dy \right]$$

$$C_2 \approx I_0 \epsilon \delta \frac{m}{(h+m)} \left[ \frac{e^{-(h+m)t_0} - e^{\lambda+t_0}}{h+m+\lambda_+} - \frac{2}{\alpha} \left(\frac{2\sqrt{\beta\sigma}}{\alpha}\right)^{-\frac{\gamma+\epsilon\delta+\sigma-2(h+m)}{\alpha} + \frac{1}{2}} \times e^{\lambda+t_0 + \frac{2\sqrt{\beta\sigma}}{\alpha}} \int_0^{\frac{2\sqrt{\beta\sigma}}{\alpha}} y^{\frac{\gamma+\epsilon\delta+\sigma-2(h+m)}{\alpha} - \frac{3}{2}} e^{-y} dy \right]$$

$$C_1(t) \approx -\frac{2I_0 \epsilon \delta}{\alpha} \frac{m}{h+m} \left(\frac{2\sqrt{\beta\sigma}}{\alpha}\right)^{-\frac{\gamma+\epsilon\delta+\sigma}{\alpha} + \frac{1}{2}} e^{\lambda+t_0 + \frac{2\sqrt{\beta\sigma}}{\alpha}}$$

$$\begin{aligned}
 & \times \int_0^{2\sqrt{e^{-\alpha t} \beta \sigma}} y^{\frac{\gamma + \epsilon \delta + \sigma}{\alpha} - \frac{3}{2}} e^{-y} dy \\
 C_2(t) & \approx \frac{2I_0 \epsilon \delta}{\alpha} \frac{m}{h+m} \left( \frac{2\sqrt{\beta \sigma}}{\alpha} \right)^{-\frac{\gamma + \epsilon \delta + \sigma}{\alpha} + \frac{1}{2}} e^{\lambda + t_0 + \frac{2\sqrt{\beta \sigma}}{\alpha}} \\
 & \times \int_0^{2\sqrt{e^{-\alpha t} \beta \sigma}} y^{\frac{\gamma + \epsilon \delta + \sigma - 2(h+m)}{\alpha} - \frac{3}{2}} e^{-y} dy, \quad (48)
 \end{aligned}$$

where we also used the same approximation given by Eq. (47) for modified Bessel function of the second kind contained in  $C$  and  $C_0$ . Note that the second terms of  $C_1$  and  $C_1(t)$  on one side, and the second terms of  $C_2$  and  $C_2(t)$  on the other have the same exponents (keep in mind that, according to Eq. (34), there is still a remaining factor  $(2\sqrt{\beta \sigma} / \alpha)^{\frac{2(h+m)}{\alpha}}$  multiplying  $C_2(t)$ ).

In Eq. (48), we encounter the lower incomplete gamma function [66]  $\gamma(s, x) = \int_0^x t^{s-1} e^{-t} dt$ , which we go about by utilizing [66]:

$$\gamma(s, x) = \Gamma(s) - \Gamma(s, x), \quad (49)$$

where  $\Gamma(s, x) = \int_x^\infty t^{s-1} e^{-t} dt$  represents the upper incomplete gamma function [66].

Finally, upon implementing thus calculated constants of Eq. (48) in Eq. (34), and by taking into account Eq. (29), we obtain the expression (16) for the general solution of Eq. (10) at the entire  $t$  region.

### A.2 Analytical derivation of detected cases

Next, we concentrate on the time evolution of detected counts. To this end, we make use of Eqs. (6) and (9), i.e.

$$D(t) = \epsilon \delta \int I(t) dt + C_i, \quad (50)$$

where  $C_i$  ( $i = 3, 4$ ) stands for the constant of integration. In region I the integration of  $I_I(t)$  (the first term in Eq. (9)) is straightforward and yields  $D_I(t) = \frac{I_0 \epsilon \delta}{\lambda_+} e^{\lambda + t} + C_3$ , while  $C_3$  is obtained from the initial conditions  $D_I(t = 0) = D_0 \equiv \frac{I_0 \epsilon \delta}{\lambda_+}$ , leading to:

$$D_I(t) = \frac{I_0 \epsilon \delta}{\lambda_+} e^{\lambda + t}. \quad (51)$$

In region II, the integration is more demanding, due to the form of  $I_{II}(t)$  (the second term of Eq. (9)). To

address this, we employ the following substitution of variable  $t - t_0 \rightarrow x = \frac{2\sqrt{\beta \sigma}}{\alpha} e^{-\frac{\alpha(t-t_0)}{2}}$ . Thus:

$$\begin{aligned}
 D_{II}(t) & = -2C_0 \frac{h+m}{m} \left( \frac{2\sqrt{\beta \sigma}}{\alpha} \right)^{-\frac{\gamma + \epsilon \delta + \sigma}{\alpha}} \\
 & \times \int_{\frac{2\sqrt{\beta \sigma}}{\alpha}}^{2\sqrt{e^{-\alpha(t-t_0)} \beta \sigma}} x^{\frac{\gamma + \epsilon \delta + \sigma}{\alpha} - 1} \\
 & \mathbb{K} \left( \frac{\gamma + \epsilon \delta - \sigma}{\alpha}, x \right) dx + C_4. \quad (52)
 \end{aligned}$$

Note that, as opposed to our previous notation during the derivation of  $F_{II}(t)$ , now we do not make use of the substitution  $t - t_0 \rightarrow t$ . Because of this, the boundary condition reads:  $D_{II}(t_0) = D_I(t_0)$ , which is used for determining the integration constant  $C_4 = \frac{I_0 \epsilon \delta}{\lambda_+} e^{\lambda + t_0}$ . So, the expression for detected cases reads:

$$\begin{aligned}
 D(t) & = \theta(t_0 - t) \frac{I_0 \epsilon \delta}{\lambda_+} e^{\lambda + t} + \theta(t - t_0) \\
 & \left\{ \frac{I_0 \epsilon \delta}{\lambda_+} e^{\lambda + t_0} + C_0 \frac{h+m}{m} \right. \\
 & \times \left[ \left( \frac{\sqrt{\beta \sigma}}{\alpha} \right)^{-\frac{\gamma + \epsilon \delta - \sigma}{\alpha}} \Gamma \left( \frac{\sigma}{\alpha} \right) \right. \\
 & \quad {}_1\tilde{F}_2 \left( \frac{\sigma}{\alpha}; 1 + \frac{\sigma}{\alpha}, 1 + \frac{\sigma - \gamma - \epsilon \delta}{\alpha}; \frac{\beta \sigma}{\alpha^2} \right) \\
 & \quad - \left( \frac{\sqrt{\beta \sigma}}{\alpha} \right)^{\frac{\gamma + \epsilon \delta - \sigma}{\alpha}} \Gamma \left( \frac{\gamma + \epsilon \delta}{\alpha} \right) \\
 & \quad \times {}_1\tilde{F}_2 \left( \frac{\gamma + \epsilon \delta}{\alpha}; 1 + \frac{\gamma + \epsilon \delta}{\alpha}, 1 + \frac{\gamma + \epsilon \delta - \sigma}{\alpha}; \frac{\beta \sigma}{\alpha^2} \right) \\
 & \quad + \left( \frac{\sqrt{\beta \sigma}}{\alpha} \right)^{\frac{\gamma + \epsilon \delta - \sigma}{\alpha}} e^{-(\gamma + \epsilon \delta)(t-t_0)} \Gamma \left( \frac{\gamma + \epsilon \delta}{\alpha} \right) \\
 & \quad \times {}_1\tilde{F}_2 \left( \frac{\gamma + \epsilon \delta}{\alpha}; 1 + \frac{\gamma + \epsilon \delta}{\alpha}, 1 \right. \\
 & \quad \quad \left. + \frac{\gamma + \epsilon \delta - \sigma}{\alpha}; \frac{e^{-\alpha(t-t_0)} \beta \sigma}{\alpha^2} \right) \\
 & \quad - \left( \frac{\sqrt{\beta \sigma}}{\alpha} \right)^{-\frac{\gamma + \epsilon \delta - \sigma}{\alpha}} e^{-\sigma(t-t_0)} \Gamma \left( \frac{\sigma}{\alpha} \right) \\
 & \quad \times {}_1\tilde{F}_2 \left( \frac{\sigma}{\alpha}; 1 + \frac{\sigma}{\alpha}, 1 \right. \\
 & \quad \quad \left. + \frac{\sigma - \gamma - \epsilon \delta}{\alpha}; \frac{e^{-\alpha(t-t_0)} \beta \sigma}{\alpha^2} \right) \left. \right] \\
 & \left. \frac{\pi}{2} \times \csc \left[ \frac{\pi(\gamma + \epsilon \delta - \sigma)}{\alpha} \right] \right\}. \quad (53)
 \end{aligned}$$



After performing the same algebraic manipulations of regularized generalized hypergeometric functions as in the previous Subsect. A.1, as well as applying Hankel’s approximation (47), we obtain the expression (19) for the general solution of Eq. (11) at the entire  $t$  region.

Alternatively, the same expression (19) could be obtained more straightforwardly. Namely, the expression for the number of infectious individuals (Eq. (9)) can be simplified by utilizing Eq. (47):

$$\begin{aligned}
 I(t) &= \theta(t_0 - t)I_0e^{\lambda+t} + \theta(t - t_0) \\
 &I_0e^{\lambda+t_0+\frac{2\sqrt{\beta\sigma}}{\alpha}} e^{-\frac{\alpha(t-t_0)}{2}\left(\frac{\gamma+\epsilon\delta+\sigma}{\alpha}-\frac{1}{2}\right)} \\
 &\times e^{-\frac{2\sqrt{e^{-\alpha(t-t_0)}\beta\sigma}}{\alpha}}.
 \end{aligned}
 \tag{54}$$

Now that  $I(t)$  has been determined in the desired form, the detected counts can be calculated from Eq. (11). In region I, the derivation is straightforward (and therefore omitted) and leads to Eq. (51). In region II, the integration is more demanding, due to the form of  $I_{II}(t) = I_0e^{\lambda+t_0+\frac{2\sqrt{\beta\sigma}}{\alpha}} e^{-\frac{\alpha(t-t_0)}{2}\left(\frac{\gamma+\epsilon\delta+\sigma}{\alpha}-\frac{1}{2}\right)} e^{-\frac{2\sqrt{e^{-\alpha(t-t_0)}\beta\sigma}}{\alpha}}$ . To address this, again we employ the following substitution of variable  $t - t_0 \rightarrow x = \frac{2\sqrt{\beta\sigma}}{\alpha} e^{-\frac{\alpha(t-t_0)}{2}}$ , resulting in the boundary condition  $D_{II}(t_0) = D_I(t_0)$  (which is used for determining the integration constant  $C_4$ ). In a similar manner as before, we again encounter the incomplete gamma functions [66]:

$$\begin{aligned}
 D_{II}(t) &= -\frac{2I_0\epsilon\delta}{\alpha} \left(\frac{2\sqrt{\beta\sigma}}{\alpha}\right)^{-\frac{\gamma+\epsilon\delta+\sigma}{\alpha}+\frac{1}{2}} e^{\frac{2\sqrt{\beta\sigma}}{\alpha}+\lambda+t_0} \\
 &\times \int_{\frac{2\sqrt{\beta\sigma}}{\alpha}}^{\frac{2\sqrt{e^{-\alpha(t-t_0)}\beta\sigma}}{\alpha}} x^{\frac{\gamma+\epsilon\delta+\sigma}{\alpha}-\frac{3}{2}} e^{-x} dx + C_4.
 \end{aligned}
 \tag{55}$$

The only difference compared to Eq. (48) is that now the lower boundary of integration is not zero but some positive real number. This integral is solved by applying the identity  $\int_a^b x^{s-1}e^{-x} dx = \int_0^b x^{s-1}e^{-x} dx - \int_0^a x^{s-1}e^{-x} dx = \Gamma(s, a) - \Gamma(s, b)$ . By combining this result with Eq. (51), we finally arrive at the expression (19) for the number of detected cases.

### A.3 Simplified expressions for fatalities and detected cases

In this section, we show that certain terms in the expressions for fatalities and detected cases can be neglected (when epidemiological parameters are in realistic ranges), without significant loss of predictive precision. First, we start with Eq. (16) for fatality counts. We notice that for  $t > t_0$  first two terms are much smaller than the remaining terms, due to  $2\sqrt{\beta\sigma}/\alpha \gg 1$ , and therefore can be neglected. Additionally, for the same reason all  $\Gamma(s, 2\sqrt{\beta\sigma}/\alpha) \rightarrow \Gamma(s, \infty)$  are approximately equal to zero (i.e., the gamma integral is effectively  $\int_\infty^\infty$ ). Therefore, instead of Eq. (16), the following formula can be safely used in practice:

$$\begin{aligned}
 F_{simp}(t) &\approx I_0\epsilon\delta \frac{m}{h+m} \\
 &\left\{ \theta(t_0 - t) \left( \frac{e^{\lambda+t} - 1}{\lambda_+} + \frac{e^{-(h+m)t} - e^{\lambda+t}}{h+m+\lambda_+} \right) \right. \\
 &+ \theta(t - t_0) \frac{2}{\alpha} \left( \frac{2\sqrt{\beta\sigma}}{\alpha} \right)^{-\frac{\gamma+\epsilon\delta+\sigma}{\alpha}+\frac{1}{2}} e^{\lambda+t_0+\frac{2\sqrt{\beta\sigma}}{\alpha}} \\
 &\times \left[ \Gamma\left( \frac{\gamma + \epsilon\delta + \sigma}{\alpha} - \frac{1}{2}, \frac{2\sqrt{e^{-\alpha(t-t_0)}\beta\sigma}}{\alpha} \right) \right. \\
 &- \left. \left( \frac{2\sqrt{e^{-\alpha(t-t_0)}\beta\sigma}}{\alpha} \right)^{\frac{2(h+m)}{\alpha}} \right. \\
 &\times \Gamma\left( \frac{\gamma + \epsilon\delta + \sigma - 2(h+m)}{\alpha} \right. \\
 &\left. \left. - \frac{1}{2}, \frac{2\sqrt{e^{-\alpha(t-t_0)}\beta\sigma}}{\alpha} \right) \right] \left. \right\}.
 \end{aligned}
 \tag{56}$$

Continuing in the same manner, the simplified form of the number of detected cases is easily obtained:

$$\begin{aligned}
 D_{simp}(t) &\approx I_0\epsilon\delta \\
 &\left[ \theta(t_0 - t) \frac{e^{\lambda+t}}{\lambda_+} + \theta(t - t_0) \frac{2}{\alpha} \right. \\
 &\left( \frac{2\sqrt{\beta\sigma}}{\alpha} \right)^{-\frac{\gamma+\epsilon\delta+\sigma}{\alpha}+\frac{1}{2}} \\
 &\times e^{\lambda+t_0+\frac{2\sqrt{\beta\sigma}}{\alpha}} \\
 &\left. \Gamma\left( \frac{\gamma + \epsilon\delta + \sigma}{\alpha} - \frac{1}{2}, \frac{2\sqrt{e^{-\alpha(t-t_0)}\beta\sigma}}{\alpha} \right) \right].
 \end{aligned}
 \tag{57}$$

We have numerically tested and confirmed that the full-fledged (given by Eq. (16)) and simplified (given by Eq. (56)) fatality curves are practically overlapping (and the same for the detected cases).

#### A.4 Expressions for fatalities and detected cases at saturation

We will evaluate the saturation values of fatalities and detected counts, that is, their expressions in the limit of very large  $t$ . This means that we can concentrate only on  $t > t_0$ , i.e., region II, where we set  $t \rightarrow \infty$ . Building on the results of the previous section, from Eq. (56) we observe that, in this limit, the second term in the square brackets can be neglected, due to  $e^{-(h+m)(t-t_0)} \rightarrow 0$ . Likewise,

$$\begin{aligned} & \Gamma\left(\frac{\gamma + \epsilon\delta + \sigma}{\alpha} - \frac{1}{2}, \frac{2\sqrt{e^{-\alpha(t-t_0)}\beta\sigma}}{\alpha}\right) \\ & \rightarrow \Gamma\left(\frac{\gamma + \epsilon\delta + \sigma}{\alpha} - \frac{1}{2}, 0\right) \\ & \equiv \Gamma\left(\frac{\gamma + \epsilon\delta + \sigma}{\alpha} - \frac{1}{2}\right). \end{aligned}$$

Therefore, we obtain the expressions (17) and (20) for the saturation values.

#### A.5 Expressions for the epidemics peak and tipping points

Other important quantities characterizing infection dynamics during the first wave are epidemics peak time and inflection (tipping and turning) points, for which we here provide analytic expressions. Namely, the epidemics peak time is the moment when infected curve reaches its maximal value (i.e.,  $dI/dt = 0$ ), or equivalently  $d^2D/dt^2 = 0$ . The second derivative of Eq. (19) in region II (or equivalently Eq. (57) in the same region) yields:

$$\begin{aligned} \frac{d^2D_{II}}{dt^2} &= I_0\epsilon\delta e^{\lambda+t_0+\frac{2\sqrt{\beta\sigma}}{\alpha}} \\ & e^{-\frac{\alpha(t-t_0)}{2}\left(\frac{\gamma+\epsilon\delta+\sigma}{\alpha}-\frac{1}{2}\right)} e^{-\frac{2\sqrt{e^{-\alpha(t-t_0)}\beta\sigma}}{\alpha}} \\ & \times \left(-\frac{\gamma + \epsilon\delta + \sigma}{2} + \frac{\alpha}{4} + \sqrt{e^{-\alpha(t-t_0)}\beta\sigma}\right). \end{aligned} \tag{58}$$

In deriving the above expression, we made use of equality  $d\Gamma(s, x)/dx = -x^{s-1}e^{-x}$ , following from the definition of incomplete gamma functions [66]. Note that, in this subsection, we are interested in region II, where all relevant points lay. After equating the second derivative of  $D_{II}$  with zero, for the epidemics peak time, we obtain:

$$t_{max} = t_0 + \frac{1}{\alpha} \ln \left[ \frac{16\beta\sigma}{(2(\gamma + \epsilon\delta + \sigma) - \alpha)^2} \right]. \tag{59}$$

By evaluating  $\frac{dD}{dt}$  at  $t = t_{max}$ , we can straightforwardly obtain the maximum of detected cases per day, given by

$$\begin{aligned} \left(\frac{dD}{dt}\right)_{max} &= D_0\lambda_+ e^{\lambda_+(t_0+\frac{2}{\alpha})+\frac{1}{2}} \\ & \left(\frac{4\sqrt{\beta\sigma}}{2(\gamma + \epsilon\delta + \sigma) - \alpha}\right)^{\frac{1}{2}-\frac{\gamma+\epsilon\delta+\sigma}{\alpha}}. \end{aligned} \tag{60}$$

Along the same lines, the epidemics inflection points are defined as  $d^2I/dt^2 = 0$ , or equivalently  $d^3D/dt^3 = 0$ :

$$\begin{aligned} \frac{d^3D_{II}}{dt^3} &= I_0\epsilon\delta e^{\lambda+t_0+\frac{2\sqrt{\beta\sigma}}{\alpha}} e^{-\frac{\alpha(t-t_0)}{2}\left(\frac{\gamma+\epsilon\delta+\sigma}{\alpha}-\frac{1}{2}\right)} \\ & e^{-\frac{2\sqrt{e^{-\alpha(t-t_0)}\beta\sigma}}{\alpha}} \\ & \times \left[\left(\frac{\gamma + \epsilon\delta + \sigma}{2} - \frac{\alpha}{4} - \sqrt{e^{-\alpha(t-t_0)}\beta\sigma}\right)^2 - \frac{\alpha}{2}\sqrt{e^{-\alpha(t-t_0)}\beta\sigma}\right] \\ & = 0. \end{aligned} \tag{61}$$

Eq. (61) has two solutions, which correspond to the infection tipping points

$$t_{1,2} = t_0 + \frac{2}{\alpha} \ln \left( \frac{2\sqrt{\beta\sigma}}{\gamma + \delta\epsilon + \sigma \mp \sqrt{\alpha(\gamma + \epsilon\delta + \sigma - \frac{\alpha}{4})}} \right). \tag{62}$$

The duration of the epidemic peak can then be defined as a difference between these two tipping points and is equal to:

$$\Delta t_{peak} = \frac{4}{\alpha} \ln \left( \frac{\gamma + \epsilon\delta + \sigma + \sqrt{\alpha(\gamma + \epsilon\delta + \sigma - \frac{\alpha}{4})}}{\gamma + \epsilon\delta + \sigma - \alpha/2} \right). \tag{63}$$

## References

1. Liu, X., Zheng, X., Balachandran, B.: COVID-19: data-driven dynamics, statistical and distributed delay models, and observations. *Nonlinear Dyn.* **101**, 1527–1543 (2020). <https://doi.org/10.1007/s11071-020-05863-5>
2. Mondal, J., Khajanchi, S.: Mathematical modeling and optimal intervention strategies of the COVID-19 outbreak. *Nonlinear Dyn.* (2022). <https://doi.org/10.1007/s11071-022-07235-7>
3. Zhou, B., Jiang, D., Dai, Y., Hayat, T.: Stationary distribution and density function expression for a stochastic SIQRS epidemic model with temporary immunity. *Nonlinear Dyn.* **105**, 931–955 (2021). <https://doi.org/10.1007/s11071-020-06151-y>
4. Han, C., Li, M., Haihambro, N., Babuna, P., Liu, Q., Zhao, X., Jaeger, C., Li, Y., Yang, S.: Mechanisms of recurrent outbreak of COVID-19: a model-based study. *Nonlinear Dyn.* **106**, 1169–1185 (2021). <https://doi.org/10.1007/s11071-021-06371-w>
5. Al-Darabsah, I.: Threshold dynamics of a time-delayed epidemic model for continuous imperfect-vaccine with a generalized nonmonotone incidence rate. *Nonlinear Dyn.* **101**, 1281–1300 (2020). <https://doi.org/10.1007/s11071-020-05825-x>
6. Zhai, S., Luo, G., Huang, T., Wang, X., Tao, J., Zhou, P.: Vaccination control of an epidemic model with time delay and its application to COVID-19. *Nonlinear Dyn.* **106**, 1279–1292 (2021). <https://doi.org/10.1007/s11071-021-06533-w>
7. Raza, A., Rafiq, M., Awrejcewicz, J., Ahmed, N., Mohsin, M.: Dynamical analysis of coronavirus disease with crowding effect, and vaccination: a study of third strain. *Nonlinear Dyn.* (2022). <https://doi.org/10.1007/s11071-021-07108-5>
8. Das, P., Upadhyay, R.K., Misra, A.K., Rihan, F.A., Das, P., Ghosh, D.: Mathematical model of COVID-19 with comorbidity and controlling using non-pharmaceutical interventions and vaccination. *Nonlinear Dyn.* **106**, 1213–1227 (2021). <https://doi.org/10.1007/s11071-021-06517-w>
9. Guan, G., Guo, Z.: Stability behavior of a two-susceptibility SHIR epidemic model with time delay in complex networks. *Nonlinear Dyn.* **106**, 1083–1110 (2021). <https://doi.org/10.1007/s11071-021-06804-6>
10. Das, P., Nadim, S.S., Das, S., Das, P.: Dynamics of COVID-19 transmission with comorbidity: a data driven modelling based approach. *Nonlinear Dyn.* **106**, 1197–1211 (2021). <https://doi.org/10.1007/s11071-021-06324-3>
11. Babajanyan, S.G., Cheong, K.H.: Age-structured SIR model and resource growth dynamics: a COVID-19 study. *Nonlinear Dyn.* **104**, 2853–2864 (2021). <https://doi.org/10.1007/s11071-021-06384-5>
12. Vilar, J.M.G., Saiz, L.: Reliably quantifying the evolving worldwide dynamic state of the COVID-19 outbreak from death records, clinical parametrization, and demographic data. *Sci. Rep.* **11**, 19952 (2021). <https://doi.org/10.1038/s41598-021-99273-1>
13. Vilar, J.M.G., Saiz, L.: Ascertaining the initiation of epidemic resurgences: an application to the COVID-19 second surges in Europe and the Northeast United States. *R Soc. Open Sci.* **8**, 210773 (2021). <https://doi.org/10.1098/rsos.210773>
14. Xu, L., Zhang, H., Xu, H., Yang, H., Zhang, L., Zhang, W., Gu, F., Lan, X.: The coSIR model predicts effective strategies to limit the spread of SARS-CoV-2 variants with low severity and high transmissibility. *Nonlinear Dyn.* **105**, 2757–2773 (2021). <https://doi.org/10.1007/s11071-021-06705-8>
15. Khyar, O., Allali, K.: Global dynamics of a multi-strain SEIR epidemic model with general incidence rates: application to COVID-19 pandemic. *Nonlinear Dyn.* **102**, 489–509 (2020). <https://doi.org/10.1007/s11071-020-05929-4>
16. Ahmed, N., Elsonbaty, A., Raza, A., Rafiq, M., Adel, W.: Numerical simulation and stability analysis of a novel reaction-diffusion COVID-19 model. *Nonlinear Dyn.* **106**, 1293–1310 (2021). <https://doi.org/10.1007/s11071-021-06623-9>
17. Di Giamberardino, P., Iacoviello, D., Papa, F., Sinigalli, C.: A data-driven model of the COVID-19 spread among interconnected populations: epidemiological and mobility aspects following the lockdown in Italy. *Nonlinear Dyn.* **106**, 1239–1266 (2021). <https://doi.org/10.1007/s11071-021-06840-2>
18. Jia, Q., Li, J., Lin, H., Tian, F., Zhu, G.: The spatiotemporal transmission dynamics of COVID-19 among multiple regions: a modeling study in Chinese provinces. *Nonlinear Dyn.* **107**, 1313–1327 (2022). <https://doi.org/10.1007/s11071-021-07001-1>
19. Sun, G.Q., Wang, S.F., Li, M.T., Li, L., Zhang, J., Zhang, W., Jin, Z., Feng, G.L.: Transmission dynamics of COVID-19 in Wuhan, China: effects of lockdown and medical resources. *Nonlinear Dyn.* **101**, 1981–1993 (2020). <https://doi.org/10.1007/s11071-020-05770-9>
20. Zlatić, V., Barjašić, I., Kadović, A., Štefančić, H., Gabrielli, A.: Bi-stability of SUDR+K model of epidemics and test kits applied to COVID-19. *Nonlinear Dyn.* **101**, 1635–1642 (2020). <https://doi.org/10.1007/s11071-020-05888-w>
21. Pacheco, P.M.C.L., Savi, M.A., Savi, P.V.: COVID-19 dynamics considering the influence of hospital infrastructure: an investigation into Brazilian scenarios. *Nonlinear Dyn.* **106**, 1325–1346 (2021). <https://doi.org/10.1007/s11071-021-06323-4>
22. Li, T., Xiao, Y.: Complex dynamics of an epidemic model with saturated media coverage and recovery. *Nonlinear Dyn.* (2022). <https://doi.org/10.1007/s11071-021-07096-6>
23. Rai, R.K., Khajanchi, S., Tiwari, P.K., Venturino, E., Misra, A.K.: Impact of social media advertisements on the transmission dynamics of COVID-19 pandemic in India. *J. Appl. Math. Comput.* **68**, 19–44 (2022). <https://doi.org/10.1007/s12190-021-01507-y>
24. WHO report. URL <https://www.who.int/emergencies/diseases/novel-coronavirus-2019/situation>
25. Diekmann, O., Heesterbeek, H., Britton, T.: *Mathematical tools for understanding infectious disease dynamics*. Princeton University Press, Princeton, NJ, USA (2012)
26. Martcheva, M.: *An introduction to mathematical epidemiology*. Springer, Berlin, Germany (2015)
27. Keeling, M.J., Rohani, P.: *Modeling infectious diseases in humans and animals*. Princeton University Press, Princeton, NJ, USA (2011)
28. Alagoz, O., Sethi, A.K., Patterson, B.W., Churpek, M., Safdar, N.: Effect of Timing of and Adherence to Social Distancing Measures on COVID-19 Burden in the United States.






- Ann. Intern. Med. **174**(1), 50–57 (2021). <https://doi.org/10.7326/m20-4096>
29. Oraby, T., Tyshenko, M.G., Maldonado, J.C., Vatcheva, K., Elsaadany, S., Alali, W.Q., Longenecker, J.C., Al-Zoughool, M.: Modeling the effect of lockdown timing as a COVID-19 control measure in countries with differing social contacts. *Sci. Rep.* **11**, 3354 (2021)
  30. Dressler, D.D.: Social Distancing's Effects on COVID-19: Roles of Timing and Adherence. *NEJM COVID Watch*. <https://www.jwatch.org/na52712/2020/11/03/social-distancings-effects-covid-19-roles-timing-and> (2020)
  31. Nande, A., Adlam, B., Sheen, J., Levy, M.Z., Hill, A.L.: Dynamics of COVID-19 under social distancing measures are driven by transmission network structure. *PLoS Comput. Biol.* **17**(2), e1008684 (2021). <https://doi.org/10.1371/journal.pcbi.1008684>
  32. Benjamin, M.F., Brockmann, D.: Effective containment explains subexponential growth in recent confirmed COVID-19 cases in China. *Science* **368**, 742–746 (2020). <https://doi.org/10.1126/science.abb4557>
  33. He, S., Peng, Y., Sun, K.: SEIR modeling of the COVID-19 and its dynamics. *Nonlinear Dyn.* **101**, 1667–1680 (2020). <https://doi.org/10.1007/s11071-020-05743-y>
  34. Hametner, C., Kozek, M., Boehler, L., Wasserburger, A., Du, Z.P., Kölbl, R., Bergmann, M., Bachleitner-Hofmann, T., Jakubek, S.: Estimation of exogenous drivers to predict COVID-19 pandemic using a method from nonlinear control theory. *Nonlinear Dyn.* **106**, 1111–1125 (2021). <https://doi.org/10.1007/s11071-021-06811-7>
  35. Carvalho, T., Cristiano, R., Rodrigues, D.S., Tonon, D.J.: Global analysis of a piecewise smooth epidemiological model of COVID-19. *Nonlinear Dyn.* **105**, 3763–3773 (2021). <https://doi.org/10.1007/s11071-021-06801-9>
  36. Saha, S., Samanta, G.P., Nieto, J.J.: Epidemic model of COVID-19 outbreak by inducing behavioural response in population. *Nonlinear Dyn.* **102**, 455–487 (2020). <https://doi.org/10.1007/s11071-020-05896-w>
  37. Huang, J., Qi, G.: Effects of control measures on the dynamics of COVID-19 and double-peak behavior in Spain. *Nonlinear Dyn.* **101**, 1889–1899 (2020). <https://doi.org/10.1007/s11071-020-05901-2>
  38. Saikia, D., Bora, K., Bora, M.P.: COVID-19 outbreak in India: an SEIR model-based analysis. *Nonlinear Dyn.* **104**, 4727–4751 (2021). <https://doi.org/10.1007/s11071-021-06536-7>
  39. Kwuimy, C.A.K., Nazari, F., Jiao, X., Rohani, P., Nataraj, C.: Nonlinear dynamic analysis of an epidemiological model for COVID-19 including public behavior and government action. *Nonlinear Dyn.* **101**, 1545–1559 (2020). <https://doi.org/10.1007/s11071-020-05815-z>
  40. Kermack, W.O., McKendrick, A.G.: A contribution to the mathematical theory of epidemics. In: *Proceedings of the Royal Society of London. Series A, Mathematical and Physical Sciences* **115**, 700–721 (1927)
  41. Friedman, A., Kao, C.Y.: *Mathematical modeling of biological processes*. Springer, Berlin, Germany (2014)
  42. Newman, M.E.J.: The spread of epidemic disease on networks. *Phys. Rev. E* **66**, 016128 (2002). <https://doi.org/10.1103/PhysRevE.66.016128>
  43. Schutz, G.M., Brandaut, M., Trimper, S.: Exact solution of a stochastic susceptible-infectious-recovered model. *Phys. Rev. E* **78**, 061132 (2008). <https://doi.org/10.1103/PhysRevE.78.061132>
  44. Awawdeh, F., Adawi, A., Mustafa, Z.: Solutions of the SIR models of epidemics using HAM. *Chaos Solitons Fractals* **42**, 3047–3052 (2009). <https://doi.org/10.1016/j.chaos.2009.04.012>
  45. Khan, H., Mohapatra, R.N., Vajravelu, K., Liao, S.J.: The explicit series solution of SIR and SIS epidemic models. *Appl. Math. Comput.* **38**, 653–669 (2009). <https://doi.org/10.1016/j.amc.2009.05.051>
  46. Harko, T., Lobo, F.S.N., Mak, M.K.: Exact analytical solutions of the susceptible-infected-recovered (SIR) epidemic model and of the SIR model with equal death and birth rates. *Appl. Math. Comput.* **236**, 184 (2014). <https://doi.org/10.1016/j.amc.2014.03.030>
  47. Barlow, N.S., Weinstein, S.J.: Accurate closed-form solution of the SIR epidemic model. *Physica D* **408**, 132540 (2020). <https://doi.org/10.1016/j.physd.2020.132540>
  48. Carvalho, A.M., Goncalves, S.: An analytical solution for the Kermack–McKendrick model. *Physica A* **566**, 125659 (2021). <https://doi.org/10.1016/j.physa.2020.125659>
  49. Sadurni, E., Luna-Acosta, G.: Exactly solvable SIR models, their extensions and their application to sensitive pandemic forecasting. *Nonlinear Dyn.* **103**, 2955–2971 (2021). <https://doi.org/10.1007/s11071-021-06248-y>
  50. Kroeger, M., Schlickeiser, R.: Analytical solution of the SIR-model for the temporal evolution of epidemics. Part A: time-independent reproduction factor. *J. Phys. A* **53**, 505601 (2020). <https://doi.org/10.1088/1751-8121/abc65d>
  51. Schlickeiser, R., Kroeger, M.: Analytical solution of the SIR-model for the temporal evolution of epidemics. Part B: semi-time case. *J. Phys. A* **54**, 175601 (2021). <https://doi.org/10.1088/1751-8121/abed66>
  52. Weinstein, S.J., Holland, M.S., Rogers, K.E., Barlow, N.S.: Analytic solution of the SEIR epidemic model via asymptotic approximant. *Physica D: Nonlinear Phenomena* **411**, 132633 (2020). <https://doi.org/10.1016/j.physd.2020.132633>
  53. Piovella, N.: Analytical solution of SEIR model describing the free spread of the COVID-19 pandemic. *Chaos Solitons Fractals* **140**, 110243 (2020). <https://doi.org/10.1016/j.chaos.2020.110243>
  54. Miller, J.C.: A note on the derivation of epidemic final sizes. *Bull. Math. Biol.* **74**, 2125–2141 (2012). <https://doi.org/10.1007/s11538-012-9749-6>
  55. Turkyilmazoglu, M.: Explicit formulae for the peak time of an epidemic from the SIR model. *Physica D: Nonlinear Phenomena* **422**, 132902 (2021). <https://doi.org/10.1016/j.physd.2021.132902>
  56. Kroeger, M., Turkyilmazoglu, M., Schlickeiser, R.: Explicit formulae for the peak time of an epidemic from the SIR model. Which approximant to use? *Physica D: Nonlinear Phenomena* **425**, 132981 (2021). <https://doi.org/10.1016/j.physd.2021.132981>
  57. Djordjevic, M., Rodic, A., Salom, I., Zigic, D., Milicevic, O., Ilic, B., Djordjevic, M.: A systems biology approach to COVID-19 progression in population. *Adv. Protein. Chem. Struct. Biol.* **127**, 291–314 (2021). <https://doi.org/10.1016/bs.apcsb.2021.03.003>

58. Djordjevic, M., Djordjevic, M., Ilic, B., Stojku, S., Salom, I.: Understanding infection progression under strong control measures through universal COVID-19 growth signatures. *Glob. Chall.* **5**, 2000101 (2021). <https://doi.org/10.1002/gch2.202170051>
59. Li, R., Pei, S., Chen, B., Song, Y., Zhang, T., Yang, W., Shaman, J.: Substantial undocumented infection facilitates the rapid dissemination of novel coronavirus (SARS-CoV-2). *Science* **368**, 489–493 (2020). <https://doi.org/10.1126/science.abb3221>
60. He, X., Lau, E.H.Y., Wu, P., Deng, X., Wang, J., Hao, X., Lau, Y.C., Wong, J.Y., Guan, Y., Tan, X., Mo, X., Chen, Y., Liao, B., Chen, W., Hu, F., Zhang, Q., Zhong, M., Wu, Y., Zhao, L., Zhang, F., Cowling, B.J., Li, F., Leung, G.M.: Temporal dynamics in viral shedding and transmissibility of COVID-19. *Nat. Med.* **26**, 672–675 (2020). <https://doi.org/10.1038/s41591-020-0869-5>
61. Bar-On, Y.M., Flamholz, A.I., Phillips, R., Milo, R.: Science forum: SARS-CoV-2 (COVID-19) by the numbers. *eLife* **9**, e57309 (2020)
62. Phillips, R., Kondev, J., Theriot, J., Garcia, H.: *Physical biology of the cell*. Garland Science, New York, NY, USA (2012)
63. Worldometer: COVID-19 coronavirus pandemic. <https://www.worldometers.info/coronavirus/> (2020)
64. Bowman, F.: *Introduction to Bessel functions*. Dover, New York NY, USA (1958)
65. Weisstein, E.W.: *CRC concise encyclopedia of mathematics*. Chapman & Hall, CRC Press, Boca Raton, FL, USA (2003)
66. Abramowitz, M., Stegun, I.A.: *Handbook of Mathematical Functions*. Dover Publications, New York, NY, USA (1972)
67. Markovic, S., Rodic, A., Salom, I., Milicevic, O., Djordjevic, M., Djordjevic, M.: COVID-19 severity determinants inferred through ecological and epidemiological modeling. *One Health* **13**, 100355 (2021). <https://doi.org/10.1016/j.onehlt.2021.100355>
68. Zwillinger, D.: *CRC standard mathematical tables and formulae*. CRC Press, Boca Raton, FL, USA (1995)
69. Sarkar, K., Khajanchi, S., Nieto, J.J.: Modeling and forecasting the COVID-19 pandemic in India. *Chaos, Solitons Fractals* **139**, 110049 (2020)
70. Salom, I., Rodic, A., Milicevic, O., Zigic, D., Djordjevic, M., Djordjevic, M.: Effects of demographic and weather parameters on COVID-19 basic reproduction number. *Front. Ecol. Evol.* **8**, 617841 (2021). <https://doi.org/10.3389/fevo.2020.617841>
71. Milicevic, O., Salom, I., Rodic, A., Markovic, S., Tumbas, M., Zigic, D., Djordjevic, M., Djordjevic, M.: PM2.5 as a major predictor of COVID-19 basic reproduction number in the USA. *Environ. Res.* **201**, 111526 (2021). <https://doi.org/10.1016/j.envres.2021.111526>
72. Djordjevic, M., Salom, I., Markovic, S., Rodic, A., Milicevic, O., Djordjevic, M.: Inferring the main drivers of SARS-CoV-2 global transmissibility by feature selection methods. *GeoHealth* **5**(9), e2021GH000432 (2021). <https://doi.org/10.1029/2021GH000432>
73. Tadic, B., Melnik, R.: Modeling latent infection transmissions through biosocial stochastic dynamics. *PloS One* **15**(10), e0241163 (2020). <https://doi.org/10.1371/journal.pone.0241163>
74. Tadic, B., Melnik, R.: Microscopic dynamics modeling unravels the role of asymptomatic virus carriers in SARS-CoV-2 epidemics at the interplay between biological and social factors. *Comput. Biol. Med.* **133**, 104422 (2021). <https://doi.org/10.1016/j.combiomed.2021.104422>
75. Frieden, T.R., Buissonniere, M., McClelland, A.: The world must prepare now for the next pandemic. *BMJ Glob. Health* **6**, e005184 (2021). <https://doi.org/10.1136/bmjgh-2021-005184>
76. Boyce, W.E., DiPrima, R.C., Rosatone, L.: *Elementary differential equations and boundary value problems*. Wiley, Hoboken, NJ, USA (2012)
77. Kreyszig, E.: *Advanced engineering mathematics*. Wiley, Hoboken, NJ, USA (2006)

**Publisher's Note** Springer Nature remains neutral with regard to jurisdictional claims in published maps and institutional affiliations.

Springer Nature or its licensor (e.g. a society or other partner) holds exclusive rights to this article under a publishing agreement with the author(s) or other rightsholder(s); author self-archiving of the accepted manuscript version of this article is solely governed by the terms of such publishing agreement and applicable law.



**Constraining  $\eta/s$  through high- $p_{\perp}$  theory and data**Bithika Karmakar , Dusan Zigic , Igor Salom , and Magdalena Djordjevic <sup>\*</sup>  
*Institute of Physics Belgrade, University of Belgrade, Belgrade 11080, Serbia*Jussi Auvinen   
*Institute of Physics Belgrade, University of Belgrade, Belgrade 11080, Serbia  
and University of Jyväskylä, Jyväskylä P.O. Box 35, FI-40014, Finland*Pasi Huovinen  
*Incubator of Scientific Excellence—Centre for Simulations of Superdense Fluids, University of Wrocław, Wrocław 50-204, Poland*Marko Djordjevic  
*Faculty of Biology, University of Belgrade, Belgrade 11000, Serbia*

(Received 19 June 2023; accepted 26 September 2023; published 24 October 2023)

We study whether it is possible to use high- $p_{\perp}$  data/theory to constrain the temperature dependence of the shear viscosity over entropy density ratio  $\eta/s$  of the matter formed in ultrarelativistic heavy-ion collisions at the BNL Relativistic Heavy Ion Collider (RHIC) and the CERN Large Hadron Collider (LHC). We use two approaches: (i) We calculate high- $p_{\perp}$   $R_{AA}$  and flow coefficients  $v_2$ ,  $v_3$ , and  $v_4$  assuming different  $(\eta/s)(T)$  of the fluid-dynamically evolving medium. (ii) We calculate the quenching strength  $(\hat{q}/T^3)$  from our dynamical energy loss model and convert it to  $\eta/s$  as a function of temperature. It turned out that the first approach cannot distinguish between different  $(\eta/s)(T)$  assumptions when the evolution is constrained to reproduce the low- $p_{\perp}$  data. In distinction,  $(\eta/s)(T)$  calculated using the second approach agrees surprisingly well with the  $(\eta/s)(T)$  inferred through state-of-the-art Bayesian analyses of the low- $p_{\perp}$  data even in the vicinity of  $T_c$ , while providing much smaller uncertainties at high temperatures.

DOI: [10.1103/PhysRevC.108.044907](https://doi.org/10.1103/PhysRevC.108.044907)**I. INTRODUCTION**

Quantum chromodynamics (QCD) predicts that at extremely high densities matter undergoes a transition to a state consisting of deconfined and interacting quarks, antiquarks, and gluons [1,2]. According to the current cosmology, this new state of matter, called quark-gluon plasma (QGP) [3], existed immediately after the big bang [4]. Today, QGP is created in “little bangs,” when heavy ions collide at ultrarelativistic energies [5] in experiments at the BNL Relativistic Heavy Ion Collider (RHIC) and the CERN Large Hadron Collider (LHC). Such collisions lead to an expanding fireball of quarks and gluons, which thermalizes to form QGP. The QGP cools down, and quarks and gluons hadronize when the temperature  $T$  drops to the critical temperature  $T_c$ .

Extracting useful information from “little bangs” requires comparing theoretical predictions with experimental data. By such comparisons, it is established that QGP is formed in the RHIC and LHC experiments [6] through two main lines of evidence [5–7]: (i) by comparison of low transverse momentum ( $p_{\perp}$ ) measurements with relativistic hydrodynamical predictions, which imply that created QGP is consistent with the description of a nearly perfect fluid [8–10], and (ii) by comparison of perturbative QCD (pQCD) predictions with high- $p_{\perp}$  data [11–14], which showed that high- $p_{\perp}$  partons (jets) significantly interact with the opaque medium [5]. Beyond the discovery phase, the current challenge is to investigate the properties of this extreme form of matter [15–25].

The QGP was expected to behave as a weakly interacting gas based on ideas of asymptotic freedom and color screening [26]. Thus, the agreement of the fluid-dynamical predictions, which assumed the QGP to behave as a nearly inviscid fluid, with the data came as a surprise [10]. Furthermore, subsequent calculations revealed [10] that reproduction of the data required the shear viscosity to entropy density ratio ( $\eta/s$ ) of QGP to be near the lower bound predicted by anti-de Sitter and conformal field theory (AdS/CFT) correspondence [27].

However, the temperature of the QGP changes significantly [28] during the evolution of the collision system. For example, in the LHC experiments, the temperature is estimated

<sup>\*</sup>Email: [magda@ipb.ac.rs](mailto:magda@ipb.ac.rs)

Published by the American Physical Society under the terms of the [Creative Commons Attribution 4.0 International](https://creativecommons.org/licenses/by/4.0/) license. Further distribution of this work must maintain attribution to the author(s) and the published article’s title, journal citation, and DOI. Funded by SCOAP<sup>3</sup>.

to span the range from  $4T_c$  to  $T_c$ . Even if the QGP behaves as a perfect fluid close to  $T_c$  (the “soft,” strongly coupled regime), its  $\eta/s$  may significantly increase with increasing  $T$  if the QGP becomes weakly coupled at higher temperatures (the “hard,” weakly coupled regime). We call this possibility the “soft-to-hard” medium hypothesis.

Testing this hypothesis has turned out to be surprisingly difficult. Reproduction of the observed anisotropies of low- $p_\perp$  particles necessitates low  $\eta/s$  in the vicinity of  $T_c$ , but the value of shear viscosity in higher temperatures has only a weak effect on anisotropies in collisions at LHC energies, and basically no effect at all at RHIC [29–31]. In the recent Bayesian analyses of the data, this is manifested in a well constrained  $\eta/s$  in the  $T_c \lesssim T \lesssim 1.5T_c$  temperature range and weak constraints at larger temperatures [17–20]. Some of the most recent Bayesian analyses [32,33] even suggest that  $\eta/s$  may decrease in the region  $T_c-2T_c$ , where the reason for such a decrease still remains to be understood.

Thus, it is evident that a complementary theory and observables are needed to investigate the “soft-to-hard” medium hypothesis. Since most of the jet energy loss takes place when the system is hottest, it is reasonable to expect the high- $p_\perp$  observables to be sensitive to the properties of the system at that stage. To use jet energy loss and high- $p_\perp$  data to provide constraints to the bulk properties of the collision system, we developed the state-of-the-art DREENA tomography tool [34,35] based on the dynamical energy loss formalism [36–38]. So far, we have used this tool to, e.g., provide constraints to the early evolution of the collision system [22] and map how the shape of the collision system is manifested in the high- $p_\perp$  data [23].

In this study, we explore whether high- $p_\perp$  data can provide constraints on the  $\eta/s$  ratio of QGP at high temperatures. As is known, shear viscosity generates entropy, which means that the system with larger viscosity cools slower or, alternatively, to reach the same final entropy, the system with larger viscosity must have a lower initial temperature. Thus, different assumed  $\eta/s$  during the early evolution of the system may lead to different jet energy loss and therefore different nuclear suppression factor  $R_{AA}$ . As well, azimuthal anisotropy in path lengths and temperature along the paths leads to azimuthal dependence of jet suppression [5], which is measured as  $v_n$  of high- $p_\perp$  particles. High- $p_\perp$   $v_n$  are known to be sensitive to the details of the medium evolution [34,35,39], and, since viscosity changes the evolution of the anisotropy of the system, the changes in  $\eta/s$  can lead to changes in high- $p_\perp$   $v_n$ . We choose three different parametrizations of  $(\eta/s)(T)$ , adjust the parameters to reproduce the low- $p_\perp$  data measured in  $\sqrt{s_{NN}} = 200$  GeV Au + Au collisions (RHIC) and  $\sqrt{s_{NN}} = 5.02$  TeV Pb + Pb collisions (LHC), calculate the temperature evolution of the system, and energy loss of jets traversing this system in each case, and evaluate the  $R_{AA}$  and high- $p_\perp$   $v_2$ ,  $v_3$ , and  $v_4$  to see if different assumptions of  $\eta/s$  lead to differences in these observables.

Complementary to this phenomenological approach to infer the  $\eta/s$  ratio from the experimental data, we also provide a fully theoretical estimate of  $\eta/s$  based on jet energy loss: The jet quenching strength is quantified through the jet quenching parameter  $\hat{q}$ . It has been argued that in a weakly coupled

regime  $T^3/\hat{q}$  is directly proportional to  $\eta/s$  [40], and thus evaluating one allows one to know the other. We estimate the quenching parameter  $\hat{q}$  as function of temperature using our dynamical energy loss formalism, convert it to  $\eta/s$ , and compare the resulting  $(\eta/s)(T)$  to constraints obtained from state-of-the-art Bayesian analyses [18,19].

## II. METHODS

### A. Modeling the bulk evolution

To calculate the temperature evolution and the low- $p_\perp$  observables we use the version of VISHNEW [41,42] used in Refs. [17,18,43].<sup>1</sup> It is a code to solve the dissipative fluid-dynamical equations in 2+1 dimensions, i.e., assuming boost invariance. Shear stress and bulk pressure are taken as dynamical variables and evolved according to the Israel-Stewart type equations [45]. We use an equation of state (EoS) [43] that combines the lattice QCD-based EoS of the HotQCD Collaboration [46] at large temperatures and a hadron resonance gas EoS at low temperatures. At a constant temperature  $T_{sw} = 151$  MeV hypersurface, we convert the fluid to particle ensembles according to the Cooper-Frye prescription [47]. These ensembles are fed to the UrQMD hadron cascade [48,49], which describes the evolution of the hadronic stage of the system until freeze-out.

We generate the event-by-event fluctuating initial states using the T<sub>R</sub>ENTo model [50]. In this model nucleus-nucleus collisions are considered as a superposition of nucleon-nucleon collisions. The nucleons are represented by Gaussian distributions, which in this study have the width  $w = 0.5$  fm while the minimum nucleon-nucleon distance within the nucleus is also set to  $d = 0.5$  fm. The inelastic nucleon-nucleon cross section is 70 mb at  $\sqrt{s_{NN}} = 5.02$  TeV (energy of Pb + Pb collisions) and 42 mb at  $\sqrt{s_{NN}} = 200$  GeV (energy of Au + Au collisions). For the other parameters we use the maximum *a posteriori* (MAP) values found in Ref. [18]. We do not allow any preequilibrium evolution (free-streaming or otherwise), and use  $\tau_0 = 1$  fm/c as the initial time for fluid-dynamical evolution, since the reproduction of the high- $p_\perp$  observables does not allow strong transverse expansion earlier [22].

We include both bulk and shear viscosity in our fluid-dynamical calculation. The temperature dependence of the bulk viscosity coefficient  $\zeta$  is parametrized as a Cauchy distribution [18]:

$$(\zeta/s)(T) = \frac{(\zeta/s)_{\max}}{1 + \left(\frac{T-T_0}{(\zeta/s)_{\text{width}}}\right)^2}. \quad (1)$$

We consider a small bulk viscosity with a maximum value  $(\zeta/s)_{\max} = 0.03$ , the width parameter  $(\zeta/s)_{\text{width}} = 0.022$ , and  $T_0 = 0.183$  GeV. As in the case of the T<sub>R</sub>ENTo parameters described above, the width and  $T_0$  correspond to MAP parameter values from Ref. [18]. However, the maximum of the bulk viscosity  $[(\zeta/s)_{\max}]$  is decreased compared to the MAP

<sup>1</sup>Code available at [44].

value in [18] to compensate for the lack of preequilibrium free streaming and still reach agreement with the  $p_\perp$  spectra.

As mentioned, our main objective is to find out whether high- $p_\perp$  data can provide constraints to  $\eta/s$  at high temperatures. Naively one can expect the jet energy loss to be proportional to the third power of temperature ( $T^3$ ), but a detailed calculation has shown it to be proportional to only

$$(\eta/s)(T) = \begin{cases} (\eta/s)_{\min}, & T < T_c, \\ (\eta/s)_{\min} + (\eta/s)_{\text{slope}}(T - T_c)\left(\frac{T}{T_c}\right)^{(\eta/s)_{\text{crv}}}, & T > T_c, \end{cases} \quad (2)$$

where  $(\eta/s)_{\min}$  is the minimum value of the specific shear viscosity,  $(\eta/s)_{\text{slope}}$  is the slope above  $T_c$ , and  $(\eta/s)_{\text{crv}}$  controls the curvature above  $T_c$ .  $T_c$  is fixed to the pseudo-critical temperature  $T_c = 154$  MeV evaluated by the HotQCD Collaboration [46].

We study three different scenarios, each capable of describing a subset of low- $p_\perp$  data at RHIC and LHC with reasonable accuracy:

- (1) constant  $\eta/s$  (0.15 for Pb + Pb collision at LHC and 0.12 for Au + Au collision at RHIC),
- (2)  $(\eta/s)_{\min} = 0.1$ ,  $(\eta/s)_{\text{slope}} = 1.11$ ,  $(\eta/s)_{\text{crv}} = -0.48$ ,
- (3)  $(\eta/s)_{\min} = 0.04$ ,  $(\eta/s)_{\text{slope}} = 3.30$ ,  $(\eta/s)_{\text{crv}} = 0$ .

The parameters in our second scenario are within the 90% credible intervals of the analysis of Ref. [18]. Therefore, we label it as ‘‘Nature.’’ Nevertheless, our  $(\eta/s)_{\min}$  is larger than in Ref. [18] since we require the reproduction of the RHIC data, not only the LHC data. As is known, including the RHIC data tends to increase the favored minimum value of  $\eta/s$  [20]. Our third scenario with its very rapidly rising  $\eta/s$  (see Fig. 8) is inspired by the ‘‘LHHQ’’ parametrization in Ref. [30]. Consequently, we label it as such.

To calculate the low- $p_\perp$  and high- $p_\perp$  predictions, we generated  $10^4$  minimum-bias events and sorted the events in centrality classes according to the number of participants. While using the final particle multiplicity would be closer to the centrality selection done in experiments, participant number sorting allows us to reduce the number of hydrodynamic simulations by focusing on the narrower (10–50)% centrality range, thus saving computational resources (we numerically tested that this approximation would have a negligible effect on theoretical predictions). Finally, we evaluated the event-averaged observables in each centrality bin.

We reproduced the pion, kaon, and proton multiplicities and charged hadron four-particle cumulant elliptic flow  $v_2\{4\}$  in Au + Au collisions at  $\sqrt{s_{NN}} = 200$  GeV (RHIC) and Pb + Pb collisions at  $\sqrt{s_{NN}} = 5.02$  TeV (LHC) in 10–20%, 20–30%, 30–40%, and 40–50% centrality classes by varying only the nucleon-nucleon cross section according to the collision energy and the overall normalization factor according to the collision energy and choice of  $(\eta/s)(T)$ . All the other T<sub>R</sub>ENTO parameters were kept the same in all cases. For the LHHQ parametrization, the minimum value of  $\eta/s$  is chosen to get an acceptable agreement of  $v_2\{4\}$  with both Pb + Pb and Au + Au collision data. The centrality dependence of charged

$T^{1.2}$  [51,52]. Since the sensitivity to temperature is weaker than expected, we want to maximize the difference in temperature due to differences in  $\eta/s$ . Therefore we do not take as our  $(\eta/s)(T)$  the upper and lower limits suggested by the Bayesian analyses [18,19] but something more extreme. We parametrize the temperature dependence of  $\eta/s$  as [17,18]

particle multiplicities ( $p_\perp$ -integrated yields) for Pb + Pb and Au + Au collisions with three different  $(\eta/s)(T)$  parametrizations found from the hydrodynamical simulation are shown in the left panels of Fig. 1. The four-particle elliptic flow coefficient  $v_2\{4\}$  at different centrality classes for Pb + Pb and Au + Au collisions are shown in the right panels of Fig. 1.

## B. Overview of DREENA framework

After evaluating the temperature evolution, we use the ‘‘generalized DREENA-A’’ framework to calculate the high- $p_\perp$  observables: Nuclear suppression factor  $R_{AA}$  and high- $p_\perp$  flow harmonics  $v_2$ ,  $v_3$ , and  $v_4$ . DREENA (Dynamical Radiative and Elastic ENergy loss Approach) is a computationally efficient tool for QGP tomography [34,35], based on generalized hard thermal loop (HTL) perturbation theory [57] with naturally regulated infrared divergences [36,58]. In this formalism both the radiative [37,38] and collisional energy loss [36] of high energy particles have been computed in an evolving QCD medium of finite size at finite temperature. Furthermore, the framework is extended to account for running coupling [59], finite magnetic mass [60], and beyond soft-gluon approximation [58]. We also recently extended the formalism towards finite orders in opacity [61], but showed that higher-order effects can be neglected for high- $p_\perp$  predictions. Thus, a computationally more efficient version with one scattering center is used in this study. Additionally, in this framework, all parameters are fixed to standard literature values stated below (i.e., no fitting parameters are used) [22,23]. This allows systematic comparison of data and the predictions from the simulation obtained using the same formalism and parameter set.

We use the generic pQCD convolution formula [59,62] to generate the final quenched ( $q$ ) and unquenched ( $u$ ) spectra of hadrons as

$$\frac{E_f d^3 \sigma_q(H_Q)}{dp_f^3} = \frac{E_i d^3 \sigma(Q)}{dp_i^3} \otimes P(E_i \rightarrow E_f) \otimes D(Q \rightarrow H_Q), \quad (3)$$

$$\frac{E_f d^3 \sigma_u(H_Q)}{dp_f^3} = \frac{E_i d^3 \sigma(Q)}{dp_i^3} \otimes D(Q \rightarrow H_Q), \quad (4)$$

where  $i$  and  $f$  denote the initial parton ( $Q$ ) and the final hadron ( $H_Q$ ) respectively.  $\frac{E_i d^3 \sigma(Q)}{dp_i^3}$  represents the initial parton spectrum calculated at the next-to-leading order for light

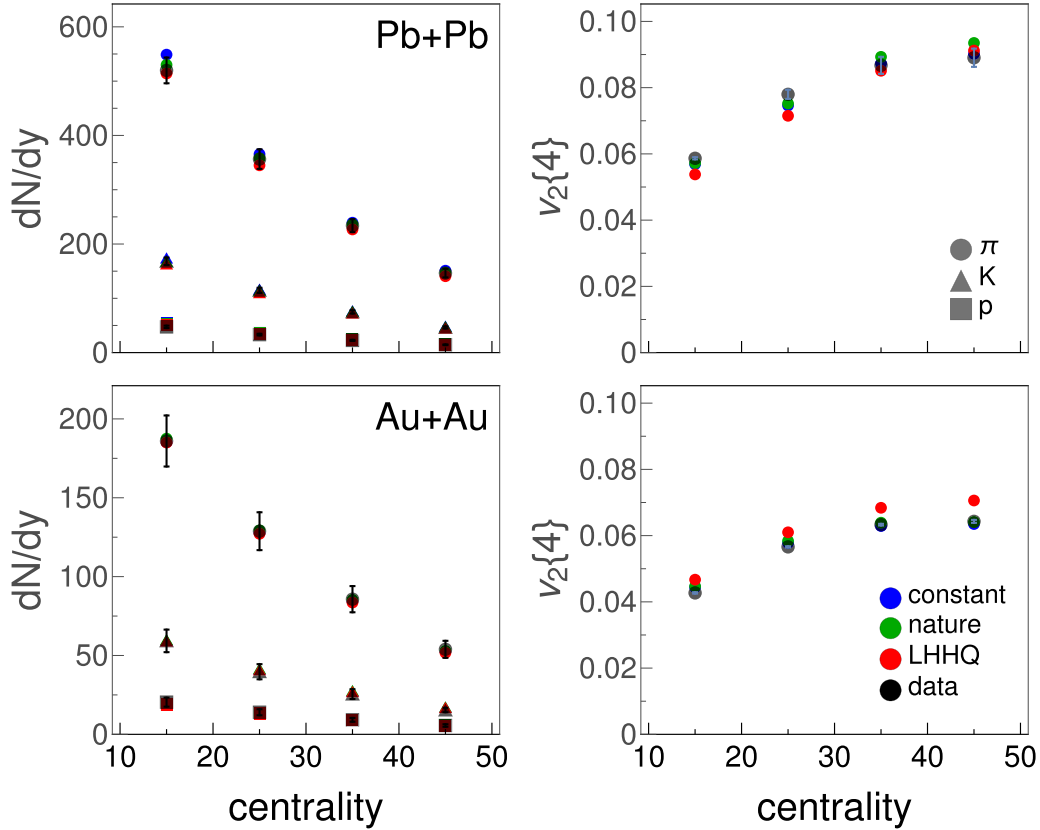


FIG. 1. Left panels: Centrality dependence of the  $p_{\perp}$ -integrated yields of pions, kaons, and protons are shown in different centrality classes. The pion multiplicity is scaled by 0.5. The upper panel corresponds to 5.02 TeV Pb + Pb collisions, where the ALICE experimental data are taken from Ref. [53]. The lower panel corresponds to 200 GeV Au + Au collisions, where the PHENIX experimental data are taken from Ref. [54]. Right panels:  $v_2\{4\}$  is shown at different centrality classes. The upper panel corresponds to 5.02 TeV Pb + Pb collisions, where the ALICE experimental data are taken from Ref. [55]. The lower panel corresponds to 200 GeV Au + Au collisions, where the STAR experimental data are taken from Ref. [56].

and heavy partons [63–65].  $P(E_i \rightarrow E_f)$  is the energy loss probability computed within finite temperature field theory.  $D(Q \rightarrow H_Q)$  represents the fragmentation function. DSS [66], BCFY [67,68], and KLP [69] fragmentation functions were used for charged hadrons,  $D$  mesons, and  $B$  mesons, respectively. DREENA-A [35], where “A” stands for adaptive (i.e., arbitrary) temperature profiles, has been optimized to incorporate any event-by-event fluctuating temperature profile [34]. For parameters, we use  $\Lambda_{\text{QCD}} = 0.2$  GeV [70–72] and the effective numbers of light quark flavors,  $n_f = 3$  and 2.5 for Pb + Pb and Au + Au collision systems, respectively. We also consider the gluon mass  $m_g = \mu_E/\sqrt{2}$  [73], where  $\mu_E$  is the temperature-dependent Debye mass computed following the procedure in Ref. [70] (outlined in the next subsection). We assume the mass of the light quarks to be  $\mu_E/6$ , and the masses of the charm and bottom quarks to be 1.2 and 4.75 GeV, respectively. The magnetic-to-electric mass ratio is  $\mu_M/\mu_E = 0.6$  [74].

### C. Derivation of transport coefficient $\hat{q}$ from dynamical energy loss formalism

To derive the transport coefficient  $\hat{q}$ , which is the squared average transverse momentum exchange between the medium

and the fast parton per unit path length [75], we start from dynamical *perturbative* QCD medium, where the interaction between high- $p_{\perp}$  partons and QGP constituents can be characterized by the HTL resummed elastic collision rate [76]:

$$\frac{d\Gamma_{el}}{d^2q} = 4C_A \left(1 + \frac{n_f}{6}\right) T^3 \frac{\alpha_s^2}{q^2(q^2 + \mu_E^2)}. \quad (5)$$

While  $\alpha_s$  in Eq. (5) is presumed to be constant, for RHIC and LHC, it is necessary to include running coupling constant in the kernel due to the wide kinematic range covered in these experiments. To include running coupling in dynamical energy loss formalism, we adopt the procedure from Ref. [77] where

$$\alpha_s^2 \rightarrow \alpha_s(ET)\alpha_s(\mu_E^2), \quad (6)$$

and  $\mu_E$  is obtained [70] as a self-consistent solution to

$$\mu_E^2 = \left(1 + \frac{n_f}{6}\right) 4\pi\alpha(\mu_E^2)T^2, \quad (7)$$

where

$$\alpha(t) = \frac{4\pi}{(11 - \frac{2}{3}n_f) \ln(\frac{t}{\Lambda^2})}, \quad (8)$$



leading to

$$\mu_E = \sqrt{\Lambda^2 \frac{\xi(T)}{W(\xi(T))}}, \quad (9)$$

where

$$\xi(T) = \frac{1 + \frac{n_f}{6}}{11 - \frac{2}{3}n_f} \left( \frac{4\pi T}{\Lambda} \right)^2, \quad (10)$$

and  $W$  is Lambert's  $W$  function. Note that  $\mu_E$  obtained through this procedure agrees with lattice QCD results [70].

By using Eqs. (9) and (6), Eq. (5) reduces to

$$\frac{d\Gamma_{el}}{d^2q} = \frac{C_A}{\pi} T \frac{\alpha(ET)\mu_E^2}{q^2(q^2 + \mu_E^2)}, \quad (11)$$

which reproduces Eq. (16) from Ref. [76] in the case of constant coupling  $\alpha(ET) = g^2/4\pi$ . Following Ref. [60], finite magnetic mass can be introduced into Eq. (11), reducing the collision rate to

$$\frac{d\Gamma_{el}}{d^2q} = \frac{C_A}{\pi} T \alpha(ET) \frac{\mu_E^2 - \mu_M^2}{(q^2 + \mu_E^2)(q^2 + \mu_M^2)}, \quad (12)$$

where  $\mu_M$  is the magnetic mass defined in the previous subsection, and  $C_A = 4/3$ . This expression [i.e., Eq. (12)] can be further reduced to

$$\frac{d\Gamma_{el}}{d^2q} = \frac{C_A}{\pi} T \alpha(ET) \left( \frac{1}{q^2 + \mu_M^2} - \frac{1}{q^2 + \mu_E^2} \right). \quad (13)$$

In the fluid rest frame, the transport coefficient  $\hat{q}$  can then be computed as [76,78]

$$\begin{aligned} \hat{q} &= \int_0^{\sqrt{6ET}} d^2q q^2 \frac{d\Gamma_{el}}{d^2q} \\ &= C_A T \alpha(ET) \int_0^{6ET} dq^2 q^2 \left( \frac{1}{q^2 + \mu_M^2} - \frac{1}{q^2 + \mu_E^2} \right) \\ &= C_A T \frac{4\pi}{(11 - \frac{2}{3}n_f)} \frac{(\mu_E^2 \ln[\frac{6ET + \mu_E^2}{\mu_E^2}] - \mu_M^2 \ln[\frac{6ET + \mu_M^2}{\mu_M^2}])}{\ln(\frac{ET}{\Lambda^2})}. \end{aligned} \quad (14)$$

In the limit  $ET \rightarrow \infty$ , Eq. (14) reduces to an expression independent of jet  $E$ :

$$\begin{aligned} \hat{q} &= C_A T \frac{4\pi}{11 - \frac{2}{3}n_f} \left( \mu_E^2 \frac{\ln \frac{ET}{\mu_E^2/6}}{\ln \frac{ET}{\Lambda^2}} - \mu_M^2 \frac{\ln \frac{ET}{\mu_M^2/6}}{\ln \frac{ET}{\Lambda^2}} \right) \\ &\approx C_A T \frac{4\pi}{11 - \frac{2}{3}n_f} (\mu_E^2 - \mu_M^2) \\ &= C_A T \frac{4\pi}{11 - \frac{2}{3}n_f} \frac{1 + \frac{n_f}{6}}{11 - \frac{2}{3}n_f} \frac{(4\pi)^2 T^2}{W(\xi(T))} (1 - x_{ME}^2) \\ &= C_A \left( \frac{4\pi}{11 - \frac{2}{3}n_f} \right)^2 \frac{4\pi (1 + \frac{n_f}{6})}{W(\xi(T))} (1 - x_{ME}^2) T^3, \end{aligned} \quad (15)$$

where  $x_{ME} = \mu_M/\mu_E$  is the magnetic-to-electric mass ratio. It is worth noticing that this is expected behavior: As a property of the medium,  $\hat{q}$  should be independent (or

weakly dependent) on jet energy [76]. Nevertheless, many models/approaches fail to describe this behavior [76].

### III. RESULTS

#### A. Constraining $\eta/s$ through high- $p_\perp$ data

To examine the sensitivity of the high- $p_\perp$  observables on the specific shear viscosity of the medium, we compare in Fig. 2 the experimental charged hadron  $R_{AA}$  and high- $p_\perp$  flow harmonics  $v_2$ ,  $v_3$ , and  $v_4$  in Pb + Pb collisions at  $\sqrt{s_{NN}} = 5.02$  TeV to the theoretical predictions calculated using three different  $(\eta/s)(T)$  parametrizations (see Sec. II A). The high- $p_\perp$  flow harmonics are computed using the scalar product method [34]. As seen in all three cases, the calculated charged hadron  $R_{AA}$  and flow anisotropies are almost indistinguishable from each other. Furthermore, the predicted charged hadron  $v_4$  significantly underestimates the experimental data even when the current large experimental uncertainties are taken into account. We previously reported a similar observation in Ref. [34], where high- $p_\perp$   $v_4$  was calculated using several different initializations of the fluid dynamical evolution.

Unfortunately, the heavy flavor high- $p_\perp$  observables shown in Fig. 3 are hardly more sensitive to the  $(\eta/s)(T)$  parametrizations. The calculated  $D$  and  $B$  meson  $R_{AA}$ ,  $v_2$ , and  $v_3$  in Pb + Pb collisions at  $\sqrt{s_{NN}} = 5.02$  TeV do not depend on our assumptions about  $\eta/s$ , whereas  $v_4$  in the 10–30% centrality class shows some sensitivity. Nevertheless, given the large experimental uncertainties of  $v_2$  and  $v_3$ , it is doubtful whether the small difference in  $v_4$  is experimentally detectable, especially when our  $v_4$  predictions are very close to 0.

Since the collisions at LHC reach larger initial temperatures than collisions at RHIC, we may expect them to be more sensitive to  $\eta/s$  at large temperatures, and thus to our  $(\eta/s)(T)$  parametrizations. Nevertheless, for the sake of completeness and to allow for surprises in the evolution, we checked whether the high- $p_\perp$  observables measured in collisions at the full RHIC energy ( $\sqrt{s_{NN}} = 200$  GeV) allow us to distinguish between different  $(\eta/s)(T)$  parametrizations.

The theoretical predictions for charged hadron and  $D$  and  $B$  meson high- $p_\perp$  observables in Au + Au collisions at  $\sqrt{s_{NN}} = 200$  GeV collision energy are shown in Figs. 4 and 5, respectively. Again, we calculated our predictions using the generalized DRENA-A framework with three different  $(\eta/s)(T)$  parametrizations. As can be seen, the high- $p_\perp$  observables are not sensitive to the  $\eta/s$  ratio at high temperatures, and thus we cannot further constrain  $(\eta/s)(T)$  using high- $p_\perp$  observables.

As was argued in the Introduction, different  $\eta/s$  require different initial temperatures. However, as shown in Fig. 6, temperature difference during the evolution is small and, as demonstrated above, insufficient to lead to observable differences in high- $p_\perp$  observables. In Fig. 6, we characterize the system temperature using the so-called average jet-perceived temperature: At each time  $\tau$  we average the system temperature in the transverse plane using the number of jets at each point as weight; e.g., while the average initial temperature in (10–20)% centrality class for Pb + Pb collisions at



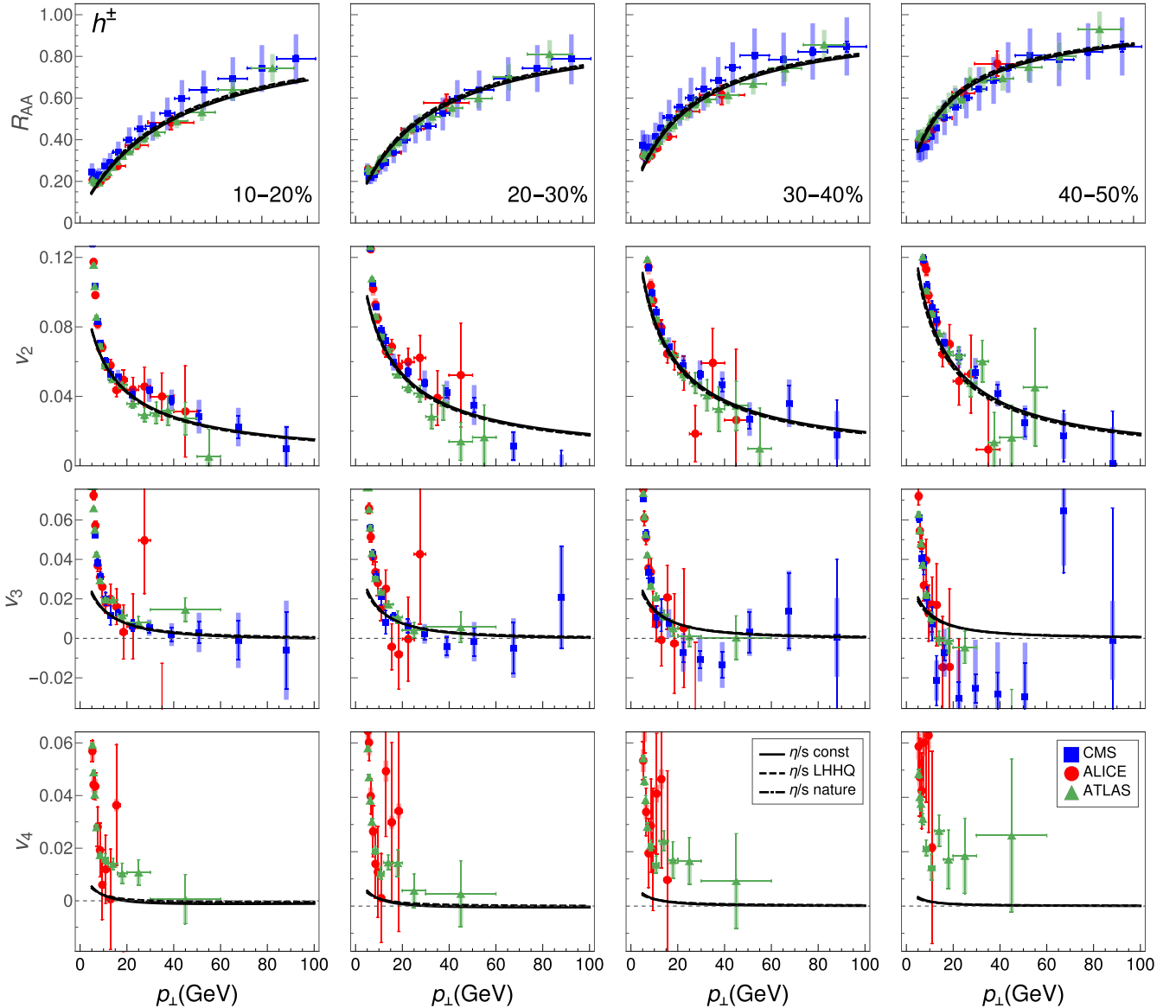


FIG. 2. Charged hadron  $R_{AA}$  (first row) and high- $p_{\perp}$  flow harmonics  $v_2$  (second row),  $v_3$  (third row), and  $v_4$  (fourth row) as a function of transverse momentum in Pb + Pb collisions at  $\sqrt{s_{NN}} = 5.02$  TeV for different  $(\eta/s)(T)$  parametrizations indicated in the legend. CMS (blue squares) [79,80], ALICE (red circles) [81,82], and ATLAS (green triangles) [83,84] experimental data are also shown for comparison. Columns 1–4 represent the centrality classes 10–20%, 20–30%, 30–40%, and 40–50%, respectively.

$\sqrt{s} = 5.02$  TeV is 370 MeV, the maximal temperature experienced by the jet can reach up to 600 MeV. The jet-perceived temperatures calculated using all three  $(\eta/s)(T)$  parametrizations are almost identical, differing less than 4% at the early stages of the evolution and settling for less than 2% for most of the evolution. The differences in the anisotropy of the jet-perceived temperature,  $\langle jT_2 \rangle$ , introduced in Ref. [23], are equally small (not shown). The investigated high- $p_{\perp}$  observables turned out to be insensitive to such small differences in temperature.

Even if our calculated high- $p_{\perp}$   $R_{AA}$  and  $v_2$  agree with the data (see Fig. 2), the calculated  $\langle jT_2 \rangle$  are slightly below the experimentally favored values. This deviation is possible since our results for both  $R_{AA}$  and  $v_2$  are at the lower end of experimental uncertainty. When taking the ratio

$v_2/(1 - R_{AA})$ , which constrains  $\langle jT_2 \rangle$ , this deviation from the data is magnified, and the calculated  $\langle jT_2 \rangle$  is below the experimental constraint. Nevertheless the values of  $\langle jT_2 \rangle$  obtained in these calculations are close to the largest values obtained in Ref. [23] for various initialization models.

### B. Calculating $\eta/s$ from the dynamical energy loss $\hat{q}$

In our previous publications, we have seen that the DREENA framework is capable of reproducing the observed  $R_{AA}$  without fitting parameters [59,93,94] (see also comparison to  $R_{AA}$  in the previous subsection). This agreement suggests that the dynamical energy loss formalism can adequately describe interactions between high- $p_{\perp}$  particles and the QCD medium. Thus, it seems reasonable to estimate  $(\eta/s)(T)$  theoretically using the dynamical energy loss model.

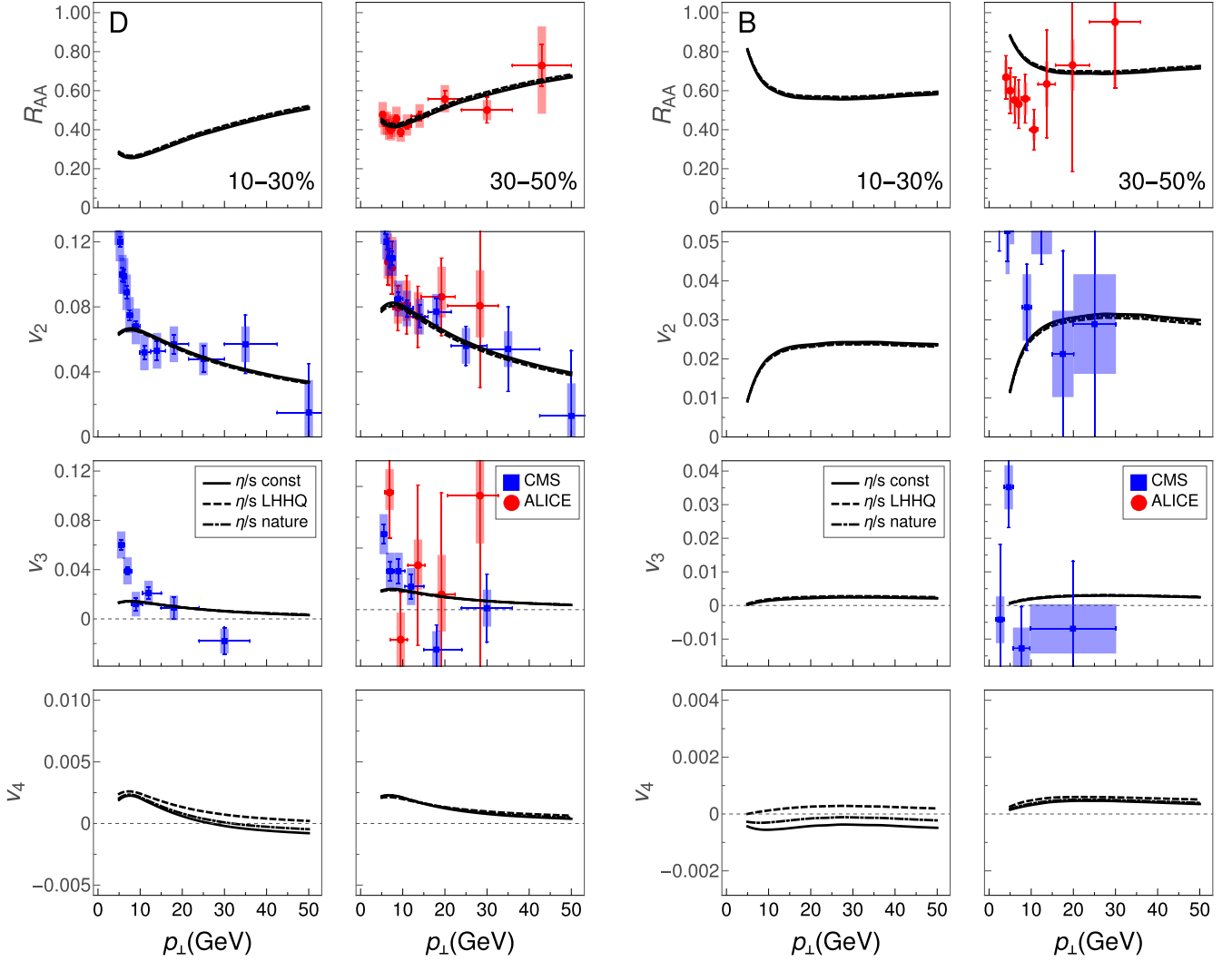


FIG. 3. Predictions for  $D$  (left  $4 \times 2$  panel) and  $B$  meson (right  $4 \times 2$  panel)  $R_{AA}$  (first row) and high- $p_{\perp}$  flow harmonics  $v_2$  (second row),  $v_3$  (third row), and  $v_4$  (fourth row) using three different  $(\eta/s)(T)$  parametrizations at various centralities in Pb + Pb collisions at  $\sqrt{s_{NN}} = 5.02$  TeV. The theoretical predictions for  $D$  mesons are compared with the CMS (blue squares) [85] and ALICE (red circles) [86,87] data, whereas  $B$  meson predictions are compared to preliminary CMS (blue squares) [88] and preliminary ALICE (red circles) [89] data.

For this purpose, we need to estimate the jet quenching parameter  $\hat{q}$ , quantifying the transverse momentum broadening of fast parton due to its elastic scatterings with the medium [75]. This parameter is a key quantity in estimating the interaction strength between jet partons and nuclear matter [76,97–101]. It has been proposed to be a valuable tool for various purposes, including gaining insights into the jet quenching phenomenon, estimating the bulk medium property  $(\eta/s)(T)$  [40,102], and, more recently, exploring the QCD phase diagram [103].

We presented the derivation of the transport coefficient  $\hat{q}$  from our dynamical energy loss model in Sec. II C. We note that  $\hat{q}$  is weakly dependent on  $E$  due to  $\ln(ET)$  appearing both in the numerator and the denominator of Eq. (14), as desired for a medium property such as transport coefficient.

Before discussing our results further, we outline the theoretical expectations for  $\hat{q}$  and its relationship to  $\eta/s$ . To account for the temperature dependence of the coefficients  $\eta$  and  $\hat{q}$ , it is common practice to examine their dimensionless

counterparts:  $\eta/s$ , and  $\hat{q}/T^3$  [102]. Both quantities are sensitive to the effective coupling strength in QGP. If the coupling is weak,  $\eta/s$  is large, while  $\hat{q}/T^3$  is small. Conversely, when the coupling is strong,  $\eta/s$  becomes small, while  $\hat{q}/T^3$  is large. In the case of weak coupling, it has been argued that these two quantities are related by  $\frac{\eta}{s} \frac{\hat{q}}{T^3} \approx \text{const}$ , i.e., more specifically [40,102],

$$\frac{\eta}{s} \approx 1.25 \frac{T^3}{\hat{q}}. \quad (16)$$

Furthermore, to explain the large observed high- $p_{\perp}$   $v_2$ , it was proposed in Ref. [104], that the jet-quenching factor  $\hat{q}/T^3$  must rise rapidly when approaching  $T_c$  from above. We *schematically* depicted such behavior in Fig. 7(a). This behavior is neither straightforward nor trivial to obtain from a model calculation.

The expected (qualitative) relation of the  $T^3/\hat{q}$  and  $(\eta/s)(T)$ —based on the existing knowledge from previous

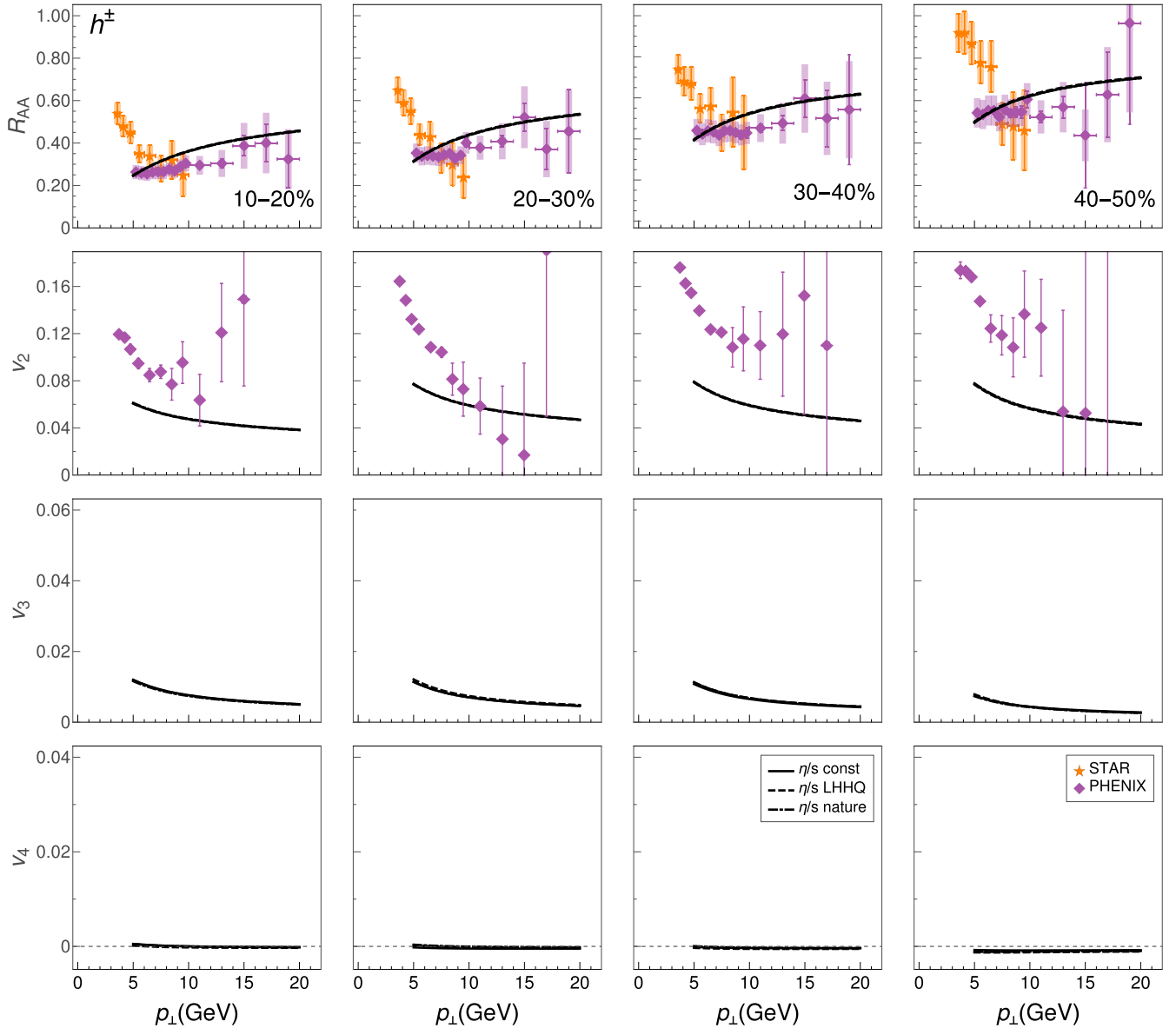


FIG. 4. The calculated charged hadron  $R_{AA}$  (first row), high- $p_{\perp}$   $v_2$  (second row),  $v_3$  (third row), and  $v_4$  (fourth row) in  $\sqrt{s_{NN}} = 200$  GeV Au + Au collisions. The experimental data from the STAR (orange stars) [90] and PHENIX (purple diamonds) [91,92] Collaborations are also shown. Columns 1–4 represent the centrality classes 10–20%, 20–30%, 30–40%, and 40–50%, respectively.

studies—is *schematically* depicted in Fig. 7(b) [40]. At large temperatures, we expect the system to be weakly coupled. At that limit, our dynamical energy loss model should be applicable, and Eq. (16) should be a good approximation. Thus, we expect the calculated  $T^3/\hat{q}$  to agree well with the inferred  $\eta/s$  as shown in the grey area at the right part of Fig. 7(b). On the other hand, in the strongly coupled limit [the left gray area in Fig. 7(b)] close to  $T_c$ , the calculated  $T^3/\hat{q}$  is expected to significantly deviate from the inferred  $\eta/s$ . Interestingly, the  $T^3/\hat{q}$  calculated using weak coupling methods is expected to drop below the inferred  $\eta/s$  [40], which, as known, is very close to the AdS-CFT lower limit of  $1/(4\pi)$  in the vicinity of  $T_c$ .

The region between strongly and weakly coupled limits is the so-called “soft-to-hard” boundary [105], i.e., the region

where the transition from a strongly to a weakly coupled regime could take place. Therefore, plotting together  $\eta/s$  and  $T^3/\hat{q}$  as a function of  $T$  might allow estimating the “soft-to-hard” boundary as the region where these two curves start to deviate, as schematically shown in Fig. 7(b).

We calculate  $\hat{q}/T^3$  from our dynamical energy loss using Eq. (14) in the initial jet energy range  $3 < E < 10$  GeV, as  $p_{\perp}$  has to be low enough to mimic interactions of partons within the medium. The obtained result is shown in Fig. 8(a), and qualitatively similar to the expectation shown in Fig. 7(a). In particular, near  $T_c$ , we obtain an enhanced quenching, which is considerably larger than quenching in other energy loss models [76] (with the exception of [101], which got a substantial increase in  $\hat{q}/T^3$  near  $T_c$ , due to a very large coupling in their model). Some models even

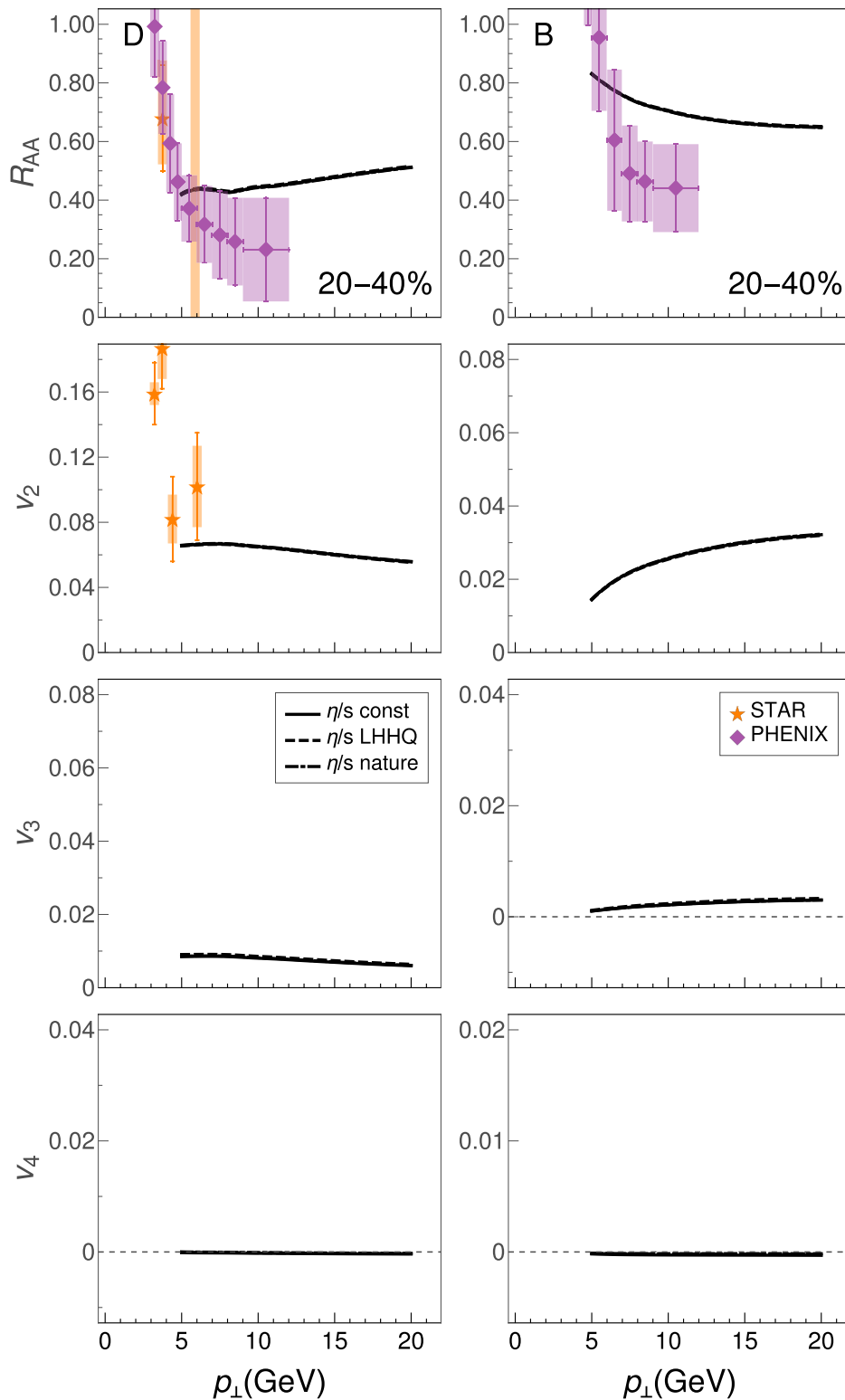


FIG. 5.  $D$  (left panel) and  $B$  meson (right panel)  $R_{AA}$  (first row) and high- $p_{\perp}$  flow harmonics  $v_2$  (second row),  $v_3$  (third row), and  $v_4$  (fourth row) in  $\sqrt{s_{NN}} = 200$  GeV Au + Au collisions in 20–40% centrality class. Theoretical predictions for  $D$  meson are compared with STAR (orange stars) [95] and preliminary PHENIX (purple diamonds) [96] data, whereas  $B$  meson predictions are compared with the preliminary PHENIX (purple diamonds) [96] data.

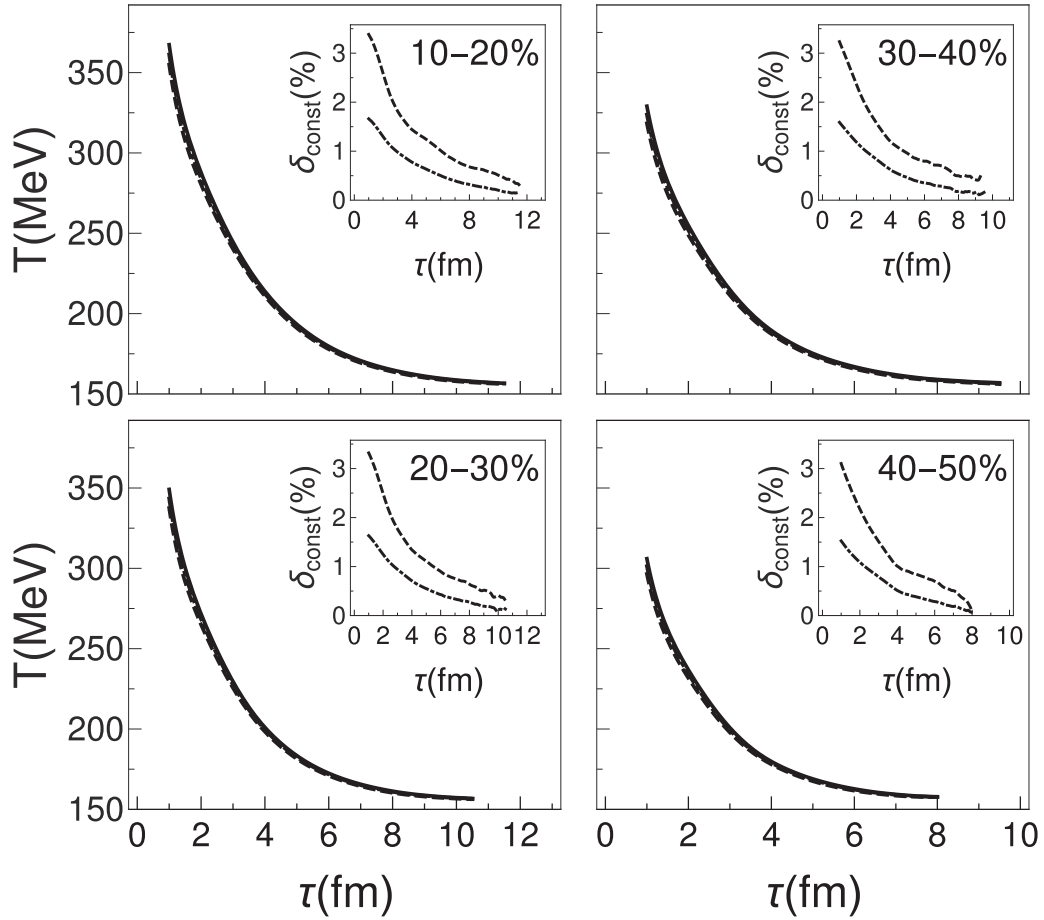


FIG. 6. The average temperature experienced by the jets as a function of proper time for three different  $(\eta/s)(T)$  parametrizations in  $\sqrt{s_{NN}} = 5.02$  TeV Pb + Pb collisions for four different centrality regions (10–20%, 20–30%, 30–40%, and 40–50%, as indicated in each panel). The inset shows the relative difference in jet-perceived temperature in case of “Nature” (dot-dashed curve) and “LHHQ” (dashed curve) with respect to constant  $\eta/s$  parametrizations.

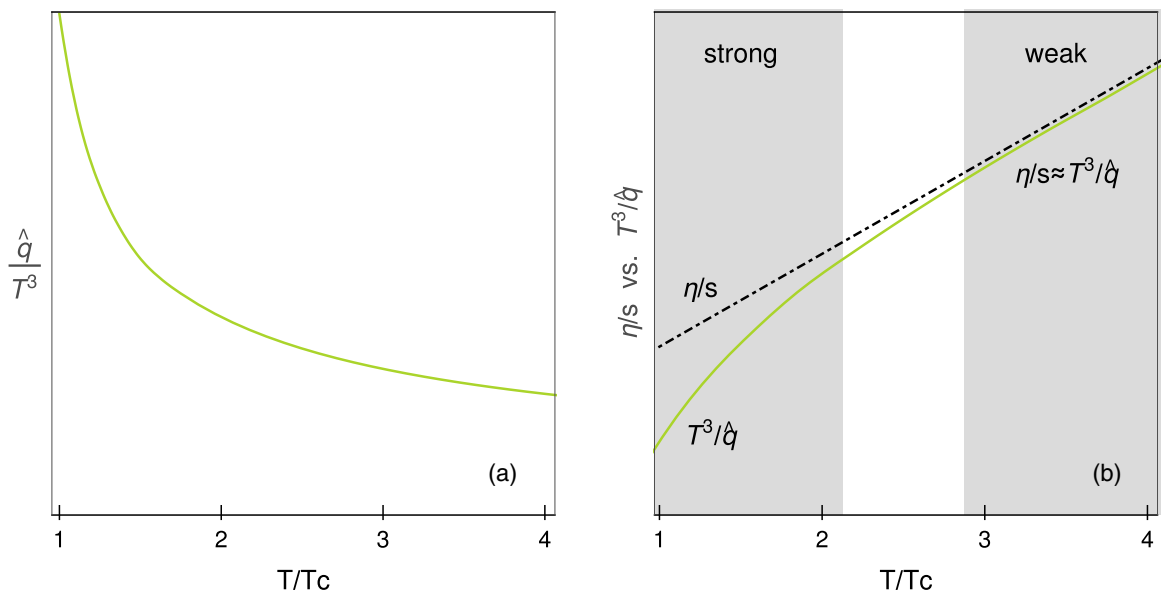


FIG. 7. (a) A schematic  $T$  dependence of quenching strength  $\hat{q}/T^3$  proposed in [104]. (b) A scheme for mapping soft-to-hard boundary based on Ref. [40].



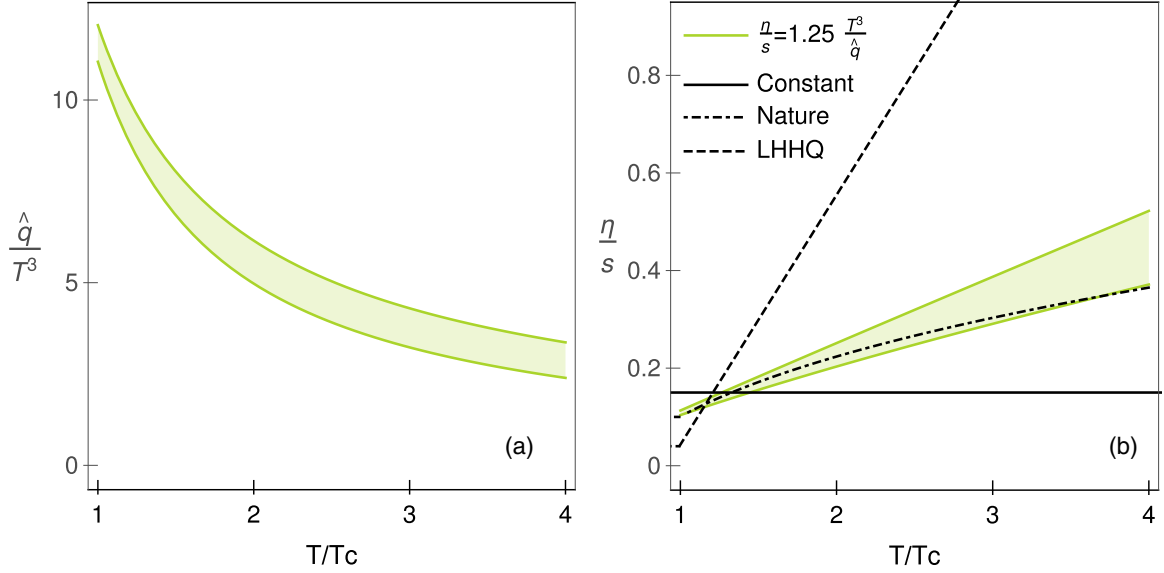


FIG. 8. (a)  $T$  dependence of  $\hat{q}/T^3$  extracted from dynamical energy loss for initial jet energy in the range  $E = 3$  GeV (lower boundary) to  $E = 10$  GeV (upper boundary) [76]. (b) Comparison of  $\eta/s$  extracted from  $\hat{q}/T^3$  [shown in (a)], with three different choices of the specific shear viscosity considered in this study and indicated in the legend.

predicted a decrease of  $\hat{q}/T^3$  (or increase in  $\eta/s$ ) when the temperature is approaching  $T_c$  from above [76,106,107]. The enhancement near  $T_c$ , obtained in Fig. 8(a), is due to an interplay between chromoelectric and chromomagnetic screenings [60]. As the magnetic component is inherently related to the dynamical nature of the medium constituents, it cannot exist in widely used static models, making the evolving medium an important feature of the dynamical energy loss model.

We convert our calculated  $\hat{q}/T^3$  to  $(\eta/s)(T)$  using Eq. (16), and compare it to the parametrizations used in this study in Fig. 8(b). First, the uncertainty due to the relevant initial jet energy is way smaller than the range of our  $(\eta/s)(T)$  parametrizations. Second, our result is surprisingly close to the parametrization inspired by the Bayesian analysis of Ref. [18], “Nature,” and, third, unexpectedly, our result obtained using weak coupling approximation does not drop significantly below the inferred  $\eta/s$  values in the vicinity of  $T_c$ .

To further gauge the significance of our result, we compare it to the 90% credible intervals for  $(\eta/s)(T)$  obtained in two state-of-the-art Bayesian analyses [18,19] in Fig. 9. Interestingly, the  $\eta/s$  dependence extracted from our  $\hat{q}/T^3$  shows an excellent agreement with both of these analyses in the entire  $T$  range, i.e., it falls precisely in the overlap of the two intervals. Our result agrees not only at large temperatures, where the Bayesian constraints are weakest, but even in the vicinity of  $T_c$ , where we expected our result to drop below the inferred values of  $\eta/s$  [as depicted in Fig. 7(b)]. This is a surprising result, as one might expect that our calculation of  $\hat{q}$  from the dynamical energy loss model and Eq. (16) are reliable only in the weakly coupled regime. However, the agreement extends to  $T_c$ , i.e., to the regime corresponding to strong coupling.

While the extended agreement observed in Fig. 9 is encouraging in terms of the prediction ability of the dynamical

energy loss formalism, it leads to the question of why the expected behavior [shown schematically in Fig. 7(b)] is not observed in Fig. 9. It is unlikely that the weak coupling regime would extend down to  $T_c$ . Instead, it was suggested [40] that Eq. (16) is valid as long as the quasiparticle picture of QGP is applicable. The same is required for the validity of energy loss calculations, including our dynamical energy loss model. Therefore, it is an intriguing (and potentially significant)

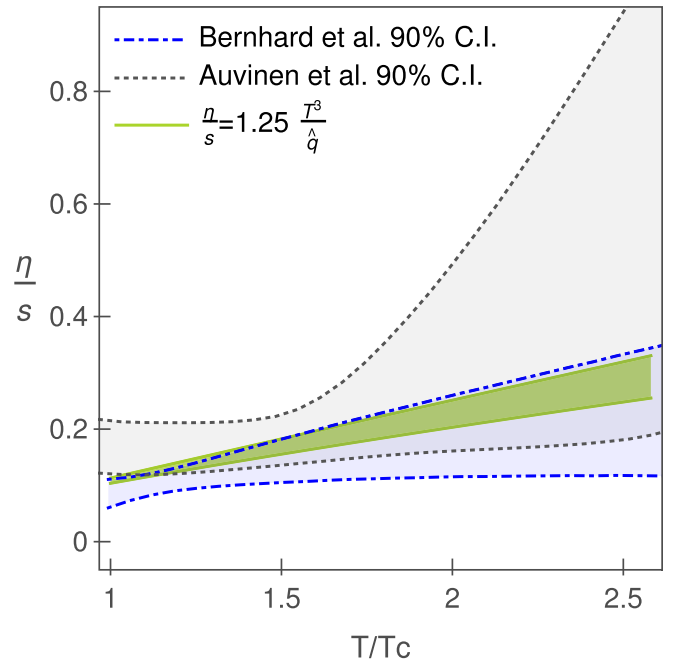


FIG. 9. Comparison of  $\eta/s$  extracted from  $\hat{q}/T^3$  to the 90% credible intervals of the Bayesian analyses of Refs. [18,19] (Bernhard *et al.* and Auvinen *et al.*, respectively).

hypothesis that the quasiparticle picture used for describing interactions between jet and QGP is consistent with the QCD medium created at RHIC and LHC at the entire temperature range. In practical terms, this hypothesis is consistent with the dynamical energy loss model's ability to explain a wide range of experimental data.

Lastly, one of the open issues of QGP physics is mapping the “soft-to-hard” boundary. As discussed, a possible approach for estimating the boundary is to compare estimates of the same quantity (like  $\eta/s$ ) from the high- $p_{\perp}$  and low- $p_{\perp}$  sectors, as schematically presented in Fig. 7(b). However, as shown here, the  $\eta/s$  obtained from high- $p_{\perp}$  theory and inferred from the low- $p_{\perp}$  data agree in the entire  $T$  range, providing no guidance on locating the boundary.

#### IV. SUMMARY

Our previous studies showed that combining high- $p_{\perp}$  predictions/data with temperature profiles from bulk medium simulations can constrain QGP medium properties, such as its early evolution and medium averaged anisotropy. Here we used an equivalent approach, where temperature profiles corresponding to different  $(\eta/s)(T)$  parametrizations were generated and subsequently used by our generalized DREENA-A framework to generate predictions for  $R_{AA}$  and high- $p_{\perp}$   $v_2$ ,  $v_3$ , and  $v_4$ . However, we found that this approach cannot differentiate between temperature profiles generated using different  $(\eta/s)(T)$  parametrizations, since the differences in  $T$  profiles and jet-perceived anisotropies [23] turned out to be small, and consequently the differences in high- $p_{\perp}$  predictions were also small. It is unrealistic to expect that the experiments at RHIC and LHC will (in a reasonable time frame) achieve the precision needed to distinguish between these predictions.

On the other hand, our second approach, based on calculating the quenching strength  $\hat{q}/T^3$  from our dynamical

energy loss model, showed a surprisingly good agreement with the constraints to  $(\eta/s)(T)$  extracted from low- $p_{\perp}$  data by state-of-the-art Bayesian analysis. Such agreement is highly nontrivial as it originates from two entirely different approaches: A theoretical calculation based on finite temperature field theory through generalized HTL approach (dynamical energy loss) and inferring  $(\eta/s)(T)$  from experimental data using fluid-dynamical modeling and advanced statistical (Bayesian) methods. The agreement is also surprising, as it extends all the way to  $T_c$ , where a strongly coupled regime should apply, and where a disagreement between energy loss calculation based on weak coupling approximation and inferred value of  $\eta/s$  is expected. We interpret the absence of such a disagreement in terms of the quasiparticle picture being valid even close to  $T_c$ . However, this obscures estimating soft-to-hard boundary, whose inference remains one of the field's major (to our knowledge, unresolved) problems. Overall, this work further emphasizes the utility of jet tomography, where low- and high- $p_{\perp}$  theory and data are jointly used to constrain the QGP properties.

#### ACKNOWLEDGMENTS

This work is supported by the European Research Council, Grant No. ERC-2016-COG: 725741, and by the Ministry of Science and Technological Development of the Republic of Serbia. P.H. was also supported by the program Excellence Initiative—Research University of the University of Wrocław of the Ministry of Education and Science. J.A. acknowledges the financial support from the Academy of Finland Project No. 330448. J.A.'s research was also funded as a part of the Center of Excellence in Quark Matter of the Academy of Finland (Project No. 346325). This research is part of the European Research Council Project No. ERC-2018-ADG-835105 Yoc-toLHC.

- 
- [1] J. C. Collins and M. J. Perry, *Phys. Rev. Lett.* **34**, 1353 (1975).
  - [2] G. Baym and S. A. Chin, *Phys. Lett. B* **62**, 241 (1976).
  - [3] E. V. Shuryak, *Phys. Lett. B* **78**, 150 (1978).
  - [4] R. Stock, *Nature (London)* **337**, 319 (1989).
  - [5] M. Gyulassy and L. McLerran, *Nucl. Phys. A* **750**, 30 (2005).
  - [6] B. Jacak and P. Steinberg, *Phys. Today* **63**(5), 39 (2010).
  - [7] J. Stachel, *Int. J. Mod. Phys. A* **21**, 1750 (2006).
  - [8] P. F. Kolb and U. Heinz, in *Quark-Gluon Plasma 3*, edited by R. C. Hwa and X. N. Wang (World Scientific, Singapore, 2004).
  - [9] P. Romatschke and U. Romatschke, *Phys. Rev. Lett.* **99**, 172301 (2007).
  - [10] U. Heinz and R. Snellings, *Annu. Rev. Nucl. Part. Sci.* **63**, 123 (2013).
  - [11] J. Adams *et al.* (STAR Collaboration), *Nucl. Phys. A* **757**, 102 (2005).
  - [12] K. Adcox *et al.* (PHENIX Collaboration), *Nucl. Phys. A* **757**, 184 (2005).
  - [13] G. Aad *et al.* (ATLAS Collaboration), *Phys. Rev. Lett.* **105**, 252303 (2010).
  - [14] K. Aamodt *et al.* (ALICE Collaboration), *Phys. Lett. B* **696**, 30 (2011).
  - [15] J. Novak, K. Novak, S. Pratt, J. Vredevoogd, C. Coleman-Smith, and R. Wolpert, *Phys. Rev. C* **89**, 034917 (2014).
  - [16] S. Pratt, E. Sangaline, P. Sorensen, and H. Wang, *Phys. Rev. Lett.* **114**, 202301 (2015).
  - [17] J. E. Bernhard, *arXiv:1804.06469*.
  - [18] J. E. Bernhard, J. S. Moreland, and S. A. Bass, *Nat. Phys.* **15**, 1113 (2019).
  - [19] J. Auvinen, K. J. Eskola, P. Huovinen, H. Niemi, R. Paatelainen, and P. Petreczky, *Phys. Rev. C* **102**, 044911 (2020).
  - [20] D. Everett *et al.* (JETSCAPE Collaboration), *Phys. Rev. C* **103**, 054904 (2021).
  - [21] D. Everett *et al.* (JETSCAPE Collaboration), *Phys. Rev. Lett.* **126**, 242301 (2021).
  - [22] S. Stojku, J. Auvinen, M. Djordjevic, P. Huovinen, and M. Djordjevic, *Phys. Rev. C* **105**, L021901 (2022).
  - [23] S. Stojku, J. Auvinen, L. Zivkovic, P. Huovinen, and M. Djordjevic, *Phys. Lett. B* **835**, 137501 (2022).

- [24] O. Soloveva, J. Aichelin, and E. Bratkovskaya, *Phys. Rev. D* **105**, 054011 (2022).
- [25] W. J. Xing, S. Cao, and G. Y. Qin, [arXiv:2303.12485](https://arxiv.org/abs/2303.12485).
- [26] C. V. Johnson and P. Steinberg, *Phys. Today* **63**(5), 29 (2010).
- [27] P. Kovtun, D. T. Son, and A. Starinets, *Phys. Rev. Lett.* **94**, 111601 (2005).
- [28] U. Heinz *et al.*, [arXiv:1501.06477](https://arxiv.org/abs/1501.06477).
- [29] J. L. Nagle, I. G. Bearden, and W. A. Zajc, *New J. Phys.* **13**, 075004 (2011).
- [30] H. Niemi, G. S. Denicol, P. Huovinen, E. Molnar, and D. H. Rischke, *Phys. Rev. Lett.* **106**, 212302 (2011).
- [31] H. Niemi, G. S. Denicol, P. Huovinen, E. Molnar, and D. H. Rischke, *Phys. Rev. C* **86**, 014909 (2012).
- [32] G. Nijs and W. van der Schee, *Phys. Rev. Lett.* **129**, 232301 (2022).
- [33] M. R. Heffernan, C. Gale, S. Jeon, and J. F. Paquet, [arXiv:2302.09478](https://arxiv.org/abs/2302.09478).
- [34] D. Zigic, J. Auvinen, I. Salom, M. Djordjevic, and P. Huovinen, *Phys. Rev. C* **106**, 044909 (2022).
- [35] D. Zigic, I. Salom, J. Auvinen, P. Huovinen, and M. Djordjevic, *Front. Phys.* **10**, 957019 (2022).
- [36] M. Djordjevic, *Phys. Rev. C* **74**, 064907 (2006).
- [37] M. Djordjevic, *Phys. Rev. C* **80**, 064909 (2009).
- [38] M. Djordjevic and U. W. Heinz, *Phys. Rev. Lett.* **101**, 022302 (2008).
- [39] T. Renk, *Phys. Rev. C* **85**, 044903 (2012).
- [40] A. Majumder, B. Müller, and X.-N. Wang, *Phys. Rev. Lett.* **99**, 192301 (2007).
- [41] H. Song and U. W. Heinz, *Phys. Rev. C* **77**, 064901 (2008).
- [42] H. Song and U. W. Heinz, *Phys. Rev. C* **78**, 024902 (2008).
- [43] J. E. Bernhard, J. S. Moreland, S. A. Bass, J. Liu, and U. Heinz, *Phys. Rev. C* **94**, 024907 (2016).
- [44] <https://github.com/Duke-QCD/hic-eventgen>.
- [45] W. Israel and J. M. Stewart, *Ann. Phys.* **118**, 341 (1979).
- [46] A. Bazavov *et al.* (HotQCD Collaboration), *Phys. Rev. D* **90**, 094503 (2014).
- [47] F. Cooper and G. Frye, *Phys. Rev. D* **10**, 186 (1974).
- [48] S. A. Bass *et al.*, *Prog. Part. Nucl. Phys.* **41**, 255 (1998).
- [49] M. Bleicher *et al.*, *J. Phys. G* **25**, 1859 (1999).
- [50] J. S. Moreland, J. E. Bernhard, and S. A. Bass, *Phys. Rev. C* **92**, 011901 (2015).
- [51] M. Djordjevic and M. Djordjevic, *Phys. Rev. C* **92**, 024918 (2015).
- [52] M. Djordjevic, S. Stojku, M. Djordjevic, and P. Huovinen, *Phys. Rev. C* **100**, 031901 (2019).
- [53] S. Acharya *et al.* (ALICE Collaboration), *Phys. Rev. C* **101**, 044907 (2020).
- [54] S. S. Adler *et al.* (PHENIX Collaboration), *Phys. Rev. C* **69**, 034909 (2004).
- [55] J. Adam *et al.* (ALICE Collaboration), *Phys. Rev. Lett.* **116**, 132302 (2016).
- [56] J. Adams *et al.* (STAR Collaboration), *Phys. Rev. C* **72**, 014904 (2005).
- [57] J. I. Kapusta, *Finite Temperature Field Theory* (Cambridge University Press, Cambridge, 1989).
- [58] B. Blagojevic, M. Djordjevic, and M. Djordjevic, *Phys. Rev. C* **99**, 024901 (2019).
- [59] M. Djordjevic and M. Djordjevic, *Phys. Lett. B* **734**, 286 (2014).
- [60] M. Djordjevic and M. Djordjevic, *Phys. Lett. B* **709**, 229 (2012).
- [61] S. Stojku, B. Ilic, I. Salom, and M. Djordjevic, *Phys. Rev. C* **108**, 044905 (2023).
- [62] S. Wicks, W. Horowitz, M. Djordjevic, and M. Gyulassy, *Nucl. Phys. A* **784**, 426 (2007).
- [63] Z. B. Kang, I. Vitev, and H. Xing, *Phys. Lett. B* **718**, 482 (2012).
- [64] R. Sharma, I. Vitev, and B. W. Zhang, *Phys. Rev. C* **80**, 054902 (2009).
- [65] M. Cacciari, S. Frixione, N. Houdeau, M. L. Mangano, P. Nason, and G. Ridolfi, *J. High Energy Phys.* **10** (2012) 137.
- [66] D. de Florian, R. Sassot, and M. Stratmann, *Phys. Rev. D* **75**, 114010 (2007).
- [67] M. Cacciari and P. Nason, *J. High Energy Phys.* **09** (2003) 006.
- [68] E. Braaten, K. Cheung, S. Fleming, and T. C. Yuan, *Phys. Rev. D* **51**, 4819 (1995).
- [69] V. G. Kartvelishvili, A. K. Likhoded, and V. A. Petrov, *Phys. Lett. B* **78**, 615 (1978).
- [70] A. Peshier, [arXiv:hep-ph/0601119](https://arxiv.org/abs/hep-ph/0601119).
- [71] S. Cao and X. N. Wang, *Rep. Prog. Phys.* **84**, 024301 (2021).
- [72] A. Nakamura, T. Saito, and S. Sakai, *Phys. Rev. D* **69**, 014506 (2004).
- [73] M. Djordjevic and M. Gyulassy, *Phys. Rev. C* **68**, 034914 (2003).
- [74] S. Borsányi, Z. Fodor, S. D. Katz, A. Pásztor, K. K. Szabó, and C. Török, *J. High Energy Phys.* **04** (2015) 138.
- [75] R. Baier, Y. Dokshitzer, A. Mueller, S. Peigne, and D. Schiff, *Nucl. Phys. B* **484**, 265 (1997).
- [76] K. M. Burke *et al.* (JET Collaboration), *Phys. Rev. C* **90**, 014909 (2014).
- [77] S. Peigne and A. Peshier, *Phys. Rev. D* **77**, 114017 (2008).
- [78] R. Rapp *et al.*, *Nucl. Phys. A* **979**, 21 (2018).
- [79] A. M. Sirunyan *et al.* (CMS Collaboration), *Phys. Lett. B* **776**, 195 (2018).
- [80] V. Khachatryan *et al.* (CMS Collaboration), *J. High Energy Phys.* **04** (2017) 039.
- [81] S. Acharya *et al.* (ALICE Collaboration), *J. High Energy Phys.* **11** (2018) 013.
- [82] S. Acharya *et al.* (ALICE Collaboration), *J. High Energy Phys.* **07** (2018) 103.
- [83] M. Aaboud *et al.* (ATLAS), *Eur. Phys. J. C* **78**, 997 (2018).
- [84] G. Aad *et al.* (ATLAS), *J. High Energy Phys.* **07** (2023) 074.
- [85] A. M. Sirunyan *et al.* (CMS Collaboration), *Phys. Lett. B* **816**, 136253 (2021).
- [86] S. Acharya *et al.* (ALICE Collaboration), *J. High Energy Phys.* **01** (2022) 174.
- [87] S. Acharya *et al.* (ALICE Collaboration), *Phys. Lett. B* **813**, 136054 (2021).
- [88] Contribution link: <https://indico.cern.ch/event/895086/contributions/4314625/>.
- [89] Contribution link: <https://indico.cern.ch/event/895086/contributions/4715758/>.
- [90] J. Adams *et al.* (STAR Collaboration), *Phys. Rev. Lett.* **91**, 172302 (2003).
- [91] A. Adare *et al.* (PHENIX Collaboration), *Phys. Rev. C* **87**, 034911 (2013).
- [92] A. Adare *et al.* (PHENIX Collaboration), *Phys. Rev. C* **99**, 054903 (2019).
- [93] M. Djordjevic, M. Djordjevic, and B. Blagojevic, *Phys. Lett. B* **737**, 298 (2014).
- [94] D. Zigic, I. Salom, J. Auvinen, M. Djordjevic, and M. Djordjevic, *J. Phys. G* **46**, 085101 (2019).

- [95] L. Adamczyk *et al.* (STAR Collaboration), *Phys. Rev. Lett.* **113**, 142301 (2014); **121**, 229901(E) (2018).
- [96] Contribution link: <https://indico.cern.ch/event/895086/contributions/4744010/>.
- [97] X. Guo and X.-N. Wang, *Phys. Rev. Lett.* **85**, 3591 (2000).
- [98] A. Majumder, *Phys. Rev. D* **85**, 014023 (2012).
- [99] J. Barata, Y. Mehtar-Tani, A. Soto-Ontoso, and K. Tywoniuk, *Phys. Rev. D* **104**, 054047 (2021).
- [100] C. Sirimanna, S. Cao, and A. Majumder, *Phys. Rev. C* **105**, 024908 (2022).
- [101] I. Grishmanovskii, T. Song, O. Soloveva, C. Greiner, and E. Bratkovskaya, *Phys. Rev. C* **106**, 014903 (2022).
- [102] B. Müller, *Phys. Rev. D* **104**, L071501 (2021).
- [103] J. Wu, S. Cao, and F. Li, [arXiv:2208.14297](https://arxiv.org/abs/2208.14297).
- [104] J. Liao and E. Shuryak, *Phys. Rev. Lett.* **102**, 202302 (2009).
- [105] B. Betz and M. Gyulassy, *Nucl. Phys. A* **931**, 410 (2014).
- [106] A. Majumder and M. Van Leeuwen, *Prog. Part. Nucl. Phys.* **66**, 41 (2011).
- [107] R. Marty, E. Bratkovskaya, W. Cassing, J. Aichelin, and H. Berrehrh, *Phys. Rev. C* **88**, 045204 (2013).

## Importance of higher orders in opacity in quark-gluon plasma tomography

Stefan Stojku , Bojana Ilic , Igor Salom , and Magdalena Djordjevic <sup>\*</sup>

*Institute of Physics Belgrade, University of Belgrade, Serbia*



(Received 4 May 2023; accepted 27 September 2023; published 16 October 2023)

We consider the problem of including a finite number of scattering centers in dynamical energy loss and classical DGLV formalism. Previously, either one or an infinite number of scattering centers were considered in energy loss models, while efforts to relax such approximations require a more conclusive and complete treatment. In reality, however, the number of scattering centers is generally estimated to be 4–5 at the BNL Relativistic Heavy Ion Collider (RHIC) and the CERN Large Hadron Collider (LHC), making the above approximations (*a priori*) inadequate and this theoretical problem significant for QGP tomography. We derived explicit analytical expressions for dynamical energy loss and DGLV up to the fourth order in opacity, resulting in complex, highly oscillatory, mathematical expressions. These expressions were then implemented into an appropriately generalized DREENA framework to calculate the effects of higher orders in opacity on a wide range of high- $p_{\perp}$  light and heavy flavor predictions. Results of extensive numerical analysis and interpretations of nonintuitive results are presented. We find that, for both RHIC and the LHC, higher-order effects on high- $p_{\perp}$  observables are small, and the approximation of a single scattering center is adequate for dynamical energy loss and DGLV formalisms.

DOI: [10.1103/PhysRevC.108.044905](https://doi.org/10.1103/PhysRevC.108.044905)

### I. INTRODUCTION

Quark-gluon plasma (QGP) [1–4] is a new form of matter consisting of quarks, antiquarks, and gluons that are no longer confined. It has been created in landmark experiments at the BNL Relativistic Heavy Ion Collider (RHIC) and the CERN Large Hadron Collider (LHC) (so-called little bangs), where heavy ions collide at ultrarelativistic energies [2,3]. Hard probes are one of the main tools for understanding and characterizing the QGP properties [2], where hard processes dominate interactions of these probes with QGP constituents. These interactions are dominantly described by energy loss, where radiative is one of the most important mechanisms at high transverse momentum  $p_{\perp}$ . The radiative energy loss can be analytically computed through pQCD approaches, typically under the assumption of the optically thick or optically thin medium [e.g., BDMPS-Z [5,6], ASW [7], (D)GLV [8,9], HT and HT-M [10,11], AMY [12], dynamical energy loss [13,14] and different applications and extensions of these methods] and tested against the experimental data.

Optically thick medium corresponds to the approximation of a jet experiencing infinite scatterings with medium constituents. While such an approximation would be adequate for QGP created in the early universe (big bang), little bangs are characterized by short, finite-size droplets of QCD matter. Another widely used approximation is an optically thin medium, assuming one scattering center. However, the medium created in little bangs is typically several femtometers in size (with mean free path  $\lambda \approx 1$  fm), so considering

several scattering centers in energy loss calculations is needed. Thus, it is evident that both approaches represent two extreme limits to the realistic situations considered in RHIC and LHC experiments, and relaxing these approximations to the case of a finite number of scattering centers is necessary. Thus, relaxing such an approximation is a highly nontrivial problem, addressed in Ref. [8], with recently renewed interest [15–21]. Some of these approaches are analytically quite advanced, e.g., providing full expressions for a gluon radiation spectrum (or splitting functions) with relaxed soft-gluon approximation in DGLV formalism [19,20] or derivation of gluon emission spectrum with full resummation of multiple scatterings within the BDMPS-Z framework [15,17,18]. However, in our view, this issue requires a more conclusive and complete treatment. Namely, the importance of including higher orders in opacity effects on experimental observables is still not addressed. In relaxing this approximation, it is not only needed to estimate these effects on, e.g., the energy loss and gluon radiation spectrum, but also to implement these corrections in the numerical frameworks needed to generate predictions for high- $p_{\perp}$  observables measured at RHIC and the LHC experiments. Furthermore, most of these studies were done in massless quarks and gluons limit and/or use the approximation of an uncorrelated medium (i.e., where the spacings between collisions are considered to be mutually independent, see Ref. [21] for more details). Since we, *a priori*, do not know the magnitude of the effects of the inclusion of multiple scattering centers, nor how the mentioned approximations can influence this magnitude, we find it questionable to discuss higher-order corrections while ignoring the effects which might potentially overshadow or alter the final effects. For example, due to a finite-temperature medium, light quarks

<sup>\*</sup> magda@ipb.ac.rs



and gluons gain mass in QGP, which can significantly numerically modify the importance of these effects on experimental observables.

In this study, we start from our dynamical energy loss formalism [13,14], computed under the approximation of an optically thin QCD medium, i.e., one scattering center. We use general expressions from Ref. [21] to relax this approximation to the case of finite number of scattering centers, where explicit analytical expressions up to the fourth order in opacity (scattering centers) are presented. These expressions are implemented in our (appropriately modified) DREENA-C [22] framework (which assumes a constant-temperature medium), enabling us to more straightforwardly estimate the effects of higher orders in opacity on high- $p_\perp$   $R_{AA}$  and  $v_2$  observables. Based on these results, we also provide estimates for the fully evolving medium, while a rigorous study in this direction is left for future work.

While the initial expressions taken from Ref. [21] were, strictly speaking, derived in the approximation of static scattering centers, we apply them here in the context of a dynamic QCD medium. Namely, by careful calculation, we have shown in Ref. [14] that—at least in the first order in opacity—the generalization from the static to dynamic medium eventually amounts to a mere appropriate replacement of the mean free path and effective potential in the final expressions. Following general arguments given in Ref. [8] and the expectations expressed in Ref. [21], we assume that the same prescription for progressing from static to dynamic medium remains valid in higher orders of opacity.

The outline of the paper is as follows: Sections II and III present the outline of theoretical and numerical

frameworks used in this study, with more detailed analytical results presented in the Appendixes. In the Results section, we numerically analyze the effects of higher orders in opacity on the gluon radiation spectrum and high- $p_\perp$   $R_{AA}$  and  $v_2$  predictions. Intuitive explanations behind obtained results will be presented. This section will also analyze a special case of static QCD medium (extension of (D)GLV [8,9] to the finite number of scattering centers). The main results will be summarized in the last section.

## II. THEORETICAL FRAMEWORK

In this study, we use our dynamical radiative energy loss [13,14] formalism, which has the following features: (i) QCD medium of *finite* size  $L$  and temperature  $T$ , which consists of dynamical (i.e., moving) partons, in a distinction to models with widely used static approximation and/or vacuum-like propagators [5,7,8,10]. (ii) Calculations based on generalized hard-thermal-loop approach [23,24], with naturally regulated infrared divergences [13,14,25]. (iii) Generalization towards running coupling [26] and finite magnetic mass [27].

However, as noted in the Introduction, this radiative energy loss is developed up to the first order in opacity. Thus, to improve the applicability of this formalism for QGP tomography, it is necessary to relax this approximation. To generalize the dynamical energy loss to finite number in scattering centers, we start from a closed-form expression—Eq. (46) from Ref. [21] and Eq. (20) from Ref. [9]—derived for static QCD medium [i.e., (D)GLV case [8,9]] but applicable for a generalized form of effective potential and mean free path  $\lambda$  [21]:

$$x \frac{dN^{(n)}}{dx d^2\mathbf{k}} = \int_0^L dz_1 \cdots \int_{z_{n-1}}^L dz_n \int \prod_{i=1}^n \left( d^2\mathbf{q}_i \frac{v^2(\mathbf{q}_i) - \delta^2(\mathbf{q}_i)}{\lambda(z)} \right) \times \frac{C_R \alpha_s(Q_k^2)}{\pi^2} \left( -2 \mathbf{C}_{(1\dots n)} \cdot \mathbf{B}_n \left[ \cos \sum_{k=2}^n \omega_{(k\dots n)} \Delta z_k - \cos \sum_{k=1}^n \omega_{(k\dots n)} \Delta z_k \right] \right), \quad (1)$$

where  $|v_i(\mathbf{q}_i)|^2$  is defined as the normalized distribution of momentum transfers from the  $i$ th scattering center (i.e., “effective potential”),  $\lambda(i)$  is the mean free path of the emitted gluon,  $C_R$  is the color Casimir of the jet. Note that, for consistency with our previous work, we denote transverse two-dimensional (2D) vectors as bold  $\mathbf{p}$ .

The running coupling is defined as in Ref. [26]:

$$\alpha_s(Q^2) = \frac{4\pi}{(11 - 2/3n_f) \ln(Q^2/\Lambda_{\text{QCD}})}, \quad (2)$$

where  $Q_k^2 = (\mathbf{k}^2 + M^2 x^2 + m_g^2)/x$ , appearing in Eq. (1) above is the off-shellness of the jet before gluon radiation [26].

$\omega_{(m\dots n)}$  is the inverse of the formation time or the (longitudinal) momentum,

$$\omega_{(m\dots n)} = \frac{\chi^2 + (\mathbf{k} - \mathbf{q}_m - \cdots - \mathbf{q}_n)^2}{2xE}, \quad (3)$$

where  $n$  is the final scatter, while  $m$  varies from the first up to the final scatter.  $\chi^2 \equiv M^2 x^2 + m_g^2$ , where  $x$  is the longitudinal momentum fraction of the quark jet carried away by the emitted gluon,  $M$  is the mass of the quark,  $m_g = \mu_E/\sqrt{2}$  is the effective mass for gluons with hard momenta [25], and  $\mu_E$  is the Debye mass (i.e., electric screening).

“Cascade” terms represent the shifting of the momentum of the radiated gluon due to momentum kicks from the medium:

$$\mathbf{C}_{(i_1 i_2 \dots i_m)} = \frac{(\mathbf{k} - \mathbf{q}_{i_1} - \mathbf{q}_{i_2} - \cdots - \mathbf{q}_{i_m})}{\chi^2 + (\mathbf{k} - \mathbf{q}_{i_1} - \mathbf{q}_{i_2} - \cdots - \mathbf{q}_{i_m})^2}. \quad (4)$$

A special case of  $\mathbf{C}$  without any momentum shifts is defined as the “hard” term:

$$\mathbf{H} = \frac{\mathbf{k}}{\chi^2 + \mathbf{k}^2} \quad \text{and} \quad \mathbf{B}_i = \mathbf{H} - \mathbf{C}_i. \quad (5)$$

In Refs. [13,14,27], we showed that, despite much more involved analytical calculations, at first order in opacity the

radiative energy loss in a dynamical medium has the same form as in the static medium, except for two straightforward substitutions in mean free path and effective potential:

$$\lambda_{\text{stat}} \rightarrow \lambda_{\text{dyn}}, \quad (6)$$

where

$$\lambda_{\text{stat}}^{-1} = 6 \frac{1.202}{\pi^2} \frac{1 + n_f/4}{1 + n_f/6} \lambda_{\text{dyn}}^{-1},$$

while the ‘‘dynamical mean free path’’ is given by  $\lambda_{\text{dyn}}^{-1} = 3\alpha_s(Q_v^2)T$  [13,14], with  $Q_v^2 = ET$  [26]. Running coupling  $\alpha_s(Q_v^2)$  corresponds to the interaction between the jet and the virtual (exchanged) gluon, while  $E$  is the jet’s energy.

$$\left[ \frac{\mu_E^2}{\pi(\mathbf{q}^2 + \mu_E^2)^2} \right]_{\text{stat}} \rightarrow \left[ \frac{\mu_E^2 - \mu_M^2}{\pi(\mathbf{q}^2 + \mu_E^2)(\mathbf{q}^2 + \mu_M^2)} \right]_{\text{dyn}}, \quad (7)$$

where  $\mu_M$  is magnetic screening. Thus, we assume that Eq. (1) can also be used in our case, with the above modification of effective potential and mean free path. In Appendixes A and B, we use this general expression to derive an explicit expression for the gluon radiation spectrum for first, second, third, and fourth order in opacity ( $dN_g^{(1)}/dx$ ,  $dN_g^{(2)}/dx$ ,  $dN_g^{(3)}/dx$ ,  $dN_g^{(4)}/dx$ , respectively).

### III. NUMERICAL FRAMEWORK

To generate the results presented in this work, we used our (appropriately generalized, see below) DREENA-C framework. For completeness, we here give a brief outline of this framework, while a detailed description is presented in Ref. [22]. The quenched spectra of light and heavy quarks are calculated according to the generic pQCD convolution given by

$$\frac{E_f d^3\sigma}{dp_f^3} = \frac{E_i d^3\sigma(Q)}{dp_i^3} \otimes P(E_i \rightarrow E_f) \otimes D(Q \rightarrow H_Q). \quad (8)$$

Here, the indices  $i$  and  $f$  stand for ‘‘initial’’ and ‘‘final,’’ respectively, while  $Q$  denotes initial high-energy parton (light quarks, heavy quarks, or gluons).  $E_i d^3\sigma(Q)/dp_i^3$  is the initial momentum spectrum for the given parton, which is calculated according to Ref. [28],  $P(E_i \rightarrow E_f)$  represents the energy loss probability for the given particle which was calculated within the dynamical energy loss formalism [13,14], which includes multigluon [29] and path-length fluctuations [22,30].  $D(Q \rightarrow H_Q)$  represents the fragmentation function of light and heavy partons into hadrons, where for light hadrons, D and B mesons, we use the DSS [31], BCFY [32], KLP [33] fragmentation functions, respectively. The geometry is averaged over by using path-length distributions, i.e., probability distributions of the path lengths of hard partons in Pb + Pb collisions, in the same way as in the original DREENA-C framework [22]. They are used as weight functions when integrating over the path-length in our numerical procedure.

We use the following parameters in the numerical procedure:  $\Lambda_{\text{QCD}} = 0.2$  GeV and  $n_f = 3$ . The temperature-dependent Debye chromoelectric mass  $\mu_E(T)$  has been extracted from Ref. [34]. For the mass of light quarks, we

take the thermal mass  $M \approx \mu_E/\sqrt{6}$ , and for the gluon mass, we use  $m_g = \mu_E/\sqrt{2}$  [25]. The mass of the charm (bottom) quark is  $M = 1.2$  GeV ( $M = 4.75$  GeV). The magnetic and electric mass ratio is  $0.4 < \mu_M/\mu_E < 0.6$  [35,36]. All the results presented in this paper are generated for the Pb + Pb collision system at  $\sqrt{s_{NN}} = 5.02$  TeV.

As DREENA-C [22] does not include suppression from multiple scattering centers in the medium, we now upgrade this framework to include the second and third order in opacity contributions. We integrate the expressions obtained from (1) analytically for  $z_i$  (see Appendixes A and B), and then numerically for momenta  $\mathbf{k}$  and  $\mathbf{q}_i$  using the quasi-Monte Carlo method to obtain  $dN_g/dx$  up to third order in opacity. Also, to test the importance of multiple scattering centers on radiative energy loss, we exclude the collisional [37] contributions from the DREENA-C framework and only generate predictions for radiative energy loss. Appendixes A and B also include expressions for the fourth order in opacity. We implemented fourth order into DREENA-C, but as the resulting integrals are highly oscillatory, we could not reach convergence for this order using our available computational resources. Notably, this numerical complexity is significantly higher, estimated to be  $\approx 2$  orders of magnitude larger than for the third order (e.g., for the first order, we needed  $\approx 25$  CPU h; for the second order  $\approx 2500$  CPU h; for the third order  $\approx 70\,000$  CPU h). Nevertheless, at specific points where we reached a convergence, we found the fourth-order contribution negligible, as expected from the results presented in the next section.

### IV. RESULTS

In Fig. 1, the effect of higher orders in opacity on  $dN_g/dx$  as a function of  $x$  is shown for typical medium length  $L = 5$  fm. In each plot, we use double axes for clarity: the lower axis corresponds to magnetic to electric mass ratio  $\mu_M/\mu_E = 0.6$  (and the curves with the peak on the left side), while the upper axis corresponds to  $\mu_M/\mu_E = 0.4$  (and the curves with the peak on the right side). Note that, in each case, maximum is reached for low values of  $x$ . We see that the importance of higher orders of opacity decreases with the increase of jet energy and mass. They also decrease with decreasing the size of the medium, as shown in Appendix C [equivalent figures for  $L = 3$  fm (Fig. 6, left) and  $L = 1$  fm (Fig. 6, right)]. For bottom quarks, higher-order effects are negligible independently of the jet momentum. In contrast, these effects are moderate for charm and light quarks and can influence the jet observables, as discussed below. Note that, due to color triviality, the results for light quarks show the (scaled) result for gluons, too. This holds up to the fact that, due to the indistinguishability of the radiated gluon from the gluon in the jet, the limits for subsequent integration of  $dN_g/dx$  with respect to  $x$  is performed from  $x_{\text{lower}} = 0$  to  $x_{\text{upper}} = 1/2$  (as opposed to  $x_{\text{upper}} = 1$  for light quarks).

In Fig. 2, we show the effect of higher orders in opacity on radiative  $R_{AA}$  observable. Our computations have shown that the effect on  $v_2$  is similar to the one on  $R_{AA}$  (see Fig. 8 in Appendix D). Thus, to avoid redundancy, we further concentrate only on  $R_{AA}$ .

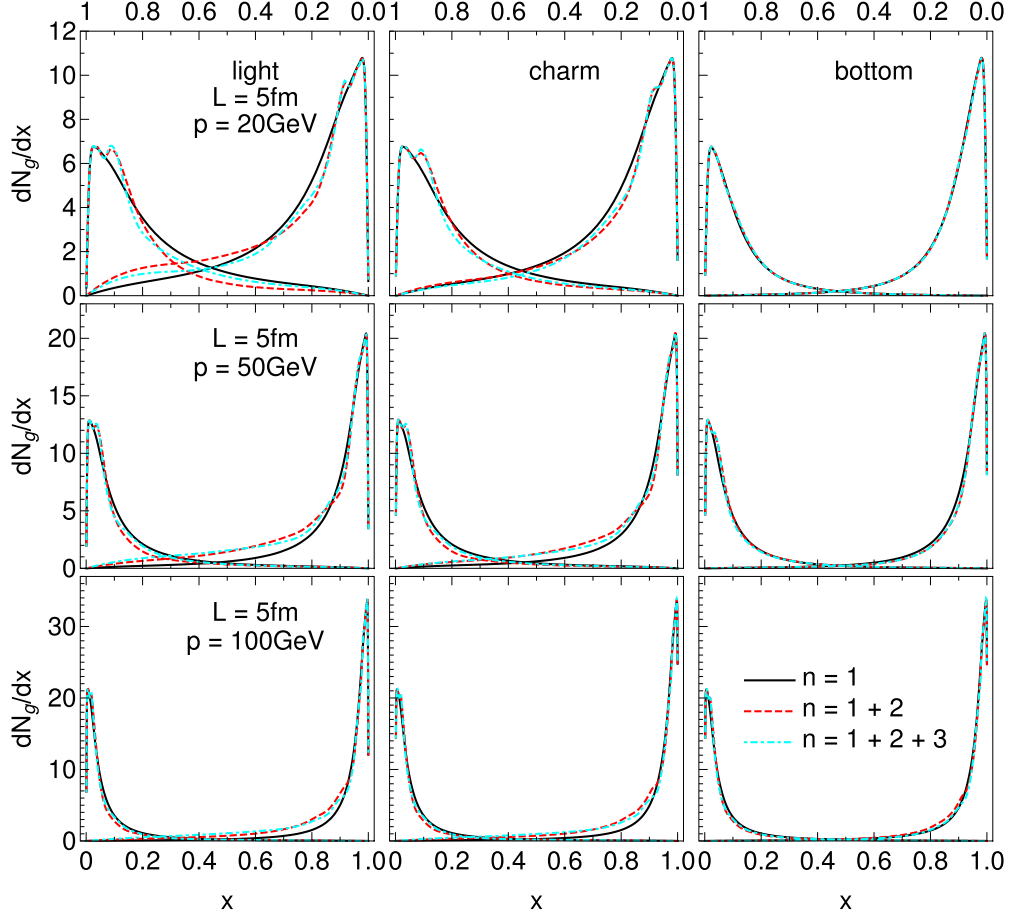


FIG. 1. Gluon radiation spectrum  $dN_g/dx$  as a function of  $x$ , for the typical medium length of  $L = 5$  fm and various jet momenta. Different columns correspond to light, charm, and bottom quarks. Solid black curves show the first order in opacity results, red dashed curves show the results up to the second order, while cyan dot-dashed curves up to the third order in opacity. Curves with the peaks on the left (right) side of each of the plots correspond to the  $\mu_M/\mu_E=0.6$  ( $\mu_M/\mu_E = 0.4$ ) case, and the numerical values should be read off on the lower (upper)  $x$  axis.

We first observe that the effect on  $R_{AA}$  is smaller for more peripheral collisions. This is expected because the medium is shorter on average, so including multiple scattering centers becomes less important.

Furthermore, we find that higher orders in opacity are negligible for B mesons, while these effects increase with decreasing mass, as expected from Fig. 1. The reason behind this is the decrease in the gluon formation time with increasing jet mass. When the gluon formation time is short, the energy loss approaches the incoherent limit, where it was previously shown that the effects of higher orders in opacity are negligible [9]. Thus, our results are consistent with the previous findings. On the other hand, for large gluon formation time (massless quark and gluon limit), the higher orders in opacity effects become significant, also in general agreement with the previous findings [15]. In finite-temperature QGP (considered in this study), light quarks and gluons gain mass due to Debye screening, reducing the effects of higher orders in opacity on the energy loss, consistent with Fig. 2.

Unexpectedly, we also observe that, for different magnetic mass limiting cases, these effects on  $R_{AA}$  are opposite in sign: for  $\mu_M/\mu_E = 0.6$ , the inclusion of higher orders in opacity reduces energy loss (and, consequently, suppression). In

contrast, for  $\mu_M/\mu_E = 0.4$ , the effect is both opposite in sign and larger in magnitude. What is the reason behind these unexpected results?

To answer this question, we go back to the effective potential [27]  $v(\mathbf{q})$  in dynamical QCD medium, which can be written in the following form:

$$v(\mathbf{q}) = v_L(\mathbf{q}) - v_T(\mathbf{q}), \quad (9)$$

where  $v_L(\mathbf{q})$  is longitudinal (electric), and  $v_T(\mathbf{q})$  is transverse (magnetic), contribution to the effective potential. The general expressions for the transverse and longitudinal contributions to the effective potentials are

$$v_L(\mathbf{q}) = \frac{1}{\pi} \left( \frac{1}{(\mathbf{q}^2 + \mu_{pl}^2)} - \frac{1}{(\mathbf{q}^2 + \mu_E^2)} \right), \quad (10)$$

$$v_T(\mathbf{q}) = \frac{1}{\pi} \left( \frac{1}{(\mathbf{q}^2 + \mu_{pl}^2)} - \frac{1}{(\mathbf{q}^2 + \mu_M^2)} \right),$$

where  $\mu_E$ ,  $\mu_M$ , and  $\mu_{pl} = \mu_E/\sqrt{3}$  are electric, magnetic, and plasmon masses, respectively. As seen from Eq. (9), this potential has two contributions: electric and magnetic, where the electric contribution is always positive due to  $\mu_{pl} < \mu_E$ . On

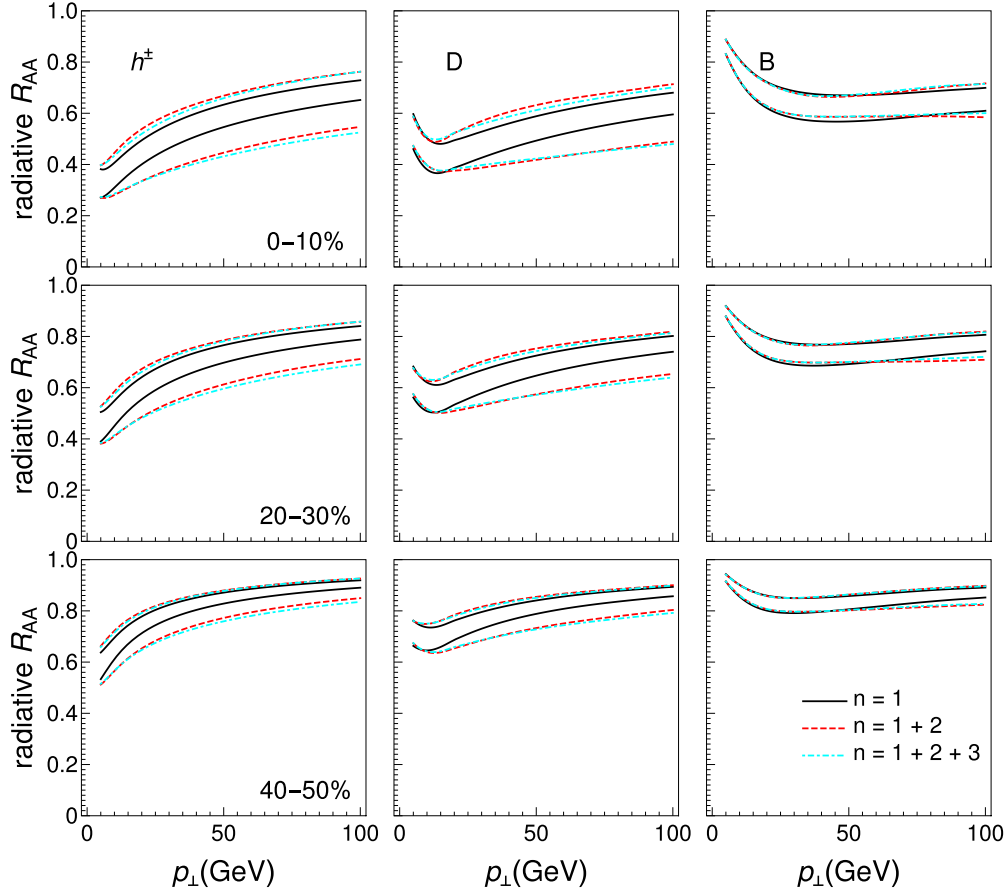


FIG. 2. Radiative  $R_{AA}$  results obtained within DREENA-C—the effects of different orders in opacity. The results are generated for the Pb + Pb collision system at  $\sqrt{s_{NN}} = 5.02$  TeV, and all the other figures in the manuscript show the results for the same collision system and energy. Different columns correspond to charged hadrons, D and B mesons, while different rows show different centrality classes. Solid black curves show the first order in opacity results, red dashed curves show the results up to the second order, while cyan dot-dashed curves up to the third order in opacity. The upper (lower) boundary of each band corresponds to the  $\mu_M/\mu_E = 0.6$  ( $\mu_M/\mu_E = 0.4$ ) case.

the other hand, the magnetic contribution depends nontrivially on the value of magnetic mass. That is, for  $\mu_M > \mu_{pl}$ , we see that the magnetic contribution decreases the energy loss, while for  $\mu_M < \mu_{pl}$  it increases the energy loss and consequently suppression, as shown in Fig. 2, which may intuitively explain the observed energy-loss behavior.

Furthermore, the Debye mass  $\mu_E$  is well defined from lattice QCD, where the perturbative calculations are also consistent [34]. Thus, the electric potential is well defined in dynamical energy loss, and we can separately test the effect of higher orders in opacity on this contribution [by replacing  $v(\mathbf{q})$  by  $v_L(\mathbf{q})$  in the DREENA framework]. We surprisingly find it to be negligible, as shown in Fig. 3. Thus, higher orders in opacity essentially do not influence the electric contribution in a dynamical QCD medium, which is an interesting and intuitively unexpected result. That is, the higher orders mainly influence the magnetic contribution to energy loss (keeping the electric contribution unaffected), where the sign of the effect depends on the magnetic mass value. For example, as  $\mu_M/\mu_E = 0.4$  is notably smaller than  $\mu_{pl}/\mu_E = 1/\sqrt{3}$ , the higher orders in opacity are significant for this limit and increase the suppression, in agreement with Fig. 2. On the

other hand,  $\mu_M/\mu_E = 0.6$  is close to (but slightly larger than)  $\mu_{pl}/\mu_E$ , so higher orders in opacity are small for this magnetic mass limit and reduce the suppression, also in agreement with Fig. 2. Additionally, note that the most recent 2 + 1 flavor lattice QCD results with physical quark masses further constrain the magnetic screening to  $0.58 < \mu_M/\mu_E < 0.64$  [38]. Thus, for this range of magnetic screening, we conclude that the effects of higher orders in opacity are small in a dynamical QCD medium and can be safely neglected.

Furthermore, Fig. 3 raises another important question: as is well known, only electric contribution exist in the *static* QCD medium approximation [23,24] (although it has a different functional form compared to the electric contribution in dynamical QCD medium). That is, the magnetic contribution is inherently connected with the dynamic nature of the QCD medium. As most existing energy loss calculations assume (simplified) static QCD medium approximation, does this mean that higher orders in opacity can be neglected under such approximation?

We first note that this does not necessarily have to be the case, because the effective potential for electric contribution is significantly different in static compared with the dynamical

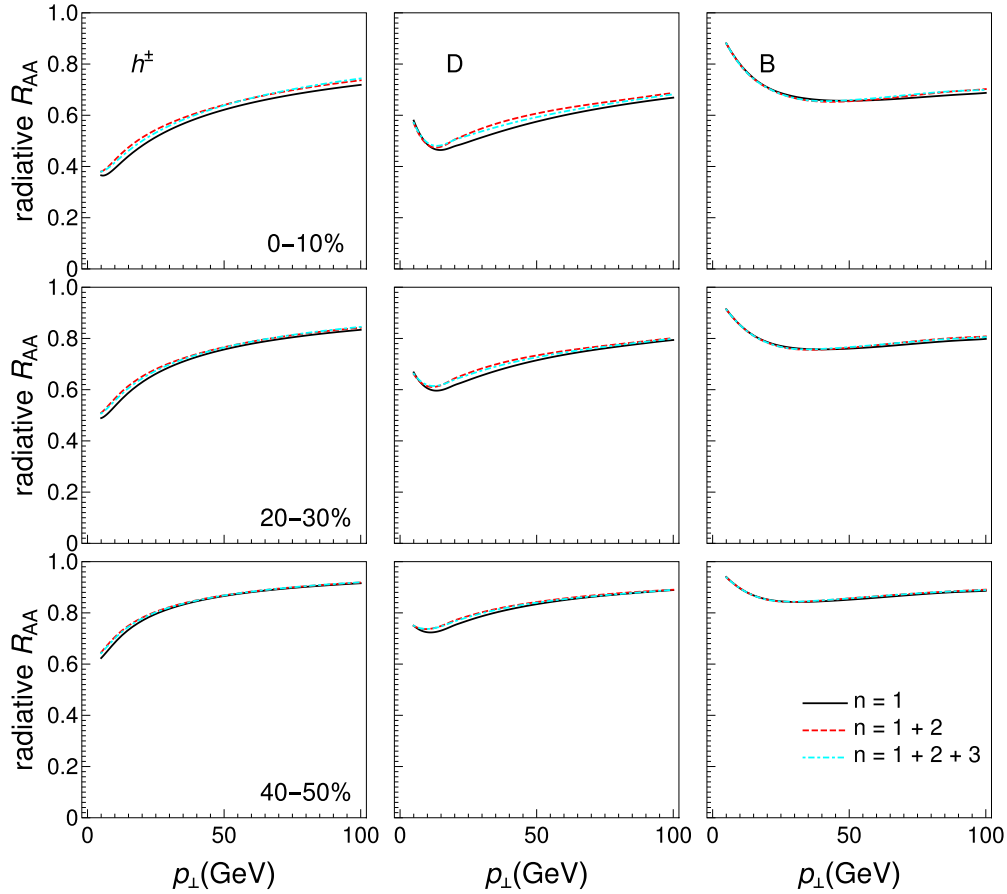


FIG. 3.  $R_{AA}$  results, obtained within DREENA-C when only electric contribution  $v_L(\mathbf{q})$  to radiative energy loss is considered. Different columns correspond to charged hadrons, D and B mesons, while different rows show different centrality classes. Solid black curves show the first order in opacity results, red dashed curves show the results up to the second order, while cyan dot-dashed curves up to the third order in opacity.

medium. However, to address this question, we repeat the same analyses as above, this time assuming the static medium effective potential [left-hand side of Eq. (7)] and mean free path  $\lambda_{\text{stat}}$ . Figure 4 shows the effects of higher orders in opacity in static medium approximation. While larger than those in Fig. 3, we see that these effects are still small (i.e., less than 6%). Thus, for optically thin medium models with static approximation, we show that including multiple scattering centers has a small effect on the numerical results, i.e., these effects can also be neglected.

Finally, we ask how the inclusion of evolving medium would modify these results. Including higher-order effects in evolving medium is very demanding and out of the scope of this paper. However, it can be partially addressed by studying how higher-order effects depend on the temperature, which changes in the evolving medium. To address this, in Fig. 5, we focus on D meson  $R_{AA}$ ,  $\mu_M/\mu_E = 0.6$  (per agreement with Ref. [38]) and study the effects of higher orders in opacity for three different temperatures  $T = 200, 400, 600$  MeV (which broadly covers the range of temperatures accessible at RHIC and the LHC). We find that the higher-order effects are largely independent of these values. Thus, we do not expect that including medium evolution will significantly influence

the results presented in this study, i.e., expect the effect of multiple scattering centers to remain small.

## V. SUMMARY

In this paper, we generalized our dynamical energy loss and DGLV formalisms towards finite orders in opacity. For bottom quarks, we find that higher orders in opacity are insignificant due to short gluon formation time, i.e. the incoherent limit. For charm and light quarks, including second order in opacity is sufficient, i.e., the third order numerical results almost overlap with the second. Surprisingly, we also find that for limits of magnetic screening,  $\mu_M/\mu_E = 0.4$  and  $\mu_M/\mu_E = 0.6$ , the effects on the  $R_{AA}$  are opposite in sign. That is, for  $\mu_M/\mu_E = 0.6$  ( $\mu_M/\mu_E = 0.4$ ), higher orders in opacity decrease (increase) the energy loss and subsequently suppression. The intuitive reason behind such behavior is the magnetic contribution to the dynamical energy loss. That is, while electric contribution remains almost insensitive to increases in the order of opacity, magnetic screening larger (smaller) than the plasmon mass value decreases (increases) the energy loss and suppression, in agreement with theoretical expectations. We also show that in the static QCD medium approximation, in



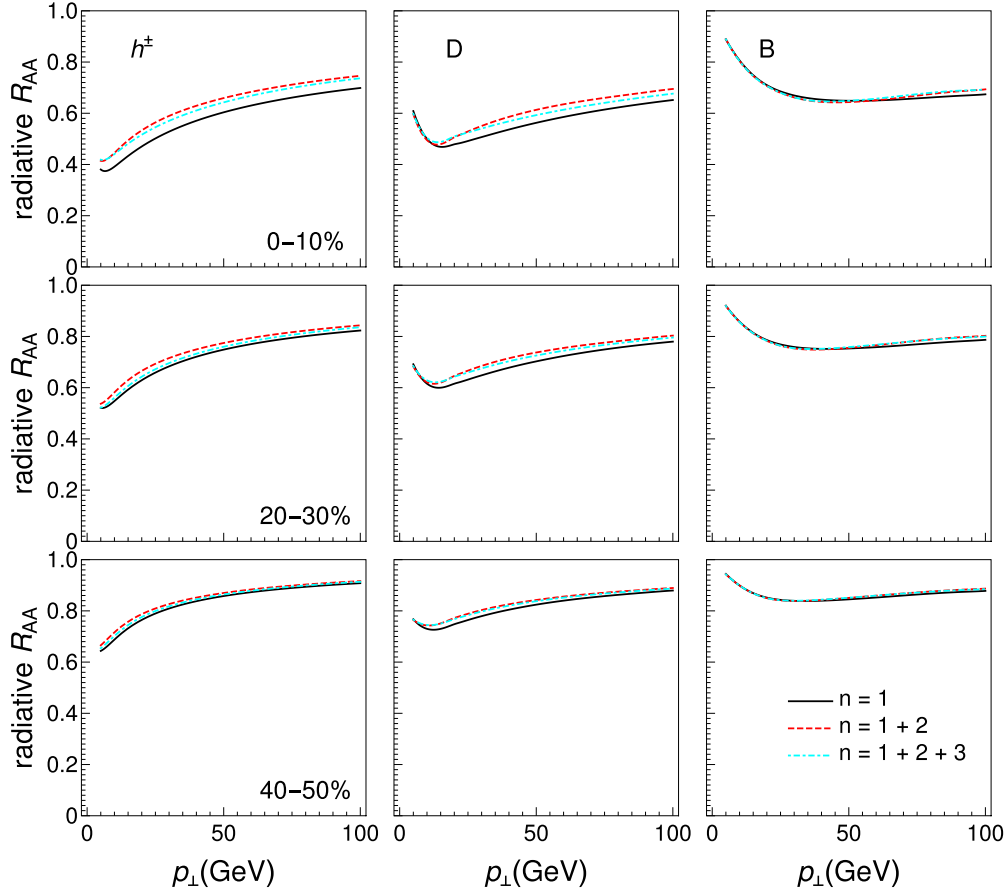


FIG. 4. Radiative  $R_{AA}$  results obtained within DREENA-C under the *static* medium approximation. Different columns correspond to charged hadrons, D and B mesons, while different rows show different centrality classes. Solid black curves show the first order in opacity results, red dashed curves show the results up to the second order, while cyan dot-dashed curves up to the third order in opacity.

which (per definition) only electric contribution remains, the effects of higher orders in opacity on high- $p_{\perp}$  observables are small and can be safely neglected. Thus, for static QCD

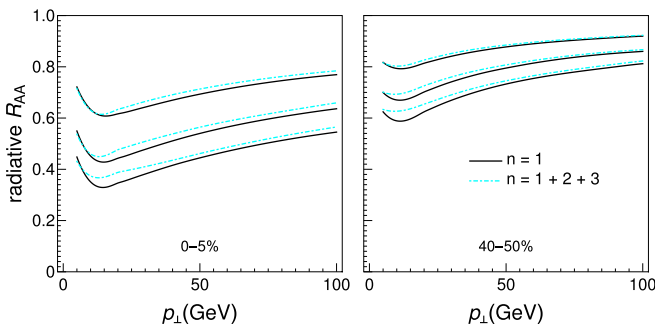


FIG. 5. D meson radiative  $R_{AA}$  results obtained within DREENA-C for different temperatures. The left panel corresponds to 0%–5% centrality, while the right panel corresponds to 40%–50% centrality. The values of temperature are  $T = 200$  MeV (the uppermost curves), 400 MeV (the middle curves), and 600 MeV (the lowest curves). The solid black curves show the first order in opacity results, while cyan dot-dashed curves show the results up to the third order in opacity. The chromomagnetic and chromoelectric mass ratio is fixed at  $\mu_M/\mu_E = 0.6$ .

medium, the first order in opacity is an adequate approximation for finite-size QCD medium created at RHIC and the LHC. For dynamical energy loss, both the sign and the size of the effects depend on the magnetic screening, as outlined above. However, for most of the current estimates of magnetic screening [38], these effects remain less than 5%, so they can also be safely neglected.

The analyses presented here are obtained for a constant-temperature medium (and adequately generalized DREENA-C framework). However, we also tested how the effects of including multiple scatterers depend upon temperature and found this influence to be also small (affecting the radiative  $R_{AA}$  for less than 5%). Thus, we expect that including higher orders in opacity in the evolving medium will not change the qualitative results obtained here, but this remains to be rigorously tested in the future.

## ACKNOWLEDGMENTS

We thank Jussi Auvinen for the useful discussions. This work is supported by the European Research Council, Grant No. ERC-2016-COG: 725741, and by the Ministry of Science, Technological Development and Innovations of the Republic of Serbia.

### APPENDIX A: ANALYTICAL EXPRESSIONS FOR $dN_g/dx$ : GENERAL FORM

The gluon radiation spectrum up to the fourth order in opacity contains the following terms, which are here given in detail:

$$\begin{aligned} \left(\frac{dN_g}{dx}\right) &= \left(\frac{dN_g^{(1)}}{dx}\right) + \left(\frac{dN_g^{(2)}}{dx}\right)_1 - \left(\frac{dN_g^{(2)}}{dx}\right)_2 + \left(\frac{dN_g^{(3)}}{dx}\right)_1 - \left(\frac{dN_g^{(3)}}{dx}\right)_2 - \left(\frac{dN_g^{(3)}}{dx}\right)_3 + \left(\frac{dN_g^{(3)}}{dx}\right)_4 + \left(\frac{dN_g^{(4)}}{dx}\right)_1 \\ &\quad - \left(\frac{dN_g^{(4)}}{dx}\right)_2 - \left(\frac{dN_g^{(4)}}{dx}\right)_3 + \left(\frac{dN_g^{(4)}}{dx}\right)_4 - \left(\frac{dN_g^{(4)}}{dx}\right)_5 + \left(\frac{dN_g^{(4)}}{dx}\right)_6 + \left(\frac{dN_g^{(4)}}{dx}\right)_7 - \left(\frac{dN_g^{(4)}}{dx}\right)_8. \end{aligned} \quad (\text{A1})$$

Numerical integrations with respect to the momentum  $\mathbf{k}$  are performed over  $0 < |\mathbf{k}| < 2Ex(1-x)$ , and the ones with respect to momenta  $\mathbf{q}_i$  are performed over  $0 < |\mathbf{q}_i| < \sqrt{4ET}$  [39]. The integrations with respect to angles  $\varphi_i$  are performed over  $0 < \varphi_i < 2\pi$ . Under the constant- $T$  approximation considered in this manuscript, the expressions presented below can be analytically integrated over  $z_i$ , significantly simplifying subsequent numerical calculations (see Appendix B).

In the expressions below, the following equations hold for  $i, j \in \{1, 2, 3, 4\}$ :

$$\mathbf{k} \cdot \mathbf{q}_i = |\mathbf{k}||\mathbf{q}_i| \cos \varphi_i, \quad (\text{A2})$$

$$\mathbf{q}_i \cdot \mathbf{q}_j = |\mathbf{q}_i||\mathbf{q}_j| \cos(\varphi_i - \varphi_j). \quad (\text{A3})$$

The first order in opacity term is given by

$$\begin{aligned} \left(\frac{dN_g^{(1)}}{dx}\right) &= \frac{4C_R}{\pi x} \int_0^L dz_1 \int \frac{d^2\mathbf{k}}{\pi} \int \frac{d^2\mathbf{q}_1}{\pi} \alpha_s(Q_k^2) \frac{1}{\lambda_{\text{dyn}}} \frac{\mu_E^2 - \mu_M^2}{(\mathbf{q}_1^2 + \mu_E^2)(\mathbf{q}_1^2 + \mu_M^2)} \\ &\quad \times \frac{\chi^2[\mathbf{q}_1 \cdot (\mathbf{q}_1 - \mathbf{k})] + (\mathbf{q}_1 \cdot \mathbf{k})(\mathbf{k} - \mathbf{q}_1)^2}{(\chi^2 + \mathbf{k}^2)[\chi^2 + (\mathbf{k} - \mathbf{q}_1)^2]} \sin^2\left(\frac{\chi^2 + (\mathbf{k} - \mathbf{q}_1)^2}{4xE} z_1\right). \end{aligned} \quad (\text{A4})$$

After integration with respect to  $z_1$ , this expression reduces to the expression used to obtain  $dN_g/dx$  in the original DREENA-C framework [22].

The second order in opacity contains two terms, which are given by

$$\begin{aligned} \left(\frac{dN_g^{(2)}}{dx}\right)_1 &= \frac{4C_R}{\pi x} \int_0^L \int_{z_1}^L dz_1 dz_2 \int \frac{d^2\mathbf{k}}{\pi} \iint \frac{d^2\mathbf{q}_1}{\pi} \frac{d^2\mathbf{q}_2}{\pi} \alpha_s(Q_k^2) \frac{1}{\lambda_{\text{dyn}}^2} \frac{\mu_E^2 - \mu_M^2}{(\mathbf{q}_1^2 + \mu_E^2)(\mathbf{q}_1^2 + \mu_M^2)} \frac{\mu_E^2 - \mu_M^2}{(\mathbf{q}_2^2 + \mu_E^2)(\mathbf{q}_2^2 + \mu_M^2)} \\ &\quad \times \frac{\chi^2[\mathbf{q}_2 \cdot (\mathbf{q}_1 + \mathbf{q}_2 - \mathbf{k})] + (\mathbf{q}_2 \cdot \mathbf{k})(\mathbf{k} - \mathbf{q}_2)^2 + (\mathbf{k} \cdot \mathbf{q}_1)[\mathbf{q}_2 \cdot (\mathbf{q}_2 - 2\mathbf{k})] + \mathbf{k}^2(\mathbf{q}_2 \cdot \mathbf{q}_1)}{(\chi^2 + \mathbf{k}^2)[\chi^2 + (\mathbf{k} - \mathbf{q}_2)^2][\chi^2 + (\mathbf{k} - \mathbf{q}_1 - \mathbf{q}_2)^2]} \\ &\quad \times \sin\left(\frac{\chi^2 + (\mathbf{k} - \mathbf{q}_1 - \mathbf{q}_2)^2}{4xE} z_1\right) \sin\left(\frac{\chi^2 + (\mathbf{k} - \mathbf{q}_1 - \mathbf{q}_2)^2}{4xE} z_1 + \frac{\chi^2 + (\mathbf{k} - \mathbf{q}_2)^2}{2xE} z_2\right), \end{aligned} \quad (\text{A5})$$

$$\begin{aligned} \left(\frac{dN_g^{(2)}}{dx}\right)_2 &= \frac{4C_R}{\pi x} \int_0^L \int_{z_1}^L dz_1 dz_2 \int \frac{d^2\mathbf{k}}{\pi} \int \frac{d^2\mathbf{q}_2}{\pi} \alpha_s(Q_k^2) \frac{1}{\lambda_{\text{dyn}}^2} \frac{\mu_E^2 - \mu_M^2}{(\mathbf{q}_2^2 + \mu_E^2)(\mathbf{q}_2^2 + \mu_M^2)} \\ &\quad \times \frac{\chi^2[\mathbf{q}_2 \cdot (\mathbf{q}_2 - \mathbf{k})] + (\mathbf{q}_2 \cdot \mathbf{k})(\mathbf{k} - \mathbf{q}_2)^2}{(\chi^2 + \mathbf{k}^2)[\chi^2 + (\mathbf{k} - \mathbf{q}_2)^2]} \sin\left(\frac{\chi^2 + (\mathbf{k} - \mathbf{q}_2)^2}{4xE} z_1\right) \sin\left[\frac{\chi^2 + (\mathbf{k} - \mathbf{q}_2)^2}{2xE} \left(\frac{z_1}{2} + z_2\right)\right]. \end{aligned} \quad (\text{A6})$$

The third order in opacity contains four terms, which are given by

$$\begin{aligned} \left(\frac{dN_g^{(3)}}{dx}\right)_1 &= \frac{4C_R}{\pi x} \int_0^L \int_{z_1}^L \int_{z_2}^L dz_1 dz_2 dz_3 \int \frac{d^2\mathbf{k}}{\pi} \iiint \frac{d^2\mathbf{q}_1}{\pi} \frac{d^2\mathbf{q}_2}{\pi} \frac{d^2\mathbf{q}_3}{\pi} \\ &\quad \times \alpha_s(Q_k^2) \frac{1}{\lambda_{\text{dyn}}^3} \frac{\mu_E^2 - \mu_M^2}{(\mathbf{q}_1^2 + \mu_E^2)(\mathbf{q}_1^2 + \mu_M^2)} \frac{\mu_E^2 - \mu_M^2}{(\mathbf{q}_2^2 + \mu_E^2)(\mathbf{q}_2^2 + \mu_M^2)} \frac{\mu_E^2 - \mu_M^2}{(\mathbf{q}_3^2 + \mu_E^2)(\mathbf{q}_3^2 + \mu_M^2)} \\ &\quad \times \frac{\chi^2[\mathbf{q}_3 \cdot (\mathbf{q}_1 + \mathbf{q}_2 + \mathbf{q}_3 - \mathbf{k})] + (\mathbf{q}_3 \cdot \mathbf{k})(\mathbf{k} - \mathbf{q}_3)^2 + [\mathbf{k} \cdot (\mathbf{q}_1 + \mathbf{q}_2)][\mathbf{q}_3 \cdot (\mathbf{q}_3 - 2\mathbf{k})] + \mathbf{k}^2[\mathbf{q}_3 \cdot (\mathbf{q}_1 + \mathbf{q}_2)]}{(\chi^2 + \mathbf{k}^2)[\chi^2 + (\mathbf{k} - \mathbf{q}_3)^2][\chi^2 + (\mathbf{k} - \mathbf{q}_1 - \mathbf{q}_2 - \mathbf{q}_3)^2]} \\ &\quad \times \sin\left(\frac{\chi^2 + (\mathbf{k} - \mathbf{q}_1 - \mathbf{q}_2 - \mathbf{q}_3)^2}{4xE} z_1\right) \\ &\quad \times \sin\left(\frac{\chi^2 + (\mathbf{k} - \mathbf{q}_1 - \mathbf{q}_2 - \mathbf{q}_3)^2}{4xE} z_1 + \frac{\chi^2 + (\mathbf{k} - \mathbf{q}_2 - \mathbf{q}_3)^2}{2xE} z_2 + \frac{\chi^2 + (\mathbf{k} - \mathbf{q}_3)^2}{2xE} z_3\right), \end{aligned} \quad (\text{A7})$$

$$\begin{aligned}
 \left(\frac{dN_g^{(3)}}{dx}\right)_2 &= \frac{4C_R}{\pi x} \int_0^L \int_{z_1}^L \int_{z_2}^L dz_1 dz_2 dz_3 \int \frac{d^2\mathbf{k}}{\pi} \iint \frac{d^2\mathbf{q}_1}{\pi} \frac{d^2\mathbf{q}_3}{\pi} \\
 &\times \alpha_s(Q_k^2) \frac{1}{\lambda_{\text{dyn}}^3} \frac{\mu_E^2 - \mu_M^2}{(\mathbf{q}_1^2 + \mu_E^2)(\mathbf{q}_1^2 + \mu_M^2)} \frac{\mu_E^2 - \mu_M^2}{(\mathbf{q}_3^2 + \mu_E^2)(\mathbf{q}_3^2 + \mu_M^2)} \\
 &\times \frac{\chi^2[\mathbf{q}_3 \cdot (\mathbf{q}_1 + \mathbf{q}_3 - \mathbf{k})] + (\mathbf{q}_3 \cdot \mathbf{k})(\mathbf{k} - \mathbf{q}_3)^2 + (\mathbf{k} \cdot \mathbf{q}_1)[\mathbf{q}_3 \cdot (\mathbf{q}_3 - 2\mathbf{k})] + \mathbf{k}^2(\mathbf{q}_3 \cdot \mathbf{q}_1)}{(\chi^2 + \mathbf{k}^2)[\chi^2 + (\mathbf{k} - \mathbf{q}_3)^2][\chi^2 + (\mathbf{k} - \mathbf{q}_1 - \mathbf{q}_3)^2]} \\
 &\times \sin\left(\frac{\chi^2 + (\mathbf{k} - \mathbf{q}_1 - \mathbf{q}_3)^2}{4xE} z_1\right) \sin\left(\frac{\chi^2 + (\mathbf{k} - \mathbf{q}_1 - \mathbf{q}_3)^2}{4xE} z_1 + \frac{\chi^2 + (\mathbf{k} - \mathbf{q}_3)^2}{2xE} (z_2 + z_3)\right), \quad (\text{A8})
 \end{aligned}$$

$$\begin{aligned}
 \left(\frac{dN_g^{(3)}}{dx}\right)_3 &= \frac{4C_R}{\pi x} \int_0^L \int_{z_1}^L \int_{z_2}^L dz_1 dz_2 dz_3 \int \frac{d^2\mathbf{k}}{\pi} \iint \frac{d^2\mathbf{q}_2}{\pi} \frac{d^2\mathbf{q}_3}{\pi} \alpha_s(Q_k^2) \frac{1}{\lambda_{\text{dyn}}^3} \frac{\mu_E^2 - \mu_M^2}{(\mathbf{q}_2^2 + \mu_E^2)(\mathbf{q}_2^2 + \mu_M^2)} \frac{\mu_E^2 - \mu_M^2}{(\mathbf{q}_3^2 + \mu_E^2)(\mathbf{q}_3^2 + \mu_M^2)} \\
 &\times \frac{\chi^2[\mathbf{q}_3 \cdot (\mathbf{q}_2 + \mathbf{q}_3 - \mathbf{k})] + (\mathbf{q}_3 \cdot \mathbf{k})(\mathbf{k} - \mathbf{q}_3)^2 + (\mathbf{k} \cdot \mathbf{q}_2)[\mathbf{q}_3 \cdot (\mathbf{q}_3 - 2\mathbf{k})] + \mathbf{k}^2(\mathbf{q}_3 \cdot \mathbf{q}_2)}{(\chi^2 + \mathbf{k}^2)[\chi^2 + (\mathbf{k} - \mathbf{q}_3)^2][\chi^2 + (\mathbf{k} - \mathbf{q}_2 - \mathbf{q}_3)^2]} \\
 &\times \sin\left(\frac{\chi^2 + (\mathbf{k} - \mathbf{q}_2 - \mathbf{q}_3)^2}{4xE} z_1\right) \sin\left[\frac{\chi^2 + (\mathbf{k} - \mathbf{q}_2 - \mathbf{q}_3)^2}{2xE} \left(\frac{z_1}{2} + z_2\right) + \frac{\chi^2 + (\mathbf{k} - \mathbf{q}_3)^2}{2xE} z_3\right], \quad (\text{A9})
 \end{aligned}$$

$$\begin{aligned}
 \left(\frac{dN_g^{(3)}}{dx}\right)_4 &= \frac{4C_R}{\pi x} \int_0^L \int_{z_1}^L \int_{z_2}^L dz_1 dz_2 dz_3 \int \frac{d^2\mathbf{k}}{\pi} \int \frac{d^2\mathbf{q}_3}{\pi} \alpha_s(Q_k^2) \frac{1}{\lambda_{\text{dyn}}^3} \frac{\mu_E^2 - \mu_M^2}{(\mathbf{q}_3^2 + \mu_E^2)(\mathbf{q}_3^2 + \mu_M^2)} \\
 &\times \frac{\chi^2[\mathbf{q}_3 \cdot (\mathbf{q}_3 - \mathbf{k})] + (\mathbf{q}_3 \cdot \mathbf{k})(\mathbf{k} - \mathbf{q}_3)^2}{(\chi^2 + \mathbf{k}^2)[\chi^2 + (\mathbf{k} - \mathbf{q}_3)^2]} \sin\left(\frac{\chi^2 + (\mathbf{k} - \mathbf{q}_3)^2}{4xE} z_1\right) \sin\left[\frac{\chi^2 + (\mathbf{k} - \mathbf{q}_3)^2}{2xE} \left(\frac{z_1}{2} + z_2 + z_3\right)\right]. \quad (\text{A10})
 \end{aligned}$$

The fourth order in opacity is given by eight terms, which are given by

$$\begin{aligned}
 \left(\frac{dN_g^{(4)}}{dx}\right)_1 &= \frac{4C_R}{\pi x} \int_0^L \int_{z_1}^L \int_{z_2}^L \int_{z_3}^L dz_1 dz_2 dz_3 dz_4 \int \frac{d^2\mathbf{k}}{\pi} \iiint \frac{d^2\mathbf{q}_1}{\pi} \frac{d^2\mathbf{q}_2}{\pi} \frac{d^2\mathbf{q}_3}{\pi} \frac{d^2\mathbf{q}_4}{\pi} \\
 &\times \alpha_s(Q_k^2) \frac{1}{\lambda_{\text{dyn}}^4} \frac{\mu_E^2 - \mu_M^2}{(\mathbf{q}_1^2 + \mu_E^2)(\mathbf{q}_1^2 + \mu_M^2)} \frac{\mu_E^2 - \mu_M^2}{(\mathbf{q}_2^2 + \mu_E^2)(\mathbf{q}_2^2 + \mu_M^2)} \frac{\mu_E^2 - \mu_M^2}{(\mathbf{q}_3^2 + \mu_E^2)(\mathbf{q}_3^2 + \mu_M^2)} \frac{\mu_E^2 - \mu_M^2}{(\mathbf{q}_4^2 + \mu_E^2)(\mathbf{q}_4^2 + \mu_M^2)} \\
 &\times \frac{\chi^2[\mathbf{q}_4 \cdot (\mathbf{q}_1 + \mathbf{q}_2 + \mathbf{q}_3 + \mathbf{q}_4 - \mathbf{k})] + (\mathbf{q}_4 \cdot \mathbf{k})(\mathbf{k} - \mathbf{q}_4)^2 + [\mathbf{k} \cdot (\mathbf{q}_1 + \mathbf{q}_2 + \mathbf{q}_3)][\mathbf{q}_4 \cdot (\mathbf{q}_4 - 2\mathbf{k})] + \mathbf{k}^2[\mathbf{q}_4 \cdot (\mathbf{q}_1 + \mathbf{q}_2 + \mathbf{q}_3)]}{(\chi^2 + \mathbf{k}^2)[\chi^2 + (\mathbf{k} - \mathbf{q}_4)^2][\chi^2 + (\mathbf{k} - \mathbf{q}_1 - \mathbf{q}_2 - \mathbf{q}_3 - \mathbf{q}_4)^2]} \\
 &\times \sin\left(\frac{\chi^2 + (\mathbf{k} - \mathbf{q}_1 - \mathbf{q}_2 - \mathbf{q}_3 - \mathbf{q}_4)^2}{4xE} z_1 + \frac{\chi^2 + (\mathbf{k} - \mathbf{q}_2 - \mathbf{q}_3 - \mathbf{q}_4)^2}{2xE} z_2 + \frac{\chi^2 + (\mathbf{k} - \mathbf{q}_3 - \mathbf{q}_4)^2}{2xE} z_3\right. \\
 &\left. + \frac{\chi^2 + (\mathbf{k} - \mathbf{q}_4)^2}{2xE} z_4\right) \sin\left(\frac{\chi^2 + (\mathbf{k} - \mathbf{q}_1 - \mathbf{q}_2 - \mathbf{q}_3 - \mathbf{q}_4)^2}{4xE} z_1\right), \quad (\text{A11})
 \end{aligned}$$

$$\begin{aligned}
 \left(\frac{dN_g^{(4)}}{dx}\right)_2 &= \frac{4C_R}{\pi x} \int_0^L \int_{z_1}^L \int_{z_2}^L \int_{z_3}^L dz_1 dz_2 dz_3 dz_4 \int \frac{d^2\mathbf{k}}{\pi} \iiint \frac{d^2\mathbf{q}_1}{\pi} \frac{d^2\mathbf{q}_2}{\pi} \frac{d^2\mathbf{q}_4}{\pi} \\
 &\times \alpha_s(Q_k^2) \frac{1}{\lambda_{\text{dyn}}^4} \frac{\mu_E^2 - \mu_M^2}{(\mathbf{q}_1^2 + \mu_E^2)(\mathbf{q}_1^2 + \mu_M^2)} \frac{\mu_E^2 - \mu_M^2}{(\mathbf{q}_2^2 + \mu_E^2)(\mathbf{q}_2^2 + \mu_M^2)} \frac{\mu_E^2 - \mu_M^2}{(\mathbf{q}_4^2 + \mu_E^2)(\mathbf{q}_4^2 + \mu_M^2)} \\
 &\times \frac{\chi^2[\mathbf{q}_4 \cdot (\mathbf{q}_1 + \mathbf{q}_2 + \mathbf{q}_4 - \mathbf{k})] + (\mathbf{q}_4 \cdot \mathbf{k})(\mathbf{k} - \mathbf{q}_4)^2 + [\mathbf{k} \cdot (\mathbf{q}_1 + \mathbf{q}_2)][\mathbf{q}_4 \cdot (\mathbf{q}_4 - 2\mathbf{k})] + \mathbf{k}^2[\mathbf{q}_4 \cdot (\mathbf{q}_1 + \mathbf{q}_2)]}{(\chi^2 + \mathbf{k}^2)[\chi^2 + (\mathbf{k} - \mathbf{q}_4)^2][\chi^2 + (\mathbf{k} - \mathbf{q}_1 - \mathbf{q}_2 - \mathbf{q}_4)^2]} \\
 &\times \sin\left(\frac{\chi^2 + (\mathbf{k} - \mathbf{q}_1 - \mathbf{q}_2 - \mathbf{q}_4)^2}{4xE} z_1 + \frac{\chi^2 + (\mathbf{k} - \mathbf{q}_2 - \mathbf{q}_4)^2}{2xE} z_2 + \frac{\chi^2 + (\mathbf{k} - \mathbf{q}_4)^2}{2xE} (z_3 + z_4)\right) \\
 &\times \sin\left(\frac{\chi^2 + (\mathbf{k} - \mathbf{q}_1 - \mathbf{q}_2 - \mathbf{q}_4)^2}{4xE} z_1\right), \quad (\text{A12})
 \end{aligned}$$

$$\begin{aligned}
\left(\frac{dN_g^{(4)}}{dx}\right)_3 &= \frac{4C_R}{\pi x} \int_0^L \int_{z_1}^L \int_{z_2}^L \int_{z_3}^L dz_1 dz_2 dz_3 dz_4 \int \frac{d^2\mathbf{k}}{\pi} \iiint \frac{d^2\mathbf{q}_1}{\pi} \frac{d^2\mathbf{q}_3}{\pi} \frac{d^2\mathbf{q}_4}{\pi} \\
&\times \alpha_s(Q_k^2) \frac{1}{\lambda_{\text{dyn}}^4} \frac{\mu_E^2 - \mu_M^2}{(\mathbf{q}_1^2 + \mu_E^2)(\mathbf{q}_1^2 + \mu_M^2)} \frac{\mu_E^2 - \mu_M^2}{(\mathbf{q}_3^2 + \mu_E^2)(\mathbf{q}_3^2 + \mu_M^2)} \frac{\mu_E^2 - \mu_M^2}{(\mathbf{q}_4^2 + \mu_E^2)(\mathbf{q}_4^2 + \mu_M^2)} \\
&\times \frac{\chi^2[\mathbf{q}_4 \cdot (\mathbf{q}_1 + \mathbf{q}_3 + \mathbf{q}_4 - \mathbf{k})] + (\mathbf{q}_4 \cdot \mathbf{k})(\mathbf{k} - \mathbf{q}_4)^2 + [\mathbf{k} \cdot (\mathbf{q}_1 + \mathbf{q}_3)][\mathbf{q}_4 \cdot (\mathbf{q}_4 - 2\mathbf{k})] + \mathbf{k}^2[\mathbf{q}_4 \cdot (\mathbf{q}_1 + \mathbf{q}_3)]}{(\chi^2 + \mathbf{k}^2)[\chi^2 + (\mathbf{k} - \mathbf{q}_4)^2][\chi^2 + (\mathbf{k} - \mathbf{q}_1 - \mathbf{q}_3 - \mathbf{q}_4)^2]} \\
&\times \sin\left(\frac{\chi^2 + (\mathbf{k} - \mathbf{q}_1 - \mathbf{q}_3 - \mathbf{q}_4)^2}{4xE} z_1 + \frac{\chi^2 + (\mathbf{k} - \mathbf{q}_3 - \mathbf{q}_4)^2}{2xE} (z_2 + z_3) + \frac{\chi^2 + (\mathbf{k} - \mathbf{q}_4)^2}{2xE} z_4\right) \\
&\times \sin\left(\frac{\chi^2 + (\mathbf{k} - \mathbf{q}_1 - \mathbf{q}_3 - \mathbf{q}_4)^2}{4xE} z_1\right), \tag{A13}
\end{aligned}$$

$$\begin{aligned}
\left(\frac{dN_g^{(4)}}{dx}\right)_4 &= \frac{4C_R}{\pi x} \int_0^L \int_{z_1}^L \int_{z_2}^L \int_{z_3}^L dz_1 dz_2 dz_3 dz_4 \int \frac{d^2\mathbf{k}}{\pi} \iint \frac{d^2\mathbf{q}_1}{\pi} \frac{d^2\mathbf{q}_4}{\pi} \\
&\times \alpha_s(Q_k^2) \frac{1}{\lambda_{\text{dyn}}^4} \frac{\mu_E^2 - \mu_M^2}{(\mathbf{q}_1^2 + \mu_E^2)(\mathbf{q}_1^2 + \mu_M^2)} \frac{\mu_E^2 - \mu_M^2}{(\mathbf{q}_4^2 + \mu_E^2)(\mathbf{q}_4^2 + \mu_M^2)} \\
&\times \frac{\chi^2[\mathbf{q}_4 \cdot (\mathbf{q}_1 + \mathbf{q}_4 - \mathbf{k})] + (\mathbf{q}_4 \cdot \mathbf{k})(\mathbf{k} - \mathbf{q}_4)^2 + (\mathbf{k} \cdot \mathbf{q}_1)[\mathbf{q}_4 \cdot (\mathbf{q}_4 - 2\mathbf{k})] + \mathbf{k}^2(\mathbf{q}_4 \cdot \mathbf{q}_1)}{(\chi^2 + \mathbf{k}^2)[\chi^2 + (\mathbf{k} - \mathbf{q}_4)^2][\chi^2 + (\mathbf{k} - \mathbf{q}_1 - \mathbf{q}_4)^2]} \\
&\times \sin\left(\frac{\chi^2 + (\mathbf{k} - \mathbf{q}_1 - \mathbf{q}_4)^2}{4xE} z_1\right) \sin\left(\frac{\chi^2 + (\mathbf{k} - \mathbf{q}_1 - \mathbf{q}_4)^2}{4xE} z_1 + \frac{\chi^2 + (\mathbf{k} - \mathbf{q}_4)^2}{2xE} (z_2 + z_3 + z_4)\right), \tag{A14}
\end{aligned}$$

$$\begin{aligned}
\left(\frac{dN_g^{(4)}}{dx}\right)_5 &= \frac{4C_R}{\pi x} \int_0^L \int_{z_1}^L \int_{z_2}^L \int_{z_3}^L dz_1 dz_2 dz_3 dz_4 \int \frac{d^2\mathbf{k}}{\pi} \iiint \frac{d^2\mathbf{q}_2}{\pi} \frac{d^2\mathbf{q}_3}{\pi} \frac{d^2\mathbf{q}_4}{\pi} \\
&\times \alpha_s(Q_k^2) \frac{1}{\lambda_{\text{dyn}}^4} \frac{\mu_E^2 - \mu_M^2}{(\mathbf{q}_2^2 + \mu_E^2)(\mathbf{q}_2^2 + \mu_M^2)} \frac{\mu_E^2 - \mu_M^2}{(\mathbf{q}_3^2 + \mu_E^2)(\mathbf{q}_3^2 + \mu_M^2)} \frac{\mu_E^2 - \mu_M^2}{(\mathbf{q}_4^2 + \mu_E^2)(\mathbf{q}_4^2 + \mu_M^2)} \\
&\times \frac{\chi^2[\mathbf{q}_4 \cdot (\mathbf{q}_2 + \mathbf{q}_3 + \mathbf{q}_4 - \mathbf{k})] + (\mathbf{q}_4 \cdot \mathbf{k})(\mathbf{k} - \mathbf{q}_4)^2 + [\mathbf{k} \cdot (\mathbf{q}_2 + \mathbf{q}_3)][\mathbf{q}_4 \cdot (\mathbf{q}_4 - 2\mathbf{k})] + \mathbf{k}^2[\mathbf{q}_4 \cdot (\mathbf{q}_2 + \mathbf{q}_3)]}{(\chi^2 + \mathbf{k}^2)[\chi^2 + (\mathbf{k} - \mathbf{q}_4)^2][\chi^2 + (\mathbf{k} - \mathbf{q}_2 - \mathbf{q}_3 - \mathbf{q}_4)^2]} \\
&\times \sin\left[\frac{\chi^2 + (\mathbf{k} - \mathbf{q}_2 - \mathbf{q}_3 - \mathbf{q}_4)^2}{2xE} \left(\frac{z_1}{2} + z_2\right) + \frac{\chi^2 + (\mathbf{k} - \mathbf{q}_3 - \mathbf{q}_4)^2}{2xE} z_3 + \frac{\chi^2 + (\mathbf{k} - \mathbf{q}_4)^2}{2xE} z_4\right] \\
&\times \sin\left(\frac{\chi^2 + (\mathbf{k} - \mathbf{q}_2 - \mathbf{q}_3 - \mathbf{q}_4)^2}{4xE} z_1\right), \tag{A15}
\end{aligned}$$

$$\begin{aligned}
\left(\frac{dN_g^{(4)}}{dx}\right)_6 &= \frac{4C_R}{\pi x} \int_0^L \int_{z_1}^L \int_{z_2}^L \int_{z_3}^L dz_1 dz_2 dz_3 dz_4 \int \frac{d^2\mathbf{k}}{\pi} \iint \frac{d^2\mathbf{q}_2}{\pi} \frac{d^2\mathbf{q}_4}{\pi} \\
&\times \alpha_s(Q_k^2) \frac{1}{\lambda_{\text{dyn}}^4} \frac{\mu_E^2 - \mu_M^2}{(\mathbf{q}_2^2 + \mu_E^2)(\mathbf{q}_2^2 + \mu_M^2)} \frac{\mu_E^2 - \mu_M^2}{(\mathbf{q}_4^2 + \mu_E^2)(\mathbf{q}_4^2 + \mu_M^2)} \\
&\times \frac{\chi^2[\mathbf{q}_4 \cdot (\mathbf{q}_2 + \mathbf{q}_4 - \mathbf{k})] + (\mathbf{q}_4 \cdot \mathbf{k})(\mathbf{k} - \mathbf{q}_4)^2 + (\mathbf{k} \cdot \mathbf{q}_2)[\mathbf{q}_4 \cdot (\mathbf{q}_4 - 2\mathbf{k})] + \mathbf{k}^2(\mathbf{q}_4 \cdot \mathbf{q}_2)}{(\chi^2 + \mathbf{k}^2)[\chi^2 + (\mathbf{k} - \mathbf{q}_4)^2][\chi^2 + (\mathbf{k} - \mathbf{q}_2 - \mathbf{q}_4)^2]} \\
&\times \sin\left(\frac{\chi^2 + (\mathbf{k} - \mathbf{q}_2 - \mathbf{q}_4)^2}{4xE} z_1\right) \sin\left[\frac{\chi^2 + (\mathbf{k} - \mathbf{q}_2 - \mathbf{q}_4)^2}{2xE} \left(\frac{z_1}{2} + z_2\right) + \frac{\chi^2 + (\mathbf{k} - \mathbf{q}_4)^2}{2xE} (z_3 + z_4)\right], \tag{A16}
\end{aligned}$$

$$\begin{aligned}
 \left(\frac{dN_g^{(4)}}{dx}\right)_7 &= \frac{4C_R}{\pi x} \int_0^L \int_{z_1}^L \int_{z_2}^L \int_{z_3}^L dz_1 dz_2 dz_3 dz_4 \int \frac{d^2\mathbf{k}}{\pi} \iint \frac{d^2\mathbf{q}_3}{\pi} \frac{d^2\mathbf{q}_4}{\pi} \\
 &\times \alpha_s(Q_k^2) \frac{1}{\lambda_{\text{dyn}}^4} \frac{\mu_E^2 - \mu_M^2}{(\mathbf{q}_3^2 + \mu_E^2)(\mathbf{q}_3^2 + \mu_M^2)} \frac{\mu_E^2 - \mu_M^2}{(\mathbf{q}_4^2 + \mu_E^2)(\mathbf{q}_4^2 + \mu_M^2)} \\
 &\times \frac{\chi^2[\mathbf{q}_4 \cdot (\mathbf{q}_3 + \mathbf{q}_4 - \mathbf{k})] + (\mathbf{q}_4 \cdot \mathbf{k})(\mathbf{k} - \mathbf{q}_4)^2 + (\mathbf{k} \cdot \mathbf{q}_3)[\mathbf{q}_4 \cdot (\mathbf{q}_4 - 2\mathbf{k})] + \mathbf{k}^2(\mathbf{q}_4 \cdot \mathbf{q}_3)}{(\chi^2 + \mathbf{k}^2)[\chi^2 + (\mathbf{k} - \mathbf{q}_4)^2][\chi^2 + (\mathbf{k} - \mathbf{q}_3 - \mathbf{q}_4)^2]} \\
 &\times \sin\left(\frac{\chi^2 + (\mathbf{k} - \mathbf{q}_3 - \mathbf{q}_4)^2}{4xE} z_1\right) \sin\left[\frac{\chi^2 + (\mathbf{k} - \mathbf{q}_3 - \mathbf{q}_4)^2}{2xE} \left(\frac{z_1}{2} + z_2 + z_3\right) + \frac{\chi^2 + (\mathbf{k} - \mathbf{q}_4)^2}{2xE} z_4\right], \quad (\text{A17})
 \end{aligned}$$

$$\begin{aligned}
 \left(\frac{dN_g^{(4)}}{dx}\right)_8 &= \frac{4C_R}{\pi x} \int_0^L \int_{z_1}^L \int_{z_2}^L \int_{z_3}^L dz_1 dz_2 dz_3 dz_4 \int \frac{d^2\mathbf{k}}{\pi} \int \frac{d^2\mathbf{q}_4}{\pi} \\
 &\times \alpha_s(Q_k^2) \frac{1}{\lambda_{\text{dyn}}^4} \frac{\mu_E^2 - \mu_M^2}{(\mathbf{q}_4^2 + \mu_E^2)(\mathbf{q}_4^2 + \mu_M^2)} \frac{\chi^2[\mathbf{q}_4 \cdot (\mathbf{q}_4 - \mathbf{k})] + (\mathbf{q}_4 \cdot \mathbf{k})(\mathbf{k} - \mathbf{q}_4)^2}{(\chi^2 + \mathbf{k}^2)[\chi^2 + (\mathbf{k} - \mathbf{q}_4)^2]^2} \\
 &\times \sin\left(\frac{\chi^2 + (\mathbf{k} - \mathbf{q}_4)^2}{4xE} z_1\right) \sin\left[\frac{\chi^2 + (\mathbf{k} - \mathbf{q}_4)^2}{2xE} \left(\frac{z_1}{2} + z_2 + z_3 + z_4\right)\right]. \quad (\text{A18})
 \end{aligned}$$

### APPENDIX B: ANALYTICAL EXPRESSIONS FOR $dN_g/dx$ WITHIN DREENA-C

Within the DREENA-C framework, under the assumption of constant medium temperature, we can explicitly perform analytical integrations for  $z_i$ , where ( $i = 1, 2, 3, 4$ ).  $\omega_{(m\dots n)}$  coefficients are defined in the Theoretical Framework section. The expression for the first order in opacity then became

$$\left(\frac{dN_g^{(1)}}{dx}\right) = \frac{2C_R}{\pi x} \int \frac{d^2\mathbf{k}}{\pi} \int \frac{d^2\mathbf{q}_1}{\pi} \alpha_s(Q_k^2) \frac{L}{\lambda_{\text{dyn}}} \frac{\mu_E^2 - \mu_M^2}{(\mathbf{q}_1^2 + \mu_E^2)(\mathbf{q}_1^2 + \mu_M^2)} \frac{\chi^2[\mathbf{q}_1 \cdot (\mathbf{q}_1 - \mathbf{k})] + (\mathbf{q}_1 \cdot \mathbf{k})(\mathbf{k} - \mathbf{q}_1)^2}{(\chi^2 + \mathbf{k}^2)[\chi^2 + (\mathbf{k} - \mathbf{q}_1)^2]^2} \left(1 - \frac{\sin(L\omega_{(1)})}{L\omega_{(1)}}\right), \quad (\text{B1})$$

The expressions for higher orders in opacity became

$$\begin{aligned}
 \left(\frac{dN_g^{(2)}}{dx}\right)_1 &= \frac{2C_R}{\pi x} \int \frac{d^2\mathbf{k}}{\pi} \iint \frac{d^2\mathbf{q}_1}{\pi} \frac{d^2\mathbf{q}_2}{\pi} \alpha_s(Q_k^2) \frac{1}{\lambda_{\text{dyn}}^2} \frac{\mu_E^2 - \mu_M^2}{(\mathbf{q}_1^2 + \mu_E^2)(\mathbf{q}_1^2 + \mu_M^2)} \frac{\mu_E^2 - \mu_M^2}{(\mathbf{q}_2^2 + \mu_E^2)(\mathbf{q}_2^2 + \mu_M^2)} \\
 &\times \frac{\chi^2[\mathbf{q}_2 \cdot (\mathbf{q}_1 + \mathbf{q}_2 - \mathbf{k})] + (\mathbf{q}_2 \cdot \mathbf{k})(\mathbf{k} - \mathbf{q}_2)^2 + (\mathbf{k} \cdot \mathbf{q}_1)[\mathbf{q}_2 \cdot (\mathbf{q}_2 - 2\mathbf{k})] + \mathbf{k}^2(\mathbf{q}_2 \cdot \mathbf{q}_1)}{(\chi^2 + \mathbf{k}^2)[\chi^2 + (\mathbf{k} - \mathbf{q}_2)^2][\chi^2 + (\mathbf{k} - \mathbf{q}_1 - \mathbf{q}_2)^2]} \\
 &\times \frac{1}{\omega_{(2)}} \left( \frac{\omega_{(2)} \cos[(\omega_{(2)} + \omega_{(12)})]}{(\omega_{(2)} + \omega_{(12)})\omega_{(12)}} + L \sin(L\omega_{(2)}) - \frac{(\omega_{(2)} - \omega_{(12)}) \cos(L\omega_{(2)})}{\omega_{(2)}\omega_{(12)}} - \frac{\omega_{(12)}}{\omega_{(2)}(\omega_{(2)} + \omega_{(12)})} \right), \quad (\text{B2})
 \end{aligned}$$

$$\begin{aligned}
 \left(\frac{dN_g^{(2)}}{dx}\right)_2 &= \frac{2C_R}{\pi x} \int \frac{d^2\mathbf{k}}{\pi} \int \frac{d^2\mathbf{q}_2}{\pi} \alpha_s(Q_k^2) \frac{1}{\lambda_{\text{dyn}}^2} \frac{\mu_E^2 - \mu_M^2}{(\mathbf{q}_2^2 + \mu_E^2)(\mathbf{q}_2^2 + \mu_M^2)} \\
 &\times \frac{\chi^2[\mathbf{q}_2 \cdot (\mathbf{q}_2 - \mathbf{k})] + (\mathbf{q}_2 \cdot \mathbf{k})(\mathbf{k} - \mathbf{q}_2)^2 \sin(L\omega_{(2)})[L\omega_{(2)} - \sin(L\omega_{(2)})]}{(\chi^2 + \mathbf{k}^2)[\chi^2 + (\mathbf{k} - \mathbf{q}_2)^2]^2 \omega_{(2)}^2}, \quad (\text{B3})
 \end{aligned}$$

$$\begin{aligned}
 \left(\frac{dN_g^{(3)}}{dx}\right)_1 &= \frac{2C_R}{\pi x} \int \frac{d^2\mathbf{k}}{\pi} \iiint \frac{d^2\mathbf{q}_1}{\pi} \frac{d^2\mathbf{q}_2}{\pi} \frac{d^2\mathbf{q}_3}{\pi} \alpha_s(Q_k^2) \frac{1}{\lambda_{\text{dyn}}^3} \frac{\mu_E^2 - \mu_M^2}{(\mathbf{q}_1^2 + \mu_E^2)(\mathbf{q}_1^2 + \mu_M^2)} \frac{\mu_E^2 - \mu_M^2}{(\mathbf{q}_2^2 + \mu_E^2)(\mathbf{q}_2^2 + \mu_M^2)} \frac{\mu_E^2 - \mu_M^2}{(\mathbf{q}_3^2 + \mu_E^2)(\mathbf{q}_3^2 + \mu_M^2)} \\
 &\times \frac{\chi^2[\mathbf{q}_3 \cdot (\mathbf{q}_1 + \mathbf{q}_2 + \mathbf{q}_3 - \mathbf{k})] + (\mathbf{q}_3 \cdot \mathbf{k})(\mathbf{k} - \mathbf{q}_3)^2 + [\mathbf{k} \cdot (\mathbf{q}_1 + \mathbf{q}_2)][\mathbf{q}_3 \cdot (\mathbf{q}_3 - 2\mathbf{k})] + \mathbf{k}^2[\mathbf{q}_3 \cdot (\mathbf{q}_1 + \mathbf{q}_2)]}{(\chi^2 + \mathbf{k}^2)[\chi^2 + (\mathbf{k} - \mathbf{q}_3)^2][\chi^2 + (\mathbf{k} - \mathbf{q}_1 - \mathbf{q}_2 - \mathbf{q}_3)^2]} \\
 &\times \left\{ \frac{\omega_{(3)}\omega_{(123)} + 2\omega_{(23)}\omega_{(123)} - \omega_{(23)}^2 - \omega_{(3)}\omega_{(23)}}{\omega_{(23)}^2(\omega_{(3)} + \omega_{(23)})^2\omega_{(123)}} \sin[L(\omega_{(3)} + \omega_{(23)})] - \frac{\omega_{(123)} \sin(L\omega_{(3)})}{\omega_{(3)}\omega_{(23)}^2(\omega_{(23)} + \omega_{(123)})} \right. \\
 &\left. + \frac{\sin[L(\omega_{(3)} + \omega_{(23)} + \omega_{(123)})]}{\omega_{(123)}(\omega_{(23)} + \omega_{(123)})(\omega_{(3)} + \omega_{(23)} + \omega_{(123)})} - \frac{L \cos[L(\omega_{(3)} + \omega_{(23)})]}{\omega_{(23)}(\omega_{(3)} + \omega_{(23)})} \right\}, \quad (\text{B4})
 \end{aligned}$$



$$\begin{aligned}
\left(\frac{dN_g^{(3)}}{dx}\right)_2 &= \frac{C_R}{\pi x} \int \frac{d^2\mathbf{k}}{\pi} \iint \frac{d^2\mathbf{q}_1}{\pi} \frac{d^2\mathbf{q}_3}{\pi} \alpha_s(Q_k^2) \frac{1}{\lambda_{\text{dyn}}^3} \frac{\mu_E^2 - \mu_M^2}{(\mathbf{q}_1^2 + \mu_E^2)(\mathbf{q}_1^2 + \mu_M^2)} \frac{\mu_E^2 - \mu_M^2}{(\mathbf{q}_3^2 + \mu_E^2)(\mathbf{q}_3^2 + \mu_M^2)} \\
&\times \frac{\chi^2[\mathbf{q}_3 \cdot (\mathbf{q}_1 + \mathbf{q}_3 - \mathbf{k})] + (\mathbf{q}_3 \cdot \mathbf{k})(\mathbf{k} - \mathbf{q}_3)^2 + (\mathbf{k} \cdot \mathbf{q}_1)[\mathbf{q}_3 \cdot (\mathbf{q}_3 - 2\mathbf{k})] + \mathbf{k}^2(\mathbf{q}_3 \cdot \mathbf{q}_1)}{(\chi^2 + \mathbf{k}^2)[\chi^2 + (\mathbf{k} - \mathbf{q}_3)^2][\chi^2 + (\mathbf{k} - \mathbf{q}_1 - \mathbf{q}_3)^2]} \\
&\times \left( \frac{\left(\frac{3\omega_{(13)}}{2} - \omega_{(3)}\right) \sin(2L\omega_{(3)})}{\omega_{(3)}^3 \omega_{(13)}} - \frac{2\omega_{(13)} \sin(L\omega_{(3)})}{\omega_{(3)}^3 (\omega_{(3)} + \omega_{(13)})} + \frac{\sin\left[2L\left(\omega_{(3)} + \frac{\omega_{(13)}}{2}\right)\right]}{(\omega_{(3)} + \frac{\omega_{(13)}}{2})\omega_{(13)}(\omega_{(3)} + \omega_{(13)})} - \frac{L \cos(2L\omega_{(3)})}{\omega_{(3)}^2} \right), \tag{B5}
\end{aligned}$$

$$\begin{aligned}
\left(\frac{dN_g^{(3)}}{dx}\right)_3 &= \frac{2C_R}{\pi x} \int \frac{d^2\mathbf{k}}{\pi} \iint \frac{d^2\mathbf{q}_2}{\pi} \frac{d^2\mathbf{q}_3}{\pi} \alpha_s(Q_k^2) \frac{1}{\lambda_{\text{dyn}}^3} \frac{\mu_E^2 - \mu_M^2}{(\mathbf{q}_2^2 + \mu_E^2)(\mathbf{q}_2^2 + \mu_M^2)} \frac{\mu_E^2 - \mu_M^2}{(\mathbf{q}_3^2 + \mu_E^2)(\mathbf{q}_3^2 + \mu_M^2)} \\
&\times \frac{\chi^2[\mathbf{q}_3 \cdot (\mathbf{q}_2 + \mathbf{q}_3 - \mathbf{k})] + (\mathbf{q}_3 \cdot \mathbf{k})(\mathbf{k} - \mathbf{q}_3)^2 + (\mathbf{k} \cdot \mathbf{q}_2)[\mathbf{q}_3 \cdot (\mathbf{q}_3 - 2\mathbf{k})] + \mathbf{k}^2(\mathbf{q}_3 \cdot \mathbf{q}_2)}{(\chi^2 + \mathbf{k}^2)[\chi^2 + (\mathbf{k} - \mathbf{q}_3)^2](\chi^2 + (\mathbf{k} - \mathbf{q}_2 - \mathbf{q}_3)^2)} \\
&\times \left( \frac{\sin\left[2L\left(\frac{\omega_{(3)}}{2} + \omega_{(23)}\right)\right]}{4\omega_{(23)}^2\left(\frac{\omega_{(3)}}{2} + \omega_{(23)}\right)} - \frac{\sin(L\omega_{(3)})}{2\omega_{(23)}^2\omega_{(3)}} + \frac{\sin[L(\omega_{(3)} + \omega_{(23)})] - L \cos[L(\omega_{(3)} + \omega_{(23)})]}{\omega_{(23)}(\omega_{(3)} + \omega_{(23)})} \right), \tag{B6}
\end{aligned}$$

$$\begin{aligned}
\left(\frac{dN_g^{(3)}}{dx}\right)_4 &= \frac{C_R}{\pi x} \int \frac{d^2\mathbf{k}}{\pi} \int \frac{d^2\mathbf{q}_3}{\pi} \alpha_s(Q_k^2) \frac{1}{\lambda_{\text{dyn}}^3} \frac{\mu_E^2 - \mu_M^2}{(\mathbf{q}_3^2 + \mu_E^2)(\mathbf{q}_3^2 + \mu_M^2)} \frac{\chi^2[\mathbf{q}_3 \cdot (\mathbf{q}_3 - \mathbf{k})] + (\mathbf{q}_3 \cdot \mathbf{k})(\mathbf{k} - \mathbf{q}_3)^2}{(\chi^2 + \mathbf{k}^2)[\chi^2 + (\mathbf{k} - \mathbf{q}_3)^2]} \\
&\times \frac{1}{\omega_{(3)}^2} \left( -\frac{\sin(L\omega_{(3)})}{\omega_{(3)}} + \frac{\sin(2L\omega_{(3)})}{2\omega_{(3)}} + \frac{\sin(3L\omega_{(3)})}{3\omega_{(3)}} - L \cos(2L\omega_{(3)}) \right), \tag{B7}
\end{aligned}$$

$$\begin{aligned}
\left(\frac{dN_g^{(4)}}{dx}\right)_1 &= \frac{2C_R}{\pi x} \int \frac{d^2\mathbf{k}}{\pi} \iiint \frac{d^2\mathbf{q}_1}{\pi} \frac{d^2\mathbf{q}_2}{\pi} \frac{d^2\mathbf{q}_3}{\pi} \frac{d^2\mathbf{q}_4}{\pi} \\
&\times \alpha_s(Q_k^2) \frac{1}{\lambda_{\text{dyn}}^4} \frac{\mu_E^2 - \mu_M^2}{(\mathbf{q}_1^2 + \mu_E^2)(\mathbf{q}_1^2 + \mu_M^2)} \frac{\mu_E^2 - \mu_M^2}{(\mathbf{q}_2^2 + \mu_E^2)(\mathbf{q}_2^2 + \mu_M^2)} \frac{\mu_E^2 - \mu_M^2}{(\mathbf{q}_3^2 + \mu_E^2)(\mathbf{q}_3^2 + \mu_M^2)} \frac{\mu_E^2 - \mu_M^2}{(\mathbf{q}_4^2 + \mu_E^2)(\mathbf{q}_4^2 + \mu_M^2)} \\
&\times \frac{\chi^2[\mathbf{q}_4 \cdot (\mathbf{q}_1 + \mathbf{q}_2 + \mathbf{q}_3 + \mathbf{q}_4 - \mathbf{k})] + (\mathbf{q}_4 \cdot \mathbf{k})(\mathbf{k} - \mathbf{q}_4)^2 + [\mathbf{k} \cdot (\mathbf{q}_1 + \mathbf{q}_2 + \mathbf{q}_3)][\mathbf{q}_4 \cdot (\mathbf{q}_4 - 2\mathbf{k})] + \mathbf{k}^2[\mathbf{q}_4 \cdot (\mathbf{q}_1 + \mathbf{q}_2 + \mathbf{q}_3)]}{(\chi^2 + \mathbf{k}^2)[\chi^2 + (\mathbf{k} - \mathbf{q}_4)^2][\chi^2 + (\mathbf{k} - \mathbf{q}_1 - \mathbf{q}_2 - \mathbf{q}_3 - \mathbf{q}_4)^2]} \\
&\times \left\{ -\frac{L \sin[L(\omega_{(4)} + \omega_{(34)} + \omega_{(234)})]}{\omega_{(234)}(\omega_{(34)} + \omega_{(234)})(\omega_{(4)} + \omega_{(34)} + \omega_{(234)})} \right. \\
&\quad - \frac{\cos[L(\omega_{(4)} + \omega_{(34)} + \omega_{(234)} + \omega_{(1234)})]}{\omega_{(1234)}(\omega_{(234)} + \omega_{(1234)})(\omega_{(34)} + \omega_{(234)} + \omega_{(1234)})(\omega_{(4)} + \omega_{(34)} + \omega_{(234)} + \omega_{(1234)})} \\
&\quad + \frac{F_{41}}{\omega_{(234)}^2(\omega_{(34)} + \omega_{(234)})^2(\omega_{(4)} + \omega_{(34)} + \omega_{(234)})^2\omega_{(1234)}} \cos[L(\omega_{(4)} + \omega_{(34)} + \omega_{(234)})] \\
&\quad + \frac{\omega_{(1234)} \cos[L(\omega_{(4)} + \omega_{(34)})]}{\omega_{(34)}(\omega_{(4)} + \omega_{(34)})\omega_{(234)}^2(\omega_{(234)} + \omega_{(1234)})} - \frac{\omega_{(1234)} \cos(L\omega_{(4)})}{\omega_{(4)}\omega_{(34)}(\omega_{(34)} + \omega_{(234)})^2(\omega_{(34)} + \omega_{(234)} + \omega_{(1234)})} \\
&\quad \left. + \frac{\omega_{(1234)}}{\omega_{(4)}(\omega_{(4)} + \omega_{(34)})(\omega_{(4)} + \omega_{(34)} + \omega_{(234)})^2(\omega_{(4)} + \omega_{(34)} + \omega_{(234)} + \omega_{(1234)})} \right\}, \tag{B8}
\end{aligned}$$

where  $F_{41} = (\omega_{(34)} + \omega_{(234)})(\omega_{(4)} + \omega_{(34)})(\omega_{(234)} - \omega_{(1234)}) + \omega_{(234)}^2 - 3\omega_{(234)}\omega_{(1234)}] - \omega_{(4)}\omega_{(234)}\omega_{(1234)}$ ,

$$\begin{aligned} \left(\frac{dN_g^{(4)}}{dx}\right)_2 &= \frac{C_R}{\pi x} \int \frac{d^2\mathbf{k}}{\pi} \iiint \frac{d^2\mathbf{q}_1}{\pi} \frac{d^2\mathbf{q}_2}{\pi} \frac{d^2\mathbf{q}_4}{\pi} \\ &\times \alpha_s(Q_k^2) \frac{1}{\lambda_{\text{dyn}}^4} \frac{\mu_E^2 - \mu_M^2}{(\mathbf{q}_1^2 + \mu_E^2)(\mathbf{q}_1^2 + \mu_M^2)} \frac{\mu_E^2 - \mu_M^2}{(\mathbf{q}_2^2 + \mu_E^2)(\mathbf{q}_2^2 + \mu_M^2)} \frac{\mu_E^2 - \mu_M^2}{(\mathbf{q}_4^2 + \mu_E^2)(\mathbf{q}_4^2 + \mu_M^2)} \\ &\times \frac{\chi^2[\mathbf{q}_4 \cdot (\mathbf{q}_1 + \mathbf{q}_2 + \mathbf{q}_4 - \mathbf{k})] + (\mathbf{q}_4 \cdot \mathbf{k})(\mathbf{k} - \mathbf{q}_4)^2 + [\mathbf{k} \cdot (\mathbf{q}_1 + \mathbf{q}_2)][\mathbf{q}_4 \cdot (\mathbf{q}_4 - 2\mathbf{k})] + \mathbf{k}^2[\mathbf{q}_4 \cdot (\mathbf{q}_1 + \mathbf{q}_2)]}{(\chi^2 + \mathbf{k}^2)[\chi^2 + (\mathbf{k} - \mathbf{q}_4)^2][\chi^2 + (\mathbf{k} - \mathbf{q}_1 - \mathbf{q}_2 - \mathbf{q}_4)^2]} \\ &\times \left\{ \frac{2[\omega_{(24)}(2\omega_{(4)}^2 + 3\omega_{(24)}\omega_{(4)} + \omega_{(24)}^2) - (2\omega_{(4)}^2 + 6\omega_{(24)}\omega_{(4)} + 3\omega_{(24)}^2)\omega_{(124)}] \cos[L(2\omega_{(4)} + \omega_{(24)})]}{\omega_{(24)}^2(\omega_{(4)} + \omega_{(24)})^2(2\omega_{(4)} + \omega_{(24)})^2\omega_{(124)}} \right. \\ &- \frac{2 \cos[L(2\omega_{(4)} + \omega_{(24)} + \omega_{(124)})]}{\omega_{(124)}(\omega_{(24)} + \omega_{(124)})(\omega_{(4)} + \omega_{(24)} + \omega_{(124)})(2\omega_{(4)} + \omega_{(24)} + \omega_{(124)})} + \frac{\omega_{(124)} \cos(2L\omega_{(4)})}{\omega_{(4)}^2\omega_{(24)}^2(\omega_{(24)} + \omega_{(124)})} \\ &- \frac{2L \sin[L(2\omega_{(4)} + \omega_{(24)})]}{\omega_{(24)}(\omega_{(4)} + \omega_{(24)})(2\omega_{(4)} + \omega_{(24)})} - \frac{2\omega_{(124)} \cos(L\omega_{(4)})}{\omega_{(4)}^2(\omega_{(4)} + \omega_{(24)})^2(\omega_{(4)} + \omega_{(24)} + \omega_{(124)})} \\ &\left. + \frac{\omega_{(124)}}{\omega_{(4)}^2(2\omega_{(4)} + \omega_{(24)})^2(2\omega_{(4)} + \omega_{(24)} + \omega_{(124)})} \right\}, \end{aligned} \quad (\text{B9})$$

$$\begin{aligned} \left(\frac{dN_g^{(4)}}{dx}\right)_3 &= \frac{C_R}{2\pi x} \int \frac{d^2\mathbf{k}}{\pi} \iiint \frac{d^2\mathbf{q}_1}{\pi} \frac{d^2\mathbf{q}_3}{\pi} \frac{d^2\mathbf{q}_4}{\pi} \\ &\times \alpha_s(Q_k^2) \frac{1}{\lambda_{\text{dyn}}^4} \frac{\mu_E^2 - \mu_M^2}{(\mathbf{q}_1^2 + \mu_E^2)(\mathbf{q}_1^2 + \mu_M^2)} \frac{\mu_E^2 - \mu_M^2}{(\mathbf{q}_3^2 + \mu_E^2)(\mathbf{q}_3^2 + \mu_M^2)} \frac{\mu_E^2 - \mu_M^2}{(\mathbf{q}_4^2 + \mu_E^2)(\mathbf{q}_4^2 + \mu_M^2)} \\ &\times \frac{\chi^2[\mathbf{q}_4 \cdot (\mathbf{q}_1 + \mathbf{q}_3 + \mathbf{q}_4 - \mathbf{k})] + (\mathbf{q}_4 \cdot \mathbf{k})(\mathbf{k} - \mathbf{q}_4)^2 + [\mathbf{k} \cdot (\mathbf{q}_1 + \mathbf{q}_3)][\mathbf{q}_4 \cdot (\mathbf{q}_4 - 2\mathbf{k})] + \mathbf{k}^2[\mathbf{q}_4 \cdot (\mathbf{q}_1 + \mathbf{q}_3)]}{(\chi^2 + \mathbf{k}^2)[\chi^2 + (\mathbf{k} - \mathbf{q}_4)^2][\chi^2 + (\mathbf{k} - \mathbf{q}_1 - \mathbf{q}_3 - \mathbf{q}_4)^2]} \\ &\times \left\{ -\frac{2L \sin[L(\omega_{(4)} + 2\omega_{(34)})]}{\omega_{(34)}^2(\omega_{(4)} + 2\omega_{(34)})} - \frac{4 \cos[L(\omega_{(4)} + 2\omega_{(34)} + \omega_{(134)})]}{\omega_{(134)}(\omega_{(34)} + \omega_{(134)})(2\omega_{(34)} + \omega_{(134)})(\omega_{(4)} + 2\omega_{(34)} + \omega_{(134)})} \right. \\ &+ \frac{[2\omega_{(34)}(\omega_{(4)} + 2\omega_{(34)}) - (3\omega_{(4)} + 8\omega_{(34)})\omega_{(134)}] \cos[L(\omega_{(4)} + 2\omega_{(34)})]}{\omega_{(34)}^3(\omega_{(4)} + 2\omega_{(34)})^2\omega_{(134)}} - \frac{\omega_{(134)} \cos(L\omega_{(4)})}{\omega_{(4)}\omega_{(34)}^3(2\omega_{(34)} + \omega_{(134)})} \\ &\left. + \frac{4\omega_{(134)}}{(\omega_{(4)} + \omega_{(34)})} \left( \frac{\cos[L(\omega_{(4)} + \omega_{(34)})]}{\omega_{(34)}^3(\omega_{(34)} + \omega_{(134)})} + \frac{1}{\omega_{(4)}(\omega_{(4)} + 2\omega_{(34)})^2(\omega_{(4)} + 2\omega_{(34)} + \omega_{(134)})} \right) \right\}, \end{aligned} \quad (\text{B10})$$

$$\begin{aligned} \left(\frac{dN_g^{(4)}}{dx}\right)_4 &= \frac{C_R}{3\pi x} \int \frac{d^2\mathbf{k}}{\pi} \iint \frac{d^2\mathbf{q}_1}{\pi} \frac{d^2\mathbf{q}_4}{\pi} \alpha_s(Q_k^2) \frac{1}{\lambda_{\text{dyn}}^4} \frac{\mu_E^2 - \mu_M^2}{(\mathbf{q}_1^2 + \mu_E^2)(\mathbf{q}_1^2 + \mu_M^2)} \frac{\mu_E^2 - \mu_M^2}{(\mathbf{q}_4^2 + \mu_E^2)(\mathbf{q}_4^2 + \mu_M^2)} \\ &\times \frac{\chi^2[\mathbf{q}_4 \cdot (\mathbf{q}_1 + \mathbf{q}_4 - \mathbf{k})] + (\mathbf{q}_4 \cdot \mathbf{k})(\mathbf{k} - \mathbf{q}_4)^2 + (\mathbf{k} \cdot \mathbf{q}_1)[\mathbf{q}_4 \cdot (\mathbf{q}_4 - 2\mathbf{k})] + \mathbf{k}^2(\mathbf{q}_4 \cdot \mathbf{q}_1)}{(\chi^2 + \mathbf{k}^2)[\chi^2 + (\mathbf{k} - \mathbf{q}_4)^2][\chi^2 + (\mathbf{k} - \mathbf{q}_1 - \mathbf{q}_4)^2]} \\ &\times \frac{1}{\omega_{(4)}^3} \left\{ -\frac{6\omega_{(4)}^3 \cos[L(3\omega_{(4)} + \omega_{(14)})]}{\omega_{(14)}(\omega_{(4)} + \omega_{(14)})(2\omega_{(4)} + \omega_{(14)})(3\omega_{(4)} + \omega_{(14)})} + \left( \frac{1}{\omega_{(14)}} - \frac{11}{6\omega_{(4)}} \right) \cos(3L\omega_{(4)}) \right. \\ &\left. - L \sin(3L\omega_{(4)}) - \frac{3\omega_{(14)} \cos(L\omega_{(4)})}{4\omega_{(4)}^2 + 2\omega_{(14)}\omega_{(4)}} + \frac{3\omega_{(14)} \cos(2L\omega_{(4)})}{(\omega_{(4)} + \omega_{(14)})\omega_{(4)}} + \frac{\omega_{(14)}}{9\omega_{(4)}^2 + 3\omega_{(14)}\omega_{(4)}} \right\}, \end{aligned} \quad (\text{B11})$$

$$\begin{aligned}
\left(\frac{dN_g^{(4)}}{dx}\right)_5 &= \frac{C_R}{\pi x} \int \frac{d^2\mathbf{k}}{\pi} \iiint \frac{d^2\mathbf{q}_2}{\pi} \frac{d^2\mathbf{q}_3}{\pi} \frac{d^2\mathbf{q}_4}{\pi} \\
&\times \alpha_s(Q_k^2) \frac{1}{\lambda_{\text{dyn}}^4} \frac{\mu_E^2 - \mu_M^2}{(\mathbf{q}_2^2 + \mu_E^2)(\mathbf{q}_2^2 + \mu_M^2)} \frac{\mu_E^2 - \mu_M^2}{(\mathbf{q}_3^2 + \mu_E^2)(\mathbf{q}_3^2 + \mu_M^2)} \frac{\mu_E^2 - \mu_M^2}{(\mathbf{q}_4^2 + \mu_E^2)(\mathbf{q}_4^2 + \mu_M^2)} \\
&\times \frac{\chi^2[\mathbf{q}_4 \cdot (\mathbf{q}_2 + \mathbf{q}_3 + \mathbf{q}_4 - \mathbf{k})] + (\mathbf{q}_4 \cdot \mathbf{k})(\mathbf{k} - \mathbf{q}_4)^2 + [\mathbf{k} \cdot (\mathbf{q}_2 + \mathbf{q}_3)][\mathbf{q}_4 \cdot (\mathbf{q}_4 - 2\mathbf{k})] + \mathbf{k}^2[\mathbf{q}_4 \cdot (\mathbf{q}_2 + \mathbf{q}_3)]}{(\chi^2 + \mathbf{k}^2)[\chi^2 + (\mathbf{k} - \mathbf{q}_4)^2][\chi^2 + (\mathbf{k} - \mathbf{q}_2 - \mathbf{q}_3 - \mathbf{q}_4)^2]} \\
&\times \frac{1}{\omega_{(234)}^2} \left( \frac{2\omega_{(234)}^3}{\omega_{(4)}(\omega_{(4)} + \omega_{(34)})(\omega_{(4)} + \omega_{(34)} + \omega_{(234)})^2(\omega_{(4)} + \omega_{(34)} + 2\omega_{(234)})} + \frac{\cos[L(\omega_{(4)} + \omega_{(34)})]}{\omega_{(34)}(\omega_{(4)} + \omega_{(34)})} \right. \\
&- \frac{2\omega_{(234)}^3 \cos(L\omega_{(4)})}{\omega_{(4)}\omega_{(34)}(\omega_{(34)} + \omega_{(234)})^2(\omega_{(34)} + 2\omega_{(234)})} - \frac{2L\omega_{(234)} \sin[L(\omega_{(4)} + \omega_{(34)} + \omega_{(234)})]}{(\omega_{(34)} + \omega_{(234)})(\omega_{(4)} + \omega_{(34)} + \omega_{(234)})} \\
&\left. - \frac{\cos[L(\omega_{(4)} + \omega_{(34)} + 2\omega_{(234)})]}{(\omega_{(34)} + 2\omega_{(234)})(\omega_{(4)} + \omega_{(34)} + 2\omega_{(234)})} - \frac{2\omega_{(234)}(\omega_{(4)} + 2\omega_{(34)} + 2\omega_{(234)}) \cos[L(\omega_{(4)} + \omega_{(34)} + \omega_{(234)})]}{(\omega_{(34)} + \omega_{(234)})^2(\omega_{(4)} + \omega_{(34)} + \omega_{(234)})^2} \right), \tag{B12}
\end{aligned}$$

$$\begin{aligned}
\left(\frac{dN_g^{(4)}}{dx}\right)_6 &= \frac{C_R}{\pi x} \int \frac{d^2\mathbf{k}}{\pi} \iint \frac{d^2\mathbf{q}_2}{\pi} \frac{d^2\mathbf{q}_4}{\pi} \alpha_s(Q_k^2) \frac{1}{\lambda_{\text{dyn}}^4} \frac{\mu_E^2 - \mu_M^2}{(\mathbf{q}_2^2 + \mu_E^2)(\mathbf{q}_2^2 + \mu_M^2)} \frac{\mu_E^2 - \mu_M^2}{(\mathbf{q}_4^2 + \mu_E^2)(\mathbf{q}_4^2 + \mu_M^2)} \\
&\times \frac{\chi^2[\mathbf{q}_4 \cdot (\mathbf{q}_2 + \mathbf{q}_4 - \mathbf{k})] + (\mathbf{q}_4 \cdot \mathbf{k})(\mathbf{k} - \mathbf{q}_4)^2 + (\mathbf{k} \cdot \mathbf{q}_2)[\mathbf{q}_4 \cdot (\mathbf{q}_4 - 2\mathbf{k})] + \mathbf{k}^2(\mathbf{q}_4 \cdot \mathbf{q}_2)}{(\chi^2 + \mathbf{k}^2)[\chi^2 + (\mathbf{k} - \mathbf{q}_4)^2][\chi^2 + (\mathbf{k} - \mathbf{q}_2 - \mathbf{q}_4)^2]} \\
&\times \left\{ \frac{\omega_{(24)}}{8\omega_{(4)}^2(\omega_{(4)} + \frac{\omega_{(24)}}{2})^2(\omega_{(4)} + \omega_{(24)})} - \frac{L \sin[L(2\omega_{(4)} + \omega_{(24)})] + \frac{(\frac{3\omega_{(4)}}{2} + \omega_{(24)}) \cos[2L(\omega_{(4)} + \frac{\omega_{(24)}}{2})]}{(\omega_{(4)} + \frac{\omega_{(24)}}{2})(\omega_{(4)} + \omega_{(24)})}}{(\omega_{(4)} + \frac{\omega_{(24)}}{2})(\omega_{(4)} + \omega_{(24)})\omega_{(24)}} \right. \\
&\left. + \frac{(\frac{\cos(2L\omega_{(4)})}{2\omega_{(4)}} - \frac{\omega_{(4)} \cos[2L(\omega_{(4)} + \omega_{(24)})]}{4(\frac{\omega_{(4)}}{2} + \omega_{(24)})(\omega_{(4)} + \omega_{(24)})})}{\omega_{(4)}\omega_{(24)}^2} - \frac{\omega_{(24)} \cos(L\omega_{(4)})}{\omega_{(4)}^2(\frac{\omega_{(4)}}{2} + \omega_{(24)})(\omega_{(4)} + \omega_{(24)})^2} \right\}, \tag{B13}
\end{aligned}$$

$$\begin{aligned}
\left(\frac{dN_g^{(4)}}{dx}\right)_7 &= \frac{C_R}{2\pi x} \int \frac{d^2\mathbf{k}}{\pi} \iint \frac{d^2\mathbf{q}_3}{\pi} \frac{d^2\mathbf{q}_4}{\pi} \alpha_s(Q_k^2) \frac{1}{\lambda_{\text{dyn}}^4} \frac{\mu_E^2 - \mu_M^2}{(\mathbf{q}_3^2 + \mu_E^2)(\mathbf{q}_3^2 + \mu_M^2)} \frac{\mu_E^2 - \mu_M^2}{(\mathbf{q}_4^2 + \mu_E^2)(\mathbf{q}_4^2 + \mu_M^2)} \\
&\times \frac{\chi^2[\mathbf{q}_4 \cdot (\mathbf{q}_3 + \mathbf{q}_4 - \mathbf{k})] + (\mathbf{q}_4 \cdot \mathbf{k})(\mathbf{k} - \mathbf{q}_4)^2 + (\mathbf{k} \cdot \mathbf{q}_3)[\mathbf{q}_4 \cdot (\mathbf{q}_4 - 2\mathbf{k})] + \mathbf{k}^2(\mathbf{q}_4 \cdot \mathbf{q}_3)}{(\chi^2 + \mathbf{k}^2)[\chi^2 + (\mathbf{k} - \mathbf{q}_4)^2][\chi^2 + (\mathbf{k} - \mathbf{q}_3 - \mathbf{q}_4)^2]} \\
&\times \left\{ \frac{1}{\omega_{(34)}^2(\frac{\omega_{(4)}}{2} + \omega_{(34)})} \left( \frac{2\omega_{(34)}^3}{\omega_{(4)}(\omega_{(4)} + \omega_{(34)})(\omega_{(4)} + 2\omega_{(34)})(\omega_{(4)} + 3\omega_{(34)})} - \frac{(\frac{\omega_{(4)}}{2} + 2\omega_{(34)}) \cos[L(\omega_{(4)} + 2\omega_{(34)})]}{(\omega_{(4)} + 2\omega_{(34)})\omega_{(34)}} \right. \right. \\
&\left. \left. - L \sin[L(\omega_{(4)} + 2\omega_{(34)})] - \frac{(\frac{\omega_{(4)}}{2} + \omega_{(34)}) \left( \frac{\cos(L\omega_{(4)})}{\omega_{(4)}} - \frac{6 \cos[L(\omega_{(4)} + \omega_{(34)})]}{\omega_{(4)} + \omega_{(34)}} + \frac{2 \cos[L(\omega_{(4)} + 3\omega_{(34)})]}{\omega_{(4)} + 3\omega_{(34)}} \right)}{3\omega_{(34)}} \right) \right\}, \tag{B14}
\end{aligned}$$

$$\begin{aligned}
\left(\frac{dN_g^{(4)}}{dx}\right)_8 &= \frac{C_R}{3\pi x} \int \frac{d^2\mathbf{k}}{\pi} \int \frac{d^2\mathbf{q}_4}{\pi} \alpha_s(Q_k^2) \frac{1}{\lambda_{\text{dyn}}^4} \frac{\mu_E^2 - \mu_M^2}{(\mathbf{q}_4^2 + \mu_E^2)(\mathbf{q}_4^2 + \mu_M^2)} \frac{\chi^2\mathbf{q}_4 \cdot (\mathbf{q}_4 - \mathbf{k}) + (\mathbf{q}_4 \cdot \mathbf{k})(\mathbf{k} - \mathbf{q}_4)^2}{(\chi^2 + \mathbf{k}^2)[\chi^2 + (\mathbf{k} - \mathbf{q}_4)^2]} \\
&\times \frac{1}{\omega_{(4)}^3} \left( \frac{1}{12\omega_{(4)}} - L \sin(3L\omega_{(4)}) - \frac{\cos(L\omega_{(4)})}{2\omega_{(4)}} + \frac{3 \cos(2L\omega_{(4)})}{2\omega_{(4)}} - \frac{5 \cos(3L\omega_{(4)})}{6\omega_{(4)}} - \frac{\cos(4L\omega_{(4)})}{4\omega_{(4)}} \right). \tag{B15}
\end{aligned}$$

**APPENDIX C:  $dN_g/dx$  RESULTS FOR  $L = 3$  AND  $L = 1$** 

In this section, we show  $dN_g/dx$  as a function of  $x$  for medium lengths  $L = 3\text{ fm}$  [Fig. (6)] and  $L = 1\text{ fm}$  [Fig. (7)].

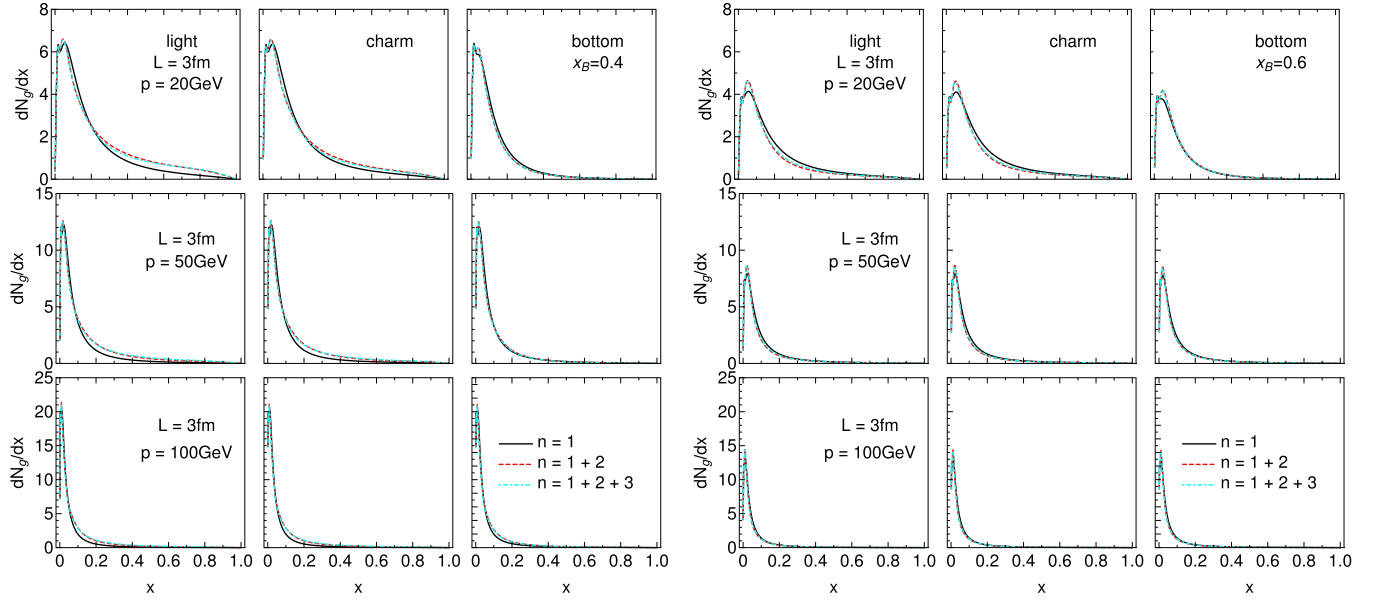


FIG. 6. Gluon radiation spectrum  $dN_g/dx$  as a function of  $x$ , for the medium length of  $L = 3\text{ fm}$  and various jet momenta. The panel on the left (right) side shows the result for  $\mu_M/\mu_E = 0.4$  (0.6). The figure caption is the same as for Fig. 1.

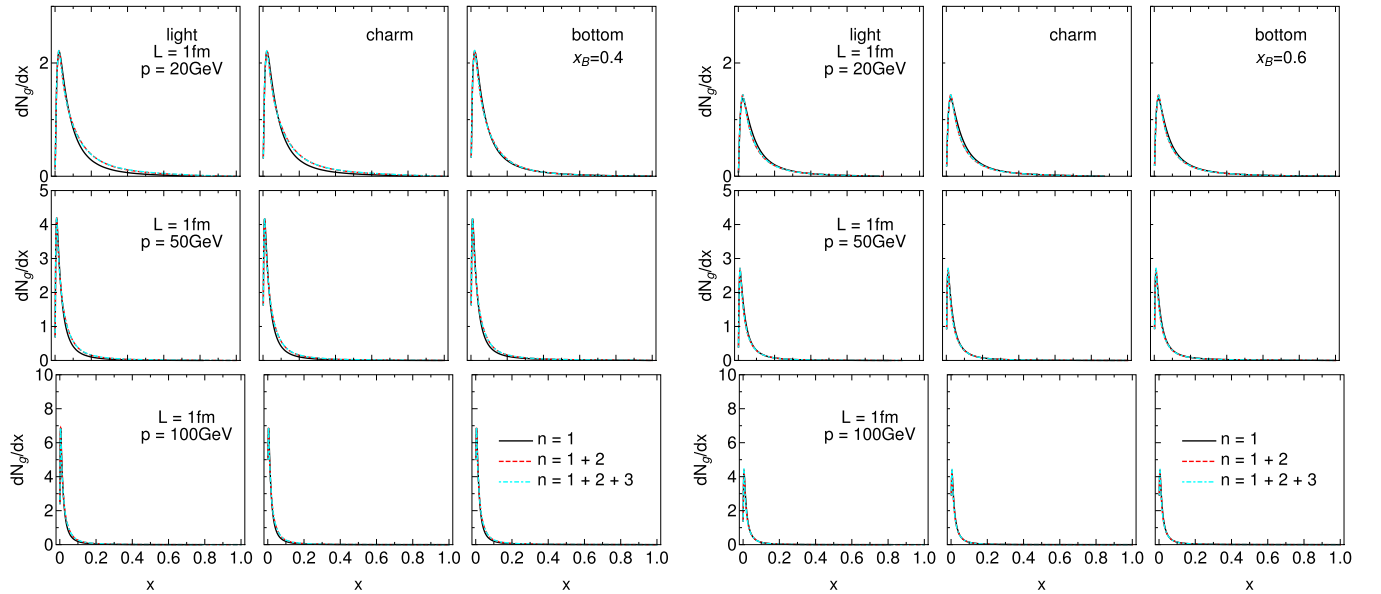


FIG. 7. Gluon radiation spectrum  $dN_g/dx$  as a function of  $x$ , for the medium length of  $L = 1\text{ fm}$  and various jet momenta. The panel on the left (right) side shows the result for  $\mu_M/\mu_E = 0.4$  (0.6). The figure caption is the same as for Fig. 1.

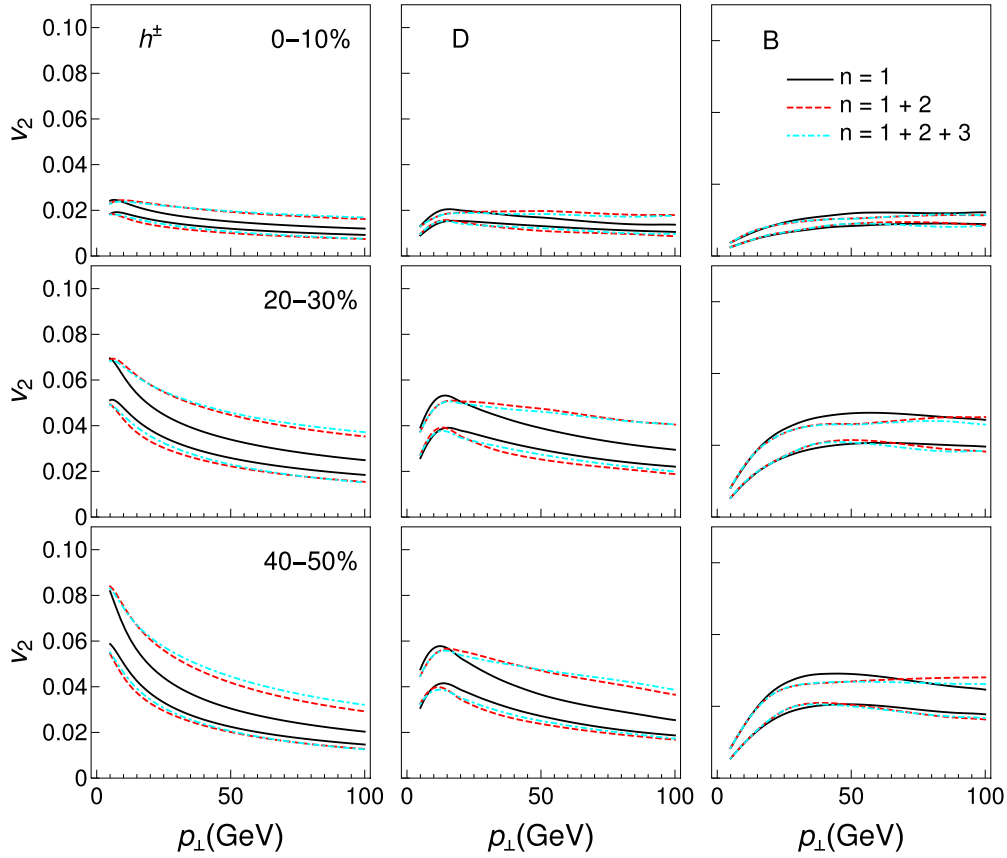


FIG. 8.  $v_2$  results obtained within DREENA-C – the effects of different orders in opacity. Different columns correspond to charged hadrons, D, and B mesons, while different rows show different centrality classes. Only radiative energy loss is taken into account. Solid black curves show the first order in opacity results, red dashed curves show the results up to the second order, while cyan dot-dashed curves up to the third order in opacity. The lower (upper) boundary of each band corresponds to the  $\mu_M/\mu_E = 0.6$  ( $\mu_M/\mu_E = 0.4$ ) case.





#### APPENDIX D: $v_2$ RESULTS UP TO THIRD ORDER IN OPACITY

We here show the results for  $v_2$  up to the third order in opacity (Fig. 8). Note that here the lower (upper) boundary of each band corresponds to the  $\mu_M/\mu_E = 0.6$  ( $\mu_M/\mu_E = 0.4$ ) case (opposite with respect to  $R_{AA}$  results). We observe the same behavior as for  $R_{AA}$ .

- 
- [1] E. V. Shuryak, *Nucl. Phys. A* **750**, 64 (2005); *Rev. Mod. Phys.* **89**, 035001 (2017).
- [2] M. Gyulassy and L. McLerran, *Nucl. Phys. A* **750**, 30 (2005).
- [3] B. Jacak and P. Steinberg, *Phys. Today* **63**(5), 39 (2010).
- [4] B. Müller, J. Schukraft, and B. Wyslouch, *Annu. Rev. Nucl. Part. Sci.* **62**, 361 (2012).
- [5] R. Baier, Y. Dokshitzer, A. Mueller, S. Peigne, and D. Schiff, *Nucl. Phys. B* **484**, 265 (1997).
- [6] B. Zakharov, *JETP Lett.* **63**, 952 (1996); **65**, 615 (1997).
- [7] N. Armesto, C. A. Salgado, and U. A. Wiedemann, *Phys. Rev. D* **69**, 114003 (2004).
- [8] M. Gyulassy, P. Levai, and I. Vitev, *Nucl. Phys. B* **594**, 371 (2001).
- [9] M. Djordjevic and M. Gyulassy, *Nucl. Phys. A* **733**, 265 (2004).
- [10] W. Xin-Nian and X. Guo, *Nucl. Phys. A* **696**, 788 (2001).
- [11] A. Majumder and M. Van Leeuwen, *Prog. Part. Nucl. Phys.* **66**, 41 (2011).
- [12] P. Arnold, G. D. Moore, and L. G. Yaffe, *J. High Energy Phys.* **11** (2001) 057; **12** (2001) 009.
- [13] M. Djordjevic, *Phys. Rev. C* **80**, 064909 (2009).
- [14] M. Djordjevic and U. Heinz, *Phys. Rev. Lett.* **101**, 022302 (2008).
- [15] C. Andres, L. Apolinário, and F. Dominguez, *J. High Energy Phys.* **07** (2020) 114.
- [16] C. Andres, F. Dominguez, and M. Gonzalez Martinez, *J. High Energy Phys.* **03** (2021) 102.
- [17] Y. Mehtar-Tani, *J. High Energy Phys.* **07** (2019) 057.
- [18] Y. Mehtar-Tani and K. Tywoniuk, *J. High Energy Phys.* **06** (2020) 187.



- [19] M. D. Sievert and I. Vitev, *Phys. Rev. D* **98**, 094010 (2018).
- [20] M. D. Sievert, I. Vitev, and B. Yoon, *Phys. Lett. B* **795**, 502 (2019).
- [21] S. Wicks, [arXiv:0804.4704](https://arxiv.org/abs/0804.4704).
- [22] D. Zigic, I. Salom, J. Auvinen, M. Djordjevic, and M. Djordjevic, *J. Phys. G* **46**, 085101 (2019).
- [23] J. I. Kapusta, *Finite-Temperature Field Theory* (Cambridge University Press, Cambridge, 1989).
- [24] M. Le Bellac, *Thermal Field Theory* (Cambridge University Press, Cambridge, 1996).
- [25] M. Djordjevic and M. Gyulassy, *Phys. Rev. C* **68**, 034914 (2003).
- [26] M. Djordjevic and M. Djordjevic, *Phys. Lett. B* **734**, 286 (2014).
- [27] M. Djordjevic, *Phys. Lett. B* **709**, 229 (2012).
- [28] Z. B. Kang, I. Vitev, and H. Xing, *Phys. Lett. B* **718**, 482 (2012); R. Sharma, I. Vitev, and B. W. Zhang, *Phys. Rev. C* **80**, 054902 (2009).
- [29] M. Gyulassy, P. Levai, and I. Vitev, *Phys. Lett. B* **538**, 282 (2002).
- [30] S. Wicks, W. Horowitz, M. Djordjevic, and M. Gyulassy, *Nucl. Phys. A* **784**, 426 (2007).
- [31] D. de Florian, R. Sassot, and M. Stratmann, *Phys. Rev. D* **75**, 114010 (2007).
- [32] M. Cacciari and P. Nason, *J. High Energy Phys.* **09** (2003) 006; E. Braaten, K.-M. Cheung, S. Fleming, and T. C. Yuan, *Phys. Rev. D* **51**, 4819 (1995).
- [33] V. G. Kartvelishvili, A. K. Likhoded, and V. A. Petrov, *Phys. Lett. B* **78**, 615 (1978).
- [34] A. Peshier, [arXiv:hep-ph/0601119](https://arxiv.org/abs/hep-ph/0601119).
- [35] Y. Maezawa, S. Aoki, S. Ejiri, T. Hatsuda, N. Ishii, K. Kanaya, N. Ukita, and T. Umeda (WHOT-QCD Collaboration), *Phys. Rev. D* **81**, 091501(R) (2010).
- [36] A. Nakamura, T. Saito, and S. Sakai, *Phys. Rev. D* **69**, 014506 (2004).
- [37] M. Djordjevic, *Phys. Rev. C* **74**, 064907 (2006).
- [38] S. Borsányi, Z. Fodor, S. D. Katz, A. Pásztor, K. K. Szabó, and C. Török, *J. High Energy Phys.* **04** (2015) 138.
- [39] M. Djordjevic, M. Gyulassy, and S. Wicks, *Phys. Rev. Lett.* **94**, 112301 (2005).

**Importance of higher harmonics and  $v_4$  puzzle in quark-gluon plasma tomography**Dusan Zigic , Jussi Auvinen , Igor Salom , and Magdalena Djordjevic <sup>\*</sup>*Institute of Physics Belgrade, 11080 Belgrade, Serbia*

Pasi Huovinen

*Institute of Physics Belgrade, University of Belgrade, 11080 Belgrade, Serbia**and Incubator of Scientific Excellence—Centre for Simulations of Superdense Fluids, University of Wrocław, 50-137 Wrocław, Poland*

(Received 8 June 2022; accepted 2 August 2022; published 20 October 2022)

Quark-gluon plasma (QGP) tomography aims to constrain the parameters characterizing the properties and evolution of QGP formed in heavy-ion collisions, by exploiting low- and high- $p_{\perp}$  theory and data. Higher-order harmonics  $v_n$  ( $n > 2$ ) are an important—but seldom explored—part of this approach. However, to take full advantage of them, several issues have to be addressed: (i) consistency of different methods for calculating  $v_n$ , (ii) importance of event-by-event fluctuations to high- $p_{\perp}$   $R_{AA}$  and  $v_2$  predictions, and (iii) sensitivity of higher harmonics to the initial state of fluid-dynamical evolution. We obtain that (i) several methods for calculating harmonics are compatible with each other, (ii) event-by-event calculations are important in mid-central collisions, and (iii) various initializations of the evolution of the medium lead to quantitatively and qualitatively different predictions, likely to be distinguished by future measurements. We also find that the present high- $p_{\perp}$   $v_4$  data cannot be reproduced using initial states for fluid-dynamical evolution given by state-of-the-art models. We call this discrepancy the high- $p_{\perp}$   $v_4$  puzzle at the Large Hadron Collider.

DOI: [10.1103/PhysRevC.106.044909](https://doi.org/10.1103/PhysRevC.106.044909)**I. INTRODUCTION**

During the past two decades, an impressive experimental and theoretical effort has been invested in generating and exploring a new form of matter called quark-gluon plasma (QGP) [1–4]. This form of matter consists of interacting and no longer confined quarks, antiquarks, and gluons [5,6] and is created at extremely high energy densities achieved in ultrarelativistic heavy ion collisions in experiments at the Relativistic Heavy Ion Collider (RHIC) and the Large Hadron Collider (LHC). An unprecedented amount of data for different collision systems (large and small), collision energies, types of particles, momentum regions, centralities, etc., are generated in these experiments, and one of the major current goals is to optimally use these data to investigate the properties of this exciting form of matter.

As one of the latest experimental achievements, the high momentum (high- $p_{\perp}$ ) higher harmonics have recently become available at RHIC and the LHC. For example, for charged hadrons, the data are available up to the seventh harmonic (for ATLAS [7]) and cover the  $p_{\perp}$  region up to 100 GeV

(for CMS [8]). For heavy flavor, the coverage is not that extensive (for both harmonics and momentum region); still, the upcoming experimental data at high-luminosity LHC Run 3 should provide these data for both light and heavy flavor with much higher precision. In the upcoming RHIC (sPHENIX and STAR) experiments, similar quality data is expected, with  $p_{\perp}$  coverage up to 20 GeV. Even if the  $p_{\perp}$  range accessible at RHIC is narrower than at the LHC, it is particularly useful for QGP tomography due to the pronounced difference between light and heavy flavor in that region. While these data (will) represent the state of the art in the experimental sector, theoretically the higher harmonics at high  $p_{\perp}$  have not been well explored.

To use these data for QGP tomography, i.e., for exploring the bulk QGP properties through high- $p_{\perp}$  theory and data, one should first identify and address potential limitations, in particular related to coverage and design of different experiments. For example, four different methods are commonly used in the literature to evaluate  $v_n$ : two-particle cumulant  $v_n\{2\}$ , four-particle cumulant  $v_n\{4\}$ , event plane  $v_n\{\text{EP}\}$ , and scalar product  $v_n\{\text{SP}\}$  methods (see Sec. II C for more details). Do these methods provide consistent results, especially when different experimental collaborations even define  $v_n\{\text{SP}\}$  in different ways?

Furthermore, in experimental analysis, the scalar product method correlates the particle of interest at midrapidity with the bulk medium constituents at higher rapidity regions to avoid nonflow effects on measured  $v_n$  [7,8]. From the theoretical perspective, this means the use of the experimental definition for  $v_n\{\text{SP}\}$  necessitates 3+1-dimensional

<sup>\*</sup> magda@ipb.ac.rs

Published by the American Physical Society under the terms of the [Creative Commons Attribution 4.0 International](https://creativecommons.org/licenses/by/4.0/) license. Further distribution of this work must maintain attribution to the author(s) and the published article's title, journal citation, and DOI. Funded by SCOAP<sup>3</sup>.

(3+1D) hydrodynamic modeling for event-by-event simulations. However, 3+1D simulations are computationally several orders of magnitude more demanding than 2+1D simulations, and consequently they are timewise impractical for high-precision QGP tomography. Thus, the question arises whether it would be plausible to compare  $v_n\{\text{SP}\}$  obtained in boost-invariant 2+1D simulations to experimental data in a model where the high- and low- $p_\perp$  particles have separate sources (fragmenting jets and a thermal fireball, respectively), and are thus uncorrelated.

Next, for the second harmonic,  $v_2$ , event-by-event fluctuations are expected to either have a significant effect on  $v_2$  values [9] or to be small enough to be considered negligible [10,11]. However, these studies were done in limited and different centrality regions. It is expected [12] that the effects of event-by-event fluctuations increase with decreasing centrality. Thus, it is important to systematically investigate and quantify these effects for the high- $p_\perp$  region at different centralities.

Therefore, the study presented in this paper has the following main goals:

- (i) Explore to what extent the different methods for calculating higher harmonics are compatible with each other.
- (ii) Explore the importance of event-by-event fluctuations and correlations to high- $p_\perp$   $v_2$  and  $R_{AA}$ .
- (iii) Explore the qualitative and quantitative effects of different medium evolution scenarios on high- $p_\perp$  higher harmonics, and how well the existing high- $p_\perp$  data can be reproduced without further tuning of parameters.

Overall, this study explores whether and how high- $p_\perp$  higher harmonics, with an adequate theoretical framework, can provide further constraints to the bulk QGP properties.

## II. METHODS

### A. Outline of DREENA-A framework

To use the high- $p_\perp$  particles to explore the bulk properties, we developed a fully optimized modular framework DREENA-A [13], where ‘‘DREENA’’ stands for dynamical radiative and elastic energy loss approach, while ‘‘A’’ stands for adaptive. We further optimized the framework for this study to efficiently incorporate any arbitrary event-by-event fluctuating temperature profile within the dynamical energy loss formalism. Due to the very large amount of temperature profile data processed in event-by-event calculations, we optimized file handling and formats. Also, we reorganized the parallelization of computation, and ensured that spatio-temporal resolution and calculation precision are optimal and adjusted to the event-by-event type of profiles.

The framework does not have fitting parameters within the energy loss model (i.e., all parameters used in the model correspond to standard literature values), which allows one to systematically compare the data and predictions obtained by the same formalism and parameter set. Therefore different temperature profiles (which are the only input in the

DREENA-A framework) resulting from different initial states and QGP properties can be distinguished by the high- $p_\perp$  observables they lead to, and the bulk QGP properties can be further constrained by studying low- and high- $p_\perp$  theory and data jointly.

The dynamical energy loss formalism [14–16] has several important features, all of which are needed for accurate predictions [17]: (i) QCD medium of *finite* size and temperature consisting of dynamical (i.e., moving) partons. (ii) Calculations are based on a generalized hard-thermal-loop approach [18], with naturally regulated infrared divergences [14,16,19]. (iii) Both radiative [14,15] and collisional [16] energy losses are calculated in the same theoretical framework and apply to both light and heavy flavors. (iv) The framework is generalized toward running coupling [20] and finite magnetic mass [21]. We have also investigated the validity of the widely used soft-gluon approximation [22], but found it a very good approximation which does not need to be relaxed.

The initial quark spectrum, for light and heavy partons, is computed at next to leading order [23]. We use de Florian–Sassot–Stratmann (DSS) [24] fragmentation functions to generate charged hadrons, and Braaten–Cheung–Fleming–Yuan (BCFY) [25] and Kartvelishvili–Likhoded–Petrov (KLP) [26] fragmentation functions for  $D$  and  $B$  mesons, respectively. To generate high- $p_\perp$  predictions, we use the same parameter set as in DREENA-A [13]. Specifically, we assume effective light quark flavors  $n_f = 3$  and  $\Lambda_{\text{QCD}} = 0.2$  GeV. The temperature-dependent Debye mass  $\mu_E$  is obtained by applying the procedure from [27] and leads to results compatible with lattice QCD [28]. For the gluon mass we assume  $m_g = \mu_E/\sqrt{2}$  [19], and for light quark mass  $M = \mu_E/\sqrt{6}$ . The charm mass is  $M = 1.2$  GeV and the bottom mass is  $M = 4.75$  GeV. For magnetic to electric mass ratio, we use  $\mu_M/\mu_E = 0.5$  [29,30].

### B. Modeling the bulk evolution

We investigate three different event-by-event initializations for the bulk evolution. The first is Monte Carlo Glauber (MC-Glauber) initialization at initial time  $\tau_0 = 1.0$  fm without initial transverse flow. We assign the binary collision points at halfway between the two colliding nucleons and convert these points to a continuous binary collision density using 2D Gaussian distributions

$$n_{BC}(x, y) = \frac{1}{2\pi\sigma_{BC}^2} \sum_{i=1}^{N_{BC}} \exp\left(-\frac{(x-x_i)^2 + (y-y_i)^2}{2\sigma_{BC}^2}\right) \quad (1)$$

with a width parameter  $\sigma_{BC} = 0.35$  fm. The binary collision density is then converted to energy density with the formula

$$\epsilon(x, y) = C_0(n_{BC} + c_1 n_{BC}^2 + c_2 n_{BC}^3), \quad (2)$$

and further extended in the longitudinal direction using the LHC parametrization from Ref. [31]. The evolution of the fluid is calculated using a 3+1D viscous fluid code [31], with a constant shear viscosity over entropy density ratio

$\eta/s = 0.03$  and no bulk viscosity. The equation of state (EoS) parametrization is  $s95p$ -PCE-v1 [32]. The model parameters were tuned to ALICE charged particle multiplicity [33] and  $v_n(p_\perp)$  data [34] for 10–20%, 20–30%, and 30–40% centrality classes in Pb + Pb collisions at  $\sqrt{s_{NN}} = 5.02$  TeV.

The second model is the TRENTo initialization [35] with a free streaming stage until  $\tau_0 = 1.16$  fm, further evolved using the VISH2+1 code [36] as described in [37,38]. The parameters in this calculation are based on a Bayesian analysis of the data at Pb + Pb collisions at  $\sqrt{s_{NN}} = 2.76$  and 5.02 TeV [38]. In particular the calculation includes temperature dependent shear and bulk viscosity coefficients with the minimum value of  $\eta/s = 0.081$  and maximum of  $\zeta/s = 0.052$ . The EoS [37] is based on the lattice results by the HotQCD Collaboration [39].

The third investigated initialization model is IP-Glasma [40,41]. The calculated event-by-event fluctuating initial states [42] are further evolved [43] using the MUSIC code [44–46] constrained to boost-invariant expansion. In these calculations, the switch from Yang-Mills to fluid-dynamical evolution takes place at  $\tau_{\text{switch}} = 0.4$  fm, shear viscosity over entropy density ratio is constant  $\eta/s = 0.12$ , and the temperature-dependent bulk viscosity coefficient over entropy density ratio has the maximum value  $\zeta/s = 0.13$ . The equation of state is based on the HotQCD lattice results [39] as presented in Ref. [47].

## C. Flow analysis

### 1. Scalar product and event plane methods

We start by defining the low- $p_\perp$  normalized flow vector for the  $n$ th harmonic based on  $M$  particles as

$$Q_n = \frac{1}{M} \sum_{j=1}^M e^{in\phi_j} \equiv |v_n| e^{in\Psi_n}, \quad (3)$$

where  $\Psi_n$  is the event plane angle:  $\Psi_n = \arctan(\frac{\text{Im} Q_n}{\text{Re} Q_n})/n$ .

Similarly to low  $p_\perp$ , we can define the flow vector for a high  $p_\perp$  bin as  $[R_{AA}(p_\perp)] = \frac{1}{2\pi} \int_0^{2\pi} R_{AA}(p_\perp, \phi) d\phi$

$$q_n^{\text{hard}} = \frac{\frac{1}{2\pi} \int_0^{2\pi} e^{in\phi} R_{AA}(p_\perp, \phi) d\phi}{R_{AA}(p_\perp)}, \quad (4)$$

and single-event high- $p_\perp$  flow coefficients  $v_n^{\text{hard}}$  as [9]

$$v_n^{\text{hard}} = \frac{\frac{1}{2\pi} \int_0^{2\pi} \cos[n\{\phi - \Psi_n^{\text{hard}}(p_\perp)\}] R_{AA}(p_\perp, \phi) d\phi}{R_{AA}(p_\perp)}, \quad (5)$$

where the event plane angle  $\Psi_n^{\text{hard}}(p_\perp)$  is defined as

$$\Psi_n^{\text{hard}}(p_\perp) = \frac{1}{n} \arctan \left( \frac{\int_0^{2\pi} \sin(n\phi) R_{AA}(p_\perp, \phi) d\phi}{\int_0^{2\pi} \cos(n\phi) R_{AA}(p_\perp, \phi) d\phi} \right). \quad (6)$$

The high- $p_\perp$   $v_n$  is then calculated by correlating  $q_n$  with  $Q_n$  [9,10,48]:

$$\begin{aligned} v_n^{\text{hard}}\{\text{SP}\} &= \frac{\langle \text{Re} [q_n^{\text{hard}}(Q_n^*)] \rangle_{\text{ev}}}{\sqrt{\langle Q_n(Q_n^*) \rangle_{\text{ev}}}} \\ &= \frac{\langle |v_n^{\text{hard}}| |v_n| \cos[n\{\Psi_n^{\text{hard}}(p_\perp) - \Psi_n\}] \rangle_{\text{ev}}}{\sqrt{\langle |v_n|^2 \rangle_{\text{ev}}}}. \end{aligned} \quad (7)$$

We may also simply calculate the high- $p_\perp$  anisotropy with respect to the event plane  $\Psi_n$ , which we shall denote as the “event plane”  $v_n$  [10]:

$$\begin{aligned} v_n\{\text{EP}\} &= \langle \langle \cos[n(\phi^{\text{hard}} - \Psi_n)] \rangle \rangle_{\text{ev}} \\ &= \langle v_n^{\text{hard}} \cos[n(\Psi_n^{\text{hard}} - \Psi_n)] \rangle_{\text{ev}}. \end{aligned} \quad (8)$$

For our theoretical  $v_n\{\text{SP}\}$ , the reference flow vector  $Q_n$  is calculated using only midrapidity particles. In order to reduce nonflow effects, it is common in experiments to introduce a rapidity gap between the particles of interest and the reference flow particles. ATLAS defines the scalar product  $v_n$  as [7]

$$v_n\{\text{SP}_{\text{ATLAS}}\} = \frac{\text{Re} \langle \langle e^{in\phi} (Q_n^{-+})^* \rangle \rangle_{\text{ev}}}{\sqrt{\langle Q_n^-(Q_n^+) \rangle_{\text{ev}}}}, \quad (9)$$

where  $Q_n^- = \frac{1}{M^-} \sum_{j=1}^{M^-} e^{in\phi_j}$  refers to particles in the rapidity interval  $-4.9 < \eta < -3.2$  and  $Q_n^+$  similarly to particles in the interval  $3.2 < \eta < 4.9$ , while  $e^{in\phi}$  is associated with particles in midrapidity  $|\eta| < 2.5$ .  $Q_n^{-+}$  indicates that particle of interest with  $\eta < 0$  are coupled to  $Q_n^+$  and particles with  $\eta > 0$  to  $Q_n^-$  to maximize the rapidity gap.<sup>1</sup>

The CMS definition for the scalar product is [8]

$$v_n\{\text{SP}_{\text{CMS}}\} = \frac{\text{Re} \langle Q_n Q_{nA}^* \rangle_{\text{ev}}}{\sqrt{\frac{\langle Q_{nA} Q_{nB}^* \rangle_{\text{ev}} \langle Q_{nA} Q_{nC}^* \rangle_{\text{ev}}}{\langle Q_{nB} Q_{nC}^* \rangle_{\text{ev}}}}}, \quad (10)$$

where the flow vector  $Q_n = \sum_{j=1}^M e^{in\phi_j}$  consists of particles of interest in midrapidity  $|\eta| < 1.0$ , vectors  $Q_{nA}, Q_{nB} = \sum_{j=1}^{M_{A,B}} E_T e^{in\phi_j}$  are measured from the HF calorimeters at  $2.9 < |\eta| < 5.2$ , one at the negative and the other at the positive rapidity, and the third reference vector  $Q_{nC} = \sum_{j=1}^{M_C} p_\perp e^{in\phi_j}$  is obtained from tracks with  $|\eta| < 0.75$ . If the particle of interest comes from the positive- $\eta$  side of the tracker, then  $Q_{nA}$  is calculated using the negative- $\eta$  side of HF, and vice versa.

### 2. Cumulant method

For two- and four-particle cumulant analysis, we use the unnormalized flow vector:

$$\tilde{Q}_n = \sum_{j=1}^M e^{in\phi_j}. \quad (11)$$

The low- $p_\perp$  integrated reference flow is calculated using Eqs. (8)–(19) from Ref. [49]: The two-particle cumulant  $v_n$  is

<sup>1</sup>Since our high- $p_\perp$  particles are produced at  $\eta = 0$ , the choice of  $Q_n^+$  or  $Q_n^-$  for the correlation is arbitrary.

defined as

$$v_n\{2\} = \sqrt{c_n\{2\}}, \quad (12)$$

where the second-order cumulant  $c_n\{2\}$  equals the event-averaged two-particle correlation  $\langle\langle 2 \rangle\rangle_{\text{ev}}$ . The four-particle cumulant  $v_n$  is

$$v_n\{4\} = \sqrt[4]{-c_n\{4\}}, \quad (13)$$

where  $c_n\{4\}$  is the fourth-order cumulant  $\langle\langle 4 \rangle\rangle_{\text{ev}} - 2\langle\langle 2 \rangle\rangle_{\text{ev}}^2$ .

For a single event, the two-particle correlation is

$$\langle 2 \rangle = \frac{|\tilde{Q}_n|^2 - M}{W_2} \quad (14)$$

with a combinatorial weight factor  $W_2 = M(M-1)$ , and the single-event four-particle correlation is

$$\begin{aligned} \langle 4 \rangle &= \frac{|\tilde{Q}_n|^4 + |\tilde{Q}_{2n}|^2 - 2\text{Re}[\tilde{Q}_{2n}\tilde{Q}_n^*\tilde{Q}_n^*]}{W_4} \\ &\quad - 2\frac{2(M-2)|\tilde{Q}_n|^2 - M(M-3)}{W_4} \end{aligned} \quad (15)$$

with  $W_4 = M(M-1)(M-2)(M-3)$ .

Using the weight factors defined above, the weighted average of a  $k$ -particle correlation over multiple events is then

$$\langle\langle k \rangle\rangle_{\text{ev}} = \frac{\sum_{i=1}^{N_{\text{events}}} W_{k,i} \langle k \rangle_i}{\sum_{i=1}^{N_{\text{events}}} W_{k,i}}. \quad (16)$$

Once the reference flow has been determined, the  $p_T$ -differential flow can be calculated using Eqs. (20)–(35) of [49]. Here we denote the flow vector in a  $p_\perp$  bin with  $m_q$  particles as

$$q_n = \sum_{j=1}^{m_q} e^{in\phi_j}. \quad (17)$$

For high- $p_\perp$  particles,  $q_n$  is calculated from the distribution

$$q_n = \int_0^{2\pi} e^{in\phi} \frac{dN}{dp_\perp d\phi} d\phi \quad (18)$$

with the associated multiplicity

$$m_q = \int_0^{2\pi} \frac{dN}{dp_\perp d\phi} d\phi. \quad (19)$$

For high- $p_\perp$  differential flow, none of the particles in a  $p_\perp$  bin are included in the calculation of the reference flow, so the weight factors are  $W'_2 = m_q M$  and  $W'_4 = m_q M(M-1)(M-2)$ , and the two-particle correlation is simply

$$\langle 2' \rangle = \frac{q_n \tilde{Q}_n^*}{W'_2}, \quad (20)$$

while the four-particle correlation is

$$\langle 4' \rangle = \frac{q_n \tilde{Q}_n \tilde{Q}_n^* \tilde{Q}_n^* - q_n \tilde{Q}_n \tilde{Q}_{2n}^* - 2M q_n \tilde{Q}_n^* + 2q_n \tilde{Q}_n^*}{W'_4}. \quad (21)$$

With the knowledge of the correlations, we can calculate the differential cumulants

$$\begin{aligned} d_n\{2\} &= \langle\langle 2' \rangle\rangle_{\text{ev}}, \\ d_n\{4\} &= \langle\langle 4' \rangle\rangle_{\text{ev}} - 2\langle\langle 2' \rangle\rangle_{\text{ev}} \langle\langle 2 \rangle\rangle_{\text{ev}} \end{aligned} \quad (22)$$

and the differential flows

$$\begin{aligned} v'_n\{2\} &= \frac{d_n\{2\}}{\sqrt{c_n\{2\}}}, \\ v'_n\{4\} &= -\frac{d_n\{4\}}{(-c_n\{4\})^{3/4}}. \end{aligned} \quad (23)$$

### III. RESULTS AND DISCUSSION

#### A. Compatibility of analysis methods

In Fig. 1, we compare  $v_n(p_\perp)$  for high- $p_\perp$  particles obtained using six different methods: two-particle cumulant  $v_n\{2\}$  given by Eq. (12), four-particle cumulant  $v_n\{4\}$  given by Eq. (13), event plane  $v_n\{\text{EP}\}$  defined by Eq. (8), midrapidity scalar product  $v_n\{\text{SP}\}$  calculated using Eq. (7), scalar product  $v_n\{\text{SP}_{\text{ATLAS}}\}$  as defined by the ATLAS Collaboration [Eq. (9)], and scalar product  $v_n\{\text{SP}_{\text{CMS}}\}$  as defined by the CMS Collaboration [Eq. (10)]. High- $p_\perp$   $R_{AA}$  and  $v_n$  predictions were obtained using generalized DREENA-A framework with the temperature profiles calculated using the combination of 3+1D viscous fluid code and MC-Glauber initial conditions (i.e., the first bulk model described in the Sec. II B).

As illustrated in Fig. 1, different scalar product methods for evaluating the  $v_n$  coefficients, and the two-particle cumulant method, lead to the same results with  $\approx 5\%$  level accuracy. In agreement with Refs. [10,11,50], the event plane results are also comparable to the scalar product results, deviating only  $\approx 10\%$ , i.e., less than the current experimental uncertainty. The only method with significantly different results is the four-particle cumulant method  $v_n\{4\}$ , which is expected to differ from  $v_n\{2\}$  in the presence of event-by-event fluctuations [12,51]. The equivalence of different approaches simplifies comparison between theoretical predictions and experimental results, since a theoretical prediction calculated using any method (with the exception of the four-particle cumulant method) can be directly compared to experimental data analyzed using any method. We have also checked that, in the scalar product method, the rapidity of particles used to calculate the reference flow vector has a negligible impact on high- $p_\perp$  particle  $v_n$  in our framework and setup, allowing us to make meaningful  $v_n\{\text{SP}\}$  data comparisons using the boost-invariant hydro simulations. However, it must be remembered that the scalar product method with large rapidity gap can be affected by the event plane decorrelation at different rapidities [52,53]. In our approach the event plane is the same



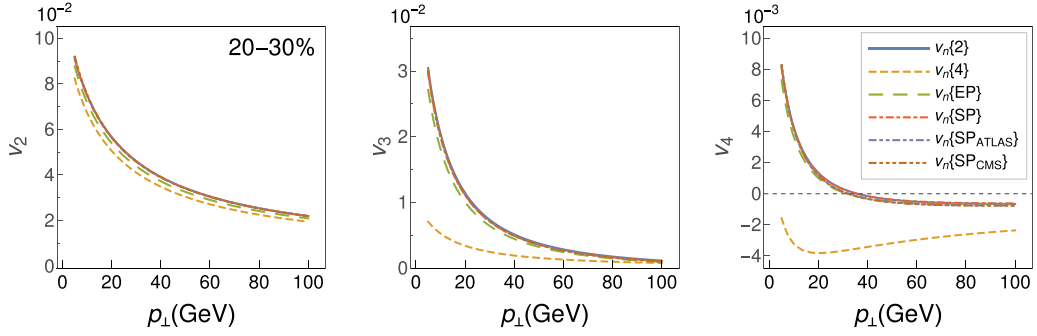


FIG. 1. Charged hadron  $v_2$  (left),  $v_3$  (middle), and  $v_4$  (right) in Pb + Pb collisions at  $\sqrt{s_{NN}} = 5.02$  TeV for 20–30% centrality class, computed using different analysis methods: two-particle cumulant, four-particle cumulant, event plane, midrapidity scalar product, ATLAS-defined scalar product, and CMS-defined scalar product, each described in the Sec. II C. Energy loss calculation was performed on MC-Glauber + 3d-hydro temperature profiles, with  $\mu_M/\mu_E = 0.5$ .

independent of rapidity, and thus the effect of decorrelation is not included. How the event plane depends on rapidity depends on the model used to create the longitudinal structure of the initial state, and, since there are very few theoretical constraints for it, we leave these studies for a later work.

### B. Event-by-event fluctuations

To investigate the influence of event-by-event fluctuations on high- $p_\perp$  observables, MC-Glauber initial conditions for all events within a single centrality class were averaged we kept reaction planes aligned, and averaged binary collision densities before converting to energy density [Eq. (2)], and then evolved using the 3+1D viscous fluid code (in a single run, instead of one run for each event). The obtained smooth

temperature profile was used to calculate high- $p_\perp$  predictions, and  $R_{AA}$  as well as  $v_2\{2\}$  and  $v_2\{4\}$  results were compared to those obtained using full event-by-event calculations (evolved separately for each event); see Fig. 2.

We see that event-by-event fluctuations increase both  $R_{AA}$  and  $v_2$ . While the effect on the  $R_{AA}$  values is rather small ( $\approx 7\%$ ) and does not have clear centrality dependence, the effect on  $v_2\{2\}$  is more pronounced and increases with decreasing centrality. Quantitatively, we obtain that the average difference between event-by-event  $v_2\{2\}$  and  $v_2\{2\}$  calculated using the smooth temperature profile goes from 14% for the 40–50% centrality class to 32% in the 10–20% centrality class. The observed centrality dependence can be explained by the fact that, with the increase in centrality, the influence of geometry on  $v_2\{2\}$  becomes larger, while at low

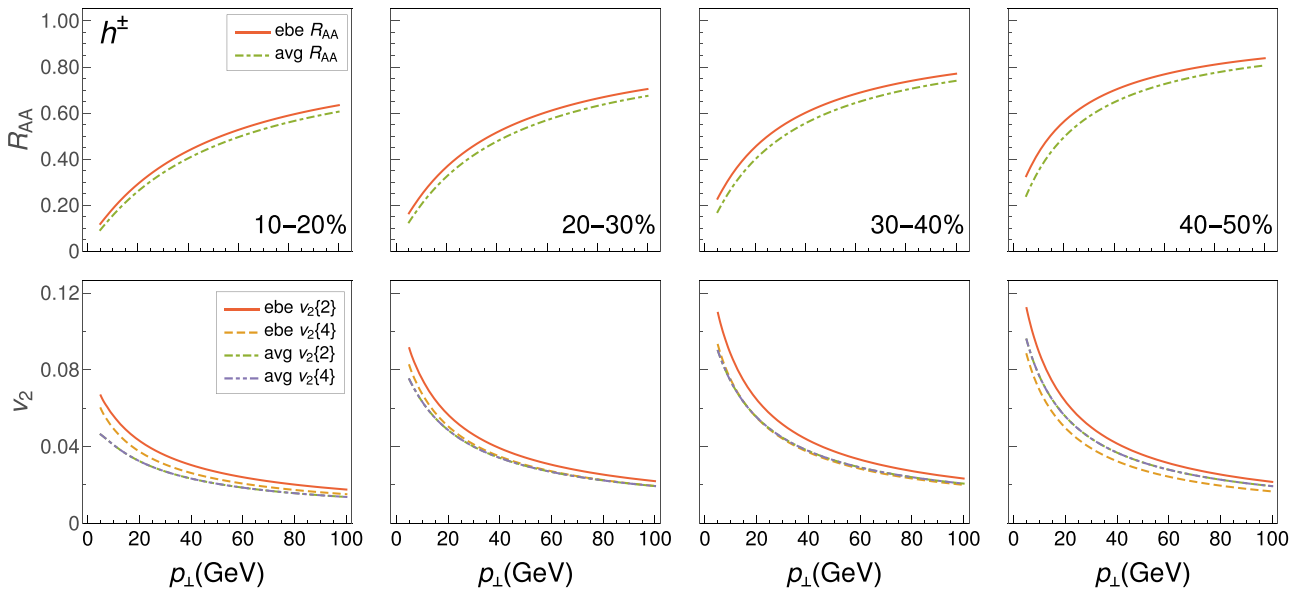


FIG. 2. *Upper panels:* charged hadron  $R_{AA}$  calculated using event-by-event (ebe) fluctuating temperature profiles compared to  $R_{AA}$  calculated using a smooth temperature profile (avg). *Lower panels:* charged hadron  $v_n\{2\}$  and  $v_n\{4\}$  calculated using event-by-event (ebe) fluctuating temperature profiles compared to  $v_n\{2\}$  and  $v_n\{4\}$  calculated using a smooth temperature profile (avg). Calculation was done for Pb + Pb collisions at  $\sqrt{s_{NN}} = 5.02$  TeV,  $\mu_M/\mu_E = 0.5$ , using MC-Glauber + 3d-hydro bulk evolution. Each column represents different centrality class (from left to right: 10–20%, 20–30%, 30–40%, and 40–50%).

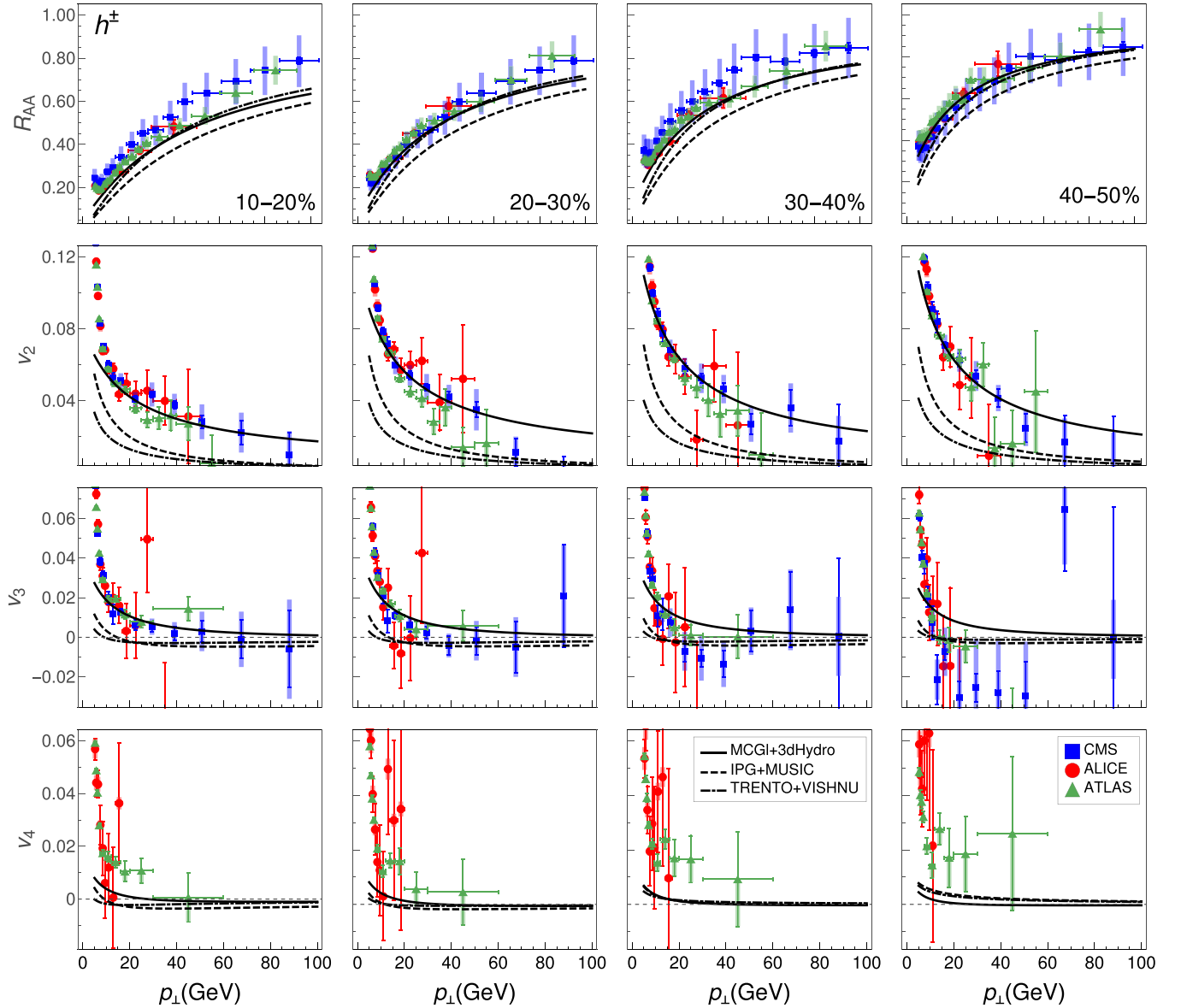


FIG. 3. Charged hadron  $R_{AA}$  (first row)  $v_2$  (second row),  $v_3$  (third row), and  $v_4$  (fourth row) in Pb + Pb collisions at  $\sqrt{s_{NN}} = 5.02$  TeV for different initializations of the QGP evolution (indicated in the legend). Theoretical predictions, obtained using SP method, are compared to CMS [8,54] (blue squares), ALICE [55,56] (red circles), and ATLAS [7,57] (green triangles) data. Columns 1–4 correspond to, respectively, 10–20%, 20–30%, 30–40%, and 40–50% centrality classes.  $\mu_M/\mu_E = 0.5$ .

centralities, event-by-event fluctuations have the dominant impact on  $v_2\{2\}$ . We also observe a  $p_\perp$  dependence of these differences (generally decreasing with increasing  $p_\perp$ ) and no notable difference between  $v_2\{2\}$  and  $v_2\{4\}$  when calculated on the smooth temperature profile, where initial state eccentricity fluctuations are absent.

### C. Effects of initial state

To demonstrate the applicability of high- $p_\perp$  theoretical predictions as a QGP tomography tool, we generated three different sets of temperature profiles using three different initial conditions and hydrodynamics codes. Generalized DREENA-A [13] was then used to calculate high- $p_\perp$  predictions, which

are compared to experimental data and, for charged hadrons, presented in Fig. 3, and for  $D$  and  $B$  mesons in Fig. 4. As can be seen, different initializations of fluid-dynamical evolution lead to different high- $p_\perp$  predictions for both  $R_{AA}$  and  $v_2$ ,  $v_3$ , and  $v_4$ , even though they all provide good agreement with low- $p_\perp$  data. Specific differences are visible already on the level of  $R_{AA}$  values, where the IP-Glasma model results in discernibly stronger suppression. The differences in predictions become even higher when we consider the  $v_2$  observable, with TRENTO leading to lower  $v_2$  than IP-Glasma, while MC-Glauber predictions are far above the two. A similar magnitude of relative differences is also obtained for  $v_3$  and  $v_4$  predictions, with an additional qualitative signature appearing for these observables: we notice that some initializations lead

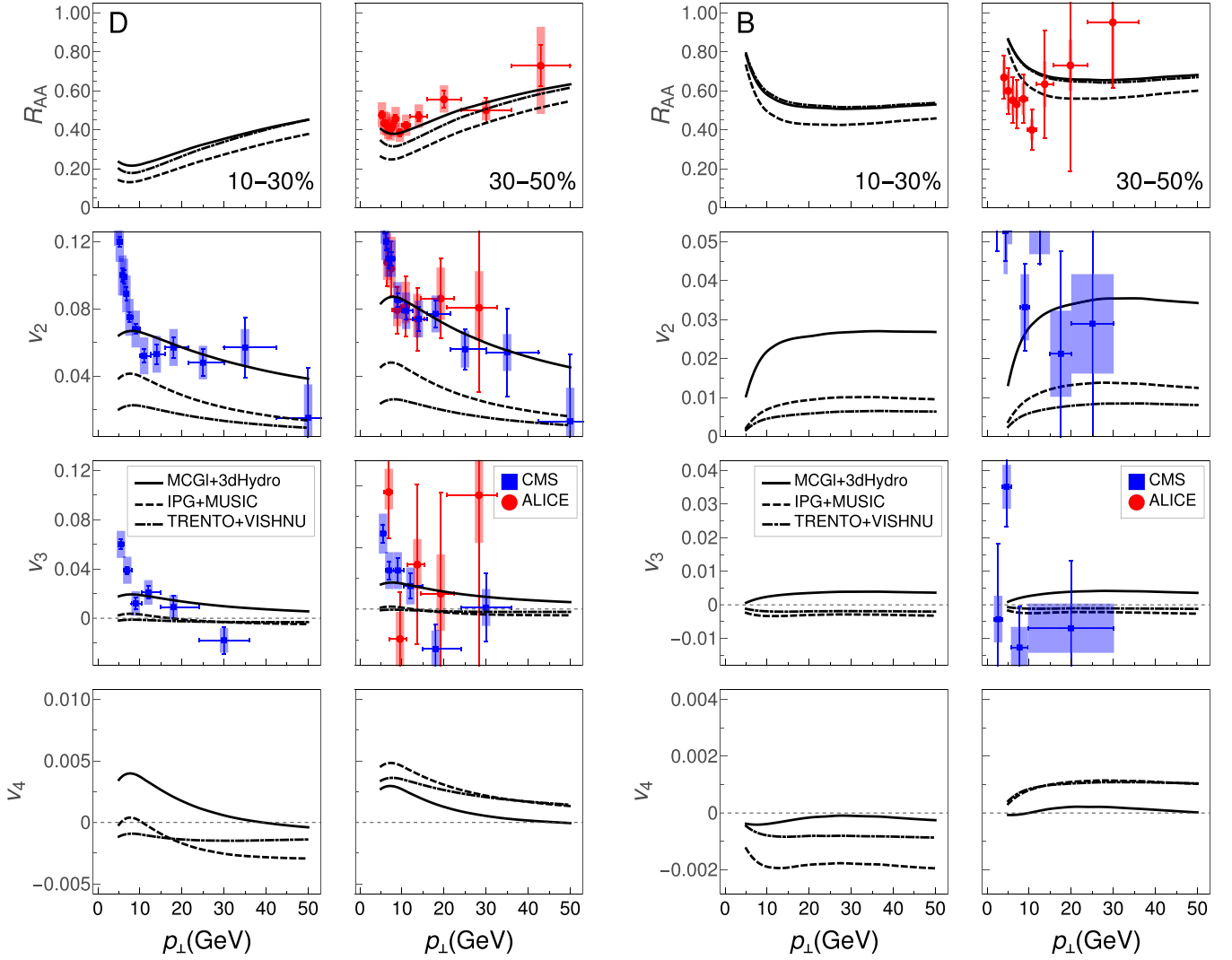


FIG. 4.  $D$  meson (left  $4 \times 2$  panel) and  $B$  meson (right  $4 \times 2$  panel) predictions in Pb + Pb collisions at  $\sqrt{s_{NN}} = 5.02$  TeV for different initializations of QGP evolution (indicated in the legend). In each  $4 \times 2$  panel, the first row corresponds to  $R_{AA}$ , the second, third, fourth to  $v_2$ ,  $v_3$ ,  $v_4$ , respectively, while the left (right) column corresponds to 10–30% (30–50%) centrality class.  $D$  meson theoretical predictions are compared to CMS [58] (blue squares) and ALICE [59,60] (red circles) data, while  $B$  meson predictions are compared to preliminary CMS [61] (blue squares) and preliminary ALICE [62] (red circles) data for nonprompt  $D$  mesons from  $b$  decay.  $\mu_M/\mu_E = 0.5$ .

to negative values of high- $p_{\perp}$   $v_3$  and  $v_4$ , i.e., models can differ even in the expected sign of the flow coefficients.

Since DREENA-A does not have fitting parameters in the energy loss (the only inputs are the temperature profile and binary collisions, which come as a direct output from fluid-dynamical calculation and the initial state model), Figs. 3 and 4 demonstrate that high- $p_{\perp}$   $R_{AA}$  and higher harmonics can distinguish between different initializations and temperature profiles, and subsequently further constrain their parameters. Furthermore, Fig. 4 suggests that heavy flavor high- $p_{\perp}$  observables are even more sensitive to different temperature profiles than the light flavor. We also see that predictions for high- $p_{\perp}$  higher harmonics can be either positive or negative. Thus, the high- $p_{\perp}$  sector can provide both quantitative and qualitative constraints for different initial states.

Presently, of the considered models, the best agreement is observed for MC-Glauber. This result is compatible with our earlier findings [63], where the best agreement with high- $p_{\perp}$  data was found by delaying the start of transverse expansion and energy loss to time  $\tau_0 \approx 1.0$  fm. However, all models seem to vastly underestimate the  $v_4$  values, though the error bars for the available  $v_4$  data are quite large. If this tendency is preserved in future high luminosity experiments (e.g., in LHC Run 3), it will present a new “high- $p_{\perp}$   $v_4$  puzzle,” whose solution will require modifications to the present initial state models and/or energy loss mechanisms. Additionally, better quality heavy flavor data are needed, especially  $D$ - and  $B$ -meson data, as they present valuable constraints to the evolution of the medium.

#### IV. SUMMARY

We obtained four main conclusions in this work: (i) We found that different methods to calculate higher harmonics at high- $p_{\perp}$  are compatible with each other within  $\approx 5\text{--}10\%$  accuracy, which is less than the current experimental uncertainties. (ii) Event-by-event calculations are particularly important for high- $p_{\perp}$   $v_2$  in mid-central collisions. (iii) Predictions for high- $p_{\perp}$  observables, and especially for higher harmonics, are sensitive to the initial state of fluid-dynamical evolution, and can distinguish between different initial state models. (iv) All initial state models lead to way smaller high- $p_{\perp}$   $v_4$  than is experimentally observed, and this disparity deserves to be called a “ $v_4$  puzzle.” Overall, the higher harmonics provide an exciting opportunity to obtain further constraints to the QGP properties and its evolution in heavy-ion collisions by combining new theoretical developments (with the corresponding predictions) and upcoming higher luminosity experimental measurements.

#### ACKNOWLEDGMENTS

We thank Chun Shen for sharing his results with us. We thank Marko Djordjevic, Bojana Ilic, and Stefan Stojku for useful discussions. This work is supported by the European Research Council, Grant No. ERC-2016-COG:725741, and by the Ministry of Science and Technological Development of the Republic of Serbia. P.H. was also supported by the program Excellence Initiative—Research University of the University of Wrocław of the Ministry of Education and Science.

- 
- [1] E. V. Shuryak, *Nucl. Phys. A* **750**, 64 (2005); *Rev. Mod. Phys.* **89**, 035001 (2017).
- [2] M. Gyulassy and L. McLerran, *Nucl. Phys. A* **750**, 30 (2005).
- [3] B. Jacak and P. Steinberg, *Phys. Today* **63**(5), 39 (2010).
- [4] B. Müller, J. Schukraft, and B. Wyslouch, *Annu. Rev. Nucl. Part. Sci.* **62**, 361 (2012).
- [5] J. C. Collins and M. J. Perry, *Phys. Rev. Lett.* **34**, 1353 (1975).
- [6] G. Baym and S. A. Chin, *Phys. Lett. B* **62**, 241 (1976).
- [7] M. Aaboud, Jr. *et al.* (ATLAS Collaboration), *Eur. Phys. J. C* **78**, 997 (2018).
- [8] A. M. Sirunyan, Jr. *et al.* (CMS Collaboration), *Phys. Lett. B* **776**, 195 (2018).
- [9] J. Noronha-Hostler, B. Betz, J. Noronha, and M. Gyulassy, *Phys. Rev. Lett.* **116**, 252301 (2016).
- [10] Y. He, W. Chen, T. Luo, S. Cao, L. G. Pang, and X. N. Wang, *arXiv:2201.08408*.
- [11] S. Shi, J. Liao, and M. Gyulassy, *Chin. Phys. C* **43**, 044101 (2019).
- [12] J. Noronha-Hostler, B. Betz, M. Gyulassy, M. Luzum, J. Noronha, I. Portillo, and C. Ratti, *Phys. Rev. C* **95**, 044901 (2017).
- [13] D. Zigic, I. Salom, J. Auvinen, P. Huovinen, and M. Djordjevic, *arXiv:2110.01544*.
- [14] M. Djordjevic, *Phys. Rev. C* **80**, 064909 (2009).
- [15] M. Djordjevic and U. Heinz, *Phys. Rev. Lett.* **101**, 022302 (2008).
- [16] M. Djordjevic, *Phys. Rev. C* **74**, 064907 (2006).
- [17] B. Blagojevic and M. Djordjevic, *J. Phys. G: Nucl. Part. Phys.* **42**, 075105 (2015).
- [18] J. I. Kapusta, *Finite-Temperature Field Theory* (Cambridge University Press, Cambridge, 1989).
- [19] M. Djordjevic and M. Gyulassy, *Phys. Rev. C* **68**, 034914 (2003).
- [20] M. Djordjevic and M. Djordjevic, *Phys. Lett. B* **734**, 286 (2014).
- [21] M. Djordjevic, *Phys. Lett. B* **709**, 229 (2012).
- [22] B. Blagojevic, M. Djordjevic, and M. Djordjevic, *Phys. Rev. C* **99**, 024901 (2019).
- [23] Z. B. Kang, I. Vitev, and H. Xing, *Phys. Lett. B* **718**, 482 (2012); R. Sharma, I. Vitev, and B. W. Zhang, *Phys. Rev. C* **80**, 054902 (2009).
- [24] D. de Florian, R. Sassot, and M. Stratmann, *Phys. Rev. D* **75**, 114010 (2007).
- [25] M. Cacciari and P. Nason, *J. High Energy Phys.* **09** (2003) 006; E. Braaten, K.-M. Cheung, S. Fleming, and T. C. Yuan, *Phys. Rev. D* **51**, 4819 (1995).
- [26] V. G. Kartvelishvili, A. K. Likhoded, and V. A. Petrov, *Phys. Lett. B* **78**, 615 (1978).
- [27] A. Peshier, *arXiv:hep-ph/0601119* (2006).
- [28] O. Kaczmarek, F. Karsch, F. Zantow, and P. Petreczky, *Phys. Rev. D* **70**, 074505 (2004); O. Kaczmarek and F. Zantow, *ibid.* **71**, 114510 (2005).
- [29] Y. Maezawa, S. Aoki, S. Ejiri, T. Hatsuda, N. Ishii, K. Kanaya, N. Ukita, and T. Umeda (WHOT-QCD Collaboration), *Phys. Rev. D* **81**, 091501(R) (2010).
- [30] A. Nakamura, T. Saito, and S. Sakai, *Phys. Rev. D* **69**, 014506 (2004).
- [31] E. Molnar, H. Holopainen, P. Huovinen, and H. Niemi, *Phys. Rev. C* **90**, 044904 (2014).
- [32] P. Huovinen and P. Petreczky, *Nucl. Phys. A* **837**, 26 (2010).
- [33] J. Adam *et al.* (ALICE Collaboration), *Phys. Rev. Lett.* **116**, 222302 (2016).
- [34] J. Adam *et al.* (ALICE Collaboration), *Phys. Rev. Lett.* **116**, 132302 (2016).
- [35] J. S. Moreland, J. E. Bernhard, and S. A. Bass, *Phys. Rev. C* **92**, 011901(R) (2015).
- [36] H. Song and U. W. Heinz, *Phys. Rev. C* **77**, 064901 (2008).
- [37] J. E. Bernhard, *arXiv:1804.06469*.
- [38] J. E. Bernhard, J. S. Moreland and S. A. Bass, *Nat. Phys.* **15**, 1113 (2019).
- [39] A. Bazavov *et al.* (HotQCD Collaboration), *Phys. Rev. D* **90**, 094503 (2014).
- [40] B. Schenke, P. Tribedy, and R. Venugopalan, *Phys. Rev. Lett.* **108**, 252301 (2012).
- [41] B. Schenke, P. Tribedy, and R. Venugopalan, *Phys. Rev. C* **86**, 034908 (2012).
- [42] B. Schenke, C. Shen, and P. Tribedy, *Phys. Rev. C* **102**, 044905 (2020).
- [43] C. Shen (private communication).
- [44] B. Schenke, S. Jeon, and C. Gale, *Phys. Rev. C* **82**, 014903 (2010).
- [45] B. Schenke, S. Jeon, and C. Gale, *Phys. Rev. Lett.* **106**, 042301 (2011).
- [46] B. Schenke, S. Jeon, and C. Gale, *Phys. Rev. C* **85**, 024901 (2012).

- [47] J. S. Moreland and R. A. Soltz, *Phys. Rev. C* **93**, 044913 (2016).
- [48] C. Andres, N. Armesto, H. Niemi, R. Paatelainen, and C. A. Salgado, *Phys. Lett. B* **803**, 135318 (2020).
- [49] A. Bilandzic, R. Snellings, and S. Voloshin, *Phys. Rev. C* **83**, 044913 (2011).
- [50] J. F. Paquet, C. Shen, G. S. Denicol, M. Luzum, B. Schenke, S. Jeon, and C. Gale, *Phys. Rev. C* **93**, 044906 (2016).
- [51] S. A. Voloshin, A. M. Poskanzer, A. Tang, and G. Wang, *Phys. Lett. B* **659**, 537 (2008).
- [52] J. Jia and P. Huo, *Phys. Rev. C* **90**, 034905 (2014).
- [53] V. Khachatryan *et al.* (CMS Collaboration), *Phys. Rev. C* **92**, 034911 (2015).
- [54] V. Khachatryan, Jr. *et al.* (CMS Collaboration), *J. High Energy Phys.* **04** (2017) 039.
- [55] S. Acharya *et al.* (ALICE Collaboration), *J. High Energy Phys.* **11** (2018) 013.
- [56] S. Acharya *et al.* (ALICE Collaboration), *J. High Energy Phys.* **07** (2018) 103.
- [57] ATLAS Collaboration, Report No. ATLAS-CONF-2017-012 (unpublished).
- [58] A. M. Sirunyan, Jr. *et al.* (CMS Collaboration), *Phys. Lett. B* **816**, 136253 (2021).
- [59] S. Acharya *et al.* (ALICE Collaboration), *J. High Energy Phys.* **01** (2022) 174.
- [60] S. Acharya *et al.* (ALICE Collaboration), *Phys. Lett. B* **813**, 136054 (2021).
- [61] Y. Kim, presented at Quark Matter 2022, 29th International Conference on Ultrarelativistic Nucleus-Nucleus Collisions, April 4–10. 2022. Kraków (unpublished), <https://indico.cern.ch/event/895086/contributions/4314625/>.
- [62] X. Peng, presented at Quark Matter 2022, 29th International Conference on Ultrarelativistic Nucleus-Nucleus Collisions, April 4–10. 2022. Kraków (unpublished), <https://indico.cern.ch/event/895086/contributions/4715758/>.
- [63] S. Stojku, J. Auvinen, M. Djordjevic, P. Huovinen, and M. Djordjevic, *Phys. Rev. C* **105**, L021901 (2022).





## OPEN ACCESS

## EDITED BY

Andrea Beraudo,  
National Institute of Nuclear Physics of  
Turin, Italy

## REVIEWED BY

Plumari Salvatore,  
University of Catania, Italy  
Ralf Rapp,  
Texas A&M University, United States

## \*CORRESPONDENCE

Magdalena Djordjevic,  
magda@ipb.ac.rs

## SPECIALTY SECTION

This article was submitted to Nuclear  
Physics,  
a section of the journal  
Frontiers in Physics

RECEIVED 30 May 2022

ACCEPTED 03 October 2022

PUBLISHED 02 November 2022

## CITATION

Zigic D, Salom I, Auvinen J, Huovinen P  
and Djordjevic M (2022), DREENA-A  
framework as a QGP tomography tool.  
*Front. Phys.* 10:957019.  
doi: 10.3389/fphy.2022.957019

## COPYRIGHT

© 2022 Zigic, Salom, Auvinen, Huovinen  
and Djordjevic. This is an open-access  
article distributed under the terms of the  
[Creative Commons Attribution License  
\(CC BY\)](https://creativecommons.org/licenses/by/4.0/). The use, distribution or  
reproduction in other forums is  
permitted, provided the original  
author(s) and the copyright owner(s) are  
credited and that the original  
publication in this journal is cited, in  
accordance with accepted academic  
practice. No use, distribution or  
reproduction is permitted which does  
not comply with these terms.

# DREENA-A framework as a QGP tomography tool

Dusan Zigic<sup>1</sup>, Igor Salom<sup>1</sup>, Jussi Auvinen<sup>1</sup>, Pasi Huovinen<sup>1,2</sup> and  
Magdalena Djordjevic<sup>1\*</sup>

<sup>1</sup>Laboratory for High-Energy Physics, Institute of Physics Belgrade, University of Belgrade, Belgrade, Serbia, <sup>2</sup>Incubator of Scientific Excellence—Centre for Simulations of Superdense Fluids, University of Wroclaw, Wroclaw, Poland

QGP tomography aims to constrain the QGP parameters by exploiting both low and high- $p_{\perp}$  theory and data. With this goal in mind, we present a fully optimised framework DREENA-A based on a state-of-the-art energy loss model. The framework can include any, in principle arbitrary, temperature profile within the dynamical energy loss formalism. Thus, “DREENA” stands for Dynamical Radiative and Elastic ENergy loss Approach, while “A” stands for Adaptive. DREENA-A does not adjust parameters within the energy loss model, allowing it to exploit differences in temperature profiles which are the only input in the framework. The framework applies to light and heavy flavor observables, different collision energies, and large and smaller systems. This, together with the ability to systematically compare data and predictions within the same formalism and parameter set, makes DREENA-A a unique multipurpose QGP tomography tool. The provided code allows researchers to use their own QGP evolution models to straightforwardly generate high- $p_{\perp}$  predictions.

## KEYWORDS

relativistic heavy ion collisions, quark-gluon plasma, QGP tomography, predictions for high- $p_{\perp}$  observables, light and heavy flavor

## 1 Introduction

QCD predicted that a new form of matter [1, 2]— consisting of quarks, antiquarks, and gluons that are no longer confined—is created at extremely high energy densities. According to the current cosmology, this new state of matter, called Quark-Gluon Plasma (QGP) [3–7], existed immediately after the Big Bang [8]. Today, QGP is created in ‘Little Bangs’, when heavy ions collide at ultra-relativistic energies [5, 6]. Such collisions lead to an expanding fireball of quarks and gluons, which thermalises to form QGP; the QGP then cools down, and when the temperature reaches a critical point, quarks and gluons hadronise.

Successful production of this exotic state of matter at the Relativistic Heavy Ion Collider (RHIC) and the Large Hadron Collider (LHC) allowed systematic testing of different models of QGP evolution against experimental data. Up to now, it has been established that QGP is formed at the LHC and RHIC experiments through two main lines [5, 6, 9] of evidence: 1) by comparison of low momentum ( $p_{\perp}$ ) measurements with relativistic hydrodynamic predictions, which implied that

created QGP is consistent with the description of a nearly perfect fluid [10–12], 2) by comparison of high- $p_{\perp}$  data [13–17] with pQCD predictions, which showed that high- $p_{\perp}$  partons (jets) significantly interact with an opaque medium. Beyond this discovery phase, the current challenge is to investigate the properties of this extreme form of matter.

While high- $p_{\perp}$  physics had a decisive role in the QGP discovery [5], it was rarely used for understanding the bulk medium properties. On the other hand, low- $p_{\perp}$  observables do not provide stringent constraints to all parameters of the models used to describe the evolution of QGP [18–21]. Thus, it is desirable to explore QGP properties through independent theory and data set. We argue that this is provided by jet energy loss and high- $p_{\perp}$  data, complementing the low- $p_{\perp}$  constraints to QGP.

To use high- $p_{\perp}$  theory and data as a QGP tomography tool, it is necessary to have a realistic high- $p_{\perp}$  parton energy loss model. We use our dynamical energy loss formalism, which has the following properties: 1) It is based on finite size, finite temperature field theory [22, 23], and takes into account that QGP constituents are dynamical (moving) particles. Consequently, all divergences are naturally regulated in the model. 2) Both collisional [24] and radiative [25, 26] energy losses are calculated in the same theoretical framework. In radiative energy loss, finite size effects induce a non-linear path length dependence of the energy loss, recovering both the incoherent Gunion Bertsch and destructive Landau-Pomeanchuk-Migdal limit [25, 26]. For collisional energy loss, we show that finite size effects can be neglected [24], i.e., path-length dependence is close to linear. 3) It is applicable to both light and heavy flavors, so it can provide predictions for an extensive set of probes. 4) Temperature is a natural variable in the framework [27], so that the  $T$  profiles resulting from bulk medium simulations are a direct input in the model. 5) The non-perturbative effects related to screening of the chromo-magnetic and chromo-electric fields are included [28] through the generalized hard-thermal-loop (HTL) approach. For radiative energy loss, the effective cross-section is handled through sum-rules [29], which allows consistent inclusion of non-perturbative medium-related interactions captured by lattice QCD (see [28] for more details). For collisional energy loss, the nonperturbative effects were included at the leading order through modification of the running coupling, following the procedure from [30] (see [31] for more details). 6) No parameters are adjusted when comparing the dynamical energy loss predictions with high- $p_{\perp}$  data [32, 33], i.e., we use fixed parameter values consistent with other studies (specified in Subsection 2.1). The formalism explained a wide range of high- $p_{\perp}$  data [31, 34–37], including puzzling data [37] and generating predictions for future experiments [35]. This suggests that the model realistically describes high-

$p_{\perp}$  parton-medium interactions. While other available energy loss models (see e.g. [38–48]) have some of the above properties, none have all (or even most of them), making the dynamical energy loss an advanced framework for QGP tomography<sup>1</sup>. As the temperature is the only input in the energy loss model, this allows further exploiting different temperature profiles that agree with low- $p_{\perp}$  data by testing their agreement with high- $p_{\perp}$  data. Consequently, a systematic comparison of data and predictions obtained by the same formalism and parameter set allows constraining the QGP parameters from both low and high- $p_{\perp}$  theory and data.

Including full medium evolution in the dynamical energy loss is, however, a highly non-trivial task, as all the model properties have to be preserved [49], without additional simplifications in the numerical procedure. Furthermore, to be effectively used as a precision QGP tomography tool, the framework needs to efficiently (timewise) generate a comprehensive set of light and heavy flavor suppression predictions through the same numerical framework and the same parameter set. Such predictions can then be compared with the available experimental data, sometimes even repeatedly (i.e., iteratively)—for different combinations of QGP medium parameters—to extract medium properties that are consistent with both low and high- $p_{\perp}$  data.

To introduce the medium evolution in the dynamical energy loss, we took a step-by-step approach, allowing us to check the consistency of each consecutive step by comparing its results with the previous (simpler) framework versions. Consequently, we first developed the DREENA-C framework [50] ('C' stands for constant temperature), continuing to DREENA-B [51] ('B' stands for Bjorken expansion). In this manuscript, we present a fully optimised DREENA-A framework, where 'A' stands for 'adaptive' (i.e., arbitrary) temperature evolution. The convergence speed of the developed numerical procedure is analysed, as well as consistency with other (earlier) versions of the framework, as necessary for the reliable and efficient QGP tomography tool. Finally, as a utility check of the DREENA-A framework, the sensitivity of high- $p_{\perp}$  observables to different temperature profiles is presented.

The link to the software code implementing the DREENA-A framework (with usage instructions and example data) is provided at <https://github.com/DusanZigic/DREENA-A>. Using this software, researchers can generate high- $p_{\perp}$  predictions for their own (different) models of medium evolution and compare the results with experimental data.

<sup>1</sup> While it is challenging to implement further improvements into the analytical calculations while keeping all existing ingredients, some possible directions for advances include, e.g., flow velocity of the bulk medium and transverse gradients of temperature and density (see e.g. [45–48]).

## 2 Methods

### 2.1 Theoretical outline

The calculation of the final hadron spectrum includes initial high- $p_{\perp}$  parton (quark and gluon) distributions from perturbative QCD, energy loss (if the QCD medium is formed), and fragmentation into hadrons. The cross section for quenched spectra is schematically written as [52, 53]:

$$\frac{E_f d^3 \sigma_q(H_Q)}{d p_f^3} = \frac{E_i d^3 \sigma(Q)}{d p_i^3} \otimes P(E_i \rightarrow E_f) \otimes D(Q \rightarrow H_Q), \quad (1)$$

where  $\otimes$  is a generic convolution, and the change in the initial spectra due to energy loss in QGP is denoted  $P(E_i \rightarrow E_f)$ . If the medium is not created, then Eq. 1 reduces to cross section for unquenched spectra

$$\frac{E_f d^3 \sigma_u(H_Q)}{d p_f^3} = \frac{E_i d^3 \sigma(Q)}{d p_i^3} \otimes D(Q \rightarrow H_Q). \quad (2)$$

More specifically,  $\frac{E_f d^3 \sigma_q(H_Q)}{d p_f^3}$  is the final hadron spectrum in the presence of QGP, while  $\frac{E_i d^3 \sigma_u(H_Q)}{d p_i^3}$  is the spectrum in the absence of QGP. ‘ $i$ ’ and ‘ $f$ ’ correspond to ‘initial’ and ‘final’, respectively.  $Q$  denotes quarks and gluons, while  $H_Q$  denotes hadrons. Initial parton spectrum is denoted by  $E_i d^3 \sigma(Q)/d p_i^3$ , and computed at next to leading order [54–56] for light and heavy partons.  $P(E_i \rightarrow E_f)$  is the probability for energy transfer, which includes medium induced radiative [25, 26] and collisional [24] contributions in a finite size dynamical QCD medium with running coupling [31]. Both contributions include multi-gluon fluctuations, introduced according to Refs. [31, 57] for radiative and [52, 58] for collisional energy loss (for more details, see below).  $Q$  to hadron  $H_Q$  fragmentation is denoted by  $D(Q \rightarrow H_Q)$ . For charged hadrons we use DSS [59], for D mesons BCFY [60, 61] and for B mesons KLP [62] fragmentation functions, respectively.

In DREENA-A, the medium temperature needed to calculate  $P(E_i \rightarrow E_f)$  depends on the position of the parton according to a temperature profile given as an input. Therefore, the temperature that the parton experiences along its path, becomes a function of the coordinates of its origin  $(x_0, y_0)$ , the angle of its trajectory  $\phi$ , and the proper time  $\tau$ :

$$T(x_0, y_0, \phi, \tau) = T_{profile}(x_0 + \tau \cos \phi, y_0 + \tau \sin \phi, \tau), \quad (3)$$

where  $T_{profile}$  is, in principle, arbitrary. This temperature then appears in the expressions below.

The collisional energy loss is given by the following analytical expression [51]:

$$\begin{aligned} \frac{dE_{coll}}{d\tau} = & \frac{2C_R \alpha_S(ET) \alpha_S(\mu_E^2(T))}{\pi v^2} \\ & \times \int_0^{\infty} n_{eq}(|\vec{k}|, T) d|\vec{k}| \left( \int_0^{|\vec{k}|/(1+v)} d|\vec{q}| \int_{-|\vec{q}|}^{|\vec{q}|} \omega d\omega + \int_{|\vec{q}|/(1+v)}^{|\vec{q}|_{max}} d|\vec{q}| \int_{|\vec{q}|/(1+v)}^{|\vec{q}|} \omega d\omega \right) \\ & \times \left( |\Delta_L(q, T)|^2 \frac{(2|\vec{k}| + \omega)^2 - |\vec{q}|^2}{2} + |\Delta_T(q, T)|^2 \frac{(|\vec{q}|^2 - \omega^2)((2|\vec{k}| + \omega)^2 + |\vec{q}|^2)}{4|\vec{q}|^4} (v^2 |\vec{q}|^2 - \omega^2) \right). \end{aligned} \quad (4)$$

Here we used the following notation:  $k$  is the 4-momentum of the incoming medium parton;  $T$  is the current temperature along the path, given by Eq. 3;  $n_{eq}(|\vec{k}|, T) = \frac{N}{e^{|\vec{k}|/T} - 1} + \frac{N_f}{e^{|\vec{k}|/T} + 1}$  is the equilibrium momentum distribution [63] at temperature  $T$  including quarks and gluons.  $N = 3$  and  $N_f$  represent, respectively, the number of colors and flavors, where we assume  $N_f = 3$  for the LHC and  $N_f = 2.5$  for RHIC;  $q = (\omega, \vec{q})$  is the 4-momentum of the exchanged gluon;  $E^2 = p^2 + M^2$  denotes the initial jet energy,  $p$  is the jet momentum, while  $M$  is the mass (specified below) of the quark or gluon jet;  $v = p/\sqrt{p^2 + M^2}$  denotes velocity of the incoming jet;  $C_R = \frac{4}{3}$  for quark jet and three for gluon jet;  $\Delta_L(T)$  and  $\Delta_T(T)$  are effective longitudinal and transverse gluon propagators [64, 65], while the electric screening (the Debye mass)  $\mu_E(T)$  is obtained by self-consistently solving the expression from [66] ( $\Lambda_{QCD}$  is perturbative QCD scale):

$$\frac{\mu_E(T)^2}{\Lambda_{QCD}^2} \ln \left( \frac{\mu_E(T)^2}{\Lambda_{QCD}^2} \right) = \frac{1 + N_f/6}{11 - 2/3 N_f} \left( \frac{4\pi T}{\Lambda_{QCD}} \right)^2. \quad (5)$$

Note that such solution leads to the Debye mass consistent with lattice QCD results [66, 67].

Running coupling  $\alpha_S(Q^2)$  is defined as [68].

$$\alpha_S(Q^2) = \frac{4\pi}{(11 - 2/3 N_f) \ln(Q^2/\Lambda_{QCD}^2)}, \quad (6)$$

where, in the collisional energy loss case, the coupling appears through the term  $\alpha_S^2$  [24], which can be factorised to  $\alpha_S(\mu_E^2) \alpha_S(ET)$  [30] (see also [31]).

The radiation spectrum [51] is:

$$\begin{aligned} \frac{d^2 N_{rad}}{dx d\tau} = & \int \frac{d^2 k}{\pi} \frac{d^2 q}{\pi} \frac{2C_R C_2(G) T}{x} \frac{\mu_E(T)^2 - \mu_M(T)^2}{(q^2 + \mu_M(T)^2)(q^2 + \mu_E(T)^2)} \frac{\alpha_S(ET) \alpha_S\left(\frac{k^2 + \chi(T)}{x}\right)}{\pi} \\ & \times \frac{(\mathbf{k} + \mathbf{q})}{(\mathbf{k} + \mathbf{q})^2 + \chi(T)} \left( 1 - \cos\left(\frac{(\mathbf{k} + \mathbf{q})^2 + \chi(T)}{x(E + p_z)} \tau\right) \right) \left( \frac{(\mathbf{k} + \mathbf{q})}{(\mathbf{k} + \mathbf{q})^2 + \chi(T)} - \frac{\mathbf{k}}{k^2 + \chi(T)} \right). \end{aligned} \quad (7)$$

Here  $C_2(G) = 3$ ;  $\chi(T) \equiv M^2 x^2 + m_g(T)^2$ , where  $x$  is the longitudinal momentum fraction of the jet carried away by the emitted gluon,  $p_z$  is longitudinal component of initial jet momentum, and  $m_g(T) = \mu_E(T)/\sqrt{2}$  is the effective gluon mass in finite temperature QCD medium [69], where  $\mu_E(T)$  is Debye mass defined above;  $M = 1.3$  GeV for charm, 4.5 GeV for bottom [54–56, 70, 71] and  $\mu_E(T)/\sqrt{6}$  for light quarks (where thermal mass originates from gluon propagators);  $\mu_M(T)$  is magnetic screening, where different non-perturbative approaches suggest  $0.4 < \mu_M(T)/\mu_E(T) < 0.6$  [67, 72];  $\mathbf{q}$  and  $\mathbf{k}$  are transverse momenta of exchanged (virtual) and radiated gluon, respectively.  $Q_k^2 = \frac{k^2 + \chi(T)}{x}$  in

$\alpha_S(\frac{k^2+\chi(T)}{x})$  corresponds to the off-shellness of the jet prior to the gluon radiation [25]. Note that, all  $\alpha_S$  terms in Eqs 4, 7 are infrared safe (and moreover of a moderate value) [31]. Thus, contrary to majority of other approaches, we do not need to introduce a cut-off in  $\alpha_S(Q^2)$ .

We further assume that radiative and collisional energy losses can be separately treated in  $P(E_i \rightarrow E_f)$ , i.e., jet quenching is performed *via* two independent branching processes [31, 52]. We first calculate the modification of the quark and gluon spectrum due to radiative energy loss, then collisional energy loss (we checked that change of order is unimportant within our model). This is a reasonable approximation when the radiative and collisional energy losses can be considered small (which is in the essence of the soft-gluon, soft-rescattering approximation widely used in energy loss calculations) and when radiative and collisional energy loss processes are decoupled, as is the case in the generalized HTL approach [73] used in our energy loss calculations.

To obtain the radiative energy loss contribution to the suppression [57], we start with Eq. 7 and, for a given trajectory, we first compute the mean number of gluons emitted due to induced radiation (further denoted as  $\bar{N}_{tr}(E)$ ), as well as the mean number of gluons emitted per fractional energy loss  $x$  (i.e.,  $\frac{d\bar{N}_{tr}(E)}{dx}$ , for compactness further denoted as  $\bar{N}'_{tr}(E, x)$ ):

$$\bar{N}_{tr}(E) = \int_{tr} \left( \int \frac{d^2 N_{rad}}{dx d\tau} dx \right) d\tau, \quad \bar{N}'_{tr}(E, x) = \int_{tr} \frac{d^2 N_{rad}}{dx d\tau} d\tau, \tag{8}$$

where the subscript *tr* indicates that the value depends on the trajectory. Radiative energy loss suppression takes multi-gluon fluctuations into account, where we assume that the fluctuations of gluon number are uncorrelated. Such assumption is reasonable, as Ref. [74] studied full splitting cascade and found that independent branchings reasonably well approximate a full branching. The radiative energy loss probability can then be expressed *via* Poisson expansion [31, 57]:

$$P_{rad}^{tr}(E_i \rightarrow E_f) = \frac{\delta(E_i - E_f)}{e^{\bar{N}_{tr}(E_i)}} + \frac{\bar{N}'_{tr}(E_i, 1 - \frac{E_f}{E_i})}{E_i e^{\bar{N}_{tr}(E_i)}} + \sum_{n=2}^{\infty} \frac{e^{-\bar{N}_{tr}(E_i)}}{n! E_i} \int dx_1 \dots dx_n \bar{N}'_{tr}(E_i, x_1) \dots \bar{N}'_{tr}(E_i, x_{n-1}) \bar{N}'_{tr}(E_i, 1 - \frac{E_f}{E_i} - x_1 - \dots - x_{n-1}). \tag{9}$$

$E_i$  and  $E_f$  are initial and final jet energy (before and after) radiative process.

To calculate the parton spectrum after radiative energy loss, we apply

$$\frac{E_{f,R} d^3 \sigma}{dp_{f,R}^3} = \frac{E_i d^3 \sigma(Q)}{dp_i^3} \otimes P_{rad}^{tr}(E_i \rightarrow E_{f,R}), \tag{10}$$

where the final spectra is obtained after integrating over  $p_i > p_{f,R}$ .

To find collisional energy loss contribution, Eq. 4 is first integrated over the given trajectory:

$$\bar{E}_{col}^{tr}(E) = \int_{tr} \frac{dE_{col}}{d\tau} d\tau. \tag{11}$$

For collisional energy loss, the full fluctuation spectrum is approximated by a Gaussian centered at the average energy loss  $\bar{E}_{col}^{tr}(E)$  [52, 58].

$$P_{col}^{tr}(E_i, E_f) = \frac{1}{\sqrt{2\pi\sigma_{col}^{tr}(E_i)}} \exp\left(-\frac{(E_i - E_f - \bar{E}_{col}^{tr}(E_i))^2}{2\sigma_{col}^{tr}(E_i)^2}\right), \tag{12}$$

with a variance

$$\sigma_{col}^{tr}(E) = \sqrt{2\overline{T^{tr}} \bar{E}_{col}^{tr}(E)}, \tag{13}$$

where  $\overline{T^{tr}}$  is the average temperature along the trajectory,  $E_i$  and  $E_f$  are initial and final energy (before and after collisional processes).

To calculate the quenched hadron spectrum after collisional energy loss, we apply

$$\frac{E_f d^3 \sigma_q(H_Q)}{dp_f^3} = \frac{E_{i,C} d^3 \sigma(Q)}{dp_{i,C}^3} \otimes P_{col}^{tr}(E_{i,C} \rightarrow E_f) \otimes D(Q \rightarrow H_Q), \tag{14}$$

where we assume  $E_{i,C} = E_{f,R}$ , i.e. the final jet energy after radiative quenching corresponds to the initial jet energy for collisional quenching. Since both collisional energy loss and gain contribute to the final spectra [24, 52], both  $E_{i,C} > E_f$  and  $E_{i,C} < E_f$  have to be taken into account in Eq. 14. Finally, the hadron suppression  $R_{AA}^{tr}(p_f, H_Q)$  for the single trajectory, after radiative and collisional energy loss, is equal to the ratio of quenched and unquenched momentum spectra

$$R_{AA}^{tr}(p_f, H_Q) = \frac{E_f d^3 \sigma_q(H_Q)}{dp_f^3} / \frac{E_f d^3 \sigma_u(H_Q)}{dp_f^3}, \tag{15}$$

where  $\frac{E_f d^3 \sigma_u(H_Q)}{dp_f^3}$  is given by Eq. 2.  $R_{AA}^{tr}(p_f, H_Q)$  then needs to be averaged over trajectories with the same direction angle  $\phi$  to obtain the suppression as a function of angle,  $R_{AA}(p_f, \phi, H_Q)$ . This is an important intermediary step since, depending on the details of QGP temperature evolution and the spatial variations in the temperature profile, energy loss may significantly depend on the parton's direction of motion<sup>2</sup>. Once we have calculated  $R_{AA}(p_f, \phi, H_Q)$ , we can easily evaluate  $R_{AA}$  and  $v_2$  observables as [75] (we here omit  $H_Q$  in the expressions, and denote  $p_f = p_{\perp}$ )<sup>3</sup>:

<sup>2</sup> In earlier DREENA frameworks, this dependence was also present but was solely a consequence of the path-length distribution dependence on the angle.

<sup>3</sup> Note that, in Eq. 17, using  $R_{AA}(p_{\perp}, \phi)$ , instead of the hadron  $p_{\perp}$  spectrum, is computationally more efficient since  $R_{AA}(p_{\perp}, \phi)$  is a well-behaved function, and the number of  $p_{\perp}$  points where we need to evaluate  $R_{AA}(p_{\perp}, \phi)$  is significantly smaller.

$$R_{AA}(p_{\perp}) = \frac{1}{2\pi} \int_0^{2\pi} R_{AA}(p_{\perp}, \phi) d\phi, \quad (16)$$

$$v_2(p_{\perp}) = \frac{\frac{1}{2\pi} \int_0^{2\pi} \cos(2\phi) R_{AA}(p_{\perp}, \phi) d\phi}{R_{AA}(p_{\perp})}. \quad (17)$$

While the general expressions of the dynamical energy loss formalism are the same as in the DREENA-B framework [51], the fact that, in DREENA-A, the temperature entering the Eqs 4–7 explicitly depends on the current parton position, notably complicates the implementation of these formulas, as we discuss in the following section.

## 2.2 Framework outline

Our previous DREENA-C and DREENA-B frameworks were based on computationally useful, but rough, approximations of the medium evolution: while in DREENA-C, there was no evolution, and the temperature remained constant both in time and along spatial dimensions, in DREENA-B, the medium was assumed to evolve according to 1D Bjorken approximation [76]. Due to these approximations, parton energy loss depended on its path length independently of its direction or production point. This allowed to analytically integrate energy-loss formulas to a significant extent, which notably reduced the number of required numerical integrations. Furthermore  $R_{AA}$  only needed to be averaged out over precalculated path-length distributions. Thus, these approximations of the medium evolution straightforwardly led to efficient computational algorithms for DREENA-C and DREENA-B.

DREENA-A framework, on the other hand, addresses fully general medium dynamics, with arbitrary spatio-temporal temperature distribution. The main input to the algorithm is the temperature profile  $T_{profile}$  given as a three-dimensional matrix of temperature values at points with coordinates  $(x, y, \tau)$  (in the input file, the values should be arranged in an array of quartets of the form  $(\tau, x, y, T_{profile})$ , and the lowest value of  $\tau$  appearing in the data is taken to be  $\tau_0$ ). In addition to the temperature profile, the DREENA-A algorithm also takes, as inputs, the initial parton  $p_{\perp}$  distributions  $\frac{d^2\sigma}{dp_{\perp}^2}$  (each as an array of  $(p_{\perp}, \frac{d^2\sigma}{dp_{\perp}^2})$  pairs) and the jet production probability distribution (as a matrix of probability density values in the transversal plane, formatted analogously as the profile temperature values). This level of generality requires a different approach than in previous frameworks. Since the DREENA-A algorithm takes arbitrary medium temperature evolution as the input, the energy loss has to be individually calculated for each parton trajectory.

This means that for each trajectory—given by the coordinates  $x_0$  and  $y_0$  of the parton origin (in the transversal plane) and the direction angle  $\phi$ —we must first numerically evaluate integrals (8) and (11). Since the current parton position—for a given

trajectory—becomes a function of the proper time  $\tau$ , integrands in Eqs 8, 11 also become functions of  $\tau$ , either through an explicit dependence, or *via* position and time dependent medium temperature (3). We numerically integrate these functions along the trajectory (parametrized by  $\tau$  as  $x = x_0 + \tau \cos \phi$ ,  $y = y_0 + \tau \sin \phi$ ), starting from the origin at  $(x_0, y_0)$  and moving in small integration steps along the direction  $\phi$  (in practice, 0.1 fm step is sufficiently small for most of the profiles). The integration is terminated when the medium temperature at the current parton's position drops below  $T_c = 155$  MeV [77], i.e., when the parton leaves the QGP phase. Also, we approximate that there are no energy losses before the initial time  $\tau_0$  (which is a parameter of the temperature profile evolution) and thus the first part of the trajectory, corresponding to  $\tau < \tau_0$ , is effectively skipped (i.e.,  $\tau_0$  is taken as the lower limit of integration in Eqs 8, 11).

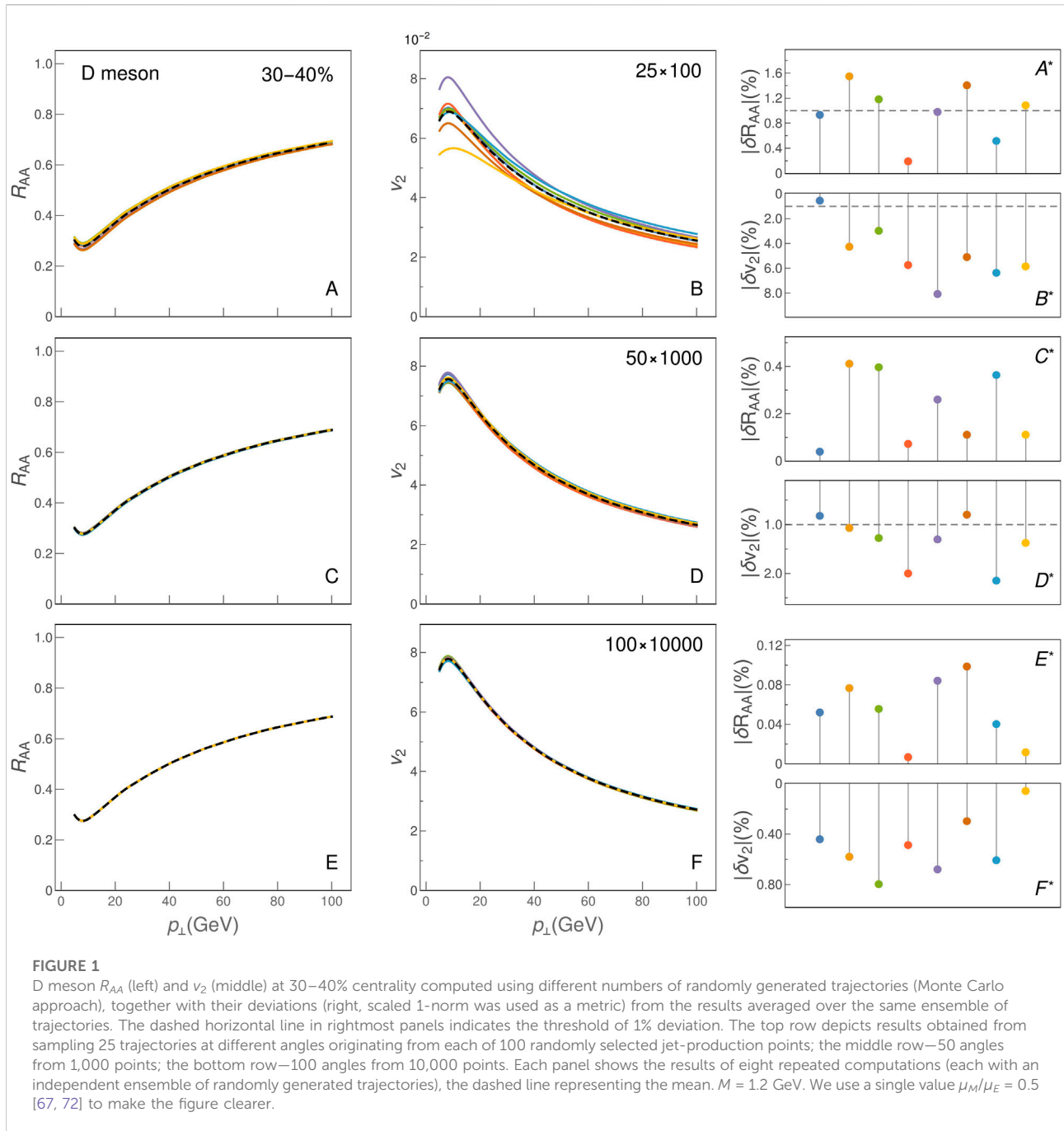
Once we, for a given trajectory, compute the integrals (8) and (11), we then perform the rest of procedure laid out by Eqs 8–15. Most of the computation time is spent on numerical integrations, in particular for evaluating integrals in Eqs 9, 10. While, in principle,  $n \rightarrow \infty$  in Eq. 9, in practice we show that  $n = 5$  is sufficient for convergence in the case of quark jets, while for gluon jets  $n = 7$  is needed. In general, the Quasi-Monte Carlo integration method turned out to be the most efficient and is used for all these integrals (as quasirandom numbers, we use precalculated and stored Halton sequences). The result of the integration (15) is the final hadron suppression  $R_{AA}^r(p_{\perp}, H_Q)$  for the jet moving along the chosen trajectory, given as the function of its transversal momentum.

To obtain  $R_{AA}(p_{\perp}, \phi, H_Q)$ , we have to average this result over all production points (taking into account the provided jet production probability distribution) and repeat the procedure for many angles  $\phi$ . In practice, this means that we must evaluate energy loss along a very large number of trajectories. This has significantly increased the computational complexity of the problem compared to DREENA-C and DREENA-B and required a number of optimisations.

## 2.3 Numerical optimisation of DREENA-A

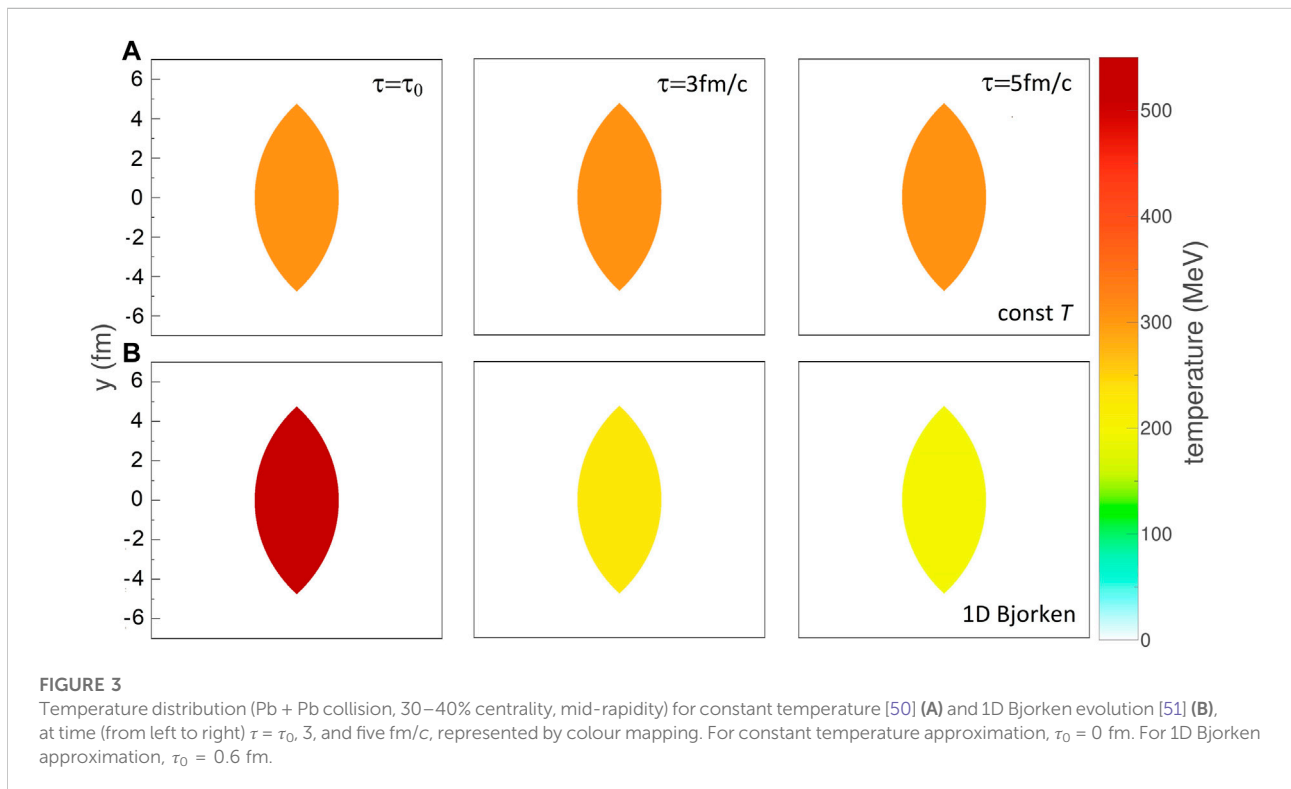
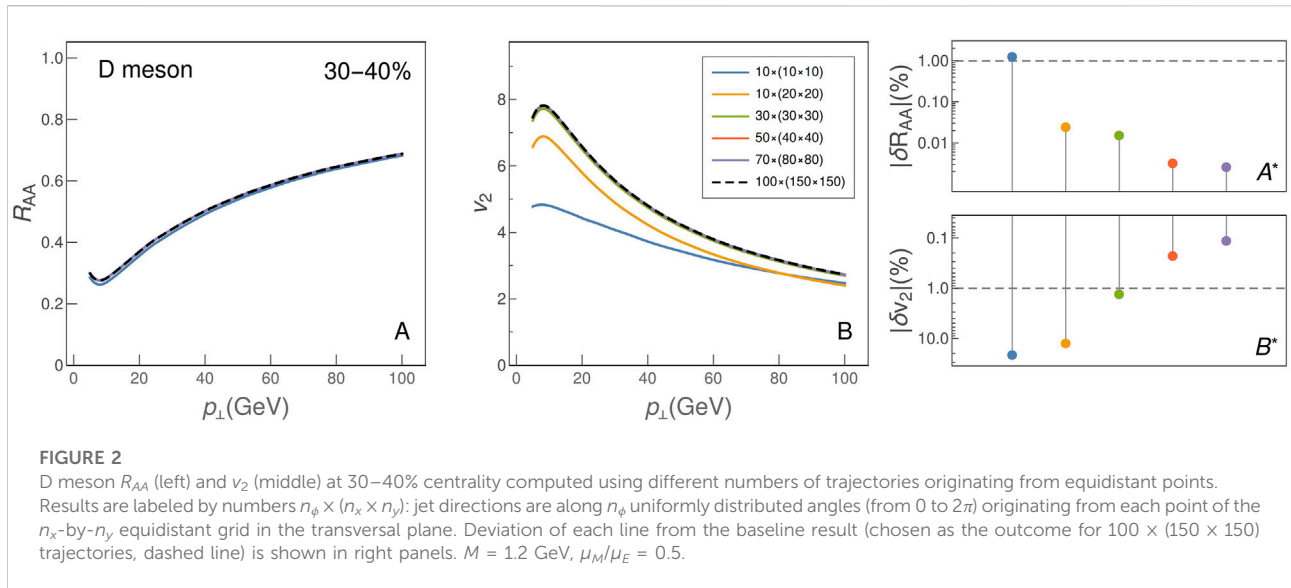
We started by adapting optimisation methods that we successfully implemented in earlier versions. One useful approach was a tabulation and consequent interpolation of values for computationally expensive functions. In particular, this is crucial for the complicated integrals (4–7): while a two dimensional array is sufficient to tabulate  $\frac{dE_{col}}{d\tau}$  (which is a function of  $T$  and  $p$ ), values of  $\frac{d^2N_{part}}{dx d\tau}$  (depending on  $\tau$ ,  $T$ ,  $p$  and  $x$ ) must be stored in a four-dimensional array. Tabulating such functions is done adaptively, with the density of evaluated points varying, depending on the function behaviour (i.e., using a denser grid where the functions change rapidly and sparser





where the behaviour is smooth). In the case of these two functions, not only that the consequent interpolation can significantly reduce the overall number of integral evaluations, but the corresponding tables (for each particle type) can be evaluated only once and then permanently stored and reused for all trajectories and even for different temperature profiles. To further optimise the algorithm, we also precalculate the integral  $\int \frac{d^2 N_{rad}}{dx d\tau} dx$  values and store a corresponding three-dimensional array (since it is a function of  $\tau$ ,  $T$ , and  $p$ ).

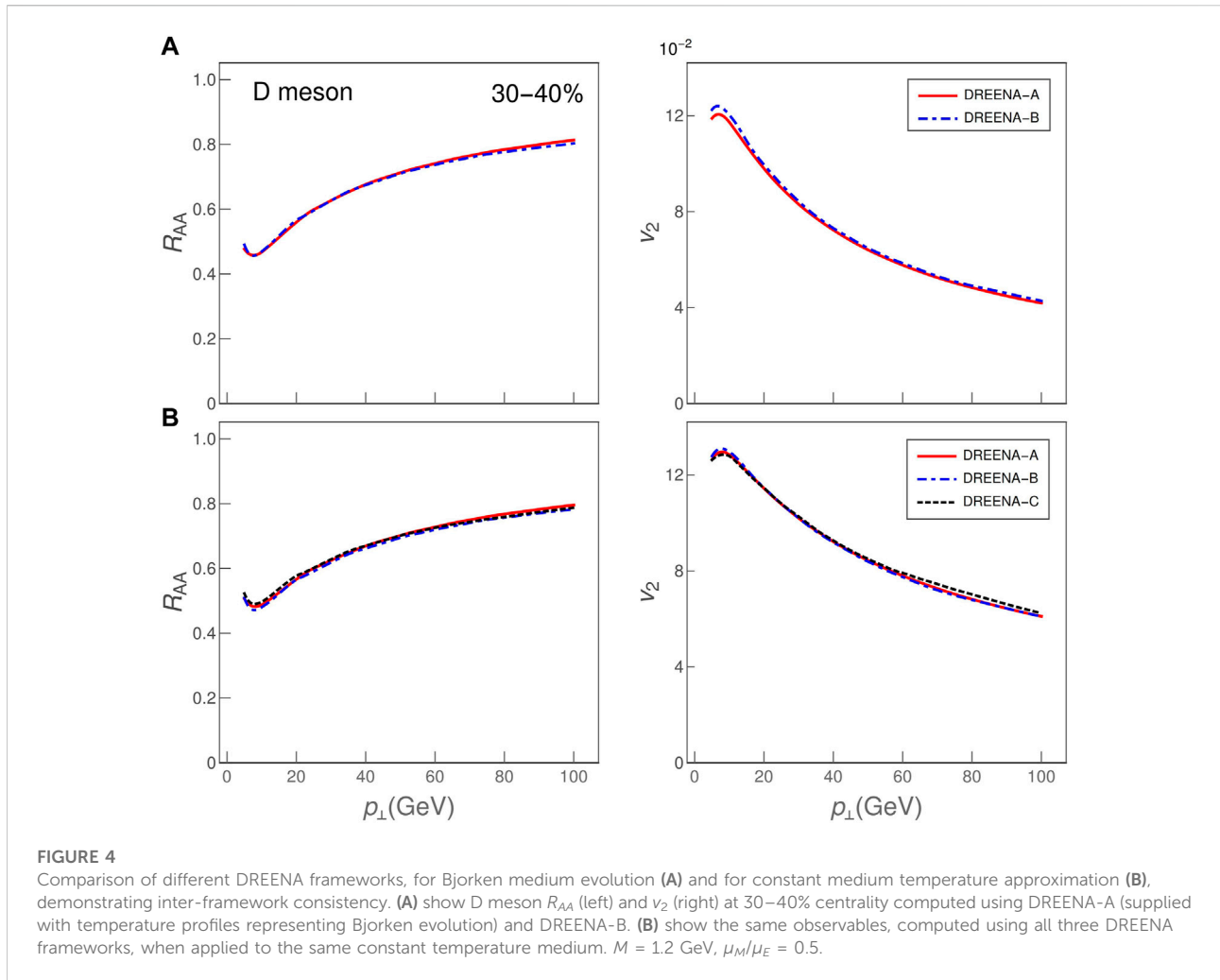
When using this table-interpolation method, it is often necessary to make a function transformation before tabulation: e.g., it is more efficient and accurate to sample and later interpolate logarithm of a rapidly (nearly or approximately-exponentially) increasing function than the function itself (similarly, it is sometimes more optimal to tabulate ratio, or a product of functions than each of the functions separately). For example, it is much more optimal to tabulate and consecutively interpolate  $R_{AA}$ s (and other similarly behaving expressions) than



the corresponding momentum distributions. This methodology is now extensively applied throughout DREENA-A (from some intermediate-level energy loss results to evaluating multi-dimensional integrals in the calculation of radiated gluon rates). Given the size of some of these tables and that many

interpolations are needed, we ensured that the table lookup and interpolation algorithm are efficient.

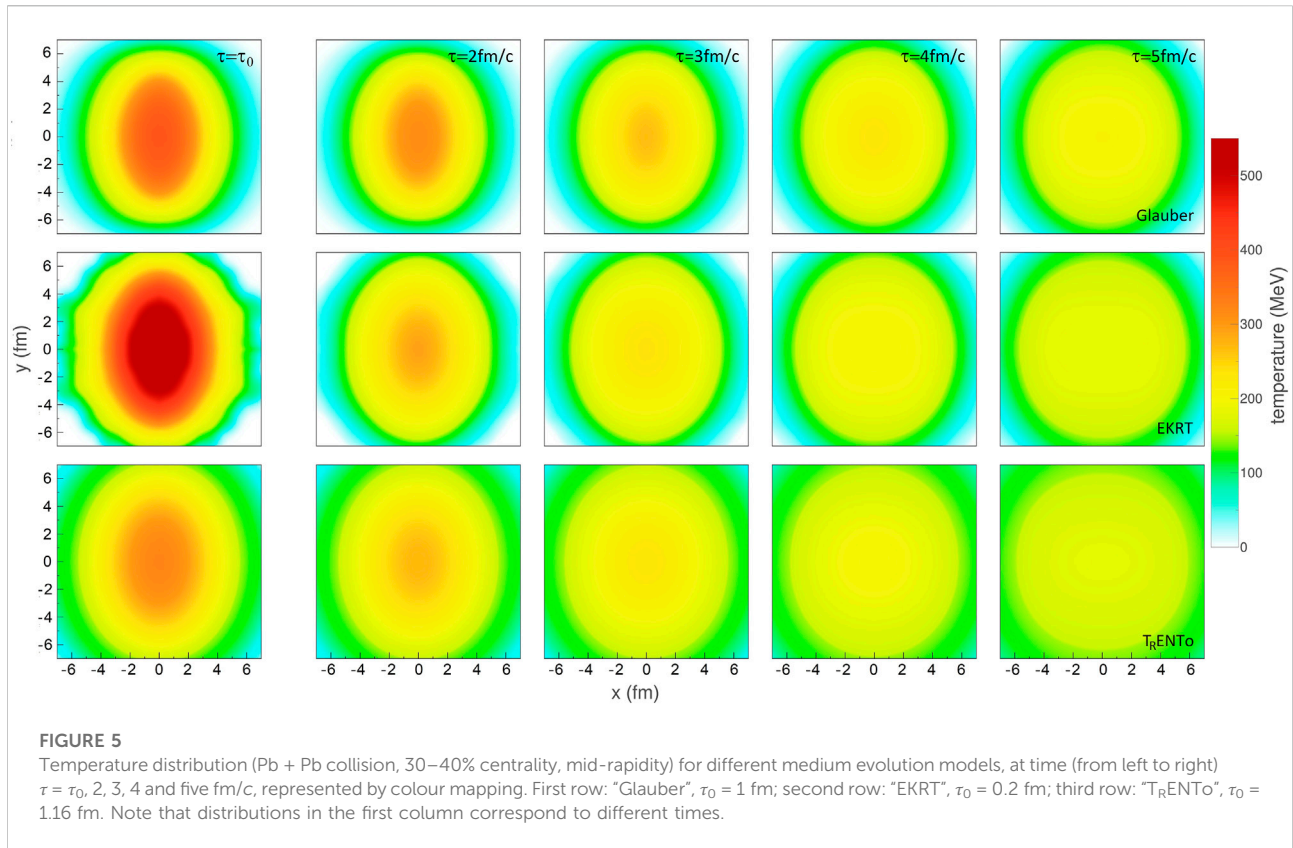
As we encounter multiple numerical integrations at different stages of the computation, modifying their order was another type of optimisation, where the natural order (from the



theoretical viewpoint) is not necessarily followed but is instead adapted to the particular function behaviour. Specifically, it turned out that a different order of integration (for radiative contribution) is optimal for heavy flavor particles compared to gluons. I.e., while it is natural, from the physical perspective, to start with the initial momentum distributions of partons and integrate over the radiative energy loss (see Eqs 9 and 10), it turned out that (for heavy flavors) the shape of the initial distributions necessitates a very high number of integration points to achieve the required computation precision. Reorganising the formulas and postponing the integration over initial distributions to the very end turned much more computationally optimal for heavy flavor. A similar procedure in the case of light quarks allowed much of the integration to be carried out jointly for all quarks, since their effective masses are the same, but initial  $p_{\perp}$  distributions differ.

The crucial optimisation in DREENA-A is the method used for averaging over the particle trajectories. In suppression calculations, it is common to carry out the averaging over

production points and directions by Monte Carlo (MC) sampling, but it turned out that the equidistant sampling of both jet production points and direction angles was here significantly more efficient. We initially implemented the Monte Carlo approach, randomly selecting both the origin coordinates and the angles of particle trajectories. The binary collision density was used as the probability density for coordinates of origins, while the angles were generated from a uniform distribution. Convergence of the results by using this method required a large number of sampled trajectories, as illustrated in Figure 1. The figure shows  $R_{AA}$  and  $v_2$  results obtained by the DREENA-A algorithm for a different total number of trajectories (the computation was done for D meson traversing the temperature evolution generated using a Glauber initialised viscous hydrodynamic code [78], at 30–40% centrality class). The plots in the right column of Figure 1 show the magnitude of the deviation of the particular curve from the median curve, where the latter is the arithmetic mean of all curves in the plot (as the measure of deviation of a function  $f(p)$  from a



reference function  $\bar{f}(p)$  we use  $|\delta f| = \frac{\int |f(p) - \bar{f}(p)| dp}{\int \bar{f}(p) dp}$ . We see that  $R_{AA}$  convergence is easily achieved, where relative deviations of the order of 1% are obtained by taking into account only 2,500 trajectories (see Figure 1-A and Figure 1-A\*). Computing the  $\nu_2$  value requires much more trajectories, i.e., we see a substantial scattering of the Monte Carlo results with 2,500 trajectories, while  $\sim 10^6$  trajectories are needed to reduce relative deviation below 1%. Note that a small number of sampled trajectories also causes a systematic error: the smaller the number of trajectories, the lower the averaged  $\nu_2$ .

When using the equidistant sampling method instead of Monte Carlo, we divide the transverse plane into an equidistant grid, whose points are used as jet origins. Energy loss for each trajectory is then weighted with the jet production probability at each point, and summed up. As production probability, we used the binary collision density evaluated using the optical Glauber model. In Figure 2, we see that, for already  $\sim 10,000$  evaluated trajectories, the integral has converged within 1% of the estimated ‘proper’ value. This modification resulted in a more than two orders of magnitude reduction of the execution time. We also tested two hybrid variants: 1) where trajectory origins were randomly selected but directions equidistantly, and 2) where production points were equidistantly selected, but directions randomly sampled. The convergence of the two variants interpolated between the

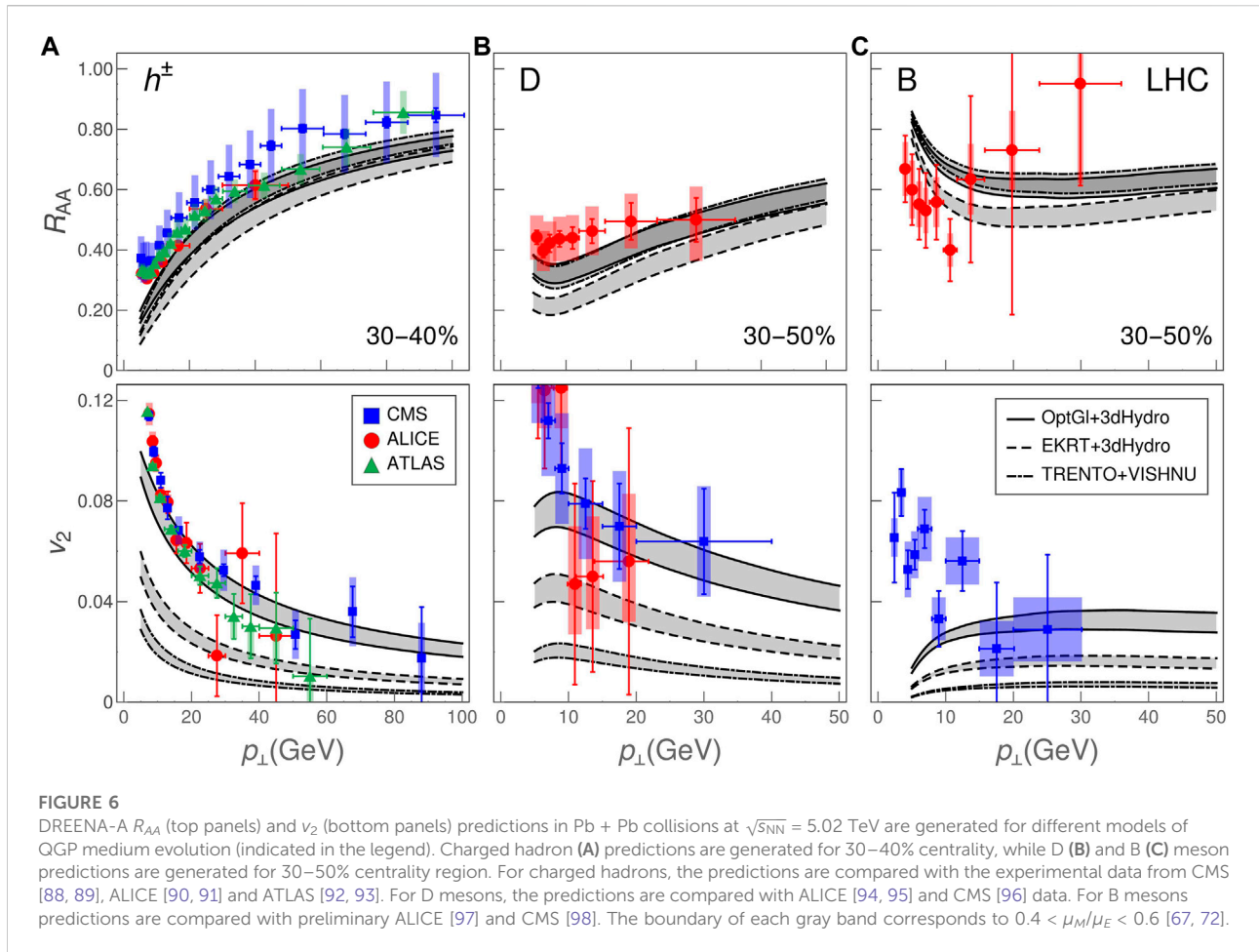
MC sampling and the equidistant sampling (Figures 1, 2, respectively).

## 2.4 Convergence test of different DREENA methods

Finally, as a consistency check for DREENA-A, we compared its predictions with DREENA-C and DREENA-B results. For this purpose, we generated artificial  $T$  profiles suitable for this comparison, illustrated in Figure 3. The results of the DREENA-A and DREENA-B comparison, for  $R_{AA}$  and  $\nu_2$ , are shown in the upper panels of Figure 4, respectively. Lower panels of Figure 4 show the comparison of all three frameworks on the hard-cylinder collision profile constant in time (for this comparison, we modified the DREENA-B code to remove temperature dependence on time). We see that all frameworks lead to consistent results (up to computational precision), supporting the reliability of the DREENA-A.

## 3 Results and discussion

To demonstrate the utility of the DREENA-A approach, we generated temperature profiles for Pb + Pb collisions at the full



LHC energy ( $\sqrt{s_{NN}} = 5.02$  TeV) and Au + Au collisions at the full RHIC energy ( $\sqrt{s_{NN}} = 200$  GeV) using three different initialisations of the fluid-dynamical expansion.

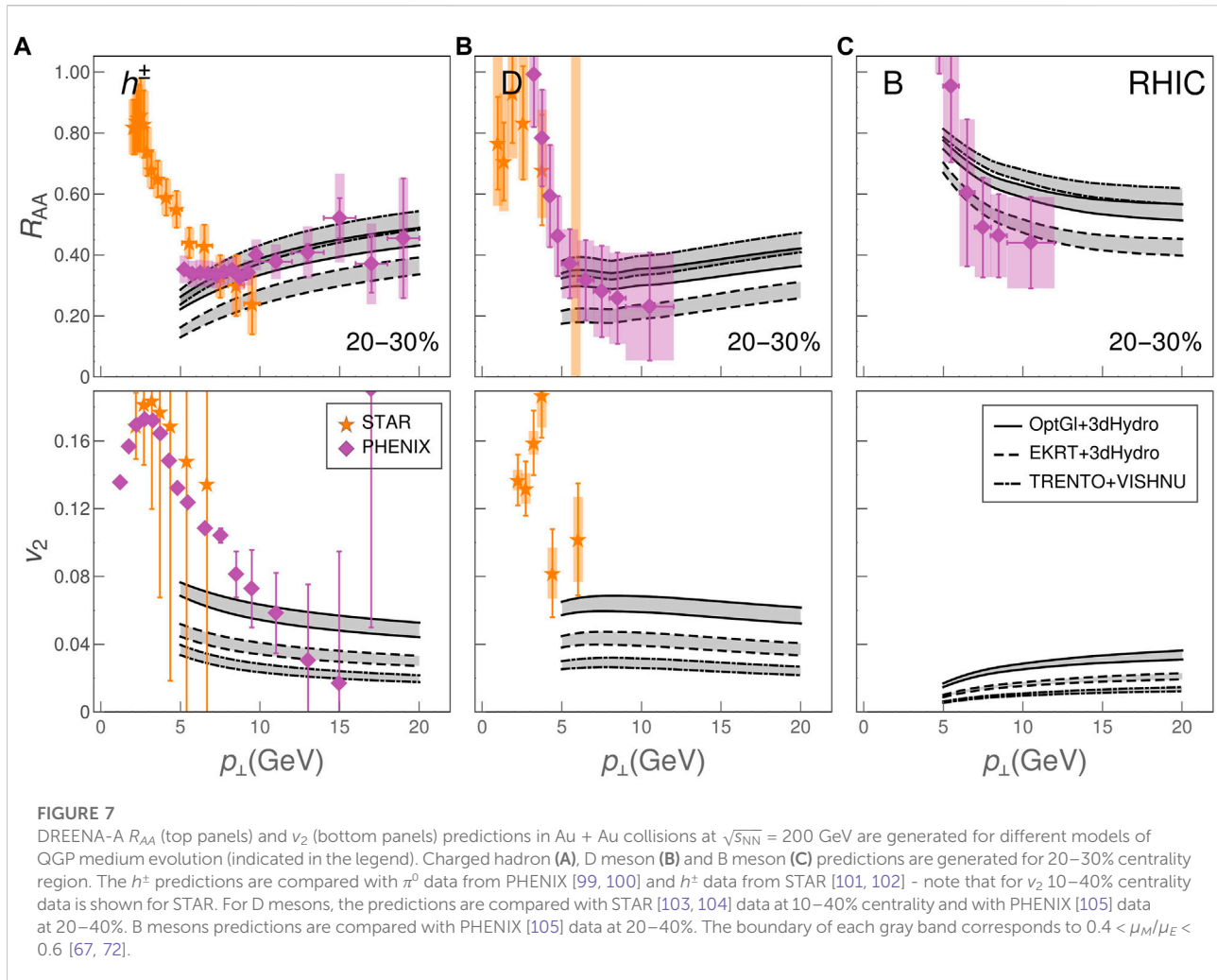
First, we used optical Glauber initialisation at initial time  $\tau_0 = 1.0$  fm without initial transverse flow. The evolution of the fluid was calculated using a 3+1D viscous fluid code from Ref. [78]. The parameters to describe collisions at the LHC energy were tuned to reproduce the low- $p_{\perp}$  data obtained in Pb + Pb collisions at  $\sqrt{s_{NN}} = 5.02$  TeV [32]. In particular, shear viscosity over entropy density ratio was constant  $\eta/s = 0.12$ , there was no bulk viscosity, and the equation of state (EoS) parametrisation was  $s95p$ -PCE-v1 [79]. For RHIC energy we used ‘LH-LQ’ parameters from Ref. [78], except that we used constant  $\eta/s = 0.16$ . Binary collision density from Glauber model was used as the probability distribution for the initial points of jets, while their directions were sampled from a uniform angular distribution.

Second, we used the EKRT initialisation [80–82], and evolved it using the same code we used to evolve the Glauber initialisation, but restricted to a boost-invariant expansion. In this case, the initial time was  $\tau_0 = 0.2$  fm, and parameters were the favoured values of a Bayesian analysis of the data from Pb + Pb

collisions at  $\sqrt{s_{NN}} = 2.76$  and 5.02 GeV, and from Au + Au collisions at  $\sqrt{s_{NN}} = 200$  GeV using the EoS parametrisation  $s83s_{18}$  [19]. In particular, there was no bulk viscosity and the minimum value of temperature-dependent  $\eta/s$  was 0.18. Origins of the high- $p_{\perp}$  particles were sampled using the binary collision density of Glauber model, while the distribution of their directions was uniform.

Our third option was the T<sub>R</sub>ENTo initialisation [83] evolved using the VISH2+1 code [84] as described in [85, 86]. To describe collisions at LHC, parameters were based on a Bayesian analysis of the data at the above mentioned two LHC collision energies [86], although the analysis was done event-by-event, whereas we carried out the calculations using simple event-averaged initial states. In particular, the calculation included free streaming stage until  $\tau_0 = 1.16$  fm, EoS based on the lattice results by the HotQCD collaboration [77], and temperature-dependent shear and bulk viscosity coefficients with the minimum value of  $(\eta/s)_{\min} = 0.081$  and maximum of  $(\zeta/s)_{\max} = 0.052$ . For RHIC, we used the ‘PTB’ maximum *a posteriori* parameter values from Ref. [87], but changed the temperature-dependent shear viscosity coefficient  $(\eta/s)(T)$  to a constant  $\eta/s = 0.16$ . The initial event-by-event





collision points were used to generate the spatial probability distribution for the initial coordinates of the high- $p_\perp$  particles, while their angular distribution was uniform.

All these calculations lead to an acceptable fit to measured charged hadron multiplicities, low- $p_\perp$  spectra, and  $p_\perp$ -differential  $v_2$  in 10–20%, 20–30%, 30–40%, and 40–50% centrality classes. As we may expect, different initialisations and initial times lead to a visibly different temperature evolution. This is demonstrated in Figure 5 where we show the calculated temperature distributions in collisions at the LHC energy at various times. Looking at the profiles, it is easily noticeable that they evolve differently in space and time. Even if the initial anisotropy of the Glauber initialisation is lowest, later in time, its anisotropy is largest, since the very early start of EKRT initialisation, or the early free streaming of T<sub>R</sub>ENTo, dilute the spatial anisotropy very fast. That is, “Glauber” exhibits larger asymmetry throughout the QGP evolution compared to the other two profiles (though “EKRT” has larger asymmetry than “Trento”), which might accordingly translate to differences in high- $p_\perp$   $v_2$ . Similarly,

the early start of EKRT leads to a large initial temperature, which is expected to result in a smaller  $R_{AA}$  than the other two profiles.

To test if these visual differences can be quantified through high- $p_\perp$  data at the LHC and RHIC, we used these profiles as an input to the DREENA-A to generate high- $p_\perp$   $R_{AA}$  and  $v_2$  predictions for charged hadrons, D and B mesons. As can be seen in Figures 6, 7, both  $R_{AA}$  and  $v_2$  show notable differences for both experiments and all types of flavor. For example, “EKRT” leads to the smallest  $R_{AA}$ , i.e., largest suppression, as can be expected based on the largest temperature. Similarly, the calculated high- $p_\perp$   $v_2$  depicts the same ordering as the system anisotropy during the evolution: “Glauber” leads to the largest, followed by “EKRT”, while T<sub>R</sub>ENTo leads to the lowest  $v_2$ . Consequently, the DREENA-A framework can differentiate between temperature profiles by corresponding differences in high- $p_\perp$  observables, where these differences agree with the qualitative observations from Figure 5. Since the differences in evolution are due to different initialisations, and different

properties of the fluid (EoS and/or dissipative coefficients),  $R_{AA}$  and  $v_2$  observables can be used to provide further constraints to the fluid properties. We note here that even low- $p_{\perp}$  data could be used to differentiate our three evolution scenarios, but such analysis would require evaluating  $\chi^2$  or a similar measure of the quality of the fit, or computing Bayes factors [87]. The high- $p_{\perp}$  observables, on the other hand, show clear differences visible by the naked eye.

Moreover, from Figures 6, 7, we see that all types of flavor, at both RHIC and LHC, show apparent sensitivity to differences in medium evolution, making them equally suitable for exploring the bulk QGP properties with high- $p_{\perp}$  data. With the expected availability of precision data from the upcoming high-luminosity experiments at RHIC and LHC (see e.g. [106–108]), the DREENA-A framework provides a unique opportunity for exploring the bulk QGP properties. We propose that the adequate medium evolution should be able to reproduce high- $p_{\perp}$  observables in both RHIC and LHC experiments for different collision energies and collision systems, with reasonable accuracy. As demonstrated in this study, an equal emphasis should be given to light and heavy flavor, as they provide a valuable independent constraint for bulk medium evolution. Overall, DREENA-A provides a versatile tool to put large amounts of data generated at RHIC and LHC experiments to optimal use.

We also observe that none of the profiles analysed in Figures 6, 7 lead to satisfactory agreement with high- $p_{\perp}$   $R_{AA}$  and  $v_2$  data. However, we note that the goal of this study is not to get a good agreement with the experimental data, but to demonstrate that 1) different temperature profiles lead to different high- $p_{\perp}$  predictions, 2) high- $p_{\perp}$  data can provide an important further constraint in exploring the QGP properties. Finding suitable temperature profiles (i.e., QGP parameters) that would lead to a reasonable agreement with high- $p_{\perp}$  data is a highly non-trivial task which is left for further work.

## 4 Summary

We presented the DREENA-A computational framework for tomography of Quark-Gluon Plasma created in heavy-ion collisions at RHIC and the LHC. The tool is based on state-of-the-art energy loss calculation and can include arbitrary temperature profiles. This feature allows fully exploiting different temperature profiles as the only input in the framework. We showed that the calculated high- $p_{\perp}$   $R_{AA}$  and  $v_2$  exhibit notable sensitivity to the details of the temperature profiles, consistent with intuitive expectations based on the profile visualisation. The DREENA-A framework applies to different types of flavor, collision systems, and collision energies. It can, consequently, provide an efficient and versatile QGP tomography tool for further constraining the bulk properties of this extreme form of matter. To facilitate

this, we also provided the fully optimized, publicly available software for generating DREENA-A predictions. The code allows straightforwardly generating high- $p_{\perp}$  predictions for diverse models of QGP evolution.

## Data availability statement

The original contributions presented in the study are included in the article, further inquiries can be directed to the corresponding author. The source code of the DREENA-A algorithm (together with usage instructions and example data), can be found at <https://github.com/DusanZigic/DREENA-A>.

## Author contributions

All authors listed have made a substantial, direct, and intellectual contribution to the work and approved it for publication.

## Funding

This work is supported by the European Research Council, grant ERC-2016-COG: 725741, and by the Ministry of Science and Technological Development of the Republic of Serbia. PH was also supported by the program Excellence Initiative–Research University of the University of Wrocław of the Ministry of Education and Science.

## Acknowledgments

We thank Marko Djordjevic, Bojana Ilic, and Stefan Stojku for useful discussions.

## Conflict of interest

The authors declare that the research was conducted in the absence of any commercial or financial relationships that could be construed as a potential conflict of interest.

## Publisher's note

All claims expressed in this article are solely those of the authors and do not necessarily represent those of their affiliated organizations, or those of the publisher, the editors and the reviewers. Any product that may be evaluated in this article, or claim that may be made by its manufacturer, is not guaranteed or endorsed by the publisher.

## References

- Collins JC, Perry MJ. Superdense matter: Neutrons or asymptotically free quarks? *Phys Rev Lett* (1975) 34:1353–6. doi:10.1103/PhysRevLett.34.1353
- Baym G, Chin S. Can a neutron star be a giant mit bag? *Phys Lett B* (1976) 62: 241–4. doi:10.1016/0370-2693(76)90517-7
- Shuryak EV. What RHIC experiments and theory tell us about properties of quark-gluon plasma? *Nucl Phys A* (2005) 750:64–83. doi:10.1016/j.nuclphysa.2004.10.022
- Shuryak E. Strongly coupled quark-gluon plasma in heavy ion collisions. *Rev Mod Phys* (2017) 89:035001. doi:10.1103/RevModPhys.89.035001
- Gyulassy M, McLerran L. New forms of QCD matter discovered at RHIC. *Nucl Phys A* (2005) 750:30–63. doi:10.1016/j.nuclphysa.2004.10.034
- Jacak B, Steinberg P. Creating the perfect liquid in heavy-ion collisions. *Phys Today* (2010) 63N5:39–43. doi:10.1063/1.3431330
- Muller B, Schukraft J, Wyslouch B. First results from Pb+Pb collisions at the LHC. *Annu Rev Nucl Part Sci* (2012) 62:361–86. doi:10.1146/annurev-nucl-102711-094910
- Stock R. The physics of dense nuclear matter from supernovae to quark gluon plasma. *Nature* (1989) 337:319–24. doi:10.1038/337319a0
- Stachel J. Has the quark-gluon plasma been seen? *Int J Mod Phys A* (2006) 21: 1750–63. doi:10.1142/S0217751X06032733
- Kolb PF, Heinz UW. Hydrodynamic description of ultrarelativistic heavy ion collisions. In: *Quark-Gluon Plasma* (2004) 3: 634–714. doi:10.1142/9789812795533\_0010
- Romatschke P, Romatschke U. Viscosity information from relativistic nuclear collisions: How perfect is the fluid observed at RHIC? *Phys Rev Lett* (2007) 99: 172301. doi:10.1103/PhysRevLett.99.172301
- Heinz U, Snellings R. Collective flow and viscosity in relativistic heavy-ion collisions. *Annu Rev Nucl Part Sci* (2013) 63:123–51. doi:10.1146/annurev-nucl-102212-170540
- Adams J, Aggarwal M, Ahammed Z, Amonett J, Anderson B, Arkhipkin D, et al. Experimental and theoretical challenges in the search for the quark gluon plasma: The STAR Collaboration's critical assessment of the evidence from RHIC collisions. *Nucl Phys A* (2005) 757:102–83. doi:10.1016/j.nuclphysa.2005.03.085
- Adcox K, Adler S, Afanasiev S, Aidala C, Ajitanand N, Akiba Y, et al. Formation of dense partonic matter in relativistic nucleus-nucleus collisions at RHIC: Experimental evaluation by the PHENIX collaboration. *Nucl Phys A* (2005) 757:184–283. doi:10.1016/j.nuclphysa.2005.03.086
- Aad G, Abbott B, Abdallah J, Abdelalim AA, Abdesselam A, Abidinov O, et al. Observation of a centrality-dependent dijet asymmetry in lead-lead collisions at  $\sqrt{s_{NN}} = 2.76$  TeV with the ATLAS detector at the LHC. *Phys Rev Lett* (2010) 105: 252303. doi:10.1103/PhysRevLett.105.252303
- Aamodt K, Abrahantes Quintana A, Adamova D, Adare A, Aggarwal M, Aglieri Rinella G, et al. Suppression of charged particle production at large transverse momentum in central Pb–Pb collisions at  $\sqrt{s_{NN}} = 2.76$  TeV. *Phys Lett B* (2011) 696:30–9. doi:10.1016/j.physletb.2010.12.020
- Chatrchyan S, Khachatryan V, Sirunyan AM, Tumasyan A, Adam W, Bergauer T, et al. Observation and studies of jet quenching in PbPb collisions at  $\sqrt{s_{NN}} = 2.76$  TeV. *Phys Rev C* (2011) 84:024906. doi:10.1103/PhysRevC.84.024906
- Nagle JL, Bearden IG, Zajc WA. Quark-gluon plasma at RHIC and the LHC: Perfect fluid too perfect? *New J Phys* (2011) 13:075004. doi:10.1088/1367-2630/13/7/075004
- Auvinen J, Eskola KJ, Huovinen P, Niemi H, Paatelainen R, Petreczky P. Temperature dependence of  $\eta/s$  of strongly interacting matter: Effects of the equation of state and the parametric form of  $(\eta/s)(T)$ . *Phys Rev C* (2020) 102: 044911. doi:10.1103/PhysRevC.102.044911
- Orjuela Koop JD, Adare A, McGlinchey D, Nagle JL. Azimuthal anisotropy relative to the participant plane from a multiphase transport model in central p + Au, d + Au, and  $^3\text{He} + \text{Au}$  collisions at  $\sqrt{s_{NN}} = 200$  GeV. *Phys Rev C* (2015) 92: 054903. doi:10.1103/PhysRevC.92.054903
- Auvinen J, Bernhard JE, Bass SA, Karpenko I. Investigating the collision energy dependence of  $\eta/s$  in the beam energy scan at the BNL Relativistic Heavy Ion Collider using Bayesian statistics. *Phys Rev C* (2018) 97:044905. doi:10.1103/PhysRevC.97.044905
- Kapusta JJ. *Finite temperature field theory*. Cambridge: Cambridge Monographs on Mathematical Physics Cambridge University Press (1989).
- Bellac ML. *Thermal field theory*. Cambridge, UK: Cambridge Monographs on Mathematical Physics Cambridge University Press (2011).
- Djordjevic M. Collisional energy loss in a finite size QCD matter. *Phys Rev C* (2006) 74:064907. doi:10.1103/PhysRevC.74.064907
- Djordjevic M. Theoretical formalism of radiative jet energy loss in a finite size dynamical QCD medium. *Phys Rev C* (2009) 80:064909. doi:10.1103/PhysRevC.80.064909
- Djordjevic M, Heinz UW. Radiative energy loss in a finite dynamical QCD medium. *Phys Rev Lett* (2008) 101:022302. doi:10.1103/PhysRevLett.101.022302
- Stojku S, Ilic B, Djordjevic M, Djordjevic M. Extracting the temperature dependence in high- $p_{\perp}$  particle energy loss. *Phys Rev C* (2021) 103:024908. doi:10.1103/PhysRevC.103.024908
- Djordjevic M, Djordjevic M. Generalization of radiative jet energy loss to non-zero magnetic mass. *Phys Lett B* (2012) 709:229–33. doi:10.1016/j.physletb.2012.02.019
- Aurenche P, Gelis F, Zaraket H. A Simple sum rule for the thermal gluon spectral function and applications. *J High Energy Phys* (2002) 05:043. doi:10.1088/1126-6708/2002/05/043
- Peigne S, Peshier A. Collisional energy loss of a fast heavy quark in a quark-gluon plasma. *Phys Rev D* (2008) 77:114017. doi:10.1103/PhysRevD.77.114017
- Djordjevic M, Djordjevic M. LHC jet suppression of light and heavy flavor observables. *Phys Lett B* (2014) 734:286–9. doi:10.1016/j.physletb.2014.05.053
- Stojku S, Auvinen J, Djordjevic M, Huovinen P, Djordjevic M. Early evolution constrained by high- $p_{\perp}$  quark-gluon plasma tomography. *Phys Rev C* (2022) 105: L021901. doi:10.1103/PhysRevC.105.L021901
- Stojku S, Auvinen J, Zivkovic L, Huovinen P, Djordjevic M. Jet-temperature anisotropy revealed through high- $p_{\perp}$  data. *Physics Letters B*, in press (2022).
- Djordjevic M, Djordjevic M, Blagojevic B. RHIC and LHC jet suppression in non-central collisions. *Phys Lett B* (2014) 737:298–302. doi:10.1016/j.physletb.2014.08.063
- Djordjevic M, Djordjevic M. Predictions of heavy-flavor suppression at 5.1 TeV Pb + Pb collisions at the CERN large hadron collider. *Phys Rev C* (2015) 92:024918. doi:10.1103/PhysRevC.92.024918
- Djordjevic M. Heavy flavor puzzle at LHC: A serendipitous interplay of jet suppression and fragmentation. *Phys Rev Lett* (2014) 112:042302. doi:10.1103/PhysRevLett.112.042302
- Djordjevic M. Complex suppression patterns distinguish between major energy loss effects in Quark-Gluon Plasma. *Phys Lett B* (2016) 763:439–44. doi:10.1016/j.physletb.2016.10.077
- Baier R, Dokshitzer YL, Mueller AH, Peigne S, Schiff D. Radiative energy loss and  $p_{\perp}$  broadening of high energy partons in nuclei. *Nucl Phys B* (1997) 484:265–82. doi:10.1016/S0550-3213(96)00581-0
- Zakharov BG. Fully quantum treatment of the Landau-Pomeranchik-Migdal effect in QED and QCD. *JETP Lett* (1996) 63:952–7. doi:10.1134/1.567126
- Zakharov BG. Radiative energy loss of high-energy quarks in finite size nuclear matter and quark-gluon plasma. *JETP Lett* (1997) 65:615–20. doi:10.1134/1.567389
- Armesto N, Salgado CA, Wiedemann UA. Medium induced gluon radiation off massive quarks fills the dead cone. *Phys Rev D* (2004) 69:114003. doi:10.1103/PhysRevD.69.114003
- Gyulassy M, Levai P, Vitev I. Reaction operator approach to nonAbelian energy loss. *Nucl Phys B* (2001) 594:371–419. doi:10.1016/S0550-3213(00)00652-0
- Arnold PB, Moore GD, Yaffe LG. Photon emission from ultrarelativistic plasmas. *J High Energy Phys* (2001) 11:057. doi:10.1088/1126-6708/2001/11/057
- Arnold PB, Moore GD, Yaffe LG. Photon emission from quark gluon plasma: Complete leading order results. *J High Energy Phys* (2001) 12:009. doi:10.1088/1126-6708/2001/12/009
- Li H, Liu F, Ma G, Wang XN, Zhu Y. Mach cone induced by  $\gamma$ -triggered jets in high-energy heavy-ion collisions. *Phys Rev Lett* (2011) 106:012301. doi:10.1103/PhysRevLett.106.012301
- Sadofyev AV, Sievert MD, Vitev I. *Ab initio* coupling of jets to collective flow in the opacity expansion approach. *Phys Rev D* (2021) 104:094044. doi:10.1103/PhysRevD.104.094044
- Antiporda L, Bahder J, Rahman H, Sievert MD. Jet drift and collective flow in heavy-ion collisions. *Phys Rev D* (2022) 105:054025. doi:10.1103/PhysRevD.105.054025

48. Barata J, Sadofyev AV, Salgado CA. Jet broadening in dense inhomogeneous matter. *Phys Rev D* (2022) 105:114010. doi:10.1103/PhysRevD.105.114010
49. Blagojevic B, Djordjevic M. Importance of different energy loss effects in jet suppression at the RHIC and the LHC. *J Phys G: Nucl Part Phys* (2015) 42:075105. doi:10.1088/0954-3899/42/7/075105
50. Zigic D, Salom I, Auvinen J, Djordjevic M, Djordjevic M. DREENA-C framework: Joint  $R_{AA}$  and  $v_2$  predictions and implications to QGP tomography. *J Phys G: Nucl Part Phys* (2019) 46:085101. doi:10.1088/1361-6471/ab2356
51. Zigic D, Salom I, Auvinen J, Djordjevic M, Djordjevic M. DREENA-B framework: First predictions of  $R_{AA}$  and  $v_2$  within dynamical energy loss formalism in evolving QCD medium. *Phys Lett B* (2019) 791:236–41. doi:10.1016/j.physletb.2019.02.020
52. Wicks S, Horowitz W, Djordjevic M, Gyulassy M. Elastic, inelastic, and path length fluctuations in jet tomography. *Nucl Phys A* (2007) 784:426–42. doi:10.1016/j.nuclphysa.2006.12.048
53. Djordjevic M, Gyulassy M, Vogt R, Wicks S. Influence of bottom quark jet quenching on single electron tomography of au+au. *Phys Lett B* (2006) 632:81–6. doi:10.1016/j.physletb.2005.09.087
54. Kang ZB, Vitev I, Xing H. Nuclear modification of high transverse momentum particle production in p+A collisions at RHIC and LHC. *Phys Lett B* (2012) 718:482–7. doi:10.1016/j.physletb.2012.10.046
55. Sharma R, Vitev I, Zhang BW. Light-cone wave function approach to open heavy flavor dynamics in QCD matter. *Phys Rev C* (2009) 80:054902. doi:10.1103/PhysRevC.80.054902
56. Cacciari M, Frixione S, Houdeau N, Mangano ML, Nason P, Ridolfi G. Theoretical predictions for charm and bottom production at the LHC. *J High Energy Phys* (2012) 10:137. doi:10.1007/jhep10(2012)137
57. Gyulassy M, Levai P, Vitev I. Jet tomography of Au+Au reactions including multigluon fluctuations. *Phys Lett B* (2002) 538:282–8. doi:10.1016/S0370-2693(02)01990-1
58. Moore GD, Teaney D. How much do heavy quarks thermalize in a heavy ion collision? *Phys Rev C* (2005) 71:064904. doi:10.1103/PhysRevC.71.064904
59. de Florian D, Sassot R, Stratmann M. Global analysis of fragmentation functions for pions and kaons and their uncertainties. *Phys Rev D* (2007) 75:114010. doi:10.1103/PhysRevD.75.114010
60. Cacciari M, Nason P. Charm cross-sections for the tevatron run II. *J High Energy Phys* (2003) 09:006. doi:10.1088/1126-6708/2003/09/006
61. Braaten E, Cheung K, Fleming S, Yuan TC. Perturbative QCD fragmentation functions as a model for heavy quark fragmentation. *Phys Rev D* (1995) 51:4819–29. doi:10.1103/PhysRevD.51.4819
62. Kartvelishvili VG, Likhoded AK, Petrov VA. On the fragmentation functions of heavy quarks into hadrons. *Phys Lett B* (1978) 78:615–7. doi:10.1016/0370-2693(78)90653-6
63. Braaten E, Thoma MH. Energy loss of a heavy fermion in a hot QED plasma. *Phys Rev D* (1991) 44:1298–310. doi:10.1103/PhysRevD.44.1298
64. Selikhov A, Gyulassy M. Color diffusion and conductivity in a quark-gluon plasma. *Phys Lett B* (1993) 316:373–80. doi:10.1016/0370-2693(93)90341-E
65. Selikhov AV, Gyulassy M. QCD Fokker-Planck equations with color diffusion. *Phys Rev C* (1994) 49:1726–9. doi:10.1103/PhysRevC.49.1726
66. Peshier A. *Running coupling and screening in the (s)QGP* hep-ph/0601119 (2006).
67. Nakamura A, Saito T, Sakai S. Lattice calculation of gluon screening masses. *Phys Rev D* (2004) 69:014506. doi:10.1103/PhysRevD.69.014506
68. Field RD, Pines DA. *Appl Perturbative QCD*. Cambridge, Massachusetts: Perseus Books (1995).
69. Djordjevic M, Gyulassy M. Ter-Mikayelian effect on QCD radiative energy loss. *Phys Rev C* (2003) 68:034914. doi:10.1103/PhysRevC.68.034914
70. Tanabashi M, Hagiwara K, Hikasa K, Nakamura K, Sumino Y, Takahashi F, et al. Review of particle physics. *Phys Rev D* (2018) 98:030001. doi:10.1103/PhysRevD.98.030001
71. Beraudo A, Gossiaux P, Andronic A, Auerbeck R, Masciocchi S. Extraction of heavy-flavor transport coefficients in QCD matter. *Nucl Phys A* (2018) 979:21–86. doi:10.1016/j.nuclphysa.2018.09.002
72. Maezawa Y, Aoki S, Ejiri S, Hatsuda T, Ishii N, Kanaya K, et al. Electric and magnetic screening masses at finite temperature from generalized Polyakov-line correlations in two-flavor lattice QCD. *Phys Rev D* (2010) 81:091501. doi:10.1103/PhysRevD.81.091501
73. Djordjevic M. Heavy quark energy loss: Collisional vs radiative. *Nucl Phys A* (2007) 783:197–204. doi:10.1016/j.nuclphysa.2006.11.008
74. Fickinger M, Ovanessian G, Vitev I. Angular distributions of higher order splitting functions in the vacuum and in dense QCD matter. *J High Energy Phys* (2013) 07:059. doi:10.1007/JHEP07(2013)059
75. Luzum M, Petersen H. Initial state fluctuations and final state correlations in relativistic heavy-ion collisions. *J Phys G: Nucl Part Phys* (2014) 41:063102. doi:10.1088/0954-3899/41/6/063102
76. Bjorken JD. Highly relativistic nucleus-nucleus collisions: The central rapidity region. *Phys Rev D* (1983) 27:140–51. doi:10.1103/PhysRevD.27.140
77. Bazavov A, Bhattacharya T, DeTar C, Ding HT, Gottlieb S, Gupta R, et al. Equation of state in (2+1)-flavor QCD. *Phys Rev D* (2014) 90:094503. doi:10.1103/PhysRevD.90.094503
78. Molnar E, Holopainen H, Huovinen P, Niemi H. Influence of temperature-dependent shear viscosity on elliptic flow at backward and forward rapidities in ultrarelativistic heavy-ion collisions. *Phys Rev C* (2014) 90:044904. doi:10.1103/PhysRevC.90.044904
79. Huovinen P, Petreczky P. QCD equation of state and hadron resonance gas. *Nucl Phys A* (2010) 837:26–53. doi:10.1016/j.nuclphysa.2010.02.015
80. Eskola KJ, Kajantie K, Ruuskanen PV, Tuominen K. Scaling of transverse energies and multiplicities with atomic number and energy in ultrarelativistic nuclear collisions. *Nucl Phys B* (2000) 570:379–89. doi:10.1016/S0550-3213(99)00720-8
81. Paatelainen R, Eskola KJ, Holopainen H, Tuominen K. Multiplicities and  $p_T$  spectra in ultrarelativistic heavy ion collisions from a next-to-leading order improved perturbative QCD + saturation + hydrodynamics model. *Phys Rev C* (2013) 87:044904. doi:10.1103/PhysRevC.87.044904
82. Paatelainen R, Eskola KJ, Niemi H, Tuominen K. Fluid dynamics with saturated minijet initial conditions in ultrarelativistic heavy-ion collisions. *Phys Lett B* (2014) 731:126–30. doi:10.1016/j.physletb.2014.02.018
83. Moreland JS, Bernhard JE, Bass SA. Alternative ansatz to wounded nucleon and binary collision scaling in high-energy nuclear collisions. *Phys Rev C* (2015) 92:011901. doi:10.1103/PhysRevC.92.011901
84. Song H, Heinz UW. Causal viscous hydrodynamics in 2+1 dimensions for relativistic heavy-ion collisions. *Phys Rev C* (2008) 77:064901. doi:10.1103/PhysRevC.77.064901
85. Bernhard JE. *Bayesian parameter estimation for relativistic heavy-ion collisions*. Ph.D. thesis. Duke U. arXiv:1804.06469 (2018).
86. Bernhard JE, Moreland JS, Bass SA. Bayesian estimation of the specific shear and bulk viscosity of quark-gluon plasma. *Nat Phys* (2019) 15:1113–7. doi:10.1038/s41567-019-0611-8
87. Everett D, Ke W, Paquet JF, Vujanovic G, Bass SA, Du L, et al. Multisystem Bayesian constraints on the transport coefficients of QCD matter. *Phys Rev C* (2021) 103:054904. doi:10.1103/PhysRevC.103.054904
88. Khachatryan V, Sirunyan AM, Tumasyan A, Adam W, Asilar E, Bergauer T, et al. Charged-particle nuclear modification factors in PbPb and pPb collisions at  $\sqrt{s_{NN}} = 5.02$  TeV. *J High Energy Phys* (2017) 04:039. doi:10.1007/JHEP04(2017)039
89. Sirunyan AM, Tumasyan A, Adam W, Asilar E, Bergauer T, Brandstetter J, et al. Azimuthal anisotropy of charged particles with transverse momentum up to 100 GeV/c in PbPb collisions at  $\sqrt{s_{NN}} = 5.02$  TeV. *Phys Lett B* (2018) 776:195–216. doi:10.1016/j.physletb.2017.11.041
90. Acharya S, Acosta FT, Adamova D, Adolphsson J, Aggarwal MM, Aglieri Rinella G, et al. Transverse momentum spectra and nuclear modification factors of charged particles in pp, p-Pb and Pb-Pb collisions at the LHC. *J High Energy Phys* (2018) 11:013. doi:10.1007/JHEP11(2018)013
91. Acharya S, Acosta FT, Adamova D, Adolphsson J, Aggarwal MM, Aglieri Rinella G, et al. Energy dependence and fluctuations of anisotropic flow in Pb-Pb collisions at  $\sqrt{s_{NN}} = 5.02$  TeV and 2.76 TeV. *J High Energy Phys* (2018) 07:103. doi:10.1007/JHEP07(2018)103
92. *Measurement of nuclear modification factor  $R_{AA}$  in Pb+Pb collisions at  $\sqrt{s_{NN}} = 5.02$  TeV with the ATLAS detector at the LHC* ATLAS-CONF-2017-012 (2017).
93. Aaboud M, Aad G, Abbott B, Abdinov O, Abeloos B, Abhayasinghe DK, et al. Measurement of the azimuthal anisotropy of charged particles produced in  $\sqrt{s_{NN}} = 5.02$  TeV Pb+Pb collisions with the ATLAS detector. *Eur Phys J C* (2018) 78:997. doi:10.1140/epjc/s10052-018-6468-7
94. Acharya S. Measurement of  $D^0$ ,  $D^+$ ,  $D^{*+}$  and  $D_s^+$  production in Pb-Pb collisions  $\sqrt{s_{NN}} = 5.02$  TeV. *JHEP* (2018) 10:174. doi:10.1007/JHEP10.174
95. Acharya S, Adamova D, Adolphsson J, Aggarwal MM, Aglieri Rinella G, Agnello M, et al. D-meson azimuthal anisotropy in midcentral Pb-Pb collisions at  $\sqrt{s_{NN}} = 5.02$  TeV. *Phys Rev Lett* (2018) 120:102301. doi:10.1103/PhysRevLett.120.102301

96. Sirunyan AM, Tumasyan A, Adam W, Ambrogio F, Asilar E, Bergauer T, et al. Measurement of prompt  $D^0$  meson azimuthal anisotropy in Pb-Pb collisions at  $\sqrt{s_{NN}} = 5.02$  TeV. *Phys Rev Lett* (2018) 120:202301. doi:10.1103/PhysRevLett.120.202301
97. Peng X. *Beauty production in heavy-ion collisions with ALICE at the LHC*, arXiv:2207.10259 (2022).
98. Kim Y. Highlights from the CMS experiment. In: Plenary talk at Quark Matter 2022 conference (2022).
99. Adare A, Afanasiev S, Aidala C, Ajitanand NN, Akiba Y, Al-Bataineh H, et al. Neutral pion production with respect to centrality and reaction plane in Au+Au collisions at  $\sqrt{s_{NN}} = 200$  GeV. *Phys Rev C* (2013) 87:034911. doi:10.1103/PhysRevC.87.034911
100. Adare A, Afanasiev S, Aidala C, Ajitanand NN, Akiba Y, Al-Bataineh H, et al. Azimuthal anisotropy of  $\pi^0$  Production in Au + Au Collisions at  $\sqrt{s_{NN}} = 200$  GeV: Path-length dependence of jet quenching and the role of initial geometry. *Phys Rev Lett* (2010) 105:142301. doi:10.1103/PhysRevLett.105.142301
101. Adams J, Adler C, Aggarwal MM, Ahammed Z, Amonett J, Anderson BD, et al. Transverse-momentum and collision-energy dependence of High- $p_T$  Hadron Suppression in Au + Au Collisions at ultrarelativistic Energies. *Phys Rev Lett* (2003) 91:172302. doi:10.1103/PhysRevLett.91.172302
102. Abelev BI, Aggarwal MM, Ahammed Z, Anderson BD, Arkhipkin D, Averichev GS, et al. Centrality dependence of charged hadron and strange hadron elliptic flow from  $\sqrt{s_{NN}} = 200$  GeV. *Phys Rev C* (2008) 77:054901. doi:10.1103/PhysRevC.77.054901
103. Adamczyk L, Adkins J, Agakishiev G, Aggarwal M, Ahammed Z, Alekseev I, et al. Observation of  $D^0$  meson nuclear modifications in Au+Au collisions at  $\sqrt{s_{NN}} = 200$  GeV. *Phys Rev Lett* (2014) 113:142301. [Erratum: Phys.Rev.Lett. 121, 229901 (2018)]. doi:10.1103/PhysRevLett.113.142301
104. Adamczyk L, Adkins J, Agakishiev G, Aggarwal M, Ahammed Z, Ajitanand N, et al. Measurement of  $D^0$  azimuthal anisotropy at midrapidity in Au+Au collisions at  $\sqrt{s_{NN}} = 200$  GeV. *Phys Rev Lett* (2017) 118:212301. doi:10.1103/PhysRevLett.118.212301
105. Hachiya T. Charm and Bottom quark energy loss and flow measurements in Au+Au collisions by the PHENIX experiment. In: Plenary talk at Quark Matter 2022 conference (2022).
106. *sPHENIX beam use proposal* (2021). [https://indico.bnl.gov/event/11884/attachments/34524/56472/sPHENIX\\_BUP\\_2021.pdf](https://indico.bnl.gov/event/11884/attachments/34524/56472/sPHENIX_BUP_2021.pdf).
107. BUR Committee. *The STAR beam use request for run-22 and data taking in 2023-25* (2021). [https://drupal.star.bnl.gov/STAR/files/STAR\\_Beam\\_Use\\_Request\\_Runs22\\_25.pdf](https://drupal.star.bnl.gov/STAR/files/STAR_Beam_Use_Request_Runs22_25.pdf).
108. Fartoukh S. *LHC configuration and operational scenario for run 3* (2021). CERN-ACC-2021-0007.





OPEN

## Analyzing the GHSI puzzle of whether highly developed countries fared worse in COVID-19

Sofija Markovic<sup>1</sup>, Igor Salom<sup>2</sup>, Andjela Rodic<sup>1</sup> & Marko Djordjevic<sup>1✉</sup>

Global Health Security Index (GHSI) categories are formulated to assess the capacity of world countries to deal with infectious disease risks. Thus, higher values of these indices were expected to translate to lower COVID-19 severity. However, it turned out to be the opposite, surprisingly suggesting that higher estimated country preparedness to epidemics may lead to higher disease mortality. To address this puzzle, we: (i) use a model-derived measure of COVID-19 severity; (ii) employ a range of statistical learning approaches, including non-parametric machine learning methods; (iii) consider the overall excess mortality, in addition to official COVID-19 fatality counts. Our results suggest that the puzzle is, to a large extent, an artifact of oversimplified data analysis and a consequence of misclassified COVID-19 deaths, combined with the higher median age of the population and earlier epidemics onset in countries with high GHSI scores.

It is natural to assume that the most prosperous world countries, well organized and with the most advanced medical institutions, would soon gain an advantage in the global race to minimize the harm from a new viral infection. This expectation is quantified in the form of the Global Health Security Index (GHSI)—a measure of preparedness for various health emergencies, precisely of the kind of the present COVID-19 pandemic<sup>1</sup>. The categories included in this index were carefully designed to help countries identify weaknesses primarily in their healthcare systems but also in their political and socio-economic structure, as well as to guide the process of reinforcing their health security capacities<sup>2–4</sup>. To this end, capacities to prevent medical hazards, to timely detect and report them, to rapidly respond in these situations, to comply in all these with international norms, as well as the health system capacity, and the overall vulnerability to biological threats—are all separately assessed and assigned a specific GHSI category: Prevent, Detect, Respond, Norms, Health and Risk, respectively.

With the COVID-19 pandemic, the GHSI scores were put for the first time to a real-life global test – which they failed, according to most of the published attempts to assess their correlation with the epidemic scale<sup>5–18</sup>. An unexpected positive correlation between the GHSI categories and differently calculated mortality<sup>5–7,12,14,17</sup> and infection spread<sup>5,7,8,10,12–14</sup> – deserving to be called the "GHSI puzzle" – suggested that the GHSI cannot be used to describe the national pandemic preparedness<sup>19</sup>. As this result seemed highly convincing, the focus was shifted to the search for explanations of the GHSI inappropriateness<sup>19</sup>. Thereby, the observed large COVID-19 infection counts in highly developed (high GHSI countries) motivated the firm opinion that their responses were "sclerotic and delayed at best"<sup>20</sup>. The first-ranked country in the GHSI 2019 list, the USA, provided a striking example. Despite its top overall score of 76/100—equaling roughly twice the average score of 38.9—COVID-19 has taken a devastating toll in the US, especially in the first wave of the pandemic<sup>21,22</sup>, introducing a two-year drop in life expectancy<sup>23</sup>. It was pointed out that GHSI scores cannot anticipate how a country decides to respond to epidemics, so these scores cannot be expected to necessarily be predictive of reported infections and fatalities<sup>24,25</sup>.

However, it is also necessary to revisit the methodological approaches that lead to the unintuitive relation of GHSI scores to the observed pandemic effects. First, the outcome variable, assumed to depend on the GHSI, should measure the relevant, effective epidemic burden to reasonably represent the country's overall success in minimizing the harm from the epidemic. Significantly, it should predominantly depend on the aspects of preparedness rather than other prevailing factors. As noted above, the GHSI predictivity was analyzed for different mortality and infection rates, yielding mostly positive correlations, and these variables depend on factors that directly or indirectly increase the frequency and range of personal contacts<sup>26</sup> and thus promote the disease spread<sup>27</sup>. Developed countries, typically carrying high GHSI scores, are characterized by intense population mobility and mixing due to ease of travel, higher local concentrations of people, and business and social activities. So,

<sup>1</sup>Quantitative Biology Group, Faculty of Biology, University of Belgrade, Belgrade, Serbia. <sup>2</sup>Institute of Physics Belgrade, National Institute of the Republic of Serbia, University of Belgrade, Belgrade, Serbia. ✉email: dmarko@bio.bg.ac.rs

the consequential rapid disease spread may cancel and overshadow the ameliorating effects of large preparedness capacities, explaining the lack of a negative correlation of the GHSI with COVID-19 growth numbers. In addition, these outcome variables depend on the calculation time frame, and there are even examples of incidence rates with negative dependence on the GHSI<sup>18</sup>. Therefore, it is quite nontrivial to select the appropriate outcome variable (among mortality and incidence rates) for describing the relationship between the GHSI and the epidemic burden.

The relation of the GHSI with clinical severity measured by the Case Fatality Ratio (CFR), as a more obvious indicator of the burden magnitude, was considered in a few papers<sup>8,13,16</sup>, with the most extensive study (for a large number of countries and with including numerous other potential predictors) carried out in<sup>13</sup>—and the connection turned out to be positive. This is genuinely perplexing since CFR is an objective measure of disease severity, thus expected to be causally independent of the disease transmissibility. Consequently, there is no obvious explanation why higher GHSI would be linked to a worse case fatality ratio.

While CFR is a specific measure of severity, its shortcoming is being time-dependent and affected by the varying lag between case detections and fatal outcomes (in addition to lacking a direct mechanistic interpretation in terms of the disease dynamics)<sup>28</sup>. Instead, we choose a timing-independent measure of severity:  $m/r$  value that we previously derived from an epidemic model<sup>29</sup>, which represents the ratio of population-averaged mortality to recovery rates (so that many fatalities and/or slow recovery correspond to higher epidemic severity). It can be shown that this measure is independent of the SARS-CoV-2 transmissibility and directly relates to the asymptotic CFR value calculated at the end of the epidemic wave, so it does not rely on an arbitrary time frame. Thus, we could estimate it straightforwardly using the data from the end of the first pandemic's peak, avoiding interpretation of complex effects of vaccination and different SARS-CoV-2 strains on the disease severity.

Furthermore, we aimed to check if the observed positive GHSI correlations with various measures of epidemics intensity may be an artifact of the applied methods that are not well adapted for the problem complexity – i.e., cannot extract the impacts specific to individual factors entangled in mutual correlations. To that end, we searched for the  $m/r$  predictors among a number of variables on 85 countries using methods such as the regularization-based linear regressions (Lasso and Elastic Net)<sup>30</sup>, and non-parametric machine learning techniques (Random Forest and Gradient Boost)<sup>30</sup>. Together with different GHS Indices, we also included a number of sociodemographic and health-related variables in the analysis, in line with a recent result that factors external to GHSI may aid in characterizing countries' ability to respond to epidemic outbursts<sup>31</sup>. Finally, we investigated the relationship between the GHSI and the total excess deaths, which was not performed before; the main advantage of such analysis is that, unlike official COVID-19 figures, total excess deaths counts do not depend on diagnosis and reporting policies<sup>17,18</sup>. Combined together, our results, to a large extent, solve—or more precisely dissolve—the puzzle: it is not justified to relate high GHSI values (i.e., high estimated country preparedness) with an unsatisfactory pandemic response and high severity/mortality burden.

## Results

**Analysis based on COVID-19 case counts.** Univariate analysis (Fig. 1) reveals a statistically significant positive correlation of all selected GHSI categories with our severity measure ( $m/r$ ), demonstrating the puzzle. Strikingly, GHSI categories show the highest positive correlations compared to all other variables in the analysis. Also, they are highly correlated with measures of a country's development (e.g., GDP per capita and HDI), so that, on average, more developed countries have higher GHSI.

However, the univariate analysis does not control for simultaneous effects of multiple factors that can influence the disease severity. Additionally, many factors that we initially included as potentially important (and thus considered in the analysis) may not significantly influence the severity, so retaining them in the final model would introduce large noise. Another problem is that many factors are mutually highly correlated. Consequently, we next applied linear regressions with regularizations and feature selection (Lasso and Elastic Net, which can eliminate non-significant predictors), combined with PCA on groups of related variables (to partially decorrelate the variable set while retaining its interpretability).

Mutually related variables were thus grouped in three categories (age, chronic disease, prosperity) on which PCA was performed (Supplement Fig. 1, Supplement Table 2), while the other variables remained unchanged (Supplement Table 1). The data were then independently analyzed using Lasso (Fig. 2A) and Elastic net regressions (Fig. 2B), which were implemented in the so-called “relaxed”<sup>30</sup> way to reduce noise from the multidimensional data.

From Fig. 2, we see that age PC1 is the dominant predictor in both methods, unsurprisingly suggesting that the older population is more severely affected by COVID-19. Furthermore, epidemic onset appears to be an important factor negatively associated with the disease severity, meaning that earlier epidemic onset is associated with higher severity of the disease. Of all four analyzed GHSI categories, the disease detection index is selected as the most important, with an (unintuitive) positive effect on  $m/r$ . While positive contribution was also obtained through univariate analysis, its magnitude diminishes when the more advanced analysis is used, i.e., in Fig. 2, PCA followed by multivariate regressions with regularization. Consequently, while the paradox is still there (positive contribution of one of GHSI categories), the regression coefficient of this predictor significantly decreases (e.g., compared to age) as the analysis progresses from univariate to multivariate (with feature selection and correlated variables accounted for). Also, in Elastic net regression (Fig. 2B), net immigration appears to contribute negatively to the disease severity, which we will further discuss below. The obtained results remain robust when the regression methods are applied to the initial data without PCA, when besides 18 demographic parameters, Detect, Respond, Health and Risk GHSI categories (Supplement Fig. 2), or Covid index (Supplement Fig. 3) are used.

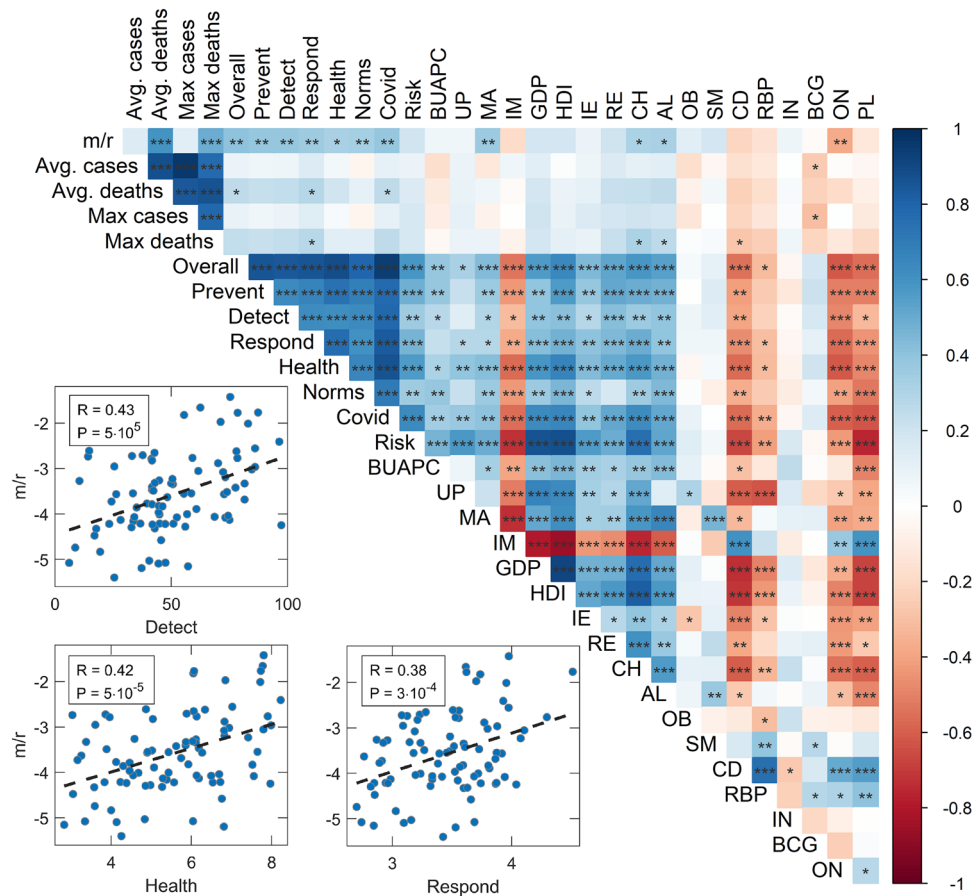


**Figure 1.** Graphical representation of the predictor correlation matrix (as the matrix is symmetric, only its upper half is shown). Colors correspond to the magnitude of Person correlation coefficients, as indicated by the color bar on the right, while asterisks correspond to the statistical significance of the results (‘ ’ –  $P > 0.05$ , ‘ \* ’ –  $0.05 > P > 0.01$ , ‘ \*\* ’ –  $0.01 > P > 0.001$ , ‘ \*\*\* ’ –  $P < 0.001$  ). Correlations of m/r and selected three Global Health Security Index categories, relevant for the pandemic, are also represented by scatterplots in the inset. m/r – disease severity measure, Overall – Overall GHSI, Prevent – GHSI Prevent category, Detect – GHSI Detect category, Respond – GHSI Respond category, Health – GHSI Health category, Norms – GHSI Norms category, Risk – GHSI Risk category, Covid – a combination of COVID-related GHSI indicators, BUAPC – built-up area per capita, UP – urban population, MA – median age, IM – infant mortality, GDP – gross domestic product per capita, HDI – human development index, IE – net immigration, RE – refugees, CH – blood cholesterol level, AL – alcohol consumption, OB – prevalence of obesity, SM – prevalence of smoking, CD – prevalence of cardiovascular diseases, RBP – raised blood pressure, IN – physical inactivity, BCG – BCG vaccination coverage, ON – the onset of the epidemic, PL – air pollution. The figure was created using R<sup>55</sup> corrplot package<sup>56</sup>, in RStudio integrated development environment for R<sup>57</sup>.

In the analysis above, we grouped variables in subsets according to their natural interpretation (e.g., age-related, chronic diseases, country prosperity) for PCA. While this approach facilitates the interpretation of the regression results, there is also some arbitrariness in the grouping criteria. This motivated us to perform supervised PCA—a mathematically well-defined procedure that chooses the variables for PCA solely based on their numerical correlation with the response variable. The optimal hyperparameter values, selected through cross-validation, were  $\theta = 0.05$  for correlation coefficient cutoff and  $n = 6$  for the number of retained principal components. The selected six principal components were used as predictors in a linear regression model with m/r as the response variable. As only two principal components, PC1 and PC4, turned out to be significant predictors (with the standard significance cutoff of  $P < 0.05$ ) in the linear regression, we proceeded to further analyze these principal components. The results in Fig. 3 show scatterplots of PC1 and PC4 vs. m/r and variables entering PCA. One can see a high correlation of m/r with PC1, which technically makes it a good risk index for COVID-19 severity – though some of its constituents, such as GHSI, have an unintuitive contribution to m/r. More importantly, PC1 shows that the composite variable, which can explain much of the variability in m/r, contains GHSI categories intertwined with HDI and GDP in terms of their effect on m/r. Consequently, the unintuitive positive contribution of GHSI to m/r (as well as the absence of negative contribution in more complex models) may be an indirect consequence of some effect that increases m/r for more developed countries (for which both HDI/GDP and GHSI are high). We will further explore this possibility through the analysis of excess deaths.

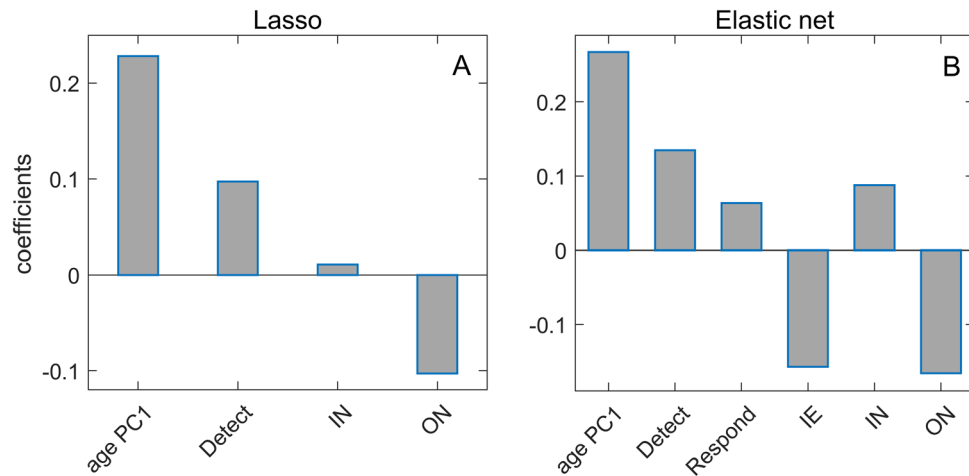


**Figure 2.** Lasso and Elastic Net regressions with  $m/r$  as the response variable. (A) Regression coefficients of variables selected by Relaxed Lasso regression, (B) Regression coefficients of variables selected by Relaxed Elastic Net regression, age PC1 – age principal component 1, Detect – GHSI Detect category, Respond – GHSI Respond category, IE – net immigration, IN – physical inactivity, ON – the onset of the epidemic.

The regression methods used so far do not account for nonlinearities or possible interactions between predictor variables. For this reason, we applied machine learning methods based on ensembles of weak learners (decision trees), Random Forest, and Gradient Boost, on the same set of predictors and PCs used in the linear regression models above. Figure 4 shows the estimate of variable importance (A and D) and Partial Dependence (PD) plots (B, C, E, F) for the variables with the highest importance in explaining disease severity. PD plots also provide information about the direction (positive or negative) in which the predictors affect  $m/r$ . We obtain age PC1 as by far the most important variable, where older age promotes the disease severity. Detect GHSI and epidemic onset also appear above the standard importance threshold. However, the estimated effect of Detect GHSI is now small, based on both the variable importance and PD plots that show a much larger dependence of  $m/r$  on age PC1.

**Analysis of excess deaths.** We next focus on excess deaths (see the definition in Methods), where we again use several univariate and multivariate approaches. As predictors, we here use COVID-19 counts, GHSI, and demographic variables, which we separated into mutually related subsets on which PCA was performed (see Supplement Table 3 and Supplement Fig. 4). In Fig. 5, which shows Random Forest results, we see that Counts PC1, which equally well reflect COVID-19 infection and death case counts, are by far the most dominant predictor of excess deaths. While expected, this is also a highly nontrivial result, given that the two quantities (excess deaths and classified COVID-19 deaths) are inferred in an entirely independent manner, and that in-principle ununiform policies of COVID-19 related deaths classification are applied in different countries<sup>32</sup>. This result is robust, i.e., consistently obtained through different methods, ranging from simple univariate regressions to linear regressions (with variable selection and regularization), see Supplement Figs. 5 and 6 and Supplement Table 4. The only other predictor with importance above the threshold in Fig. 5 is CFR (which we also calculate in saturation, i.e., at the end of the first wave), which has a small to moderate positive effect on  $m/r$ , though much smaller than the COVID-19 case counts.

We then analyzed the unexplained deaths with the same approach described above for the excess deaths. The unexplained deaths are the difference between the excess deaths and COVID-19 deaths, i.e., those excess deaths not attributed to COVID-19 (for the definition, see Methods). From Fig. 6, we see that the most important predictor is demo PC1, which has a clear *negative* association with unexplained deaths (see the corresponding PD plot). These results are robust, i.e., independently obtained by several different univariate and multivariate analyses (Supplement Figs. 7 and 8 and Supplement Table 5). As demo PC1 is strongly related to country GDP/HDI (see Supplement Fig. 4), more developed countries are associated with a smaller number of unexplained deaths. The other demographic-related PC components above the importance threshold (demo PC 4 and 6) have a smaller influence on unexplained deaths and can also be related to the negative influence of HDI/GDP (see Supplement Fig. 4). Interestingly, GHSI PC1 (highly correlated to all GHSI categories) is also selected as a significant predictor, negatively associated with unexplained deaths. This implies that higher GHSI (significantly correlated to HDI/GDP) is associated with fewer unexplained COVID-19 deaths.

## Discussion

Although the  $m/r$  quantity does not depend on the epidemic growth rate, which is boosted by the large contact rate in countries with high GDP, HDI, and GHSI, the univariate analysis shows that GHSI categories significantly correlate with this measure of severity – having the highest correlation of all considered variables. This could be naively interpreted as a higher likelihood of dying from COVID-19 in well-equipped medical facilities than in settings ranked by far lower GHSI. In the subsequent two parallel analyses—Lasso and Elastic Net on PCs

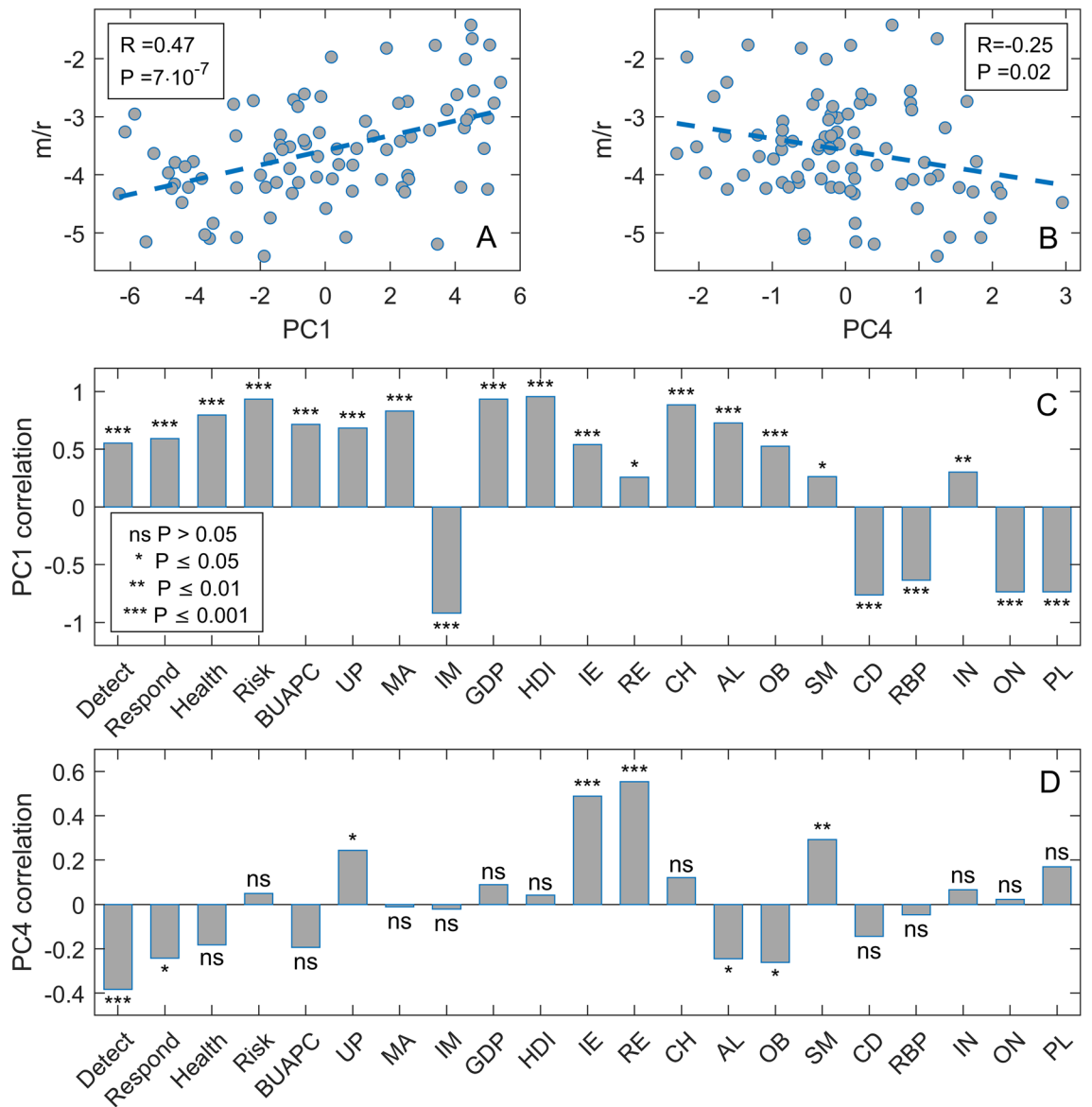


**Figure 3.** Supervised Principal Component Analysis. Scatterplot of (A) PC1 and  $m/r$ , (B) PC4 and  $m/r$ , (C) PC1 and variables entering PCA, (D) PC4, and variables entering PCA.  $m/r$  – mortality over recovery rate, Detect – GHS Detect category, Respond – GHSI Respond category, Health – GHSI Health category, Risk – GHSI Risk category, BUAPC – built-up area per capita, UP – urban population, MA – median age, IM – infant mortality, GDP – gross domestic product per capita, HDI – human development index, IE – net immigration, RE – refugees, CH – blood cholesterol level, AL – alcohol consumption, OB – prevalence of obesity, SM – prevalence of smoking, CD – prevalence of cardiovascular diseases, RBP – raised blood pressure, IN – physical inactivity, BCG – BCG vaccination coverage, ON – the onset of the epidemic, PL – air pollution.

obtained from three predefined groups of variables, on one side, and the Supervised PCA, on the other – the positive effect of GHSI is acknowledged, primarily through the Detect category. However, it is smaller than the effects of PCs brought to the fore, determined by factors like the population median age, the epidemic onset, and the net immigration. Thereby, the diversity of the variables constituting PC1 in the supervised PCA, together with multiple GHSI categories, additionally questions the GHSI significance, as it makes it hard to separate the influence of the GHSI from the influences of other variables related to the country development level (HDI/GDP). Finally, the variable importance analysis points to a robust and dominant influence of the age PC1, while a positive influence of the GHSI Detect category is present but almost negligible compared to the age PC1 effect.

Moreover, the Random Forest method selects the Onset as an additional variable with higher significance than the GHSI Detect. Therefore, our results show that oversimplified analytical methods play a major role in the puzzle: While simple pairwise correlations indeed strongly suggest that "better healthcare leads to higher COVID-19 mortality", there is hardly any hint of such paradox with advanced machine-learning analyses. Instead, old age and an earlier epidemic onset are likely behind the increased disease severity—and simple univariate analysis fails to identify these confounding variables, both significantly correlated with the GHSI.



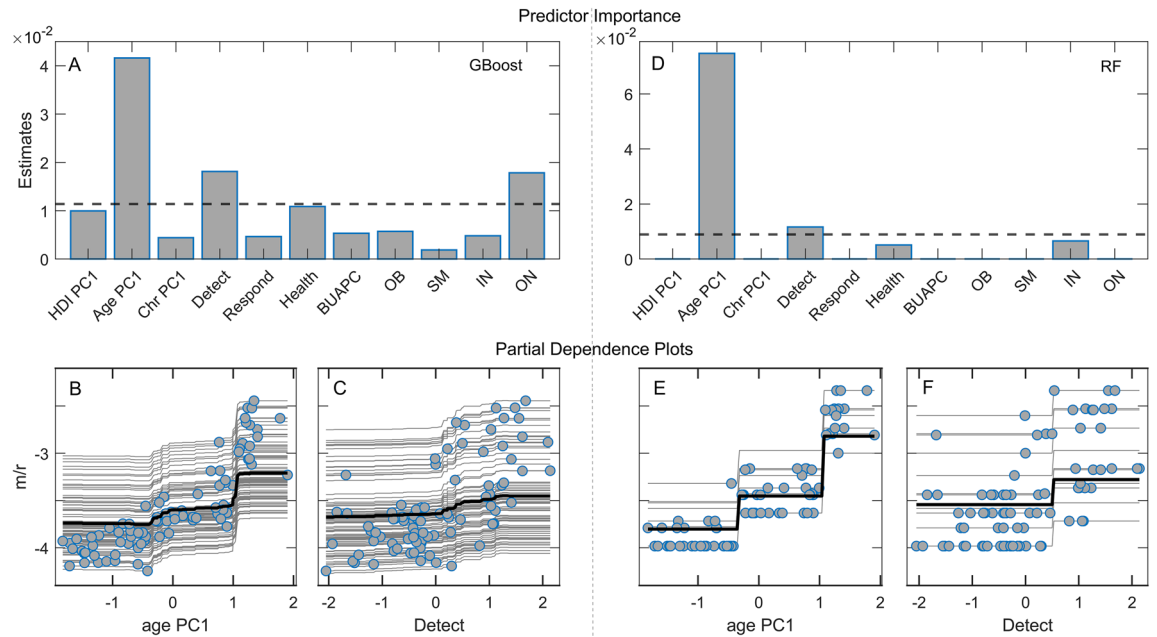


**Figure 4.** Machine learning algorithms and Partial dependence (PD) plots with disease severity as the response variable. **(A)** Variable importance estimates for Random Forest regression, **(B–C)** PD plots corresponding to Random Forest, **(D)** Variable importance estimates from Gradient Boost regression, **(E–F)** PD plots corresponding to Gradient Boost. The dashed lines in A and D correspond to the mean variable importance in the given model. HDI PC1 – human development index PC1, Chr PC1 – chronic diseases PC1, Detect – GHSI Detect category, Respond – GHSI Respond category, Health – GHSI Health category, BUAPC – built-up area per capita, OB – obesity, SM – smoking, IN – physical inactivity, ON – epidemic onset, m/r – disease severity measure.

Three severity predictors robustly selected by different methods – the median age, the epidemic onset, and the net immigrations – are generally supported by other studies' results, obtained in combinations with other predictors<sup>6,8,11,13,14</sup>. The fact that our analysis singled them out argues about their dominant roles. Old age is undoubtedly a dominant risk factor for developing severe illness and dying from COVID-19<sup>6,8,13,14</sup>. The onset variable, not acknowledged only by the Random Forest, is obtained with a negative association to severity<sup>11,33</sup>. The time in which the pandemic reached a country may have been a significant factor in the first wave, as countries could use it to organize medical resources and adjust treatment protocols, learning from the experiences of those affected earlier. The Elastic net and the supervised PCA results identify the net immigration as a negative contributor to the COVID-19 severity. The supervised PCA groups this variable inside the same PC with the percent of refugees. This negative effect of immigration in the broader sense on the severity should not be interpreted through a hypothetical mitigating effect of the full lockdowns on the virus spread, rapidly imposed in those countries expecting a massive inflow of people<sup>13,34</sup>, because m/r is independent of the disease transmissibility. Rather than being more efficient in treating COVID-19, countries leading in net immigration probably had an additional under-privileged population<sup>35</sup> whose deaths from COVID-19 were more frequently misattributed to other causes, e.g., a lack of medical insurance or a general reluctance to go to hospitals<sup>36,37</sup>. If so, the presence of immigrants did not decrease the actual COVID-19 mortality, but only the officially recognized toll (further discussed below).

We further demonstrate that the reliability of COVID-19 data also plays an important role. Many factors can lead to underreporting, or even overreporting, of COVID-19 deaths: testing capabilities, protocols for classifying causes of death, to outright political influences<sup>38</sup>. Since these factors can be highly variable between countries, we considered the overall excess deaths as an alternative measure to official COVID-19 mortality statistics. We obtain that, similarly to<sup>39</sup>, the excess deaths variable depends almost only on the sheer number of COVID-19 cases (itself not significantly correlated with any other of our predictor variables, see Fig. 1), together with some influence of the CFR value (where CFR itself is dominantly correlated with median age, and with epidemic onset—possibly due to the accumulated experience in medical treatments). The counterintuitive connection of COVID-19 severity with GHSI categories (and country's prosperity) does not appear when considering the overall excess mortality. Another perspective on the phenomenon is gained by considering the "unexplained deaths" variable, quantifying the part of the overall excess deaths not officially attributed to COVID-19 mortality. We obtained that unexplained deaths are smaller in developed countries with high GHSI scores. Other studies also found a similar relationship between unaccounted excess deaths and the lower average income/fewer physicians per capita<sup>6,8,14,37,38,40</sup>. This strongly suggests that underreporting COVID-19 deaths plays another crucial role in the GHSI puzzle, i.e., that the actual COVID-19 toll in low GHSI countries is higher than the official figures reveal.

For our present purposes, it is not crucial whether the excess deaths represent direct COVID-19 victims or indirect pandemic casualties of reduced access to healthcare services (i.e., due to overwhelmed medical facilities):

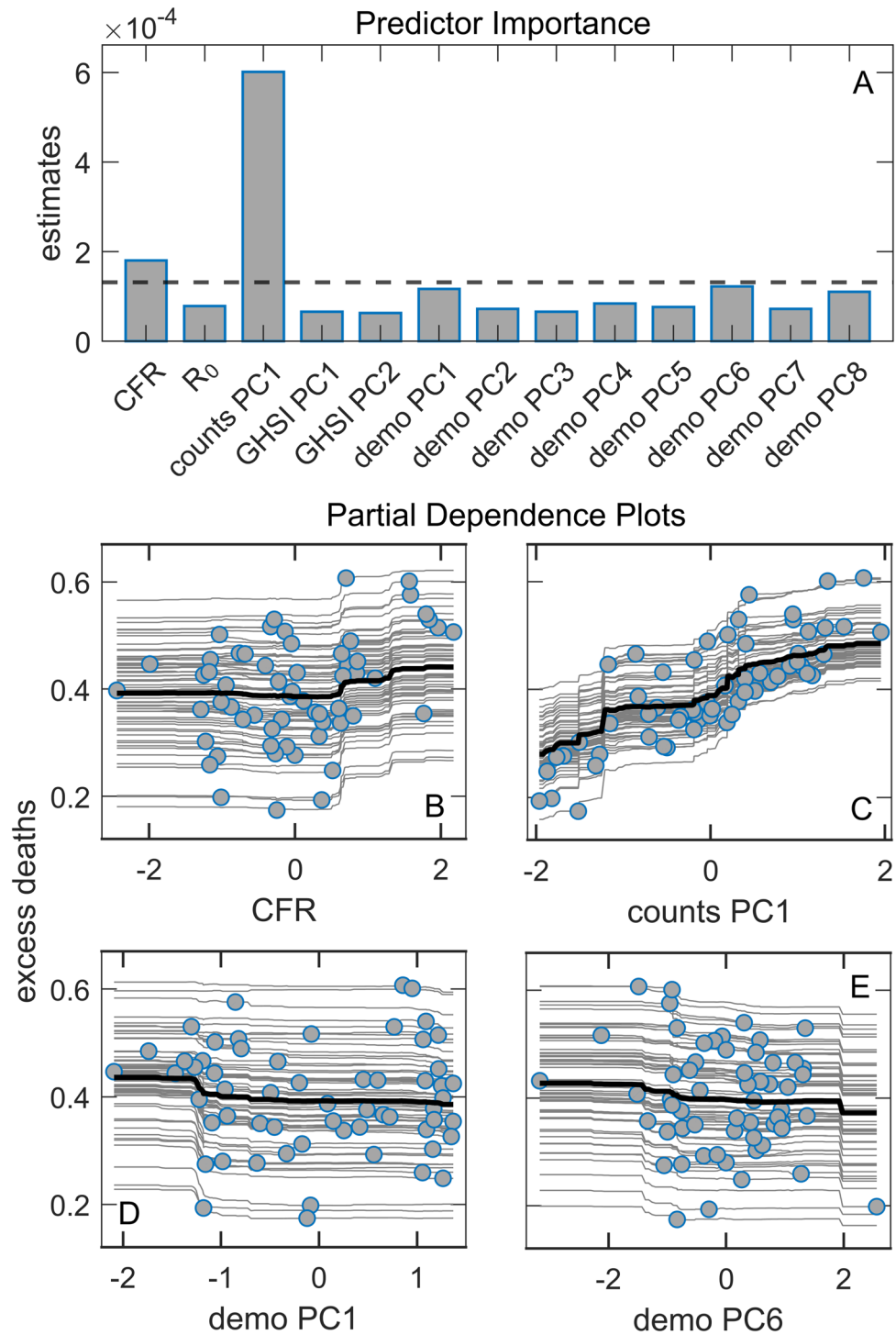


**Figure 5.** Random Forest regression with excess deaths as the response. (A) Predictor importance estimates from Random Forest regression, where dashed line represents the importance threshold, i.e., the mean importance value, (B–E) Partial dependence plots of predictors with the highest importance estimates from Random Forest regression model, CFR – case fatality rate,  $R_0$  – basic reproductive number of the virus.

GHSI scores should reflect capabilities to cope with both aspects of the pandemic consequences. Nevertheless, most of the unaccounted deaths likely represent direct consequences of SARS-CoV-2 infection, especially in countries where the difference between the official COVID-19 mortality and the excess of deaths is substantial. Namely, our results are based on the excess of deaths that occurred during a relatively short time window of the first pandemic wave (a few months), where the negligence of other/chronic medical conditions (e.g., postponed oncological or cardiological check-ups and treatments) will unlikely have such immediate effects on mortality.

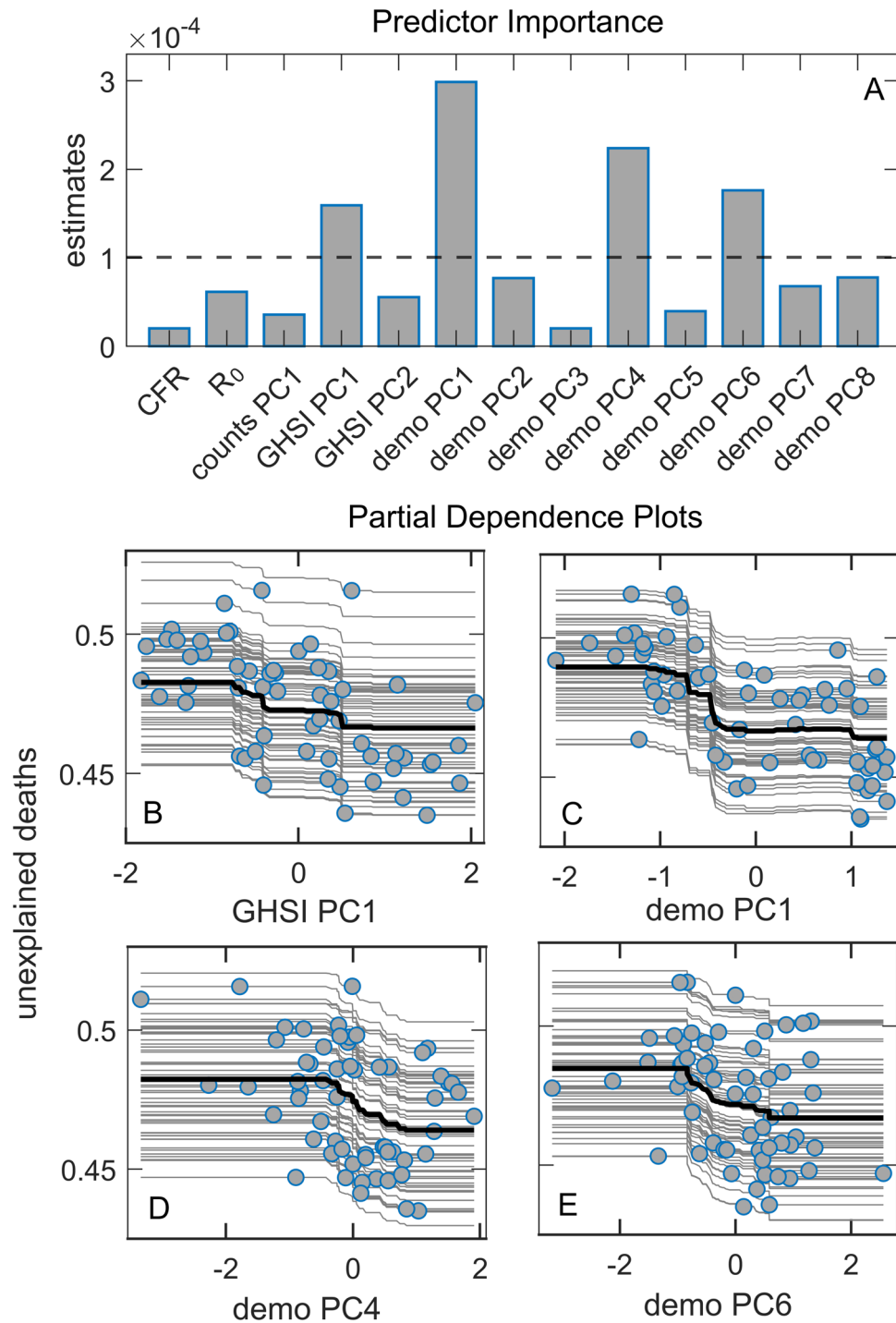


**Figure 6.** Random Forest regression with unexplained deaths as the response. (A) Predictor importance estimates from Random Forest regression, where dashed line represents the importance threshold (the mean value of the variables), (B–E) Partial dependence plots of predictor with the highest importance estimates from Random Forest regression model, CFR – case fatality rate,  $R_0$  – basic reproductive number of the virus.

Besides, if the unexplained deaths were primarily an indirect consequence of saturation of medical resources, COVID-19 case counts should reflect this saturation and thus be expected to appear as a relevant predictor of unexplained deaths—but this does not happen. On similar grounds, the authors of<sup>39</sup> support the same interpretation of excess mortality in regions of Italy. As an additional argument, we note that, of all GHS indices, both the linear regressions with feature selection (Fig. 2) and the machine learning techniques (Fig. 4) consistently single out the Detect score (quantifying testing capabilities) as the one most affecting m/r. This is consistent with the interpretation that high GHSI scores—and the Detect index category in particular—are not connected to higher

COVID-19 mortality but rather reflect better capacity to recognize (i.e., "detect") COVID-19 deaths as such, and thus lead to less unexplained deaths. On the other hand, a lower Detect score relates to a larger number of unrecognized COVID-19 deaths and falsely lower mortality, adding to the apparent paradox.

We have provided ample arguments that the puzzling connection of high GHSI scores with severe COVID-19 epidemic outcomes is an artifact of oversimplified analyses and low-quality data, but neither of our methods could directly establish the anticipated negative correlation. Notably, the negative correlation with the scale of under-reporting of COVID-19 deaths is suggested by our results, demonstrating the effectiveness of better detection capacity of high-GHSI countries. However, it seems that the anticipated benefits of the elaborated preparedness capacities for minimizing the overall harm did not manifest, at least not directly. Note that our results clearly show the strong influence of population age and, in the second place, the epidemic onset on the m/r measure of severity. The latter predictor emphasizes the particular vulnerability of the initial pandemic period<sup>11,12</sup>. Not only did a later onset provide more time to organize a response, but the large unpredictability effect when the world encountered an unknown virus, obstructing any organizational efforts<sup>1,41,42</sup>, put the first-hit countries in an additionally vulnerable position. The lack of knowledge and experience could have primarily determined the reach of the initial efforts to minimize severity regardless of the pre-established capacities, and this factor would be hard to incorporate in a static preparedness measure such as the GHSI. Nevertheless, the GHSI might show a better, anticipated agreement later during the pandemic, when the advantages of the prepared system start to reveal. Previous studies, like ours, assessed the GHSI predictivity focusing on the pre-vaccination period, so its performance separated from the sensitive, first outbreak period remains largely unexplored.

On the other hand, GHS indices are positively correlated with the population age and negatively correlated with the onset time. In turn, if there was no direct influence of GHSI scores on mortality (nor additional confounding correlations), we should expect more excess deaths in countries with higher GHS indices—simply because the population is, on average, older, while the epidemic came earlier, in these countries. However, since the plot in Fig. 6 does not reveal such a trend, and overall excess mortality seems to depend almost solely on the number of infected individuals (with neither age nor GHSI playing any role in Fig. 5), there must be a factor that compensates for this age and early epidemic onset disadvantage. While we cannot rule out possible confounders, it is plausible that the difference in levels of medical care—reflected via GHSI scores—counterbalances these two effects.

In summary, the main goal of this study was to reinvestigate the "GHSI puzzle," giving attention to three essential aspects (i) the choice of the effective epidemic burden measure, (ii) the advanced multivariate data analysis, suiting the data complexity, and (iii) the analysis of excess deaths data, in addition to more questionable official COVID-19 infection and mortality figures. Our results point to a major weak point in the previous efforts to assess the predictivity of the GHS index – namely, using the oversimplified methodology, which emphasizes the importance of implementing the three essential steps in our analysis mentioned above. We show that high GHSI scores cannot be associated with low efficacy in combating epidemics, contrary to the dominant claim in academic literature. On the contrary, more developed countries with high GHSI values likely provided better quality data due to more reliable reporting of COVID-19 fatality counts. This becomes particularly significant in light of the notion strongly supported by our results: that a majority of excess deaths after the first wave should be attributed to direct COVID-19 fatalities instead of indirect consequences of the pandemic or other concurrent causes.

GHSI categories, therefore, do not contradict the observed data and can still be a valuable instrument in ameliorating the consequences of future global health-related crises, especially with some refinement to account for the country's vulnerability to a high level of initial unpredictability when it faces an unknown, fast-transmitting virus. Refining this and developing similar measures can aid the prevention of future epidemic catastrophes, where our study may provide some guidelines on how to perform an accurate assessment of their appropriateness. Some of the GHSI shortcomings have already been reported<sup>31</sup> and addressed in the revised GHSI Index 2021<sup>43</sup>, where the authors have attempted to improve the index by adding several new subcategories, which can certainly be viewed as a step in the right direction. While the lack of a positive association between higher GHSI scores and lower disease severity cannot be fully explained by our results, it is possible that including more variables in the research and obtaining excess and unexplained deaths data for a higher number of countries (which would allow for introducing more predictor variables without the danger of overfitting the data) would help bring to light some of the dependencies we were unable to capture in this research. One such variable could be countries' corruption index, as it is reasonable to assume that countries with a higher corruption prevalence, would be less transparent in reporting COVID-19-related deaths. Less reported deaths would lead to lower disease severity estimates in countries with a higher corruption index, contributing to the paradox. Higher perceptions of corruption and social polarization have already been identified as contributing to higher excess mortality<sup>31</sup>.

Also, the results from later COVID-19 peaks might differ from the first peak, as it is reasonable to anticipate that more developed countries, with higher GHSI and, on average, higher healthcare budgets, given enough time and resources, would be better prepared for the later COVID-19 waves<sup>44,45</sup>. Additionally, a quicker vaccine rollout in developed countries could lead to quicker drop in disease severity, regardless of the increasing transmissibility of new viral strains<sup>46</sup>.

## Methods

**Data collection and processing.** The majority of the data used in this research, including 18 demographic and health parameters, and the basic reproduction number of the virus was taken from the dataset previously assembled in<sup>27</sup>. Additionally, Global Health Security Index (GHSI) data were taken from<sup>1</sup>. In addition to the main (Overall) GHSI and six index categories (Prevent, Detect, Respond, Health, Norms, and Risk), the Covid index was calculated from the averaged values of COVID-19 related GHSI indicators, according to<sup>17</sup>.

COVID-19 counts (average and maximal daily cases and deaths) were taken from<sup>48</sup>. At the end of the first peak, the case fatality rate and severity measure (m/r) for each country were calculated according to the methodology described in<sup>29</sup>. To determine the numbers of total and excess deaths during the first peak of the pandemic, data from<sup>49</sup> was used. Relative excess deaths and relative unexplained deaths (excess and unexplained deaths in further text and figures) were calculated as follows:

$$\text{relative excess deaths} = \frac{\text{excess deaths}}{\text{total deaths} - \text{excess deaths}}$$

$$\text{relative unexplained deaths} = \frac{\text{excess deaths} - \text{COVID19 deaths}}{\text{total deaths} - \text{excess deaths}}.$$

For the research two datasets were constructed: (i) m/r dataset—a subset of the dataset used in<sup>27</sup>, consisting of the data from 85 countries for which both GHSI were available and m/r was inferred; (ii) excess deaths dataset—a subset of (i) for which total and excess deaths data was available (59 countries). Since the distribution of most variables initially deviated from normality, data was transformed, so that the skewness of the variables was as close to zero as possible, with the minimal number of remaining outliers. To obtain the best possible results, transformations were applied separately for variables in each dataset. Interpretation of all the variables and the used transformation for both datasets are presented in Supplementary Table 1. For easier tracking of the course of the research, analyses performed on each dataset are graphically represented by a flowchart in Fig. 7.

**Principal component analysis.** To partially decorrelate data and reduce dimensionality while retaining relatively simple interpretation of principal components, some of the variables were grouped into mutually related groups, on which Principal Component Analysis (PCA) was performed. The number of principal components retained from each group after the PCA was determined to explain over 85% of the variance of the data. PCA grouping was performed independently for both datasets and variables entering PCA; retained principal components, and the percentage of variance they account for are presented in Supplementary Table 2 (m/r dataset) and 3 (excess deaths dataset). New datasets, now consisting of both retained principal components and remaining variables that did not enter PCA, were next used as input in univariate and multivariate analyses. For easier interpretation of the most relevant principal components, their correlation with the variables entering PCA is given in Supplementary Figs. 1 and 4. Two now obtained sets of predictors were: (i) variables used in m/r regression analysis, consisting of: Detect, Respond, and Health GHSI categories, five selected PCs from Supplementary Table 2, and remaining demographic and health parameters that did not enter PCA (BUAPC, UP, IE, RE, OB, SM, IN, BCG, ON) (ii) variables used in excess and unexplained deaths analysis with principal components consisting of  $R_0$ , CFR and 11 principal components from Supplementary Table 3.

**Linear regression models.** LASSO and Elastic net regressions were used as the implementations of L1 (LASSO) and L1 and L2 norms (Elastic net) on three variations of the m/r dataset and on excess deaths dataset with principal components (regressions were implemented separately for excess and unexplained deaths as response variables). The variables (and PCs) were standardized before the regressions, so the regression coefficients obtained by these methods can be interpreted as the relative importance of predictors in explaining the response variables. Values of the hyperparameters  $\lambda$  in LASSO and  $\alpha$  and  $\lambda$  in Elastic Net were determined through fivefold cross-validation, with the data repartitioned 40 times. In m/r dataset regressions, the sparsest model—with mean squared error (MSE) within 1 standard error (SE) from the minimal MSE—model was chosen. To further reduce the noise in m/r dataset regressions (where the number of predictors retained after the first round of regression was relatively high), LASSO and Elastic Net were implemented as “Relaxed”<sup>50</sup>, meaning that the regression was performed in two rounds so that only the variables selected in the first round were used as the input for the second round of regression. Regressions were performed on the initial m/r dataset, without grouping and PCA and with Detect, Respond, Health and Risk GHSI categories (Supplementary Fig. 2); on a dataset containing Covid index and 18 demographic and health variables, without any other GHSI categories (Supplementary Fig. 3); and on m/r dataset with principal components (Fig. 2). Since the number of selected variables after the first round of regression with both excess and unexplained deaths data was relatively small (even though this time minimal MSE model was selected instead of the sparsest), the second round of regression was not performed. As an addition to LASSO and Elastic Net for the excess and unexplained deaths analysis, Forward stepwise linear regression<sup>30</sup> was performed. In this method, starting from the constant model, a predictor is added to the regression if it improves the fit significantly ( $P < 0.05$  in F-statistics). The process is repeated sequentially, adding significant and removing non-significant terms until the best fit is obtained.

**Random forest and gradient boost regressions.** Two non-parametric, decision tree-based methods – Random Forest<sup>30,51</sup> and Gradient Boost<sup>30,52</sup>—were implemented on both m/r and excess deaths datasets with principal components. These methods are of particular importance, as they can accommodate potential interaction between the variables and highly non-linear relations between the predictors and the response variable. In the analysis of disease severity, the m/r dataset with principal components was used, with a constraint that only variables correlated to m/r with  $P < 0.1$  in either Pierson, Kendall, or Spearman correlation are used as the input in the model. This way, overfitting, which would present a problem for these algorithms, is avoided. As the number of input variables was smaller in the excess/unexplained deaths dataset, preselection was not required before those regressions. Values of the hyperparameters in Random Forest and Gradient Boost methods were selected through extensive grid search, by the same method of cross-validation used for LASSO and Elastic Net regres-



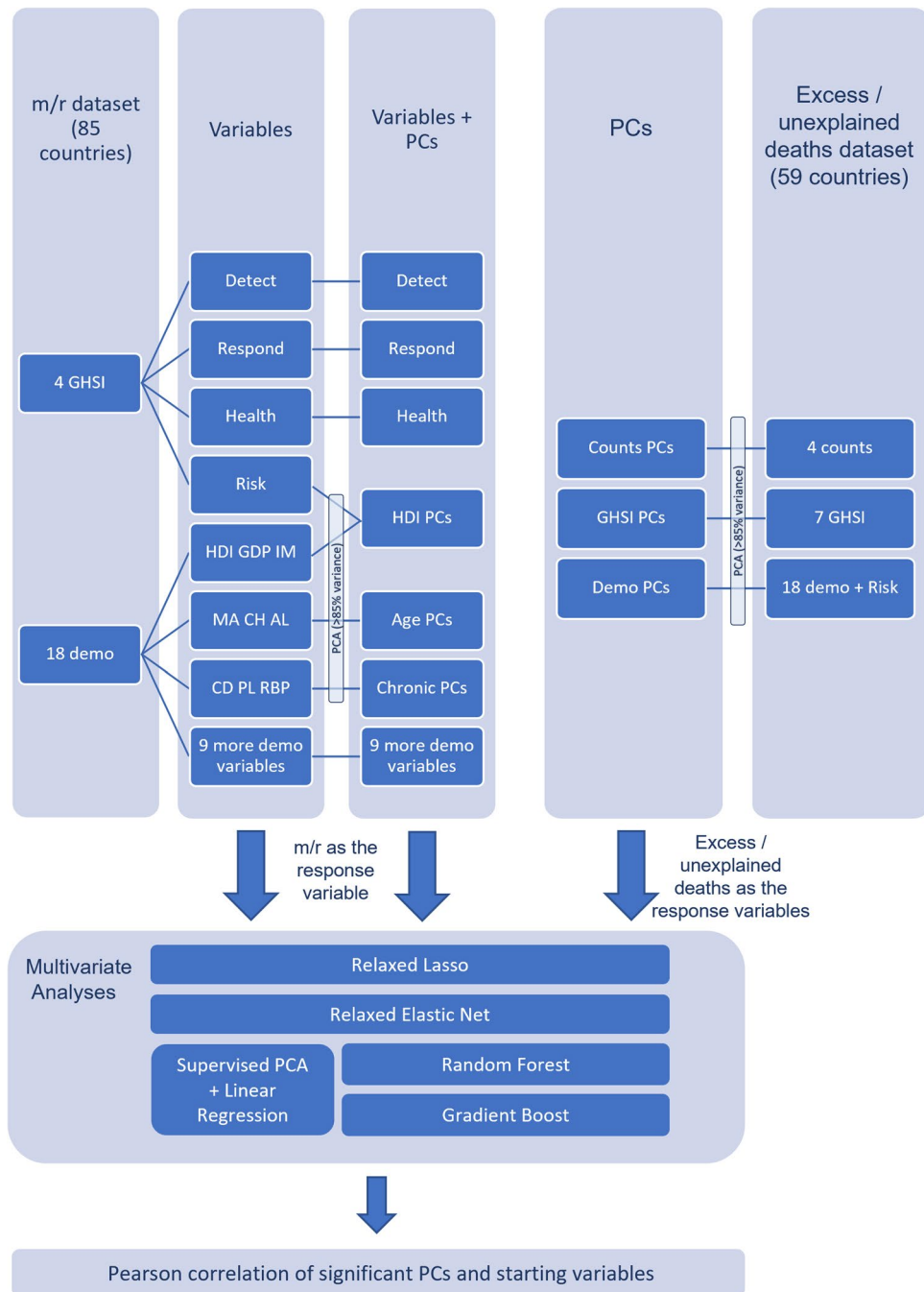


**Figure 7.** Flowchart of the methods applied on each of the datasets. m/r – disease severity measure, GHSI – Global Health Security Index, demo – demographic, counts – COVID-19 counts, PCs – principal components, Detect – GHSI Detect category, Respond – GHSI Respond category, Health – GHSI Health category, Risk – GHSI Risk category, MA – median age, IM – infant mortality, GDP – gross domestic product per capita, HDI – human development index, CH – blood cholesterol level, AL – alcohol consumption, CD – prevalence of cardiovascular diseases, RBP – raised blood pressure, PL – air pollution.

sions, and a model with the minimal MSE was chosen to be retained on the entire (reduced) dataset. Unlike linear regression models, where regression coefficients measure the impact of each feature on the outcome variable, in these two methods, the contribution of each of the features is measured by feature importance. For each decision tree, the feature importance is calculated as the sum of changes in the node risk due to splits for each feature, divided by the total number of branch nodes<sup>53</sup>. The feature importance for the ensemble is obtained by averaging over all the trees<sup>54</sup>. Note that, unlike regression coefficients, feature importance does not indicate the direction of the association (that is, whether the feature affects the outcome positively or negatively). Therefore, the contribution of the relevant variables in Random Forest and Gradient Boost was estimated through Partial

Dependence (PD) plots<sup>30</sup>, which estimate the effect of a single predictor by considering the average effects of all other predictors.

**Supervised PCA.** Supervised Principle Component Analysis<sup>30</sup> was performed. In this method, PCA is done only on those variables that show sufficiently high correlation with the response variable (m/r), where a certain number of PCs is then used in multiple regression with m/r as the response. The univariate correlation constant cutoff (i.e., the number of variables retained for PCA), and the number of retained PCs, are treated as hyper-parameters, i.e., determined through cross-validation. Principal components that appeared significant in the multivariable regressions were further analyzed.

### Data availability

We confirm that all methods were carried out in accordance with relevant guidelines and regulations as publicly available data set is used. All data generated or analyzed during this study are included in this published article and its Supplementary material.

### Code availability

All source codes are available at [https://github.com/Q-bio-Belgrade/GHSI\\_puzzle](https://github.com/Q-bio-Belgrade/GHSI_puzzle).

Received: 15 March 2022; Accepted: 17 October 2022

Published online: 21 October 2022

### References

1. GHS Index. The 2019 Global Health Security Index. *GHS Index* <https://www.ghsindex.org/> (2019).
2. Nuzzo, J. B. *et al.* What makes health systems resilient against infectious disease outbreaks and natural hazards? Results from a scoping review. *BMC Public Health* **19**, 1310 (2019).
3. Meyer, D. *et al.* A checklist to improve health system resilience to infectious disease outbreaks and natural hazards. *BMJ Glob. Health* **5**, e002429 (2020).
4. Ravi, S. J. *et al.* Establishing a theoretical foundation for measuring global health security: A scoping review. *BMC Public Health* **19**, 954 (2019).
5. Aitken, T., Chin, K. L., Liew, D. & Ofori-Asenso, R. Rethinking pandemic preparation: Global Health Security Index (GHSI) is predictive of COVID-19 burden, but in the opposite direction. *J. Infect.* **81**, 318–356 (2020).
6. Amadu, I. *et al.* Assessing sub-regional-specific strengths of healthcare systems associated with COVID-19 prevalence, deaths and recoveries in Africa. *PLoS ONE* **16**, e0247274 (2021).
7. Bouba, Y. *et al.* The determinants of the low COVID-19 transmission and mortality rates in Africa: A cross-country analysis. *Front. Public Health* **9**, 751197 (2021).
8. Chakravarty, S., Grover, G. & Aggarwal, S. Association of socioeconomic and demographic factors With COVID-19 related health outcomes in SAARC nations. *Stat. Appl.* **19**, 367–386 (2021).
9. Dewi, A. *et al.* Global policy responses to the COVID-19 pandemic: Proportionate adaptation and policy experimentation: A study of country policy response variation to the COVID-19 pandemic. *Health Promot. Perspect.* **10**, 359–365 (2020).
10. Duhon, J., Bragazzi, N. & Kong, J. D. The impact of non-pharmaceutical interventions, demographic, social, and climatic factors on the initial growth rate of COVID-19: A cross-country study. *Sci. Total Environ.* **760**, 144325 (2021).
11. Haider, N. *et al.* The global health security index and joint external evaluation score for health preparedness are not correlated with countries' COVID-19 detection response time and mortality outcome. *Epidemiol. Infect.* **148**, e210 (2020).
12. Ji, Y. *et al.* Are we ready to deal with a global COVID-19 pandemic? Rethinking countries' capacity based on the Global Health Security Index. *Int. J. Infect. Dis.* **106**, 289–294 (2021).
13. Kim, J. *et al.* Factors associated with the difference between the incidence and case-fatality ratio of coronavirus disease 2019 by country. *Sci. Rep.* **11**, 18938 (2021).
14. Kumru, S., Yiğit, P. & Hayran, O. Demography, inequalities and global health security index as correlates of COVID-19 morbidity and mortality. *Int. J. Health Plan. Manag.* **37**(2), 944–962. <https://doi.org/10.1002/hpm.3384> (2022).
15. Leichtweis, B. G., de Faria Silva, L., da Silva, F. L. & Peterelli, L. A. How the global health security index and environment factor influence the spread of COVID-19: A country level analysis. *One Health* **12**, 100235 (2021).
16. Maraghi, E., Saki Malehi, A. & Rahim, F. Global health security capacity against COVID-19 outbreak: An analysis of annual data from 210 countries and territories. *Jundishapur J. Health Sci.* **12**, e110814 (2020).
17. Stribling, J., Clifton, A., McGill, G. & de Vries, K. Examining the UK Covid-19 mortality paradox: Pandemic preparedness, health-care expenditure, and the nursing workforce. *J. Adv. Nurs.* **76**, 3218–3227 (2020).
18. Wong, M. C., Huang, J., Wong, S. H. & Yuen-Chun Teoh, J. The potential effectiveness of the WHO International Health Regulations capacity requirements on control of the COVID-19 pandemic: a cross-sectional study of 114 countries. *J. R. Soc. Med.* **114**, 121–131 (2021).
19. Baum, F. *et al.* Explaining covid-19 performance: What factors might predict national responses?. *BMJ* **372**, n91 (2021).
20. Dalglish, S. L. COVID-19 gives the lie to global health expertise. *Lancet* **395**, 1189 (2020).
21. Baker, H. A., Safavynia, S. A. & Evered, L. A. The 'third wave': Impending cognitive and functional decline in COVID-19 survivors. *Br. J. Anaesth.* **126**, 44–47 (2021).
22. James, N., Menzies, M. & Radchenko, P. COVID-19 second wave mortality in Europe and the United States. *Chaos* **31**, 031105 (2021).
23. Stephenson, J. COVID-19 deaths helped drive largest drop in US life expectancy in more than 75 years. *JAMA Health Forum* **3**, e215286 (2022).
24. Ravi, S. J. *et al.* The value proposition of the global health security index. *BMJ Glob. Health* **5**, e003648 (2020).
25. Nuzzo, J. B., Bell, J. A. & Cameron, E. E. Suboptimal US response to COVID-19 despite robust capabilities and resources. *JAMA* **324**, 1391–1392 (2020).
26. Gangemi, S., Billeci, L. & Tonacci, A. Rich at risk: Socio-economic drivers of COVID-19 pandemic spread. *Clinic. Mol. Allergy* **18**, 12 (2020).
27. Djordjevic, M. *et al.* Inferring the main drivers of SARS-CoV-2 Global transmissibility by feature selection methods. *GeoHealth* **5**, e2021GH000432 (2021).
28. Böttcher, L., Xia, M. & Chou, T. Why case fatality ratios can be misleading: Individual- and population-based mortality estimates and factors influencing them. *Phys. Biol.* **17**, 065003 (2020).

29. Markovic, S. *et al.* COVID-19 severity determinants inferred through ecological and epidemiological modeling. *One Health* **13**, 100355 (2021).
30. Hastie, T., Tibshirani, R. & Friedman, J. *The Elements of Statistical Learning: Data Mining, Inference, and Prediction* (Springer, New York, 2009).
31. Rose, S. M. *et al.* Analysing COVID-19 outcomes in the context of the 2019 Global Health Security (GHS) Index. *BMJ Glob. Health* **6**, e007581 (2021).
32. Beaney, T. *et al.* Excess mortality: The gold standard in measuring the impact of COVID-19 worldwide?. *J R Soc. Med.* **113**, 329–334 (2020).
33. Milani, F. COVID-19 outbreak, social response, and early economic effects: A global VAR analysis of cross-country interdependencies. *J. Popul. Econ.* **34**, 223–252 (2021).
34. Chaudhry, R., Dranitsaris, G., Mubashir, T., Bartoszko, J. & Riazi, S. A country level analysis measuring the impact of government actions, country preparedness and socioeconomic factors on COVID-19 mortality and related health outcomes. *EClinicalMedicine* **25**, 100464 (2020).
35. Kong, J. D., Tekwa, E. W. & Gignoux-Wolfsohn, S. A. Social, economic, and environmental factors influencing the basic reproduction number of COVID-19 across countries. *PLoS ONE* **16**, e0252373 (2021).
36. Calderón-Larrañaga, A. *et al.* High excess mortality in areas with young and socially vulnerable populations during the COVID-19 outbreak in Stockholm Region, Sweden. *BMJ Glob. Health* **5**, e003595 (2020).
37. Stokes, A. C. *et al.* Association of health care factors with excess deaths not assigned to COVID-19 in the US. *JAMA Netw. Open* **4**, e2125287 (2021).
38. Stokes, A. C. *et al.* COVID-19 and excess mortality in the United States: A county-level analysis. *PLoS Med.* **18**, e1003571 (2021).
39. Modi, C., Böhm, V., Ferraro, S., Stein, G. & Seljak, U. Estimating COVID-19 mortality in Italy early in the COVID-19 pandemic. *Nat. Commun.* **12**, 2729 (2021).
40. Sanmarchi, F. *et al.* Exploring the gap between excess mortality and COVID-19 deaths in 67 countries. *JAMA Netw. Open* **4**, e2117359 (2021).
41. Cohen, J. & Rodgers, Y. van der M. Contributing factors to personal protective equipment shortages during the COVID-19 pandemic. *Prev Med* **141**, 106263 (2020).
42. Ranney, M. L., Griffith, V. & Jha, A. K. Critical supply shortages — the need for ventilators and personal protective equipment during the Covid-19 pandemic. *N. Engl. J. Med.* **382**, e41 (2020).
43. GHS Index. The 2021 Global Health Security Index. *GHS Index* <https://www.ghsindex.org/> (2021).
44. Oshinubi, K., Rachdi, M. & Demongeot, J. Analysis of reproduction number R0 of COVID-19 using current health expenditure as gross domestic product percentage (CHE/GDP) across countries. *Healthcare* **9**, 1247 (2021).
45. Oshinubi, K., Rachdi, M. & Demongeot, J. Modeling of COVID-19 pandemic vis-à-vis some socio-economic factors. *Front. Appl. Math. Stat.* **7**, 786983. <https://doi.org/10.3389/fams.2021.786983> (2022).
46. Waku, J., Oshinubi, K. & Demongeot, J. Maximal reproduction number estimation and identification of transmission rate from the first inflection point of new infectious cases waves: COVID-19 outbreak example. *Math. Comput. Simul.* **198**, 47–64 (2022).
47. GHS Index. COVID-19: Identifying the most vulnerable countries using the GHS index and global flight data. *GHS Index* <https://www.ghsindex.org/news/covid-19-identifying-the-most-vulnerable-countries-using-the-ghs-index-and-global-flight-data/> (2020).
48. Worldometer. Coronavirus Pandemic. <https://www.worldometers.info/coronavirus> (2020).
49. Karlinsky, A. & Kobak, D. Tracking excess mortality across countries during the COVID-19 pandemic with the World Mortality Dataset. *Elife* **10**, e69336 (2021).
50. Meinshausen, N. Relaxed lasso. *Comput. Stat. Data Anal.* **52**, 374–393 (2007).
51. Breiman, L. Random forests. *Mach. Learn.* **45**, 5–32 (2001).
52. Friedman, J. H. Greedy function approximation: A gradient boosting machine. *Ann. Stat.* **29**, 1189–1232 (2001).
53. MathWorks. Estimates of predictor importance for regression tree - MATLAB. <https://www.mathworks.com/help/stats/compactregressiontree.predictorimportance.html> (2022).
54. MathWorks. Estimates of predictor importance for regression ensemble - MATLAB. <https://www.mathworks.com/help/stats/compactregressionensemble.predictorimportance.html> (2022).
55. R Core Team. R: A Language and Environment for Statistical Computing. (2021).
56. Wei, T. & Simko, V. R package 'corrplot': Visualization of a Correlation Matrix. (2021).
57. RStudio Team. RStudio: Integrated Development Environment for R. (2020).

## Author contributions

Conceptualization: M.D., I.S., and S.M. Formal analysis: S.M. and M.D. Methodology: S.M., M.D., and A.R. Software: S.M. Supervision: M.D. and I.S. Validation: all authors. Visualization: S.M. and M.D. Manuscript writing, review, and editing: all authors.

## Funding

This work was partially supported by the Ministry of Education, Science, and Technological Development of the Republic of Serbia.

## Competing interests

The authors declare no competing interests.

## Additional information

**Supplementary Information** The online version contains supplementary material available at <https://doi.org/10.1038/s41598-022-22578-2>.

**Correspondence** and requests for materials should be addressed to M.D.

**Reprints and permissions information** is available at [www.nature.com/reprints](http://www.nature.com/reprints).

**Publisher's note** Springer Nature remains neutral with regard to jurisdictional claims in published maps and institutional affiliations.



**Open Access** This article is licensed under a Creative Commons Attribution 4.0 International License, which permits use, sharing, adaptation, distribution and reproduction in any medium or format, as long as you give appropriate credit to the original author(s) and the source, provide a link to the Creative Commons licence, and indicate if changes were made. The images or other third party material in this article are included in the article's Creative Commons licence, unless indicated otherwise in a credit line to the material. If material is not included in the article's Creative Commons licence and your intended use is not permitted by statutory regulation or exceeds the permitted use, you will need to obtain permission directly from the copyright holder. To view a copy of this licence, visit <http://creativecommons.org/licenses/by/4.0/>.

© The Author(s) 2022



# Effects of Demographic and Weather Parameters on COVID-19 Basic Reproduction Number

Igor Salom<sup>1</sup>, Andjela Rodic<sup>2</sup>, Ognjen Milicevic<sup>3</sup>, Dusan Zigic<sup>1</sup>, Magdalena Djordjevic<sup>1</sup> and Marko Djordjevic<sup>2\*</sup>

<sup>1</sup> Institute of Physics Belgrade, National Institute of the Republic of Serbia, University of Belgrade, Belgrade, Serbia,

<sup>2</sup> Quantitative Biology Group, Faculty of Biology, University of Belgrade, Belgrade, Serbia, <sup>3</sup> Department for Medical Statistics and Informatics, School of Medicine, University of Belgrade, Belgrade, Serbia

It is hard to overstate the importance of a timely prediction of the COVID-19 pandemic progression. Yet, this is not possible without a comprehensive understanding of environmental factors that may affect the infection transmissibility. Studies addressing parameters that may influence COVID-19 progression relied on either the total numbers of detected cases and similar proxies (which are highly sensitive to the testing capacity, levels of introduced social distancing measures, etc.), and/or a small number of analyzed factors, including analysis of regions that display a narrow range of these parameters. We here apply a novel approach, exploiting widespread growth regimes in COVID-19 detected case counts. By applying nonlinear dynamics methods to the exponential regime, we extract basic reproductive number  $R_0$  (i.e., the measure of COVID-19 inherent biological transmissibility), applying to the completely naïve population in the absence of social distancing, for 118 different countries. We then use bioinformatics methods to systematically collect data on a large number of potentially interesting demographics and weather parameters for these countries (where data was available), and seek their correlations with the rate of COVID-19 spread. While some of the already reported or assumed tendencies (e.g., negative correlation of transmissibility with temperature and humidity, significant correlation with UV, generally positive correlation with pollution levels) are also confirmed by our analysis, we report a number of both novel results and those that help settle existing disputes: the absence of dependence on wind speed and air pressure, negative correlation with precipitation; significant positive correlation with society development level (human development index) irrespective of testing policies, and percent of the urban population, but absence of correlation with population density *per se*. We find a strong positive correlation of transmissibility on alcohol consumption, and the absence of correlation on refugee numbers, contrary to some widespread beliefs. Significant tendencies with health-related factors are reported, including a detailed analysis of the blood type group showing consistent tendencies on Rh factor, and a strong positive correlation of transmissibility with cholesterol levels. Detailed comparisons of obtained results with previous findings, and limitations of our approach, are also provided.

**Keywords:** COVID-19 transmissibility, environmental factors, basic reproduction number, COVID-19 demographic dependence, COVID-19 weather dependence

## OPEN ACCESS

### Edited by:

Matteo Convertino,  
Hokkaido University, Japan

### Reviewed by:

Essam Rashed,  
Nagoya Institute of Technology, Japan  
Subhas Khajanchi,  
Presidency University, India  
Kankan Sarkar,  
Malda College, India

### \*Correspondence:

Marko Djordjevic  
dmarko@bio.bg.ac.rs

### Specialty section:

This article was submitted to  
Models in Ecology and Evolution,  
a section of the journal  
Frontiers in Ecology and Evolution

**Received:** 15 October 2020

**Accepted:** 28 December 2020

**Published:** 25 January 2021

### Citation:

Salom I, Rodic A, Milicevic O, Zigic D,  
Djordjevic M and Djordjevic M (2021)  
Effects of Demographic and Weather  
Parameters on COVID-19 Basic  
Reproduction Number.  
Front. Ecol. Evol. 8:617841.  
doi: 10.3389/fevo.2020.617841



## INTRODUCTION

The ancient wisdom teaches us that “knowing your adversary” is essential in every battle—and this equally applies to the current global struggle against the COVID-19 pandemic. Understanding the parameters that influence the course of the pandemic is of paramount importance in the ongoing worldwide attempts to minimize the devastating effects of the virus which, to the present moment, has already taken a toll of more than a million lives (Dong et al., 2020), and resulted in double-digit recession among some of the major world economies (World Bank, 2020a). Of all such factors, the ecological ones (both abiotic such as meteorological factors and biotic such as demographic and health-related population properties) likely play a prominent role in determining the dynamics of disease progression (Qu et al., 2020).

However, making good estimates of the effects that general demographic, health-related, and weather conditions, have on the spread of COVID-19 infection is beset by many difficulties. First of all, these dependencies are subtle and easily overshadowed by larger-scale effects. Furthermore, as the effective rate of disease spread is an interplay of numerous biological, medical, social, and physical factors, a particular challenge is to differentiate the dominating effects of local COVID-19-related policies, which are both highly heterogeneous and time-varying, often in an inconsistent manner. And this is precisely where, in our view, much of the previous research on this subject falls short.

There are not many directly observable variables that can be used to trace the progression of the epidemics on a global scale (i.e., for a large number of diverse countries). The most obvious one—the number of detected cases—is heavily influenced both by the excessiveness of the testing (which, in turn, depends on non-uniform medical guidelines, variable availability of testing kits, etc.) and by the introduced infection suppression measures (where the latter are not only non-homogeneous but are also erratically observed (Cohen and Kupferschmidt, 2020). Nevertheless, the majority of the research aimed to establish connections of the weather and/or demographic parameters with the spread of COVID-19 seeks correlations exactly with the raw number of detected cases (Adhikari and Yin, 2020; Correa-Araneda et al., 2020; Fareed et al., 2020; Gupta et al., 2020; Iqbal et al., 2020; Li et al., 2020; Pourghasemi et al., 2020; Rashed et al., 2020; Singh and Agarwal, 2020). For the aforementioned reasons, the conclusions reached in this way are questionable. Other variables that can be directly measured, such as the number of hospitalized patients or the number of COVID-19 induced deaths (Pranata et al., 2020; Tosepu et al., 2020; Ward, 2020), again depend on many additional parameters that are difficult to take into account: level of medical care and current hospital capacity, advancements, and changing practices in treating COVID-19 patients, the prevalence of risk groups, and even on the diverging definitions of when hospitalization or death should be attributed to the COVID-19 infection. As such, these variables are certainly not suitable as proxies of the SARS-CoV-2 transmissibility *per se*.

On the other hand, as we here empirically find [and as theoretically expected (Anderson and May, 1992; Keeling and

Rohani, 2011)] the initial stage of the COVID-19 epidemic (in a given country or area) is marked by a period of a nearly perfect exponential growth for a wide range of countries, which typically lasts for about 2 weeks (based on our analysis of the available data). One can observe widespread dynamical growth patterns for many countries, with a sharp transition between exponential, superlinear (growth faster than linear), and sublinear (growth slower than linear) regimes (see **Figure 1**)—the last two representing a subexponential growth. We here concentrate on the initial exponential growth of the detected-case data (marked in red in **Figure 1**), characterizing the period *before* the control measures took effect, and with a negligible fraction of the population resistant to infection. Note that dates which correspond to the exponential growth regime (included in **Supplementary Table 1**) are different for each country, corresponding to the different start of COVID-19 epidemic in those countries.

We use the exponential growth regime to deduce the basic reproduction number  $R_0$  (Martcheva, 2015), following a simple and robust mathematical (dynamical) model presented here.  $R_0$  is a straightforward and important epidemiological parameter characterizing the inherent biological transmissibility of the virus, in a completely naïve population, and the absence of social distancing measures (Bar-On et al., 2020; Eubank et al., 2020). To emphasize the absence of social distancing in the definition (and inference) of  $R_0$  used here, the term  $R_{0,free}$  is also used, — for simplicity, we further denote  $R_0 \equiv R_{0,free}$ .  $R_0$  is largely independent of the implemented COVID-19 policies and thus truly reflects the characteristics of the disease itself, as it starts to spread unhampered through the given (social and meteorological) settings. Namely, the exponential period ends precisely when the effect of control measures kick in, which happens with a delay of  $\sim 10$  days after their introduction

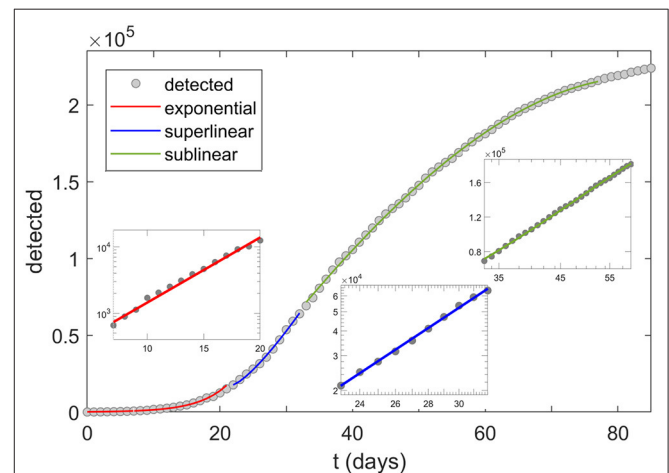


**FIGURE 1** | COVID-19 growth regimes. Transitions of the growth patterns (here shown for Italy) from exponential (red), to superlinear (blue) and sublinear (green) regime. The three insets correspond to the log-linear scale (exponential), log-log scale (superlinear), and linear-log scale (sublinear). Dots correspond to detected infections, starting from 20.02.2020. In this study,  $R_{0,free}$  is extracted from the slope of the first (exponential, i.e., log-linear) inset, corresponding to dates 29.02–13.03 in the case of Italy.

(The Novel Coronavirus Pneumonia Emergency Response Epidemiology Team, 2020), corresponding to the disease latent period, and to the time between the symptom onset and the disease confirmation. Not only that very few governments had enacted any social measures before the occurrence of a substantial number of cases (Cohen and Kupferschmidt, 2020), but also the length of the incubation period makes it likely that the infection had been already circulating for some time through the community even before the first detected case (and that the effects of the measures are inescapably delayed in general). Also, the transition from the exponential to the subsequent subexponential phase of the epidemics is readily visible in the COVID data (see **Figure 1**). Furthermore,  $R_0$  is invariant to the particular testing guidelines, as long as these do not significantly vary over the (here relatively short) studied period. Note that in **Figure 1** cumulative number of positive cases (also known as cumulative infection incidence) is shown, which has to monotonically increase—though with a decreasing rate, once the infection starts to slow down, i.e., once the subexponential growth (sublinear and superlinear regimes) is reached.

In the analysis presented here, we consider 42 different weather, demographic, and health-related population factors, whose analyzed ranges correspond to their variations exhibited in 118 world countries (not all of the parameters were available for all of the countries, as discussed in Section “Demographic and Weather Data Acquisition”). While some authors prefer more coherent data samples to avoid confusing effects of too many different factors (Adhikari and Yin, 2020; Correa-Araneda et al., 2020; Fareed et al., 2020; Rashed et al., 2020; Singh and Agarwal, 2020; Tosepu et al., 2020), this consideration is outweighed by the fact that large ranges of the analyzed parameters serve to amplify the effects we are seeking to recognize and to more reliably determine the underlying correlations. For example, while the value of the Human Development Index (HDI, a composite index of life expectancy, education, and per capita income indicators) varies from 0.36 to 0.96 over the set of analyzed countries, this range would drop by an order of magnitude (Global Data Lab, 2020) if the states of the US were chosen as the scope of the study (other demographic parameters exhibit similar behavior). The input parameters must take values in some substantial ranges to have measurable effects on  $R_0$  (i.e., small variations may lead to effects that are easily lost in statistical fluctuations).

The number of considered parameters is also significant, especially when compared to other similar studies (Adhikari and Yin, 2020; Copat et al., 2020; Fareed et al., 2020; Iqbal et al., 2020; Rashed et al., 2020; Rychter et al., 2020; Singh and Agarwal, 2020; Thangriyal et al., 2020; Tosepu et al., 2020). In a model where a large number of factors are analyzed under the same framework, consistency of the obtained results, in terms of agreement with other studies, common-sense expectations, and their self-consistency, becomes an important check of applied methodology and analysis. Furthermore, a comprehensive and robust analysis is expected to generate new findings and lead to novel hypotheses on how environmental factors influence COVID-19 spread. Overall, we expect that the understanding achieved here will contribute to the ability to understand the behavior of the pandemics in the future and, by the same token,

to timely and properly take measures in an attempt to ameliorate the disease effects.

## MODEL AND PARAMETER EXTRACTION

### Modified SEIR Model and Relevant Approximations

There are various theoretical models and tools used to investigate and predict the progress of an epidemic (Keeling and Rohani, 2011; Martcheva, 2015). We here opted for the SEIR compartmental model, up to now used to predict or explain different features of COVID-19 infection dynamics (Maier and Brockmann, 2020; Maslov and Goldenfeld, 2020; Perkins and España, 2020; Tian et al., 2020; Weitz et al., 2020). The model is sufficiently simple to be applied to a wide range of countries while capturing all the features of COVID-19 progression relevant for extracting the  $R_0$  values. The model assumes dividing the entire population into four (mutually exclusive) compartments with labels: (S)usceptible, (E)xposed, (I)nfected, and (R)ecovered.

The dynamics of the model (which considers gradual transitions of the population from one compartment to the other) directly reflects the disease progression. Initially, a healthy individual has no developed SARS-CoV-2 virus immunity and is considered as “susceptible.” Through contact with another infected individual, this person may become “exposed”—denoting that the transmission of the virus has occurred, but the newly infected person at this point has neither symptoms nor can yet transmit the disease. An exposed person becomes “infected”—in the sense of becoming contagious—on average after the so-called “latent” period which is, in the case of COVID-19, approximately 3 days. After a certain period of the disease, this person ceases to be contagious and is then considered as “recovered” (from the mathematical perspective of the model, “recovered” are all individuals who are no longer contagious, which therefore also includes deceased persons). In the present model, the recovered individuals are taken to be no longer susceptible to new infections (irrespective of whether the COVID-19 immunity is permanent or not, it is certainly sufficiently long in the context of our analysis).

Accordingly, almost the entire population initially belongs to the susceptible class. Subsequently, parts of the population become exposed, then infected, and finally recovered. SARS-CoV-2 epidemic is characterized by a large proportion of asymptomatic cases (or cases with very mild symptoms) (Day, 2020), which leads to a large number of cases that remain undiagnosed. For this reason, only a portion of the infected will be identified (diagnosed) in the population, and we classify them as “detected.” This number is important since it is the only direct observable in our model, i.e., the only number that can be directly related to the actual COVID-19 data.

This dynamic is schematically represented in **Figure 2**, and is governed by the following set of differential equations:

$$\frac{dS}{dt} = -\frac{\beta SI}{N} \quad (1)$$

$$\frac{dE}{dt} = \frac{\beta SI}{N} - \sigma E \quad (2)$$

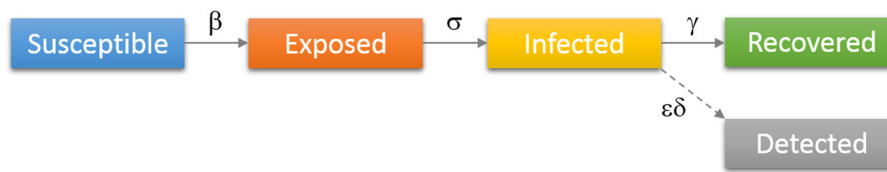


**FIGURE 2** | Diagrammatic representation of the SEIR model with the added class of “Detected” patients. Individuals move (denoted by solid arrows) from Susceptible to Exposed to Infected to Recovered, with the rates indicated above arrows in the figure. Some of the infected are detected (diagnosed/confirmed), indicated by the dashed arrow.

$$\frac{dI}{dt} = \sigma E - \gamma I \quad (3)$$

$$\frac{dR}{dt} = \gamma I \quad (4)$$

$$\frac{dD}{dt} = \varepsilon \delta I \quad (5)$$

In the above equations,  $S$ ,  $E$ ,  $I$ , and  $R$  denote numbers of individuals belonging to, respectively, susceptible, exposed, infected, and recovered compartments,  $D$  is the cumulative number of detected cases, while  $N$  is the total population. Parameter  $\beta$  denotes the transmission rate, which is proportional to the probability of disease transmission in contact between a susceptible and an infectious subject. Incubation rate  $\sigma$  determines the rate at which exposed individuals become infected and corresponds to the inverse of the average incubation period. Recovery rate  $\gamma$  determines the transition rate between infected and recovered parts of the population, (i.e.,  $1/\gamma$  is the average period during which an individual is infectious). Finally,  $\varepsilon$  and  $\delta$  are detection efficiency and the detection rate. All these rate parameters are considered constant during the analyzed (brief) period. Also, note that the constants in our model do not correspond to transition probabilities *per se*, but rather to transition rates (with units 1/time), so that e.g.  $\gamma$  and  $\varepsilon\delta$  do not add to one. While rates in the model can be rescaled and normalized to directly correspond to transition probabilities, our formulation (with rates rather than probabilities) is rather common (see e.g., Keeling and Rohani, 2011), and also has a direct intuitive interpretation, where the transition rates correspond to the inverse of the period that individuals spend in a given compartment (see e.g., the explanation for  $\gamma$  above).

In the first stage of the epidemic, when essentially the entire population is susceptible (i.e.,  $S/N \approx 1$ ) and no distancing measures are enforced, the average number of secondary infections, caused directly by primary-infected individuals, corresponds to the basic reproduction number  $R_0$ . The infectious disease can spread through the population only when  $R_0 > 1$  (Khajanchi et al., 2020a), and in these cases, the initial growth of the infected cases is exponential. Though  $R_0$  is a characteristic of the pathogen, it also depends on environmental abiotic (e.g., local weather conditions), as well as biotic factors (e.g., prevalence of health conditions, and population mobility tightly related to the social development level).

Note that, as we seek to extract the basic reproduction number  $R_0$  from the model for a wide range of countries,

the social distancing effects are not included in the model presented above. That is, the introduced model serves only to explain the exponential growth phase—note that this growth regime characterizes part of the infection progression where the social distancing interventions still did not take effect, and where the fraction of resistant (non-susceptible) population is still negligible. It is only this phase which is relevant for extracting  $R_0$  that is used in the subsequent analysis.  $R_0$  should not be confused with the effective reproduction number  $R_e$ , which takes into account also the effects of social distancing interventions and the decrease in the number of susceptibles due to acquired infection resistance.  $R_e$  is not considered in this work, as we are concerned with the factors that affect the inherent biological transmissibility of the virus, independently from the applied measures. That is, by considering  $R_0$  rather than  $R_e$ , we disentangle the influence of meteorological and demographic factors on transmissibility (the goal of this study), from the effects of social distancing interventions (not analyzed here). The model can, however, be straightforwardly extended to include social distancing measures, as we did in (Djordjevic et al., 2020)—social distancing measures were also included through other frameworks (Khajanchi and Sarkar, 2020; Maier and Brockmann, 2020; Maslov and Goldenfeld, 2020; Perkins and España, 2020; Samui et al., 2020; Sarkar et al., 2020; Tian et al., 2020; Weitz et al., 2020). Such extensions are needed to explain the subexponential growth that emerges due to intervention measures (i.e., superlinear and sublinear growth regimes that are illustrated in **Figure 1** for Italy but are common for other countries as well).

## COVID-19 Growth Regimes

If we observe the number of total COVID-19 cases (e.g., in a given country) as a function of time, there is a regular pattern that we observe: the growth of the detected COVID cases is initially exponential but slows down after some time—when we say it enters the subexponential regime. The subexponential regime can be further divided into the superlinear (growing asymptotically faster than a linear function) and sublinear regime (the growth is asymptotically slower than a linear function). This typical behavior is illustrated, in the case of Italy, in **Figure 1** above. The transition to the subexponential regime occurs relatively soon, much before a significant portion of the population gains immunity, and is a consequence of the introduction of the infection suppression measures.

## Inference of the Basic Reproduction Number $R_0$

In the initial exponential regime, a linear approximation to the model can be applied. Namely, in this stage, almost the entire population is susceptible to the virus, i.e.,  $S/N \approx 1$ , which simplifies the Equation (2) to:

$$\frac{dE}{dt} = -\sigma E + \beta I. \quad (6)$$

By combining expressions (3) and (6) one obtains:

$$\frac{d}{dt} \begin{pmatrix} E \\ I \end{pmatrix} = \begin{pmatrix} -\sigma & \beta \\ \sigma & -\gamma \end{pmatrix} \begin{pmatrix} E \\ I \end{pmatrix} = A \begin{pmatrix} E \\ I \end{pmatrix}, \quad (7)$$

where we have introduced a two-by-two matrix:

$$A = \begin{pmatrix} -\sigma & \beta \\ \sigma & -\gamma \end{pmatrix} \quad (8)$$

The solution for the number of infected individuals can now be written:

$$I(t) = C_1 \cdot e^{\lambda_+ t} + C_2 \cdot e^{\lambda_- t}, \quad (9)$$

where  $\lambda_+$  and  $\lambda_-$  denote eigenvalues of the matrix A, i.e., the solutions of the equation:

$$\det(A - \lambda I) = 0. \quad (10)$$

The eigenvalues must satisfy:

$$\begin{vmatrix} -\sigma - \lambda & \beta \\ \sigma & -\gamma - \lambda \end{vmatrix} = 0,$$

leading to:

$$(\lambda + \sigma) \cdot (\lambda + \gamma) - \beta \cdot \sigma = 0. \quad (11)$$

The solutions of (11) are:

$$\lambda_{\pm} = \frac{-(\gamma + \sigma) \pm \sqrt{(\gamma - \sigma)^2 + 4\beta\sigma}}{2}. \quad (12)$$

Since  $\lambda_- < 0$ , the second term in (9) can be neglected for sufficiently large  $t$ . More precisely, numerical analysis shows that this approximation is valid already after the second day, while, for the extraction of  $R_0$  value we will anyhow ignore all data before the fifth day (for the analyzed countries, numbers of cases before the fifth day were generally too low, hence this early data is dominated by stochastic effects/fluctuations). Hence,  $I(t)$  is proportional to  $\exp(\lambda_+ t)$ , i.e.:

$$I(t) = I(0) \cdot e^{\lambda_+ t}. \quad (13)$$

By using  $\beta$  from (12) and  $R_0 = \frac{\beta}{\gamma}$  (Keeling and Rohani, 2011; Martcheva, 2015), we obtain:

$$R_0 = 1 + \frac{\lambda_+ \cdot (\gamma + \sigma) + \lambda_+^2}{\gamma \cdot \sigma}. \quad (14)$$

From (13) and (5) we compute:

$$D(t) = \varepsilon \cdot \delta \cdot I(0) \cdot \frac{(e^{\lambda_+ t} - 1)}{\lambda_+}. \quad (15)$$

By taking the logarithm, the above expression leads to:

$$\log(D(t)) = \log(\varepsilon \delta I(0) / \lambda_+) + \lambda_+ \cdot t, \quad (16)$$

from which  $\lambda_+$  can be obtained as the slope of the  $\log(D(t))$  function. From Equation (14), we thus obtain the  $R_0$  value as a function of the slope of  $\log(D(t))$ , where the latter can be efficiently inferred from the plot of the number of detected COVID-19 cases for a large set of countries.

The SEIR model and the above derivation of  $R_0$  assume that the population belonging to different compartments is uniformly mixed. Possible heterogeneities may tend to increase  $R_0$  values (Keeling and Rohani, 2011). However, this would not influence the results obtained below, as our  $R_0$  values are consistently inferred for all analyzed countries by using the same model, methodology, and parameter set. Moreover, our  $R_0$  values are in agreement with the prevailing estimates in the literature (Najafimehr et al., 2020).

## Demographic and Weather Data Acquisition

For the countries for which  $R_0$  was determined through the procedure above, we also collect a broad spectrum of meteorological and demographic parameter values. Overall, 118 countries were selected for our analysis, based on the relevance of the COVID-19 epidemiological data. Namely, a country was considered as relevant for the analysis if the number of detected cases on June 15th was higher than a threshold value of 1,000. A few countries were then discarded from this initial set, where the case count growth was too irregular to extract any results, possibly due to inconsistent or irregular testing policies. As a source for detected cases, we used (World Bank, 2020b; Worldometer, 2020).

In the search for factors correlated with COVID-19 transmissibility, we have analyzed overall 42 parameters, 11 of which are related to weather conditions, 30 to demographics or health-related population characteristics, and one parameter quantifying a delay in the epidemic's onset (data provided in **Supplementary Tables 2–5**). Not all of these parameters were available for all of the considered countries. In particular, data on the prevalence of blood types (**Supplementary Table 4** in the Supplement) was possible to find for 83 of the 118 countries, while, primarily due to scarce data on pollutant concentrations during the epidemics, almost 30% of entries in **Supplementary Table 5** in Supplement had to be left blank for this category. Nevertheless, we opted to include these parameters in our report: despite the lower number of values, some of these parameters exhibited strong and highly statistically significant correlations with  $R_0$ , warranting their inclusion.

Our main source of weather data was project POWER (Prediction of Worldwide Energy Resources) of the NASA agency (NASA Langley Research Center, 2020). A dedicated



Python script was written and used to acquire weather data via the provided API (Application Programming Interface). NASA project API allows a large set of weather parameters to be obtained for any given location (specified by latitude and longitude) and given date (these data are provided in the **Supplementary Table 7**). From this source, we gathered data on temperature (estimated at 2 m above ground), specific humidity (estimated at 2 m above ground), wind speed (estimated at 2 m above ground), and precipitation (defined as the total column of precipitable water). Data on air pressure (at ground level) and UV index (international standard measurement of the strength of sunburn-producing ultraviolet radiation) were collected via similar API from World Weather Online source (World Weather Online, 2020), using the same averaging methodology. Since we needed to assign a single value to each country (for each analyzed parameter), the following method was used for averaging meteorological data. In each country, a number of largest cities<sup>1</sup> were selected and weather data was taken for the corresponding locations. These data was then averaged, weighted by the population of each city, followed by averaging over the period used for  $R_0$  estimation (more precisely, to account for the time between disease transmission and the case confirmation, we shifted this period 12 days into the past). The applied averaging method used here can be of limited adequacy in countries spreading over multiple climate zones, but is still expected to provide reasonable single-value estimates of the weather parameters, particularly since the averaging procedure was formulated to reflect the most likely COVID-19 hotspots in a given country.

Demographic data was collected from several sources. Percentage of the urban population, refugees, net migration, social and medical insurance coverage, infant mortality, and disease (CVD, cancer, diabetes, and CRD) risk was taken from the World Bank organization (World Bank, 2020b). The HDI was taken from the Our World in Data source (Our World in Data, 2020), while median age information was obtained from the CIA website. The source of most of the considered medical parameters: cholesterol, raised blood pressure, obesity, inactivity, BSG vaccination as well as data on alcohol consumption and smoking prevalence was World Health Organization (World Health Organization, 2020). Data for blood types were taken from the Wikidata web site. BUCAP parameter, representing population density in the built-up area, was taken from GHS Urban Center Database 2015 (European Commission Global Human Settlement, 2020). The onset parameter, determining the delay (in days) of the epidemic's start, was inferred from COVID-19 counts data. We used the most recent available data for all the parameters.

## RESULTS

The  $\log(D(t))$  function, for a subset of selected countries, is shown in **Figure 3**. The obvious linear dependence confirms that

<sup>1</sup>This number was determined for each country by the following condition: the total population of the cities taken into consideration had to surpass 10 percent of the overall population of the country.

the progression of the epidemic in this stage is almost perfectly exponential. Note that our model exactly reproduces this early exponential growth (see Equation 13), happening under the assumption of a small fraction of the population being resistant, and the absence of the effect of social distancing interventions. From **Figure 3**, we see that this behavior, predicted by the model for the early stage of the epidemic, is also directly supported by the data, i.e., the exponential growth in the cumulative number of confirmed cases is indeed observed for a wide range of countries. For each country, the parameter  $\lambda_+$  is directly obtained as the slope of the corresponding linear fit of the  $\log(D(t))$ , and the basic reproduction number  $R_0$  is then calculated from Equation (14). Here, we used the following values for the incubation rate,  $\sigma = 1/3 \text{ day}^{-1}$ , and for the recovery rate  $\gamma = 1/4 \text{ day}^{-1}$ , per the commonly accepted values in the literature (Bar-On et al., 2020). Note that possible variations in these two values would not significantly affect any conclusions about  $R_0$  correlations, due to the mathematical properties of the relation (14): it is a strictly monotonous function of  $\lambda_+$  and the linear term  $\lambda_+ \cdot (\gamma + \sigma) / \gamma \cdot \sigma$  dominantly determines the value of  $R_0$ .

Supplementary tables contain the values for 42 variables, for all countries. Correlations of each of the variables with  $R_0$  are given in **Supplementary Table 6**. Values for the Pearson correlation coefficient are further shown below, though consistent conclusions are also obtained by Kendall and Spearman correlation coefficients (which do not assume a linear relationship between variables). Correlation coefficients were calculated in the usual manner: as the correlation of the vector of parameter values with the vector of  $R_0$  values, by taking into account all available data (for parameters that were available across all of the countries, both of the vectors were 118 dimensional; if values were missing for certain countries, these countries were simply ignored and lower-dimensional vectors were compared).

The first set of results that corresponds to, roughly speaking, general demographic data, is presented in **Figure 4**. The plot in panel A shows the distribution of  $R_0$  vs. HDI values for all countries, where a higher HDI score indicates the more prosperous country concerning life expectancy, education, and per capita income (Sagar and Najam, 1998). This parameter was included in the study due to a reasonable expectation that a higher level of social development also implies a higher level of population interconnectedness and mixing (stronger business and social activity, more travelers, more frequent contacts, etc.), and hence that HDI could be related to the SARS-CoV-2 transmissibility. Indeed, we note a strong, statistically highly significant correlation between the HDI and the  $R_0$  value, with  $R = 0.37$ , and  $p = 4 \cdot 10^{-5}$ , demonstrating that the initial expansion of COVID-19 was faster in more developed societies.

The social security and health insurance coverage (INS) “shows the percentage of population participating in programs that provide old age contributory pensions (including survivors and disability) and social security and health insurance benefits (including occupational injury benefits, paid sick leave, maternity, and other social insurance)” (World Bank, 2020b). Reflecting the percentage of the population covered by medical insurance and likely feeling more protected from the financial



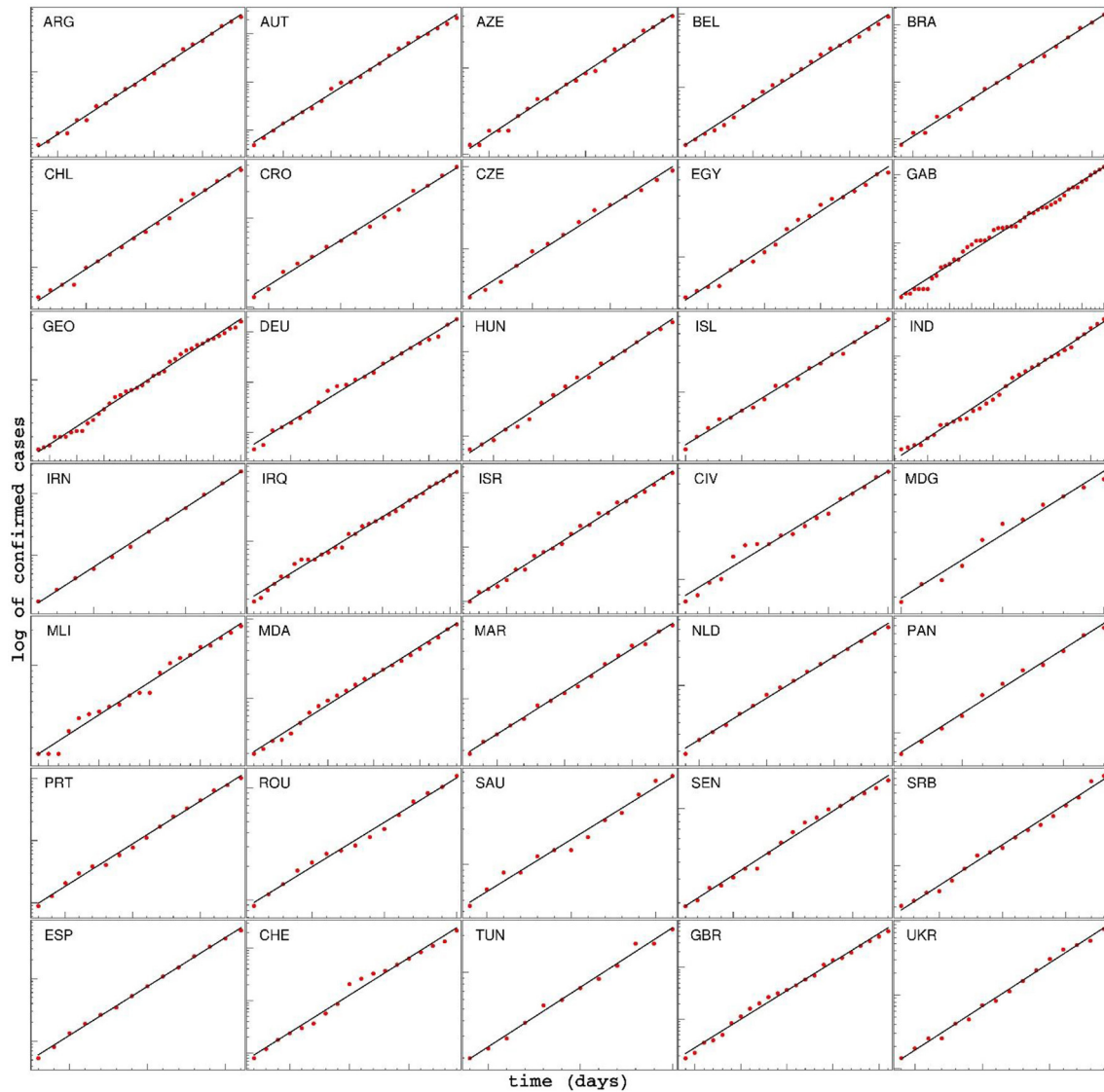
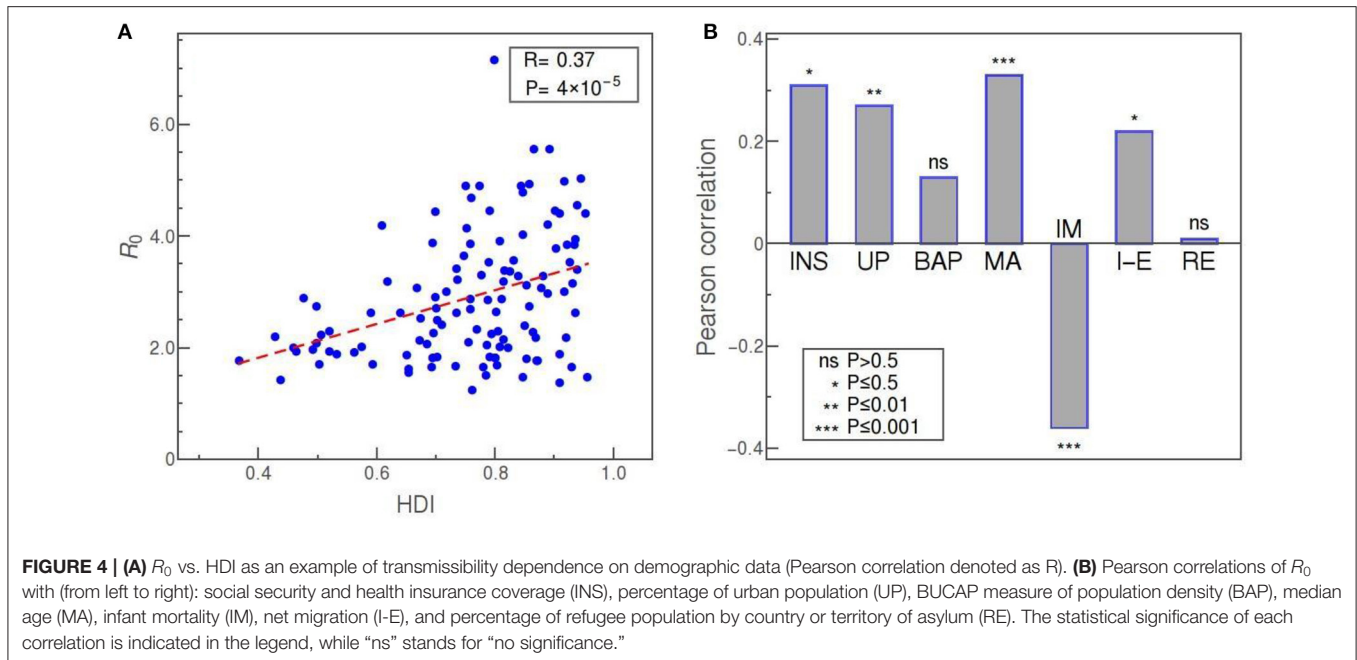


**FIGURE 3 |** Time dependence of the detected cases for various countries, during the initial period of the epidemic, shown on a log-linear scale. The linear fit of  $\log(D)$  shows that the spread of COVID-19 in this phase is very well approximated by exponential growth. Note that the values on axes are chosen differently for each country, in order to emphasize the exponential character of the growth. For each country, the start and end dates of the exponential regime, together with the extracted slope  $\lambda_+$ , are provided in the **Supplementary Table 1**. ARG, Argentina; AUT, Austria; AZE, Azerbaijan; BEL, Belgium; BRA, Brazil; CHL, Chile; CRO, Croatia; CZE, Czech Republic; EGY, Egypt; GAB, Gabon; GEO, Georgia; DEU, Germany; HUN, Hungary; ISL, Iceland; IND, India; IRN, Iran; IRQ, Iraq; ISR, Israel; CIV, Cote d'Ivoire; MDG, Madagascar; MLI, Mali; MDA, Moldova; MAR, Morocco; NLD, Netherlands; PAN, Panama; PRT, Portugal; ROU, Romania; SAU, Saudi Arabia; SEN, Senegal; SRB, Serbia; ESP, Spain; CHE, Switzerland; TUN, Tunisia; GBR, Great Britain; UKR, Ukraine.

effects of the epidemics, this indicator shows a strong ( $R = 0.4$ ) and highly significant ( $p = 4 \cdot 10^{-4}$ ) positive correlation with  $R_0$ . The percentage of urban population (UP) and BUCAP density (BAP) are both included as measures of how concentrated is the population of the country. While the UP value simply shows what percentage of the population lives in cities, the BUCAP parameter denotes the amount of built-up area per person. Of the two, the former shows a highly significant positive correlation with the COVID-19 basic reproduction number, whereas the latter shows no correlation. Median age (MA) should be of obvious potential relevance in COVID-19 studies since it is well

known that the disease more severely affects the older population (Jordan et al., 2020). Thus, we wanted to investigate also if there is any connection of age with the virus transmissibility. Our results are suggestive of such a connection, since we obtained a strong positive correlation of age with  $R_0$ , with very high statistical confidence. Infant mortality (IM) is defined as the number of infants dying before reaching 1 year of age, per 1,000 live births. Lower IM rates can serve as another indicator of the prosperity of a society, and it turns out that this measure is also strongly correlated, but negatively, with  $R = -0.36$  and  $p = 8 \cdot 10^{-5}$  (showing again that more developed countries, i.e.,

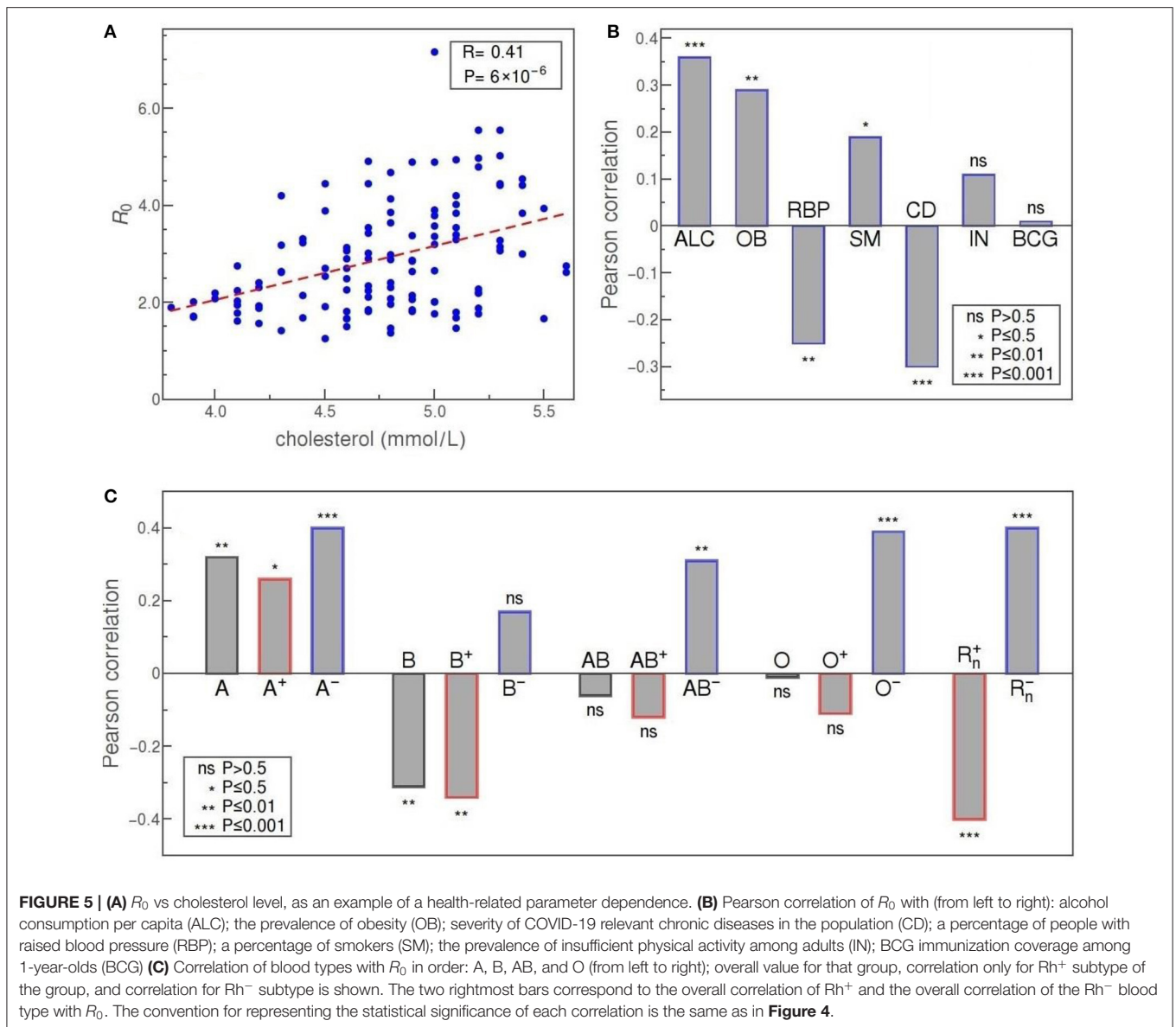


those with lower IM rates, have experienced more rapid spread of the virus infection). Net migration (I-E) represents the 5-year estimates of the total number of immigrants less the annual number of emigrants, including both citizens and non-citizens. This number, related to the net influx of foreigners, turns out to be positively correlated, in a statistically significant way, with  $R_0$ . However, according to our data, the percentage of refugees, defined as the percentage of the people in the country who are legally recognized as refugees and were granted asylum in that country, is not correlated with  $R_0$  at all.

Another set of parameters corresponds to medically-related demographic parameters and is shown in the upper part of **Figure 5**. The plot in panel A represents the average blood cholesterol level (in mmol/L) in the population of various countries, plotted against the value of  $R_0$ . The two parameters are strongly correlated, with  $R = 0.4$ , and  $p = 6 \cdot 10^{-6}$ . Another demographic parameter with clear medical relevance, that has a comparatively strong and significant positive correlation with  $R_0$ , is the alcohol consumption per capita (ALC), as shown in panel B of **Figure 5**. Our data shows that  $R_0$  is also positively correlated, with high statistical significance, with the prevalence of obesity and to a somewhat smaller extent with the percentage of smokers. Here, obesity is defined as having a body-mass index over 30. A medical parameter that is strongly, but negatively, correlated with  $R_0$ , is a measure of prevalence and severity of COVID-19 relevant chronic diseases in the population (CD). This parameter is defined as “the percent of 30-year-old-people who would die before their 70th birthday from any of cardiovascular disease, cancer, diabetes, or chronic respiratory disease, assuming that s/he would experience current mortality rates at every age and s/he would not die from any other cause of death” (World Bank, 2020b). The percentage of people with raised blood pressure (RBP) is also negatively

correlated with  $R_0$ , though this correlation is not as strong and as statistically significant as in the case of the CD parameter. Here, raised blood pressure is defined as systolic blood pressure over 140 or diastolic blood pressure over 90, in the population older than 18. The percentage of smokers exhibits statistically significant (though not large) positive correlation. Two medical-demographic parameters that show no correlation with  $R_0$  in our data are the prevalence of insufficient physical activity among adults aged over 18 (IN) and BCG immunization coverage among 1-year-olds (BCG).

In **Figure 5C** we see that blood types are, in general, strongly correlated with  $R_0$ . The highest positive correlation is exhibited by  $A^-$  and  $O^-$  types, with a Pearson correlation of 0.4 and 0.39, and a very high statistical significance of  $p = 10^{-4}$  and  $p = 2 \cdot 10^{-4}$ , respectively. Taken as a whole, group A is still strongly and positively correlated with  $R_0$ , albeit with a bit lower statistical significance ( $A^+$  type correlation has  $p$ -value two orders of magnitude higher than  $A^-$ ). This is not so for group O that, overall, does not seem to be correlated to  $R_0$  ( $O^+$  even shows a certain negative correlation but without statistical significance). Our data reveals a highly significant positive correlation also for  $AB^-$  subtype ( $R = 0.31$ ,  $p = 0.003$ ), while neither the  $AB^+$  subtype nor overall AB group is significantly correlated with the basic reproduction number. Clear negative correlation is exhibited only by B blood group ( $R = -0.31$ ,  $p = 0.004$ ), mostly due to the negative correlation of its  $B^+$  subtype ( $R = -0.34$ ,  $p = 0.001$ ), whereas  $B^-$  subtype is not significantly correlated with  $R_0$  in our data. If we consider the rhesus factor alone, we again observe very strong correlations with  $R_0$  and with very high statistical significance:  $Rh^-$  and  $Rh^+$  correlate positively ( $R = 0.4$ ) and negatively ( $R = -0.4$ ), respectively, with very high statistical significance ( $p = 2 \cdot 10^{-4}$ ). The tendency of  $Rh^-$  and  $Rh^+$  to, respectively, increase and decrease the transmissibility,



is therefore consistent with the results obtained for all four individual blood-groups.

In **Figure 6**, the onset represents the delay of the exponential phase and is defined, for each country, as the number of days from February 15 to the start of the exponential growth of detected cases. The motivation was to check for a possible correlation between the delay in the onset of the epidemic and the rate at which it spreads. Indeed, our data shows that such correlation exists and that it is strong and statistically significant:  $R = -0.48$  and  $p = 4 \cdot 10^{-8}$ . In other words, the later the epidemic started, the lower (on average) is the basic reproduction number.

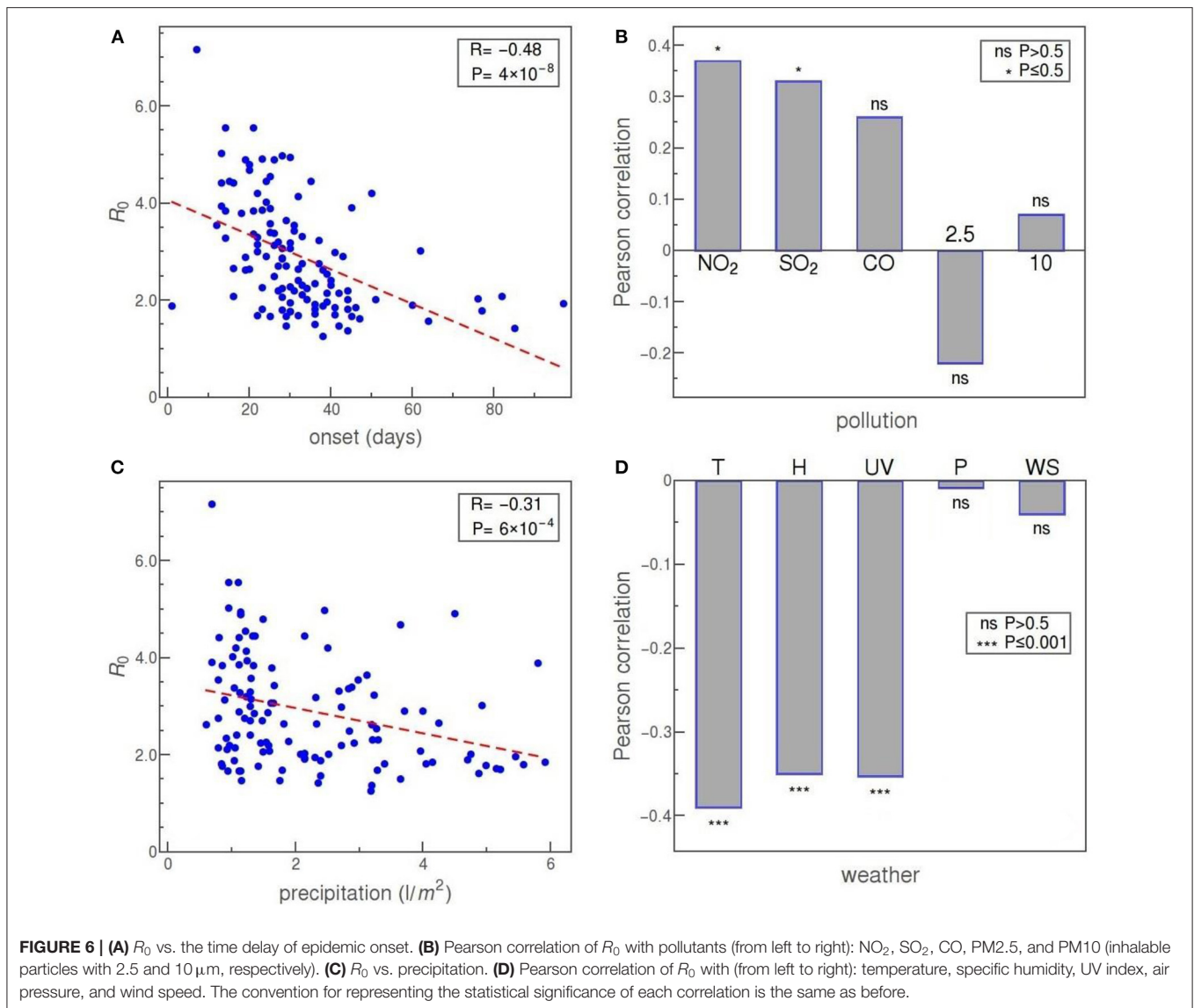
Panel B of **Figure 6** shows the correlation of  $R_0$  with some of the commonly considered air pollutants. Our data reveal a statistically significant positive correlation of  $R_0$  with  $\text{NO}_2$  and  $\text{SO}_2$  concentrations. Other pollutants—CO, PM<sub>2.5</sub> (fine inhalable particles, with diameters that are generally 2.5  $\mu\text{m}$

and smaller), and PM<sub>10</sub> (inhalable particles, up to 10 nm in diameter)—show no statistically significant correlation with  $R_0$ .

Next, we consider weather factors. Panels C and D of **Figure 6** show correlations of precipitation, temperature, specific humidity, UV index, air pressure, and wind speed with the reproduction number  $R_0$ . Of these, precipitation, temperature, specific humidity, and UV index show a strong negative correlation, at a high level of statistical significance. Of the other two parameters, both air pressure and wind speed are not correlated at all with  $R_0$  in our data.

## DISCUSSION

The present paper aimed to establish relations between the COVID-19 transmissibility and a large number of



demographic and weather parameters. As a measure of COVID-19 transmissibility, we have chosen the basic reproduction number  $R_0$ —a quantity that is essentially independent of the variations in both the testing policies and the introduced social measures (as discussed in the Introduction), in distinction to many studies on transmissibility that relied on the total number of detected case counts [see e.g., (Adhikari and Yin, 2020; Correa-Araneda et al., 2020; Fareed et al., 2020; Gupta et al., 2020; Iqbal et al., 2020; Li et al., 2020; Pourghasemi et al., 2020; Rashed et al., 2020; Singh and Agarwal, 2020)]. We have covered a substantial number of demographic and weather parameters, and included in our analysis all world countries that were significantly affected by the COVID-19 pandemic (and had a reasonable consistency in tracking the early phase of infection progression). While a number of manuscripts have been devoted to factors that may influence COVID-19 progression, only a few used an estimate of  $R_0$  or some of its

proxies (Coccia, 2020; Contini and Costabile, 2020; Copiello and Grillenzoni, 2020)—these studies were however limited to China, and included a small set of meteorological variables, with conflicting results obtained for their influence on  $R_0$ . Therefore, a combination of (i) using a reliable and robust measure of COVID-19 transmissibility, and (ii) considering a large number of factors that may influence this transmissibility within the same study/framework, distinguishes our study over prior work. We, however, must be cautious when it comes to further interpretation of the obtained data. As always, we must keep in mind that “correlation does not imply causation” and that further research is necessary to identify possible confounding factors and establish which of these parameters truly affect the COVID-19 transmissibility. Due to the sheer number of studied variables, an even larger number of parameters that might be relevant but are inaccessible to study (or even impossible to quantify), as well as due to possible intricate mutual relations of



the factors that may influence COVID-19 transmission, this is a highly non-trivial task. While we postpone any further analysis in this direction to future studies, we will, nevertheless, consider here the possible interpretations of the obtained correlations, assuming that they also probably indicate the existence of at least some causation. We below provide a detailed comparison between our results and previous findings. While a detailed discussion is presented, despite our best effort, we may have missed some of the relevant references due to an extremely rapidly developing field. Nevertheless, we point out a clear distinction of our work with previous studies, as outlined in this paragraph.

We will first consider the demographic variables presented in **Figure 4**. The obtained correlation of the HDI with the basic reproduction number is both strong and hardly surprising. The level of prosperity and overall development of a society is necessarily tied with the degree of population mobility and mixing, traffic intensity (in particular air traffic), business and social activity, higher local concentrations of people, and other factors that directly or indirectly increase the frequency and range of personal contacts (Gangemi et al., 2020), rendering the entire society more vulnerable to the spread of viruses. In this light, it is reasonably safe to assume that the obtained strong and highly statistically significant correlation of HDI with  $R_0$  reflects a truly causal connection. However, some authors offer also a different explanation: that higher virus transmission in more developed countries is a consequence of more efficient detection of COVID-19 cases due to the better-organized health system (Gangemi et al., 2020)—but since our  $R_0$  measure does not depend on detection efficiency, presented results can be taken as evidence against such hypothesis.

The interpretation is less clear for other demographic parameters, for example, the percentage of the population covered by medical and social insurance programs (INS). While there seem to be no previous studies discussing this parameter, one possibility is to attribute its strong positive correlation with  $R_0$  to a hypothetical tendency of population to more easily indulge in the epidemiologically-risky behavior if they feel well-protected, both medically and financially, from the risks posed by the virus; conversely, that the population that cannot rely on professional medical care in the case of illness is likely to be more cautious not to contract the virus. The other is, of course, to see this correlation as an indirect consequence of the strong correlation of this parameter with HDI—which is also, almost certainly, the underlying explanation of the infant mortality (IM) correlation, where low mortality ratios point to a better medical system, which goes hand in hand with the overall prosperity and development of the country (Ruiz et al., 2015) (thus the negative correlation with  $R_0$ ).

Similarly, the strong positive correlation of median age (MA) with  $R_0$  might be a mere consequence of its clear relation with the overall level of development of the country (Gangemi et al., 2020), but it can be also considered in the light of the fact that clinical and epidemiological studies have unanimously shown that the elderly are at higher risk of developing a more severe clinical picture, and our result may indicate that the virus also spreads more efficiently in the elderly population. Possible

explanations may include: drugs frequently prescribed to this population that increase levels of ACE2 receptors (Shahid et al., 2020), a general weakening of the immune system with age leading to a greater susceptibility to viral infections (Pawelec and Larbi, 2008), and a large number of elderly people grouped in nursing homes, where the virus can expand very quickly (Kimball et al., 2020).

The correlation of population density with  $R_0$ , or the lack of thereof, is more challenging to explain. Naively, one could expect that COVID-19 spreads much more rapidly in areas with a large concentration of people, but, if exists, this effect is not that easily numerically captured. As the standard population density did not show any correlation with the reproduction number  $R_0$  (not shown), we explored some more subtle variants. Namely, the simplest reason why the data shows no correlation of  $R_0$  with population density would be that the density, calculated in the usual way, is too averaged out: the most densely-populated country on our list, Monaco, has roughly 10,000 times more people per square kilometer than the least densely-populated Australia. However, Melbourne downtown has a similar population density as Monaco and far more people, so one would expect no a priori reason that its infection progression would be slower (and the  $R_0$  rate for Australia as a whole will be dominantly determined by the fastest exponential expansion occurring anywhere on its territory). For this reason, we included the BUCAP parameter into the analysis, which takes into account only population density in built-up areas. Surprisingly, even this parameter did not exhibit any statistically significant correlation. Actually, several studies may serve as examples showing that the correlation of population density with the rate of COVID-19 expansion can be expected only under certain conditions since the frequency of contacts between people is to a large extent modulated by additional geographical, economic, and sociological factors (Berg et al., 2020; Carozzi, 2020; Pourghasemi et al., 2020; Rashed et al., 2020). Our observed absence of a correlation could be therefore expected and possibly indicates that such a correlation should be sought at the level of smaller populated areas—for example, individual cities (Yu et al., 2020). This conclusion is somewhat supported by the obtained highly significant and strong positive correlation of  $R_0$  with the percentage of the population living in cities (UP) and which probably reflects the higher number of encounters between people in a more densely populated, urban environment (Li et al., 2020). It is also possible that virus spread might have a highly non-linear dependence on the population density—namely, that an outbreak in a susceptible population requires a certain threshold value of its density, while below that value population density ceases to be a significant factor influencing virus (Scheffer, 2009; Carozzi, 2020; Coro, 2020).

Another demographic parameter that exhibits a significant correlation with  $R_0$  in our data is the net migration (I-E), denoting the number of immigrants less the number of emigrants. Unlike this number, which shows a positive correlation, the number of refugees (RE) seems not to be correlated at all. By definition, migrants deliberately choose to move to improve their prospects, while refugees have to move to save their lives or preserve their freedom. Migrants (e.g., in



economic or academic migration), arguably tend to stay in closer contact with the country of their origin and have more financial means for that, which likely contributes to more frequent border crossings and more intensive passenger traffic (Fan et al., 2020), thereby promoting the infection spread. On the other hand, refugees are mostly stationed in refugee camps, there is less possibility of spreading the virus outside through contacts with residents, but there is a high possibility of escalation of the epidemic within camps with a high concentration of people (Hargreaves et al., 2020). We did not find any other attempt in the literature to examine this issue. In any case, our results demonstrate that refugees are certainly not a primary cause of concern in the pandemics, contrary to fears expressed in some media.

Of the medical factors, the strongest correlation of  $R_0$  is established with elevated cholesterol levels, as shown in **Figure 5**. Cholesterol may be associated with a viral infection and further disease development through a complex network of direct and indirect effects. *In vitro* studies of the role of cholesterol in virus penetration into the host body, done on several coronaviruses, indicate that its presence in the lipid rafts of the cell membrane is essential for the interaction of the virus with the ACE2 receptor, and also for the latter endocytosis of the virus (Radenkovic et al., 2020). Obesity prevalence (OB) also exhibits a highly significant, though somewhat weaker correlation with  $R_0$ , which might be a consequence of the common connection between obesity and cholesterol: in principle, obesity might be a relevant factor in the COVID-19 epidemic exactly due to the effects of cholesterol on SARS-CoV-2 susceptibility. Of course, other effects might be at play, e.g., the fact that the adipose tissue of obese people excessively produces pro-inflammatory cytokines (Sattar et al., 2020). In the case of obesity, a simple explanation via relation to HDI is not available, since obesity does not show a simple correlation with the society development (Haidar and Cosman, 2011). Overall, while the correlation of obesity with a more severe prognosis in COVID-19 is well established in the literature, its relation to COVID-19 transmissibility is only mentioned in Li et al. (2020) and hitherto unexplained.

Often related to obesity is also raised blood pressure (RBP), and we have discovered that this factor is also correlated, at high statistical significance, with  $R_0$ . While this seems to be the first study correlating high blood pressure with the SARS-CoV-2 transmission rate, it is known that, based on clinical studies, RBP appears to be a risk factor for hospitalization and death due to COVID-19 (Ran et al., 2020a; Schiffrin et al., 2020). In this light, it might be surprising that the correlation between RBP and  $R_0$  turns out to be negative. On the other hand, this result supports the existing hypothesis about the beneficial effect of ACE inhibitors and ARBs (Ran et al., 2020a; Schiffrin et al., 2020) (standardly used in the treatment of hypertension). Similarly unintuitive correlation we report in the case of chronic diseases that are known to be relevant for the COVID-19 outcome. Namely, our data show, at very high statistical significance, a strong negative correlation of  $R_0$  with the risk of death from a batch of chronic diseases (cardiovascular disease, cancer, diabetes, and chronic respiratory disease), agreeing in this regard with some recent research

(Chiang et al., 2020; Li et al., 2020). These diseases are identified as relevant comorbidities in the context of COVID-19, leading to a huge increase in the severity of the infection and poorer prognosis (An et al., 2020; Zheng et al., 2020) and, therefore, the discovered negative correlation comes as a surprise—particularly when contrasted to the positive correlation of obesity (where both are recognized risk factors in COVID-19 illness). One possible explanation is that the correlation may be due to potentially lower mobility of people with chronic diseases compared to the general mobility of the population. Additionally, it is possible that these people, being aware to belong to a high-risk group, behaved more cautiously even before the official introduction of social distancing measures.

According to our analysis, the prevalence of certain health-hazard habits is also significantly correlated to COVID-19 transmissibility. Chronic excessive alcohol consumption has, in general, a detrimental effect on immunity to viral and bacterial infections, which, judging by the strong positive correlation we obtained, most likely applies also to SARS-CoV-2 virus infection. This correlation contradicts the belief that alcohol can be used as a protective nostrum against COVID-19, which has spread in some countries and even led to cases of alcohol poisoning (Chick, 2020).

Regarding the impact of smoking on SARS-CoV-2 virus infection—the results are controversial (Chatkin and Godoy, 2020). The positive correlation of smoking with COVID-19 transmissibility that we obtained seems to support the reasoning that, since the SARS-CoV-2 virus enters cells by binding to angiotensin-converting enzyme 2 (ACE2) receptors and that the number of these receptors is significantly higher in the lungs of smokers, the smokers will be more affected and easily infected (Brake et al., 2020; Hoffmann et al., 2020). Accordingly, our result contradicts the hypothesis that a weakened immune response of smokers to virus infection may prove beneficial in the context of inflammation caused by intense cytokine release (Garufi et al., 2020).

Another result that addresses the association of unhealthy lifestyle with greater susceptibility to SARS-CoV-2 infection is the slight positive correlation we obtained for the prevalence of insufficient physical activity (IN) in adults, which is however not statistically significant. In this sense, in the case of COVID-19, we could not fully confirm the findings from (Jurak et al., 2020), who found that physical activity significantly reduces the risk of viral infections.

Despite the recent media interest (Gallagher, 2020), our findings neither could confirm that BCG immunization has any beneficial effect in the case of COVID-19, at least as far as reducing the risk of contracting and transmitting the disease is concerned. While it is known that the BCG vaccine provides some protection against various infectious agents, unfortunately, there is no clear evidence for such an effect against SARS-CoV-2 (O'Neill and Netea, 2020). Our analysis suggests that BCG immunization simply does not correlate with SARS-CoV-2 virus transmission.

SARS-CoV-2 target cells are typically capable of synthesizing ABH antigens and certain arguments exist, both theoretical and experimental, for a potential relation of blood groups

with COVID-19 progression and transmission (Guillon et al., 2008; Dai, 2020; Gérard et al., 2020). While the results of epidemiological studies on COVID-19 patients mostly support the proposed effect of blood groups on the development of COVID-19 disease, the relationship between virus transmission and blood group prevalence and Rh phenotype has been significantly less studied. Our analysis showed strong positive correlations of virus transmission with the presence of A blood group and Rh<sup>-</sup> phenotype, as well as strong negative correlations for B blood group and Rh<sup>+</sup> phenotype, while for AB and O blood group no significant correlations were obtained (**Figure 5C**). This result coincides significantly with the correlations obtained in a study conducted for 86 countries (Ansari-Lari and Saadat, 2020). However, another study focused on hospitalized patients in Turkey reported that the Rh<sup>+</sup> phenotype represents a predisposition to infection (Arac et al., 2020), contradicting our findings. Similar results regarding the Rh factor were obtained in a study (Latz et al., 2020) on hospitalized patients in the US (this study further reported no correlation of blood types with the severity of the disease). One way to reconcile these results with ours would be to speculate that the virus is more efficiently transmitted in a population with a higher proportion of Rh<sup>-</sup> phenotype because these people show a milder clinical picture compared to Rh<sup>+</sup>, so their movement is not equally limited, which is why they have more ability to pass on the infection.

Our data (**Figure 6A**) shows a strong negative correlation with the date of the epidemic onset. Curiously, it seems that the later the epidemic started in a given country, it is more likely that the disease expansion will be slower. Instead of interpreting this result as an indication that the virus has mutated and changed its properties over such a short period, we offer the following simpler explanation: pandemic reached first those countries that are most interconnected with the rest of the world (at the same time, those are the countries characterized by great mobility of people overall), so it is expected that also the progression of the local epidemics in these countries is more rapid. Another contributing factor could be the effect of media, which had more time to raise awareness about the risks of COVID-19 in the countries that were hit later (Khajanchi et al., 2020b).

Another segment of our interest were air pollutants, shown in **Figure 6B**. Air pollution can have a detrimental effect on the human immune system and lead to the development (or to worsening) of respiratory diseases, including those caused by respiratory viral infections (Becker and Soukup, 1999; Copat et al., 2020). Several papers have already investigated air pollution in the context of COVID-19 and reported a positive correlation between the death rate due to COVID-19 and the concentration of PM<sub>2.5</sub> in the environment (Wu et al., 2020; Yao et al., 2020c). Positive correlations were also found for the spread of the SARS-CoV-2 virus, but mainly by considering daily numbers of newly discovered cases—a method that, as we have already argued, may strongly depend on testing policies, as well as on state measures to combat the epidemic (Copat et al., 2020). It has been suggested that virus RNA can be adsorbed to airborne particles facilitating thus its spread over greater distances (Coccia, 2020; Setti et al., 2020), but these arguments were contested by examination of air samples in Wuhan (Contini and Costabile, 2020; Liu et al., 2020).

The latter conclusions concur with the results of a study in which no correlation was obtained between the basic reproductive number of SARS-CoV-2 infection for 154 Chinese cities and the concentration of PM<sub>2.5</sub> and PM<sub>10</sub> particles, while the correlation of these factors with the death rate (CFR) was shown (Ran et al., 2020b). The statistically insignificant and relatively weak correlations we obtained for PM<sub>2.5</sub> and PM<sub>10</sub> pollutants also do not support the hypothesis of a potentially significant role of these particles in the transmission of this virus. In contrast, significant positive correlations were shown by our analysis for concentrations of NO<sub>2</sub>, SO<sub>2</sub>, and CO in the air (although the correlation for CO is not statistically significant), which is generally supported by the results of other studies. For example, a positive correlation of NO<sub>2</sub> levels with the basic reproductive number of infection was obtained from data for 63 Chinese cities (Yao et al., 2020a). Also, it has been shown that the number of detected cases of COVID-19 in China is strongly positively correlated with the level of CO, while in Italy and the USA such correlation exists with NO<sub>2</sub> (Pansini and Fornacca, 2020). The mentioned study failed to establish a clear correlation with the level of SO<sub>2</sub>. Possible mechanisms of interaction were also proposed (Darai et al., 2020). Also, it is important to emphasize that the atmospheric concentration of NO<sub>2</sub> strongly depends on the levels of local exhaust emissions, so its correlation with virus transmission can be interpreted by the connection with the urban environment, characterized by more intensive traffic (Goldberg et al., 2020).

Finally, we have also obtained some interesting correlations of the meteorological parameters with  $R_0$ , shown in **Figures 6C,D**. The statistically very highly significant negative correlation of the basic reproductive number of SARS-CoV-2 virus infection with both the mean temperature and humidity obtained in our research (**Figure 6D**) is consistent with the results of other relevant papers, e.g., (Mecenas et al., 2020). For example, a similar correlation was obtained in a study that analyzed COVID-19 outbreak in the cities of Chile—a country that covers several climate zones, but where it is still safe to assume that social patterns of behavior and introduced epidemic control measures do not drastically differ throughout the country (Correa-Araneda et al., 2020). Effectively the same conclusion—that fewer COVID-19 cases were reported in countries with higher temperatures and humidities—was reached in a study covering over 200 countries in the world (Iqbal et al., 2020). While an established correlation between virus transmission and a certain factor is not, in general, a telltale sign of a direct causal relationship between them, in the case of temperature and humidity such connection is firmly indicated also by results of experimental research (Lowen et al., 2007; Casanova et al., 2010; Chan et al., 2011; van Doremalen et al., 2020). Nevertheless, some studies yielded different conclusions, most likely due to the method of calculating  $R_0$  or due to choosing a small/uninformative sample of populations in which the number of infected cases was monitored (Guo et al., 2020; Lin et al., 2020; Yao et al., 2020b). For example, a study focused on the suburbs of New York, Queens, obtained a positive correlation between virus transmission and temperature, which seems unexpected given the prevailing observations of other studies (Adhikari and Yin,

2020). This result is most likely a consequence of analyzing data for a small area (Queens only) where the temperature varies in a relatively narrow range of values, as well as correlating the number of detected cases, which may be sensitive to variations in the testing procedure.

Another environmental agent that can destroy or inactivate viruses is UV radiation from sunlight, and the properties of a particular virus determine how long it can remain infectious when exposed to radiation. For example, epidemics of influenza have a seasonal character precisely due to the susceptibility of influenza viruses to UV radiation (Sagripanti and Lytle, 2007). Our analysis found, at very high statistical significance, a strong negative correlation between the transmission of the SARS-CoV-2 virus and the intensity of UV radiation, which is consistent with the results of other studies obtained for the cities of Brazil and the provinces of Iran (Ahmadi et al., 2020; Mendonça et al., 2020). It is worth mentioning that lower temperatures, humidity, and sunlight levels usually occur in combination and directly affect not only the virus but also the human behavior, so the observed higher transmission of the virus in such conditions can alternatively be interpreted by indirect effects of other factors that act together in cold weather, such as more time spent indoors where the virus spreads more easily, or weakening of the immune system that increases susceptibility to infections (Abdullahi et al., 2020).

While the results related to COVID-19 correlations with temperature, humidity, and UV radiation are fairly frequent in the literature, this is less so for the results on the precipitation levels. Very few other studies have examined the association of precipitation with SARS-CoV-2 transmission, with either no correlation found (Pourghasemi et al., 2020), or looking at precipitation as a surrogate for humidity and generally receiving a negative correlation with infection rate (Araujo and Naimi, 2020; Coro, 2020). Our results, however, shown in **Figure 6D**, confirm natural expectations: just like humidity, the precipitation exhibits a strong negative correlation with  $R_0$ , only slightly lower than in the case of T, H, and UV, at a very high level of statistical significance. Such results also concur with some general conclusions about the behavior of similar viruses (Agrawal et al., 2009; Pica and Bouvier, 2012).

Our analysis did not reveal any statistically significant correlation either between the wind speed or between air pressure and SARS-CoV-2 transmissibility. In the case of wind speed, this result agrees with the findings in some other papers (Gupta et al., 2020; Oliveiros et al., 2020). A positive correlation of wind speed with COVID-19 transmissibility was obtained in a study in Chilean cities, but, as the authors themselves note, the interpretation of the effect of this factor is complicated by its observed significant interaction with temperature (Correa-Araneda et al., 2020). The role of wind in transmitting the virus to neighboring buildings is predicted by the SARS virus spread model within the Amoy Gardens residential complex in Hong Kong, but such an effect may relate to local air currents and virus transmission over relatively short distances and does not imply a correlation of mean wind speeds in the area with virus transmission (McKinney et al., 2006; Pica and Bouvier, 2012). As for the air pressure, the potential connection is hardly at all investigated in the literature. An

exception is a study (Cambaza et al., 2020) reporting a positive correlation of air pressure with the number of COVID-19 cases in parts of Mozambique, but our results do not confirm such a conclusion.

## CONCLUSION

While there is by now a significant amount of research on a crucial problem of how environmental factors affect COVID-19 spread, several features set this analysis apart from the existing research. First is the applied methodology: instead of basing analysis directly on the number of detected COVID-19 cases (or some of its simple derivatives), we employ an adapted SEIR model to extract the basic reproduction number  $R_0$  from the initial stage of the epidemic. By taking into account only data in the exponential growth regime, i.e., before the social measures took effect (as explained in the “Methods” section), we ensured that the correlations we have later identified were not confounded with the effects of local COVID-19 policies. Even more importantly, our method is also invariant to variations in COVID-19 testing practices, which, as is well known, used to vary in quite an unpredictable manner between different countries. Another important factor is the large geographical scope of our research: we collected data from 118 countries worldwide, more precisely, from all the countries that were above a certain threshold for the number of confirmed COVID-19 cases (except for several countries with clearly irregular early growth data). The third factor was the number of analyzed parameters: we calculated correlations for the selected 42 different variables (of more than a hundred that we initially considered overall) and looked for viable interpretations of the obtained results.

These results should also help in resolving some of the existing disputes in the literature. For example, our findings indicate that correlation of HDI with  $R_0$  is not a consequence of the COVID-19 testing bias, as was occasionally argued. Of the opposing opinions, our data seem to support assertions that blood types are indeed related to COVID-19 transmissibility, as well as arguments that the higher prevalence of smoking does increase the virus transmissibility (though weakly). On the other hand, in the dispute about the effects of the pollution, our correlations give an edge to claims that there is no correlation between PM2.5 and PM10 particles and transmissibility (whereas we agree with the prevailing conclusions about the positive correlation of other considered pollutants). In the case of the effects of the wind, based on the obtained results we tend to side with those denying any connection. In certain cases our findings contradict popular narratives: there are no clear indications that either number of refugees or physical inactivity intensifies the spread of COVID-19. Unfortunately, our data also suggest that BCG immunization may not help in subduing the epidemic. Additionally, the obtained correlations hint to possible new alleys of research, e.g., those that would help us understand the connection between cholesterol levels and SARS-CoV-2 transmissibility.

Overall, we believe that the presented results can be a useful contribution to the ongoing attempts to better understand the first pandemic of the twenty-first century—and the better we understand it, the sooner we may hope to overcome it.



## DATA AVAILABILITY STATEMENT

The original contributions presented in the study are included in the article/**Supplementary Material**, further inquiries can be directed to the corresponding author/s.

## AUTHOR CONTRIBUTIONS

MarD and MagD conceived the research. The work was supervised by IS, MagD, and MarD. Data acquisition by OM, IS, DZ, and AR. Data analysis by DZ, OM, and IS, with the help of MagD. Figures and tables made by DZ and AR with the help of MagD. A literature search by AR. Manuscript written by IS, AR, and MarD. All authors contributed to the article and approved the submitted version.

## REFERENCES

- Abdullahi, I. N., Emeribe, A. U., Mustapha, J. O., Fasogbon, S. A., Ofor, I. B., Opeyemi, I. S., et al. (2020). Exploring the genetics, ecology of SARS-CoV-2 and climatic factors as possible control strategies against COVID-19. *Infez. Med.* 28, 166–173.
- Adhikari, A., and Yin, J. (2020). Short-term effects of ambient ozone, PM<sub>2.5</sub>, and meteorological factors on COVID-19 confirmed cases and deaths in queens, New York. *Int. J. Environ. Res. Public Health* 17:4047. doi: 10.3390/ijerph17114047
- Agrawal, A. S., Sarkar, M., Chakrabarti, S., Rajendran, K., Kaur, H., Mishra, A. C., et al. (2009). Comparative evaluation of real-time PCR and conventional RT-PCR during a 2 year surveillance for influenza and respiratory syncytial virus among children with acute respiratory infections in Kolkata, India, reveals a distinct seasonality of infection. *J. Med. Microbiol.* 58, 1616–1622. doi: 10.1099/jmm.0.011304-0
- Ahmadi, M., Sharifi, A., Dorosti, S., Ghouschi, S. J., and Ghanbari, N. (2020). Investigation of effective climatology parameters on COVID-19 outbreak in Iran. *Sci. Total Environ.* 729:138705. doi: 10.1016/j.scitotenv.2020.138705
- An, C., Lim, H., Kim, D. W., Chang, J. H., Choi, Y. J., and Kim, S. W. (2020). Machine learning prediction for mortality of patients diagnosed with COVID-19: a nationwide Korean cohort study. *Sci. Rep.* 10:18716. doi: 10.1038/s41598-020-75767-2
- Anderson, R. M., and May, R. M. (1992). *Infectious Diseases of Humans: Dynamics and Control*. New York, NY: Oxford University Press.
- Ansari-Lari, M., and Saadat, M. (2020). The morbidity and mortality of COVID-19 are associated with ABO and Rh blood groups. *Eur. J. Prev. Cardiol.* doi: 10.1177/2047487320939216. [Epub ahead of print].
- Arac, E., Solmaz, I., Akkoc, H., Donmezdil, S., Karahan, Z., Kaya, S., et al. (2020). Association between the Rh blood group and the Covid-19 susceptibility. *UHOD-Uluslar. Hematol.* 30, 81–86. doi: 10.4999/uhod.204247
- Araujo, M. B., and Naimi, B. (2020). Spread of SARS-CoV-2 coronavirus likely constrained by climate. medRxiv [Preprint]. Available online at <https://europepmc.org/article/ppr/ppr117563> (accessed December 16, 2020).
- Bar-On, Y. M., Flamholz, A., Phillips, R., and Milo, R. (2020). SARS-CoV-2 (COVID-19) by the numbers. *Elife* 9:e57309. doi: 10.7554/eLife.57309.sa2
- Becker, S., and Soukup, J. M. (1999). Exposure to urban air particulates alters the macrophage-mediated inflammatory response to respiratory viral infection. *J. Toxicol. Environ. Health Part A* 57, 445–457. doi: 10.1080/009841099157539
- Berg, M. K., Yu, Q., Salvador, C. E., Melani, I., and Kitayama, S. (2020). Mandated Bacillus Calmette-Guérin (BCG) vaccination predicts flattened curves for the spread of COVID-19. *Sci. Adv.* 6:eabc1463. doi: 10.1126/sciadv.abc1463
- Brake, S. J., Barnsley, K., Lu, W., McAlinden, K. D., Eapen, M. S., and Sohal, S. S. (2020). Smoking upregulates angiotensin-converting enzyme-2 receptor: a potential adhesion site for novel coronavirus SARS-CoV-2 (Covid-19). *J. Clin. Med.* 9:841. doi: 10.3390/jcm9030841
- Cambaza, E. M., Viegas, G. C., and Cambaza, C. M. (2020). Potential impact of temperature and atmospheric pressure on the number of cases of COVID-19 in Mozambique, Southern Africa. *J. Public Health Epidemiol.* 12, 246–260. doi: 10.5897/JPHE2020.1258
- Carozzi, F. (2020). Urban density and COVID-19. *Institute for the Study of Labor (IZA)* [Online], 13440. Available online at <https://ssrn.com/abstract=3643204> (accessed December 16, 2020).
- Casanova, L. M., Jeon, S., Rutala, W. A., Weber, D. J., and Sobsey, M. D. (2010). Effects of air temperature and relative humidity on coronavirus survival on surfaces. *Appl. Environ. Microbiol.* 76, 2712–2717. doi: 10.1128/AEM.02291-09
- Chan, K.-H., Peiris, J. M., Lam, S., Poon, L., Yuen, K., and Seto, W. H. (2011). The effects of temperature and relative humidity on the viability of the SARS coronavirus. *Adv. Virol.* 2011:734690. doi: 10.1155/2011/734690
- Chatkin, J. M., and Godoy, I. (2020). Are smoking, environmental pollution, and weather conditions risk factors for COVID-19? *J. Bras. Pneumol.* 46:e20200183. doi: 10.36416/1806-3756/e20200183
- Chiang, W.-H., Liu, X., and Mohler, G. (2020). Hawkes process modeling of COVID-19 with mobility leading indicators and spatial covariates. *medRxiv [Preprint]*. Available online at: <https://europepmc.org/article/ppr/ppr172763> (accessed December 16, 2020).
- Chick, J. (2020). Alcohol and COVID-19. *Alcohol Alcohol.* 55, 341–342. doi: 10.1093/alcal/agaa039
- Coccia, M. (2020). The effects of atmospheric stability with low wind speed and of air pollution on the accelerated transmission dynamics of COVID-19. *Int. J. Environ. Stud.* doi: 10.1080/00207233.2020.1802937. [Epub ahead of print].
- Cohen, J., and Kupferschmidt, K. (2020). Countries test tactics in 'war' against COVID-19. *Science* 367, 1287–1288. doi: 10.1126/science.367.6484.1287
- Contini, D., and Costabile, F. (2020). Does air pollution influence COVID-19 outbreaks? *Atmosphere* 11:377. doi: 10.3390/atmos11040377
- Copat, C., Cristaldi, A., Fiore, M., Grasso, A., Zuccarello, P., Signorelli, S. S., et al. (2020). The role of air pollution (PM and NO<sub>2</sub>) in COVID-19 spread and lethality: a systematic review. *Environ. Res.* 191:110129. doi: 10.1016/j.envres.2020.110129
- Copiello, S., and Grillenzoni, C. (2020). The spread of 2019-nCoV in China was primarily driven by population density. Comment on "Association between short-term exposure to air pollution and COVID-19 infection: evidence from China" by Zhu et al. *Sci. Total Environ.* 744:141028. doi: 10.1016/j.scitotenv.2020.141028
- Coro, G. (2020). A global-scale ecological niche model to predict SARS-CoV-2 coronavirus infection rate. *Ecol. Modell.* 431:109187. doi: 10.1016/j.ecolmodel.2020.109187
- Correa-Araneda, F., Ulloa-Yañez, A., Núñez, D., Boyero, L., Tonin, A., Cornejo, A., et al. (2020). Environmental determinants of COVID-19 transmission across a

## FUNDING

This work was partially supported by the Ministry of Education, Science and Technological Development of the Republic of Serbia.

## ACKNOWLEDGMENTS

The authors thank Anica Brzakovic for reproducing a subset of the results presented in this manuscript.

## SUPPLEMENTARY MATERIAL

The Supplementary Material for this article can be found online at: <https://www.frontiersin.org/articles/10.3389/fevo.2020.617841/full#supplementary-material>

- wide climatic gradient in Chile. Research Square [Preprint]. Available online at: <https://europepmc.org/article/ppr/ppr166276> (accessed December 16, 2020).
- Dai, X. (2020). ABO blood group predisposes to COVID-19 severity and cardiovascular diseases. *Eur. J. Prev. Cardiol.* 27, 1436–1437. doi: 10.1177/2047487320922370
- Daraei, H., Toolabian, K., Kazempour, M., and Javanbakht, M. (2020). The role of the environment and its pollution in the prevalence of COVID-19. *J. Infect.* 81, e168–e169. doi: 10.1016/j.jinf.2020.06.019
- Day, M. (2020). Covid-19: four fifths of cases are asymptomatic, China figures indicate. *BMJ* 369:m1375. doi: 10.1136/bmj.m1375
- Djordjevic, M., Djordjevic, M., Salom, I., Rodic, A., Zigic, D., Milicevic, O., et al. (2020). COVID-19 puzzle in China: a serendipitous interplay between transmissibility and social distancing measures. arXiv [Preprint]. Available online at: <https://arxiv.org/abs/2005.09630> (accessed December 16, 2020).
- Dong, E., Du, H., and Gardner, L. (2020). An interactive web-based dashboard to track COVID-19 in real time. *Lancet. Infect. Dis.* 20, 533–534. doi: 10.1016/S1473-3099(20)30120-1
- Eubank, S., Eckstrand, I., Lewis, B., Venkatraman, S., Marathe, M., and Barrett, C. (2020). Commentary on Ferguson, et al., “Impact of non-pharmaceutical interventions (NPIs) to reduce COVID-19 mortality and healthcare demand”. *Bull. Math. Biol.* 82:52. doi: 10.1007/s11538-020-00726-x
- European Commission Global Human Settlement (2020). *Urban Centre Database UCDB R2019A* [Online]. Available online at: [https://ghsl.jrc.ec.europa.eu/ghs\\_stat\\_ucdb2015mt\\_r2019a.php](https://ghsl.jrc.ec.europa.eu/ghs_stat_ucdb2015mt_r2019a.php) (accessed September 26, 2020).
- Fan, C., Cai, T., Gai, Z., and Wu, Y. (2020). The relationship between the migrant population's migration network and the risk of COVID-19 transmission in China—empirical analysis and prediction in prefecture-level cities. *Int. J. Environ. Res. Public Health* 17:2630. doi: 10.3390/ijerph17082630
- Fareed, Z., Iqbal, N., Shahzad, F., Shah, S. G. M., Zulfqar, B., Shahzad, K., et al. (2020). Co-variance nexus between COVID-19 mortality, humidity, and air quality index in Wuhan, China: new insights from partial and multiple wavelet coherence. *Air Qual. Atmos. Health* 8, 1–10. doi: 10.1007/s11869-020-00847-1
- Gallagher, J. (2020, October 11). BCG: can a vaccine from 1921 save lives from Covid-19? *BBC News*.
- Gangemi, S., Billeci, L., and Tonacci, A. (2020). Rich at risk: socio-economic drivers of COVID-19 pandemic spread. *Clin. Mol. Allergy* 18:12. doi: 10.1186/s12948-020-00127-4
- Garufi, G., Carbognin, L., Orlandi, A., Tortora, G., and Bria, E. (2020). Smoking habit and hospitalization for severe acute respiratory syndrome coronavirus 2 (SARS-CoV-2)-related pneumonia: the unsolved paradox behind the evidence. *Eur. J. Intern. Med.* 77, 121–122. doi: 10.1016/j.ejim.2020.04.042
- Gérard, C., Maggipinto, G., and Minon, J.-M. (2020). COVID-19 and ABO blood group: another viewpoint. *Brit. J. Haematol.* 190, e57–e94. doi: 10.1111/bjh.16884
- Global Data Lab (2020). *Subnational Human Development Index (4.0)* [Online]. Available online at: <http://globaldatalab.org/shdi/> (accessed September 27, 2020).
- Goldberg, D. L., Anenberg, S. C., Griffin, D., McLinden, C. A., Lu, Z., and Streets, D. G. (2020). Disentangling the impact of the COVID-19 lockdowns on urban NO<sub>2</sub> from natural variability. *Geophys. Res. Lett.* 47:e2020GL089269. doi: 10.1002/essoar.10503396.1
- Guillon, P., Clément, M., Sébille, V., Rivain, J.-G., Chou, C.-F., Ruvoën-Clouet, N., et al. (2008). Inhibition of the interaction between the SARS-CoV spike protein and its cellular receptor by anti-histo-blood group antibodies. *Glycobiology* 18, 1085–1093. doi: 10.1093/glycob/cwn093
- Guo, X.-J., Zhang, H., and Zeng, Y.-P. (2020). Transmissibility of COVID-19 in 11 major cities in China and its association with temperature and humidity in Beijing, Shanghai, Guangzhou, and Chengdu. *Infect. Dis. Poverty* 9:87. doi: 10.1186/s40249-020-00708-0
- Gupta, A., Banerjee, S., and Das, S. (2020). Significance of geographical factors to the COVID-19 outbreak in India. *Model. Earth Syst. Environ.* 6, 2645–2653. doi: 10.1007/s40808-020-00838-2
- Haidar, Y. M., and Cosman, B. C. (2011). Obesity epidemiology. *Clin. Colon Rectal Surg.* 24, 205–210. doi: 10.1055/s-0031-1295684
- Hargreaves, S., Kumar, B. N., McKee, M., Jones, L., and Veizis, A. (2020). Europe's migrant containment policies threaten the response to covid-19. *BMJ* 368:m1213. doi: 10.1136/bmj.m1213
- Hoffmann, M., Kleine-Weber, H., Schroeder, S., Krüger, N., Herrler, T., Erichsen, S., et al. (2020). SARS-CoV-2 cell entry depends on ACE2 and TMPRSS2 and is blocked by a clinically proven protease inhibitor. *Cell* 181, 271–280. doi: 10.1016/j.cell.2020.02.052
- Iqbal, M. M., Abid, I., Hussain, S., Shahzad, N., Waqas, M. S., and Iqbal, M. J. (2020). The effects of regional climatic condition on the spread of COVID-19 at global scale. *Sci. Total Environ.* 739:140101. doi: 10.1016/j.scitotenv.2020.140101
- Jordan, R. E., Adab, P., and Cheng, K. K. (2020). Covid-19: risk factors for severe disease and death. *BMJ* 368:m1198. doi: 10.1136/bmj.m1198
- Jurak, G., Morrison, S. A., Leskošek, B., Kovač, M., Hadžić, V., Vodičar, J., et al. (2020). Physical activity recommendations during the coronavirus disease-2019 virus outbreak. *J. Sport Health Sci.* 9, 325–327. doi: 10.1016/j.jshs.2020.05.003
- Keeling, M. J., and Rohani, P. (2011). *Modeling Infectious Diseases in Humans and Animals*. Princeton, NJ: Princeton University Press. doi: 10.2307/j.ctvc4m4gk0
- Khajanchi, S., Bera, S., and Roy, T. K. (2020a). Mathematical analysis of the global dynamics of a HTLV-I infection model, considering the role of cytotoxic T-lymphocytes. *Math. Comput. Simulat.* 180, 354–378. doi: 10.1016/j.matcom.2020.09.009
- Khajanchi, S., and Sarkar, K. (2020). Forecasting the daily and cumulative number of cases for the COVID-19 pandemic in India. *Chaos* 30:071101. doi: 10.1063/5.0016240
- Khajanchi, S., Sarkar, K., Mondal, J., and Perc, M. (2020b). Dynamics of the COVID-19 pandemic in India. arXiv [Preprint]. Available at: <https://arxiv.org/abs/2005.06286> (accessed December 16, 2020). doi: 10.21203/rs.3.rs-27112/v1
- Kimball, A., Hatfield, K. M., Arons, M., James, A., Taylor, J., Spicer, K., et al. (2020). Asymptomatic and presymptomatic SARS-CoV-2 infections in residents of a long-term care skilled nursing facility—King County, Washington, March 2020. *MMWR Morb. Mortal. Wkly Rep.* 69, 377–381. doi: 10.15585/mmwr.mm6913e1
- Latz, C. A., DeCarlo, C., Boitano, L., Png, C. M., Patell, R., Conrad, M. F., et al. (2020). Blood type and outcomes in patients with COVID-19. *Ann. Hematol.* 99, 2113–2118. doi: 10.1007/s00277-020-04169-1
- Li, M., Zhang, Z., Cao, W., Liu, Y., Du, B., Chen, C., et al. (2020). Identifying novel factors associated with COVID-19 transmission and fatality using the machine learning approach. *Sci. Total Environ.* 142810. doi: 10.1016/j.scitotenv.2020.142810. [Epub ahead of print].
- Lin, S., Wei, D., Sun, Y., Chen, K., Yang, L., Liu, B., et al. (2020). Region-specific air pollutants and meteorological parameters influence COVID-19: a study from mainland China. *Ecotoxicol. Environ. Saf.* 204:111035. doi: 10.1016/j.ecoenv.2020.111035
- Liu, Y., Ning, Z., Chen, Y., Guo, M., Gali, N. K., Sun, L., et al. (2020). Aerodynamic analysis of SARS-CoV-2 in two Wuhan hospitals. *Nature* 582, 557–560. doi: 10.1038/s41586-020-2271-3
- Lowen, A. C., Mubareka, S., Steel, J., and Palese, P. (2007). Influenza virus transmission is dependent on relative humidity and temperature. *PLoS Pathog.* 3, 1470–1476. doi: 10.1371/journal.ppat.0030151
- Maier, B. F., and Brockmann, D. (2020). Effective containment explains subexponential growth in recent confirmed COVID-19 cases in China. *Science* 368, 742–746. doi: 10.1126/science.abb4557
- Martcheva, M. (2015). *An Introduction to Mathematical Epidemiology*. Boston, MA: Springer. doi: 10.1007/978-1-4899-7612-3
- Maslov, S., and Goldenfeld, N. (2020). Window of opportunity for mitigation to prevent overflow of ICU capacity in Chicago by COVID-19. medRxiv [Preprint]. Available online at: <https://europepmc.org/article/ppr/ppr118721> (accessed December 16, 2020).
- McKinney, K. R., Yu, Y. G., and Lewis, T. G. (2006). Environmental transmission of SARS at amoy gardens. *J. Environ. Health* 68, 26–30.
- Mecenas, P., Bastos, R., Vallinoto, A. C. R., and Normando, D. (2020). Effects of temperature and humidity on the spread of COVID-19: a systematic review. *PLoS ONE* 15:e0238339. doi: 10.1371/journal.pone.0238339
- Mendonça, F., Anjos, M., Collischonn, E., Murara, P., DE, F., Limberger, L., et al. (2020). Climate and Covid-19—upgrade and solar radiation influences based on Brazil cases. Research Square [Preprint]. Available online at: <https://europepmc.org/article/ppr/ppr174953> (accessed December 16, 2020).



- Najafimehr, H., Mohamed Ali, K., Safari, S., Yousefifard, M., and Hosseini, M. (2020). Estimation of basic reproduction number for COVID-19 and the reasons for its differences. *Int. J. Clin. Pract.* 74:e13518. doi: 10.1111/ijcp.13518
- NASA Langley Research Center (2020). *The Prediction of Worldwide Energy Resources (POWER) Project [Online]*. Available online at: <https://power.larc.nasa.gov/> (accessed October 6, 2020).
- Oliveiros, B., Caramelo, L., Ferreira, N. C., and Caramelo, F. (2020). Role of temperature and humidity in the modulation of the doubling time of COVID-19 cases. medRxiv [Preprint]. Available online at: <https://europepmc.org/article/ppr/ppr116498> (accessed December 16, 2020).
- O'Neill, L. A., and Netea, M. G. (2020). BCG-induced trained immunity: can it offer protection against COVID-19? *Nat. Rev. Immunol.* 20, 335–337. doi: 10.1038/s41577-020-0337-y
- Our World in Data (2020). *Research and Data to Make Progress Against the World's Largest Problems [Online]*. Available online at: <https://ourworldindata.org/> (accessed May, 2020).
- Pansini, R., and Fornacca, D. (2020). COVID-19 higher induced mortality in Chinese regions with lower air quality. medRxiv [Preprint]. Available online at <https://www.medrxiv.org/content/10.1101/2020.05.28.20115832v2> (accessed December 16, 2020).
- Pawelec, G., and Larbi, A. (2008). Immunity and ageing in man: annual review 2006/2007. *Exp. Gerontol.* 43, 34–38. doi: 10.1016/j.exger.2007.09.009
- Perkins, T. A., and España, G. (2020). Optimal control of the COVID-19 pandemic with non-pharmaceutical interventions. *Bull. Math. Biol.* 82:118. doi: 10.1007/s11538-020-00795-y
- Pica, N., and Bouvier, N. M. (2012). Environmental factors affecting the transmission of respiratory viruses. *Curr. Opin. Virol.* 2, 90–95. doi: 10.1016/j.coviro.2011.12.003
- Pourghasemi, H. R., Pouyan, S., Heidari, B., Farajzadeh, Z., Fallah Shamsi, S. R., Babaei, S., et al. (2020). Spatial modeling, risk mapping, change detection, and outbreak trend analysis of coronavirus (COVID-19) in Iran (days between February 19 and June 14, 2020). *Int. J. Infect. Dis.* 98, 90–108. doi: 10.1016/j.ijid.2020.06.058
- Pranata, R., Lim, M. A., Huang, I., Raharjo, S. B., and Lukito, A. A. (2020). Hypertension is associated with increased mortality and severity of disease in COVID-19 pneumonia: a systematic review, meta-analysis and meta-regression. *J. Renin Angiotensin Aldosterone Syst.* 21:1470320320926899. doi: 10.1177/1470320320926899
- Qu, G., Li, X., Hu, L., and Jiang, G. (2020). An imperative need for research on the role of environmental factors in transmission of novel coronavirus (COVID-19). *Environ. Sci. Technol.* 54, 3730–3732. doi: 10.1021/acs.est.0c01102
- Radenkovic, D., Chawla, S., Pirro, M., Sahebkar, A., and Banach, M. (2020). Cholesterol in relation to COVID-19: should we care about it? *J. Clin. Med.* 9:1909. doi: 10.3390/jcm9061909
- Ran, J., Song, Y., Zhuang, Z., Han, L., Zhao, S., Cao, P., et al. (2020a). Blood pressure control and adverse outcomes of COVID-19 infection in patients with concomitant hypertension in Wuhan, China. *Hypertens. Res.* 43, 1267–1276. doi: 10.1038/s41440-020-00541-w
- Ran, J., Zhao, S., Han, L., Qiu, Y., Cao, P., Yang, Z., et al. (2020b). Effects of particulate matter exposure on the transmissibility and case fatality rate of COVID-19: a Nationwide Ecological Study in China. *J. Travel Med.* 27:taaa133. doi: 10.1093/jtm/taaa133
- Rashed, E. A., Kodera, S., Gomez-Tames, J., and Hirata, A. (2020). Influence of absolute humidity, temperature and population density on COVID-19 spread and decay durations: multi-prefecture study in Japan. *Int. J. Environ. Res. Public Health* 17:5354. doi: 10.3390/ijerph17155354
- Ruiz, J. I., Nuhu, K., McDaniel, J. T., Popoff, F., Izcovich, A., and Criniti, J. M. (2015). Inequality as a powerful predictor of infant and maternal mortality around the world. *PLoS ONE* 10:e0140796. doi: 10.1371/journal.pone.0140796
- Rychter, A. M., Zawada, A., Ratajczak, A. E., Dobrowolska, A., and Krela-Kazmierczak, I. (2020). Should patients with obesity be more afraid of COVID-19? *Obes. Rev.* 21:e13083. doi: 10.1111/obr.13083
- Sagar, A. D., and Najam, A. (1998). The human development index: a critical review. *Ecol. Econ.* 25, 249–264. doi: 10.1016/S0921-8009(97)00168-7
- Sagripanti, J.-L., and Lytle, C. D. (2007). Inactivation of influenza virus by solar radiation. *Photochem. Photobiol.* 83, 1278–1282. doi: 10.1111/j.1751-1097.2007.00177.x
- Samui, P., Mondal, J., and Khajanchi, S. (2020). A mathematical model for COVID-19 transmission dynamics with a case study of India. *Chaos Solitons Fractals* 140:110173. doi: 10.1016/j.chaos.2020.110173
- Sarkar, K., Khajanchi, S., and Nieto, J. J. (2020). Modeling and forecasting the COVID-19 pandemic in India. *Chaos Solitons Fractals* 139:110049. doi: 10.1016/j.chaos.2020.110049
- Sattar, N., McInnes, I. B., and McMurray, J. J. (2020). Obesity a risk factor for severe COVID-19 infection: multiple potential mechanisms. *Circulation* 142, 4–6. doi: 10.1161/CIRCULATIONAHA.120.047659
- Scheffer, M. (2009). *Critical Transitions in Nature and Society*. Princeton, NJ: Princeton University Press. doi: 10.1515/9781400833276
- Schiffirin, E. L., Flack, J. M., Ito, S., Muntner, P., and Webb, R. C. (2020). Hypertension and COVID-19. *Am. J. Hypertens.* 33, 373–374. doi: 10.1093/ajh/hpaa057
- Setti, L., Passarini, F., De Gennaro, G., Barbieri, P., Perrone, M. G., Borelli, M., et al. (2020). SARS-Cov-2RNA found on particulate matter of Bergamo in Northern Italy: first evidence. *Environ. Res.* 188:109754. doi: 10.1016/j.envres.2020.109754
- Shahid, Z., Kalayanamitra, R., McClafferty, B., Kepko, D., Ramgobin, D., Patel, R., et al. (2020). COVID-19 and older adults: what we know. *J. Am. Geriatr. Soc.* 68, 926–929. doi: 10.1111/jgs.16472
- Singh, K., and Agarwal, A. (2020). Impact of weather indicators on the COVID-19 outbreak: a multi-state study in India. medRxiv [Preprint]. Available online at <https://europepmc.org/article/ppr/ppr176027> (accessed December 16, 2020).
- Thangriyal, S., Rastogi, A., Tomar, A., and Baweja, S. (2020). Impact of temperature and sunshine duration on daily new cases and death due to COVID-19. medRxiv [Preprint]. Available online at: <https://europepmc.org/article/ppr/ppr176097> (accessed December 16, 2020).
- The Novel Coronavirus Pneumonia Emergency Response Epidemiology Team (2020). The epidemiological characteristics of an outbreak of 2019 novel coronavirus diseases (COVID-19)—China, 2020. *China CDC Weekly* [Online], 2. Available online at: <https://slma.lk/wp-content/uploads/2020/02/TheEpidemiologicalCharacteristicsofanOutbreakof2019NovelCoronavirusDiseases28COVID-1929E28094China2C20201.pdf>. doi: 10.46234/ccdcw2020.032
- Tian, H., Liu, Y., Li, Y., Wu, C. H., Chen, B., Kraemer, M. U. G., et al. (2020). An investigation of transmission control measures during the first 50 days of the COVID-19 epidemic in China. *Science* 368, 638–642. doi: 10.1126/science.abb6105
- Tosepu, R., Gunawan, J., Effendy, D. S., Ahmad, O. A. I., Lestari, H., Bahar, H., et al. (2020). Correlation between weather and Covid-19 pandemic in Jakarta, Indonesia. *Sci. Total Environ.* 725:138436. doi: 10.1016/j.scitotenv.2020.138436
- van Doremalen, N., Bushmaker, T., Morris, D. H., Holbrook, M. G., Gamble, A., Williamson, B. N., et al. (2020). Aerosol and surface stability of SARS-CoV-2 as compared with SARS-CoV-1. *N. Engl. J. Med.* 382, 1564–1567. doi: 10.1056/NEJMc2004973
- Ward, D. (2020). *Actions Speak Louder Than Age: Explaining Wide Variations in COVID-19 Deaths* [Online]. Available online at: [https://www.researchgate.net/publication/341599695\\_Actions\\_Speak\\_Louder\\_than\\_Age\\_Explaining\\_Wide\\_Variations\\_in\\_COVID-19\\_Deaths](https://www.researchgate.net/publication/341599695_Actions_Speak_Louder_than_Age_Explaining_Wide_Variations_in_COVID-19_Deaths) (accessed December 16, 2020).
- Weitz, J. S., Beckett, S. J., Coenen, A. R., Demory, D., Dominguez-Mirazo, M., Dushoff, J., et al. (2020). Modeling shield immunity to reduce COVID-19 epidemic spread. *Nat. Med.* 26, 849–854. doi: 10.1038/s41591-020-0895-3
- World Bank (2020a). *Global Economic Prospects, June 2020*. Washington, DC: World Bank.
- World Bank (2020b). *World Bank Open Data* [Online]. Available online at: <https://www.worldbank.org/> (accessed May, 2020).
- World Health Organization (2020). *The Global Health Observatory: Explore a World of Health Data* [Online]. Available online at: <https://www.who.int/data/gho> (accessed October 6, 2020).
- World Weather Online (2020). *Local Weather History API* [Online]. Available online at: <https://www.worldweatheronline.com/developer/api/historical-weather-api.aspx> (accessed December 9, 2020).

- Worldometer (2020). *COVID-19 Coronavirus Pandemic* [Online]. Available online at: <https://www.worldometers.info/coronavirus/> (accessed June 14, 2020).
- Wu, X., Nethery, R. C., Sabath, M. B., Braun, D., and Dominici, F. (2020). Air pollution and COVID-19 mortality in the United States: strengths and limitations of an ecological regression analysis. *Sci. Adv.* 6:eabd4049. doi: 10.1126/sciadv.abd4049
- Yao, Y., Pan, J., Liu, Z., Meng, X., Wang, W., Kan, H., et al. (2020a). Ambient nitrogen dioxide pollution and spread ability of COVID-19 in Chinese cities. *Ecotoxicol. Environ. Saf.* 208:111421. doi: 10.1016/j.ecoenv.2020.111421
- Yao, Y., Pan, J., Liu, Z., Meng, X., Wang, W., Kan, H., et al. (2020b). No association of COVID-19 transmission with temperature or UV radiation in Chinese cities. *Eur. Respir. J.* 55:2000517. doi: 10.1183/13993003.00517-2020
- Yao, Y., Pan, J., Wang, W., Liu, Z., Kan, H., Qiu, Y., et al. (2020c). Association of particulate matter pollution and case fatality rate of COVID-19 in 49 Chinese cities. *Sci. Total Environ.* 741:140396. doi: 10.1016/j.scitotenv.2020.140396
- Yu, Q., Salvador, C., Melani, I., Berg, M., Neblett, E., and Kitayama, S. (2020). Racial residential segregation and economic disparity jointly exacerbate the COVID-19 fatality in large American cities. *PsyArXiv [Preprint]*. Available online at: <https://psyarxiv.com/xgbpy/> (accessed December 16, 2020).
- Zheng, Z., Peng, F., Xu, B., Zhao, J., Liu, H., Peng, J., et al. (2020). Risk factors of critical and mortal COVID-19 cases: a systematic literature review and meta-analysis. *J. Infect.* 81:e16–e25. doi: 10.1016/j.jinf.2020.04.021

**Conflict of Interest:** The authors declare that the research was conducted in the absence of any commercial or financial relationships that could be construed as a potential conflict of interest.

Copyright © 2021 Salom, Rodic, Milicevic, Zigic, Djordjevic and Djordjevic. This is an open-access article distributed under the terms of the Creative Commons Attribution License (CC BY). The use, distribution or reproduction in other forums is permitted, provided the original author(s) and the copyright owner(s) are credited and that the original publication in this journal is cited, in accordance with accepted academic practice. No use, distribution or reproduction is permitted which does not comply with these terms.

# Understanding Infection Progression under Strong Control Measures through Universal COVID-19 Growth Signatures

Magdalena Djordjevic,\* Marko Djordjevic,\* Bojana Ilic, Stefan Stojku, and Igor Salom

Widespread growth signatures in COVID-19 confirmed case counts are reported, with sharp transitions between three distinct dynamical regimes (exponential, superlinear, and sublinear). Through analytical and numerical analysis, a novel framework is developed that exploits information in these signatures. An approach well known to physics is applied, where one looks for common dynamical features, independently from differences in other factors. These features and associated scaling laws are used as a powerful tool to pinpoint regions where analytical derivations are effective, get an insight into qualitative changes of the disease progression, and infer the key infection parameters. The developed framework for joint analytical and numerical analysis of empirically observed COVID-19 growth patterns can lead to a fundamental understanding of infection progression under strong control measures, applicable to outbursts of both COVID-19 and other infectious diseases.

COVID-19 pandemic introduced unprecedented worldwide social distancing measures.<sup>[1]</sup> While interventions such as quarantine or vaccination have been extensively studied in quantitative epidemiology, effects of social distancing are not well understood,<sup>[2–4]</sup> and when addressed, they have been studied only numerically. Unique opportunity to understand these effects has been provided by COVID-19 tracing through confirmed case counts, active cases and fatalities, in a variety of countries with different demographic and environmental conditions.<sup>[5,6]</sup> We here show that focusing on analytical and numerical derivations in distinct epidemics growth regimes, is

a novel and effective approach in revealing infection progression mechanisms that may be a valuable alternative to detailed numerical simulations.


We start by introducing our COVID-19 dynamics model. We then extract COVID-19 count data<sup>[7]</sup> and select those countries that systematically trace not only confirmed cases and fatalities, but also active cases (Andorra, Austria, Czechia, Croatia, Cuba, Germany, Israel, New Zealand, Switzerland and Turkey), which allows tight constraint of numerical analysis. We observe three characteristic growth regimes in confirmed case counts, show that our model is well constrained by these regimes for a wide range of countries, and provide an intuitive explanation behind the emergence of such regimes. Our analytical results

for the characteristic (inflection and maximum) points of the infective curve will allow to i) explain the nearly constant value of the scaling exponent in the superlinear regime of confirmed counts; ii) understand the relation between the duration of this regime and strength of social distancing; iii) pinpoint changes in the reproduction number from outburst to extinguishing the infection, and iv) constrain the main parameter quantifying the effect of social distancing by analyzing scaling of the infection growth with time in the sub-linear regime. The obtained constraints provide a basis for successful analysis of countries that did not continuously track the active cases (here demonstrated for France, Italy, Spain, United Kingdom, and Serbia). We will finally present the key infection parameters inferred through combined analytical and numerical analysis.

We develop a mechanistic model (nonlinear and nonhomogeneous), which takes into account gradual introduction of social distancing (as relevant for most countries' response), in addition to other important infection progression mechanisms. We start from standard compartments for epidemiological models, that is, susceptible ( $S$ ), exposed ( $E$ ), infective ( $I$ ), and recovered ( $R$ ).<sup>[2–4]</sup> To account for social distancing and observable quantities, we introduce additional compartments: protected ( $P$ )—where individuals effectively move from susceptible category due to social distancing; total number of diagnosed (confirmed and consequently quarantined) cases ( $D$ ), active cases ( $A$ ), and fatalities ( $F$ ).  $D$ ,  $A$ , and  $F$  correspond to directly observable (measured) quantities, but are indirect observables of  $I$ , as only part of infective individuals gets diagnosed, due to a large number of mild/asymptomatic cases.<sup>[8]</sup>

Dr. M. Djordjevic, Dr. B. Ilic, S. Stojku, Dr. I. Salom  
Institute of Physics Belgrade  
University of Belgrade  
Belgrade 11080, Serbia  
E-mail: magda@ipb.ac.rs

Prof. M. Djordjevic  
Quantitative Biology Group  
Faculty of Biology  
University of Belgrade  
Belgrade 11000, Serbia  
E-mail: dmarko@bio.bg.ac.rs

 The ORCID identification number(s) for the author(s) of this article can be found under <https://doi.org/10.1002/gch2.202000101>.

© 2021 The Authors. *Global Challenges* published by Wiley-VCH GmbH. This is an open access article under the terms of the Creative Commons Attribution License, which permits use, distribution and reproduction in any medium, provided the original work is properly cited.

DOI: 10.1002/gch2.202000101

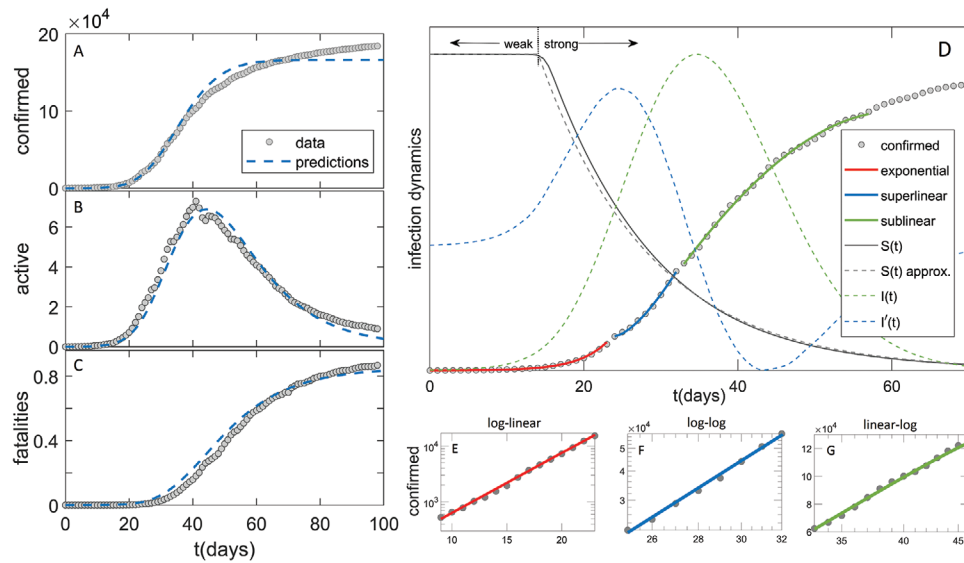


**Figure 1.** Comparison of the model (dashed blue curves) with the data in the case of Germany (grey circles) for A) confirmed case counts, B) active cases, C) fatalities. D) Exponential, superlinear, and sublinear fit to confirmed case data, is shown. Arrows “weak” and “strong” indicate, respectively, the regions with a small and large magnitude of social distancing. The full grey curve denotes susceptibles ( $S(t)$ ), where the dashed grey curve shows an approximation to  $S(t)$ . The dashed green curve denotes the number of infectious cases ( $I(t)$ ), where the dashed blue curve is  $I'(t)$ , whose maxima indicate  $I(t)$  inflection points. The confirmed case counts in the three regimes are shown on E) log-linear, F) log-log and G) linear-log scale.

We implement the model deterministically, as COVID-19 count numbers are very high wherever reasonable testing capacities are employed. This makes model analytically tractable, and allows robust parameter inference through combination of analytically derived expressions and tightly constrained numerical analysis, as we show below. Our analysis is applied separately to each country, as the effect of social distancing, initial numbers of infected and exposed cases, diagnosis/detection efficiency and transmission rates may be different. However, within a given country, we do not take into account different heterogeneities—demographic, spatial, population activity, or seasonality effects.<sup>[2,9,10]</sup> Alternatively, global dynamical properties of the outbreak can be analyzed in a probabilistic framework employing partial differential equations in an age-structured model.<sup>[11,12]</sup> These can readily be included in our model, but would lead to model structure which is not analytically tractable, so these extensions are left for future work.

Given this, the model equations are:

$$dS/dt = -\beta IS/N - dP/dt; \quad dP/dt = \alpha/(1+(t_0/t)^n)S \quad (1)$$

$$dE/dt = \beta IS/N - \sigma E; \quad dI/dt = \sigma E - \gamma I - \varepsilon \delta I; \quad dR/dt = \gamma I \quad (2)$$

$$dD/dt = \varepsilon \delta I; \quad dA/dt = \varepsilon \delta I - hA - mA; \quad dF/dt = mA \quad (3)$$

where  $N$  is the total population number;  $\beta$ —the transmission rate;  $\sigma$ —inverse of the latency period;  $\gamma$ —inverse of the infectious period;  $\delta$ —inverse of the detection/diagnosis period;  $\varepsilon$ —detection efficiency;  $h$ —the recovery rate;  $m$ —the mortality rate. Social distancing is included through Equation (1) (second equation), which represents the rate at which the

population moves (on average) from susceptible to protected category. The term  $\frac{\alpha}{1+(t_0/t)^n}$  corresponds to a sigmoidal dependence

(similar to Fermi–Dirac function, in quantitative biology known as the Hill function<sup>[13]</sup>). Time  $t_0$  determines the half-saturation, so that well before  $t_0$  the social distancing is negligible, while well after  $t_0$  the rate of transition to the protected category approaches  $\alpha$ . Parameter  $n$  (the Hill constant) determines how rapidly the social distancing is introduced, that is, large  $n$  leads to rapid transition from OFF to ON state, and vice versa.<sup>[13]</sup> Equation (3) considers that only a fraction of the infected is diagnosed, so that  $\varepsilon \delta I$  takes into account the diagnosis and the subsequent quarantine process.

To make the problem analytically tractable, we approximate the Hill function in the first relation of Equation (1) by unit step function, so that after  $t_0$  the second term in Equation (1) becomes  $-\alpha S$  and dominates over the first term, that is,  $S(t) \approx e^{-\alpha t}$ . We checked that this approximation agrees well with full-fledged numerical simulations (Figure 1D and Supporting Information). In all comparisons with analytical results, numerical analysis is done with the full model, allowing an independent check of both analytical derivations and employed approximations. Under this assumption, Equations (1) and (2) reduce to:

$$\frac{d^2 I(t)}{dt^2} + (\gamma + \varepsilon \delta + \sigma) \frac{dI(t)}{dt} = \sigma \{ \beta [\theta(t_0 - t) + e^{-(t-t_0)\alpha} \theta(t-t_0)] - (\gamma + \varepsilon \delta) \} I(t) \quad (4)$$

We next introduce two time regions: I)  $t \leq t_0$  and II)  $t > t_0$  and solve Equations (4) separately within these regions, where corresponding solutions are denoted as  $I_I(t)$  and  $I_{II}(t)$ . As in the above expressions  $\gamma + \varepsilon \delta$  always appear together, we further denote  $\gamma + \varepsilon \delta \rightarrow \gamma$ .

For  $I_1(t)$ , we take  $I(t=0) \equiv I_0$ , and restrict to dominant (positive) Jacobian eigenvalue, leading to the exponential regime:

$$I_1(t) = I_0 e^{2^{\frac{1}{2} - (\gamma + \sigma) + \sqrt{(\gamma - \sigma)^2 + 4\beta\sigma}} t} \quad (5)$$

By shifting  $t - t_0 \rightarrow t$ ,  $I_{II}(t)$  is determined by

$$\frac{d^2 I_{II}(t)}{dt^2} + (\gamma + \sigma) \frac{dI_{II}(t)}{dt} = \sigma(\beta e^{-\alpha t} - \gamma) I_{II}(t) \quad (6)$$

Equation (6) is highly nontrivial, due to variable coefficient ( $\sigma\beta e^{-\alpha t}$ ). By substituting variable  $t \rightarrow x = \frac{-2i\sqrt{\beta\sigma}}{\alpha} e^{-\frac{\alpha t}{2}}$  it can be shown that Equation (6) reduces to transformed form of Bessel differential equation:<sup>[14]</sup>

$$x^2 \frac{d^2 \gamma}{dx^2} + (1 - 2\alpha_1)x \frac{d\gamma}{dx} + (\beta_1^2 \gamma_1^2 x^{2\gamma_1} + \alpha_1^2 - v^2 \gamma_1^2) \gamma = 0 \quad (7)$$

whose general solution for noninteger  $v$  is given by:

$$\gamma(x) = x^{\alpha_1} [C_1 J(v, \beta_1 x^{\gamma_1}) + C_2 J(-v, \beta_1 x^{\gamma_1})] \quad (8)$$

where  $J(v, x)$  represents Bessel function of the first kind, and  $C_1, C_2$  are arbitrary constants. In our case  $\alpha_1 = \frac{\gamma + \sigma}{\alpha}$ ,  $\gamma_1 = \beta_1 = 1$ , while  $v = \frac{\gamma - \sigma}{\alpha}$  is indeed noninteger. If we return to  $t$  variable, taking into account the following relation between standard and modified ( $I(v, x)$ ) Bessel functions of the first kind:<sup>[15,16]</sup>  $I(v, x) = i^{-v} J(v, ix)$ , the general solution of Equation (6) reads:

$$I_{II}(t) = \left(\frac{\beta\sigma}{\alpha^2} e^{-\alpha t}\right)^{\frac{\gamma+\sigma}{2\alpha}} \left\{ C_1 (-1)^{\frac{\gamma}{\alpha}} I\left(\frac{\gamma-\sigma}{\alpha}, \frac{2\sqrt{e^{-\alpha t}\beta\sigma}}{\alpha}\right) \Gamma\left(1 + \frac{\gamma-\sigma}{\alpha}\right) + C_2 (-1)^{\frac{\sigma}{\alpha}} I\left(-\frac{\gamma-\sigma}{\alpha}, \frac{2\sqrt{e^{-\alpha t}\beta\sigma}}{\alpha}\right) \Gamma\left(1 - \frac{\gamma-\sigma}{\alpha}\right) \right\} \quad (9)$$

To determine  $C_1, C_2$ , we use the following boundary conditions:  $I_{II}(0) = I_1(t_0)$  and  $I'_{II}(0) = I'_1(t_0)$ , where the first derivative in region II has the following expression:

$$I'_{II}(0) = \left(\frac{\beta\sigma}{\alpha^2}\right)^{\frac{\gamma+\sigma}{2\alpha}} \left\{ C_1 (-1)^{\frac{\alpha+\gamma}{\alpha}} \Gamma\left(1 + \frac{\gamma-\sigma}{\alpha}\right) \left[ \gamma I\left(\frac{\gamma-\sigma}{\alpha}, \frac{2\sqrt{\beta\sigma}}{\alpha}\right) + \sqrt{\beta\sigma} I\left(1 + \frac{\gamma-\sigma}{\alpha}, \frac{2\sqrt{\beta\sigma}}{\alpha}\right) \right] + C_2 (-1)^{\frac{\alpha+\sigma}{\alpha}} \Gamma\left(1 - \frac{\gamma-\sigma}{\alpha}\right) \left[ \sigma I\left(-\frac{\gamma-\sigma}{\alpha}, \frac{2\sqrt{\beta\sigma}}{\alpha}\right) + \sqrt{\beta\sigma} I\left(1 - \frac{\gamma-\sigma}{\alpha}, \frac{2\sqrt{\beta\sigma}}{\alpha}\right) \right] \right\} \quad (10)$$

In obtaining the expression above, the following identities were frequently used:<sup>[15,16]</sup>

$$\frac{dI(v, x)}{dx} = I(v-1, x) - \frac{v}{x} I(v, x); I(v-1, x) - I(v+1, x) = \frac{2vI(v, x)}{x} \quad (11)$$

After derivations, where the following relation<sup>[16]</sup>

$$I(v+1, x)I(-v, x) - I(v, x)I(-v-1, x) = \frac{2\sin(\pi v)}{\pi x} \quad (12)$$

together with  $\sin((v \pm 1)\pi) = -\sin(v\pi)$  and the identity relating modified Bessel function of the first and second kind  $K(v, x) = \frac{\pi}{2} \frac{I(-v, x) - I(v, x)}{\sin v\pi}$  are used,<sup>[15,16]</sup> we finally obtain a surprisingly simple result:

$$I_{II}(t) = I_1(t_0) e^{-\frac{\gamma+\sigma}{2} t} \frac{K\left(\frac{\gamma-\sigma}{\alpha}, \frac{2\sqrt{e^{-\alpha t}\beta\sigma}}{\alpha}\right)}{K\left(\frac{\gamma-\sigma}{\alpha}, \frac{2\sqrt{\beta\sigma}}{\alpha}\right)} \quad (13)$$

where  $K(v, x)$  is the modified Bessel function of the second kind.

At maximum and inflection points,  $I'_{II} = 0$  and  $I''_{II} = 0$ , respectively. After extensive simplification of the results, this leads to  $(\gamma = R_{0,free} e^{-\alpha t})$ , where  $R_{0,free} = \beta/\gamma$  is the basic reproduction number in the absence of social distancing:<sup>[6,17]</sup>

$$\sqrt{\gamma} K\left(\frac{\gamma-\sigma}{\alpha} + 1, \frac{2\sqrt{\gamma\sigma}}{\alpha} \sqrt{\gamma}\right) = \sqrt{\frac{\gamma}{\sigma}} K\left(\frac{\gamma-\sigma}{\alpha}, \frac{2\sqrt{\gamma\sigma}}{\alpha} \sqrt{\gamma}\right) \quad (14)$$

$$\sqrt{\gamma} K\left(\frac{\gamma-\sigma}{\alpha} + 1, \frac{2\sqrt{\gamma\sigma}}{\alpha} \sqrt{\gamma}\right) = \sqrt{\frac{\gamma}{\sigma}} \left(\frac{\gamma+\gamma}{\sigma}\right) K\left(\frac{\gamma-\sigma}{\alpha}, \frac{2\sqrt{\gamma\sigma}}{\alpha} \sqrt{\gamma}\right) \left(\frac{\gamma}{\sigma} + 1\right) \quad (15)$$

Equations (14) and (15) have to be solved numerically, but, as  $\gamma$  and  $\sigma$  are constants, we, interestingly, obtain that solutions will depend only on  $\alpha$ . Since, for the analysis of superlinear and sublinear regimes, only the left inflection point and the maximum are important, we will further omit the second solution of Equation (15) (Equation (14) has one solution), and denote  $\gamma_i = f_{i1}(\alpha) \equiv f_i(\alpha)$ ,  $\gamma_m = f_m(\alpha)$  (these two solutions are presented as upper and lower curves on **Figure 2C**, respectively), so that the effective reproduction numbers at inflection and maximum points ( $R_{e,i}$  and  $R_{e,m}$ ) are:

$$R_{e,i} \equiv R_{0,free} e^{-\alpha t_i} = f_i(\alpha), \quad R_{e,m} \equiv R_{0,free} e^{-\alpha t_m} = f_m(\alpha). \quad (16)$$

From this follows the length of superlinear regime (between inflection and maximum points):

$$\Delta t \equiv t_m - t_i = \frac{1}{\alpha} \ln\left(\frac{f_i(\alpha)}{f_m(\alpha)}\right) \quad (17)$$

We further Taylor expand  $I_{II}(t)$  around the inflection point:



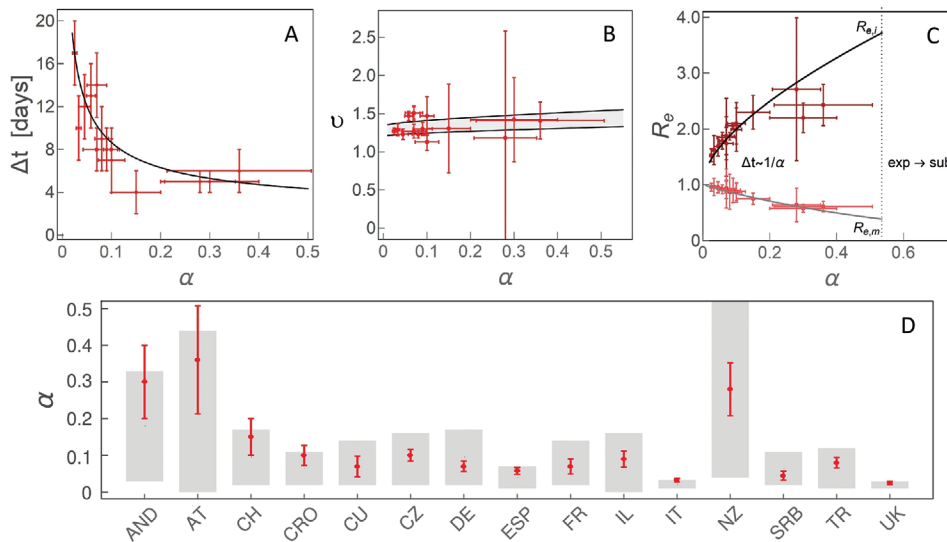


**Figure 2.** The dependence on the effective social distancing strength ( $\alpha$ ) of A)  $\Delta t$ , the duration of the superlinear regime, B)  $\nu$ , the scaling exponent of the superlinear regime, C)  $R_e$ , effective reproduction number at the left inflection point ( $R_{e,i}$ ) and the maximum ( $R_{e,m}$ ) of  $I(t)$ .  $\Delta t \approx 1/\alpha$  indicates that the time, in which the change from  $R_{e,i}$  to  $R_{e,m}$  is exhibited, is approximately inversely proportional to  $\alpha$ . “exp  $\rightarrow$  sub” indicates the region of  $\alpha$  where we predict a direct transition from exponential to sublinear growth. D) Comparison of  $\alpha$  constrained from analytical derivations (the grey bands) and numerical analysis, with countries indicated on the horizontal axis by their abbreviations. Results obtained by independent numerical analysis are presented by red dots with corresponding errorbars.

$$I_{II}(t) = I_1(t_0) e^{-\frac{\gamma+\sigma}{2}(t-t_0)} \frac{K\left(\frac{\gamma-\sigma}{\alpha}, \frac{2\sqrt{\gamma\sigma}}{\alpha} \sqrt{f_i(\alpha)}\right)}{K\left(\frac{\gamma-\sigma}{\alpha}, \frac{2\sqrt{\beta\sigma}}{\alpha}\right)} \left[1 - \frac{\gamma\sigma}{\gamma+\sigma}(1-f_i(\alpha))(t-t_0) + \mathcal{O}((t-t_0)^2)\right] \quad (18)$$

In the superlinear regime  $D(t) \approx (t-t_s)^\nu$ , where  $\nu$  is the scaling exponent and  $t_s$  marks the beginning of this regime. By Taylor expanding  $D(t)$  around  $t_s$ , using Equations (18) and (3):

$$\nu = 1 + \frac{1}{k\alpha} \frac{\gamma\sigma}{\gamma+\sigma} [f_i(\alpha) - 1] \ln\left(\frac{f_i(\alpha)}{f_m(\alpha)}\right) \quad (19)$$

which is always larger than 1, as expected for the superlinear regime. As  $t_s$  is localized toward the beginning of the regime, we estimate  $t_i - t_s \approx \frac{\Delta t}{k}$ , where  $k \approx 3, 4$ .

Finally, to provide analytical constrain on  $\alpha$ , we Taylor expand  $I_{II}(t)$  around the maximum:

$$I_{II}(t) = I_1(t_0) e^{-\frac{\gamma+\sigma}{2}(t-t_0)} \frac{K\left(\frac{\gamma-\sigma}{\alpha}, \frac{2\sqrt{\gamma\sigma}}{\alpha} \sqrt{f_m(\alpha)}\right)}{K\left(\frac{\gamma-\sigma}{\alpha}, \frac{2\sqrt{\beta\sigma}}{\alpha}\right)} \left[1 - \frac{\gamma\sigma}{2}(1-f_m(\alpha))(t-t_m)^2 + \mathcal{O}((t-t_m)^3)\right] \quad (20)$$

As  $f_m(\alpha) < 0$ , we see that the quadratic term in Equation (20) is always negative, that is,  $D(t)$  curve enters sublinear regime around maximum of the infection. By fitting  $D(t)$

to  $c+d(t-t_m)-f(t-t_m)^3$  in this regime, and by using Equation (20) together with Equation (3), we obtain:

$$\frac{f}{d} = \frac{\gamma\sigma}{6} [1 - f_m(\alpha)] \quad (21)$$

which allows to directly constrain  $\alpha$ .

We first numerically analyze outbreak dynamics in the countries that continuously updated<sup>[18]</sup> three observable categories ( $D$ ,  $A$ , and  $F$ ). For a large majority of countries active cases were either not tracked or were not continuously updated, so the analysis is done for ten countries listed in the outline above.

In the exponential regime, the analytical closed-form solution is given by Equation (5). From this, and the initial slope of  $\ln(D)$  curve (once the number of counts are out of the stochastic regime),  $\beta$  can be directly determined, while the corresponding eigenvector sets the ratio of  $I_0$  to  $E_0$ . The intercept of the initial exponential growth of  $D$  at  $t = 0$  sets the product of  $I_0$  and  $\varepsilon\delta$ .  $h$  and  $m$  can also be readily constrained, as from Equation (3), they depend only on integrals of the corresponding counts; here note that  $d(D-A-F)/dt = hA$ . Also,<sup>[17,19,20]</sup>  $\sigma = 1/3 \text{ day}^{-1}$  and  $\gamma = 1/4 \text{ day}^{-1}$ , characterize fundamental infectious process, which we assume not to change between different countries.

Only parameters related with the intervention measures ( $\alpha, t_0, n, \varepsilon\delta$ ) are left to be inferred numerically, leading to tightly constrained numerical results. For this, we individually performed joint fit to all three observable quantities ( $A, D, F$ ) for each country. The errors are estimated through Monte-Carlo<sup>[21,22]</sup> simulations, assuming that count numbers follow Poisson distribution.

Representative numerical results are shown in Figure 1 for Germany, while other countries are shown in the Supporting

Information. In Figure 1A–C (and Supporting Information) we see a good agreement of our numerical analysis with all three classes of the case counts. In Figure 1D, we see sharp transitions between the three growth patterns indicated in the figure: i) exponential growth, observed as a straight line in log–linear plot in Figure 1E; ii) superlinear growth, a straight line in log–log plot in Figure 1F; iii) sublinear growth, a straight line in linear–log plot in Figure 1G.

Transition between the growth patterns can be qualitatively understood from Equation (3), and  $I(t)$  curve in Figure 1D. The exponential growth has to break after the inflection point of  $I(t)$ , that is, once the maximum of its first derivative ( $I'(t)$  in Figure 1D) is reached. In the superlinear regime, confirmed counts case ( $D(t)$ ) curve is convex ( $D''(t) > 0$ ), so this regime breaks once  $I'(t)$  (dashed blue curve) becomes negative. Equivalently,  $D(t)$  curve becomes concave (enters sublinear regime) once the maximum of the  $I(t)$  is reached. Note that the growth of  $D(t)$  can reemerge if the social distancing measures are alleviated. Our model can account for this by allowing transition from protected back to susceptible category, which is out of the scope of this study, but may improve the agreement with the data at later times (see Figure 1A–C). In addition to this numerical/intuitive understanding, we also showed that we analytically reproduce the emergence of these growth regimes (Equations (6), (14), (15)). Can we also analytically derive the parameters that characterize these regimes?

The exponential regime is straightforward to explain, as described above. The superlinear regime is in between the left inflection point and the maximum of  $I(t)$ , so that infective numbers grow, but with a decreasing rate. While the derivations are straightforward in the exponential regime, they are highly non-trivial during the subsequent subexponential (superlinear and sublinear) growth. As the superlinear regime spans the region between the left inflection point ( $t_i, I''(t_i) = 0$ ) and the maximum ( $t_m, I'(t_m) = 0$ ), its duration is  $\Delta t = t_m - t_i$  given by Equation (17), with  $\approx 1/\alpha$  dependence, so that weak measures lead to protracted superlinear growth (see Figure 2A). This tendency is also confirmed by independent numerical analysis in Figure 2A, where for each individual country we numerically infer  $\alpha$  and extract the length of the superlinear regime. Therefore, the duration of the superlinear regime indicates the effectiveness of introduced social distancing.

The scaling exponent  $\nu$  of the superlinear regime is given by Equation (19), and shown in Figure 2B, where we predict that all countries are roughly in the same range of  $1.2 < \nu < 1.5$  (surprisingly, weakly dependent on  $\alpha$ ), despite significant differences in the applied measures, demographic and environmental factors. This result is (independently from our model) confirmed from case count numbers (the slope in Figure 1F, and equivalently for other countries, see Figure 2B).

How the effective reproduction number  $R_e$  changes during this regime, that is, between the left inflection point and the maximum of  $I(t)$ ?  $R_e$  quantifies the average number of secondary cases per infectious case, so that  $R_e > 1$  signifies disease outburst, while for  $R_e < 1$  the disease starts to be eliminated from the population.<sup>[17]</sup> The Equation (16) provides expressions for  $R_{e,i}$  (at the inflection point) and  $R_{e,m}$  (at the maximum). Interestingly, from Figure 2C, we observe that  $R_{e,i}$  and  $R_{e,m}$

do not depend on  $R_{0,free}$  and are, respectively, significantly larger and smaller than 1, which shows that transition from infection outburst to extinguishing happens during the superlinear growth. Consequently, the steepness of  $R_e$  change over the superlinear regime significantly increases (larger change over smaller time interval, see Figure 2C) with the measure strength.

Finally, in the sublinear regime, in a wide vicinity of  $I(t)$  maximum (which marks the beginning of the sublinear growth) leading non-linear term of  $D(t)$  is cubic ( $\approx t^3$ , with negative prefactor). This is consistent with the expansion of  $I(t)$  around  $t_m$ , which has leading negative quadratic ( $t^2$ ) dependence (see Equations (3) and (20)). The ratio between the prefactors in  $D(t)$  expansion is given by Equation (21), from which we see that  $\alpha$  can be directly constrained, as shown in Figure 2D. For the ten countries with consistent tracking of  $D, A$ , and  $F$ , we independently numerically determined  $\alpha$  and compared it with analytical results coming from Equation (21), obtaining an excellent agreement between our derivations and numerical results. The obtained  $\alpha$  values should be understood as an effective epidemic containment measure—that is, estimating the true result of the introduced measures, which can be used to evaluate the practical effectiveness of the official policies.

To demonstrate how constraining  $\alpha$  can aid numerical analysis in the cases when  $A$  is not continuously tracked, we next analyze five additional countries listed in the outline above, so that altogether our study covers majority of COVID-19 hotspots, which (at the time of this analysis) are close to saturation in confirmed counts. Furthermore, in the specific cases of UK and Italy, where we analytically obtained both very low and very constrained  $\alpha$  ( $0.01 < \alpha < 0.04$ ), we chose five times larger parameter span in  $\alpha$  in the numerical analysis, to confirm that these low values are indeed preferred by the exhaustive numerical search. For example, the finally obtained  $\alpha$  for Italy ( $0.033 \pm 0.005$ ) and UK ( $0.025 \pm 0.005$ ), together with previously obtained agreements shown in Figure 2A–C, strongly confirm that the observed growth patterns provide invaluable information for successful analysis of the infection progression data.

To further illustrate this, the synergy of analytical derivations and numerical analysis presented above enables us to, directly from the publicly available data, infer key infection parameters necessary to assess epidemics risks (provided in Table S1, Supporting Information). We estimate these parameters by the same model/analysis, for a number of diverse countries, allowing their direct comparison. In **Figure 3**, we show together case fatality rate (CFR), infected fatality rate (IFR) and infection attack rate (AR).<sup>[17,24]</sup> CFR is the number of fatalities per confirmed cases. CFR can, in principle, be inferred directly from the data, but since different countries are in different phases of infection, we project forward the number of confirmed cases until a saturation is reached for each country, from which we calculate CFR. IFR (crucial parameter for assessing the risks for infection progression under different scenarios) is the number of fatalities per total number of infected cases, which is a genuine model estimate, due to the unknown total number of infected cases. AR (necessary for understanding the virus recurrence risk) is also determined from our model and provides an estimate of the fraction of the total population that got infected and possibly resistant.

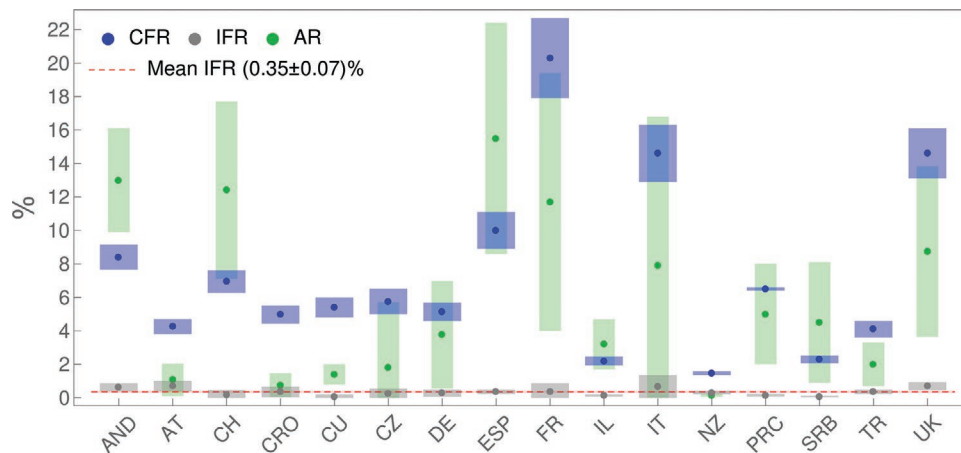


**Figure 3.** CFR, IFR, and AR, inferred for countries whose abbreviations are indicated on the horizontal axis, are denoted, respectively, by blue, grey, and green dots, with errorbars indicated by corresponding bands. The dashed red horizontal line stands for IFR consistent with a mean value (indicated in the legend). Values for PRC are from ref. [23].

From Figure 3, we see that CFR takes very different values for different countries, from below 2% (New Zealand) to above 20% (France). On the other hand, IFR is consistent with a constant value (the dashed red line in the figure) of  $\approx 0.3\text{--}0.4\%$ . In distinction to IFR, AR also takes diverse values for different countries, ranging from  $\approx 1\%$  to as high as  $\approx 15\%$  (though with large errorbars). Although diverse, these AR values are well below the classical herd immunity threshold of 60–70%.

To summarize, we here developed a novel quantitative framework through which we showed that: i) The emergence of three distinct growth regimes in COVID-19 case counts can be reproduced both analytically and numerically. ii) Typically, a brief superlinear regime is characterized by a sharp transition from outburst to extinguishing the infection, where effective reproduction number changes from much larger to much smaller than one; more effective measures lead to shorter superlinear growth, and to a steeper change of the effective reproduction number. iii) Scaling exponent of the superlinear regime is surprisingly uniform for countries with diverse environmental and demographic factors and epidemics containment policies; this highly non-trivial empirical result is well reproduced by our model. iv) Scaling prefactors in the sublinear regime contain crucial information for analytically constraining infection progression parameters, so that they can be straightforwardly extracted through numerical analysis. Interestingly, we found that the number of COVID-19 fatalities per total number of infected is highly uniform across diverse analyzed countries, in distinction to other (highly variable) infection parameters, and about twice higher than commonly quoted for influenza (0.3–0.4% compared to 0.1–0.2%), which may be valuable for direct assessment of the epidemics risks.

While state-of-the-art approach in epidemiological modeling uses computationally highly demanding numerical simulations, the results above demonstrate a shift of paradigm toward simpler, but analytically tractable models, that can both explain common dynamical features of the system and be used for straightforward and highly constrained parameter inference. This shift is based on a novel framework that relates universal growth patterns with characteristic points of the infective curve, followed by analytical derivations in the vicinity of these points, in an approach akin to those in a number of

physics problems. The framework presented here can be, in principle, further extended toward, for example, including stochastic effects or different heterogeneities such as age-structure. However, these are non-trivial tasks, and it remains to be seen to what extent the analytical results can be obtained in those more complex models. Overall, as our approach does not depend on any COVID-19 specifics, the developed framework can also be readily applied to potential outbursts of future infections.

## Supporting Information

Supporting Information is available from the Wiley Online Library or from the author.

## Acknowledgements

This work was supported by the Ministry of Education, Science and Technological Development of the Republic of Serbia.

## Conflict of Interest

The authors declare no conflict of interest.

## Data Availability Statement

The data used in this study are openly available in Worldometer at <https://www.worldometers.info/coronavirus/>, reference number [7]. Parameters inferred through the analysis are available in the supplementary material of this article.

## Keywords

dynamical growth patterns, infections disease modeling, physics and society, scaling of epidemics growth

Received: October 8, 2020  
Revised: January 16, 2021  
Published online: March 1, 2021

- [1] WHO report. <https://www.who.int/emergencies/diseases/novel-coronavirus-2019/situation>.
- [2] O. Diekmann, H. Heesterbeek, T. Britton, *Mathematical Tools for Understanding Infectious Disease Dynamics*, Princeton University Press, Princeton, NJ **2012**.
- [3] M. Martcheva, *An Introduction to Mathematical Epidemiology*, Springer, Berlin **2015**.
- [4] M. J. Keeling, P. Rohani, *Modeling Infectious Diseases in Humans and Animals*, Princeton University Press, Princeton, NJ **2011**.
- [5] H. Tian, Y. Liu, Y. Li, C. H. Wu, B. Chen, U. G. Kraemer, B. Li, J. Cai, B. Xu, Q. Yang, B. Wang, P. Yang, Y. Cui, Y. Song, P. Zheng, Q. Wang, O. N. Bjornstad, R. Yang, B. T. Grenfell, O. G. Pybus, C. Dye, *Science* **2020**, 368, 638.
- [6] G. Chowell, L. Sattenspiel, S. Bansal, C. Viboud, *Physics of Life Reviews* **2016**, 18, 66.
- [7] Worldometer **2020**. COVID-19 Coronavirus Pandemic. <https://www.worldometers.info/coronavirus/> (accessed: June 2020).
- [8] M. Day, *BMJ: British Medical Journal* **2020**, 368, m1165.
- [9] G. N. Wong, Z. J. Weiner, A. V. Tkachenko, A. Elbanna, S. Maslov, N. Goldenfeld, *arXiv:200602036*, **2020**.
- [10] J. R. Dormand, P. J. Prince, *J. Comput. Appl. Math.* **1980**, 6, 19.
- [11] J. M. Vilar, L. Saiz. medRxiv 2020.11.26.20239434, **2020**.
- [12] N. C. Grassly, C. Fraser, *Nat. Rev. Microbiol.* **2008**, 6, 477.
- [13] R. Phillips, J. Kondev, J. Theriot, H. Garcia, *Physical Biology of the Cell*, Garland Science, New York, NY **2012**.
- [14] F. Bowman, *Introduction to Bessel Functions*, Dover Publications, New York, NY **1958**.
- [15] D. Zwillinger, *Standard Mathematical Tables and Formulae*, CRC Press, Boca Raton, FL **1995**.
- [16] M. Abramowitz, T. A. Stegun, *Handbook of Mathematical Functions* (Ed: M. Abramowitz), Dover Publications, New York, NY **1972**.
- [17] Y. M. Bar-On, A. I. Flamholz, R. Phillips, R. Milo, *eLife* **2020**, 9, e57309.
- [18] E. Dong, H. Du, L. Gardner, *Lancet Infect. Dis.* **2020**, 20, 533.
- [19] R. Li, S. Pei, B. Chen, Y. Song, T. Zhang, W. Yang, J. Shaman, *Science* **2020**, 368, 489.
- [20] X. He, E. H. Y. Lau, P. Wu, X. Deng, J. Wang, X. Hao, Y. C. Lau, J. Y. Wong, Y. Guan, X. Tan, X. Mo, Y. Chen, B. Liao, W. Chen, F. Hu, Q. Zhang, M. Zhong, Y. Wu, L. Zhao, F. Zhang, B. J. Cowling, F. Li, G. M. Leung, *Nat. Med.* **2020**, 26, 672.
- [21] W. H. Press, B. P. Flannery, S. A. Teukolsky, W. T. Vetterling, *Numerical Recipes: The Art of Scientific Computing*, Cambridge University Press, Cambridge **1986**.
- [22] R. W. Cunningham, *Comput. Phys.* **1993**, 7, 570.
- [23] M. Djordjevic, M. Djordjevic, I. Salom, A. Rodic, D. Zigic, O. Milicevic, B. Ilic, *arXiv:2005.09630*, **2020**.
- [24] S. Eubank, I. Eckstrand, B. Lewis, S. Venkatramanan, M. Marathe, C. L. Barrett, *Bull. Math. Biol.* **2020**, 82, 1.
- [25] T. Britton, F. Ball, P. Trapman, *arXiv:2005.03085*, **2020**.
- [26] F. P. Havers, C. Reed, T. Lim, J. M. Montgomery, J. D. Klena, A. J. Hall, A. M. Fry, D. L. Cannon, C.-F. Chiang, A. Gibbons, I. Krapiunaya, M. Morales-Betoulle, K. Roguski, M. Ata Ur Rasheed, B. Freeman, S. Lester, L. Mills, D. S. Carroll, S. M. Owen, J. A. Johnson, V. Semenova, C. Blackmore, D. Blog, S. J. Chai, A. Dunn, J. Hand, S. Jain, S. Lindquist, R. Lynfield, S. Pritchard, et al., *JAMA Intern. Med.* **2020**, 180, 1576.

**Special Section:**

The COVID-19 pandemic:  
linking health, society and  
environment

**Key Points:**

- Machine learning techniques are utilized to select the most influential environmental factors behind COVID-19 transmissibility
- The country's wealth/development level is identified as the main global predictor of SARS-CoV-2 spread in a population
- Other important factors are indoor space per person, unhealthy living determinants, spontaneous behavior change, and weather seasonality

**Correspondence to:**

M. Djordjevic,  
[dmarko@bio.bg.ac.rs](mailto:dmarko@bio.bg.ac.rs)

**Citation:**

Djordjevic, M., Salom, I., Markovic, S., Rodic, A., Milicevic, O., & Djordjevic, M. (2021). Inferring the main drivers of SARS-CoV-2 global transmissibility by feature selection methods. *GeoHealth*, 5, e2021GH000432. <https://doi.org/10.1029/2021GH000432>

Received 29 MAR 2021

Accepted 18 AUG 2021

**Author Contributions:**

**Conceptualization:** Marko Djordjevic, Igor Salom, Ognjen Milicevic, Magdalena Djordjevic

**Formal analysis:** Marko Djordjevic, Sofija Markovic

**Methodology:** Marko Djordjevic, Andjela Rodic, Ognjen Milicevic, Magdalena Djordjevic

**Software:** Marko Djordjevic, Sofija Markovic

**Supervision:** Marko Djordjevic, Igor Salom

© 2021 The Authors. GeoHealth published by Wiley Periodicals LLC on behalf of American Geophysical Union. This is an open access article under the terms of the [Creative Commons Attribution License](https://creativecommons.org/licenses/by/4.0/), which permits use, distribution and reproduction in any medium, provided the original work is properly cited.

## Inferring the Main Drivers of SARS-CoV-2 Global Transmissibility by Feature Selection Methods

Marko Djordjevic<sup>1</sup> , Igor Salom<sup>2</sup>, Sofija Markovic<sup>1</sup>, Andjela Rodic<sup>1</sup>, Ognjen Milicevic<sup>3</sup>, and Magdalena Djordjevic<sup>2</sup>

<sup>1</sup>Faculty of Biology, Quantitative Biology Group, Institute of Physiology and Biochemistry, University of Belgrade, Belgrade, Serbia, <sup>2</sup>Institute of Physics Belgrade, National Institute of the Republic of Serbia, University of Belgrade, Belgrade, Serbia, <sup>3</sup>Department for Medical Statistics and Informatics, School of Medicine, University of Belgrade, Belgrade, Serbia

**Abstract** Identifying the main environmental drivers of SARS-CoV-2 transmissibility in the population is crucial for understanding current and potential future outbreaks of COVID-19 and other infectious diseases. To address this problem, we concentrate on the basic reproduction number  $R_0$ , which is not sensitive to testing coverage and represents transmissibility in an absence of social distancing and in a completely susceptible population. While many variables may potentially influence  $R_0$ , a high correlation between these variables may obscure the result interpretation. Consequently, we combine Principal Component Analysis with feature selection methods from several regression-based approaches to identify the main demographic and meteorological drivers behind  $R_0$ . We robustly obtain that country's wealth/development (GDP per capita or Human Development Index) is the most important  $R_0$  predictor at the global level, probably being a good proxy for the overall contact frequency in a population. This main effect is modulated by built-up area per capita (crowdedness in indoor space), onset of infection (likely related to increased awareness of infection risks), net migration, unhealthy living lifestyle/conditions including pollution, seasonality, and possibly BCG vaccination prevalence. Also, we argue that several variables that significantly correlate with transmissibility do not directly influence  $R_0$  or affect it differently than suggested by naïve analysis.

**Plain Language Summary** While numerous studies tried to assess the correlations of different factors with the SARS-CoV-2, the next step should be predicting the environmental risk of the high transmissibility in a certain population. Specifically, a relatively small number of the most influential meteorological and demographic factors should be selected for a predictive risk measure that is accurate enough and practical for use. To achieve this, we here utilize a combination of Principal Component Analysis and feature selection techniques. We identify that the main drivers behind COVID-19 transmissibility are the country's wealth/development level corrected by the available indoor space per person and net migration; pollution levels, and some of the unhealthy living factors; spontaneous behavior change due to developing epidemics; weather seasonality; (less significantly) BCG vaccination. On the other hand, we show that several variables that appear significantly related to the disease progression through naïve pairwise correlation analysis do not directly influence transmissibility. These results may provide useful guidelines for future strategies of imposing epidemic mitigation measures.

### 1. Introduction

Despite the unprecedented worldwide campaign of mass immunization, due to the relatively slow vaccine rollout and to the appearance of new, more contagious (Tegally et al., 2020), and maybe even more deadly SARS-CoV-2 strains (Mallapaty, 2021), COVID-19 still takes its toll on human lives, stifles the world economy, and forces the majority of countries to keep unpopular lockdowns. In the absence of a prompt solution to the first pandemic of the century, the goal to identify the main environmental and demographic parameters that influence the dynamics of infection transmission remains as important as ever.

Investigating which factors influence the rate of COVID-19 expansion is a highly involved matter, primarily due to many possibly relevant modes of SARS-CoV-2 transmission. It is generally undisputed that COVID-19 transmission occurs by droplets between people in close proximity (Rahimi et al., 2021). Consequently,



**Validation:** Marko Djordjevic, Igor Salom, Sofija Markovic, Andjela Rodic, Ognjen Milicevic, Magdalena Djordjevic  
**Visualization:** Sofija Markovic, Magdalena Djordjevic  
**Writing – original draft:** Marko Djordjevic, Igor Salom, Andjela Rodic  
**Writing – review & editing:** Marko Djordjevic, Igor Salom, Andjela Rodic, Magdalena Djordjevic

various factors that influence the frequency of interpersonal contacts and intensity of social mixing between people arriving from different/distant areas will necessarily strongly impact the rate of the epidemic spread. However, other means of transmission may also play important roles. It has been established that contact with surfaces in the immediate environment of infected persons (or with objects used by them) can lead to infection. Also, there is an increasing body of evidence that the airborne transmission of COVID-19 cannot be neglected and, moreover, that small air pollutant particles may aid the long-range virus transmission (Coccia, 2020b; Rahimi et al., 2021). Some authors even suggest the relevance of contaminated wastewater in the infection spread (Rahimi et al., 2021). Such various modes of transmission open up the possibility not only of direct influence of numerous environmental factors (e.g., temperature, humidity, wind speed, and air pollution) (Sarkodie & Owusu, 2020) but also of nontrivial interactions between these factors (e.g., the interplay between the pollution, wind speed, and population density is discussed in Coccia, 2021b). It must also be taken into account that the level of personal susceptibility to the given virus can strongly affect the rate of an epidemic, and thus a comprehensive study must also consider more subtle demographic/medical variables (Notari & Torrieri, 2020).

We recently published a comprehensive study of the correlation of 42 different demographic and weather parameters with COVID-19 basic reproduction number  $R_0$  across 118 world countries (Salom et al., 2021).  $R_0$  is a well-established epidemiological measure of virus transmissibility. Its major advantage is independence on the testing policy/capacity and intervention measures, which can be highly variable (and almost impossible to consistently control) between different countries (Salom et al., 2021). In Salom et al. (2021), we selected all the countries that exhibited regular exponential growth in the case numbers before the introduction of intervention measures (Djordjevic et al., 2021), from which their  $R_0$  values can be reliably extracted. Tracking a wide range of countries allows achieving a maximal variability in the data set, that is, a maximal possible range in the values of analyzed variables, as another advantage of this study. This data set will be used as a starting point in this work.

Our present goal is to go a step further than the previous study by applying and combining various advanced data analysis methods. Namely, while (Salom et al., 2021) covered a broad scope of variables and countries, it focused on establishing pairwise correlations between  $R_0$  and each of the studied factors, ignoring the fact that many of these variables are highly mutually correlated. This is most obvious in the case of the weather parameters such as for example, temperature and UV radiation (which both reflect the local climate in a similar way and follow comparable seasonal trends), but also in the case of many demographic parameters, for example, the strong positive correlation between the Human Development Index (HDI) and cholesterol levels. Based on pairwise correlations alone, it is thus hard to estimate, which of these variables might be truly influencing the spread of the disease, to what extent, and in which direction.

Therefore, in the present paper, our task is to go beyond mere pairwise correlations, and by using a combination of principal component analysis (PCA) and four different regression-based approaches, establish which of these factors significantly affect  $R_0$  (by at the same time controlling for the impact of other factors). To achieve this, the number of variables necessary to explain the virus transmissibility needs to be reduced to only a few without losing predictiveness. However, this is not the only challenge, because of variable redundancy. In particular, one may select different combinations of variables accounting together for a similar proportion of variance in the virus transmissibility, which presents an ambiguity that is difficult to resolve. Consequently, there is a challenge to narrow down the possibilities and illuminate important contributions of the seemingly small differences between highly correlated variables. Notably, numerous studies examined the correlations of several selected (Lin et al., 2020; Ran et al., 2020; Xie et al., 2020) or many different (Hassan et al., 2021; Li et al., 2020; Salom et al., 2021) sociodemographic and meteorological factors with the magnitude of the COVID-19 epidemic. However, only a few studies tried to select a handful of key factors whose combination can explain a large portion of the variance between regions (Allel et al., 2020; Coccia, 2020d; Gupta & Gharehgozli, 2020; Notari & Torrieri, 2020). Even a smaller number of studies included data from multiple countries (Allel et al., 2020; Notari & Torrieri, 2020). Furthermore, a similar effort to relate the rate of exponential case growth to a smaller set of variables by PCA was made (Notari, 2021; Notari & Torrieri, 2020). To conduct a thorough investigation and reach robust conclusions, we partially decorrelate 24 different factors and apply several specialized feature selection methods independently. While disentangling the various effects on the epidemic spread is undeniably a challenging task,

by comparing the results obtained by different methods one can identify the variables that are selected by all or most of them, which provides valuable evidence in favor of their true significance.

The main idea of this study is to develop a novel approach, which can robustly identify the most important predictors of  $R_0$ . The development of such an approach will (a) provide a straightforward solution to the known problem of selecting the important ones among the highly correlated variables, (b) enable a better understanding of which environmental and demographic variables may dominantly and/or independently influence the progression of the COVID-19 epidemics, and what is the direction of this influence. With these goals, we organize the study as follows:

1. The variables are first naturally split into two groups. The first group comprises six meteorological parameters, sampled and averaged (for each country) during the initial stage of the local epidemic outbreak: air temperature (T), precipitation (PR), specific humidity (H), ultra-violet radiation index (UV), air pressure (P), and wind speed (WS). Eighteen (broadly speaking) demographic parameters form the second group: human development index (HDI), percentage of the urban population (UP), gross domestic product per capita (GDP), amount of the built-up area per person (BUAPC), percentage of refugees (RE), net migration (i.e., the number of immigrants minus emigrants, I-E), infant mortality (IM), median age (MA), long-term average of PM2.5 pollution (PL), prevalence and severity of COVID-19 relevant chronic diseases in the population (CD), average blood cholesterol level (CH), the prevalence of raised blood pressure (RBP), the prevalence of obesity (OB), the prevalence of insufficient physical activity among adults (IN), BCG immunization coverage (BCG), alcohol consumption per capita (ALC), smoking prevalence (SM), and the delay of the epidemic onset (ON).
2. Due to strong correlations between parameters within each group (as well as across the groups, but at a lower extent), on each group, we will perform the PCA (Jolliffe, 2002). This step will allow us to notably reduce the dimensionality, that is, proceed to work with a smaller number of (mostly) uncorrelated variables. Such a dimensionality reduction will significantly simplify the further analysis and improve the reliability of the results.
3. The linear regression analysis will next be performed in four independent ways, ranging from our custom-developed to more formal regression-based approaches, to select important variables. In our custom-developed approach, multiple linear regressions are applied, first separately to demographic and meteorological principal components (PCs) to narrow down the number of relevant PCs within each of the two groups, before doing overall linear regression with the remaining PCs to assess their importance in explaining  $R_0$ . A major advantage of such an analysis is an intuitive understanding of the data structure and its relation to  $R_0$ . This analysis is next independently redone by more formal feature selection methods, commonly employed in bioinformatics and systems biology: Stepwise regression and regressions utilizing both regularization and variable selection—Lasso (Least Absolute Selection and Shrinkage Operator) and Elastic net (Hastie et al., 2009; Tibshirani, 1996; Zou & Hastie, 2005). Lasso and Elastic net are regressions based on regularization, which can shrink coefficients exactly to zero, allowing variable selection. Such a feature selection is quite important, as the variables that do not affect the response ( $R_0$ ) may introduce significant noise in the model. This would lead to overfitting (high variance), which is exacerbated by a small/limited data set and correlated predictors (as applicable here). Note that regressions with regularization are not ordinary fits, for example, hyperparameters that control coefficient shrinkage have to be carefully tuned through cross-validation. Overall, this comprehensive analysis will ensure the consistency and robustness of the reported results.
4. Finally, an intuitive interpretation of the obtained results will be presented. This will permit a much more specific understanding of COVID-19 transmissibility, by focusing on the main driving factors behind the disease spread in the population.

## 2. Methods

### 2.1. Sample and Data

Data for demographic and meteorological parameters were assembled as described in Salom et al. (2021). Briefly, the data correspond to six meteorological and eighteen demographic variables outlined above. The differences between this data set and the one used in Salom et al. (2021) is the following: IMS (Social security and health insurance coverage), Prevalence of ABO and Rhesus blood groups, and Ambient levels

of different pollutants ( $\text{NO}_2$ ,  $\text{SO}_2$ , CO, PM2.5, and PM10) are not used in this analysis, as they contain too many missing values. Instead of the pollutant levels measured from air pollution monitoring stations during the epidemic's exponential growth (available for only ~40 countries), we use the yearly average PM2.5 pollutant levels in 2017 (World Bank, 2020b). Also, we consider GDP per capita (GDPpc), taken from World Bank (2020a), as a more direct (average) indicator of a country's economic wealth/productivity.

There are no missing values in the meteorological data, while we substitute the missing values in the demographic data (which were sparse for the used variables) with the median values of the respective variables. The discarded variables have at least 30% missing values (occurring for blood groups) and going up to 72% (for CO). On the other hand, for the variables that we retained, the missing values are sparse. Specifically, the maximal fraction is 6% (for refugees).

Basic reproduction number ( $R_0$ ), that is, a measure of SARS-CoV-2 transmissibility in a fully susceptible population and in the absence of intervention measures (social distancing, quarantine), was also taken from Salom et al. (2021), where it was inferred from nonlinear dynamics modeling. Overall, demographic data, meteorological data, and  $R_0$  were assembled for 118 different countries from which we could reliably infer  $R_0$ . We used the following criteria to select the countries for which  $R_0$  was inferred and consequently used in the further analysis:

1. We initially selected 165 world countries, with the following criteria: more than 1,000 tests performed by 12.06.2020, with the ratio between performed tests and detected cases larger than five. This accounts for reliable testing capacity, that is, in this way, we avoid countries with low testing capacity.
2.  $R_0$  is inferred from the regime, which has reached the deterministic limit, that is, the starting time is such that the number of detected cases is ~10 or more. Each country is processed/inspected manually to determine the time period that is used in the analysis (i.e., exactly which interval corresponds to the exponential growth)—this is necessary as we found that this interval significantly varies for different countries. The manual inspection corresponds to recognizing a straight line on a semi-logarithmic plot, which is straightforward and reproducible.
3. Clear exponential growth is observed for at least 7 days, corresponding to the straight line in the number of detected cases versus time on the log scale.

In this way, we avoid the cases where too small (or irregular) testing is preventing reliable inference of  $R_0$ . Two 'filters' ensure this: The first is a condition (a) which directly accounts for those countries with too small testing capacity. Second, the countries with 'irregular' testing are also filtered by condition (b), as they exhibit an irregular behavior in the case count numbers, rather than regular exponential growth, which is robustly observed across other countries. Finally, condition (c) ensures that stochastic fluctuations (and possible very early testing inconsistencies) do not influence results, while the manual inspection for each country ensures adequacy of the time interval used in the analysis.

## 2.2. Measures of Variables

Several variables, particularly among demographic data, show a significant deviation from normality when visually inspected. Such deviations generate large outliers and would significantly impact the necessary normality of the model error residuals. We consequently transform the data (where necessary) to make the resulting distributions closer to normal, by using standard transformations that reduce the right and left skewness. We chose the strength of the applied transformations (e.g., square root, cubic root, or log) so that skewness of the transformed distribution is as close as possible to zero. Applied transformations are provided in Table 1. Each transformed variable whose direction was changed by the transformation was taken with a minus sign, so that the original and the transformed variable are oriented in the same direction, allowing for easier result interpretation.

After transformations, the remaining (now sparse, less than 2% of the data set) outliers were removed by substituting them with the median of each variable; the outliers were identified as having more than three scaled median absolute deviation (MAD) from the (transformed) variable median. Removal of the outliers is important, as they may substantially (both quantitatively and qualitatively) obscure the multivariate regression analysis, including regressions with regularization (Hastie et al., 2009).

**Table 1**  
*Data Transformations*

Variable	Acronym	Transformation
Built-up area per capita	BUAPC	$(x - \min(x))^{1/3}$
Urban population	UP	$x^2$
Infant mortality	IM	$\log(x)$
Gross domestic product per capita	GDPpc	$\log(x)$
Human development index	HDI	$(\max(x) - x)^{1/2}$
Number of immigrants minus emigrants	I-E	$(\max(x) - x)^{1/2}$
Percentage of refugees	RE	$\log(x)$
Average blood cholesterol level	CH	$(\max(x) - x)^{1/2}$
Prevalence of obesity	OB	$(\max(x) - x)^{1/2}$
Prevalence and severity of chronic diseases	CD	$x^{1/3}$
Prevalence of insufficient physical activity	IN	$\log(\max(x) - x)$
BCG immunization coverage	BCG	$(\max(x) - x)^{1/2}$
Epidemic onset	ON	$\log(x)$
Long-term PM2.5 pollution	PL	$\log(x)$
Precipitation	PR	$\log(x)$
Wind speed	WS	$x^{1/3}$
Basic reproduction number of SARS-CoV-2	$R_0$	$\log(x)$

The dimensionality of the transformed data was later reduced and the data decorrelated through PCA (Jolliffe, 2002). PCA was done separately for demographic and meteorological variables to allow for a more straightforward interpretation of the obtained PCs. Since different variables are expressed in different units and correspond to diverse scales, each variable in the data set was standardized (the mean subtracted and divided by the standard deviation) before PCA. For both data sets, we retained as many PCs (starting from the most dominant one) as needed to (cumulatively) explain >85% of the data variance. It was inspected that PCs reasonably follow a normal distribution (as expected, based on the transformation of the original variables). Few remaining outliers were then substituted by medians. For easier interpretation of PCs and their contribution to  $R_0$ , each PC was oriented in the same direction as the variable with which it has a maximal magnitude of Pearson correlation (i.e., when needed, the sign of the PC was flipped to render the positive sign of this correlation).

### 2.3. Data Analysis

*Custom regression analysis* was done by applying multiple linear regression (PC regression) to only demographic PCs (Hastie et al., 2009). Only linear terms were included in the regression to allow straightforward interpretation, that is, the selection of PCs that significantly affect  $R_0$ . Significant PCs were selected as those appearing in the regression with  $P < 0.05$ , where the significance in the regression was estimated in the standard way (through F-statistics) (Alexopoulos, 2010). The same regression was then repeated with only meteorological PCs, and those significant in explaining  $R_0$  were retained. Finally, multiple linear regression was performed with all retained demographic and meteorological PCs. The significant PCs from this last step were recognized as PCs relevant for the  $R_0$  explanation. Before regression, each PC was standardized so that coefficients obtained in the regression provided a measure of the variable importance in explaining  $R_0$ . For both the custom analysis and stepwise regression, OLS (Ordinary Least Squares) were used as the regression metrics.

*Stepwise regression* was used to select PCs that significantly affect  $R_0$ . In Stepwise regression, as well as in LASSO and Elastic net described below, all PCs (demographic and meteorological) were included in the regression. Briefly, starting from a constant model, at each step a term is added to the model if its significance (calculated with F-statistics) meets the condition  $P < 0.05$  (Pope & Webster, 1972). Only linear terms are added to the model (i.e., interaction and quadratic terms are not considered) to allow for straightforward interpretation of the PCs which significantly affect  $R_0$ . All PCs are standardized before regression so that contributions of the terms (PCs) in the model can be assessed by the magnitude of the regression coefficient.

*Lasso regression* (Hastie et al., 2009; Tibshirani, 1996) was used to implement L1 regularization. As needed with the Lasso regularization, all PCs were standardized before regression, which allowed direct comparison of the coefficients obtained by the regression. The value  $\lambda$  in Lasso was treated as the hyperparameter, that is,  $\lambda_{min}$  value was determined through cross-validation, so that MSE (Mean Squared Error) on the testing set was minimal. A total of 100  $\lambda$  values were put on the grid, corresponding to the geometric sequence, where the largest value produces all zero terms. Note that larger  $\lambda$  corresponds to a sparser model, that is, a smaller number of nonzero components in the regression, while the small  $\lambda$  limit corresponds to OLS regression. To obtain the maximally sparse model,  $\lambda_{1SE} = \lambda_{min} + 1SE$ , where 1SE corresponds to the standard error of MSE obtained by cross-validation, was used. 1,000 cross-validations were performed—in each repetition, 20% of the data were randomly selected for the testing set, with the remainder used for training. All nonzero terms, and the corresponding coefficients obtained through Lasso, were reported.

*Elastic net regression* was used to implement a combination of L1 and L2 regularization (Zou & Hastie, 2005). Analogously to our Lasso analysis, that is, as needed due to regularization, all PCs were standardized. In the regression, both  $\alpha$  and  $\lambda$  were treated as hyperparameters, that is, their optimal values were found by cross-validation. Cross-validation was repeated 1,000 times. In each repetition, testing and training sets were formed in the same way as for Lasso.  $\alpha$  and  $\lambda$  values were put on a grid consisting of 100  $\alpha$  and 100  $\lambda$  values.  $\alpha$  values on the grid were chosen uniformly in the range (0,1)— $\alpha$  approaching zero corresponds to Ridge (L2) regression, and 1 corresponds to Lasso regression. For each  $\alpha$  value,  $\lambda$  values were chosen as described for the Lasso regression. For each repetition of cross-validation, a combination of  $\alpha$  and  $\lambda$  that leads to the minimal MSE was chosen.  $\alpha$  and  $\lambda$  values in  $(\alpha, \lambda)$  pairs from each cross-validation run were then standardized so that  $\alpha$  and  $\lambda$  values are on the same scale and centered to the origin of the  $\alpha$ - $\lambda$  plane.  $(\alpha_{min}, \lambda_{min})$  was then chosen as the  $(\alpha, \lambda)$  point closest to the origin. With this  $(\alpha_{min}, \lambda_{min})$  value, the model was then retrained on the entire data set. All nonzero terms and the corresponding regression coefficients were reported.

### 3. Results

PCA was first applied to the data set consisting of 18 demographic and health factors for 118 countries. Cumulative data variance that is explained jointly by the first  $n$  PCs is shown in Figure 1a (with  $n$  represented on the  $x$ -axis). In particular, Figure 1a shows the first PC alone already accounts for 45% of the variance, while the first 9 PCs (PC1–PC9), which we retain in further analysis, explain more than 85% (precisely, 89%).

To obtain a basic interpretation of these nine PCs, we related each PC with the original (transformed) variable it is most correlated with. The corresponding associations—with the values of correlations coefficients presented on the  $y$ -axis—are shown in Figure 1b (however, one should have in mind that some PCs are highly correlated with more than one original variable, as we discuss in more detail below). Among all principal components, the PC1 and the PC5 have the highest correlation coefficients (close to 1) with individual demographic factors—the HDI and the BCG immunization coverage, respectively. Moderately high correlation coefficients ( $\sim 0.75$ ) characterize the relations between the PC2 and the prevalence of smokers, and the PC3 and the percentage of refugees, while the coefficient values of  $\sim 0.5$  were obtained for the correlations of the PC4, the PC6, the PC7, the PC8, and the PC9 with, respectively, the prevalence of obesity, the prevalence of insufficient physical activity, the amount of the built-up area per person, the percentage of refugees, and the epidemic onset.

In particular, the first PC, accounting alone for the largest portion of the variance in the demographic data, is almost perfectly correlated with the Human Development Index (Figure 1c). On the other hand, the HDI variable itself strongly correlates with several other demographic variables (Figure 1d), most prominently



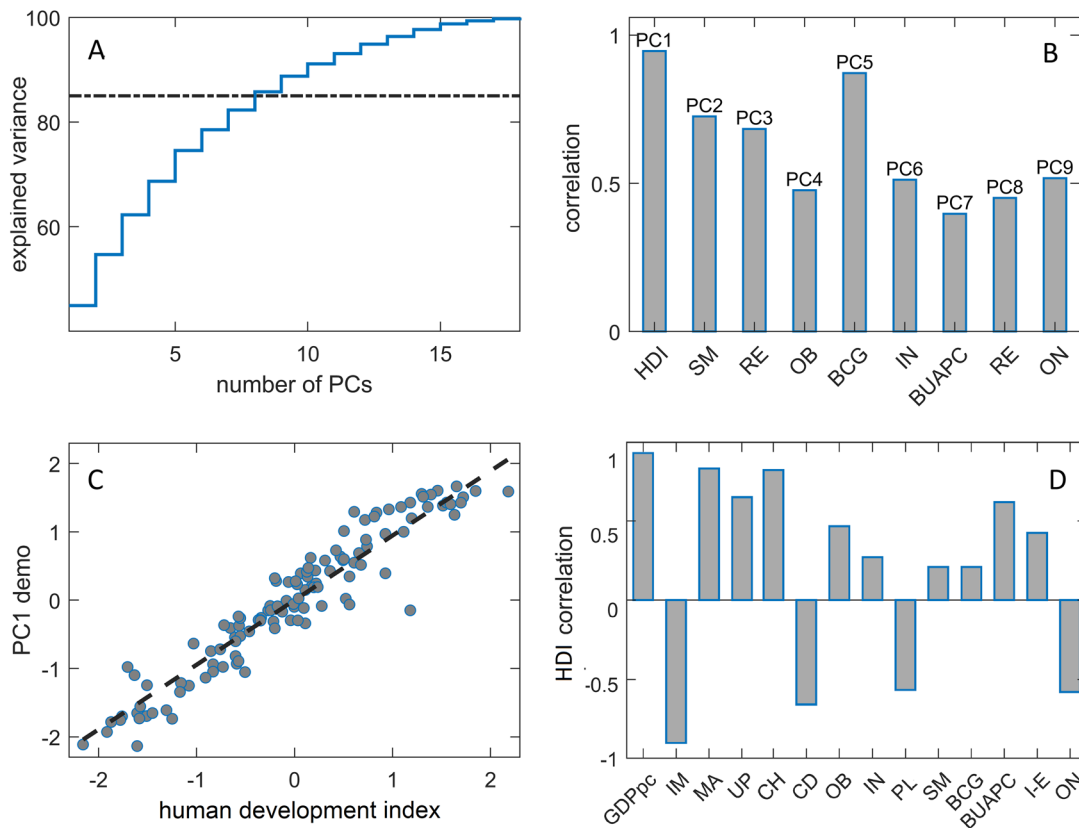


**Figure 1.** Principal component analysis for demographic data. (a) Cumulative explained variance. (b) Variables best correlated with demographic principal components (PCs). The labels above and below each bar present, respectively, the demographic PC and the variable with which that PC has the highest correlation. (c) Scatter plot PC1 versus HDI. (d) Correlations of selected demographic variables with HDI. HDI—Human development index, SM—prevalence of smoking, RE—the percentage of refugees, OB—prevalence of obesity, BCG—BCG immunization coverage, IN—prevalence of insufficient physical activity, BUAPC—Built-up area per capita, ON—epidemic onset, GDPpc—GDP per capita, IM—infant mortality, MA—median age, UP—urban population, CH—average blood cholesterol level, CD—prevalence of chronic diseases, PL—PM2.5 pollution, I-E—number of immigrants minus emigrants.

with per capita GDP, infant mortality, and cholesterol levels. As elaborated in the Discussion section, such extremely high correlations will eventually preclude us from differentiating between the separate effects of each of these variables on  $R_0$ . On the other hand, the prevalence of obesity, the built-up area per person, and the epidemic onset are significantly correlated with the HDI (Figure 1d), and thereby the PC1 (Figure 1c), but they are markedly featured also in separate principal components (Figure 1b), namely—the PCs 4, 7, and 9. This will help us to infer whether their specific (additional) contributions to the variance in the data (apart from that along the PC1) impact the virus transmissibility.

Meteorological factors for 118 countries were reduced similarly as for the demographic data set. PCA generated six uncorrelated, orthogonal principal components. Thereby, the first PC alone explains 62% of the variance, while the first three PCs (PC1–PC3) capture 95%, which is significantly above the targeted 85% of the total variance (Figure 2a). Pairwise correlations showed that the retained three PCs have the highest correlations with the temperature, the wind speed, and the air pressure, respectively (Figure 2b), where the correlation of PC1 with the temperature is close to 1 (Figures 2b and 2c). There are also notable correlations of the temperature with humidity, the levels of UV radiation, and precipitation (Figure 2d). Therefore, PC1 presents seasonality, that is, a set of mutually correlated meteorological variables that can be related to yearly weather changes. PCA, thus, effectively separated the impacts of seasonality (PC1), the wind speed (through the PC2), and the air pressure (through the PC3). The variables determining the PC1 are also correlated with the HDI. These inter-data set correlations are not resolved at this level by our PCA and represent the trade-off that allows interpreting the PCs more easily within each of the two smaller, thematic groups of factors.

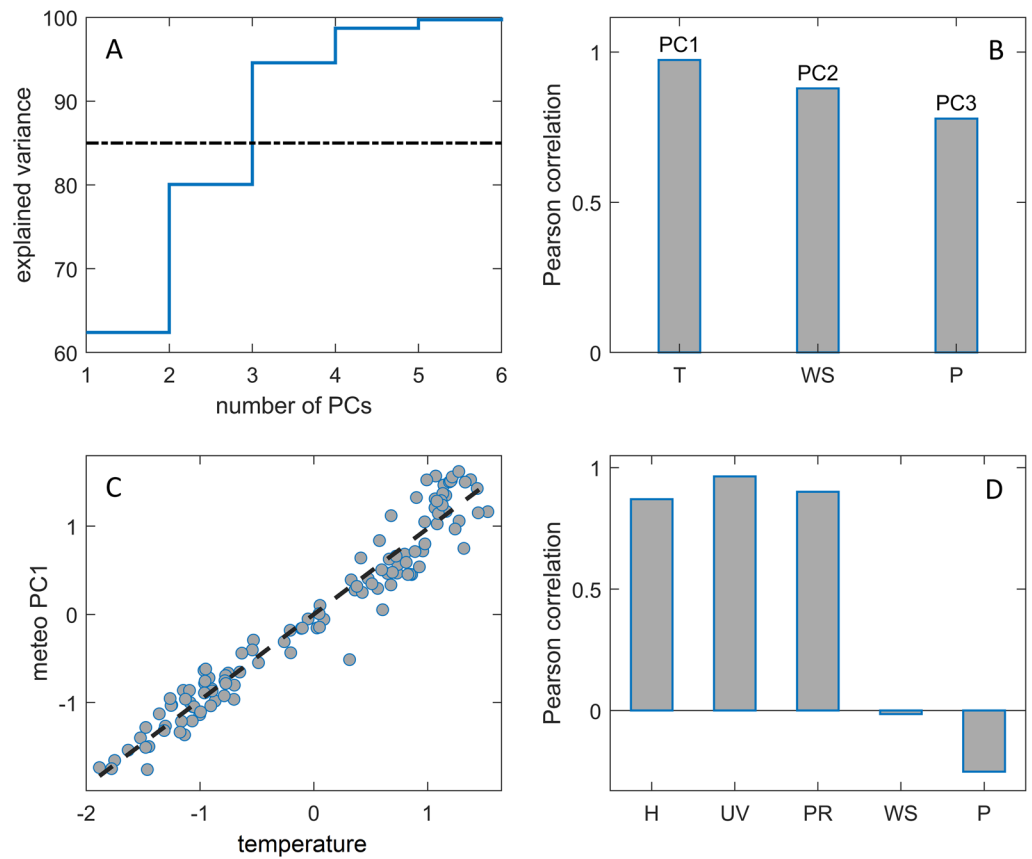


**Figure 2.** Principal component analysis for meteorological data. (a) Cumulative explained variance. (b) Variables best correlated with meteorological principal components (PCs). (c) Scatter plot meteo PC1 versus temperature. (d) Correlation of meteorological variables with temperature. T—temperature, WS—wind speed, P—air pressure, H—specific humidity, UV—ultra-violet radiation index, PR—precipitation.

After PCA, we applied the linear regression analysis using four different methods, as explained in Methods. The first, “custom” method included the additional step of “preselecting,” that is, further narrowing down the number of PCs that will enter the final regression analysis. The multiple linear regression, applied on the group of nine demographic PCs, selected first, fourth, seventh, and ninth component as the most relevant predictors of  $R_0$  (the remaining 5 PCs appeared in the linear regression with  $p$  values above 0.05 threshold and were consequently excluded from the further analysis, see Table 2. Analogously, the “preselection” of meteorological PCs singled out the first component as the only statistically relevant predictor of  $R_0$  from this group (see Table 3). The multiple linear regression was then applied on these five selected PCs (four demographic and one meteorological) and yielded a regression model with the corresponding linear coefficients represented in Figure 3a (see also Table 4). Meteo PC1 component does not appear in the results of the custom method due to the lack of statistical significance ( $p > 0.305$ ) in the final regression. Thus, according to our custom regression methodology, weather parameters do not significantly influence  $R_0$ .  $R_0$  in this model is, therefore, determined by a combination of demographic PC1, PC4, PC7, and PC9, where coefficients multiplying PC1 and PC4 are positive, while for PC7 and PC9 are negative. As can be inferred from the values represented in Figure 3a, the demographic PC1 has the most dominant influence on  $R_0$ —a robustly obtained result throughout all four methods (see below).

**Table 2**  
Multiple Linear Regression for Demographic Principal Components

Principal component	Coefficient	Standard error	$P$ -value
Demo PC1	0.15	0.03	$10^{-6}$
Demo PC2	0.02	0.03	0.4
Demo PC3	−0.00	0.03	0.97
Demo PC4	0.06	0.03	0.03
Demo PC5	−0.05	0.03	0.08
Demo PC6	0.02	0.03	0.6
Demo PC7	−0.12	0.03	$10^{-4}$
Demo PC8	−0.00	0.03	0.9
Demo PC9	−0.10	0.03	$4 \times 10^{-4}$

Note. Root Mean Squared Error = 0.31, Adjusted R-Squared = 0.33, F-statistics versus constant model = 7,  $P$ -value  $\sim 2 \cdot 10^{-8}$ .

After PCA, we applied the linear regression analysis using four different methods, as explained in Methods. The first, “custom” method included the additional step of “preselecting,” that is, further narrowing down the number of PCs that will enter the final regression analysis. The multiple linear regression, applied on the group of nine demographic PCs, selected first, fourth, seventh, and ninth component as the most relevant predictors of  $R_0$  (the remaining 5 PCs appeared in the linear regression with  $p$  values above 0.05 threshold and were consequently excluded from the further analysis, see Table 2. Analogously, the “preselection” of meteorological PCs singled out the first component as the only statistically relevant predictor of  $R_0$  from this group (see Table 3). The multiple linear regression was then applied on these five selected PCs (four demographic and one meteorological) and yielded a regression model with the corresponding linear coefficients represented in Figure 3a (see also Table 4). Meteo PC1 component does not appear in the results of the custom method due to the lack of statistical significance ( $p > 0.305$ ) in the final regression. Thus, according to our custom regression methodology, weather parameters do not significantly influence  $R_0$ .  $R_0$  in this model is, therefore, determined by a combination of demographic PC1, PC4, PC7, and PC9, where coefficients multiplying PC1 and PC4 are positive, while for PC7 and PC9 are negative. As can be inferred from the values represented in Figure 3a, the demographic PC1 has the most dominant influence on  $R_0$ —a robustly obtained result throughout all four methods (see below).

**Table 3**  
*Multiple Linear Regression for Meteorological Principal Components*

Principal component	Coefficient	Standard error	P-value
Meteo PC1	-0.14	0.03	$4 \times 10^{-5}$
Meteo PC2	0.00	0.03	0.99
Meteo PC3	-0.04	0.03	0.3

Note. Root Mean Squared Error = 0.35, Adjusted R-Squared = 0.12, F-statistics versus constant model = 6, P-value  $\sim 4 \cdot 10^{-4}$ .

We have already related each of these four PCs with the dominantly correlated variable (Figure 1b), but a more detailed interpretation of the results is obtained if all significant correlations (not just the dominant one) are taken into account. In addition to the very high correlation with HDI, demographic PC1 is also highly positively correlated with GDP, cholesterol levels, median age, and percentage of the urban population, while it is highly negatively correlated with infant mortality and the prevalence of chronic diseases (Figure 4a). Such strong correlations with HDI, GDP, IM, MA, and UP show that this component indeed expresses an overall, both social and financial, the prosperity of the country (which seemingly also goes hand in hand with high average cholesterol levels and low

prevalence of COVID-19 relevant chronic diseases). Similarly, by considering the correlations of demo PC4 with all demographic variables, we see that this component is significantly positively correlated not only with obesity but also with smoking, physical inactivity, and air pollution (Figure 4b)—in other words, with major indicators of an unhealthy lifestyle and living conditions. Apart from its correlation with the BUAPC parameter, the component demo PC7 is also significantly positively correlated with net migration (Figure 4c). In the case of the demo PC9 component, its only significant correlation is with the onset variable. Results of the custom method can, therefore, be summarized as follows: the country's prosperity, as well

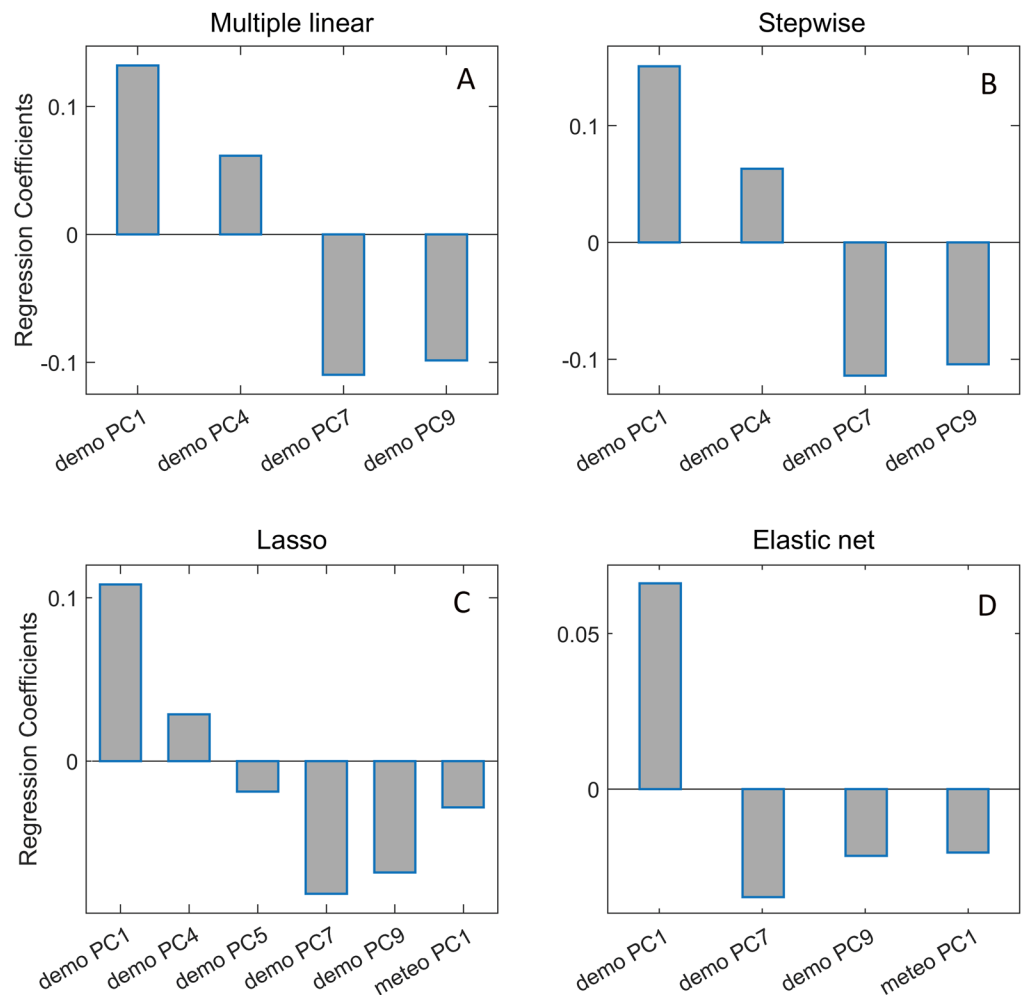


**Figure 3.** Results of: (a) multiple linear regression (“custom”) method, (b) Stepwise regression, (c) Lasso regression, and (d) Elastic net regression. Bar charts represent the values of regression coefficients for each of the PCs selected by the method.

**Table 4**  
Multiple Linear Regression for Relevant Principal Components

Principal component	Coefficient	Standard error	P-value
Demo PC1	0.13	0.03	$2 \times 10^{-4}$
Demo PC4	0.06	0.03	0.03
Demo PC7	-0.11	0.03	$2 \times 10^{-4}$
Demo PC9	-0.10	0.03	$9 \times 10^{-4}$
Meteo PC1	-0.04	0.03	0.3

Note. Root Mean Squared Error = 0.31, Adjusted R-Squared = 0.34, F-statistics versus constant model = 13, P-value  $\sim 10^{-9}$ .

as unhealthy living conditions and lifestyle, tend to increase the value of  $R_0$ , while the larger built-up area per person and the later epidemic outbreak tend to slow the spread of the disease. Also, the results seem to indicate—via demo PC7 component—a surprising diminishing effect of the net migration on the rate of epidemic progress (though the sign of this variable may not be easy to interpret, as the net migration is a difference of two quantities).

Equivalently to Figures 3a–3d represent the results of, respectively, Stepwise, Lasso, and Elastic net regression. Results (and the corresponding graph) of the Stepwise method almost coincide with the results of our custom method—in spite that in the Stepwise regression (as well as in Lasso and Elastic net methods), there is no intermediate “preselection” step.

Lasso results, shown in Figure 3c, find two additional PCs as relevant: demo PC5 and meteo PC1 (in addition to demo PC1, demo PC4, demo PC7, and demo PC9). The component demo PC5, appearing in Lasso

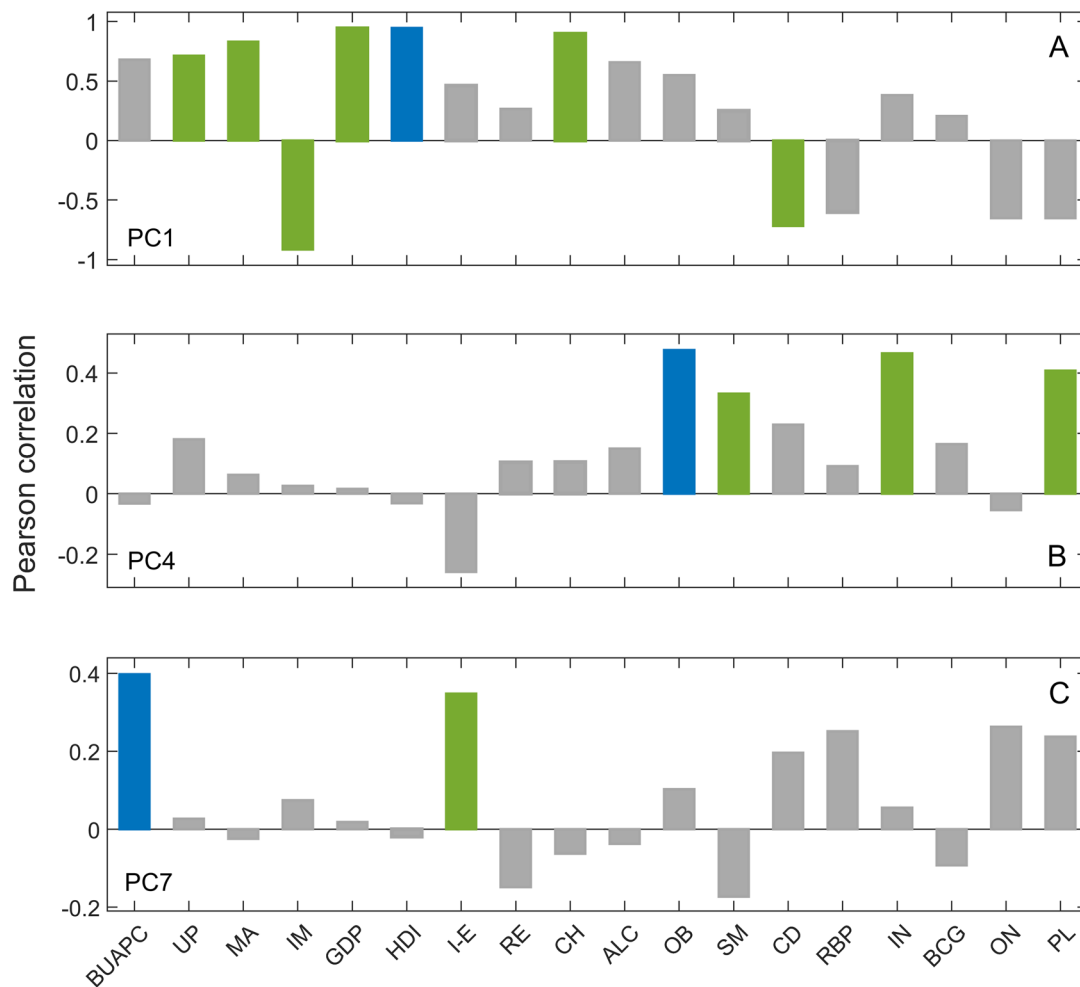


**Figure 4.** Pearson correlation coefficients between principal components and demographic variables for (a) demo PC1, (b) demo PC4, and (c) demo PC7. BUAPC—built-up area per capita, UP—urban population, MA—median age, IM—infant mortality, GDP—gross domestic product per capita, HDI—human development index, I-E—number of immigrants minus emigrants, RE—percentage of refugees, CH—average blood cholesterol level, ALC—alcohol consumption per capita, OB—prevalence of obesity, SM—prevalence of smoking, CD—prevalence and severity chronic diseases, RBP—prevalence of raised blood pressure, IN—prevalence of insufficient physical activity, BCG—BCG immunization coverage, ON—epidemic onset, and PL—long-term average PM2.5 pollution.

results with a small negative coefficient, is significantly correlated only with the BCG variable, hinting at possible beneficial effects of BCG vaccination. Meteorological principal component meteo PC1 reflects seasonality (see above). In addition to supporting the conclusions of the custom and stepwise methods, the Lasso method thus also implicates a significance of seasonality changes and (to some extent) BCG vaccination in reducing the rate of SARS-CoV2 spread.

The results of the Elastic net method, shown in Figure 3d, are again a bit more restrictive. While further bolstering our confidence in the importance of demo PC1, demo PC7, and demo PC9, these results also reinforce that the seasonal weather variables influence the COVID-19 epidemic (in agreement with the Lasso method) but, for the first time, we do not find an indication of the relevance of the unhealthy lifestyle and living conditions—as revealed by the absence of demo PC4 component in Figure 3d.

Finally, as much as the PCs appearing in Figure 3 are important, the absence of the remaining PCs in the results can be of comparative significance for some of our conclusions. For example, we note that PCs highly correlated with the urban population, alcohol consumption, and chronic diseases do not show up as relevant in any of the methods used. While it is true that these variables are moderately correlated with demo PC1, absence in the results of additional PCs tied with these variables supports the view that these variables are not directly influencing  $R_0$  value, but only via indirect relation to the country's prosperity.

#### 4. Discussion

Our goal was to identify the most predictive factors influencing the risk of the SARS-CoV-2 virus spreading in a population in the absence of any epidemic mitigation measures. Since many potentially relevant factors strongly correlate with each other, we divided them into two groups—meteorological and sociodemographic—and applied the PCA to the variables in each group. In this way, we were able to decorrelate variables within each group while still retaining intuitive interpretation for the new variables (demographic and meteorological PCs) used in further analysis. While a similar approach was proposed in Notari and Torrieri (2020); Notari (2021), dimensionality reduction and predictor decorrelation through PCA were, in our study, combined with different variable selection and regularization techniques—namely, Lasso and Elastic net—to select PCs that are most predictive of  $R_0$  for COVID-19 epidemics. Examining correlations of these PCs with the original variables allowed pinpointing the main drivers of COVID-19 transmissibility. Therefore, this approach, which is reminiscent of the analysis of complex data in systems biology and bioinformatics, to our knowledge represents the most thorough effort to disentangle true COVID-19-related effects from indirect correlations.

Three principal components are robustly selected as the most important predictors by all the methods. Of these, the prosperity of the country has the most significant influence on  $R_0$ : the spread of the epidemic is faster in economically more developed countries. Specifically, this is the most dominant PC from the demographic group of variables, which is by far most important in explaining  $R_0$ , and very strongly correlated with HDI (Pearson's correlation coefficient  $r = 0.95$ ) and GDP ( $r = 0.94$ )—therefore, effectively reflecting prosperity and wealth. The second PC is dominantly related to the BUAPC, and the third with the epidemic onset, where the increase of these reduces the infection spread. We also robustly obtained (by three out of four methods) that unhealthy living conditions/lifestyle is another important factor that exacerbates the epidemic—this PC is dominantly (and consistently positively) correlated with obesity, physical inactivity, smoking, and air pollution. The group of four weather conditions, represented by seasonality, was selected by two independent methods. One is the Elastic net, which is well adapted for selecting among correlated variables (Hastie et al., 2009; Zou & Hastie, 2005)—note that correlations between meteorological and demographic PCs were not abolished by our approach. The PC dominantly correlated with BCG immunization appears only in Lasso regression. In favor of our results, we notice that the analysis of 13 selected variables conducted by Notari and Torrieri (2020) pointed to several similar factors as significant, such as the epidemic starting date, temperature, and the factors characteristic of general poor health and, thus, lower resistance to the virus infection (i.e., smoking, obesity and lung cancer as related to the chronic diseases).

HDI (alternatively, GDPpc) shows the highest correlation with the first demographic PC, which singles out this variable as the main index quantifying the virus transmissibility risk. Higher HDI leads to a higher rate of social contacts and more intense population mixing (especially over long distances), as high HDI is



strongly related to high GDPpc implying intensive economic activity, trade, and transportation, including large-distance flights (Allel et al., 2020; Gangemi et al., 2020). While it is true that the intensity of social binding might often be even higher in low-income societies, such interpersonal relations are prevalently of spatially local character and may less contribute to a large scale epidemic than the intense business activity (trade, transport, tourism, and education), which connects and mixes people over large distances/areas. Thus, in our view, much higher contact frequency (especially of contacts that mix individuals over large distances) in societies with higher HDI is likely the main cause behind the dominant role of the first demographic PC in explaining  $R_0$ .

There is, however, no reason to expect this relation of HDI with  $R_0$  to uniformly hold across the entire range of HDI (prosperity PC) values: indeed, analysis performed in Notari and Torrieri, 2020 shows that GDP (strongly correlated to HDI and our prosperity PC) ceases to be a significant predictor of COVID-19 transmission rate once the low-income countries are excluded. One possible interpretation is that above a certain threshold of HDI, there is a focus on fully developed modern societies. The impact of further increasing country prosperity on the frequency of social contacts then becomes overshadowed by other factors. This was obtained in our recent study of the rate of COVID-19 transmission in USA states (Milicevic et al., 2021), where different factors, in the first place pollution, become dominant in that data set.

This explanation of the impact of prosperity PC is still a hypothesis, which should be tested by further investigating the relation of HDI to some more direct measures of frequency of actual physical contact between individuals (unfortunately, such measures are not readily available) (Bontempi et al., 2020). We think that the obtained strong association of the PC closely related with GDP/HDI with  $R_0$  is an important result (allowing a better understanding of epidemic risks), regardless of whether our interpretation (entirely) captures the true underlying causes of this connection.

An advantage of our approach is that it is based on the analysis of  $R_0$  rather than other measures used as transmissibility proxies. The most commonly used measure, confirmed case counts, strongly depends on the number of performed tests, which is generally much higher in high-GDPpc countries, so the analysis would become strongly influenced by testing policies. For example, in Allel et al. (2020), the importance of HDI for predicting cumulative case counts was noted. However, this perceived effect may be due to the lack of testing in lower-income countries, as already noted in Notari (2021), rather than genuine HDI influence. Our results are, on the other hand, insensitive to the testing capacity differences. Namely, since our  $R_0$  estimation procedure relies on the scale-invariant slope of the case growth curve logarithm (in the distinct early exponential phase) (Djordjevic et al., 2021), it does not depend on the percentage of the infected individuals that get tested/diagnosed (i.e., multiplying daily case counts by arbitrary number will not affect  $R_0$ ). As long as this percentage is roughly constant (i.e., testing is performed consistently) during the (relatively short) examined period, our  $R_0$  estimate remains valid irrespectively of whether the country must reserve testing kits only for symptomatic cases, or the country has the means to (preventively) test asymptomatic individuals. On the other hand, if testing policies/criteria happen to irregularly change during the observed period (e.g., due to a sudden lack of testing resources), this would be accounted for (i.e., filtered out) as described in Methods. Therefore, our analysis indeed strongly suggests that HDI/GDPpc are the main/genuine predictors of COVID-19 spread in the population.

Many correlations previously reported between SARS-CoV-2 transmissibility and various weather, sociodemographic, and health factors (see e.g., Li et al., 2020; Salom et al., 2021) may be captured by HDI. From our results, one can note that several demographic factors significantly correlate with both HDI/GDPpc and the first demographic PC, but are not noticeably related with other demographic PCs (4, 5, 7, and 9) that significantly contribute to  $R_0$ . These demographic factors can be further divided into two groups using the correlation of BUAPC with HDI as the reference. The percentage of the urban population, the prevalence of alcohol consumption, and chronic diseases, which have similar (just somewhat higher) correlations with HDI compared to BUAPC, comprise the first group. Their absence from the independent PCs significantly related with  $R_0$  (in contrast to BUAPC that prominently appears in the demographic PC7), indicates that they do not have independent effects on  $R_0$ . Consequently, their significant correlation with  $R_0$  (Salom et al., 2021) is likely due to their generic correlation with HDI, rather than a consequence of the independent effect that they exhibit on  $R_0$ . This result is especially interesting for the percentage of the urban population, whose relation with  $R_0$  is sometimes taken for granted (Carozzi, 2020). It also explains

the previously obtained negative correlation of the prevalence of chronic diseases with  $R_0$ , where one might expect the opposite, as it is generally known that people with chronic diseases are seriously affected by COVID-19 (Zheng et al., 2020). We can now claim that this result is due to a generically lower incidence of chronic diseases in more developed countries (i.e., due to their significant negative correlation with HDI) rather than a direct effect on  $R_0$ .

A significant positive correlation with the first demographic PC is also exhibited by the net economic migration (the difference between immigrants and emigrants), population median age, infant mortality, and the average blood cholesterol level. However, their correlation with HDI is very high (in distinction to the three factors mentioned before), that is, visibly higher compared to the correlation of BUAPC with HDI. So, even though they do not appear in demographic PCs that significantly contribute to  $R_0$  other than PC1, we cannot make any reliable conclusion about their direct effect on  $R_0$  based on our analysis. Therefore, it is relevant to discuss evidence from other sources, that is, possible mechanisms for distinguishing their direct influence on  $R_0$ . Regarding infant mortality, a mechanism of its direct contribution to  $R_0$  is hard to imagine, so its involvement in PC1, and high negative correlation with  $R_0$ , is almost certainly an indirect consequence of this variable being a proxy of HDI (Ruiz et al., 2015). On the other hand, the median age and the blood cholesterol level are real contenders for direct  $R_0$  modifiers, as mechanisms for their contribution to COVID-19 transmissibility have been proposed. Aging is generally associated with the weakening of the immune response to infectious diseases making the elderly more susceptible to the viruses like the SARS-CoV-2 (Pawelec & Larbi, 2008). Additionally, many of them due to some chronic diseases take ACE inhibitors and angiotensin-receptor blockers, which cause an increased expression of ACE2 serving as a receptor for the SARS-CoV-2 virus entry (Shahid et al., 2020). Their residing in care homes, which is particularly common in high-income countries, also well suits the spreading of the infection (Kapitsinis, 2020). Similarly, high cholesterol levels can increase susceptibility to the infection by SARS-CoV-2 through systemic adverse effects on the immune and inflammatory responses and through direct implication in the virus life cycle (especially at the level of its endocytosis). To that end, statins, blocking cholesterol synthesis, were proposed for usage in COVID-19 treatment, which is supported by studies showing that previous statin usage is associated with a milder pneumonia outcome in the case of several other viral infections (Frost et al., 2007; Schmidt et al., 2020).

Other demographic PCs (4, 5, 7, and 9) that are selected to have a significant influence on  $R_0$  are by construction independent (decorrelated) from PC1. Variables associated with these PCs can be interpreted as effects on  $R_0$  independent from those related to PC1. These variables then importantly identify corrections to the main effect of HDI/GDPpc. Specifically, these are available to an individual in an indoor area and the net migration (demographic PC7), the delay in the epidemic onset, which is associated with more awareness of the virus threat (demographic PC9), the prevalence of unhealthy lifestyle and environment (demographic PC4), and the weather seasonality (meteorological PC1). The slower spread of the virus with a larger built-up area per capita, as an independent and significant  $R_0$  predictor, is an interesting and new result, though intuitively plausible. It can be understood as having a less crowded indoor space (where the virus transmission dominantly happens) so that people are less exposed to each other and the virus. For example, on the Diamond Princess cruise ship, both the population density and  $R_0$  were estimated as four times greater than those in Wuhan (Rocklöv & Sjödin, 2020). On the other hand, a correlation of the virus transmissibility with the large territory population density is weakly established in the literature, whereby it seems that one should rather seek a correlation with a local population density, directly determining the number of contacts that an individual can make (Diao et al., 2021; Garland et al., 2020).

A positive contribution to the transmissibility is also made by the principal component strongly correlated with the onset variable, representing the number of days from February 15th to the epidemic's start in a particular country. The importance of the delay in the epidemic onset may be due to the psychological effect of hearing the news about the spread of COVID-19 in other countries (Khajanchi et al., 2020). Namely, the longer the epidemic was growing outside of a particular country, the larger impact this had on its people to change their usual behavior to prevent the infection, which could slow down the virus transmission even before the introduction of the official intervention measures (Salom et al., 2021).

Another distinguished principal component appears to encompass multiple indicators of an unhealthy lifestyle and environment—specifically, the prevalence of obesity, physical inactivity, and smoking, together

with the level of air pollution. We obtained that all these factors promote virus transmission. It is well established that they can impair immune function and adversely affect different organ systems. Furthermore, their association with mechanisms specifically facilitating the infection by the SARS-CoV-2 virus has been proposed (Domingo & Rovira, 2020; Haddad et al., 2021; Heidari-Beni & Kelishadi, 2020). Notably, the association of air pollution with COVID-19 transmission has been shown in several studies (Bashir et al., 2020; Coccia, 2020b; Milicevic et al., 2021). Two of the remaining relevant PCs are strongly determined by temperature (and/or three other highly related weather factors) and the prevalence of BCG vaccinated children, respectively. Although not selected by all the methods, the weather component seems important as it was chosen by the Elastic net algorithm (in addition to Lasso), which is specifically designed to deal with (highly) correlated variables, and yet it did not exclude this PC despite its correlation with the first demographic PC. Moreover, a decrease of the transmissibility with the temperature increase appears as a robust result in COVID-19 literature (Haque & Rahman, 2020; Rosario et al., 2020; Sarkodie & Owusu, 2020), although conflicting conclusions are also present (Islam et al., 2021; Srivastava, 2021; Xie & Zhu, 2020). Higher temperatures may shorten the period of virus viability in aerosols, enhance the immune system functioning, and/or impact the time that people spend together in poorly ventilated indoor spaces (Notari, 2021). Since temperature is highly positively correlated with the intensity of UV radiation, humidity, and the level of precipitation, we cannot exclude the possibility that some of these other factors are in a significant causal relationship with virus transmissibility. Importantly, some experimental findings support the inactivating effects of high temperature, humidity, and UV radiation on SARS-CoV-2 and related viruses (Casanova et al., 2010; Chan et al., 2011; Heilingloh et al., 2020; Sagripanti & Lytle, 2020; van Doremalen et al., 2020). Anyhow, our results suggest the dependence of virus transmissibility on seasonal weather variations related to our meteorological PC1 component. On the other hand, while some authors suggest the importance of wind speed in virus dissemination (Coccia, 2020a, 2020b; Islam et al., 2021; Sarkodie & Owusu, 2020), our study could not confirm this connection—as reflected by the absence of the wind-related principal component PC2 in our results. This might be the consequence of a strong interplay between wind speed and pollution effects (Coccia, 2021b) that our study is not suited to detect. The last demographic principal component occurred as important only in Lasso regression. It, however, closely follows the extent of BCG vaccination, which is known to provide some protection against various respiratory tract infections through the induction of the trained immunity (O'Neill & Netea, 2020), so BCG immunization may influence the SARS-CoV-2 spread, although, according to our results, to a lesser extent than the other discussed factors.

Our study is also an example of how assessing the effect of one factor, while controlling for the presence of other relevant variables can change the obtained conclusions. We will illustrate this with four examples, where we obtained qualitatively different conclusions, compared to single-variable correlation analysis (Salom et al., 2021): BUAPC, net migration, air pollution, and raised blood pressure. BUAPC showed an absence of a significant correlation with  $R_0$  (Salom et al., 2021), which is a consequence of canceling the two effects. The first is its direct effect on  $R_0$  (exhibited through demographic PC7), which tends to slow the spread of COVID-19 in a population. The second is collinearity with PC1, which reflects a generic correlation of BUAPC with GDPpc, caused by more construction (higher built-up area) per capita with the increase in GDPpc. Our combination of PC and regression analysis revealed this nontrivial conclusion, which cannot (even qualitatively) be obtained from the pairwise correlation analysis.

Similar reasoning, though perhaps harder to understand intuitively, applies to net migration. Net migration is also significantly positively correlated with HDI (and consequently also with PC1), reflecting a generic tendency of immigrants to flow to countries with higher GDPpc. The direct effect of net migration (exhibited through PC7) is harder to intuitively understand, as I-E negatively contributes to  $R_0$ , so that faster spread (at least in the initial phase of the epidemic) appears to be associated with a higher number of emigrants. As these are economic migrations (to be distinguished from the movement of refugees), possibly the part of the emigrants returned to their countries with the pandemic's start. The significant effect of net migration on  $R_0$  (inferred through our analysis) is again highly nontrivial and in the opposite direction from the positive pairwise correlation of  $R_0$  with I-E. Refugees (i.e., percentage of refugee population by country) exhibit high correlations only with PC3 and PC8, where neither significantly contributes to  $R_0$ . There is also no significant pairwise correlation of refugees with  $R_0$ , which robustly shows that this variable does not affect transmissibility.

Pollution negatively contributes to demographic PC1 (with the corresponding negative correlation with HDI) and positively to demographic PC4. The pairwise correlation between the pollution and  $R_0$  is negative ( $-0.31$ ), which is counterintuitive, as it is generally expected that higher pollution should increase COVID-19 transmissibility. This is, however, an artifact of negative correlation between pollution and HDI, while its genuine (direct) effect on  $R_0$  is reflected through PC4. Our analysis, therefore, revealed the direct effect of long-term air pollution on transmissibility, which is consistent with previously published observations that it can damage the respiratory system and reduce resistance to infections (Domingo & Rovira, 2020; Fattorini & Regoli, 2020) but opposite to naive pairwise correlation analysis.

Finally, raised blood pressure also shows a statistically significant (counterintuitively negative) correlation with  $R_0$ . However, in addition to PC1, raised blood pressure shows a notable correlation only with PC2, which does not significantly affect  $R_0$ . This indicates that the negative correlation of this variable with  $R_0$  is a consequence of its generically negative correlation with HDI, instead of a direct effect on COVID-19 transmissibility.

## 5. Conclusion and Outlook

Numerous studies tried to assess the correlations of different factors with the SARS-CoV-2 virus transmissibility (Li et al., 2020; Notari & Torrieri, 2020; Salom et al., 2021), but the next step should be predicting the environmental risk of the high spreadability in a certain population (Allel et al., 2020; Coccia, 2020d; Gupta & Gharehgozli, 2020). Specifically, a relatively small number of the most influential meteorological and demographic factors should be selected for a predictive risk measure that is accurate enough and practical for use. Such risk assessment is very useful in guiding the future strategies of imposing epidemic mitigation measures (Coccia, 2021a).

Here, we demonstrated that taking into account joint effects of different factors can point to qualitatively different conclusions about their influence on the virus transmissibility than considering them individually as in Salom et al., 2021. Utilizing a combination of PCA and feature selection techniques, we were able to disentangle with high confidence, the variables of which independently (and significantly) influence the rate of the infection spread, and which only have an indirect influence or no influence at all (here found for alcohol consumption, chronic diseases, percentage of the urban population, raised blood pressure, and refugees).

While PCA brings clear advantages to regression analysis, such as working with a smaller number of variables and abolishing collinearity, the main disadvantage is harder interpretation in terms of original variables. We were, however, able to interpret PCs that significantly affect  $R_0$ , so that the main driving factors behind COVID-19 transmissibility are (a) the country's wealth/development level, corrected by the available indoor space per person and net migration), (b) pollution levels and some of the unhealthy living factors, (c) spontaneous behavior change due to developing epidemics, (d) weather seasonality and (e) possibly (marginally) BCG vaccination. These conclusions, and the direction of the corresponding effects, crucially depend on the more complex analysis performed here.

Certain limitations of this study should also be addressed. When the alignment between certain variables is too high, even the analysis performed here cannot differentiate between the factors genuinely affecting  $R_0$  and mere accidental correlations. In such cases, further, specifically designed (such as targeted epidemiological) studies are needed. For example, based on this analysis alone and due to the very high correlation between the cholesterol levels and HDI/GDP, it cannot be excluded that cholesterol is a contributing factor to the observed significance of the PC1 component, in addition to the country's prosperity that likely mimics the contact rate in population (as a crucial disease transmission property). For this reason, our research suggests that a separate study of cholesterol levels in the COVID-19 context (e.g., by measuring cholesterol blood levels along with PCR tests) could be, potentially, of high value since a hypothetical unexpected discovery of inherent cholesterol importance could lead to novel treatments of SARS-CoV-2 infection. Similarly, studies that disentangle the effect of the overall country's prosperity from the intrinsic effects of median age on  $R_0$  would also be quite welcome. Furthermore, some of the variables that were not included in our study, but were found as significant by other studies (Notari & Torrieri, 2020), and are closely related to HDI, such as lung cancer prevalence (Youlden et al., 2008), or frequency of tourist arrivals (Anggraeni, 2017), may



also contribute to the strong association of HDI with  $R_0$ , which we observe. Another problem might occur due to possible nontrivial interactions between different factors: for example, the effects of pollution on the airborne COVID-19 transmission can be significantly dependent on the wind speed (Coccia, 2020b, 2021b). Unfortunately, our study is not well-suited to detect such effects (while, in principle, these effects could be included through higher-order terms in regression, this might lead to overfitting). A nontrivial future task may be a systematic attempt to unify (and standardize, to the extent possible) different approaches and variables used in the studies of the environmental factor effects on COVID-19 transmissibility.

Some suggestions that could improve COVID-19 mitigation policies may already follow from this study. Deliberately reducing (in the long run) the overall population prosperity, which we identified as the most important predictor of  $R_0$  in an attempt to indirectly reduce the frequency of social contacts is impractical. However, the widely implemented lockdowns, proven to inhibit the infection spread, are the measures that reduce the frequency of interpersonal contacts, but also economic activity, so the epidemic behavior seems consistent with the predicted HDI dependence. Our conclusions about the importance of HDI, as a predictor of  $R_0$ , could be further tested by studies of epidemiological relevance of higher resolution HDI-analogs, such as Subnational HDI (SHDI) or City Development Index. If HDI and GDP parameters are confirmed to dominantly influence  $R_0$  values simply since they highly and naturally correlate with the frequency of social contacts (as we anticipate to be the case), identifying this as one of the major factors is not without implications. That is, recognizing the importance of this parameter can help make better predictions of the disease dynamic and locate in advance high-risk spots/areas.

Moreover, since we identified the built-up area per person as another relevant factor, future urban policies should put more emphasis on avoiding very high population concentrations (Coccia, 2020c). The relevance of the onset variable may indicate the importance of timely informing the public about all the risks and perils of the incoming epidemic. More obviously, pointing to unhealthy living conditions and lifestyle as a significant driver of COVID-19 pandemic, underscores the importance of measures to reduce obesity, smoking prevalence, physical inactivity, and air pollution (Coccia, 2021a), also by subsidizing energy from renewable resources (Coccia, 2020c). Overall, the results presented here emphasize the importance of understanding environmental factors that impact transmissibility for both COVID-19 and other (including potential future) infectious diseases.

### Conflict of Interest

The authors declare that the research was conducted in the absence of any commercial or financial relationships that could be construed as a potential conflict of interest.

### Data Availability Statement

Data are available through Salom et al., 2021.

### Acknowledgments

This work was partially supported by the Ministry of Education, Science and Technological Development of the Republic of Serbia.

### References

- Alexopoulos, E. C. (2010). Introduction to multivariate regression analysis. *Hippokratia*, 14(Suppl 1), 23–38. <https://doi.org/10.1201/b10289-6>
- Allel, K., Tapia-Muñoz, T., & Morris, W. (2020). Country-level factors associated with the early spread of COVID-19 cases at 5, 10 and 15 days since the onset. *Global Public Health*, 15(11), 1589–1602. <https://doi.org/10.1080/17441692.2020.1814835>
- Anggraeni, G. N. (2017). The relationship between numbers of international tourist arrivals and economic growth in the Asean-8: Panel data approach. *JDE (Journal of Developing Economies)*, 2(1), 40–49. <https://doi.org/10.20473/jde.v2i1.5118>
- Bashir, M. F., Ma, B. J., Bilal, B., Komal, M. A., Farooq, T. H., Iqbal, N., & Bashir, M. (2020). Correlation between environmental pollution indicators and COVID-19 pandemic: A brief study in Californian context. *Environmental Research*, 187, 109652. <https://doi.org/10.1016/j.envres.2020.109652>
- Bontempi, E., Vergalli, S., & Squazzoni, F. (2020). Understanding COVID-19 diffusion requires an interdisciplinary, multi-dimensional approach. *Environmental Research*, 188, 109814. <https://doi.org/10.1016/j.envres.2020.109814>
- Carozzi, F. (2020). *Urban density and COVID-19*. Institute for the Study of Labor. (IZA) [Online], 13440. Retrieved from <https://ssrn.com/abstract=3643204>
- Casanova, L. M., Jeon, S., Rutala, W. A., Weber, D. J., & Sobsey, M. D. (2010). Effects of air temperature and relative humidity on coronavirus survival on surfaces. *Applied and Environmental Microbiology*, 76(9), 2712–2717. <https://doi.org/10.1128/AEM.02291-09>
- Chan, K.-H., Peiris, J. M., Lam, S., Poon, L., Yuen, K., & Seto, W. H. (2011). The effects of temperature and relative humidity on the viability of the SARS coronavirus. *Advances in Virology*, 2011, 734690. <https://doi.org/10.1155/2011/734690>



- Coccia, M. (2020a). The effects of atmospheric stability with low wind speed and of air pollution on the accelerated transmission dynamics of COVID-19. *International Journal of Environmental Studies*, 78(1), 1–27. <https://doi.org/10.1080/00207233.2020.1802937>
- Coccia, M. (2020b). Factors determining the diffusion of COVID-19 and suggested strategy to prevent future accelerated viral infectivity similar to COVID. *The Science of the Total Environment*, 729, 138474. <https://doi.org/10.1016/j.scitotenv.2020.138474>
- Coccia, M. (2020c). How (Un)sustainable environments are related to the diffusion of COVID-19: The relation between coronavirus disease 2019, air pollution, wind resource and energy. *Sustainability*, 12(22), 9709. <https://doi.org/10.3390/su12229709>
- Coccia, M. (2020d). An index to quantify environmental risk of exposure to future epidemics of the COVID-19 and similar viral agents: Theory and practice. *Environmental Research*, 191, 110155. <https://doi.org/10.1016/j.envres.2020.110155>
- Coccia, M. (2021a). Effects of the spread of COVID-19 on public health of polluted cities: Results of the first wave for explaining the déjà vu in the second wave of COVID-19 pandemic and epidemics of future vital agents. *Environmental Science and Pollution Research International*, 28(15), 19147–19154. <https://doi.org/10.1007/s11356-020-11662-7>
- Coccia, M. (2021b). How do low wind speeds and high levels of air pollution support the spread of COVID-19? *Atmospheric Pollution Research*, 12(1), 437–445. <https://doi.org/10.1016/j.apr.2020.10.002>
- Diao, Y., Kodera, S., Anzai, D., Gomez-Tames, J., Rashed, E. A., & Hirata, A. (2021). Influence of population density, temperature, and absolute humidity on spread and decay durations of COVID-19: A comparative study of scenarios in China, England, Germany, and Japan. *One Health*, 12, 100203. <https://doi.org/10.1016/j.onehlt.2020.100203>
- Djordjevic, M., Djordjevic, M., Ilic, B., Stojku, S., & Salom, I. (2021). Understanding infection progression under strong control measures through universal COVID-19 growth signatures. *Global Challenges*, 2021, 2000101. <https://doi.org/10.1002/gch2.202000101>
- Domingo, J., & Rovira, J. (2020). Effects of air pollutants on the transmission and severity of respiratory viral infections. *Environmental Research*, 187, 109650. <https://doi.org/10.1016/j.envres.2020.109650>
- Fattorini, D., & Regoli, F. (2020). Role of the chronic air pollution levels in the Covid-19 outbreak risk in Italy. *Environmental Pollution*, 264, 114732. <https://doi.org/10.1016/j.envpol.2020.114732>
- Frost, F., Petersen, H., Tollestrup, K., & Skipper, B. (2007). Influenza and COPD mortality protection as pleiotropic, dose-dependent effects of statins. *Chest*, 131(4), 1006–1012. <https://doi.org/10.1378/chest.06-1997>
- Gangemi, S., Billeci, L., & Tonacci, A. (2020). Rich at risk: Socio-economic drivers of COVID-19 pandemic spread. *Clinical and Molecular Allergy*, 18, 12. <https://doi.org/10.1186/s12948-020-00127-4>
- Garland, P., Babbitt, D., Bondarenko, M., Sorichetta, A., Tatem, A. J., & Johnson, O. (2020). *The COVID-19 pandemic as experienced by the individual*. (Accessed March 12, 2021) arXiv [Preprint] Retrieved from <https://ui.adsabs.harvard.edu/abs/2020arXiv200501167G/abstract>
- Gupta, A., & Gharegozli, A. (2020). *Developing a machine learning framework to determine the spread of COVID-19*. Accessed 12 March 2021 SSRN [Preprint] Retrieved from [https://papers.ssrn.com/sol3/papers.cfm?abstract\\_id=3635211](https://papers.ssrn.com/sol3/papers.cfm?abstract_id=3635211)
- Haddad, C., Bou Malhab, S., Sacre, H., & Salameh, P. (2021). Smoking and COVID-19: A scoping review. *Tobacco Use Insights*, 14. <https://doi.org/10.1177/1179173X21994612>
- Haque, S. E., & Rahman, M. (2020). Association between temperature, humidity, and COVID-19 outbreaks in Bangladesh. *Environmental Science & Policy*, 114, 253–255. <https://doi.org/10.1016/j.envsci.2020.08.012>
- Hassan, M., Bhuiyan, M., Tareq, F., Bodrud-Doza, M., Tanu, S., & Rabbani, K. (2021). Relationship between COVID-19 infection rates and air pollution, geo-meteorological, and social parameters. *Environmental Monitoring and Assessment*, 193(1), 29. <https://doi.org/10.1007/s10661-020-08810-4>
- Hastie, T., Tibshirani, R., & Friedman, J. (2009). *The elements of statistical learning: Data mining, inference, and prediction*. Springer.
- Heidari-Beni, M., & Kelishadi, R. (2020). Reciprocal impacts of obesity and coronavirus disease 2019. *Journal of Research in Medical Sciences*, 25(1), 110. [https://doi.org/10.4103/jrms.JRMS\\_416\\_20](https://doi.org/10.4103/jrms.JRMS_416_20)
- Heilingloh, C. S., Aufderhorst, U. W., Schipper, L., Dittmer, U., Witzke, O., Yang, D., et al. (2020). Susceptibility of SARS-CoV-2 to UV irradiation. *American Journal of Infection Control*, 48(10), 1273–1275. <https://doi.org/10.1016/j.ajic.2020.07.031>
- Islam, N., Bukhari, Q., Jameel, Y., Shabnam, S., Erzurumluoglu, A. M., Siddique, M. A., et al. (2021). COVID-19 and climatic factors: A global analysis. *Environmental Research*, 193, 110355. <https://doi.org/10.1016/j.envres.2020.110355>
- Jolliffe, I. T. (2002). *Principal component analysis*. Springer.
- Kapitsinis, N. (2020). The underlying factors of the COVID-19 spatially uneven spread. Initial evidence from regions in nine EU countries. *Regional Science Policy & Practice*, 12(6), 1027–1045. <https://doi.org/10.1111/rsp3.12340>
- Khajanchi, S., Sarkar, K., Mondal, J., & Perc, M. (2020). *Dynamics of the COVID-19 pandemic in India*. Accessed March 12, 2021 arXiv [Preprint] Retrieved from <https://arxiv.org/abs/2005.06286>
- Li, M., Zhang, Z., Cao, W., Liu, Y., Du, B., Chen, C., et al. (2020). Identifying novel factors associated with COVID-19 transmission and fatality using the machine learning approach. *The Science of the Total Environment*, 764, 142810. <https://doi.org/10.1016/j.scitotenv.2020.142810>
- Lin, S., Wei, D., Sun, Y., Chen, K., Yang, L., Liu, B., et al. (2020). Region-specific air pollutants and meteorological parameters influence COVID-19: A study from mainland China. *Ecotoxicology and Environmental Safety*, 204, 111035. <https://doi.org/10.1016/j.ecoenv.2020.111035>
- Mallapaty, S. (2021). *What's the risk of dying from a fast-spreading COVID-19 variant?* Accessed 12 March 2021 [Online] Retrieved from <https://www.nature.com/articles/d41586-021-00299-2>
- Milicevic, O., Salom, I., Rodic, A., Markovic, S., Tumbas, M., Zigic, D., et al. (2021). PM2.5 as a major predictor of COVID-19 basic reproduction number in the USA. *Environmental Research*, 201, 111526. <https://doi.org/10.1016/j.envres.2021.111526>
- Notari, A. (2021). Temperature dependence of COVID-19 transmission. *The Science of the Total Environment*, 763, 144390. <https://doi.org/10.1016/j.scitotenv.2020.144390>
- Notari, A., & Torrieri, G. (2020). *COVID-19 transmission risk factors*. (Accessed March 12, 2021) Authorea [Preprint] Retrieved from <https://authorea.com/users/360787/articles/482318-covid-19-transmission-risk-factors>
- O'Neill, L. A., & Netea, M. G. (2020). BCG-induced trained immunity: Can it offer protection against COVID-19? *Nature Reviews Immunology*, 20(6), 335–337. <https://doi.org/10.1038/s41577-020-0337-y>
- Pawelec, G., & Larbi, A. (2008). Immunity and ageing in man: Annual review 2006/2007. *Experimental Gerontology*, 43(1), 34–38. <https://doi.org/10.1016/j.exger.2007.09.009>
- Pope, P., & Webster, J. (1972). The use of an F-statistic in stepwise regression procedures. *Technometrics*, 14(2), 327–340. <https://doi.org/10.1080/00401706.1972.10488919>
- Rahimi, N. R., Fouladi-Fard, R., Aali, R., Shahyari, A., Rezaali, M., Ghafouri, Y., et al. (2021). Bidirectional association between COVID-19 and the environment: A systematic review. *Environmental Research*, 194, 110692. <https://doi.org/10.1016/j.envres.2020.110692>

- Ran, J., Zhao, S., Han, L., Qiu, Y., Cao, P., Yang, Z., et al. (2020). Effects of particulate matter exposure on the transmissibility and case fatality rate of COVID-19: A Nationwide Ecological Study in China. *Journal of Travel Medicine*, 27(6). <https://doi.org/10.1093/jtm/taaa133>
- Rocklöv, J., & Sjödin, H. (2020). High population densities catalyse the spread of COVID-19. *Journal of Travel Medicine*, 27(3). <https://doi.org/10.1093/jtm/taaa038>
- Rosario, D. K. A., Mutz, Y. S., Bernardes, P. C., & Conte-Junior, C. A. (2020). Relationship between COVID-19 and weather: Case study in a tropical country. *International Journal of Hygiene and Environmental Health*, 229, 113587. <https://doi.org/10.1016/j.ijheh.2020.113587>
- Ruiz, J. I., Nuhu, K., McDaniel, J. T., Popoff, F., Izcovich, A., & Criniti, J. M. (2015). Inequality as a powerful predictor of infant and maternal mortality around the world. *PLoS One*, 10(10), e0140796. <https://doi.org/10.1371/journal.pone.0140796>
- Sagripanti, J. L., & Lytle, C. D. (2020). Estimated inactivation of coronaviruses by solar radiation with special reference to COVID-19. *Photochemistry and Photobiology*, 96(4), 731–737. <https://doi.org/10.1111/php.13293>
- Salom, I., Rodic, A., Milicevic, O., Zigic, D., Djordjevic, M., & Djordjevic, M. (2021). Effects of demographic and weather parameters on COVID-19 basic reproduction number. *Frontiers in Ecology and Evolution*, 8(524), 617841. <https://doi.org/10.3389/fevo.2020.617841>
- Sarkodie, S. A., & Owusu, P. A. (2020). Impact of meteorological factors on COVID-19 pandemic: Evidence from top 20 countries with confirmed cases. *Environmental Research*, 191, 110101. <https://doi.org/10.1016/j.envres.2020.110101>
- Schmidt, N., Wing, P., McKeating, J., & Maini, M. (2020). Cholesterol-modifying drugs in COVID-19. *Oxford Open Immunology*, 1(1), iqaa001. <https://doi.org/10.1093/oxfimm/iqaa001>
- Shahid, Z., Kalayanamitra, R., McClafferty, B., Kepko, D., Ramgobin, D., Patel, R., et al. (2020). COVID-19 and older adults: What we know. *Journal of the American Geriatrics Society*, 68(5), 926–929. <https://doi.org/10.1111/jgs.16472>
- Srivastava, A. (2021). COVID-19 and air pollution and meteorology-an intricate relationship: A review. *Chemosphere*, 263, 128297. <https://doi.org/10.1016/j.chemosphere.2020.128297>
- Tegally, H., Wilkinson, E., Giovanetti, M., Iranzadeh, A., Fonseca, V., Giandhari, J., et al. (2020). Emergence and rapid spread of a new severe acute respiratory syndrome-related coronavirus 2 (SARS-CoV-2) lineage with multiple spike mutations in South Africa. Accessed March 12, 2021 | medRxiv [Preprint] Retrieved from <https://www.medrxiv.org/content/10.1101/2020.12.21.20248640v1>
- Tibshirani, R. (1996). Regression shrinkage and selection via the lasso. *Journal of the Royal Statistical Society. Series B (Methodological)*, 58(1), 267–288. <https://doi.org/10.1111/j.2517-6161.1996.tb02080.x>
- van Doremalen, N., Bushmaker, T., Morris, D. H., Holbrook, M. G., Gamble, A., Williamson, B. N., et al. (2020). Aerosol and surface stability of SARS-CoV-2 as compared with SARS-CoV-1. *New England Journal of Medicine*, 382(16), 1564–1567. <https://doi.org/10.1056/NEJMc2004973>
- World Bank. (2020a). *GDP per capita (current US\$)*. [Accessed January, 2021] [Online] Retrieved from <https://data.worldbank.org/indicator/NY.GDP.PCAP.CD>
- World Bank. (2020b). *World Bank open data*. Accessed May 2020 [Online] Retrieved from <https://www.worldbank.org/>
- Xie, J., & Zhu, Y. (2020). Association between ambient temperature and COVID-19 infection in 122 cities from China. *The Science of the Total Environment*, 724, 138201. <https://doi.org/10.1016/j.scitotenv.2020.138201>
- Xie, Z., Qin, Y., Li, Y., Shen, W., Zheng, Z., & Liu, S. (2020). Spatial and temporal differentiation of COVID-19 epidemic spread in mainland China and its influencing factors. *The Science of the Total Environment*, 744, 140929. <https://doi.org/10.1016/j.scitotenv.2020.140929>
- Youlden, D. R., Cramb, S. M., & Baade, P. D. (2008). The international epidemiology of lung cancer: Geographical distribution and secular trends. *Journal of Thoracic Oncology*, 3(8), 819–831. <https://doi.org/10.1097/JTO.0b013e31818020eb>
- Zheng, Z., Peng, F., Xu, B., Zhao, J., Liu, H., Peng, J., et al. (2020). Risk factors of critical & mortal COVID-19 cases: A systematic literature review and meta-analysis. *Journal of Infection*, 81(2), e16–e25. <https://doi.org/10.1016/j.jinf.2020.04.021>
- Zou, H., & Hastie, T. (2005). Regularization and variable selection via the elastic net. *Journal of the Royal Statistical Society: Series B*, 67(2), 301–320. <https://doi.org/10.1111/j.1467-9868.2005.00503.x>



# Rational $so(3)$ Gaudin model with general boundary terms

N. Manojlović<sup>a,\*</sup>, I. Salom<sup>b</sup>

<sup>a</sup> *Departamento de Matemática, Faculdade de Ciências e Tecnologia, Universidade do Algarve, Campus de Gambelas, Faro, PT-8005-139, Portugal*

<sup>b</sup> *Institute of Physics, University of Belgrade, Belgrade, P.O. Box 57, 11080, Serbia*

Received 29 October 2021; received in revised form 28 February 2022; accepted 22 March 2022

Available online 28 March 2022

Editor: Hubert Saleur

---

## Abstract

We study the  $so(3)$  Gaudin model with general boundary K-matrix in the framework of the algebraic Bethe ansatz. The off-shell action of the generating function of the  $so(3)$  Gaudin Hamiltonians is determined. The proof based on the mathematical induction is presented on the algebraic level without any restriction whatsoever on the boundary parameters. The  $so(3)$  Gaudin Hamiltonians with general boundary terms are given explicitly as well as their off-shell action on the Bethe states. The correspondence between the Bethe states and the solutions to the generalized  $so(3)$  Knizhnik-Zamolodchikov equations is established. In this context, the on-shell norm of the Bethe states is determined as well as their off-shell scalar product.

© 2022 The Author(s). Published by Elsevier B.V. This is an open access article under the CC BY license (<http://creativecommons.org/licenses/by/4.0/>). Funded by SCOAP<sup>3</sup>.

---

## 1. Introduction

The systems obtained as the quasi-classical limit of the Heisenberg spin chains [1] were first studied by Gaudin [2–4]. In the framework of the coordinate as well as the algebraic Bethe ansatz Gaudin has found the spectrum of the generating function of the corresponding Hamiltonians [2–4]. This system has been recasted in the framework of the quantum inverse scattering method [5–7] by exploring the so-called Sklyanin linear bracket using an  $s\ell(2)$  invariant, unitary classical

---

\* Corresponding author.

E-mail address: [nmanoj@ualg.pt](mailto:nmanoj@ualg.pt) (N. Manojlović).

$r$ -matrix [8]. This result enabled further generalisations based on other unitary solutions to the classical Yang-Baxter equation [9,10], prompting the interest in the Gaudin systems based on higher-rank simple Lie algebras [11–13] as well as Lie superalgebras [14–18]. The relation with the Knizhnik-Zamolodchikov equations of conformal field theory in two dimension [19] and the representation theory of the Kac-Moody algebras [20] was further strengthened when the connection between the Bethe states of the Gaudin model and the solution to the Knizhnik-Zamolodchikov equations was established [21,22,15–17,23]. It is also interesting to note that, in a somewhat more physical approach, the long-range interaction of these systems was studied in [24,25]. The Gaudin system on an elliptic curve was studied in [26], while the  $s\ell(2)$  Gaudin with the Jordanian twist was studied in [27–29]. On the classical level, the Gaudin model corresponds to the so-called Schlesinger system in the theory of isomonodromic deformation [30–36].

In our considerations of the quantum Heisenberg spin chains with non-periodic boundary conditions we follow Sklyanin's approach where the boundary conditions are expressed in the form of the left and right reflection matrices [37]. The so-called reflection equation and the dual reflection equation represent the compatibility conditions between the bulk and the boundary of the system at the left and, respectively, right site of the system. The commutativity of the transfer matrix, in this case, is guaranteed on the one hand by the fact that the matrix form of the exchange relations between the entries of the Sklyanin monodromy matrix is analogous to the reflection equation and on the other hand, by the dual reflection equation [37–39].

Renewed interest has emerged in the implementation of algebraic Bethe ansatz on solvable Heisenberg chains with non-periodic boundary conditions [40–48]. As for alternative approaches, a review of the coordinate Bethe ansatz in this case is given in [49], the Bethe ansatz based on the functional relation between the eigenvalues of the transfer matrix and the quantum determinant, as well as the associated T-Q relation are studied in [50–52], functional relations for the eigenvalues of the transfer matrix based on fusion hierarchy were discussed in [53] and the Vertex-IRF correspondence in [54,55], while the Jordanian deformation of the open XXX chain is analysed in [56]. For the latest results, as well as an excellent review on the application of the separation of variables method on the 6-vertex model and the associate XXZ quantum chains see [57].

Our interest in open Heisenberg spin chains was twofold. On the one hand, we were interested in the implementation of the algebraic Bethe ansatz, and on the other hand, we wanted to consider the quasi-classical limit which yields the corresponding Gaudin model [58,59]. As it is well known [41,42,58], due to the symmetry of the R-matrix of the non-periodic XXX spin chain, the accomplishment of the algebraic Bethe ansatz does not imply any restriction on the boundary parameters. However, in the case of the open XXZ chain [60], the existence of the so-called vacuum vector requires the triangular form of the boundary K-matrix [43,44,59]. As for the quasi-classical limit, Hikami showed, in complete analogy with the periodic case [24,25], how the expansion of the XXZ transfer matrix, calculated at the special values of the spectral parameter, yields the Gaudin Hamiltonians in the case when both reflection matrices are diagonal [61]. Similar expansion was done for the Jordanian deformation of the rational  $s\ell(2)$  Gaudin model with generic boundaries [62]. The algebraic Bethe ansatz was applied to open Gaudin model in the context of the Vertex-IRF correspondence [63–65]. Also, results were obtained for the open Gaudin models based on Lie superalgebras [66]. Returning back to the quasi-classical limit, following the Sklyanin proposal for the periodic boundary conditions [8,67], we have derived the generating function of the Gaudin Hamiltonians both for the XXX [58] and the XXZ chain [59] as well as for the Jordanian deformation of the XXX Heisenberg spin chain [68]. Moreover, we have shown [69] how, in the context of the quasi-classical limit, the solutions to

the classical Yang-Baxter equation [9,10] can be combined with the solutions to the classical reflection equation [70,71] to yield solutions to the so-called generalized classical Yang-Baxter equation [72–75]. These solutions are the non-unitary classical r-matrices [76–82]. In particular, the generic elliptic  $sl(2)$  non-unitary r-matrix was studied in [83]. Also, we draw attention to the recent study of the generalized Gaudin and Richardson models based on a class of non-unitary r-matrices [84].

An approach to the implementation of the algebraic Bethe ansatz for the rational as well as the trigonometric  $sl(2)$  Gaudin model based on the corresponding Maillet linear bracket was developed in [85–89]. Once a suitable set of generators of the relevant generalized Gaudin algebra is found, the local realization of these generators becomes compact and it naturally leads to the definition of the so-called creation operators. In both the rational and trigonometric case [86,89], these creation operators define Bethe states in such a way that the off-shell action of the generating function of the Gaudin Hamiltonians can be computed explicitly, and a completely algebraic proof of this action given.

This paper is centred on the application of the algebraic Bethe ansatz to the rational  $so(3)$  Gaudin model with generic classical boundary K-matrix. We recall that this K-matrix can be obtained by the so-called fusion procedure [6,90,91], starting from the  $sl(2)$  K-matrix [58,92–94]. The outline of this method in the trigonometric  $so(3)$  case was given in [95]. Alternatively, one can use the so-called scaling limit [96], to obtain the K-matrix from the trigonometric  $so(3)$  boundary K-matrix [95,97]. The non-unitary  $so(3)$  classical r-matrix (B.8) is then obtained by combining the unitary  $so(3)$  invariant classical r-matrix and the K-matrix. This non-unitary classical r-matrix defines the  $so(3)$  Maillet linear bracket, for the suitable Lax operator, and provides an algebraic framework for our study of the non-periodic  $so(3)$  Gaudin model. As an immediate consequence of the definition of the  $so(3)$  Maillet bracket follows the mutual commutativity of the generating function for different values of the spectral parameter. However, as it will be confirmed in the following, the natural set of generators unfortunately turns out not to be adequate for the implementation of the algebraic Bethe ansatz. Thus we will here propose a new set of generators. Besides the relative simplicity of the local realization of the new generators, their most striking feature will be the compact form of their commutation relations. This is of great significance since it efficiently enables the algebraic proof of the off-shell action of the generating function on the Bethe states. Furthermore, it is important to stress that these results will be obtained without any restriction whatsoever on the boundary parameters. It is only when solving the generalized  $so(3)$  Knizhnik-Zamolodchikov equations that the key identity in the proof will require one of four boundary parameters to be set to zero. However, in spite of this constraint we will retain a large improvement in generality over the previous studies: while the formulas that we here provide for the solutions to the generalized  $so(3)$  Knizhnik-Zamolodchikov equations, the on-shell norm of the Bethe vectors and the off-shell scalar product of the Bethe vectors do superficially look similar to the analogous formulae in the  $sl(2)$  case [86], only one of the boundary parameters will be fixed here, instead of all four of them (as, for example, in [86]).

The paper is organised as follows. In Section 2 we study the  $so(3)$  Maillet linear bracket which provides the algebraic framework for implementation of the Bethe ansatz. In the same section we propose the novel set of generators with simplified commutation relations and introduce Gaudin Hamiltonians. The implementation of the algebraic Bethe ansatz is the principal topic of the Section 3. There we will obtain the expression for the off-shell action of the generating function  $\tau(\lambda)$ , as well as for the off-shell action of the  $so(3)$  Gaudin Hamiltonians with general boundary terms – and prove these formulas by mathematical induction. The solutions to the generalized  $so(3)$  Knizhnik-Zamolodchikov equations will be given in the Section 4. Our



results will be summarised in the concluding Section 5. Fundamental definitions regarding the  $so(3)$  Lie algebra, including the two  $so(3)$  invariant operators in  $\mathbb{C}^3 \otimes \mathbb{C}^3$  which generate the relevant Brauer algebra, are presented in the Appendix A. Finally, the cornerstone of our study – the non-unitary  $so(3)$  classical r-matrix – is given in the Appendix B.

## 2. The $so(3)$ Maillet linear bracket

In this section we show how the non-unitary  $so(3)$  classical r-matrix (B.8) helps define the  $so(3)$  Maillet linear bracket (8) for the suitable Lax operator (7). Although this Maillet bracket provides an appropriate algebraic framework for studying the quantum  $so(3)$  Gaudin model, yielding the generating function of the  $so(3)$  Gaudin Hamiltonians with general boundary terms, it will be shown below that the natural set of generators unfortunately does not provide the most efficient way for implementing the algebraic Bethe ansatz in this case. Thus we will propose a new set off generators of the corresponding generalized  $so(3)$  Gaudin algebra.

In our study we use the Lax operator

$$L_0(\lambda) = \sum_{m=1}^N \frac{\vec{S}_0 \cdot \vec{S}_m}{\lambda - \alpha_m} = \sum_{m=1}^N \frac{1}{\lambda - \alpha_m} \left( S_0^3 \otimes S_m^3 + \frac{1}{2} (S_0^+ \otimes S_m^- + S_0^- \otimes S_m^+) \right), \quad (1)$$

where the spin operators  $S_m^\alpha$ , with  $\alpha = +, -, 3$  and  $m = 1, 2, \dots, N$ , are introduced in (A.12) and the matrices  $S_0^3$  and  $S_0^\pm$  in the auxiliary space  $\mathbb{C}^3$  are specified by (A.1) and (A.3), respectively. The Lax operator (1) can also be represented in the following form

$$L_0(\lambda) = \vec{S}_0 \cdot \vec{S}(\lambda), \quad (2)$$

where the generators of the  $so(3)$  Gaudin algebra are defined by [2–4]

$$S^3(\lambda) = \sum_{m=1}^N \frac{S_m^3}{\lambda - \alpha_m}, \quad S^\pm(\lambda) = \sum_{m=1}^N \frac{S_m^\pm}{\lambda - \alpha_m}. \quad (3)$$

The so-called Sklyanin linear bracket [8,15,16] for the Lax operator (1) and the r-matrix (B.1)

$$[L_1(\lambda), L_2(\mu)] = [r_{12}(\lambda - \mu), L_1(\lambda) + L_2(\mu)] \quad (4)$$

yields nontrivial commutation relations for the generators (3)

$$\begin{aligned} [S^3(\lambda), S^\pm(\mu)] &= \mp \frac{S^\pm(\lambda) - S^\pm(\mu)}{\lambda - \mu}, \\ [S^+(\lambda), S^-(\mu)] &= (-2) \frac{S^3(\lambda) - S^3(\mu)}{\lambda - \mu}. \end{aligned} \quad (5)$$

The Lax operator corresponding to the generalized  $so(3)$  Gaudin algebra is given by

$$\mathcal{L}_0(\lambda) = L_0(\lambda) - K_0(\lambda)L_0(-\lambda)K_0^{-1}(\lambda), \quad (6)$$

where  $L_0(\lambda)$  is the Lax operator (1) and  $K_0(\lambda)$  is the reflection K-matrix defined in (B.4). This form of the Lax operator can be obtained by following a relatively general procedure of quasi-classical expansion of the Sklyanin monodromy [69]. By direct substitution we obtain

$$\begin{aligned} \mathcal{L}_0(\lambda) &= \vec{S}_0 \cdot \vec{S}(\lambda) - \left( K_0(\lambda) \vec{S}_0 K_0^{-1}(\lambda) \right) \cdot \vec{S}(-\lambda) \\ &= \begin{pmatrix} H(\lambda) & \frac{1}{\sqrt{2}} F(\lambda) & 0 \\ \frac{1}{\sqrt{2}} E(\lambda) & 0 & \frac{1}{\sqrt{2}} F(\lambda) \\ 0 & \frac{1}{\sqrt{2}} E(\lambda) & -H(\lambda) \end{pmatrix}. \end{aligned} \tag{7}$$

The Lax operator (7) obeys the following  $so(3)$  Maillet linear bracket [73–75,38,69]

$$[\mathcal{L}_0(\lambda), \mathcal{L}_0(\mu)] = \left[ r_{00}^K(\lambda, \mu), \mathcal{L}_0(\lambda) \right] - \left[ r_{00}^K(\mu, \lambda), \mathcal{L}_0(\mu) \right]. \tag{8}$$

This linear bracket is obviously anti-symmetric and it obeys the Jacobi identity because the  $r$ -matrix (B.6) satisfies the generalized classical Yang-Baxter equation (B.7).

The  $so(3)$  Maillet bracket (8) implies the following commutation relations for the generators  $E(\lambda)$ ,  $F(\lambda)$  and  $H(\lambda)$  (7)

$$\begin{aligned} [E(\lambda), E(\mu)] &= \frac{-2\varphi^2}{\lambda + \mu} \left( \frac{\mu^2}{\xi^2 - (\psi\varphi + \nu^2)\mu^2} H(\lambda) - \frac{\lambda^2}{\xi^2 - (\psi\varphi + \nu^2)\lambda^2} H(\mu) \right), \\ &+ \frac{2\varphi}{\lambda + \mu} \left( \frac{(\xi + \nu\mu)\mu}{\xi^2 - (\psi\varphi + \nu^2)\mu^2} E(\lambda) - \frac{(\xi + \nu\lambda)\lambda}{\xi^2 - (\psi\varphi + \nu^2)\lambda^2} E(\mu) \right), \end{aligned} \tag{9}$$

$$\begin{aligned} [F(\lambda), F(\mu)] &= \frac{2\psi^2}{\lambda + \mu} \left( \frac{\mu^2}{\xi^2 - (\psi\varphi + \nu^2)\mu^2} H(\lambda) - \frac{\lambda^2}{\xi^2 - (\psi\varphi + \nu^2)\lambda^2} H(\mu) \right) \\ &+ \frac{2\psi}{\lambda + \mu} \left( \frac{(\xi - \nu\mu)\mu}{\xi^2 - (\psi\varphi + \nu^2)\mu^2} F(\lambda) - \frac{(\xi - \nu\lambda)\lambda}{\xi^2 - (\psi\varphi + \nu^2)\lambda^2} F(\mu) \right), \end{aligned} \tag{10}$$

$$\begin{aligned} [H(\lambda), H(\mu)] &= \frac{-\psi}{\lambda + \mu} \left( \frac{(\xi + \nu\mu)\mu}{\xi^2 - (\psi\varphi + \nu^2)\mu^2} E(\lambda) - \frac{(\xi + \nu\lambda)\lambda}{\xi^2 - (\psi\varphi + \nu^2)\lambda^2} E(\mu) \right) \\ &+ \frac{-\varphi}{\lambda + \mu} \left( \frac{(\xi - \nu\mu)\mu}{\xi^2 - (\psi\varphi + \nu^2)\mu^2} F(\lambda) - \frac{(\xi - \nu\lambda)\lambda}{\xi^2 - (\psi\varphi + \nu^2)\lambda^2} F(\mu) \right), \end{aligned} \tag{11}$$

and

$$\begin{aligned} [H(\lambda), E(\mu)] &= \frac{\varphi}{\lambda + \mu} \left( \frac{\varphi\mu^2}{\xi^2 - (\psi\varphi + \nu^2)\mu^2} F(\lambda) - \frac{2(\xi - \nu\lambda)\lambda}{\xi^2 - (\psi\varphi + \nu^2)\lambda^2} H(\mu) \right) \\ &- \frac{1}{(\lambda - \mu)(\lambda + \mu)} \left( \frac{(2(\xi - \nu\lambda)(\xi + \nu\mu) - \psi\varphi(\lambda + \mu)\mu)\mu}{\xi^2 - (\psi\varphi + \nu^2)\mu^2} E(\lambda) \right. \\ &\left. - \frac{2(\xi^2 - (\psi\varphi\mu + \nu^2)\lambda)\lambda}{\xi^2 - (\psi\varphi + \nu^2)\lambda^2} E(\mu) \right), \end{aligned} \tag{12}$$

$$\begin{aligned} [H(\lambda), F(\mu)] &= \frac{-\psi}{\lambda + \mu} \left( \frac{\psi\mu^2}{\xi^2 - (\psi\varphi + \nu^2)\mu^2} E(\lambda) + \frac{2(\xi + \nu\lambda)\lambda}{\xi^2 - (\psi\varphi + \nu^2)\lambda^2} H(\mu) \right) \\ &+ \frac{1}{(\lambda - \mu)(\lambda + \mu)} \left( \frac{(2(\xi - \nu\mu)(\xi + \nu\lambda) - \psi\varphi(\lambda + \mu)\mu)\mu}{\xi^2 - (\psi\varphi + \nu^2)\mu^2} F(\lambda) \right. \end{aligned}$$

$$- \frac{2(\xi^2 - (\psi\varphi\mu + v^2\lambda)\lambda)\lambda}{\xi^2 - (\psi\varphi + v^2)\lambda^2} F(\mu) \Big), \tag{13}$$

$$\begin{aligned} [F(\lambda), E(\mu)] = & \frac{-2}{\lambda + \mu} \left( \frac{\varphi(\xi + v\mu)\mu}{\xi^2 - (\psi\varphi + v^2)\mu^2} F(\lambda) - \frac{\psi(\xi - v\lambda)\lambda}{\xi^2 - (\psi\varphi + v^2)\lambda^2} E(\mu) \right) \\ & + \frac{2}{(\lambda - \mu)(\lambda + \mu)} \left( \frac{(2(\xi - v\lambda)(\xi + v\mu) - \psi\varphi(\lambda + \mu)\mu)\mu}{\xi^2 - (\psi\varphi + v^2)\mu^2} H(\lambda) \right. \\ & \left. - \frac{(2(\xi - v\lambda)(\xi + v\mu) - \psi\varphi(\lambda + \mu)\lambda)\lambda}{\xi^2 - (\psi\varphi + v^2)\lambda^2} H(\mu) \right). \end{aligned} \tag{14}$$

Moreover, the Maillet linear bracket (8) yields the expression for the generating function of the  $so(3)$  Gaudin Hamiltonians with general boundary terms in terms of the Lax operator (6)

$$\tau(\lambda) = \frac{1}{2} \text{tr}_0 \left( \mathcal{L}_0^2(\lambda) \right). \tag{15}$$

Namely, using the Maillet bracket (8), it is straightforward to check that the operator  $\tau(\lambda)$  commutes for different values of the spectral parameter,

$$[\tau(\lambda), \tau(\mu)] = 0. \tag{16}$$

From (7) it follows that

$$\tau(\lambda) = H^2(\lambda) + \frac{1}{2} (E(\lambda)F(\lambda) + F(\lambda)E(\lambda)). \tag{17}$$

Our aim here is to obtain the spectrum and the corresponding states of the generating function  $\tau(\lambda)$  by algebraic methods. To this end we would have to use the relations (9) – (14). As it is evident from the formulae above, these relations do not seem to be suitable to efficiently address this problem. Therefore, we propose a new set of generators

$$\begin{aligned} \mathcal{E}(\lambda) = & \frac{1}{2\psi\sqrt{\psi\varphi + v^2}} \left( \psi^2 E(\lambda) - \left( \psi\varphi + 2v \left( v - \sqrt{\psi\varphi + v^2} \right) \right) F(\lambda) \right. \\ & \left. + 2\psi \left( v - \sqrt{\psi\varphi + v^2} \right) H(\lambda) \right), \end{aligned} \tag{18}$$

$$\begin{aligned} \mathcal{F}(\lambda) = & \frac{1}{2\psi\sqrt{\psi\varphi + v^2}} \left( -\psi^2 E(\lambda) + \left( \psi\varphi + 2v \left( v + \sqrt{\psi\varphi + v^2} \right) \right) F(\lambda) \right. \\ & \left. - 2\psi \left( v + \sqrt{\psi\varphi + v^2} \right) H(\lambda) \right), \end{aligned} \tag{19}$$

$$\mathcal{H}(\lambda) = \frac{1}{2\sqrt{\psi\varphi + v^2}} (\psi E(\lambda) + \varphi F(\lambda) + 2v H(\lambda)). \tag{20}$$

The commutation relations we obtain for the new generators are substantially simpler than the initial relations (12)–(11). In particular,

$$[\mathcal{E}(\lambda), \mathcal{E}(\mu)] = [\mathcal{F}(\lambda), \mathcal{F}(\mu)] = [\mathcal{H}(\lambda), \mathcal{H}(\mu)] = 0, \tag{21}$$

and the three non-trivial relations are

$$[\mathcal{H}(\lambda), \mathcal{E}(\mu)] = \frac{-2}{\lambda^2 - \mu^2} \left( \mu \frac{\xi - \lambda\sqrt{\psi\varphi + v^2}}{\xi - \mu\sqrt{\psi\varphi + v^2}} \mathcal{E}(\lambda) - \lambda \mathcal{E}(\mu) \right), \tag{22}$$

$$[\mathcal{H}(\lambda), \mathcal{F}(\mu)] = \frac{2}{\lambda^2 - \mu^2} \left( \mu \frac{\xi + \lambda\sqrt{\psi\varphi + v^2}}{\xi + \mu\sqrt{\psi\varphi + v^2}} \mathcal{F}(\lambda) - \lambda \mathcal{F}(\mu) \right), \tag{23}$$

$$[\mathcal{F}(\lambda), \mathcal{E}(\mu)] = \frac{4}{\lambda^2 - \mu^2} \left( \mu \frac{\xi - \lambda\sqrt{\psi\varphi + v^2}}{\xi - \mu\sqrt{\psi\varphi + v^2}} \mathcal{H}(\lambda) - \lambda \frac{\xi + \mu\sqrt{\psi\varphi + v^2}}{\xi + \lambda\sqrt{\psi\varphi + v^2}} \mathcal{H}(\mu) \right). \tag{24}$$

Furthermore, the local realization of the new generators is:

$$\begin{aligned} \mathcal{E}(\lambda) &= \frac{\lambda}{\sqrt{\psi\varphi + v^2}} \sum_{m=1}^N \frac{\xi - \alpha_m \sqrt{\psi\varphi + v^2}}{\xi - \lambda\sqrt{\psi\varphi + v^2}} \\ &\times \frac{2(v - \sqrt{\psi\varphi + v^2})S_m^3 + \psi S_m^+ - \frac{\psi\varphi + 2v(v - \sqrt{\psi\varphi + v^2})}{\psi} S_m^-}{(\lambda - \alpha_m)(\lambda + \alpha_m)}, \end{aligned} \tag{25}$$

$$\begin{aligned} \mathcal{F}(\lambda) &= \frac{-\lambda}{\sqrt{\psi\varphi + v^2}} \sum_{m=1}^N \frac{\xi + \alpha_m \sqrt{\psi\varphi + v^2}}{\xi + \lambda\sqrt{\psi\varphi + v^2}} \\ &\times \frac{2(v + \sqrt{\psi\varphi + v^2})S_m^3 + \psi S_m^+ - \frac{\psi\varphi + 2v(v + \sqrt{\psi\varphi + v^2})}{\psi} S_m^-}{(\lambda - \alpha_m)(\lambda + \alpha_m)}, \end{aligned} \tag{26}$$

$$\mathcal{H}(\lambda) = \frac{\lambda}{\sqrt{\psi\varphi + v^2}} \sum_{m=1}^N \frac{2vS_m^3 + \psi S_m^+ + \varphi S_m^-}{(\lambda - \alpha_m)(\lambda + \alpha_m)}. \tag{27}$$

A straightforward but somewhat lengthy calculation shows that the generating function  $\tau(\lambda)$  (17) has exactly the same form when expressed in terms of the new generators

$$\tau(\lambda) = \mathcal{H}^2(\lambda) + \frac{1}{2} (\mathcal{E}(\lambda)\mathcal{F}(\lambda) + \mathcal{F}(\lambda)\mathcal{E}(\lambda)). \tag{28}$$

The explicit expressions for the  $so(3)$  Gaudin Hamiltonians with general boundary terms are derived by substituting the local realization of the new generators (25) – (27) in the right-hand-side of (28)

$$\begin{aligned} H_m = (\pm) \operatorname{Res}_{\lambda = \pm\alpha_m} \tau(\lambda) &= \frac{1}{\xi^2 - (\psi\varphi + v^2)\alpha_m^2} \\ &\times \left( \frac{\xi^2 + (\psi\varphi - v^2)\alpha_m^2}{\alpha_m} (S_m^3)^2 - \frac{\alpha_m}{2} \left( \psi^2 (S_m^+)^2 + \varphi^2 (S_m^-)^2 \right. \right. \\ &\left. \left. + 2\psi v (S_m^+ S_m^3 + S_m^3 S_m^+) + 2\varphi v (S_m^- S_m^3 + S_m^3 S_m^-) \right) \right) \end{aligned}$$

$$\begin{aligned}
 & + \frac{\xi^2 + v^2 \alpha_m^2}{2\alpha_m} (S_m^+ S_m^- + S_m^- S_m^+) \\
 & + \frac{\alpha_m}{\xi^2 - (\psi\varphi + v^2) \alpha_m^2} \sum_{n \neq m}^N \left( \frac{4(\xi^2 - \psi\varphi \alpha_m \alpha_n - v^2 \alpha_m^2)}{\alpha_m^2 - \alpha_n^2} S_m^3 S_n^3 \right. \\
 & - \frac{\alpha_m}{\alpha_m + \alpha_n} (\psi^2 S_m^+ S_n^+ + \varphi^2 S_m^- S_n^- \\
 & + 2\psi v (S_m^+ S_n^3 + S_m^3 S_n^+) + 2\varphi v (S_m^- S_n^3 + S_m^3 S_n^-) \\
 & \left. + \frac{2(\xi^2 - (\psi\varphi + v^2) \alpha_m \alpha_n) - \psi\varphi \alpha_m (\alpha_m - \alpha_n)}{\alpha_m^2 - \alpha_n^2} (S_m^- S_n^+ + S_m^+ S_n^-) \right) \\
 & + \frac{\xi \cdot \alpha_m}{\xi^2 - (\psi\varphi + v^2) \alpha_m^2} \sum_{n \neq m}^N \frac{1}{\alpha_m + \alpha_n} (2\psi (S_m^+ S_n^3 - S_m^3 S_n^+) \\
 & + 2v (S_m^- S_n^+ - S_m^+ S_n^-) + 2\varphi (S_m^3 S_n^- - S_m^- S_n^3)) . \tag{29}
 \end{aligned}$$

Besides the formula above for the  $so(3)$  Gaudin Hamiltonians with general boundary terms, our main result in this section is the new form of generators of the generalized  $so(3)$  Gaudin algebra (25) – (27). Due to their strikingly simple commutation relations (21) – (24) they now provide a suitable framework for applying the algebraic Bethe ansatz without any restrictions on boundary parameters.

### 3. Implementation of the algebraic Bethe ansatz

Before we can proceed to find Bethe vectors and determine the off-shell action of the generating function  $\tau(\lambda)$ , we have to establish several intermediary results.

In the Hilbert space  $\mathcal{H}$  (A.11) of the system we have to define the so-called vacuum vector  $\Omega_+ \in \mathcal{H}$  together with the appropriate action of the generators (25) – (27) on it. To this purpose we observe that in every local space  $V_m = \mathbb{C}^3$ ,  $m \in \{1, \dots, N\}$  there exists a vector  $\omega_m \in V_m$  given by

$$\omega_m = \begin{pmatrix} \psi^2 \\ -\sqrt{2} \psi (v - \sqrt{\psi\varphi + v^2}) \\ (v - \sqrt{\psi\varphi + v^2})^2 \end{pmatrix} \in \mathbb{C}^3 = V_m , \tag{30}$$

where the parameters  $v$ ,  $\psi$  and  $\varphi$  are the parameters of the boundary K-matrix (B.4). Then it is easy to check that

$$\left( 2 \left( v - \sqrt{\psi\varphi + v^2} \right) S_m^3 + \psi S_m^+ - \frac{\psi\varphi + 2v(v - \sqrt{\psi\varphi + v^2})}{\psi} S_m^- \right) \omega_m = 0 , \tag{31}$$

$$(2v S_m^3 + \psi S_m^+ + \varphi S_m^-) \omega_m = 2\sqrt{\psi\varphi + v^2} \omega_m . \tag{32}$$



Therefore the vacuum vector  $\Omega_+$ , defined as

$$\Omega_+ = \omega_1 \otimes \cdots \otimes \omega_N \in \mathcal{H} \tag{33}$$

has the desired properties. Namely, it is annihilated by the generator  $\mathcal{E}(\lambda)$  (25) and, at the same time, it is an eigenvector of the generator  $\mathcal{H}(\lambda)$  (27), that is

$$\mathcal{E}(\lambda) \Omega_+ = 0 \quad \text{and} \quad \mathcal{H}(\lambda) \Omega_+ = \rho(\lambda) \Omega_+ \quad \text{with} \quad \rho(\lambda) = \sum_{m=1}^N \frac{2\lambda}{\lambda^2 - \alpha_m^2}. \tag{34}$$

Our next aim is to rewrite the formula for  $\tau(\lambda)$  (28) in a more suitable way so that the action of the generating function  $\tau(\lambda)$  on the vacuum vector  $\Omega_+$  (33) becomes more transparent. With this aim, we first note that the commutation relations (22) – (24) imply

$$[\mathcal{H}(\lambda), \mathcal{F}(\lambda)] = \frac{-\xi}{\lambda (\xi + \lambda \sqrt{\psi\varphi + v^2})} \mathcal{F}(\lambda) + \mathcal{F}'(\lambda), \tag{35}$$

$$[\mathcal{H}(\lambda), \mathcal{E}(\lambda)] = \frac{\xi}{\lambda (\xi - \lambda \sqrt{\psi\varphi + v^2})} \mathcal{E}(\lambda) - \mathcal{E}'(\lambda), \tag{36}$$

$$[\mathcal{F}(\lambda), \mathcal{E}(\lambda)] = 2 \left( \frac{-1}{\lambda} \frac{\xi^2 + (\psi\varphi + v^2)\lambda^2}{\xi^2 - (\psi\varphi + v^2)\lambda^2} \mathcal{H}(\lambda) + \mathcal{H}'(\lambda) \right), \tag{37}$$

where prime denotes derivative with respect to parameter. Therefore we can express the generating function  $\tau(\lambda)$  (28) as follows

$$\tau(\lambda) = \mathcal{H}^2(\lambda) + \frac{1}{\lambda} \frac{\xi^2 + (\psi\varphi + v^2)\lambda^2}{\xi^2 - (\psi\varphi + v^2)\lambda^2} \mathcal{H}(\lambda) - \mathcal{H}'(\lambda) + \mathcal{F}(\lambda)\mathcal{E}(\lambda). \tag{38}$$

Taking into account (34) and (38), it is evident that the vacuum vector  $\Omega_+$  (33) is an eigenvector of the generating function

$$\tau(\lambda) \Omega_+ = \chi_0(\lambda) \Omega_+ \quad \text{with} \quad \chi_0(\lambda) = \rho^2(\lambda) + \frac{\xi^2 + (\psi\varphi + v^2)\lambda^2}{\xi^2 - (\psi\varphi + v^2)\lambda^2} \frac{\rho(\lambda)}{\lambda} - \rho'(\lambda). \tag{39}$$

In our approach, one of the essential steps in the implementation of algebraic Bethe ansatz is to find the commutation relation between the generating function  $\tau(\lambda)$  (38) and the generator  $\mathcal{F}(\mu)$  (19). To this end, we will also need the following auxiliary result which follows from (23)

$$\begin{aligned} [\mathcal{H}'(\lambda), \mathcal{F}(\mu)] &= \frac{2}{\lambda^2 - \mu^2} \left( \frac{\xi (\lambda - \mu)}{(\lambda + \mu) (\xi + \mu \sqrt{\psi\varphi + v^2})} \mathcal{F}(\lambda) \right. \\ &\quad \left. + \frac{\lambda^2 + \mu^2}{\lambda^2 - \mu^2} (\mathcal{F}(\mu) - \mathcal{F}(\lambda)) + \mu \frac{\xi + \lambda \sqrt{\psi\varphi + v^2}}{\xi + \mu \sqrt{\psi\varphi + v^2}} \mathcal{F}'(\lambda) \right). \end{aligned} \tag{40}$$

Now we can compute the commutator by a straightforward calculation, based on the formulae (38), (23), (24) and (40):

$$\begin{aligned}
 [\tau(\lambda), \mathcal{F}(\mu)] = & -\frac{4}{\lambda^2 - \mu^2} \mathcal{F}(\mu) \left( \lambda \mathcal{H}(\lambda) + \frac{(\psi\varphi + v^2)\lambda^2}{\xi^2 - (\psi\varphi + v^2)\lambda^2} \right) \\
 & + \frac{4}{\lambda^2 - \mu^2} \frac{\lambda}{\mu} \frac{\xi - \mu\sqrt{\psi\varphi + v^2}}{\xi - \lambda\sqrt{\psi\varphi + v^2}} \mathcal{F}(\lambda) \left( \mu \mathcal{H}(\mu) + \frac{(\psi\varphi + v^2)\mu^2}{\xi^2 - (\psi\varphi + v^2)\mu^2} \right).
 \end{aligned}
 \tag{41}$$

The relative simplicity of the right hand side of the equation above has encouraged us to seek the commutator between the operator  $\tau(\lambda)$  and the product  $\mathcal{F}(\mu_1)\mathcal{F}(\mu_2)$  as the next step. In this case, an analogous direct calculation based on the previous formulae, leads to

$$\begin{aligned}
 [\tau(\lambda), \mathcal{F}(\mu_1)\mathcal{F}(\mu_2)] = & \\
 & -\frac{4}{\lambda^2 - \mu_1^2} \mathcal{F}(\mu_1)\mathcal{F}(\mu_2) \left( \lambda \mathcal{H}(\lambda) + \frac{(\psi\varphi + v^2)\lambda^2}{\xi^2 - (\psi\varphi + v^2)\lambda^2} - \frac{\lambda^2}{\lambda^2 - \mu_2^2} \right) \\
 & -\frac{4}{\lambda^2 - \mu_2^2} \mathcal{F}(\mu_1)\mathcal{F}(\mu_2) \left( \lambda \mathcal{H}(\lambda) + \frac{(\psi\varphi + v^2)\lambda^2}{\xi^2 - (\psi\varphi + v^2)\lambda^2} - \frac{\lambda^2}{\lambda^2 - \mu_1^2} \right) \\
 & + \frac{4}{\lambda^2 - \mu_1^2} \frac{\lambda}{\mu_1} \frac{\xi - \mu_1\sqrt{\psi\varphi + v^2}}{\xi - \lambda\sqrt{\psi\varphi + v^2}} \mathcal{F}(\lambda)\mathcal{F}(\mu_2) \\
 & \times \left( \mu_1 \mathcal{H}(\mu_1) + \frac{(\psi\varphi + v^2)\mu_1^2}{\xi^2 - (\psi\varphi + v^2)\mu_1^2} - \frac{2\mu_1^2}{\mu_1^2 - \mu_2^2} \right) \\
 & + \frac{4}{\lambda^2 - \mu_2^2} \frac{\lambda}{\mu_2} \frac{\xi - \mu_2\sqrt{\psi\varphi + v^2}}{\xi - \lambda\sqrt{\psi\varphi + v^2}} \mathcal{F}(\mu_1)\mathcal{F}(\lambda) \\
 & \times \left( \mu_2 \mathcal{H}(\mu_2) + \frac{(\psi\varphi + v^2)\mu_2^2}{\xi^2 - (\psi\varphi + v^2)\mu_2^2} - \frac{2\mu_2^2}{\mu_2^2 - \mu_1^2} \right).
 \end{aligned}
 \tag{42}$$

Evidently, the right hand side of (42) has extra lines and every line has extra terms in comparison with (41). While certain pattern is already visible, we will explicitly compute one more step before conjecturing the general case. The commutation relation between the generating function  $\tau(\lambda)$  and the product  $\mathcal{F}(\mu_1)\mathcal{F}(\mu_2)\mathcal{F}(\mu_3)$  is obtained in a similar manner, using the previous results,

$$\begin{aligned}
 [\tau(\lambda), \mathcal{F}(\mu_1)\mathcal{F}(\mu_2)\mathcal{F}(\mu_3)] = & \\
 & -\frac{4}{\lambda^2 - \mu_1^2} \mathcal{F}(\mu_1)\mathcal{F}(\mu_2)\mathcal{F}(\mu_3) \left( \lambda \mathcal{H}(\lambda) + \frac{(\psi\varphi + v^2)\lambda^2}{\xi^2 - (\psi\varphi + v^2)\lambda^2} - \frac{\lambda^2}{\lambda^2 - \mu_2^2} - \frac{\lambda^2}{\lambda^2 - \mu_3^2} \right) \\
 & -\frac{4}{\lambda^2 - \mu_2^2} \mathcal{F}(\mu_1)\mathcal{F}(\mu_2)\mathcal{F}(\mu_3) \left( \lambda \mathcal{H}(\lambda) + \frac{(\psi\varphi + v^2)\lambda^2}{\xi^2 - (\psi\varphi + v^2)\lambda^2} - \frac{\lambda^2}{\lambda^2 - \mu_1^2} - \frac{\lambda^2}{\lambda^2 - \mu_3^2} \right) \\
 & -\frac{4}{\lambda^2 - \mu_3^2} \mathcal{F}(\mu_1)\mathcal{F}(\mu_2)\mathcal{F}(\mu_3) \left( \lambda \mathcal{H}(\lambda) + \frac{(\psi\varphi + v^2)\lambda^2}{\xi^2 - (\psi\varphi + v^2)\lambda^2} - \frac{\lambda^2}{\lambda^2 - \mu_1^2} - \frac{\lambda^2}{\lambda^2 - \mu_2^2} \right)
 \end{aligned}$$

$$\begin{aligned}
 &+ \frac{4}{\lambda^2 - \mu_1^2} \frac{\lambda}{\mu_1} \frac{\xi - \mu_1 \sqrt{\psi\varphi + v^2}}{\xi - \lambda \sqrt{\psi\varphi + v^2}} \mathcal{F}(\lambda) \mathcal{F}(\mu_2) \mathcal{F}(\mu_3) \\
 &\quad \times \left( \mu_1 \mathcal{H}(\mu_1) + \frac{(\psi\varphi + v^2)\mu_1^2}{\xi^2 - (\psi\varphi + v^2)\mu_1^2} - \frac{2\mu_1^2}{\mu_1^2 - \mu_2^2} - \frac{2\mu_1^2}{\mu_1^2 - \mu_3^2} \right) \\
 &+ \frac{4}{\lambda^2 - \mu_2^2} \frac{\lambda}{\mu_2} \frac{\xi - \mu_2 \sqrt{\psi\varphi + v^2}}{\xi - \lambda \sqrt{\psi\varphi + v^2}} \mathcal{F}(\mu_1) \mathcal{F}(\lambda) \mathcal{F}(\mu_3) \\
 &\quad \times \left( \mu_2 \mathcal{H}(\mu_2) + \frac{(\psi\varphi + v^2)\mu_2^2}{\xi^2 - (\psi\varphi + v^2)\mu_2^2} - \frac{2\mu_2^2}{\mu_2^2 - \mu_1^2} - \frac{2\mu_2^2}{\mu_2^2 - \mu_3^2} \right) \\
 &+ \frac{4}{\lambda^2 - \mu_3^2} \frac{\lambda}{\mu_3} \frac{\xi - \mu_3 \sqrt{\psi\varphi + v^2}}{\xi - \lambda \sqrt{\psi\varphi + v^2}} \mathcal{F}(\mu_1) \mathcal{F}(\mu_2) \mathcal{F}(\lambda) \\
 &\quad \times \left( \mu_3 \mathcal{H}(\mu_3) + \frac{(\psi\varphi + v^2)\mu_3^2}{\xi^2 - (\psi\varphi + v^2)\mu_3^2} - \frac{2\mu_3^2}{\mu_3^2 - \mu_1^2} - \frac{2\mu_3^2}{\mu_3^2 - \mu_2^2} \right). \tag{43}
 \end{aligned}$$

In the general case, we conjecture validity of the following relation:

$$\begin{aligned}
 [\tau(\lambda), \mathcal{F}(\mu_1) \mathcal{F}(\mu_2) \cdots \mathcal{F}(\mu_M)] &= -\mathcal{F}(\mu_1) \mathcal{F}(\mu_2) \cdots \mathcal{F}(\mu_M) \sum_{j=1}^M \frac{4}{\lambda^2 - \mu_j^2} \times \\
 &\times \left( \lambda \mathcal{H}(\lambda) + \frac{(\psi\varphi + v^2)\lambda^2}{\xi^2 - (\psi\varphi + v^2)\lambda^2} - \sum_{k \neq j}^M \frac{\lambda^2}{\lambda^2 - \mu_k^2} \right) \\
 &+ \sum_{j=1}^M \frac{4}{\lambda^2 - \mu_j^2} \frac{\lambda}{\mu_j} \frac{\xi - \mu_j \sqrt{\psi\varphi + v^2}}{\xi - \lambda \sqrt{\psi\varphi + v^2}} \mathcal{F}(\lambda) \mathcal{F}(\mu_1) \mathcal{F}(\mu_2) \cdots \widehat{\mathcal{F}(\mu_j)} \cdots \mathcal{F}(\mu_M) \\
 &\times \left( \mu_j \mathcal{H}(\mu_j) + \frac{(\psi\varphi + v^2)\mu_j^2}{\xi^2 - (\psi\varphi + v^2)\mu_j^2} - \sum_{k \neq j}^M \frac{2\mu_j^2}{\mu_j^2 - \mu_k^2} \right), \tag{44}
 \end{aligned}$$

where the notation  $\widehat{\mathcal{F}(\mu_j)}$  means that the operator  $\mathcal{F}(\mu_j)$  is omitted.

The proof of the formula above is by mathematical induction. Our initial hypothesis is that the equation (44) is valid for some natural number  $M$ . Thus, we have to show that the analogous equation is valid for  $M + 1$ . To this end, we write

$$\begin{aligned}
 [\tau(\lambda), \mathcal{F}(\mu_1) \mathcal{F}(\mu_2) \cdots \mathcal{F}(\mu_M) \mathcal{F}(\mu_{M+1})] &= \\
 &= [\tau(\lambda), \mathcal{F}(\mu_1) \mathcal{F}(\mu_2) \cdots \mathcal{F}(\mu_M)] \mathcal{F}(\mu_{M+1}) \\
 &+ \mathcal{F}(\mu_1) \mathcal{F}(\mu_2) \cdots \mathcal{F}(\mu_M) \mathcal{F}(\mu_{M+1}) [\tau(\lambda), \mathcal{F}(\mu_{M+1})] \\
 &= [[\tau(\lambda), \mathcal{F}(\mu_1) \mathcal{F}(\mu_2) \cdots \mathcal{F}(\mu_M)], \mathcal{F}(\mu_{M+1})] \tag{45}
 \end{aligned}$$

$$\begin{aligned}
 & + \mathcal{F}(\mu_{M+1}) [\tau(\lambda), \mathcal{F}(\mu_1)\mathcal{F}(\mu_2) \cdots \mathcal{F}(\mu_M)] \\
 & + \mathcal{F}(\mu_1)\mathcal{F}(\mu_2) \cdots \mathcal{F}(\mu_M)\mathcal{F}(\mu_{M+1}) [\tau(\lambda), \mathcal{F}(\mu_{M+1})] .
 \end{aligned} \tag{46}$$

It follows from (44) that the first term on the right hand side of (46) yields two type of terms. In the second term of (46) we can just substitute the right hand side of (44). Finally, in the last term of (46) we use (41). In this way we obtain

$$\begin{aligned}
 & [\tau(\lambda), \mathcal{F}(\mu_1)\mathcal{F}(\mu_2) \cdots \mathcal{F}(\mu_M)\mathcal{F}(\mu_{M+1})] = \\
 & - \mathcal{F}(\mu_1)\mathcal{F}(\mu_2) \cdots \mathcal{F}(\mu_M) \sum_{j=1}^M \frac{4\lambda}{\lambda^2 - \mu_j^2} [\mathcal{H}(\lambda), \mathcal{F}(\mu_{M+1})] \\
 & + \sum_{j=1}^M \frac{4\lambda}{\lambda^2 - \mu_j^2} \frac{\xi - \mu_j \sqrt{\psi\varphi + v^2}}{\xi - \lambda \sqrt{\psi\varphi + v^2}} \times \\
 & \quad \times \mathcal{F}(\lambda)\mathcal{F}(\mu_1)\mathcal{F}(\mu_2) \cdots \widehat{\mathcal{F}(\mu_j)} \cdots \mathcal{F}(\mu_M) [\mathcal{H}(\mu_j), \mathcal{F}(\mu_{M+1})] \\
 & - \mathcal{F}(\mu_1)\mathcal{F}(\mu_2) \cdots \mathcal{F}(\mu_M)\mathcal{F}(\mu_{M+1}) \times \\
 & \quad \times \sum_{j=1}^M \frac{4}{\lambda^2 - \mu_j^2} \left( \lambda \mathcal{H}(\lambda) + \frac{(\psi\varphi + v^2)\lambda^2}{\xi^2 - (\psi\varphi + v^2)\lambda^2} - \sum_{k \neq j}^M \frac{\lambda^2}{\lambda^2 - \mu_k^2} \right) \\
 & + \sum_{j=1}^M \frac{4}{\lambda^2 - \mu_j^2} \frac{\lambda}{\mu_j} \frac{\xi - \mu_j \sqrt{\psi\varphi + v^2}}{\xi - \lambda \sqrt{\psi\varphi + v^2}} \mathcal{F}(\lambda)\mathcal{F}(\mu_1)\mathcal{F}(\mu_2) \cdots \widehat{\mathcal{F}(\mu_j)} \cdots \mathcal{F}(\mu_M)\mathcal{F}(\mu_{M+1}) \times \\
 & \quad \times \left( \mu_j \mathcal{H}(\mu_j) + \frac{(\psi\varphi + v^2)\mu_j^2}{\xi^2 - (\psi\varphi + v^2)\mu_j^2} - \sum_{k \neq j}^M \frac{2\mu_j^2}{\mu_j^2 - \mu_k^2} \right) \\
 & + \mathcal{F}(\mu_1)\mathcal{F}(\mu_2) \cdots \mathcal{F}(\mu_M) \left( - \frac{4}{\lambda^2 - \mu_{M+1}^2} \mathcal{F}(\mu_{M+1}) \left( \lambda \mathcal{H}(\lambda) + \frac{(\psi\varphi + v^2)\lambda^2}{\xi^2 - (\psi\varphi + v^2)\lambda^2} \right) \right) \\
 & + \frac{4}{\lambda^2 - \mu_{M+1}^2} \frac{\lambda}{\mu_{M+1}} \frac{\xi - \mu_{M+1} \sqrt{\psi\varphi + v^2}}{\xi - \lambda \sqrt{\psi\varphi + v^2}} \mathcal{F}(\lambda) \times \\
 & \quad \times \left( \mu_{M+1} \mathcal{H}(\mu_{M+1}) + \frac{(\psi\varphi + v^2)\mu_{M+1}^2}{\xi^2 - (\psi\varphi + v^2)\mu_{M+1}^2} \right) .
 \end{aligned} \tag{47}$$

In the first two terms on the right hand side of (47) we used the equation (23) and the remaining terms we rewrite in a more appropriate order

$$\begin{aligned}
 & [\tau(\lambda), \mathcal{F}(\mu_1)\mathcal{F}(\mu_2) \cdots \mathcal{F}(\mu_M)\mathcal{F}(\mu_{M+1})] = - \mathcal{F}(\mu_1)\mathcal{F}(\mu_2) \cdots \mathcal{F}(\mu_M) \sum_{j=1}^M \frac{4\lambda}{\lambda^2 - \mu_j^2} \times \\
 & \quad \times \frac{2}{\lambda^2 - \mu_{M+1}^2} \left( \mu_{M+1} \frac{\xi + \lambda \sqrt{\psi\varphi + v^2}}{\xi + \mu_{M+1} \sqrt{\psi\varphi + v^2}} \mathcal{F}(\lambda) - \lambda \mathcal{F}(\mu_{M+1}) \right)
 \end{aligned}$$

$$\begin{aligned}
 & + \sum_{j=1}^M \frac{4\lambda}{\lambda^2 - \mu_j^2} \frac{\xi - \mu_j \sqrt{\psi\varphi + v^2}}{\xi - \lambda \sqrt{\psi\varphi + v^2}} \mathcal{F}(\lambda) \mathcal{F}(\mu_1) \mathcal{F}(\mu_2) \cdots \widehat{\mathcal{F}(\mu_j)} \cdots \mathcal{F}(\mu_M) \times \\
 & \quad \times \frac{2}{\mu_j^2 - \mu_{M+1}^2} \left( \mu_{M+1} \frac{\xi + \mu_j \sqrt{\psi\varphi + v^2}}{\xi + \mu_{M+1} \sqrt{\psi\varphi + v^2}} \mathcal{F}(\mu_j) - \mu_j \mathcal{F}(\mu_{M+1}) \right) \\
 & - \mathcal{F}(\mu_1) \mathcal{F}(\mu_2) \cdots \mathcal{F}(\mu_M) \mathcal{F}(\mu_{M+1}) \times \\
 & \quad \times \sum_{j=1}^M \frac{4}{\lambda^2 - \mu_j^2} \left( \lambda \mathcal{H}(\lambda) + \frac{(\psi\varphi + v^2)\lambda^2}{\xi^2 - (\psi\varphi + v^2)\lambda^2} - \sum_{k \neq j}^M \frac{\lambda^2}{\lambda^2 - \mu_k^2} \right) \\
 & - \mathcal{F}(\mu_1) \mathcal{F}(\mu_2) \cdots \mathcal{F}(\mu_M) \mathcal{F}(\mu_{M+1}) \times \\
 & \quad \times \frac{4}{\lambda^2 - \mu_{M+1}^2} \left( \lambda \mathcal{H}(\lambda) + \frac{(\psi\varphi + v^2)\lambda^2}{\xi^2 - (\psi\varphi + v^2)\lambda^2} \right) \\
 & + \sum_{j=1}^M \frac{4}{\lambda^2 - \mu_j^2} \frac{\lambda}{\mu_j} \frac{\xi - \mu_j \sqrt{\psi\varphi + v^2}}{\xi - \lambda \sqrt{\psi\varphi + v^2}} \mathcal{F}(\lambda) \mathcal{F}(\mu_1) \mathcal{F}(\mu_2) \cdots \widehat{\mathcal{F}(\mu_j)} \cdots \mathcal{F}(\mu_M) \mathcal{F}(\mu_{M+1}) \times \\
 & \quad \times \left( \mu_j \mathcal{H}(\mu_j) + \frac{(\psi\varphi + v^2)\mu_j^2}{\xi^2 - (\psi\varphi + v^2)\mu_j^2} - \sum_{k \neq j}^M \frac{2\mu_j^2}{\mu_j^2 - \mu_k^2} \right) \\
 & + \frac{4}{\lambda^2 - \mu_{M+1}^2} \frac{\lambda}{\mu_{M+1}} \frac{\xi - \mu_{M+1} \sqrt{\psi\varphi + v^2}}{\xi - \lambda \sqrt{\psi\varphi + v^2}} \mathcal{F}(\mu_1) \mathcal{F}(\mu_2) \cdots \mathcal{F}(\mu_M) \mathcal{F}(\lambda) \times \\
 & \quad \times \left( \mu_{M+1} \mathcal{H}(\mu_{M+1}) + \frac{(\psi\varphi + v^2)\mu_{M+1}^2}{\xi^2 - (\psi\varphi + v^2)\mu_{M+1}^2} \right). \tag{48}
 \end{aligned}$$

Now it is just a question of reordering the terms in a more suitable manner

$$\begin{aligned}
 & [\tau(\lambda), \mathcal{F}(\mu_1) \mathcal{F}(\mu_2) \cdots \mathcal{F}(\mu_M) \mathcal{F}(\mu_{M+1})] = \\
 & - \mathcal{F}(\mu_1) \mathcal{F}(\mu_2) \cdots \mathcal{F}(\mu_M) \mathcal{F}(\mu_{M+1}) \times \\
 & \quad \times \sum_{j=1}^M \frac{4}{\lambda^2 - \mu_j^2} \left( \lambda \mathcal{H}(\lambda) + \frac{(\psi\varphi + v^2)\lambda^2}{\xi^2 - (\psi\varphi + v^2)\lambda^2} - \sum_{k \neq j}^{M+1} \frac{\lambda^2}{\lambda^2 - \mu_k^2} \right) \\
 & - \mathcal{F}(\mu_1) \mathcal{F}(\mu_2) \cdots \mathcal{F}(\mu_M) \mathcal{F}(\mu_{M+1}) \times \\
 & \quad \times \frac{4}{\lambda^2 - \mu_{M+1}^2} \left( \lambda \mathcal{H}(\lambda) + \frac{(\psi\varphi + v^2)\lambda^2}{\xi^2 - (\psi\varphi + v^2)\lambda^2} - \sum_{k=1}^M \frac{\lambda^2}{\lambda^2 - \mu_k^2} \right) \\
 & + \sum_{j=1}^M \frac{4}{\lambda^2 - \mu_j^2} \frac{\lambda}{\mu_j} \frac{\xi - \mu_j \sqrt{\psi\varphi + v^2}}{\xi - \lambda \sqrt{\psi\varphi + v^2}} \mathcal{F}(\lambda) \mathcal{F}(\mu_1) \mathcal{F}(\mu_2) \cdots \widehat{\mathcal{F}(\mu_j)} \cdots
 \end{aligned}$$



$$\begin{aligned}
 & \cdots \mathcal{F}(\mu_M)\mathcal{F}(\mu_{M+1}) \left( \mu_j \mathcal{H}(\mu_j) + \frac{(\psi\varphi + v^2)\mu_j^2}{\xi^2 - (\psi\varphi + v^2)\mu_j^2} - \sum_{k \neq j}^{M+1} \frac{2\mu_j^2}{\mu_j^2 - \mu_k^2} \right) \\
 & + \frac{4}{\lambda^2 - \mu_{M+1}^2} \frac{\lambda}{\mu_{M+1}} \frac{\xi - \mu_{M+1}\sqrt{\psi\varphi + v^2}}{\xi - \lambda\sqrt{\psi\varphi + v^2}} \mathcal{F}(\mu_1)\mathcal{F}(\mu_2)\cdots\mathcal{F}(\mu_M)\mathcal{F}(\lambda) \times \\
 & \times \left( \mu_{M+1}\mathcal{H}(\mu_{M+1}) + \frac{(\psi\varphi + v^2)\mu_{M+1}^2}{\xi^2 - (\psi\varphi + v^2)\mu_{M+1}^2} - \sum_{k=1}^M \frac{2\mu_{M+1}^2}{\mu_{M+1}^2 - \mu_k^2} \right). \tag{49}
 \end{aligned}$$

To obtain all the terms in the last sum (in the last line above) we had to use a generally valid, purely algebraic identity:

$$\begin{aligned}
 & \frac{-1}{(\lambda^2 - \mu_j^2)(\lambda^2 - \mu_{M+1}^2)} \frac{\xi^2 - (\psi\varphi + v^2)\lambda^2}{\xi^2 - (\psi\varphi + v^2)\mu_{M+1}^2} + \frac{1}{(\lambda^2 - \mu_j^2)(\mu_j^2 - \mu_{M+1}^2)} \times \\
 & \times \frac{\xi^2 - (\psi\varphi + v^2)\mu_j^2}{\xi^2 - (\psi\varphi + v^2)\mu_{M+1}^2} = \frac{-1}{(\lambda^2 - \mu_{M+1}^2)(\mu_{M+1}^2 - \mu_j^2)}, \tag{50}
 \end{aligned}$$

which is valid for every  $j = 1, 2, \dots, M$ .

Finally, to complete the proof we can simply combine together similar terms and obtain the desired result

$$\begin{aligned}
 & [\tau(\lambda), \mathcal{F}(\mu_1)\mathcal{F}(\mu_2)\cdots\mathcal{F}(\mu_M)\mathcal{F}(\mu_{M+1})] = \\
 & - \mathcal{F}(\mu_1)\mathcal{F}(\mu_2)\cdots\mathcal{F}(\mu_M)\mathcal{F}(\mu_{M+1}) \times \\
 & \times \sum_{j=1}^{M+1} \frac{4}{\lambda^2 - \mu_j^2} \left( \lambda \mathcal{H}(\lambda) + \frac{(\psi\varphi + v^2)\lambda^2}{\xi^2 - (\psi\varphi + v^2)\lambda^2} - \sum_{k \neq j}^{M+1} \frac{\lambda^2}{\lambda^2 - \mu_k^2} \right) \\
 & + \sum_{j=1}^{M+1} \frac{4}{\lambda^2 - \mu_j^2} \frac{\lambda}{\mu_j} \frac{\xi - \mu_j\sqrt{\psi\varphi + v^2}}{\xi - \lambda\sqrt{\psi\varphi + v^2}} \mathcal{F}(\lambda)\mathcal{F}(\mu_1)\mathcal{F}(\mu_2)\cdots\widehat{\mathcal{F}(\mu_j)}\cdots \\
 & \cdots \mathcal{F}(\mu_M)\mathcal{F}(\mu_{M+1}) \left( \mu_j \mathcal{H}(\mu_j) + \frac{(\psi\varphi + v^2)\mu_j^2}{\xi^2 - (\psi\varphi + v^2)\mu_j^2} - \sum_{k \neq j}^{M+1} \frac{2\mu_j^2}{\mu_j^2 - \mu_k^2} \right). \tag{51}
 \end{aligned}$$

This completes the proof by mathematical induction of the formula (44). It should be stressed that the right hand side is in an algebraically closed form. Thus the off-shell action of the generating function of the  $so(3)$  Gaudin Hamiltonians with general boundary terms becomes a simple corollary of this result.

Namely, from (44) it follows that, for an arbitrary natural number  $M$ , the off-shell action of the generating function  $\tau(\lambda)$  on the Bethe vectors

$$\Phi_M(\mu_1, \mu_2, \dots, \mu_M) = \mathcal{F}(\mu_1)\mathcal{F}(\mu_2)\cdots\mathcal{F}(\mu_M)\Omega_+, \tag{52}$$

is given by

$$\begin{aligned} \tau(\lambda)\Phi_M(\mu_1, \mu_2, \dots, \mu_M) &= \chi_M(\lambda, \mu_1, \mu_2, \dots, \mu_M) \Phi_M(\mu_1, \mu_2, \dots, \mu_M) \\ &+ \sum_{j=1}^M \frac{4\lambda}{\lambda^2 - \mu_j^2} \frac{\xi - \mu_j \sqrt{\psi\varphi + v^2}}{\xi - \lambda \sqrt{\psi\varphi + v^2}} \left( \rho(\mu_j) + \frac{(\psi\varphi + v^2)\mu_j}{\xi^2 - (\psi\varphi + v^2)\mu_j^2} - \sum_{k \neq j}^M \frac{2\mu_j}{\mu_j^2 - \mu_k^2} \right) \times \\ &\times \Phi_M(\lambda, \mu_1, \dots, \widehat{\mu}_j, \dots, \mu_M), \end{aligned} \tag{53}$$

where the eigenvalue  $\chi_M(\lambda, \mu_1, \mu_2, \dots, \mu_M)$  is given by

$$\begin{aligned} \chi_M(\lambda, \mu_1, \mu_2, \dots, \mu_M) &= \\ \chi_0(\lambda) - \sum_{j=1}^M \frac{4\lambda}{\lambda^2 - \mu_j^2} \left( \rho(\lambda) + \frac{(\psi\varphi + v^2)\lambda}{\xi^2 - (\psi\varphi + v^2)\lambda^2} - \sum_{k \neq j}^M \frac{\lambda}{\lambda^2 - \mu_k^2} \right). \end{aligned} \tag{54}$$

The unwanted terms on the right hand side of (53) are annihilated once the Bethe equations

$$\rho(\mu_j) + \frac{(\psi\varphi + v^2)\mu_j}{\xi^2 - (\psi\varphi + v^2)\mu_j^2} - \sum_{k \neq j}^M \frac{2\mu_j}{\mu_j^2 - \mu_k^2} = 0, \quad j = 1, 2, \dots, M, \tag{55}$$

are imposed on the parameters  $\mu_1, \mu_2, \dots, \mu_M$ .

The off-shell action of the  $so(3)$  Gaudin Hamiltonians with general boundary terms (29) on the Bethe vectors (52) is obtained by taking the residue, at  $\lambda = \alpha_m$ , of the equation (53)

$$\begin{aligned} H_m \Phi_M(\mu_1, \mu_2, \dots, \mu_M) &= \mathcal{E}_{m,M} \Phi_M(\mu_1, \mu_2, \dots, \mu_M) \\ &+ \sum_{j=1}^M \frac{4\alpha_m}{\alpha_m^2 - \mu_j^2} \frac{\xi - \mu_j \sqrt{\psi\varphi + v^2}}{\xi - \alpha_m \sqrt{\psi\varphi + v^2}} \times \\ &\times \left( \rho(\mu_j) + \frac{(\psi\varphi + v^2)\mu_j}{\xi^2 - (\psi\varphi + v^2)\mu_j^2} - \sum_{k \neq j}^M \frac{2\mu_j}{\mu_j^2 - \mu_k^2} \right) \times \\ &\times \left( \frac{-2(v + \sqrt{\psi\varphi + v^2})S_m^3 - \psi S_m^+ + \frac{\psi\varphi + 2v(v + \sqrt{\psi\varphi + v^2})}{\psi} S_m^-}{2\sqrt{\psi\varphi + v^2}} \right) \times \\ &\times \Phi_{M-1}(\mu_1, \dots, \widehat{\mu}_j, \dots, \mu_M), \end{aligned} \tag{56}$$

where

$$H_m = \text{Res}_{\lambda=\alpha_m} \tau(\lambda) \tag{57}$$

and the eigenvalues  $\mathcal{E}_{m,M}$  of the  $so(3)$  Gaudin Hamiltonians are the residues of the eigenvalues  $\chi_M(\lambda, \mu_1, \mu_2, \dots, \mu_M)$  (54) of the generating function  $\tau(\lambda)$  at  $\lambda = \alpha_m$ ,

$$\begin{aligned} \mathcal{E}_{m,M} &= \text{Res}_{\lambda=\alpha_m} \chi_M(\lambda, \mu_1, \mu_2, \dots, \mu_M) \\ &= \frac{2\xi^2}{(\xi^2 - (\psi\varphi + v^2)\alpha_m^2)\alpha_m} + \sum_{n \neq m}^N \frac{4\alpha_m}{\alpha_m^2 - \alpha_n^2} - \sum_{j=1}^M \frac{4\alpha_m}{\alpha_m^2 - \mu_j^2}, \end{aligned} \tag{58}$$

and

$$\begin{aligned} \operatorname{Res}_{\lambda=\alpha_m} \Phi_M(\lambda, \mu_1, \dots, \widehat{\mu}_j, \dots, \mu_M) &= \operatorname{Res}_{\lambda=\alpha_m} (\mathcal{F}(\lambda)) \cdot \Phi_{M-1}(\mu_1, \dots, \widehat{\mu}_j, \dots, \mu_M) \\ &= \left( \frac{-2(v + \sqrt{\psi\varphi + v^2})S_m^3 - \psi S_m^+ + \frac{\psi\varphi + 2v(v + \sqrt{\psi\varphi + v^2})}{\psi} S_m^-}{2\sqrt{\psi\varphi + v^2}} \right) \cdot \Phi_{M-1}(\mu_1, \dots, \widehat{\mu}_j, \dots, \mu_M), \end{aligned} \tag{59}$$

where the notation  $\widehat{\mu}_j$  means that the argument  $\mu_j$  is omitted.

As a closing remark for this section we must underline the complete generality of these results: the formulae for the off-shell action of the generating function  $\tau(\lambda)$  (53) and the  $so(3)$  Gaudin Hamiltonians on the Bethe vectors (52) are obtained for an arbitrary natural number  $M$  and without any restriction whatsoever on all four boundary parameters. In this sense we can say that these formulae are as general as they can possibly be. In the next section we will establish a correspondence between the Bethe vectors (52) established here and the solutions to the generalized  $so(3)$  Knizhnik-Zamolodchikov equations.

#### 4. Generalized $so(3)$ Knizhnik-Zamolodchikov equations

In this section we study solutions to the generalized  $so(3)$  Knizhnik-Zamolodchikov equations. To proceed further, we now have to set the parameter  $\xi$  to zero, i.e.  $\xi = 0$ . Consequently, the local realization of the generators (25) – (27) simplifies to

$$\widetilde{\mathcal{E}}(\lambda) = \sum_{m=1}^N \frac{\alpha_m}{\sqrt{\psi\varphi + v^2}} \frac{2(v - \sqrt{\psi\varphi + v^2})S_m^3 + \psi S_m^+ - \frac{\psi\varphi + 2v(v - \sqrt{\psi\varphi + v^2})}{\psi} S_m^-}{\lambda^2 - \alpha_m^2}, \tag{60}$$

$$\widetilde{\mathcal{F}}(\lambda) = \sum_{m=1}^N \frac{-\alpha_m}{\sqrt{\psi\varphi + v^2}} \frac{2(v + \sqrt{\psi\varphi + v^2})S_m^3 + \psi S_m^+ - \frac{\psi\varphi + 2v(v + \sqrt{\psi\varphi + v^2})}{\psi} S_m^-}{\lambda^2 - \alpha_m^2}, \tag{61}$$

$$\mathcal{H}(\lambda) = \frac{\lambda}{\sqrt{\psi\varphi + v^2}} \sum_{m=1}^N \frac{2vS_m^3 + \psi S_m^+ + \varphi S_m^-}{\lambda^2 - \alpha_m^2}. \tag{62}$$

These generators have the following non-trivial commutation relations

$$[\mathcal{H}(\lambda), \widetilde{\mathcal{E}}(\mu)] = \frac{-2\lambda}{\lambda^2 - \mu^2} (\widetilde{\mathcal{E}}(\lambda) - \widetilde{\mathcal{E}}(\mu)), \tag{63}$$

$$[\mathcal{H}(\lambda), \widetilde{\mathcal{F}}(\mu)] = \frac{2\lambda}{\lambda^2 - \mu^2} (\widetilde{\mathcal{F}}(\lambda) - \widetilde{\mathcal{F}}(\mu)), \tag{64}$$

$$[\widetilde{\mathcal{E}}(\lambda), \widetilde{\mathcal{F}}(\mu)] = \frac{-4}{\lambda^2 - \mu^2} (\lambda \mathcal{H}(\lambda) - \mu \mathcal{H}(\mu)). \tag{65}$$

Thus, in this case, the first Bethe vector is here defined by

$$\tilde{\Phi}_1(\mu) = \Phi_1(\mu) \Big|_{\xi=0} = \tilde{\mathcal{F}}(\mu)\Omega_+, \tag{66}$$

and, in general case, for the Bethe vectors  $\tilde{\Phi}_M(\mu_1, \mu_2, \dots, \mu_M)$  we have

$$\tilde{\Phi}_M(\mu_1, \mu_2, \dots, \mu_M) = \Phi_M(\mu_1, \mu_2, \dots, \mu_M) \Big|_{\xi=0} = \tilde{\mathcal{F}}(\mu_1)\tilde{\mathcal{F}}(\mu_2) \cdots \tilde{\mathcal{F}}(\mu_M)\Omega_+. \tag{67}$$

It is useful to explicitly write  $H_m$  for  $\xi = 0$ :

$$\begin{aligned} \tilde{H}_m = H_m \Big|_{\xi=0} &= \frac{1}{2(\psi\varphi + v^2)\alpha_m} \left( 2(v^2 - \psi\varphi)(S_m^3)^2 \right. \\ &+ \psi^2 (S_m^+)^2 + \varphi^2 (S_m^-)^2 + 2\psi v (S_m^+ S_m^3 + S_m^3 S_m^+) \\ &+ 2\varphi v (S_m^- S_m^3 + S_m^3 S_m^-) - v^2 (S_m^+ S_m^- + S_m^- S_m^+) \Big) \\ &+ \frac{1}{\psi\varphi + v^2} \sum_{n \neq m}^N \left( \frac{4(\psi\varphi\alpha_n + v^2\alpha_m)}{\alpha_m^2 - \alpha_n^2} S_m^3 S_n^3 + \frac{1}{\alpha_m + \alpha_n} \times \right. \\ &\times \left( \psi^2 S_m^+ S_n^+ + \varphi^2 S_m^- S_n^- + 2\psi v (S_m^+ S_n^3 + S_m^3 S_n^+) + 2\varphi v (S_m^- S_n^3 + S_m^3 S_n^-) \right) \\ &\left. + \frac{2v^2\alpha_n + \psi\varphi(\alpha_m + \alpha_n)}{\alpha_m^2 - \alpha_n^2} (S_m^- S_n^+ + S_m^+ S_n^-) \right). \end{aligned} \tag{68}$$

Therefore the off-shell action of these Hamiltonians reads

$$\begin{aligned} \tilde{H}_m \tilde{\Phi}_M(\mu_1, \mu_2, \dots, \mu_M) &= \\ \tilde{\mathcal{E}}_{m,M} \tilde{\Phi}_M(\mu_1, \mu_2, \dots, \mu_M) &+ \sum_{j=1}^M \frac{(-2)\mu_j}{\alpha_m^2 - \mu_j^2} \beta_M(\mu_j) \tilde{\Phi}_{M-1}^{(j,m)}, \end{aligned} \tag{69}$$

where

$$\tilde{\mathcal{E}}_{m,M} = \mathcal{E}_{m,M} \Big|_{\xi=0} = \sum_{n \neq m}^N \frac{4\alpha_m}{\alpha_m^2 - \alpha_n^2} - \sum_{j=1}^M \frac{4\alpha_m}{\alpha_m^2 - \mu_j^2}, \tag{70}$$

$$\beta_M(\mu_j) = -2 \left( \rho(\mu_j) - \frac{1}{\mu_j} - \sum_{k \neq j}^M \frac{2\mu_j}{\mu_j^2 - \mu_k^2} \right), \tag{71}$$

and

$$\begin{aligned} \tilde{\Phi}_{M-1}^{(j,m)} &= \left( \frac{-2(v + \sqrt{\psi\varphi + v^2})S_m^3 - \psi S_m^+ + \frac{\psi\varphi + 2v(v + \sqrt{\psi\varphi + v^2})}{\psi} S_m^-}{2\sqrt{\psi\varphi + v^2}} \right) \\ &\cdot \tilde{\Phi}_{M-1}(\mu_1, \dots, \hat{\mu}_j, \dots, \mu_M). \end{aligned} \tag{72}$$

Our main objective in this section is to show how to each Bethe vector (67) we can relate a solution to the generalized  $so(3)$  Knizhnik-Zamolodchikov equations

$$\kappa \partial_{\alpha_m} \Psi(\alpha_1, \alpha_2, \dots, \alpha_N) = \tilde{H}_m \Psi(\alpha_1, \alpha_2, \dots, \alpha_N). \tag{73}$$

Within our approach [22,61,15–17,86,89] this correspondence is defined by a closed contour integration with respect to the variables  $\mu_1, \mu_2, \dots, \mu_M$

$$\Psi(\alpha_1, \alpha_2, \dots, \alpha_N) = \oint \oint \dots \oint \Upsilon(\vec{\mu}; \vec{\alpha}) \cdot \tilde{\Phi}_M(\vec{\mu}; \vec{\alpha}) d\mu_1 d\mu_2 \dots d\mu_M. \tag{74}$$

The scalar function  $\Upsilon(\vec{\mu}; \vec{\alpha})$  is defined by

$$\Upsilon(\vec{\mu}; \vec{\alpha}) = \exp\left(\frac{S(\vec{\mu}; \vec{\alpha})}{\kappa}\right), \tag{75}$$

with the constant  $\kappa$  and the function  $S(\vec{\mu}; \vec{\alpha})$  specified by

$$S(\vec{\mu}; \vec{\alpha}) = \sum_{m=1}^N \left( \sum_{n \neq m}^N \ln(\alpha_n^2 - \alpha_m^2) - \sum_{j=1}^M 2 \ln(\mu_j^2 - \alpha_m^2) \right) \tag{76}$$

$$+ \sum_{j=1}^M \left( \ln(\mu_j^2) + \sum_{k \neq j}^M \ln(\mu_j^2 - \mu_k^2) \right). \tag{77}$$

It is straightforward to check that the function  $\Upsilon(\vec{\mu}; \vec{\alpha})$  satisfies the system

$$\kappa \partial_{\alpha_m} \Upsilon = \tilde{\mathcal{E}}_{m,M} \Upsilon, \tag{78}$$

$$\kappa \partial_{\mu_j} \Upsilon = \beta_M(\mu_j) \Upsilon, \tag{79}$$

where  $\tilde{\mathcal{E}}_{m,M}$  and  $\beta_M(\mu_j)$  are defined in (70) and (71), respectively.

The crucial identity in our approach is

$$\partial_{\alpha_m} \tilde{\Phi}_M = \sum_{j=1}^M \partial_{\mu_j} \left( \frac{2\mu_j}{\alpha_m^2 - \mu_j^2} \tilde{\Phi}_{M-1}^{(j,m)} \right). \tag{80}$$

It takes a few rather simple steps to confirm that the function  $\Psi(\alpha_1, \alpha_2, \dots, \alpha_N)$  (74) is a solution to the generalized  $so(3)$  Knizhnik-Zamolodchikov equations (73). As the first step, using the Leibniz rule, we calculate

$$\kappa \partial_{\alpha_m} (\Upsilon \cdot \tilde{\Phi}_M) = (\kappa \partial_{\alpha_m} \Upsilon) \cdot \tilde{\Phi}_M + \Upsilon \cdot (\kappa \partial_{\alpha_m} \tilde{\Phi}_M). \tag{81}$$

Then we use the equation (78) in the first term on the right hand side of the equation above and the identity (80) in the second term

$$\kappa \partial_{\alpha_m} (\Upsilon \cdot \tilde{\Phi}_M) = \mathcal{E}_{m,M} (\Upsilon \cdot \tilde{\Phi}_M) + \Upsilon \cdot \kappa \sum_{j=1}^M \partial_{\mu_j} \left( \frac{2\mu_j}{\alpha_m^2 - \mu_j^2} \tilde{\Phi}_{M-1}^{(j,m)} \right). \tag{82}$$

In the following step we use the equation (69) in the first term and the Leibniz rule in the second term on the right hand side of the equation above



$$\begin{aligned} \kappa \partial_{\alpha_m} (\Upsilon \cdot \tilde{\Phi}_M) &= \tilde{H}_m (\Upsilon \cdot \tilde{\Phi}_M) + \sum_{j=1}^M \frac{2\mu_j}{\alpha_m^2 - \mu_j^2} \beta_M(\mu_j) \cdot \Upsilon \cdot \tilde{\Phi}_{M-1}^{(j,m)} \\ &+ \kappa \sum_{j=1}^M \partial_{\mu_j} \left( \frac{2\mu_j}{\alpha_m^2 - \mu_j^2} \Upsilon \cdot \tilde{\Phi}_{M-1}^{(j,m)} \right) - \kappa \sum_{j=1}^M (\partial_{\mu_j} \Upsilon) \frac{2\mu_j}{\alpha_m^2 - \mu_j^2} \tilde{\Phi}_{M-1}^{(j,m)}. \end{aligned} \tag{83}$$

Now it remains to rewrite the last terms on the right hand side using the equation (79)

$$\begin{aligned} \kappa \partial_{\alpha_m} (\Upsilon \cdot \tilde{\Phi}_M) &= \tilde{H}_m (\Upsilon \cdot \tilde{\Phi}_M) + \sum_{j=1}^M \frac{2\mu_j}{\alpha_m^2 - \mu_j^2} \beta_M(\mu_j) \cdot \Upsilon \cdot \tilde{\Phi}_{M-1}^{(j,m)} \\ &+ \kappa \sum_{j=1}^M \partial_{\mu_j} \left( \frac{2\mu_j}{\alpha_m^2 - \mu_j^2} \Upsilon \cdot \tilde{\Phi}_{M-1}^{(j,m)} \right) - \sum_{j=1}^M \frac{2\mu_j}{\alpha_m^2 - \mu_j^2} \beta_M(\mu_j) \cdot \Upsilon \cdot \tilde{\Phi}_{M-1}^{(j,m)}. \end{aligned} \tag{84}$$

As the final step of this demonstration, we simplify the second and the last term in the equation above in order to obtain the desired result

$$\kappa \partial_{\alpha_m} (\Upsilon \cdot \tilde{\Phi}_M) = \tilde{H}_m (\Upsilon \cdot \tilde{\Phi}_M) + \kappa \sum_{j=1}^M \partial_{\mu_j} \left( \frac{2\mu_j}{\alpha_m^2 - \mu_j^2} \Upsilon \cdot \tilde{\Phi}_{M-1}^{(j,m)} \right). \tag{85}$$

This shows that the function  $\Psi(\alpha_1, \alpha_2, \dots, \alpha_N)$  (74) is a solution to the generalized  $so(3)$  Knizhnik-Zamolodchikov equations (73) since the terms in the sum will not contribute to the closed contour integrals with respect to the variables  $\mu_j, j = 1, 2, \dots, M$ .

In the final part of this section we determine the on-shell norm as well as the off-shell scalar products of the Bethe vectors (67). In particular, the on-shell norm of the Bethe vector (66) is obtained to be

$$\begin{aligned} \|\tilde{\Phi}_1(\mu)\|^2 &= \lim_{\nu \rightarrow \mu} \langle \Omega_+, \tilde{\mathcal{E}}(\nu) \tilde{\mathcal{F}}(\mu) \Omega_+ \rangle = -2 \left( \rho'(\mu) + \frac{\rho(\mu)}{\mu} \right) \\ &= \frac{\partial \beta_1(\mu)}{\partial \mu} \Big|_{\beta_1(\mu)=0} = \frac{\partial^2 S(\mu)}{\partial \mu^2} \Big|_{\beta_1(\mu)=0}. \end{aligned} \tag{86}$$

Similarly, the norm of the Bethe vector

$$\tilde{\Phi}_2(\mu_1, \mu_2) = \tilde{\mathcal{F}}(\mu_1) \tilde{\mathcal{F}}(\mu_2) \Omega_+, \tag{87}$$

when the Bethe equations are imposed on the parameters  $\mu_1$  and  $\mu_2$ , is given by

$$\begin{aligned} \|\tilde{\Phi}_2(\mu_1, \mu_2)\|^2 &= \lim_{\substack{\nu_1 \rightarrow \mu_1 \\ \nu_2 \rightarrow \mu_2}} \langle \Omega_+, \tilde{\mathcal{E}}(\nu_1) \tilde{\mathcal{E}}(\nu_2) \tilde{\mathcal{F}}(\mu_2) \tilde{\mathcal{F}}(\mu_1) \Omega_+ \rangle \\ &= 4 \rho'(\mu_1) \rho'(\mu_2) + 4 \rho'(\mu_1) \left( \frac{1}{\mu_2^2} + \frac{2}{\mu_2^2 - \mu_1^2} + \frac{4\mu_1^2}{(\mu_2^2 - \mu_1^2)^2} \right) \\ &+ 4 \rho'(\mu_2) \left( \frac{1}{\mu_1^2} + \frac{2}{\mu_1^2 - \mu_2^2} + \frac{4\mu_2^2}{(\mu_2^2 - \mu_1^2)^2} \right) + 12 \frac{(\mu_1^2 + \mu_2^2)^2}{\mu_1^2 \mu_2^2 (\mu_2^2 - \mu_1^2)^2} \end{aligned} \tag{88}$$

$$= \det \left( \begin{array}{cc} \frac{\partial \beta_2(\mu_1)}{\partial \mu_1} & \frac{\partial \beta_2(\mu_2)}{\partial \mu_1} \\ \frac{\partial \beta_2(\mu_1)}{\partial \mu_2} & \frac{\partial \beta_2(\mu_2)}{\partial \mu_2} \end{array} \right) \Bigg|_{\substack{\beta_2(\mu_1)=0 \\ \beta_2(\mu_2)=0}} = \det \left( \begin{array}{cc} \frac{\partial^2 S}{\partial \mu_1^2} & \frac{\partial^2 S}{\partial \mu_1 \partial \mu_2} \\ \frac{\partial^2 S}{\partial \mu_2 \partial \mu_1} & \frac{\partial^2 S}{\partial \mu_2^2} \end{array} \right) \Bigg|_{\substack{\beta_2(\mu_1)=0 \\ \beta_2(\mu_2)=0}} .$$

In the general case, for an arbitrary positive integer  $M$ , the norm of the Bethe vector  $\tilde{\Phi}_M(\mu_1, \mu_2, \dots, \mu_M)$  (67), when the Bethe equations

$$\beta_M(\mu_j) = -2 \left( \rho(\mu_j) - \frac{1}{\mu_j} - \sum_{k \neq j}^M \frac{2\mu_j}{\mu_j^2 - \mu_k^2} \right) = 0, \quad j = 1, 2, \dots, M, \tag{89}$$

are imposed on the parameter  $\mu_1, \dots, \mu_M$ , is obtained to be

$$\|\tilde{\Phi}_M(\mu_1, \mu_2, \dots, \mu_M)\|^2 = \det \left( \begin{array}{cccc} \frac{\partial^2 S}{\partial \mu_1^2} & \frac{\partial^2 S}{\partial \mu_1 \partial \mu_2} & \cdots & \frac{\partial^2 S}{\partial \mu_1 \partial \mu_M} \\ \vdots & \ddots & & \vdots \\ \frac{\partial^2 S}{\partial \mu_M \partial \mu_1} & \frac{\partial^2 S}{\partial \mu_M \partial \mu_2} & \cdots & \frac{\partial^2 S}{\partial \mu_M^2} \end{array} \right) \Bigg|_{\substack{\beta_M(\mu_1)=0 \\ \vdots \\ \beta_M(\mu_M)=0}} . \tag{90}$$

Finally, we also calculate the off-shell scalar products of the Bethe vectors  $\tilde{\Phi}_M(\mu_1, \mu_2, \dots, \mu_M)$  (67). As our first step, we observe that in the case when  $M = 1$  the scalar product is

$$\langle \tilde{\Phi}_1(\mu), \tilde{\Phi}_1(v) \rangle = 4 \left( -\frac{\mu \rho(\mu) - v \rho(v)}{\mu^2 - v^2} \right) . \tag{91}$$

For  $M = 2$ , a straightforward calculation yields

$$\langle \tilde{\Phi}_2(\mu_1, \mu_2), \tilde{\Phi}_2(v_1, v_2) \rangle = 4^2 \sum_{\sigma \in \mathcal{S}_2} \det \mathcal{M}^\sigma = 16 \left( \det \mathcal{M}^1 + \det \mathcal{M}^2 \right) , \tag{92}$$

where  $\mathcal{S}_2$  is the symmetric group of degree two and the two-by-two matrices  $\mathcal{M}^1$  and  $\mathcal{M}^2$  are given by

$$\begin{aligned} \mathcal{M}_{11}^1 &= -\frac{\mu_1 \rho(\mu_1) - v_1 \rho(v_1)}{\mu_1^2 - v_1^2} - \frac{\mu_2^2 + v_2^2}{(\mu_1^2 - \mu_2^2)(v_1^2 - v_2^2)} , \\ \mathcal{M}_{12}^1 &= -\frac{\mu_2^2 + v_2^2}{(\mu_1^2 - \mu_2^2)(v_1^2 - v_2^2)} , \\ \mathcal{M}_{22}^1 &= -\frac{\mu_2 \rho(\mu_2) - v_2 \rho(v_2)}{\mu_2^2 - v_2^2} - \frac{\mu_1^2 + v_1^2}{(\mu_2^2 - \mu_1^2)(v_2^2 - v_1^2)} , \\ \mathcal{M}_{21}^1 &= -\frac{\mu_1^2 + v_1^2}{(\mu_2^2 - \mu_1^2)(v_2^2 - v_1^2)} , \end{aligned} \tag{93}$$

and

$$\begin{aligned}
 \mathcal{M}_{11}^2 &= -\frac{\mu_1 \rho(\mu_1) - \nu_2 \rho(\nu_2)}{\mu_1^2 - \nu_2^2} - \frac{\mu_2^2 + \nu_1^2}{(\mu_1^2 - \mu_2^2)(\nu_2^2 - \nu_1^2)}, \\
 \mathcal{M}_{12}^2 &= -\frac{\mu_2^2 + \nu_1^2}{(\mu_1^2 - \mu_2^2)(\nu_2^2 - \nu_1^2)}, \\
 \mathcal{M}_{22}^2 &= -\frac{\mu_2 \rho(\mu_2) - \nu_1 \rho(\nu_1)}{\mu_2^2 - \nu_1^2} - \frac{\mu_1^2 + \nu_2^2}{(\mu_2^2 - \mu_1^2)(\nu_1^2 - \nu_2^2)}, \\
 \mathcal{M}_{21}^2 &= -\frac{\mu_1^2 + \nu_2^2}{(\mu_2^2 - \mu_1^2)(\nu_1^2 - \nu_2^2)}.
 \end{aligned} \tag{94}$$

In general case, for an arbitrary positive integer  $M$ , we have

$$(\tilde{\Phi}_M(\mu_1, \mu_2, \dots, \mu_M), \tilde{\Phi}_M(\nu_1, \nu_2, \dots, \nu_M)) = 4^M \sum_{\sigma \in \tilde{S}_M} \det \mathcal{M}^\sigma, \tag{95}$$

where  $\tilde{S}_M$  is the symmetric group of degree  $M$  and the matrix entries of the  $M \times M$  matrix  $\mathcal{M}^\sigma$  are given by

$$\mathcal{M}_{jj}^\sigma = -\frac{\mu_j \rho(\mu_j) - \nu_{\sigma(j)} \rho(\nu_{\sigma(j)})}{\mu_j^2 - \nu_{\sigma(j)}^2} - \sum_{k \neq j} \frac{\mu_k^2 + \nu_{\sigma(k)}^2}{(\mu_j^2 - \mu_k^2)(\nu_{\sigma(j)}^2 - \nu_{\sigma(k)}^2)}, \tag{96}$$

$$\mathcal{M}_{jk}^\sigma = -\frac{\mu_k^2 + \nu_{\sigma(k)}^2}{(\mu_j^2 - \mu_k^2)(\nu_{\sigma(j)}^2 - \nu_{\sigma(k)}^2)}, \quad \text{for } j, k = 1, 2, \dots, M. \tag{97}$$

The off-shell scalar products of the Bethe vectors  $\tilde{\Phi}_M(\mu_1, \mu_2, \dots, \mu_M)$  (67) in the  $M = 1$  case (91) and in the  $M = 2$  case (92) were derived by a direct, straightforward calculations. The formula (95) was obtained by symbolic computer calculations for  $M = 3, 4, 5$ , for some values of  $N$ . In the general case, the proof of these formulae by induction would be very difficult, since it would require some highly non-trivial relations between a certain type of determinants of a different order. In this sense, the general formula (95), strictly speaking, remains a conjecture.

### 5. Conclusions

The cornerstone of our study of the non-periodic  $so(3)$  Gaudin model was the  $so(3)$  Maillet linear bracket (8) for the suitable Lax operator (7) and the non-unitary  $so(3)$  classical r-matrix (B.8) constructed from the generic boundary K-matrix (B.4). Based on Maillet bracket we obtained the generating function (15) of the  $so(3)$  Gaudin Hamiltonians with general boundary terms. However it turned out that the natural set of generators was not the most efficient choice for implementing the algebraic Bethe ansatz due to the cumbersome commutation relations (9) - (14). For this reason we proposed a new set of generators: (18) - (20). Not only that their commutation relations had a strikingly compact form (21) - (24) but also their local realization was fairly simple (25) - (27), yielding the explicit expression for the Gaudin Hamiltonians with all four boundary parameters (29).

There were several preceding objectives which we had to address before attempting to find the off-shell action of the generating function  $\tau(\lambda)$  (28). In the first place, we had to define the

so-called vacuum vector  $\Omega_+$  (30) - (33). Then we had to confirm the action of the generators on the vacuum vectors (34) and to show that the vector  $\Omega_+$  is the eigenvector of the generating function  $\tau(\lambda)$  (39). As our next step, we have calculated the commutation relations between the generating function  $\tau(\lambda)$  and the remaining generator  $\mathcal{F}(\mu)$  of the generalized  $so(3)$  Gaudin algebra (41). The idea of using the generator  $\mathcal{F}(\mu)$  as the so-called creation operator prompted us to calculate the commutation relations between the generating function  $\tau(\lambda)$  and the product  $\mathcal{F}(\mu_1)\mathcal{F}(\mu_2)$  (42) as well as the product  $\mathcal{F}(\mu_1)\mathcal{F}(\mu_2)\mathcal{F}(\mu_3)$  (43). Hence, we have conjectured the formula (44), in the general case, for the commutator between the generating function  $\tau(\lambda)$  and the product  $\mathcal{F}(\mu_1)\mathcal{F}(\mu_2)\cdots\mathcal{F}(\mu_M)$ , for an arbitrary natural number  $M$ . The proof of the formula (44) based on the mathematical induction was presented in (45) - (51). Once we have accordingly defined the Bethe vectors (52), the off-shell action (53) of the generating function  $\tau(\lambda)$ , including the formulae for the eigenvalues (54) and the Bethe equations (55), followed from (44). Moreover, the off-shell action (56) of the Gaudin Hamiltonians (29) on the Bethe vectors (52) was obtained by taking the residue, at  $\lambda = \alpha_m$ , of the left and the right hand side of (53). It should be stressed that the formulae of the off-shell action (53) and (56) have been obtained without any restriction whatsoever on any of the four boundary parameters and therefore we can say that these formulae are as general as they can possibly be.

Next, we found the solutions to the generalized  $so(3)$  Knizhnik-Zamolodchikov equations (73). In spite that the key identity (80) in the proof required the parameter  $\xi$  to be set to zero, the formulae we obtained for the solutions to the generalized  $so(3)$  Knizhnik-Zamolodchikov equations (74), the on-shell norm of the Bethe vectors (90) and the off-shell scalar product of the Bethe vectors (95) – all possess higher degree of generality than the analogous formulae in the  $s\ell(2)$  case [86] (here we have fixed only one of the four boundary parameters instead of all four).

In our future research we hope to address the remaining open problem of correlation functions for the  $so(3)$  Gaudin model with general boundary, following Sklyanin approach in the periodic  $s\ell(2)$  case [100].

## CRediT authorship contribution statement

**N. Manojlović:** Conceptualization, Formal analysis, Methodology, Writing – original draft.  
**I. Salom:** Formal analysis, Methodology, Software, Writing – review & editing.

## Declaration of competing interest

The authors declare the following financial interests/personal relationships which may be considered as potential competing interests:

Igor Salom reports financial support was provided by Republic of Serbia Ministry of Education Science and Technological Development.

## Acknowledgements

The authors thank to Rodrigo Pimenta for helpful discussions. IS is supported by the Ministry of Education, Science and Technological Development (MPNTR) of the Republic of Serbia, and by the Science Fund of the Republic of Serbia, Program DIASPORA, No. 6427195, SQ2020.

### Appendix A. Preliminaries

Some essential definitions regarding the  $so(3)$  Lie algebra and its fundamental representation are given in the Appendix A. Namely, we consider the spin one operators

$$S^x = \frac{1}{\sqrt{2}} \begin{pmatrix} 0 & 1 & 0 \\ 1 & 0 & 1 \\ 0 & 1 & 0 \end{pmatrix}, \quad S^y = \frac{i}{\sqrt{2}} \begin{pmatrix} 0 & -1 & 0 \\ 1 & 0 & -1 \\ 0 & 1 & 0 \end{pmatrix}, \quad S^z = \begin{pmatrix} 1 & 0 & 0 \\ 0 & 0 & 0 \\ 0 & 0 & -1 \end{pmatrix} \quad (\text{A.1})$$

acting in the space  $V^{(1)} = \mathbb{C}^3$  with the commutation relations

$$[S^x, S^y] = iS^z, \quad [S^z, S^x] = iS^y, \quad [S^y, S^z] = iS^x$$

and the Casimir element

$$c_2 = \vec{S} \cdot \vec{S} = (S^x)^2 + (S^y)^2 + (S^z)^2 = 2\mathbb{1}. \quad (\text{A.2})$$

Introducing raising and lowering operators

$$S^+ = S^x + iS^y = \begin{pmatrix} 0 & \sqrt{2} & 0 \\ 0 & 0 & \sqrt{2} \\ 0 & 0 & 0 \end{pmatrix}, \quad S^- = S^x - iS^y = \begin{pmatrix} 0 & 0 & 0 \\ \sqrt{2} & 0 & 0 \\ 0 & \sqrt{2} & 0 \end{pmatrix}, \quad (\text{A.3})$$

the relations above can also be written as

$$[S^z, S^\pm] = \pm S^\pm, \quad [S^+, S^-] = 2S^z, \quad (\text{A.4})$$

and

$$c_2 = (S^z)^2 + \frac{1}{2}(S^+S^- + S^-S^+) = (S^z)^2 + S^z + S^-S^+. \quad (\text{A.5})$$

It is useful to notice that the tensor Casimir operator can be expressed as follows

$$c_2^\otimes(1, 2) = \vec{S}_1 \cdot \vec{S}_2 = \mathcal{P} - 3\mathcal{K}. \quad (\text{A.6})$$

The permutation operator

$$\mathcal{P} = \left( \begin{array}{ccc|ccc|ccc} 1 & 0 & 0 & 0 & 0 & 0 & 0 & 0 & 0 \\ 0 & 0 & 0 & 1 & 0 & 0 & 0 & 0 & 0 \\ 0 & 0 & 0 & 0 & 0 & 0 & 1 & 0 & 0 \\ \hline 0 & 1 & 0 & 0 & 0 & 0 & 0 & 0 & 0 \\ 0 & 0 & 0 & 0 & 1 & 0 & 0 & 0 & 0 \\ 0 & 0 & 0 & 0 & 0 & 0 & 0 & 1 & 0 \\ \hline 0 & 0 & 1 & 0 & 0 & 0 & 0 & 0 & 0 \\ 0 & 0 & 0 & 0 & 0 & 1 & 0 & 0 & 0 \\ 0 & 0 & 0 & 0 & 0 & 0 & 0 & 0 & 1 \end{array} \right), \quad (\text{A.7})$$

the rank 1 projector



$$\mathcal{K} = \frac{1}{3} \left( \begin{array}{ccc|ccc|ccc} 0 & 0 & 0 & 0 & 0 & 0 & 0 & 0 & 0 \\ 0 & 0 & 0 & 0 & 0 & 0 & 0 & 0 & 0 \\ 0 & 0 & 1 & 0 & -1 & 0 & 1 & 0 & 0 \\ \hline 0 & 0 & 0 & 0 & 0 & 0 & 0 & 0 & 0 \\ 0 & 0 & -1 & 0 & 1 & 0 & -1 & 0 & 0 \\ 0 & 0 & 0 & 0 & 0 & 0 & 0 & 0 & 0 \\ \hline 0 & 0 & 1 & 0 & -1 & 0 & 1 & 0 & 0 \\ 0 & 0 & 0 & 0 & 0 & 0 & 0 & 0 & 0 \\ 0 & 0 & 0 & 0 & 0 & 0 & 0 & 0 & 0 \end{array} \right) \quad (\text{A.8})$$

and the identity operator  $\mathbb{1}$  satisfy the relations

$$\mathcal{P}^2 = \mathbb{1}, \quad \mathcal{K}^2 = \mathcal{K}, \quad \mathcal{P}\mathcal{K} = \mathcal{K}\mathcal{P} = \mathcal{K}. \quad (\text{A.9})$$

and therefore define the representation of the Brauer algebra in  $\mathbb{C}^3 \otimes \mathbb{C}^3$ . Moreover these are the three invariant operators acting on  $\mathbb{C}^3 \otimes \mathbb{C}^3$

$$[\mathcal{S}^\alpha \otimes \mathbb{1} + \mathbb{1} \otimes \mathcal{S}^\alpha, \mathcal{P}] = 0, \quad [\mathcal{S}^\alpha \otimes \mathbb{1} + \mathbb{1} \otimes \mathcal{S}^\alpha, \mathcal{K}] = 0, \quad (\text{A.10})$$

here  $\alpha = x, y, z$ .

In our study of the  $so(3)$  Gaudin model with  $N$  sites, characterised by the local space  $V_m = \mathbb{C}^3$  together with the corresponding inhomogeneous parameter  $\alpha_m$ , the Hilbert space is given by

$$\mathcal{H} = \bigotimes_{m=1}^N V_m = (\mathbb{C}^3)^{\otimes N}. \quad (\text{A.11})$$

The local spin operators

$$S_m^\alpha = \mathbb{1} \otimes \dots \otimes \underbrace{S_m^\alpha}_m \otimes \dots \otimes \mathbb{1}, \quad (\text{A.12})$$

with  $\alpha = x, y, z$  and  $m = 1, 2, \dots, N$ , are given by the matrices (A.3) and (A.1) in every local space  $V_m = \mathbb{C}^3$ . Evidently, they satisfy the usual commutation relations

$$[S_m^3, S_n^\pm] = \pm S_m^\pm \delta_{mn}, \quad [S_m^+, S_n^-] = 2S_m^3 \delta_{mn}. \quad (\text{A.13})$$

### Appendix B. The non-unitary $so(3)$ classical r-matrix

The cornerstone of our study presented in this paper is the non-unitary  $so(3)$  classical r-matrix (B.8). Here, in the Appendix B, we recount how the r-matrix (B.8) can be obtained starting from the unitary,  $so(3)$  invariant classical r-matrix

$$r(\lambda) = -\frac{\vec{S}_1 \cdot \vec{S}_2}{\lambda} = -\frac{\mathcal{P} - 3\mathcal{K}}{\lambda}, \quad (\text{B.1})$$

where we have used the notation introduced in the Appendix A. In particular, the classical r-matrix (B.1) can be obtained as a quasi-classical limit of the  $SO(3)$  quantum R-matrix [98,99,6]. Evidently, this classical r-matrix satisfies the classical Yang-Baxter equation [10]

$$[r_{12}(\lambda - \mu), r_{13}(\lambda - \nu)] + [r_{12}(\lambda - \mu), r_{23}(\mu - \nu)] + [r_{13}(\lambda - \nu), r_{23}(\mu - \nu)] = 0, \quad (\text{B.2})$$

and has the unitarity property

$$r_{21}(-\lambda) = -r_{12}(\lambda). \quad (\text{B.3})$$

We also consider the following reflection matrix

$$K(\lambda) = \begin{pmatrix} (\xi - \nu\lambda)^2 & -\sqrt{2}\psi\lambda(\xi - \nu\lambda) & \psi^2\lambda^2 \\ -\sqrt{2}\varphi\lambda(\xi - \nu\lambda) & \xi^2 + (\psi\varphi - \nu^2)\lambda^2 & -\sqrt{2}\psi\lambda(\xi + \nu\lambda) \\ \varphi^2\lambda^2 & -\sqrt{2}\varphi\lambda(\xi + \nu\lambda) & (\xi + \nu\lambda)^2 \end{pmatrix}, \tag{B.4}$$

here  $\xi, \nu, \psi, \varphi$  are arbitrary parameters. As it is well known, this K-matrix can be obtained by the so-called fusion procedure [6,90,91], starting from the  $sl(2)$  K-matrix [58,92–94]. This method is outlined, in the trigonometric  $so(3)$ , in [95]. Alternatively, the so-called scaling limit [96] can be used to obtain the K-matrix (B.4) from the trigonometric  $so(3)$  boundary K-matrix [95,97]. Evidently, this K-matrix satisfies the classical reflection equation

$$r_{12}(\lambda - \mu)K_1(\lambda)K_2(\mu) + K_1(\lambda)r_{21}(\lambda + \mu)K_2(\mu) = K_2(\mu)r_{12}(\lambda + \mu)K_1(\lambda) + K_2(\mu)K_1(\lambda)r_{21}(\lambda - \mu). \tag{B.5}$$

It is worth mentioning that, while in the context of Heisenberg’s open spin chain, one should also consider the dual reflection equation, this is not the case in the Gaudin model. Namely, as a consequence of long-range Gaudin model interactions, the “two ends of the chain” cannot have the same interpretation as in the case of Heisenberg’s spin chain. In the Gaudin case, boundary parameters must be fixed in a way that the reflection equation and its dual effectively degenerate into a single equation.

Therefore, it follows that the corresponding non-unitary classical r-matrix, given by [69,76–82]

$$r_{12}^K(\lambda, \mu) = r_{12}(\lambda - \mu) - K_2(\mu)r_{12}(\lambda + \mu)K_2^{-1}(\mu), \tag{B.6}$$

satisfies the generalized classical Yang-Baxter equation [69,72–75]

$$\left[ r_{32}^K(\nu, \mu), r_{13}^K(\lambda, \nu) \right] + \left[ r_{12}^K(\lambda, \mu), r_{13}^K(\lambda, \nu) \right] + \left[ r_{12}^K(\lambda, \mu), r_{23}^K(\mu, \nu) \right] = 0. \tag{B.7}$$

The explicit form of this non-unitary  $so(3)$  classical r-matrix is the following

$$r_{12}^K(\lambda, \mu) = - \left( \frac{\vec{\mathfrak{S}}_1 \cdot \vec{\mathfrak{S}}_2}{\lambda - \mu} - \frac{\vec{\mathfrak{S}}_1 \cdot \left( K_2(\mu)\vec{\mathfrak{S}}_2 K_2^{-1}(\mu) \right)}{\lambda + \mu} \right). \tag{B.8}$$

## References

- [1] W. Heisenberg, Zur Theorie der Ferromagnetismus, *Z. Phys.* 49 (1928) 619–636.
- [2] M. Gaudin, Diagonalisation d’une classe d’hamiltoniens de spin, *J. Phys.* 37 (1976) 1087–1098.
- [3] M. Gaudin, *La fonction d’onde de Bethe*, Masson, Paris, 1983.
- [4] M. Gaudin, *The Bethe Wavefunction*, Cambridge University Press, 2014.
- [5] L.A. Takhtajan, L.D. Faddeev, The quantum method for the inverse problem and the XYZ Heisenberg model, *Usp. Mat. Nauk* 34 (5) (1979) 13–63 (in Russian); translation in *Russ. Math. Surv.* 34 (5) (1979) 11–68.
- [6] P.P. Kulish, E.K. Sklyanin, Quantum spectral transform method. Recent developments, *Lect. Notes Phys.* 151 (1982) 61–119.
- [7] L.D. Faddeev, How the algebraic Bethe ansatz works for integrable models, in: A. Connes, K. Gawedzki, J. Zinn-Justin (Eds.), *Quantum Symmetries / Symetries Quantiques, Proceedings of the les Houches Summer School, Session LXIV*, North-Holland, 1998, pp. 149–219, arXiv:hep-th/9605187.
- [8] E.K. Sklyanin, Separation of variables in the Gaudin model, *Zap. Nauč. Semin.* 164 (1987) 151–169, <https://doi.org/10.1007/BF01840429>.

- [9] P.P. Kulish, E.K. Sklyanin, Solutions of the Yang-Baxter equation, *Zap. Nauč. Semin. POMI* 95 (1980) 129–160 (in Russian); translation in *J. Sov. Math.* 19 (1982) 1596–1620.
- [10] A.A. Belavin, V.G. Drinfeld, Solutions of the classical Yang-Baxter equation for simple Lie algebras, *Funkc. Anal. Prilozh.* 16 (3) (1982) 1–29 (in Russian); translation in *Funct. Anal. Appl.* 16 (3) (1982) 159–180.
- [11] B. Jurčo, Classical Yang-Baxter equations and quantum integrable systems (Gaudin models), in quantum groups, in: *Quantum Groups*, Clausthal, 1989, in: *Lecture Notes in Phys.*, vol. 370, 1990, pp. 219–227.
- [12] M.A. Semenov-Tian-Shansky, Quantum and classical integrable systems, in: *Integrability of Nonlinear Systems*, in: *Lecture Notes in Physics*, vol. 495, 1997, pp. 314–377.
- [13] F. Wagner, A.J. Macfarlane, Solvable Gaudin models for higher rank symplectic algebras, in: *Quantum Groups and Integrable Systems*, Prague, 2000, *Czechoslov. J. Phys.* 50 (2000) 1371–1377.
- [14] T. Brzezinski, A.J. Macfarlane, On integrable models related to the  $osp(1,2)$  Gaudin algebra, *J. Math. Phys.* 35 (7) (1994) 3261–3272.
- [15] P.P. Kulish, N. Manojlović, Bethe vectors of the  $osp(1|2)$  Gaudin model, *Lett. Math. Phys.* 55 (2001) 77–95, <https://doi.org/10.1023/A:1010950003268>.
- [16] P.P. Kulish, N. Manojlović, Creation operators and Bethe vectors of the  $osp(1|2)$  Gaudin model, *J. Math. Phys.* 42 (2001) 4757–4778, <https://doi.org/10.1063/1.1398584>.
- [17] P.P. Kulish, N. Manojlović, Trigonometric  $osp(1|2)$  Gaudin model, *J. Math. Phys.* 44 (2003) 676–700, <https://doi.org/10.1063/1.1531250>.
- [18] A. Lima-Santos, W. Utiel, Off-shell Bethe ansatz equation for  $osp(2|1)$  Gaudin magnets, *Nucl. Phys. B* 600 (2001) 512–530.
- [19] V.G. Knizhnik, A.B. Zamolodchikov, Current algebras and Wess-Zumino model in two dimensions, *Nucl. Phys. B* 247 (1984) 83–103.
- [20] N. Reshetikhin, A. Varchenko, Quasiclassical asymptotics of solutions to the KZ equations, in: *Geometry, Topology & Physics for Raul Bott*, in: *Conference Proceedings Lecture Notes Geometry Topology VI*, Int. Press, Cambridge, MA, 1995, pp. 293–322.
- [21] B. Fagin, E. Frenkel, N. Reshetikhin, Gaudin model, Bethe ansatz and critical level, *Commun. Math. Phys.* 166 (1994) 27–62.
- [22] H.M. Babujian, R. Flume, Off-shell Bethe ansatz equations for Gaudin magnets and solutions of Knizhnik-Zamolodchikov equations, *Mod. Phys. Lett. A* 9 (22) (1994) 2029–2039.
- [23] V. Kurak, A. Lima-Santos,  $sl(2|1)^{(2)}$  Gaudin magnet and its associated Knizhnik-Zamolodchikov equation, *Nucl. Phys. B* 701 (2004) 497–515.
- [24] K. Hikami, P.P. Kulish, M. Wadati, Integrable spin systems with long-range interaction, *Chaos Solitons Fractals* 2 (5) (1992) 543–550.
- [25] K. Hikami, P.P. Kulish, M. Wadati, Construction of integrable spin systems with long-range interaction, *J. Phys. Soc. Jpn.* 61 (9) (1992) 3071–3076.
- [26] E.K. Sklyanin, T. Takebe, Algebraic Bethe ansatz for the XYZ Gaudin model, *Phys. Lett. A* 219 (1996) 217–225.
- [27] N. Cirilo António, N. Manojlović,  $sl_2$  Gaudin model with jordanian twist, *J. Math. Phys.* 46 (10) (2005) 102701, <https://doi.org/10.1063/1.2036932>.
- [28] P.P. Kulish, N. Manojlović, M. Samsonov, A. Stolin, Bethe ansatz for deformed Gaudin model, in: *AGMF Tartu08 Workshop Proceedings*, *Proc. Est. Acad. Sci.* 59 (4) (2010) 326–331.
- [29] N. Cirilo Antonio, N. Manojlović, A. Stolin, Algebraic Bethe ansatz for deformed Gaudin model, *J. Math. Phys.* 52 (2011) 103501, <https://doi.org/10.1063/1.3644345>.
- [30] L. Schlesinger, Über eine Klasse von Differentialsystemen beliebiger Ordnung mit festen kritischen Punkten, *J. Reine Angew. Math.* 141 (1912) 96–145.
- [31] M. Jimbo, T. Miwa, a.K. Ueno, Monodromy preserving deformation of linear ordinary differential equations with rational coefficients: I. General theory and  $\tau$ -function, *Physica D* 2 (1981) 306–352.
- [32] M. Jimbo, T. Miwa, Monodromy preserving deformation of linear ordinary differential equations with rational coefficients. II, *Physica D* 2 (1981) 407–448.
- [33] M. Jimbo, T. Miwa, Monodromy preserving deformation of linear ordinary differential equations with rational coefficients. III, *Physica D* 4 (1981) 26–46.
- [34] D. Korotkin, N. Manojlović, H. Samtleben, Schlesinger transformations for elliptic isomonodromic deformations, *J. Math. Phys.* 41 (2000) 3125–3141, <https://doi.org/10.1063/1.533296>.
- [35] N. Manojlović, H. Samtleben, Schlesinger transformations and quantum R matrices, *Commun. Math. Phys.* 230 (2002) 517–537, <https://doi.org/10.1007/s00220-002-0716-1>.
- [36] B. Dubrovin, M. Mazzocco, Canonical structure and symmetries of the Schlesinger equations, *Commun. Math. Phys.* 271 (2007) 289–373, <https://doi.org/10.1007/s00220-006-0165-3>.

- [37] E.K. Sklyanin, Boundary conditions for integrable quantum systems, *J. Phys. A, Math. Gen.* 21 (1988) 2375–2389.
- [38] L. Freidel, J.M. Maillet, Quadratic algebras and integrable systems, *Phys. Lett. B* 262 (1991) 278–284.
- [39] L. Freidel, J.M. Maillet, On classical and quantum integrable field theories associated to Kac-Moody current algebras, *Phys. Lett. B* 263 (1991) 403–410.
- [40] C.S. Melo, G.A.P. Ribeiro, M.J. Martins, Bethe ansatz for the  $XXX - S$  chain with non-diagonal open boundaries, *Nucl. Phys. B* 711 (3) (2005) 565–603.
- [41] S. Belliard, N. Crampé, E. Ragoucy, Algebraic Bethe ansatz for open XXX model with triangular boundary matrices, *Lett. Math. Phys.* 103 (5) (2013) 493–506.
- [42] S. Belliard, N. Crampé, Heisenberg XXX model with general boundaries: eigenvectors from algebraic Bethe ansatz, *SIGMA* 9 (2013) 072.
- [43] R.A. Pimenta, A. Lima-Santos, Algebraic Bethe ansatz for the six vertex model with upper triangular K-matrices, *J. Phys. A* 46 (45) (2013) 455002.
- [44] S. Belliard, Modified algebraic Bethe ansatz for XXZ chain on the segment - I: triangular cases, *Nucl. Phys. B* 892 (2015) 1–20.
- [45] S. Belliard, R.A. Pimenta, Modified algebraic Bethe ansatz for XXZ chain on the segment - II - general cases, *Nucl. Phys. B* 894 (2015) 527–552.
- [46] J. Avan, S. Belliard, N. Grosjean, R.A. Pimenta, Modified algebraic Bethe ansatz for XXZ chain on the segment - III - proof, *Nucl. Phys. B* 899 (2015) 229–246.
- [47] A.M. Gainutdinov, R.I. Nepomechie, Algebraic Bethe ansatz for the quantum group invariant open XXZ chain at roots of unity, *Nucl. Phys. B* 909 (2016) 796–839.
- [48] S. Belliard, R.A. Pimenta, N.A. Slavnov, Scalar product for the XXZ spin chain with general integrable boundaries, arXiv:2103.12501.
- [49] E. Ragoucy, Coordinate Bethe ansätze for non-diagonal boundaries, *Rev. Math. Phys.* 25 (10) (2013) 1343007.
- [50] L. Frappat, R.I. Nepomechie, E. Ragoucy, A complete Bethe ansatz solution for the open spin- $s$  XXZ chain with general integrable boundary terms, *J. Stat. Mech. Theory Exp.* 0709 (2007) P09009.
- [51] J. Cao, W.-L. Yang, K. Shi, Y. Wang, Off-diagonal Bethe ansatz solution of the XXX spin chain with arbitrary boundary conditions, *Nucl. Phys. B* 875 (2013) 152–165.
- [52] X. Zhang, Y.-Y. Li, J. Cao, W.-L. Yang, K. Shi, Y. Wang, Bethe states of the XXZ spin- $\frac{1}{2}$  chain with arbitrary boundary fields, *Nucl. Phys. B* 893 (2015) 70–88.
- [53] R.I. Nepomechie, Bethe ansatz solution of the open XXZ chain with nondiagonal boundary terms, *J. Phys. A, Math. Theor.* 37 (2) (2004) 433–440.
- [54] M. Jimbo, R. Kedem, T. Kojima, H. Konno, T. Miwa, XXZ chain with a boundary, *Nucl. Phys. B* 441 (1995) 437–470.
- [55] J. Cao, H. Lin, K. Shi, Y. Wang, Exact solutions and elementary excitations in the XXZ spin chain with unparallel boundary fields, *Nucl. Phys. B* 663 (2003) 487–519.
- [56] P.P. Kulish, N. Manojlović, Z. Nagy, Jordanian deformation of the open XXX-spin chain, *Theor. Math. Phys.* 163 (2010) 644–652, <https://doi.org/10.1007/s11232-010-0047-x>.
- [57] J.M. Maillet, G. Niccoli, B. Pezelier, Transfer matrix spectrum for cyclic representations of the 6-vertex reflection algebra I, *SciPost Phys.* 2 (2017) 009.
- [58] N. Cirilo António, N. Manojlović, I. Salom, Algebraic Bethe ansatz for the XXX chain with triangular boundaries and Gaudin model, *Nucl. Phys. B* 889 (2014) 87–108, <https://doi.org/10.1016/j.nuclphysb.2014.10.014>.
- [59] N. Manojlović, I. Salom, Algebraic Bethe ansatz for the XXZ Heisenberg spin chain with triangular boundaries and the corresponding Gaudin model, *Nucl. Phys. B* 923 (2017) 73–106, <https://doi.org/10.1016/j.nuclphysb.2017.07.017>.
- [60] N. Cirilo António, N. Manojlović, Z. Nagy, Trigonometric  $sl(2)$  Gaudin model with boundary terms, *Rev. Math. Phys.* 25 (10) (2013) 1343004, <https://doi.org/10.1142/S0129055X13430046>.
- [61] K. Hikami, Gaudin magnet with boundary and generalized Knizhnik-Zamolodchikov equation, *J. Phys. A, Math. Gen.* 28 (1995) 4997–5007.
- [62] N. Cirilo António, N. Manojlović, Z. Nagy, Jordanian deformation of the open  $sl(2)$  Gaudin model, *Theor. Math. Phys.* 179 (2014) 462–471, <https://doi.org/10.1007/s11232-014-0155-0>.
- [63] W.L. Yang, R. Sasaki, Y.Z. Zhang,  $\mathbb{Z}_n$  elliptic Gaudin model with open boundaries, *J. High Energy Phys.* 09 (2004) 046.
- [64] W.L. Yang, R. Sasaki, Y.Z. Zhang,  $A_{n-1}$  Gaudin model with open boundaries, *Nucl. Phys. B* 729 (2005) 594–610.
- [65] K. Hao, W.-L. Yang, H. Fan, S.Y. Liu, K. Wu, Z.Y. Yang, Y.Z. Zhang, Determinant representations for scalar products of the XXZ Gaudin model with general boundary terms, *Nucl. Phys. B* 862 (2012) 835–849.
- [66] A. Lima-Santos, The  $sl(2|1)^{(2)}$  Gaudin magnet with diagonal boundary terms, *J. Stat. Mech.* (2009) P07025.

- [67] N. Manojlović, Z. Nagy, I. Salom, Derivation of the trigonometric Gaudin Hamiltonians, in: Proceedings of the 8th Mathematical Physics Meeting: Summer School and Conference on Modern Mathematical Physics, 24–31 August 2014, Belgrade, Serbia, in: SFIN XXVIII Series A: Conferences, vol. A1, ISBN 978-86-82441-43-4, 2015, pp. 127–135.
- [68] N. Manojlović, N. Cirilo António, I. Salom, Quasi-classical limit of the open Jordanian XXX spin chain, in: Proceedings of the 9th Mathematical Physics Meeting: Summer School and Conference on Modern Mathematical Physics, 18–23 September 2017, Belgrade, Serbia, in: SFIN XXXI Series A: Conferences, vol. A1, ISBN 978-86-82441-48-9, 2018, pp. 259–266.
- [69] N. Cirilo António, N. Manojlović, E. Ragoucy, I. Salom, Algebraic Bethe ansatz for the  $sl(2)$  Gaudin model with boundary, Nucl. Phys. B 893 (2015) 305–331, <https://doi.org/10.1016/j.nuclphysb.2015.02.011>.
- [70] E.K. Sklyanin, Boundary conditions for integrable equations, Funkc. Anal. Prilozh. 21 (1987) 86–87 (Russian); translation in Funct. Anal. Appl. 21 (2) (1987) 164–166.
- [71] E.K. Sklyanin, Boundary conditions for integrable systems, in: Proceedings of the VIIIth International Congress on Mathematical Physics, Marseille, 1986, World Sci. Publishing, Singapore, 1987, pp. 402–408.
- [72] J.M. Maillet, Kac-Moody algebra and extended Yang-Baxter relations in the  $O(N)$  non-linear  $\sigma$ -model, Phys. Lett. B 162 (1985) 137–142.
- [73] J.M. Maillet, New integrable canonical structures in two-dimensional models, Nucl. Phys. B 269 (1986) 54–76.
- [74] O. Babelon, C. Viallet, Hamiltonian structures and Lax equations, Phys. Lett. B 237 (1990) 411.
- [75] J. Avan, M. Talon, Rational and trigonometric constant non-antisymmetric r-matrices, Phys. Lett. B 241 (1990) 77–82.
- [76] T. Skrypnyk, Generalized quantum Gaudin spin chains, involutive automorphisms and twisted classical r-matrices, J. Math. Phys. 47 (2006) 033511, <https://doi.org/10.1063/1.2179052>.
- [77] T. Skrypnyk, Generalized Gaudin spin chains, non-skew-symmetric r-matrices and reflection equation algebras, J. Math. Phys. 48 (2007) 113521, <https://doi.org/10.1063/1.2816256>.
- [78] T. Skrypnyk, Non-skew-symmetric classical r-matrix, algebraic Bethe ansatz, and Bardeen-Cooper-Schrieffer-type integrable systems, J. Math. Phys. 50 (2009) 033540.
- [79] T. Skrypnyk, Generalized Knizhnik-Zamolodchikov equations, off-shell Bethe ansatz and non-skew-symmetric classical r-matrices, Nucl. Phys. B 824 (2010) 436–451.
- [80] T. Skrypnyk, Isomonodromic deformations, generalized Knizhnik-Zamolodchikov equations and non-skew-symmetric classical r-matrices, J. Math. Phys. 51 (2010) 083516.
- [81] T. Skrypnyk, “Z2-graded” Gaudin models and analytical Bethe ansatz, Nucl. Phys. B 870 (3) (2013) 495–529.
- [82] T. Skrypnyk, “Generalized” algebraic Bethe ansatz, Gaudin-type models and  $\mathbb{Z}_p$ -graded classical r-matrices, Nucl. Phys. B 913 (2016) 327–356.
- [83] N. Manojlović, I. Salom, N. Cirilo António, XYZ Gaudin model with boundary terms, in: Proceedings of the 10th Mathematical Physics Meeting: Summer School and Conference on Modern Mathematical Physics, 9–14 September 2019, Belgrade, Serbia, in: SFIN XXXIII Series A: Conferences, vol. A1, ISBN 978-86-82441-51-9, 2020, pp. 143–160.
- [84] T. Skrypnyk, N. Manojlović, Twisted rational r-matrices and algebraic Bethe ansatz: application to generalized Gaudin and Richardson models, Nucl. Phys. B 967 (2021) 115424, <https://doi.org/10.1016/j.nuclphysb.2021.115424>.
- [85] I. Salom, N. Manojlović, Creation operators of the non-periodic  $sl(2)$  Gaudin model, in: Proceedings of the 8th Mathematical Physics Meeting: Summer School and Conference on Modern Mathematical Physics, 24–31 August 2014, Belgrade, Serbia, in: SFIN XXVIII Series A: Conferences, vol. A1, ISBN 978-86-82441-43-4, 2015, pp. 149–155.
- [86] I. Salom, N. Manojlović, N. Cirilo António, Generalized  $sl(2)$  Gaudin algebra and corresponding Knizhnik-Zamolodchikov equation, Nucl. Phys. B 939 (2019) 358–371, <https://doi.org/10.1016/j.nuclphysb.2018.12.025>.
- [87] N. Manojlović, I. Salom, Algebraic Bethe ansatz for the trigonometric  $sl(2)$  Gaudin model with triangular boundary, Symmetry 12 (3) (2020) 352, <https://doi.org/10.3390/sym12030352>.
- [88] N. Crampé, Algebraic Bethe ansatz for the XXZ Gaudin models with generic boundary, SIGMA 13 (2017) 094, [arXiv:1710.08490](https://arxiv.org/abs/1710.08490).
- [89] I. Salom, N. Manojlović, Bethe states and Knizhnik-Zamolodchikov equations of the trigonometric Gaudin model with triangular boundary, Nucl. Phys. B 969 (2021) 115462, <https://doi.org/10.1016/j.nuclphysb.2021.115462>.
- [90] L. Mezincescu, R.I. Nepomechie, Fusion procedure for open chains, J. Phys. A 25 (1992) 2533–2544.
- [91] P.P. Kulish, N. Manojlović, Z. Nagy, Symmetries of spin systems and Birman-Wenzl-Murakami algebra, J. Math. Phys. 51 (2010) 043516, <https://doi.org/10.1063/1.3366259>.



- [92] H.J. de Vega, A. González Ruiz, Boundary  $K$ -matrices for the  $XYZ$ ,  $XXZ$ ,  $XXX$  spin chains, *J. Phys. A, Math. Gen.* 27 (1994) 6129–6137.
- [93] S. Ghoshal, A.B. Zamolodchikov, Boundary S-matrix and boundary state in two-dimensional integrable quantum field theory, *Int. J. Mod. Phys. A* 09 (3841) (1994) 3841–3885.
- [94] S. Ghoshal, A.B. Zamolodchikov, Errata: boundary S-matrix and boundary state in two-dimensional integrable quantum field theory, *Int. J. Mod. Phys. A* 09 (4353) (1994) 4353.
- [95] I. Salom, N. Manojlović, N. Cirilo António, The spin 1  $XXZ$  Gaudin model with boundary, in: *Proceedings of the 10th Mathematical Physics Meeting: Summer School and Conference on Modern Mathematical Physics*, 9–14 September 2019, Belgrade, Serbia, in: *SFIN XXXIII Series A: Conferences*, vol. A1, ISBN 978-86-82441-51-9, 2020, pp. 277–286.
- [96] P.P. Kulish, Twist deformations of quantum integrable spin chains, *Lect. Notes Phys.* 774 (2009) 165–188.
- [97] T. Inami, S. Odake, Y.Z. Zhang, Reflection  $K$  matrices of the 19 vertex model and  $XXZ$  spin 1 chain with general boundary terms, *Nucl. Phys. B* 470 (1996) 419–434, [https://doi.org/10.1016/0550-3213\(96\)00133-2](https://doi.org/10.1016/0550-3213(96)00133-2).
- [98] Alexander B. Zamolodchikov, Alexey B. Zamolodchikov, Relativistic factorized S-matrix in two dimensions having  $O(N)$  isotopic symmetry, *Nucl. Phys. B* 133 (1978) 525–535.
- [99] Alexander B. Zamolodchikov, Alexey B. Zamolodchikov, Factorized S-matrices in two dimensions as the exact solutions of certain relativistic quantum field theory models, *Ann. Phys.* 120 (1979) 253–291.
- [100] E.K. Sklyanin, Generating function of correlators in the  $sl(2)$  Gaudin model, *Lett. Math. Phys.* 47 (1999) 275–292, <https://doi.org/10.1023/A:1007585716273>.



# Bethe states and Knizhnik-Zamolodchikov equations of the trigonometric Gaudin model with triangular boundary

I. Salom<sup>a,\*</sup>, N. Manojlović<sup>b,c</sup>

<sup>a</sup> *Institute of Physics, University of Belgrade, P.O. Box 57, 11080 Belgrade, Serbia*

<sup>b</sup> *Departamento de Matemática, Faculdade de Ciências e Tecnologia, Universidade do Algarve, Campus de Gambelas, PT-8005-139 Faro, Portugal*

<sup>c</sup> *Grupo de Física Matemática da Universidade de Lisboa, Departamento de Matemática, Faculdade de Ciências, Campo Grande, Edifício C6, PT-1749-016 Lisboa, Portugal*

Received 20 February 2021; received in revised form 12 May 2021; accepted 27 May 2021

Available online 7 June 2021

Editor: Hubert Saleur

## Abstract

We present a comprehensive treatment of the non-periodic trigonometric  $sl(2)$  Gaudin model with triangular boundary, with an emphasis on specific freedom found in the local realization of the generators, as well as in the creation operators used in the algebraic Bethe ansatz. First, we give Bethe vectors of the non-periodic trigonometric  $sl(2)$  Gaudin model both through a recurrence relation and in a closed form. Next, the off-shell action of the generating function of the trigonometric Gaudin Hamiltonians with general boundary terms on an arbitrary Bethe vector is shown, together with the corresponding proof based on mathematical induction. The action of the Gaudin Hamiltonians is given explicitly. Furthermore, by careful choice of the arbitrary functions appearing in our more general formulation, we additionally obtain: i) the solutions to the Knizhnik-Zamolodchikov equations (each corresponding to one of the Bethe states); ii) compact formulas for the on-shell norms of Bethe states; and iii) closed-form expressions for the off-shell scalar products of Bethe states.

© 2021 The Authors. Published by Elsevier B.V. This is an open access article under the CC BY license (<http://creativecommons.org/licenses/by/4.0/>). Funded by SCOAP<sup>3</sup>.

\* Corresponding author.

E-mail addresses: [isalom@ipb.ac.rs](mailto:isalom@ipb.ac.rs) (I. Salom), [nmanoj@ualg.pt](mailto:nmanoj@ualg.pt) (N. Manojlović).

## 1. Introduction

Gaudin systems have been a subject of study for almost half a century. Gaudin originally introduced them as a quasi-classical limit of the Heisenberg spin chains [1–3]. Sklyanin used a suitable unitary classical r-matrix [4] in the study of the rational  $sl(2)$  model [5]. A generalisation of these results to the skew-symmetric classical r-matrices of simple Lie algebras [6–8] and Lie superalgebras [9–12] was relatively straightforward as well as their Jordanian deformation [13–15].

Non-periodic Gaudin systems have also attracted considerable attention [16–30]. Particularly compelling is the approach based on the non-unitary r-matrices [31–33]. Recently we have studied the rational  $sl(2)$  Gaudin model with general boundary K-matrices, both as a limit of the spin-chain model [34] and independently [35], and provided a number of additional interesting results, from the solutions to Knizhnik-Zamolodchikov (KZ) equations to compact formulas for on-shell norms and for off-shell scalar products of the Bethe states [36].

A number of results are already available also for the trigonometric  $sl(2)$  Gaudin model with nontrivial boundary. The generating function of the trigonometric  $sl(2)$  Gaudin Hamiltonians with triangular boundary terms was obtained in [37]. Moreover, we have shown that in this case a suitable non-unitary trigonometric classical r-matrix is an essential tool in the implementation of the algebraic Bethe ansatz [38] and we have conjectured the spectrum of the generating function and the corresponding Bethe equations [38]. Restricting boundary conditions to triangular K-matrices was here essential for the existence of unique lowest weight state, which then allowed straightforward application of the algebraic Bethe ansatz and finding the off-shell action of the generating function. The so-called modified Bethe ansatz for this model was studied in [39]. In a special case (when the number of excitations matched a specific value) this approach allowed a more general form of boundary conditions, while in the rest of the cases it was again necessary to restrict boundary conditions to triangular K-matrices (after which our earlier results [37,38] would be recovered). In spite of all this progress, a number of other important problems has remained hitherto open and we intend to address them in the present paper.

Although we have conjectured the form of full off-shell action of the generating function on Bethe vectors in [38], the strict mathematical proof of the obtained formulas was lacking. More importantly, one of the main goals here was to provide solutions to the corresponding KZ equations, as well as to find the formulas for on-shell norms of Bethe vectors and for their off-shell scalar products – the tasks we have already successfully accomplished in the rational case. However, we faced serious obstacles in pursuing these goals: the straightforward approach adapted from the rational case was failing to produce either KZ solutions or norm/scalar product formulas. It was not before we noticed and employed a combination of freedom in defining the local realization of Gaudin algebra generators and a freedom in defining the effective creation operators for the Bethe vectors, that we could achieve our established objectives. This realisation and the corresponding technique is another novel contribution of this paper.

The approach taken here differs in many aspects from our previous work on the subject [37, 38]. As a crucial step towards the complete proof (by mathematical induction) of the off-shell action of the generating function, we here define Bethe states through a particular recurrence relation. Next, our study is here based on the unitary, trigonometric  $sl(2)$  classical r-matrix and the corresponding reflection K-matrix, both given in the so-called homogeneous gradation [21], as opposed to our previous papers [37,38] where we have used the trigonometric r-matrix and the classical reflection K-matrix in the principal gradation. Although the two formulations are equivalent, the motivation for making the present choice is related to the forementioned freedom

in the local realization of the new set of generators of the generalized trigonometric  $sl(2)$  Gaudin algebra. This approach yields a neat form of the off-shell action of the generating function on the Bethe vectors while at the same time enables the quest for the solutions to the corresponding Knizhnik-Zamolodchikov equations. Once this freedom – represented by two initially arbitrary functions – is fixed by solving appropriate differential equations, we not only find solutions to KZ equations, but also recover the compact determinant representation for the norms and the scalar products of the Bethe vectors, analogous to the expressions we have obtained in the rational case [36].

The composition of the paper is the following. In Section 2 the local realisation of the new generators of the relevant Gaudin algebra is given. The novel feature of this realisation is an arbitrary function of the local inhomogeneous parameter whose introduction does not affect the algebraic Bethe ansatz. The suitable creation operators and the complete details of the algebraic Bethe ansatz for the first two Bethe states are given in Section 3. It should be emphasised that the creation operator contains the second arbitrary function, this time of the rapidity parameter. In Section 4 we present the recurrent relation which defines the Bethe states of this system as well as the complete proof of the off-shell action of the generating function. The action of Gaudin Hamiltonians on the Bethe vectors is shown in Section 5. The solutions of the Knizhnik-Zamolodchikov equations are obtained in Section 6 by solving the appropriate differential equations for the two previously introduced arbitrary functions. The same choice for these functions allows us to derive, in Section 7, very compact relations for the on-shell norm and the scalar product of the Bethe vectors. Finally, our conclusions are presented in Section 8. For the sake of completeness, the fundamental structure on which this work is based (e.g. the classical r-matrix and the corresponding classical K-matrix) is presented in Appendix A. The standard definition of the Hilbert space of the system is given in Appendix B. The generalized Gaudin Lax operator as well as the Gaudin Hamiltonians with the boundary terms, both in the parametrization we have considered here, are given in Appendix C. In Appendix D we present the key formula in the proof of the off-shell action of the generating function of the trigonometric Gaudin Hamiltonians with boundary terms.

## 2. Generalized trigonometric Gaudin algebra

Our approach adopted here is established upon the non-unitary r-matrix (A.5) and the Lax operator (C.3), which in turn follow from the unitary, trigonometric  $sl(2)$  classical r-matrix (A.1) and the corresponding reflection K-matrix (A.3), both given in the so-called homogeneous gradation [21]. We will focus on the triangular case when the boundary parameter  $\phi$  is set to zero. As it follows from the linear bracket (C.4), the entries of the Lax matrix (C.3) generate the generalized  $sl(2)$  trigonometric Gaudin algebra [38]. Furthermore, it is convenient to apply a linear triangular transformation that yields a particularly convenient set of generators which will be used below. These generators admit the following local realization

$$e(\lambda) = \sum_{m=1}^N \frac{(\xi e^{-2\alpha_m} + \nu) Z(\alpha_m) S_m^+}{\sinh(\lambda - \alpha_m) \sinh(\lambda + \alpha_m)}, \tag{2.1}$$

$$h(\lambda) = \sum_{m=1}^N \frac{S_m^3 + \frac{\psi}{2\xi\nu} (\xi e^{-2\alpha_m} - \nu) Z(\alpha_m) S_m^+}{\sinh(\lambda - \alpha_m) \sinh(\lambda + \alpha_m)}, \tag{2.2}$$

$$f(\lambda) = \sum_{m=1}^N \frac{(\xi e^{2\alpha_m} + v) \frac{S_m^-}{Z(\alpha_m)} - \frac{\psi}{\xi v} (\xi^2 - v^2 - 2\xi v \sinh(2\alpha_m)) S_m^3 + \frac{\psi^2}{\xi v} e^{-2\alpha_m} (\xi e^{2\alpha_m} + v) Z(\alpha_m) S_m^+}{\sinh(\lambda - \alpha_m) \sinh(\lambda + \alpha_m)}, \tag{2.3}$$

where  $Z(\alpha_m)$  is an arbitrary function of the inhomogeneous parameter  $\alpha_m$ . As it will be shown in the next two sections, the function  $Z(\alpha_m)$  will remain arbitrary throughout the implementation of the algebraic Bethe ansatz. However, it will be of utmost importance both for finding the solutions to the Knizhnik-Zamolodchikov equations (6.7) and for finding formulas for norms and scalar products of Bethe vectors 7.

An important feature of these generators is that their commutation relations are quite simple. Namely, the trivial commutation relations are

$$[e(\lambda), e(\mu)] = [h(\lambda), h(\mu)] = [f(\lambda), f(\mu)] = 0, \tag{2.4}$$

and the only nontrivial ones are given by

$$[h(\lambda), e(\mu)] = \frac{1}{\sinh(\lambda - \mu) \sinh(\lambda + \mu)} (e(\mu) - e(\lambda)), \tag{2.5}$$

$$[h(\lambda), f(\mu)] = \frac{1}{\sinh(\lambda - \mu) \sinh(\lambda + \mu)} \left( f(\lambda) - f(\mu) + \frac{\psi^2}{2\xi^2 v^2} \times \right. \\ \left. \times \left( (\xi^2 + v^2 + 2\xi v \cosh(2\mu)) e(\mu) - (\xi^2 + v^2 + 2\xi v \cosh(2\lambda)) e(\lambda) \right) \right), \tag{2.6}$$

$$[e(\lambda), f(\mu)] = \frac{2}{\sinh(\lambda - \mu) \sinh(\lambda + \mu)} \times \\ \times \left( (\xi^2 + v^2 + 2\xi v \cosh(2\mu)) h(\mu) - (\xi^2 + v^2 + 2\xi v \cosh(2\lambda)) h(\lambda) \right). \tag{2.7}$$

Note that function the function  $Z(\alpha_m)$  does not appear in the relations above.

Next, for the study of the algebraic Bethe ansatz it is essential to have the expression of the generating function  $\tau(\lambda)$  (C.5) in terms of the generators (2.1)–(2.3).

$$\tau(\lambda) = 2 \sinh^2(2\lambda) \left( h^2(\lambda) - \frac{4\xi v h(\lambda)}{\xi^2 + v^2 + 2\xi v \cosh(2\lambda)} - \frac{h'(\lambda)}{\sinh(2\lambda)} \right) \\ + 2 \sinh^2(2\lambda) \left( \frac{f(\lambda)}{\xi^2 + v^2 + 2\xi v \cosh(2\lambda)} - \frac{\psi^2}{4\xi^2 v^2} e(\lambda) \right) e(\lambda). \tag{2.8}$$

As we have shown in [38] the trigonometric  $sl(2)$  Gaudin Hamiltonians with the boundary terms are obtained as the residues of the generating function  $\tau(\lambda)$  at poles  $\lambda = \pm\alpha_m$ . For completeness, the explicit expressions of the Gaudin Hamiltonians  $H_m$  in the parametrisation used here are given in the Appendix C, more precisely, in the equation (C.7).

### 3. The algebraic Bethe ansatz

As it is well known [40–42], the existence of the pseudo-vacuum is essential for the algebraic Bethe ansatz. In the present case, the vector  $\Omega_+$  (see the definition in the Appendix B, in particular relations (B.3) and (B.4)), is annihilated by the generator  $e(\lambda)$ , i.e.



$$e(\lambda)\Omega_+ = 0, \tag{3.1}$$

and is an eigenvector of the generator  $h(\lambda)$ ,

$$h(\lambda)\Omega_+ = \rho(\lambda)\Omega_+, \quad \text{with} \quad \rho(\lambda) = \sum_{m=1}^N \frac{s_m}{\sinh(\lambda + \alpha_m) \sinh(\lambda - \alpha_m)}. \tag{3.2}$$

From the expression for the generating function  $\tau(\lambda)$  that we have obtained in the previous section (2.8) and from the relations above (3.1) and (3.2) it is evident that the pseudo-vacuum is an eigenvector

$$\tau(\lambda)\Omega_+ = \chi_0(\lambda)\Omega_+, \tag{3.3}$$

with the eigenvalue  $\chi_0(\lambda)$  given by

$$\chi_0(\lambda) = 2 \sinh^2(2\lambda) \left( \rho^2(\lambda) - \frac{4\xi v \rho(\lambda)}{\xi^2 + v^2 + 2\xi v \cosh(2\lambda)} - \frac{\rho'(\lambda)}{\sinh(2\lambda)} \right). \tag{3.4}$$

One way to define the Bethe states of the system is to introduce the appropriate creation operators [11,42]. In this case, it is of interest to consider the following creation operators

$$\mathcal{C}_M(\lambda) = \mathcal{A}(\lambda) \left( f(\lambda) + 2\psi \left( (2M - 1) - \frac{\xi^2 + v^2 + 2\xi v \cosh(2\lambda)}{2\xi v} \left( h(\lambda) + \frac{\psi}{2\xi v} e(\lambda) \right) \right) \right), \tag{3.5}$$

where  $\mathcal{A}(\lambda)$  is an arbitrary function of the parameter  $\lambda$ . Being an overall multiplier of the creation operator, it is not surprising that the function  $\mathcal{A}(\lambda)$  will not be relevant for the algebraic Bethe ansatz. However, it will play an important role in relation to the solutions to the Knizhnik-Zamolodchikov equations, together with the function  $Z(\alpha_m)$  that we have introduced in the local realization of the generators of the generalized  $sl(2)$  trigonometric Gaudin algebra (2.1)–(2.3). The constant values for functions  $\mathcal{A}(\lambda)$  and  $Z(\alpha_m)$  would effectively (i.e. up to technical differences in used gradation) correspond to our earlier results [37,38]. (Similarly, with a suitable choice of these functions the creation operators (3.5) exactly correspond to those in the triangular boundary case of [39].)

In particular, it holds:

$$[\mathcal{C}_1(\lambda), \mathcal{C}_1(\mu)] = 4\psi (\mathcal{A}(\lambda)\mathcal{C}_1(\mu) - \mathcal{A}(\mu)\mathcal{C}_1(\lambda)), \tag{3.6}$$

as well as

$$[\mathcal{C}_1(\lambda), e(\mu)] = \frac{\mathcal{A}(\lambda)}{\xi v \sinh(\lambda - \mu) \sinh(\lambda + \mu)} \left( (2v\xi \cosh(2\lambda) + v^2 + \xi^2) \times (\psi e(\lambda) - \psi e(\mu) + 2v\xi h(\lambda)) - 2v\xi h(\mu) (2v\xi \cosh(2\mu) + v^2 + \xi^2) \right), \tag{3.7}$$

$$[\mathcal{C}_1(\lambda), h(\mu)] = \mathcal{A}(\lambda) \left( \frac{2\psi^2 e(\mu)}{v\xi} + \frac{1}{\sinh(\lambda - \mu) \sinh(\lambda + \mu)} (f(\mu) - f(\lambda)) \right), \tag{3.8}$$

$$[\mathcal{C}_1(\lambda), f(\mu)] = \frac{\psi \mathcal{A}(\lambda)}{2v^3 \xi^3 \sinh(\lambda - \mu) \sinh(\lambda + \mu)} \left( 2v\xi \cosh(2\lambda) + v^2 + \xi^2 \right) \times (\psi^2 e(\lambda) (2v\xi \cosh(2\lambda) + v^2 + \xi^2) - \psi^2 e(\mu) (2v\xi \cosh(2\mu) + v^2 + \xi^2) +$$

$$2v\xi(-v\xi f(\lambda) + v\xi f(\mu) + \psi h(\lambda) (2v\xi \cosh(2\lambda) + v^2 + \xi^2) - \psi h(\mu) (2v\xi \cosh(2\mu) + v^2 + \xi^2))). \tag{3.9}$$

Another useful relation is:

$$\begin{aligned} \tau(\lambda) = & 2 \sinh^2(2\lambda) \left( h^2(\lambda) - \frac{4\xi v h(\lambda)}{\xi^2 + v^2 + 2\xi v \cosh(2\lambda)} - \frac{h'(\lambda)}{\sinh(2\lambda)} \right) \\ & + 2 \sinh^2(2\lambda) \left( \frac{\mathcal{C}_1(\lambda) - 2\psi \mathcal{A}(\lambda)}{\mathcal{A}(\lambda)(\xi^2 + v^2 + 2\xi v \cosh(2\lambda))} + \frac{\psi}{\xi v} \left( h(\lambda) + \frac{\psi}{4\xi v} e(\lambda) \right) \right) e(\lambda). \end{aligned} \tag{3.10}$$

Now it is not difficult to show that the Bethe vector  $\varphi_1(\mu)$  has the form

$$\varphi_1(\mu) = \mathcal{C}_1(\mu)\Omega_+, \tag{3.11}$$

where the operator  $\mathcal{C}_1(\mu)$  is given in (3.5), with  $M = 1$ . Evidently, the action of the generating function of the Gaudin Hamiltonians (2.8) reads

$$\tau(\lambda)\varphi_1(\mu) = [\tau(\lambda), \mathcal{C}_1(\mu)]\Omega_+ + \chi_0(\lambda)\varphi_1(\mu). \tag{3.12}$$

In this case, a direct calculation shows that the commutator in the first term on the right hand side of (3.12) is given by

$$\begin{aligned} & [\tau(\lambda), \mathcal{C}_1(\mu)]\Omega_+ \\ &= -\frac{2 \sinh^2(2\lambda)}{\sinh(\lambda + \mu) \sinh(\lambda - \mu)} \left( 2\rho(\lambda) - \frac{4\xi v}{\xi^2 + v^2 + 2\xi v \cosh(2\lambda)} \right) \varphi_1(\mu) \\ &+ \frac{\mathcal{A}(\mu)}{\mathcal{A}(\lambda)} \frac{2 \sinh^2(2\lambda)}{\sinh(\lambda + \mu) \sinh(\lambda - \mu)} \frac{\xi^2 + v^2 + 2\xi v \cosh(2\mu)}{\xi^2 + v^2 + 2\xi v \cosh(2\lambda)} \times \\ &\times \left( 2\rho(\mu) - \frac{4\xi v}{\xi^2 + v^2 + 2\xi v \cosh(2\mu)} \right) \varphi_1(\lambda). \end{aligned} \tag{3.13}$$

Consequently, the action of the generating function  $\tau(\lambda)$  on  $\varphi_1(\mu)$  is given by

$$\begin{aligned} \tau(\lambda)\varphi_1(\mu) = & \chi_1(\lambda, \mu)\varphi_1(\mu) + \frac{\mathcal{A}(\mu)}{\mathcal{A}(\lambda)} \frac{4 \sinh^2(2\lambda)}{\sinh(\lambda + \mu) \sinh(\lambda - \mu)} \frac{\xi^2 + v^2 + 2\xi v \cosh(2\mu)}{\xi^2 + v^2 + 2\xi v \cosh(2\lambda)} \times \\ & \times \left( \rho(\mu) - \frac{2\xi v}{\xi^2 + v^2 + 2\xi v \cosh(2\mu)} \right) \varphi_1(\lambda), \end{aligned} \tag{3.14}$$

where

$$\chi_1(\lambda, \mu) = \chi_0(\lambda) - \frac{2 \sinh^2(2\lambda)}{\sinh(\lambda + \mu) \sinh(\lambda - \mu)} \left( 2\rho(\lambda) - \frac{4\xi v}{\xi^2 + v^2 + 2\xi v \cosh(2\lambda)} \right). \tag{3.15}$$

The unwanted term in (3.14) vanishes when the following Bethe equation is imposed on the parameter  $\mu$ ,

$$\rho(\mu) - \frac{2\xi v}{\xi^2 + v^2 + 2\xi v \cosh(2\mu)} = 0. \tag{3.16}$$

Thus we have shown that  $\varphi_1(\mu)$  (3.11) is a desired Bethe vector of the generating function  $\tau(\lambda)$  with the eigenvalue  $\chi_1(\lambda, \mu)$  (3.15), for arbitrary choices of the functions  $\mathcal{A}(\mu)$  and  $Z(\alpha_m)$ .

As the next step, we will show that the Bethe vector  $\varphi_2(\mu_1, \mu_2)$  can be given in a similar form:

$$\varphi_2(\mu_1, \mu_2) = \mathcal{C}_1(\mu_1)\varphi_1(\mu_2) + 4\psi \mathcal{A}(\mu_2)\varphi_1(\mu_1). \tag{3.17}$$

With the aim of obtaining the off-shell action of the generating function  $\tau(\lambda)$  on  $\varphi_2(\mu_1, \mu_2)$  we observe that

$$\tau(\lambda)\varphi_2(\mu_1, \mu_2) = [\tau(\lambda), \mathcal{C}_1(\mu_1)]\varphi_1(\mu_2) + \mathcal{C}_1(\mu_1)\tau(\lambda)\varphi_1(\mu_2) + 4\psi \mathcal{A}(\mu_2)\tau(\lambda)\varphi_1(\mu_1). \tag{3.18}$$

As the action of  $\tau(\lambda)$  on  $\varphi_1(\mu)$  known (3.14), now it is only necessary to calculate the first term on the right hand side of the equation above. Its straightforward to obtain

$$\begin{aligned} [\tau(\lambda), C_1(\mu_1)]\varphi_1(\mu_2) &= -\frac{2 \sinh^2(2\lambda)}{\sinh(\lambda + \mu_1) \sinh(\lambda - \mu_1)} \times \\ &\times \left( 2\rho(\lambda) - \frac{4\xi v}{\xi^2 + v^2 + 2\xi v \cosh(2\lambda)} - \frac{2}{\sinh(\lambda + \mu_2) \sinh(\lambda - \mu_2)} \right) \varphi_2(\mu_1, \mu_2) \\ &+ \frac{\mathcal{A}(\mu_1)}{\mathcal{A}(\lambda)} \frac{2 \sinh^2(2\lambda)}{\sinh(\lambda + \mu_1) \sinh(\lambda - \mu_1)} \frac{\xi^2 + v^2 + 2\xi v \cosh(2\mu_1)}{\xi^2 + v^2 + 2\xi v \cosh(2\lambda)} \times \\ &\times \left( 2\rho(\mu_1) - \frac{4\xi v}{\xi^2 + v^2 + 2\xi v \cosh(2\mu_1)} - \frac{2}{\sinh(\mu_1 + \mu_2) \sinh(\mu_1 - \mu_2)} \right) \varphi_2(\lambda, \mu_2) \\ &- \frac{\mathcal{A}(\mu_2)}{\mathcal{A}(\lambda)} \frac{2 \sinh^2(2\lambda)}{\sinh(\lambda + \mu_2) \sinh(\lambda - \mu_2)} \frac{\xi^2 + v^2 + 2\xi v \cosh(2\mu_2)}{\xi^2 + v^2 + 2\xi v \cosh(2\lambda)} \\ &\times \frac{2}{\sinh(\mu_2 + \mu_1) \sinh(\mu_2 - \mu_1)} \varphi_2(\mu_1, \lambda) \\ &+ \frac{8\psi \mathcal{A}(\mu_2) \sinh^2(2\lambda)}{\sinh(\lambda + \mu_1) \sinh(\lambda - \mu_1)} \frac{\sinh(\mu_1 + \mu_2) \sinh(\mu_1 - \mu_2)}{\sinh(\lambda + \mu_2) \sinh(\lambda - \mu_2)} \\ &\times \left( 2\rho(\lambda) - \frac{4\xi v}{\xi^2 + v^2 + 2\xi v \cosh(2\lambda)} \right) \varphi_1(\mu_1) \\ &- \frac{8\psi \mathcal{A}(\mu_1) \mathcal{A}(\mu_2) \sinh^2(2\lambda)}{\mathcal{A}(\lambda) \sinh(\lambda + \mu_1) \sinh(\lambda - \mu_1)} \frac{\xi^2 + v^2 + 2\xi v \cosh(2\mu_1)}{\xi^2 + v^2 + 2\xi v \cosh(2\lambda)} \\ &\times \left( 2\rho(\mu_1) - \frac{4\xi v}{\xi^2 + v^2 + 2\xi v \cosh(2\mu_1)} \right) \varphi_1(\lambda) \\ &+ \frac{8\psi \mathcal{A}(\mu_2) \sinh^2(2\lambda)}{\sinh(\lambda + \mu_2) \sinh(\lambda - \mu_2)} \frac{\xi^2 + v^2 + 2\xi v \cosh(2\mu_2)}{\xi^2 + v^2 + 2\xi v \cosh(2\lambda)} \\ &\times \left( 2\rho(\mu_2) - \frac{4\xi v}{\xi^2 + v^2 + 2\xi v \cosh(2\mu_2)} \right) \varphi_1(\mu_1). \end{aligned} \tag{3.19}$$

Then, after substituting this formula into the equation (3.18), twice using the action of  $\tau(\lambda)$  on  $\varphi_1(\mu)$  (3.14) and then rearranging some terms, the desired off-shell action of  $\tau(\lambda)$  on the vector  $\varphi_2(\mu_1, \mu_2)$  is obtained

$$\begin{aligned} \tau(\lambda)\varphi_2(\mu_1, \mu_2) &= \chi_2(\lambda, \mu_1, \mu_2)\varphi_2(\mu_1, \mu_2) \\ &+ \sum_{j=1}^2 \frac{\mathcal{A}(\mu_j)}{\mathcal{A}(\lambda)} \frac{4 \sinh^2(2\lambda)}{\sinh(\lambda + \mu_j) \sinh(\lambda - \mu_j)} \frac{\xi^2 + v^2 + 2\xi v \cosh(2\mu_j)}{\xi^2 + v^2 + 2\xi v \cosh(2\lambda)} \times \\ &\times \left( \rho(\mu_j) - \frac{2\xi v}{\xi^2 + v^2 + 2\xi v \cosh(2\mu_j)} - \frac{1}{\sinh(\mu_j + \mu_{3-j}) \sinh(\mu_j - \mu_{3-j})} \right) \\ &\times \varphi_2(\lambda, \mu_{3-j}), \end{aligned} \tag{3.20}$$

with the eigenvalue

$$\begin{aligned} \chi_2(\lambda, \mu_1, \mu_2) &= \chi_0(\lambda) - \sum_{i=1}^2 \frac{2 \sinh^2(2\lambda)}{\sinh(\lambda + \mu_i) \sinh(\lambda - \mu_i)} \times \\ &\times \left( 2\rho(\lambda) - \frac{4\xi v}{\xi^2 + v^2 + 2\xi v \cosh(2\lambda)} - \frac{1}{\sinh(\lambda + \mu_{3-i}) \sinh(\lambda - \mu_{3-i})} \right). \end{aligned}$$

The two unwanted terms in the action above (3.20) vanish when the Bethe equations are imposed on the parameters  $\mu_1$  and  $\mu_2$ ,

$$\rho(\mu_j) - \frac{2\xi v}{\xi^2 + v^2 + 2\xi v \cosh(2\mu_j)} - \frac{1}{\sinh(\mu_j + \mu_{3-j}) \sinh(\mu_j - \mu_{3-j})} = 0, \tag{3.21}$$

with  $j = 1, 2$ . In this way, we have demonstrated that, for an arbitrary choice of the functions  $\mathcal{A}(\mu_j)$  and  $Z(\alpha_m)$ , the vector  $\varphi_2(\mu_1, \mu_2)$ , as defined in (3.17), is the Bethe state of the generating function of the Gaudin Hamiltonians with the eigenvalue  $\chi_2(\lambda, \mu_1, \mu_2)$ .

#### 4. The general form of Bethe vectors

In this section we will obtain the general form of Bethe states as well as the off-shell action of the generating function on these states. For arbitrary natural number  $M$ , the Bethe states of the system can be defined by the following recurrence relation

$$\begin{aligned} \varphi_M(\mu_1, \mu_2, \dots, \mu_M) &= \mathcal{C}_1(\mu_1)\varphi_{M-1}(\mu_2, \mu_3, \dots, \mu_M) \\ &+ 4\psi \sum_{j=2}^M \mathcal{A}(\mu_j) \varphi_{M-1}(\mu_1, \mu_2, \dots, \widehat{\mu}_j, \dots, \mu_{M-1}, \mu_M), \end{aligned} \tag{4.1}$$

where the notation  $\widehat{\mu}_j$  means that the argument  $\mu_j$  is not present. Thus the action of the generating function of the Gaudin Hamiltonians on  $\varphi_M(\mu_1, \mu_2, \dots, \mu_M)$  can be obtained as follows

$$\begin{aligned} \tau(\lambda)\varphi_M(\mu_1, \mu_2, \dots, \mu_M) &= [\tau(\lambda), \mathcal{C}_1(\mu_1)]\varphi_{M-1}(\mu_2, \dots, \mu_M) + \mathcal{C}_1(\mu_1) \tau(\lambda)\varphi_{M-1}(\mu_2, \dots, \mu_M) \\ &+ 4\psi \sum_{j=2}^M \mathcal{A}(\mu_j) \tau(\lambda)\varphi_{M-1}(\mu_1, \mu_2, \dots, \widehat{\mu}_j, \dots, \mu_{M-1}, \mu_M). \end{aligned} \tag{4.2}$$

According to the principle of mathematical induction, on the right hand side of the equation above, it is assumed that the action of  $\tau(\lambda)$  on  $\varphi_{M-1}$  is known. Therefore the essential step in the proof consists in determining the off-shell action of the commutator between the generating function and the creation operator, i.e.  $[\tau(\lambda), \mathcal{C}_1(\mu_1)]$ , on the Bethe vector  $\varphi_{M-1}(\mu_2, \dots, \mu_M)$ . This can be done by a straightforward calculation and the result is a somewhat cumbersome one-page formula given in Appendix D, equation (D.1). Then, after substituting this formula into the equation (4.2) and using the action of  $\tau(\lambda)$  on  $\varphi_{M-1}$  in the remaining  $M$  terms on the right hand side of (4.2), it is also necessary to make some obvious steps which consist in rearranging some terms and simplifying others. Finally, as required by the mathematical induction, we obtain the action of the generating function on  $\varphi_M(\mu_1, \mu_2, \dots, \mu_M)$  in the desired form

$$\begin{aligned} \tau(\lambda)\varphi_M(\mu_1, \dots, \mu_M) &= \chi_M(\mu_1, \dots, \mu_M)\varphi_M(\mu_1, \dots, \mu_M) \\ &+ \sum_{j=1}^M \frac{\mathcal{A}(\mu_j)}{\mathcal{A}(\lambda)} \frac{4 \sinh^2(2\lambda)}{\sinh(\lambda + \mu_j) \sinh(\lambda - \mu_j)} \frac{\xi^2 + v^2 + 2\xi v \cosh(2\mu_j)}{\xi^2 + v^2 + 2\xi v \cosh(2\lambda)} \times \\ &\times \left( \rho(\mu_j) - \frac{2\xi v}{\xi^2 + v^2 + 2\xi v \cosh(2\mu_j)} - \sum_{k \neq j}^M \frac{1}{\sinh(\mu_j + \mu_k) \sinh(\mu_j - \mu_k)} \right) \\ &\times \varphi_M(\lambda, \mu_1, \dots, \widehat{\mu}_j, \dots, \mu_M), \end{aligned} \tag{4.3}$$

where the notation  $\widehat{\mu}_j$  means that the argument  $\mu_j$  is not present and the eigenvalue  $\chi_M(\lambda, \mu_1, \mu_2, \dots, \mu_M)$  is given by

$$\begin{aligned} \chi_M(\lambda, \mu_1, \mu_2, \dots, \mu_M) &= \chi_0(\lambda) - \sum_{j=1}^M \frac{2 \sinh^2(2\lambda)}{\sinh(\lambda + \mu_j) \sinh(\lambda - \mu_j)} \times \\ &\times \left( 2\rho(\lambda) - \frac{4\xi v}{\xi^2 + v^2 + 2\xi v \cosh(2\lambda)} - \sum_{k \neq j}^M \frac{1}{\sinh(\lambda + \mu_k) \sinh(\lambda - \mu_k)} \right). \end{aligned} \tag{4.4}$$

In order to guarantee that the  $M$  unwanted terms in (4.3) will vanish, the Bethe equations have to be imposed on the rapidity parameters  $\mu_j$ :

$$\rho(\mu_j) - \frac{2\xi v}{\xi^2 + v^2 + 2\xi v \cosh(2\mu_j)} - \sum_{k \neq j}^M \frac{1}{\sinh(\mu_j + \mu_k) \sinh(\mu_j - \mu_k)} = 0, \tag{4.5}$$

with  $j = 1, 2, \dots, M$ . In this way, we have concluded the proof.

While the form (4.1) for Bethe vectors is more convenient for the proof of the off-shell action relation (4.3), it is relatively straightforward to show that Bethe vectors can be also written in a much more compact form that was conjectured in [38]:

$$\varphi_M(\mu_1, \mu_2, \dots, \mu_M) = \mathcal{C}_1(\mu_1)\mathcal{C}_2(\mu_2)\cdots\mathcal{C}_M(\mu_M)\Omega_+ \tag{4.6}$$

As it is evident from the formulas above, the choice of functions  $\mathcal{A}(\mu_j)$  and  $Z(\alpha_m)$  does not affect the algebraic Bethe ansatz and therefore they may still remain arbitrary. This will remain so until the Section 6 where will have to fix these functions in order to derive solutions to the related Knizhnik-Zamolodchikov equations.



### 5. The action of Gaudin Hamiltonians

To deal with KZ equations we must first find the off-shell action of the Gaudin Hamiltonians (C.7) on an arbitrary Bethe vector  $\varphi_M(\mu_1, \dots, \mu_M)$  (4.1). It is obtained by taking the residuum of (4.3) at  $\lambda = \alpha_m$  and dividing both sides of the equation by four

$$\begin{aligned}
 H_m \varphi_M(\mu_1, \mu_2, \dots, \mu_M) &= \mathcal{E}_{m,M} \varphi_M(\mu_1, \mu_2, \dots, \mu_M) \\
 &+ \sum_{j=1}^M \frac{\mathcal{A}(\mu_j)}{\mathcal{A}(\alpha_m)} \frac{\sinh^2(2\lambda)}{\sinh(\alpha_m + \mu_j) \sinh(\alpha_m - \mu_j)} \frac{\xi^2 + v^2 + 2\xi v \cosh(2\mu_j)}{\xi^2 + v^2 + 2\xi v \cosh(2\alpha_m)} \times \\
 &\times \left( \rho(\mu_j) - \frac{2\xi v}{\xi^2 + v^2 + 2\xi v \cosh(2\mu_j)} - \sum_{k \neq j}^M \frac{1}{\sinh(\mu_j + \mu_k) \sinh(\mu_j - \mu_k)} \right) \times \\
 &\times \text{Res}_{\lambda=\alpha_m} \varphi_M(\lambda, \mu_1, \dots, \widehat{\mu}_j, \dots, \mu_M),
 \end{aligned} \tag{5.1}$$

where the eigenvalues of the Gaudin Hamiltonians (C.7) are given by

$$\begin{aligned}
 \mathcal{E}_{m,M} &= \frac{1}{4} \text{Res}_{\lambda=\alpha_m} \chi_M(\lambda, \mu_1, \mu_2, \dots, \mu_M) = s_m(s_m + 1) \coth(2\alpha_m) + s_m \sinh(2\alpha_m) \times \\
 &\times \left( -\frac{2\xi v}{\xi^2 + v^2 + 2\xi v \cosh(2\alpha_m)} + \sum_{n \neq m}^N \frac{s_n}{\sinh(\alpha_m + \alpha_n) \sinh(\alpha_m - \alpha_n)} \right) \\
 &- \sum_{i=1}^M \frac{s_m \sinh(2\alpha_m)}{\sinh(\alpha_m + \mu_i) \sinh(\alpha_m - \mu_i)},
 \end{aligned} \tag{5.2}$$

and, for example,

$$\begin{aligned}
 \text{Res}_{\lambda=\alpha_m} \varphi_M(\lambda, \mu_2, \dots, \mu_M) &= \text{Res}_{\lambda=\alpha_m} \mathcal{C}_1(\lambda) (\varphi_{M-1}(\mu_2, \dots, \mu_M) \\
 &+ 4\psi \sum_{j=2}^M \mathcal{A}(\mu_j) \varphi_{M-2}(\mu_2, \dots, \widehat{\mu}_j, \dots, \mu_M) \\
 &+ (4\psi)^2 \cdot 2 \sum_{\substack{j,k=2 \\ k \neq j}}^M \mathcal{A}(\mu_j) \mathcal{A}(\mu_k) \varphi_{M-3}(\mu_2, \dots, \widehat{\mu}_j, \dots, \widehat{\mu}_k, \dots, \mu_M) + \dots \\
 &+ (4\psi)^{M-1} \cdot (M-1)! \mathcal{A}(\mu_2) \mathcal{A}(\mu_3) \dots \mathcal{A}(\mu_M) \Omega_+).
 \end{aligned} \tag{5.3}$$

Here the residuum of the creation operator (3.5) at the pole  $\lambda = \alpha_m$  is given by

$$\text{Res}_{\lambda=\alpha_m} \mathcal{C}_1(\lambda) = \frac{\mathcal{A}(\alpha_m) (\xi e^{2\alpha_m} + v)}{\sinh(2\alpha_m)} \left( \frac{S_m^-}{Z(\alpha_m)} - 2 \frac{\psi}{v} e^{-2\alpha_m} S_m^3 - \frac{\psi^2}{v^2} e^{-4\alpha_m} Z(\alpha_m) S_m^+ \right). \tag{5.4}$$

This action will be essential in obtaining solutions to the corresponding Knizhnik-Zamolodchikov equations in the following section.

### 6. Knizhnik-Zamolodchikov equations

Even before writing down the form of Knizhnik-Zamolodchikov equations in this context, we note that the results in this section will be obtained under the condition that the boundary parameter  $\psi$  is set to zero. Having in mind the local realization (2.1)–(2.3), it should be emphasised that then the creation operator (3.5) simplifies to become

$$\tilde{\mathcal{C}}(\lambda) = \mathcal{C}_M(\lambda) \Big|_{\psi=0} = \mathcal{A}(\lambda) \sum_{m=1}^N \frac{\xi e^{2\alpha_m + \nu}}{Z(\alpha_m) \sinh(\lambda - \alpha_m) \sinh(\lambda + \alpha_m)} S_m^-, \tag{6.1}$$

and therefore the Bethe vectors (4.1) simplify as well

$$\tilde{\varphi}_M(\mu_1, \mu_2, \dots, \mu_M) = \varphi_M(\mu_1, \mu_2, \dots, \mu_M) \Big|_{\psi=0} = \tilde{\mathcal{C}}(\mu_1) \tilde{\mathcal{C}}(\mu_2) \cdots \tilde{\mathcal{C}}(\mu_M) \Omega_+. \tag{6.2}$$

Moreover, when  $\psi = 0$ , the Gaudin Hamiltonians (C.7) reduce to

$$\begin{aligned} \tilde{H}_m = H_m \Big|_{\psi=0} &= \sum_{n \neq m}^N \left( \coth(\alpha_m - \alpha_n) S_m^3 \cdot S_n^3 + \frac{e^{\alpha_m - \alpha_n} S_m^- \cdot S_n^+ + e^{-(\alpha_m - \alpha_n)} S_m^+ \cdot S_n^-}{2 \sinh(\alpha_m - \alpha_n)} \right) \\ &+ \sum_{n=1}^N \coth(\alpha_m + \alpha_n) \left( \frac{S_m^3 \cdot S_n^3 + S_n^3 \cdot S_m^3}{2} \right) \\ &+ \sum_{n=1}^N \frac{e^{-(\alpha_m + \alpha_n)}}{\sinh(\alpha_m + \alpha_n)} \left( \frac{\xi e^{2\alpha_m + \nu}}{\xi e^{-2\alpha_m + \nu}} \frac{S_m^- \cdot S_n^+ + S_n^+ \cdot S_m^-}{4} \right) \\ &+ \sum_{n=1}^N \frac{e^{\alpha_m + \alpha_n}}{\sinh(\alpha_m + \alpha_n)} \left( \frac{\xi e^{-2\alpha_m + \nu}}{\xi e^{2\alpha_m + \nu}} \frac{S_m^+ \cdot S_n^- + S_n^- \cdot S_m^+}{4} \right). \end{aligned} \tag{6.3}$$

Also, observe that, in this case, the equation (5.1) takes the following form

$$\begin{aligned} \tilde{H}_m \tilde{\varphi}_M(\mu_1, \mu_2, \dots, \mu_M) &= \mathcal{E}_{m,M} \tilde{\varphi}_M(\mu_1, \mu_2, \dots, \mu_M) \\ &+ \sum_{j=1}^M \frac{\mathcal{A}(\mu_j)}{\mathcal{A}(\alpha_m)} \frac{\sinh^2(2\lambda)}{\sinh(\alpha_m + \mu_j) \sinh(\alpha_m - \mu_j)} \frac{\xi^2 + \nu^2 + 2\xi\nu \cosh(2\mu_j)}{\xi^2 + \nu^2 + 2\xi\nu \cosh(2\alpha_m)} \times \\ &\times \left( \rho(\mu_j) - \frac{2\xi\nu}{\xi^2 + \nu^2 + 2\xi\nu \cosh(2\mu_j)} - \sum_{k \neq j}^M \frac{1}{\sinh(\mu_j + \mu_k) \sinh(\mu_j - \mu_k)} \right) \times \\ &\times \operatorname{Res}_{\lambda=\alpha_m} \tilde{\varphi}_M(\lambda, \mu_1, \dots, \hat{\mu}_j, \dots, \mu_M), \end{aligned} \tag{6.4}$$

where the eigenvalue  $\mathcal{E}_{m,M}$  of the Gaudin Hamiltonian  $\tilde{H}_m$  is given by (5.2), the notation  $\hat{\mu}_j$  means that the argument  $\mu_j$  is not present and

$$\operatorname{Res}_{\lambda=\alpha_m} \tilde{\varphi}_M(\lambda, \mu_1, \dots, \hat{\mu}_j, \dots, \mu_M) = \operatorname{Res}_{\lambda=\alpha_m} \tilde{\mathcal{C}}(\lambda) \tilde{\varphi}_{M-1}(\mu_1, \dots, \hat{\mu}_j, \dots, \mu_M) \tag{6.5}$$

with

$$\text{Res}_{\lambda=\alpha_m} \tilde{\mathcal{C}}(\lambda) = \frac{\mathcal{A}(\alpha_m)}{Z(\alpha_m)} \frac{\xi e^{2\alpha_m} + \nu}{\sinh(2\alpha_m)} S_m^- \tag{6.6}$$

The interplay between the Bethe vectors of the Gaudin models and solutions to the corresponding Knizhnik-Zamolodchikov equations have attracted some attention [11,12,36,43–48]. The main objective of this section is to consider the Knizhnik-Zamolodchikov equations

$$\kappa \partial_{\alpha_m} \Psi(\alpha_1, \alpha_2, \dots, \alpha_N) = \tilde{H}_m \Psi(\alpha_1, \alpha_2, \dots, \alpha_N), \tag{6.7}$$

where the Hamiltonians  $\tilde{H}_m$  are given by (6.3). The goal is to find the functions (i.e. states)  $\Psi(\alpha_1, \alpha_2, \dots, \alpha_N)$  with the curious property that the action of the Gaudin Hamiltonians  $\tilde{H}_m$  on these states reduces to mere derivation with respect to parameters  $\alpha_m$ .

Following a common approach [11,12,36,45,46], we seek solutions to the equations above in the form of contour integrals with respect to the variables  $\mu_1, \mu_2, \dots, \mu_M$

$$\Psi(\alpha_1, \alpha_2, \dots, \alpha_N) = \oint \dots \oint \Phi(\vec{\mu}|\vec{\alpha}) \cdot \tilde{\varphi}_M(\vec{\mu}|\vec{\alpha}) d\mu_1 \dots d\mu_M, \tag{6.8}$$

where the integrating factor is a scalar function  $\Phi(\vec{\mu}|\vec{\alpha})$  that we will seek in the form:

$$\Phi(\vec{\mu}|\vec{\alpha}) = \exp\left(\frac{S(\vec{\mu}|\vec{\alpha})}{\kappa}\right). \tag{6.9}$$

We choose the function  $S(\vec{\mu}|\vec{\alpha})$  to be:

$$\begin{aligned} S(\vec{\mu}|\vec{\alpha}) = & \sum_{m=1}^N \frac{s_m(s_m + 1)}{2} \ln(\sinh(2\alpha_m)) - \sum_{m=1}^N \frac{s_m}{2} \ln(\xi^2 + \nu^2 + 2\xi\nu \cosh(2\alpha_m)) \\ & + \sum_{m>n}^N s_m s_n (\ln(\sinh(\alpha_m - \alpha_n)) + \ln(\sinh(\alpha_m + \alpha_n))) \\ & - \sum_{j=1}^M \sum_{m=1}^N s_m (\ln(\sinh(\alpha_m - \mu_j)) + \ln(\sinh(\alpha_m + \mu_j))) \\ & + \sum_{j=1}^M \ln(\xi^2 + \nu^2 + 2\xi\nu \cosh(2\mu_j)) + \sum_{j>k}^M (\ln(\sinh(\mu_j - \mu_k)) \\ & + \ln(\sinh(\mu_j + \mu_k))), \end{aligned} \tag{6.10}$$

so that it becomes straightforward to check that the function  $\phi(\vec{\mu}|\vec{\alpha})$ , as defined above, satisfies the following system of linear partial differential equations

$$\kappa \partial_{\alpha_m} \Phi = \mathcal{E}_{m,M} \Phi, \tag{6.11}$$

$$\kappa \partial_{\mu_j} \Phi = \beta_M(\mu_j) \Phi, \tag{6.12}$$

with  $\mathcal{E}_{m,M}$  given by (5.2) and

$$\beta_M(\mu_j) = -\sinh(2\mu_j) \left( \rho(\mu_j) - \frac{2\xi v}{\xi^2 + v^2 + 2\xi v \cosh(2\mu_j)} - \sum_{k \neq j}^M \frac{1}{\sinh(\mu_j + \mu_k) \sinh(\mu_j - \mu_k)} \right). \tag{6.13}$$

Note that, up to multiplication by  $-\sinh(2\mu_j)$ , the functions  $\beta_M(\mu_j)$  coincide with the left-hand sides of Bethe equations (4.5). Alternatively, we might have imposed Bethe equations in the form  $\beta_M(\mu_j) = 0$ .

For later convenience we rewrite the equation (6.4) as follows

$$\begin{aligned} \tilde{H}_m \tilde{\varphi}_M(\mu_1, \mu_2, \dots, \mu_M) &= \mathcal{E}_{m,M} \tilde{\varphi}_M(\mu_1, \mu_2, \dots, \mu_M) \\ &+ \sum_{j=1}^3 \frac{\sinh(2\alpha_m)}{\sinh(\mu_j + \alpha_m) \sinh(\mu_j - \alpha_m)} \frac{\xi^2 + v^2 + 2\xi v \cosh(2\mu_j)}{Z(\alpha_m) (\xi e^{-2\alpha_m} + v)} \\ &\times \frac{\mathcal{A}(\mu_j)}{\sinh(2\mu_j)} \beta_M(\mu_j) \cdot \tilde{\varphi}_{M-1}^{(j,m)}, \end{aligned} \tag{6.14}$$

where we have used the notation

$$\tilde{\varphi}_{M-1}^{(j,m)} = S_m^- \tilde{\varphi}_{M-1}(\mu_1, \dots, \hat{\mu}_j, \dots, \mu_M), \tag{6.15}$$

once more,  $\hat{\mu}_j$  means that the argument  $\mu_j$  is not present.

Now, for the KZ equations to be satisfied, the following must hold:

$$\begin{aligned} \partial_{\alpha_m} \tilde{\varphi}_M &= \sum_{j=1}^M \partial_{\mu_j} \left( \frac{\xi^2 + v^2 + 2\xi v \cosh(2\mu_j)}{\sinh(\alpha_m + \mu_j) \sinh(\alpha_m - \mu_j)} \frac{\mathcal{A}(\mu_j)}{\sinh(2\mu_j)} \right. \\ &\times \left. \frac{\sinh(2\alpha_m)}{Z(\alpha_m) (\xi e^{-2\alpha_m} + v)} \tilde{\varphi}_{M-1}^{(j,m)} \right). \end{aligned} \tag{6.16}$$

The novel feature in the present case is that the functions  $\mathcal{A}(\mu_j)$  of the rapidity parameter  $\mu_j$  and  $Z(\alpha_m)$  of the inhomogeneous parameter  $\alpha_m$  appear on both sides of the equation (6.16). It is easy to check that, without these functions, equality (6.16) simply would not hold. But in their presence, we can try to determine these functions in such a way that the equation (6.16) is valid for an arbitrary natural number  $M$ .

With the aim of satisfying the equation (6.16) for arbitrary  $M$ , we write the same equation in the case when  $M = 1$

$$\begin{aligned} \partial_{\alpha_m} \tilde{\mathcal{C}}(\mu) \Omega_+ &= \partial_{\mu} \left( \frac{\xi^2 + v^2 + 2\xi v \cosh(2\mu)}{\sinh(\alpha_m + \mu) \sinh(\alpha_m - \mu)} \frac{\mathcal{A}(\mu)}{\sinh(2\mu)} \frac{\sinh(2\alpha_m)}{Z(\alpha_m) (\xi e^{-2\alpha_m} + v)} \right. \\ &\times \left. S_m^- \Omega_+ \right) \end{aligned} \tag{6.17}$$

On the left hand side of the equation above we substitute the expression for the operator  $\tilde{\mathcal{C}}(\mu)$  (6.1) and we use the identity

$$\begin{aligned} \partial_{\alpha_m} \frac{\sinh(2\mu)}{\sinh(\mu - \alpha_m) \sinh(\mu + \alpha_m)} &= \partial_{\mu} \left( \frac{\xi^2 + \nu^2 + 2\xi\nu \cosh(2\mu)}{\sinh(\alpha_m - \mu) \sinh(\alpha_m + \mu)} \right) \\ &\times \frac{\sinh(2\alpha_m)}{\xi^2 + \nu^2 + 2\xi\nu \cosh(2\alpha_m)}, \end{aligned} \tag{6.18}$$

to obtain the following equation

$$\frac{Z(\alpha_m) (\xi e^{-2\alpha_m} + \nu)}{\sinh(2\alpha_m)} \partial_{\alpha_m} \frac{\xi e^{2\alpha_m} + \nu}{Z(\alpha_m)} = - \frac{\xi^2 + \nu^2 + 2\xi\nu \cosh(2\mu)}{\mathcal{A}(\mu)} \partial_{\mu} \frac{\mathcal{A}(\mu)}{\sinh(2\mu)}. \tag{6.19}$$

Evidently, in the equation above the variables are separated and therefore we have to solve

$$\frac{\partial_{\alpha_m} Z(\alpha_m)}{Z(\alpha_m)} - \frac{2\xi e^{2\alpha_m}}{\xi e^{2\alpha_m} + \nu} + \frac{C \sinh(2\alpha_m)}{\xi^2 + \nu^2 + 2\xi\nu \cosh(2\alpha_m)} = 0, \tag{6.20}$$

and

$$\frac{\partial_{\mu} \mathcal{A}(\mu)}{\mathcal{A}(\mu)} - 2 \coth(2\mu) + \frac{C \sinh(2\mu)}{\xi^2 + \nu^2 + 2\xi\nu \cosh(2\mu)} = 0, \tag{6.21}$$

where  $C$  is an arbitrary constant. The general solution of the equations above is

$$Z(\alpha_m) = C_1 \frac{\xi e^{2\alpha_m} + \nu}{(\xi^2 + \nu^2 + 2\xi\nu \cosh(2\alpha_m))^{\frac{C}{4\xi\nu}}}, \tag{6.22}$$

$$\mathcal{A}(\mu) = C_2 \frac{\sinh(2\mu)}{(\xi^2 + \nu^2 + 2\xi\nu \cosh(2\mu))^{\frac{C}{4\xi\nu}}}, \tag{6.23}$$

where  $C_1$  and  $C_2$  are additional arbitrary constants. One possible solution is obtained if we set  $C = 0$  and  $C_1 = C_2 = 1$ . In this case, forms of the functions become extremely simple:

$$Z(\alpha_m) = \xi e^{2\alpha_m} + \nu, \quad \text{and} \quad \mathcal{A}(\mu) = \sinh(2\mu). \tag{6.24}$$

After substituting these expressions into (6.1) and (6.2), it is not difficult to confirm that (6.16) is valid for an arbitrary positive integer  $M$ . However, we will nevertheless choose  $C = 2\xi\nu$  and  $C_1 = C_2 = 1$ , since these values will turn out to be far more suitable in the next section, when we discuss norms and scalar products of Bethe vectors. With these values, we obtain:

$$Z(\alpha_m) = \frac{\xi e^{2\alpha_m} + \nu}{\sqrt{\xi^2 + \nu^2 + 2\xi\nu \cosh(2\alpha_m)}} \quad \text{and} \quad \mathcal{A}(\mu) = \frac{\sinh(2\mu)}{\sqrt{\xi^2 + \nu^2 + 2\xi\nu \cosh(2\mu)}}. \tag{6.25}$$

It is straightforward to verify that (6.16) is valid also in this case.

For completeness, we proceed to show that the functions  $\Psi(\alpha_1, \alpha_2, \dots, \alpha_N)$  (6.8) are solutions to the Knizhnik-Zamolodchikov equations (6.7)

$$\kappa \partial_{\alpha_m} (\Phi \cdot \tilde{\varphi}_M) = (\kappa \partial_{\alpha_m} \Phi) \cdot \tilde{\varphi}_M + \Phi \cdot (\kappa \partial_{\alpha_m} \tilde{\varphi}_M). \tag{6.26}$$

As the next step, in the first term, we substitute the right-hand-side of (6.11) and in the second term we use (6.16), with (6.25), to obtain



$$\begin{aligned} \kappa \partial_{\alpha_m} (\Phi \cdot \tilde{\varphi}_M) &= \mathcal{E}_{m,M} (\Phi \cdot \tilde{\varphi}_M) + \Phi \cdot \kappa \sum_{j=1}^M \partial_{\mu_j} \left( \frac{\sqrt{\xi^2 + \nu^2 + 2\xi\nu \cosh(2\mu_j)}}{\sinh(\alpha_m + \mu_j) \sinh(\alpha_m - \mu_j)} \right. \\ &\quad \left. \times \frac{\sinh(2\alpha_m)}{\sqrt{\xi^2 + \nu^2 + 2\xi\nu \cosh(2\alpha_m)}} \tilde{\varphi}_{M-1}^{(j,m)} \right). \end{aligned} \tag{6.27}$$

We use (6.14), with (6.25), to express the first term and we rewrite the second term of the equation above using the Leibniz rule

$$\begin{aligned} \kappa \partial_{\alpha_m} (\Phi \cdot \tilde{\varphi}_M) &= H_m (\Phi \cdot \tilde{\varphi}_M) + \sum_{j=1}^M \frac{\sqrt{\xi^2 + \nu^2 + 2\xi\nu \cosh(2\mu_j)}}{\sinh(\alpha_m + \mu_j) \sinh(\alpha_m - \mu_j)} \\ &\quad \times \frac{\sinh(2\alpha_m)}{\sqrt{\xi^2 + \nu^2 + 2\xi\nu \cosh(2\alpha_m)}} \times \\ &\quad \times \beta_M(\mu_j) \cdot \Phi \cdot \tilde{\varphi}_{M-1}^{(j,m)} + \kappa \sum_{j=1}^M \partial_{\mu_j} \left( \frac{\sqrt{\xi^2 + \nu^2 + 2\xi\nu \cosh(2\mu_j)}}{\sinh(\alpha_m + \mu_j) \sinh(\alpha_m - \mu_j)} \right. \\ &\quad \left. \times \frac{\sinh(2\alpha_m)}{\sqrt{\xi^2 + \nu^2 + 2\xi\nu \cosh(2\alpha_m)}} \Phi \cdot \tilde{\varphi}_{M-1}^{(j,m)} \right) \\ &\quad - \kappa \sum_{j=1}^M (\partial_{\mu_j} \Phi) \frac{\sqrt{\xi^2 + \nu^2 + 2\xi\nu \cosh(2\mu_j)}}{\sinh(\alpha_m + \mu_j) \sinh(\alpha_m - \mu_j)} \frac{\sinh(2\alpha_m)}{\sqrt{\xi^2 + \nu^2 + 2\xi\nu \cosh(2\alpha_m)}} \tilde{\varphi}_{M-1}^{(j,m)}. \end{aligned} \tag{6.28}$$

Then, in the last term we use (6.12) to obtain

$$\begin{aligned} \kappa \partial_{\alpha_m} (\Phi \cdot \tilde{\varphi}_M) &= H_m (\Phi \cdot \tilde{\varphi}_M) + \sum_{j=1}^M \frac{\sqrt{\xi^2 + \nu^2 + 2\xi\nu \cosh(2\mu_j)}}{\sinh(\alpha_m + \mu_j) \sinh(\alpha_m - \mu_j)} \\ &\quad \frac{\sinh(2\alpha_m)}{\sqrt{\xi^2 + \nu^2 + 2\xi\nu \cosh(2\alpha_m)}} \times \\ &\quad \times \beta_M(\mu_j) \cdot \Phi \cdot \tilde{\varphi}_{M-1}^{(j,m)} + \kappa \sum_{j=1}^M \partial_{\mu_j} \left( \frac{\sqrt{\xi^2 + \nu^2 + 2\xi\nu \cosh(2\mu_j)}}{\sinh(\alpha_m + \mu_j) \sinh(\alpha_m - \mu_j)} \right. \\ &\quad \left. \times \frac{\sinh(2\alpha_m)}{\sqrt{\xi^2 + \nu^2 + 2\xi\nu \cosh(2\alpha_m)}} \Phi \cdot \tilde{\varphi}_{M-1}^{(j,m)} \right) \\ &\quad - \sum_{j=1}^M \frac{\sqrt{\xi^2 + \nu^2 + 2\xi\nu \cosh(2\mu_j)}}{\sinh(\alpha_m + \mu_j) \sinh(\alpha_m - \mu_j)} \frac{\sinh(2\alpha_m)}{\sqrt{\xi^2 + \nu^2 + 2\xi\nu \cosh(2\alpha_m)}} \beta_M(\mu_j) \cdot \Phi \cdot \tilde{\varphi}_{M-1}^{(j,m)}. \end{aligned} \tag{6.29}$$

Finally, we simplify the second and the last term to conclude

$$\begin{aligned} \kappa \partial_{\alpha_m} (\Phi \cdot \tilde{\varphi}_M) &= H_m (\Phi \cdot \tilde{\varphi}_M) \\ &+ \kappa \sum_{j=1}^M \partial_{\mu_j} \left( \frac{\sqrt{\xi^2 + v^2 + 2\xi v \cosh(2\mu_j)}}{\sinh(\alpha_m + \mu_j) \sinh(\alpha_m - \mu_j)} \frac{\sinh(2\alpha_m)}{\sqrt{\xi^2 + v^2 + 2\xi v \cosh(2\alpha_m)}} \Phi \cdot \tilde{\varphi}_{M-1}^{(j,m)} \right). \end{aligned} \tag{6.30}$$

Evidently, the terms in the second line of (6.30) will not contribute to the contour integrals with respect to variables  $\mu_j, j = 1, 2, \dots, M$ , in (6.8). Therefore, we have shown that every Bethe vector  $\tilde{\varphi}_M(\mu_1, \mu_2, \dots, \mu_M)$  (6.2) yields a solution  $\Psi(\alpha_1, \alpha_2, \dots, \alpha_N)$  (6.8) to the Knizhnik-Zamolodchikov equations (6.7).

### 7. Norms and scalar products

In this section we will first study the on-shell norms of the Bethe vectors  $\tilde{\varphi}_M(\mu_1, \mu_2, \dots, \mu_M)$  (6.2). With the choice we made for the function  $Z(\alpha_m)$ , the local realization of the generators is given by:

$$e(\lambda) = \sum_{m=1}^N \frac{\sqrt{\xi^2 + v^2 + 2\xi v \cosh(2\alpha_m)} S_m^+}{\sinh(\lambda - \alpha_m) \sinh(\lambda + \alpha_m)}, \tag{7.1}$$

$$h(\lambda) = \sum_{m=1}^N \frac{S_m^3}{\sinh(\lambda - \alpha_m) \sinh(\lambda + \alpha_m)}, \tag{7.2}$$

$$f(\lambda) = \sum_{m=1}^N \frac{\sqrt{\xi^2 + v^2 + 2\xi v \cosh(2\alpha_m)} S_m^-}{\sinh(\lambda - \alpha_m) \sinh(\lambda + \alpha_m)}. \tag{7.3}$$

As the first step, the norm of the Bethe vector

$$\tilde{\varphi}_1(\mu) = \tilde{\mathcal{C}}(\mu)\Omega_+ = \frac{\sinh(2\mu)}{\sqrt{\xi^2 + v^2 + 2\xi v \cosh(2\mu)}} \tilde{f}(\mu)\Omega_+, \tag{7.4}$$

is calculated, when the Bethe equation (3.16) is imposed on the parameter  $\mu$ , to be

$$\begin{aligned} \|\tilde{\varphi}_1(\mu)\|^2 &= -2 \sinh(2\mu) \left( \rho'(\mu) + \frac{4\xi v \sinh(2\mu)}{\xi^2 + v^2 + 2\xi v \cosh(2\mu)} \rho(\mu) \right) \\ &= 2 \frac{\partial \beta_1(\mu)}{\partial \mu} \Big|_{\beta_1(\mu)=0} = 2 \frac{\partial^2 S(\mu)}{\partial \mu^2} \Big|_{\beta_1(\mu)=0}. \end{aligned} \tag{7.5}$$

As the next step, we obtain the norm of the Bethe vector

$$\begin{aligned} \tilde{\varphi}_2(\mu_1, \mu_2) &= \tilde{\mathcal{C}}(\mu_1)\tilde{\mathcal{C}}(\mu_2)\Omega_+ \\ &= \frac{\sinh(2\mu_1)}{\sqrt{\xi^2 + \eta^2 + 2\xi v \cosh(2\mu_1)}} \frac{\sinh(2\mu_2)}{\sqrt{\xi^2 + \eta^2 + 2\xi v \cosh(2\mu_2)}} \tilde{f}(\mu_1)\tilde{f}(\mu_2)\Omega_+, \end{aligned} \tag{7.6}$$

when the Bethe equation (3.21) is imposed on the parameter  $\mu_1$  and  $\mu_2$ , to be

$$\begin{aligned} \|\tilde{\varphi}_2(\mu_1, \mu_2)\|^2 &= 2^2 \det \left( \begin{array}{cc} \frac{\partial \beta_2(\mu_1)}{\partial \mu_1} & \frac{\partial \beta_2(\mu_2)}{\partial \mu_1} \\ \frac{\partial \beta_2(\mu_1)}{\partial \mu_2} & \frac{\partial \beta_2(\mu_2)}{\partial \mu_2} \end{array} \right) \Bigg|_{\substack{\beta_2(\mu_1)=0 \\ \beta_2(\mu_2)=0}} \\ &= 2^2 \det \left( \begin{array}{cc} \frac{\partial^2 S}{\partial \mu_1^2} & \frac{\partial^2 S}{\partial \mu_1 \partial \mu_2} \\ \frac{\partial^2 S}{\partial \mu_2 \partial \mu_1} & \frac{\partial^2 S}{\partial \mu_2^2} \end{array} \right) \Bigg|_{\substack{\beta_2(\mu_1)=0 \\ \beta_2(\mu_2)=0}}. \end{aligned} \tag{7.7}$$

In general, the norm of the Bethe vector

$$\tilde{\varphi}_M(\mu_1, \mu_2, \dots, \mu_M) = \tilde{\mathcal{C}}(\mu_1) \cdots \tilde{\mathcal{C}}(\mu_M) \Omega_+, \tag{7.8}$$

where  $M$  is an arbitrary natural number, is calculated to be

$$\|\tilde{\varphi}_M(\mu_1, \mu_2, \dots, \mu_M)\|^2 = 2^M \det \left( \begin{array}{cccc} \frac{\partial^2 S}{\partial \mu_1^2} & \frac{\partial^2 S}{\partial \mu_1 \partial \mu_2} & \cdots & \frac{\partial^2 S}{\partial \mu_1 \partial \mu_M} \\ \vdots & \ddots & & \vdots \\ \frac{\partial^2 S}{\partial \mu_M \partial \mu_1} & \frac{\partial^2 S}{\partial \mu_M \partial \mu_2} & \cdots & \frac{\partial^2 S}{\partial \mu_M^2} \end{array} \right) \Bigg|_{\substack{\beta_M(\mu_1)=0 \\ \vdots \\ \beta_M(\mu_M)=0}}, \tag{7.9}$$

when the Bethe equation (4.5) is imposed on the parameters  $\mu_1, \dots, \mu_M$ . Therefore, we confirm that relations for norm, analogous to those in rational case [36], now hold also in the trigonometric case, thanks to the proper choices of  $Z(\alpha_m)$  and  $\mathcal{A}(\mu)$  functions.

Furthermore, with this choice for  $Z(\alpha_m)$  and  $\mathcal{A}(\mu)$ , it is also possible to calculate more general expression for the off-shell scalar product of the Bethe vectors, again analogous as in the rational case [36]. It turns out that the scalar product

$$\begin{aligned} &\langle \tilde{\varphi}_M(\mu_1, \mu_2, \dots, \mu_M), \tilde{\varphi}_M(v_1, v_2, \dots, v_M) \rangle \\ &= \langle \Omega_+, \tilde{\mathcal{C}}^*(\mu_1) \cdots \tilde{\mathcal{C}}^*(\mu_M) \tilde{\mathcal{C}}(v_1) \cdots \tilde{\mathcal{C}}(v_M) \Omega_+ \rangle, \end{aligned} \tag{7.10}$$

is proportional to

$$\langle \Omega_+, e(\mu_1) \cdots e(\mu_M) f(v_M) \cdots f(v_1) \Omega_+ \rangle = 2^M \sum_{\sigma \in \mathcal{S}_M} \det \mathcal{M}^\sigma, \tag{7.11}$$

where  $\mathcal{S}_M$  is the symmetric group of degree  $M$  and the entries of the  $M \times M$  matrix  $\mathcal{M}^\sigma$  are given by

$$\begin{aligned} \mathcal{M}_{jj}^\sigma &= - \frac{(\xi^2 + v^2 + 2\xi v \cosh(2\mu_j)) \rho(\mu_j) - (\xi^2 + v^2 + 2\xi v \cosh(2v_{\sigma(j)})) \rho(v_{\sigma(j)})}{\sinh(\mu_j - v_{\sigma(j)}) \sinh(\mu_j + v_{\sigma(j)})} \\ &\quad - \frac{1}{2} \sum_{k \neq j}^M \frac{(\xi^2 + v^2 + 2\xi v \cosh(2\mu_k)) + (\xi^2 + v^2 + 2\xi v \cosh(2v_{\sigma(k)}))}{\sinh(\mu_j - \mu_k) \sinh(\mu_j + \mu_k) \sinh(v_{\sigma(j)} - v_{\sigma(k)}) \sinh(v_{\sigma(j)} + v_{\sigma(k)})}, \end{aligned} \tag{7.12}$$

$$\mathcal{M}_{jk}^\sigma = - \frac{1}{2} \frac{(\xi^2 + v^2 + 2\xi v \cosh(2\mu_k)) + (\xi^2 + v^2 + 2\xi v \cosh(2v_{\sigma(k)}))}{\sinh(\mu_j - \mu_k) \sinh(\mu_j + \mu_k) \sinh(v_{\sigma(j)} - v_{\sigma(k)}) \sinh(v_{\sigma(j)} + v_{\sigma(k)})}, \tag{7.13}$$

where  $j, k = 1, 2, \dots, M$ .

## 8. Conclusions

We have demonstrated the implementation of the algebraic Bethe ansatz for the trigonometric Gaudin model with boundary terms, which we have conjectured in our previous paper [38]. The Bethe vectors are here defined by the recurrent relation (4.1). We have shown the action of the generating function  $\tau(\lambda)$  on an arbitrary Bethe vector (4.3). The proof was based on mathematical induction. The key step in the proof is calculating the off-shell action of the commutator between the generating function and the relevant creation operator on the previous Bethe vector. This was done by a straightforward calculation and the result is presented in Appendix D, equation (D.1), and is valid for an arbitrary natural number  $M$ .

The work we have presented here is based on the non-unitary classical r-matrix (A.5) which is given in the so-called homogeneous gradation, as opposed to our previous papers [37,38] where we have used the r-matrix in the principal gradation. As we have shown, the novel feature in this approach is the certain freedom we have found in the local realization of the generators of the generalized trigonometric  $sl(2)$  Gaudin algebra as well as in the creation operators we have used in the algebraic Bethe ansatz. It is precisely this structure that supports the interplay with the corresponding Knizhnik-Zamolodchikov equations. As a result we have obtained not only the solutions to the Knizhnik-Zamolodchikov equations, each of which corresponding to every Bethe state we have constructed, but also some neat formulas for the on-shell norms and off-self scalar products of these Bethe states, in some sense, analogous to the ones we have obtained previously in the rational case [36].

### CRedit authorship contribution statement

**I. Salom:** Formal analysis, Methodology, Software, Writing – review & editing. **N. Manojlović:** Conceptualization, Formal analysis, Writing – original draft.

### Declaration of competing interest

The authors declare that they have no known competing financial interests or personal relationships that could have appeared to influence the work reported in this paper.

### Acknowledgements

IS is supported by the Ministry of Education, Science and Technological Development (MP-NTR) of the Republic of Serbia, and by the Science Fund of the Republic of Serbia, Program DIASPORA, No. 6427195, SQ2020.

### Appendix A. Classical r-matrix

The study presented in this paper is based on the following classical r-matrix [20,49,50]

$$r(\lambda) = -\frac{\coth(\lambda)}{2} \sigma^3 \otimes \sigma^3 - \frac{1}{4 \sinh(\lambda)} (e^{-\lambda} \sigma^+ \otimes \sigma^- + e^{\lambda} \sigma^- \otimes \sigma^+), \quad (\text{A.1})$$

where  $\sigma^\alpha$ , with  $\alpha = +, -, 3$  are the Pauli matrices

$$\sigma^\alpha = \begin{pmatrix} \delta_{\alpha 3} & 2\delta_{\alpha+} \\ 2\delta_{\alpha-} & -\delta_{\alpha 3} \end{pmatrix}.$$

This unitarity classical r-matrix is a solution to the (proper) classical Yang-Baxter equation and it has the following symmetry [4].

$$[\sigma_1^3 + \sigma_2^3, r_{12}(\lambda)] = 0. \tag{A.2}$$

In this case, the relevant K-matrix is given by [20,49,50]

$$K(\lambda) = \begin{pmatrix} \xi e^{-2\lambda} + \nu & 2\psi \sinh(2\lambda) \\ 2\phi \sinh(2\lambda) & \xi e^{2\lambda} + \nu \end{pmatrix}, \tag{A.3}$$

where we use the standard parametrization of [51]. This K-matrix and the r-matrix (A.1) satisfy the classical reflection equation [35,52,53]

$$\begin{aligned} r_{12}(\lambda - \mu)K_1(\lambda)K_2(\mu) + K_1(\lambda)r_{21}(\lambda + \mu)K_2(\mu) = \\ = K_2(\mu)r_{12}(\lambda + \mu)K_1(\lambda) + K_2(\mu)K_1(\lambda)r_{21}(\lambda - \mu). \end{aligned} \tag{A.4}$$

Thus, the corresponding non-unitary r-matrix defined by [35]

$$r_{12}^K(\lambda, \mu) = r_{12}(\lambda - \mu) - K_2(\mu)r_{12}(\lambda + \mu)K_2^{-1}(\mu), \tag{A.5}$$

satisfies the generalized classical Yang-Baxter equation [31–33,35,54–56]

$$[r_{32}^K(\nu, \mu), r_{13}^K(\lambda, \nu)] + [r_{12}^K(\lambda, \mu), r_{13}^K(\lambda, \nu)] + [r_{12}^K(\lambda, \mu), r_{23}^K(\mu, \nu)] = 0. \tag{A.6}$$

Moreover, it is straightforward to check the following useful identities

$$K(\lambda)K(-\lambda) = \det(K(\lambda)) \mathbb{1}, \tag{A.7}$$

$$K(-\lambda) = \text{tr}(K(\lambda)) \mathbb{1} - K(\lambda). \tag{A.8}$$

When the parameters are chosen so that  $\xi^2 + 4\psi\phi \neq 0$ , the K-matrix (A.3) admits two distinct eigenvalues

$$\epsilon_{\pm}(\lambda) = \xi \cosh(2\lambda) \pm \sqrt{\xi^2 + 4\psi\phi \sinh(2\lambda) + \nu}. \tag{A.9}$$

In this case, for  $\phi \neq 0$ , there exists the matrix

$$\mathcal{U} = \begin{pmatrix} \xi + \sqrt{\xi^2 + 4\psi\phi} & \xi - \sqrt{\xi^2 + 4\psi\phi} \\ -2\phi & -2\phi \end{pmatrix} \tag{A.10}$$

such that

$$K(\lambda) = \mathcal{U} D(\lambda) \mathcal{U}^{-1}, \quad \text{with} \quad D(\lambda) = \begin{pmatrix} \epsilon_{-}(\lambda) & 0 \\ 0 & \epsilon_{+}(\lambda) \end{pmatrix}. \tag{A.11}$$

Under the conditions above there exists the matrix

$$\mathcal{M} = \begin{pmatrix} \xi + \sqrt{\xi^2 + 4\psi\phi} & -2\phi \\ -2\phi & \xi + \sqrt{\xi^2 + 4\psi\phi} \end{pmatrix} \tag{A.12}$$

such that

$$\mathcal{M}^{-1} K(\lambda) \mathcal{M} = \begin{pmatrix} \epsilon_{-}(\lambda) & 2(\psi + \phi) \sinh(2\lambda) \\ 0 & \epsilon_{+}(\lambda) \end{pmatrix}. \tag{A.13}$$

An analogous diagonalization can be obtained for  $\psi \neq 0$ . However, when  $\xi^2 + 4\psi\varphi = 0$ , the matrix (A.3) cannot be diagonalized. In this case, its Jordan form is given by

$$K(\lambda) = \mathcal{V}(\lambda) J(\lambda) \mathcal{V}^{-1}(\lambda), \tag{A.14}$$

where

$$\mathcal{V}(\lambda) = \begin{pmatrix} -\xi \sinh(2\lambda) & 1 \\ 2\phi \sinh(2\lambda) & 0 \end{pmatrix}, \quad \text{and} \quad J(\lambda) = \begin{pmatrix} \xi \cosh(2\lambda) + \nu & 1 \\ 0 & \xi \cosh(2\lambda) + \nu \end{pmatrix}. \tag{A.15}$$

### Appendix B. Hilbert space

It is well known that the Hilbert space of the inhomogeneous trigonometric  $sl(2)$  Gaudin model with  $N$  sites, characterised by the local space  $V_m = \mathbb{C}^{2s+1}$  together with the corresponding inhomogeneous parameter  $\alpha_m$ , is given by [20,37–39]

$$\mathcal{H} = \bigotimes_{m=1}^N V_m = (\mathbb{C}^{2s+1})^{\otimes N}. \tag{B.1}$$

The local spin operators  $S_m^\alpha$ , here  $\alpha = +, -, 3$ , satisfy the usual commutation relations

$$[S_m^3, S_n^\pm] = \pm S_m^\pm \delta_{mn}, \quad [S_m^+, S_n^-] = 2S_m^3 \delta_{mn}. \tag{B.2}$$

Moreover, for every  $m \in \{1, \dots, N\}$

$$\exists \omega_m \in V_m : S_m^3 \omega_m = s_m \omega_m \quad \text{and} \quad S_m^+ \omega_m = 0. \tag{B.3}$$

Then the vector  $\Omega_+$  is defined to be

$$\Omega_+ = \omega_1 \otimes \dots \otimes \omega_N \in \mathcal{H}. \tag{B.4}$$

### Appendix C. Linear bracket

The Lax operator

$$L_0(\lambda) = \sum_{m=1}^N \left( \coth(\lambda - \alpha_m) \sigma_0^3 \otimes S_m^3 + \frac{1}{2 \sinh(\lambda - \alpha_m)} (e^{-\lambda + \alpha_m} \sigma_0^+ \otimes S_m^- + e^{\lambda - \alpha_m} \sigma_0^- \otimes S_m^+) \right), \tag{C.1}$$

and the r-matrix (A.1) satisfy the so-called Sklyanin linear bracket [5,10–12]

$$[L_0(\lambda), L_0(\mu)] = [r_{00}(\lambda - \mu), L_0(\lambda) + L_0(\mu)]. \tag{C.2}$$

Consequently, the entries of the Lax operator (C.1) generate the  $sl(2)$  trigonometric Gaudin algebra.

In the study of the generalized trigonometric  $sl(2)$  Gaudin algebra the relevant the Lax operator is given by

$$\mathcal{L}_0(\lambda) = L_0(\lambda) - K_0(\lambda) L_0(-\lambda) K_0^{-1}(\lambda), \tag{C.3}$$



where  $L_0(\lambda)$  is the Lax operator (C.1) and  $K_0(\lambda)$  the reflection K-matrix is defined in (A.3). The Lax operator (C.3) obeys the following linear bracket [31–33,35,54–56]

$$[\mathcal{L}_0(\lambda), \mathcal{L}_0(\mu)] = \left[ r_{00'}^K(\lambda, \mu), \mathcal{L}_0(\lambda) \right] - \left[ r_{0'0}^K(\mu, \lambda), \mathcal{L}_0(\mu) \right]. \tag{C.4}$$

This linear bracket is obviously anti-symmetric and it obeys the Jacobi identity because the  $r$ -matrix (A.5) satisfies the classical Yang-Baxter equation (A.6).

The generating function of the Gaudin Hamiltonians with boundary terms is given by

$$\tau(\lambda) = \text{tr}_0 \left( \mathcal{L}_0^2(\lambda) \right), \tag{C.5}$$

and it generates an Abelian subalgebra since it commutes for different values of the spectral parameter,

$$[\tau(\lambda), \tau(\mu)] = 0. \tag{C.6}$$

In this formulation the trigonometric Gaudin Hamiltonians with boundary terms have slightly different form in terms of local operators

$$\begin{aligned} H_m &= \frac{(\pm 1)}{4} \text{Res}_{\lambda=\pm\alpha_m} \tau(\lambda) \\ &= \sum_{n \neq m}^N \left( \coth(\alpha_m - \alpha_n) S_m^3 \cdot S_n^3 + \frac{e^{\alpha_m - \alpha_n} S_m^- \cdot S_n^+ + e^{-(\alpha_m - \alpha_n)} S_m^+ \cdot S_n^-}{2 \sinh(\alpha_m - \alpha_n)} \right) \\ &+ \sum_{n=1}^N \coth(\alpha_m + \alpha_n) \left( \frac{S_m^3 \cdot S_n^3 + S_n^3 \cdot S_m^3}{2} - \frac{2\psi \sinh(2\alpha_m)}{\xi e^{2\alpha_m + \nu}} \frac{S_m^+ \cdot S_n^3 + S_n^3 \cdot S_m^+}{2} \right) \\ &+ \sum_{n=1}^N \frac{e^{-(\alpha_m + \alpha_n)}}{\sinh(\alpha_m + \alpha_n)} \left( \frac{2\psi \sinh(2\alpha_m)}{\xi e^{-2\alpha_m + \nu}} \frac{S_m^3 \cdot S_n^+ + S_n^+ \cdot S_m^3}{2} \right. \\ &+ \left. \frac{\xi e^{2\alpha_m + \nu}}{\xi e^{-2\alpha_m + \nu}} \frac{S_m^- \cdot S_n^+ + S_n^+ \cdot S_m^-}{4} \right) \\ &+ \sum_{n=1}^N \frac{e^{-(\alpha_m + \alpha_n)}}{\sinh(\alpha_m + \alpha_n)} \left( - \frac{2\psi^2 \sinh^2(2\alpha_m)}{(\xi e^{2\alpha_m + \nu})(\xi e^{-2\alpha_m + \nu})} \frac{S_m^+ \cdot S_n^+ + S_n^+ \cdot S_m^+}{2} \right) \\ &+ \sum_{n=1}^N \frac{e^{\alpha_m + \alpha_n}}{\sinh(\alpha_m + \alpha_n)} \left( \frac{\xi e^{-2\alpha_m + \nu}}{\xi e^{2\alpha_m + \nu}} \frac{S_m^+ \cdot S_n^- + S_n^- \cdot S_m^+}{4} \right). \end{aligned} \tag{C.7}$$

### Appendix D. Crucial formula

Obtained by direct calculation, the action of the commutator between  $\tau(\lambda)$  and the creation operator on the Bethe vector  $\varphi_{M-1}(\mu_2, \dots, \mu_M)$  represents the crucial step in the proof of the off-shell action of the generating function

$$\begin{aligned}
 & [\tau(\lambda), C_1(\mu_1)] \varphi_{M-1}(\mu_2, \dots, \mu_M) = -\frac{2 \sinh^2(2\lambda)}{\sinh(\lambda + \mu_1) \sinh(\lambda - \mu_1)} \times \\
 & \times \left( 2\rho(\lambda) - \frac{4\xi v}{\xi^2 + v^2 + 2\xi v \cosh(2\lambda)} - \sum_{j=2}^M \frac{2}{\sinh(\lambda + \mu_j) \sinh(\lambda - \mu_j)} \right) \\
 & \times \varphi_M(\mu_1, \mu_2, \dots, \mu_M) \\
 & + \frac{\mathcal{A}(\mu_1)}{\mathcal{A}(\lambda)} \frac{2 \sinh^2(2\lambda)}{\sinh(\lambda + \mu_1) \sinh(\lambda - \mu_1)} \frac{\xi^2 + v^2 + 2\xi v \cosh(2\mu_1)}{\xi^2 + v^2 + 2\xi v \cosh(2\lambda)} \times \\
 & \times \left( 2\rho(\mu_1) - \frac{4\xi v}{\xi^2 + v^2 + 2\xi v \cosh(2\mu_1)} - \sum_{j=2}^M \frac{2}{\sinh(\mu_1 + \mu_j) \sinh(\mu_1 - \mu_j)} \right) \\
 & \times \varphi_M(\lambda, \mu_2, \dots, \mu_M) \\
 & + \sum_{j=2}^M \frac{\mathcal{A}(\mu_j)}{\mathcal{A}(\lambda)} \frac{2 \sinh^2(2\lambda)}{\sinh(\lambda + \mu_j) \sinh(\lambda - \mu_j)} \frac{\xi^2 + v^2 + 2\xi v \cosh(2\mu_j)}{\xi^2 + v^2 + 2\xi v \cosh(2\lambda)} \times \\
 & \times \frac{2}{\sinh(\mu_1 + \mu_j) \sinh(\mu_1 - \mu_j)} \varphi_M(\lambda, \mu_1, \mu_2, \dots, \widehat{\mu}_j, \dots, \mu_M) \\
 & + \sum_{j=2}^M \frac{8\psi \mathcal{A}(\mu_j) \sinh^2(2\lambda)}{\sinh(\lambda + \mu_1) \sinh(\lambda - \mu_1)} \frac{\sinh(\mu_1 + \mu_j) \sinh(\mu_1 - \mu_j)}{\sinh(\lambda + \mu_j) \sinh(\lambda - \mu_j)} \times \\
 & \times \left( 2\rho(\lambda) - \frac{4\xi v}{\xi^2 + v^2 + 2\xi v \cosh(2\lambda)} - \sum_{k \neq 1, j}^M \frac{2}{\sinh(\lambda + \mu_k) \sinh(\lambda - \mu_k)} \right) \\
 & \times \varphi_{M-1}(\mu_1, \mu_2, \dots, \widehat{\mu}_j, \dots, \mu_M) \\
 & + \sum_{j=2}^M \frac{4\psi \mathcal{A}(\mu_j)}{\mathcal{A}(\lambda)} \frac{2 \sinh^2(2\lambda)}{\sinh(\lambda + \mu_j) \sinh(\lambda - \mu_j)} \frac{\xi^2 + v^2 + 2\xi v \cosh(2\mu_j)}{\xi^2 + v^2 + 2\xi v \cosh(2\lambda)} \times \\
 & \times \sum_{k \neq 1, j}^M \frac{2 \mathcal{A}(\mu_k) \sinh(\mu_1 + \mu_k) \sinh(\mu_1 - \mu_k)}{\sinh(\mu_j + \mu_1) \sinh(\mu_j - \mu_1) \sinh(\mu_j + \mu_k) \sinh(\mu_j - \mu_k)} \\
 & \times \varphi_{M-1}(\lambda, \mu_1, \mu_2, \dots, \widehat{\mu}_j, \dots, \widehat{\mu}_k, \dots, \mu_M) \\
 & - \sum_{j=2}^M \frac{4\psi \mathcal{A}(\mu_1) \mathcal{A}(\mu_j)}{\mathcal{A}(\lambda)} \frac{2 \sinh^2(2\lambda)}{\sinh(\lambda + \mu_1) \sinh(\lambda - \mu_1)} \frac{\xi^2 + v^2 + 2\xi v \cosh(2\mu_1)}{\xi^2 + v^2 + 2\xi v \cosh(2\lambda)} \times \\
 & \times \left( 2\rho(\mu_1) - \frac{4\xi v}{\xi^2 + v^2 + 2\xi v \cosh(2\mu_1)} - \sum_{k \neq 1, j}^M \frac{2}{\sinh(\mu_1 + \mu_k) \sinh(\mu_1 - \mu_k)} \right) \\
 & \times \varphi_{M-1}(\lambda, \mu_2, \dots, \widehat{\mu}_j, \dots, \mu_M)
 \end{aligned}$$

$$\begin{aligned}
 & + \sum_{j=2}^M \frac{8\psi \mathcal{A}(\mu_j) \sinh^2(2\lambda)}{\sinh(\lambda + \mu_j) \sinh(\lambda - \mu_j)} \frac{\xi^2 + \nu^2 + 2\xi\nu \cosh(2\mu_j)}{\xi^2 + \nu^2 + 2\xi\nu \cosh(2\lambda)} \times \\
 & \times \left( 2\rho(\mu_j) - \frac{4\xi\nu}{\xi^2 + \nu^2 + 2\xi\nu \cosh(2\mu_j)} - \sum_{k \neq 1, j}^M \frac{2}{\sinh(\mu_j + \mu_k) \sinh(\mu_j - \mu_k)} \right) \\
 & \times \varphi_{M-1}(\mu_1, \dots, \widehat{\mu}_j, \dots, \mu_M). \tag{D.1}
 \end{aligned}$$

**References**

[1] M. Gaudin, Diagonalisation d’une classe d’hamiltoniens de spin, *J. Phys.* 37 (1976) 1087–1098.  
 [2] M. Gaudin, La fonction d’onde de Bethe, chapter 13 Masson, Paris, 1983.  
 [3] M. Gaudin, The Bethe Wavefunction, Cambridge University Press, 2014.  
 [4] A.A. Belavin, V.G. Drinfeld, Solutions of the classical Yang-Baxter equation for simple Lie algebras, *Funct. Anal. Appl.* 16 (3) (1982) 159–180.  
 [5] E.K. Sklyanin, Separation of variables in the Gaudin model, *Zap. Nauchn. Sem. Leningrad. Otdel. Mat. Inst. Steklov. (LOMI)* 164 (1987) 151–169; translation in *J. Sov. Math.* 47 (1989) 2473–2488.  
 [6] M.A. Semenov-Tian-Shansky, Quantum and classical integrable systems, in: *Integrability of Nonlinear Systems*, in: *Lecture Notes in Physics*, vol. 495, 1997, pp. 314–377.  
 [7] B. Jurčo, Classical Yang-Baxter equations and quantum integrable systems (Gaudin models), in: *Quantum Groups*, Clausthal, 1989, in: *Lecture Notes in Phys.*, vol. 370, 1990, pp. 219–227.  
 [8] F. Wagner, A.J. Macfarlane, Solvable Gaudin models for higher rank symplectic algebras. Quantum groups and integrable systems (Prague, 2000), *Czechoslov. J. Phys.* 50 (2000) 1371–1377.  
 [9] T. Brzezinski, A.J. Macfarlane, On integrable models related to the  $osp(1, 2)$  Gaudin algebra, *J. Math. Phys.* 35 (7) (1994) 3261–3272.  
 [10] P.P. Kulish, N. Manojlović, Bethe vectors of the  $osp(1|2)$  Gaudin model, *Lett. Math. Phys.* 55 (2001) 77–95.  
 [11] P.P. Kulish, N. Manojlović, Creation operators and Bethe vectors of the  $osp(1|2)$  Gaudin model, *J. Math. Phys.* 42 (10) (2001) 4757–4778.  
 [12] P.P. Kulish, N. Manojlović, Trigonometric  $osp(1|2)$  Gaudin model, *J. Math. Phys.* 44 (2) (2003) 676–700.  
 [13] N. Cirilo António, N. Manojlović,  $sl(2)$  Gaudin models with Jordanian twist, *J. Math. Phys.* 46 (10) (2005) 102701.  
 [14] P.P. Kulish, N. Manojlović, M. Samsonov, A. Stolin, Bethe Ansatz for deformed Gaudin model (AGMF Tartu08 workshop proceedings), *Proc. Est. Acad. Sci.* 59 (4) (2010) 326–331.  
 [15] N. Cirilo António, N. Manojlović, A. Stolin, Algebraic Bethe Ansatz for deformed Gaudin model, *J. Math. Phys.* 52 (10) (2011) 103501, arXiv:1002.4951.  
 [16] W.L. Yang, R. Sasaki, Y.Z. Zhang,  $\mathbb{Z}_n$  elliptic Gaudin model with open boundaries, *J. High Energy Phys.* 09 (2004) 046.  
 [17] W.L. Yang, R. Sasaki, Y.Z. Zhang,  $A_{n-1}$  Gaudin model with open boundaries, *Nucl. Phys. B* 729 (2005) 594–610.  
 [18] A. Lima-Santos, The  $sl(2|1)^{(2)}$  Gaudin magnet with diagonal boundary terms, *J. Stat. Mech.* (2009) P07025.  
 [19] K. Hao, W.-L. Yang, H. Fan, S.-Y. Liu, K. Wu, Z.-Y. Yang, Y.Z. Zhang, Determinant representations for scalar products of the XXX Gaudin model with general boundary terms, *Nucl. Phys. B* 862 (2012) 835–849.  
 [20] N. Cirilo António, N. Manojlović, Z. Nagy, Trigonometric  $s\ell(2)$  Gaudin model with boundary terms, *Rev. Math. Phys.* 25 (10) (2013) 1343004, arXiv:1303.2481.  
 [21] N. Cirilo António, N. Manojlović, Z. Nagy, Jordanian deformation of the open  $s\ell(2)$  Gaudin model, *Theor. Math. Phys.* 179 (1) (2014) 462–471, arXiv:1304.6918.  
 [22] I. Salom, N. Manojlović, Creation operators of the non-periodic  $sl(2)$  Gaudin model, in: *Proceedings of the 8th Mathematical Physics Meeting: Summer School and Conference on Modern Mathematical Physics*, 24–31 August 2014, Belgrade, Serbia, in: *SFIN XXVIII Series A: Conferences No. A1*, ISBN 978-86-82441-43-4, June 2015, pp. 149–155.  
 [23] N. Manojlović, N. Cirilo António, I. Salom, Quasi-classical limit of the open Jordanian XXX spin chain, in: *Proceedings of the 9th Mathematical Physics Meeting: Summer School and Conference on Modern Mathematical Physics*, 18–23 September 2017, Belgrade, Serbia, in: *SFIN XXXI Series A: Conferences No. A1*, ISBN 978-86-82441-48-9, April 2018, pp. 259–266.  
 [24] I. Lukyanenko, P.S. Isaac, J. Links, On the boundaries of quantum integrability for the spin-1/2 Richardson-Gaudin system, *Nucl. Phys. B* 886 (2014) 364–398.

- [25] J. Links, Solution of the classical Yang-Baxter equation with an exotic symmetry, and integrability of a multi-species boson tunnelling model, *Nucl. Phys. B* 916 (2017) 117–131.
- [26] E.A. Yuzbashyan, Integrable time-dependent Hamiltonians, solvable Landau-Zener models and Gaudin magnets, *Ann. Phys.* 392 (2018) 323–339.
- [27] Y. Shen, P.S. Isaac, J. Links, Ground-state energies of the open and closed  $p + ip$ -pairing models from the Bethe Ansatz, *Nucl. Phys. B* 937 (2018) 28–55.
- [28] C. Dimo, A. Faribault, Quadratic operator relations and Bethe equations for spin-1/2 Richardson-Gaudin models, *J. Phys. A, Math. Theor.* 51 (32) (2018) 325202.
- [29] P. Claeys, C. Dimo, S. De Baerdemacker, A. Faribault, Integrable spin- $\frac{1}{2}$  Richardson-Gaudin XYZ models in an arbitrary magnetic field, *J. Phys. A, Math. Theor.* 52 (8) (2019) 08LT01.
- [30] V. Caudrelier, N. Crampé, Classical  $N$ -reflection equation and Gaudin models, *Lett. Math. Phys.* 109 (4) (2019) 843–856.
- [31] T. Skrypnik, Generalized quantum Gaudin spin chains, involutive automorphisms and twisted classical r-matrices, *J. Math. Phys.* 47 (2006) 033511.
- [32] T. Skrypnik, Generalized Gaudin spin chains, non-skew-symmetric r-matrices and reflection equation algebras, *J. Math. Phys.* 47 (2007) 113521.
- [33] T. Skrypnik, Non-skew-symmetric classical r-matrix, algebraic Bethe ansatz, and Bardeen-Cooper-Schrieffer-type integrable systems, *J. Math. Phys.* 50 (2009) 033540.
- [34] N. Cirilo António, N. Manojlović, I. Salom, Algebraic Bethe ansatz for the XXX chain with triangular boundaries and Gaudin model, *Nucl. Phys. B* 889 (2014) 87–108, arXiv:1405.7398.
- [35] N. Cirilo António, N. Manojlović, E. Ragoucy, I. Salom, Algebraic Bethe ansatz for the  $sl(2)$  Gaudin model with boundary, *Nucl. Phys. B* 893 (2015) 305–331, arXiv:1412.1396.
- [36] I. Salom, N. Manojlović, N. Cirilo António, Generalized  $sl(2)$  Gaudin algebra and corresponding Knizhnik-Zamolodchikov equation, *Nucl. Phys. B* 939 (2019) 358–371.
- [37] N. Manojlović, I. Salom, Algebraic Bethe ansatz for the XXZ Heisenberg spin chain with triangular boundaries and the corresponding Gaudin model, *Nucl. Phys. B* 923 (2017) 73–106, arXiv:1705.02235.
- [38] N. Manojlović, I. Salom, Algebraic Bethe ansatz for the trigonometric  $sl(2)$  Gaudin model with triangular boundary, *Symmetry* 12 (2020) 352, arXiv:1709.06419.
- [39] N. Crampé, Algebraic Bethe Ansatz for the XXZ Gaudin models with generic boundary, *SIGMA* 13 (2017) 094.
- [40] L.D. Faddeev, How the algebraic Bethe Ansatz works for integrable models, in: A. Connes, K. Gawedzki, J. Zinn-Justin (Eds.), *Quantum Symmetries/Symmetries Quantiques*, in: *Proceedings of the Les Houches Summer School, Session LXIV, North-Holland, 1998*, pp. 149–219, arXiv:hep-th/9605187.
- [41] E.K. Sklyanin, T. Takebe, Algebraic Bethe ansatz for the XYZ Gaudin model, *Phys. Lett. A* 219 (1996) 217–225.
- [42] N. Manojlović, Z. Nagy, Creation operators and algebraic Bethe ansatz for the elliptic quantum group  $E_{\tau, \eta}(so_3)$ , *J. Phys. A, Math. Theor.* 40 (2007) 4181–4191.
- [43] B. Feigin, E. Frenkel, N. Reshetikhin, Gaudin model, Bethe ansatz and correlation functions at the critical level, *Commun. Math. Phys.* 166 (1994) 27–62.
- [44] N. Reshetikhin, A. Varchenko, Quasiclassical asymptotics of solutions to the KZ equations, in: *Geometry, Topology & Physics for Raul Bott*, in: *Conference Proceedings Lecture Notes Geometry Topology VI*, Int. Press, Cambridge, MA, 1995, pp. 293–322.
- [45] H.M. Babujian, R. Flume, Off-shell Bethe Ansatz equations for Gaudin magnets and solutions of Knizhnik-Zamolodchikov equations, *Mod. Phys. Lett. A* 9 (22) (1994) 2029–2039.
- [46] K. Hikami, Gaudin magnet with boundary and generalized Knizhnik-Zamolodchikov equation, *J. Phys. A, Math. Gen.* 28 (1995) 4997–5007.
- [47] T. Skrypnik, Generalized Knizhnik-Zamolodchikov equations, off-shell Bethe ansatz and non-skew-symmetric classical r-matrices, *Nucl. Phys. B* 824 (2010) 436–451.
- [48] T. Skrypnik, Isomonodromic deformations, generalized Knizhnik-Zamolodchikov equations and non-skew-symmetric classical r-matrices, *J. Math. Phys.* 51 (2010) 083516.
- [49] A. Doikou, From affine Hecke algebras to boundary symmetries, *Nucl. Phys. B* 725 (3) (2005) 493–530, arXiv:math-ph/0409060.
- [50] P.P. Kulish, A.I. Mudrov, Baxterization of solutions to reflection equation with Hecke R-matrix, *Lett. Math. Phys.* 75 (2006) 151–170.
- [51] H.J. de Vega, A. González Ruiz, Boundary  $K$ -matrices for the XYZ, XXZ, XXX spin chains, *J. Phys. A, Math. Gen.* 27 (1994) 6129–6137.
- [52] E.K. Sklyanin, Boundary conditions for integrable equations, *Funct. Anal. Appl.* 21 (2) (1987) 164–166.
- [53] E.K. Sklyanin, Boundary conditions for integrable systems, in: *Proceedings of the VIIIth International Congress on Mathematical Physics, Marseille, 1986*, World Sci. Publishing, Singapore, 1987, pp. 402–408.

- [54] J. Avan, M. Talon, Rational and trigonometric constant non-antisymmetric r-matrices, *Phys. Lett. B* 241 (1990) 77–82.
- [55] O. Babelon, C. Viallet, Hamiltonian structures and Lax equations, *Phys. Lett. B* 237 (1990) 411.
- [56] L. Freidel, J.M. Maillet, Quadratic algebras and integrable systems, *Phys. Lett. B* 262 (1991) 278–284.



XXVIIIth International Conference on Ultrarelativistic Nucleus-Nucleus Collisions  
(Quark Matter 2019)

## From high $p_{\perp}$ theory and data to inferring anisotropy of Quark-Gluon Plasma

Magdalena Djordjevic<sup>a</sup>, Stefan Stojku<sup>a</sup>, Dusan Zigic<sup>a</sup>, Bojana Ilic<sup>a</sup>, Jussi  
Auvinen<sup>a</sup>, Igor Salom<sup>a</sup>, Marko Djordjevic<sup>b</sup> and Pasi Huovinen<sup>a</sup>

<sup>a</sup> Institute of Physics Belgrade, University of Belgrade, Serbia

<sup>b</sup> Faculty of Biology, University of Belgrade, Serbia

### Abstract

High  $p_{\perp}$  theory and data are commonly used to study high  $p_{\perp}$  parton interactions with QGP, while low  $p_{\perp}$  data and corresponding models are employed to infer QGP bulk properties. On the other hand, with a proper description of high  $p_{\perp}$  parton-medium interactions, high  $p_{\perp}$  probes become also powerful tomography tools, since they are sensitive to global QGP features, such as different temperature profiles or initial conditions. This tomographic role of high  $p_{\perp}$  probes can be utilized to assess the spatial anisotropy of the QCD matter. With our dynamical energy loss formalism, we show that a (modified) ratio of  $R_{AA}$  and  $v_2$  presents a reliable and robust observable for straightforward extraction of initial state anisotropy. We analytically estimated the proportionality between the  $v_2/(1-R_{AA})$  and anisotropy coefficient  $\epsilon_{2L}$ , and found surprisingly good agreement with full-fledged numerical calculations. Within the current error bars, the extraction of the anisotropy from the existing LHC data using this approach is still inaccessible. However, with the expected accuracy improvement in the upcoming LHC runs, the anisotropy of the QGP formed in heavy ion collisions can be straightforwardly derived from the data. Such a data-based anisotropy parameter would present an important test to models describing the initial stages of heavy-ion collision and formation of QGP, and demonstrate the usefulness of high  $p_{\perp}$  theory and data in obtaining QGP properties.

**Keywords:** Quark-gluon plasma, High  $p_{\perp}$  probes, Initial anisotropy

### 1. Introduction

Understanding the properties of the new form of matter named Quark-Gluon Plasma (QGP) is the major goal of relativistic heavy ion physics [1, 2]. However, to explore the properties of QGP, one needs good probes. With regards to that, it is commonly assumed that high  $p_{\perp}$  theory and data are good probes for exploring the high  $p_{\perp}$  parton interactions with QGP, while low  $p_{\perp}$  theory and data are considered as good probes for bulk QGP properties. Contrary to this common assumption, the goal of this contribution is to demonstrate that high  $p_{\perp}$  particles can also be useful independent probes of *bulk* QGP properties.

To put it simply, the main idea is that when high  $p_{\perp}$  particles transverse QGP, they lose energy, where this energy loss is sensitive to bulk QGP properties, such as its temperature profiles or initial conditions.



Consequently, with a realistic and sophisticated high  $p_{\perp}$  parton energy loss model, high  $p_{\perp}$  probes can indeed become powerful tomographic tools. So, in this contribution, we will present how we can use these probes to infer some of the bulk QGP properties, i.e., for precision QGP tomography. Note that only the main results are presented here; for a more detailed version, see [3], and references therein.

## 2. DREENA framework

To achieve the goal of utilizing high  $p_{\perp}$  theory and data for inferring the bulk QGP properties, as previously implied, a reliable high  $p_{\perp}$  parton energy loss model is necessary. With this goal in mind, we developed a dynamical energy loss formalism [4, 5], which takes into account some more realistic and unique features, such as: i) The calculations are performed within finite temperature field theory and generalized Hard-Thermal-Loop [6] approach, in which the infrared divergences are naturally regulated, excluding the need for artificial cutoffs. ii) The formalism assumes QCD medium of finite size and finite temperature, consisting of dynamical partons (i.e., energy exchange with medium constituents is included), in distinction to commonly considered static scatterers approximation and/or models with vacuum-like propagators. iii) Both radiative [4] and collisional [5] energy losses are calculated within the same theoretical framework, and are equally applicable to light and heavy flavors. iv) The formalism is generalized to include a finite chromomagnetic mass [7], running coupling, and to relax the widely used soft-gluon approximation [8]. Finally, the formalism is integrated in a numerical framework DREENA (Dynamical Radiative and Elastic ENergy loss Approach) [9, 10], to provide predictions for high  $p_{\perp}$  observables.

Within this framework, we generated a wide set of high  $p_{\perp}$  predictions using 1D Bjorken expansion [11] (i.e., DREENA-B framework [10]). Thus we obtained a good joint agreement with a wide range of high  $p_{\perp}$   $R_{AA}$  and  $v_2$  data, by applying the same numerical procedure, the same parameter set, and no fitting parameters in model testing. That is, there is no  $v_2$  puzzle [12] within our model, which then strongly suggests that the model provides a realistic description of high  $p_{\perp}$  parton-medium interactions. Moreover, our preliminary findings suggest that, within our formalism, moving from 1D Bjorken to full 3D hydrodynamical expansion does not significantly affect the agreement of our predictions with high  $p_{\perp}$   $R_{AA}$  and  $v_2$  data [13]. Consequently, in order to adequately address the high  $p_{\perp}$  measurements, a proper description of high  $p_{\perp}$  parton interactions with the medium appears to be much more important than an advanced medium evolution description. Furthermore, we have also analyzed the sensitivity of high  $p_{\perp}$   $R_{AA}$  and  $v_2$  to different initial stages, giving an additional insight in the usefulness of both high  $p_{\perp}$  observables in the precision QGP tomography [14].

## 3. Inferring QGP anisotropy through high $p_{\perp}$ theory and data

As one example of QGP tomography, in this contribution, we will address how to infer the QGP anisotropy from high  $p_{\perp}$   $R_{AA}$  and  $v_2$  data. The initial state anisotropy is one of the main properties of QGP and a major limiting factor for precision QGP tomography. However, despite its essential importance, it is still not possible to directly infer the initial anisotropy from experimental measurements. Several theoretical studies [15, 16, 17, 18] have provided different methods for calculating the initial anisotropy, leading to notably different predictions, with a notable effect in the resulting predictions for both low and high  $p_{\perp}$  data. Therefore, approaches for inferring anisotropy from the data are necessary. Optimally, these approaches should be complementary to existing predictions, i.e., based on a method that is fundamentally different from models of early stages of QCD matter.

To this end, we here propose a novel approach to extract the initial state anisotropy. Our method is based on inference from high  $p_{\perp}$  data, by using already available  $R_{AA}$  and  $v_2$  measurements, which will moreover be measured with much higher precision in the future. Such an approach is substantially different from the existing approaches, as it is based on the inference from experimental data (rather than on calculations of early stages of QCD matter) exploiting the information from interactions of rare high  $p_{\perp}$  partons with the QCD medium. This also presents an improvement/optimization in utilizing high  $p_{\perp}$  data as, to date, these data were mostly constrained on studying the parton-medium interactions, rather than assessing bulk QGP parameters, such as spatial asymmetry.

In the literature, the initial state anisotropy is quantified in terms of eccentricity parameter  $e_2$

$$e_2 = \frac{\langle y^2 - x^2 \rangle}{\langle y^2 + x^2 \rangle} = \frac{\int dx dy (y^2 - x^2) \rho(x, y)}{\int dx dy (y^2 + x^2) \rho(x, y)}, \quad (1)$$

where  $\rho(x, y)$  denotes the initial density distribution of the formed QGP. Regarding high  $p_\perp$  observables, we note that  $v_2$  is sensitive to both the anisotropy of the system and its size, while  $R_{AA}$  is sensitive only to the size of the system. Therefore, it is plausible that the adequate observable for extracting eccentricity from high  $p_\perp$  data depends on both  $v_2$  and  $R_{AA}$ , and the question is how.

To address this question, we will use the dynamical energy loss formalism, and DREENA-B framework outlined above. For high  $p_\perp$ , the fractional energy loss scales as [3]  $\Delta E/E \sim \chi \langle T \rangle^a \langle L \rangle^b$ , where  $\langle T \rangle$  stands for the average temperature along the path of high  $p_\perp$  parton,  $\langle L \rangle$  is the average path-length traversed by the parton,  $\chi$  is a proportionality factor that depends on the initial parton transverse momentum, and  $a$  and  $b$  are exponents which govern the temperature and path-length dependence of the energy loss. Within our model,  $a \approx 1.2$  and  $b \approx 1.4$ , which is contrary to simpler models, and consistent with a wide range of experimental data [19, 20]. From this simple scaling argument, we can straightforwardly obtain the following expressions for  $R_{AA}$  and  $v_2$  (for more details we refer the reader to [3]):

$$R_{AA} \approx 1 - \xi(\chi) \langle T \rangle^a \langle L \rangle^b, \quad v_2 \approx \frac{1}{2} \frac{R_{AA}^{in} - R_{AA}^{out}}{R_{AA}^{in} + R_{AA}^{out}} \approx \xi(\chi) \langle T \rangle^a \langle L \rangle^b \left( \frac{b}{2} \frac{\Delta L}{\langle L \rangle} - \frac{a}{2} \frac{\Delta T}{\langle T \rangle} \right), \quad (2)$$

where we see that  $\xi(\chi) \langle T \rangle^a \langle L \rangle^b$  corresponds to  $1 - R_{AA}$ . Therefore, if we divide  $v_2$  by  $(1 - R_{AA})$ , we see that this ratio is given by the following simple expression:

$$\frac{v_2}{1 - R_{AA}} \approx \left( \frac{b}{2} \frac{\Delta L}{\langle L \rangle} - \frac{a}{2} \frac{\Delta T}{\langle T \rangle} \right). \quad (3)$$

Note that, while this ratio exposes the dependence on the asymmetry of the system (through spatial  $(\Delta L/\langle L \rangle)$  and temperature  $(\Delta T/\langle T \rangle)$  parts), the dependence only on spatial anisotropy is still not isolated. However, by plotting together spatial and temperature anisotropy, we obtain a linear dependence [3], with a proportionality factor given by  $c \approx 4.3$ . Therefore,  $v_2/(1 - R_{AA})$  reduces to the following expression:

$$\frac{v_2}{1 - R_{AA}} \approx \frac{1}{2} \left( b - \frac{a}{c} \right) \frac{\langle L_{out} \rangle - \langle L_{in} \rangle}{\langle L_{out} \rangle + \langle L_{in} \rangle} \approx 0.57\zeta, \quad \text{where } \zeta = \frac{\langle L_{out} \rangle - \langle L_{in} \rangle}{\langle L_{out} \rangle + \langle L_{in} \rangle} \text{ and } \frac{1}{2} \left( b - \frac{a}{c} \right) \approx 0.57. \quad (4)$$

Consequently, the asymptotic scaling behavior of observables  $v_2$  and  $R_{AA}$ , at high  $p_\perp$ , reveals that their (moderated) ratio is determined only by the geometry of the initial QGP droplet. Therefore, the anisotropy parameter  $\zeta$  could, in principle, be directly obtained from the high  $p_\perp$  experimental data.

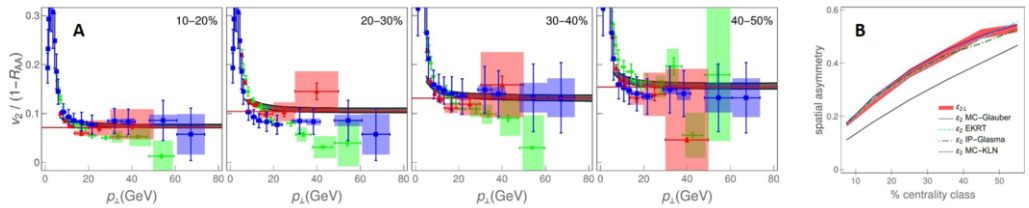


Fig. 1. **A**) Comparison of theoretical predictions for charged hadron  $v_2/(1 - R_{AA})$  as a function of  $p_\perp$  with 5.02 TeV  $Pb + Pb$  CMS [21, 22] (blue squares), ALICE [23, 24] (red triangles) and ATLAS [25, 26] (green circles) data. Each panel corresponds to different centrality range, as indicated in the upper right corners, while red lines denote the limit  $0.57\zeta$  from Eq. (4). **B**) Comparison of  $e_{2L}$  (red band) extracted from our full-fledged calculations, with  $e_2$  obtained from MC-Glauber [15] (gray full curve), EKRT [16] (cyan dashed curve), IP-Glasma [17] (green dot-dashed curve) and MC-KLN [18] (blue dotted curve) models. MC-Glauber and EKRT curves correspond to 5.02 TeV, whereas IP-Glasma and MC-KLN curves correspond to 2.76 TeV  $Pb + Pb$  collisions at the LHC.

To test the adequacy of the analytical estimate given by Eqs. (2)-(4), Fig. 1A is displayed, which comprises our  $v_2/(1 - R_{AA})$  predictions (gray bands), stemming from our full-fledged recently developed

DREENA-B framework (outlined in the previous section), the ALICE, CMS and ATLAS data, and analytically derived asymptote  $0.57\zeta$  (red lines). Importantly, for each centrality range and for  $p_{\perp} \gtrsim 20$  GeV,  $v_2/(1 - R_{AA})$  is independent on  $p_{\perp}$ , and approaches the asymptote, i.e., is determined by the geometry of the system - depicted by the solid red line, up to 5% accuracy. Moreover, the experimental data for all three experiments also display the independence on the  $p_{\perp}$  and agree with our predictions, although the error bars are rather large. Therefore, we conclude that our scaling estimates are valid and that  $v_2/(1 - R_{AA})$  indeed carries the information about the anisotropy of the fireball, which can be simply (from the straight line fit to data at high  $p_{\perp}$  limit) and robustly (in the same way for each centrality) inferred from the experimental data.

However, note that the anisotropy parameter  $\zeta$  is not the widely-considered anisotropy parameter  $\epsilon_2$  (given by Eq. (1)). To facilitate comparison with  $\epsilon_2$  values in the literature, we define  $\epsilon_{2L} = \frac{(L_{out})^2 - (L_{in})^2}{(L_{out})^2 + (L_{in})^2} = \frac{2\zeta}{1+\zeta^2}$ , and in Fig. 1B compare it with the results from different initial-state models [15, 16, 17, 18]. First, we should note that as a starting point, our initial  $\epsilon_2$ , through which we generate our path-length distributions, agrees with EKRT and IP-Glasma. However, what is highly non-trivial is that, as an outcome of this procedure, in which  $v_2/(1 - R_{AA})$  is calculated (based on the full-fledged DREENA-B framework), we obtain  $\epsilon_{2L}$  which practically coincides with our initial  $\epsilon_2$  and also with some of the conventional initial-state models. As an overall conclusion, the straightforward extraction of  $\epsilon_{2L}$  and its agreement with values of the prevailing initial-state models' eccentricity (and our initial  $\epsilon_2$ ) is highly non-trivial and supports  $v_2/(1 - R_{AA})$  as a reliable and robust observable for anisotropy. Additionally, the width of our  $\epsilon_{2L}$  band is smaller than the difference in the  $\epsilon_2$  values obtained by using different models (e.g., MC-Glauber vs. MC-KLN). Therefore, our approach provides genuine resolving power to distinguish between different initial-state models, although it may not be possible to separate the finer details of more sophisticated models. This resolving power, moreover, comes from an entirely different perspective, i.e., from high  $p_{\perp}$  theory and data, supporting the usefulness of utilizing high  $p_{\perp}$  theory and data for inferring the bulk QGP properties.

**Acknowledgements:** This work is supported by the European Research Council, grant ERC-2016-COG: 725741, and by the Ministry of Science and Technological Development of the Republic of Serbia, under project numbers ON171004, ON173052 and ON171031.

## References

- [1] M. Gyulassy and L. McLerran, Nucl. Phys. A **750**, 30 (2005); E. V. Shuryak, Nucl. Phys. A **750**, 64 (2005).
- [2] B. Jacak and P. Steinberg, Phys. Today **63**, 39 (2010); C. V. Johnson and P. Steinberg, Phys. Today **63**, 29 (2010).
- [3] M. Djordjevic, S. Stojku, M. Djordjevic and P. Huovinen, Phys. Rev. C **100**, no. 3, 031901 (2019).
- [4] M. Djordjevic, Phys. Rev. C **80**, 064909 (2009); M. Djordjevic and U. Heinz, Phys. Rev. Lett. **101**, 022302 (2008).
- [5] M. Djordjevic, Phys. Rev. C **74**, 064907 (2006).
- [6] J. I. Kapusta, *Finite-Temperature Field Theory* (Cambridge University Press, 1989).
- [7] M. Djordjevic and M. Djordjevic, Phys. Lett. B **709**, 229 (2012).
- [8] B. Blagojevic, M. Djordjevic and M. Djordjevic, Phys. Rev. C **99**, 024901 (2019).
- [9] D. Zigic, I. Salom, J. Auvinen, M. Djordjevic and M. Djordjevic, J. Phys. G **46**, 085101 (2019).
- [10] D. Zigic, I. Salom, M. Djordjevic and M. Djordjevic, Phys. Lett. B **791**, 236 (2019).
- [11] J. D. Bjorken, Phys. Rev. D **27**, 140 (1983).
- [12] J. Noronha-Hostler, B. Betz, J. Noronha and M. Gyulassy, Phys. Rev. Lett. **116**, no. 25, 252301 (2016); B. Betz and M. Gyulassy, JHEP **1408**, 090 (2014); S. K. Das, F. Scardina, S. Plumari and V. Greco, Phys. Lett. B **747**, 260 (2015).
- [13] D. Zigic, *et al.*, to be submitted.
- [14] D. Zigic, B. Ilic, M. Djordjevic and M. Djordjevic, arXiv:1908.11866 [hep-ph].
- [15] C. Loizides, J. Kamin and D. d'Enterria, Phys. Rev. C **97**, 054910 (2018).
- [16] K. J. Eskola, H. Niemi, R. Paatelainen and K. Tuominen, Phys. Rev. C **97**, 034911 (2018).
- [17] J. E. Bernhard, J. S. Moreland, S. A. Bass, J. Liu and U. Heinz, Phys. Rev. C **94**, 024907 (2016).
- [18] T. Hirano, P. Huovinen, K. Murase and Y. Nara, Prog. Part. Nucl. Phys. **70**, 108 (2013).
- [19] M. Djordjevic and M. Djordjevic, Phys. Rev. C **92**, 024918 (2015).
- [20] M. Djordjevic, D. Zigic, M. Djordjevic and J. Auvinen, Phys. Rev. C **99**(R), 061902 (2019).
- [21] V. Khachatryan *et al.* [CMS Collaboration], JHEP **1704**, 039 (2017).
- [22] A. M. Sirunyan *et al.* [CMS Collaboration], Phys. Lett. B **776**, 195 (2018).
- [23] S. Acharya *et al.* [ALICE Collaboration], JHEP **1811**, 013 (2018).
- [24] S. Acharya *et al.* [ALICE Collaboration], JHEP **1807**, 103 (2018).
- [25] [ATLAS Collaboration], ATLAS-CONF-2017-012.
- [26] M. Aaboud *et al.* [ATLAS Collaboration], Eur. Phys. J. C **78**, no. 12, 997 (2018).



# A systems biology approach to COVID-19 progression in population

Magdalena Djordjevic<sup>a</sup>, Andjela Rodic<sup>b</sup>, Igor Salom<sup>a</sup>, Dusan Zigic<sup>a</sup>,  
Ognjen Milicevic<sup>c</sup>, Bojana Ilic<sup>a</sup>, and Marko Djordjevic<sup>b,\*</sup>

<sup>a</sup>Institute of Physics Belgrade, University of Belgrade, Belgrade, Serbia

<sup>b</sup>Computational Systems Biology Group, Faculty of Biology, University of Belgrade, Belgrade, Serbia

<sup>c</sup>Department for Medical Statistics and Informatics, Faculty of Medicine, University of Belgrade, Belgrade, Serbia

\*Corresponding author: e-mail address: dmarko@bio.bg.ac.rs

## Contents

1. Introduction	292
2. An overview of compartmental models of epidemic progression	295
3. Systems biology approach to compartmental modeling of the COVID-19 epidemic	297
3.1 Virus transmission in the early stages of epidemics	300
4. Parameter analysis and inference	301
5. Analysis of COVID-19 transmission in China	303
6. Conclusions	311
Acknowledgment	312
References	312

## Abstract

A number of models in mathematical epidemiology have been developed to account for control measures such as vaccination or quarantine. However, COVID-19 has brought unprecedented social distancing measures, with a challenge on how to include these in a manner that can explain the data but avoid overfitting in parameter inference. We here develop a simple time-dependent model, where social distancing effects are introduced analogous to coarse-grained models of gene expression control in systems biology. We apply our approach to understand drastic differences in COVID-19 infection and fatality counts, observed between Hubei (Wuhan) and other Mainland China provinces. We find that these unintuitive data may be explained through an interplay of differences in transmissibility, effective protection, and detection efficiencies between Hubei and other provinces. More generally, our results demonstrate that regional differences may drastically shape infection outbursts. The obtained results demonstrate the applicability of our developed method to extract key infection parameters directly from publically available data so that it can be globally applied to outbreaks of COVID-19

in a number of countries. Overall, we show that applications of uncommon strategies, such as methods and approaches from molecular systems biology research to mathematical epidemiology, may significantly advance our understanding of COVID-19 and other infectious diseases.



## 1. Introduction

As the novel COVID-19 disease caused by the SARS-CoV-2 virus took the world by a storm, the new pandemic quickly gained priority in scientific research in a wide range of biological and medical science disciplines. Despite that their prior expertise was in unrelated research fields, many researchers have successfully adapted their approaches and methods to examine various aspects of this viral infection and, thus, contributed to finding the necessary solutions. The systems biology community is not an exception (Alon, Mino, & Yashiv, 2020; Bar-On, Flamholz, Phillips, & Milo, 2020; Djordjevic, Djordjevic, Ilic, Stojku, & Salom, 2021; Eilersen & Sneppen, 2020; Karin et al., 2020; Saad-Roy et al., 2021; Vilar & Saiz, 2020; Wong et al., 2020): those involved in modeling the dynamics of biological systems at the molecular and cellular level can directly apply the similar methodology in epidemiological studying of the virus spread—and this exactly is the central point of the present paper. In particular, dynamic models of biochemical reaction networks, in which the reaction kinetics follow the law of mass action, are analogous to compartmental epidemiological models which, instead of concentrations of chemical species, track the prevalence of individuals in defined population classes over time (Voit, Martens, & Omholt, 2015). Moreover, gene expression dynamics is usually a result of the interplay between the changing rate of cell growth, on which the global physiological rates of molecule synthesis and degradation depend, and complex transcription regulation (Djordjevic, Rodic, & Graovac, 2019). Therefore, modeling dynamics of gene circuits implies combining kinetic models, often relying on the law of mass action, with appropriate non-linear functions describing the regulation part. In the case of the COVID-19 epidemic, one can note that the virus transmission in a population, driven by the biological capacity of the particular virus in the given environment, is coupled with strong, time-dependent regulation, represented by the epidemic mitigation measures imposed by governments. These similarities between the modeled systems may facilitate the application of

the systems biology techniques to the epidemiology field of research. In this paper, we will show how such an approach can be used to assess the basic parameters of the COVID-19 epidemic progression in a given population. In particular, we will use the analogy outlined above to study the COVID-19 spread in Mainland China and test the hypothesis about possible reasons for the uneven disease spread in China provinces.

Our interest in Mainland China infection progression comes from Fig. 1. The progression seems highly intriguing, as Hubei (with only 4% of China population) shows an order of magnitude larger number of detected infection cases (Fig. 1A) and two orders of magnitude higher fatalities (Fig. 1B) compared to the *total* sum in all other Mainland China provinces. The epidemic was unfolding well before the Wuhan closure (with the reported symptom onset of the first patient on December 1, 2019) and within the period of huge population movement, which started 2 weeks before January 25 (the Chinese Lunar New Year) (Chen, Yang, Yang, Wang, & Bärnighausen, 2020). As a rough baseline, a modeling study of the infection spread from Wuhan (Wu, Leung, & Leung, 2020) estimated more than  $10^5$  new cases per day in Chongqing alone—instead, the actual (reported) peak number for *all* Mainland China provinces outside Hubei was just 831.

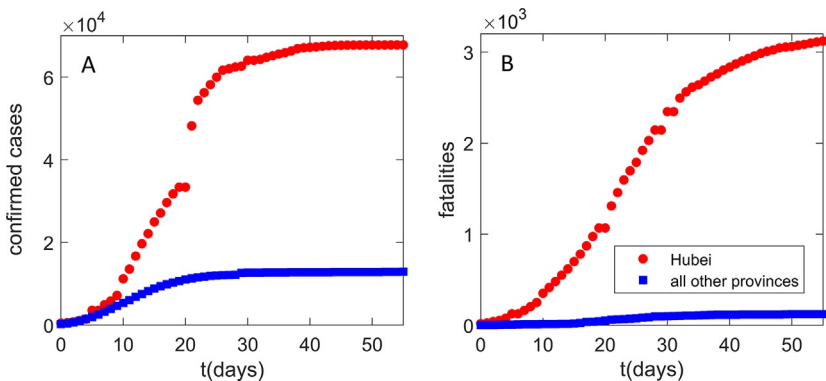


**Fig. 1** Infection and fatality counts for Hubei vs all other provinces. The number of (A) detected infections, (B) fatality cases. Zero on the horizontal axis corresponds to the time from which the data (Hu et al., 2020) are taken (January 23), which also coincides with the Wuhan closure. Red circles correspond to the observed Hubei counts. Blue squares correspond to the sum of the number of counts for all other provinces. The figure illustrates a puzzling difference in the number of counts between Hubei alone and the sum of all other Mainland China provinces.



Consequently, it is a notable challenge for computational modeling to understand drastic differences in COVID-19 infection and fatality counts observed between Hubei (Wuhan) and other Mainland China provinces. These drastic differences may be a consequence of an interplay between the virus transmissibility (influenced by environmental and demographic factors) and the effectiveness of the protection measures. Both can significantly change between different provinces (more generally different countries/regions), and the model has to infer this from available data (commonly the number of confirmed cases, publicly available for a large number of countries/regions).

The study presented here will therefore demonstrate the usefulness of the systems biology approach to the analysis of non-trivial COVID-19 data from China. In particular, the developed method will allow us to analyze the puzzling differences in dynamics trajectories in Mainland China provinces, and it will also turn out to be more generally applicable for understanding regional differences in outbreak dynamics. The surprising differences in COVID-19 progression in different provinces may put strong constraints on the underlying infection progression parameters and allow us to understand:

- i. What interplay between the inherent disease transmissibility and the effects of social distancing is responsible for the large difference in the count numbers between Hubei and the rest of Mainland China? Addressing this question in a proper way would make easier to comprehend how regional differences may shape the infection outbreaks, which is important both locally (for explaining this puzzle), and more generally in the context of global COVID-19 pandemics progression.
- ii. What is the Infected Fatality Rate (IFR, the number of fatalities per total number of *infected* cases) in China? Case Fatality Rate (CFR, the number of fatalities per *confirmed/detected* cases) can be obtained directly from the data but is highly sensitive to the testing coverage. IFR is a more fundamental mortality parameter, as it does not depend on the testing coverage, but is however much harder to determine, due to the unknown number of infected cases.

Addressing these questions allows understanding both the different response policies, and the inherent risks posed by the pandemics and will enable future cross-country comparisons. The developed methodology (i) demonstrates the usefulness of applying transdisciplinary expertise to efficiently analyze problems of nationwide importance, (ii) allows to readily analyze future

outbreaks of COVID-19 and other infectious diseases, as it depends only on inference from straightforward and publically available data.



## 2. An overview of compartmental models of epidemic progression

In epidemiology, for practical and ethical reasons, it is fairly impossible to conduct scientific experiments in controlled conditions in order to investigate the spread of the disease in the human population (Brauer, 2008). Therefore, epidemiologists usually resort to collecting data from clinical reports on the observed situation in the field and, then, using mathematical models to interpret these data, i.e., to infer the principles underlying the process of disease spreading. These principles may point to potentially successful control strategies, as well as to the probable future status of the disease in the population. Epidemiological data can often be incomplete or inaccurate due to poorly controlled or non-standardized collection methods, which significantly complicates modeling. However, even a qualitative agreement of the model with the data can provide useful information of great practical importance. Hence, model predictions are widely used for making various estimates and answering important questions about the seriousness of the epidemic consequences. For example, how many people will be infected, require treatment, or die, or how many patients should the public health facilities expect at any given time? Also, how long will the epidemic last? To what extent could quarantine and self-isolation of the infected contribute to mitigating the effects of the epidemic? Model predictions guide the development of strategies to control the epidemic spread, including vaccination programs.

When the goal is to discover the general principles of epidemic progression, simple mathematical models, which can be solved and analyzed with a “pencil on paper,” are a logical choice as they give insight into the properties of the examined process despite failing to reproduce it in detail. In 1927, Kermack and McKendrick formulated a simple model that predicted behavior similar to that observed in numerous epidemics (Kermack & McKendrick, 1927). It was a type of compartmental model describing the infection spread in a population by analogy with a system of vessels connected by pipes through which a fluid flows. Namely, the population is divided into compartments, and assumptions are made about the nature and the rate of the flow between them. The structure of the compartmental

model—which sections and how many of them it will contain and how they will be connected—depends on the characteristics of transmission of a given infectious disease and whether the past disease provides immunity to re-infections or not. The model set by these two scientists is known as SIR (from **S**usceptible–**I**nfected–**R**ecovered). It divides the population into three classes which correspond to compartments (Fig. 2): Susceptible (*S*) class includes healthy individuals susceptible to infection, which have never been exposed to the virus; Those who are infected and can infect others belong to the Infected (*I*) class; Recovered (*R*) class encompasses those who are excluded from the population, either by quarantining the infected, or by acquiring immunity through recovery from disease or immunization, or by the death of the infected (Brauer, 2008).

Mathematically, this model is represented by a system of ordinary differential equations. The time derivative of the number of individuals in a compartment, i.e., the rate of their change, is given by the difference between the rates at which the compartment is filled and emptied. Analogous to the processes in which chemical species (e.g., proteins) are degraded or converted into others within a biochemical reaction network (Ingalls, 2013), the rate of transition of individuals from one compartment to another follows the law of mass action. For example, a person moves from compartment *S* to compartment *I* at the rate which is proportional to the product of the *S* and *I*, as the encounter with an infected person enables virus transmission to the susceptible one (Voit et al., 2015).

By formulating such (or similar) models, one assumes that the epidemic is a deterministic process. Namely, the state of the population at all times is completely determined by its previous state and the rules described by the model. This is a reasonable approximation in cases where the numbers of individuals in the compartments are large, i.e., in a commonly considered



**Fig. 2** Schematic representation of the SIR model. Rectangles denote model compartments containing susceptible (*S*), infected (*I*), and recovered (*R*) individuals in the population of size *N*. Permitted directions of flow between compartments are denoted by arrows, with the rates of flow indicated above them. The rates are expressed according to the law of mass action, where  $\kappa_1$  and  $\kappa_2$  are the rate constants. The dashed curve corresponds to bimolecular reaction, where newly infected are generated through interactions (contacts) between susceptible and already infected individuals.

deterministic range ( $>10$ ). Such approximation (i.e., deterministic modeling) is well suited for the spread of COVID-19, which is up to now known for a large number of individuals in all compartments.



### 3. Systems biology approach to compartmental modeling of the COVID-19 epidemic

The above-introduced SIR model is likely the simplest compartmental model in mathematical epidemiology and many subsequent models are derivatives of this basic form. Among others, these extensions have also been developed toward including control measures such as vaccination or quarantine (Diekmann, Heesterbeek, & Britton, 2012; Keeling & Rohani, 2011; Martcheva, 2015). However, COVID-19 brought a challenge to account for previously unprecedented social distancing measures, taken by most countries. When included, these effects have been, up to now, accounted for by the direct changes in the transmissibility term (Chowell, Sattenspiel, Bansal, & Viboud, 2016; Tian et al., 2020), which, however, corresponds to introducing a phenomenological dependence in otherwise mechanistic models. That is, to be included consistently in the model, social distancing should move individuals from one compartment to the other, just as vaccination and quarantine are usually implemented. On the other hand, it is necessary to construct a minimal mechanistic model in terms of the ability to explain the data with the smallest number of parameters, so that relevant infection progression properties can be inferred without overfitting. With this goal in mind, we used our systems biology background to develop a minimal model that accounts for all the main qualitative features of the SARS-CoV-2 infection spread under epidemic mitigation measures. As outlined above, we opt for a deterministic model due to the robust and computationally less demanding parameter inference (Wilkinson, 2018).

To describe the COVID-19 epidemic, we developed SPEIRD model depicted schematically in Fig. 3. It assumes that healthy persons susceptible to infection ( $S$ ), can be infected, but in the case of this (and many other) viruses they do not immediately become contagious to other people, but first spend some time in the compartment  $E$  (Exposed to the virus) and then develop symptoms and pass to the compartment  $I$ . Infected persons can either recover at home, moving to the compartment  $R$ , or they can be diagnosed with SARS-CoV-2 virus infection (Active detected cases).  $A$  (Active) cases can, further, either become healed ( $H$ ) or die from the disease ( $F$ ). To consistently implement the social distancing within this model structure, we

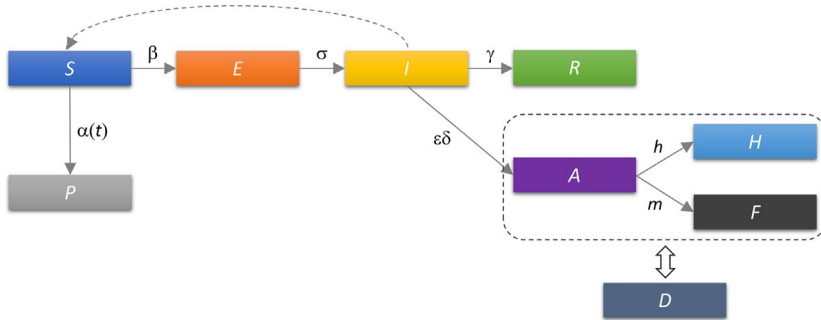


**Fig. 3** Schematic representation of the SPEIRD model. Compartments and the transition rates are as indicated in the text, where transitions between different compartments are marked by arrows. The time-dependent transition rate from susceptible to protected category  $\alpha(t)$  is indicated by the solid arrow. The infected can transition to the recovered category either without being diagnosed (transition to  $R$ ), or being diagnosed and then transitioning to confirmed healed or fatality cases. The dashed rectangle indicates that  $A$ ,  $H$ , and  $F$  categories in the starting model are substituted for the cumulative case counts ( $D$ ), which removes  $h$  and  $m$  from the analysis, where  $D$  is fitted to the observed data.

included a compartment  $P$  (**P**rotected) in the model, which contains susceptible persons who are protected from exposure to the virus as a result of the epidemic mitigation measures, such as self-imposed isolation, social distancing, and advised changes in individual behavior.

The following differential equations describe how different categories change with time:

$$\frac{dS}{dt} = -\beta \cdot I \cdot S/N - \alpha(t) \cdot S \quad (1)$$

$$\frac{dE}{dt} = \beta \cdot I \cdot S/N - \sigma \cdot E \quad (2)$$

$$\frac{dI}{dt} = \sigma \cdot E - \gamma \cdot I - \varepsilon \cdot \delta \cdot I \quad (3)$$

$$\frac{dA}{dt} = \varepsilon \cdot \delta \cdot I - h \cdot A - m \cdot A \quad (4)$$

$$\frac{dH}{dt} = h \cdot A \quad (5)$$

$$\frac{dF}{dt} = m \cdot A \quad (6)$$

where  $\beta$  is the infection rate in a fully susceptible population;  $\alpha(t)$ , the time-dependent protection rate, i.e., the rate at which the population moves from susceptible to the protected category, quantifying the impact of the social protection measures;  $\sigma$ , the inverse of the exposed period;  $\gamma$ , the inverse of the infectious period;  $\delta$ , the inverse of the period of the infection diagnosis;  $\varepsilon$ , the detection efficiency;  $h$ , the healing rate of diagnosed cases;  $m$ , the mortality rate.

The probability that an infected person will meet a susceptible person is proportional to  $S/N$ , where  $N$  is the total number of individuals in the population. The rate at which individuals move from  $S$  to  $E$  is obtained when the product of  $I$  and  $S/N$  is multiplied by the infection rate,  $\beta$ , which quantifies the efficiency of transmission of a particular virus in the population with certain demographic characteristics and meteorological conditions, and it does not depend on epidemic suppression measures. Thus,  $\beta$  is a characteristic of the virus, the population, and the external conditions in which the virus is transmitted. Since the compartment  $S$  is being emptied, the corresponding rate in the first equation is specified with the minus sign.

$S$  also decays by moving the individuals to  $P$  with a protection rate that may vary with time. While mitigation measures are commonly accounted for by models with time-independent terms (Martcheva, 2015), we note that the social distancing term should depend on time, as this measure is introduced at a certain point in epidemics and may also evolve gradually. We denote the time point (more specifically, the date) of the onset of the social distancing measures in the examined population with  $t_0$ . The protection rate  $\alpha(t)$  is then taken as 0 before  $t_0$  and a constant value  $\alpha$  afterwards.

One may notice a direct parallel between the model outlined above, and e.g., modeling gene expression regulation in systems biology with a step function that approximates the activity of a promoter to which repressor proteins are highly cooperatively bound: the promoter is initially silenced and upon receiving a signal which leads to the abrupt removal of repression, promoter activity rises sharply to its maximum value. We notice that the step function is a satisfactory approximation of the dynamics of social distancing, i.e., it may not be necessary to further increase the number of parameters by applying the Hill function (which describes a more gradual activation), since governments quickly introduced these measures, together with their effective implementation. Note however that in (Djordjevic et al., 2021) we introduced a more complex model with Hill function, and provided analytical results for key properties of this model.

Compartment  $E$  is filled by infecting the susceptibles and emptied by moving the individuals to  $I$ , with the rate  $\sigma$  representing the inverse value of the latent period during which the person is not contagious. While compartment  $I$  is filled with individuals from  $E$ , it is depleted through two channels. Individuals move to  $R$  with the rate  $\gamma$ , which is the inverse of the period of contagiousness, and to  $A$  with the rate  $\delta$ , which is the inverse of the time required for diagnosis, multiplied by  $\epsilon$ , reflecting that only a fraction (likely small due to many asymptomatic infections) of the total infected are



detected. Note that case detection reduces the number of individuals in  $I$  that can infect susceptibles: the model assumes that the detected cases are quarantined and thus isolated from the general population. The numbers in compartments  $A$ ,  $H$ , and  $F$  change following the same logic described for the other compartments.

We can further simplify the analysis by looking at the total number of detected cases ( $D$ ), which is the sum of  $A$ ,  $H$ , and  $F$ . By adding the Eqs. (4)–(6), we obtain:

$$dD/dt = \varepsilon \cdot \delta \cdot I, \quad (7)$$

and thus lose two parameters,  $h$  and  $m$ . The total number of detected cases in time is a measurable quantity from which we can determine the dynamics of other model compartments since this is the data that is available for various different regions and countries. Thereby, we assume that before  $t_0$  social distancing does not take effect, and the measures introduced at  $t_0$  will take effect on  $D \sim 10$  days later, as this is about the time that elapses between infection and detection/diagnosis (Feng et al., 2020). Consequently, for the first  $t_0 + 10$  days, the  $D$  curve reflects disease transmission without epidemic suppression measures.

### 3.1 Virus transmission in the early stages of epidemics

We will now focus on the dynamics of the infection spread at the very beginning of the epidemic, i.e., on the period before the introduction and practice of any control measures (Salom et al., 2021). Regarding the model, we assume that there is no social distancing (no transition from  $S$  to  $P$ ), there is no quarantine, and almost the entire population consists of people susceptible to infection, so  $S/N = 1$ . This gives us an even simpler mathematical model which appears to be very useful because it allows analytical derivation of the expressions we need. Our system of Eqs. (1)–(3) and (7) is reduced to two linear differential equations that we can write in matrix form

$$\frac{d}{dt} \begin{pmatrix} E \\ I \end{pmatrix} = \begin{pmatrix} -\sigma & \beta \\ \sigma & -\gamma \end{pmatrix} \begin{pmatrix} E \\ I \end{pmatrix} = A \begin{pmatrix} E \\ I \end{pmatrix}, \quad (8)$$

determine the eigenvalues and eigenvectors of the matrix and, subsequently, the solutions of the system,  $E(t)$  and  $I(t)$ . Specifically, the cumulative number of infected in time,  $I(t)$ , is obtained according to the following equation:

$$I(t) = C_1 \exp(\lambda_+ t) + C_2 \exp(\lambda_- t), \quad (9)$$

where  $\lambda_s$  are eigenvalues of the matrix. Since one of the eigenvalues, here denoted by  $\lambda_-$ , is negative, the corresponding term of the Eq. (9) will decrease over time, and  $I(t)$  will be effectively described by the first term, already after few days from the epidemic outbreak (Salom et al., 2021). We can further derive this equation for the dependence of the logarithm of the number of detected cases in time:

$$\log(D(t)) = \log(\varepsilon \cdot \delta \cdot I(0)/\lambda_+) + \lambda_+ \cdot t \quad (10)$$

This is the straight line equation whose slope is given by the value of  $\lambda_+$  (the dominant, positive eigenvalue of the matrix in Eq. (8)).

Once we know  $\lambda_+$ , we can calculate the value of the so-called basic reproduction number,  $R_{0,free}$ , by fixing mean values of the latency period and the infectivity period ( $\gamma = 0.4 \text{ days}^{-1}$ ,  $\sigma = 0.2 \text{ days}^{-1}$ ), which are known from the literature and characterize the fundamental infection processes (Kucharski et al., 2020; Li et al., 2020):

$$R_{0,free} = \frac{\beta}{\gamma} = 1 + \frac{\lambda_+(\gamma + \sigma) + \lambda_+^2}{\gamma\sigma} \quad (11)$$

$R_{0,free}$  is an important epidemiological parameter that characterizes the inherent biological transmission of the virus in a completely unprotected population. In particular, it is the mean number of secondarily infected by one infected person introduced in a completely susceptible population. It depends on the biology of the specific virus, as well as the demographic characteristics of the population and the environmental conditions, while it does not depend on the applied infection control measures (Brauer, 2008). In Salom et al. (2021) we utilized a bioinformatics analysis, akin to those often used to understand complex data in systems biology, to pinpoint demographic and meteorological factors that affect  $R_{0,free}$  (i.e., inherent virus transmissibility in population). This furthermore underlines that a rich array of techniques developed and/or widely used within systems biology can be successfully employed within infectious disease modeling.



#### 4. Parameter analysis and inference

$R_{0,free}$ ,  $\alpha$ ,  $t_0$ , two initial conditions ( $I_0$  and  $E_0$ ), and the detection efficiency  $\varepsilon$ , are unknown and may differ between the provinces. Is it possible to determine these unknown parameters from different properties of the  $D$  curve? Early in the infection, almost the entire population is susceptible ( $S \approx N$ ), so Eqs. (2) and (3) become linear, and decoupled from the rest of the

system, as discussed in the previous section. This sets the ratio of  $I_0$  to  $E_0$ , through the eigenvector components with the dominant (positive) eigenvalue of the Jacobian for this subsystem. This eigenvalue, corresponding to the initial slope of the  $\log(D)$  curve, sets the value of  $\lambda_+$  and subsequently, of  $R_{0,\text{free}}$  (see Eq. 11). From Eq. (7) one can see that the product of  $I_0$  and  $\varepsilon \cdot \delta$  is set by  $dD/dt$  at the initial time ( $t=0$ ). Later dynamics of the  $D$  curve is determined solely by the combination  $t_\alpha = t_0 + 1/\alpha$  (which we denote as protection time), setting the time at which  $\sim 1/2$  of the population moves to the protected category. We also numerically checked this, and confirmed that  $t_0$  can be lowered at the expense of increasing  $1/\alpha$ , without affecting the fit quality. We allowed for  $t_0$  to vary in reasonable proximity of January 23, as the social distancing was generally introduced close to Wuhan closure (e.g., on that date, all major events in Beijing were canceled) (Chen et al., 2020; Du et al., 2020), but we cannot be sure when the measures effectively took place. Our inferred  $t_0$  values are within a week from Wuhan closure, appearing as reasonable. The remaining independent parameter ( $I_0$ ) is then left to be determined from  $D$  curve properties at the late infection stage, such as its saturation time. The number of characteristic dynamics features is thus at least equal to the number of fit parameters, leading to constrained numerical analysis, so that overfitting is not expected. For few provinces, we however observed that  $I_0$  can be decreased compared to the best fit value, without noticeably affecting the fit quality. For these provinces, we chose the lowest  $I_0$  value that still leads to a comparably good fit. This allows obtaining the most conservative (i.e., as high as possible while still consistent with data) IFR estimate, as the reported fatality counts for provinces other than Hubei is surprisingly low.

Parameter inference and uncertainties are estimated separately for each province. However, within a given province, demographic, special, or population activity (network effects) heterogeneities (Britton, Ball, & Trapman, 2020; Diekmann et al., 2012), or seasonality effects (Wong et al., 2020), are not taken into account. These are potentially important, particularly for projections (longer-term predictions of infection dynamics under different scenarios), and can be readily included in our model. Such extensions would however complicate parameter inference, due to an increase in parameter number, as this may either lead to overfitting or require special/additional data that may be available only for a limited number of countries/regions (which would limit the generality of our proposed method). A more complex model structure may also obscure a straightforward relationship between the model parameters and distinct dynamical features of the

confirmed case count curve analyzed above. While the inclusion of additional effects is left for future work, we here employ the model structure and parameter inference introduced above on widely available case count data, as proof of the principle for the generality of our proposed approach. Moreover, a major advantage of our approach is that it allows consistent analysis for all provinces with the same model, numerical procedure, and parameter set, allowing an objective comparison of the obtained results.

Our model was numerically solved by the Runge–Kutta method (Dormand & Prince, 1980) for each parameter combination. Parameter values were inferred by exhaustive search over a wide parameter range, to avoid reaching a local minimum of the objective function ( $R^2$ ). To infer the unknown parameters, we fit (by minimizing  $R^2$ ) the model to the observed total number of detected  $D$  for each province. As an alternative to exhaustive search, some of many optimization techniques used in epidemics modeling, such as the Markov chain Monte Carlo (MCMC) approach, can be used instead (Keeling & Rohani, 2011; Wong et al., 2020)—exhaustive search is however straightforward, guarantees that the global minimum is reached, and is in this case not computationally demanding. Errors were estimated through Monte–Carlo simulations (Press, Flannery, Teukolsky, & Vetterling, 1986), individually for each province with the assumption that count numbers follow the Poisson distribution. Monte–Carlo simulations were found as the most reliable estimate of the fit parameter uncertainties for a non-linear fit (Cunningham, 1993). This also serves as an independent check for overfitting, as in that case, data point perturbations would lead to large parameter uncertainties. We find no indication of this in the results reported below, as the inferred uncertainties (consistently indicated with all results) are reasonably small. In particular, the differences in the inferred parameter values, which are relevant for the reported results/conclusions, are statistically highly significant.  $P$  values for extracted parameter differences between provinces are estimated by the  $t$ -test.



---

## 5. Analysis of COVID-19 transmission in China

We used our SPEIRD model with the parameter inference described above, to analyze all Mainland China provinces, except Tibet, where only one COVID-19 case was reported. Parameters were estimated separately for each of the 30 provinces by the same model and parameter set, which enables an impartial comparison of the results presented below. To allow

for a straightforward comparison of the infection progression between different provinces, the starting date (i.e.,  $t=0$ ) in our analysis is the same for all the provinces and corresponds to January 23 (when the data for all the provinces became publically available and continuously tracked (Hu et al., 2020)).

In Fig. 4A and B, we show that our model can robustly explain the observed  $D$ , in the cases of large outburst (Hubei on Fig. 4A), as well as for all other provinces, where  $D$  is in the range from intermediate (e.g., Guangdong) to low (e.g., Inner Mongolia). Provinces in Fig. 2B were selected to cover the entire range of observed  $D$  (from lower to higher counts), while comparably good fits were obtained for other provinces, which were all included in the further analysis. Our method is also robust to data perturbations (which might be frequent), e.g., in the case of Hubei (Wuhan), a large number of counts was added on February 12, based on clinical diagnosis (CT scan) (Feng et al., 2020), which is apparent as a discontinuity in observed  $D$  in Fig. 4A. The model however interpolates this discontinuity, finding a reasonable description of the overall data.

We backpropagated the dynamics inferred for Hubei, to estimate that January 5 ( $\pm 4$  days) was the onset of the infection's exponential growth in the population (not to be confused with the appearance of first infections, which likely happened in December (Feng et al., 2020)). This agrees well with (Feng et al., 2020) (cf. Fig. 3A), which tracked cases according to their symptom onset (shifted for  $\sim 12$  days with respect to detection/diagnosis, cf. Fig. 3B), and coincides with WHO reports on social media that there is a cluster of pneumonia cases—with no deaths—in Wuhan (WHO, 2020). Since our analysis does not directly use any information before January 23, this agreement provides confidence in our  $I_0$  estimate. Note that we infer  $I_0$  separately for each province of interest, through which we also take into account different times of the infection onset in different provinces (so that earlier onset time would generally lead to a larger number of infected on January 23).

Key parameters inferred from our analysis are summarized in Fig. 4C–F, with individual results and errors for all the provinces shown in Table 1. Fig. 4C shows the distribution of  $R_{0,\text{free}}$ . Note that  $R_{0,\text{free}}$  might depend on demographic (population density, etc.) and climate factors (temperature, humidity...), which are not controllable, but are unrelated to the applied social distancing measures (see above). It is known that the  $R_0$  value can strongly depend on the model, e.g., the number of introduced compartments (Keeling & Rohani, 2011); accordingly, a wide range of  $R_0$  values

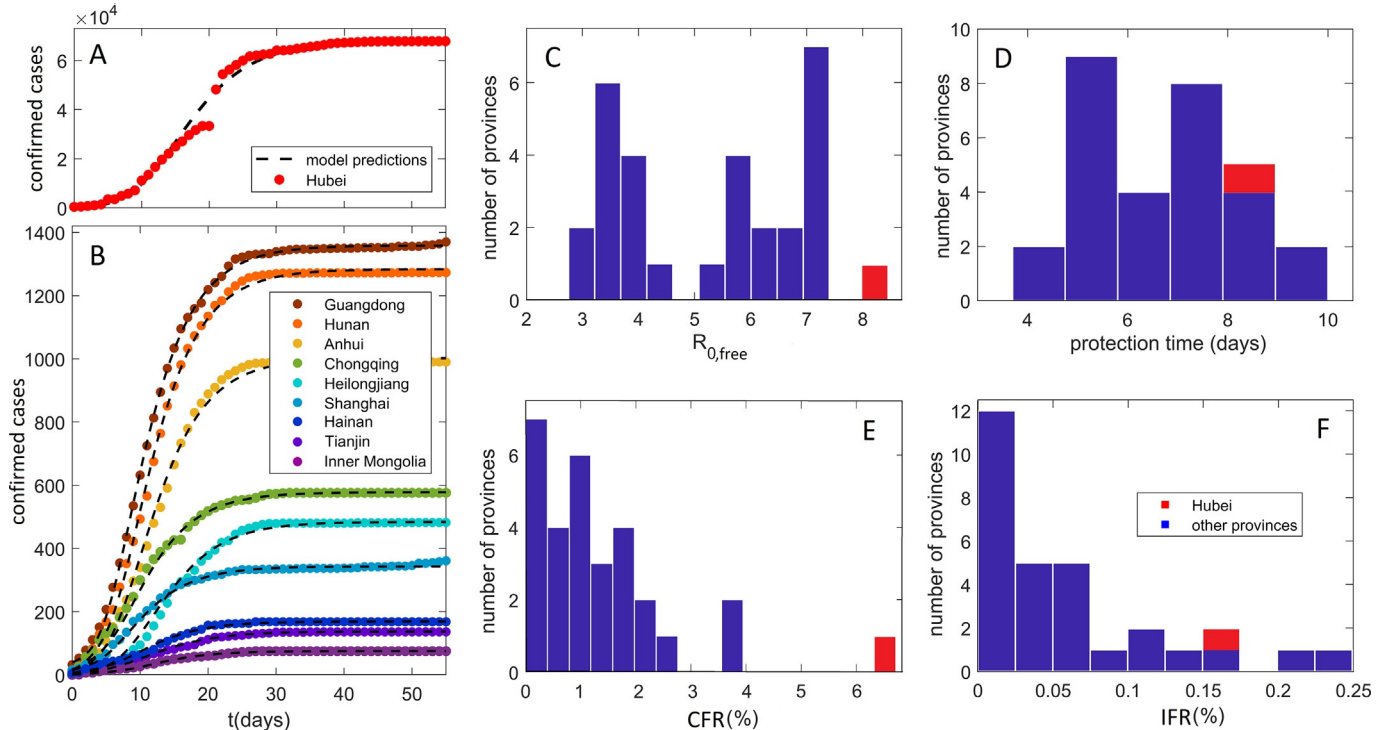


**Fig. 4** Model predictions: comparison with data and key parameter estimates. Predictions (compared to data) of detected infection counts for (A) Hubei, (B) other Mainland China provinces. Zeros on the horizontal axis correspond to January 23, which is the initial time in our numerical analysis for all the provinces. The observed counts are shown by dots and our model predictions by dashed curves. Names of the provinces are indicated in the legend, with provinces selected to cover the full range of the observed total detected counts. The distribution with respect to provinces of (C) the basic reproduction number in the absence of social distancing,  $R_{0,free}$ , (D) the protection time  $t_p$ , (E) Case Fatality Rate, calculated directly from the reported data. (F) Infected Fatality Rate. The values for Hubei are indicated by the red bars.



**Table 1** Inferred COVID-19 infection progression parameters for Mainland China provinces

Province	$t_\alpha$ (days)	$R_0$	$E_0$	$I_0$	IFR (%)	CFR (%)	Detected (%)
Anhui	$6.6 \pm 0.5$	$5.5 \pm 0.8$	$920 \pm 30$	$220 \pm 20$	$0.04 \pm 0.02$	$0.6 \pm 0.3$	$6 \pm 3$
Beijing	$7.9 \pm 0.5$	$3.5 \pm 0.4$	$610 \pm 20$	$180 \pm 10$	$0.12 \pm 0.05$	$1.7 \pm 0.7$	$7 \pm 3$
Chongqing	$7.0 \pm 0.2$	$3.5 \pm 0.2$	$1900 \pm 40$	$560 \pm 20$	$0.04 \pm 0.03$	$1.0 \pm 0.5$	$4 \pm 2$
Fujian	$3.7 \pm 0.4$	$7 \pm 2$	$1660 \pm 40$	$360 \pm 20$	$0.007 \pm 0.003$	$0.3 \pm 0.4$	$2 \pm 1$
Gansu	$5 \pm 1$	$6 \pm 3$	$630 \pm 20$	$150 \pm 10$	$0.03 \pm 0.04$	$1 \pm 1$	$2 \pm 3$
Guangdong	$5.0 \pm 0.1$	$7 \pm 1$	$1360 \pm 40$	$290 \pm 20$	$0.04 \pm 0.01$	$0.6 \pm 0.2$	$7 \pm 2$
Guangxi	$7 \pm 1$	$3.8 \pm 0.8$	$1000 \pm 30$	$290 \pm 20$	$0.02 \pm 0.02$	$0.8 \pm 0.6$	$3 \pm 3$
Guizhou	$8.1 \pm 0.6$	$7 \pm 1$	$53 \pm 7$	$11 \pm 3$	$0.06 \pm 0.03$	$1 \pm 1$	$4 \pm 2$
Hainan	$7.6 \pm 0.8$	$3.3 \pm 0.7$	$300 \pm 20$	$90 \pm 10$	$0.21 \pm 0.09$	$4 \pm 2$	$6 \pm 3$
Hebei	$6.0 \pm 0.6$	$7 \pm 2$	$240 \pm 20$	$52 \pm 7$	$0.11 \pm 0.03$	$1.8 \pm 0.8$	$6 \pm 2$
Heilongjiang	$7 \pm 1$	$6 \pm 2$	$260 \pm 20$	$59 \pm 7$	$0.15 \pm 0.07$	$2.9 \pm 0.9$	$5 \pm 3$
Henan	$7.0 \pm 0.3$	$4.5 \pm 0.5$	$1780 \pm 40$	$460 \pm 20$	$0.09 \pm 0.04$	$1.7 \pm 0.4$	$5 \pm 2$
Hubei	$8.3 \pm 0.2$	$8.2 \pm 0.4$	$31,900 \pm 400$	$6600 \pm 200$	$0.15 \pm 0.09$	$6.5 \pm 0.1$	$2 \pm 2$
Hunan	$5.1 \pm 0.1$	$6.8 \pm 0.8$	$1430 \pm 40$	$310 \pm 20$	$0.02 \pm 0.01$	$0.4 \pm 0.2$	$5 \pm 2$
I. Mongolia	$10.0 \pm 0.8$	$2.8 \pm 0.4$	$940 \pm 30$	$300 \pm 20$	$0.01 \pm 0.03$	$1 \pm 1$	$1 \pm 3$
Jiangsu	$5.5 \pm 0.5$	$7 \pm 2$	$500 \pm 20$	$110 \pm 10$	$0 \pm 0$	$0 \pm 0$	$6 \pm 2$

Jiangxi	$7.0 \pm 0.2$	$5.6 \pm 0.9$	$890 \pm 30$	$210 \pm 10$	$0.005 \pm 0.002$	$0.1 \pm 0.1$	$5 \pm 2$
Jilin	$10.0 \pm 0.7$	$4.0 \pm 0.8$	$270 \pm 20$	$76 \pm 9$	$0.02 \pm 0.02$	$1 \pm 1$	$1 \pm 2$
Liaoning	$7 \pm 1$	$2.9 \pm 0.7$	$1240 \pm 40$	$390 \pm 20$	$0.02 \pm 0.04$	$2 \pm 2$	$1 \pm 2$
Ningxia	$5.3 \pm 0.9$	$7 \pm 3$	$72 \pm 9$	$15 \pm 4$	$0 \pm 0$	$0 \pm 0$	$6 \pm 23$
Qinghai	$6.1 \pm 0.6$	$4.0 \pm 0.5$	$2260 \pm 50$	$640 \pm 30$	$0 \pm 0$	$0 \pm 0$	$0 \pm 2$
Shaanxi	$5.2 \pm 0.5$	$6 \pm 1$	$380 \pm 20$	$90 \pm 10$	$0.07 \pm 0.03$	$1.3 \pm 0.8$	$6 \pm 2$
Shandong	$9 \pm 1$	$3.5 \pm 0.5$	$900 \pm 30$	$260 \pm 20$	$0.06 \pm 0.01$	$1.0 \pm 0.4$	$6 \pm 1$
Shanghai	$5.0 \pm 0.4$	$6 \pm 1$	$1570 \pm 40$	$370 \pm 20$	$0.02 \pm 0.02$	$0.8 \pm 0.5$	$2 \pm 3$
Shanxi	$5.2 \pm 0.5$	$6 \pm 2$	$1600 \pm 40$	$370 \pm 20$	$0 \pm 0$	$0 \pm 0$	$1 \pm 2$
Sichuan	$7.7 \pm 0.8$	$3.7 \pm 0.5$	$990 \pm 30$	$280 \pm 20$	$0.03 \pm 0.02$	$0.6 \pm 0.3$	$5 \pm 3$
Tianjin	$7 \pm 2$	$4 \pm 2$	$170 \pm 10$	$46 \pm 7$	$0.14 \pm 0.06$	$2 \pm 1$	$7 \pm 3$
Xinjiang	$7.3 \pm 0.9$	$6 \pm 1$	$42 \pm 7$	$10 \pm 3$	$0.25 \pm 0.09$	$3 \pm 2$	$8 \pm 2$
Yunnan	$4.0 \pm 0.2$	$7 \pm 2$	$360 \pm 20$	$76 \pm 9$	$0.06 \pm 0.03$	$1.2 \pm 0.9$	$5 \pm 2$
Zhejiang	$5.0 \pm 0.1$	$7.2 \pm 0.8$	$1340 \pm 40$	$290 \pm 20$	$0.005 \pm 0.002$	$0.1 \pm 0.1$	$7 \pm 3$

$t_{gr}$ , protection time;  $R_{0,free}$ , basic reproduction number;  $E_0$ , initial exposed;  $I_0$ , initial infected;  $IFR$ , Infected Fatality Rate;  $CFR$ , Case Fatality Rate; *detected* %, fraction of the infected population that has been detected. Error of the quantities correspond to one standard deviation.

were reported for China in the literature (Sanche et al., 2020; Wu, Leung, Bushman, et al., 2020). Consequently, a clear advantage of our study is that parameters for all China provinces were determined from the same model and data set, which allows direct comparisons. Our obtained average  $R_{0,\text{free}}$  for provinces outside of Hubei is  $5.3 \pm 0.3$ , in a reasonable agreement with a recent estimate ( $\approx 5.7$ ) (Sanche et al., 2020). Furthermore, we observe that  $R_{0,\text{free}}$  for Hubei is a far outlier with a value of  $8.2 \pm 0.4$ , which is notably larger than for other provinces with  $p \sim 10^{-11}$ . This then strongly suggests that demographic and climate factors that determine  $R_{0,\text{free}}$ , played a decisive role in a large outburst in Hubei vs other provinces, which we further address below.

The distribution of protection time  $t_\alpha$  for the provinces is shown in Fig. 4D, with the value for Hubei indicated in red. The mean for the other provinces is  $6.6 \pm 0.2$  days. That is, we observe that the suppression measures were efficiently implemented, with  $\sim 1/2$  of the population moving to the protected category within a week from Wuhan closure. The protection time for Hubei of  $8.3 \pm 0.2$  days was longer, which is statistically significant at the  $p \sim 10^{-11}$  level. The estimated less efficient protection in the case of Hubei may also be an important contributing factor in the surprising difference in Hubei vs other provinces, which we further investigate below.

CFR distribution, based on the fatality numbers reported for Hubei and other provinces is shown in Fig. 4E. These numbers are not based on the model predictions, i.e., can be straightforwardly obtained by dividing the total number of fatalities by the total number of detected cases. CFR for other provinces with a mean of  $1.2 \pm 0.4\%$  is significantly smaller compared to CFR for Hubei, which was 4.6% before the correction on April 17, and 6.5% after the correction (with 1290 fatalities added to Wuhan). This large difference in CFR between Hubei and other provinces further accentuates the differences noted in Fig. 1.

IFR is harder to determine than CFR, as a majority of COVID-19 infections correspond to asymptomatic or mild cases that are by large not diagnosed (Day, 2020). We consequently calculate IFR as the total number of fatalities divided by the total number of infections (cumulative incidence) for the entire outburst, where cumulative incidence is estimated from our model. As the infections precede fatalities, both the total number of fatalities and the cumulative incidence in our estimate correspond to the entire outburst, so that all the infections had a sufficient time to recover or lead to fatalities—this is directly feasible for the provinces in China, where all detected case counts reached saturation. Note that IFR calculated in this

way corresponds to an averaged quantity so that it does not capture possible time-dependent change over the outburst interval (in fact, for Wuhan it is known that the fatality rate was larger at the very beginning of the outburst). Nevertheless, the estimated IFR's present a reasonable measure of COVID-19 mortality across China provinces.

IFR distribution, which provides a much less biased measure of the infection mortality, is shown in Fig. 4F. In distinction to CFR, estimated IFR shows a much smaller difference between Hubei ( $0.15 \pm 0.09\%$ ) and other provinces ( $0.056 \pm 0.007\%$ ). Therefore, while Hubei is a clear outlier with respect to CFR, we observe similar IFR values for all Mainland China provinces, where few provinces have even higher IFR than Hubei. The ratio of IFR to CFR equals the fraction of all infected that got detected (*detection coverage*). We estimate that the mean detection coverage for all provinces except Hubei is higher than detection coverage for Hubei ( $4.5 \pm 0.9\%$  vs  $2 \pm 2\%$ ). This difference is responsible for a decrease by a factor of two from CFR to IFR for Hubei, compared to the other provinces, and consequently for more uniform mortality estimates at the IFR level. Xinjiang has the highest IFR of  $0.25 \pm 0.09\%$  so that Hubei is not an outlier anymore. Estimated IFR's of up to 0.3% in China provinces are in general agreement with the estimates reported elsewhere (see e.g., (Bar-On et al., 2020; Djordjevic et al., 2021; Mizumoto, Kagaya, & Chowell, 2020)).

In Fig. 5A, two key infection progression parameters are plotted against each other: protection time  $t_\alpha$  vs basic reproduction number  $R_{0,\text{free}}$ . Unexpectedly, there is a high negative correlation, with Pearson correlation coefficient  $R = -0.70$ , which is statistically highly significant  $p \sim 10^{-5}$ , where these two are a priori unrelated (see above). Actually, stronger social distancing measures—which by definition are not included in  $R_{0,\text{free}}$ —would lead to a decrease in *effective* transmissibility. This would then lead to a tendency of transmissibility to positively correlate with  $t_\alpha$ , oppositely from the strong negative correlation observed in Fig. 5A. Therefore, higher basic reproduction number is genuinely related to a shorter protection time (larger effect of the suppression measures). Intuitively, this could be understood as a negative feedback loop, commonly observed in systems biology (Alon, 2019; Phillips, Kondev, Theriot, & Garcia, 2012), where larger  $R_{0,\text{free}}$  leads to steeper initial growth in the infected numbers, which may elicit stronger measures and better observing of these measures by the population faced with a more serious outbreak. Interestingly, similar negative feedback was also obtained in the context of epidemics research other than COVID-19 (Wang, Andrews, Wu, Wang, & Bauch, 2015).

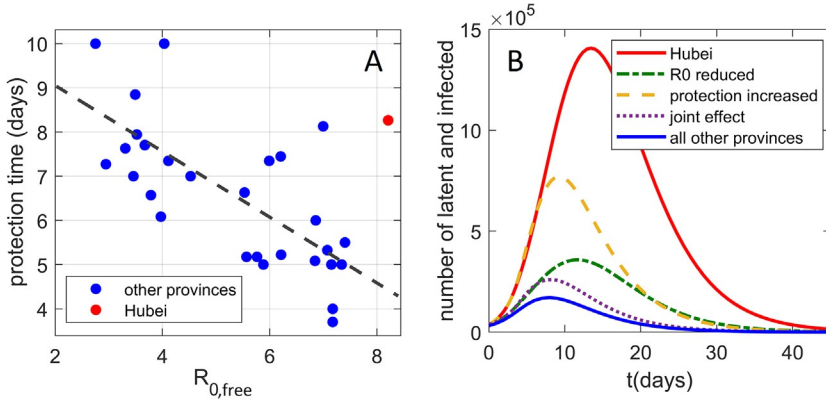


**Fig. 5** The interplay of transmissibility and effective social distancing. (A) The correlation plot of  $t_\alpha$  vs  $R_{0,free}$  for all provinces, where the point corresponding to Hubei is marked in red. (B) The effect (on the Hubei dynamics of infected and latent cases) of reducing  $R_{0,free}$  and  $t_\alpha$  to the mean values of other Mainland China provinces. Both the unperturbed Hubei dynamics and the sum of infected and latent cases for all other provinces are included as references.

The two main properties of the Hubei outburst are therefore higher  $R_{0,free}$  and  $t_\alpha$  compared to other provinces. In Fig. 5B, we investigate how these two properties separately affect the Wuhan outburst for latent and infected cases, where unperturbed Hubei dynamics is shown by the red full curve. We first reduce only  $R_{0,free}$  from the Hubei value, to the mean value for all other provinces (the dash-dotted green curve). We see that this reduction substantially lowers the peak of the curve, though it still remains wide. Next, instead of decreasing  $R_{0,free}$ , we decrease the protection time  $t_\alpha$  to the mean value for all other provinces (dashed orange curve). While reducing  $t_\alpha$  also significantly lowers the peak of the curve, its main effect is in narrowing the curve, i.e., reducing the outburst time. Finally, when  $R_{0,free}$  and  $t_\alpha$  are jointly reduced, we obtain the (dotted purple) curve that is both significantly lower and narrower than the original Hubei progression. This curve comes quite close to the curve that presents the sum of all other provinces (full blue curve)—the dotted curve remains somewhat above this sum, mainly because the initial number of latent and infected cases is somewhat higher for Hubei compared to the sum of all other provinces. This synergy between the transmissibility and the control measures will be further discussed below.



## 6. Conclusions

In this study, we applied a systems biology approach to develop a novel method of COVID-19 transmission dynamics. The model includes (time-dependent) social distancing measures in a simple manner, consistent with the compartmental mechanistic nature of the underlying process. The model has a major advantage that it is independent of the specific transmission process considered, and requires only commonly available count data as an input. The model allows extracting key infection parameters from the data that are readily available and publicly accessible (both for China and other countries), so that, in a nutshell, our approach is of wide applicability. To our best knowledge, such parameters (necessary to assess any future COVID-19 risks), were not extracted by other computational approaches.

The developed method is subsequently applied to the problem that appears highly non-trivial, i.e., to understand the puzzle created by the drastic differences in the infection and fatality counts between Hubei and the rest of Mainland China. The goal was to determine if it is possible to consistently explain such drastic differences by the same model, and what are the resulting numerical estimates and conclusions. We found that Hubei was a suitable ground for infection transmission, being an outlier with respect to two key infection progression parameters: having significantly larger  $R_{0,free}$ , and a longer time needed to move a sizable fraction of the population from susceptible to a protected category. While stricter measures were formally introduced in Hubei, the initial phase of the outburst put a large strain on the system, arguably leading to less effective measures compared to other provinces.

The fact that the initial epidemic in Hubei was not followed by similar outbursts in the rest of Mainland China may be understood as a serendipitous interplay of the two factors noted above. While both smaller  $R_{0,free}$  and lower half-protection time (more efficient measures) significantly suppress the infection curve, their effect is also qualitatively different. While lowering  $R_{0,free}$  more significantly suppresses the peak, decreasing the half-protection time significantly reduces the outburst duration. Consequently, the synergy of these two effects appears to lead to drastically suppressed infection dynamics in other Mainland China provinces compared to Hubei. The number of detected (diagnosed) cases in the entire Mainland China is, therefore, though unintuitive, well consistent with the model, and is explainable by a seemingly reasonable combination of circumstances. Our obtained



negative feedback between transmissibility and effects of social distancing may be understood in terms of larger transmissibility triggering more stringent social distancing measures, where a similar conclusion was also obtained through entirely different means (a combination of real-time human mobility data and regression analysis) (Kraemer et al., 2020).

In summary, we showed that unintuitive dissimilarity in the infection progression for Hubei vs other Mainland China provinces is consistent with our model, and can be attributed to the interplay of transmissibility and effective protection, demonstrating that regional differences may drastically shape the infection outbursts. This also shows that comparisons in terms of the confirmed cases, or fatality counts (even when normalized for population size), between COVID-19 and other infectious diseases, or between different regions for COVID-19, are not feasible, and that parameter inference from quantitative models (individually for different affected regions) is necessary. Consequently, this paper illustrates that utilization of uncommon strategies, such as systems biology application to mathematical epidemiology, may significantly advance our understanding of COVID-19 and other infectious diseases.

## Acknowledgment

This work was supported by the Ministry of Education, Science and Technological Development of the Republic of Serbia.

## References

- Alon, U. (2019). *An introduction to systems biology: Design principles of biological circuits*. CRC press.
- Alon, U., Mino, R., & Yashiv, E. (2020). 10–4: How to reopen the economy by exploiting the coronavirus's weak spot. *The New York Times*.
- Bar-On, Y. M., Flamholz, A., Phillips, R., & Milo, R. (2020). Science forum: SARS-CoV-2 (COVID-19) by the numbers. *eLife*, 9, e57309.
- Brauer, F. (2008). Compartmental models in epidemiology. In *Mathematical epidemiology* (pp. 19–79). Springer.
- Britton, T., Ball, F., & Trapman, P. (2020). A mathematical model reveals the influence of population heterogeneity on herd immunity to SARS-CoV-2. *Science*, 369(6505), 846–849.
- Chen, S., Yang, J., Yang, W., Wang, C., & Bärnighausen, T. (2020). COVID-19 control in China during mass population movements at New Year. *The Lancet*, 395(10226), 764–766.
- Chowell, G., Sattenspiel, L., Bansal, S., & Viboud, C. (2016). Mathematical models to characterize early epidemic growth: A review. *Physics of Life Reviews*, 18, 66–97.
- Cunningham, R. W. (1993). Comparison of three methods for determining fit parameter uncertainties for the Marquardt Compromise. *Computers in Physics*, 7(5), 570–576.
- Day, M. (2020). Covid-19: Identifying and isolating asymptomatic people helped eliminate virus in Italian village. *British Medical Journal*, 368(m1165)(Online).

- Diekmann, O., Heesterbeek, H., & Britton, T. (2012). Mathematical tools for understanding infectious disease dynamics. In (Vol. 7). Princeton University Press.
- Djordjevic, M., Djordjevic, M., Ilic, B., Stojku, S., & Salom, I. (2021). Understanding infection progression under strong control measures through universal COVID-19 growth strategies. *Global Challenges*, 5, 2000101.
- Djordjevic, M., Rodic, A., & Graovac, S. (2019). From biophysics to 'omics and systems biology. *European Biophysics Journal*, 48(5), 413–424.
- Dormand, J. R., & Prince, P. J. (1980). A family of embedded Runge–Kutta formulae. *Journal of Computational and Applied Mathematics*, 6(1), 19–26.
- Du, Z., Xu, X., Wang, L., Fox, S. J., Cowling, B. J., Galvani, A. P., et al. (2020). Effects of proactive social distancing on COVID-19 outbreaks in 58 cities, China. *Emerging Infectious Diseases*, 26(9), 2267.
- Eilersen, A., & Sneppen, K. (2020). Cost–benefit of limited isolation and testing in COVID-19 mitigation. *Scientific Reports*, 10(1), 1–7.
- Feng, Z., et al. (2020). The epidemiological characteristics of an outbreak of 2019 novel coronavirus diseases (COVID-19)—China, 2020. *China CDC Weekly*, 2(8), 113–122.
- Hu, T., Weihe, W. G., Zhu, X., Shao, Y., Liu, L., Du, J., et al. (2020). Building an open resources repository for COVID-19 research. *Data and Information Management*, 4(3), 130–147.
- Ingalls, B. P. (2013). *Mathematical modeling in systems biology: An introduction*. MIT Press.
- Karin, O., Bar-On, Y. M., Milo, T., Katzir, I., Mayo, A., Korem, Y., et al. (2020). Cyclic exit strategies to suppress COVID-19 and allow economic activity. *medRxiv* 2020.04.04.20053579.
- Keeling, M. J., & Rohani, P. (2011). *Modeling infectious diseases in humans and animals*. Princeton University Press.
- Kermack, W. O., & McKendrick, A. G. (1927). A contribution to the mathematical theory of epidemics. *Proceedings of the Royal Society of London Series A, Containing Papers of a Mathematical and Physical Character*, 115(772), 700–721.
- Kraemer, M. U., Yang, C.-H., Gutierrez, B., Wu, C.-H., Klein, B., Pigott, D. M., et al. (2020). The effect of human mobility and control measures on the COVID-19 epidemic in China. *Science*, 368(6490), 493–497.
- Kucharski, A. J., Russell, T. W., Diamond, C., Liu, Y., Edmunds, J., Funk, S., et al. (2020). Early dynamics of transmission and control of COVID-19: A mathematical modelling study. *The Lancet Infectious Diseases*, 20(5), 553–558.
- Li, Q., Guan, X., Wu, P., Wang, X., Zhou, L., Tong, Y., et al. (2020). Early transmission dynamics in Wuhan, China, of novel coronavirus-infected pneumonia. *New England Journal of Medicine*, 382(13), 1199–1207.
- Martcheva, M. (2015). An introduction to mathematical epidemiology. In (Vol. 61) Springer.
- Mizumoto, K., Kagaya, K., & Chowell, G. (2020). Early epidemiological assessment of the transmission potential and virulence of coronavirus disease 2019 (COVID-19) in Wuhan City, China, January–February, 2020. *BMC Medicine*, 18(1), 1–9.
- Phillips, R., Kondev, J., Theriot, J., & Garcia, H. (2012). *Physical biology of the cell*. Garland Science.
- Press, W. H., Flannery, B. P., Teukolsky, S. A., & Vetterling, W. T. (1986). *Numerical recipes: The art of scientific computing*. Cambridge: Cambridge University Press.
- Saad-Roy, C. M., Grenfell, B. T., Levin, S. A., Pellis, L., Stage, H. B., van den Driessche, P., et al. (2021). Superinfection and the evolution of an initial asymptomatic stage. *Royal Society Open Science*, 8(1), 202212.
- Salom, I., Rodic, A., Milicevic, O., Zigic, D., Djordjevic, M., & Djordjevic, M. (2021). Effects of demographic and weather parameters on COVID-19 basic reproduction number. *Frontiers in Ecology and Evolution*, 8, 617841.
- Sanche, S., Lin, Y. T., Xu, C., Romero-Severson, E., Hengartner, N., & Ke, R. (2020). High contagiousness and rapid spread of severe acute respiratory syndrome coronavirus 2. *Emerging Infectious Diseases*, 26(7), 1470–1477.

- Tian, H., Liu, Y., Li, Y., Wu, C.-H., Chen, B., Kraemer, M. U., et al. (2020). An investigation of transmission control measures during the first 50 days of the COVID-19 epidemic in China. *Science*, *368*(6491), 638–642.
- Vilar, J. M., & Saiz, L. (2020). The evolving worldwide dynamic state of the COVID-19 outbreak. *medRxiv*.
- Voit, E., Martens, H., & Omholt, S. (2015). 150 years of the mass action law. *PLoS Computational Biology*, *11*(1), e1004012.
- Wang, Z., Andrews, M. A., Wu, Z.-X., Wang, L., & Bauch, C. T. (2015). Coupled disease–behavior dynamics on complex networks: A review. *Physics of Life Reviews*, *15*, 1–29.
- WHO. (2020). *WHO timeline—COVID-19*. <https://www.who.int/news-room/detail/27-04-2020-who-timeline—covid-19>: World Health Organization.
- Wilkinson, D. J. (2018). *Stochastic modelling for systems biology* (3rd ed.). London: Chapman and Hall/CRC.
- Wong, G. N., Weiner, Z. J., Tkachenko, A. V., Elbanna, A., Maslov, S., & Goldenfeld, N. (2020). Modeling COVID-19 dynamics in Illinois under nonpharmaceutical interventions. *Physical Review X*, *10*(4), 041033.
- Wu, J. T., Leung, K., Bushman, M., Kishore, N., Niehus, R., de Salazar, P. M., et al. (2020). Estimating clinical severity of COVID-19 from the transmission dynamics in Wuhan, China. *Nature Medicine*, *26*(4), 506–510.
- Wu, J. T., Leung, K., & Leung, G. M. (2020). Nowcasting and forecasting the potential domestic and international spread of the 2019-nCoV outbreak originating in Wuhan, China: A modelling study. *The Lancet*, *395*(10225), 689–697.

Article

# Algebraic Bethe Ansatz for the Trigonometric $sl(2)$ Gaudin Model with Triangular Boundary

Nenad Manojlović <sup>1,†</sup>  and Igor Salom <sup>2,\*,†</sup> 

<sup>1</sup> Departamento de Matemática, F. C. T., Universidade do Algarve, Campus de Gambelas, PT-8005-139 Faro, Portugal; nmanoj@ualg.pt

<sup>2</sup> Institute of Physics, University of Belgrade, P.O. Box 57, 11080 Belgrade, Serbia

\* Correspondence: isalom@ipb.ac.rs

† These authors contributed equally to this work.

Received: 28 January 2020; Accepted: 19 February 2020; Published: 1 March 2020



**Abstract:** In this paper we deal with the trigonometric Gaudin model, generalized using a nontrivial triangular reflection matrix (corresponding to non-periodic boundary conditions in the case of anisotropic XXZ Heisenberg spin-chain). In order to obtain the generating function of the Gaudin Hamiltonians with boundary terms we follow an approach based on Sklyanin's derivation in the periodic case. Once we have the generating function, we obtain the corresponding Gaudin Hamiltonians with boundary terms by taking its residues at the poles. As the main result, we find the generic form of the Bethe vectors such that the off-shell action of the generating function becomes exceedingly compact and simple. In this way—by obtaining Bethe equations and the spectrum of the generating function—we fully implement the algebraic Bethe ansatz for the generalized trigonometric Gaudin model.

**Keywords:** Gaudin model; Algebraic Bethe Ansatz; non-unitary r-matrix

## 1. Introduction

The so-called rational  $sl(2)$  Gaudin model was first introduced in [1] as a model of “long-range” interacting spins in a chain. Having non-trivial long-range (pairwise) interactions and yet being fully integrable, the model was of clear potential interest in many areas of physics. Naturally, the most promising were its applications in condensed matter physics, where the need for exactly (or even only quasi-exactly) solvable interacting many-body models was maybe the most acute, and where the generalizations of Gaudin algebra arguably play a significant role [2]. However, the potential physical significance of Gaudin model is not confined to this area; for example, its connection with Wess–Zumino–Novikov–Witten model was pointed out in [3], more recently it was also related to AGT correspondence [4], and applied to obtain classical integrable field theories [5].

Therefore it is not surprising that many generalizations ensued soon after the Gaudin's original paper, along various directions: to other simple Lie algebras [6,7], in the context of the quantum inverse scattering method [8–10], to other cases where skew-symmetric r-matrix fulfills the classical Yang–Baxter equation [11,12]. In general, not only Gaudin models corresponding to the classical r-matrices of simple Lie algebras [3,13–17], but also those of Lie superalgebras [18–22] attracted considerable attention.

One particular approach to the relation between Heisenberg spin-chains and Gaudin models was due to Hikami, Kulish and Wadati, who showed that the Gaudin Hamiltonians can be obtained by making the so-called quasi-classical expansion of the transfer matrix of the periodic chain [23,24]. This was soon demonstrated also for cases with non-periodic boundary conditions [25]. The progress paved the way for further studies of open Gaudin models, and algebraic Bethe ansatz (ABA)

was soon applied to open Gaudin model in the context of Lie superalgebras [26] and of the the Vertex-IRF correspondence [27–29]. Open Gaudin models were also studied in the light of the classical reflection equation [30–32] and, more recently, an approach utilizing non-unitary  $r$ -matrices was demonstrated [33,34]. A more detailed review of the open Gaudin model can be found in [35].

Due to the close mathematical connection between Heisenberg spin-chains and Gaudin models, development in one area inevitably led also to the progress in the other. Further generalizations in applications of ABA to spin-chains with non-periodic boundary conditions [36–53] recently influenced study of the corresponding Gaudin model [54,55]. A new method to obtain the eigenvalues of the Gaudin Hamiltonians and the corresponding Bethe ansatz equations was derived in [56], based on  $T$ - $Q$  approach to implementation of Bethe ansatz [41,42]. Also, in [53], by taking the so-called quasi-classical limit we obtained the off-shell action of the generating function on the Bethe vectors for the trigonometric Gaudin model with boundary terms.

While in [53] we considered expansion of the XXZ spin-chain expressions to obtain Bethe vectors for the Gaudin model (i.e., by exploiting the mathematical relation between the two models), the open trigonometric Gaudin model can be treated in its own right, by fully implementing the algebraic Bethe ansatz for this case. This is the essential goal of the present paper.

The first important goal of an independent treatment of the Gaudin model is to obtain the generating function of the Gaudin Hamiltonians. Similarly like in the rational case [55], we will follow the approach based on Sklyanin's method in the periodic case [10,57]. Once we have the generating function, taking its residues at the poles will yield the Gaudin Hamiltonians with the boundary terms.

The next step is to establish the algebra of Bethe operators. This will be accomplished by first constructing non-unitary classical  $r$ -matrix (which satisfies the generalized classical Yang-Baxter equation) and the corresponding modified Lax matrix—both of which depend on the reflection  $K$ -matrix (following the analogy with the spin-chain case, we may say that the  $K$ -matrix encodes non-period boundary conditions). These two entities are mutually related via linear bracket, which is anti-symmetric, obeys the Jacobi identity and will lead us to algebraic relations between Bethe operators (matrix elements of the Lax matrix). Additionally, as an important nontrivial step, we will demonstrate how an appropriate change of generator basis can result in significant simplification of the initial Bethe algebra relations.

The most difficult part of the ABA implementation is to find the Bethe vectors and the corresponding off-shell action of the generating function. After explicitly solving the first few particular cases, we will conjecture the general form of a Bethe vector using a family of suitably defined creation operators. Such Bethe vectors will turn out to yield strikingly simple off-shell action of the generating function—so simple that it is hardly any more complex than the corresponding formula when the boundary matrix is diagonal [25]. As usual, off-shell action of the generating function provides us both with the spectrum of the system and with the corresponding Bethe equations (the latter are the necessary conditions to eliminate the unwanted terms and promote Bethe vectors into true solutions of the eigenproblem).

This paper is organized as follows. In Section 2 we establish the fundamentals of the framework, defining the reflection matrix, Lax matrix and  $r$ -matrix that correspond to the Gaudin model with nontrivial boundary. The generating function, as well as the Gaudin Hamiltonians are also derived in this section. Section 3 deals with the algebraic Bethe ansatz of the model: we derive the relevant algebraic structure and proceed to solve the generating function eigenproblem by finding the appropriate Bethe vectors and the formula for the off-shell action. We summarize our results in the Section 4. In Appendix A we provide proof for the essential commutativity property of the generating function of the Gaudin Hamiltonians, while the Appendix B contains some explicit formulas regarding the Bethe vector  $\varphi_3(\mu_1, \mu_2, \mu_3)$ .

## 2. Trigonometric Gaudin Model with Boundary

Lax matrix of the trigonometric Gaudin model with periodic boundary conditions [20] is of the following form [53,57]:

$$L_0(\lambda) = \sum_{m=1}^N \frac{\sigma_0^3 \otimes \cosh(\lambda - \alpha_m) S_m^3 + \frac{1}{2} (\sigma_0^+ \otimes S_m^- + \sigma_0^- \otimes S_m^+)}{\sinh(\lambda - \alpha_m)}, \quad (1)$$

where spin operators  $S_m^\alpha$ ,  $\alpha = +, -, 3$ , living in the product Hilbert space

$$\mathcal{H} = \bigotimes_{m=1}^N V_m = (\mathbb{C}^{2s+1})^{\otimes N}, \quad (2)$$

satisfy the usual commutation relations:

$$[S_m^3, S_n^\pm] = \pm S_m^\pm \delta_{mn}, \quad [S_m^+, S_n^-] = 2S_m^3 \delta_{mn}. \quad (3)$$

The corresponding classical r-matrix is given by:

$$r(\lambda) = \frac{-1}{2 \sinh(\lambda)} \left( \cosh(\lambda) (\mathbb{1} \otimes \mathbb{1} + \sigma^3 \otimes \sigma^3) + \frac{1}{2} (\sigma^+ \otimes \sigma^- + \sigma^- \otimes \sigma^+) \right). \quad (4)$$

The r-matrix (4) satisfies the classical Yang-Baxter equation

$$[r_{13}(\lambda), r_{23}(\mu)] + [r_{12}(\lambda - \mu), r_{13}(\lambda) + r_{23}(\mu)] = 0, \quad (5)$$

and also has the following unitarity property

$$r_{21}(-\lambda) = -r_{12}(\lambda). \quad (6)$$

Crucially, Lax matrix and r-matrix satisfy the so-called Sklyanin linear bracket relation:

$$[L_1(\lambda), L_2(\mu)] = [r_{12}(\lambda - \mu), L_1(\lambda) + L_2(\mu)]. \quad (7)$$

The Sklyanin linear bracket (7) obeys the Jacobi identity and is also anti-symmetric. From here it follows that the entries of the Lax matrix (1) generate a Lie algebra (Gaudin algebra), which in this case corresponds to the trigonometric Gaudin model with periodic boundary conditions [20].

The Gaudin model described by the above Lax matrix (1) and r-matrix (4) is mathematically tightly related to the trigonometric spin-chain model with periodic boundary: the former can be obtained from the latter by the so-called quasi-classical expansion [23,24]. This can be verified by considering linear terms in the  $\eta$  expansion of the XXZ Heisenberg spin-chain Lax operator and R-matrix, taken from [53], in a full analogy with the rational case [55]:

$$\begin{aligned} \mathbb{L}_{0m}(\lambda - \alpha_m) &= \mathbb{1}_0 \otimes \mathbb{1}_m + \eta \left( \sigma_0^3 \otimes \coth(\lambda - \alpha_m) S_m^3 + \frac{1}{2 \sinh(\lambda - \alpha_m)} (\sigma_0^+ \otimes S_m^- + \sigma_0^- \otimes S_m^+) \right) \\ &+ \frac{\eta^2}{2} \mathbb{1}_0 \otimes (S_m^3)^2 + \mathcal{O}(\eta^3); \end{aligned} \quad (8)$$

and

$$\frac{1}{\sinh(\lambda)} R(\lambda) = \mathbb{1} - \eta r(\lambda) + \mathcal{O}(\eta^2). \quad (9)$$

To extend the generality of the model it is possible to introduce the reflection K-matrix, in a mathematically similar manner as when the periodic Heisenberg spin-chain model is extended



to account for nontrivial boundary conditions. K-matrix must then satisfy the classical reflection equation [30,31,55]:

$$\begin{aligned} r_{12}(\lambda - \mu)K_1(\lambda)K_2(\mu) + K_1(\lambda)r_{21}(\lambda + \mu)K_2(\mu) = \\ = K_2(\mu)r_{12}(\lambda + \mu)K_1(\lambda) + K_2(\mu)K_1(\lambda)r_{21}(\lambda - \mu). \end{aligned} \quad (10)$$

In the spin chain case, parameters of  $K^-$  and  $K^+$  matrices (encoding, respectively, boundary conditions on the left and on the right end of the chain) are allowed to be different. However, in the Gaudin model case we must impose the following additional condition on the reflection matrices [35,55]:

$$\lim_{\eta \rightarrow 0} \left( K^+(\lambda)K^-(\lambda) \right) = \left( \kappa^2 \sinh(\xi - \lambda) \sinh(\xi + \lambda) - \phi\psi \sinh^2(\lambda) \right) \mathbb{1}. \quad (11)$$

In turn, this implies that parameters of the  $K^-$  and  $K^+$  cannot be mutually independent, and effectively, we cannot speak of two reflection matrices but of a single one. Intuitively, this is not surprising, since the long-range Gaudin interactions actually do not single out any nodes as boundary nodes and thus, physically, K-matrices cannot be literally interpreted as describing any boundary conditions but merely as parameters that provide further generalization of the model (this can be best inferred from the Hamiltonian Expression (23) below). In spite of this, we will say for such a Gaudin model—incorporating a nontrivial K-matrix—that it satisfies nontrivial boundary conditions (or denote it as “open”), simply due to the analogy and direct relation with the corresponding spin-chain model (the strict mathematical connection can be again established by the quasi-classical expansion procedure).

The solutions for  $K^-(\lambda)$  and  $K^+(\lambda)$  can be thus given in terms of a single K-matrix, and they take the following form [58,59]:

$$K^-(\lambda) \equiv K(\lambda) = \begin{pmatrix} \kappa \sinh(\xi + \lambda) & \psi \sinh(2\lambda) \\ \phi \sinh(2\lambda) & \kappa \sinh(\xi - \lambda) \end{pmatrix} \quad (12)$$

and

$$K^+(\lambda) = K(-\lambda - \eta) = \begin{pmatrix} \kappa \sinh(\xi - \lambda - \eta) & -\psi \sinh(2(\lambda + \eta)) \\ -\phi \sinh(2(\lambda + \eta)) & \kappa \sinh(\xi + \lambda + \eta) \end{pmatrix}. \quad (13)$$

Moreover, it is straightforward to check the following useful identities

$$K(-\lambda)K(\lambda) = \det(K(\lambda)) \mathbb{1}, \quad (14)$$

$$K(-\lambda) = \text{tr} K(\lambda) - K(\lambda). \quad (15)$$

Now, the new Gaudin Lax matrix generalized by the K-matrix, is given by

$$\mathcal{L}_0(\lambda) = L_0(\lambda) - K_0(\lambda)L_0(-\lambda)K_0^{-1}(\lambda), \quad (16)$$

and the corresponding non-unitary r-matrix is given by:

$$r_{00'}^K(\lambda, \mu) = r_{00'}(\lambda - \mu) - K_{0'}(\mu)r_{00'}(\lambda + \mu)K_0^{-1}(\mu). \quad (17)$$

It is not difficult to check that this r-matrix satisfies the classical Yang-Baxter equation

$$[r_{32}^K(\lambda_3, \lambda_2), r_{13}^K(\lambda_1, \lambda_3)] + [r_{12}^K(\lambda_1, \lambda_2), r_{13}^K(\lambda_1, \lambda_3)] + r_{23}^K(\lambda_2, \lambda_3) = 0 \quad (18)$$

and that the linear bracket for the modified Lax operator is now preserved:

$$[\mathcal{L}_0(\lambda), \mathcal{L}_{0'}(\mu)] = [r_{00'}^K(\lambda, \mu), \mathcal{L}_0(\lambda)] - [r_{0'0}^K(\mu, \lambda), \mathcal{L}_{0'}(\mu)]. \tag{19}$$

This linear bracket is also anti-symmetric. Since the  $r$ -matrix (17) satisfies the classical Yang-Baxter equation, it additionally obeys the Jacobi identity.

We have now set the stage to introduce the generating function of the Gaudin Hamiltonians with boundary terms:

$$\tau(\lambda) = \text{tr}_0 \mathcal{L}_0^2(\lambda) \tag{20}$$

The essential property of  $\tau(\lambda)$  is that it commutes for different values of the spectral parameter:

$$[\tau(\lambda), \tau(\mu)] = 0. \tag{21}$$

The proof of this relation is given in the Appendix A.

Next, we obtain the Gaudin Hamiltonians with the boundary terms by taking the residues of the generating function (20) at poles  $\lambda = \pm\alpha_m$  :

$$\text{Res}_{\lambda=\alpha_m} \tau(\lambda) = 4 H_m \quad \text{and} \quad \text{Res}_{\lambda=-\alpha_m} \tau(\lambda) = (-4) H_m \tag{22}$$

where

$$\begin{aligned} H_m = & \sum_{n \neq m}^N \left( \coth(\alpha_m - \alpha_n) S_m^3 S_n^3 + \frac{S_m^+ S_n^- + S_m^- S_n^+}{2 \sinh(\alpha_m - \alpha_n)} \right) + \sum_{n=1}^N \coth(\alpha_m + \alpha_n) \frac{S_m^3 S_n^3 + S_n^3 S_m^3}{2} \\ & + \frac{\psi}{\kappa} \frac{\sinh(2\alpha_m)}{\sinh(\xi + \alpha_m)} \sum_{n=1}^N \frac{S_m^3 S_n^+ + S_n^+ S_m^3}{2 \sinh(\alpha_m + \alpha_n)} + \frac{\sinh(\xi - \alpha_m)}{2 \sinh(\xi + \alpha_m)} \sum_{n=1}^N \frac{S_m^- S_n^+ + S_n^+ S_m^-}{2 \sinh(\alpha_m + \alpha_n)} \\ & - \frac{\psi}{\kappa} \frac{\sinh(2\alpha_m)}{\sinh(\xi - \alpha_m)} \sum_{n=1}^N \coth(\alpha_m + \alpha_n) \frac{S_m^+ S_n^3 + S_n^3 S_m^+}{2} + \frac{\sinh(\xi + \alpha_m)}{2 \sinh(\xi - \alpha_m)} \sum_{n=1}^N \frac{S_m^+ S_n^- + S_n^- S_m^+}{2 \sinh(\alpha_m + \alpha_n)} \\ & - \frac{\psi^2}{\kappa^2} \frac{\sinh^2(2\alpha_m)}{2 \sinh(\xi - \alpha_m) \sinh(\xi + \alpha_m)} \sum_{n=1}^N \frac{S_m^+ S_n^+ + S_n^+ S_m^+}{2 \sinh(\alpha_m + \alpha_n)}. \end{aligned} \tag{23}$$

In the next section we will deal with the arduous task of obtain the spectrum and the corresponding Bethe vectors of the generating function.

### 3. Algebraic Bethe Ansatz

Implementation of the algebraic Bethe ansatz requires triangularity of the K-matrix (12). As opposed to the rational case [55] where the triangularity of the K-matrix can be guaranteed by the similarity transformation independent of the spectral parameter, in the present case there is no, in general,  $U(1)$  symmetry transformation that can bring the reflection matrix to the upper triangular form. For this reason, we are forced to impose an extra condition on the parameters of  $K(\lambda)$ . By setting

$$\phi = 0$$

the reflection matrix becomes upper triangular

$$K(\lambda) = \begin{pmatrix} \kappa \sinh(\xi + \lambda) & \psi \sinh(2\lambda) \\ 0 & \kappa \sinh(\xi - \lambda) \end{pmatrix}. \tag{24}$$

The inverse matrix has the following form:

$$K^{-1}(\lambda) = \frac{1}{\kappa^2 \sinh(\xi + \lambda) \sinh(\xi - \lambda)} \begin{pmatrix} \kappa \sinh(\xi - \lambda) & -\psi \sinh(2\lambda) \\ 0 & \kappa \sinh(\xi + \lambda) \end{pmatrix}. \tag{25}$$

By substituting these formulas into (16),

$$\mathcal{L}_0(\lambda) = \begin{pmatrix} H(\lambda) & F(\lambda) \\ E(\lambda) & -H(\lambda) \end{pmatrix} = L_0(\lambda) - K_0(\lambda)L_0(-\lambda)K_0^{-1}(\lambda), \tag{26}$$

we obtain local realisation for the entries of the Lax matrix of the following form:

$$E(\lambda) = \sum_{m=1}^N \left( \frac{S_m^+}{\sinh(\lambda - \alpha_m)} + \frac{\sinh(\xi - \lambda) S_m^+}{\sinh(\xi + \lambda) \sinh(\lambda + \alpha_m)} \right), \tag{27}$$

$$H(\lambda) = \sum_{m=1}^N \left( \coth(\lambda - \alpha_m) S_m^3 + \coth(\lambda + \alpha_m) S_m^3 + \frac{\psi \sinh(2\lambda) S_m^+}{\kappa \sinh(\xi + \lambda) \sinh(\lambda + \alpha_m)} \right), \tag{28}$$

$$F(\lambda) = \sum_{m=1}^N \left( \frac{S_m^-}{\sinh(\lambda - \alpha_m)} + \frac{\sinh(\xi + \lambda) S_m^-}{\sinh(\xi - \lambda) \sinh(\lambda + \alpha_m)} - \frac{2\psi \sinh(2\lambda)}{\kappa \sinh(\xi - \lambda)} \coth(\lambda + \alpha_m) S_m^3 - \frac{\psi^2 \sinh^2(2\lambda) S_m^+}{\kappa^2 \sinh(\xi - \lambda) \sinh(\xi + \lambda) \sinh(\lambda + \alpha_m)} \right). \tag{29}$$

Similarly, by using (4), (24), (25) and (17) we obtain explicit expression for  $r_{00'}^K(\lambda, \mu)$ . This non-unitary, classical r-matrix together with the Lax matrix (26) defines the Lie algebra relevant for the open trigonometric Gaudin model. By explicitly rewriting the relation (19) we find the following commutation relations for the generators  $E(\lambda)$ ,  $H(\lambda)$  and  $F(\lambda)$ :

$$[E(\lambda), E(\mu)] = 0, \tag{30}$$

$$[H(\lambda), E(\mu)] = \frac{1}{\sinh(\lambda - \mu) \sinh(\lambda + \mu)} \left( \sinh(2\lambda) E(\mu) - \frac{\sinh(\xi + \lambda)}{\sinh(\xi + \mu)} \sinh(2\mu) E(\lambda) \right), \tag{31}$$

$$[E(\lambda), F(\mu)] = \frac{2\psi}{\kappa} \coth(\lambda + \mu) \frac{\sinh(2\mu)}{\sinh(\xi - \mu)} E(\lambda) + \frac{2}{\sinh(\lambda - \mu) \sinh(\lambda + \mu)} \times \left( \frac{\sinh(\xi + \mu)}{\sinh(\xi + \lambda)} \sinh(2\lambda) H(\mu) - \frac{\sinh(\xi - \lambda)}{\sinh(\xi - \mu)} \sinh(2\mu) H(\lambda) \right), \tag{32}$$

$$[H(\lambda), H(\mu)] = \frac{-\psi}{\kappa \sinh(\lambda + \mu)} \left( \frac{\sinh(2\lambda)}{\sinh(\xi + \lambda)} E(\mu) - \frac{\sinh(2\mu)}{\sinh(\xi + \mu)} E(\lambda) \right), \tag{33}$$

$$[H(\lambda), F(\mu)] = -\frac{1}{\sinh(\lambda - \mu) \sinh(\lambda + \mu)} \left( \sinh(2\lambda) F(\mu) - \frac{\sinh(\xi - \lambda)}{\sinh(\xi - \mu)} \sinh(2\mu) F(\lambda) \right) + \frac{2\psi \sinh(2\lambda)}{\kappa \sinh(\lambda + \mu) \sinh(\xi + \lambda)} H(\mu) - \frac{\psi^2 \sinh^2(2\mu)}{\kappa^2 \sinh(\lambda + \mu) \sinh(\xi - \mu) \sinh(\xi + \mu)} E(\lambda), \tag{34}$$

$$[F(\lambda), F(\mu)] = \frac{2\psi}{\kappa} \coth(\lambda + \mu) \left( \frac{\sinh(2\lambda)}{\sinh(\xi - \lambda)} F(\mu) - \frac{\sinh(2\mu)}{\sinh(\xi - \mu)} F(\lambda) \right) - \frac{2\psi^2}{\kappa^2 \sinh(\lambda + \mu)} \left( \frac{\sinh^2(2\lambda)}{\sinh(\xi - \lambda) \sinh(\xi + \lambda)} H(\mu) - \frac{\sinh^2(2\mu)}{\sinh(\xi - \mu) \sinh(\xi + \mu)} H(\lambda) \right). \tag{35}$$

In terms of the entries of the Lax matrix, the generating function of the Gaudin Hamiltonians (20) has the following form:

$$\tau(\lambda) = \text{tr}_0 \mathcal{L}_0^2(\lambda) = 2H^2(\lambda) + 2F(\lambda)E(\lambda) + [E(\lambda), F(\lambda)], \tag{36}$$

where, from (32) we evaluate the last term to be

$$[E(\lambda), F(\lambda)] = 2 \frac{\cosh(2\xi) \cosh(2\lambda) - 1}{\sinh(2\lambda) \sinh(\xi + \lambda) \sinh(\xi - \lambda)} H(\lambda) - 2H'(\lambda) + \frac{2\psi \cosh(2\lambda)}{\kappa \sinh(\xi - \lambda)} E(\lambda), \tag{37}$$

and thus the final expression becomes

$$\tau(\lambda) = 2 \left( H^2(\lambda) + \frac{\cosh(2\xi) \cosh(2\lambda) - 1}{\sinh(2\lambda) \sinh(\xi + \lambda) \sinh(\xi - \lambda)} H(\lambda) - H'(\lambda) \right) + \left( 2F(\lambda) + \frac{2\psi \cosh(2\lambda)}{\kappa \sinh(\xi - \lambda)} \right) E(\lambda). \tag{38}$$

In order to simplify commutation relations (30)–(35) we switch to new generators  $e(\lambda), h(\lambda)$  and  $f(\lambda)$ , defined as linear combinations of the original ones:

$$e(\lambda) = \frac{\sinh(\xi + \lambda)}{\sinh(2\lambda)} E(\lambda) = \sum_{m=1}^N \frac{\sinh(\xi + \alpha_m) S_m^+}{\sinh(\lambda - \alpha_m) \sinh(\lambda + \alpha_m)}, \tag{39}$$

$$h(\lambda) = \frac{1}{\sinh(2\lambda)} \left( H(\lambda) - \frac{\psi \sinh(\lambda)}{\kappa \sinh(\xi)} E(\lambda) \right) = \sum_{m=1}^N \frac{S_m^3 - \frac{\psi \sinh(\alpha_m)}{\kappa \sinh(\xi)} S_m^+}{\sinh(\lambda - \alpha_m) \sinh(\lambda + \alpha_m)}, \tag{40}$$

$$f(\lambda) = \frac{1}{\sinh(2\lambda)} \left( \sinh(\xi - \lambda) F(\lambda) + \frac{\psi}{\kappa} \sinh(2\lambda) H(\lambda) \right) = \sum_{m=1}^N \frac{\sinh(\xi - \alpha_m) S_m^- + \frac{\psi}{\kappa} \sinh(2\alpha_m) S_m^3}{\sinh(\lambda - \alpha_m) \sinh(\lambda + \alpha_m)}. \tag{41}$$

The essential property of the new basis operators is:

$$[e(\lambda), e(\mu)] = [h(\lambda), h(\mu)] = [f(\lambda), f(\mu)] = 0. \tag{42}$$

Therefore there are only three remaining nontrivial commutation relations

$$[h(\lambda), e(\mu)] = \frac{1}{\sinh(\lambda - \mu) \sinh(\lambda + \mu)} (e(\mu) - e(\lambda)), \tag{43}$$

$$\begin{aligned} [h(\lambda), f(\mu)] &= \frac{-1}{\sinh(\lambda - \mu) \sinh(\lambda + \mu)} (f(\mu) - f(\lambda)) + \frac{2\psi \coth(\xi)}{\kappa \sinh(\lambda - \mu) \sinh(\lambda + \mu)} \times \\ &\times \left( \sinh^2(\mu) h(\mu) - \sinh^2(\lambda) h(\lambda) \right) + \frac{2\psi^2}{\kappa^2 \sinh(\lambda - \mu) \sinh(\lambda + \mu) \sinh^2(\xi)} \times \\ &\times \left( \sinh^2(\mu) e(\mu) - \sinh^2(\lambda) e(\lambda) \right), \end{aligned} \tag{44}$$

$$\begin{aligned} [e(\lambda), f(\mu)] &= \frac{-2\psi \coth(\xi)}{\kappa \sinh(\lambda - \mu) \sinh(\lambda + \mu)} \left( \sinh^2(\mu) e(\mu) - \sinh^2(\lambda) e(\lambda) \right) + \frac{2}{\sinh(\lambda - \mu) \sinh(\lambda + \mu)} \times \\ &\times \left( \sinh(\xi - \mu) \sinh(\xi + \mu) h(\mu) - \sinh(\xi - \lambda) \sinh(\xi + \lambda) h(\lambda) \right). \end{aligned} \tag{45}$$

Lie algebra (42)–(45) will be the basis of our implementation of the algebraic Bethe ansatz. The first step is to find the expression for the generating function  $\tau(\lambda)$  as a function of the new generators  $e(\lambda), h(\lambda)$  and  $f(\lambda)$ . To this end, we will invert the relations (39)–(41)

$$E(\lambda) = \frac{\sinh(2\lambda)}{\sinh(\xi + \lambda)} e(\lambda), \tag{46}$$

$$H(\lambda) = \sinh(2\lambda) \left( h(\lambda) + \frac{\psi \sinh(\lambda)}{\kappa \sinh(\xi) \sinh(\xi + \lambda)} e(\lambda) \right), \tag{47}$$

$$F(\lambda) = \frac{\sinh(2\lambda)}{\sinh(\xi - \lambda)} \left( f(\lambda) - \frac{\psi \sinh(2\lambda)}{\kappa} h(\lambda) - \frac{\psi^2 \sinh(\lambda) \sinh(2\lambda)}{\kappa^2 \sinh(\xi) \sinh(\xi + \lambda)} e(\lambda) \right). \tag{48}$$

In particular, we find

$$\begin{aligned}
 H^2(\lambda) &= \sinh^2(2\lambda) \left( h^2(\lambda) + \frac{\psi \sinh(\lambda)}{\kappa \sinh(\xi) \sinh(\xi + \lambda)} (2h(\lambda)e(\lambda) - [h(\lambda), e(\lambda)]) \right. \\
 &\quad \left. + \frac{\psi^2 \sinh^2(\lambda)}{\kappa^2 \sinh^2(\xi) \sinh^2(\xi + \lambda)} e^2(\lambda) \right) \\
 &= \sinh^2(2\lambda) \left( h^2(\lambda) + \frac{\psi \sinh(\lambda)}{\kappa \sinh(\xi) \sinh(\xi + \lambda)} \left( 2h(\lambda)e(\lambda) + \frac{e'(\lambda)}{\sinh(2\lambda)} \right) \right. \\
 &\quad \left. + \frac{\psi^2 \sinh^2(\lambda)}{\kappa^2 \sinh^2(\xi) \sinh^2(\xi + \lambda)} e^2(\lambda) \right). \tag{49}
 \end{aligned}$$

Substitution of (46)–(49) into (38) yields the desired expression for the the generating function

$$\begin{aligned}
 \tau(\lambda) &= 2 \sinh^2(2\lambda) \left( h^2(\lambda) + \frac{h(\lambda)}{\sinh(\xi + \lambda) \sinh(\xi - \lambda)} - \frac{h'(\lambda)}{\sinh(2\lambda)} \right) + \frac{2 \sinh^2(2\lambda)}{\sinh(\xi + \lambda) \sinh(\xi - \lambda)} \times \\
 &\quad \times \left( f(\lambda) - 2 \frac{\psi}{\kappa} \coth(\xi) \sinh^2(\lambda) h(\lambda) - \frac{\psi^2 \sinh^2(\lambda)}{\kappa^2 \sinh^2(\xi)} e(\lambda) + \frac{\psi}{\kappa} \coth(\xi) \right) e(\lambda). \tag{50}
 \end{aligned}$$

In every factor-space  $V_m = \mathbb{C}^{2s+1}$  from the Hilbert space  $\mathcal{H}$  (2) there exists a vector  $\omega_m \in V_m$  such that

$$S_m^3 \omega_m = s_m \omega_m \quad \text{and} \quad S_m^+ \omega_m = 0. \tag{51}$$

We define a vector  $\Omega_+$  to be

$$\Omega_+ = \omega_1 \otimes \dots \otimes \omega_N \in \mathcal{H}. \tag{52}$$

The action of the generators  $e(\lambda)$  and  $h(\lambda)$  on the vector  $\Omega_+$  can be obtained from the definitions above and the formulas (27)–(28) and (39)–(41):

$$e(\lambda)\Omega_+ = 0 \quad \text{and} \quad h(\lambda)\Omega_+ = \rho(\lambda)\Omega_+, \quad \text{with} \quad \rho(\lambda) = \sum_{m=1}^N \frac{s_m}{\sinh(\lambda + \alpha_m) \sinh(\lambda - \alpha_m)}. \tag{53}$$

Of a crucial importance in what follows is to note that the vector  $\Omega_+$  (52) is an eigenvector of the generating function  $\tau(\lambda)$ . This can be shown by using (53)

$$\tau(\lambda)\Omega_+ = \chi_0(\lambda)\Omega_+ = 2 \sinh^2(2\lambda) \left( \rho^2(\lambda) + \frac{\rho(\lambda)}{\sinh(\xi + \lambda) \sinh(\xi - \lambda)} - \frac{\rho'(\lambda)}{\sinh(2\lambda)} \right) \Omega_+. \tag{54}$$

By using the explicit expression for the function  $\rho(\lambda)$  (53) the eigenvalue  $\chi_0(\lambda)$  can be also written as

$$\begin{aligned}
 \chi_0(\lambda) &= 2 \sinh^2(2\lambda) \left( \sum_{m=1}^N \frac{s_m(s_m + 1)}{\sinh^2(\lambda + \alpha_m) \sinh^2(\lambda - \alpha_m)} + \sum_{m=1}^N \frac{s_m}{\sinh(\lambda + \alpha_m) \sinh(\lambda - \alpha_m)} \times \right. \\
 &\quad \left. \times \left( \frac{1}{\sinh(\xi + \lambda) \sinh(\xi - \lambda)} + \sum_{n>m}^N \frac{2s_n}{\sinh(\lambda + \alpha_n) \sinh(\lambda - \alpha_n)} \right) \right). \tag{55}
 \end{aligned}$$

The essential goal of the implementation of the algebraic Bethe ansatz is to find the corresponding Bethe vectors. Due to the existence of Bethe conditions, it turns out that their form is not unique, and we seek the solution that renders the off-shell action of the generating function of the Gaudin

Hamiltonians as simple as possible. We proceed by demonstrating that the Bethe vector  $\varphi_1(\mu)$  has the form

$$\varphi_1(\mu) = \left( f(\mu) + c_1^{(1)}(\mu) \right) \Omega_+, \tag{56}$$

where  $c_1(\mu)$  is given by

$$c_1^{(1)}(\mu) = \frac{\psi}{\kappa} \left( 1 + \left( e^{-2\xi} - \cosh(2\mu) \right) \rho(\mu) \right). \tag{57}$$

We proceed by explicit calculation to find

$$\tau(\lambda)\varphi_1(\mu) = [\tau(\lambda), f(\mu)] \Omega_+ + \chi_0(\lambda)\varphi_1(\mu), \tag{58}$$

where the commutator in the first term of (58) becomes

$$\begin{aligned} [\tau(\lambda), f(\mu)] \Omega_+ = & -\frac{2 \sinh^2(2\lambda)}{\sinh(\lambda + \mu) \sinh(\lambda - \mu)} \left( 2\rho(\lambda) + \frac{1}{\sinh(\xi + \lambda) \sinh(\xi - \lambda)} \right) \varphi_1(\mu) \\ & + \frac{2 \sinh^2(2\lambda)}{\sinh(\lambda + \mu) \sinh(\lambda - \mu)} \frac{\sinh(\xi + \mu) \sinh(\xi - \mu)}{\sinh(\xi + \lambda) \sinh(\xi - \lambda)} \times \\ & \times \left( 2\rho(\mu) + \frac{1}{\sinh(\xi + \mu) \sinh(\xi - \mu)} \right) \varphi_1(\lambda). \end{aligned} \tag{59}$$

Hence the action of the generating function  $\tau(\lambda)$  on  $\varphi_1(\mu)$  is

$$\begin{aligned} \tau(\lambda)\varphi_1(\mu) = & \chi_1(\lambda, \mu)\varphi_1(\mu) + \frac{2 \sinh^2(2\lambda)}{\sinh(\lambda + \mu) \sinh(\lambda - \mu)} \frac{\sinh(\xi + \mu) \sinh(\xi - \mu)}{\sinh(\xi + \lambda) \sinh(\xi - \lambda)} \times \\ & \times \left( 2\rho(\mu) + \frac{1}{\sinh(\xi + \mu) \sinh(\xi - \mu)} \right) \varphi_1(\lambda), \end{aligned} \tag{60}$$

with

$$\chi_1(\lambda, \mu) = \chi_0(\lambda) - \frac{2 \sinh^2(2\lambda)}{\sinh(\lambda + \mu) \sinh(\lambda - \mu)} \left( 2\rho(\lambda) + \frac{1}{\sinh(\xi + \lambda) \sinh(\xi - \lambda)} \right). \tag{61}$$

We can make the unwanted term in (60) vanish in the standard manner, i.e., by imposing the following Bethe equation:

$$2\rho(\mu) + \frac{1}{\sinh(\xi + \mu) \sinh(\xi - \mu)} = 0. \tag{62}$$

Therefore, we have shown that  $\varphi_1(\mu)$  (56) is indeed a Bethe vector of the generating function  $\tau(\lambda)$  with the eigenvalue  $\chi_1(\lambda, \mu)$  (61).

Next, we seek the Bethe vector  $\varphi_2(\mu_1, \mu_2)$  in the form of the following symmetric function

$$\varphi_2(\mu_1, \mu_2) = f(\mu_1)f(\mu_2)\Omega_+ + c_2^{(1)}(\mu_2; \mu_1)f(\mu_1)\Omega_+ + c_2^{(1)}(\mu_1; \mu_2)f(\mu_2)\Omega_+ + c_2^{(2)}(\mu_1, \mu_2)\Omega_+. \tag{63}$$

We now proceed to show that a proper solution for the scalar coefficients  $c_2^{(1)}(\mu_1; \mu_2)$  and  $c_2^{(2)}(\mu_1, \mu_2)$  is

$$c_2^{(1)}(\mu_1; \mu_2) = \frac{\psi}{\kappa} \left( 1 + \left( e^{-2\xi} - \cosh(2\mu_1) \right) \left( \rho(\mu_1) - \frac{1}{\sinh(\mu_1 - \mu_2) \sinh(\mu_1 + \mu_2)} \right) \right), \tag{64}$$

$$\begin{aligned} c_2^{(2)}(\mu_1, \mu_2) = & \frac{\psi^2}{\kappa^2} \left( 3 + \left( e^{-2\xi} - \cosh(2\mu_1) \right) \left( e^{-2\xi} - \cosh(2\mu_2) \right) \rho(\mu_1)\rho(\mu_2) + \right. \\ & + \frac{2e^{-4\xi} + 2e^{-2\xi} (\cosh(2\mu_1) - 3 \cosh(2\mu_2)) - (3 + \cosh(4\mu_1) - 6 \cosh(2\mu_1) \cosh(2\mu_2))}{4 \sinh(\mu_1 - \mu_2) \sinh(\mu_1 + \mu_2)} \rho(\mu_1) \\ & \left. + \frac{2e^{-4\xi} + 2e^{-2\xi} (\cosh(2\mu_2) - 3 \cosh(2\mu_1)) - (3 + \cosh(4\mu_2) - 6 \cosh(2\mu_2) \cosh(2\mu_1))}{4 \sinh(\mu_2 - \mu_1) \sinh(\mu_2 + \mu_1)} \rho(\mu_2) \right). \end{aligned} \tag{65}$$



The action of  $\tau(\lambda)$  on  $\varphi_2(\mu_1, \mu_2)$  can be written as

$$\begin{aligned} \tau(\lambda)\varphi_2(\mu_1, \mu_2) &= [[\tau(\lambda), f(\mu_1)], f(\mu_2)] \Omega_+ + \left( f(\mu_2) + c_2^{(1)}(\mu_2; \mu_1) \right) [\tau(\lambda), f(\mu_1)] \Omega_+ \\ &+ \left( f(\mu_1) + c_2^{(1)}(\mu_1; \mu_2) \right) [\tau(\lambda), f(\mu_2)] \Omega_+ + \chi_0(\lambda)\varphi_2(\mu_1, \mu_2). \end{aligned} \tag{66}$$

Then, we already have the Expression (59) for the second and third term above, and we use the relations

$$\begin{aligned} \left( f(\mu_1) + c_2^{(1)}(\mu_1; \mu_2) \right) \varphi_1(\mu_2) &= \varphi_2(\mu_1, \mu_2) - \frac{\psi}{\kappa} \frac{e^{-2\xi} - \cosh(2\mu_2)}{\sinh(\mu_1 - \mu_2) \sinh(\mu_1 + \mu_2)} \varphi_1(\mu_1) \\ &- \left( c_2^{(2)}(\mu_1, \mu_2) - c_1^{(1)}(\mu_1)c_1^{(1)}(\mu_2) + \frac{\psi}{\kappa} \frac{(e^{-2\xi} - \cosh(2\mu_1)) c_1^{(1)}(\mu_2) - (e^{-2\xi} - \cosh(2\mu_2)) c_1^{(1)}(\mu_1)}{\sinh(\mu_1 - \mu_2) \sinh(\mu_1 + \mu_2)} \right) \Omega_+, \end{aligned} \tag{67}$$

$$\begin{aligned} \left( f(\mu_1) + c_2^{(1)}(\mu_1; \mu_2) \right) \varphi_1(\lambda) &= \varphi_2(\mu_1, \lambda) - \frac{\psi}{\kappa} \frac{e^{-2\xi} - \cosh(2\lambda)}{\sinh(\lambda - \mu_1) \sinh(\lambda + \mu_1)} \varphi_1(\mu_1) \\ &+ \left( c_2^{(1)}(\mu_1; \mu_2) - c_2^{(1)}(\mu_1; \lambda) \right) \varphi_1(\lambda) \\ &- \left( c_2^{(2)}(\mu_1, \lambda) - c_1^{(1)}(\mu_1)c_1^{(1)}(\lambda) + \frac{\psi}{\kappa} \frac{(e^{-2\xi} - \cosh(2\lambda)) c_1^{(1)}(\mu_1) - (e^{-2\xi} - \cosh(2\mu_1)) c_1^{(1)}(\lambda)}{\sinh(\lambda - \mu_1) \sinh(\lambda + \mu_1)} \right) \Omega_+, \end{aligned} \tag{68}$$

which follow from the definition (63). After expressing appropriately the first term on the right-hand side of (66) and using twice the expression for the action of the commutator of  $\tau(\lambda)$  with the generator  $f(\lambda)$  on the vector  $\Omega_+$  (59) as well as the identities (67) and (68), a straightforward calculation shows that the off-shell action of the generating function  $\tau(\lambda)$  on  $\varphi_2(\mu_1, \mu_2)$  is given by

$$\begin{aligned} \tau(\lambda)\varphi_2(\mu_1, \mu_2) &= \chi_2(\lambda, \mu_1, \mu_2)\varphi_2(\mu_1, \mu_2) + \sum_{i=1}^2 \frac{2 \sinh^2(2\lambda)}{\sinh(\lambda + \mu_i) \sinh(\lambda - \mu_i)} \frac{\sinh(\xi + \mu_i) \sinh(\xi - \mu_i)}{\sinh(\xi + \lambda) \sinh(\xi - \lambda)} \times \\ &\times \left( 2\rho(\mu_i) + \frac{1}{\sinh(\xi + \mu_i) \sinh(\xi - \mu_i)} - \frac{2}{\sinh(\mu_i + \mu_{3-i}) \sinh(\mu_i - \mu_{3-i})} \right) \varphi_2(\lambda, \mu_{3-i}), \end{aligned} \tag{69}$$

with the eigenvalue

$$\begin{aligned} \chi_2(\lambda, \mu_1, \mu_2) &= \chi_0(\lambda) - \sum_{i=1}^2 \frac{2 \sinh^2(2\lambda)}{\sinh(\lambda + \mu_i) \sinh(\lambda - \mu_i)} \times \\ &\times \left( 2\rho(\lambda) + \frac{1}{\sinh(\xi + \lambda) \sinh(\xi - \lambda)} - \frac{1}{\sinh(\lambda + \mu_{3-i}) \sinh(\lambda - \mu_{3-i})} \right). \end{aligned} \tag{70}$$

Again, we can take care of the two unwanted terms in (69) by imposing the Bethe equations on the parameters  $\mu_1$  and  $\mu_2$ :

$$2\rho(\mu_i) + \frac{1}{\sinh(\xi + \mu_i) \sinh(\xi - \mu_i)} - \frac{2}{\sinh(\mu_i + \mu_{3-i}) \sinh(\mu_i - \mu_{3-i})} = 0, \tag{71}$$

with  $i = 1, 2$ . Thus, we have established that  $\varphi_2(\mu_1, \mu_2)$  is the Bethe vector of the generating function of the Gaudin Hamiltonians corresponding to the eigenvalue  $\chi_2(\lambda, \mu_1, \mu_2)$ .

The form of the Bethe vector  $\varphi_3(\mu_1, \mu_2, \mu_3)$  is given explicitly (as a symmetric function of these parameters) in the Appendix B. By a straightforward (but lengthy) computation one can show that the action of the generating function  $\tau(\lambda)$  on  $\varphi_3(\mu_1, \mu_2, \mu_3)$  has the following form:

$$\begin{aligned} \tau(\lambda)\varphi_3(\mu_1, \mu_2, \mu_3) &= \chi_3(\lambda, \mu_1, \mu_2, \mu_3)\varphi_3(\mu_1, \mu_2, \mu_3) \\ &+ \sum_{i=1}^3 \frac{2 \sinh^2(2\lambda)}{\sinh(\lambda + \mu_i) \sinh(\lambda - \mu_i)} \frac{\sinh(\xi + \mu_i) \sinh(\xi - \mu_i)}{\sinh(\xi + \lambda) \sinh(\xi - \lambda)} \times \\ &\times \left( 2\rho(\mu_i) + \frac{1}{\sinh(\xi + \mu_i) \sinh(\xi - \mu_i)} - \sum_{j \neq i}^3 \frac{2}{\sinh(\mu_i + \mu_j) \sinh(\mu_i - \mu_j)} \right) \varphi_3(\lambda, \{\mu_j\}_{j \neq i}), \end{aligned} \quad (72)$$

where the eigenvalue is

$$\begin{aligned} \chi_3(\lambda, \mu_1, \mu_2, \mu_3) &= \chi_0(\lambda) - \sum_{i=1}^3 \frac{2 \sinh^2(2\lambda)}{\sinh(\lambda + \mu_i) \sinh(\lambda - \mu_i)} \times \\ &\times \left( 2\rho(\lambda) + \frac{1}{\sinh(\xi + \lambda) \sinh(\xi - \lambda)} - \sum_{j \neq i}^3 \frac{1}{\sinh(\lambda + \mu_j) \sinh(\lambda - \mu_j)} \right). \end{aligned} \quad (73)$$

The three unwanted terms in (72) vanish upon imposing the following Bethe conditions on the parameters  $\mu_i$ :

$$2\rho(\mu_i) + \frac{1}{\sinh(\xi + \mu_i) \sinh(\xi - \mu_i)} - \sum_{j \neq i}^3 \frac{2}{\sinh(\mu_i + \mu_j) \sinh(\mu_i - \mu_j)} = 0, \quad (74)$$

with  $i = 1, 2, 3$ .

Instead of processing further in a brute-force manner to find the form of  $\varphi_4(\mu_1, \mu_2, \mu_3, \mu_4)$ , it turns out that it is possible to unify the obtained expressions for  $\varphi_1$ ,  $\varphi_2$  and  $\varphi_3$  by introducing a family of operators

$$\begin{aligned} \mathcal{C}_K(\mu) &= f(\mu) + \frac{\psi}{\kappa} \left( (2K - 1) + (e^{-2\xi} - \cosh(2\mu)) h(\mu) \right) + \frac{\psi^2}{\kappa^2} \frac{e^{-\xi}}{2 \sinh(\xi)} \times \\ &\times (e^{-2\xi} + 1 - 2 \cosh(2\mu)) e(\mu), \end{aligned} \quad (75)$$

for any natural number  $K$ . Now, it can be shown by a direct calculation that the Bethe vectors (56), (63) and (A8) can be expressed as

$$\varphi_1(\mu) = \mathcal{C}_1(\mu)\Omega_+, \quad \varphi_2(\mu_1, \mu_2) = \mathcal{C}_1(\mu_1)\mathcal{C}_2(\mu_2)\Omega_+ \quad \text{and} \quad \varphi_3(\mu_1, \mu_2, \mu_3) = \mathcal{C}_1(\mu_1)\mathcal{C}_2(\mu_2)\mathcal{C}_3(\mu_3)\Omega_+. \quad (76)$$

Although in general the operators  $\mathcal{C}_K(\mu)$  (75) do not commute, it is easy to verify that the Bethe vector  $\varphi_2(\mu_1, \mu_2)$  is a symmetric function

$$\varphi_2(\mu_1, \mu_2) = \mathcal{C}_1(\mu_1)\mathcal{C}_2(\mu_2)\Omega_+ = \mathcal{C}_1(\mu_2)\mathcal{C}_2(\mu_1)\Omega_+ = \varphi_2(\mu_2, \mu_1). \quad (77)$$

Analogously, it is straightforward to check that the Bethe vector  $\varphi_3(\mu_1, \mu_2, \mu_3)$  is a symmetric function of its arguments

$$\varphi_3(\mu_1, \mu_2, \mu_3) = \mathcal{C}_1(\mu_1)\mathcal{C}_2(\mu_2)\mathcal{C}_3(\mu_3)\Omega_+ = \mathcal{C}_1(\mu_2)\mathcal{C}_2(\mu_1)\mathcal{C}_3(\mu_3)\Omega_+ = \varphi_3(\mu_2, \mu_1, \mu_3), \quad (78)$$

etc. Moreover using the formulae above (76) for the Bethe vectors it is somewhat simpler to calculate the off-shell action of the generating function. Evidently,

$$[\tau(\lambda), C_1(\mu)] \Omega_+ = [\tau(\lambda), f(\mu)] \Omega_+,$$

and consequently, the action (60) of the generating function  $\tau(\lambda)$  on the Bethe vector  $\varphi_1(\mu)$  follows directly from (59). In order to show (69), we calculate

$$\begin{aligned} & [[\tau(\lambda), C_1(\mu_1)], C_2(\mu_2)] \Omega_+ = \frac{4 \sinh^2(2\lambda)}{\sinh(\lambda + \mu_1) \sinh(\lambda - \mu_1) \sinh(\lambda + \mu_2) \sinh(\lambda - \mu_2)} \varphi_2(\mu_1, \mu_2) \\ & - \sum_{i=1}^2 \frac{2 \sinh^2(2\lambda)}{\sinh(\lambda + \mu_i) \sinh(\lambda - \mu_i)} \frac{\sinh(\xi + \mu_i) \sinh(\xi - \mu_i)}{\sinh(\xi + \lambda) \sinh(\xi - \lambda)} \frac{2}{\sinh(\mu_i + \mu_{3-i}) \sinh(\mu_i - \mu_{3-i})} \varphi_2(\lambda, \mu_{3-i}) \\ & + \frac{\psi}{\kappa} \frac{4 \sinh^2(2\lambda)}{\sinh(\lambda + \mu_1) \sinh(\lambda - \mu_1)} \left( 2\rho(\lambda) + \frac{1}{\sinh(\xi + \lambda) \sinh(\xi - \lambda)} \right) (\varphi_1(\mu_1) - \varphi_1(\mu_2)) \\ & - \frac{\psi}{\kappa} \frac{4 \sinh^2(2\lambda)}{\sinh(\lambda + \mu_1) \sinh(\lambda - \mu_1)} \frac{\sinh(\xi + \mu_1) \sinh(\xi - \mu_1)}{\sinh(\xi + \lambda) \sinh(\xi - \lambda)} \left( 2\rho(\mu_1) + \frac{1}{\sinh(\xi + \mu_1) \sinh(\xi - \mu_1)} \right) \times \quad (79) \\ & \times (\varphi_1(\lambda) - \varphi_1(\mu_2)) \\ & - \frac{\psi}{\kappa} \frac{4 \sinh^2(2\lambda)}{\sinh(\lambda + \mu_2) \sinh(\lambda - \mu_2)} \left( 2\rho(\lambda) + \frac{1}{\sinh(\xi + \lambda) \sinh(\xi - \lambda)} \right) \varphi_1(\mu_1) \\ & + \frac{\psi}{\kappa} \frac{4 \sinh^2(2\lambda)}{\sinh(\lambda + \mu_2) \sinh(\lambda - \mu_2)} \frac{\sinh(\xi + \mu_2) \sinh(\xi - \mu_2)}{\sinh(\xi + \lambda) \sinh(\xi - \lambda)} \left( 2\rho(\mu_2) + \frac{1}{\sinh(\xi + \mu_2) \sinh(\xi - \mu_2)} \right) \varphi_1(\mu_1) \end{aligned}$$

and use (59) appropriately. Finally, the action (72) of the generating function  $\tau(\lambda)$  on the Bethe vector  $\varphi_3(\mu_1, \mu_2, \mu_3)$  can be obtained by expressing  $[[[\tau(\lambda), C_1(\mu_1)], C_2(\mu_2)], C_3(\mu_3)] \Omega_+$  conveniently and using (59) and (79) adequately.

We proceed in a natural way and conjecture that the Bethe vector  $\varphi_4(\mu_1, \dots, \mu_4)$  can be written in the form

$$\varphi_4(\mu_1, \dots, \mu_4) = C_1(\mu_1)C_2(\mu_2)C_3(\mu_3)C_4(\mu_4)\Omega_+. \quad (80)$$

With the aim of calculating the action of the generating function of the Gaudin Hamiltonians on the vector above we calculate  $[[[[\tau(\lambda), C_1(\mu_1)], C_2(\mu_2)], C_3(\mu_3)], C_4(\mu_4)] \Omega_+$ , expressing it appropriately as a linear combination of all the previous Bethe vectors. This formula is very long and cumbersome and for this reason, is not presented in the text. Using this result it is possible to obtain the desired off-shell action in the following form

$$\begin{aligned} & \tau(\lambda) \varphi_4(\mu_1, \mu_2, \mu_3, \mu_4) = \chi_4(\lambda, \mu_1, \mu_2, \mu_3, \mu_4) \varphi_4(\mu_1, \mu_2, \mu_3, \mu_4) \\ & + \sum_{i=1}^4 \frac{2 \sinh^2(2\lambda)}{\sinh(\lambda + \mu_i) \sinh(\lambda - \mu_i)} \frac{\sinh(\xi + \mu_i) \sinh(\xi - \mu_i)}{\sinh(\xi + \lambda) \sinh(\xi - \lambda)} \times \quad (81) \\ & \times \left( 2\rho(\mu_i) + \frac{1}{\sinh(\xi + \mu_i) \sinh(\xi - \mu_i)} - \sum_{j \neq i}^4 \frac{2}{\sinh(\mu_i + \mu_j) \sinh(\mu_i - \mu_j)} \right) \varphi_4(\lambda, \{\mu_j\}_{j \neq i}), \end{aligned}$$

where the eigenvalue is

$$\begin{aligned} & \chi_4(\lambda, \mu_1, \mu_2, \mu_3, \mu_4) = \chi_0(\lambda) - \sum_{i=1}^4 \frac{2 \sinh^2(2\lambda)}{\sinh(\lambda + \mu_i) \sinh(\lambda - \mu_i)} \times \quad (82) \\ & \times \left( 2\rho(\lambda) + \frac{1}{\sinh(\xi + \lambda) \sinh(\xi - \lambda)} - \sum_{j \neq i}^4 \frac{1}{\sinh(\lambda + \mu_j) \sinh(\lambda - \mu_j)} \right). \end{aligned}$$

This result we have confirmed also by computer algorithms for symbolical calculation. Upon putting constrains on parameters  $\mu_i$  in the form of the following Bethe equations:

$$2\rho(\mu_i) + \frac{1}{\sinh(\xi + \mu_i) \sinh(\xi - \mu_i)} - \sum_{j \neq i}^4 \frac{2}{\sinh(\mu_i + \mu_j) \sinh(\mu_i - \mu_j)} = 0, \quad (83)$$

with  $i = 1, 2, 3, 4$ , the four unwanted terms vanish in (81).

We readily proceed to define  $\varphi_M(\mu_1, \mu_2, \dots, \mu_M)$ , for an arbitrary positive integer  $M$ ,

$$\varphi_M(\mu_1, \mu_2, \dots, \mu_M) = \mathcal{C}_1(\mu_1) \mathcal{C}_2(\mu_2) \cdots \mathcal{C}_M(\mu_M) \Omega_+, \quad (84)$$

and the operators  $\mathcal{C}_K(\mu)$  are given in (75). Although the operators  $\mathcal{C}_K(\mu)$  do not commute, the Bethe vector  $\varphi_M(\mu_1, \mu_2, \dots, \mu_M)$  is nonetheless a symmetric function of its arguments, since these operators satisfy the following identity,

$$\mathcal{C}_K(\mu) \mathcal{C}_{K+1}(\tilde{\mu}) - \mathcal{C}_K(\tilde{\mu}) \mathcal{C}_{K+1}(\mu) = 0, \quad (85)$$

for  $K = 1, \dots, M - 1$ . It can be confirmed by explicit calculation that the off-shell action of the generating function  $\tau(\lambda)$  on the Bethe vector  $\varphi_M(\mu_1, \mu_2, \dots, \mu_M)$ , is given by

$$\begin{aligned} \tau(\lambda) \varphi_M(\mu_1, \mu_2, \dots, \mu_M) &= \chi_M(\mu_1, \mu_2, \dots, \mu_M) \varphi_M(\mu_1, \mu_2, \dots, \mu_M) \\ &+ \sum_{i=1}^M \frac{2 \sinh^2(2\lambda)}{\sinh(\lambda + \mu_i) \sinh(\lambda - \mu_i)} \frac{\sinh(\xi + \mu_i) \sinh(\xi - \mu_i)}{\sinh(\xi + \lambda) \sinh(\xi - \lambda)} \times \\ &\times \left( 2\rho(\mu_i) + \frac{1}{\sinh(\xi + \mu_i) \sinh(\xi - \mu_i)} - \sum_{j \neq i}^M \frac{2}{\sinh(\mu_i + \mu_j) \sinh(\mu_i - \mu_j)} \right) \varphi_M(\lambda, \{\mu_j\}_{j \neq i}), \end{aligned} \quad (86)$$

with the eigenvalue

$$\begin{aligned} \chi_M(\mu_1, \mu_2, \dots, \mu_M) &= \chi_0(\lambda) - \sum_{i=1}^M \frac{2 \sinh^2(2\lambda)}{\sinh(\lambda + \mu_i) \sinh(\lambda - \mu_i)} \times \\ &\times \left( 2\rho(\lambda) + \frac{1}{\sinh(\xi + \lambda) \sinh(\xi - \lambda)} - \sum_{j \neq i}^M \frac{1}{\sinh(\lambda + \mu_j) \sinh(\lambda - \mu_j)} \right). \end{aligned} \quad (87)$$

Imposing the following Bethe equations on parameters  $\mu_i$ :

$$2\rho(\mu_i) + \frac{1}{\sinh(\xi + \mu_i) \sinh(\xi - \mu_i)} - \sum_{j \neq i}^M \frac{2}{\sinh(\mu_i + \mu_j) \sinh(\mu_i - \mu_j)} = 0, \quad (88)$$

with  $i = 1, 2, \dots, M$ , results in vanishing of  $M$  unwanted terms in (86).

The obtained formula (86) for the action of the generating function  $\tau(\lambda)$  has a strikingly compact form. This simplicity stems from our suitable definition of the Bethe vector  $\varphi_M(\mu_1, \mu_2, \dots, \mu_M)$  (84) and of the corresponding creation operators  $\mathcal{C}_K(\mu)$  (75). In this sense we have successfully implemented the algebraic Bethe ansatz for the trigonometric Gaudin model, with triangular K-matrix (24). The implementation was based on the non-unitary classical r-matrix (17) and the corresponding linear bracket (19).

#### 4. Conclusions

Our first step was to derive the generating function of the Gaudin Hamiltonians with boundary terms. We followed the approach based on Sklyanin's method in the periodic case, just as we previously

did in the rational case. Having obtained the generating function, we could calculate its residues at poles and find the corresponding Gaudin Hamiltonians with boundary terms.

Our next step was the implementation of the algebraic Bethe ansatz for the trigonometric Gaudin model with triangular reflection matrix (24). To this end we have introduced the non-unitary classical  $r$ -matrix (17), which satisfies the generalized classical Yang-Baxter Equation (18), as well as the modified Lax matrix (16). Together they define the linear bracket (19), which is obviously anti-symmetric and obeys the Jacobi identity. As a consequence, it follows that the entries of the modified Lax matrix generate an infinite dimensional Lie algebra, which is the basis of the open trigonometric Gaudin model. A suitable set of generators (39)–(41) simplifies the commutation relations (42)–(45) and therefore facilitates the algebraic Bethe ansatz. Another crucial observation for the implementation of the algebraic Bethe ansatz was the existence of the so-called pseudo-vacuum or the reference state  $\Omega_+$  (52) (see also (53) and (54)). The simplest way to define the relevant Bethe vectors turned out to be by using the family of the creation operators  $C_K(\mu)$  (75). Obtained Bethe vectors  $\varphi_M(\mu_1, \mu_2, \dots, \mu_M)$  (84) are symmetric functions of their arguments and they result in exceedingly simple and compact form of off-shell action of the generating function. In this sense, we have fully implemented the algebraic Bethe ansatz: we have obtained the spectrum of the generating function and found the corresponding Bethe equations.

Having in mind the already discussed range of potential applications that Gaudin model and its generalizations have in various areas of physics (from condensed matter physics to field theory [2–5]), we believe that the inclusion of nontrivial boundary conditions while retaining the integrability of the model—demonstrated here—also has its share of significance. In this regard, it would be of further considerable interest to establish a relationship between the presented Bethe vectors of the trigonometric Gaudin model and the solutions to the related generalized Knizhnik-Zamolodchikov equations, analogously as we did it for the rational case in [60]. These results will be reported elsewhere. Also, we intend to give a mathematical completion of the work presented here by providing a strict analytical proof (omitted here primarily due to its length) of the general Expression (86) for the off-shell action.

**Author Contributions:** Investigation, N.M. and I.S.; methodology N.M.; software, I.S.; writing—original draft preparation, N.M.; writing—review and editing, I.S. All authors have read and agreed to the published version of the manuscript.

**Funding:** I.S. was supported in part by the Serbian Ministry of Science and Technological Development under grant number ON 171031.

**Conflicts of Interest:** The authors declare no conflict of interest.

## Appendix A. Commutativity of the Generating Function

There are multiple ways to prove the commutation relation (21). Here we will employ the relation of the present Gaudin model with the XXZ Heisenberg spin-chain model with boundary, explored in detail in [53]. Thus, in this appendix, we will extensively reference expressions from that paper.

We will begin by computing the expansion (with respect to the quasi-classical parameter  $\eta$ ) of the monodromy matrix taken from [53]:

$$\begin{aligned}
 T(\lambda) = & \mathbb{1} + \eta L_0(\lambda) + \frac{\eta^2}{2} \mathbb{1}_0 \otimes \sum_{m=1}^N (S_m^3)^2 \\
 & + \frac{\eta^2}{2} \sum_{\substack{n,m=1 \\ n \neq m}}^N \frac{\mathbb{1}_0 \otimes \left( \cosh(\lambda - \alpha_m) \cosh(\lambda - \alpha_n) S_m^3 S_n^3 + \frac{1}{2} (S_m^+ S_n^- + S_m^- S_n^+) \right)}{\sinh(\lambda - \alpha_m) \sinh(\lambda - \alpha_n)} \\
 & + \frac{\eta^2}{2} \sum_{m=1}^N \sum_{n < m}^N \frac{\sigma_0^3 \otimes (S_m^- S_n^+ - S_m^+ S_n^-) + \sigma_0^+ \otimes (\cosh(\lambda - \alpha_m) S_m^3 S_n^- - \cosh(\lambda - \alpha_n) S_m^- S_n^3)}{2 \sinh(\lambda - \alpha_m) \sinh(\lambda - \alpha_n)} \\
 & + \frac{\eta^2}{2} \sum_{m=1}^N \sum_{n < m}^N \frac{\sigma_0^- \otimes (\cosh(\lambda - \alpha_n) S_m^+ S_n^3 - \cosh(\lambda - \alpha_m) S_m^3 S_n^-)}{2 \sinh(\lambda - \alpha_m) \sinh(\lambda - \alpha_n)} \\
 & + \frac{\eta^2}{2} \sum_{m=1}^N \sum_{n > m}^N \frac{\sigma_0^3 \otimes (S_n^- S_m^+ - S_n^+ S_m^-) + \sigma_0^+ \otimes (\cosh(\lambda - \alpha_n) S_n^3 S_m^- - \cosh(\lambda - \alpha_m) S_n^- S_m^3)}{2 \sinh(\lambda - \alpha_n) \sinh(\lambda - \alpha_m)} \\
 & + \frac{\eta^2}{2} \sum_{m=1}^N \sum_{n > m}^N \frac{\sigma_0^- \otimes (\cosh(\lambda - \alpha_m) S_n^+ S_m^3 - \cosh(\lambda - \alpha_n) S_n^3 S_m^-)}{2 \sinh(\lambda - \alpha_n) \sinh(\lambda - \alpha_m)} + \mathcal{O}(\eta^3). \tag{A1}
 \end{aligned}$$

Analogously, it is straightforward to obtain the expansion of the  $\tilde{T}(\lambda)$  monodromy matrix from [53] in the powers the quasi-classical parameter  $\eta$

$$\begin{aligned}
 \tilde{T}(\lambda) = & \mathbb{1} - \eta L_0(-\lambda) + \frac{\eta^2}{2} \sum_{m=1}^N \left( \mathbb{1}_0 \otimes (S_m^3)^2 - \frac{2 \left( \sigma_0^3 \otimes S_m^3 + \frac{1}{2} \cosh(\lambda + \alpha_m) (\sigma_0^+ \otimes S_m^- + \sigma_0^- \otimes S_m^+) \right)}{\sinh^2(\lambda + \alpha_m)} \right) \\
 & + \frac{\eta^2}{2} \sum_{\substack{n,m=1 \\ n \neq m}}^N \frac{\mathbb{1}_0 \otimes \left( \cosh(\lambda + \alpha_m) \cosh(\lambda + \alpha_n) S_m^3 S_n^3 + \frac{1}{2} (S_m^+ S_n^- + S_m^- S_n^+) \right)}{\sinh(\lambda + \alpha_m) \sinh(\lambda + \alpha_n)} \\
 & + \frac{\eta^2}{2} \sum_{m=1}^N \sum_{n < m}^N \frac{\sigma_0^3 \otimes (S_m^- S_n^+ - S_m^+ S_n^-) + \sigma_0^+ \otimes (\cosh(\lambda + \alpha_m) S_m^3 S_n^- - \cosh(\lambda + \alpha_n) S_m^- S_n^3)}{2 \sinh(\lambda + \alpha_m) \sinh(\lambda + \alpha_n)} \\
 & + \frac{\eta^2}{2} \sum_{m=1}^N \sum_{n < m}^N \frac{\sigma_0^- \otimes (\cosh(\lambda - \alpha_n) S_m^+ S_n^3 - \cosh(\lambda + \alpha_m) S_m^3 S_n^-)}{2 \sinh(\lambda + \alpha_m) \sinh(\lambda + \alpha_n)} \\
 & + \frac{\eta^2}{2} \sum_{m=1}^N \sum_{n > m}^N \frac{\sigma_0^3 \otimes (S_n^- S_m^+ - S_n^+ S_m^-) + \sigma_0^+ \otimes (\cosh(\lambda + \alpha_n) S_n^3 S_m^- - \cosh(\lambda + \alpha_m) S_n^- S_m^3)}{2 \sinh(\lambda + \alpha_n) \sinh(\lambda - \alpha_m)} \\
 & + \frac{\eta^2}{2} \sum_{m=1}^N \sum_{n > m}^N \frac{\sigma_0^- \otimes (\cosh(\lambda + \alpha_m) S_n^+ S_m^3 - \cosh(\lambda + \alpha_n) S_n^3 S_m^-)}{2 \sinh(\lambda + \alpha_n) \sinh(\lambda + \alpha_m)} + \mathcal{O}(\eta^3). \tag{A2}
 \end{aligned}$$

Using these formulas, as well as the first three terms in the power series of the K-matrix (13), we can deduce the expansion of the transfer matrix of the chain  $t(\lambda)$  in powers of  $\eta$ . We similarly obtain the expansion of the so-called Sklyanin determinant  $\Delta [T(\lambda)]$  in powers of  $\eta$ . However these formulas



are long and cumbersome, therefore we will not present them here. Instead we will give the expansion of the difference between the transfer matrix of the chain and the Sklyanin determinant:

$$\begin{aligned}
 t(\lambda) - \frac{\Delta[\mathcal{T}(\lambda)]}{\sinh(2\lambda)} &= \frac{1}{2} \text{tr}_0 K_0(\lambda) K_0(-\lambda) + \eta (\text{tr}_0 K'_0(-\lambda) K_0(\lambda) + \text{tr}_{00'} P_{00'}^- K_0(\lambda) r_{00'}(2\lambda) K_{0'}(\lambda)) \\
 &+ \eta^2 (\text{tr}_0 K'_0(-\lambda) \mathcal{L}_0(\lambda) K_0(\lambda) + \text{tr}_{00'} P_{00'}^- (\mathcal{L}_0(\lambda) K_0(\lambda) r_{00'}(2\lambda) K_{0'}(\lambda) + K_0(\lambda) r_{00'}(2\lambda) \mathcal{L}_{0'}(\lambda) K_{0'}(\lambda))) \\
 &- \eta^2 \text{tr}_{00'} P_{00'}^- \mathcal{L}_0(\lambda) K_0(\lambda) \mathcal{L}_{0'}(\lambda) K_{0'}(\lambda) + \frac{\eta^2}{2} \left( \text{tr}_0 K''_0(-\lambda) K_0(\lambda) - \frac{1}{4} \text{tr}_0 K''_0(\lambda) K_0(-\lambda) \right. \\
 &\left. + \frac{1}{2} \text{tr}_{00'} P_{00'}^- K'_0(\lambda) K'_{0'}(\lambda) - \frac{1}{\sinh(2\lambda)} \text{tr}_{00'} P_{00'}^- K_0(\lambda) \partial_\eta^2 R_{00'}(2\lambda) \Big|_{\eta=0} K_{0'}(\lambda) \right) + \mathcal{O}(\eta^3). \quad (\text{A3})
 \end{aligned}$$

Note the explicit appearance of the K-modified Lax matrix (16) in the above result.

Actually, a straightforward calculation shows that the terms in the second line of the expression above vanish

$$\text{tr}_0 K'_0(-\lambda) \mathcal{L}_0(\lambda) K_0(\lambda) + \text{tr}_{00'} P_{00'}^- (\mathcal{L}_0(\lambda) K_0(\lambda) r_{00'}(2\lambda) K_{0'}(\lambda) + K_0(\lambda) r_{00'}(2\lambda) \mathcal{L}_{0'}(\lambda) K_{0'}(\lambda)) = 0. \quad (\text{A4})$$

Also, it is important to notice that using the following identity

$$\mathcal{L}_0(\lambda) K_0(\lambda) - \text{tr}_{0'} (\mathcal{L}_{0'}(\lambda) K_{0'}(\lambda)) \mathbb{1}_0 = K_0(-\lambda) \mathcal{L}_0(\lambda), \quad (\text{A5})$$

the first term in the third line of (A3) can be simplified

$$\text{tr}_0 K_0(-\lambda) \mathcal{L}_0(\lambda) \mathcal{L}_0(\lambda) K_0(\lambda) = \det K_0(\lambda) \text{tr}_0 \mathcal{L}_0^2(\lambda). \quad (\text{A6})$$

Finally, the Expansion (A3) reads

$$\begin{aligned}
 t(\lambda) - \frac{\Delta[\mathcal{T}(\lambda)]}{\sinh(2\lambda)} &= \det K_0(\lambda) + \eta (\text{tr}_0 K'_0(-\lambda) K_0(\lambda) + \text{tr}_{00'} P_{00'}^- K_0(\lambda) r_{00'}(2\lambda) K_{0'}(\lambda)) \\
 &+ \frac{\eta^2}{2} \det K_0(\lambda) \text{tr}_0 \mathcal{L}_0^2(\lambda) + \frac{\eta^2}{2} \left( \text{tr}_0 K''_0(-\lambda) K_0(\lambda) - \frac{1}{4} \text{tr}_0 K''_0(\lambda) K_0(-\lambda) \right. \\
 &\left. + \frac{1}{2} \text{tr}_{00'} P_{00'}^- K'_0(\lambda) K'_{0'}(\lambda) - \frac{1}{\sinh(2\lambda)} \text{tr}_{00'} P_{00'}^- K_0(\lambda) \partial_\eta^2 R_{00'}(2\lambda) \Big|_{\eta=0} K_{0'}(\lambda) \right) + \mathcal{O}(\eta^3). \quad (\text{A7})
 \end{aligned}$$

Since both the transfer matrix  $t(\lambda)$  and the Sklyanin determinant  $\Delta[\mathcal{T}(\lambda)]$  commute (as well as their difference) for different values of the spectral parameter, the result (21) directly follows from the previous relation.

## Appendix B. Bethe Vector $\varphi_3(\mu_1, \mu_2, \mu_3)$

Here we provide explicit formulas of the Bethe vector  $\varphi_3(\mu_1, \mu_2, \mu_3)$ :

$$\begin{aligned}
 \varphi_3(\mu_1, \mu_2, \mu_3) &= f(\mu_1) f(\mu_2) f(\mu_3) \Omega_+ + c_3^{(1)}(\mu_1; \mu_2, \mu_3) f(\mu_2) f(\mu_3) \Omega_+ + c_3^{(1)}(\mu_2; \mu_3, \mu_1) f(\mu_3) f(\mu_1) \Omega_+ \\
 &+ c_3^{(1)}(\mu_3; \mu_1, \mu_2) f(\mu_1) f(\mu_2) \Omega_+ + c_3^{(2)}(\mu_1, \mu_2; \mu_3) f(\mu_3) \Omega_+ + c_3^{(2)}(\mu_2, \mu_3; \mu_1) f(\mu_1) \Omega_+ \\
 &+ c_3^{(2)}(\mu_3, \mu_1; \mu_2) f(\mu_2) \Omega_+ + c_3^{(3)}(\mu_1, \mu_2, \mu_3) \Omega_+, \quad (\text{A8})
 \end{aligned}$$

where the three scalar coefficients above are given by

$$c_3^{(1)}(\mu_1; \mu_2, \mu_3) = \frac{\psi}{\kappa} \left( 1 + \left( \rho(\mu_1) - \frac{1}{\sinh(\mu_1 - \mu_2) \sinh(\mu_1 + \mu_2)} - \frac{1}{\sinh(\mu_1 - \mu_3) \sinh(\mu_1 + \mu_3)} \right) \times \right. \\ \left. \times \left( e^{-2\xi} - \cosh(2\mu_1) \right) \right), \quad (\text{A9})$$

$$c_3^{(2)}(\mu_1, \mu_2; \mu_3) = \frac{\psi^2}{\kappa^2} \left( 3 + \left( e^{-2\xi} - \cosh(2\mu_1) \right) \left( e^{-2\xi} - \cosh(2\mu_2) \right) \times \right. \\ \times \left( \rho(\mu_1) - \frac{1}{\sinh(\mu_1 - \mu_3) \sinh(\mu_1 + \mu_3)} \right) \left( \rho(\mu_2) - \frac{1}{\sinh(\mu_2 - \mu_3) \sinh(\mu_2 + \mu_3)} \right) \\ + \frac{2e^{-4\xi} + 2e^{-2\xi} (\cosh(2\mu_1) - 3 \cosh(2\mu_2)) - (3 + \cosh(4\mu_1) - 6 \cosh(2\mu_1) \cosh(2\mu_2))}{4 \sinh(\mu_1 - \mu_2) \sinh(\mu_1 + \mu_2)} \\ \times \left( \rho(\mu_1) - \frac{1}{\sinh(\mu_1 - \mu_3) \sinh(\mu_1 + \mu_3)} \right) \\ + \frac{2e^{-4\xi} + 2e^{-2\xi} (\cosh(2\mu_2) - 3 \cosh(2\mu_1)) - (3 + \cosh(4\mu_2) - 6 \cosh(2\mu_2) \cosh(2\mu_1))}{4 \sinh(\mu_2 - \mu_1) \sinh(\mu_2 + \mu_1)} \\ \left. \times \left( \rho(\mu_2) - \frac{1}{\sinh(\mu_2 - \mu_3) \sinh(\mu_2 + \mu_3)} \right) \right), \quad (\text{A10})$$

$$c_3^{(3)}(\mu_1, \mu_2, \mu_3) = \frac{\psi^3}{\kappa^3} \left( 15 + \left( e^{-2\xi} - \cosh(2\mu_1) \right) \left( e^{-2\xi} - \cosh(2\mu_2) \right) \left( e^{-2\xi} - \cosh(2\mu_3) \right) \rho(\mu_1) \rho(\mu_2) \rho(\mu_3) \right. \\ + \left( \left( 5 - 2 \coth(\xi) \left( \frac{\sinh^2(\mu_1)}{\sinh(\mu_1 - \mu_3) \sinh(\mu_1 + \mu_3)} + \frac{\sinh^2(\mu_2)}{\sinh(\mu_2 - \mu_3) \sinh(\mu_2 + \mu_3)} \right) \right) \left( e^{-2\xi} - \cosh(2\mu_1) \right) \right. \\ \times \left( e^{-2\xi} - \cosh(2\mu_2) \right) - \frac{e^{-\xi}}{\sinh(\xi)} \left( \frac{\sinh(\xi - \mu_1) \sinh(\xi + \mu_1)}{\sinh(\mu_1 - \mu_3) \sinh(\mu_1 + \mu_3)} \left( e^{-2\xi} + 1 - 2 \cosh(2\mu_1) \right) \times \right. \\ \left. \left. \times \left( e^{-2\xi} - \cosh(2\mu_2) \right) + \frac{\sinh(\xi - \mu_2) \sinh(\xi + \mu_2)}{\sinh(\mu_2 - \mu_3) \sinh(\mu_2 + \mu_3)} \left( e^{-2\xi} - \cosh(2\mu_1) \right) \left( e^{-2\xi} + 1 - 2 \cosh(2\mu_2) \right) \right) \right) \\ \times \rho(\mu_1) \rho(\mu_2) \\ + \left( \left( 5 - 2 \coth(\xi) \left( \frac{\sinh^2(\mu_1)}{\sinh(\mu_1 - \mu_2) \sinh(\mu_1 + \mu_2)} + \frac{\sinh^2(\mu_3)}{\sinh(\mu_3 - \mu_2) \sinh(\mu_3 + \mu_2)} \right) \right) \left( e^{-2\xi} - \cosh(2\mu_1) \right) \right. \\ \times \left( e^{-2\xi} - \cosh(2\mu_3) \right) - \frac{e^{-\xi}}{\sinh(\xi)} \left( \frac{\sinh(\xi - \mu_1) \sinh(\xi + \mu_1)}{\sinh(\mu_1 - \mu_2) \sinh(\mu_1 + \mu_2)} \left( e^{-2\xi} + 1 - 2 \cosh(2\mu_1) \right) \times \right. \\ \left. \left. \times \left( e^{-2\xi} - \cosh(2\mu_3) \right) + \frac{\sinh(\xi - \mu_3) \sinh(\xi + \mu_3)}{\sinh(\mu_3 - \mu_2) \sinh(\mu_3 + \mu_2)} \left( e^{-2\xi} - \cosh(2\mu_1) \right) \left( e^{-2\xi} + 1 - 2 \cosh(2\mu_3) \right) \right) \right) \\ \left. \times \rho(\mu_1) \rho(\mu_3) \right)$$

$$\begin{aligned}
& + \left( \left( 5 - 2 \coth(\xi) \left( \frac{\sinh^2(\mu_2)}{\sinh(\mu_2 - \mu_1) \sinh(\mu_2 + \mu_1)} + \frac{\sinh^2(\mu_3)}{\sinh(\mu_3 - \mu_1) \sinh(\mu_3 + \mu_1)} \right) \right) \left( e^{-2\xi} - \cosh(2\mu_2) \right) \right. \\
& \times \left( e^{-2\xi} - \cosh(2\mu_3) \right) - \frac{e^{-\xi}}{\sinh(\xi)} \left( \frac{\sinh(\xi - \mu_2) \sinh(\xi + \mu_2)}{\sinh(\mu_2 - \mu_1) \sinh(\mu_2 + \mu_1)} \left( e^{-2\xi} + 1 - 2 \cosh(2\mu_2) \right) \times \right. \\
& \times \left. \left. \left( e^{-2\xi} - \cosh(2\mu_3) \right) + \frac{\sinh(\xi - \mu_3) \sinh(\xi + \mu_3)}{\sinh(\mu_3 - \mu_1) \sinh(\mu_3 + \mu_1)} \left( e^{-2\xi} - \cosh(2\mu_2) \right) \left( e^{-2\xi} + 1 - 2 \cosh(2\mu_3) \right) \right) \right) \\
& \times \rho(\mu_2) \rho(\mu_3) \\
& + \left( 8e^{-6\xi} + 4e^{-4\xi} (4 \cosh(2\mu_1) - 5 (\cosh(2\mu_2) + \cosh(2\mu_3))) + 2e^{-2\xi} (-5 + 7 \cosh(4\mu_1) + 30 \cosh(2\mu_2) \times \right. \\
& \times \cosh(2\mu_3) - 10 \cosh(2\mu_1) (\cosh(2\mu_2) + \cosh(2\mu_3))) - 3 \cosh(6\mu_1) + 10 (3 + \cosh(4\mu_1)) \times \\
& \times (\cosh(2\mu_2) + \cosh(2\mu_3)) - 5 \cosh(2\mu_1) (5 + 12 \cosh(2\mu_2) \cosh(2\mu_3)) \left. \right) \times \\
& \times \frac{\rho(\mu_1)}{16 \sinh(\mu_1 - \mu_2) \sinh(\mu_1 + \mu_2) \sinh(\mu_1 - \mu_3) \sinh(\mu_1 + \mu_3)} \\
& + \left( 8e^{-6\xi} + 4e^{-4\xi} (4 \cosh(2\mu_2) - 5 (\cosh(2\mu_1) + \cosh(2\mu_3))) + 2e^{-2\xi} (-5 + 7 \cosh(4\mu_2) + 30 \cosh(2\mu_1) \times \right. \\
& \times \cosh(2\mu_3) - 10 \cosh(2\mu_2) (\cosh(2\mu_1) + \cosh(2\mu_3))) - 3 \cosh(6\mu_2) + 10 (3 + \cosh(4\mu_2)) \times \\
& \times (\cosh(2\mu_1) + \cosh(2\mu_3)) - 5 \cosh(2\mu_2) (5 + 12 \cosh(2\mu_1) \cosh(2\mu_3)) \left. \right) \times \\
& \times \frac{\rho(\mu_2)}{16 \sinh(\mu_2 - \mu_1) \sinh(\mu_2 + \mu_1) \sinh(\mu_2 - \mu_3) \sinh(\mu_2 + \mu_3)} \\
& + \left( 8e^{-6\xi} + 4e^{-4\xi} (4 \cosh(2\mu_3) - 5 (\cosh(2\mu_1) + \cosh(2\mu_2))) + 2e^{-2\xi} (-5 + 7 \cosh(4\mu_3) + 30 \cosh(2\mu_1) \times \right. \\
& \times \cosh(2\mu_2) - 10 \cosh(2\mu_3) (\cosh(2\mu_1) + \cosh(2\mu_2))) - 3 \cosh(6\mu_3) + 10 (3 + \cosh(4\mu_3)) \times \\
& \times (\cosh(2\mu_1) + \cosh(2\mu_2)) - 5 \cosh(2\mu_3) (5 + 12 \cosh(2\mu_1) \cosh(2\mu_2)) \left. \right) \times \\
& \times \frac{\rho(\mu_3)}{16 \sinh(\mu_3 - \mu_1) \sinh(\mu_3 + \mu_1) \sinh(\mu_3 - \mu_2) \sinh(\mu_3 + \mu_2)} \tag{A11}
\end{aligned}$$

## References

- Gaudin, M. Diagonalisation d'une classe d'hamiltoniens de spin. *J. Phys.* **1976**, *37*, 1087–1098. [\[CrossRef\]](#)
- Ortiz, G.; Somma, R.; Dukelsky, J.; Rombouts, S. Exactly-solvable models derived from a generalized Gaudin algebra. *Nuclear Phys. B* **2005**, *707*, 421–457. [\[CrossRef\]](#)
- Feigin, B.; Frenkel, E.; Reshetikhin, N. Gaudin model, Bethe ansatz and correlation functions at the critical level. *Commun. Math. Phys.* **1994**, *166*, 27–62. [\[CrossRef\]](#)
- Mironov, A.; Morozov, A.; Runov, B.; Zenkevich, Y.; Zotov, A. Spectral Duality between Heisenberg Chain and Gaudin Model. *Lett. Math. Phys.* **2013**, *103*, 299–329. [\[CrossRef\]](#)
- Delduc, F.; Lacroix, S.; Magro, M.; Vicedo, B. Assembling integrable sigma-models as affine Gaudin models. *J. High Energy Phys.* **2019**, *2019*, 17. [\[CrossRef\]](#)
- Gaudin, M. *La Fonction D'onde de Bethe*; Masson: Paris, France, 1983.
- Gaudin, M. *The Bethe Wavefunction*; Cambridge University Press: Cambridge, UK, 2014.
- Takhtajan, L.A.; Faddeev, L.D. The quantum method for the inverse problem and the XYZ Heisenberg model. *Uspekhi Mat. Nauk* **1979**, *34*, 13–63; translation in *Russ. Math. Surv.* **1979**, *34*, 11–68. (In Russian) [\[CrossRef\]](#)
- Kulish, P.P.; Sklyanin, E.K. Quantum spectral transform method. Recent developments. *Lect. Notes Phys.* **1982**, *151*, 61–119.
- Sklyanin, E.K. Separation of variables in the Gaudin model. *Zap. Nauchn. Sem. Leningrad. Otdel. Mat. Inst. Steklov. (LOMI)* **1987**, *164*, 151–169; translation in *J. Soviet Math.* **1989**, *47*, 2473–2488. [\[CrossRef\]](#)
- Sklyanin, E.K.; Takebe, T. Algebraic Bethe ansatz for the XYZ Gaudin model. *Phys. Lett. A* **1996**, *219*, 217–225. [\[CrossRef\]](#)

12. Semenov-Tian-Shansky, M.A. Quantum and classical integrable systems. *Integr. Nonlinear Syst.* **1997**, *495*, 314–377.
13. Jurčo, B. Classical Yang-Baxter equations and quantum integrable systems. *J. Math. Phys.* **1989**, *30*, 1289–1293. [[CrossRef](#)]
14. Jurčo, B. Classical Yang-Baxter equations and quantum integrable systems (Gaudin models). *Lect. Notes Phys.* **1990**, *370*, 219–227.
15. Babujian, H.M.; Flume, R. Off-shell Bethe ansatz equation for Gaudin magnets and solutions of Knizhnik-Zamolodchikov equations. *Mod. Phys. Lett. A* **1994**, *9*, 2029–2039. [[CrossRef](#)]
16. Reshetikhin, N.; Varchenko, A. Quasiclassical asymptotics of solutions to the KZ equations. In *Geometry, Topology and Physics. Conf. Proc. Lecture Notes Geom. Topology IV*; Internat. Press: Cambridge, MA, USA, 1995; pp. 293–322.
17. Wagner, F.; Macfarlane, A.J. Solvable Gaudin models for higher rank symplectic algebras. Quantum groups and integrable systems (Prague, 2000). *Czechoslovak J. Phys.* **2000**, *50*, 1371–1377. [[CrossRef](#)]
18. Brzezinski, T.; Macfarlane, A.J. On integrable models related to the  $osp(1,2)$  Gaudin algebra. *J. Math. Phys.* **1994**, *35*, 3261–3272. [[CrossRef](#)]
19. Kulish, P.P.; Manojlović, N. Creation operators and Bethe vectors of the  $osp(1|2)$  Gaudin model. *J. Math. Phys.* **2001**, *42*, 4757–4778. [[CrossRef](#)]
20. Kulish, P.P.; Manojlović, N. Trigonometric  $osp(1|2)$  Gaudin model. *J. Math. Phys.* **2003**, *44*, 676–700. [[CrossRef](#)]
21. Lima-Santos, A.; Utiel, W. Off-shell Bethe ansatz equation for  $osp(2|1)$  Gaudin magnets. *Nucl. Phys. B* **2001**, *600*, 512–530. [[CrossRef](#)]
22. Kurak, V.; Lima-Santos, A.  $sl(2|1)^{(2)}$  Gaudin magnet and its associated Knizhnik-Zamolodchikov equation. *Nuclear Phys. B* **2004**, *701*, 497–515. [[CrossRef](#)]
23. Hikami, K.; Kulish, P.P.; Wadati, M. Integrable Spin Systems with Long-Range Interaction. *Chaos Solitons Fractals* **1992**, *2*, 543–550. [[CrossRef](#)]
24. Hikami, K.; Kulish, P.P.; Wadati, M. Construction of Integrable Spin Systems with Long-Range Interaction. *J. Phys. Soc. Jpn.* **1992**, *61*, 3071–3076. [[CrossRef](#)]
25. Hikami, K. Gaudin magnet with boundary and generalized Knizhnik-Zamolodchikov equation. *J. Phys. A Math. Gen.* **1995**, *28*, 4997–5007. [[CrossRef](#)]
26. Lima-Santos, A. The  $sl(2|1)^{(2)}$  Gaudin magnet with diagonal boundary terms. *J. Stat. Mech.* **2009**. [[CrossRef](#)]
27. Yang, W.L.; Sasaki, R.; Zhang, Y.Z.  $\mathbb{Z}_n$  elliptic Gaudin model with open boundaries. *J. High Energy Phys.* **2004**, *9*, 046. [[CrossRef](#)]
28. Yang, W.L.; Sasaki, R.; Zhang, Y.Z.  $A_{n-1}$  Gaudin model with open boundaries. *Nuclear Phys. B* **2005**, *729*, 594–610. [[CrossRef](#)]
29. Hao, K.; Yang, W.-L.; Fan, H.; Liu, S.Y.; Wu, K.; Yang, Z.Y.; Zhang, Y.Z. Determinant representations for scalar products of the XXZ Gaudin model with general boundary terms. *Nuclear Phys. B* **2012**, *862*, 835–849. [[CrossRef](#)]
30. Sklyanin, E.K. Boundary conditions for integrable equations. *Funktsional. Anal. Prilozhen.* **1987**, *21*, 86–87; translation in *Funct. Anal. Its Appl.* **1987**, *21*, 164–166. (In Russian) [[CrossRef](#)]
31. Sklyanin, E.K. Boundary conditions for integrable systems. In Proceedings of the VIIIth International Congress on Mathematical Physics, Marseille, France, 16–25 July 1986; World Sci. Publishing: Singapore, 1987; pp. 402–408.
32. Sklyanin, E.K. Boundary conditions for integrable quantum systems. *J. Phys. A Math. Gen.* **1988**, *21*, 2375–2389. [[CrossRef](#)]
33. Skrypnyk, T. Non-skew-symmetric classical r-matrix, algebraic Bethe ansatz, and Bardeen-Cooper-Schrieffer-type integrable systems. *J. Math. Phys.* **2009**, *50*, 033540. [[CrossRef](#)]
34. Skrypnyk, T. “ $\mathbb{Z}_2$ -graded” Gaudin models and analytical Bethe ansatz. *Nuclear Phys. B* **2013**, *870*, 495–529. [[CrossRef](#)]
35. Cirilo António, N.; Manojlović, N.; Nagy, Z. Trigonometric  $sl(2)$  Gaudin model with boundary terms. *Rev. Math. Phys.* **2013**, *25*, 1343004. [[CrossRef](#)]
36. Cao, J.; Lin, H.; Shi, K.; Wang, Y. Exact solutions and elementary excitations in the XXZ spin chain with unparallel boundary fields. *Nucl. Phys. B* **2003**, *663*, 487–519. [[CrossRef](#)]

37. Nepomechie, R.I. Bethe ansatz solution of the open XXZ chain with nondiagonal boundary terms. *J. Phys. A* **2004**, *37*, 433–440. [[CrossRef](#)]
38. Arnaudon, D.; Doikou, A.; Frappat, L.; Ragoucy, E.; Crampé, N. Analytical Bethe ansatz in  $gl(N)$  spin chains. *Czechoslovak J. Phys.* **2006**, *56*, 141–148. [[CrossRef](#)]
39. Melo, C.S.; Ribeiro, G.A.P.; Martins, M.J. Bethe ansatz for the XXX-S chain with non-diagonal open boundaries. *Nuclear Phys. B* **2005**, *711*, 565–603. [[CrossRef](#)]
40. Frappat, L.; Nepomechie, R.I.; Ragoucy, E. A complete Bethe ansatz solution for the open spin-s XXZ chain with general integrable boundary terms. *J. Stat. Mech.* **2007**, *2007*, P09009. [[CrossRef](#)]
41. Cao, J.; Yang, W.-L.; Shi, K.; Wang, Y. Off-diagonal Bethe ansatz solution of the XXX spin chain with arbitrary boundary conditions. *Nuclear Phys. B* **2013**, *875*, 152–165. [[CrossRef](#)]
42. Cao, J.; Yang, W.-L.; Shi, K.; Wang, Y. Off-diagonal Bethe ansatz solutions of the anisotropic spin-1/2 chains with arbitrary boundary fields. *Nuclear Phys. B* **2013**, *877*, 152–175. [[CrossRef](#)]
43. Ragoucy, E. Coordinate Bethe ansätze for non-diagonal boundaries. *Rev. Math. Phys.* **2013**, *25*, 1343007. [[CrossRef](#)]
44. Belliard, S.; Crampé, N.; Ragoucy, E. Algebraic Bethe ansatz for open XXX model with triangular boundary matrices. *Lett. Math. Phys.* **2013**, *103*, 493–506. [[CrossRef](#)]
45. Belliard, S.; Crampé, N. Heisenberg XXX model with general boundaries: Eigenvectors from algebraic Bethe ansatz. *SIGMA Symm. Integr. Geom. Methods Appl.* **2013**, *9*, 072. [[CrossRef](#)]
46. Pimenta, R.A.; Lima-Santos, A. Algebraic Bethe ansatz for the six vertex model with upper triangular K-matrices. *J. Phys. A* **2013**, *46*, 455002. [[CrossRef](#)]
47. Belliard, S. Modified algebraic Bethe ansatz for XXZ chain on the segment—I: Triangular cases. *Nuclear Phys. B* **2015**, *892*, 1–20. [[CrossRef](#)]
48. Belliard, S.; Pimenta, R.A. Modified algebraic Bethe ansatz for XXZ chain on the segment—II—General cases. *Nuclear Phys. B* **2015**, *894*, 527–552. [[CrossRef](#)]
49. Avan, J.; Belliard, S.; Grosjean, N.; Pimenta, R.A. Modified algebraic Bethe ansatz for XXZ chain on the segment—III—Proof. *Nuclear Phys. B* **2015**, *899*, 229–246. [[CrossRef](#)]
50. Gainutdinov, A.M.; Nepomechie, R.I. Algebraic Bethe ansatz for the quantum group invariant open XXZ chain at roots of unity. *Nuclear Phys. B* **2016**, *909*, 796–839. [[CrossRef](#)]
51. Zhang, X.; Li, Y.-Y.; Cao, J.; Yang, W.-L.; Shi, K.; Wang, Y. Bethe states of the XXZ spin- $\frac{1}{2}$  chain with arbitrary boundary fields. *Nuclear Phys. B* **2015**, *893*, 70–88. [[CrossRef](#)]
52. Cirilo António, N.; Manojlović, N.; Salom, I. Algebraic Bethe ansatz for the XXX chain with triangular boundaries and Gaudin model. *Nuclear Phys. B* **2014**, *889*, 87–108. [[CrossRef](#)]
53. Manojlović, N.; Salom, I. Algebraic Bethe ansatz for the XXZ Heisenberg spin chain with triangular boundaries and the corresponding Gaudin model. *Nuclear Phys. B* **2017**, *923*, 73–106. [[CrossRef](#)]
54. Lukyanenko, I.; Isaac, P.S.; Links, J. On the boundaries of quantum integrability for the spin-1/2 Richardson-Gaudin system. *Nuclear Phys. B* **2014**, *886*, 364–398. [[CrossRef](#)]
55. Cirilo António, N.; Manojlović, N.; Ragoucy, E.; Salom, I. Algebraic Bethe ansatz for the  $sl(2)$  Gaudin model with boundary. *Nuclear Phys. B* **2015**, *893*, 305–331. [[CrossRef](#)]
56. Hao, K.; Cao, J.; Yang, T.; Yang, W.-L. Exact solution of the XXX Gaudin model with the generic open boundaries. *Ann. Phys.* **2015**, *354*, 401–408. [[CrossRef](#)]
57. Manojlović, N.; Nagy, Z.; Salom, I. Derivation of the trigonometric Gaudin Hamiltonians. In Proceedings of the 8th Mathematical Physics Meeting: Summer School and Conference on Modern Mathematical Physics, Belgrade, Serbia, 24–31 August 2014; Institute of Physics: Belgrade, Serbia, 2015; pp. 127–135.
58. De Vega, H.J.; González Ruiz, A. Boundary K-matrices for the XYZ, XXZ, XXX spin chains. *J. Phys. A Math. Gen.* **1994**, *27*, 6129–6137. [[CrossRef](#)]
59. Ghoshal, S.; Zamolodchikov, A.B. Boundary S-matrix and boundary state in two-dimensional integrable quantum field theory. *Int. J. Modern Phys. A* **1994**, *9*, 3841–3885; Errata in **1994**, *9*, 4353. [[CrossRef](#)]
60. Salom, I.; Manojlović, N.; Cirilo António, N. Generalized  $sl(2)$  Gaudin algebra and corresponding Knizhnik-Zamolodchikov equation. *Nuclear Phys. B* **2019**, *939*, 358–371. [[CrossRef](#)]





## Systems Biology Approaches to Understanding COVID-19 Spread in the Population

Sofija Marković, Igor Salom, and Marko Djordjevic

### Abstract

In essence, the COVID-19 pandemic can be regarded as a systems biology problem, with the entire world as the system, and the human population as the element transitioning from one state to another with certain transition rates. While capturing all the relevant features of such a complex system is hardly possible, compartmental epidemiological models can be used as an appropriate simplification to model the system's dynamics and infer its important characteristics, such as basic and effective reproductive numbers of the virus. These measures can later be used as response variables in feature selection methods to uncover the main factors contributing to disease transmissibility. We here demonstrate that a combination of dynamic modeling and machine learning approaches can represent a powerful tool in understanding the spread, not only of COVID-19, but of any infectious disease of epidemiological proportions.

**Key words** COVID-19 transmissibility, Epidemics dynamics, Compartmental epidemiological models, Regularized regressions, Machine learning, Feature selection methods

---

## 1 Introduction

### 1.1 *Pandemics from the Systems Biology Perspective*

Similarly to many scientific disciplines, systems biology was urged to adapt to the research of COVID-19, which practically overnight became the priority of almost the entire scientific community. It was soon apparent that many approaches used in systems biology for exploring molecular-level phenomena can be employed in the population-level epidemiological study. In essence, the pandemic represents a systems biology problem, where the entire world is the system, with the human population as the elements transitioning from one state to another. Compartmental models, similar to those used to describe transport dynamics and biochemical reactions in cellular compartments [1], can be utilized to analyze epidemics' dynamics. Here, instead of the molecular species, the transition of individuals from one epidemiological population class to another is observed over time [2]. During the pandemic, the population size



in each compartment is relatively large. Thus, the entire epidemic can be considered a deterministic process, where the system's previous state and the model constraints determine the state of the population at any given time.

Epidemiological models of this type were first described in 1927 by Kermack and McKendrick [3]. In their SIR (Susceptible-Infected-Recovered) model, the entire population is divided into susceptible, infected, and recovered classes (i.e., compartments), with certain transition rates between them. Numerous other epidemiological models of a similar type have been proposed since then, most notably the SEIR model [4], aiming to better describe the dynamics of different infectious diseases. In ref [5], the modified SEIR model was used as a starting point for modeling the dynamics of COVID-19 spread during the first wave of the pandemic. To model the later stages of the infection outburst, when the disease mitigation measures, such as strong social distancing, already took effect, a more complex model is needed. In ref [2, 6], the SPEIRD model was introduced to capture the dynamic of the later epidemiological stages and, subsequently, used to analytically and numerically explain different (almost universally observed) epidemic growth regimes.

A parallel can be drawn between the modeling of virus transmission in the population and gene expression dynamics [2, 7]. While the dynamics of gene expression is influenced by both the global physiological state of the cell, driven by the changing rate of cell growth [8], and the complex (nonlinear) transcription regulation [9], the virus transmissibility also depends on the combination of the inherent properties of the virus in the given environment, represented by its basic reproduction number ( $R_0$ ), and the complex effects of epidemiological measures introduced by each country. That is, from the systems biology point of view, the classical models for epidemic dynamics (such as SIR and SEIR) are an example of the mass action law kinetics [10]. However, COVID-19 also brought additional challenges, such as unprecedented control measures, which are analogous to the control mechanisms at the cellular level—a widely studied problem in systems biology, which is addressed using methods ranging from nonlinear differential equations to network theory. Therefore, it is unsurprising that many system biologists have used different approaches to tackle this problem [11–16]. For example, in ref [12], agent-based simulation was combined with the SEIR model to mimic the structure of society and social contacts in the context of the pandemic to determine the most efficient epidemic mitigation strategies. On the other hand, in ref [13], the authors employ a non-Markovian age-of-infection model to estimate the effective reproduction number of the virus.

## **1.2 Challenges in Uncovering the Main Transmissibility Drivers of COVID-19**

In the context of the ongoing COVID-19 pandemic, besides estimating the basic reproduction number of the virus in the given country, it is crucial to understand the observed differences in transmissibility between different countries. Unmasking the main environmental, demographic, and health-related factors responsible for the severe outbreaks in some countries and regions worldwide was one of the highest priorities in early COVID-19 epidemiological studies. That is, although in the first wave of the pandemic, only one (initial Wuhan) strain was present, significant discrepancies in viral transmissibility (and severity) were observed in different countries, with  $R_0$  ranging from 1.5 to 5.5 [5].

In the absence of previous knowledge of the environmental and social factors influencing the transmissibility of a novel disease, a large set of potential transmissibility drivers for a relatively small number of countries for which the relevant data is available needs to be considered. The matter is further complicated by the often-high correlation of these predictors and their potentially nonlinear relationship with the response variable. This makes feature selection a highly nontrivial problem whose solution goes beyond standard statistical techniques and allows for more advanced machine-learning approaches. This is also analogous to many machine-learning applications in molecular systems biology and bioinformatics [17–19]. There, one often has to understand the influence of many heterogeneous factors, which are hard to account for by mechanistic modeling alone, so the complementarity of mechanistic dynamical models (deterministic or stochastic) and machine learning is increasingly emphasized [20–22]. We proceed similarly in epidemics modeling and data analysis, starting with methods based on dynamical compartmental models and proceeding to machine learning methods.

## **1.3 Definition of an Appropriate Transmissibility Measure**

The first step in studying disease dynamics in the population is defining an appropriate disease transmissibility measure. This measure must meet several criteria before being implemented as the response variable in feature selection methods. Although the most practical, using the number of registered disease cases is inappropriate when examining an epidemic of global proportions, such as COVID-19, due to several reasons, such as being sensitive to differences in testing policies and introduced epidemiological measures between countries. A way to overcome these difficulties is using the basic reproduction number of the virus, extracted from the dynamical model of the exponential phase of the epidemics, as a measure of disease transmissibility [5].  $R_0$ , defined in this way, represents the number of secondarily infected people per infected individual in a fully susceptible population, and is equal to the infection rate and recovery rate ratio. Infectious diseases with  $R_0 > 1$  can spread through the population and have epidemiological potential. Without any epidemiological measures, an initial

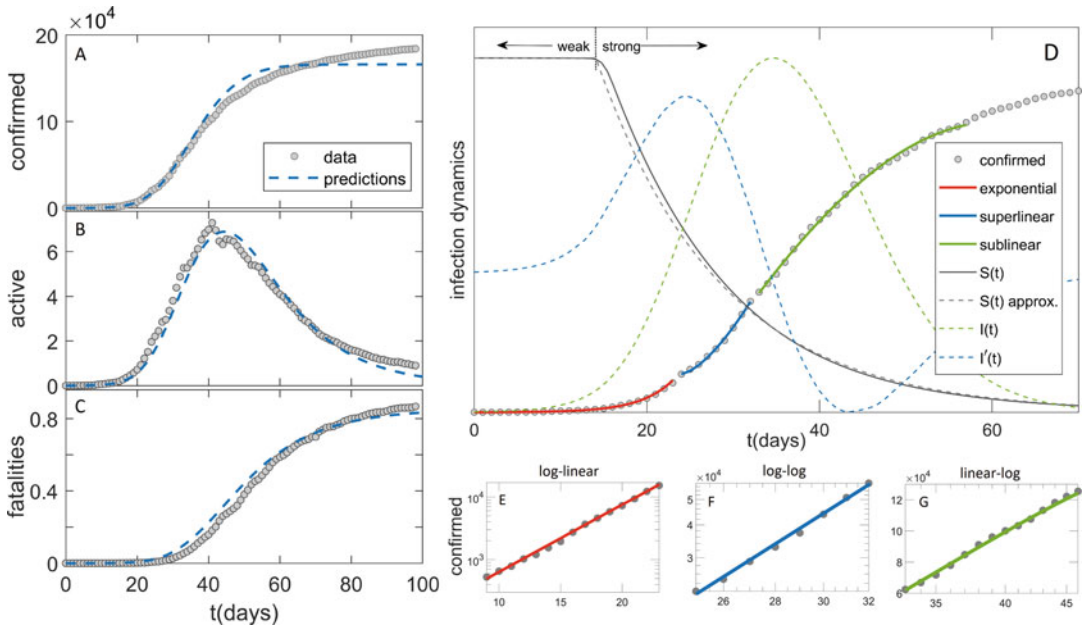


**Fig. 1** Growth regimes of COVID-19. SPEIRD model predictions are compared with the data for (a) confirmed cases, (b) active cases, and (c) fatalities; (d) Exponential, superlinear, and sublinear growth regimes are represented by red, blue, and green curves, respectively, with arrows representing a transition from “weak” to “strong” social distancing measures. The confirmed (i.e., detected) case count and the corresponding fit are represented on (e) log-linear, (f) log-log, and (g) linear-log scale for the corresponding regime. (Figure reproduced from ref [7])

increase in the number of cases of such diseases is exponential due to the large number of susceptible individuals at the beginning of the epidemic. Although  $R_0$  is the inherent characteristic of the virus, it is affected by environmental conditions and hence varies in different countries. During the later stages of the pandemic, when epidemiological measures have been introduced and not all population members are susceptible to the disease,  $R_0$  is no longer an appropriate measure of disease transmissibility. Instead, the effective reproduction number,  $R_e$ , is used.

**1.4 Growth Regime of COVID-19**

Typically, the time course of the COVID-19 epidemic can be divided into three regimes: exponential, superlinear, and sublinear (see Fig. 1). During the initial exponential phase, no measures have been implemented, and the number of cases grows exponentially. In countries with a clear exponential growth regime,  $R_0$  can be calculated from the SEIR-based compartmental epidemiological model presented in Fig. 2 [5]. This model is a simplification of a more complex SPEIRD model, introduced in ref [2] and suitable for dynamic modeling of the early epidemiological stages when the following assumptions are met: (i) No epidemiological measures have been introduced; (ii) The entire population is susceptible to

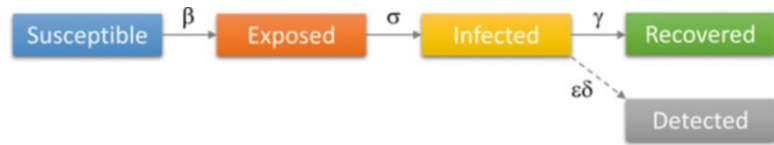


**Fig. 2** SEIR-based compartmental model of the early stages of the epidemic. Each block represents an epidemiological compartment with a suitable label, while arrows represent possible transitions from one compartment to another, which occurs at the rates denoted above the arrows,  $\beta$  – transmission rate,  $\sigma$  – incubation rate,  $\gamma$  – recovery rate,  $\epsilon$  – detection efficiency,  $\delta$  – detection rate. (Figure reproduced from ref [5])

the disease (there is no immunity); (iii) Only a single strain of the virus is present. Introducing epidemiological measures causes a transition from exponential to subexponential (superlinear and sublinear) growth. This typically occurs 10–14 days after introducing the measures (*see* Fig. 1d). The sublinear and superlinear growth regimes have been analyzed in more detail in ref [6, 7].

## 2 Methods

### 2.1 A Simplified Compartmental Model of the Epidemic and Inference of $R_0$

During the exponential regime, the compartmental model of COVID-19 progression in the population can be simplified to the SEIR-based model [5] presented in Fig. 2. In this model, the entire population is divided into five compartments: Susceptible ( $S$ ), Exposed ( $E$ ), Infected ( $I$ ), Recovered ( $R$ ), and, as an addition to the SEIR model, Detected ( $D$ ). The transition between the compartments is denoted by arrows, with the appropriate transition rates above them. At the initial stage of the epidemic, an entire population is treated as susceptible to the disease. With the infection rate  $\beta$ , a certain proportion of the susceptible population is exposed to the disease, moving to the Exposed compartment. After a latent period, the exposed individuals become infected (at which point they also become infectious). Infected can either recover without detection, moving to the Recovered compartment, or are diagnosed with COVID-19 at a certain detection rate, which depends on the detection efficiency and time needed for diagnostics. At this point, they transition to the detected compartment. In our model, which studies the brief initial infection period, all the described rates are considered constant.

Mathematically, the described model can be represented by a system of ordinary differential equations:

$$\begin{aligned}\frac{dS}{dt} &= -\beta \cdot I \cdot \frac{S}{N}, \\ \frac{dE}{dt} &= \beta \cdot I \cdot \frac{S}{N} - \sigma \cdot E,\end{aligned}$$

$$\frac{dI}{dt} = \sigma \cdot E - \gamma \cdot I - \varepsilon \cdot \delta \cdot I,$$

$$\frac{dR}{dt} = \gamma \cdot I,$$

$$\frac{dD}{dt} = \varepsilon \cdot \delta \cdot I,$$

where capital letters  $S$ ,  $E$ ,  $I$ ,  $R$ , and  $D$  represent the number of people in the corresponding compartment,  $N$  denotes population size,  $\beta$  denotes infection rate,  $\sigma$  denotes incubation rate, that is, the inverse value of the average latent period,  $\gamma$  denotes the recovery rate, defined as the inverse value of the infectious period, and  $\varepsilon$  and  $\delta$  represent the detected fraction of infected and reciprocal value of the time needed for diagnosis, respectively.

The cumulative number of detected disease cases,  $D$ , is a measurable quantity, with the data publicly available for most countries [23]. In ref [5], we showed that the basic reproduction number of the virus, defined as the infection rate multiplied by the infectious period ( $R_0 = \frac{\beta}{\gamma}$ ), can be calculated from the slope of the  $\log(D(t))$  curve during the exponential growth period, by applying the formula:

$$R_0 = 1 + \frac{\lambda_+(\gamma + \sigma) + \lambda_+^2}{\gamma \cdot \sigma}$$

Here  $\lambda_+$  is the slope of the  $\log(D(t))$  function, and  $\gamma$  and  $\sigma$  are approximated to  $1/4 \text{ day}^{-1}$  and  $1/3 \text{ day}^{-1}$ , respectively, according to the findings from the literature [14].

The basic reproduction number of the virus represents the mean number of secondarily infected individuals by one infected individual in a completely susceptible population, and with the absence of epidemic mitigation measures. It depends on the biology of the virus, environmental factors, and socio-demographic characteristics of the population, but it is independent of the testing policies.

Using the methodology above, described in ref [5],  $R_0$  can be inferred for all countries at the beginning of the epidemic, given that exponential growth in the number of detected cases, lasting at least 7 days, is observed, during which at least 1000 tests are performed, with less than 20% reported positive test results.  $R_0$  is inferred from the exponential regime for these countries, assuming a deterministic limit (valid when the number of detected cases is around 10 or more). The manual inspection of growth profiles for each country is needed to determine this interval, as it can vary from country to country.

Therefore, the steps to obtain  $R_0$  are:

1. Obtain daily values of Detected cases  $D(t)$  and performed tests numbers in the initial stage of epidemic for various countries/

regions (ignore the non-deterministic pre-exponential period with less than 10 daily detected cases).

2. Discard countries/regions with more than 20% of positive test results as regions with insufficient testing coverage.
3. For each country/region, manually identify the initial exponential-growth interval, in the duration of at least 7 days, with overall at least 1000 performed tests.
4. Make a plot of  $\log(D(t))$  function and discard the country/region if it is not close to linear.
5. Calculate  $R_0$  value from the slope of  $\log(D(t))$ , using the above formula.

While this absence of epidemiological measures and immunity among the population allows calculating  $R_0$  as the inherent virus property, it is also worth mentioning that, although more complicated, it is possible to derive the effective reproductive number of the virus ( $R_e$ ) during later stages of the epidemics, as shown in ref [2, 7]. However, extracting  $R_e$  from these models, with the control measures fully considered, is complicated and requires a high-quality data set [7]. Consequently, in the machine learning methods explained below, we will use publicly available  $R_e$  values extracted from a simplified SIR model [24].

## **2.2 Univariate Correlations – Valuable First Insight**

Simple linear correlation is a valuable tool for quickly analyzing the strength of the linear relationship between two variables. Although it does not account for the effects of other (confounding) factors, it is a relatively simple method that provides a helpful first insight into the strength and direction of the relationship between the variables.

The protocol for univariate correlations is the following:

1. Collect data for variables of interest.
2. Calculate Pearson's correlation coefficient between each variable and the target variable.
3. Graphically represent the results via bar plots or scatter graphs to visualize the strength of correlation for selected variables.
4. Interpret the results to identify potential risk factors and assess the strength and direction of the relationship between variables.
5. Consider the limitations of the univariate correlation method, including the lack of accounting for confounding factors, and plan for further analysis if needed.
6. Utilize the results for various purposes, such as interpretation of principal components and preselection of variables for machine learning regressions.



As an illustration of this procedure, in ref [5], Pearson's correlation of  $R_0$ , inferred for 118 world countries, was determined together with 42 demographic, meteorological, and health-related variables. This way, potential risk factors were singled out among many variables. These univariate correlations can be graphically represented via bar plots (for representing univariate correlation coefficients of a group of variables with  $R_0$ ) and scatter graphs (to emphasize the strength of correlation for selected variables), as presented in Fig. 3. This figure shows significant positive correlations between  $R_0$  and the human development index (HDI), the median population age, and the urban population percentage. At the same time, the highest negative correlation is observed for infant mortality rate and weather parameters related to a warmer climate (i.e., higher temperatures, precipitation, humidity, and UV radiation). The correlation between  $R_0$  and the delay of the epidemic onset is also significant and negative.

Besides exploring the strength of the linear relationship between  $R_0$  and potential risk factors, univariate correlation can be used for a number of purposes, including interpretation of principal components with respect to the variables entering PCA, as well as for preselection of variables entering the machine learning regressions, all of which will later be discussed.

### **2.3 Data Transformation and Outlier Substitution**

Many linear regression methods used for feature selection are sensitive to outliers and require approximately normal distribution. Thus:

1. Check the distribution of collected environmental and demographic data before running regression.
2. If the distribution deviates significantly from normal, apply appropriate transformations.
3. Use standard transformations ( $x^2$ ,  $\log x$ ,  $\sqrt{x}$ ,  $\sqrt[3]{x}$ ) that lead to the skewness coefficient closest to zero, and the minimal number of outliers in the transformed data.
4. Substitute remaining outliers with the median of the transformed variable.

### **2.4 Dealing with Multicollinearity of High-Dimensional Data – PCA and mRMR Approach**

Principal component analysis (PCA) [25] is an unsupervised machine learning method widely used to analyze high-dimensional data sets. This relatively simple technique allows for dimensionality reduction and partial data decorrelation while keeping the desired percentage of the variance. As the result of PCA, the initial data are linearly transformed into a new coordinate system based on the variables' covariance, so that the new set of variables, i.e., principal components (PCs), contain a descending amount of information. That is, the first principal component contains most of the variance of the original data, followed by the second principal component,

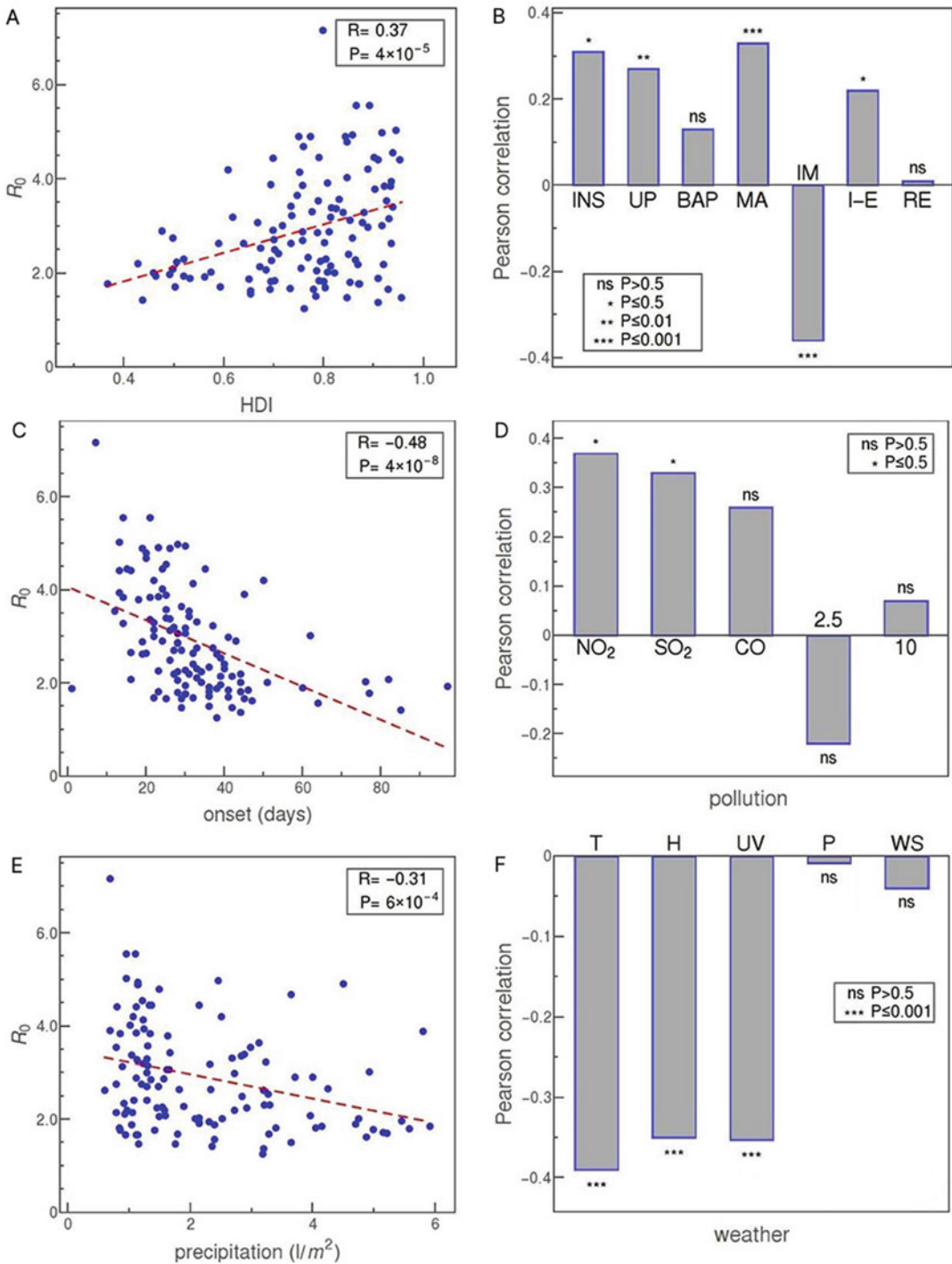


**Fig. 3** Pearson's correlation of  $R_0$  and potential transmissibility drivers. **(a)** Scatter graph of  $R_0$  vs. HDI; **(b)** Bar plot of Pearson's correlation coefficients of  $R_0$  with socio-demographic variables, INS – social security and health insurance coverage, UP – percentage of urban population, BAP – built-up area per capita (measure of population density), MA – median age, IM – infant mortality, I-E – net immigration, RE – percentage of refugees; **(c)** Scatter graph of  $R_0$  vs. days since the epidemic onset; **(d)** Bar plot of Pearson's correlation coefficients of  $R_0$  with air pollutants, 2.5 –  $PM_{2.5}$  concentration, 10 –  $PM_{10}$  concentration; **(e)** Scatter graph of

etc. Commonly, we keep only the number of components required to explain over 85% of the variance of the original data. This way, a minimal number of maximally informative components can be used as input in regression models, making the analysis significantly more straightforward and reliable. The standard PCA protocol is the following:

1. Collect high-dimensional data for analysis.
2. Standardize the data by subtracting the mean from each data point and dividing the result by the standard deviation (required for PCA).
3. Perform PCA on the standardized data.
4. Examine the distribution of the PCs and substitute the outliers (if they appeared).
5. Determine the number of principal components that explain over 85% of the variance of the original data and retain only them in the following regression-based analysis.
6. Interpret the principal components by assessing their correlation with the variables entering PCA.

The biggest downside of this approach is a somewhat complicated interpretation of principal components. For example, in ref [26], the correlation of each of the PCs relevant for the analysis with the variables entering the PCA was determined, and PCs were later discussed based on the variable(s) with which they had the highest correlation. An approach used by [27] to overcome this problem was to group the variables in smaller, mutually related subsets prior to the PCA, making their subsequent interpretation more straightforward. In ref [26], PCA was performed on nine demographic variables obtained from 118 world countries. The increase of the cumulative variance explained by a larger number of PCs and the 85% cut-off point for the principal components are represented in Fig. 4a. The correlation of the 9 selected PCs (which cumulatively explain over 85% of the data variance) and the variables entering PCA were examined. The variables with the highest correlation with each of the PCs, along with the corresponding Pearson's correlation coefficient, are represented in Fig. 4b. PC1, containing the highest portion of the explained variance, shows the highest correlation with the Human Development Index (HDI) (see Fig. 4c). HDI is, in turn, significantly correlated with many variables related to society's prosperity (see Fig. 4d), interpreting PC1 as the prosperity measure.

---

**Fig. 3** (continued)  $R_0$  vs. precipitation; (f) Bar plot of Pearson's correlation coefficients of  $R_0$  with five meteorological variables, T – temperature, H – specific humidity, UV – UV index, P – air pressure, WS – the wind speed. (Figure adapted from ref [5])

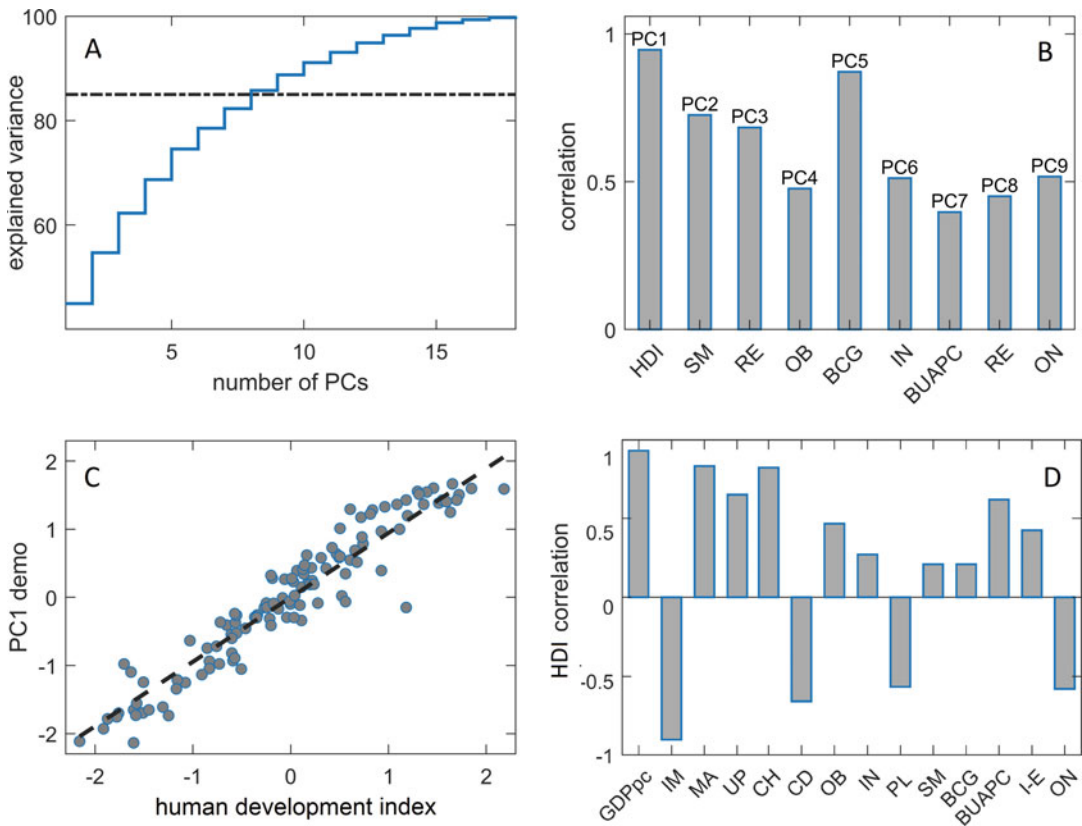


**Fig. 4** Principal Component Analysis of selected demographic variables. (a) Cumulative variance explained by first  $n$  principal components, with the dashed line representing 85% variance cut-off; (b) Pearson's correlation coefficients of the variables with the highest correlation with each of the selected principal components; (c) Scatter plot of PC1 vs. HDI; (d) Pearson's correlation of HDI and demographic variables which entered PCA, HDI – human development index, SM – prevalence of smoking, RE – the percentage of refugees, OB – prevalence of obesity, BCG – BCG immunization coverage, IN – prevalence of insufficient physical activity, BUAPC – built-up area per capita, ON – delay of the epidemic onset, GDPpc – GDP per capita, IM – infant mortality, MA – median age, UP – urban population, CH – average blood cholesterol level, CD – prevalence of chronic diseases, PL –  $\text{PM}_{2.5}$  pollution, I-E – net immigration. (Figure reproduced from ref [26])

A generalization of PCA, Supervised Principal Component Analysis [28, 29], is a PCA-based regression and classification method aimed at analyzing data sets in which the number of observations is smaller than the number of their features. In the Supervised PCA, principal component analysis is performed only on the variables whose Pearson's correlation coefficient with the response variable is higher than a certain threshold,  $\theta$ . Only  $m$  principal components obtained this way are used as input in the multiple linear regression model. In ref [30], supervised PCA was used to analyze COVID-19 global severity determinants, with  $\theta$  and  $m$  treated as hyperparameters and selected through cross-validation.

The Minimum Redundancy Maximum Relevance (mRMR) [31] feature selection method can be used for variable preselection as an alternative to PCA. This method's features are ordered based on their maximal correlation with the response variable (maximal relevance) and minimal correlation with the previously selected features (minimal redundancy). Only the predetermined number of highest-ranking features are selected. The mRMR algorithm is executed in the following way:

1. Calculate relevance of the features as F-statistics between the target variable and each feature.
2. Calculate the redundancy of each feature with respect to the remaining features as sum of the absolute values of their Pearson's correlation coefficients.
3. Divide relevance with redundancy to obtain the score.
4. Choose the feature with the highest score as the first feature.
5. Iteratively select the remaining features based on their score.
6. The selected features can then be used as input in regression models or other analyses.

This method was recently proved effective with the Random Forest algorithm [32]. In ref [33], this approach was used in the large-scale analysis of COVID-19 severity determinants in the United States. The number of best-ranking features retained by mRMR in this research was treated as a hyperparameter and determined through cross-validation.

## **2.5 Regularization-Based Linear Regression Methods**

Although multiple linear regression models (MLRM) are practical and easy to implement, they are prone to overfitting, especially for small data sets with many variables, such as the data set used in ref [27], consisting of 74 initial variables observed in 46 US states. Regularization-based models aim to resolve this issue by balancing bias and variance. This is accomplished by penalizing a higher number of variables in the model. While Lasso (Least Absolute Shrinkage and Selection Operator) [34] implements an  $L_1$  penalty, Elastic Net [35] is the combination of Ridge [36] and Lasso regression, which implements both  $L_1$  and  $L_2$  penalties. In both methods, significant predictors are selected by shrinking the coefficients of all other (insignificant) predictors to zero. The parameter  $\lambda$  determines the significance threshold for Lasso and  $\lambda$  and  $\alpha$  for Elastic Net regression. Parameter  $\lambda$  can take any positive value, with higher values associated with a stricter penalty (i.e., for  $\lambda = 0$  regression model is equal to MLRM, and for  $\lambda \rightarrow \infty$ , all the model coefficients are equal to zero). On the other hand, parameter  $\alpha$  can take values from 0 to 1. It represents the balance between Lasso and Ridge regressions: for  $\alpha = 1$ , the model turns to Lasso regression, and for  $\alpha = 0$ , it turns to Ridge regression.

The optimal values of  $\alpha$  and  $\lambda$  can be found through cross-validation. In MATLAB implementation of this procedure used in ref [37], 100  $\lambda$  values for cross-validation are obtained through a scanning round of Lasso regression performed on the entire data set. In the case of Elastic Net regression, corresponding 100 linearly spaced  $\alpha$  values in the range from 0 to 1 are assigned to each  $\lambda$  value. The model is then trained for every 100  $\lambda$  values for Lasso regression, or every 10,000  $\alpha$ - $\lambda$  combinations for Elastic Net, using fivefold cross-validation, with the data repartitioned 40 times, and determining Mean Square Error (MSE) on the testing set for each model. Depending on the problem at hand, the final model is selected as the model with minimal MSE on the testing set or the sparsest model among those with MSE within one standard error from the minimal MSE—that is, the model with the smallest number of predictors among the models with the smallest error. If the response variable strongly correlates with the higher number of predictors, the sparsest model is usually more informative (as the noise is reduced). If the response variable is not strongly correlated with most predictors, the minimal MSE model is preferable. While choosing the sparsest model is trivial for Lasso regression (the model with the highest  $\lambda$  value among the models with MSE close to minimal), for the Elastic Net, the number of predictors for all the models with MSE within 1 SE from the minimal MSE needs to be determined for the sparsest model to be selected.

The association of a higher Human Development Index (HDI) on COVID-19 transmissibility, which was observed by [5] (see Fig. 3a), was confirmed by [26], where the principal component associated with higher prosperity of the country (and most notably, HDI, see Fig. 4b, c) was selected by both Lasso and Elastic Net regression as the most important global COVID-19 transmissibility predictor (Fig. 5c, d). This research also performed an MLRM-based approach and stepwise linear regression (Fig. 5a, b). While the shortcomings of MLRM compared to regularization-based methods have already been discussed, it is worth mentioning that Forward stepwise regression also offers certain advantages compared to MLRM. In this method, starting from the null model (i.e., a model containing no variables), a linear term is added to the model if its significance, estimated using F-statistics, falls below the standard threshold of  $P = 0.05$  [38]. Forward stepwise selection proved a useful yet straightforward feature selection method, especially when the number of predictors is comparable to the sample size, i.e., when MLRM would likely lead to overfitting [29]. However, unlike regularization-based methods, Forward stepwise regression is affected by multicollinearity and may fail to select relevant predictors among a group of mutually correlated variables. Also, this model's significant drawback is that it is biased in parameter estimation and produces inflated  $R^2$  values [39]. For all the mentioned reasons, regularization-based techniques, although more complex and computationally demanding, remain preferable.



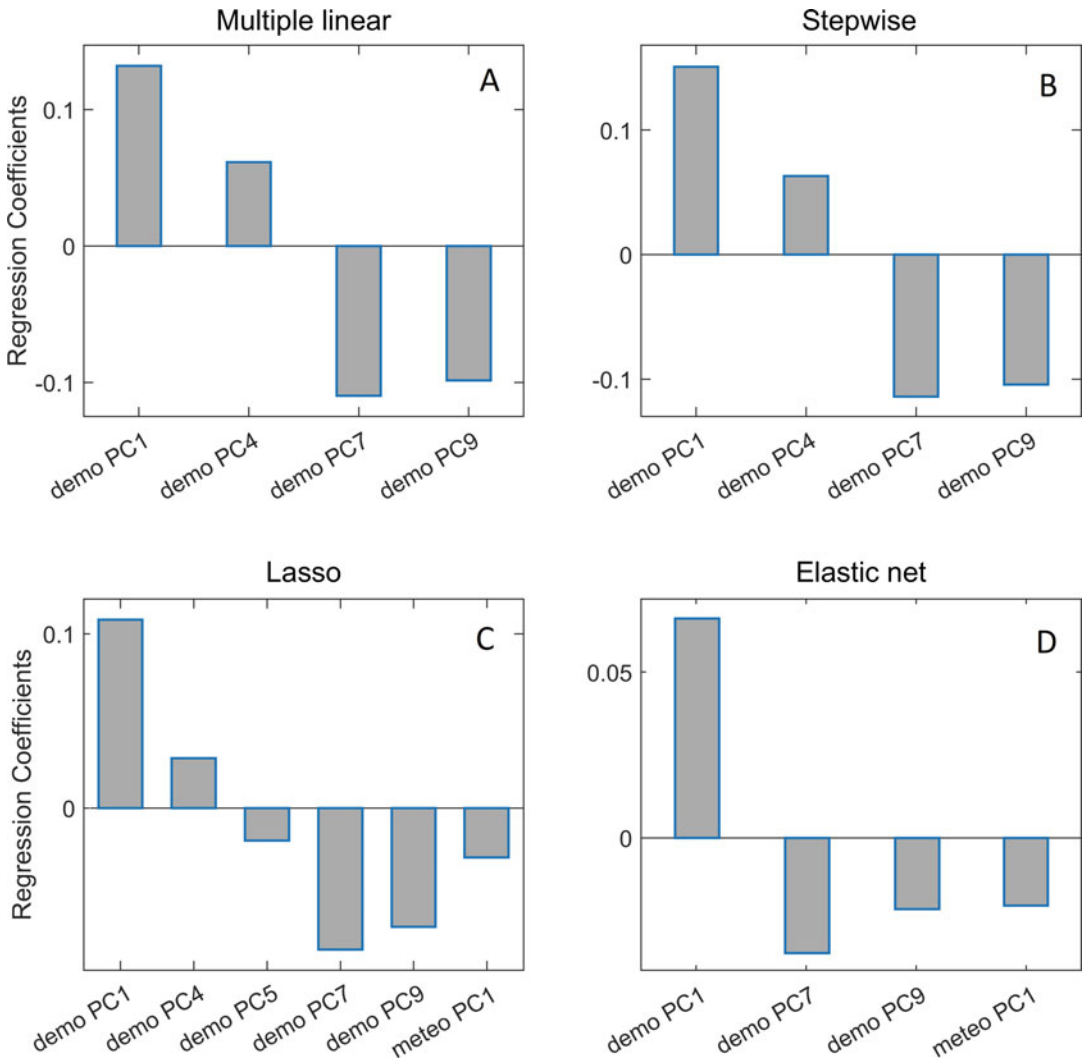


**Fig. 5** Regression coefficient obtained by four linear regression models of COVID-19 transmissibility. Principal components obtained from selected demographic (*see* Fig. 4) and meteorological variables were used as input, (a) Multiple linear regression model on the previously selected subset of predictors; (b) Forward stepwise linear regression model; (c) Lasso regression; (d) Elastic Net regression. (Figure reproduced from ref [26])

Relaxed Lasso [40] and Elastic Net procedures can be implemented to reduce noise when the response variable is highly correlated with many predictors. In this setup, regression is performed in two rounds of selection. While the first round is identical to the procedure described above, only the predictors selected as important in the first round are used as input for the second round of regression. In ref [37, 41], a relaxed approach was successfully implemented to analyze COVID-19 severity determinants in the USA and worldwide.

To summarize, for (Relaxed) Lasso/Elastic Net regression:

1. Collect data for the variables of interest, preprocess and standardize them, as previously described.
2. Choose the appropriate regularization-based method (Lasso or Elastic Net).
3. Choose an appropriate values of lambda (and alpha for Elastic Net) to be tested during cross-validation. A good rule of thumb is to test values ranging from 0 to 1, in increments of 0.01 for alpha and select 100 lambda values through a “scanning” round of regression for each alpha value.
4. Perform k-fold cross-validation (e.g., fivefold), with the data repartitioned sufficiently many times (e.g., 40), using the chosen method and lambda/alpha values, and record the mean squared error (MSE) for each model.
5. Determine the optimal lambda/alpha value(s) based on the MSE values obtained in step 4. A common approach is to choose the lambda/alpha value that results in the model with the smallest MSE, or the sparsest model with MSE within one standard error of the minimum MSE.
6. Train the final model on the entire training set using the optimal lambda/alpha value(s).
7. If implementing the relaxed approach, repeat the whole procedure while taking only the selected predictors (i.e., predictors with non-zero coefficients from **step 6**) as the new input.

## **2.6 Decision-Tree-Based Methods**

Potential interactions between predictors and their often nonlinear relationship with the response variable cannot be captured by linear feature selection methods presented so far. To further inspect these relations, a different approach is needed. Nonlinear supervised machine learning methods, based on ensembles of decision trees, such as Random Forest and Gradient Boost regressions, have proven particularly useful for solving these problems.

Decision trees are relatively simple classification and prediction tools with a wide range of applications, most commonly used in data mining [29, 42]. These tree-like models aim to classify the given data in the best possible way by creating a set of branching criteria, separating the data into two or more subsets. That is, a decision tree consists of root, internal, and terminal nodes (or leaves). The root node represents the first branching criterion, i.e., the criterion by which the data is separated into two branches. Internal nodes are the branching points in between, and leaves are the terminal subsets in which data is separated. The branching criteria are determined for each node based on how well they separate the data according to the response variable. Calculating each leaf node’s entropy or Gini index is a standard method for

accomplishing this in classification problems [42] while minimizing the residual sum of squares is usually used in regression trees [43]. To prevent the tree from “growing” too complex and consequentially overfitting the data, minimal leaf size and the maximal number of splits can be used as stopping criteria [42].

Unlike the linear regression methods, these methods do not require normal data or scaling distribution and are not sensitive to outliers or missing data. However, while fast and easy to interpret, decision trees are prone to overfitting when facing small, high-dimensional data sets. To overcome this problem, Random Forest [44] and Gradient Boosting [45] methods use ensembles of decision trees combined with bootstrapping and bagging [46] or boosting approaches for solving classification and prediction problems.

In the Random Forest algorithm [44], the model is created using the bagging approach [46]. Each decision tree in the ensemble is trained on a bootstrapped data set, following the methodology described above but considering only a randomly chosen subset of predictors at each branching step. This way, a set of decorrelated decision trees with a large number of splits is created. In the final model, each decision tree’s aggregate “votes” are used to predict the value of the response variable, reducing the relatively high variance of a single decision tree.

In our MATLAB implementation of these algorithms [37, 41], the number of trees in the ensemble, minimal number of splits, and maximal number of leaves were all treated as hyperparameters (similar to  $\alpha$  and  $\lambda$  in Lasso and Elastic Net) and selected through grid search, with fivefold cross-validation and the data repartitioned 40 times. The model with minimal MSE was considered optimal and evaluated on the entire data set. The features were relevant if their importance estimates were above the mean threshold.

Gradient Boost [45] implements a boosting algorithm similar to the widely used Ada Boost method [47]. In this method, the trees are constructed to correct the error produced by the previous tree (i.e., “pseudo-residual”), with the weight of each tree (i.e., its impact on the final prediction) scaled by the set learning rate. This way, by adding each tree to the ensemble, the prediction improves as the pseudo-residuals get closer to 0. Hyperparameter tuning for the Gradient Boost method is similar to the above-explained procedure for the Random Forest regression, with the learning rate as an additional parameter.

To further reduce noise in both Random Forest and Gradient Boost, in ref [41], the procedure was repeated, analog to the Relaxed Lasso and Elastic Net settings, using only the features with the importance estimates above the mean importance threshold.

The importance estimates produced by Random Forest and Gradient Boost, unlike the regression coefficient from the linear regression methods, do not indicate the direction of the association. That is why partial dependence plots [29] should be used to assess the effect of each relevant predictor on the response variable while considering the average effects of the remaining predictors.

In practice, the steps for implementation of the Random Forest algorithm (and similarly for the Gradient Boost) are the following:

1. Prepare your data set for analysis. No need to normalize data or remove outliers.
2. Treat the number of trees in the ensemble, minimal number of splits, and maximal number of leaves as hyperparameters in Random Forest algorithms; additionally, learning rate is also used as a hyperparameter in Gradient Boost.
3. The hyperparameter values should be selected through grid search, e.g. with fivefold cross-validation and the data repartitioned 40 times.
4. For each set of hyperparameter values evaluate the performance of the model by comparing the predicted values to the actual values using mean squared error (MSE) as metrics.
5. Choose the model with minimal MSE as optimal and evaluate it on the entire data set.
6. Determine the importance of the features by examining their importance estimates. Relevant features should have importance estimates above the mean threshold.
7. Refine the model by selecting a subset of the relevant features and repeating the procedure.
8. Generate partial dependence plots to determine the direction of the predictor influence.

In Fig. 6, obtained from [41], the average effective reproductive number of the virus ( $R_{\text{avg}}$ ) was used as the response variable, leading to the importance estimates from Relaxed Random Forest and Gradient Boost regressions. The dependence between the variables with the highest importance—immunity proxy and transit mobility and  $R_{\text{avg}}$  is represented by partial dependence plots.

## **2.7 New Variant Outburst Analysis**

The inference of  $R_0$ , as described previously, is possible only for the initial epidemiological peak when the premises of susceptibility of the entire population and the absence of epidemiological measures are fulfilled. For the analysis of later epidemiological stages, a different approach is needed. For example, in ref [41], the late outburst of the Omicron strain of COVID-19 was analyzed in the following way:

1. The estimated effective reproductive number ( $R_c$ ) was inferred for over a hundred countries, following the methodology introduced in ref [24].

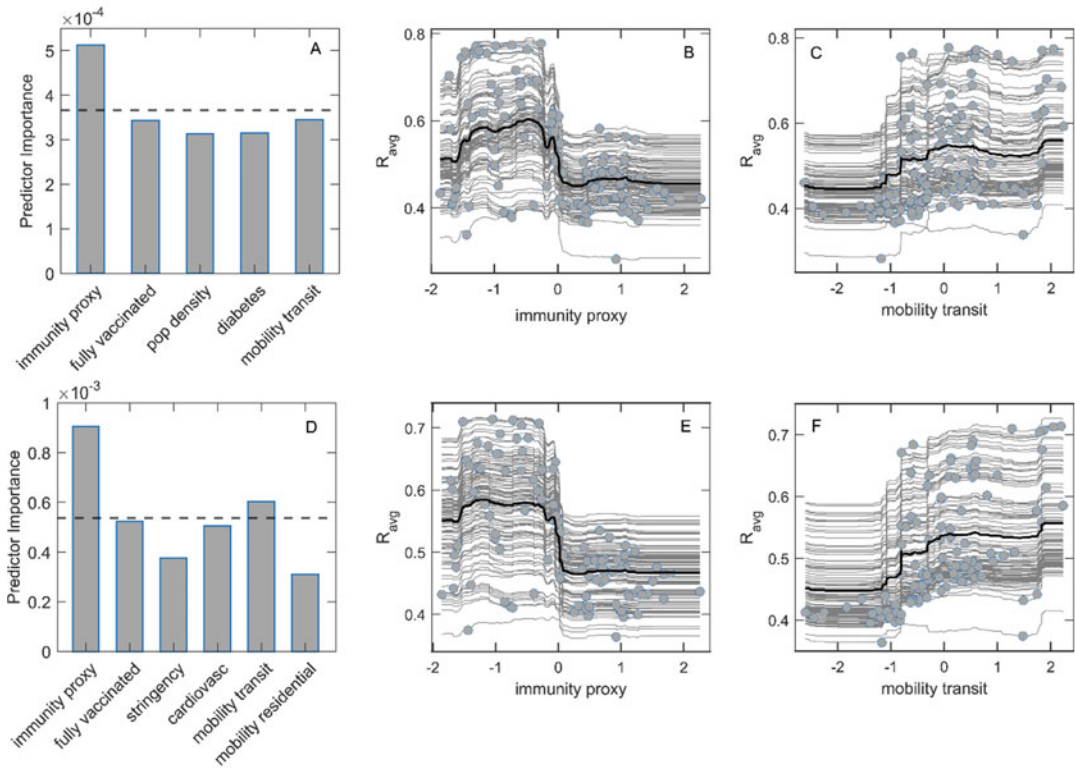


**Fig. 6** Relaxed Random Forest and Gradient Boost regressions. (a) Importance estimates from the Relaxed Random Forest regression; (b, c) Partial dependence plots of variables with highest importance estimates in Random Forest; (d) Importance estimates for the Relaxed Gradient Boost regression; (e, f) Partial dependence plots of variables with highest importance estimates in Gradient Boost; Dashed line in (a) and (d) represents the mean importance estimate. (Figure reproduced from ref [41])

2. To dampen data fluctuations, the  $R_c$  value was averaged over 21 days around the epidemiological peak (the day with the maximal estimated  $R_c$ ).
3. A large data set containing a number of possibly relevant environmental and social predictors for these countries was assembled.
4. All discussed feature selection methods were then applied, implemented in relaxed settings, with the averaged  $R_c$  as the response variable.

The method singled out the younger population age, earlier epidemic onset, higher population mobility, as well as lower COVID-19 immunity and booster vaccination prevalence as most likely transmissibility risks (Fig. 6). Therefore, all the described methods are also effective when considering factors relevant to the later epidemiological stages, such as vaccination and natural immunity.

---

### 3 Conclusion

Machine learning is a powerful tool in systems biology, as mechanistic models are often hard to formulate due to heterogeneous signals. This problem transfers to the epidemiological field, where numerous factors impact disease transmissibility. Mechanistic models have proved valuable input for machine learning methods, as they provide epidemiological measures insensitive to the epidemiological phase and testing policies. The methodology presented in this chapter is well-adjusted to analyze these factors. It can easily be modified to analyze the spread of any potential future infectious disease of epidemiological proportions. While regularization-based methods offer an easily understandable parametric approach for selecting important features among numerous mutually correlated predictors, even in relatively small data sets, non-parametric, decision-tree-based algorithms go a step further and enable us to infer the potential risk factors by taking into account interactions between variables and their nonlinear relationship to output. Moreover, combining supervised statistical learning with unsupervised approaches or variable preselection techniques such as PCA or mRMR may alleviate the problem of highly correlated input variables. Overall, as also recently increasingly argued for other areas of systems biology, machine learning and mechanistic models can effectively complement each other to advance understanding of infectious disease spread in the population. Here, we review some of the methods and specific examples of their application on real-world data, which can efficiently achieve these results. We expect exciting future developments in this area, particularly given the abundance of data available from the COVID-19 pandemic, which will be used to improve the methodology further so that we become increasingly better prepared for future epidemics.

---

### Acknowledgements

This work was supported by the Ministry of Education, Science and Technological Development of the Republic of Serbia.

### References

1. Bassingthwaight JB, Butterworth E, Jardine B, Raymond GM (2012) Compartmental modeling in the analysis of biological systems. *Methods Mol Biol Clifton NJ* 929: 391–438. [https://doi.org/10.1007/978-1-62703-050-2\\_17](https://doi.org/10.1007/978-1-62703-050-2_17)
2. Djordjevic M, Rodic A, Salom I et al (2021) A systems biology approach to COVID-19 progression in population. *Adv Protein Chem Struct Biol* 127:291–314. <https://doi.org/10.1016/bs.apcsb.2021.03.003>
3. Kermack WO, McKendrick AG (1927) A contribution to the mathematical theory of epidemics. *Proc R Soc Lond Ser Contain Pap Math Phys Char* 115:700–721. <https://doi.org/10.1098/rspa.1927.0118>



4. Aron JL, Schwartz IB (1984) Seasonality and period-doubling bifurcations in an epidemic model. *J Theor Biol* 110:665–679. [https://doi.org/10.1016/S0022-5193\(84\)80150-2](https://doi.org/10.1016/S0022-5193(84)80150-2)
5. Salom I, Rodic A, Milicevic O et al (2021) Effects of demographic and weather parameters on COVID-19 basic reproduction number. *Front Ecol Evol* 8:617841. <https://doi.org/10.3389/fevo.2020.617841>
6. Ilic B, Salom I, Djordjevic M, Djordjevic M (2022) An analytical framework for understanding infection progression under social mitigation measures. [Preprint] available at Research Square. <https://doi.org/10.21203/rs.3.rs-1331002/v1>
7. Djordjevic M, Djordjevic M, Ilic B et al (2021) Understanding infection progression under strong control measures through universal COVID-19 growth signatures. *Glob Chall* 5: 2000101. <https://doi.org/10.1002/gch2.202000101>
8. Klumpp S, Hwa T (2014) Bacterial growth: global effects on gene expression, growth feedback and proteome partition. *Curr Opin Biotechnol* 28:96–102. <https://doi.org/10.1016/j.copbio.2014.01.001>
9. Rodic A, Blagojevic B, Djordjevic M (2018) Systems biology of bacterial immune systems: regulation of restriction-modification and CRISPR-Cas systems. In: Rajewsky N, Jurga S, Barciszewski J (eds) *Systems biology*. Springer International Publishing, Cham, pp 37–58
10. Voit EO, Martens HA, Omholt SW (2015) 150 years of the Mass Action Law. *PLoS Comput Biol* 11:e1004012. <https://doi.org/10.1371/journal.pcbi.1004012>
11. Karin O, Bar-On YM, Milo T, et al (2020) Cyclic exit strategies to suppress COVID-19 and allow economic activity. [Preprint] available at medRxiv. 2020.04.04.20053579. <https://doi.org/10.1101/2020.04.04.20053579>
12. Eilersen A, Sneppen K (2020) Cost–benefit of limited isolation and testing in COVID-19 mitigation. *Sci Rep* 10:18543. <https://doi.org/10.1038/s41598-020-75640-2>
13. Wong GN, Weiner ZJ, Tkachenko AV et al (2020) Modeling COVID-19 dynamics in Illinois under nonpharmaceutical interventions. *Phys Rev X* 10:041033. <https://doi.org/10.1103/PhysRevX.10.041033>
14. Bar-On YM, Flamholz A, Phillips R, Milo R (2020) SARS-CoV-2 (COVID-19) by the numbers. *elife* 9:e57309. <https://doi.org/10.7554/eLife.57309>
15. Rossman H, Shilo S, Meir T et al (2021) COVID-19 dynamics after a national immunization program in Israel. *Nat Med* 27:1055–1061. <https://doi.org/10.1038/s41591-021-01337-2>
16. Xue L, Jing S, Miller JC et al (2020) A data-driven network model for the emerging COVID-19 epidemics in Wuhan, Toronto and Italy. *Math Biosci* 326:108391. <https://doi.org/10.1016/j.mbs.2020.108391>
17. Li R, Li L, Xu Y, Yang J (2022) Machine learning meets omics: applications and perspectives. *Brief Bioinform* 23:bbab460. <https://doi.org/10.1093/bib/bbab460>
18. Tang B, Pan Z, Yin K, Khateeb A (2019) Recent advances of deep learning in bioinformatics and computational biology. *Front Genet* 10. <https://doi.org/10.3389/fgene.2019.00214>
19. Iuchi H, Kawasaki J, Kubo K et al (2023) Bioinformatics approaches for unveiling virus-host interactions. *Comput Struct Biotechnol J* 21: 1774–1784. <https://doi.org/10.1016/j.csbj.2023.02.044>
20. Wang S, Fan K, Luo N et al (2019) Massive computational acceleration by using neural networks to emulate mechanism-based biological models. *Nat Commun* 10:4354. <https://doi.org/10.1038/s41467-019-12342-y>
21. Gilpin W, Huang Y, Forger DB (2020) Learning dynamics from large biological data sets: machine learning meets systems biology. *Curr Opin Syst Biol* 22:1–7. <https://doi.org/10.1016/j.coisb.2020.07.009>
22. Torregrosa G, Garcia-Ojalvo J (2021) Mechanistic models of cell-fate transitions from single-cell data. *Curr Opin Syst Biol* 26:79–86. <https://doi.org/10.1016/j.coisb.2021.04.004>
23. Worldometer (2022) COVID live - Coronavirus statistics - Worldometer. In: Worldometer. <https://www.worldometers.info/coronavirus/?msclkid=7812e8b9bf0011ecae993ad5fa9b7f49>. Accessed 18 Apr 2022
24. Arroyo-Marioli F, Bullano F, Kucinkas S, Rondón-Moreno C (2021) Tracking R of COVID-19: a new real-time estimation using the Kalman filter. *PLoS One* 16:e0244474. <https://doi.org/10.1371/journal.pone.0244474>
25. Jolliffe IT (2002) *Principal component analysis*, 2nd edn. Springer, New York, NY
26. Djordjevic M, Salom I, Markovic S et al (2021) Inferring the main drivers of SARS-CoV-2 global transmissibility by feature selection

- methods. *GeoHealth* 5:e2021GH000432. <https://doi.org/10.1029/2021GH000432>
27. Milicevic O, Salom I, Rodic A et al (2021) PM2.5 as a major predictor of COVID-19 basic reproduction number in the USA. *Environ Res* 201:111526. <https://doi.org/10.1016/j.envres.2021.111526>
  28. Barshan E, Ghodsi A, Azimifar Z, Zolghadri Jahromi M (2011) Supervised principal component analysis: visualization, classification and regression on subspaces and submanifolds. *Pattern Recogn* 44:1357–1371. <https://doi.org/10.1016/j.patcog.2010.12.015>
  29. Hastie T, Tibshirani R, Friedman J (2009) The elements of statistical learning data mining, inference, and prediction, 2nd edn. Springer, New York
  30. Markovic S, Salom I, Rodic A, Djordjevic M (2022) Analyzing the GHSI puzzle of whether highly developed countries fared worse in COVID-19. *Sci Rep* 12:17711. <https://doi.org/10.1038/s41598-022-22578-2>
  31. Ding C, Peng H (2005) Minimum redundancy feature selection from microarray gene expression data. *J Bioinforma Comput Biol* 03:185–205. <https://doi.org/10.1142/S0219720005001004>
  32. Zhao Z, Anand R, Wang M (2019) Maximum relevance and minimum redundancy feature selection methods for a marketing machine learning platform. In: 2019 IEEE international conference on data science and advanced analytics (DSAA), pp 442–452
  33. Tumbas M, Markovic S, Salom I, Djordjevic M (2023) A large-scale machine learning study of socio-demographic factors contributing to COVID-19 severity. *Front Big Data* 6:1038283
  34. Tibshirani R (1996) Regression Shrinkage and selection via the Lasso. *J R Stat Soc Ser B Methodol* 58:267–288. <https://doi.org/10.1111/j.2517-6161.1996.tb02080.x>
  35. Zou H, Hastie T (2005) Regularization and variable selection via the elastic net. *J R Stat Soc Ser B Stat Methodol* 67:301–320. <https://doi.org/10.1111/j.1467-9868.2005.00503.x>
  36. Hoerl AE, Kennard RW (1970) Ridge regression: applications to nonorthogonal problems. *Technometrics* 12:69–82. <https://doi.org/10.1080/00401706.1970.10488635>
  37. Markovic S, Rodic A, Salom I et al (2021) COVID-19 severity determinants inferred through ecological and epidemiological modeling. *One Health* 13:100355. <https://doi.org/10.1016/j.onehlt.2021.100355>
  38. Pope PT, Webster JT (1972) The use of an F-statistic in stepwise regression procedures. *Technometrics* 14:327–340. <https://doi.org/10.1080/00401706.1972.10488919>
  39. Whittingham MJ, Stephens PA, Bradbury RB, Freckleton RP (2006) Why do we still use stepwise modelling in ecology and behaviour? *J Anim Ecol* 75:1182–1189. <https://doi.org/10.1111/j.1365-2656.2006.01141.x>
  40. Meinshausen N (2007) Relaxed Lasso. *Comput Stat Data Anal* 52:374–393. <https://doi.org/10.1016/j.csda.2006.12.019>
  41. Djordjevic M, Markovic S, Salom I, Djordjevic M (2023) Understanding risk factors of a new variant outbreak through global analysis of Omicron transmissibility. *Environ Res* 216:114446. <https://doi.org/10.1016/j.envres.2022.114446>
  42. Song Y, Lu Y (2015) Decision tree methods: applications for classification and prediction. *Shanghai Arch Psychiatry* 27:130–135. <https://doi.org/10.11919/j.issn.1002-0829.215044>
  43. James G, Witten D, Hastie T, Tibshirani R (2021) Tree-based methods. In: James G, Witten D, Hastie T, Tibshirani R (eds) An introduction to statistical learning: with applications in R. Springer US, New York, NY, pp 327–365
  44. Breiman L (2001) Random Forests. *Mach Learn* 45:5–32. <https://doi.org/10.1023/A:1010933404324>
  45. Friedman JH (2002) Stochastic gradient boosting. *Comput Stat Data Anal* 38:367–378. [https://doi.org/10.1016/S0167-9473\(01\)00065-2](https://doi.org/10.1016/S0167-9473(01)00065-2)
  46. Breiman L (1996) Bagging predictors. *Mach Learn* 24:123–140. <https://doi.org/10.1007/BF00058655>
  47. Freund Y, Schapire RE (1995) A decision-theoretic generalization of on-line learning and an application to boosting. In: Vitányi P (ed) Computational learning theory. Springer, Berlin, Heidelberg, pp 23–37

# THREE NONRELATIVISTIC QUARKS IN THE LATTICE QCD POTENTIAL: CAN ONE SEE THE DIFFERENCE IN BARYON SPECTRA?\*

IGOR SALOM, V. DMITRAŠINOVIĆ

Institute of Physics, Belgrade University  
Pregrevica 118, Zemun, P.O.Box 57, 11080 Beograd, Serbia

(Received September 30, 2020)

We used the  $U(1) \otimes SO(3)_{\text{rot}} \subset U(3) \subset SO(6)$  hyperspherical harmonics of I. Salom, V. Dmitrašinović, *Nucl. Phys. B* **920**, 521 (2017). to calculate the energy-spectrum of three nonrelativistic quarks in the (interpolation of the) lattice QCD potential. We show that the first clear difference between the  $\Delta$ , or the Y-string confinement and the lattice QCD potential can be seen only in the third shell of excited states. This is beyond experimental access, even in the light-quark sector. We also briefly discuss the role of relativity.

DOI:10.5506/APhysPolBSupp.14.121

## 1. Introduction

The form of the three-heavy-quark potential in (lattice) QCD is substantially better known after the recent lattice work by Sakumichi and Suganuma [1], and by Koma and Koma [2]. The form of this potential has been analysed in terms of hyperspherical variables by Leech *et al.* [3, 4], as well as in another contribution to this workshop [5], where an upper and a lower bound (a band of small width) on the triangle-shape dependence of the confining part of the potential has been established.

These upper and lower bounds on the potential in two sectors/lines in the shape space can be extrapolated to the whole shape space due to its periodicity, and certain inequalities can be inferred about the value of the  $v_{66}$  hyperspherical expansion coefficient. In this light, one may even discuss the consequences of this lattice potential in three-heavy-quark spectroscopy. The aim of this work is to briefly discuss the effects of the lattice QCD 3-quark potential, as extracted in Refs. [3–5], in the heavy-baryon spectrum, as calculated in the hyperspherical approach, see Refs. [6–9].

---

\* Presented at *Excited QCD 2020*, Krynica Zdrój, Poland, February 2–8, 2020.

## 2. The nonrelativistic quantum-mechanical three-body problem in hyperspherical coordinates

### 2.1. $O(6)$ hyperspherical coordinates

Any (spin-independent) three-body potential must be invariant under: (1) translations; (2) overall (“ordinary  $O(3)$ ”) rotations; (3) permutations, if three identical particles are involved. Thus, due to (1), it may depend only on the relative position (Jacobi) vectors  $\boldsymbol{\rho} = \frac{1}{\sqrt{2}}(\mathbf{x}_1 - \mathbf{x}_2)$ ,  $\boldsymbol{\lambda} = \frac{1}{\sqrt{6}}(\mathbf{x}_1 + \mathbf{x}_2 - 2\mathbf{x}_3)$ ; (2) is a function of three scalar products of the two vectors,  $\boldsymbol{\rho} \cdot \boldsymbol{\lambda}$ ,  $\boldsymbol{\rho}^2$ , and  $\boldsymbol{\lambda}^2$ ; (3) it must be permutation-symmetric.

It can be transcribed in hyperspherical coordinates as  $f(R, \Omega_5)$ , where  $R = \sqrt{\boldsymbol{\rho}^2 + \boldsymbol{\lambda}^2}$  is the hyperradius, and five angles  $\Omega_5$  that parametrize a hypersphere in the six-dimensional Euclidean space. Three ( $\Phi_i$ ;  $i = 1, 2, 3$ ) of these five angles ( $\Omega_5$ ) are just the Euler angles associated with the orientation in a three-dimensional space of a spatial reference frame defined by the (plane of) three bodies; the remaining two hyperangles describe the shape of the triangle subtended by three bodies; they are functions of three independent scalar three-body variables, *e.g.*,  $\boldsymbol{\rho} \cdot \boldsymbol{\lambda}$ ,  $\boldsymbol{\rho}^2$ , and  $\boldsymbol{\lambda}^2$ . One linear combination ( $\boldsymbol{\rho}^2 + \boldsymbol{\lambda}^2$ ) of the two variables is already taken by the hyperradius  $R$ , so the shape-space is two-dimensional, and topologically equivalent to the surface of a three-dimensional sphere. We define the hyperangles  $(\alpha, \phi)$  as  $(\sin \alpha)^2 = 1 - \left(\frac{2\boldsymbol{\rho} \cdot \boldsymbol{\lambda}}{R^2}\right)^2$ ,  $\tan \phi = \left(\frac{2\boldsymbol{\rho} \cdot \boldsymbol{\lambda}}{\boldsymbol{\rho}^2 - \boldsymbol{\lambda}^2}\right)$ , which reveal the full  $S_3$  permutation symmetry of the problem: the angle  $\alpha$  does not change under permutations, so that all permutation properties are encoded in the  $\phi$ -dependence of the wave functions. This leads to permutation-adapted hyperspherical harmonics, as explained in Refs. [6, 7] wherein specific hyperspherical harmonics used here are displayed.

### 2.2. $O(6)$ harmonics

Labelling the  $O(6)$  hyperspherical harmonics with labels  $K$ , the Abelian hyperangular momentum quantum number  $Q$  conjugated with the Iwai angle  $\phi$ , the (total orbital) angular momentum quantum numbers  $L$  and  $L_z = m$ , and  $\nu$  which is the multiplicity label that distinguishes between hyperspherical harmonics with remaining four quantum numbers that are identical, as defined in Refs. [6, 7], corresponds to the subgroup chain  $U(1) \otimes SO(3)_{\text{rot}} \subset U(3) \subset SO(6)$ . We expand the wave function  $\Psi(R, \Omega_5)$  in terms of hyperspherical harmonics  $\mathcal{Y}_{[m]}^K(\Omega_5)$ ,  $\Psi(R, \Omega_5) = \sum_{K, [m]} \psi_{[m]}^K(R) \mathcal{Y}_{[m]}^K(\Omega_5)$ .

### 2.3. Hyperspherical expansion of three-body Schrödinger equation

The hyperspherical harmonics turn the Schrödinger equation of three particles in a factorizable three-body potential  $V(R, \alpha, \phi) = V(R)V(\alpha, \phi)$  into a set of coupled hyperradial equations

$$\begin{aligned}
 & -\frac{1}{2\mu} \left[ \frac{d^2}{dR^2} + \frac{5}{R} \frac{d}{dR} - \frac{K(K+4)}{R^2} + 2\mu E \right] \psi_{[m]}^K(R) \\
 & + V_{\text{eff}}(R) \sum_{K', [m']} C_{[m][m']}^{K K'} \psi_{[m']}^{K'}(R) = 0
 \end{aligned} \tag{1}$$

with a hyperangular coupling coefficients matrix  $C_{[m][m']}^{K K'}$  defined by

$$\begin{aligned}
 V_{\text{eff}}(R) C_{[m][m']}^{K' K} &= \left\langle \mathcal{Y}_{[m']}^{K'}(\Omega_5) \left| V(R, \alpha, \phi) \right| \mathcal{Y}_{[m]}^K(\Omega_5) \right\rangle \\
 &= V(R) \left\langle \mathcal{Y}_{[m']}^{K'}(\Omega_5) \left| V(\alpha, \phi) \right| \mathcal{Y}_{[m]}^K(\Omega_5) \right\rangle.
 \end{aligned} \tag{2}$$

Factorizability of the potential is a simplifying assumption that leads to analytic results in the energy spectrum. It holds for the power-law ones, but also other homogeneous ones.

### 2.4. Hyperspherical expansion of three-body potentials

The hyperangular part  $V(\alpha, \phi)$  of a factorizable potential can be expanded in terms of  $O(6)$  hyperspherical harmonics with zero angular momenta  $L = m = 0$  as

$$V(\alpha, \phi) = \sum_{K, Q}^{\infty} v_{K, Q}^{\text{3-body}} \mathcal{Y}_{00}^{K Q \nu}(\alpha, \phi), \tag{3}$$

where

$$v_{K, Q}^{\text{3-body}} = \int \mathcal{Y}_{00}^{K Q \nu*}(\Omega_5) V(\alpha, \phi) d\Omega_5 \tag{4}$$

leading to

$$\begin{aligned}
 V_{\text{eff}}(R) C_{[m''] [m']}^{K'' K'} &= V(R) \sum_{K, Q}^{\infty} v_{K, Q}^{\text{3-body}} \\
 &\times \left\langle \mathcal{Y}_{[m'']}^{K''}(\Omega_5) \left| \mathcal{Y}_{00}^{K Q \nu}(\alpha, \phi) \right| \mathcal{Y}_{[m']}^{K'}(\Omega_5) \right\rangle.
 \end{aligned} \tag{5}$$

In the case of three identical particles, the sum runs only over double-even-order ( $K = 0, 4, \dots$ )  $O(6)$  hyperspherical harmonics with zero value of the

democracy quantum number  $G_3 = Q = 0$ , as well as over  $K = 6, 12, 18 \dots$   $O(6)$  hyperspherical harmonics with democracy quantum number  $G_3 \equiv Q \equiv 0 \pmod{6}$ , always with vanishing angular momentum  $L = m = 0$ .

The numerical values for the first four allowed (nonvanishing)  $v_{K,Q}^{3\text{-body}}$  coefficients for  $K \leq 11$ , in the Y- and  $\Delta$ -string and Coulomb potential's hyperspherical expansions are tabulated in Table I. All other coefficients vanish for  $K < 12$ . Smallness of the coefficient  $v_{6,\pm 6}$  (Y-string) indicates (an additional) dynamical symmetry of the Y-string potential.

TABLE I

Expansion coefficients  $v_{KQ}$  of the Y- and  $\Delta$ -string as well as of the Coulomb and Logarithmic potentials in terms of  $O(6)$  hyperspherical harmonics  $\mathcal{Y}_{0,0}^{K,0,0}$ , for  $K = 0, 4, 8$ , respectively, and of the hyperspherical harmonics  $\mathcal{Y}_{0,0}^{6,\pm 6,0}$ .

$(K, Q)$	$v_{KQ}$ (Y-string)	$v_{KQ}$ ( $\Delta$ -string)	$v_{KQ}$ (CM-string)	$v_{KQ}$ (Coulomb)
(0,0)	8.22	16.04	$16.04/\sqrt{3}$	20.04
(4,0)	-0.398	-0.445	$-0.445/\sqrt{3}$	2.93
(6, $\pm 6$ )	-0.027	-0.14	$0.14/\sqrt{3}$	1.88
(8,0)	-0.064	-0.04	$-0.04/\sqrt{3}$	1.41

### 3. Consequences for the low-lying spectrum

The lowest-lying states in which the energy splittings depend on the  $v_{66}$  coefficient are the odd-parity resonances in the  $K = 3$  shell. In Ref. [8], one finds that only two pairs of levels in the  $K = 3$  shell are split by the  $v_{66}$  coefficient

$$\begin{aligned}
 [20, 1^-] & \frac{1}{\pi\sqrt{\pi}} \left( v_{00} + \frac{1}{\sqrt{3}}v_{40} - \frac{2}{7}v_{66} \right), \\
 [56, 1^-] & \frac{1}{\pi\sqrt{\pi}} \left( v_{00} + \frac{1}{\sqrt{3}}v_{40} + \frac{2}{7}v_{66} \right), \\
 [20, 3^-] & \frac{1}{\pi\sqrt{\pi}} \left( v_{00} - \frac{\sqrt{3}}{7}v_{40} - v_{66} \right), \\
 [56, 3^-] & \frac{1}{\pi\sqrt{\pi}} \left( v_{00} - \frac{\sqrt{3}}{7}v_{40} + v_{66} \right). \tag{6}
 \end{aligned}$$

In Table I, one can find the hyperspherical harmonic expansion coefficients of several standard potentials. In a separate contribution to this conference [5], we have analysed the lattice QCD data from Refs. [1, 2] in terms of



permutation-adapted hyperspherical variables. We found that the confining lattice QCD potential lies roughly half-way between the pure Y-string and the pure  $\Delta$ -string within the region of acute triangles. This allows us to set an upper and a lower bound on the value of the lattice coefficient:  $-0.14 \leq v_{66} \leq -0.027$  using the values from Table I. Unfortunately, no  $K = 3$  shell levels have been experimentally identified among the heavy-quark baryons as yet [12].

One possibility is to search for  $K = 3$  states among light-quark baryons [12], which, however, involve significant contributions from relativity. In order to get a feeling for, or at least the sign of relativistic corrections, we shall employ a special case of the three-body problem: the extreme-relativistic three-body harmonic oscillator.

#### 4. Extreme-relativistic three-body harmonic oscillator

The (extreme) relativistic three-quark Hamiltonian in configuration space is the  $m_a \rightarrow 0$  limit of

$$H = \sum_a \sqrt{m_a^2 + \mathbf{p}_i^2} + \frac{k}{2} (\boldsymbol{\rho}^2 + \boldsymbol{\lambda}^2) \quad (7)$$

with the confining 3-body harmonic oscillator potential  $V_{\text{HO}}$ . The Hamiltonian in momentum space and CM frame reads

$$\tilde{H} = \frac{k}{2} \left( \frac{\partial^2}{\partial \mathbf{p}_\rho^2} + \frac{\partial^2}{\partial \mathbf{p}_\lambda^2} \right) + \sum_{i=1}^3 |\mathbf{p}_i|,$$

which, after the substitutions  $\mathbf{p}_\rho \leftrightarrow \boldsymbol{\rho}$  and  $\mathbf{p}_\lambda \leftrightarrow \boldsymbol{\lambda}$ , is equivalent to the (nonrelativistic) Schrödinger equation

$$\tilde{H}\tilde{\Psi} = \tilde{E}\tilde{\Psi}$$

for three identical particles with a mass  $m = k$  and interacting with a linearly rising ‘‘CM-string’’ potential with unit string tension  $\sigma = 1$ . As we have developed hyperspherical harmonic methods [6, 7, 9] to deal with such three-body Schrödinger equations, we simply use the solution worked out in Ref. [11]. In Table I, we can see that the  $v_{66}$  coefficient has opposite signs in the Y- and  $\Delta$ -string potentials, on the one hand, and the CM-string, *i.e.*, in the relativistic case and the Coulomb one, on the other. Thus we see that the relativistic effects, as well as the residual QCD Coulomb interaction, may reduce or even annihilate the  $\Delta$ -string effects, which makes an identification of the confining potential more difficult.

## 5. Discussion and conclusions

We have shown how the lattice QCD data interpreted in terms of the hyperspherical variables can be used to put bounds on the mass-splittings of certain higher-lying odd-parity baryons using  $O(6)$  hyperspherical harmonics.

The Serbian Ministry of Science and Technological Development supported V.D. under grant numbers OI 171037 and III 41011, and I.S. under grant number OI 171031.

## REFERENCES

- [1] N. Sakumichi, H. Suganuma, *Phys. Rev. D* **92**, 034511 (2015).
- [2] Y. Koma, M. Koma, *Phys. Rev. D* **95**, 094513 (2017).
- [3] J. Leech, M. Šuvakov, V. Dmitrašinović, «Hyperspherical Three-Body Variables Applied to Lattice QCD Data», in: B. Dragovich, I. Salom, M. Vojinović (Eds.) «Proceedings of the “Ninth Mathematical Physics Meeting”», *Institute of Physics*, Belgrade, Serbia 2017, pp. 253–258.
- [4] J. Leech, M. Šuvakov, V. Dmitrašinović, *Acta Phys. Pol. B Proc. Suppl.* **11**, 435 (2018).
- [5] J. Leech, M. Šuvakov, V. Dmitrašinović, *Acta Phys. Pol. B Proc. Suppl.* **13**, 215 (2020), this issue.
- [6] I. Salom, V. Dmitrašinović, «Permutation-Symmetric Three-Body  $O(6)$  Hyperspherical Harmonics in Three Spatial Dimensions», in: V. Dobrev (Ed.) «Lie Theory and Its Applications in Physics. LT 2015. Springer Proceedings in Mathematics & Statistics, Vol. 191», *Springer, Singapore* 2016, p. 431.
- [7] I. Salom, V. Dmitrašinović, *Nucl. Phys. B* **920**, 521 (2017).
- [8] V. Dmitrašinović, I. Salom, *Phys. Rev. D* **97**, 094011 (2018).
- [9] I. Salom, V. Dmitrašinović, *Phys. Lett. A* **380**, 1904 (2016).
- [10] V. Dmitrašinović, T. Sato, M. Šuvakov, *Phys. Rev. D* **80**, 054501 (2009).
- [11] I. Salom, V. Dmitrašinović, «Relativistic Three-Body Harmonic Oscillator», to appear in Proceedings of the Lie Theory and Its Applications in Physics, Varna, Bulgaria, June 2019, in Springer Proceedings in Mathematics & Statistics, 2020.
- [12] V. Credé, W. Roberts, *Rep. Prog. Phys.* **76**, 076301 (2013).

PAPER • OPEN ACCESS

## Higher category theory and n-groups as gauge symmetries for quantum gravity

To cite this article: Bojan Nikolić *et al* 2023 *J. Phys.: Conf. Ser.* **2667** 012019

View the [article online](#) for updates and enhancements.

You may also like

- [Unification mechanism for gauge and spacetime symmetries](#)  
András László
- [Top down approach to 6D SCFTs](#)  
Jonathan J Heckman and Tom Rudelius
- [Cosmological solutions from 4D  \$N=4\$  matter-coupled supergravity](#)  
H L Dao



**UNITED THROUGH SCIENCE & TECHNOLOGY**

 **The Electrochemical Society**  
Advancing solid state & electrochemical science & technology

**248th  
ECS Meeting**  
Chicago, IL  
October 12-16, 2025  
*Hilton Chicago*

**Science +  
Technology +  
YOU!**

**SUBMIT  
ABSTRACTS by  
March 28, 2025**

**SUBMIT NOW**

The banner features a woman in a brown blazer smiling and gesturing, set against a blue background with a network of nodes and lines. The top and bottom of the banner are decorated with a repeating pattern of circular icons containing stylized molecular or atomic structures.

# Higher category theory and $n$ -groups as gauge symmetries for quantum gravity

Bojan Nikolić, Danijel Obrić, Tijana Radenković, Igor Salom and Marko Vojinović

Institute of Physics, University of Belgrade, Pregrevica 118, 11080 Belgrade, Serbia

E-mail: vmarko@ipb.ac.rs

**Abstract.** Higher category theory can be employed to generalize the notion of a gauge group to the notion of a gauge  $n$ -group. This novel algebraic structure is designed to generalize notions of connection, parallel transport and holonomy from curves to manifolds of dimension higher than one. Thus it generalizes the concept of gauge symmetry, giving rise to a topological action called  $nBF$  action, living on a corresponding  $n$ -principal bundle over a spacetime manifold. Similarly as for the Plebanski action, one can deform the topological  $nBF$  action by adding appropriate simplicity constraints, in order to describe the correct dynamics of both gravity and matter fields. Specifically, one can describe the whole Standard Model coupled to gravity as a constrained  $3BF$  or  $4BF$  action. The split of the full action into a topological sector and simplicity constraints sector is adapted to the spinfoam quantization technique, with the aim to construct a full model of quantum gravity with matter. In addition, the properties of the gauge  $n$ -group structure open up a possibility of a nontrivial unification of all fields. An  $n$ -group naturally contains additional novel gauge groups which specify the spectrum of matter fields present in the theory, in a similar way to the ordinary gauge group that prescribes the spectrum of gauge vector bosons in the Yang-Mills theory. The presence and the properties of these new gauge groups has the potential to explain fermion families, and other structure in the matter spectrum of the theory.

## 1. Introduction

The formulation of a quantum theory of gravity represents one of the fundamental open problems in modern theoretical physics. Among the many approaches to this problem, some have developed into vast research frameworks, such as Loop Quantum Gravity, which aims to formulate a model of quantum gravity (QG) in a nonperturbative fashion, both canonically and covariantly [1, 2, 3]. The covariant approach aims to give a tentative rigorous definition of the path integral for the gravitational field,

$$Z = \int \mathcal{D}g e^{iS[g]}. \quad (1)$$

One of the essential assumptions is a triangulation of a spacetime manifold, and the path integral is introduced as a discrete state sum of the gravitational field configurations, living on the simplicial complex structure. This approach to quantization of gravity is usually called the *spinfoam* quantization method. It is performed via the following three steps:



- (1) one reformulates the classical action  $S[g]$  as a constrained  $BF$  action, separating the topological  $BF$  part and the constraint part of the action;
- (2) one employs the underlying Lie group structure of the  $BF$  sector of the action, in order to define a triangulation-independent state sum  $Z$ ;
- (3) finally, one deforms the topological state sum by applying the simplicity constraints, and therefore redefining it into a triangulation-dependent state sum, which plays the role of a definition for the path integral (1).

This type of quantization prescription has been implemented in a number of cases, for various choices of the gravitational action, of the Lie group, and of the spacetime dimension. Historically the first spinfoam model was the Ponzano-Regge model [4], defined in 3 spacetime dimensions. In 4 dimensions multiple models have been formulated, differing in the choice of the Lie group and the way one imposes the simplicity constraints [5, 6, 7, 8, 9]. While all these models do represent definitions of the gravitational path integral, none of them are able to include matter fields in a seamless way. Introducing the latter into a spinfoam QG model has so far had only limited success [10], predominantly due to the lack of the tetrad fields in the topological part of the model.

Recently, a new approach has been developed to address the issue of matter fields, which employs the framework of *higher gauge theory* (see [11] for a review). Specifically, one uses the notion of a *categorical ladder* to generalize the  $BF$  action (based on a Lie group) to a  $2BF$  action (based on the so-called 2-group structure), and further to a  $3BF$  action (based on a 3-group structure). A convenient choice of the *Poincaré 2-group* gives rise to the needed tetrad fields in the topological sector of the action [12], while an additional extension to the 3-group naturally introduces the matter fields (fermions and scalars) into the model [13]. The steps of the categorical ladder and their corresponding structures are summarized as follows:

categorical structure	algebraic structure	linear structure	topological action	degrees of freedom
Lie group	Lie group	Lie algebra	$BF$ theory	gauge fields
Lie 2-group	Lie crossed module	differential Lie crossed module	$2BF$ theory	tetrad fields
Lie 3-group	Lie 2-crossed module	differential Lie 2-crossed module	$3BF$ theory	scalar and fermion fields

The main aim of this work is to provide a short review of the classical pure  $BF$ ,  $2BF$  and  $3BF$  actions, in order to demonstrate the categorical ladder procedure and the construction of higher gauge theories. In other words, we mainly focus on the step 1 of the spinfoam quantization programme, with a very short review of step 2 of the programme.

The layout of the paper is as follows. Section 2 deals with first three examples of  $nBF$  theories, namely  $BF$ ,  $2BF$  and  $3BF$  actions, and their construction using the categorical ladder. After this, in Section 3 we briefly present an application of a  $3BF$  theory to the Standard Model of elementary particles coupled to Einstein-Cartan gravity. As it turns out, the scalar and fermion fields are *naturally associated to a new gauge group*, generalizing the role of an ordinary gauge group in the Yang-Mills theory. This opens up a possibility of an algebraic classification of matter fields, and (more speculatively) a possibility of the explanation of the three fermion families. Finally, Section 4 contains some discussion and our conclusions.

The notation and conventions are as follows. Spacetime indices are denoted by the Greek letters  $\mu, \nu, \dots$ , and are raised and lowered by the spacetime metric  $g_{\mu\nu} = \eta_{ab} e^a{}_{\mu} e^b{}_{\nu}$ , where  $e^a{}_{\mu}$  are the tetrad fields. The inverse tetrad is denoted as  $e^{\mu}{}_a$ . The local Lorentz indices are denoted by the Latin letters  $a, b, c, \dots$ , take values 0, 1, 2, 3, and are raised and lowered using the Minkowski metric  $\eta_{ab}$  with signature  $(-, +, +, +)$ . All other indices that appear in the paper depend on the context, and their use is explicitly defined in the text where they appear. We

work in the natural system of units where  $c = \hbar = 1$ , and  $G = l_p^2$ , where  $l_p$  is the Planck length. The exterior product in the space of differential forms is denoted with the standard “wedge” symbol,  $\wedge$ .

## 2. $nBF$ theories

We begin by giving a short review of  $nBF$  theories, for  $n = 1, 2, 3$ , which represent the most interesting cases for physics.

### 2.1. $BF$ theory

A  $BF$  theory and its various applications in physics are already well known in the literature, see for example [14, 15, 16], so here we merely give a brief definition. Given a Lie group  $G$ , and its corresponding Lie algebra as  $\mathfrak{g}$ , one defines the  $BF$  action in the form (we discuss only the 4-dimensional spacetime manifolds  $\mathcal{M}_4$ ):

$$S_{BF} = \int_{\mathcal{M}_4} \langle B \wedge \mathcal{F} \rangle_{\mathfrak{g}}. \quad (2)$$

Here,  $\mathcal{F} \equiv d\alpha + \alpha \wedge \alpha$  is the curvature 2-form for the  $\mathfrak{g}$ -valued connection 1-form  $\alpha \in \Lambda^1(\mathcal{M}_4) \otimes \mathfrak{g}$ , while  $B \in \Lambda^2(\mathcal{M}_4) \otimes \mathfrak{g}$  is a  $\mathfrak{g}$ -valued Lagrange multiplier 2-form. Also,  $\langle -, - \rangle_{\mathfrak{g}}$  denotes a  $G$ -invariant nondegenerate symmetric bilinear form over  $\mathfrak{g}$ .

Varying the action (2) with respect to  $B$  and  $\alpha$ , one obtains the equations of motion:

$$\mathcal{F} = 0, \quad \nabla B \equiv dB + \alpha \wedge B = 0. \quad (3)$$

The first equation implies that  $\alpha$  is a flat connection, in the sense that  $\alpha = 0$  up to gauge transformations. The second equation then implies that  $B$  is covariantly constant. From these one can deduce that there are no local propagating degrees of freedom, and therefore the theory is said to be *topological*.

### 2.2. $2BF$ theory

Once we have introduced the  $BF$  model, we proceed to first step of the *categorical ladder*, generalizing the algebraic notion of a group to the notion of a 2-group. This leads to the generalization of the  $BF$  theory to the  $2BF$  theory, also sometimes called  $BFCG$  theory [11, 17, 18, 19].

The categorical ladder is a procedure of generalizing various notions in mathematics, using the framework of category theory, and works as follows. One starts from the notion of a group as an algebraic structure, and notes that it can be understood as a category with only one object and invertible morphisms [11]. Then, one employs the fundamental idea that a category can be generalized to the so-called *higher categories*, which have not only objects and morphisms, but also 2-morphisms (maps between morphisms), 3-morphisms (maps between 2-morphisms), and so on. This tower of  $n$ -categories is known as the *categorical ladder*. Applying the construction to groups, it is straightforward to introduce the notion of a *2-group* as a 2-category consisting of only one object, where all the morphisms and all 2-morphisms are invertible. It was demonstrated that every strict 2-group is equivalent to a *crossed module*  $(H \xrightarrow{\partial} G, \triangleright)$ , see [13] for detailed definitions. Here  $G$  and  $H$  are groups,  $\partial$  is a homomorphism from  $H$  to  $G$ , while  $\triangleright : G \times H \rightarrow H$  is an action of  $G$  on  $H$ .

Just like an ordinary Lie group  $G$  has a naturally associated connection  $\alpha$  and gives rise to a  $BF$  theory, a Lie 2-group has a naturally associated 2-connection  $(\alpha, \beta)$ , described by the usual  $\mathfrak{g}$ -valued 1-form  $\alpha \in \Lambda^1(\mathcal{M}_4) \otimes \mathfrak{g}$  and an  $\mathfrak{h}$ -valued 2-form  $\beta \in \Lambda^2(\mathcal{M}_4) \otimes \mathfrak{h}$ , where  $\mathfrak{h}$  is a



Lie algebra of the Lie group  $H$ . This 2-connection gives rise to the so-called *fake 2-curvature*  $(\mathcal{F}, \mathcal{G})$ , defined as

$$\mathcal{F} = d\alpha + \alpha \wedge \alpha - \partial\beta, \quad \mathcal{G} = d\beta + \alpha \wedge^\triangleright \beta. \tag{4}$$

Here  $\alpha \wedge^\triangleright \beta$  means that  $\alpha$  and  $\beta$  are multiplied as forms using  $\wedge$ , and simultaneously multiplied as algebra elements using  $\triangleright$ , see [13]. The curvature pair  $(\mathcal{F}, \mathcal{G})$  is called “fake” due of the presence of the additional term  $\partial\beta$  in the definition of  $\mathcal{F}$  [11].

Using the structure of a 2-group, or equivalently the crossed module, one can introduce the so-called *2BF* action, as a generalization of the *BF* action, as follows [17, 18]:

$$S_{2BF} = \int_{\mathcal{M}_4} \langle B \wedge \mathcal{F} \rangle_{\mathfrak{g}} + \langle C \wedge \mathcal{G} \rangle_{\mathfrak{h}}. \tag{5}$$

Here the 2-form  $B \in \Lambda^2(\mathcal{M}_4) \otimes \mathfrak{g}$  and the 1-form  $C \in \Lambda^1(\mathcal{M}_4) \otimes \mathfrak{h}$  are Lagrange multipliers. Also,  $\langle -, - \rangle_{\mathfrak{g}}$  and  $\langle -, - \rangle_{\mathfrak{h}}$  denote the  $G$ -invariant nondegenerate symmetric bilinear forms over the Lie algebras  $\mathfrak{g}$  and  $\mathfrak{h}$ , respectively. As a consequence of the axiomatic structure of a crossed module (see [13]), the bilinear form  $\langle -, - \rangle_{\mathfrak{h}}$  is  $H$ -invariant as well. See [17, 18] for review and references.

The equations of motion for a *2BF* theory are an extension of the equations of motion of a *BF* theory. Varying with respect to  $B$  and  $C$  one obtains

$$\mathcal{F}^\alpha = 0, \quad \mathcal{G}^a = 0, \tag{6}$$

while varying with respect to  $\alpha$  and  $\beta$  one obtains the equations for the multipliers,

$$\nabla B + C \wedge^\mathcal{T} \beta = 0, \quad \nabla C - \partial B = 0. \tag{7}$$

Here the map  $\mathcal{T}$  is defined in [13]. A rigorous Hamiltonian analysis of the model demonstrates that in this case as well there are no local propagating degrees of freedom [20, 21] (see also [22]). Therefore the *2BF* theory is also topological.

### 2.3. 3BF theory

When constructing more realistic (nontopological) models by adding constraints to *BF* and *2BF* models, it becomes apparent that the group  $G$  with a constrained *BF* action can successfully describe ordinary gauge vector bosons, while the so-called Poincaré 2-group with a constrained *2BF* action can successfully describe general relativity. However, neither of these can suitably accomodate matter fields, such as fermions or scalars. Nevertheless, it turns out that this can be remedied if we make one further step in the categorical ladder, passing from the notion of a 2-group to the notion of a 3-group. As we shall see in the next Section, the notion of a 3-group will prove to be an excellent structure for the description of all fields that are present in the Standard Model, coupled to Einstein-Cartan gravity. Moreover, a 3-group contains one more gauge group, which is novel and specifies the spectrum of scalar and fermion fields present in the theory. This is an unexpected and beautiful result, absent from ordinary gauge theory.

Applying the categorical ladder once more, one can introduce the notion of a 3-group in the framework of higher category theory, as a 3-category with only one object where all the morphisms, 2-morphisms and 3-morphisms are invertible. Also, the equivalence between a 2-group and a crossed module has been generalized to the equivalence between a strict 3-group and a *2-crossed module* [23]. A Lie 2-crossed module, denoted as  $(L \xrightarrow{\delta} H \xrightarrow{\partial} G, \triangleright, \{-, -\})$ , is an algebraic structure specified by three Lie groups  $G, H$  and  $L$ , together with the homomorphisms  $\delta$  and  $\partial$ , an action  $\triangleright$  of the group  $G$  on all three groups, and a  $G$ -equivariant map

$$\{-, -\} : H \times H \rightarrow L.$$

called the Peiffer lifting. The maps  $\partial$ ,  $\delta$ ,  $\triangleright$  and the Peiffer lifting satisfy certain axioms, so that the resulting structure is equivalent to a 3-group [13].

Based on a given 2-crossed module  $(L \xrightarrow{\delta} H \xrightarrow{\partial} G, \triangleright, \{-, -\})$ , one can introduce a gauge invariant topological  $3BF$  action over the manifold  $\mathcal{M}_4$  as follows. Denoting  $\mathfrak{g}$ ,  $\mathfrak{h}$  and  $\mathfrak{l}$  as Lie algebras corresponding to the groups  $G$ ,  $H$  and  $L$ , respectively, the Lie 3-group structure allows one to introduce a 3-connection  $(\alpha, \beta, \gamma)$  given by the algebra-valued differential forms  $\alpha \in \Lambda^1(\mathcal{M}_4) \otimes \mathfrak{g}$ ,  $\beta \in \Lambda^2(\mathcal{M}_4) \otimes \mathfrak{h}$  and  $\gamma \in \Lambda^3(\mathcal{M}_4) \otimes \mathfrak{l}$ . The corresponding fake 3-curvature  $(\mathcal{F}, \mathcal{G}, \mathcal{H})$  is then defined as

$$\begin{aligned}\mathcal{F} &= d\alpha + \alpha \wedge \alpha - \partial\beta, & \mathcal{G} &= d\beta + \alpha \wedge^{\triangleright} \beta - \delta\gamma, \\ \mathcal{H} &= d\gamma + \alpha \wedge^{\triangleright} \gamma + \{\beta \wedge \beta\},\end{aligned}\quad (8)$$

see [23, 24] for details. Note that  $\gamma$  is a 3-form, while its corresponding field strength  $\mathcal{H}$  is a 4-form, requiring that the spacetime manifold be at least 4-dimensional. Also, for this reason, going beyond 3-groups and 4-groups in the categorical ladder does not have many applications in realistic 4-dimensional physics. A  $3BF$  action is defined as

$$S_{3BF} = \int_{\mathcal{M}_4} \langle B \wedge \mathcal{F} \rangle_{\mathfrak{g}} + \langle C \wedge \mathcal{G} \rangle_{\mathfrak{h}} + \langle D \wedge \mathcal{H} \rangle_{\mathfrak{l}}, \quad (9)$$

where  $B \in \Lambda^2(\mathcal{M}_4) \otimes \mathfrak{g}$ ,  $C \in \Lambda^1(\mathcal{M}_4) \otimes \mathfrak{h}$  and  $D \in \Lambda^0(\mathcal{M}_4) \otimes \mathfrak{l}$  are Lagrange multipliers valued in the respective algebras. Note that exclusively in 4 spacetime dimensions the Lagrange multiplier  $D$  corresponding to  $\mathcal{H}$  is a 0-form, i.e. a scalar function. As before, the bilinear forms  $\langle -, - \rangle_{\mathfrak{g}}$ ,  $\langle -, - \rangle_{\mathfrak{h}}$  and  $\langle -, - \rangle_{\mathfrak{l}}$  are  $G$ -invariant, nondegenerate and symmetric, over the algebras  $\mathfrak{g}$ ,  $\mathfrak{h}$  and  $\mathfrak{l}$ , respectively.

The equations of motion can be obtained by varying the action with respect to the multipliers  $B$ ,  $C$  and  $D$ ,

$$\mathcal{F} = 0, \quad \mathcal{G} = 0, \quad \mathcal{H} = 0, \quad (10)$$

and by varying with respect to the connections  $\alpha$ ,  $\beta$  and  $\gamma$ ,

$$\nabla B + C \wedge^{\mathcal{T}} \beta - D \wedge^{\mathcal{S}} \gamma = 0, \quad \nabla C - \partial B - D \wedge^{(\mathcal{X}_1 + \mathcal{X}_2)} \beta = 0, \quad \nabla D + \delta C = 0. \quad (11)$$

See [13] for the detailed definitions of the maps  $\mathcal{T}$ ,  $\mathcal{S}$ ,  $\mathcal{X}_1$  and  $\mathcal{X}_2$ .

### 3. The Standard Model 3-group

At this point we are finally ready to construct a realistic classical action, featuring the full Standard Model of elementary particles coupled to Einstein-Cartan gravity. The action is based on a so-called Standard Model 3-group, which is a 2-crossed module  $(L \xrightarrow{\delta} H \xrightarrow{\partial} G, \triangleright, \{-, -\})$  with a following choices for the Lie groups:

$$\begin{aligned}G &= SO(3,1) \times SU(3) \times SU(2) \times U(1), & H &= \mathbb{R}^4, \\ L &= \mathbb{C}^4 \times \mathbb{G}^{64} \times \mathbb{G}^{64} \times \mathbb{G}^{64}.\end{aligned}$$

We choose the group  $G$  as a product of the Lorentz group and the usual internal gauge symmetry group of the Standard Model. The group  $H$  is chosen to be the group of spacetime translations, motivated by the Poincaré 2-group construction [12]. Finally, we choose the group  $L$  as a product of  $\mathbb{C}^4$  accounting for the doublet of complex scalar fields, and three copies of the 64-dimensional Grassmann algebra  $\mathbb{G}^{64}$ , representing three families of fermions. The maps  $\delta$ ,  $\partial$  and  $\{-, -\}$  are

trivial, while the map  $\triangleright$  is chosen in a natural way, in accord with the usual action of the gauge group  $G$  onto translations and various components of matter fields. It is defined in detail in [13].

Once the 3-group has been completely specified, the corresponding action can be written as a  $3BF$  action with suitable constraint terms, as follows:

$$\begin{aligned}
S = & \int \overbrace{B_\alpha \wedge F^\alpha + B^{[ab]} \wedge R_{[ab]} + e_a \wedge \nabla \beta^a}^{\langle B \wedge \mathcal{F} \rangle} + \overbrace{\phi^A (\nabla \gamma)_A + \bar{\psi}_A (\overrightarrow{\nabla} \gamma)^A - (\bar{\gamma} \overleftarrow{\nabla})_A \psi^A}^{\langle D \wedge \mathcal{H} \rangle} & 3BF \\
& - \int \lambda_{[ab]} \wedge \left( B^{[ab]} - \frac{1}{16\pi l_p^2} \varepsilon^{[ab]cd} e_c \wedge e_d \right) + \frac{1}{96\pi l_p^2} \Lambda \varepsilon_{abcd} e^a \wedge e^b \wedge e^c \wedge e^d & \text{GR and CC} \\
& + \int \lambda^\alpha \wedge \left( B_\alpha - 12 C_\alpha^\beta M_{\beta ab} e^a \wedge e^b \right) + \zeta^{\alpha ab} \left( M_{\alpha ab} \varepsilon_{cdef} e^c \wedge e^d \wedge e^e \wedge e^f - F_\alpha \wedge e_a \wedge e_b \right) & \text{YM} \\
& + \int \lambda^A \wedge \left( \gamma_A - H_{abcA} e^a \wedge e^b \wedge e^c \right) + \Lambda^{abA} \wedge \left( H_{abcA} \varepsilon^{cdef} e_d \wedge e_e \wedge e_f - (\nabla \phi)_A \wedge e_a \wedge e_b \right) & \text{Higgs} \\
& - \int \frac{1}{12} \chi \left( \phi^A \phi_A - v^2 \right)^2 \varepsilon_{abcd} e^a \wedge e^b \wedge e^c \wedge e^d & \text{Higgs potential} \\
& + \int \bar{\lambda}_A \wedge \left( \gamma^A + \frac{i}{6} \varepsilon_{abcd} e^a \wedge e^b \wedge e^c \left( \gamma^d \psi \right)^A \right) - \lambda^A \wedge \left( \bar{\gamma}_A - \frac{i}{6} \varepsilon_{abcd} e^a \wedge e^b \wedge e^c \left( \bar{\psi} \gamma^d \right)_A \right) & \text{Dirac} \\
& - \int \frac{1}{12} Y_{ABC} \bar{\psi}^A \psi^B \phi^C \varepsilon_{abcd} e^a \wedge e^b \wedge e^c \wedge e^d & \text{Yukawa} \\
& + \int 2\pi i l_p^2 \bar{\psi}_A \gamma_5 \gamma^a \psi^A \varepsilon_{abcd} e^b \wedge e^c \wedge \beta^d. & \text{spin-torsion}
\end{aligned}$$

Here the first row represents the topological  $3BF$  part, while the remaining rows represent various constraint terms, each corresponding to one sector of the theory. Taking all together, the equations of motion obtained from the action  $S$  are equivalent to the full set of equations of motion for all Standard Model fields, coupled to the Einstein-Cartan theory of gravity.

The key novelty of the above structure is the role of the group  $L$ , which prescribes the spectrum of scalar and fermion fields present in the theory, via the  $\langle D \wedge \mathcal{H} \rangle$  term in the topological sector of the action.

#### 4. Conclusions

Let us summarize the results of the paper. In Section 2 we have introduced the  $nBF$  theories for  $n = 1, 2, 3$ , and explained in brief terms how the categorical ladder procedure can be applied to generalize the notion of a group to the notions of a 2-group and a 3-group, which represent more powerful ways to describe the gauge symmetry of a physical theory. These structures were employed in Section 3 to construct the constrained  $3BF$  action for the Standard Model of elementary particles coupled to the Einstein-Cartan gravity in the usual way. Within that framework, the spectrum of scalar and fermion fields happens to be determined by a *new gauge group*, in a way similar to that of the ordinary gauge group determining the spectrum of gauge vector bosons in Yang-Mills theory. This opens up a very interesting possibility of applying the structure of a 3-group to classify matter fields, and possibly gain some insight into why there are three families of fermions.

These results complete the first step of the spinfoam quantization programme, as outlined in the Introduction. The second step has also been performed in [25], for a general case of a Lie 2-crossed module  $(L \xrightarrow{\delta} H \xrightarrow{\partial} G, \triangleright, \{-, -\})$ . The resulting state sum is a novel topological

invariant of a 4-dimensional manifold, and has the following form:

$$\begin{aligned}
Z &= |G|^{-|\Lambda_0|+|\Lambda_1|-|\Lambda_2|} |H|^{|\Lambda_0|-|\Lambda_1|+|\Lambda_2|-|\Lambda_3|} |L|^{-|\Lambda_0|+|\Lambda_1|-|\Lambda_2|+|\Lambda_3|-|\Lambda_4|} \\
&\times \prod_{(jk)\in\Lambda_1} \int_G dg_{jk} \prod_{(jkl)\in\Lambda_2} \int_H dh_{jkl} \prod_{(jklm)\in\Lambda_3} \int_L dl_{jklm} \\
&\times \prod_{(jkl)\in\Lambda_2} \delta_G \left( \partial(h_{jkl}) g_{kl} g_{jk} g_{jl}^{-1} \right) \prod_{(jklm)\in\Lambda_3} \delta_H \left( \delta(l_{jklm}) h_{jlm} (g_{lm} \triangleright h_{jkl}) h_{klm}^{-1} h_{jkm}^{-1} \right) \\
&\times \prod_{(jklmn)\in\Lambda_4} \delta_L \left( l_{jlmn}^{-1} h_{jln} \triangleright' \{ h_{lmn}, (g_{mn} g_{lm}) \triangleright h_{jkl} \}_P l_{jklm}^{-1} (h_{jkn} \triangleright' l_{klmn}) l_{jkmn} h_{jmn} \triangleright' (g_{mn} \triangleright l_{jklm}) \right).
\end{aligned} \tag{12}$$

Here  $g_{ij}$ ,  $h_{ijk}$ ,  $l_{ijkl}$  are elements from groups  $G$ ,  $H$ ,  $L$ , respectively, which are assigned to simplices of the triangulation whose vertices are numerated by indices  $i, j, \dots$ . In other words,  $g_{ij}$  are assigned to edges,  $h_{ijk}$  are assigned to triangles, and  $l_{ijkl}$  are assigned to tetrahedra of the simplicial complex representing a compact 4-manifold, which has a total number of  $\Lambda_0$  vertices,  $\Lambda_1$  edges,  $\Lambda_2$  triangles,  $\Lambda_3$  tetrahedra, and  $\Lambda_4$  4-simplices.

Of course, when building a realistic theory, we are in fact not interested in a topological theory, but instead in a theory which contains local propagating degrees of freedom. Thus the state sum  $Z$  should be appropriately deformed. This is the task of step 3 of the spinfoam quantization programme, by imposing the simplicity constraints on  $Z$ . The classical action from Section 3 manifestly distinguishes the topological sector from the simplicity constraints. Imposing those constraints should thus complete the spinfoam quantization programme, and would ultimately lead us to a tentative model of quantum gravity with matter, by providing a rigorous definition for the path integral

$$Z = \int \mathcal{D}g \int \mathcal{D}\phi e^{iS[g,\phi]}, \tag{13}$$

which is a generalization of (1) in the sense that it contains matter fields as well as gravity, at the quantum level.

In addition to the construction of a full quantum theory of gravity, there are also many additional possible studies of the classical constrained  $3BF$  action. For example, a full Hamiltonian analysis of the  $3BF$  action has been done for the example of scalar electrodynamics [26], and then also for a general choice of a Lie 3-group [27], and the complete gauge symmetry group has been discussed in detail [27, 28]. Also, it is worth looking into the idea of imposing the simplicity constraints using a spontaneous symmetry breaking mechanism, and some work has already begun in this area. Finally, one can also study in more depth the mathematical structure and properties of the simplicity constraints. The list is not conclusive, and there may be many other interesting topics to study.

## Acknowledgments

This research was supported by the Ministry of Science, Technological Development and Innovations of the Republic of Serbia, and by the Science Fund of the Republic of Serbia, grant 7745968, ‘‘Quantum Gravity from Higher Gauge Theory 2021’’ — QGHG-2021. The contents of this publication are the sole responsibility of the authors and can in no way be taken to reflect the views of the Science Fund of the Republic of Serbia.

## References

- [1] Rovelli C 2004 *Quantum Gravity* (Cambridge University Press: Cambridge)
- [2] Rovelli C and Vidotto F 2014 *Covariant Loop Quantum Gravity* (Cambridge University Press: Cambridge)
- [3] Thiemann T 2007 *Modern Canonical Quantum General Relativity* (Cambridge University Press: Cambridge)
- [4] Ponzano G and Regge T 1968 *Semiclassical limit of Racah coefficients* (Spectroscopic and Group Theoretical Methods in Physics) ed F Bloch (Amsterdam: North Holland)

- [5] Barrett J W and Crane L 1998 *J. Math. Phys.* **39** 3296
- [6] Barrett J W and Crane L 2000 *Class. Quant. Grav.* **17** 3101
- [7] Ooguri H 1992 *Mod. Phys. Lett. A* **7** 279
- [8] Engle J, Livine E R, Pereira R and Rovelli C 2008 *Nucl. Phys.* **B799** 136
- [9] Freidel L and Krasnov K 2008 *Class. Quant. Grav.* **25** 125018
- [10] Bianchi E, Han M, Magliaro E, Perini C, Rovelli C and Wieland W 2013 *Class. Quantum Grav.* **30** 235023
- [11] Baez J C and Huerta J 2011 *Gen. Relativ. Gravit.* **43** 2335
- [12] Miković A and Vojinović M 2012 *Class. Quant. Grav.* **29** 165003
- [13] Radenković T and Vojinović M 2019 *JHEP* **10** 222
- [14] Celada M, González D and Montesinos M 2016 *Class. Quant. Grav.* **33** 213001
- [15] Rovelli C 2011 Zakopane lectures on loop gravity *Preprint* arXiv:1102.3660
- [16] Plebanski J F 1977 *J. Math. Phys.* **18** 2511
- [17] Girelli F, Pfeiffer H and Popescu E M 2008 *Jour. Math. Phys.* **49** 032503
- [18] Martins J F and Miković A 2011 *Adv. Theor. Math. Phys.* **15** 1059
- [19] Crane L and Sheppeard M D 2003 2-categorical Poincare Representations and State Sum Applications *Preprint* math/0306440
- [20] Miković A and Oliveira M A 2015 *Gen. Relativ. Gravit.* **47** 58
- [21] Miković A, Oliveira M A and Vojinović M 2016 Hamiltonian analysis of the BFCG theory for a generic Lie 2-group *Preprint* arXiv:1610.09621
- [22] Miković A, Oliveira M A and Vojinović M 2019 *Class. Quant. Grav.* **36** 015005
- [23] Martins J F and Picken R 2011 *Differ. Geom. Appl. Journal* **29** 179
- [24] Wang W 2014 *Jour. Math. Phys.* **55** 043506
- [25] Radenković T and Vojinović M 2022 *JHEP* **7** 105
- [26] Radenković T and Vojinović M 2020 *Symmetry* **12** 620
- [27] Radenković T and Vojinović M 2022 *Class. Quant. Grav.* **39** 135009
- [28] Djordjević M, Radenković T, Stipsić P and Vojinović M 2023 *Universe* **9** 281

Home > Lie Theory and Its Applications in Physics > Conference paper

# $sl(2)$ Gaudin Model with General Boundary Terms

Conference paper | First Online: 30 January 2023

pp 371–379 | [Cite this conference paper](#)



**Lie Theory and Its Applications in Physics**  
(LT 2021)

I. Salom & N. Manojlović

Part of the book series: [Springer Proceedings in Mathematics & Statistics](#) ((PROMS, volume 396))

Included in the following conference series:  
[International Workshop on Lie Theory and Its Applications in Physics](#)

834 Accesses

## Abstract

We study the  $sl(2)$  Gaudin model with general boundary K-matrix in the framework of the algebraic Bethe ansatz. The off-shell action of the generating function of the  $so(3)$  Gaudin Hamiltonians is determined without any restriction whatsoever on the boundary parameters.

This is a preview of subscription content, [log in via an institution](#) to check access.

### Access this chapter

Log in via an institution

### Subscribe and save

Springer+ Basic €32.70 /Month

- Get 10 units per month
- Download Article/Chapter or eBook
- 1 Unit = 1 Article or 1 Chapter
- Cancel anytime

Subscribe now →

### Buy Now

Chapter EUR 29.95 Price includes VAT (Serbia) eBook EUR 192.59 Softcover Book EUR 229.99

- Available as PDF
- Read on any device
- Instant download
- Own it forever

Buy Chapter



# $sl(2)$ Gaudin model with general boundary terms

I. Salom and N. Manojlović

**Abstract** We study the  $sl(2)$  Gaudin model with general boundary K-matrix in the framework of the algebraic Bethe ansatz. The off-shell action of the generating function of the  $so(3)$  Gaudin Hamiltonians is determined without any restriction whatsoever on the boundary parameters.

## 1 Introduction

In the framework of the Bethe ansatz, Gaudin has studied the system obtained as the quasi-classical limit of the Heisenberg spin chain [1, 2]. This system has been recast in the framework of the quantum inverse scattering method with the help of the so-called Sklyanin linear bracket, corresponding to an  $sl(2)$  invariant, unitary classical r-matrix [3]. This result enabled further generalizations based on other unitary solutions to the classical Yang-Baxter equation corresponding to higher-rank simple Lie algebras as well as Lie superalgebras [4–6] and the corresponding Jordanian deformation [7–9].

In our considerations of the non-periodic rational as well as trigonometric Gaudin model we have studied them as the quasi-classical limit, respectively, of the open XXX and XXZ Heisenberg spin chains [10, 11]. Also, we have shown how the expansion of the XXZ transfer matrix, calculated at the special values of the spectral parameter, yields the Gaudin Hamiltonians in the

---

I. Salom

Institute of Physics, University of Belgrade, P.O. Box 57, 11080 Belgrade, Serbia,  
e-mail: isalom@ipb.ac.rs

N. Manojlović

Departamento de Matemática, Faculdade de Ciências e Tecnologia, Universidade do Algarve, Campus de Gambelas, PT-8005-139 Faro, Portugal and Grupo de Física Matemática da Universidade de Lisboa, Faculdade de Ciências, Campo Grande, Edifício C6, PT-1749-016 Lisboa, Portugal e-mail: nmanoj@ualg.pt

trigonometric case [12] as well as for the Jordanian deformation of the rational  $sl(2)$  Gaudin model with generic boundaries [13]. Returning back to the quasi-classical limit, following the Sklyanin proposal for the periodic boundary conditions [3, 14], we have derived the generating function of the Gaudin Hamiltonians both for the XXX [10], the XXZ chain [11] and for the Jordanian deformation of the XXX Heisenberg spin chain [15]. Moreover, we have shown [16] how, in the context of the quasi-classical limit, the solutions to the classical Yang-Baxter equation can be combined with the solutions to the classical reflection equation to yield solutions to the so-called generalized classical Yang-Baxter equation. These solutions are the non-unitary classical r-matrices [17]. In particular, the generic elliptic  $sl(2)$  non-unitary r-matrix was studied in [18]. Also, we have developed an approach to the implementation of the algebraic Bethe ansatz for the rational as well as the trigonometric  $sl(2)$  Gaudin model, in the case when the classical boundary K-matrix has a triangular form [19–22].

Following our approach to the generic  $so(3)$  Gaudin [23, 24], here we study the non-periodic  $sl(2)$  Gaudin model with the general boundary K-matrix. Namely, we show that it is possible to keep all of the K-matrix parameters arbitrary, though this requires a more complex form of the vacuum state.

The paper is organized as follows. In Section 2 we study the  $sl(2)$  linear bracket which provides the algebraic framework for implementation of the Bethe ansatz. In the same section we propose the novel set of generators with simplified commutation relations. In Section 3 we will introduce an explicit form of the vacuum state which, together with the suitable choice of algebra generators, allows the implementation of the algebraic Bethe ansatz without reducing generality of the K-matrix. In this way, we will finally obtain the expression for the off-shell action of the generating function of the  $sl(2)$  Gaudin Hamiltonians with general boundary terms.

## 2 The $sl(2)$ linear bracket

We consider the classical r-matrix

$$r(\lambda) = -\frac{\mathcal{P}}{\lambda}, \quad (1)$$

where  $\mathcal{P}$  is the permutation matrix in  $\mathbb{C}^2 \otimes \mathbb{C}^2$ . This classical r-matrix (1) has the unitarity property

$$r_{21}(-\lambda) = -r_{12}(\lambda), \quad (2)$$

and it satisfies the classical Yang-Baxter equation

$$[r_{12}(\lambda-\mu), r_{13}(\lambda-\nu)] + [r_{12}(\lambda-\mu), r_{23}(\mu-\nu)] + [r_{13}(\lambda-\nu), r_{23}(\mu-\nu)] = 0. \quad (3)$$

The corresponding Gaudin Lax matrix is defined by [3]

$$L_0(\lambda) = \sum_{m=1}^N \frac{\vec{\sigma}_0 \cdot \vec{S}_m}{\lambda - \alpha_m}, \quad (4)$$

as usual,  $\{\alpha_m, m = 1, \dots, N\}$  are the inhomogeneous parameters,  $\sigma_0^\alpha$ , with  $\alpha = +, -, 3$ , are the Pauli matrices

$$\sigma^\alpha = \begin{pmatrix} \delta_{\alpha 3} & 2\delta_{\alpha +} \\ 2\delta_{\alpha -} & -\delta_{\alpha 3} \end{pmatrix}, \quad (5)$$

in the auxiliary space  $V_0 = \mathbb{C}^2$  and the spin  $\frac{1}{2}$  operators  $S^\alpha = \frac{1}{2}\sigma^\alpha$  are acting on the local space  $V_m = \mathbb{C}^2$  at each site of the chain

$$S_m^\alpha = 1 \otimes \dots \otimes \underbrace{S_m^\alpha}_m \otimes \dots \otimes 1, \quad (6)$$

with  $\alpha = +, -, 3$  and  $m = 1, 2, \dots, N$ . The Gaudin Lax matrix (4) and the classical r-matrix (1) obey the so-called Sklyanin linear bracket [3]

$$[L_1(\lambda), L_2(\mu)] = [r_{12}(\lambda - \mu), L_1(\lambda) + L_2(\mu)]. \quad (7)$$

The next step is the generalization of the model by introduction of the  $K$ -matrix, which must satisfy the reflection equation. The general, spectral parameter dependent solutions of the classical reflection equation [10]:

$$\begin{aligned} r_{12}(\lambda - \mu)K_1(\lambda)K_2(\mu) + K_1(\lambda)r_{21}(\lambda + \mu)K_2(\mu) = \\ = K_2(\mu)r_{12}(\lambda + \mu)K_1(\lambda) + K_2(\mu)K_1(\lambda)r_{21}(\lambda - \mu), \end{aligned} \quad (8)$$

where the classical r-matrix is the one given in (1), can be written as follows [10]

$$K(\lambda) = \begin{pmatrix} \xi - \lambda & \psi\lambda \\ \phi\lambda & \xi + \lambda \end{pmatrix}. \quad (9)$$

Moreover, by introducing the non-unitary, classical r-matrix [16]

$$r_{12}^K(\lambda, \mu) = r_{12}(\lambda - \mu) - K_2(\mu)r_{12}(\lambda + \mu)K_2^{-1}(\mu), \quad (10)$$

the two equations (3) and (8) can be combined into the generalized classical Yang-Baxter equation [16]

$$[r_{32}^K(\nu, \mu), r_{13}^K(\lambda, \nu)] + [r_{12}^K(\lambda, \mu), r_{13}^K(\lambda, \nu)] + [r_{12}^K(\lambda, \mu), r_{23}^K(\mu, \nu)] = 0. \quad (11)$$

As we have shown [16], the appropriate Lax matrix is given by

$$\begin{aligned}\mathcal{L}_0(\lambda) &= L_0(\lambda) - K_0(\lambda)L_0(-\lambda)K_0^{-1}(\lambda) = \begin{pmatrix} H(\lambda) & F(\lambda) \\ E(\lambda) & -H(\lambda) \end{pmatrix} \\ &= \sum_{m=1}^N \left( \frac{\vec{\sigma}_0 \cdot \vec{S}_m}{\lambda - \alpha_m} + \frac{K_0(\lambda)\vec{\sigma}_0 K_0^{-1}(\lambda) \cdot \vec{S}_m}{\lambda + \alpha_m} \right).\end{aligned}\quad (12)$$

The corresponding linear bracket based on the  $r$ -matrix  $r^K(\lambda, \mu)$  (10) is defined by [16]

$$[\mathcal{L}_0(\lambda), \mathcal{L}_{0'}(\mu)] = [r_{00'}^K(\lambda, \mu), \mathcal{L}_0(\lambda)] - [r_{0'0}^K(\mu, \lambda), \mathcal{L}_{0'}(\mu)]. \quad (13)$$

This linear bracket is obviously anti-symmetric and it obeys the Jacobi identity because the  $r$ -matrix  $r_{00'}^K(\lambda, \mu)$  (10) satisfies the generalized classical Yang-Baxter equation (11).

As it is well known [16], the linear bracket (13) yields the expression for the generating function of the  $sl(2)$  Gaudin Hamiltonians with general boundary terms in terms of the Lax operator (12)

$$\tau(\lambda) = \frac{1}{2} \text{tr}_0 (\mathcal{L}_0^2(\lambda)) = H^2(\lambda) + \frac{1}{2} (E(\lambda)F(\lambda) + F(\lambda)E(\lambda)). \quad (14)$$

Using the bracket (13), it is straightforward to check that the operator  $\tau(\lambda)$  commutes for different values of the spectral parameter

$$[\tau(\lambda), \tau(\mu)] = 0. \quad (15)$$

Our aim here is to study the Gaudin system without any restriction whatsoever on the boundary parameters. Consequently, the commutation relations for the generators  $H(\lambda)$ ,  $E(\lambda)$  and  $F(\lambda)$  turn out to be long and cumbersome and, thus, we will not present them here. Technically, these commutation relations are the principal difficulty in implementing the algebraic Bethe ansatz in this, fully general, case. To overcome this problem we propose the new set of generators

$$\mathcal{H}(\lambda) = \frac{1}{2\nu} (2H(\lambda) - \varphi F(\lambda) - \psi E(\lambda)), \quad (16)$$

$$\mathcal{E}(\lambda) = -\frac{1-\nu}{2\nu} \left( 2H(\lambda) - \frac{\varphi}{1+\nu} F(\lambda) - \frac{\psi}{1-\nu} E(\lambda) \right), \quad (17)$$

$$\mathcal{F}(\lambda) = \frac{1+\nu}{2\nu} \left( 2H(\lambda) - \frac{\varphi}{1-\nu} F(\lambda) - \frac{\psi}{1+\nu} E(\lambda) \right). \quad (18)$$

The commutation relations for the new generators are substantially simpler than the relations for the initial generators. In particular,

$$[\mathcal{E}(\lambda), \mathcal{E}(\mu)] = [\mathcal{F}(\lambda), \mathcal{F}(\mu)] = [\mathcal{H}(\lambda), \mathcal{H}(\mu)] = 0, \quad (19)$$

and the three non-trivial relations are

$$[\mathcal{H}(\lambda), \mathcal{E}(\mu)] = \frac{-2}{\lambda^2 - \mu^2} \left( \mu \frac{\xi - \lambda\nu}{\xi - \mu\nu} \mathcal{E}(\lambda) - \lambda \mathcal{E}(\mu) \right), \quad (20)$$

$$[\mathcal{H}(\lambda), \mathcal{F}(\mu)] = \frac{2}{\lambda^2 - \mu^2} \left( \mu \frac{\xi + \lambda\nu}{\xi + \mu\nu} \mathcal{F}(\lambda) - \lambda \mathcal{F}(\mu) \right), \quad (21)$$

$$[\mathcal{E}(\lambda), \mathcal{F}(\mu)] = \frac{-4}{\lambda^2 - \mu^2} \left( \mu \frac{\xi + \lambda\nu}{\xi + \mu\nu} \mathcal{H}(\lambda) - \lambda \frac{\xi - \mu\nu}{\xi - \lambda\nu} \mathcal{H}(\mu) \right). \quad (22)$$

A straightforward but somewhat lengthy calculation shows that the generating function  $\tau(\lambda)$  (14) has exactly the same form when expressed in terms of the new generators

$$\tau(\lambda) = \mathcal{H}^2(\lambda) + \frac{1}{2} (\mathcal{E}(\lambda)\mathcal{F}(\lambda) + \mathcal{F}(\lambda)\mathcal{E}(\lambda)). \quad (23)$$

Our main result in this section are the new generators of the generalized  $sl(2)$  Gaudin algebra (16) – (18). Due to their strikingly simple commutation relations (19) – (22) they provide a suitable framework for applying the algebraic Bethe ansatz without any restrictions on boundary parameters.

### 3 Implementation of the algebraic Bethe ansatz

A necessary prerequisite for the implementation of the algebraic Bethe ansatz is the existence of an appropriate vacuum vector  $\Omega_+ \in \mathcal{H}$  in the Hilbert space

$$\mathcal{H} = \bigotimes_{m=1}^N V_m = (\mathbb{C}^2)^{\otimes N}. \quad (24)$$

The standard approach relies on its property to be annihilated by one of the algebra generators – usually:  $\mathcal{E}(\lambda) \Omega_+ = 0$ . To this end we obtain the local representation of the generators (16) – (18):

$$\mathcal{H}(\lambda) = \frac{\lambda}{\nu} \sum_{m=1}^N \frac{2S_m^3 - \psi S_m^+ - \varphi S_m^-}{(\lambda - \alpha_m)(\lambda + \alpha_m)}, \quad (25)$$

$$\mathcal{E}(\lambda) = \frac{-\lambda(1 - \nu)}{\nu} \sum_{m=1}^N \frac{\xi - \alpha_m \nu}{\xi - \lambda \nu} \frac{2S_m^3 - \frac{\psi}{1 - \nu} S_m^+ - \frac{\varphi}{1 + \nu} S_m^-}{(\lambda - \alpha_m)(\lambda + \alpha_m)}, \quad (26)$$

$$\mathcal{F}(\lambda) = \frac{\lambda(1 + \nu)}{\nu} \sum_{m=1}^N \frac{\xi + \alpha_m \nu}{\xi + \lambda \nu} \frac{2S_m^3 - \frac{\psi}{1 + \nu} S_m^+ - \frac{\varphi}{1 - \nu} S_m^-}{(\lambda - \alpha_m)(\lambda + \alpha_m)}. \quad (27)$$

A simple approach to ensure  $\mathcal{E}(\lambda) \Omega_+ = 0$  is by fixing some of the  $K$ -matrix parameters – e.g. setting  $\phi = 0$  and choosing the vacuum state as the tensorial product of highest spin states in each of the local spaces  $V_m$  [22]. Another approach, allowing for general boundary parameter in a set of special cases can be found in [25].

However, here we show that, for the  $sl(2)$  Gaudin model, it is possible to retain the full generality of the  $K$ -matrix parameters by choosing a somewhat more complicated vacuum vector. To this purpose we observe that in every local space  $V_m = \mathbb{C}^2$ ,  $m \in \{1, \dots, N\}$  there exists a vector  $\omega_m \in V_m$  given by

$$\omega_m = \begin{pmatrix} \frac{\psi}{1 - \sqrt{1 + \psi\varphi}} \\ 1 \end{pmatrix} \in \mathbb{C}^2 = V_m, \quad (28)$$

where the parameters  $\nu$ ,  $\psi$  and  $\varphi$  are the parameters of the boundary  $K$ -matrix (9). Then it is easy to check that

$$\left( 2S_m^3 - \frac{\psi}{1 - \nu} S_m^+ - \frac{\varphi}{1 + \nu} S_m^- \right) \omega_m = 0, \quad (29)$$

$$(2S_m^3 - \psi S_m^+ - \varphi S_m^-) \omega_m = \nu \omega_m. \quad (30)$$

Therefore the vacuum vector  $\Omega_+$ , defined as

$$\Omega_+ = \omega_1 \otimes \dots \otimes \omega_N \in \mathcal{H} \quad (31)$$

is annihilated by the generator  $\mathcal{E}(\lambda)$  (26) and, at the same time, it is an eigenvector of the generator  $\mathcal{H}(\lambda)$  (25), that is

$$\mathcal{E}(\lambda) \Omega_+ = 0 \quad \text{and} \quad \mathcal{H}(\lambda) \Omega_+ = \rho(\lambda) \Omega_+ \quad \text{with} \quad \rho(\lambda) = \sum_{m=1}^N \frac{\lambda}{\lambda^2 - \alpha_m^2}. \quad (32)$$

Our next aim is to rewrite the formula for  $\tau(\lambda)$  (23) in a more suitable way so that the action of the generating function  $\tau(\lambda)$  on the vacuum vector  $\Omega_+$  (31) becomes more transparent. As it can be shown, the generating function  $\tau(\lambda)$  (23) can be expressed as follows

$$\tau(\lambda) = \mathcal{H}^2(\lambda) + \frac{1}{\lambda} \frac{\xi^2 + \lambda^2 \nu^2}{\xi^2 - \lambda^2 \nu^2} \mathcal{H}(\lambda) - \mathcal{H}'(\lambda) + \mathcal{F}(\lambda) \mathcal{E}(\lambda). \quad (33)$$

Taking into account (32) and (33), it is evident that the vacuum vector  $\Omega_+$  (31) is an eigenvector of the generating function

$$\tau(\lambda) \Omega_+ = \chi_0(\lambda) \Omega_+ \quad \text{with} \quad \chi_0(\lambda) = \rho^2(\lambda) + \frac{\xi^2 + \lambda^2 \nu^2}{\xi^2 - \lambda^2 \nu^2} \frac{\rho(\lambda)}{\lambda} - \rho'(\lambda). \quad (34)$$



Now we can compute the commutator by a straightforward calculation, based on the formulae (33), (21) and (22)

$$\begin{aligned} [\tau(\lambda), \mathcal{F}(\mu)] &= -\frac{4}{\lambda^2 - \mu^2} \mathcal{F}(\mu) \left( \lambda \mathcal{H}(\lambda) + \frac{\lambda^2 \nu^2}{\xi^2 - \lambda^2 \nu^2} \right) \\ &\quad + \frac{4}{\lambda^2 - \mu^2} \frac{\lambda}{\mu} \frac{\xi - \mu \nu}{\xi - \lambda \nu} \mathcal{F}(\lambda) \left( \mu \mathcal{H}(\mu) + \frac{\mu^2 \nu^2}{\xi^2 - \mu^2 \nu^2} \right). \end{aligned} \quad (35)$$

The relative simplicity of the right hand side of the equation above has encouraged us to seek the commutator between the operator  $\tau(\lambda)$  and the product  $\mathcal{F}(\mu_1)\mathcal{F}(\mu_2)$  as the next step. In this case, an analogous direct calculation based on the previous formulae, leads to

$$\begin{aligned} [\tau(\lambda), \mathcal{F}(\mu_1)\mathcal{F}(\mu_2)] &= -\frac{4}{\lambda^2 - \mu_1^2} \mathcal{F}(\mu_1)\mathcal{F}(\mu_2) \left( \lambda \mathcal{H}(\lambda) + \frac{\lambda^2 \nu^2}{\xi^2 - \lambda^2 \nu^2} - \frac{\lambda^2}{\lambda^2 - \mu_2^2} \right) \\ &\quad - \frac{4}{\lambda^2 - \mu_2^2} \mathcal{F}(\mu_1)\mathcal{F}(\mu_2) \left( \lambda \mathcal{H}(\lambda) + \frac{\lambda^2 \nu^2}{\xi^2 - \lambda^2 \nu^2} - \frac{\lambda^2}{\lambda^2 - \mu_1^2} \right) \\ &\quad + \frac{4}{\lambda^2 - \mu_1^2} \frac{\lambda}{\mu_1} \frac{\xi - \mu_1 \nu}{\xi - \lambda \nu} \mathcal{F}(\lambda)\mathcal{F}(\mu_2) \left( \mu_1 \mathcal{H}(\mu_1) + \frac{\mu_1^2 \nu^2}{\xi^2 - \mu_1^2 \nu^2} - \frac{2\mu_1^2}{\mu_1^2 - \mu_2^2} \right) \\ &\quad + \frac{4}{\lambda^2 - \mu_2^2} \frac{\lambda}{\mu_2} \frac{\xi - \mu_2 \nu}{\xi - \lambda \nu} \mathcal{F}(\mu_1)\mathcal{F}(\lambda) \left( \mu_2 \mathcal{H}(\mu_2) + \frac{\mu_2^2 \nu^2}{\xi^2 - \mu_2^2 \nu^2} - \frac{2\mu_2^2}{\mu_2^2 - \mu_1^2} \right). \end{aligned} \quad (36)$$

From these relations it is not difficult to infer, and to prove by mathematical induction, e.g. as in [22] that, for an arbitrary natural number  $M$ , the off-shell action of the generating function  $\tau(\lambda)$  on the Bethe vectors takes the form:

$$\Phi_M(\mu_1, \mu_2, \dots, \mu_M) = \mathcal{F}(\mu_1)\mathcal{F}(\mu_2) \cdots \mathcal{F}(\mu_M)\Omega_+, \quad (37)$$

is given by

$$\begin{aligned} \tau(\lambda)\Phi_M(\mu_1, \mu_2, \dots, \mu_M) &= \chi_M(\lambda, \mu_1, \mu_2, \dots, \mu_M) \Phi_M(\mu_1, \mu_2, \dots, \mu_M) \\ &\quad + \sum_{j=1}^M \frac{4\lambda}{\lambda^2 - \mu_j^2} \frac{\xi - \mu_j \nu}{\xi - \lambda \nu} \left( \rho(\mu_j) + \frac{\mu_j \nu^2}{\xi^2 - \mu_j^2 \nu^2} - \sum_{k \neq j}^M \frac{2\mu_j}{\mu_j^2 - \mu_k^2} \right) \Phi_M(\lambda, \mu_1, \dots, \hat{\mu}_j, \dots, \mu_M), \end{aligned} \quad (38)$$

where the eigenvalue  $\chi_M(\lambda, \mu_1, \mu_2, \dots, \mu_M)$  is given by

$$\chi_M(\lambda, \mu_1, \mu_2, \dots, \mu_M) = \chi_0(\lambda) - \sum_{j=1}^M \frac{4\lambda}{\lambda^2 - \mu_j^2} \left( \rho(\lambda) + \frac{\lambda \nu^2}{\xi^2 - \lambda^2 \nu^2} - \sum_{k \neq j}^M \frac{\lambda}{\lambda^2 - \mu_k^2} \right). \quad (39)$$

The unwanted terms on the right hand side of (38) are annihilated once the Bethe equations

$$\rho(\mu_j) + \frac{\mu_j \nu^2}{\xi^2 - \mu_j^2 \nu^2} - \sum_{k \neq j}^M \frac{2\mu_j}{\mu_j^2 - \mu_k^2} = 0, \quad j = 1, 2, \dots, M, \quad (40)$$

are imposed on the parameters  $\mu_1, \mu_2, \dots, \mu_M$ .

## 4 Conclusion

The usual approaches to nontrivial boundary conditions for the  $sl(2)$  Gaudin model commonly require additional constraints on the  $K$ -matrix parameters [22], with the exception of some special cases for the trigonometric  $sl(2)$  Gaudin model [25]. In this paper, we have demonstrated that, by the suitable choices of generators of the generalized  $sl(2)$  Gaudin algebra and of the corresponding vacuum vector, it is possible to retain full generality of the  $K$ -matrix, i.e. without any restriction whatsoever on the boundary parameters. While here this was realized for fixed values of spin  $-\frac{1}{2}$  at each node, we believe that the approach can be further generalized to the case of arbitrary spins.

**Acknowledgements** The cooperation between IS and NM was supported by the bilateral project ‘‘Symmetry and Quantization’’, 337-00-00227/2019-09/57. IS is supported by the Ministry of Education, Science and Technological Development (MP-NTR) of the Republic of Serbia.

## References

1. M. Gaudin, *La fonction d'onde de Bethe*, Masson, Paris, 1983.
2. M. Gaudin, *The Bethe Wavefunction*, Cambridge University Press, 2014.
3. E. K. Sklyanin, *Zap. Nauchn. Semin.*, doi:10.1007/BF01840429
4. P. P. Kulish and N. Manojlovic, *Lett. Math. Phys.*, doi:10.1023/A:1010913532054
5. P. P. Kulish and N. Manojlovic, *J. Math. Phys.*, doi:10.1063/1.1398584
6. P. P. Kulish and N. Manojlovic, *J. Math. Phys.*, doi:10.1063/1.1531250
7. N. Cirilo António and N. Manojlović, *J. Math. Phys.*, doi:10.1063/1.2036932
8. P. P. Kulish, N. Manojlović, M. Samsonov and A. Stolin, *Bethe Ansatz for deformed Gaudin model*, (AGMF Tartu08 Workshop Proceedings) in the Proceedings of the Estonian Academy of Sciences **Vol 59** No. 4 (2010) 326–331.
9. N. Cirilo Antonio, N. Manojlovic and A. Stolin, *J. Math. Phys.*, doi:10.1063/1.3644345
10. N. Cirilo António, N. Manojlović and I. Salom, *Nucl. Phys. B*, doi:10.1016/j.nuclphysb.2014.10.014
11. N. Manojlović and I. Salom, *Nucl. Phys. B*, doi:10.1016/j.nuclphysb.2017.07.017

12. N. Cirilo António, N. Manojlović and Z. Nagy, *Rev. Math. Phys.*, doi:10.1142/S0129055X13430046
13. N. Cirilo António, N. Manojlović and Z. Nagy, *Theor. Math. Phys.*, doi:10.1007/s11232-014-0155-0
14. N. Manojlović, Z. Nagy and I. Salom, *Derivation of the trigonometric Gaudin Hamiltonians*, SFIN **XXVIII** Series A: Conferences No. A1(2015) 127–135; ISBN: 978-86-82441-43-4.
15. N. Manojlović, N. Cirilo António and I. Salom, *Quasi-classical limit of the open Jordanian XXX spin chain*, SFIN **XXXI** Series A: Conferences No. A1 (2018) 259–266; ISBN: 978-86-82441-48-9.
16. N. Cirilo António, N. Manojlović, E. Ragoucy and I. Salom, *Nucl. Phys. B*, doi:10.1016/j.nuclphysb.2015.02.011
17. T. Skrypnyk and N. Manojlović, *Nucl. Phys. B*, doi:10.1016/j.nuclphysb.2021.115424
18. N. Manojlovic, I. Salom and N. Cirilo António, *XYZ Gaudin model with boundary terms*, SFIN **XXXIII** Series A: Conferences, No. A1 (2020) 143 – 160; ISBN 978-86-82441-51-9.
19. I. Salom and N. Manojlović, *Creation operators of the non-periodic  $sl(2)$  Gaudin model*, SFIN **XXVIII** Series A: Conferences No. A1 (2015) 149–155; ISBN: 978-86-82441-43-4.
20. I. Salom, N. Manojlović and N. Cirilo António, *Nucl. Phys. B*, doi:10.1016/j.nuclphysb.2018.12.025
21. N. Manojlović and I. Salom, *Symmetry*, doi:10.3390/sym12030352.
22. I. Salom and N. Manojlović, *Nucl. Phys. B*, doi:10.1016/j.nuclphysb.2021.115462
23. I. Salom, N. Manojlovic and N. Cirilo António, *The spin 1 XXZ Gaudin model with boundary*, SFIN **XXXIII** Series A: Conferences, No. A1 (2020) 277 – 286; ISBN 978-86-82441-51-9.
24. N. Manojlović and I. Salom, *Rational  $so(3)$  Gaudin model with general boundary terms*, submitted to the Nuclear Physics **B**.
25. N. Crampé, *Symmetry, Integrability and Geometry: Methods and Applications*, doi:10.3842/SIGMA.2017.094

Home &gt; Lie Theory and Its Applications in Physics &gt; Conference paper

# Relativistic Three-Body Harmonic Oscillator

| Conference paper | First Online: 16 October 2020

| pp 473–480 | [Cite this conference paper](#)

**Lie Theory and Its Applications in  
Physics**  
(LT 2019)

Igor Salom &amp; V. Dmitrašinović

Part of the book series: [Springer Proceedings in Mathematics & Statistics](#) ((PROMS, volume 335))Included in the following conference series:  
[International Workshop on Lie Theory and Its Applications in Physics](#)

762 Accesses 1 Citations

## Abstract

We discuss the relativistic three-body harmonic oscillator problem, and show that in the extreme relativistic limit its energy spectrum is closely related to that of the non-relativistic three-body problem in the  $\Delta$ -string potential, which blurs the distinction between relativistic and confinement effects. This, perhaps unexpected, feature can be understood in terms of permutation properties of the two problems, and as such can be expected to persist in confining potentials other than the harmonic oscillator.

This is a preview of subscription content, [log in via an institution](#) to check access.

### Access this chapter

[Log in via an institution](#)

### Subscribe and save

 Springer+ Basic

€32.70 /Month

Get 10 units per month

Download Article/Chapter or eBook

1 Unit = 1 Article or 1 Chapter

Cancel anytime

[Subscribe now](#) →

### Buy Now

 ChapterEUR 29.95  
Price includes VAT (Serbia) eBook

EUR 117.69

 Softcover Book

EUR 149.99

Available as PDF

Read on any device

Instant download

Own it forever

[Buy Chapter](#)

# Relativistic Three-Body Harmonic Oscillator

Igor Salom and V. Dmitrašinović

**Abstract** We discuss the relativistic three-body harmonic oscillator problem, and show that in the extreme relativistic limit its energy spectrum is closely related to that of the non-relativistic three-body problem in the  $\Delta$ -string potential, which blurs the distinction between relativistic and confinement effects. This, perhaps unexpected, feature can be understood in terms of permutation properties of the two problems, and as such can be expected to persist in confining potentials other than the harmonic oscillator.

## 1 Introduction

The harmonic oscillator is the quintessential example of a solvable/integrable problem in physics, both classical and quantum. It is (always) understood to be non-relativistic, the (special) relativistic version being neither easily solvable, nor integrable in the formal sense of the word<sup>1</sup>. Consequently, the relativistic harmonic oscillator is mentioned only rarely in the literature. Nevertheless, it can be an instructive example, as we shall show below, especially in the (quantum mechanical) three-quark problem, where relativity is expected to play an important role, particularly in excited states.

Over the past five years, or so, we have developed an  $O(6)$  hyper-spherical harmonics (HSH) approach to the quantum-mechanical non-relativistic three-

---

Igor Salom  
Institute of Physics, University of Belgrade, Pregrevica 118, Zemun, 11080 Beograd,  
Serbia e-mail: isalom@ipb.ac.rs

V. Dmitrašinović  
Institute of Physics, University of Belgrade, Pregrevica 118, Zemun, 11080 Beograd,  
Serbia e-mail: dmitrasin@ipb.ac.rs

<sup>1</sup> Indeed, so-called relativistic “No Interaction Theorems” suggest that the interaction must vanish in a relativistic setting, see Sect. 5

body problem [1, 2, 3]. This approach relies on the fact that the non-relativistic kinetic energy has an  $O(6)$  symmetry, which is generally not shared by the three-body potential. In the case of the harmonic oscillator interaction, the potential shares the same  $O(6)$  symmetry, and in conjunction with the non-relativistic kinetic energy, leads to the higher  $U(6)$  dynamical symmetry, which ensures its super-integrability. What happens to this system when the motion becomes relativistic? We shall explore this question here, and show that (in the ultra-relativistic limit) the energy spectrum is equivalent to that of the non-relativistic three-body system in a linearly rising potential.

We start from the (obvious) observation that under the transition from the configuration-space to the momentum-space representation, one does a Fourier transformation of the whole Schrödinger equation, the wave function included. A necessary condition for this transformation to hold is that all of the functions involved be square-integrable. Whereas that is certainly true of the bound-state wave functions, it does not hold for the harmonic oscillator, or any other infinitely rising (i.e., confining) potential. Therefore, the Fourier transform of the harmonic-oscillator Schrödinger equation is not the usual Lippmann-Schwinger integro-differential equation, but rather, (the same) differential equation, except for the fact that the variables are in the momentum space. In Boukraa and Basdevant's [4] words: "These integral equations appear to be singular for confining potentials and hence need particular treatment." For an arbitrary confining potential this "particular treatment" has been presented in some detail in Ref. [4].

In the special case of the harmonic oscillator potential, however, this "particular treatment" turns out to be simple and yields an elegant solution: instead of an integro-differential equation, one ends up with a purely differential equation of the second order that looks just like an ordinary nonrelativistic Schrödinger equation, see problem V.17, Chapter V in Ref. [5], albeit with a (different) potential, that is the Fourier transform of the relativistic kinetic energy operator. Indeed the relativistic 1-body harmonic oscillator was treated in this way by Li et al. [6]. The Fourier transform of the relativistic kinetic energy be evaluated in closed form with the (possibly not-so-surprising) result that it asymptotically grows linearly with the resulting "separation of quarks in momentum space", which corresponds to a linearly confining potential.

Thus the *relativistic* harmonic oscillator three-body problem is reduced to a *non-relativistic* three-body problem in a linearly growing potential in momentum space<sup>2</sup>. In this light, we do not seem to have gained much, just trading one three-body problem for another. The actual advantage is that the new three-body problem is non-relativistic, which allows us to use the  $O(6)$  hyper-spherical harmonics.

---

<sup>2</sup> This was noted by Hall et al [7].



From this point onwards, one can employ our previously developed hyper-spherical harmonics methods [1, 2, 3] to solve the resulting equations of motion. The new potential is expanded in hyper-spherical harmonics and the resulting expansion coefficients inserted into the (reduced) hyper-radial Schrödinger equations, that can be solved numerically at least in the extreme relativistic limit (zero masses).

The resulting energy spectrum is curious and instructive: instead of the highly degenerate spectrum of the non-relativistic harmonic oscillator, we find that the degeneracy has been maximally lifted, the only remnants of degeneracy being those decreed by the  $S_3$  permutation symmetry. Moreover, degeneracy-lifting effects have the same amplitudes, and (sometimes) the opposite sign to those in the  $\Delta$ -string potential, at least in the extreme relativistic limit.

Of course, the more realistic case of non-zero masses is expected to interpolate between the two extreme cases of non-relativity and extreme relativity, but that cannot be handled as simply as in the case shown here.

## 2 Semi-relativistic three-body harmonic oscillator in momentum space

The semi-relativistic three-quark Hamiltonian in configuration space is

$$H = \sum_a \sqrt{m_a^2 + \mathbf{p}_i^2} + V_{3b}(|\boldsymbol{\rho}|, |\boldsymbol{\lambda}|, \boldsymbol{\rho} \cdot \boldsymbol{\lambda}), \quad (1)$$

where the confining 3-body harmonic oscillator potential reads (for the sake of simplicity we shall work with three identical particles):

$$\begin{aligned} V_{3b}(|\boldsymbol{\rho}|, |\boldsymbol{\lambda}|, \boldsymbol{\rho} \cdot \boldsymbol{\lambda}) &= V_{\text{HO}} = \frac{k}{2} (\boldsymbol{\rho}^2 + \boldsymbol{\lambda}^2) \\ &= \frac{k'}{2} \left( (\mathbf{x}_1 - \mathbf{x}_2)^2 + (\mathbf{x}_2 - \mathbf{x}_3)^2 + (\mathbf{x}_3 - \mathbf{x}_1)^2 \right) \end{aligned} \quad (2)$$

and  $k' = 3k$ . Here we used the standard notation for Jacobi coordinates  $\boldsymbol{\rho}$  and  $\boldsymbol{\lambda}$ , defined as the following linear combinations of the positions of the three identical particles  $\mathbf{x}_i$ :

$$\boldsymbol{\rho} = \frac{1}{\sqrt{2}}(\mathbf{x}_1 - \mathbf{x}_2), \quad \boldsymbol{\lambda} = \frac{1}{\sqrt{6}}(\mathbf{x}_1 + \mathbf{x}_2 - 2\mathbf{x}_3).$$

The Fourier transform of the harmonic oscillator potential, as is well known, see problem V.17, Chapter V in Ref. [5], is proportional to the Laplacian operator, i.e., to the kinetic energy (in the configuration representation). This property holds in the three-body problem, as well, with the distinction

that the Laplacian operates in six-dimensional space

$$\tilde{V}_{\text{HO}} = -\frac{k}{2} \left( \frac{\partial^2}{\partial \mathbf{p}_\rho^2} + \frac{\partial^2}{\partial \mathbf{p}_\lambda^2} \right).$$

The major difference is in what happens to the relativistic kinetic energy in the momentum space: the kinetic energy

$$T = \sum_{a=1}^3 \sqrt{m_a^2 + \mathbf{p}_i^2},$$

is a differential operator in configuration representation (because  $\mathbf{p}_j = -i\hbar \frac{\partial}{\partial \mathbf{x}_j}$  is a differential operator), but a multiplicative operator in the momentum representation. In the center-of-momentum (CM) frame it holds:

$$\sum_{i=1}^3 \mathbf{p}_i = 0$$

and, subjected to this constraint, it is possible to express all three spatial momenta  $\mathbf{p}_i$  as linear combinations of just two Jacobi vectors  $\mathbf{p}_\rho$  and  $\mathbf{p}_\lambda$ .

Note that kinetic energy  $T$  does not have the  $O(6)$  symmetry of its non-relativistic analogon. Moreover, in the extreme relativistic limit  $m_a \rightarrow 0$ , or  $T_{\text{CM}} \rightarrow \infty$ , we can write center-of-momentum kinetic energy as:

$$T_{\text{CM}} = \sum_{i=1}^3 |\mathbf{p}_i| = \sqrt{\frac{2}{3} \mathbf{p}_\lambda^2} + \sqrt{\frac{1}{2}} \left( \left| \mathbf{p}_\rho + \frac{\mathbf{p}_\lambda}{\sqrt{3}} \right| + \left| \mathbf{p}_\rho - \frac{\mathbf{p}_\lambda}{\sqrt{3}} \right| \right), \quad (3)$$

and it is only a linearly (rather than quadratically as in the non relativistic case) rising function of momenta magnitudes.

Thus, the Hamiltonian in momentum space and CM frame reads

$$\tilde{H} = -\frac{k}{2} \left( \frac{\partial^2}{\partial \mathbf{p}_\rho^2} + \frac{\partial^2}{\partial \mathbf{p}_\lambda^2} \right) + \sum_{i=1}^3 |\mathbf{p}_i|,$$

which, after the substitutions  $\mathbf{p}_\rho \leftrightarrow \boldsymbol{\rho}$  and  $\mathbf{p}_\lambda \leftrightarrow \boldsymbol{\lambda}$ , is equivalent to the Schrödinger equation

$$\tilde{H}\tilde{\Psi} = \tilde{E}\tilde{\Psi}$$

for three identical particles with a mass  $m = k$  and interacting with a CM-string potential with unit string tension  $\sigma = 1$ . We have developed hyper-spherical harmonic methods [1, 2, 3] for the solution of such three-body Schrödinger equations.

### 3 Barycentric-string three-body potential

The potential:

$$V_{\text{CM}} = \sigma_{\text{CM}} \left( \sqrt{\frac{2}{3}\lambda^2} + \sqrt{\frac{1}{2}} \left( \left| \boldsymbol{\rho} + \frac{\boldsymbol{\lambda}}{\sqrt{3}} \right| + \left| \boldsymbol{\rho} - \frac{\boldsymbol{\lambda}}{\sqrt{3}} \right| \right) \right) \quad (4)$$

corresponding to the expression (3) is known as the barycentric-junction (instead of Torricelli-junction) string

$$V_{\text{CM}} = \sigma_{\text{CM}} \sum_{i=1}^3 |\mathbf{x}_i - \mathbf{x}_{\text{CM}}|,$$

in the literature [8]. In terms of Iwai-Smith angles it reads

$$\begin{aligned} V_{\text{CM}}(R, \alpha, \phi) = \frac{\sigma_{\text{CM}}}{\sqrt{3}} R & \left( \sqrt{1 - \sin(\alpha) \cos\left(\phi - \frac{\pi}{3}\right)} \right. \\ & + \sqrt{1 - \sin(\alpha) \cos\left(\phi + \frac{\pi}{3}\right)} \\ & \left. + \sqrt{1 + \sin(\alpha) \cos(\phi)} \right). \end{aligned} \quad (5)$$

The barycentric string 3-body potential is closely related to the  $\Delta$ -string one,

$$V_{\Delta} = \sigma_{\Delta} \sum_{i>j=1}^3 |\mathbf{x}_i - \mathbf{x}_j|, \quad (6)$$

which, written in terms of Jacobi vectors reads

$$\begin{aligned} V_{\Delta} = \sigma_{\Delta} & \left( \sqrt{2\rho^2} + \sqrt{\frac{1}{2} \left( \rho^2 + 3\lambda^2 - 2\sqrt{3}\boldsymbol{\rho} \cdot \boldsymbol{\lambda} \right)} \right. \\ & \left. + \sqrt{\frac{1}{2} \left( \rho^2 + 3\lambda^2 + 2\sqrt{3}\boldsymbol{\rho} \cdot \boldsymbol{\lambda} \right)} \right). \end{aligned} \quad (7)$$

Note that the expression Eq. (4) for  $V_{\text{CM}}$  can be obtained from the expression Eq. (7) for  $V_{\Delta}$  by exchanging  $\boldsymbol{\rho}$  and  $\boldsymbol{\lambda}$  (together with setting  $\sigma_{\Delta} = \sigma_{\text{CM}}/\sqrt{3}$ ).

The  $\Delta$ -string potential Eq. (7), in terms of Iwai-Smith angles, reads

$$V_{\Delta}(R, \alpha, \phi) = \sigma_{\Delta} R \left( \sqrt{1 + \sin(\alpha) \sin\left(\frac{\pi}{6} - \phi\right)} \right)$$

$$\begin{aligned}
& + \sqrt{1 + \sin(\alpha) \sin\left(\phi + \frac{\pi}{6}\right)} \\
& + \sqrt{1 - \sin(\alpha) \cos(\phi)} \Big) \quad (8)
\end{aligned}$$

which is just a rotation of angle  $\phi$  through  $\pi$  as compared with Eq. (5). An interchange of the  $\boldsymbol{\rho}$  and  $\boldsymbol{\lambda}$  vectors has exactly such the effect of a  $\phi$ -rotation through  $\pi$  on the hyper-spherical harmonic expansion coefficients,  $v_{K,Q}^\Delta$ , defined in Eq. (9).

In order to find the general hyper-spherical harmonic expansion of the  $\Delta$ -string potential we note that it factors into the hyper-radial  $V_\Delta(R) = \sigma_\Delta R$  and the hyper-angular part  $V_\Delta(\alpha, \phi)$ , and thus:

$$\begin{aligned}
V_\Delta(R, \alpha, \phi) &= V_\Delta(R)V_\Delta(\alpha, \phi) \\
&= \sigma_\Delta R \sum_{K,Q}^\infty v_{K,Q}^\Delta \mathcal{Y}_{00}^{KQ\nu}(\alpha, \phi). \quad (9)
\end{aligned}$$

This circumstance, of course, leaves consequences for the hyper-spherical harmonic expansion coefficients of these two potentials: 1) the  $Q = 0$  coefficients  $v_{K,Q=0}$  of these two potentials are identical (modulo  $\sqrt{3}$  in the definitions of the string tensions); 2) the  $Q \neq 0$  coefficients  $v_{K,Q \neq 0}$  of these two potentials have the same absolute value, with opposite signs.

We have already calculated the expansion coefficients  $v_{K,Q}^\Delta$  in Ref. [10], and we can use our above conclusions to directly infer values of the corresponding coefficients in the hyper-spherical decomposition of the potential  $V_{\text{CM}}$  (4). All these coefficients (and some additional for comparison) are tabulated in Table 1.

**Table 1** Expansion coefficients  $v_{KQ}$  of the Y- and  $\Delta$ -string as well as of the Coulomb and Logarithmic potentials in terms of O(6) hyper-spherical harmonics  $\mathcal{Y}_{0,0}^{K,0,0}$ , for  $K = 0, 4, 8, 12$ , respectively, and of the hyper-spherical harmonics  $\mathcal{Y}_{0,0}^{6,\pm 6,0}$ .

$(K, Q)$	$v_{KQ}(\text{Y-string})$	$v_{KQ}(\Delta)$	$v_{KQ}(\text{CM-string})$	$v_{KQ}(\text{Coulomb})$	$v_{KQ}(\text{Log})$
(0,0)	8.22	16.04	$16.04/\sqrt{3}$	20.04	-6.58
(4,0)	-0.398	-0.445	$-0.445/\sqrt{3}$	2.93	-1.21
(6, $\pm 6$ )	-0.027	-0.14	$0.14/\sqrt{3}$	1.88	-0.56
(8,0)	-0.064	-0.04	$-0.04/\sqrt{3}$	1.41	-0.33
(12,0)	-0.01	0	0	0	-0.17

## 4 Results: Energy spectra

This means that the relativistic 3-body harmonic oscillator spectrum is closely related to that of the non-relativistic  $\Delta$ -string one, which has been studied in detail Ref. [10], see also Basdevant and Boukraa, [11, 4]. The precise energy eigenvalues depend on the absolute value of the (1-body) mass, and can be bounded from above and below as shown in [6]. In the extreme relativistic limit ( $m \rightarrow 0$ ) the ground-state energy is equal to the (rescaled)  $\Delta$ -string ground state energy (cf. Table 5 in Ref. [8]). Thus we find that the

**Table 2** The eigen-energies (in units of  $\left(\frac{\sigma_{\#}}{\sqrt{2m}}\right)^{\frac{2}{3}}$ ) of the  $\#$ -string potentials (where  $\# = Y, \Delta, \text{CM}$ ) for all  $K = 0, 1, 2$  states. The CM-string eigen-energies are obtained from the  $\Delta$  by dividing the latter by  $\sqrt[3]{3}$ , which is equivalent to the substitution  $\sigma_{\Delta} = \sqrt{3}\sigma_{\text{CM}}$  in the above formula for units.

K	$N_K$	$[SU(6), L^P]$	$E_{N_K, K, L}^{(Y)}$	$E_{N_K, K, L}^{(\Delta)}$	$E_{N_K, K, L}^{(\text{CM})}$
0	0	[56, 0 <sup>+</sup> ]	5.1761	6.1348	4.2536
1	0	[70, 1 <sup>-</sup> ]	6.3160	7.4858	5.1904
0	1	[56, 0 <sup>+</sup> ]	7.1360	8.4577	5.8643
2	0	[70, 0 <sup>+</sup> ]	7.1733	8.6322	5.9852
2	0	[56, 2 <sup>+</sup> ]	7.2437	8.6691	6.0108
2	0	[70, 2 <sup>+</sup> ]	7.3968	8.7430	6.0621
2	0	[20, 1 <sup>+</sup> ]	7.5550	8.8168	6.1132

degeneracy of energy levels has been maximally lifted, the only remnants of degeneracy being those allowed/decreed by the  $S_3$  permutation symmetry and by angular momentum conservation. Moreover, degeneracy-lifting effects have the same amplitudes, and in some cases the opposite sign(s) to those in the  $\Delta$ -string potential, at least in the extreme ultra-relativistic limit. This stands in stark contrast to the highly degenerate spectrum of the non-relativistic harmonic oscillator.

Moreover, this shows that the relativistic effects can either enhance, or reduce the  $(K, Q) = (6, \pm 6)$  coefficient, which is a benchmark signal of the Y-string confinement potential, thus possibly confusing the issue of  $\Delta$ - vs. Y-string further still.

Of course, the more realistic case of non-zero masses is expected to interpolate between the two extreme cases of non-relativistic and extremely relativistic motion, but that cannot be handled as simply as in the case shown here. Once the masses are turned on, the problem's Hamiltonian loses its homogeneity, and has to be (re)calculated separately at every mass value.

Next we compare our ground state energy (see the right-most column in Table 5 in Ref. [8])  $E_{00} = 5.3592 \times \sqrt[3]{\frac{3}{2}k^{1/3}} = 6.13475k^{1/3}$  which is slightly (0.12 %) larger than Hall et al's [7] (rigorous) lower bound of  $2.33810741 \times \sqrt[3]{18}k^{1/3} = 6.12757k^{1/3}$ . The difference may well be down to the numerical

inaccuracy (4th significant digit) in the numerical evaluation of the eigenvalue in Table 11 in Ref. [8].

## 5 Discussion and Conclusions

In this paper we have explicitly established a direct relation between ultra-relativistic three-particle harmonic oscillator problem, and the non-relativistic three particle problem in a linear  $\Delta$  potential. This relation allowed us to directly infer the harmonic oscillator spectrum from the already known properties of the three particle non-relativistic system in the  $\Delta$  potential.

In conferences one can still occasionally hear comments to the effect that the Dirac's formulation(s) of (special) relativistic mechanics [12] precludes any and all interaction within few-body systems - the so-called "No Interaction Theorems" of Currie, Jordan, and Sudarshan [13]. It is far less known that in a series of papers [14, 15], Luis Bel has reviewed which assumption(s) lay at the root of this apparent difficulty, as well as several assumptions supplanting the Currie-Jordan-Sudarshan ones, which permit one to circumvent this "No Interaction theorem". In this regard, see also Jordan's own more recent views [16]. Thus there are no formal grounds for viewing our present results with suspicion.

## References

1. Igor Salom and V. Dmitrašinović, Phys. Lett. **A 380**, 1904-1911 (2016).
2. Igor Salom and V. Dmitrašinović, Springer Proc. Math. Stat. **191**, 431 (2016).
3. Igor Salom and V. Dmitrašinović, Nucl. Phys. B **920**, 521 (2017).
4. S. Boukraa and J.-L. Basdevant, Jour. Math. Phys. **30**, 1060 (1989).
5. F. Constantinescu and E. Magyari, "PROBLEMS IN QUANTUM MECHANICS", Pergamon Press, Oxford (1971).
6. Zhi-Feng Li, Jin-Jin Liu, Wolfgang Lucha, Wen-Gan Ma and Franz F. Schöberl, J. Math. Phys. **46**, 103514 (2005).
7. Richard L. Hall, Wolfgang Lucha, Franz F. Schöberl, Phys. Lett. **A 320**, 127-130 (2003) and J. Math. Phys. **45**, 3086 (2004).
8. V. Dmitrašinović, T. Sato and M. Šuvakov, Eur. Phys. J. C **62**, 383 (2009).
9. V. Dmitrašinović and Igor Salom, J. Math. Phys. **55**, 082105 (16) (2014).
10. V. Dmitrašinović and I. Salom, Phys. Rev. D **97**, 094011 (2018), [arXiv:1805.00386 [nucl-th]].
11. J.-L. Basdevant, and S. Boukraa, Z. Phys. **C 30**, 103 (1986).
12. P.A.M. Dirac, Rev. Mod. Phys. **21** (1949) 392;
13. D.G. Currie, T.F. Jordan, E.C.G. Sudarshan, Rev. Mod. Phys. **35** (1963) 350; D.G. Currie, J. Math. Phys. **4** (1963) 1470.
14. Luis Bel, Ann. Inst. Henri Poincaré, Section A : Vol. XIV, no. 3, p. 189 - 203 (1971). Physique théorique.
15. Luis Bel, Ann. Inst. Henri Poincaré, Section A : Vol. XVII, no. 1, p. 57 - 76 (1973). Physique théorique.
16. Thomas F. Jordan, Phys. Lett. **A 310**, 123-130 (2003).



# The spin 1 XXZ Gaudin model with boundary\*

**Igor Salom**<sup>†</sup>

Institute of Physics, University of Belgrade  
Pregrevica 118, 11080 Belgrade, Serbia

**Nenad Manojlović**<sup>‡</sup>

Departamento de Matemática, Faculdade de Ciências e Tecnologia  
Universidade do Algarve, Campus de Gambelas,  
8005-139 Faro, Portugal

and

Grupo de Física Matemática da Universidade de Lisboa  
Departamento de Matemática, Faculdade de Ciências  
Campo Grande, Edifício C6, 1749-016 Lisboa, Portugal

**Nuno Cirilo António**<sup>§</sup>

Centro de Análise Funcional e Aplicações  
Instituto Superior Técnico, Universidade de Lisboa  
Av. Rovisco Pais, 1049-001 Lisboa, Portugal

## ABSTRACT

We obtain the non-unitary classical r-matrix of the spin 1 trigonometric Gaudin model with boundary terms. Starting from the R-matrix and corresponding K-matrix of the spin  $\frac{1}{2}$  XXZ Heisenberg chain the so-called fusion procedure yields the R and K matrices of the spin 1 XXZ Heisenberg chain. We demonstrate that the corresponding classical r and K matrices satisfy, respectively, the classical Yang-Baxter equation and the classical reflection equation. Consequently, we show that the relevant non-unitary classical r-matrix satisfies the generalized classical Yang-Baxter equation and therefore defines the non-periodic spin 1 trigonometric Gaudin model.

## 1. Introduction

An approach to study periodic Gaudin models [1, 2, 3] is based on the unitary classical r-matrices [4, 5, 6, 7] and the corresponding Sklyanin linear

---

\* N.M. gratefully acknowledges useful discussions with Eric Ragoucy. I.S. was supported in part by the Serbian Ministry of Education, Science and Technological Development under grant number ON 171031.

<sup>†</sup> e-mail address: isalom@ipb.ac.rs

<sup>‡</sup> e-mail address: nmanoj@ualg.pt

<sup>§</sup> e-mail address: nantonio@math.ist.utl.pt

bracket [5, 6, 7, 8, 9, 10, 11]. The algebra generated by the entries of the relevant Lax operators can be used to completely solve the system through the algebraic Bethe ansatz, or the separation of variable method [5, 6, 7, 8, 9, 10, 11].

Similar approach to the non-periodic Gaudin models, based on the non-unitary classical r-matrices and corresponding linear bracket, enabled full implementation of the algebraic Bethe ansatz in the spin  $\frac{1}{2}$  case [12, 13, 14, 15, 16, 17, 18, 19]. In this paper we initiate the study of the spin 1 non-periodic Gaudin models by deriving the relevant non-unitary classical r-matrix. This classical r-matrix is a solution to the generalized classical Yang-Baxter equation. An important advantage of this approach is that the generalized classical Yang-Baxter equation is equivalent to both the classical Yang-Baxter equation and classical reflection equation [15]. To obtain this non-unitary r-matrix we use the fusion procedure starting from the quantum R-matrix and the reflection K-matrix of the spin  $\frac{1}{2}$  XXZ Heisenberg chain. The classical r-matrix we obtain defines completely the non-periodic spin 1 Gaudin model.

This paper is organized as follows. In the section 2. we describe briefly the fusion procedure as applied to the R and K matrices of the spin  $\frac{1}{2}$  XXZ Heisenberg chain. The results of the second section are then presented and analysed in the section 3.. The quasi-classical limit which leads to the spin 1 non-unitary r-matrix is presented in the section 4..

## 2. Spin $\frac{1}{2}$ XXZ Heisenberg chain

In our study of the spin  $\frac{1}{2}$  XXZ Heisenberg spin chain [16] the starting point is always the R-matrix [20, 21, 22, 23]

$$R(\lambda, \eta) = \begin{pmatrix} \sinh(\lambda + \eta) & 0 & 0 & 0 \\ 0 & \sinh(\lambda) & \sinh(\eta) & 0 \\ 0 & \sinh(\eta) & \sinh(\lambda) & 0 \\ 0 & 0 & 0 & \sinh(\lambda + \eta) \end{pmatrix}. \quad (1)$$

This R-matrix satisfies the Yang-Baxter equation [24, 22, 23, 20, 21] in the space  $\mathbb{C}^2 \otimes \mathbb{C}^2 \otimes \mathbb{C}^2$

$$R_{12}(\lambda - \mu)R_{13}(\lambda)R_{23}(\mu) = R_{23}(\mu)R_{13}(\lambda)R_{12}(\lambda - \mu), \quad (2)$$

and it also has other relevant properties such as

$U(1)$ symmetry	$[\sigma_1^3 + \sigma_2^3, R_{12}(\lambda)] = 0;$
unitarity	$R_{12}(\lambda)R_{21}(-\lambda) = \sinh(\eta - \lambda) \sinh(\eta + \lambda) \mathbb{1};$
parity invariance	$R_{21}(\lambda) = R_{12}(\lambda);$
temporal invariance	$R_{12}^t(\lambda) = R_{12}(\lambda);$
crossing symmetry	$R(\lambda) = \mathcal{J}_1 R^{t_2}(-\lambda - \eta) \mathcal{J}_1,$

where  $t_2$  denotes the transpose in the second space and the two-by-two matrix  $\mathcal{J}$  is proportional to the Pauli matrix  $\sigma^2$ , i.e.  $\mathcal{J} = \iota\sigma^2$ .

A way to introduce non-periodic boundary conditions which are compatible with the integrability of the bulk model, was developed in [25]. Boundary conditions on the left and right sites of the chain are encoded in the left and right reflection matrices  $K^-$  and  $K^+$ . The compatibility condition between the bulk and the boundary of the system takes the form of the so-called reflection equation. It is written in the following form for the left reflection matrix acting on the space  $\mathbb{C}^2$  at the first site  $K^-(\lambda) \in \text{End}(\mathbb{C}^2)$

$$R_{12}(\lambda - \mu)K_1^-(\lambda)R_{21}(\lambda + \mu)K_2^-(\mu) = K_2^-(\mu)R_{12}(\lambda + \mu)K_1^-(\lambda)R_{21}(\lambda - \mu). \tag{3}$$

Due to the properties of the R-matrix (1) the dual reflection equation can be presented in the following form

$$R_{12}(\mu - \lambda)K_1^+(\lambda)R_{21}(-\lambda - \mu - 2\eta)K_2^+(\mu) = K_2^+(\mu)R_{12}(-\lambda - \mu - 2\eta)K_1^+(\lambda)R_{21}(\mu - \lambda). \tag{4}$$

One can then verify that the mapping

$$K^+(\lambda) = K^-(-\lambda - \eta) \tag{5}$$

is a bijection between solutions of the reflection equation and the dual reflection equation. After substitution of (5) into the dual reflection equation (4) one gets the reflection equation (3) with shifted arguments.

The general, spectral parameter dependent, solutions of the reflection equation (3) and the dual reflection equation (4) can be written as follows [26, 27, 28]

$$K^-(\lambda) = \begin{pmatrix} \kappa^- \sinh(\xi^- + \lambda) & \psi^- \sinh(2\lambda) \\ \phi^- \sinh(2\lambda) & \kappa^- \sinh(\xi^- - \lambda) \end{pmatrix}, \tag{6}$$

$$K^+(\lambda) = \begin{pmatrix} \kappa^+ \sinh(\xi^+ - \lambda - \eta) & -\psi^+ \sinh(2(\lambda + \eta)) \\ -\phi^+ \sinh(2(\lambda + \eta)) & \kappa^+ \sinh(\xi^+ + \lambda + \eta) \end{pmatrix}. \tag{7}$$

Due to the fact that the reflection matrices  $K^\mp(\lambda)$  are defined up to multiplicative constants the values of parameters  $\kappa^\mp$  are not essential, as long as they are different from zero. Although the R-matrix (1) has the  $U(1)$  symmetry the reflection matrices  $K^\mp(\lambda)$  (6) and (7) cannot be brought to the upper triangular form by the symmetry transformations like in the case of the XXX Heisenberg spin chain [14].

We will not discuss the Lax operators and the corresponding monodromies, relevant for the study of the spin  $\frac{1}{2}$  XXZ Heisenberg spin chain [16]. Our aim is to obtain the R and K matrices corresponding the spin 1 XXZ Heisenberg chain. As our first step we use the fusion procedure [29, 21] in the space  $\mathbb{C}^2 \otimes \mathbb{C}^2 \otimes \mathbb{C}^2 \otimes \mathbb{C}^2$  with the aim of deriving the spin 1

XXZ R-matrix. To this end we observe that the R-matrix (1) at  $\lambda = -\eta$  is proportional to the projector onto the antisymmetric subspace of the space  $\mathbb{C}^2 \otimes \mathbb{C}^2$ ,

$$P^- = \frac{-1}{2 \sinh(\eta)} \begin{pmatrix} 0 & 0 & 0 & 0 \\ 0 & \frac{1}{2} & -\frac{1}{2} & 0 \\ 0 & -\frac{1}{2} & \frac{1}{2} & 0 \\ 0 & 0 & 0 & 0 \end{pmatrix}. \quad (8)$$

For our purpose, the relevant projector is the complementary one, which projects onto the symmetric subspace of the space  $\mathbb{C}^2 \otimes \mathbb{C}^2$ ,

$$P^+ = \mathbb{1} - P^-. \quad (9)$$

We obtain the spin 1 representation in the tensor product of the last two spaces,

$$R_{1(34)}(\lambda) = P_{34}^+ R_{14}(\lambda - \eta) R_{13}(\lambda) P_{34}^+. \quad (10)$$

It straightforward the check that the corresponding Yang-Baxter equation is satisfied

$$R_{12}(\lambda - \mu) R_{1(34)}(\lambda) R_{2(34)}(\mu) = R_{2(34)}(\mu) R_{1(34)}(\lambda) R_{12}(\lambda - \mu). \quad (11)$$

Analogously, we have

$$R_{(12)3}(\lambda) = P_{12}^+ R_{13}(\lambda) R_{23}(\lambda + \eta) P_{12}^+. \quad (12)$$

Finally, we obtain the relevant R-matrix

$$R_{(12)(34)}(\lambda) = P_{34}^+ R_{(12)4}(\lambda - \eta) R_{(12)3}(\lambda) P_{34}^+. \quad (13)$$

In this case, the fusion procedure for the  $K$ -matrix [30] yields

$$K_{(12)}^-(\lambda) = P_{12}^+ K_1^-(\lambda) R_{12}(2\lambda + \eta) K_2^-(\lambda + \eta) P_{12}^+. \quad (14)$$

A direct calculation shows that the corresponding reflection equation is satisfied

$$\begin{aligned} & R_{(12)(34)}(\lambda - \mu) K_{(12)}^-(\lambda) R_{(34)(12)}(\lambda + \mu) K_{(34)}^-(\mu) = \\ & = K_{(34)}^-(\mu) R_{(12)(34)}(\lambda + \mu) K_{(12)}^-(\lambda) R_{(34)(12)}(\lambda - \mu). \end{aligned} \quad (15)$$

Therefore we have achieved our main objective in obtaining the relevant R and K matrices. In the following section we will look at their explicit form and some important properties.

### 3. Spin 1 XXZ Heisenberg chain

In the appropriate bases the R-matrix (13) of the spin one XXZ Heisenberg chain can be represented as the following  $9 \times 9$  matrix

$$R(\lambda, \eta) = \left( \begin{array}{ccc|ccc} a_1 & & & b_1 & & \\ & a_2 & & & b_2 & \\ & & a_3 & & & b_3 \\ \hline & b_1 & & a_2 & & \\ & & b_2 & & a_4 & \\ & & & & a_2 & b_1 \\ \hline & & b_3 & & b_2 & \\ & & & & & a_3 \\ & & & & b_1 & \\ & & & & & a_2 \\ & & & & & & a_1 \end{array} \right), \quad (16)$$

where the entries are given by

$$\begin{aligned} a_1 &= \sinh(\lambda + \eta) \sinh(\lambda + 2\eta), & b_1 &= \sinh(\lambda + \eta) \sinh(2\eta), \\ a_2 &= \sinh(\lambda) \sinh(\lambda + \eta), & b_2 &= \sinh^2(\lambda) \sinh(2\eta) \cosh(\eta), \\ a_3 &= \sinh(\lambda) \sinh(\lambda - \eta), & b_3 &= \sinh(\eta) \sinh(2\eta) \sinh(\lambda) \sinh(\lambda + \eta), \\ a_4 &= \sinh(\lambda) \sinh(\lambda + \eta) + \sinh(\eta) \sinh(2\eta). \end{aligned}$$

This R-matrix satisfies the Yang-Baxter equation in the space  $\mathbb{C}^3 \otimes \mathbb{C}^3 \otimes \mathbb{C}^3$

$$R_{12}(\lambda - \mu)R_{13}(\lambda)R_{23}(\mu) = R_{23}(\mu)R_{13}(\lambda)R_{12}(\lambda - \mu), \quad (17)$$

and has the  $U(1)$  symmetry

$$[h_1 + h_2, R_{12}(\lambda, \eta)] = 0, \quad (18)$$

where  $h = \text{diag}(1, 0, -1)$ . The similarity transformation

$$\text{Ad exp}(\alpha\lambda(h_1 - h_2))R_{12}(\lambda, \eta), \quad (19)$$

with  $\alpha = \frac{1}{2}$ , yields the  $O(3)$  invariant form of this R-matrix [31, 32, 33]. The R-matrix 16 has some important properties such as regularity, unitarity, PT-symmetry and crossing symmetry. The regularity condition at  $\lambda = 0$  reads

$$R(0, \eta) = \sinh(\eta) \sinh(2\eta)\mathcal{P}, \quad (20)$$

where  $\mathcal{P}$  is the permutation matrix of  $\mathbb{C}^3 \otimes \mathbb{C}^3$ . The unitarity relation is

$$R_{12}(\lambda)R_{12}(-\lambda) = \rho(\lambda)\mathbb{1}, \quad (21)$$

here  $\rho$  is the following function

$$\rho(\lambda) = \sinh(\lambda + \eta) \sinh(\lambda + 2\eta) \sinh(\lambda - \eta) \sinh(\lambda - 2\eta). \quad (22)$$

The so-called PT-symmetry states

$$R_{12}^t(\lambda) = R_{12}(\lambda). \quad (23)$$

Finally, the R-matrix (16) has the following crossing symmetry property:

$$R(\lambda) = (\mathcal{J} \otimes \mathbb{1}) R^{t_2}(-\lambda - \eta) (\mathcal{J}^{-1} \otimes \mathbb{1}), \quad (24)$$

where  $t_2$  denotes the transpose in the second space and the matrix  $\mathcal{J}$  is given by

$$\mathcal{J} = \begin{pmatrix} 0 & 0 & -1 \\ 0 & 1 & 0 \\ -1 & 0 & 0 \end{pmatrix}. \quad (25)$$

In the basis in which the R-matrix (13) takes the form (16) the K-matrix (14) is given by

$$K^-(\lambda, \eta) = \sinh(2\lambda + \eta) \begin{pmatrix} k_{11} & k_{12} & k_{13} \\ k_{21} & k_{22} & k_{23} \\ k_{31} & k_{32} & k_{33} \end{pmatrix}, \quad (26)$$

where

$$\begin{aligned} k_{11} &= \kappa^{-2} \sinh(\xi^- + \lambda + \frac{\eta}{2}) \sinh(\xi^- + \lambda - \frac{\eta}{2}) + \psi^- \phi^- \sinh(2\lambda - \eta) \sinh(\eta), \\ k_{22} &= \kappa^{-2} \sinh(\xi^- - \lambda + \frac{\eta}{2}) \sinh(\xi^- + \lambda - \frac{\eta}{2}) + \psi^- \phi^- \sinh(2\lambda - \eta) \sinh(2\lambda + \eta), \\ k_{33} &= \kappa^{-2} \sinh(\xi^- - \lambda + \frac{\eta}{2}) \sinh(\xi^- - \lambda - \frac{\eta}{2}) + \psi^- \phi^- \sinh(2\lambda - \eta) \sinh(\eta), \\ k_{12} &= \kappa^- \psi^- \sqrt{2} \sqrt{\cosh(\eta)} \sinh(\xi^- + \lambda - \frac{\eta}{2}) \sinh(2\lambda), \\ k_{23} &= \kappa^- \psi^- \sqrt{2} \sqrt{\cosh(\eta)} \sinh(\xi^- - \lambda + \frac{\eta}{2}) \sinh(2\lambda), \\ k_{13} &= \psi^{-2} \sinh(2\lambda - \eta) \sinh(2\lambda), \\ k_{21} &= \kappa^- \phi^- \sqrt{2} \sqrt{\cosh(\eta)} \sinh(\xi^- + \lambda - \frac{\eta}{2}) \sinh(2\lambda), \\ k_{32} &= \kappa^- \phi^- \sqrt{2} \sqrt{\cosh(\eta)} \sinh(\xi^- - \lambda + \frac{\eta}{2}) \sinh(2\lambda), \\ k_{31} &= \phi^{-2} \sinh(2\lambda - \eta) \sinh(2\lambda). \end{aligned} \quad (27)$$

The R-matrix (16) and the above K-matrix satisfy the reflection equation

$$R_{12}(\lambda - \mu) K_1^-(\lambda) R_{21}(\lambda + \mu) K_2^-(\mu) = K_2^-(\mu) R_{12}(\lambda + \mu) K_1^-(\lambda) R_{21}(\lambda - \mu). \quad (28)$$

The study of the spin 1 XXZ Heisenberg chain would require the dual reflection equation and the relevant  $K^+$  matrix. Although, now this would be straightforward we will not proceed in this direction since our main aim is to derive the corresponding Gaudin model through the so-called quasi-classical limit [14, 16].

### 4. Spin 1 XXZ Gaudin model

The classical r-matrices are essential tools in the study of the Gaudin models [5, 4, 6, 7, 8, 9, 10]. To this end we observe the quasi-classical property of the R-matrix (16)

$$\frac{1}{\sinh^2(\lambda)}R(\lambda, \eta) = \mathbb{1} + \eta r(\lambda) + \mathcal{O}(\eta^2), \tag{29}$$

where the classical r-matrix is given by [4, 6]

$$r(\lambda) = \frac{2}{\sinh(\lambda)} \left( \begin{array}{cc|cc|cc} \cosh(\lambda) & & & & & & & \\ & -\cosh(\lambda) & & 1 & & & & \\ \hline & & 1 & & & & & \\ & & & & 1 & & & \\ \hline & & & & & & 1 & \\ & & & & & & & 1 \\ \hline & & & & 1 & & -\cosh(\lambda) & \\ & & & & & 1 & & \\ & & & & & & & \cosh(\lambda) \end{array} \right) + \coth(\lambda)\mathbb{1}. \tag{30}$$

As it is very well known[4, 6], the above r-matrix has the unitarity property

$$r_{21}(-\lambda) = -r_{12}(\lambda), \tag{31}$$

and it satisfies the classical Yang-Baxter equation

$$[r_{13}(\lambda), r_{23}(\mu)] + [r_{12}(\lambda - \mu), r_{13}(\lambda) + r_{23}(\mu)] = 0. \tag{32}$$

Our objective is the non-periodic Gaudin model and therefore we also need the classical K-matrix [14, 15, 16] which is obtained from the K-matrix (26) by setting  $\eta = 0$ ,

$$K(\lambda) \equiv K^-(\lambda, 0). \tag{33}$$

A direct consequence of the equation (28) is the classical reflection equation [34, 35, 15]:

$$\begin{aligned} r_{12}(\lambda - \mu)K_1(\lambda)K_2(\mu) + K_1(\lambda)r_{21}(\lambda + \mu)K_2(\mu) = \\ = K_2(\mu)r_{12}(\lambda + \mu)K_1(\lambda) + K_2(\mu)K_1(\lambda)r_{21}(\lambda - \mu). \end{aligned} \tag{34}$$

It can be shown [15, 12] that by defining the non-unitary classical r-matrix

$$r_{12}^K(\lambda, \mu) = r_{12}(\lambda - \mu) - K_2(\mu)r_{12}(\lambda + \mu)K_2^{-1}(\mu), \tag{35}$$

the classical Yang-Baxter equation (32) and (34) combine into one equation, the so-called generalized classical Yang-Baxter equation

$$[r_{32}^K(\nu, \mu), r_{13}^K(\lambda, \nu)] + [r_{12}^K(\lambda, \mu), r_{13}^K(\lambda, \nu) + r_{23}^K(\mu, \nu)] = 0. \tag{36}$$



As the classical  $r$ -matrix defines the Sklyanin linear bracket, an essential tool in the study of the periodic Gaudin model [5, 6, 7, 8, 9, 10], the non-unitary  $r$ -matrix (34), through the relevant linear bracket, defines the so-called generalized Gaudin algebra essential in the study of the non-periodic model [12, 15, 17, 18, 19].

## References

- [1] M. Gaudin, *Diagonalisation d'une classe d'hamiltoniens de spin*, J. Physique 37 (1976) 1087–1098.
- [2] M. Gaudin, *La fonction d'onde de Bethe*, chapter 13 Masson, Paris, 1983.
- [3] M. Gaudin, *The Bethe Wavefunction*, Cambridge University Press, 2014.
- [4] A. A. Belavin and V. G. Drinfeld. *Solutions of the classical Yang-Baxter equation for simple Lie algebras* (in Russian), Funktsional. Anal. i Prilozhen. 16 (1982), no. 3, 1–29; translation in Funct. Anal. Appl. 16 (1982) no. 3, 159–180.
- [5] E. K. Sklyanin, *Separation of variables in the Gaudin model*, Zap. Nauchn. Sem. Leningrad. Otdel. Mat. Inst. Steklov. (LOMI) 164 (1987) 151–169; translation in J. Soviet Math. 47 (1989) 2473–2488.
- [6] M. A. Semenov-Tian-Shansky, *Quantum and classical integrable systems*, in Integrability of Nonlinear Systems, Lecture Notes in Physics Volume 495 (1997) 314–377.
- [7] B. Jurčo, *Classical Yang-Baxter equations and quantum integrable systems (Gaudin models)*, in Quantum groups (Clausthal, 1989), Lecture Notes in Phys. Volume 370 (1990) 219–227.
- [8] P. P. Kulish and N. Manojlović, *Bethe vectors of the  $osp(1|2)$  Gaudin model*, Letters in Mathematical Physics **Vol. 55** (2001) 77–95.
- [9] P. P. Kulish and N. Manojlović, *Creation operators and Bethe vectors of the  $osp(1|2)$  Gaudin model*, Journal of Mathematical Physics **Vol. 42** No. 10 (2001) 4757–4778.
- [10] P. P. Kulish and N. Manojlović, *Trigonometric  $osp(1|2)$  Gaudin model*, Journal of Mathematical Physics **Vol. 44** No. 2 (2003) 676–700.
- [11] N. Manojlović, Z. Nagy and I. Salom, *Derivation of the trigonometric Gaudin Hamiltonians*, Proceedings of the 8th Mathematical Physics meeting: Summer School and Conference on Modern Mathematical Physics, 24 - 31 August 2014, Belgrade, Serbia, SFIN **XXVIII** Series A: Conferences No. A1, ISBN: 978-86-82441-43-4, (2015) 127–135.
- [12] T. Skrypnyk, *Non-skew-symmetric classical  $r$ -matrix, algebraic Bethe ansatz, and Bardeen-Cooper-Schrieffer-type integrable systems*, J. Math. Phys. 50 (2009) 033540, 28 pages.
- [13] N. Cirilo António, N. Manojlović and Z. Nagy, *Trigonometric  $sl(2)$  Gaudin model with boundary terms*, Reviews in Mathematical Physics **Vol. 25** No. 10 (2013) 1343004 (14 pages); [arXiv:1303.2481](https://arxiv.org/abs/1303.2481).
- [14] N. Cirilo António, N. Manojlović and I. Salom, *Algebraic Bethe ansatz for the XXX chain with triangular boundaries and Gaudin model*, Nuclear Physics **B 889** (2014) 87–108; [arXiv:1405.7398](https://arxiv.org/abs/1405.7398).
- [15] N. Cirilo António, N. Manojlović, E. Ragoucy and I. Salom, *Algebraic Bethe ansatz for the  $sl(2)$  Gaudin model with boundary*, Nuclear Physics **B 893** (2015) 305–331; [arXiv:1412.1396](https://arxiv.org/abs/1412.1396).

- 
- [16] N. Manojlović and I. Salom, *Algebraic Bethe ansatz for the XXZ Heisenberg spin chain with triangular boundaries and the corresponding Gaudin model*, Nuclear Physics **B 923** (2017) 73-106; [arXiv:1705.02235](#).
- [17] I. Salom, N. Manojlović and N. Cirilo António, *Generalized  $sl(2)$  Gaudin algebra and corresponding Knizhnik-Zamolodchikov equation*, Nuclear Physics **B 939** (2019) 358-371.
- [18] N. Manojlović and I. Salom, *Algebraic Bethe ansatz for the trigonometric  $sl(2)$  Gaudin model with triangular boundary*, Symmetry **12** (2020) 352; [arXiv:1709.06419](#).
- [19] I. Salom and N. Manojlović, *Creation operators of the non-periodic  $sl(2)$  Gaudin model*, Proceedings of the 8th Mathematical Physics meeting: Summer School and Conference on Modern Mathematical Physics, 24 - 31 August 2014, Belgrade, Serbia, SFIN **XXVIII** Series A: Conferences No. A1, ISBN: 978-86-82441-43-4, (2015) 149–155.
- [20] L. A. Takhtajan and L. D. Faddeev, *The quantum method for the inverse problem and the XYZ Heisenberg model*, (in Russian) Uspekhi Mat. Nauk **34** No. 5 (1979) 13–63; translation in Russian Math. Surveys **34** No.5 (1979) 11–68.
- [21] P. P. Kulish and E. K. Sklyanin, *Quantum spectral transform method. Recent developments*, Lecture Notes in Physics **151** (1982), 61–119.
- [22] R. J. Baxter, *Partition function of the Eight-Vertex lattice model*, Annals of Physics **70** (1972) 193–228.
- [23] R. J. Baxter, *Exactly solved models in statistical mechanics*, Academic Press, London (1982).
- [24] C. N. Yang, *Some exact results for the many-body problem in one dimension with repulsive delta-function interaction*, Physical Review Letters **19** (1967) 1312-1315.
- [25] E. K. Sklyanin, *Boundary conditions for integrable quantum systems*, J. Phys. A: Math. Gen. **21** (1988) 2375–2389.
- [26] H. J. de Vega and A. González Ruiz, *Boundary K-matrices for the XYZ, XXZ, XXX spin chains*, J. Phys. A: Math. Gen. **27** (1994), 6129–6137.
- [27] S. Ghoshal and A. B. Zamolodchikov, *Boundary S-matrix and boundary state in two-dimensional integrable quantum field theory*, International Journal of Modern Physics A **09**, 3841 (1994) 3841–3885.
- [28] S. Ghoshal and A. B. Zamolodchikov, *Errata: Boundary S-matrix and boundary state in two-dimensional integrable quantum field theory*, International Journal of Modern Physics A **09**, 4353 (1994) 4353.
- [29] P. P. Kulish, N. Yu. Reshetikhin and E. K. Sklyanin, *Yang-Baxter equation and representation theory I*, Letters in Mathematical Physics **5** (1981) 393–403.
- [30] L. Mezincescu and R. Nepomechie, *Fusion procedure for open chains*, Journal of Physics A: Mathematical and Theoretical **25** (1992) 2533-2543.
- [31] Alexander B. Zamolodchikov and Alexey B. Zamolodchikov, *Relativistic factorized S-matrix in two dimensions having  $O(N)$  isotopic symmetry* Nuclear Phys. B **133** (1978) 525–535.
- [32] Alexander B. Zamolodchikov and Alexey B. Zamolodchikov, *Factorized S-matrices in two dimensions as the exact solutions of certain relativistic quantum field theory models* Annals of Physics Vol. **120** (1979) 253–291.
- [33] P. P. Kulish and E. K. Sklyanin, *Solutions of the Yang-Baxter equation*, (Russian) Zap. Nauchn. Sem. Leningrad. Otdel. Mat. Inst. Steklov. (LOMI) **95** (1980), 129–160; translation in J. Soviet Math. Vol. **19** (1982), 1596–1620.
- [34] E. K. Sklyanin, *Boundary conditions for integrable equations*, (Russian) Funktsional. Anal. i Prilozhen. **21** (1987) 86–87; translation in Functional Analysis and Its Applications Volume **21**, Issue **2** (1987) 164–166.

- [35] E. K. Sklyanin, *Boundary conditions for integrable systems*, in the Proceedings of the VIIIth international congress on mathematical physics (Marseille, 1986), World Sci. Publishing, Singapore, (1987) 402–408.

# XYZ Gaudin model with boundary terms\*

**Nenad Manojlović<sup>†</sup>**

Departamento de Matemática, Faculdade de Ciências e Tecnologia  
Universidade do Algarve, Campus de Gambelas,  
PT-8005-139 Faro, Portugal

and

Grupo de Física Matemática da Universidade de Lisboa  
Departamento de Matemática, Faculdade de Ciências  
Campo Grande, Edifício C6, 1749-016 Lisboa, Portugal

**Igor Salom<sup>‡</sup>**

Institute of Physics, University of Belgrade  
Pregrevica 118, 11080 Belgrade, Serbia

**Nuno Cirilo António<sup>§</sup>**

Centro de Análise Funcional e Aplicações  
Instituto Superior Técnico, Universidade de Lisboa  
Av. Rovisco Pais, 1049-001 Lisboa, Portugal

## ABSTRACT

We study the elliptic Gaudin model as a quasi-classical limit of the XYZ Heisenberg spin chain with the most general K-matrix. In particular, we give the generating function of the Gaudin Hamiltonians with boundary terms.

## 1. Introduction

There is extensive literature on the subject of Gaudin algebras, discussing its various generalizations in many different contexts [1, 2, 3, 4, 5, 6, 7, 8, 9, 10, 11, 12, 13, 14, 15, 16, 17, 18, 19, 20, 21, 22, 23, 24, 25, 26, 27, 28, 29, 30, 31, 32, 33, 34, 35, 36, 37, 38, 39, 40, 41, 42, 43]. Here we derive the generating function of the Gaudin Hamiltonians with boundary terms in the elliptic case following Sklyanin's approach in the periodic case [4], as we have done for the rational and trigonometric Gaudin model [44, 45, 43, 46, 47]. In the section 2. we review the XYZ Heisenberg spin chain. Our starting point is

---

\* I.S. was supported in part by the Serbian Ministry of Education, Science and Technological Development under grant number ON 171031.

<sup>†</sup> e-mail address: nmanoj@ualg.pt

<sup>‡</sup> e-mail address: isalom@ipb.ac.rs

<sup>§</sup> e-mail address: nantonio@math.ist.utl.pt

the corresponding R-matrix [48, 49] and its most relevant properties. The relevant Lax operator as well as the definition of the Sklyanin algebra [50] is our next step. Then we study the properties of the central element of the RLL-relations, the so-called quantum determinant of the Lax operator, and the representation theory of the Sklyanin algebra which follows from the fusion procedure [50, 51, 52]. Sklyanin showed how to introduce non-periodic boundary conditions which are compatible with the integrability of the bulk system [27]. Following his approach we study the general solution of the relevant Reflection Equation [53, 54, 55] which at the same time defines the corresponding solution of the so-called dual Reflection Equation. The Reflection Equation Algebra provides the suitable algebraic framework for studying the non-periodic XYZ Heisenberg spin chain. This algebra is generated by the entries of the so-called Sklyanin monodromy matrix. As Sklyanin showed [27], the trace of the product of this monodromy matrix with the solution of the dual Reflection Equation yields the transfer matrix of the chain, i.e. the generator of an Abelian subalgebra which is relevant for the dynamics of the system. Moreover, the Sklyanin monodromy matrix admits a central element of the Reflection Equation Algebra. In the section 3. we study the non-periodic elliptic Gaudin model as the quasi-classical limit of the XYZ Heisenberg spin chain. Following Sklyanin's approach in the rational case [4] we show how the linear combination of the quantum determinant of the elliptic monodromy matrix together with its trace yields the generation function of the elliptic Gaudin model, in the periodic case. To study the non-periodic elliptic Gaudin model we follow the same approach we have used successfully in the rational [44] as well as in the trigonometric case [47]. Namely, we combine the classical r-matrix together with the general solution of the classical Reflection Equation into the so-called non-unitary classical r-matrix which is the key notion in the study of the non-periodic Gaudin model. The relevant Lax operator can then be defined in somewhat natural way [44, 45, 46, 47]. This Lax operator and the non-unitary classical r-matrix determine the linear bracket which is antisymmetric and satisfies the Jacobi identity, defining the dynamical symmetry algebra which is of utmost importance for the solvability of the system. The generating function of the Gaudin Hamiltonian is then introduced in a similar way like for the other non-periodic Gaudin models [44, 45, 46, 47]. Finally, in the appendix A we summarise some fundamental identities satisfied by the Jacobi elliptic functions used in the text.

## 2. XYZ Heisenberg spin chain

The R-matrix relevant for the XYZ Heisenberg spin chain is given by [48, 49]

$$R(\lambda, \eta, \kappa) = \mathbb{1} + \sum_{\alpha=1}^3 W_{\alpha}(\lambda, \eta, \kappa) \sigma^{\alpha} \otimes \sigma^{\alpha}, \quad (1)$$

where

$$\begin{aligned} W_1(\lambda, \eta, \kappa) &= \frac{\operatorname{cn}(\lambda + \eta, \kappa) \operatorname{sn}(\eta, \kappa)}{\operatorname{sn}(\lambda + \eta, \kappa) \operatorname{cn}(\eta, \kappa)}, \\ W_2(\lambda, \eta, \kappa) &= \frac{\operatorname{dn}(\lambda + \eta, \kappa) \operatorname{sn}(\eta, \kappa)}{\operatorname{sn}(\lambda + \eta, \kappa) \operatorname{dn}(\eta, \kappa)}, \\ W_3(\lambda, \eta, \kappa) &= \frac{\operatorname{sn}(\eta, \kappa)}{\operatorname{sn}(\lambda + \eta, \kappa)}, \end{aligned} \quad (2)$$

the functions  $\operatorname{sn}(\lambda, \kappa)$ ,  $\operatorname{cn}(\lambda, \kappa)$ , and  $\operatorname{dn}(\lambda, \kappa)$  are the usual Jacobi elliptic functions,  $\lambda$  is a spectral parameter,  $\eta$  is a quasi-classical parameter,  $\kappa$  is the modulus and  $\sigma^\alpha$ ,  $\alpha = 1, 2, 3$ , are the Pauli matrices

$$\sigma^\alpha = \begin{pmatrix} \delta_{\alpha 3} & \delta_{\alpha 1} - i\delta_{\alpha 2} \\ \delta_{\alpha 1} + i\delta_{\alpha 2} & -\delta_{\alpha 3} \end{pmatrix}. \quad (3)$$

The R-matrix (1) satisfies the Yang-Baxter equation

$$R_{12}(\lambda - \mu)R_{13}(\lambda)R_{23}(\mu) = R_{23}(\mu)R_{13}(\lambda)R_{12}(\lambda - \mu). \quad (4)$$

In the present case Yang-Baxter equation reduces to the following matrix equation

$$\begin{aligned} \sum_{\alpha, \beta, \gamma=1}^3 \epsilon_{\alpha\beta\gamma} (W_\beta(\lambda - \mu)W_\gamma(\lambda) - W_\alpha(\lambda - \mu)W_\gamma(\mu) + W_\alpha(\lambda)W_\beta(\mu) \\ - W_\gamma(\lambda - \mu)W_\beta(\lambda)W_\alpha(\mu)) \sigma^\alpha \otimes \sigma^\beta \otimes \sigma^\gamma = 0, \end{aligned} \quad (5)$$

or to the six scalar equations

$$\begin{aligned} W_2(\lambda - \mu)W_3(\lambda) - W_1(\lambda - \mu)W_3(\mu) + W_1(\lambda)W_2(\mu) - W_3(\lambda - \mu)W_2(\lambda)W_1(\mu) &= 0, \\ W_3(\lambda - \mu)W_1(\lambda) - W_2(\lambda - \mu)W_1(\mu) + W_2(\lambda)W_3(\mu) - W_1(\lambda - \mu)W_3(\lambda)W_2(\mu) &= 0, \\ W_1(\lambda - \mu)W_2(\lambda) - W_3(\lambda - \mu)W_2(\mu) + W_3(\lambda)W_1(\mu) - W_2(\lambda - \mu)W_1(\lambda)W_3(\mu) &= 0, \\ W_3(\lambda - \mu)W_2(\lambda) - W_1(\lambda - \mu)W_2(\mu) + W_1(\lambda)W_3(\mu) - W_2(\lambda - \mu)W_3(\lambda)W_1(\mu) &= 0, \\ W_1(\lambda - \mu)W_3(\lambda) - W_2(\lambda - \mu)W_3(\mu) + W_2(\lambda)W_1(\mu) - W_3(\lambda - \mu)W_1(\lambda)W_2(\mu) &= 0, \\ W_2(\lambda - \mu)W_1(\lambda) - W_3(\lambda - \mu)W_1(\mu) + W_3(\lambda)W_2(\mu) - W_1(\lambda - \mu)W_2(\lambda)W_3(\mu) &= 0, \end{aligned} \quad (6)$$

which are consequences of the definition (2) of the functions  $W_\alpha(\lambda) \equiv W_\alpha(\lambda, \eta, \kappa)$ ,  $\alpha = 1, 2, 3$ , the identities (92) and the addition theorems of the Jacobi elliptic functions (93) - (95).

In the following, we study some important properties of the R-matrix (1). Evidently, this R-matrix has the parity invariance

$$R_{21}(\lambda) = R_{12}(\lambda), \quad (7)$$

temporal invariance

$$R_{12}^t(\lambda) = R_{12}(\lambda), \quad (8)$$

and it is regular at  $\lambda = 0$ ,

$$R_{12}(0) = 2\mathcal{P}, \quad (9)$$

here  $\mathcal{P}$  is the permutation matrix in  $\mathbb{C}^2 \otimes \mathbb{C}^2$ .

With the aim of checking the unitarity property we calculate the product

$$\begin{aligned} R(\lambda)R(-\lambda) &= \left( 1 + \sum_{\alpha=1}^3 W_{\alpha}(\lambda)W_{\alpha}(-\lambda) \right) \mathbb{1} + \sum_{\alpha=1}^3 (W_{\alpha}(\lambda) + W_{\alpha}(-\lambda)) \sigma^{\alpha} \otimes \sigma^{\alpha} \\ &\quad - \sum_{\alpha, \beta, \gamma, \rho=1}^3 \epsilon_{\alpha\beta\gamma} \epsilon_{\alpha\beta\rho} W_{\alpha}(\lambda)W_{\beta}(-\lambda) \sigma^{\gamma} \otimes \sigma^{\rho}. \end{aligned} \quad (10)$$

A straightforward calculation shows that

$$\begin{aligned} W_1(\lambda) + W_1(-\lambda) - W_2(\lambda)W_3(-\lambda) - W_3(\lambda)W_2(-\lambda) &= 0, \\ W_2(\lambda) + W_2(-\lambda) - W_3(\lambda)W_1(-\lambda) - W_1(\lambda)W_3(-\lambda) &= 0, \\ W_3(\lambda) + W_3(-\lambda) - W_1(\lambda)W_2(-\lambda) - W_2(\lambda)W_1(-\lambda) &= 0. \end{aligned} \quad (11)$$

Therefore the R-matrix (1) has the unitarity property

$$R(\lambda)R(-\lambda) = \rho(\lambda, \eta, \kappa) \mathbb{1} \quad (12)$$

where the function  $\rho(\lambda, \eta, \kappa)$  is given by

$$\rho(\lambda, \eta, \kappa) = \left( 1 + \sum_{\alpha=1}^3 W_{\alpha}(\lambda)W_{\alpha}(-\lambda) \right) = 4 \frac{\operatorname{sn}^2(\eta, \kappa)}{\operatorname{sn}^2(2\eta, \kappa)} \frac{\operatorname{sn}^2(\lambda, \kappa) - \operatorname{sn}^2(2\eta, \kappa)}{\operatorname{sn}^2(\lambda, \kappa) - \operatorname{sn}^2(\eta, \kappa)}. \quad (13)$$

The R-matrix (1) has the crossing symmetry

$$R(\lambda) = (\sigma^2 \otimes \mathbb{1}) R^{t_1}(-\lambda - 2\eta) (\sigma^2 \otimes \mathbb{1}), \quad (14)$$

where  $t_1$  denotes the transpositions in the first space of the tensor product  $\mathbb{C}^2 \otimes \mathbb{C}^2$ . Consequently, the crossing unitarity property holds

$$R^{t_1}(\lambda)R^{t_1}(\lambda - 4\eta) = \rho(\lambda + 2\eta, \eta, \kappa) \mathbb{1}. \quad (15)$$

In what follows we study an inhomogeneous XYZ spin chain with  $N$  sites, with the local space  $V_m$ , that is the  $2s + 1$  dimensional spin  $s$  representation space of the Sklyanin algebra and inhomogeneous parameter  $\alpha_j$ .

$$\mathcal{H} = \bigotimes_{m=1}^N V_m.$$



Following [50] we introduce the Lax operator

$$\begin{aligned} \mathbb{L}_{0q}(\lambda) &= \mathbb{1} \otimes S^0 + \sum_{\alpha=1}^3 W_{\alpha}(\lambda, \eta, \kappa) \sigma^{\alpha} \otimes S^{\alpha}, \\ &= \begin{pmatrix} S^0 + W_3(\lambda)S^3 & W_1(\lambda)S^1 - iW_2(\lambda)S^2 \\ W_1(\lambda)S^1 + iW_2(\lambda)S^2 & S^0 - W_3(\lambda)S^3 \end{pmatrix}, \end{aligned} \quad (16)$$

were  $S^0, S^1, S^2, S^3$  are the generators of the Sklyanin algebra  $U_{\tau, \eta}(sl(2))$  [50]. The generators of the Sklyanin algebra satisfy the following relations

$$\begin{aligned} [S^1, S^2] &= i(S^0S^3 + S^3S^0), \\ [S^2, S^3] &= i(S^0S^1 + S^1S^0), \\ [S^3, S^1] &= i(S^0S^2 + S^2S^0), \\ [S^0, S^1] &= iJ_{23}(S^2S^3 + S^3S^2), \\ [S^0, S^2] &= iJ_{31}(S^3S^1 + S^1S^3), \\ [S^0, S^3] &= iJ_{12}(S^1S^2 + S^2S^1), \end{aligned} \quad (17)$$

where

$$J_{23} = \frac{W_2(\lambda - \mu)W_3(\lambda)W_2(\mu) - W_3(\lambda - \mu)W_2(\lambda)W_3(\mu)}{W_1(\lambda) - W_1(\lambda - \mu)W_1(\mu)}, \quad (18)$$

$$J_{23} = \frac{W_3(\lambda - \mu)W_2(\mu)W_3(\lambda) - W_2(\lambda - \mu)W_3(\mu)W_2(\lambda)}{W_1(\mu) - W_1(\lambda - \mu)W_1(\lambda)}, \quad (19)$$

$$J_{31} = \frac{W_3(\lambda - \mu)W_1(\lambda)W_3(\mu) - W_1(\lambda - \mu)W_3(\lambda)W_1(\mu)}{W_2(\lambda) - W_2(\lambda - \mu)W_2(\mu)}, \quad (20)$$

$$J_{31} = \frac{W_1(\lambda - \mu)W_3(\mu)W_1(\lambda) - W_3(\lambda - \mu)W_1(\mu)W_3(\lambda)}{W_2(\mu) - W_2(\lambda - \mu)W_2(\lambda)}, \quad (21)$$

$$J_{12} = \frac{W_1(\lambda - \mu)W_2(\lambda)W_1(\mu) - W_2(\lambda - \mu)W_1(\lambda)W_2(\mu)}{W_3(\lambda) - W_3(\lambda - \mu)W_3(\mu)}, \quad (22)$$

$$J_{12} = \frac{W_2(\lambda - \mu)W_1(\mu)W_2(\lambda) - W_1(\lambda - \mu)W_2(\mu)W_1(\lambda)}{W_3(\mu) - W_3(\lambda - \mu)W_3(\lambda)}. \quad (23)$$

Actually, the quantities  $J_{12}$ ,  $J_{23}$  and  $J_{31}$  do not depend on the spectral parameter and are given by [50, 51]

$$J_{12} = \frac{W_1^2(\lambda) - W_2^2(\lambda)}{W_3^2(\lambda) - 1} = (1 - \kappa^2) \frac{\operatorname{sn}^2(\eta, \kappa)}{\operatorname{cn}^2(\eta, \kappa) \operatorname{dn}^2(\eta, \kappa)}, \quad (24)$$

$$J_{23} = \frac{W_2^2(\lambda) - W_3^2(\lambda)}{W_1^2(\lambda) - 1} = \kappa^2 \frac{\operatorname{sn}^2(\eta, \kappa) \operatorname{cn}^2(\eta, \kappa)}{\operatorname{dn}^2(\eta, \kappa)}, \quad (25)$$

$$J_{31} = \frac{W_3^2(\lambda) - W_1^2(\lambda)}{W_2^2(\lambda) - 1} = -\frac{\operatorname{sn}^2(\eta, \kappa) \operatorname{dn}^2(\eta, \kappa)}{\operatorname{cn}^2(\eta, \kappa)}. \quad (26)$$

A straightforward calculation shows that

$$J_{12} + J_{23} + J_{31} + J_{12}J_{23}J_{31} = 0. \quad (27)$$

Therefore

$$J_{\alpha\beta} = -\frac{J_\alpha - J_\beta}{J_\gamma}, \quad (28)$$

with

$$J_1 : J_2 : J_3 = \frac{\operatorname{cn}(2\eta, \kappa)}{\operatorname{cn}^2(\eta, \kappa)} : \frac{\operatorname{dn}(2\eta, \kappa)}{\operatorname{dn}^2(\eta, \kappa)} : 1. \quad (29)$$

Also, it is important to notice that [51]

$$\kappa = \frac{J_{12} + 1}{J_{12} + J_{23}} \sqrt{-J_{23}J_{31}}, \quad \operatorname{sn}^2(\eta, \kappa) = \frac{J_{12} + J_{23}}{J_{12} + 1}. \quad (30)$$

The quadratic Casimir elements of the Sklyanin algebra are given by

$$C_0 = (S^0)^2 + \sum_{\alpha=1}^3 (S^\alpha)^2, \quad (31)$$

$$C_2 = \sum_{\alpha=1}^3 J_\alpha (S^\alpha)^2. \quad (32)$$

Following [50], it maybe useful to introduce another Casimir element of the Sklyanin algebra

$$C_1 = C_0 - C_2 = (S^0)^2 + \sum_{\alpha=1}^3 (1 - J_\alpha) (S^\alpha)^2. \quad (33)$$

Evidently the two dimensional representation of the Sklyanin algebra is given by the R-matrix (1). Therefore in this case

$$S^0 = \mathbb{1} \quad \text{and} \quad S^\alpha = \sigma^\alpha. \quad (34)$$

In this representation, evidently,

$$C_0 = 4\mathbb{1} \quad \text{and} \quad C_2 = (J_1 + J_2 + J_3) \mathbb{1}. \quad (35)$$

The other irreducible representations of the Sklyanin algebra are constructed by the so-called fusion procedure [52, 49, 51, 50]. In particular, the three dimensional representation can be obtained from

$$\begin{aligned} R_{1(23)}(\lambda) &= P_{23}^+ R_{1,23}(\lambda) P_{23}^+ \\ &= P_{23}^+ R_{12}(\lambda + \eta) R_{13}(\lambda - \eta) P_{23}^+, \end{aligned} \quad (36)$$

where

$$P_{23}^+ = \mathbb{1} - P_{23}^- = \mathbb{1} - \frac{1}{4} R_{23}(-2\eta). \quad (37)$$

It follows that, with a suitable choice of bases, the generators of the Sklyanin algebra are represented by the following set of matrices [50]

$$S^0 = \begin{pmatrix} J_3 & 0 & J_1 - J_2 \\ 0 & J_1 + J_2 - J_3 & 0 \\ J_1 - J_2 & 0 & J_3 \end{pmatrix}, \quad (38)$$

$$S^1 = \sqrt{2J_2J_3} \begin{pmatrix} 0 & 1 & 0 \\ 1 & 0 & 1 \\ 0 & 1 & 0 \end{pmatrix}, \quad (39)$$

$$S^2 = \sqrt{2J_3J_1} \begin{pmatrix} 0 & -i & 0 \\ i & 0 & -i \\ 0 & i & 0 \end{pmatrix}, \quad (40)$$

$$S^3 = 2\sqrt{J_1J_2} \begin{pmatrix} 1 & 0 & 0 \\ 0 & 0 & 0 \\ 0 & 0 & -1 \end{pmatrix}. \quad (41)$$

Straightforward substitution of formulae (38) - (41) into (31) and (32) yields

$$C_0 = (J_1 + J_2 + J_3)^2 \mathbb{1}, \quad C_2 = (8J_1J_2J_3) \mathbb{1}. \quad (42)$$

The commutation relations of the generators of the Sklyanin algebra (17) guarantee the RLL-relations for the XYZ Lax operator (16)

$$R_{12}(\lambda - \mu) \mathbb{L}_{1q}(\lambda) \mathbb{L}_{2q}(\mu) = \mathbb{L}_{2q}(\mu) \mathbb{L}_{1q}(\lambda) R_{12}(\lambda - \mu). \quad (43)$$

The RLL-relations admit a central element

$$\mathbb{D}[\mathbb{L}(\lambda)] = \text{tr}_{00'} P_{00'}^- \mathbb{L}_{0q}(\lambda - \eta) \mathbb{L}_{0'q}(\lambda + \eta), \quad (44)$$

where

$$P_{00'}^- = \frac{\mathbb{1} - P_{00'}}{2} = \frac{1}{4} R_{00'}(-2\eta). \quad (45)$$

A straightforward calculation shows that

$$\left[ \mathbb{D}[\mathbb{L}(\mu)], \mathbb{L}(\nu) \right] = 0. \quad (46)$$

Substituting (16) into (44) yields

$$\mathbb{D}[\mathbb{L}(\lambda)] = (S^0)^2 - \sum_{\alpha=1}^3 W_\alpha(\lambda - \eta) W_\alpha(\lambda + \eta) (S^\alpha)^2. \quad (47)$$

In particular, in the case of the R-matrix, its quantum determinant is given by

$$\mathbb{D}[R(\lambda)] = \left( 1 - \sum_{\alpha=1}^3 W_{\alpha}(\lambda - \eta)W_{\alpha}(\lambda + \eta) \right) \mathbb{1} = \rho(\lambda + \eta, \eta, \kappa) \mathbb{1}. \quad (48)$$

In general, the central  $\mathbb{D}[\mathbb{L}(\lambda)]$  can be expressed in terms of the Casimir elements of the Sklyanin algebra using (28), (19), (21) and (23),

$$\mathbb{D}[\mathbb{L}(\lambda)] = C_0 - \frac{1 + W_3(\lambda - \eta)W_3(\lambda + \eta)}{J_3} C_2. \quad (49)$$

The quantum determinant  $\mathbb{D}[\mathbb{L}(\lambda)]$  can be written in terms of  $C_0$  and  $C_1$  as follows

$$\begin{aligned} \mathbb{D}[\mathbb{L}(\lambda)] &= \left( 1 - \frac{1 + W_3(\lambda - \eta)W_3(\lambda + \eta)}{J_3} \right) C_0 \\ &\quad + \left( \frac{1 + W_3(\lambda - \eta)W_3(\lambda + \eta)}{J_3} \right) C_1. \end{aligned} \quad (50)$$

The Lax operator (16) satisfies the following identity

$$\mathbb{L}_{0q}(\lambda) \sigma_0^2 \mathbb{L}_{0q}^{t_0}(\lambda - 2\eta) \sigma_0^2 = \mathbb{1} \otimes \mathbb{D}[\mathbb{L}(\lambda - \eta)], \quad (51)$$

where  $t_0$  denotes the transpositions in the auxiliary space  $\mathbb{C}^2$ .

The so-called monodromy matrix

$$T(\lambda) = \mathbb{L}_{0N}(\lambda - \alpha_N) \cdots \mathbb{L}_{01}(\lambda - \alpha_1) \quad (52)$$

is used to describe the system. Notice that  $T(\lambda)$  is a two-by-two matrix in the auxiliary space  $V_0 = \mathbb{C}^2$ , whose entries are operators acting in  $\mathcal{H}$

$$T(\lambda) = \begin{pmatrix} A(\lambda) & B(\lambda) \\ C(\lambda) & D(\lambda) \end{pmatrix}. \quad (53)$$

From RLL-relations it follows that the monodromy matrix satisfies the RTT-relations

$$R_{00'}(\lambda - \mu) T_0(\lambda) T_{0'}(\mu) = T_{0'}(\mu) T_0(\lambda) R_{00'}(\lambda - \mu). \quad (54)$$

The RTT-relations define the commutation relations for the entries of the monodromy matrix.

In the periodic case the modified Algebraic Bethe Ansatz [48, 56] yields the spectrum of the spin-s XYZ Heisenberg Hamiltonian

$$H = -\frac{1}{2} \sum_{m=1}^N (J_1 S_m^1 S_{m+1}^1 + J_2 S_m^2 S_{m+1}^2 + J_3 S_m^3 S_{m+1}^3). \quad (55)$$

A way to introduce non-periodic boundary conditions which are compatible with the integrability of the bulk system, was developed in [27].

The compatibility condition between the bulk and the boundary of the system takes the form of the so-called Reflection Equation. It is written in the following form for the left reflection matrix acting on the space  $V_1 = \mathbb{C}^2$  at the first site,  $K^-(u) \in \text{End}(\mathbb{C}^2)$

$$R_{12}(u-v)K_1^-(u)R_{21}(u+v)K_2^-(v) = K_2^-(v)R_{12}(u+v)K_1^-(u)R_{21}(u-v). \quad (56)$$

The general solution of the reflection equation above, for the R-matrix (16), can be written as follows [53, 54, 55]

$$K^-(u) = \begin{pmatrix} \text{sn}(u+a) - d \text{sn}(u-a) & b \text{sn}(2u) \frac{c(1-\tau \text{sn}^2(u)) + 1 + \tau \text{sn}^2(u)}{1 - \tau^2 \text{sn}^2(u) \text{sn}^2(a)} \\ b \text{sn}(2u) \frac{c(1-\tau \text{sn}^2(u)) - 1 - \tau \text{sn}^2(u)}{1 - \tau^2 \text{sn}^2(u) \text{sn}^2(a)} & -\text{sn}(u-a) + d \text{sn}(u+a) \end{pmatrix}, \quad (57)$$

here  $a, b, c, d$  are arbitrary constants.

Due to the properties of the Yang R-matrix the dual reflection equation can be presented in the following form

$$R_{12}(v-u)K_1^+(u)R_{21}(-u-v-2\omega)K_2^+(v) = K_2^+(v)R_{12}(-u-v-2\omega)K_1^+(u)R_{21}(v-u).$$

One can then verify that the mapping

$$K^+(u) = K^-(-u - \omega)$$

is a bijection between solutions of the reflection equation and the dual reflection equation. After substitution of into the dual reflection equation one gets the reflection equation with shifted arguments.

We use Sklyanin approach to integrable spin chains with non-periodic boundary conditions [27]. The Sklyanin monodromy matrix  $\mathcal{T}(\lambda)$  is

$$\mathcal{T}_0(\lambda) = T_0(\lambda)K_0^-(\lambda)\tilde{T}_0(\lambda). \quad (58)$$

The monodromy matrix  $\tilde{T}_0(\lambda)$  is such that its RTT-relations (54) can be recast as follows

$$\tilde{T}_{0'}(\mu)R_{00'}(\lambda+\mu)T_0(\lambda) = T_0(\lambda)R_{00'}(\lambda+\mu)\tilde{T}_{0'}(\mu), \quad (59)$$

$$\tilde{T}_0(\lambda)\tilde{T}_{0'}(\mu)R_{00'}(\mu-\lambda) = R_{00'}(\mu-\lambda)\tilde{T}_{0'}(\mu)\tilde{T}_0(\lambda). \quad (60)$$

Then, by construction, the exchange relations of the monodromy matrix  $\mathcal{T}(\lambda)$  are

$$R_{00'}(\lambda-\mu)\mathcal{T}_0(\lambda)R_{0'0}(\lambda+\mu)\mathcal{T}_{0'}(\mu) = \mathcal{T}_{0'}(\mu)R_{00'}(\lambda+\mu)\mathcal{T}_0(\lambda)R_{0'0}(\lambda-\mu). \quad (61)$$

The Reflection Equation Algebra admits a central element, the so-called Sklyanin determinant [27],

$$\Delta [\mathcal{T}(\lambda)] = \text{tr}_{00'} P_{00'}^- \mathcal{T}_0(\lambda - \eta/2) R_{00'}(2\lambda) \mathcal{T}_{0'}(\lambda + \eta/2). \quad (62)$$

The open chain transfer matrix is given by the trace of the monodromy  $\mathcal{T}(\lambda)$  over the auxiliary space  $V_0$  with an extra reflection matrix  $K^+(\lambda)$ ,

$$t(\lambda) = \text{tr}_0 (K^+(\lambda) \mathcal{T}(\lambda)). \quad (63)$$

The reflection matrix  $K^+(\lambda)$  is the corresponding solution of the dual reflection equation.

The commutativity of the transfer matrix for different values of the spectral parameter

$$[t(\lambda), t(\mu)] = 0, \quad (64)$$

is guaranteed by the dual reflection equation and the exchange relations of the monodromy matrix  $\mathcal{T}(\lambda)$ .

In the spin- $\frac{1}{2}$  case, in the homogeneous limit, this transfer matrix yields the Hamiltonian with the boundary terms of the form:

$$H = \sum_{m=1}^{N-1} H_{m,m+1} + (A_- \sigma_1^z + B_- \sigma_1^+ + C_- \sigma_1^-) + (A_+ \sigma_N^z + B_+ \sigma_N^+ + C_+ \sigma_N^-), \quad (65)$$

where the first term corresponds to the expression 55 (here without the periodic boundary condition). The separation of variables method [57, 58] was used to obtain the spectrum of the above transfer matrix by S. Faldella and G. Niccoli [59].

### 3. Generalized XYZ Gaudin model

The key observation is that the R-matrix (1) admits the following expansion [16]

$$R(\lambda, \eta) = \mathbb{1} + 2\eta r(\lambda) + \mathcal{O}(\eta^2), \quad (66)$$

where the classical r-matrix is given by

$$r(\lambda) = \sum_{\alpha=1}^3 w_\alpha(\lambda) \sigma^\alpha \otimes \sigma^\alpha, \quad (67)$$

where

$$w_1(\lambda) = \frac{\text{cn}(\lambda, \kappa)}{\text{sn}(\lambda, \kappa)}, \quad w_2(\lambda) = \frac{\text{dn}(\lambda, \kappa)}{\text{sn}(\lambda, \kappa)}, \quad w_3(\lambda) = \frac{1}{\text{sn}(\lambda, \kappa)}, \quad (68)$$

the functions  $\text{sn}(\lambda, \kappa)$ ,  $\text{cn}(\lambda, \kappa)$ , and  $\text{dn}(\lambda, \kappa)$  are the usual Jacobi elliptic functions and  $\sigma^\alpha$ ,  $\alpha = 1, 2, 3$ , are the Pauli matrices (3). Evidently, this classical r-matrix has the parity invariance property

$$r_{21}(\lambda) = r_{12}(\lambda), \tag{69}$$

and, due to the fact that  $w_\alpha(\lambda)$  (68) are odd function of  $\lambda$  cf. (91), it also has the unitarity property

$$r_{21}(-\lambda) = -r_{12}(\lambda). \tag{70}$$

Notice that in the case of the r-matrix (67) the classical Yang-Baxter equation

$$[r_{13}(\lambda), r_{23}(\mu)] + [r_{12}(\lambda - \mu), r_{13}(\lambda) + r_{23}(\mu)] = 0, \tag{71}$$

reduces to the following three identities

$$\begin{aligned} w_1(\lambda) w_2(\mu) &= -w_2(\lambda - \mu) w_3(\lambda) + w_1(\lambda - \mu) w_3(\mu), \\ w_3(\lambda) w_1(\mu) &= -w_1(\lambda - \mu) w_2(\lambda) + w_3(\lambda - \mu) w_2(\mu), \\ w_2(\lambda) w_3(\mu) &= -w_3(\lambda - \mu) w_1(\lambda) + w_2(\lambda - \mu) w_1(\mu), \end{aligned} \tag{72}$$

which are consequences of the definition (68) of the functions  $w_\alpha(\lambda)$ ,  $\alpha = 1, 2, 3$ , the identities (92) and the addition theorems of the Jacobi elliptic functions (93) - (95).

The Lax operator of the chain (16) admits the following expansion

$$\mathbb{L}_{0q}(\lambda, \eta) = \mathbb{1} + 2\eta \ell_{0q}(\lambda) + \mathcal{O}(\eta^2), \tag{73}$$

where

$$\ell_{0q}(\lambda) = \sum_{\alpha=1}^3 w_\alpha(\lambda) \sigma_0^\alpha \otimes S^\alpha. \tag{74}$$

Therefore the expansion of the monodromy matrix (52) reads

$$T_0(\lambda, \eta) = \mathbb{1} + 2\eta L_0(\lambda) + \eta^2 T_0^{(2)}(\lambda) + \mathcal{O}(\eta^3), \tag{75}$$

where the Gaudin Lax operator is given by

$$L_0(\lambda) = \sum_{m=1}^N \ell_{0n}(\lambda - \alpha_m). \tag{76}$$

The RTT-relations (54) imply the so-called Sklyanin linear bracket for the Gaudin Lax operator

$$[L_0(\lambda), L_{0'}(\mu)] = [r_{00'}(\lambda - \mu), L_0(\lambda) + L_{0'}(\mu)], \tag{77}$$



with the above classical r-matrix (67).

It can be shown that the transfer matrix of the chain and the quantum determinant of the monodromy matrix admit the following expansions

$$\begin{aligned} t(\lambda, \eta) &= 1 + \eta^2 \operatorname{tr}_0 T_0^{(2)}(\lambda) + \mathcal{O}(\eta^3), \\ \mathbb{D}[T_0(\lambda, \eta)] &= 1 + \eta^2 \left( \operatorname{tr}_0 T_0^{(2)}(\lambda) + 4 \operatorname{tr}_0 L_0^2(\lambda) \right) + \mathcal{O}(\eta^3). \end{aligned} \quad (78)$$

Thus the generating function  $\tau(\lambda)$  of the Gaudin Hamiltonians in the elliptic case can be obtain as a difference

$$\mathbb{D}[T_0(\lambda, \eta)] - t(\lambda, \eta) = 4\eta \operatorname{tr}_0 L_0^2(\lambda) + \mathcal{O}(\eta^3), \quad (79)$$

with, as expected,

$$\tau(\lambda) = \operatorname{tr}_0 L_0^2(\lambda). \quad (80)$$

Evidently,  $\tau(\lambda)$  commute for different values of the spectral parameter,

$$[\tau(\lambda), \tau(\mu)] = 0. \quad (81)$$

As in the rational and the trigonometric case, the expansion into partial fractions yields the corresponding Gaudin Hamiltonians

$$\tau(\lambda) = \sum_{m=1}^N \wp(\lambda - \alpha_m) s_m(s_m + 1) + \sum_{m=1}^N \zeta(\lambda - \alpha_m) H_m + H_0, \quad (82)$$

where  $\wp$  is the Weierstrass P function,  $\zeta$  is the zeta function,  $H_0$  is  $\lambda$  independent and

$$H_m = 2 \sum_{m \neq n} \sum_{\alpha=1}^3 w_\alpha(\alpha_n - \alpha_m) S_n^\alpha S_m^\beta. \quad (83)$$

Sklyanin and Takebe [16, 17] obtained the spectrum of the generating function both by the modified Algebraic Bethe Ansatz and by the separation of variables method.

In order to define the Gaudin model with boundary terms we consider the following non-unitary classical r-matrix [44, 47]

$$r_{00'}^K(\lambda, \mu) = r_{00'}(\lambda - \mu) - K_{0'}(\nu) r_{00'}(\lambda + \mu) K_{0'}^{-1}(\mu), \quad (84)$$

where

$$K_0(\lambda) \equiv K_0^-(\lambda). \quad (85)$$

It is straightforward to check that this r-matrix satisfies the classical Yang-Baxter equation [44, 47]

$$[r_{32}^K(\lambda_3, \lambda_2), r_{13}^K(\lambda_1, \lambda_3)] + [r_{12}^K(\lambda_1, \lambda_2), r_{13}^K(\lambda_1, \lambda_3) + r_{23}^K(\lambda_2, \lambda_3)] = 0. \quad (86)$$

The corresponding Lax operator is given by

$$\mathcal{L}_0(\lambda) = \sum_{m=1}^N (\ell_{0m}(\lambda - \alpha_m) + K_0(\lambda)\ell_{0m}(\lambda + \alpha_m)K_0^{-1}(\lambda)). \quad (87)$$

Evidently, it satisfies the following linear bracket relations

$$[\mathcal{L}_0(\lambda), \mathcal{L}_{0'}(\mu)] = [r_{00'}^K(\lambda, \mu), \mathcal{L}_0(\lambda)] - [r_{0'0}^K(\mu, \lambda), \mathcal{L}_{0'}(\mu)]. \quad (88)$$

By definition this linear bracket is obviously anti-symmetric. It obeys the Jacobi identity since the  $r$ -matrix  $r_{00'}^K(\lambda, \mu)$  satisfies the classical Yang-Baxter equation.

The generating function  $\tau(\lambda)$  of the Gaudin Hamiltonians with boundary terms is given by

$$\tau(\lambda) = \text{tr}_0 \mathcal{L}_0^2(\lambda). \quad (89)$$

The generating function for different values of the spectral parameter obviously commute,

$$[\tau(\lambda), \tau(\mu)] = 0. \quad (90)$$

Thus, defining the family of the Gaudin Hamiltonians in involution.

In this way, we have achieved the main objective of this work. Our next step will be to solve explicitly the model using either the modified algebraic Bethe ansatz [48], which was successfully used in the periodic case [16], or the separation of variables method [57, 58], used to solve the periodic elliptic Gaudin model [17] as well as the non-periodic elliptic chain [59].

## A Jacobi elliptic functions

In this appendix we briefly review some basic identities which follow from the definition of the Jacobi elliptic functions. In particular,

$$\text{sn}(-\lambda, \kappa) = -\text{sn}(\lambda, \kappa), \quad \text{cn}(-\lambda, \kappa) = \text{cn}(\lambda, \kappa), \quad \text{dn}(-\lambda, \kappa) = \text{dn}(\lambda, \kappa), \quad (91)$$

$$\text{sn}^2(\lambda, \kappa) + \text{cn}^2(\lambda, \kappa) = 1, \quad \text{dn}^2(\lambda, \kappa) + \kappa^2 \text{sn}^2(\lambda, \kappa) = 1. \quad (92)$$

The addition theorems for the Jacobi elliptic functions read

$$\text{sn}(\lambda + \mu, \kappa) = \frac{\text{sn}(\lambda, \kappa)\text{cn}(\mu, \kappa)\text{dn}(\mu, \kappa) + \text{cn}(\lambda, \kappa)\text{dn}(\lambda, \kappa)\text{sn}(\mu, \kappa)}{1 - \kappa^2 \text{sn}^2(\lambda, \kappa)\text{sn}^2(\mu, \kappa)}, \quad (93)$$

$$\text{cn}(\lambda + \mu, \kappa) = \frac{\text{cn}(\lambda, \kappa)\text{cn}(\mu, \kappa) - \text{sn}(\lambda, \kappa)\text{dn}(\lambda, \kappa)\text{sn}(\mu, \kappa)\text{dn}(\mu, \kappa)}{1 - \kappa^2 \text{sn}^2(\lambda, \kappa)\text{sn}^2(\mu, \kappa)}, \quad (94)$$

$$\text{dn}(\lambda + \mu, \kappa) = \frac{\text{dn}(\lambda, \kappa)\text{dn}(\mu, \kappa) - \kappa^2 \text{sn}(\lambda, \kappa)\text{cn}(\lambda, \kappa)\text{sn}(\mu, \kappa)\text{cn}(\mu, \kappa)}{1 - \kappa^2 \text{sn}^2(\lambda, \kappa)\text{sn}^2(\mu, \kappa)}. \quad (95)$$

Some other important identities follow from the formulae above

$$\operatorname{sn}(\lambda + \mu, \kappa) \operatorname{sn}(\lambda - \mu, \kappa) = \frac{\operatorname{sn}^2(\lambda, \kappa) - \operatorname{sn}^2(\mu, \kappa)}{1 - \kappa^2 \operatorname{sn}^2(\lambda, \kappa) \operatorname{sn}^2(\mu, \kappa)}, \quad (96)$$

$$\operatorname{cn}(\lambda + \mu, \kappa) \operatorname{cn}(\lambda - \mu, \kappa) = \frac{\operatorname{cn}^2(\mu, \kappa) - \operatorname{sn}^2(\lambda, \kappa) \operatorname{dn}^2(\mu, \kappa)}{1 - \kappa^2 \operatorname{sn}^2(\lambda, \kappa) \operatorname{sn}^2(\mu, \kappa)}, \quad (97)$$

$$\operatorname{dn}(\lambda + \mu, \kappa) \operatorname{dn}(\lambda - \mu, \kappa) = \frac{\operatorname{dn}^2(\mu, \kappa) - \kappa^2 \operatorname{sn}^2(\lambda, \kappa) \operatorname{cn}^2(\mu, \kappa)}{1 - \kappa^2 \operatorname{sn}^2(\lambda, \kappa) \operatorname{sn}^2(\mu, \kappa)}. \quad (98)$$

## References

- [1] M. Gaudin, *Diagonalisation d'une classe d'hamiltoniens de spin*, J. Physique 37 (1976) 1087–1098.
- [2] M. Gaudin, *La fonction d'onde de Bethe*, chapter 13 Masson, Paris, 1983.
- [3] M. Gaudin, *The Bethe Wavefunction*, Cambridge University Press, 2014.
- [4] E. K. Sklyanin, *Separation of variables in the Gaudin model*, Zap. Nauchn. Sem. Leningrad. Otdel. Mat. Inst. Steklov. (LOMI) 164 (1987) 151–169; translation in J. Soviet Math. 47 (1989) 2473–2488.
- [5] A. A. Belavin and V. G. Drinfeld. *Solutions of the classical Yang-Baxter equation for simple Lie algebras* (in Russian), Funktsional. Anal. i Prilozhen. 16 (1982), no. 3, 1–29; translation in Funct. Anal. Appl. 16 (1982) no. 3, 159–180.
- [6] M. A. Semenov-Tian-Shansky, *Quantum and classical integrable systems*, in Integrability of Nonlinear Systems, Lecture Notes in Physics Volume 495 (1997) 314–377.
- [7] B. Jurčo, *Classical Yang-Baxter equations and quantum integrable systems*, J. Math. Phys. Volume 30 (1989) 1289–1293.
- [8] B. Jurčo, *Classical Yang-Baxter equations and quantum integrable systems (Gaudin models)*, in Quantum groups (Clausthal, 1989), Lecture Notes in Phys. Volume 370 (1990) 219–227.
- [9] B. Feigin, E. Frenkel, and N. Reshetikhin, *Gaudin model, Bethe ansatz and correlation functions at the critical level*, Commun. Math. Phys. 166 (1994) 27–62.
- [10] N. Reshetikhin and A. Varchenko, *Quasiclassical asymptotics of solutions to the KZ equations*, in Geometry, Topology and Physics, Conf. Proc. Lecture Notes Geom., pages 293–273. Internat. Press, Cambridge, MA, 1995.
- [11] F. Wagner and A. J. Macfarlane, *Solvable Gaudin models for higher rank symplectic algebras. Quantum groups and integrable systems (Prague, 2000)* Czechoslovak J. Phys. 50 (2000) 1371–1377.
- [12] T. Brzezinski and A. J. Macfarlane, *On integrable models related to the osp(1,2) Gaudin algebra*, J. Math. Phys. 35 (1994), no. 7, 3261–3272.
- [13] P. P. Kulish and N. Manojlović, *Bethe vectors of the osp(1|2) Gaudin model*, Letters in Mathematical Physics **Vol. 55** (2001) 77–95.
- [14] P. P. Kulish and N. Manojlović, *Creation operators and Bethe vectors of the osp(1|2) Gaudin model*, J. Math. Phys. 42 no. 10 (2001) 4757–4778.
- [15] P. P. Kulish and N. Manojlović, *Trigonometric osp(1|2) Gaudin model*, J. Math. Phys. 44 no. 2 (2003) 676–700.

- 
- [16] E. K. Sklyanin and T. Takebe, *Algebraic Bethe ansatz for the XYZ Gaudin model*, Physics Letters A 219 (1996) 217–225.
- [17] E. K. Sklyanin and T. Takebe, *Separation of Variables in the Elliptic Gaudin Model*, Commun. Math. Phys. 204 (1999) 17–38.
- [18] K. Hikami, P. P. Kulish and M. Wadati, *Integrable Spin Systems with Long-Range Interaction*, Chaos, Solitons & Fractals Vol. 2 No. 5 (1992) 543–550.
- [19] K. Hikami, P. P. Kulish and M. Wadati, *Construction of Integrable Spin Systems with Long-Range Interaction*, J. Phys. Soc. Japan Vol. 61 No. 9 (1992) 3071–3076.
- [20] K. Hikami, *Gaudin magnet with boundary and generalized Knizhnik-Zamolodchikov equation*, J. Phys. A Math. Gen. **28** (1995) 4997–5007.
- [21] W. L. Yang, R. Sasaki and Y. Z. Zhang,  $\mathbb{Z}_n$  elliptic Gaudin model with open boundaries, JHEP 09 (2004) 046.
- [22] W. L. Yang, R. Sasaki and Y. Z. Zhang,  $A_{n-1}$  Gaudin model with open boundaries, Nuclear Physics B 729 (2005) 594–610.
- [23] K. Hao, W.-L. Yang, H. Fan, S. Y. Liu, K. Wu, Z. Y. Yang and Y. Z. Zhang, *Determinant representations for scalar products of the XXZ Gaudin model with general boundary terms*, Nuclear Physics **B 862** (2012) 835–849.
- [24] A. Lima-Santos, *The  $sl(2|1)^{(2)}$  Gaudin magnet with diagonal boundary terms*, J. Stat. Mech. (2009) P07025.
- [25] E. K. Sklyanin, *Boundary conditions for integrable equations*, (Russian) Funktsional. Anal. i Prilozhen. 21 (1987) 86–87; translation in Functional Analysis and Its Applications Volume 21, Issue 2 (1987) 164–166.
- [26] E. K. Sklyanin, *Boundary conditions for integrable systems*, in the Proceedings of the VIIIth international congress on mathematical physics (Marseille, 1986), World Sci. Publishing, Singapore, (1987) 402–408.
- [27] E. K. Sklyanin, *Boundary conditions for integrable quantum systems*, J. Phys. A: Math. Gen. **21** (1988) 2375–2389.
- [28] T. Skrypnyk, *Non-skew-symmetric classical r-matrix, algebraic Bethe ansatz, and Bardeen-Cooper-Schrieffer-type integrable systems*, J. Math. Phys. 50 (2009) 033540, 28 pages.
- [29] T. Skrypnyk, *“ $\mathbb{Z}_2$ -graded” Gaudin models and analytical Bethe ansatz*, Nuclear Physics B 870 (2013), no. 3, 495–529.
- [30] N. Cirilo António, N. Manojlović and Z. Nagy, *Trigonometric  $sl(2)$  Gaudin model with boundary terms*, Reviews in Mathematical Physics **Vol. 25** No. 10 (2013) 1343004 (14 pages).
- [31] J. Cao, H. Lin, K. Shi and Y. Wang, *Exact solutions and elementary excitations in the XXZ spin chain with unparallel boundary fields*, Nucl. Phys. B 663 (2003) 487–519.
- [32] R. I. Nepomechie, *Bethe ansatz solution of the open XXZ chain with nondiagonal boundary terms*, J. Phys. A 37 (2004), no. 2, 433–440.
- [33] D. Arnaudon, A. Doikou, L. Frappat, E. Ragoucy and N. Crampé, *Analytical Bethe ansatz in  $gl(N)$  spin chains*, Czechoslovak J. Phys. 56 (2006), no. 2, 141–148.
- [34] C. S. Melo, G. A. P. Ribeiro and M. J. Martins, *Bethe ansatz for the XXX – S chain with non-diagonal open boundaries*, Nuclear Phys. B 711, no. 3 (2005) 565–603.
- [35] J. Cao, W.-L. Yang, K. Shi and Y. Wang, *Off-diagonal Bethe ansatz solution of the XXX spin chain with arbitrary boundary conditions*, Nuclear Physics B 875 (2013) 152–165.

- 
- [36] J. Cao, W.-L. Yang, K. Shi and Y. Wang, *Off-diagonal Bethe ansatz solutions of the anisotropic spin-1/2 chains with arbitrary boundary fields*, Nuclear Physics B 877 (2013) 152–175.
- [37] E. Ragoucy, *Coordinate Bethe ansätze for non-diagonal boundaries*, Rev. Math. Phys. 25 (2013), no. 10, 1343007.
- [38] S. Belliard, N. Crampé and E. Ragoucy, *Algebraic Bethe ansatz for open XXX model with triangular boundary matrices*, Lett. Math. Phys. 103 No. 5 (2013) 493–506.
- [39] S. Belliard and N. Crampé *Heisenberg XXX model with general boundaries: eigenvectors from algebraic Bethe ansatz*, SIGMA Symmetry Integrability Geom. Methods Appl. 9 (2013), Paper 072, 12 pp.
- [40] R. A. Pimenta and A. Lima-Santos, *Algebraic Bethe ansatz for the six vertex model with upper triangular K-matrices*, J. Phys. A 46 No. 45 (2013) 455002, 13 pp.
- [41] N. Cirilo António, N. Manojlović and I. Salom, *Algebraic Bethe ansatz for the XXX chain with triangular boundaries and Gaudin model*, Nuclear Physics B 889 (2014) 87–108.
- [42] K. Hao, J. Cao, T. Yang and W.-L. Yang, *Exact solution of the XXX Gaudin model with the generic open boundaries*, arXiv:1408.3012.
- [43] N. Manojlović and I. Salom, *Algebraic Bethe ansatz for the XXZ Heisenberg spin chain with triangular boundaries and the corresponding Gaudin model*, Nuclear Physics B 923 (2017) 73–106; arXiv:1705.02235.
- [44] N. Cirilo António, N. Manojlović, E. Ragoucy and I. Salom, *Algebraic Bethe ansatz for the  $sl(2)$  Gaudin model with boundary*, Nuclear Physics B 893 (2015) 305–331; arXiv:1412.1396.
- [45] I. Salom and N. Manojlović, *Creation operators of the non-periodic  $sl(2)$  Gaudin model*, Proceedings of the 8th Mathematical Physics meeting: Summer School and Conference on Modern Mathematical Physics, 24 - 31 August 2014, Belgrade, Serbia, SFIN XXVIII Series A: Conferences No. A1, ISBN: 978-86-82441-43-4, (2015) 149–155.
- [46] I. Salom, N. Manojlović and N. Cirilo António, *Generalized  $sl(2)$  Gaudin algebra and corresponding Knizhnik-Zamolodchikov equation*, Nuclear Physics B 939 (2019) 358–371.
- [47] N. Manojlović and I. Salom, *Algebraic Bethe ansatz for the trigonometric  $sl(2)$  Gaudin model with triangular boundary*, Symmetry 12 (2020) 352; arXiv:1709.06419.
- [48] L. A. Takhtajan and L. D. Faddeev, *The quantum method for the inverse problem and the XYZ Heisenberg model*, (in Russian) Uspekhi Mat. Nauk 34 No. 5 (1979) 13–63; translation in Russian Math. Surveys 34 No.5 (1979) 11–68.
- [49] P. P. Kulish and E. K. Sklyanin, *Quantum spectral transform method. Recent developments*, Lect. Notes Phys. 151 (1982), 61–119.
- [50] E. K. Sklyanin, *Some algebraic structures connected with the Yang-Baxter equation*, Funkts. Analiz i ego Prilozh. 16 No. 4 (1982) 27–34; translation in Functional Analysis and Applications 17 (1983) 263–270.
- [51] E. K. Sklyanin, *Some algebraic structures connected with the Yang-Baxter equation. Representations of quantum algebras*, Funkts. Analiz i ego Prilozh. 17 No. 4 (1983) 34–48; translation in Functional Analysis and Applications 17 (1984) 273–284.
- [52] P. P. Kulish, N. Yu. Reshetikhin and E. K. Sklyanin, *Yang-Baxter equation and representation theory I*, Letters in Mathematical Physics 5 (1981) 393–403.

- 
- [53] H. J. de Vega and A. Gonzalez-Ruiz, *Boundary K matrices for the XYZ, XXZ and XXX spin chains*, J. Phys. A **27** (1994) 6129–6137.
  - [54] T. Inami and H. Konno, *Integrable XYZ spin chain with boundaries*, J. Phys. A **27** (1994) L913-L918.
  - [55] Y. Komori and K. Hikami, *Elliptic K-matrix associated with Belavin’s symmetric R-matrix*, Nucl. Phys. B **494** (1997) 687–701.
  - [56] T. Takebe, *Generalized Bethe ansatz with the general spin representations of the Sklyanin algebra*, J. Phys. A: Math. Gen. **25** (1992) 1071-1083.
  - [57] E. K. Sklyanin, *Separation of variables - new trends*, Prog. Theor. Phys. Suppl. **118** (1995) 35–60.
  - [58] J. M. Maillet and G. Niccoli, *On Separation of Variables for Reflection Algebras*, J. Stat. Mech. **1909**, no. 9, (2019) 094020.
  - [59] S. Faldella and G. Niccoli, *SOV approach for integrable quantum models associated with general representations on spin-1/2 chains of the 8-vertex reflection algebra*, J. Phys. A **47** (2014) 115202.





# **P r o c e e d i n g s**

of the

**10th MATHEMATICAL PHYSICS MEETING:**

**School and Conference on  
Modern Mathematical Physics**

September 9–14, 2019, Belgrade, Serbia

**Editors**

**B. Dragovich, I. Salom and M. Vojinović**

Institute of Physics

Belgrade, 2020

SERBIA

Igor Salom<sup>1</sup>

University of Belgrade, Institute of Physics, Belgrade

## 2022 NOBEL PRIZE IN PHYSICS AND THE END OF MECHANISTIC MATERIALISM<sup>2</sup>

### Abstract

The ideas and results that are in the background of the 2022 Nobel Prize in Physics had an immense impact on our understanding of reality. Therefore, it is crucial that these implications also reach the general public and not only the scientists in the related fields of quantum mechanics. The purpose of this review is to attempt to elucidate these revolutionary changes in our worldview that were eventually also acknowledged by the Nobel Committee, and to do it with very few references to mathematical details (which could even be ignored without undermining the take-away essence of the text).

We first look into the foundational disputes between Einstein and Bohr about the nature of quantum mechanics, which culminated in the so-called EPR paradox—the main impetus for all the research that would ensue in this context. Next, we try to explain the statement of the famous Bell's theorem—the theorem that relocated the Einstein-Bohr discussions from the realm of philosophy and metaphysics to the hard-core physics verifiable by experiments (we also give a brief derivation of the theorem's proof). Then we overview the experimental work of the last year's laureates who had the final say about who was right in the debate. The outcome of these experiments forced us to profoundly revise our understanding of the universe. Finally, we discuss in more detail the implications of such outcomes, and what

---

<sup>1</sup> isalom@ipb.ac.rs

<sup>2</sup> This research was supported by the Science Fund of the Republic of Serbia, grant 7745968, *Quantum Gravity from Higher Gauge Theory 2021* — QGHG-2021. The contents of this publication are the sole responsibility of the author and can in no way be taken to reflect the views of the Science Fund of the Republic of Serbia.

are the possible ways in which our worldviews can be modified to account for the experimental facts. As we will see, the standard mechanist picture of the universe is no longer a viable option and can never be again. Nowadays, we know this with certainty unusual for physics that only a strict mathematical theorem could provide.

**Keywords:** EPR paradox, Bell's theorem, Bell's inequality, foundations of quantum mechanics, local realism

## 1. Introduction

The 2022 Physics Nobel Prize was not quite like any other. While the Nobel prizes in physics are always of interest to the physics community, by a rule, they are merely a matter of curiosity for the general public. However, the last year's Nobel award should pertain to all of us, irrespective of profession, and remind us that it is time to rethink our basic worldviews. Indeed, the Nobel Committee's announcement in early October 2022 has elicited some bold titles across journals and news agencies worldwide, even among those not aimed at scientific circles. For example, on October 11, the business newspaper *Financial Times* came up with an article titled *What quantum physics tells us about reality*, while the non-profit news website *The Wire* had a piece titled *In the 2022 Physics Nobel Prize, a Test of Your Grip on Reality*. *Scientific American*, in its October issue, brought up the article *The Universe Is Not Locally Real, and the Physics Nobel Prize Winners Proved It*. The deep philosophical impact of the 2022 Nobel Prize was particularly nicely emphasized in the title of an article that last October showed up in *The Conversation* media network: *How philosophy turned into physics — and reality turned into information*. As we can see, the word “reality” is recurrent in these titles, and few things should be of more pervasive importance than the calls to reconsider our notion of the fundamental reality, especially when these calls (essentially) originate from the Royal Swedish Academy of Sciences.

So, in what sense do the accomplishments of the 2022 laureates Alain Aspect, John F. Clauser, and Anton Zeilinger challenge our understanding of reality? The Nobel Committee summarizes that they were awarded “for experiments with entangled photons, establishing the violation of Bell inequalities and pioneering quantum information science”, but it takes some time and effort to unwrap this ostensibly simple statement. To do so, we must start with the achievements of certain people who could not appear at the last year's Nobel ceremony.

## 2. Einstein and Bohr

### 2.1. The Debates

The first act of the deeply philosophical drama that had its (scientific) resolution in the last year's Nobel prize begins in the first half of the 20<sup>th</sup> century, in the period between the two world wars, when the “new physics” called Quantum Mechanics has begun to assume its mathematically well-defined, more or less present-day form. While there essentially existed a global consensus that the claims of the new theory seemed preposterous, there was a huge disagreement to what extent such a state of affairs reflected the true properties of nature and to what extent only the present state of (possibly highly incomplete) scientific understanding of that nature. The opinions ranged from that of the camp of (some of) the “founding fathers of quantum mechanics”, which included the likes of Niels Bohr, Werner Heisenberg, and Wolfgang Pauli, all the way to the staunch critics of quantum ideas among whom was no lesser figure than Albert Einstein himself. While the former insisted that quantum mechanics provides an accurate and complete description of reality (and if we do not like it, it is nature to blame), the latter were convinced that quantum physics is, at best, a temporary and approximate model of some more “reasonable” underlying physics that we are yet to discover.

The new physics seemed to ignore all the cornerstones of the previously known exact science. One of the more obvious departures from the previous scientific reasoning was the sudden appearance of randomness at the most fundamental level of the new theory—prompting Einstein to famously protest with “God does not play dice”. Namely, we must recall that one of the main tenets of all the prior physics, including then novel theory of relativity, was that there can be nothing inherently random in nature—everything evolves according to strict mathematical laws that precisely *determine* the future of any physical system, leaving no room for chance. Any randomness in the events that we might observe had to be a consequence of our imprecise knowledge either of the present state of the universe, or of the laws of nature, or a consequence of our technical inability to calculate the future from these basic laws. Yet, for a hypothetical being (so-called Laplace's daemon) who knows precise positions and momenta of every atom in the universe, and has both the complete knowledge of physical laws and sufficient computational capabilities—the entire future (and past also) was fixed and known. Such a view was essentially uncontested in science—until this new quantum theory. Famously, in those days, Max Born put forward his “probabilis-

tic” interpretation of the wavefunction (the wavefunction was the main mathematical object of the new physics, describing all properties of a system), according to which we could often do no more but to predict only the probabilities of experimental outcomes—and not due to any lack of technological abilities, but in principle. At face value, the quantum theory suggested that physical laws simply do not fully determine the future of systems, but only provide probabilities for the possible events. This seemed outrageous to many, including Einstein. But, it was gradually becoming clear that much more is at stake than merely this *determinism* of classical physics.

The novel “uncertainty relations”, produced by Heisenberg—stating that some mutually “incompatible” properties such as position and momentum cannot be simultaneously known with arbitrary precision—seemed to be inevitably related to the proposed indeterminism. These relations provided an intuitive rationale as to why we cannot reduce uncertainties in our knowledge of physical systems and again recover determinism. Intuitively, due to them, it was impossible to “track down” all details of the present state of the system, and thus it was also impossible to precisely predict its future state—allowing only for experimental predictions of statistical type. At least, this was intuition based on our classical understanding of systems and their properties which, of course, implied that these properties are well-defined per se, in spite of our knowledge of them possibly being quite vague. However, even here the positions of the two camps started to diverge.

Indeed, it was not clear how to interpret the uncertainty relations themselves. It was one thing to accept that we are incapable to determine certain physical quantities with arbitrary precision, even to accept that the laws of physics happen to “conspire” in such a way that this turns out to be impossible in principle, that is, irrespective of our technological abilities and experimental skills. In particular, it seemed reasonable that the very act of measurement, which must involve some interaction with the object being measured, inescapably disturbs that object in an unpredictable fashion that leads to uncertainties. Einstein seemed quite ready to accept such a possibility, even if it would, in practice, preclude any prospect of determining precise properties of the systems and forever confine our experimental predictions to the mere computation of probabilities. We are imperfect creatures, and thus it is not inconceivable that our capacities, including those to gather (precise) data about the universe, are strictly limited. In this case, it is our imperfection and our problem. Universe (and the systems themselves) certainly “know” their properties, and underlying objective reality must be well-defined,

solid real. The uncertainty relations were, in this view, technical or epistemological limitations and had nothing to do with the true ontology, which remains to be described by a deeper, more complete theory than the quantum mechanics. Consequently, Einstein maintained that deep down “God does not play dice with the universe”, no matter how that might look to us. Even Heisenberg himself seemed to initially share this view of his own relations—as can be inferred from his analysis of what is nowadays known as Heisenberg’s microscope<sup>3</sup> (the position he soon after changed, under Bohr’s influence<sup>4</sup>).

Yet, it was an entirely different thing to assume that the uncertainty relations do not merely talk about our inability to reveal the true properties of nature, but that they actually reflect the vagueness of these properties themselves, per se—that the problem is not that when the momentum of a particle is precisely known and defined, we cannot know the position of this particle, but that this particle position, in a certain sense, no longer “exists”, i.e., that it is not a well-defined property of itself. (Alternatively, following the mathematical formalism, we might then say that this property becomes blurred into a so-called superposition of various possibilities.) In other words, neither the universe nor the particle itself really “know” this location. And this was gradually becoming the position of the Bohr’s camp. Bohr, in particular, saw this via his principle of complementarity, the precursor of the contemporary notion of contextuality in quantum physics. Knowledge of one of the two “complementary” properties (i.e., of those “incompatible”<sup>5</sup> in the context of uncertainty relations) automatically renders the other one ill-defined: precise measurement of momentum does not simply make the position of the particle unknown or unpredictable (e.g., as a consequence of mechanically disturbing the particle)—it makes it fully meaningless and undefinable. In his view, the properties themselves were inseparable from the experimental context that reveals them: the setup needed to measure the momentum crucially differs from the one required to find out the position—these two properties cannot be observed or measured simultaneously. Thus, it was also wrong to assume that the position ex-

---

<sup>3</sup> Werner Heisenberg, *The Physical Principles of the Quantum Theory* (Courier Dover Publications, 1949).

<sup>4</sup> W. Heisenberg, “Über den anschaulichen Inhalt der quantentheoretischen Kinematik und Mechanik”, *Z. fur. Physik*, 43, 172 (1927). Translated as “The physical content of quantum kinematics and mechanics”, in *Quantum Theory and Measurement*, eds. J. Wheeler and W. Zurek (Princeton: Princeton University Press, 1983).

<sup>5</sup> Mathematically, operators corresponding to such properties do not commute.

ists in the context where the momentum was (precisely) measured, and vice versa.

But such a view was inevitably leading further down the rabbit hole. It was obviously altering our basic views about reality, to cite F. Frescura: “In the traditional view, it is assumed that there exists a reality in space-time and that this reality is a given thing, all of whose aspects can be viewed or articulated at any given moment. Bohr was the first to point out that quantum mechanics called this traditional outlook into question.”<sup>6</sup> Moreover, if the position, or momentum (and this also holds for basically any other property) is not always well-defined, when is it that it becomes well-defined? Answering this question eventually led to what is now called the “measurement problem” of quantum mechanics. Namely, it seemed that the properties would become well-defined and thus fully (i.e., in the traditional/classical sense) real only upon their measurement, i.e., observation. According to quantum formalism, it was only upon the measurement that the probabilities of various possible results would *collapse* into one truly realized outcome—a mere potentiality turning into actuality. This idea was often summarized as “measurement causes collapse of the wavefunction”.

Yet, what would constitute a measurement? Bohr thought it was sufficient, in this context, to note that to have a (communicable) measurement outcome requires the interaction of the measured system with a macroscopic measurement instrument, where the latter must be described in the language of classical physics.<sup>7</sup> However, this boundary between a quantum system and the classical measurement apparatus (that possessed this crucial “ability” to make system properties well-defined and thus truly real via measurement)—was itself fluid and vague. Indeed, what prevented us from seeing the measurement apparatus as yet another (albeit larger and more complicated) quantum system that also adhered to the principles of quantum mechanics? And if so, then what makes the properties of the apparatus itself (with or without the system it is measuring) well-defined, that is, when, in that case, does the reality becomes truly “real”? Such a chain of thoughts prompted Eugene Wigner, in a part of his life, to even assume that it must be the consciousness of the observer (as purportedly the only entity not describable by quantum

---

<sup>6</sup> F. A. M. Frescura and B. J. Hiley, “Algebras, quantum theory and pre-space”, in *Revista Brasileira de Fisica, Special volume “Os 70 anos de Mario Schonberg”* (1984): 49–86.

<sup>7</sup> Niels Bohr, *Atomic Physics and Human Knowledge* (London, New York: John Wiley and Sons, 1958).



laws) which truly completes the measurement process and grants the full reality to physical systems. Needless to say, such a view (if seen, as by Wigner, as a claim that consciousness causes an objective, instead of merely subjective, wavefunction collapse) would open a number of other intractable and presumably ridiculous questions (e.g., could a cat, a mouse, an amoeba or a single neuron cause the collapse?). Overall, to the present day, there has been no consensus about what a satisfactory solution to the question when (if ever) the reality becomes well-defined would be (only a plethora of different views called the interpretations of quantum mechanics), so the measurement problem remains.

In any case, Einstein would not subscribe to any of this. The novel roles of the observation and the observer in quantum mechanics, to whom was granted the ability to cause the “wavefunction collapse”<sup>8</sup>, was something abhorred by Einstein. He insisted that physics should describe objective reality independent of any observation, stressing that the moon must be there even when we do not look at it.<sup>9</sup> Therefore, he kept attempting to provide arguments that quantum mechanics must be only an approximate description of a maybe complicated but objective and deterministic underlying reality. After each of his arguments, Bohr would consequently make an effort to refute Einstein’s criticism of the theory, with the aim to show that quantum mechanics was not some effective approximation, but that the quantum wavefunction provides a complete description of reality. These exchanges are remembered as probably the most impressive contest of the two genius minds in the history of science, aka the *Einstein-Bohr debates*. Einstein would come up with a wisely constructed thought experiment, ostensibly violating the principles of quantum mechanics or demonstrating its logical inconsistency, and then it was up to Bohr to defend the theory by showing where Einstein went wrong. In all rounds of this intellectual game, Bohr would eventually come out as the winner (the most remarkable case being the one when Bohr used Einstein’s general relativity to prove Einstein’s argument wrong). Seemingly, Bohr won in all rounds but the last one.

This last and the most influential round of that contest is today known as the Einstein-Podolsky-Rosen (EPR) paradox. It was this argument and its final experimental resolution that, almost a century later, ended in the

---

<sup>8</sup> That is, to invoke the projection postulate.

<sup>9</sup> N. David Mermin, *Boojums All the Way Through* (Cambridge: Cambridge University Press, 1990), 81; J. F. Clauser, “Early History of Bell’s Theorem”, in N. P. Bigelow, J. H. Eberly, C. R. Stroud and I. A. Walmsley, eds., *Coherence and Quantum Optics VIII* (Boston, MA: Springer, 2003).

last year's Nobel Prize in Physics, and therefore, it warrants a more detailed discussion.

## 2.2 Einstein-Podolsky-Rosen Paradox

In May 1935, an article titled *Can Quantum-Mechanical Description of Physical Reality Be Considered Complete?* appeared in the journal *Physical Review*.<sup>10</sup> It was signed by Albert Einstein, Boris Podolsky, and Nathan Rosen. In spite of the question mark in the title, it was clear that the authors were confident that they have finally proved the “incompleteness” of the quantum theory. And sure they had some strong arguments.

Effectively, their claim was that the wavefunction—the mathematical object that, according to quantum mechanics, was supposed to represent the complete information about the physical system—must actually be representing only some “incomplete” approximation of the physical reality. Namely, as they argued, in a good and complete physical theory, every “element of physical reality” must find its place in the mathematical description of the universe—but, according to the authors, this was not the case in quantum mechanics. Their point was that something is likely missing from the quantum description, i.e., that some properties of the physical systems were not taken into account by the quantum theory. (Such properties we would, in modern terminology, call “hidden variables”.) Or, at the very least, that the correspondence between the wavefunction and the physical system is not so one-to-one as claimed by the proponents of the quantum theory (i.e., that the theory lacks “bijective completeness”, as this was later called by some authors<sup>11</sup>).

The novel idea was to consider cases of physical systems that interacted in the past and were then separated. For example, we may consider two particles that constituted a bound two-particle system (like an electron and a proton forming a hydrogen atom) that later decayed, resulting in the two particles leaving in opposite directions. In such cases, it is generally possible to infer some property of one of the particles indirectly, by making the corresponding measurement on the other particle in the pair. For example, if we knew the initial momentum of the overall system (e.g., it was zero) and the momentum was conserved, then afterwards, by measuring the momentum of one particle, we immediately

---

<sup>10</sup> A. Einstein, B. Podolsky and N. Rosen, “Can Quantum-Mechanical Description of Physical Reality Be Considered Complete?” *Phys. Rev.*, 47, 10 (1935): 777–780.

<sup>11</sup> A. Fine, *The Shaky Game: Einstein, Realism and the Quantum Theory*, 2nd Edition (Chicago: University of Chicago Press, 1996).

also find out the momentum of the other one (i.e., it must be of the same intensity but in the opposite direction, so that their vector sum remains zero). This, of course, holds irrespectively of the mutual distance that the separating particles reached at the moment of measurement. In principle, this allows us to find out and precisely predict the momentum of a faraway particle by performing a measurement on a nearby particle.

This fact, that we can precisely know the momentum of the distant particle, without ever disturbing it in any way (we have not performed any measurement on it, only on its peer), in the view of the EPR authors meant that there must be something *real* about this momentum. Whoever next measures the momentum of that other particle is guaranteed (i.e., with 100 percent chance) to obtain precisely the predicted result. EPR paper argues that this is only possible if the distant particle really possesses that well-defined, truly existing momentum value—in other words, if it is an *element of reality*. Quite generally, the EPR paper authors argued that: “If, without in any way disturbing a system, we can predict with certainty (i.e., with probability equal to unity) the value of a physical quantity, then there exists an element of reality corresponding to that quantity.”<sup>12</sup> In a relatively similar way, it turns out to be possible to find out the precise location of the distant particle (by measuring the position of the closer one) which, by the same reasoning, implies that the position of that particle must be a well-defined and real property—an element of reality. Now, since the two particles can be light years apart at the moment when we perform the measurement on one of them, such measurement cannot immediately affect the distant particle—therefore, if it has well-defined momentum after we measure the momentum of its peer, then it must have had it all the time. It is the same with the position. Ergo, contrary to Heisenberg relations and Bohr’s interpretation of those, the particle must possess both well-defined momentum and well-defined position (with precise values of both quantities). If quantum mechanics cannot describe both these properties simultaneously, it means that it is incomplete.

In this last part of the reasoning, they tacitly relied on what is commonly called the principle of *locality*, i.e., of the idea that no influence can be exerted immediately and directly at a distance (more specifically, that no influence can travel faster than light). Namely, a part and parcel of a fully successful mechanical description of reality was always the idea that matter should affect other matter only “locally”, that is, only the

---

<sup>12</sup> Einstein, Podolsky and Rosen, “Can Quantum-Mechanical Description of Physical Reality Be Considered Complete?”.

matter which is in its immediate vicinity (i.e., as if by mechanically “pulling and pushing”), and that only in this way any influence or interaction can propagate through space. It seemed that, at the beginning of the 20<sup>th</sup> century, Einstein cemented this view by showing that the speed of this propagation is always limited by the speed of light (and, via General Relativity, by also clarifying that the same is also true for gravitational interaction).

While this is the outline of EPR’s essential argument against the completeness of quantum mechanics, it is worthwhile to consider their discussion in some more detail, especially as a prelude to later developments.

Quite generally, the EPR authors have noticed that the type of connection (or, in mathematical terminology, type of *correlation*) that, according to quantum mechanics, often exists between particles (systems) that interacted in the past and were then separated, is very strange from the common-sense classical-physics viewpoint. Actually, as they pointed out, quantum mechanics predicted a whole class of many-particle states with such strange properties, which had no classical-physics analogues. Today we call such many-particle states “entangled”.

For example, we can consider more closely wavefunction (or, in contemporary terminology, *state vector*, or simply *state*) corresponding to two particles of spin  $\frac{1}{2}$ , which are “aligned in opposing directions” in the sense that their total spin equals zero. In other words, while each of the particles separately “rotates” in a certain sense—and thus possesses the axis and direction of this rotation (spin)—the overall angular momentum (physical measure of rotation) vanishes. This is similar to the case discussed above—of two particles of known and vanishing total momentum—only here, we consider angular instead of linear momentum, for the reasons of mathematical simplicity. (To practically obtain such a state, the two particles generally had to interact before, to constitute a bound state, or to be simultaneously generated in some physical process.) Mathematically, this two-particle state, in the so-called Dirac notation, has almost an intuitive, pictorial form:

$$|\Psi\rangle = \frac{1}{\sqrt{2}} (|\uparrow\rangle|\downarrow\rangle - |\downarrow\rangle|\uparrow\rangle). \quad (1)$$

Here,  $|\uparrow\rangle$  denotes particle spin aligned in the direction of the positive z-axis, i.e., “upwards” (meaning as if the particle “rotates” around the z-axis in anti-clockwise direction as seen from above, where the usual convention is that the z-axis goes in the “upward” direction), while  $|\downarrow\rangle$  will denote the opposite direction of spinning. The term  $|\uparrow\rangle|\downarrow\rangle$  then corresponds to the physical situation where the first particle has its spin oriented upwards, while the second particle spin has a downward spin

orientation. Hence, (the z components of) their spins cancel each other. The overall state has two similar terms of this type, but the second one is “opposite” in respect to the two particles: the first particle is this time spin-down, while the second is spin-up. To simplify referencing these two particles, we can imagine that the first of these two particles is heading to a researcher named Alice, while the second one is moving towards a researcher called Bob (here we follow the usual naming convention in papers on this subject). Then  $|\uparrow\rangle|\downarrow\rangle$  denotes that Alice’s particle is spin-up, while Bob’s is spin-down and vice-versa, for the  $|\downarrow\rangle|\uparrow\rangle$  term. The combination of the two terms, together with the relative minus sign, turns out to mathematically ensure that the total spin angular momentum is zero, along any axis (not only along the z-axis). The numerical factor  $\frac{1}{\sqrt{2}}$  is the so-called overall normalization (in principle, relevant for the evaluation of probabilities) and it is not crucial for understanding the paradox.

Taken together, the two terms have the following simple interpretation: if Alice’s particle is a spin-up, Bob’s will be a spin-down, and vice versa. More precisely, the formalism of quantum mechanics tells us a couple more things about the particles in such a state. First, if we measure the spin of Alice’s particle along the z-axis, we will get the up result in the 50% of cases, and the spin down result in the other 50% of cases. The same goes for Bob’s particle.<sup>13</sup> In addition, the formalism also tells us that if Alice’s particle, upon the z-spin measurement, turned out to be spin-up, the measurement of the z-spin of Bob’s particle will yield spin-down result with certainty, i.e., 100%. It means that, after the measurement of the spin of Alice’s particle and getting the up result, the state of Bob’s particle is no longer ambiguous (i.e., leading to up and down outcomes with equal chances), but has become precisely  $|\downarrow\rangle$ .<sup>14</sup> And vice versa: obtaining that Alice’s particle has its spin in the down direction, reveals that Bob’s particle has its spin upwards—which in turn means that, as a consequence of the measurement on Alice’s particle, the state of Bob’s particle was automatically changed, or “updated” to the  $|\uparrow\rangle$  value.

In this sense, by measuring the z-spin component of the first particle, we have automatically also found out the z-spin of the other particle and, according to the quantum formalism, by the same token, we have also altered (i.e., updated) the wavefunction of the other particle spin. And this conclusion holds irrespective of the distance between the two particles: even if the other particle is located light years away, by measur-

---

<sup>13</sup> Mathematically, we calculate the up-spin probability of the first particle by computing  $\langle\Psi||\uparrow\rangle\langle\uparrow|\otimes I|\Psi\rangle$ , where  $I$  is the identity operator.

<sup>14</sup> We can obtain this result by acting with the projector  $|\uparrow\rangle\langle\uparrow|\otimes 1$  on state  $|\Psi\rangle$ .

ing the spin of the first particle we can find out the spin orientation of the second. After all, this is not really surprising: we already knew that the two spins must be opposite, so finding one directly determines the other. In the process, we have updated our knowledge about the spin of the second particle, and as long as its wavefunction corresponds to our knowledge, there is nothing mysterious in the fact that the wavefunction has immediately changed, no matter that the particle is light years away.

So far, none of this has been particularly revealing. But the key insight of the authors was that everything said still holds if we decide to measure the spin along the x-axis, instead of the z-axis. Namely, it turns out that the same state vector  $|\Psi\rangle$  can be written, in essentially the same form, this time using “right”  $|\rightarrow\rangle$  and “left”  $|\leftarrow\rangle$  spinning states—with respect to the x-axis:<sup>15</sup>

$$|\Psi\rangle = \frac{1}{\sqrt{2}} (|\rightarrow\rangle|\leftarrow\rangle - |\leftarrow\rangle|\rightarrow\rangle). \quad (2)$$

In particular, this means that if we perform a spin-x measurement on Alice’s particle, we will immediately also know the x-spin component of Bob’s particle. Furthermore, according to the formalism, it would mean that the state of Bob’s particle will be again altered after the measurement performed by Alice on her particle: if we obtain that Alice’s is right spinning, the state of Bob’s will become  $|\leftarrow\rangle$ , and if we obtain left x-spin of Alice’s particle, Bob’s will be “projected” to  $|\rightarrow\rangle$  state.

And now the authors make two important points. The first is that by choosing what measurement to perform on her particle, Alice can partially influence what will be the new state of Bob’s particle. Namely, Alice can choose whether to measure spin along the z-axis or along the x-axis. In the first case, Bob’s particle will end up either in the down state  $|\downarrow\rangle$  (if Alice obtained up) or in the up state  $|\uparrow\rangle$  (if Alice obtained down). Alternatively, Alice can choose to perform measurement of the x-spin component, and Bob’s particle will end up either in the state  $|\rightarrow\rangle$  or  $|\leftarrow\rangle$ . Note that Alice cannot choose whether Bob’s particle will end in  $|\rightarrow\rangle$  or in  $|\leftarrow\rangle$  state—this is completely random, with probability of 50 % for both outcomes. But she can choose whether Bob’s particle will end up in the set  $\{|\uparrow\rangle, |\downarrow\rangle\}$  (if she decides to measure spin along the z-axis), or in the set  $\{|\rightarrow\rangle, |\leftarrow\rangle\}$  (if she opts for the x direction). And she can decide in which of these two mutually exclusive sets Bob’s particle will turn up af-

---

<sup>15</sup> This is not difficult to verify since, following from the so-called representation theory of the SU (2) group, it holds:  $|\rightarrow\rangle = \frac{1}{\sqrt{2}} (|\uparrow\rangle + |\downarrow\rangle)$  and  $|\leftarrow\rangle = \frac{1}{\sqrt{2}} (|\uparrow\rangle - |\downarrow\rangle)$ . Here, the relative minus sign between the two terms in (1) and (2) becomes important.

ter her measurement, even if the second particle is light years away at that moment!

This seemed clearly at odds with Einstein's theory of relativity, according to which no influence could travel faster than light. As it is widely known, light speed appears as the natural speed limit in our universe, since the theory of relativity has shown that a bunch of problems and paradoxes are related to exceeding this limit. On top of the list are problems with causality. Namely, thanks to Einstein's discoveries, we know that moving faster than light in one system of reference amounts to traveling into the past in another system. And while wishful thinking on behalf of the science fiction industry has made worldwide audiences pretty comfortable with the time travel idea (as long as one takes care not to kill their own grandfather), in reality, it is the logical inconsistencies that plague (and thus prevent) this hypothetical possibility. The mere possibility to send information into own past (on demand) is a logical contradiction: one can decide to send oneself in the past (e.g., yesterday) any piece of information that he has not already received yesterday—proving that this is either impossible or not deserving to be truly called “sending information into the past”. We emphasize that the problem has nothing to do with free will—as long as a deterministic robot has the means to send arbitrary information to its own past, a simple algorithm of this sort demonstrates the implausibility of the idea.<sup>16</sup> For these reasons, it is—and has been at the time of EPR writing—generally taken that no influences can travel faster than light.

Thus, the authors of the EPR paper drew a seemingly natural conclusion: since no real influence can travel faster than light, it must be that nothing *really* happens with Bob's particle upon the distant spin measurement performed by Alice. Consequently, it means that some of the states from the  $\{| \uparrow \rangle, | \downarrow \rangle\}$  set must correspond to the same unchanged reality of Bob's particle as one of the states from the  $\{| \rightarrow \rangle, | \leftarrow \rangle\}$  set. That is, the state vector (wavefunction) has changed, but the reality has not—hence, this matching between the wavefunction and the true reality of Bob's particle is not so one-to-one. In other words, the quantum wavefunction does not provide such a completely adequate description of reality as Bohr liked to claim. Either that, or there was some “spooky action at distance”, as Einstein liked to call this immediate influence that

---

<sup>16</sup> It should be noted, however, that the existence of the so-called “closed time loops”, as well as tachyons, is not explicitly forbidden by contemporary physical theories, but to avoid logical contradiction the related hypotheses must somehow preclude either sending information into the past altogether, or at least the ability to do so at will.



the measurement on the first particle allegedly has on the second one. For Einstein, the latter was hardly a serious option.

At this point, it is important to understand why authors could not make a stronger claim: that, since the quantum theory predicts such immediate action at a distance, it is in strict violation of special relativity (and that, thus, quantum mechanics is simply wrong). Namely, one needs to be able to send information faster than light at will in order to violate the predictions of the special theory of relativity: according to relativity, by consecutively sending information faster than light and then returning it back again faster than light from another system of reference, one can actually send it in own past—which, as we have explained, is not just weird but is logically forbidden. But, curiously, in spite of allowing the existence of this “spooky action at distance” that influences wavefunction, quantum mechanics predicts that sending information via such a channel is not possible. This has to do with the inherent randomness of quantum mechanics, due to which Alice cannot influence in which particular state vector will Bob’s particle end (i.e., she can choose only in which of the two sets it will end). And the quantum calculations show that Bob, by measuring the spin of his particle, cannot infer whether Alice has measured her spin along the z-axis or along the x-axis. (All Bob can do is to measure his particle spin along some axis, but irrespective of Alice’s choice, his spin measurement will always yield 50-50 probability along any axis.) Therefore, Alice’s decision on whether to measure x-spin or z-spin of her particle cannot be later inferred just by performing measurements on Bob’s particle, in spite of the fact that its wavefunction description will be different in the two cases.

Had the quantum mechanics predicted that entangled pairs can be used for sending faster-than-light signals (obviously then, it would allow sending information “on demand”), this would have been in contradiction with the implications of special relativity. In principle, one could then perform an actual experiment and check whether the superluminal signalling in this way is really achieved—falsifying one or the other of the two theories. But this was an awkward situation—according to the wavefunction description, some influence was spreading faster than light, yet still it was impossible to use such influence to send meaningful information. As if the two particles were somehow communicating faster than light, only in some specific conspiratorial way that we cannot use for sending information ourselves. Something like that was unconceivable in classical physics, but it was somehow now strangely allowed in quantum physics, thanks to its indeterminism. This might have contributed to Einstein calling the effect “spooky action at distance”, instead of

simply “action at distance”. Consequently, the EPR paradox could not demonstrate the inconsistency of quantum mechanics nor that it has any real (i.e., measurable) conflict with relativity, and for this reason, the EPR paper remained only a (strong) philosophical argument against the purported completeness of the quantum theory. On the other hand, for Einstein, who was a realist and did not believe that nature is truly indeterministic, whether we could use this supposed influence to send information or not certainly did not seem essential: in his view, no real influence could travel faster than light and thus the fact that, according to quantum mechanics, wavefunction was nevertheless changing at distance was simply a proof that quantum description was faulty.

The second point that the EPR authors had made was the one related to uncertainty relations, that we have already briefly discussed. Namely, Heisenberg relations also hold for  $x$  and  $z$  components of spin.<sup>17</sup> This means that, according to Bohr’s understanding of the uncertainty relations, when spin along the  $x$ -axis is precisely known, the spin along the  $z$ -axis cannot be well-defined and vice versa. But, according to Einstein, Podolsky, and Rosen, this two-particle setup demonstrates that Bohr’s understanding must be wrong, that is, that the values of spin along both axes must be well-defined and existing properties at all times, while it is only due to the imperfection of the quantum theory (i.e., due to its incompleteness) that these properties do not appear in the mathematical formalism.

Their argument goes as follows. Let us assume that Alice first measures the spin of her particle along the  $z$ -axis, and obtains the up result. Now we know (and quantum formalism tells us) that if Bob measures  $z$ -spin component of his particle, he is bound to get the spin-down result, with certainty. And, according to the authors, since the  $z$ -spin of Bob’s particle is now well-defined, and has the certain, known-in-advance value, it must be that this spin- $z$  property is in some sense real, that is, there must really be “something about” this particle that would “produce” that guaranteed outcome upon future  $z$ -spin measurement. Furthermore, since these particles can be arbitrarily distant from each other (precluding any real influence of Alice’s measurement on the second particle), that property must have been there even before our measurement or, more precisely, irrespective of our measurement. Thus, this property of Bob’s particle that determines its  $z$ -spin outcome must be there even if Alice decides not to carry out any measurement. Thus, authors call this

---

<sup>17</sup> The  $S_x$  and  $S_z$  operators, corresponding to measurements of these two values, do not commute.

real property of Bob's particle "an element of reality" corresponding to its z-spin value.

By the same reasoning, we can conclude that there must be some feature of Bob's particle—i.e., an element of reality—that determines the outcome of the x-spin measurement, since we can also, in principle, infer its x-spin value by measuring the spin of Alice's particle along the x-axis. In this reasoning, it is crucial that we are able to reveal the spin of Bob's particle without influencing, i.e., disturbing this particle, as it is here guaranteed by the spatial distance between the particles—of course, assuming the validity of the "locality" premise (which was never doubted in the paper). Namely, if any influence of Alice's measurement on Bob's particle was possible, then there would remain a possibility that the spin value of Bob's particle became well-defined only after Alice's measurement and due to it. This is why the "without in any way disturbing a system" requirement had to be present in the above EPR definition of an "element of reality".

In this way, the authors have concluded that there must exist elements of reality that determine the spin projection both along the x-axis and along the z-axis, and since these do not appear in quantum formalism, this formalism must be incomplete. While this is the entire formal conclusion of the paper, essentially, the authors expected that they have consequently proved that uncertainty relations are, therefore, a consequence of this incompleteness, i.e., of our technical inability to precisely infer these elements of reality by measurement and account for them in the theory. In other words, reality is rock-solid with always well-defined properties, while the problem is in us and our present theory. Such elements of reality that do not show up in quantum mechanics, due to its alleged incompleteness, soon become known (in general) as "hidden variables". All this was contrary to Bohr's stance that quantum mechanics provided the full picture (with no room for any "hidden variables"), while the x-spin value, after the spin z measurement, was simply a not well-defined property of nature per se (following the quantum formalism, this property existed then in a so-called superposition of different possibilities, and thus, it did not have a well-defined unique value).

The ball was now in Bohr's court. It took him a few months to reply, and he did it by publishing a paper with precisely the same title as the title of the EPR paper, in the same journal.<sup>18</sup> As we will discuss in some more detail later, the reply emphasized his "non-realist" views (in a cer-

---

<sup>18</sup> N. Bohr, "Can Quantum-Mechanical Description of Physical Reality be Considered Complete?", *Phys. Rev.*, 48, 8 (1935): 696–702.

tain sense: if something does not exist well-defined per se, what would it mean that it was changed at a distance) and that we must embrace a new view of reality, which is more holistic (instead of reductionistic) and does not allow us to see the two particles as truly separate entities. Until this day there are ongoing discussions of historians of science and philosophers as to what extent his defence of the completeness of the theory was to the point and successful.<sup>19</sup> Many were of the opinion that the reply was unclear and confusing, and even Bohr himself, some 15 years later, has regretted his choice of wording on some essential points.<sup>20</sup> However, what was certain is that he has doubled down on the completeness of quantum mechanics, even if it entailed accepting some sort of nonlocality, i.e., of the “spooky action at distance”.

In any case, both the EPR’s initial argument and Bohr’s reply were of philosophical nature, so it was rather a matter of taste who will find which side more appealing and convincing. And the conundrum seemed likely to remain undecided, maybe forever.

### 3. John Bell

#### 3.1 Hidden Variables

For the second act of the drama, we fast forward some thirty years into the future.

The success of the new physics was huge, and almost nobody really cared about Einstein’s philosophical objections. Meanwhile, the formal-

---

<sup>19</sup> For example, Arthur Fine and Thomas A. Ryckman, “The Einstein-Podolsky-Rosen Argument in Quantum Theory”, in *The Stanford Encyclopedia of Philosophy* (Summer 2020 Edition), Edward N. Zalta, ed., accessed on July 31, 2023, <https://plato.stanford.edu/archives/sum2020/entries/qtepr>; A. Fine and M. Beller, “Bohr’s response to EPR”, in eds. J. Faye and H. Folse, *Niels Bohr and Contemporary Philosophy* (New York: Kluwer, 1994), 1–31; Arthur Fine, “Bohr’s Response to EPR: Criticism and Defense.” *Iyyun: The Jerusalem Philosophical Quarterly*, 56 (2007): 31–56. JSTOR, accessed on July 31, 2023, <http://www.jstor.org/stable/23354464>. H. Halvorson and R. Clifton, “Reconsidering Bohr’s Reply to EPR. Non-locality and Modality”. Springer (2022), accessed on August 1, 2023, doi: 10.1007/978-94-010-0385-8\_1; A. Drezet, “Why Bohr was wrong in his response to EPR”, *arXiv* (2023), 2305.06859, accessed on August 1, 2023, <https://arxiv.org/abs/2305.06859v1>; Shingo Fujita, “How Did Bohr Reply to EPR?”, in “The Two Faces of Realism: Bohr and Bell”, *Journal of the Philosophy of Science*, 27 (1994).

<sup>20</sup> Fine and Ryckman, “The Einstein-Podolsky-Rosen Argument in Quantum Theory”.

ism was polished (mostly thanks to John von Neumann) and in practice it worked flawlessly, showing no traces of any incompleteness. The measurement problem still existed, but it was not showing up in any real-life applications or computations. Besides, the science of the post-World War II era was more of a pragmatic type, and physicists were increasingly leaning towards the infamous “shut up and calculate” view of quantum mechanics.

One of the few to whom the question of the true meaning of quantum mechanics was of greater importance than its applications, was Irish physicist John Bell. Working on accelerator design at CERN in the early 1960s, Bell was still managing to find time to investigate the deepest interpretational issues of quantum physics.

Personally, Bell was entirely sharing the late Einstein’s dissatisfaction with the quantum theory. Even the quantum terminology alone was, in his view, improper for a theory of physics—as we can see from his comment about the books on the subject: “For the good books known to me are not much concerned with physical precision. This is clear already from their vocabulary. Here are some words which, however legitimate and necessary in application, have no place in a formulation with any pretension to physical precision: system, apparatus, environment, microscopic, macroscopic, reversible, irreversible, observable, information, measurement. [...] On this list of bad words from good books, the worst of all is ‘measurement’.”<sup>21</sup>

So, the roles of the measurement and the observer in quantum mechanics, even more than the lack of determinism, were deeply unsettling to him, similarly as they were to Einstein. In his view, the prevailing Copenhagen interpretation of quantum physics (i.e., one following the views of Bohr and Heisenberg) had too many “subjective” elements, while he longed for a description of objective reality that would be devoid of vagueness, indeterminism, and the role of the observers.<sup>22</sup>

In particular, he was very enthusiastic about the so-called De Broglie-Bohm pilot-wave interpretation of quantum mechanics. According to the pilot-wave theory, particles had well-defined positions at all times and obeyed causal (deterministic) laws. These supposedly real and well-defined positions were an example of what the EPR authors considered as elements of reality that were not taken into account by the standard quantum mechanics. In quantum mechanics, the full description of sys-

---

<sup>21</sup> John Stewart Bell, *Speakable and Unsayable in Quantum Mechanics* (Cambridge: Cambridge University Press, 1987).

<sup>22</sup> *Ibid.*

tems was given by the wavefunction, and wavefunction only, so if these well-defined coordinates really existed, they were “hidden” in the quantum formalism. Therefore, the pilot-wave theory was an example of a model with *hidden variables* that was, nevertheless, experimentally indistinguishable from the standard, Bohr’s quantum mechanics.

However, while realistic and deterministic, this model had a terribly unwelcome feature of being manifestly nonlocal—meaning that influences could spread immediately over distance, as if acting at infinite speeds. In particular, the velocity of a particle in this theory would depend on the configuration of arbitrarily distant particles at the present moment, i.e., in principle, it could depend on what was currently happening in other galaxies. Due to special relativity, this meant that the influences could also travel into the past, as seen from some reference systems. In truth, the pilot-wave model predicted that information could not be sent faster than by light speed, so it did not experimentally conflict with relativity (otherwise it could be easily falsified), but the nonlocality feature also led to many other, either technical or conceptual complications that plagued this approach. Nevertheless, for Bell, this was an encouraging example, a proof of concept that it might be possible to find a truly satisfactory realistic underlying theory that would replace the vague and subjectivistic quantum formalism. In particular, it would have been exactly the type of theory Einstein was arguing for in the EPR paper, if only it was not for this nonlocality. The essential question was could a similar realistic, but this time also local theory exist, and how to find it?

Bell was strongly inspired by the EPR paradox. Meanwhile, the experimentalists managed (in experiments with photons) to check that the entangled pairs of particles indeed behaved as quantum mechanics predicted: the two spins in the state given by equation (1) would indeed always be opposite to one another (along arbitrary direction). Nevertheless, this confirmation did not take anything away from Einstein, Podolsky, and Rosen’s arguments of incompleteness (after all, they exactly presumed that spins would always be opposite, in deriving their conclusions). Just like Einstein, Bell was confident that the fact that two spins always turn out to be opposite, across arbitrary distances, must point to the existence of some well-defined underlying “elements of reality” that were driving such experimental outcomes. Basically, he understood that these spins must in some sense simply be real, predefined, and opposite to each other, and that the experiment’s role was just to confirm and demonstrate such a state of affairs, and not to make any of the spins well-defined at the moment of measurement (as quantum formalism suggested). He likened the case of opposing spins in the EPR pair to the

socks of his colleague Reinhold Bertlmann, who had a habit of wearing socks of different colours. In his paper *Bertlmann's socks and the nature of reality*,<sup>23</sup> he noted that when we observe one sock of Prof. Bertlmann, we immediately know that the other sock will be of a different colour, even before we spot it—and that there is nothing puzzling here (apart from Bertlmann's dressing habits), irrespective of the hypothetical distance between the socks. The colours of both socks were real and well-defined all the time, and in no way was the moment of our observation essential nor influenced any of the socks. He was positive that the matter of spins should be no more mysterious than that of his colleague's socks, once we discover the underlying true theory of quanta.

Yet, there was this question of how to prove that the spins were indeed like socks and that measurement outcomes were merely revealing the preexisting well-defined reality? Thus far, the EPR argument had remained purely a philosophical one and there had been no consensus about its implications, let alone a consensus that a more complete theory than quantum mechanics was really needed. Moving forward from there required an argument in a form of a prediction that could be experimentally verified and which would, once and for all, settle down the dispute either in Einstein's favour or in favour of Bohr.

However, this seemed impossible. Namely, the trouble was that nobody yet knew the hypothetical underlying more-complete theory that Einstein was arguing for. And if we do not know the theory, how could we possibly test and compare its predictions? All anyone knew was that such a theory had to be realistic and local, but apart from that, it could be arbitrarily complex. Einstein was not claiming that he knew it—he was only confident that it must exist, but the theory might, in principle, even be so complicated that human beings could be incapable of deducing it. Besides, if existed, why would such a theory experimentally differ at all from quantum mechanics—maybe all experimental predictions would be the same, as was the case with the pilot-wave theory?

But, Bell's intuition was different. He felt that any such locally-realistic theory must be observably different from quantum mechanics, and in 1964 he managed to prove it.<sup>24</sup> The proof is known as Bell's theorem, and it (together with the associated experimental tests) was even praised as

---

<sup>23</sup> J. S. Bell, *Bertlmann's socks and the nature of reality. Speakable and Unspeakable in Quantum Mechanics: Collected Papers on Quantum Philosophy* (Cambridge: Cambridge University Press, 2004).

<sup>24</sup> J. S. Bell, "On the Einstein Podolsky Rosen paradox", *Physica Physique Fizika*, 1(3) (1964): 195–200.



“the most profound discovery of science”.<sup>25</sup> Note that the claim was not about the most profound discovery of physics, but of all science, in the history of mankind!

### 3.2 Bell’s Theorem

The starting point was the setup with two entangled particles depicted in the EPR paper. Bell felt that the type of connection between the particles predicted by quantum theory was in some sense “stronger” than it was possible to explain by any “pre-existing” reality (such as that of the well-defined pre-existing colours of Bertlemann’s socks). It did not take long to realize that, to prove this, it was not sufficient to consider only the type of measurements that were in the spotlight of the EPR paper—that is, those where the outcomes of the measurement on the second particle were certain. Thus, Bell’s first insight was that he should in much more detail consider non-zero-or-one probabilities related to measurements on both particles, along different directions.

Once he realized this, he went on to derive a mathematical relation concerning a combination of probabilities to get particular spin outcomes on the two distant particles, but when we are measuring the spin along axes that are neither parallel nor perpendicular, but forming some intermediate angles. For example, he was considering probabilities of the following type: if Alice measures her particle spin along z-axis and obtains up, what is the probability for Bob to obtain the spin of his particle to be in the direction inclined by 45 degrees with respect to the vertical? He managed to mathematically prove that in any locally-realistic universe, a particular combination of such probabilities must satisfy a certain inequality, now known as Bell’s inequality. The main achievement here was in the word “any”. This meant that truly any universe that would respect Einstein’s (and Bell’s) expectations—i.e., where physical systems have well-defined properties irrespective of observation and where influences cannot spread infinitely fast—was bound to satisfy this inequality. This included arbitrarily complicated universes, where particles could, in principle, mutually communicate and even conspire against experimentalists in arbitrary manners, or could behave differently on Earth than on Jupiter (whether we as humans are able to infer or comprehend these complex rules or not was of no relevance here).

---

<sup>25</sup> Henry P. Stapp, “Bell’s Theorem and World Process”, *Nuovo Cimento*, 29B, 2, (1975): 270.

It is important to underline that this inequality had, per se, absolutely nothing to do with quantum mechanics. Again, this was inequality that necessarily constrained any theory in which measurement outcomes were driven by observer-independent well-defined properties of matter (i.e., adhering to realism) and in which there was a limit for the speed at which influences can travel (i.e., respecting locality). In other words, this was a limitation for all universes that meet Einstein's expectations, not for the quantum mechanical universe of Niels Bohr.

This is clear from the fact that the inequality was essentially derived from the following two seemingly naive and self-evident presumptions. The first was the premise of locality: whatever Alice decides to do in her lab, it cannot influence the outcomes (or probabilities of outcomes) of Bob's simultaneous measurements in his arbitrarily distant lab. The other was the premise of realism, which was, arguably, always tacitly present in derivations. In the original Bell's formulation, this premise was taken into account by assuming that the outcomes of spin measurements deterministically followed from some unknown (and non-existing in quantum formalism) yet well-defined properties of particles. In other words, that the outcomes were determined by some hidden variables. Mathematically, they were explicitly represented in Bell's original paper by variable(s) denoted as  $\lambda$ . In some of the following reformulations of Bell's theorem,<sup>26</sup> the requirement of determinism was removed, but the premise of realism nevertheless remained in some form through the role of the variable(s)  $\lambda$  still representing the hidden variables and through the way these hidden variables were used to derive probabilities of spin measurement outcomes. (Some authors argue that the very way the probabilities are expressed as functions of  $\lambda$  encodes the presumption about a classical-like, non-contextual reality.<sup>27</sup> Another way to see this is that, arguably, certain presumptions about underlying reality are necessary even to define the locality postulate in the sense in which it is different from "no-signalling"—while the former is claimed to be violated, the latter is not.)

To fully understand how it was possible to prove such a general inequality can be accomplished only by considering the proof itself. However, since the exposition of the proof requires some equations and

---

<sup>26</sup> Wayne Myrvold, Marco Genovese and Abner Shimony, "Bell's Theorem", in *The Stanford Encyclopedia of Philosophy (Fall 2021 Edition)*, Edward N. Zalta, ed., accessed on August 1, 2023, <https://plato.stanford.edu/archives/fall2021/entries/belltheorem>.

<sup>27</sup> Marek Żukowski and Časlav Brukner, "Quantum non-locality – it ain't necessarily so", *J. Phys. A: Math. Theor.*, 47, 42, 8 (2014): 424009.

some (though fairly basic) mathematical knowledge, we discuss it in a separate Appendix A, below.

The entire relevance of this inequality for the context of the EPR discussion of quantum physics was that Bell noticed that quantum theory actually predicted violations of this inequality! (In the Appendix B, we give a concrete mathematical example of this violation.) Hence, this was precisely what could settle Einstein-Bohr debate once and for all. This inequality was violated by physics advocated by Bohr, while it had to be satisfied by any type of physics advocated by Einstein. Whether the real physical systems satisfied this inequality or not could finally discriminate between Bohr's and Einstein's views, and thus, this inequality had the power to move the debate from pure philosophy into physics.

The very fact that such inequality existed was a proof of Bell's theorem, which essentially stated that no locally-realistic theory can ever reproduce exactly all quantum mechanical predictions. In other words, this was also a proof that it was not possible to improve the pilot-wave theory in a way to make it local but still experimentally indistinguishable from the standard quantum theory. It was now certain that any realistic model that closely reproduces experimental predictions of quantum formalism is also bound to have non-local properties. And it is important to stress that this conclusion holds irrespective of whether we are looking for a strictly deterministic theory or we are even ready to accept inherent randomness (this, however, had become clear only after some generalizations of the original Bell's derivation). Crucially, the quantities constrained by the Bell's inequality were something that could, in principle, be measured. Therefore, it finally became possible to experimentally measure values of these quantities—for some of the special cases in which quantum physics predicts violation of the inequality—and simply check if the constraint is satisfied or not. If the inequality would turn out to be preserved in such an experiment, that would be in contradiction to quantum predictions and would present definite proof that quantum mechanics requires modifications. That would mean the entire quantum theory was only some sort of approximation, with just partial validity. Bell himself thought that such an outcome was, regrettably, unlikely (discouraged by the enormous practical success of quantum mechanics), but still hoped for “an unexpected result, which would shake the world!”<sup>28</sup> and falsify the completeness of the quantum ideas.

However, if the measurement would reveal a violation of Bell's inequality, it would have groundbreaking philosophical implications for

---

<sup>28</sup> Clauser, “Early History of Bell's Theorem”.

our understanding of the universe. Once and for all, we would have to abandon any hope that a “rational” realistic explanation of phenomena in nature, of the type sought after by Einstein, could be found.

Bell, for his part, could now just sit and wait until someone managed to perform the real experiment.

#### 4. John F. Clauser, Alain Aspect and Anton Zeilinger

##### 4.1 Experimental Verdict

The history of physics had to wait almost another decade for the final act of this philosophical drama. Years were passing by after Bell’s groundbreaking proof, yet hardly anyone was noticing Bell’s discovery. Bell had to wait a couple of years even for the first citation of his work, collecting only a handful of citations in the first decade or more. It was not just that his paper was published in a less-known journal *Physics, Physique, Fizika*,<sup>29</sup> but, as the young physicist John F. Clauser working as a postdoctoral researcher at UC Berkeley at the time would later recall, this was a generally unpopular topic. Young Clauser, together with his colleague, graduate student Stuart Freedman, will be the first ever to perform an experimental test of Bell’s inequality. Even after being warned that this research might ruin their careers,<sup>30</sup> the two young scientists further pursued their idea until finally obtaining a definite experimental answer about who was right in the great Einstein-Bohr debate.

From 1964 to 1972, our understanding of physics remained in an unusual limbo state: we knew it was possible to, once and for all, find out whether our universe is “normal” in the sense of Einstein (local and real), or truly as “weird” as Bohr suggested—but still nobody knew the answer. And finally, in 1972, Clauser and Freedman managed to perform the first ever “Bell’s test”.<sup>31</sup> Unlike the original Bell’s paper, which discussed matter particles of spin equal to  $\frac{1}{2}$  (such as electrons or protons), for practical reasons this experiment dealt with photons, measuring polarizations of photon pairs emitted in an atomic cascade. While the spins in Bell’s analy-

---

<sup>29</sup> Bell, “On the Einstein Podolsky Rosen paradox”.

<sup>30</sup> Clauser, “Early History of Bell’s Theorem”; Whitney Clavin, “Proving that Quantum Entanglement is Real”, Caltech, accessed 10 July 2023, <https://www.caltech.edu/about/news/proving-thatquantum-entanglement-is-real>.

<sup>31</sup> S. J. Freedman and J. F. Clauser, “Experimental Test of Local Hidden-Variable Theories”, *Phys. Rev. Lett.*, 28, 14 (1972): 938–941.

sis were opposite, here the polarizations of the two photons in each pair were the same: every time we would let the two photons arrive at polarizing filters aligned in the same direction, either both photons would pass the filters, or neither would. The task was to measure the so-called coincidences: how often would it happen that both photons manage to pass the corresponding polarizing filter and to investigate this probability as a function of the angle between the polarizers. Instead of the probability of the spin measurement outcomes, it was these probabilities of photon coincidences that had to satisfy Bell's inequality. However, these were merely technical differences—the essence remained absolutely the same.

And, at last, we heard the Nature's ruling—no doubt, it was in favour of Bohr! The obtained experimental results perfectly followed quantum mechanical predictions, demonstrating Bell's violation at 6.3 sigma (where everything over 5 sigmas is considered in physics as statistically sure proof). Clauser himself, sympathetic to Einstein's side in the debate, would later say "I was very sad to see that my own experiment had proven Einstein wrong."<sup>32</sup> But so it was.

No doubt that Bell was even sadder than Clauser. As most dramas have some tragic character, in this one, that role was, so to say, taken by Bell. It was Bell's strong inclination towards the realist stance that led him to investigate possibilities for local hidden variable theories in the first place, finally leading him to his theorem. No one else has so openly and bluntly expressed his convictions as did Bell, and seemingly no one's convictions were as strong as Bell's. He was absolutely sure that Einstein must be right, yet he had to concede that he was not:

"For me, it is so reasonable to assume that the photons in those experiments carry with them programs, which have been correlated in advance, telling them how to behave. This is so rational that I think that when Einstein saw that, and the others refused to see it, he was the rational man. The other people, although history has justified them, were burying their heads in the sand. I feel that Einstein's intellectual superiority over Bohr, in this instance, was enormous; a vast gulf between the man who saw clearly what was needed, and the obscurantist. So for me, it is a pity that Einstein's idea doesn't work. The reasonable thing just doesn't work."<sup>33</sup>

---

<sup>32</sup> B. Skuse, "Nobel Prize in Physics 2022", Lindau Nobel Laureate Meetings, accessed on August 1, 2023, <https://www.lindau-nobel.org/blog-nobel-prize-in-physics-2022-provin-g-and-using-the-peculiar-quantumnature-of-reality>.

<sup>33</sup> Jeremy Bernstein, *Quantum Profiles* (Princeton: Princeton University Press, 1991).

On another occasion, he succinctly summarized his sentiment as: “Bohr was inconsistent, unclear, wilfully obscure and right. Einstein was consistent, clear, down-to-earth and wrong.”<sup>34</sup>

Despite his theorem and the subsequent violation of the inequality being terribly disappointing to Bell, this episode was a perfect testimony to the strength of the scientific method. While every scientist must and should have their own opinions, a truly good scientist will not allow their own wishful thinking to stand in the way of reaching the truth. Despite so fervently advocating Einstein’s positions, it was essentially Bell himself who led us to the definite falsification of these views. While Clauser was an accomplice, it was Bell who killed the worldview he cherished as the true one. And he did not hesitate to acknowledge that the outcome of his work and of the later experiments was not the one he was hoping for. By doing so, Bell established his greatness as a scientist, in yet another way.

## 4.2 Closing Loopholes

Yet, some hope for Einstein’s viewpoint still remained after the 1972 experiment. Namely, in Clauser and Freedman’s 1972 experiment, the photons were impinging on the polarizers that were a mere couple of meters away, in the same lab. The experiment was performed in cycles of 100 seconds of accumulating the detectors’ data, during which the polarizers were kept oriented along fixed angles.<sup>35</sup> But the essence of Bell’s original idea was that the two polarizers belonging to Alice and Bob need to be sufficiently distant, so that Alice’s decision about how to orient her polarizer could not have a chance to influence the photon arriving on Bob’s side. In Clauser’s experiment, the hypothetical influence of the decision on how to orient the polarizer on one side of the lab had plenty of time to reach the other side, with no need for superluminal speeds and conflict with locality principles of special relativity.

Reading the Bell’s original paper, there is an impression that not even Bell himself had hoped that the outcome of an experiment such as Clauser’s could be any different than to support quantum mechanical predictions. On the other hand, his hopes were that quantum mechanical predictions about entangled pairs of particles may be limited to the cases where the subluminal influences can arrive from one side to the

---

<sup>34</sup> Graham Farmelo, “Random Acts of Science”, *The New York Times*, June 11, 2010.

<sup>35</sup> Freedman and Clauser, “Experimental Test of Local Hidden-Variable Theories”.

other in due time, but may fail in cases when the distances are greater (or relevant times shorter):

“Of course, the situation is different if the quantum mechanical predictions are of limited validity. Conceivably they might apply only to experiments in which the settings of the instruments are made sufficiently in advance to allow them to reach some mutual rapport by exchanging signals with velocity less than the speed of light. In this connection, experiments of the type proposed by Bohm and Aharonov, in which the settings are changed during the flight of the particles, are crucial.”<sup>36</sup>

In the last sentence, we see that he urged for experiments that would remove this possibility of having any ordinary, slower-than-light signals influencing the results.

However, it must be noted that it is difficult to imagine in what way the two polarizers/detectors from different sides could “communicate” in order to fool the experimenter. Clauser, personally, saw this as a form of “paranoia” for which “it is first necessary to believe that a pair of detectors and analysers that are several meters apart are somehow conspiring with each other, so as to defeat the experimenter”.<sup>37</sup> Nevertheless, this remained a logical possibility, so it is generally accepted that Clauser and Freedman’s original experimental realization with static polarizers suffered from this “locality loophole”, as this “paranoid possibility” became known.

The first experiment to almost entirely close this locality loophole and essentially meet Bell’s original criterion was performed in 1982. It was done by our second Nobel Laureate Alain Aspect and his collaborators working at *École Supérieure d’Optique* in Orsay.<sup>38</sup> Among other experimental improvements, Aspect has found a way to effectively change the orientation of the polarizers on the fly, i.e., while the photons were on their way towards detectors. The polarizers (with the corresponding detectors behind) were situated on the opposing ends of the lab, at a distance of 6 meters from the photon source (i.e., 12 meters apart). That corresponded to the flight time of 20 nanoseconds from the creation of photons to their detection. Instead of physically rotating the polarizers—which was technically impossible to accomplish in such a short time—he replaced the polarizer on each side with a setup consisting of a so-called optical switch, and two polarizers aligned in different directions. The

---

<sup>36</sup> Bell, “On the Einstein Podolsky Rosen paradox”.

<sup>37</sup> Clauser, “Early History of Bell’s Theorem”.

<sup>38</sup> A. Aspect, J. Dalibard and G. Roger, “Experimental Test of Bell’s Inequalities Using Time-Varying Analyzers”, *Phys. Rev. Lett.*, 49, 25 (1982): 1804–1807.



switches allowed the incoming photons to be directed toward different polarizers, and this change of direction was occurring regularly, approximately every 10 nanoseconds. In this way, the photons were arriving at the polarizers whose angle varied, and this variation of the angle was happening during the flight of photons. There was no way for a signal, traveling from one side to the other at a speed not greater than that of light, to arrive in time to “inform” the physical system there about the current state of the optical switch. The results were unwavering, confirming Bohr’s expectations at 5 standard deviations. Bell’s last hopes that our universe might still be locally realistic were dispersing.

However, this was not yet precisely what Bell had envisaged. Ideally, the experimenter on one side should be capable to orient their polarizer at will, or randomly, so that there would be absolutely no way for the system on the other side to predict what angle was chosen. This was not what Aspect’s setup allowed, where variations of polarization were periodic, and thus, strictly speaking, easily predictable (if the equipment on the two sides could communicate, wanted to “conspire” against the experimenter—as Clauser would say, and was “intelligent” enough to get the pattern of variations). Regardless of whether this was an overly paranoid requirement or not, it was still a logically necessary one if we wanted to be absolutely sure that no room for any locally realistic model has remained. And the first one to definitely close this locality (or communication) loophole—by using superfast random number generators—was the third laureate, Anton Zeilinger, with his team from the University of Innsbruck, back in 1998.<sup>39</sup> His experiment demonstrated a violation of Bell’s inequality to a staggering 30 standard deviations.

But, after careful analysis, physicists have realized that, strictly speaking, the locality loophole was not the only potential loophole. Additionally, they also identified the detection loophole (related to the low efficiency of used detectors), the coincidence loophole (related to the imperfect methods used to judge which two detected photons belonged to the same pair), and the memory loophole (a pretty “paranoid” possibility that hidden variables could exploit the memory of past measurements to conspire against experimenters). However, with a combined effort of many experimental groups worldwide, finally, in 2015, we had the first “loophole-free” confirmations of Bell’s inequality violation

---

<sup>39</sup> G. Weihs et al., “Violation of Bell’s Inequality under Strict Einstein Locality Conditions”, *Phys. Rev. Lett.*, 81, 23 (1998): 5039–5043.

(one of three such experiments done in 2015 was once again performed by Zeilinger's group<sup>40</sup>).

It is also worth mentioning that some of these additional loopholes do not even appear in generalizations of Bell's theorem to entangled states of three or more particles. Generalizations of this sort were discovered by Daniel Greenberger, Michael Horne, and Anton Zeilinger in 1989 (aka GHZ theorem<sup>41</sup>), and the corresponding experimental tests<sup>42</sup>, performed also by Zeilinger's group, again falsified local realism. In these cases, the incompatibility of local realism with our universe could be verified on the level of a single measurement, without the need to gather sufficient statistics and consider any probabilities, or inequalities, at all. And, after all these experiments there was no more a single speck of doubt: our world could never be explained by any locally realistic theory, and it was Bohr who won the famous debates.

Overall, hardly to anyone's surprise, the loopholes failed to save local realism. Years later, it is time to finally get used to this fact and take the conclusions seriously.

### 4.3 Superdeterminism

It should be noted that, in a tendency to give statements of utmost mathematical precision, physicists often mention yet another hypothetical loophole. It is known by the name of "superdeterminism". If the locality loophole was already paranoid in Clauser's words, this one must be labelled as "insanely paranoid". Namely, what if the conspiracy of nature (to fool physicists and leave a false impression of Bell's inequality violation) is so grand, that neither random nor human choices for polarizing angles are sufficiently independent? In principle, the universe could still be real and local, moreover deterministic, only if it was precisely fine-tuned at the moment of the Big Bang so that each time we try to test Bell's inequality our attempts are actually futile, since everything is staged. Everything is so precisely adjusted in advance (and the deterministic assumption in this picture makes such an idea logically consistent)

---

<sup>40</sup> Marissa Giustina et al., "Significant-Loophole-Free Test of Bell's Theorem with Entangled Photons", *Phys. Rev. Lett.*, 115, 25, (2015): 250401.

<sup>41</sup> M. Daniel Greenberger, Michael A. Horne and Anton Zeilinger, "Going Beyond Bell's Theorem", in *Bell's Theorem, Quantum Theory, and Conceptions of the Universe (1st edition)*, ed. Kafatos, Menos (Heidelberg: Springer, 1989), 69–72.

<sup>42</sup> J.-W. Pan et al., "Experimental test of quantum nonlocality in three-photon Greenberger-Horne-Zeilinger entanglement", *Nature*, 403 (2000): 515–519.

that each time we attempt to measure distant particles in a Bell's pair, Bob's particle and/or equipment "knows" what angle Alice is going to choose not because it was somehow signalled/influenced faster than light, but simply because everything is evolving according to a script written long ago, by a screenwriter whose core motive was seemingly to trick physicists into a false belief.

John Clauser, together with Abner Shimony and Michael Horne (scientists who, together with Richard Holt, were responsible for the most popular CHSH variation of the Bell's inequality) illustrated this type of conspiracy ideas in their 1976 paper<sup>43</sup> by noting a possibility that manufacturers of the measurement equipment might have tweaked the instruments as to produce a prepared set of false experimental outcomes. However, for this to work, conspirators would have also had to instruct the secretaries of the experimenters on both sides to "quietly whisper in their ears" appropriate choices of polarizer angles for each run—everything carefully orchestrated in order to demonstrate the ostensible violation of Bell's inequality in a universe that is otherwise locally real. Meanwhile, it actually turned out that even this scenario would not have worked, since all the details of the conspiracy had to have been fixed much earlier, probably already at the dawn of time: a Bell test performed in 2018 has confirmed the violation by using, instead of random generators, the light emitted 7.8 billion years ago from distant quasars, to decide how to orient polarizers (so, according to superdeterminism, these quasars would also have to be a part of the conspiracy, taking care of what light to emit, so that some scientists on Earth 7.8 billion years later will be properly fooled).<sup>44</sup> Furthermore, "as a safeguard against potential systematic or conspiratorial effects", one of the loophole-free Bell tests in 2015<sup>45</sup> used a number of popular culture sources to modulate the decision of the angles to be used in the experiment. In particular, they used binary bits of digital versions of movies such as the *Back to the Future* franchise (all three parts, of which the third was used in reverse order), *Star Trek* episodes, *Doctor Who*, and the *Monty Python and the Holy Grail*. For good measure, they also performed a binary XOR operation of everything also with binary digits of the number pi. This raised the bar for the required conspiracy even further: "A hypothetical cause that achieved

---

<sup>43</sup> A. Shimony, A. Horne and J. Clauser, "Comment on 'The theory of local beables'," *Epistemological Letters*, 13 (1976): 1–8.

<sup>44</sup> D. Rauch, "Cosmic Bell test using random measurement settings from high-redshift quasars," *Physical Review Letters*, 121 (2018): 080403.

<sup>45</sup> L. K. Shalm et al., "Strong loophole-free test of local realism," *Physical Review Letters*, 115 (2015): 250402.

the observed statistics via correlation between states of the photons studied and the choice of measurements would have had to precisely orchestrate the creative processes leading up to the digitized versions of these cultural artifacts in such a way that, when processed in conjunction with the outputs of the random number generators, produced just the right sequence of experimental choices.”<sup>46</sup>

By one of the worse misnomers in physics, the negation of the “superdeterminism” hypothesis is sometimes called the “free will” requirement, potentially misleading audiences that the superdeterminism conspiracy idea has anything to do with the ancient and open philosophical problem of the existence of free will. While the existence of free will (or of true inherent randomness in nature) would indeed logically ensure that superdeterminism is not possible, the lack of free will by no means implies superdeterminism. As should be clear from the above discussion, apart from complete determinism (and thus the absence of free will), the latter also seemingly requires some sort of intentional ultra-fine tuning specifically aimed at tricking physicists interested in Bell inequalities. (Here we discuss the superdeterminism in its basic form—e.g., there are also variations that presuppose retrocausality, i.e., affecting past from the future, but this has some resemblance to the idea of putting out fire with gasoline: a rather problematic and hard-to-motivate move to avoid the milder initial problem of Bell’s nonlocality.)

As an idea of conspiracy without bounds, the superdeterminism loophole is, obviously, in principle, experimentally unfalsifiable. However, if superdeterminism is true, the inability to draw correct conclusions from the violation of Bell’s inequalities should be of our least concern. As noted by Clauser and his coauthors, the whole pursuit of science would be meaningless: “Unless we proceed under the assumption that hidden conspiracies of this sort do not occur, we have abandoned in advance the whole enterprise of discovering the laws of nature by experimentation.”<sup>47</sup>

A similar conclusion was echoed by Zeilinger when he stated that, if superdeterminism were true, “it would make no sense at all to ask nature questions in an experiment, since then nature could determine what our questions are, and that could guide our questions such that we arrive at a false picture of nature”.<sup>48</sup> Actually, there can be much worse implications of superdeterminism than making science pointless. Following the same

---

<sup>46</sup> Myrvold, Genovese and Shimony, “Bell’s Theorem”.

<sup>47</sup> Shimony, Horne and Clauser, “Comment on ‘The theory of local beables’”.

<sup>48</sup> A. Zeilinger, *Dance of the Photons* (New York: Farrar, Straus and Giroux, 2010): 266.

reasoning, the Earth could right now be flooded with hostile species of reptilian aliens that are literally all around us, but so it happens that some regrettable sets of circumstances always prevent us from looking in the right direction at the right moment—just as fine-tuned sets of circumstances dictate Alice and Bob’s decisions how to turn their polarizers. And we could never know—unless, at some moment, the script dictates that aliens begin to devour us alive.

Instead of a serious hypothesis about nature, the superdeterminism can rather be seen as a testament to the price some people are ready to pay, just to avoid the inevitable conclusion that our universe is not locally realistic (seemingly, some scientists are ready to entertain superdeterminism at least partially seriously)<sup>49</sup>. This enormity of the price only underlines the depth of the change in our worldviews that the Bell’s inequality and its violation force us to make.

## 5. Epilogue

### 5.1 Nobel Prizes

Luckily, times are changing. With only a handful of citations in the first decade, as of today, Bell’s 1964 paper has amassed more than 27,000 citations. Implications of its violation are widely discussed and brought into the spotlight of broader audiences. Finally, last year, even the Nobel Committee decided to acknowledge the momentous scientific and philosophical contributions of Bell and the experimental physicists who tested his inequality. John Clauser, Alain Aspect and Anton Zeilinger shared the 2022 Nobel Prize in Physics.

The only reason why Bell was not among the last year’s laureates was that he unfortunately died in 1990, at the age of 62. Reportedly, he was nominated for the Nobel prize in the year that he passed away.<sup>50</sup> Of the other main actors in this drama, Einstein and Bohr did not live to see Bell’s theorem and the outcomes of experimental Bell tests, but both were awarded Nobel prizes for other achievements. Stuart Freedman, who assisted J. Clauser in his experiment, also died prematurely.

Taking into account that the first experimental test of Bell’s inequality happened already in 1972 (and that hardly anyone expected any remain-

---

<sup>49</sup> Myrvold, Genovese and Shimony, “Bell’s Theorem”.

<sup>50</sup> Louisa Gilder, *The Age of Entanglement: When Quantum Physics Was Reborn* (New York: Alfred A. Knopf, 2008).

ing loopholes to change our conclusions), it is reasonable to ask why it has taken an entire half of a century for the Nobel Committee to effectively recognize, by its decision, the depth of the irrevocable shift in our perception of the reality that quantum mechanics has brought, and Bell has proved. Stated differently, what prompted the Nobel Committee to suddenly remember Bell nowadays, 50 years after the first test and 24 years after Zeilinger closed the locality loophole?

At least a part of the answer certainly has to do with the shift from pure science and philosophy into technology. As it often happens, the most fundamental research in physics, aimed at purely philosophical topics, eventually also produced some very practical spin-offs. At some point, it was realized that the strange non-classical properties of quantum entanglement—the phenomenon first brought to attention in the EPR paper—can be used in many technologies, from cryptography, highly sensitive measurement techniques, superdense information coding, all the way to the entirely novel concept of quantum computing. It actually opened a whole new branch of research called quantum information science. In this light, the achievements of the pioneers of this field, both in the theory and experiment, were also gradually becoming more and more difficult to ignore.

## 5.2 The Aftermath: Reality or Locality

And, when the dust has settled, what is it that this “most profound discovery of science”, as Henry Stapp praised Bell’s inequality and its violation, actually tells us? While this obviously is the most important question in this context, to this day, it remains a controversial one.

On multiple occasions we have stated that Bell’s violations falsify the idea of “local realism”—they show us that nature certainly cannot be both “local” and “real” at the same time. While it might be neither. This common formulation of conclusions dates back to Clauser and Shimony’s 1978 paper.<sup>51</sup> While the idea of the locality they had in mind is fairly clear (i.e., that no influence can be exerted immediately to arbitrary distance, i.e., as if mediated at infinite speed), they explained the notion of realism as follows: “Realism is a philosophical view in which external reality is assumed to exist and have definite properties, whether or not they are observed by someone.” Giving up the notion of objective reality independent of observers, which was the cornerstone of exact science from

---

<sup>51</sup> J. F. Clauser and A. Shimony, “Bell’s theorem: experimental tests and implications,” *Reports on Progress in Physics*, 41 (1978): 1881–1927.

its advent, might seem like quite a steep price to pay. The problem with violating the notion of locality, on the other hand, is not only in the fact that it is not in the spirit of Einstein's theory of relativity (it neither strictly experimentally contradicts it, since particle entanglement does not allow sending information faster than light). The additional problem is that giving up locality also jeopardizes the idea that nature can be split into separate subsystems and investigated in this way. If whatever happens in our lab can be, in principle, influenced by what is at the moment happening in another galaxy, that undermines the very reductionist approach to reality. It certainly does away with the good old mechanist ideal of reality being a set of moving pieces that influence only those in the immediate vicinity (the intuitive idea of gears and levers, or of particles bouncing off each other). We should clarify that, although the influence by "pulling and pushing", i.e., by the contact-interaction of impenetrable solid bodies was the golden standard, or at least ideal, of Newtonian classical physics, it is true that Newton himself was forced to introduce a long-range force to explain gravity. However, that idea was immediately considered as a sort of occult and definitely troubling, even by Newton.<sup>52</sup> And what was merely shunned in Newton's era, would eventually become inadmissible with Einstein's theory of relativity due to the light-speed limitation on all influences. It took a while for science to get rid of such unwelcome "occult" remnants: first, thanks to Maxwell's theory of electromagnetism, which solved this problem for the case of electric and magnetic interactions, and finally by Einstein who solved the same problem for gravity. They provided perfectly local (and of course, realist) explanations of the universe's inner workings. With these achievements, the Newtonian ideal of a mechanistic universe was seemingly completely accomplished and the universe fully gained the intuitive feel of a huge clockwork mechanism. Yet, the option opened by the Bell test—to abandon the locality of physics—all of a sudden endangered this ancient worldview, in a way that was far more disturbing than the simple inverse-square Newton's law of gravity.

Even without these purely philosophical repercussions, the huge problem of internal compatibility between nonlocal interactions and the theory of relativity means that accepting the nonlocality requires serious revisions of our understanding of space and time. Overall, as Clauser and Shimony emphasize in their paper: "The conclusions [from Bell's theorem] are philosophically startling; either one must totally abandon the

---

<sup>52</sup> W. Seager, "The Philosophical and Scientific Metaphysics of David Bohm", *Entropy*, 20, 7 (2018): 493.



realistic philosophy of most working scientists, or dramatically revise our concept of space-time.”<sup>53</sup>

We stress again that the issue of determinism is unrelated here. First we must clarify that, *per se*, realism does not inevitably entail determinism (though the two notions are often conflated). It is easy to conceive a model that would be realistic (i.e., systems have definite properties irrespective of measurement/observation) and local in spite of being stochastic (i.e., laws of physics do not allow us to predict actual outcomes of experiments, but only probabilities of different outcomes). For example, in the Bell’s context, we might consider a hypothetical model in which photons always have well-defined polarizations (hence the model is realistic), while it is nevertheless impossible to surely predict whether a particular photon will pass the polarizing filter or not (thus model is indeterministic): in particular, the probability of transmission could be proportional to the cosine squared of the angle between photon polarization and the filter orientation (such dynamics would be local and would correctly reproduce the experimentally observed Malus law).<sup>54</sup>

Importantly, giving up determinism cannot save the role of local realism in nature—since locally-realistic models like the one above must also satisfy Bell’s inequalities, despite them having sacrificed determinism. This fact was obscured in the original formulation of Bell’s inequality (which actually presumed determinism), but was recognized in later generalizations of the theorem.

---

<sup>53</sup> Clauser and Shimony, “Bell’s theorem: experimental tests and implications”.

<sup>54</sup> At first sight, it might seem possible to trade this randomness for a complex, but again, deterministic law of nature, if we would allow each photon to somehow possess within itself a long enough predefined sequence of random numbers: each time it encounters a polarizing filter, it would then “consult” this list and “decide” according to some deterministic algorithm whether to pass or not, instead of this outcome being truly undetermined until that moment. However, if each photon possessed a different list, this would have revealed itself via violation of Bose-Einstein statistics, as they would cease to be identical particles. And if this list would be identical for all photons, then it would effectively constitute a new deterministic law of physics—something that should be expected to reveal itself via repeatable patterns in behaviour of particles under identical conditions. Finally, if every particle could somehow “consult” random-like number list that is external to the particle (and thus not violate statistics of identical particles), this would be problematic from the locality perspective. This last option also includes the so-called “second time around” universe: assume there is a nondeterministic universe, we let it evolve and “record” everything that happens; if we then “play” this recorded universe, all events would be predetermined and thus the universe deterministic, but its dynamical laws would not be local. Thus, non-deterministic locally-realistic models arguably constitute an entirely separate class.

### 5.3 Locality?

On the other hand, some of the more recent discussions on the subject tend to question this Clauser's "reality or locality" formulation of the conclusions.<sup>55</sup> Careful logical analysis shows that Bell's inequality violation seemingly implies some elements of nonlocality irrespectively of our stance on realism, i.e., that "locality" assumption cannot be saved—at least not in its standard sense—even if we give up realism. Some modern scholars thus prefer to summarize implications of Bell's violation simply as a constraint that any hidden variable theory must be nonlocal, more in line with Bell's own formulation of his theorem: "If [a hidden variable theory] is local it will not agree with quantum mechanics, and if it agrees with quantum mechanics it will not be local".<sup>56</sup> To understand this emphasis on the hidden variables, but also to better understand the idea of sacrificing locality to preserve realism, we must again return to Bohm-de Broigle's hidden-variable interpretation, aka the pilot-wave theory (PWT),<sup>57</sup> which hugely influenced Bell.

Namely, this theory was, and still is, basically the only known model of nature that explicitly does away with locality premise in order to retain realism in a sense somewhat close to the classical one (though, even there the concept of reality had to be extended to include a quite abstract wavefunction that lives in a mathematically involved construct of a so-called "tensor product of single-particle Hilbert spaces", instead of keeping only the intuitively clear picture of the classical three-dimensional space). Bohmian mechanics (as PWT interpretation of quantum mechanics is often called) assumes the existence of true and precise positions of all particles—here playing the role of hidden variables—which are well-defined at all times, irrespectively of observation (despite the knowledge about these positions not being experimentally accessible). Besides, the theory is deterministic. However, as we have already discussed, the price is paid in the form of manifest nonlocality: the velocity of every particle depends on the current positions of all particles that exist in the universe, in a way determined by an additional "guiding" equation. This remote influence, which exists irrespectively of the mutual distance between par-

---

<sup>55</sup> Myrvold, Genovese, and Shimony, "Bell's Theorem".

<sup>56</sup> Bell, *Speakable and Unspeakable in Quantum Mechanics*.

<sup>57</sup> C. Zander and A. R. Plastino, "Revisiting Entanglement within the Bohmian Approach to Quantum Mechanics", *Entropy*, 20, 6 (2018); Sheldon Goldstein, "Bohmian Mechanics", *The Stanford Encyclopedia of Philosophy (Fall 2021 Edition)*, Edward N. Zalta, ed., accessed on August 1, 2023, <https://plato.stanford.edu/archives/fall2021/entries/qmbohm>.

ticles, is non-local simply by the definition and not as a consequence of any interaction potential. Apart from the guiding equation, this theory also postulates Schrödinger's equation that governs the evolution of the wavefunction in precisely the same way as in standard quantum mechanics. The theory is constructed in such a way as to produce experimental predictions mathematically equivalent to predictions of the standard quantum formalism.<sup>58</sup> This is possible since those hypothetical real positions of particles (i.e., hidden variables) do not affect the dynamics in any way—the latter is entirely determined by the standard quantum mechanical wavefunction. Since these positions cannot be inferred by measurement, their main purpose is to provide philosophical comfort of allowing one to say that the particles actually had well-defined properties (more precisely, well-defined positions—things become much more complicated with other properties like spin), in spite of our eternal lack of precise knowledge about them. Of course, it depends upon personal philosophical predilections to whom will such a possibility sound comforting, and to whom misleading and strikingly non-parsimonious. In fact, the facets of this interpretation that its proponents find most appealing are often the same ones that the critics of the theory see as unnecessary and extravagant additions to the complexity of an already complete theory. Bohmian mechanics is often criticized from the viewpoint of Occam's razor, as it requires the introduction of additional properties and an entirely new dynamical equation, and it must also go to lengths to solve technical issues non-existent in the standard formulation, while at the same time, it is not adding anything to the explanatory power of quantum mechanics.

But, philosophical preferences aside (which can hugely differ, as in the case of Einstein and Bohr), the inherent non-locality of PWT inevitably leads to both conceptual and severe technical problems in attempts to extend nonrelativistic quantum mechanics into the relativistic domain, and especially to the deeper, underlying quantum field theory.<sup>59</sup> This was likely the main reason why Einstein was not satisfied with Bohm's proposal, in spite of its realism (besides, he found it "too cheap")<sup>60</sup>. Bell, while favouring this view of quantum mechanics, was also aware of its problem with non-locality. In his opinion, the PWT would have been a perfect theory, if it was not for this problem. As we have explained, Bell eventually arrived at his theorem by attempting to answer the question of whether it was possible to improve the Bohmian mechanics in a way

---

<sup>58</sup> After assuming initial probability densities that match  $|\psi|^2$ .

<sup>59</sup> Goldstein, "Bohmian Mechanics".

<sup>60</sup> J. S. Bell, "On the impossible pilot wave", *Found. Phys.*, 12, 10 (1982): 989–999.

that would retain its realism but also remove the troubling non-local features (which motivated his formulation of the theorem statement via hidden variables). The conclusion of Bell's theorem—that no such improved theory can exist that would be compatible with predictions of quantum mechanics—was immediately disappointing to the author since the prospect of experimentally invalidating quantum theory sounded implausible. Once the Bell tests have indeed confirmed the validity of quantum predictions, from then on, the Bell's theorem implied that any hidden variable theory, which aspires to conform to the experiments, must suffer from the same non-locality problem as the Bohmian mechanics.

But instead of being viewed as a deal-breaker for hidden variable theories in general, by the proponents of PWT this was seen as an argument in favour of their interpretation: the non-locality was no longer the fault of the particular Bohmian approach, because it was now clear that no other hidden variable theory can do better, even in principle. Moreover, advocates of Bohmian mechanics particularly tend to emphasize that some sort of nonlocality is unavoidably inherent in quantum theory *per se*, irrespectively of interpretation. At the same time, they mostly dismiss that Bell's inequality violations should have any logical implications on the idea of realism (even the mention of the existence of hidden variables—which is certainly an assumption about reality—is often avoided). For example, for Tim Maudlin, who is a vocal supporter of Bohmian mechanics, the implications of Bell tests can be simply summarized as “actual physics is non-local,” period.<sup>61</sup>

#### 5.4 Reality?

While, as already mentioned, Bell's theorem indeed suggests that quantum mechanics must have some sort of non-local elements, we believe that such formulations that ignore mentions of realism (put forward mostly by Bohmian sympathizers) are at least misleading. Formulations of this type tend to wrongly reduce the deep and universal philosophical implications of Bell's inequality violations to an ostensible dichotomy between local and non-local hidden variables. They completely ignore (or obscure) the fact that violations of Bell's inequality come as the final confirmation of Bohr's predictions, in contrast to Einstein's expectations, and that, as such, the observed violations also strongly reinforce and support Bohr's view. And this view is, in the context of EPR and Bell, succinctly formulated by Clauser: “Bohr's argument is more readily understood, once that one recognizes that it is based on his denial of realism. That is,

<sup>61</sup> Tim Maudlin, “What Bell did”, *J. Phys. A: Math. Theor.*, 47, 42 (2014): 424010.

it is impossible to physically disturb something that doesn't exist! Thus, if there is no physical-space description of either the quantum mechanically entangled individual systems or of the actual disturbance process, then the required associated existence of non-local action-at-a-distance is a non-issue. The objectionable aspect of Bohr's description (action-at-a-distance) is then, consistently with Bohr's assertion of completeness, simply non-existent, by definition!"<sup>62</sup>

Accordingly, in Bohr's view, even if there is some sort of non-locality in quantum mechanics after all, it is of absolutely secondary and interpretational character. As pointed by Clauser above, what does it mean to physically disturb something at a distance, if that something does not truly exist, in the first place?

On the other hand, the premise of realism was built in from the outset: the "elements of reality" that were presumed to exist in the EPR paradox, were reflected via the variable (or set of variables)  $\lambda$  appearing in the Bell's proof and representing the hidden variables. While, in the first version of the Bell's theorem, these elements of reality were seen as giving rise to deterministic outcomes of the experiments, even the later versions of the theorem, which did not incorporate determinism, nevertheless relied on realism presumption of some sort. In a certain sense, reality presumption is an indispensable part of the theorem's proof since the way the joint probabilities are computed implies that the "values co-exist together independently of which experiment is actually performed on either side, and in this sense are 'real'".<sup>63</sup>

A part of the problem with emphasizing non-locality at the expense of considering issues with reality might be in the suggestively chosen terminology. In usual physics jargon, non-locality commonly implies, or suggests, some sort of "non-local interaction", where "interaction" generally denotes some well-defined force, or potential (or a term in the Lagrangian) that causes/mediates influence between well-defined objects of the theory (e.g., particles or fields). In other words, the very term "non-locality" is not "ontologically neutral", in the sense that it effectively presupposes, or at least suggests, some sort of realism. Therefore, if the conclusion of Bell's violations is indeed simply summarized as "actual physics is non-local", that even leaves an impression that Bell tests reinforced Einstein's position of realism, while in reality, the logical implications of Bell's violations were certainly the opposite (without a doubt, realism was far more plausible hypothesis while we still thought that such

---

<sup>62</sup> Clauser, "Early History of Bell's Theorem".

<sup>63</sup> Żukowski and Brukner, "Quantum non-locality – it ain't necessarily so".

theories could be constructed in full observance of the relativistic principles). Similar is also true for the formulations closer to the original Bell's statement, like "any hidden variable theory must be non-local"—again connoting that the entire issue is a dichotomy between local and non-local hidden variable theories, instead of between the realist Einstein's viewpoint and the "non-realist" Bohr's stance.

A much better choice would be the word "inseparable" (this word is also more closely related to the mathematical term "non-factorizable", which better corresponds to the presumptions of the Bell's theorem than "non-locality"<sup>64</sup>). For, if the conclusion is that physical systems on Alice and Bob's side cannot be thought of as separate<sup>65</sup> entities, then it is a statement that pertains to our understanding of reality as a whole (suggesting it possesses a certain holistic character) and not merely to some technical details about the speeds at which the influences can propagate. Besides, if the essence was truly in non-local interactions that somehow allow particles to "communicate" faster than light, we could naturally expect that we—and not only particles among themselves—should also be able to send faster-than-light signals. The fact that, ostensibly due to an interplay of probabilities, entanglement cannot be used for faster-than-light signalling, speaks in favour of "non-separability" rather than of "non-locality".<sup>66</sup>

As noted by Gründler,<sup>67</sup> in his reply to the EPR paradox, Bohr precisely argued that the notion of separability, as understood by classical physics and Einstein, is no longer applicable to the reality of quantum mechanics. In his paper, Bohr writes: "[...] we have to do with a feature of individuality completely foreign to classical physics", putting the word "individuality" in italics.<sup>68</sup> Seemingly, his point was that quantum mechanics does not allow us to fully consider subsystems individually, as we were accustomed to in classical thinking, since reality is in some sense not divisible ("individual" comes from Latin, literally meaning "not divisible"). So, Bohr did recognize that quantum mechanics implies some non-local effects in the sense of inseparability, but this was to him merely one

---

<sup>64</sup> Myrvold, Genovese and Shimony, "Bell's Theorem".

<sup>65</sup> There is also a formal definition of separability in quantum information theory (being the opposite of entanglement) that corresponds well to this intuitive meaning.

<sup>66</sup> Seager, "The Philosophical and Scientific Metaphysics of David Bohm".

<sup>67</sup> G. Gründler, "What exactly is proved by the violation of Bell's inequality?", arXiv, accessed on August 1, 2023, <https://arxiv.org/abs/1704.03856v6>.

<sup>68</sup> Bohr, "Can Quantum-Mechanical Description of Physical Reality be Considered Complete?".

of the features of that different sort of reality that we need to embrace. And this new reality clearly does not conform to Einstein's idea of classical "realism".

This difference between notions of locality and separability can be explained a bit better if we switch to the description using the so-called density matrix, instead of the wavefunction. The density matrix is a somewhat richer mathematical object than the wavefunction, capable of jointly describing both the quantum-mechanical lack of knowledge about systems (described by superposition) and the classical lack of knowledge (described by the so-called mixed states). Instead of using state-vector  $|\Psi\rangle$  given by (1) to describe EPR entangled state of two particles with spin (we will again denote them as Alice's and Bob's particle), we can use the density matrix  $\rho_{AB}$  that corresponds to this state and describes the joint system of both particles.<sup>69</sup> However, in addition to the density matrix that describes the joint system, we can also define density matrices corresponding to each of the particles taken individually.<sup>70</sup> These mathematical objects deal with only one of the particles and do not have anything to do with the other one. As if we took the joint two-particle description and then forgotten (erased) anything about the second particle and their mutual connection. It turns out that such density matrices of individual particles (subsystems) provide sufficient information to predict the outcome of any possible experiment carried out on that particle alone! In other words, it can be argued that this reduced density matrix of a single particle is what truly describes the "reality" of that particle. (The analogue is not possible to define on the level of wavefunctions.) Importantly, it turns out that nothing that Alice does can influence the reality of Bob's particle defined in this sense, since the quantum formalism directly implies that Alice's actions cannot change the reduced density matrix that Bob uses to describe his particle (and to successfully predict outcome probability of any possible measurement on it). For this reason, considering reduced density matrices is, mathematically, the simplest way to prove that it is impossible for Alice to send any information to Bob by using entanglement—the result that is far from obvious when considering the wavefunction.

Here, the weirdness of quantum mechanics appears through the fact that the reality of Alice's particle alone, combined with the reality of Bob's particle alone, does not represent the full reality of the system

---

<sup>69</sup> This is a two-particle operator defined as  $\rho_{AB} = |\Psi\rangle\langle\Psi|$ .

<sup>70</sup> They are obtained from  $\rho_{AB}$  by taking the "partial trace" over the other space, e.g.:  $\rho_A = \text{tr}_B(\rho_{AB})$ . The result is a single particle operator.



consisting of Alice's and Bob's particles taken together. Namely, the outcomes of measurements that require access to both particles, in general, cannot be inferred (not even probabilistically) based only on these two reduced density matrices, even in situations where our ignorance does not play any role. This is in contrast with the situation in classical physics, where analogous situation is possible only when we are lacking some piece of information. For example, in classical physics, we could have pairs of particles where Alice's spin is pointing upwards, and Bob's spin points down, and pairs where, vice versa, Alice's spin is down and Bob's is up. If, from a mixture of ten pairs of the first type and ten pairs of the second type we would be randomly given a single pair (so that we do not know from which set it originates), our classical description of such a pair would be superficially similar to the quantum state of entangled spins (1) discussed in the context of the EPR paradox. Namely, it would also have the properties that probability of both Alice's and Bob's particle spin to be up is 50% (same for down), while each time Alice's spin turns out to be up, Bob's will certainly be down, and vice versa. However, such classical correlations are always a consequence of some type of our ignorance (here, we simply did not know from which of the two sets our pair originated), but they are never the feature of the system *per se*—since, classically, particles do have well-defined properties and must “themselves know from which set they originated”.

The essence of the EPR paradox and the Bell's violation can be seen from this perspective: Einstein assumed that the only possible cause of such correlations in nature must be in our ignorance, i.e., that there must remain some hidden variables which make quantum mechanical description incomplete, but the violation of Bell's inequality showed us that quantum correlations are not always of this type.<sup>71</sup> According to quantum mechanics, even if we know everything there is to be known, sometimes reduced density matrices still do not contain sufficient information to predict outcomes of experiments performed on the joint system. The simplest example of such a joint-type experiment is measuring the spins of both particles and *comparing* the results. To predict outcomes of such measurements (in general) we need the full density matrix of the joint system—and this matrix, therefore, somehow represents the reality of the two particles taken as a whole. As the joint matrix cannot

---

<sup>71</sup> Quantum-mechanical density matrix can describe both the “mixed state” correlations of the ignorance type expected by Einstein, and the counter-intuitive inseparable “pure state” correlations of the entanglement. The former differ by the absence of off-diagonal matrix elements.

be reconstructed from the reduced density matrices—and this is not a consequence of our incomplete knowledge—the full reality turns out to be more than the sum of its parts.

In the case of the two EPR particles in state (1), the spin state of each particle is unknown and thus undefined (the reduced density matrices are proportional to unit matrices). In the language of Bohr, individual spin components of particles do not exist. However, in spite of the non-existence (indefiniteness) of individual spins, the fact that the spins are opposite is well-defined and thus very much existent (otherwise, conservation of angular momentum and rotational symmetry would be violated). And the reality of this “oppositeness” is described by the joint density matrix  $\rho_{AB}$ . As if the two Bertlmann’s socks were of different colours despite the colour of each individual sock being undefined/non-existent.

This view is intuitively easier to grasp from the viewpoint of interpretations that are closer to Wheeler’s “it from bit” doctrine, that is those in which, in one way or the other, information plays the fundamental (ontological) role. Wheeler used to liken the universe with the “twenty questions” game where the object we are trying to guess was simply not yet decided by the answerer:<sup>72</sup> our questions posed to nature by experiments and observations do not find something out about the fixed reality that is out there—instead, our questions gradually shape that reality. The answer is, in a certain sense, created only after the question, and we are only granted to always obtain mutually consistent answers. Returning to the case at hand, from this viewpoint there is nothing surprising in the fact that the two spins can be opposite and this fact real, as this opposite-ness follows from available information, while the individual spins, about which we can know nothing even in principle, are not yet defined. By our measurements required to prepare the initial state of the particles, we obtained confirmation from nature that the spins are opposite and that is all there is—before we ask anything about the individual spins, nature does not yet have to decide anything about them, and they remain vague, undefined.

However, if we follow this line of reasoning, we must be careful about who precisely is posing the question to nature. For example, in the EPR case, not only that we have two subsystems, but also two observers, so the density matrices used to describe reality by Alice and Bob can easily start to differ. This is a consequence of the fact that the density matrices take into account our classical knowledge (and the lack thereof).

---

<sup>72</sup> John Gribbin, Marry Gribbin and Jonathan Gribbin, *Q. is for Quantum: An Encyclopedia of Particle Physics* (Simon and Schuster, 2000).

Namely, when Alice obtains the measurement result of spin projection on her particle, this new information pertains also to the joint system of the two particles. She may also update her knowledge about the reality of Bob's particle spin (since the spins are opposite)—and the latter now also becomes well-defined from her viewpoint. Bob, on the other hand, does not know the outcome obtained by Alice, so he describes the joint system and the subsystems with different density matrices.<sup>73</sup>

So, what does it mean if Alice and Bob use different density matrices to describe reality? If these matrices correspond merely to Alice's and Bob's knowledge, then this sounds quite natural, since they simply possess different sets of information about the systems they want to describe. But, if we want to assume that this knowledge also directly corresponds to a given, well-defined and unique reality of the particles they describe, obviously not both descriptions can be correct. We may be tempted to say that, initially, both Alice's and Bob's descriptions were the same and correctly represented the reality of Bob's particle, but after Alice's measurement, she has learned a piece of information that Bob does not have, and thus her description is correct, while Bob's is not. If all this is so, then we indeed must concede that Alice's measurement has somehow changed the state of Bob's distant particle, i.e., that we have some sort of non-local influence.

Yet, assuming that additional reality is independent of available information is not in the spirit of Wheeler's proposal (and not even parsimoni-

---

<sup>73</sup> All this directly follows from the standard formalism of quantum mechanics. From the perspective of Bob, who does not know the outcome, Alice performing the measurement corresponding to Hermitian operator  $A$  with spectral decomposition  $A = \sum_i a_i P_i$  has no effect on Bob's reduced density matrix since  $\rho'_B = \text{tr}_A(\sum_i (P_i \otimes 1) \rho_{AB} (P_i \otimes 1)) = \text{tr}_A(\sum_i (P_i \otimes 1) \rho_{AB}) = \text{tr}_A(\rho_{AB}) = \rho_B$ , where we used cyclic property of trace. The only change Bob's reduced density operator undergoes in this view is of taxonomic nature: after the measurement, it becomes a mixed state of the first kind—reflecting the classical lack of knowledge of the result that Alice has obtained, while previously it was a mixed state of the second kind—i.e., reflecting that it was entangled with Alice's particle. This classification, of course, neither affects the form of the matrix nor the underlying reality. In interpretations of quantum mechanics in which collapse is only subjective and Alice's measurement does not result in collapse from Bob's perspective, his particle remains in the mixed state of the second kind—reflecting the entanglement which is now not only with Alice's particle, but also with Alice's measurement apparatus/environment and Alice herself. On the other hand, for Alice who knows which specific outcome  $a_i$  has occurred, the density operator of the joint system changes according to the following formula:  $\rho'_{AB} = (P_i \otimes 1) \rho_{AB} (P_i \otimes 1) / \text{tr}_{AB}(\rho_{AB} P_i)$ , leading to a nontrivial change in the reduced density matrix of Bob's particle.

ous). If we restrain from such a “realist” urge, we may say that there is one description (density matrix, or a vector state) and the corresponding reality related to Alice, and another one related to Bob. Taking such a view is literally, to a certain extent, the position of Rovelli’s “relational interpretation” of quantum mechanics. According to this interpretation, there is nothing anthropocentric here, i.e., Alice and Bob have no unique role, and we could speak about the quantum state (and “reality” in some sense) from the perspective of any physical system—since the state (wavefunction) is here observer-dependent and just encapsulates relations between the observed system and the reference system (i.e., observer). This is understood in a similar way as the lengths and time intervals are relative to observers (i.e., reference frames) in the theory of relativity. Another way to interpret different descriptions of reality by Alice and Bob, which may be ostensibly conflicting and yet both correct, is offered by the “quantum Bayesianism” (QBist) interpretation of quantum mechanics. Here, the quantum state merely represents (rational) degrees of belief that an agent can have about the outcomes of possible measurements. Yet another would be a reading of the Copenhagen interpretation where the collapse occurs strictly subjectively, and which goes hand in hand with the ontology of idealism.<sup>74</sup>

It is beyond the scope of this paper to discuss in more detail the mentioned views. Nevertheless, it is very dubious whether, and in what sense, one can say that the universe is non-local, according to these interpretations. In all of these views, the wave-function collapse after Alice’s measurement happens only from her perspective, and it is essentially nothing else but the update of knowledge (or degrees of belief) that Alice has about both hers and Bob’s particle. The fact that Bob’s particle is distant makes the update of knowledge, per se, nothing more mysterious than if Bertlmann would send a sock from his pair to Andromeda galaxy, and would only afterwards present us the other one from the pair: our update of the knowledge about the distant sock based on the one that we have just witnessed would be instantaneous, irrespectively of the light years of distance. Nonetheless, we most certainly would not describe the situation as a case of faster-than-light interaction—instead, we would simply say that we found out something about the distant sock. Note that no change in the “reality of Bob’s particle” happens from Bob’s viewpoint after Alice’s measurement, and thus, there is no objective non-local influence of Alice on the distant particle.

---

<sup>74</sup> I. Salom, “To the rescue of Copenhagen interpretation”, arXiv, accessed on August 1, 2023, <https://arxiv.org/abs/1809.01746v1>.

The mysterious part of these interpretations is not in their attitude towards locality, but towards reality. It is in the claim that the knowledge and information (given by state vector/density matrix) do not correspond to any objective, observer-independent (or system-independent) reality. And since this idea of objective reality is now inherited by this observer-dependent information-based reality, finding out something about a distant system (which consequently also defines that revealed property) might be seen as a sort of action at a distance. However, in our view, calling this simply a “non-local interaction” (or a demonstration of the non-locality of the universe) is at least misleading and a stretch of definition.

There are some additional arguments that it is our understanding of reality which we must radically revise as the consequence of Bell’s violations (and not merely the idea of locality). These are provided by the Kochen-Specker theorem<sup>75</sup> and more recent violations of the so-called Leggett (and Leggett-Garg) inequalities.<sup>76</sup> In a similar fashion as with Bell’s inequalities, these theorems and experimentally violated inequalities rule out a large class of intuitive realistic theories (e.g. macrorealistic physical theories), this time irrespectively of whether our universe respects locality or not. The corresponding experiments were again first performed by Zeilinger and his team, and they concluded: “Giving up the concept of locality is not sufficient to be consistent with quantum experiments, unless certain intuitive features of realism are abandoned.”<sup>77</sup>

While it is true that the De Broglie-Bohm hypothesis cannot be falsified in this way (since it was constructed to be experimentally indistinguishable from the standard quantum mechanics), these constraints on realistic theories explain why even PWT is very far from the realism standards set by classical physics. In particular, as a general consequence of the Kochen-Specker theorem, it is not possible to construct any hidden variable model (in agreement with experiments) that would have simultaneously well-defined values of all measurable properties of sys-

<sup>75</sup> Carsten Held, “The Kochen-Specker Theorem”, *The Stanford Encyclopedia of Philosophy (Fall 2022 Edition)*, Edward N. Zalta and Uri Nodelman, eds., accessed on August 1, 2023, <https://plato.stanford.edu/archives/fall2022/entries/kochenspecker>.

<sup>76</sup> A. J. Leggett, “Nonlocal Hidden-Variable Theories and Quantum Mechanics: An Incompatibility Theorem”, *Found. Phys.*, 33, 10 (2003): 1469–1493; A. J. Leggett and Anupam Garg. “Quantum mechanics versus macroscopic realism: Is the flux there when nobody looks?”, *Phys. Rev. Lett.*, 54, 9 (1985): 857–860.

<sup>77</sup> S. Gröblacher et al., “An experimental test of non-local realism”, *Nature*, 446 (2007): 871–875.

tems (hidden variables must be “contextual”, i.e., dependent upon the measurement “context”). For example, in PWT interpretation, a special role is given to the position of particles and they are real in the standard, classical case. However, this is not the case with spin, which cannot be taken as a genuine/intrinsic property of particle alone, but it has to do with both the wavefunction and the current experimental setup.<sup>78</sup> Even Bohm himself saw this contextuality as a huge departure from the basic principles of classical physics.<sup>79</sup> Besides, while postulating a wave-function existing in the real three-dimensional space would absolutely be in the spirit of “classical realism”, it is quite different to posit, forced by the quantum phenomenon of entanglement, a wave-function living in some abstract N-fold tensorial product of three-dimensional spaces (where N is the number of particles in the universe). Arguably, such ontology loses touch with the highest ideals of a true realist theory, where reality should be intuitively clear and sort of palpable. (The matters are only made worse by the fact that this richness of the wave-function structure, which can never be directly observed, leads to endless “zombie worlds” of the so-called empty branches.)<sup>80</sup> Thus, we see that even in the pilot wave theory the core idea of realism has suffered too much to warrant claims that ramifications of Bell’s inequalities can be constrained only to the issue of locality.

### 5.5 Something else?

Overall, we have seen that even if we are ready to sacrifice realism, some features of locality (at least in the sense of separability) must be lost as well, while the attempts to solve the problem by explicitly giving up locality again land far from any epitome of realism. Hence, Clauser’s original formulation, simply stating that we must abandon the idea of “local realism”, seems to be the closest to the mark and to reasonably summarize the true philosophical implications of the violations of Bell’s inequalities. It is up to different interpretations of quantum mechanics to emphasize either the “locality” or the “reality” part of the statement.

---

<sup>78</sup> M. Daumer et al., “Naive realism about operators”, *Erkenntnis* 45, (1996): 379–397.

<sup>79</sup> Goldstein, “Bohmian Mechanics”; David Bohm and Basil J. Hiley, *The Undivided Universe: An Ontological Interpretation of Quantum Theory* (London: Routledge and Kegan Paul, 1993).

<sup>80</sup> R. Brown, Harvey and David Wallace, “Solving the Measurement Problem: De Broglie–Bohm Loses Out to Everett”, *Found. Phys.*, 35, 4 (2005): 517–540.

However, we must mention the option that retains both the ideal of the locality of influences and the idea of observer-independent reality, at the expense of giving up a seemingly necessary and tacitly always implied assumption that experiments have unique outcomes. This is the widely known many-worlds interpretation (MWI) of quantum mechanics. It asserts that it is wrong to say that in the EPR setting, Alice will obtain either a spin-up or spin-down outcome in the z-spin measurement—in- stead, the universe will split (or multiply in some sense) into two uni- verses, identical in every minute detail, apart from the fact that in one of them, there will be Alice seeing the up outcome, whereas the other will be inhabited by Alice registering the opposite outcome. While, as with every other interpretation, this one also has its strengths and weaknes- ses (which we will not delve into), it is not difficult to see that the proof of Bell’s theorem cannot be carried out with such a wildly altered definition of measurement.

Many-world interpretation posits that the wavefunction of the uni- verse is ontologically real and observer-independent. In this sense, this is a realist interpretation. On the other hand, merely saying that MWI calls for a revision of our understanding of reality would be an understatement. Instead of having a single reality of three-dimensional space, we now have an almost infinite number of concurrent realities, i.e., “worlds”, and essentially everything that might have happened has actually hap- pened in (at least) one of these worlds. Obviously, this picture of reality is far remote from any stretch of Newtonian or classical-like worldview.

## **6. Conclusion: The Fate of the Clockwork Mechanism**

While there might not be a consensus on whether it is the idea of sepa- rability (locality) or reality that should give in, or maybe that we live in countless parallel universes, there is an absolute consensus in contempo- rary physics that the hopes of ever returning to anything resembling clas- sical physics are long over. Between the abandoning of reality or locality, the philosophy of mechanistic materialism is caught between a rock and a hard place, but with no more room left in the middle. Needless to say, the many-world option is of no help here. Therefore, the very mechanism idea, that the world can be understood as a separable set of moving/ acting parts that affect each other in the immediate vicinity, the view that was so pervasive in our science and technology of the last couple of centuries—has to be forsaken. Actually, even before Bell’s theorem, and long, long before closing all the loopholes in Bell tests, the overwhelm-



ing majority of eminent physicists involved in the development of quantum theory was already making radical shifts from the old philosophical views. Einstein, who still believed that the universe is something akin to a huge deterministic clockwork mechanism, was essentially the sole exception among this elite—and his expectations in this context were, as we have seen, proven explicitly wrong.

On the other hand, Bohr, with his “anti-realist” stance, was neither alone nor the most radical. Unsurprisingly, his close collaborator Heisenberg also deemed the speculations that “behind the perceived statistical world there still hides a ‘real’ world in which causality holds”, in his own words, “fruitless and senseless”.<sup>81</sup> No doubt that, in his opinion, it was the “reality” which we misunderstood in the previous centuries. He saw implications of quantum mechanics as a call for a switch from Democritus’ to Plato’s views: “I think that modern physics has definitely decided in favour of Plato. In fact the smallest units of matter are not physical objects in the ordinary sense; they are forms, ideas which can be expressed unambiguously only in mathematical language.”<sup>82</sup>

Non-separability was, to him, seemingly just an anticipated part of this ideological shift: “There is a fundamental error in separating the parts from the whole, the mistake of atomizing what should not be atomized. Unity and complementarity constitute reality.”<sup>83</sup>

Wolfgang Pauli was also clear that it is time to move on from the worldview based on classical prejudices: “The mechanistic world view seems to us as a historically understandable, excusable, maybe even temporarily useful, yet on the whole artificial hypothesis.”<sup>84</sup>

Fascinated by Jung’s idea of synchronicity (which he saw on par with the principle of causality, complementing it in the explanation of the world) and psychology of the unconscious, Pauli’s views are generally

---

<sup>81</sup> W. Heisenberg, “Über den anschaulichen Inhalt der quantentheoretischen Kinematik und Mechanik”, *Z. Phys.*, 43, (3 (1927): 172–198.

<sup>82</sup> W. Heisenberg, *Das Naturgesetz und die Struktur der Materie. Natural law and the structure of matter* (Stuttgart: Belsler-Press, 1967).

<sup>83</sup> B. Piechocinska, “Physics from Wholeness: Dynamical Totality as a Conceptual Foundation for Physical Theories”, *Uppsala Universitet/Acta Universitatis Uppsaliensis* (2005).

<sup>84</sup> Harald Atmanspacher and Hans Primas, *Recasting Reality: Wolfgang Pauli’s Philosophical Ideas and Contemporary Science* (Springer Science & Business Media, 2008).

classified under the heading of a dual-aspect theory and he has never highly esteemed the philosophy of materialism.<sup>85</sup>

Interestingly, while Erwin Schrödinger often supported Einstein in debates on topics in physics, his basic philosophical views were even more distant from materialism than Pauli's. Finding agreement in Upanishads, he saw Brahman and Atman as essentially the same, clearly supporting idealist philosophical views: "The external world and consciousness are one and the same thing".<sup>86</sup> He leaves no doubt which of the two is the fundamental one in his view: "Consciousness cannot be accounted for in physical terms. For consciousness is absolutely fundamental. It cannot be accounted for in terms of anything else."<sup>87</sup>

Here, by consciousness he does not consider merely individual, personal consciousness, since he finds the plurality of consciousness to be deception (Indian *maya*): "The ego or its separation is an illusion."<sup>88</sup>

Idealist views were already expressed by Max Planck: "I regard consciousness as fundamental. I regard matter as derivative from consciousness."<sup>89</sup> In other words, his opinion was that "mind is the ultimate source of matter."<sup>90</sup>

Consciousness was also essential for Eugene Wigner and John von Neumann. They were even of the opinion that it is indispensable for the quantum theory in the sense that, according to Neumann–Wigner interpretation, it is the consciousness of the observer that causes the collapse of the wavefunction. Von Neumann also recognized that the wavefunction collapse ("the process 1" as he called it) has a unique role in the universe as only it can create new information (unlike "the process 2"—the deterministic evolution by Schrödinger's equation).

We also encounter the emphasis on both information and the crucial role of the observer in the views of John Archibald Wheeler, in his already

---

<sup>85</sup> Harald Atmanspacher, "The Pauli–Jung Conjecture and Its Relatives: A Formally Augmented Outline", *Open Philosophy*, 3, 1 (2020): 527–549.

<sup>86</sup> Erwin Schrödinger, *My View of the World* (Cambridge: Cambridge University Press, 1964), quoted from R. Malhotra, *Being different: An Indian challenge to western universalism* (Princeton, N.J.: Infinity Foundation, 2018).

<sup>87</sup> The Observer, January 11, 1931; also in *Psychic Research* 25 (1931), 91.

<sup>88</sup> Walter Moore, *Schrodinger: Life and Thought* (Cambridge University Press, 1992).

<sup>89</sup> The Observer, January 25, 1931, p.17, column 3.

<sup>90</sup> "Das Wesen der Materie [The Nature of Matter]", a 1944 speech in Florence, Italy, *Archiv zur Geschichte der Max-Planck-Gesellschaft*, Abt. Va, Rep. 11 Planck, Nr. 1797.

mentioned “it from bit” doctrine, combined with the idea of a “participatory universe” (Participatory Anthropic Principle).

For him (conscious) observers were participators in creating the reality, by posing questions to nature (by measurement and observation), as in his variation of the “twenty questions” game. The information contained in the answers was the basis for the existence of all physical things.

Of all of them, the philosophical positions of Max Born were the least radical (with respect to the prevailing materialistic views of that time). Since his contribution to quantum mechanics was the probabilistic interpretation of the (modulus squared) wavefunction, he, naturally, disagreed with Einstein on the issue of determinism. This further led to differences about the existence of free will, since Born’s opinion was that the breach of causality arising from quantum mechanics provides a channel for our true agency in the physical world.<sup>91</sup> In this sense, he was also departing from the philosophy of radical (monistic) materialism.

Curiously, even David Bohm did not support Einstein’s philosophical views. This might come as a surprise, since it was he who revived and further developed De Broglie’s vague idea of pilot-wave theory, to fully develop what is now known as De Broglie–Bohm theory—and is often seen as the last refuge of people looking to salvage as much as possible of our classical intuitions about the world and objective reality. (As for De Broglie, it is known that he has changed his philosophical views a few times.) But, Bohm had far more complex metaphysical intentions than attempts to resurrect mechanical worldview. To him, the pilot-wave theory was a way to unite his holistic view of the universe, with the importance of information and mind.<sup>92</sup> He strongly believed that the reductionistic approach of classical physics, relying on the separability of subsystems, was wrong: “Ultimately, the entire universe (with all its ‘particles’, including those constituting human beings, their laboratories, observing instruments, etc.) has to be understood as a single undivided whole, in which analysis into separately and independently existent parts has no fundamental status.”<sup>93</sup>

As we can see, it turns out that Bohm advocated his mechanics not in spite of its non-locality (i.e., inseparability) features, but because of them. Furthermore, he saw the wavefunction as embodying a special kind of

---

<sup>91</sup> T. G. Cowling, *Natural Philosophy of Cause and Chance* (Nature Publishing Group, 1949).

<sup>92</sup> Seager, “The Philosophical and Scientific Metaphysics of David Bohm”.

<sup>93</sup> D. Bohm, *Wholeness and the Implicate Order* (London, UK: Routledge and Kegan Paul, 1980).

information he called “active information” that was per se of semantic character (unlike Shanon’s information). Indeed, in this informational context, the abstract and huge dimensional space in which the wavefunction exists has much more sense than in the context of attempts to explain the wavefunction as a part of a classical-like realist ontology.<sup>94</sup> And since the information was semantic, it was related to his, essentially pan-psychic view that “the particles of physics have certain primitive mind-like qualities”.<sup>95</sup> The main achievement of his theory, for him, was not in any underlying realism, but that “the way could be opened for a world view in which consciousness and reality would not be fragmented from each other”.<sup>96</sup> Overall, as Seager concluded: “In the end, Bohm’s metaphysics is about as far from that of the Newtonian classical metaphysical picture of the world as one could get”.<sup>97</sup> In this sense, we see that Bohm had much deeper and very different philosophical motives than most of his contemporary followers who are merely attracted by distant echoes of classical mechanistic views that can be found in Bohmian mechanics.<sup>98</sup>

Above, we have summarized the philosophical views of the greatest physicists of the first half of the 20<sup>th</sup> century—of essentially everyone who significantly contributed to the birth of the new quantum theory. (We missed mentioning Paul Dirac since he had a sort of aversion towards quantum interpretations and philosophical issues. He explained his attitude by writing: “I don’t want to discuss this question of the interpretation of quantum mechanics [...] I want to deal with more fundamental things”.<sup>99</sup>) Not only that Einstein was the only one of them who believed in a classical-like mechanistic conception of the world, but the vast majority of them insisted on the necessity to radically evolve our understanding of reality (not locality), often even being starkly non-materialistic and emphasizing the role of consciousness in one or the other way. And all of them were exceptional geniuses, who had the deepest available knowledge of the laws of our universe. Thus, it is safe to say that there were plenty of rational arguments that mechanical worldview was no longer a

---

<sup>94</sup> Seager, “The Philosophical and Scientific Metaphysics of David Bohm”.

<sup>95</sup> D. Bohm, “A new theory of the relationship of mind and matter”, *Philos. Psychol.*, 3 (1990): 271–286.

<sup>96</sup> Bohm, *Wholeness and the Implicate Order*.

<sup>97</sup> Seager, “The Philosophical and Scientific Metaphysics of David Bohm”.

<sup>98</sup> *Ibid.*

<sup>99</sup> H. Kragh, *Natural Philosopher. Simply Charly*, PressBooks, accessed on August 1, 2023, <https://pressbooks.pub/simplydirac/chapter/naturalphilosopher>.

plausible description of the universe, even long before we got the rock-solid mathematical proof for that, in the form of the Bell's violations.

And, finally, once it was experimentally established that Bell's inequalities are indeed violated in our universe, we encountered a truly unique situation in the entire history of science. Never before has humanity been in need to abandon an entire paradigm because of a proof of mathematical nature that could guarantee that our previous scientific view—in a quite broad sense—was plainly wrong. Namely, it was common, throughout the history of science, that one particular theory would succeed the previous one—as soon as it demonstrated to provide a better and more precise description of nature. But, this time, what was falsified was not some particular theory or model—it was a whole huge class of theories, and precisely those theories that we, just until recently, thought were the only reasonable and possible choices. We are speaking of abandoning the entire scientific worldview that was absolutely dominant for a few centuries (at least in exact sciences). It was dominant to the extent that we, for the most part, tacitly understood it surely must be the correct one, so that rarely anyone even bothered to question it. And, if it was not for the Bell's theorem, which possesses this unyielding power of a precise mathematical statement, to this day we would not be aware of the immensity and the inevitability of the quantum revolution that took place. Without Bell, some physicists could, even nowadays, see the quantum mechanics as yet another incremental step in scientific progress, possibly one of only technical nature. And there would always be a remaining chance that Einstein was right after all, and that someday we would find a reasonable mechanistic model “rationally” explaining all that quantum “mumbo-jumbo”, in a form of some good old (complicated or not) clockwork mechanism. But, thanks to the Bell's theorem, we now know that this can never happen. (Again, we stress that by a clockwork-like mechanistic model, we assume one being both local and realistic.) The word “never” is something we are basically not allowed to use in physics, except in this context—such is the extraordinary generality and pure mathematical strength of the Bell's “no go” theorem. This is the reason, and a much of justification, why Stapp saw Bell's theorem as the most profound in all of science.

With such few things that we can declare with certainty in physics, and with the debunking of mechanistic doctrine after Bell being one rare example, it is unbelievable that the perception of the universe as a (deterministic) clockwork mechanism persists to this day, even among many (obviously less well-informed) scholars of various scientific disciplines, and let alone in the general public. Ironically, most of them are clinging

to mechanistic materialism in a false belief that they are upholding strict scientific views. We hope that the Nobel Prize awarded last year can help raise awareness of the scientific and philosophical revolution that happened almost half a century ago (with the first Bell tests) and that a clockwork mechanism picture of the reality will soon be widely recognized for what it is—a “flat Earth” of philosophy.

## Appendix A: Bell's Inequality

A complete understanding of how it was possible to formulate and prove a statement so general as that of Bell's inequality can be gained only by going through its derivation. Thus, we will briefly derive the simplest version of Bell's inequalities known by the name CHSH inequality (in years after the Bell's original paper,<sup>100</sup> many variations of Bell's initial inequality appeared, all of them nowadays collectively called Bell's type inequalities, or simply, Bell's inequalities; CHSH was named after John Clauser, Michael Horne, Abner Shimony, and Richard Holt).

For simplicity of exposition of the proof, instead of considering the state of two particles with spins  $\frac{1}{2}$ , we will here analyse a system made of two photons and consider their polarizations. (Beside mathematical convenience, most of the real experiments were performed with photons, so this different choice of physical system also simplifies comparisons with actual tests of Bell's inequality). We will again assume that the first photon is heading towards Alice and her lab, while the second is heading towards Bob and his lab, which we will take to be far apart. While we were previously considering two particles with opposite spin directions, now we will focus on a case where the two photons are emitted (in opposite directions) from a common source in such a way that they have identical polarizations. Throughout this section we will keep in mind a realistic picture of the universe, where the polarizations are existing and are well-defined irrespective of observation—and, thus, we will assume both photons have the same, real polarization angle, to be denoted as  $\lambda$ . (As already stressed, the inequality we are about to prove puts a constraint on locally-realistic universes.) This value  $\lambda$  is unbeknown both to Alice and Bob, and might be thought of (in the simplest case) as a random angle (not necessarily in the sense of fundamentally-inherently random).<sup>101</sup>

Quite generally, if we direct an incoming photon towards a polarizing filter, it will either pass the filter or be absorbed. In principle, we expect this outcome to depend on at least two factors: the angle of polarization of the photon, and the angle at which we orient our polarizing filter. (Commonly, it is understood that if the two angles coincide, the photon will certainly pass the filter, while if the angles are perpendicular, the photon cannot pass. However, for this derivation we will not take anything for granted and, in any case, this will be irrelevant for the derivation.)

---

<sup>100</sup> Bell, "On the Einstein Podolsky Rosen paradox".

<sup>101</sup> Eventually, it will turn out that these assumptions of identical polarizations  $\lambda$  of both photons and of random distributions are not essential for the derivation of CHSH inequality.



Both Alice and Bob will let their photons impinge on polarization filters: Alice will orient her filter at an angle to be denoted as  $a$ , while Bob will orient his filter at angle  $b$ . We will introduce a variable  $A$ , which will take value 1 if Alice's photon manages to pass through her filter, and value  $-1$  if it gets absorbed. And here comes the crucial part of the entire theorem: what does the outcome, i.e., the  $A$  value, depend upon? Certainly, we expect  $A$  to depend on Alice's decision at which angle to orient her polarizer (that we denoted by  $a$ ), as well as on the angle of the photon polarization (denoted by  $\lambda$ ). Importantly, the outcome  $A$  cannot depend on Bob's choice of his angle of polarizing filter  $b$ , simply because Bob can be light years away from Alice, and the presumption is that the universe respects the locality principle (i.e., no instantaneous influences). Therefore, we may write  $A$  as a function of  $a$  and  $\lambda$ , that is  $A = A(a, \lambda)$ . In principle, it might be that the value  $A$  also depends on some other factors—in the end, we will see that the result trivially generalizes to include this possibility. In the same way, we introduce variable  $B$  and have  $B = B(b, \lambda)$ .

We will consider the expected value (or mathematical expectation, similar to arithmetic mean value) of the product  $A(a, \lambda)B(b, \lambda)$ . Since the angle  $\lambda$  is here the only unknown variable, to find the expected value  $E(A \cdot B)$  we must average over all possible angles:

$$E(A \cdot B) = \int_0^{2\pi} A(a, \lambda)B(b, \lambda)\rho(\lambda)d\lambda. \quad (3)$$

Since there is an infinite number of possible angles, we had to integrate over all of them to get the average. Here,  $\rho(\lambda)$  denotes the probability distribution for the angle  $\lambda$ —i.e., probability (density) that the photons have the particular polarization angle  $\lambda$ —allowing for the possibility that some angles are more probable than others. We only know that it must hold:

$$\int_0^{2\pi} \rho(\lambda)d\lambda = 1, \quad (4)$$

since it is certain that the angle  $\lambda$  must take some value between 0 and  $2\pi$ . (If the distribution is uniform, then we simply have  $\rho(\lambda) = \frac{1}{2\pi}$ .) After integration over  $\lambda$ , we see that the expectation value  $E(A \cdot B)$  depends only on the remaining variables  $a$  and  $b$ , that is, the averaged value of this product that we will obtain after many repeated experiments eventually depends only on the choices of angles that Alice and Bob make. For simplicity, we can thus write  $E(a, b) \equiv E(A(a, \lambda) \cdot B(b, \lambda))$ .

Now comes the ingenious part of the Bell's theorem (in the CHSH variant). We will consider a very specially defined value  $S$ :

$$S \equiv E(a, b) + E(a', b) + E(a, b') - E(a', b'), \quad (5)$$

and shortly it will become clear why such a choice is relevant.

Above,  $a$ ,  $a'$ ,  $b$ , and  $b'$  denote 4 different angles. Namely, the idea is that Alice and Bob first set their filters to angles  $a$  and  $b$  and find the expectation value  $E(a, b)$  by averaging over many experiments. Then Alice shifts her angle to  $a'$  and they find  $E(a', b)$  in the same way. Next, Alice sets her angle to  $a$ , and Bob to  $b'$  to find  $E(a, b')$ . In the end, they also find  $E(a', b')$ .

Finally, we can explicitly formulate the famous Bell's inequality (in the CHSH variant): in any locally-realistic universe, and for any choice of  $a$ ,  $a'$ ,  $b$  and  $b'$ , the value of  $S$  must be less or equal to 2, i.e.,

$$S(a, a', b, b') \leq 2. \quad (6)$$

Before we explain the relevance of such a result, let us first prove the inequality.

We begin by noting a simple fact: either  $A(a, \lambda) + A(a', \lambda) = 0$  or  $A(a, \lambda) - A(a', \lambda) = 0$ . This is actually a trivial statement, since both  $A(a, \lambda)$  and  $A(a', \lambda)$  can take either value 1 or  $-1$ , so that either their sum, or their difference, must vanish. In a similarly simple manner, it follows that:

$$B(b, \lambda)(A(a, \lambda) + A(a', \lambda)) + B(b', \lambda)(A(a, \lambda) - A(a', \lambda)) \leq 2.$$

This holds since one of the two terms must vanish, and the other term cannot be greater than two by absolute value:  $|A(a, \lambda) \pm A(a', \lambda)| \leq 2$  and  $|B(b, \lambda)| \leq 1$ ,  $|B(b', \lambda)| \leq 1$ . Now, if we multiply this inequality by  $\rho(\lambda)$  and integrate over all angles  $\lambda$ , we directly obtain the result we intended to prove:

$$\int_0^{2\pi} (B(b, \lambda)A(a, \lambda) + B(b, \lambda)A(a', \lambda) + B(b', \lambda)A(a, \lambda) - B(b', \lambda)A(a', \lambda))\rho(\lambda) d\lambda \leq 2 \int_0^{2\pi} \rho(\lambda) d\lambda. \quad (7)$$

Namely, by comparison with the definition (5) we recognize that, due to equation (3), the integral on the left side yields precisely  $S$  value, while the expression on the right-hand side is equal to 2, due to equation (4).

Thus, we have proved the inequality (6) which tells us something (quite specific indeed) about the averaged outcomes of the repeated experiments with photons and polarizers. Crucially, we obtained this result essentially without assuming anything about the physical laws that govern the polarizations and filters! The only thing we explicitly assumed was that Bob's choice of how to set up his apparatus cannot influence Alice's outcomes far, far away (and vice versa). For simplicity, we also initially assumed that Alice's outcome depends only on her filter angle  $a$  and the unknown polarization of the photon  $\lambda$  (same for Bob). However, we did not need this assumption, since we can repeat the same deriva-

tion while taking  $\lambda$  to represent a whole set of relevant values, instead of a single angle. Among these values in the set  $\lambda$  can be, for example, the location of Alice's lab, and/or two different angles instead of one—one for Alice's photon and a different one for Bob's, or any other value(s) that might be relevant for the outcomes. Regardless of what the set  $\lambda$  contains, we will again integrate over all possibilities, weighted by the corresponding probability density  $\rho(\lambda)$ , to get the expected value of the product  $A \cdot B$ . Note that the general form of the probability density  $\rho(\lambda)$  also allows for the possibility not only that some photon polarizations are more frequent than others, but also that the photon polarization need not be random at all (e.g., taking  $\rho(\lambda)$  proportional to delta function). It also allows for much more complex hypotheses such that polarizations on Jupiter could be more often inclined towards its moon Io, while those on Earth must be aligned to follow the angle of the Leaning Tower of Pisa. Whatever the rules are, the inequality must be satisfied!

Actually, in the derivation of (6), we have tacitly used another assumption about the underlying physics: we implied it was deterministic. Namely, this is seen from our statement that Alice's outcome  $A$  is a function of values  $a$  and  $\lambda$ , meaning that each time  $a$  and  $\lambda$  are the same, the outcome  $A$  must also be the same. However, it turns out that the inequality remains the same even if we allow the physics to be indeterministic, and if we only assume that probabilities of getting  $A = 1$  or  $A = -1$  depend on values  $a$  and  $\lambda$ . (Essentially, we only need to replace the  $A$  value with its mathematical expectation.)

In addition, during this entire analysis, we had in mind a picture of a well-defined objective reality—two photons exist in and of themselves, with their always well-defined properties such as polarization. And we assumed that outcomes  $A$  and  $B$  (or, at least, probabilities for these outcomes) depend on these real properties of the physical systems (regardless of whether these properties and their values are known, and regardless of what measurements we have or have not made).

So, to summarize, we assumed a locally-realistic universe and nothing else about the underlying physics, and obtained that the value of  $S$ , defined by (5), must always be less or equal to two.

But, why is that relevant at all? This particular definition of  $S$  is important since it turns out that, for certain choices of angles  $a$ ,  $a'$ ,  $b$  and  $b'$ , quantum mechanics predicts that the value of so-defined  $S$  will be greater than 2. This we will show in Appendix B.

## Appendix B: Quantum Violation

To show that quantum mechanics predicts violations of Bell’s inequality, we will consider the following entangled state of two photons, which nowadays can be easily realized in a lab:

$$|\Phi\rangle = \frac{1}{\sqrt{2}}(|H\rangle|H\rangle + |V\rangle|V\rangle). \quad (8)$$

This state is similar to the state  $|\Psi\rangle$  of two particles with opposing spins (1), just as the state  $|\Phi\rangle$  describes two photons whose polarizations will be the same (not opposite) upon the measurement in any chosen direction (direction of polarization is always perpendicular to the direction of photon propagation, so we here only consider these perpendicular directions). Here,  $H$  and  $V$  denote, respectively, horizontal and vertical linear polarization (with respect to some, arbitrarily chosen axes). Note, however, that individual polarizations of the two photons are not well-defined in this state: when directed into a polarization filter, each of the photons has  $\frac{1}{2}$  chance of passing through, irrespective of the polarizer angle. (The arbitrarily chosen horizontal and vertical directions  $H$  and  $V$  in expression (8) are not actually distinctive nor preferential in any sense, since this state would retain the same form when expressed in any other basis of two perpendicular directions  $H'$  and  $V'$ —the state  $|\Phi\rangle$  is isotropic.) In other words, the state  $|\Phi\rangle$  corresponds to the situation where individual polarizations are not well-defined (so, in Bohr’s sense, they are not fully real), while the fact that these two “unreal” polarizations are mutually identical is nevertheless well-defined and real. Following the analogy with socks, here we should consider a same-colour pair, and the situation would then be similar as if the colours of the two socks were not well-defined/real, but nevertheless, it was certain that the non-existent colours are the same (so that, observing one sock automatically also determines the colour of the other one).

To show a quantum violation of the CHSH inequality, we again note that, according to quantum mechanics, the first, i.e., Alice’s photon, has a 50 percent chance to pass through Alice’s filter, irrespective of the filter orientation  $a$ . Quantum formalism implies that, if this happens, Bob’s photon polarization state will be immediately projected to the vector state that corresponds to the same angle  $a$ . In other words, if we have measured that Alice’s photon was polarized in the direction  $a$ , Bob’s photon sort of immediately becomes polarized in the same way. (While a detailed discussion in this direction is beyond the scope of this review, we note that the temporal order of Alice’s and Bob’s measurements in this setting can depend upon the velocity of the frame of reference,

seemingly leading to, among some other interesting philosophical implications, strange relativity of whether an outcome was random or pre-determined.) If Bob's photon next encounters Bob's polarization filter oriented at the angle  $b$ , quantum physics predicts that it has probability  $\cos^2(a - b)$  to pass it and  $\sin^2(a - b)$  to be absorbed (this also matches the classical result known as the Malus law). Therefore, the probability that both photons pass their filters, i.e., have  $A = 1$  and  $B = 1$  outcomes, according to quantum mechanics, is  $P(A = 1, B = 1) = \frac{1}{2}\cos^2(a - b)$ . Similarly, probabilities to get the other three outcomes  $P(A = -1, B = 1)$ ,  $P(A = 1, B = -1)$ , and  $P(A = -1, B = -1)$  are, respectively,  $\frac{1}{2}\sin^2(a - b)$ ,  $\frac{1}{2}\sin^2(a - b)$ , and  $\frac{1}{2}\cos^2(a - b)$ . We should notice that no "real angle of polarization"  $\lambda$  of the two photons, or anything alike, appears in the quantum mechanical description of the situation. That is why the hypothetical angle  $\lambda$  from our prior analysis of a realistic universe would usually be called a "hidden variable". Also, note that the probability of both photons passing their polarizers cannot be written as a product of two independent probabilities for each of the photons to pass (as we previously presumed possible and necessary in a locally-realistic universe).

Knowing these probabilities, it is now easy to compute the quantum expected value of the product  $A \cdot B$ :

$$\begin{aligned} E(a, b) &= E(AB) = P(A = 1, B = 1) \cdot 1 \cdot 1 \\ &+ P(A = -1, B = 1) \cdot (-1) \cdot 1 \\ &+ P(A = 1, B = -1) \cdot 1 \cdot (-1) \\ &+ P(A = -1, B = -1) \cdot (-1) \cdot (-1) \\ &= \cos^2(a - b) - \sin^2(a - b) = \cos 2(a - b). \end{aligned} \tag{9}$$

Once we know the formula  $E(a, b)$  for the expected value of the product for given angles  $a$  and  $b$ , we can directly compute the  $S$  value for any given choice of the four angles  $a, a', b$  and  $b'$ . To complete Bell's proof, we should only find some concrete four angles for which the quantum prediction of the value of  $S$  exceeds number 2. And, for example, the inequality is violated for the following choice:  $a = 45^\circ$ ,  $a' = 0^\circ$ ,  $b = 22.5^\circ$  and  $b' = 67.5^\circ$ , because:

$$\begin{aligned} S &= \cos(2 \times 22.5) + \cos(-2 \times 22.5) + \cos(-2 \times 22.5) \\ &- (\cos(-2 \times 67.5)) = 4 \times \frac{1}{\sqrt{2}} = 2\sqrt{2} \approx 2.828 > 2. \end{aligned}$$

Therefore, the standard Bohr's version of quantum mechanics claims that Bell's inequality can be violated. In particular, that it must be violated for the above choice of angles (it can be shown that this value of  $S = 2\sqrt{2}$  represents at the same time the maximal possible violation). But in a universe that is real in Einstein's sense and respects the locality of interac-

tions, there is absolutely no way to obtain such a high value for  $S$ . Hence, the existence of this quantum mechanical example that violates Bell's inequality completes the proof of Bell's theorem—that no local-realist theory can ever reproduce all predictions of quantum mechanics.

Consequently, we have proved that the two worldviews (Einstein's and Bohr's) are not only philosophically different, but they can be also differentiated by an objective experiment! This was Bell's pivotal contribution to our understanding of the universe.

Bell's inequality, in principle, also provided general instructions on what should be experimentally measured to settle the dispute. One first needed to be able to create pairs of photons in the state given by (8), after which each photon from a pair should be directed to a polarizing filter oriented, respectively, at angle  $45^\circ$  and  $22.5^\circ$ , in order to measure  $E(a, b)$ . Then, the experiment should be repeated with angles  $0^\circ$  and  $22.5^\circ$  to measure  $E(a', b)$ , and so on. The particular expectation value is easily experimentally inferred (for any fixed choice of  $a$  and  $b$  angles) by using the first part of the equation (9), which, in practice, boils down to:

$$E = \frac{N_{++} - N_{+-} - N_{-+} + N_{--}}{N_{++} + N_{+-} + N_{-+} + N_{--}} \quad (10)$$

where  $N_{++}$  would be the number of events in which both photons passed their filters,  $N_{+-}$  would be the number of cases that the first one passed but the second was absorbed, and so on.

## Literature

1. Aspect, A., J. Dalibard and G. Roger. "Experimental Test of Bell's Inequalities Using Time-Varying Analyzers". *Phys. Rev. Lett.*, 49, 25 (1982): 1804–1807. doi: 10.1103/Phys-RevLett.49.1804.
2. Atmanspacher, Harald. "The Pauli–Jung Conjecture and Its Relatives: A Formally Augmented Outline". *Open Philosophy*. 3, 1 (2020): 527–549. doi:10.1515/opphil-2020- 0138. S2CID 222005552.
3. Atmanspacher, Harald and Hans Primas. *Recasting Reality: Wolfgang Pauli's Philosophical Ideas and Contemporary Science*. Springer Science & Business Media, 2008. ISBN 3540851984, 9783540851981.
4. Bell, J. S. "Bertlmann's socks and the nature of reality". In *Speakable and Unsayable in Quantum Mechanics: Collected Papers on Quantum Philosophy*. Cambridge University Press, 2004. doi: 10.1017/CBO9780511815676.018.
5. Bell, J. S. "On the Einstein Podolsky Rosen paradox". *Physique Physique Fizika*, 1, 3 (1964): 195–200. doi: 10.1103/PhysicsPhysiqueFizika.1.195.
6. Bell, J. S. "On the impossible pilot wave". *Found. Phys.*, 12, 10 (1982): 989–999. doi: 10.1007/BF01889272.
7. Bell, John Stewart. *Speakable and Unsayable in Quantum Mechanics*. Cambridge: Cambridge University Press, 1987. ISBN 978-0-521-36869-8.
8. Bernstein, Jeremy. *Quantum Profiles*. Princeton: Princeton University Press, 1991. <https://doi.org/10.1515/9781400820542>.
9. Bohm, D. "A new theory of the relationship of mind and matter". *Philos. Psychol.*, 3 (1990): 271–286.
10. Bohm, D. *Wholeness and the Implicate Order*. London, UK: Routledge and Kegan Paul, 1980.
11. Bohm, David and Basil J. Hiley. *The Undivided Universe: An Ontological Interpretation of Quantum Theory*. London: Routledge and Kegan Paul, 1993.
12. Bohr, N. "Can Quantum-Mechanical Description of Physical Reality be Considered Complete?". *Phys. Rev.*, 48, 8 (1935), 696–702. doi: 10.1103/PhysRev.48.696.
13. Bohr, Niels. *Atomic Physics and Human Knowledge*. London, New York: John Wiley and Sons, 1958.
14. Clauser, J. F. "Early History of Bell's Theorem". In: Bigelow, N.P., J.H. Eberly, C.R. Stroud, I.A. Walmsley, eds. *Coherence and Quantum Optics VIII*. Boston, MA: Springer, 2003. [https://doi.org/10.1007/978-1-4419-8907-9\\_2](https://doi.org/10.1007/978-1-4419-8907-9_2).
15. Clauser, J. F. and A. Shimony. "Bell's theorem: experimental tests and implications". *Reports on Progress in Physics*, 41 (1978): 1881–1927.



16. Clavin, Whitney. "Proving that Quantum Entanglement is Real". Caltech. Accessed on July 10, 2023. <https://www.caltech.edu/about/news/proving-that-quantum-entanglement-is-real>.
17. Cowling, T. G. *Natural Philosophy of Cause and Chance*. Nature Publishing Group, 1949. doi:10.1038/164419a0.
18. "Das Wesen der Materie [The Nature of Matter]". A 1944 speech in Florence, Italy, *Archiv zur Geschichte der Max-Planck-Gesellschaft*, Abt. Va, Rep. 11 Planck, Nr. 1797.
19. Daumer, M., D. Dürr, S. Goldstein et al. "Naive realism about operators". *Erkenntnis* 45, (1996): 379–397. <https://doi.org/10.1007/BF00276801>.
20. Drezet, A. "Why Bohr was wrong in his response to EPR" (2023). arXiv. Accessed on August 1, 2023. <https://arxiv.org/abs/2305.06859v1>.
21. Einstein, A., B. Podolsky and N. Rosen. "Can Quantum-Mechanical Description of Physical Reality Be Considered Complete?". *Phys. Rev.*, 47, 10 (1935): 777–780. doi: 10.1103/PhysRev.47.777.
22. Farmelo, Graham. "Random Acts of Science". *The New York Times*, June 11, 2010.
23. Fine, A. and M. Beller. "Bohr's response to EPR". In J. Faye and H. Folse, eds. *Niels Bohr and Contemporary Philosophy*, 1–31. New York: Kluwer 1994.
24. Fine, A. *The Shaky Game: Einstein, Realism and the Quantum Theory*, 2nd Edition. Chicago: University of Chicago Press, 1996.
25. Fine, Arthur and Thomas A. Ryckman. "The Einstein-Podolsky-Rosen Argument in Quantum Theory". In Edward N. Zalta, ed. *The Stanford Encyclopedia of Philosophy (Summer 2020 Edition)*. Accessed on August 1, 2023, <https://plato.stanford.edu/archives/sum2020/entries/qt-epr>.
26. Fine, Arthur. "Bohr's Response to EPR: Criticism and Defense". *Iyyun: The Jerusalem Philosophical Quarterly*, 56 (2007): 31–56. JSTOR, Accessed on July 31, 2023. <http://www.jstor.org/stable/23354464>.
27. Freedman, S. J. and J. F. Clauser. "Experimental Test of Local Hidden-Variable Theories". *Phys. Rev. Lett.*, 28, 14 (1972): 938–941.
28. Frescura, F. A. M. and B. J. Hiley. "Algebras, quantum theory and pre-space". *Revista Brasileira de Física. Special volume "Os 70 anos de Mario Schonberg"* (1984): 49–86, 2.
29. Gilder, Louisa. *The Age of Entanglement: When Quantum Physics Was Reborn*. New York: Alfred A. Knopf, 2008. ISBN 978-1-4000-4417-7. OCLC 608258970.
30. Giustina, Marissa et al. "Significant-Loophole-Free Test of Bell's Theorem with Entangled Photons." *Phys. Rev. Lett.*, 115, 25 (2015): 250401. doi:10.1103/PhysRevLett.115.250401.

31. Goldstein, Sheldon. "Bohmian Mechanics". In Edward N. Zalta, ed. *The Stanford Encyclopedia of Philosophy (Fall 2021 Edition)*. <https://plato.stanford.edu/archives/fall2021/entries/qm-bohm>.
32. Greenberger, Daniel M., Michael A. Horne and Anton Zeilinger. "Going Beyond Bell's Theorem". In Kafatos, Menos, ed. *Bell's Theorem, Quantum Theory, and Conceptions of the Universe (1 ed.)*, 69–72. Heidelberg: Springer, 1989. arXiv:0712.0921. ISBN 978-94-017-0849-4.
33. Gribbin, John, Mary Gribbin and Jonathan Gribbin. *Q is for Quantum: An Encyclopedia of Particle Physics*. Simon and Schuster, 2000. ISBN 9780684863153.
34. Gröblacher, S., T. Paterek, R. Kaltenbaek, R. Brukner, Č. Žukowski, M. Aspelmeyer and A. Zeilinger. "An experimental test of non-local realism". *Nature*, 446 (2007): 871–875. doi: 10.1038/nature05677.
35. Gründler, G. "What exactly is proved by the violation of Bell's inequality?". arXiv. Accessed on August 1, 2023. <https://arxiv.org/abs/1704.03856v6>.
36. Halvorson, H. and R. Clifton. *Reconsidering Bohr's Reply to EPR. Non-locality and Modality*. Springer, 2002. doi: 10.1007/978-94-010-0385-8 1.
37. Heisenberg, W. "Über den anschaulichen Inhalt der quantentheoretischen Kinematik und Mechanik". *Z. Phys.*, 43, 3 (1927): 172–198. doi: 10.1007/BF01397280.
38. Heisenberg, W. "Über den anschaulichen Inhalt der quantentheoretischen Kinematik und Mechanik". *Z. für Physik*, 43, 172 (1927). Translated as "The physical content of quantum kinematics and mechanics". In J. Wheeler and W. Zurek, eds. *Quantum Theory and Measurement*. Princeton: Princeton University Press, 1983.
39. Heisenberg, W. *Das Naturgesetz und die Struktur der Materie. Natural law and the structure of matter*. Belser-Press, 1967.
40. Heisenberg, Werner. *The Physical Principles of the Quantum Theory*. Courier Dover Publications, 1949.
41. Held, Carsten. "The Kochen-Specker Theorem". In Edward N. Zalta and Uri Nodelman, eds. *The Stanford Encyclopedia of Philosophy (Fall 2022 Edition)*. <https://plato.stanford.edu/archives/fall2022/entries/kochen-specker>.
42. Kragh, H. *Natural Philosopher. Simply Charly*. Accessed on August 1, 2023. <https://pressbooks.pub/simplydirac/chapter/natural-philosopher>.
43. Leggett, A. J. "Nonlocal Hidden-Variable Theories and Quantum Mechanics: An Incompatibility Theorem". *Found. Phys.*, 33, 10 (2003): 1469–1493. doi: 10.1023/A:1026096313729.
44. Leggett, A. J. and Anupam Garg. "Quantum mechanics versus macroscopic realism: Is the flux there when nobody looks?". *Phys. Rev. Lett.*, 54, 9 (1985): 857–860. doi:10.1103/PhysRevLett.54.857.
45. Maudlin, Tim. "What Bell did." *J. Phys. A: Math. Theor.*, 47, 42 (2014): 424010. doi:10.1088/1751-8113/47/42/424010.

- I. Salom, 2022 Nobel Prize in Physics and the End of Mechanistic Materialism
46. Mermin, N. David. *Boojums All The Way Through*. Cambridge University Press, 1990.
  47. Moore, Walter. *Schrodinger: Life and Thought*. Cambridge University Press, 1992.
  48. Myrvold, Wayne, Marco Genovese and Abner Shimony. "Bell's Theorem". In Edward N. Zalta, ed. *The Stanford Encyclopedia of Philosophy (Fall 2021 Edition)*. <https://plato.stanford.edu/archives/fall2021/entries/bell-theorem>.
  49. Pan, J.-W., D. Bouwmeester, M. Daniell, H. Weinfurter and A. Zeilinger. "Experimental test of quantum nonlocality in three-photon Greenberger-Horne-Zeilinger entanglement". *Nature* 403 (2000): 515–519.
  50. Piechocinska, B. "Physics from Wholeness: Dynamical Totality as a Conceptual Foundation for Physical Theories". *Uppsala Universitet/Acta Universitatis Uppsaliensis* (2005).
  51. R. Brown, Harvey and David Wallace. "Solving the Measurement Problem: De Broglie–Bohm Loses Out to Everett". *Found. Phys.*, 35, 4 (2005): 517–540. doi:10.1007/s10701-004-2009-3.
  52. Rauch, D., 2018, "Cosmic Bell test using random measurement settings from high-redshift quasars," *Physical Review Letters*, 121: 080403.
  53. Salom, I. "To the rescue of Copenhagen interpretation". arXiv. Accessed on August 1, 2023 <https://arxiv.org/abs/1809.01746v1>.
  54. Schrödinger, Erwin. *My View of the World*. Cambridge: Cambridge University Press, 1964. Quoted from Malhotra, R., Infinity Foundation. *Being different: An Indian challenge to western universalism*. N. J.: Princeton, 2018.
  55. Seager, W. "The Philosophical and Scientific Metaphysics of David Bohm". *Entropy*, 20, 7 (2018): 493. doi: 10.3390/e20070493.
  56. Shalm, L. K., et al. "Strong loophole-free test of local realism". *Physical Review Letters*, 115 (2015): 250402.
  57. Shimony, A., M. A. Horne and J. Clauser. "Comment on 'The theory of local beables'," *Epistemological Letters*, 13 (1976): 1–8.
  58. Shingo, Fujita. "How Did Bohr Reply to EPR?". In "The Two Faces of Realism: Bohr and Bell". *Journal of the Philosophy of Science*, 27 (1994).
  59. Skuse, B. "Nobel Prize in Physics 2022". Lindau Nobel Laureate Meetings. Accessed on August 1, 2023. <https://www.lindau-nobel.org/blog-nobel-prize-in-physics-2022-provin-g-and-using-the-peculiar-quantum-nature-of-reality>.
  60. Stapp, Henry P. "Bell's Theorem and World Process". *Nuovo Cimento*, 29B, 2, (1975): 270.
  61. The Observer, January 25, 1931, p. 17, column 3.
  62. The Observer, January 11, 1931; also in *Psychic Research*, 25 (1931): 91.

63. Weihs, G., T. Jennewein, C. Simon, H. Weinfurter and A. Zeilinger. "Violation of Bell's Inequality under Strict Einstein Locality Conditions". *Phys. Rev. Lett.*, 81, 23 (1998): 5039–5043. doi: 10.1103/PhysRevLett.81.5039.
64. Zander, C. and A. R. Plastino. "Revisiting Entanglement within the Bohmian Approach to Quantum Mechanics". *Entropy*, 20, 6 (2018). doi: 10.3390/e20060473.
65. Zeilinger, A. *Dance of the Photons*, 266. New York: Farrar, Straus and Giroux, 2010.
66. Żukowski, Marek and Časlav Brukner. "Quantum non-locality – it ain't necessarily so". *J. Phys. A: Math. Theor.*, 47, 42, 8 (2014): 424009. doi:10.1088/1751-8113/47/42/424009.

**Игор Салом**

Универзитет у Београду, Институт за физику, Београд

### **НОБЕЛОВА НАГРАДА ЗА ФИЗИКУ ЗА 2022. ГОДИНУ И КРАЈ ЕРЕ МЕХАНИСТИЧКОГ МАТЕРИЈАЛИЗМА**

Идеје и резултати који се налазе у позадини Нобелове награде за физику, додељене 2022. године, имали су огроман утицај на наше разумевање самих основа универзума, односно фундаменталних особина стварности у којој живимо. Зато је од изузетног значаја да импликације ових открића такође стигну и до шире јавности, а не само до уских научних кругова. Стога, овај прегледни рад представља покушај да се ова револуција у научном погледу на филозофску суштину нашег универзума, а која је коначно овековечена и потврдом Нобеловог комитета, објасни и приближи што ширем кругу читалаца. Притом, то је изведено уз што мање позивања на математичке детаље (текст је писан са идејом да се може пратити и уз потпуно занемаривање математичких исказа, којих у главном тексту, ионако да готово и нема).

Почећемо од генијалних научних расправа између Алберта Ајнштајна и Нилса Бора о самој природи квантне механике, у којима је Ајнштајн заступао своју „здраворазумску“ визију универзума, зановану на детерминизму и уверењу да физички системи морају увек поседовати добро дефинисане, реалне особине, независне од контекста и мерења, док је Бор износио своје револуционарне погледе на природу реалности, а која је, по њему, своје јасне особине попримала тек у контексту конкретног експеримента. Расправе су кулминирале када је Ајнштајн, заједно са колегама Подолским и Розеном, формулисао такозвани ЕПР парадокс – проблем који ће послужити као подстицај за многобројна каснија истраживања у овом контексту (укључујући и она крунисана прошлогодишњом Нобеловом наградом), па чак посредно довести и до нових технологија везаних за квантну теорију информација. Ајнштајн је сматрао да је ЕПР аргументом коначно доказана „некомплетност“ квантне механике, односно да ова физичка теорија не може претендовати да пружи потпуну слику стварности (у најбољем случају, може представљати само некакву апроксимативну теорију). Ипак, Ајнштајнове примедбе на рачун квантне механике су остале филозофске природе, док је њен практични успех био толики да се мало ко интересовао за потенцијалне дилеме око њене „комплетности“.

Затим ћемо се фокусирати на ирског физичара Џона Бела, који је био много више окупиран филозофским импликацијама квантне физике него њеним практичним последицама. Делећи Ајнштајнов поглед на физику и природу нашег универзума, он је био фасциниран идејом да се пронађе комплетнија и „објективнија“ теорија од квантне механике, а која би

била у духу „реализма”: у којој би физички системи увек имали добро дефинисане особине и где не би било „субјективистичких” елемената нити специјалне улоге мерења. Био је инспирисан Де Брољ-Бомовом механиком: интерпретацијом квантне механике која је, по њему, имала много пожељних карактеристика (уједно била и „реалистична” и детерминистичка), али и велики проблем такозване манифестне „нелокалности” – односно, у тој теорији, утицаји су се преносили тренутно на даљину, пркосећи Ајнштајновој теорији релативитета. Трагање за реалистичном теоријом која не би имала овај проблем нелокалности, довело га је, на крају, до данас чувене Белове теореме – резултата који неки сматрају највећим достигнућем у целокупној историји људске науке, а не само физике. Надовезавши се на поставку из ЕПР парадокса, Бел је, са математичком стогошћу, доказао да се свака (колико год компликована) „здраворазумска”, односно локална и реалистична теорија, неизбежно мора експериментално разликовати од квантне механике. Другим речима, да квантна механика или мора бити погрешна на начин који се може доказати експериментом (а Бел је показао и како), или заувек морамо променити наше схватање универзума и одбацити сваку наду да се он може објаснити у истинском духу механицистичке физике и филозофије. Након Белове теореме, остало је да експеримент донесе своју пресуду.

Конечно, размотрићемо експерименте који су пратили Белову теорему. Прво Џон Клаузер, па затим и Алан Аспе и Антон Цајлингер – тројица прошлогодишњих нобеловаца – отклонили су, кроз низ вештих експеримената, сваку сумњу: наш универзум није локално-реалистичан и никад неће бити могуће наћи теорију која би била у складу са Ајнштајновим (а и Беловим) очекивањима, а да притом буде у складу са експериментима.

Исход ових експеримената нас је приморао да дубоко преиспитамо наше разумевање универзума. Детаљније ћемо продискутовати о филозофским последицама ових експерименталних резултата и о томе какве измене нашег погледа на свет они захтевају. Као што ћемо видети, једно је извесно: стандардна слика универзума као компликованог безличног механизма, у коме се сваки утицај може испратити и ништа се не догађа волшебно и на даљину – сигурно више није научно утемељена опција и никад више не може ни бити. Данас ово знамо са сигурношћу која је необична за физику, а коју је могла да пружи само строга математичка теорема какву нам је Бел подарио.

**Кључне речи:** ЕПР парадокс, Белова теорема, Белова неједнакост, заснивање квантне механике, локални реализам

*Прихваћено за објављивање на седници  
Уређивачкој одбора 11. новембра 2023.*



## OPEN ACCESS

## EDITED BY

Firuz Kamalov,  
Canadian University of Dubai,  
United Arab Emirates

## REVIEWED BY

Emmanuel Letouzé,  
Pompeu Fabra University, Spain  
Hanjia Lyu,  
University of Rochester, United States

## \*CORRESPONDENCE

Marko Djordjevic  
✉ dmako@bio.bg.ac.rs

## SPECIALTY SECTION

This article was submitted to  
Machine Learning and Artificial Intelligence,  
a section of the journal  
Frontiers in Big Data

RECEIVED 06 September 2022

ACCEPTED 27 February 2023

PUBLISHED 24 March 2023

## CITATION

Tumbas M, Markovic S, Salom I and  
Djordjevic M (2023) A large-scale machine  
learning study of sociodemographic factors  
contributing to COVID-19 severity.  
*Front. Big Data* 6:1038283.  
doi: 10.3389/fdata.2023.1038283

## COPYRIGHT

© 2023 Tumbas, Markovic, Salom and  
Djordjevic. This is an open-access article  
distributed under the terms of the [Creative  
Commons Attribution License \(CC BY\)](#). The use,  
distribution or reproduction in other forums is  
permitted, provided the original author(s) and  
the copyright owner(s) are credited and that  
the original publication in this journal is cited, in  
accordance with accepted academic practice.  
No use, distribution or reproduction is  
permitted which does not comply with these  
terms.

# A large-scale machine learning study of sociodemographic factors contributing to COVID-19 severity

Marko Tumbas<sup>1</sup>, Sofija Markovic<sup>1</sup>, Igor Salom<sup>2</sup> and  
Marko Djordjevic<sup>1\*</sup>

<sup>1</sup>Quantitative Biology Group, Faculty of Biology, University of Belgrade, Belgrade, Serbia, <sup>2</sup>Institute of Physics Belgrade, National Institute of the Republic of Serbia, University of Belgrade, Belgrade, Serbia

Understanding sociodemographic factors behind COVID-19 severity relates to significant methodological difficulties, such as differences in testing policies and epidemics phase, as well as a large number of predictors that can potentially contribute to severity. To account for these difficulties, we assemble 115 predictors for more than 3,000 US counties and employ a well-defined COVID-19 severity measure derived from epidemiological dynamics modeling. We then use a number of advanced feature selection techniques from machine learning to determine which of these predictors significantly impact the disease severity. We obtain a surprisingly simple result, where only two variables are clearly and robustly selected—population density and proportion of African Americans. Possible causes behind this result are discussed. We argue that the approach may be useful whenever significant determinants of disease progression over diverse geographic regions should be selected from a large number of potentially important factors.

## KEYWORDS

SARS-CoV-2, sociodemographic factors, feature selection, Random Forest, XGBoost, mRMR

## 1. Introduction

More than two years into the COVID-19 pandemic, there are still many open questions regarding the spread and severity of SARS-CoV-2. Not only can we not explain, on an individual basis, who will experience severe illness or no symptoms at all, but we often lack this predictive power even on the larger scale of entire regions, where personal traits and individual genetical predispositions are averaged out. Different countries or regions within a country experience diverse numbers of new cases and fatalities, with patterns that are difficult to anticipate. On the other hand, the potential benefits of the ability to understand and foresee the regional COVID-19 behavior are clear: it would assist governments in appropriately allocating resources, help sustain economic activities, and allow to correctly and timely estimate risks and necessary measures—thus saving human lives and reducing the overall epidemic impact.



Naively, in the present era of abundant and widely available data, one could expect that most of these questions could be settled down by systematically comparing the COVID-19 numbers with various demographic and environmental parameters. However, while much progress in this direction has been made (e.g., [Adhikari and Yin, 2020](#); [Allel et al., 2020](#); [An et al., 2020](#); [Gupta and Gharehgozli, 2020](#); [Pan et al., 2020](#); [Djordjevic et al., 2021b](#); [Hradsky and Komarek, 2021](#); [Lorenzo et al., 2021](#); [Markovic et al., 2021](#); [Perone, 2021](#); [Rontos et al., 2021](#); [Salom et al., 2021](#); [Singh et al., 2021](#); [Wang et al., 2022](#)), many methodological obstacles complicate this type of research and often lead to conflicting conclusions of otherwise similar studies.

One obvious problem lies in often significant correlations between potentially relevant demographic predictors, making it challenging to disentangle their influences. This is further complicated by interactions between the variables and the nonlinear ways some of these predictors may influence COVID-19 observables. To distinguish between such delicate effects requires careful numerical analysis and sufficiently large COVID-19 data. State-of-the-art statistical and machine-learning methods can be effective if they are provided with sufficiently large, high-quality data. To train accurate models, one should collect relevant data from a large number of smaller regions. However, in the COVID-19 context, this comes with a trade-off: diverse regions tend to have inconsistent testing/reporting policies, and the data is often less reliable (or entirely unavailable) for smaller regions. In general, this dependence of COVID-19 observables (e.g., case counts and fatalities) on local policies (mostly on testing protocols and rules on which deaths are attributed to COVID-19) poses a problem in how to compare the data from various regions meaningfully. Even when policies reasonably coincide, making equal-time comparisons rarely makes sense since different counties of states belong to different phases of the epidemics curve.

Another methodological issue is to define the response variable, i.e., to quantify the precise aspect of the pandemic that we want to investigate and the appropriate proxy variables. In particular, there are two main, substantially different aspects of assessing the pandemic effects: (i) Analyzing virus transmissibility, i.e., how rapidly it spreads in the community, which is necessary to understand the evolution of COVID-19 case numbers, and (ii) Investigating SARS-CoV-2 severity—i.e., understanding individual hospitalization/morbidity/mortality risks, what causes differences in infection severity, and identifying subpopulations or regions more prone to severe forms of the disease. Of the two, much more effort has been devoted to the former, while the studies investigating the disease severity face the additional problem of choosing a relevant severity measure intrinsically independent of the transmissibility. For example, using COVID-19 fatalities is not suitable, despite being often used in this context ([Wu et al., 2020](#); [Moreira et al., 2021](#)) since it is strongly correlated with COVID-19 prevalence (i.e., transmissibility) in the population ([Markovic et al., 2021](#))—qualitatively, a larger number of cases (larger transmissibility) also leads to a larger number of fatalities.

In this paper, we focus on the problem of COVID-19 severity to address the above-mentioned caveats. As the dataset, we collect COVID-19 time series (of case numbers and deaths) with values of over one hundred diverse sociodemographic variables for more

than 3,000 U.S. counties. This dataset has optimal properties in the sense of being both large and reasonably uniform (in the sense of COVID-19 policies). That is, all considered regions belong to the same country (and therefore have reasonably uniform policies). To focus on the influence of sociodemographic and economic factors, i.e., to neglect the complex influences of vaccination and different virus strains, we concentrate on the first epidemic wave—though, in the future, our study could also be extended by including suitable predictors for these factors. For each county, we estimate a well-defined measure of severity alone, which is a priori independent of the virus transmissibility. This measure, denoted as  $m/r$ , was introduced in [Markovic et al. \(2021\)](#) and is based on epidemiological modeling, representing the ratio of population-averaged mortality to recovery rates. Intuitively, the faster rate of dying from COVID-19, and slower recovery rate, relate to larger severity.

We apply several machine learning techniques to identify which demographic variables are relevant predictors of the  $m/r$  severity measure. In particular, we use repetitive rounds of (relaxed) Lasso and Elastic net linear regressions (with feature selection and regularization) and Random Forest and XGBoost, implementing ensembles of weak learners (decision trees). Random Forest and XGBoost can also accommodate highly nonlinear relations of the response to predictors and their interactions. Both can assign importance to the predictors, allowing for straightforward selection of significant predictors (with all other advantages of these techniques). Finally, we will also use a recently popularized [within the Uber platform ([Zhao et al., 2019](#))] mRMR (minimal Redundancy Maximal Relevance) feature selection method, allowing better dealing with correlated datasets. mRMR will be integrated into Random Forest and XGBoost, which combines the advantages of these methods with mRMR. Overall, we carefully devise several state-of-the-art feature selection methods, intending to start from a large number of sociodemographic factors and, in an unbiased way (without prior assumptions), determine the most important predictors directly from the data. While machine learning has been successfully applied to a number of COVID-19-related problems, such as disease diagnosis and prognosis ([Alizadehsani et al., 2021](#); [Mahdavi et al., 2021](#); [Amini et al., 2022](#); [Kamalov et al., 2022](#); [Rajab et al., 2022](#); [Ramírez-del Real et al., 2022](#); [Yousefzadeh et al., 2022](#)) it was to our knowledge less frequently applied in the ecological study design (a transverse comparison of geographical regions) as done here ([Wang et al., 2021](#)).

The analysis presented here is also helpful from another perspective. In [Markovic et al. \(2021\)](#), we studied COVID-19 severity based on U.S. states instead of counties. Comparing the results of these studies can provide an important insight into the possible effects of spatial resolution (from 51 states to over 3,000 counties) on the obtained results. To our best knowledge, it is currently unresolved what happens with conclusions of ecological regressions (transverse/cross-sectional study design across different regions employed here) in a transition from a smaller number of spatially larger geographic regions to a substantially larger number of smaller regions. Consequently, our study can also aid a better understanding of the implications of ecological regression study design, particularly in the context of machine learning applications.

## 2. Materials and methods

### 2.1. Data collection

Demographic data at the county level were collected from several sources. The demographic composition of the U.S. population by gender, race, and population under 18 and over 65 was taken from the U.S. Census Bureau website integrating multiple different reports (U.S. Census Bureau, 2020). Information about population behavioral health risks at the county level was taken from the County Health Rankings website (County Health Rankings, 2020). The number of hospital beds and emergency unit capacity per county was obtained from the Homeland Infrastructure Foundation-Level Data (HIFLD) website (Homeland Infrastructure Foundation-Level Data, 2020). Poverty, deep poverty, median household income, per capita income, number of households, and predictor variables describing various levels of education on the county level were downloaded from the U.S. Department of Agriculture website resource Atlas of Rural and Small-Town America (U.S. Department Of Agriculture, 2021). Medical parameters such as hypertension, cardiovascular disease mortality, diabetes, obesity, inactivity, lower respiratory disease mortality, and daily smoking prevalence were downloaded from the Global Health Data Exchange website (Global Health Data Exchange, 2021). Individual county areas (U.S. Census Bureau, 2018) and exact FIPS codes (U.S. Census Bureau, 2011) were also downloaded from the U.S. Census Bureau website. Python scripts were used to map multiple county information sources using FIPS code values, and the resulting dataset is provided in Supplementary Tables 1, 2.

### 2.2. County severity measure calculation

Information about cumulative daily COVID-19 deaths and cumulative registered infection cases at the county level was retrieved from Dong et al. (2020). From these case counts, the COVID-19 severity measure  $m/r$  was calculated as previously derived (Markovic et al., 2021) using our SPEIRD infection dynamics model (Djordjevic et al., 2021a,b):

$$\frac{m}{r} = \frac{\text{CFR}(\infty)}{1 - \text{CFR}(\infty)}$$

Here  $\text{CFR}(\infty)$  is the Case Fatality Rate in saturation, i.e., calculated at the end of the epidemic wave. CFR corresponds to the ratio of cumulative fatalities and case counts, where both quantities are calculated at the end of the wave. To estimate its saturation value, without relying on a single date for the wave end, we use a mean CFR value for the time interval at the end of the wave when the case counts (and correspondingly also CFR) enter saturation. This time interval (end of the wave) was estimated at the level of states and then associated with the corresponding counties (see Supplementary Table 3), as it was shown that the wave intervals could be inferred more accurately from larger (conglomerated) spatial units (Vilar and Saiz, 2021). For more details on the derivation of  $m/r$ , see Supplementary methods.

In Markovic et al. (2021) it was shown that the  $m/r$  measure is independent of transmissibility, which is also evident from the direct (though nonlinear) relationship between  $m/r$  and CFR (due to the fact that CFR is, per se, independent from the frequency of the virus transmission). Therefore, our measure does not depend on the rate at which the epidemic spreads, and is consequently independent of the social distancing measures and/or quarantine. It also does not depend on the epidemic phase since it is a function of CFR at the end of the epidemic wave (when both the number of fatalities and cumulative case counts have stabilized). Additionally, the  $m/r$  value is not expected to significantly depend on the testing policies. That is, while both the cumulative number of (detected) COVID-19 deaths and the cumulative (detected) case counts depend on the volume of testing, their dependence is qualitatively of the same manner: fewer tests will result in lower case counts but also in more COVID-19 deaths that failed to be attributed to the pandemic. Thus, these two effects tend to cancel each other.

Several other severity/fatality measures have been proposed so far, including the total number of fatalities, as the simplest to obtain, yet inadequate measure, which is highly correlated with the total number of detected cases, making it impossible to distinguish the severity from the transmissibility of the disease (Markovic et al., 2021). Some other, more promising approaches found in the literature include the use of CFR and its variations, such as delay-adjusted CFR (Yeoh et al., 2021). These measures, however, do not have a clear mechanistic interpretation (Böttcher et al., 2020), as they are not derived from a dynamic/mechanistic model of the disease spread.

Since CFR at the end of the first peak for COVID-19 has a relatively small value for most counties ( $\sim 10^{-2}$ ), from the equation above follows that in such cases  $m/r$  and  $\text{CFR}(\infty)$  have similar values, so  $m/r$  in principle leads to the robust results compared to other measures (but only provided that CFR for these measures is calculated in saturation, i.e., at the end of the peak). However, this does not have to be the case for other infectious diseases with potentially higher CFR, for which the difference between  $m/r$  and  $\text{CFR}(\infty)$  would be more drastic, particularly since  $m/r$  is a nonlinear function of  $\text{CFR}(\infty)$ . In such a case, and for the reasons stated above, the use of  $m/r$  as the severity measure is more adequate. Even in the case of low CFR, and as explained above, using  $m/r$  has the following advantages: (i) In distinction to ordinary CFR, CFR in  $m/r$  expression is calculated at saturation (end of the peak), which naturally follows from  $m/r$  derivation and makes the measure independent of the epidemic phase. (ii) The measure has a clear mechanistic interpretation and is inherently independent of transmissibility (and by that, also of the effects of epidemiological policies and interventions), which further simplifies the result interpretation. Based on that, using  $m/r$  as the response variable in ecological regressions applied to epidemiological problems is preferable. In addition to the study of COVID-19 severity determinants at the level of USA states in Markovic et al. (2021), the measure was also successfully applied at a global level to better understand the apparently puzzling relationship between Global Health Security Index (GHSI) and COVID-19 mortality in different world countries (Markovic et al., 2022).

## 2.3. Data processing

All assembled variables were subjected to standard transformations of different strengths and directions (square, square root, cubic root, logarithm, negative square root, negative cubic root, and negative logarithm) to reduce the skewness of the data and bring them closer to normal distribution. For each variable, the transformation that minimizes the absolute value of the skewness from the Python SciPy library (Virtanen et al., 2020) was chosen, which was automated by a custom Python script. The county severity measure was transformed using the square root function (also chosen to minimize skewness).

Outliers were identified as being outside three median absolute deviations (MADs). After applying transformations, outliers were substituted with the corresponding variable median values. Transformations and subsequent outlier substitution by median values removed heavy distribution tails (observed for some variables) so that the distributions were brought closer to normal.

## 2.4. Model hyperparameter tuning

Processed data was split into training and validation sets (80-20). The validation set was set aside, while the training set was used for hyperparameter selection (through 10-fold cross-validations) and final model training. To select optimal hyperparameter values, we put them on an extensive grid (specified below for each model) and chose the parameter combination leading to the smallest cross-validation MSE (Mean Squared Error). Alternatively, to obtain sparse models (see below), hyperparameter combinations within one standard error of minimal MSE were considered. The data were standardized (the mean subtracted and divided by the standard deviation) in each cross-validation round. The hyperparameter grid search results are provided in [Supplementary Tables 4–13](#). Final models were trained on the entire training dataset with the previously selected optimal hyperparameter values. MSE calculated on the validation set was compared to (approximately) agree with the training set MSE as a consistency check.

## 2.5. Lasso regression

Lasso regression applies L1 regularization (Hastie et al., 2009), controlled by the  $\lambda$  hyperparameter value. Hyperparameter grid search was performed as described in 2.4., with exponential grid spacing and maximal  $\lambda$  value corresponding to all zero coefficients.  $\lambda$  values that lead to minimal cross-validation MSE within one standard error were selected.  $\lambda$  for training the model on the entire training dataset corresponds to the maximally sparse Lasso model (i.e., largest  $\lambda$ ) within these values. Non-zero coefficients were extracted from the model.

## 2.6. Elastic net regression

Elastic net regression applies L1 and L2 regularization (Zou and Hastie, 2005; Hastie et al., 2009), which are controlled by  $\lambda$  and

$\alpha$  hyperparameter values. Scikit-Learn library implementation of Elastic net model was used (Pedregosa et al., 2011).  $\alpha$  parameter was put on a linear grid in the range (0,1), and for each  $\alpha$  parameter, the range of  $\lambda$  values was selected as described in 2.5. This resulted in a 2-dimensional grid, searched as described in 2.4. Hyperparameter combinations within one standard error of cross-validation MSE were selected. Among these, ( $\lambda$ ,  $\alpha$ ) combination that leads to a maximally sparse Elastic net model was chosen to train the model on the entire training dataset.

## 2.7. Random Forest regression

For Random Forest regression, minimal leaf size and maximal tree depth were used as hyperparameters (Breiman, 2001; Hastie et al., 2009). The number of regression tree estimators was set to 600. Hyperparameter grid values that correspond, respectively, to minimal leaf size and maximal tree depth are: {1, 2, 4, 8, 16, 32, 64, 128, 256, 512, 1024}, {1, 106, 211, 316, 421, 526, 631, 736, 841, 946, 1051, 1156, 1261, 1366, 1471, 1576, 1681, 1786, 1891}. A 2-dimensional grid was constructed, and a search was performed as described in subsection 2.4. A hyperparameter combination that corresponds to minimal test MSE was selected. As several combinations correspond to the minimum, the one with the smallest maximal tree depth (corresponding to the shallowest tree) was selected. The Random Forest model was then trained on the whole training set, and predictors with greater than mean feature importance were selected.

## 2.8. XGBoost regression

XGBoost regression model learning rate, maximal tree depth, and the number of tree estimators were tuned hyperparameters (Friedman, 2001; Hastie et al., 2009; Chen and Guestrin, 2016). Hyperparameter values in the previously defined order are: {0.5, 0.1, 0.15, 0.2, 0.25, 0.35, 0.5}, {1, 2, 3, 4, 5, 6, 7, 8, 16, 32, 64, 128, 256, 512}, {15, 30, 45, 60, 75, 90, 100, 115, 130, 145, 160, 175}. A 3-dimensional grid was constructed, and a search was performed as described in 2.4. A Hyperparameter combination corresponding to minimal test MSE was selected and used to train the XGBoost model on the entire training dataset. Predictor variables with greater than mean feature importance were selected.

## 2.9. Relaxed models

Relaxed models (Hastie et al., 2009) were implemented through a two-step iterative training process. The first training step is described in the sections above (Lasso, Elastic net, Random Forest, and XGBoost regression). Input data for the first step contains an entire dataset with all 115 predictor variables. Hyperparameter values are optimized after the first round as described above, and predictor variables are selected for each model based on non-zero coefficients (Lasso and Elastic net) or greater than mean feature importance for Random Forest and XGBoost. In the second iteration, the input dataset contains only predictor features selected

by the first iteration, and model training is repeated in the same way as for the first iteration. Second iteration (relaxed) models are further used to extract the final predictor importance and coefficients. In the [Supplement Figures](#), we provide importance estimates for all predictors.

## 2.10. Minimum redundancy maximum relevance predictor selection

Minimum redundancy maximum relevance (mRMR) is an algorithm for selecting the minimal-optimal subset of predictor variables ([Ding and Peng, 2005](#); [Zhao et al., 2019](#)). In mRMR implementation ([Mazzanti, 2022](#)), F-statistics was used to assess association with the response (relevance) and mean Pearson correlation between predictors to assess redundancy. mRMR regression returns top  $n$  selected features, where  $n$  was added as an additional hyperparameter to Random Forest and XGBoost regressions, with the grid values: {5, 10, 15, 20, 25, 30, 40, 50, 65, 80, 100, 115}. For each grid value, (1—minimal MSE) was plotted, and the number of features was selected when the plot approached saturation. This number of features and other hyperparameter values corresponding to minimal cross-validation MSE were used to train Random Forest or XGBoost models on the entire training dataset. Predictor variables with greater than mean feature importance were selected.

## 3. Results

We started by assembling an extensive set of sociodemographic and medical variables for USA counties (115). The entire dataset is provided in [Supplementary Tables 1–3](#). The main challenge for the data analysis is a large number of input variables from which we should select the most important predictors of disease severity. While this allows for an unbiased selection of factors that can contribute to the disease severity at the level of counties, a large majority of the initial set of variables likely do not significantly contribute to the response. Therefore, keeping them in the analysis may lead to a large noise and, consequently, model overfitting. On the other hand, several sociodemographic factors can genuinely contribute to explaining severity, so multivariate analysis, in which one controls for simultaneous effects of these variables, is necessary. Consequently, we start with linear regression methods with regularizations and variable selection, Lasso ([Hastie et al., 2009](#)) and Elastic net ([Zou and Hastie, 2005](#); [Hastie et al., 2009](#)). Both methods can exclude redundant variables that do not significantly contribute to  $m/r$ . To reduce the effect of noise, both algorithms were implemented in the so-called relaxed procedure ([Hastie et al., 2009](#)), consisting of two iterations. In the first iteration, the algorithm is trained on all predictors. A hyperparameter combination within one standard error of cross-validation MSE that led to a maximally sparse model was chosen. Only non-zero coefficient predictors are used in the second training iteration to reduce noise influence on the model. Taken together, the variable selection implemented through Lasso and Elastic Net, together with the relaxed model selection procedure, allowed reducing multicollinearity by removing redundant variables.

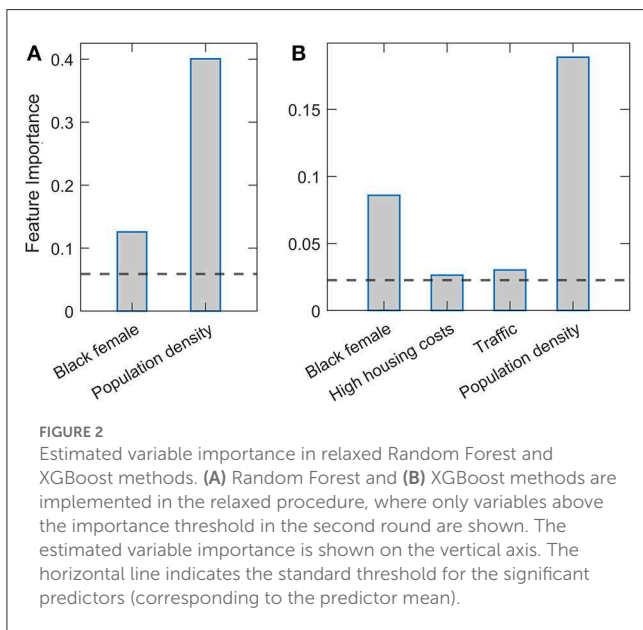
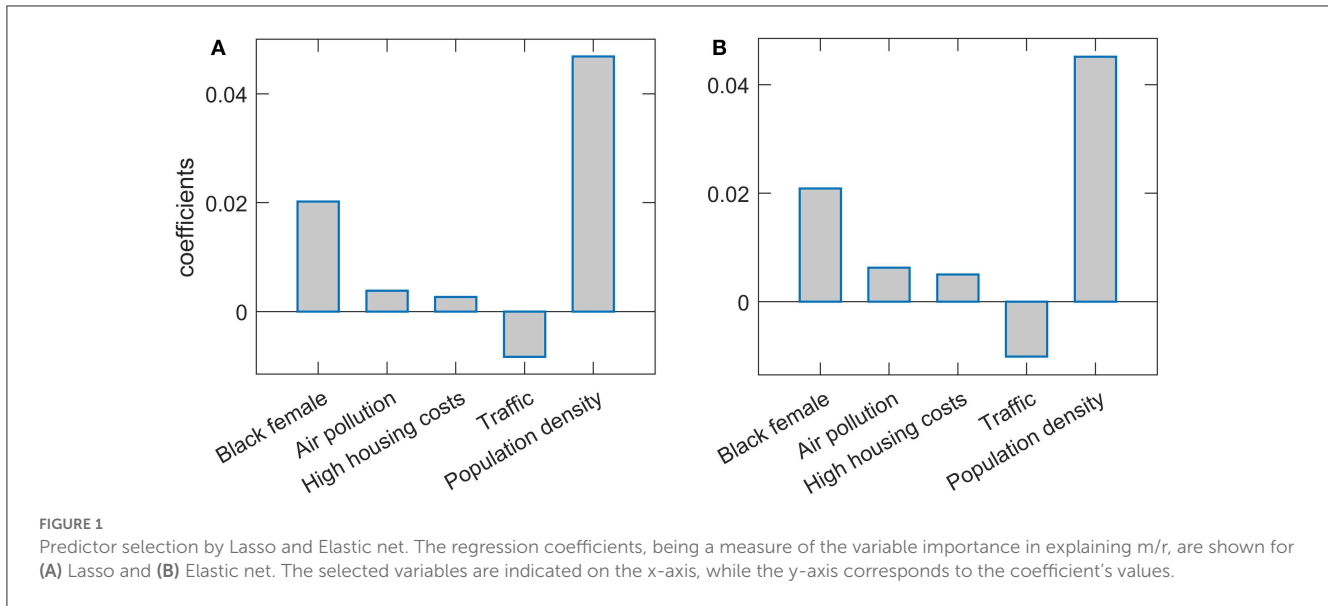
Results of the Lasso and Elastic net regressions are presented in [Figure 1](#). Hyperparameters in both models are optimized on the grid through cross-validation so that the resulting model corresponds to maximal prediction accuracies on new datasets. Note that, as the data was standardized before the regression, the obtained regression coefficients can be interpreted as the importance of the given feature in explaining COVID-19 severity, while the coefficient's sign indicates the influence's direction. Both methods lead to similar results. Population density is singled out as the severity predictor with the highest importance, followed by the percentage of Black females. Both predictors positively affect  $m/r$ , i.e., higher population density and Black female percentage are related to higher disease severity. Of the predictors with somewhat lower importance, traffic volume is negatively associated with the disease severity, while PM air pollution and high housing costs (an indication of poor socioeconomic conditions) are positively associated with the severity. However, the importance of these three features is notably smaller than the importance of the population density and percentage of African Americans. Note that “Black female” and “Black male” variables are highly correlated (Pearson Correlation Coefficient of 0.93), which in practice makes them hardly distinguishable and redundant. Due to this, in the text we merge/consolidate them as a measure of African American population prevalence (African Americans).

Lasso and Elastic net correspond to linear regression analysis. However, in reality, the predictors may have a highly nonlinear relationship with the output, while interactions between different predictors in the model may also occur. Linear regressions cannot account for such effects. Thus, we next used the ensembles of weak learners (decision trees), i.e., XGBoost and Random Forest. Another advantage of these methods is that they can better handle multicollinearity, particularly when redundant variables are removed (i.e., the most relevant variables selected), before training the ensembles of the decision trees. We extensively optimized (cross-validated) both methods over a large hyperparameter grid. We again employ both methods in the relaxed setup to reduce noise influence, i.e., only the predictors with importance above the mean (standardly used threshold) in the first round are used as the input in the second round.

[Figure 2](#) presents feature importance in Relaxed Random Forest and XGBoost. Again, robust results consistent across the two methods were obtained, where by far the highest relative importance is assigned to population density, followed by the Black female variable. These results are consistent with those previously obtained by Lasso and Elastic net regressions. Besides these two features, which are clearly above the importance threshold in both methods, traffic volume and high housing costs appear with values barely above the threshold in XGBoost.

Mutual correlations between the predictors in the dataset are another complication. To address this, we integrate the mRMR method into Random Forest and XGBoost methods. The method was initially introduced by [Ding and Peng \(2005\)](#) but recently gained popularity with its implementation within the Uber machine learning platform ([Zhao et al., 2019](#)). In essence, mRMR ranks the variables to how well they are associated with the response and how much they are redundant (where high correlations with other predictors decrease the predictor rank). In the Uber platform, the method was integrated only in Random





Forest, and fixed (preselected) hyperparameter values were used, likely to reduce computational time in a time-sensitive setup. Instead, we here carefully optimize hyperparameters by cross-validation on an extensive grid. The number of selected predictors in this cross-validation is also treated as a hyperparameter (see Methods). We also implement mRMR within XGBoost, in addition to being implemented in Random Forest.

Results of Random Forest and XGBoost with integrated mRMR methods for variable preselection are shown in Figure 3. Optimal selection of the number of variables was made through the plots on the left-hand side of the Figures 3A, C, where the prediction accuracy (assessed on the testing set in cross-validation) is shown vs. the number of selected variables. Above a certain number of included variables, the prediction accuracy enters saturation, which

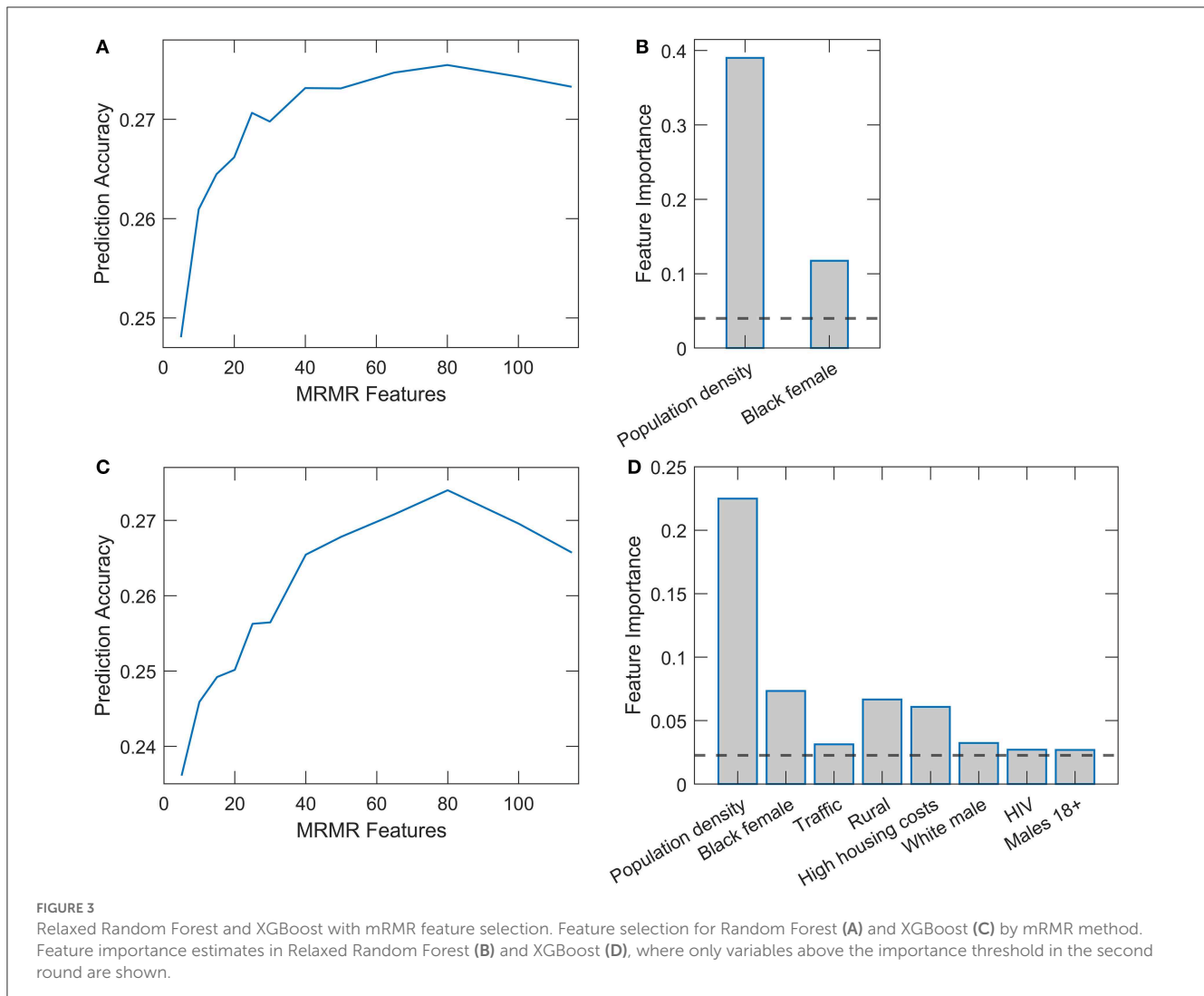
we use for selecting the number of variables for training the final model. The number of retained features was 25 for Random Forest and 38 for XGBoost. Figures 3B, D (the right side of the panel) again show the dominant importance of Population density and the Black female variable. While in Random Forest, we obtain no other features above the importance threshold, several features in XGBoost have importance estimates above the mean importance value. Most notably, the percentage of the rural population, high housing costs, percentage of white males, and traffic volume. We will see that most of these variables significantly correlate with the two main predictors.

Interestingly, only two predictors (Population density and Black female) were robustly singled out from 115 variables used in the initial input in the analysis. We finally assess the correlation of these two variables with the other variables to discuss factors related to the two main predictors associated with m/r. The variables with the highest values of the correlation coefficients are shown on the bar plots in Figure 4. All these variables have a statistically highly significant correlation ( $P \sim 10^{-100}$ ). These correlations are further discussed in the next section.

## 4. Discussion

In our large-scale high-resolution study (county-level with many predictors), we robustly obtain population density and percentage of Black females as the COVID-19 severity predictors with the highest importance in regressions. For discussion, we correlated these variables with the other predictors and selected those with the highest correlations.

This can be informative when trying to understand our somewhat surprising result: only two variables were clearly selected among a large number of starting predictors. By considering these correlations, we may also better understand possible factors that contribute to these two variables being clearly distinct in their association with COVID-19 severity.

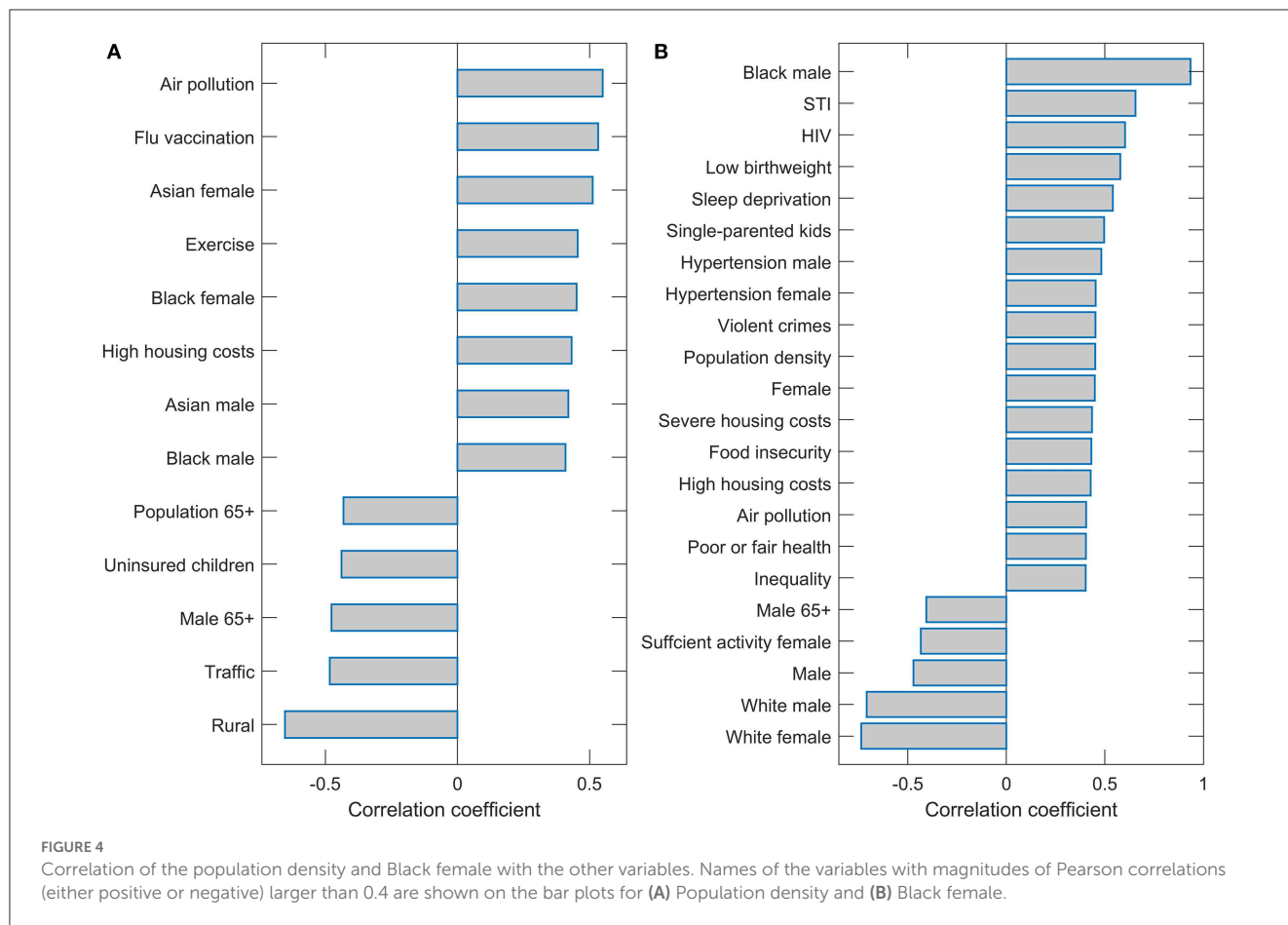


As the Black female variable is strongly positively correlated with the Black male variable, it can be considered as a measure of the percentage of African Americans of both genders. Furthermore, the fraction of the Black population is strongly negatively correlated with the proportion of the non-Hispanic white population and positively correlated with the Asian American and Hispanic populations. The Black female variable can be, thus, considered a signature of the minority population, which we found strongly positively associated with COVID-19 severity. Indeed, this association also holds for the Hispanic population, who, despite having (on average) higher life expectancy (County Health Rankings, 2020) compared to non-Hispanic whites, suffered the highest drop in life expectancy due to COVID-19 compared to any other ethnicity (Woolf et al., 2021).

The positive association between the percentage of African Americans and the severity of COVID-19 has already been documented (Azar et al., 2020; Thebault et al., 2020) and discussed in the context of several health and social factors. These are the same factors that show up in our analysis through the correlations of Blacks with other variables. First, Blacks are strongly correlated with several determinants of poverty and

disadvantaged population, such as the prevalence of sexually transmitted infections (STIs), violent crimes, different housing problems, and smaller homeownership. COVID-19 severity has also been associated with determinants of the disadvantaged population outside the USA (Gao et al., 2022). Secondly, they are strongly correlated with a number of medical factors, such as low birth weight, insufficient sleep, hypertension, cardiovascular diseases, and generally poor health. These medical conditions are well-known COVID-19 risk factors, as extensively discussed in the literature (Ssentongo et al., 2020; Ahmadi et al., 2021; Crispi et al., 2021; Du et al., 2021; Saleh et al., 2022; Zhang et al., 2022). We next focus on sociodemographic factors, whose interpretation may be less evident.

Although the direct association between the prevalence of violent crimes and COVID-19 severity is unlikely, this variable can be interpreted as another measure of socioeconomic deprivation, as it is established that both poverty and income inequality are positively associated with the rate of violent crimes (Hsieh and Pugh, 1993; Kennedy et al., 1998). While a higher rate of violent crimes is correlated with a larger proportion of African Americans, violent crimes are more likely to be class-related (Smith et al., 2021)



than associated with African Americans *per se*. Violent crime areas may also lead to high-stress levels (Berman et al., 1996; Ellen et al., 2001; County Health Rankings, 2020), which can damage health and be the underlying cause of a series of chronic conditions, such as hypertension (Zimmerman and Frohlich, 1990; Ellen et al., 2001) or obesity (Conklin et al., 2019), which are both well-known risk factors for the severe outcome of COVID-19 (Kwok et al., 2020; Du et al., 2021).

Housing issues, such as severe or high housing costs and a low homeownership percentage, indicate poor socioeconomic conditions (Dunn, 2002; County Health Rankings, 2020). Race differences also play a role in homeownership, as it is much lower among African Americans than non-Hispanic Whites (Jackman and Jackman, 1980). Households affected by housing issues would probably lack access to healthcare, as they may be unable to pay for it (Carroll et al., 2017). In the pandemic context, members of such households might not receive proper medical care, fail to timely seek medical attention, or be unable to afford the appropriate treatment and medications. Prevalence of STIs, defined as the number of newly diagnosed Chlamydia cases per 100,000 population, is also correlated with the Black female variable, which is not surprising, as it has been shown that African American adolescent women are disproportionately affected by Chlamydia (Cooksey et al., 2010). The prevalence of Chlamydia and other STIs can thus be viewed in the context of health inequality (County Health Rankings, 2020).

Therefore, all sociodemographic variables significantly correlated with Blacks correspond to underserved communities. This suggests that Black female was singled out by our regressions, not as a single severity predictor but as the variable that best captures most of these effects, indicating that minorities and socially disadvantaged populations were disproportionately severely affected by COVID-19, which is coherent with the results of several other studies (Dyer, 2020; Tirupathi et al., 2020; Arasteh, 2021; Chen and Krieger, 2021; Tai et al., 2021). Additionally, middle-aged Black females have already been recognized as the group with the highest disease burden in Mississippi (Martin and Garrett, 2022). This could be related to the higher prevalence of obesity in this social group (Martin and Garrett, 2022) or a relatively high percentage of Black females who are essential workers (Sugg et al., 2021) working in an environment with a probability of high viral exposure. High initial viral inoculum at the workplace could also lead to higher disease severity (Burgess et al., 2020). Since people in disadvantaged areas are more likely to be “essential workers” working in environments with a high risk of COVID-19 exposure while simultaneously having limited access to healthcare (Oronce et al., 2020), the obtained associations with the disease case counts are not surprising. However, as our severity measure is independent of transmissibility, our result is not a mere consequence of a larger COVID-19 exposure but rather a consequence of the interplay of medical and sociodemographic factors discussed above.



Population density appeared as, by far, the most significant predictor of COVID-19 severity. The variable with the highest correlation with population density is air pollution. This likely points to an important factor behind the strong association of population density with disease severity. Namely, the link between air pollution exposure and respiratory diseases, and COVID-19, in particular, is well established (Ogen, 2020; Wu et al., 2020; Pansini and Fornacca, 2021).

In addition to pollution, the population density is also significantly correlated with Blacks, where potential contributions of this variable to the severity are discussed above. Other variables correlated with the Black female also appear to correlate with population density (STI, housing problems, insufficient sleep). Interestingly, another racial-related factor (non-White/White residential segregation), which did not turn out to be highly correlated with Blacks, now appears significantly correlated with the population density. Regarding minorities, the Asian population of both genders is also significantly correlated with population density. The variable with the highest negative correlation with the population density is Rural, so the population density is a good proxy for urban and metropolitan areas.

Apart from the influences via pollution and African Americans (and related variables discussed above), likely, population density is also, *per se*, a prominent risk factor. A strong, nonlinear association between the epidemic's size and population density has already been proposed (Kermack et al., 1927) and empirically confirmed (Li et al., 2018). As higher population density inevitably leads to a much higher number of infected individuals in densely populated areas, the number of patients requiring hospitalization is more likely to quickly exceed the healthcare capacity. The effect of overcrowding, in this case, is dominant compared to the disparities in healthcare in rural areas, where population density is low. Namely, even though people in rural areas often struggle with poverty, lack of health insurance, and shortages in health professionals (Probst et al., 2004), a lower probability of exposure to the virus leads to the generally lower severity of the disease in these areas, so that healthcare facilities cannot quickly become saturated. Another possible explanation for the lower severity in rural areas is underreporting of COVID-19 deaths in these areas (Souch and Cossman, 2020). Namely, it has been determined that excess mortality not attributed to COVID-19 was higher in counties with a lower percentage of insured individuals, fewer primary care physicians, and more at-home deaths (Stokes et al., 2021). As most of these characteristics apply to rural areas (Probst et al., 2004), the reported cases and deaths likely do not correspond well to the actual situation.

Finally, this work provides an opportunity to compare the results of this high-resolution (county-level) analysis with our previous study at the state level (Markovic et al., 2021). While, in addition to different geographic resolutions, the two studies also use different variables—a larger number of (different) predictors are used here—interesting comparisons can still be made. First, predictors related to population density, African Americans, pollution, and prevalence of chronic diseases were obtained in that study. Although all these variables were directly selected at the state level, in the present study, pollution and chronic diseases were also identified via association with the two directly selected predictors. Also, at the state level, African Americans were less robustly

selected, i.e., only in the analysis that considers nonlinearities and interactions between the predictors, while in this study, it was robustly selected as a major predictor.

The largest difference between the two studies is the effect of the population age, which was selected as a significant predictor (with the expected positive influence on severity) in Markovic et al. (2021) but did not emerge as significant in this study. A higher proportion of African Americans and population density are associated with a younger population. It appears that, at the county level, Blacks are a much stronger signal associated with a younger population, which appears to conceal the age effect on severity. That is, counties with older populations will also have a smaller Black fraction, so they do not appear with higher  $m/r$ . At the state level, the variations of Blacks are lower (so that Blacks come out only in a more complicated machine learning analysis), which allows the age effect to come out. On the other hand, age has been clinically recognized as an important COVID-19 severity risk factor. This, therefore, shows that the analysis at lower and higher spatial resolutions are complementary, i.e., the smaller spatial resolution is not necessarily more accurate/relevant. One reason is that decreasing the size of the regions where the analysis is done also decreases the number of case counts, thereby increasing fluctuations and, consequently, the noise in the model. This consequently argues that, at least for some significant predictors, larger spatial resolution may clearly promote their proper identification.

## 5. Study limitations

We finally discuss some limitations of our study. Most importantly, while we here assembled a vast number of COVID-19 predictors, some factors that are likely very important (but would be hard to quantify) are clearly missing. In particular, our dataset consists of “static” variables and does not include “dynamic” decisions and factors that emerge during the pandemic, such as decisions on how to treat patients, medical protocols to be applied, motivation/training of medical staff, etc. In other words, static capacities or beneficial general conditions to fight pandemics may not necessarily translate to optimal decisions (and willingness to implement them), as has been well recognized in the case of, e.g., Global Health Security Index (Haider et al., 2020; Stribling et al., 2020). How to systematically include/quantify such highly complex factors remains to be seen.

On the other hand, a significant advantage of our study is that the epidemic intervention decisions (social distancing, quarantine, etc.) that impact the disease spread (transmissibility) (Hayashi et al., 2022) do not influence our severity measure (Markovic et al., 2021). This is because our severity measure  $m/r$  is independent of transmissibility, which does not apply to measures commonly used to quantify COVID-19 severity/mortality (such as the number of fatalities). We feel this is a considerable advantage of our study, as the actual effect of introduced intervention measures is hard to quantify (Soltesz et al., 2020). Also, as discussed in the Materials and Methods section,  $m/r$  is neither expected to significantly depend on the testing policies, since the variations in the volume of testing affect both the numerator and the denominator of the CFR in the same direction. However, the strict independence of  $m/r$  on testing

policies would require that the influence of the testing coverage on the case counts is exactly proportional to its effect on the number of fatalities, which need not be the case. Possible larger deviations in this sense might affect some of our conclusions.

Meteorological variables are also not included in this study. While they may impact transmissibility (Salom et al., 2021; Lin et al., 2022), they are unlikely to significantly impact the disease severity/mortality, as explicitly obtained for the state-level analysis (Markovic et al., 2021). Also, another potential limitation is that we inferred the end of the peak time from states (and then applied them to corresponding counties). It was previously shown that the peak time range could be inferred more accurately in spatially larger (conglomerated) regions (Vilar and Saiz, 2021), though we cannot exclude some counties with different peak timing. However, this should not significantly impact our results since in Markovic et al. (2021), we showed that  $m/r$  enters saturation (i.e., is nearly constant) for an extended time period, so the results should not be susceptible to exact dates for  $m/r$  inference. More generally, however, this issue corresponds to the conundrum of using smaller vs. larger geographic regions, which is generally understudied and should be better explored in the future.

Finally, as with other machine learning studies (limited to exploring data associations), the significant predictors we identified do not necessarily have to represent a causal relationship. In particular, our analysis has singled out two demographic factors—the percentage of Black females and population density—neither of which seems to have a direct medical impact on the prognosis of the disease. While this is clear for the population density, it is also less likely (though not entirely impossible) that Black females are genetically, per se, more predisposed to severe outcomes. Therefore, in an attempt to point out possible causal associations, we extensively discussed our results both in the context of previous studies and by analyzing the correlations of these two factors with the rest of the collected data. Thanks to the specific nature of the identified factors and the large overall number of variables included in the study, we believe that our interpretation of the obtained results indeed reveals some of the main drivers behind variations in the observed COVID-19 severity. Nevertheless, even if the significant predictors only partially reflect direct causal relations, they are still valuable risk assessment factors. Moreover, they may point to potential mechanistic relations that future studies should explore.

## 6. Conclusion and outlook

We addressed the challenging problem of identifying some of the potential main drivers of COVID-19 severity from a large set of assembled sociodemographic factors. We showed that machine learning methods with feature selection are well suited for this task, producing robust results across different methods. The combination of mRMR and ensembles of decision trees (Random Forest and XGBoost) seems particularly promising for similar tasks in the future, as it can simultaneously handle large, correlated sets of predictors, their interactions, and nonlinear dependences. We propose that this methodology is useful whenever there is a measure of interest (response) defined over a diverse set of geographic regions, and significant predictors of this measure (e.g.,

demographic, economic, medical variables, or their combinations) should be selected among many variables that initially seem potentially relevant. In the study of COVID-19 and any other emerging infectious disease, identifying potential transmissibility and severity determinants (and the consequent understanding of the nature of their relation to the response variable) is a very challenging problem that requires taking into account many potential risk factors. The combination of the mRMR approach (which offers a very efficient way of variable preselection while eliminating all the redundant variables), and the nonparametric, supervised machine learning methods based on the ensembles of decision trees (which are capable of selecting important features while taking into account possible nonlinear relation between the features and the response variable), can be very promising in resolving this problem, as our study illustrates.

In summary, our final result is simple and suggests that densely populated areas with a high proportion of minorities and disadvantaged populations are the main COVID-19 severity risk factors. The result is here obtained for the USA, but it is arguably more general. That is, the likely causes behind such result are disadvantaged populations, environmental factors such as pollution, and a potentially high increase of cases in densely populated areas that available medical resources might not match. These factors remain to be carefully investigated and understood in the future.

## Data availability statement

The original contributions presented in the study are included in the article/Supplementary material, further inquiries can be directed to the corresponding author.

## Author contributions

MD conceived the research. The work was supervised by MD and IS. Data acquisition and analysis by MT. Figures and tables made by MT and SM. A literature search by SM. Manuscript written by MT and IS, with the help of MD and SM. All authors contributed to the article and approved the submitted version.

## Funding

This work was partially supported by the Ministry of Education, Science and Technological Development of the Republic of Serbia.

## Acknowledgments

We thank Dusan Zigic and Magdalena Djordjevic for their help in assembling part of the input data.

## Conflict of interest

The authors declare that the research was conducted in the absence of any commercial or financial relationships

that could be construed as a potential conflict of interest.

## Publisher's note

All claims expressed in this article are solely those of the authors and do not necessarily represent those of their affiliated organizations, or those of the publisher, the editors and the reviewers. Any product that may be

evaluated in this article, or claim that may be made by its manufacturer, is not guaranteed or endorsed by the publisher.

## Supplementary material

The Supplementary Material for this article can be found online at: <https://www.frontiersin.org/articles/10.3389/fdata.2023.1038283/full#supplementary-material> (accessed January 27, 2022).

## References

- Adhikari, A., and Yin, J. (2020). Short-Term Effects of Ambient Ozone, PM(2.5), and Meteorological Factors on COVID-19 Confirmed Cases and Deaths in Queens, New York. *Int. J. Environ. Res. Public Health* 17, 4047. doi: 10.3390/ijerph17114047
- Ahmadi, M. N., Huang, B.-H., Inan-Eroglu, E., Hamer, M., and Stamatakis, E. (2021). Lifestyle risk factors and infectious disease mortality, including COVID-19, among middle aged and older adults: evidence from a community-based cohort study in the United Kingdom. *Brain Behav. Immun.* 96, 18–27. doi: 10.1016/j.bbi.2021.04.022
- Alizadehsani, R., Roshanzamir, M., Hussain, S., Khosravi, A., Koohestani, A., Zangoeei, M. H., et al. (2021). Handling of uncertainty in medical data using machine learning and probability theory techniques: a review of 30 years (1991–2020). *Annal. Operat. Res.* 6, 2. doi: 10.1007/s10479-021-04006-2
- Allel, K., Tapia-Muñoz, T., and Morris, W. (2020). Country-level factors associated with the early spread of COVID-19 cases at 5, 10 and 15 days since the onset. *Global Public Health* 15, 1589–1602. doi: 10.1080/17441692.2020.1814835
- Amini, N., Mahdavi, M., Choubdar, H., Abedini, A., Shalhaf, A., and Lashgari, R. (2022). Automated prediction of COVID-19 mortality outcome using clinical and laboratory data based on hierarchical feature selection and random forest classifier. *Comput. Methods Biomechan. Biomed. Eng.* 2, 1–14. doi: 10.1080/10255842.2022.2050906
- An, C., Lim, H., Kim, D.-W., Chang, J. H., Choi, Y. J., and Kim, S. W. (2020). Machine learning prediction for mortality of patients diagnosed with COVID-19: a nationwide Korean cohort study. *Scientific Rep.* 10, 18716. doi: 10.1038/s41598-020-75767-2
- Arasteh, K. (2021). Prevalence of Comorbidities and Risks Associated with COVID-19 Among Black and Hispanic Populations in New York City: an Examination of the 2018 New York City Community Health Survey. *J. Racial Ethnic Health Disparit.* 8, 863–869. doi: 10.1007/s40615-020-00844-1
- Azar, K. M. J., Shen, Z., Romanelli, R. J., Lockhart, S. H., Smits, K., Robinson, S., et al. (2020). Disparities in outcomes among COVID-19 patients in a large health care system in California. *Health Affairs* 39, 1253–1262. doi: 10.1377/hlthaff.2020.00598
- Berman, S. L., Kurtines, W. M., Silverman, W. K., and Serafini, L. T. (1996). The impact of exposure to crime and violence on urban youth. *Am. J. Orthopsychiatr.* 66, 329–336. doi: 10.1037/h0080183
- Böttcher, L., Xia, M., and Chou, T. (2020). Why case fatality ratios can be misleading: individual- and population-based mortality estimates and factors influencing them. *Phys. Biol.* 17, 065003. doi: 10.1088/1478-3975/ab9e59
- Breiman, L. (2001). Random forests. *Mach. Learn.* 45, 5–32. doi: 10.1023/A:1010933404324
- Burgess, S., Smith, D., Kenyon, J. C., and Gill, D. (2020). Lightening the viral load to lessen covid-19 severity. *BMJ* 371, m4763. doi: 10.1136/bmj.m4763
- Carroll, A., Corman, H., Curtis, M. A., Noonan, K., and Reichman, N. E. (2017). Housing instability and children's health insurance gaps. *Academ. Pediatr.* 17, 732–738. doi: 10.1016/j.acap.2017.02.007
- Chen, J. T., and Krieger, N. (2021). Revealing the Unequal Burden of COVID-19 by Income, Race/Ethnicity, and Household Crowding: U.S. county versus zip code analyses. *J. Public Health Manage. Pract.* 27, S43. doi: 10.1097/PHH.0000000000001263
- Chen, T., and Guestrin, C. (2016). XGBoost: A Scalable Tree Boosting System. in *Proceedings of the 22nd ACM SIGKDD International Conference on Knowledge Discovery and Data Mining KDD '16*. (New York, NY, USA: Association for Computing Machinery), 785–794.
- Conklin, A. I., Guo, S. X. R., Yao, C. A., Tam, A. C. T., and Richardson, C. G. (2019). Stressful life events, gender and obesity: a prospective, population-based study of adolescents in British Columbia. *Int. J. Pediatr. Adolesc. Med.* 6, 41–46. doi: 10.1016/j.ijpam.2019.03.001
- Cooksey, C. M. J. L., Berggren, E. K., and Lee, J. (2010). Chlamydia trachomatis Infection in minority adolescent women: a public health challenge. *Obstetric. Gynecologic. Survey* 65, 729–735. doi: 10.1097/OGX.0b013e3182110204
- County Health Rankings (2020). *2020 County Health Rankings Key Findings Report. County Health Rankings and Roadmaps*. Available online at: <https://www.countyhealthrankings.org/reports/2020-county-health-rankings-key-findings-report> (accessed January 27, 2022).
- Crispi, F., Crovetto, F., Larroya, M., Camacho, M., Tortajada, M., Sibila, O., et al. (2021). Low birth weight as a potential risk factor for severe COVID-19 in adults. *Scientific Rep.* 11, 2909. doi: 10.1038/s41598-021-82389-9
- Ding, C., and Peng, H. (2005). Minimum redundancy feature selection from microarray gene expression data. *J. Bioinform. Comput. Biol.* 03, 185–205. doi: 10.1142/S0219720005001004
- Djordjevic, M., Djordjevic, M., Ilic, B., Stojku, S., and Salom, I. (2021a). Understanding Infection Progression under Strong Control Measures through Universal COVID-19 Growth Signatures. *Glob. Challenges* 5, 2000101. doi: 10.1002/gch2.202000101
- Djordjevic, M., Rodic, A., Salom, I., Zigic, D., Milicevic, O., Ilic, B., et al. (2021b). A systems biology approach to COVID-19 progression in population. *Adv. Prot. Chemistr. Struct. Biology* 127, 291–314. doi: 10.1016/bs.apcsb.2021.03.003
- Dong, E., Du, H., and Gardner, L. (2020). An interactive web-based dashboard to track COVID-19 in real time. *Lancet Infect. Dis.* 20, 533–534. doi: 10.1016/S1473-3099(20)30120-1
- Du, Y., Zhou, N., Zha, W., and Lv, Y. (2021). Hypertension is a clinically important risk factor for critical illness and mortality in COVID-19: a meta-analysis. *Nutrit. Metabol. Cardiovascul. Dis.* 31, 745–755. doi: 10.1016/j.numecd.2020.12.009
- Dunn, J. R. (2002). Housing and inequalities in health: a study of socioeconomic dimensions of housing and self reported health from a survey of Vancouver residents. *J. Epidemiol. Commun. Health* 56, 671–681. doi: 10.1136/jech.56.9.671
- Dyer, O. (2020). Covid-19: Black people and other minorities are hardest hit in the U.S. *BMJ* 369, m1483. doi: 10.1136/bmj.m1483
- Ellen, I. G., Mijanovich, T., and Dillman, K.-N. (2001). Neighborhood effects on health: exploring the links and assessing the evidence. *J. Urban Affairs* 23, 391–408. doi: 10.1111/0735-2166.00096
- Friedman, J. H. (2001). Greedy function approximation: a gradient boosting machine. *Annal. Statistics* 29, 1189–1232. doi: 10.1214/aos/1013203451
- Gao, L., Zheng, C., Shi, Q., Wang, L., Tia, A., Liu, Z. G., et al. (2022). Multiple introduced lineages and the single native lineage co-driving the four waves of the COVID-19 pandemic in West Africa. *Front. Public Health* 30, 38. doi: 10.3389/fpubh.2022.957277
- Global Health Data Exchange (2021). *US Data | GHDx. Global Health Data Exchange*. Available online at: <http://ghdx.healthdata.org/us-data> (accessed February 11, 2022).
- Gupta, A., and Gharehgozli, A. (2020). *Developing a Machine Learning Framework to Determine the Spread of COVID-19*.
- Haider, N., Yavlinsky, A., Chang, Y.-M., Hasan, M. N., Benfield, C., Osman, A. Y., et al. (2020). The Global Health Security index and Joint External Evaluation score for health preparedness are not correlated with countries' COVID-19 detection response time and mortality outcome. *Epidemiol. Infect.* 148, e210. doi: 10.1017/S0950268820002046
- Hastie, T., Tibshirani, R., and Friedman, J. (2009). *The Elements of Statistical Learning: Data Mining, Inference, and Prediction*. 2nd ed. New York, NY: Springer-Verlag.



- Hayashi, K., Kayano, T., Anzai, A., Fujimoto, M., Linton, N., Sasanami, M., et al. (2022). Assessing public health and social measures against COVID-19 in Japan from march to june 2021. *Front. Med.* 9, 937732. doi: 10.3389/fmed.2022.937732
- Homeland Infrastructure Foundation-Level Data (2020). *Hospitals*. Available online at: <https://hifld-geoplatform.opendata.arcgis.com/datasets/hospitals/explore?location=31.724568,-93.543139,7.83> (accessed February 11, 2022).
- Hradsky, O., and Komarek, A. (2021). Demographic and public health characteristics explain a large part of variability in COVID-19 mortality across countries. *Euro. J. Public Health* 31, 12–16. doi: 10.1093/eurpub/ckaa226
- Hsieh, C.-C., and Pugh, M. D. (1993). Poverty, income inequality, and violent crime: a meta-analysis of recent aggregate data studies. *Criminal Justice Rev.* 18, 182–202. doi: 10.1177/073401689301800203
- Jackman, M. R., and Jackman, R. W. (1980). Racial inequalities in home ownership. *Soc. Forces* 58, 1221–1234. doi: 10.2307/2577321
- Kamalov, F., Cherukuri, A. K., and Thabtah, F. (2022). “Machine learning applications to Covid-19: a state-of-the-art survey,” in *2022 Advances in Science and Engineering Technology International Conferences (ASET)*, 1–6.
- Kennedy, B. P., Kawachi, I., Prothrow-Stith, D., Lochner, K., and Gupta, V. (1998). Social capital, income inequality, and firearm violent crime. *Soc. Sci. Med.* 47, 7–17. doi: 10.1016/S0277-9536(98)00097-5
- Kermack, W. O., McKendrick, A. G., and Walker, G. T. (1927). A contribution to the mathematical theory of epidemics: proceedings of the royal society of London. *Series A, Contain. Papers Mathematic. Physic. Charact.* 115, 700–721. doi: 10.1098/rspa.1927.0118
- Kwok, S., Adam, S., Ho, J. H., Iqbal, Z., Turkington, P., Razvi, S., et al. (2020). Obesity: a critical risk factor in the COVID-19 pandemic. *Clinic. Obesit.* 10, e12403. doi: 10.1111/cob.12403
- Li, R., Richmond, P., and Roehner, B. M. (2018). Effect of population density on epidemics. *Physica A: Statistic. Mechan. Applicat.* 510, 713–724. doi: 10.1016/j.physa.2018.07.025
- Lin, S., Rui, J., Xie, F., Zhan, M., Chen, Q., Zhao, B., et al. (2022). Assessing the impacts of meteorological factors on COVID-19 pandemic using generalized estimating equations. *Front. Public Health* 10, 920312. doi: 10.3389/fpubh.2022.920312
- Lorenzo, J. S. L., Tam, W. W. S., and Seow, W. J. (2021). Association between air quality, meteorological factors and COVID-19 infection case numbers. *Environ. Res.* 197, 111024. doi: 10.1016/j.envres.2021.111024
- Mahdavi, M., Choubdar, H., Zabe, E., Rieder, M., Safavi-Naeini, S., Jobbagy, Z., et al. (2021). A machine learning based exploration of COVID-19 mortality risk. *Plos One* 16, e0252384. doi: 10.1371/journal.pone.0252384
- Markovic, S., Rodic, A., Salom, I., Milicevic, O., Djordjevic, M., and Djordjevic, M. (2021). COVID-19 severity determinants inferred through ecological and epidemiological modeling. *One Health* 13, 100355. doi: 10.1016/j.onehlt.2021.100355
- Markovic, S., Salom, I., Rodic, A., and Djordjevic, M. (2022). Analyzing the GHSI puzzle of whether highly developed countries fared worse in COVID-19. *Sci. Rep.* 12, 17711. doi: 10.1038/s41598-022-22578-2
- Martin, B. E., and Garrett, M. R. (2022). Race and sex differences in vital signs associated with COVID-19 and flu diagnoses in mississippi. *J. Rac. Ethnic Health Disparit.* 12, 31. doi: 10.1007/s40615-021-01213-2
- Mazzanti, S. (2022). *mrmr-selection: minimum-Redundancy-Maximum-Relevance algorithm for feature selection*. Available online at: <https://github.com/smazzanti/mrmr> (accessed September 5, 2022).
- Moreira, A., Chorath, K., Rajasekaran, K., Burmeister, F., Ahmed, M., and Moreira, A. (2021). Demographic predictors of hospitalization and mortality in U.S. children with COVID-19. *Europ. J. Pediatrics* 180, 1659–1663. doi: 10.1007/s00431-021-03955-x
- Ogen, Y. (2020). Assessing nitrogen dioxide (NO2) levels as a contributing factor to coronavirus (COVID-19) fatality. *Sci. Total Environ.* 726, 138605. doi: 10.1016/j.scitotenv.2020.138605
- Oronce, C. I. A., Scannell, C. A., Kawachi, I., and Tsugawa, Y. (2020). Association Between State-Level Income Inequality and COVID-19 Cases and Mortality in the USA. *J. General Intern. Med.* 35, 2791–2793. doi: 10.1007/s11606-020-05971-3
- Pan, J., St. Pierre, J. M., Pickering, T. A., Demirjian, N. L., Fields, B. K. K., Desai, B., et al. (2020). Coronavirus disease 2019 (COVID-19): a modeling study of factors driving variation in case fatality rate by country. *Int. J. Environ. Res. Public Health* 17, 8189. doi: 10.3390/ijerph17218189
- Pansini, R., and Fornacca, D. (2021). COVID-19 higher mortality in chinese regions with chronic exposure to lower air quality. *Front. Public Health* 1, 53. doi: 10.3389/fpubh.2020.597753
- Pedregosa, F., Varoquaux, G., Gramfort, A., Michel, V., Thirion, B., Grisel, O., et al. (2011). Scikit-learn: machine learning in Python. *J. Machine Learn. Res.* 12, 2825–2830. doi: 10.5555/1953048.2078195
- Perone, G. (2021). The determinants of COVID-19 case fatality rate (CFR) in the Italian regions and provinces: An analysis of environmental, demographic, and healthcare factors. *Science of The Total Environment* 755, 142523. doi: 10.1016/j.scitotenv.2020.142523
- Probst, J. C., Moore, C. G., Glover, S. H., and Samuels, M. E. (2004). Person and place: the compounding effects of race/ethnicity and rurality on health. *Am. J. Public Health* 94, 1695–1703. doi: 10.2105/AJPH.94.10.1695
- Rajab, K., Kamalov, F., and Cherukuri, A. K. (2022). Forecasting COVID-19: vector autoregression-based model. *Arab. J. Sci. Eng.* 47, 6851–6860. doi: 10.1007/s13369-021-06526-2
- Ramirez-del Real, T., Martínez-García, M., Márquez, M. F., López-Trejo, L., Gutiérrez-Esparza, G., and Hernández-Lemus, E. (2022). Individual factors associated with COVID-19 infection: a machine learning study. *Front. Public Health* 10, 12099. doi: 10.3389/fpubh.2022.912099
- Rontos, K., Syrimali, M.-E., and Salvati, L. (2021). Unravelling the role of socioeconomic forces in the early stage of COVID-19 pandemic: a global analysis. *Int. J. Environ. Res. Public Health* 18, 6340. doi: 10.3390/ijerph18126340
- Saleh, M. A., Alotaibi, N., Schrapp, K., Alsaber, A., Pan, J., Almutairi, F., et al. (2022). Risk factors for mortality in patients with COVID-19: The Kuwait Experience. *Med. Princ. Pract.* 22, 166. doi: 10.1159/000522166
- Salom, I., Rodic, A., Milicevic, O., Zigic, D., Djordjevic, M., and Djordjevic, M. (2021). Effects of demographic and weather parameters on COVID-19 basic reproduction number. *Front. Ecol. Evol.* 8, 617841. doi: 10.3389/fevo.2020.617841
- Singh, B. B., Ward, M. P., Lowerison, M., Lewinson, R. T., Vallerand, I. A., Dearnod, R., et al. (2021). Meta-analysis and adjusted estimation of COVID-19 case fatality risk in India and its association with the underlying comorbidities. *One Health* 13, 100283. doi: 10.1016/j.onehlt.2021.100283
- Smith, S., Ferguson, C. J., and Henderson, H. (2021). An exploratory study of environmental stress in four high violent crime cities: what sets them apart? *Crime Delinquency* 21, 00111287211057858. doi: 10.1177/00111287211057858
- Soltész, K., Gustafsson, F., Timpka, T., Jaldén, J., Jidling, C., Heimerson, A., et al. (2020). The effect of interventions on COVID-19. *Nature* 588, E26–E28. doi: 10.1038/s41586-020-3025-y
- Souch, J. M., and Cossman, J. S. (2020). A commentary on rural-urban disparities in COVID-19 testing rates per 100,000 and risk factors. *J. Rural Health*, 10, 12450. doi: 10.1111/jrh.12450
- Ssentongo, P., Ssentongo, A. E., Heilbrunn, E. S., Ba, D. M., and Chinchilli, V. M. (2020). Association of cardiovascular disease and 10 other pre-existing comorbidities with COVID-19 mortality: A systematic review and meta-analysis. *PLOS ONE* 15, e0238215. doi: 10.1371/journal.pone.0238215
- Stokes, A. C., Lundberg, D. J., Elo, I. T., Hempstead, K., Bor, J., and Preston, S. H. (2021). COVID-19 and excess mortality in the United States: a county-level analysis. *PLOS Med.* 18, e1003571. doi: 10.1371/journal.pmed.1003571
- Stribling, J., Clifton, A., McGill, G., and de Vries, K. (2020). Examining the U.K. Covid-19 mortality paradox: Pandemic preparedness, healthcare expenditure, and the nursing workforce. *J. Adv. Nurs* 76, 3218–3227. doi: 10.1111/jan.14562
- Sugg, M. M., Runkle, J. D., Andersen, L., Weiser, J., and Michael, K. D. (2021). Crisis response among essential workers and their children during the COVID-19 pandemic. *Prev. Med.* 153, 106852. doi: 10.1016/j.ypmed.2021.106852
- Tai, D. B. G., Shah, A., Doubeni, C. A., Sia, I. G., and Wieland, M. L. (2021). The disproportionate impact of COVID-19 on racial and ethnic minorities in the United States. *Clinic. Infect. Dis.* 72, 703–706. doi: 10.1093/cid/ciaa815
- Thebault, R., Tran, A. B., and Williams, V. (2020). *The coronavirus is infecting and killing black Americans at an alarmingly high rate*. *Washington Post*. Available online at: <https://www.washingtonpost.com/nation/2020/04/07/coronavirus-is-infecting-killing-black-americans-an-alarmingly-high-rate-post-analysis-shows/> (accessed January 24, 2022).
- Tirupathi, R., Muradova, V., Shekhar, R., Salim, S. A., Al-Tawfiq, J. A., and Palabindala, V. (2020). COVID-19 disparity among racial and ethnic minorities in the U.S.: a cross sectional analysis. *Travel Med. Infect. Dis.* 38, 101904. doi: 10.1016/j.tmaid.0.2020.101904
- U.S. Census Bureau (2011). *USA Counties: 2011. U.S. Census Bureau*. Available online at: <https://www.census.gov/library/publications/2011/compendia-usa-counties-2011.html> (accessed February 11, 2022).
- U.S. Census Bureau (2018). *2018 Population Estimates FIPS Codes. U.S. Census Bureau*. Available online at: <https://www.census.gov/geographies/reference-files/2018/demo/pepost/2018-fips.html> (accessed February 11, 2022).
- U.S. Census Bureau (2020). *U.S. Census Data. U.S. Census Bureau*. Available online at: <https://www.census.gov/en.html> (accessed July 10, 2021).
- U.S. Department Of Agriculture (2021). *Atlas of Rural and Small-Town America. Economic research service U.S. Department of Agriculture*. Available at: <https://www.ers.usda.gov/data-products/atlas-of-rural-and-small-town-america> (accessed February 11, 2022).
- Vilar, J. M. G., and Saiz, L. (2021). Ascertainning the initiation of epidemic resurgences: an application to the COVID-19 second surges in Europe and the Northeast United States. *Royal Soc. Open Sci.* 8, 210773. doi: 10.1098/rsos.210773
- Virtanen, P., Gommers, R., Oliphant, T. E., Haberland, M., Reddy, T., Cournapeau, D., et al. (2020). SciPy 1.0: fundamental algorithms for scientific computing in Python. *Nat. Methods* 17, 261–272. doi: 10.1038/s41592-019-0686-2

- Wang, L., Lin, M., Wang, J., Chen, H., Yang, M., Qiu, S., et al. (2022). Quantitative analysis of the impact of various urban socioeconomic indicators on search-engine-based estimation of COVID-19 prevalence. *Infect. Dis. Modell.* 7, 117–126. doi: 10.1016/j.idm.2022.04.003
- Wang, L., Zhang, Y., Wang, D., Tong, X., Liu, T., Zhang, S., et al. (2021). Artificial Intelligence for COVID-19: a systematic review. *Front. Med.* 8, 256. doi: 10.3389/fmed.2021.704256
- Wolf, S. H., Masters, R. K., and Aron, L. Y. (2021). Effect of the COVID-19 pandemic in 2020 on life expectancy across populations in the USA and other high income countries: simulations of provisional mortality data. *BMJ* 373, n1343. doi: 10.1136/bmj.n1343
- Wu, X., Nethery, R. C., Sabath, M. B., Braun, D., and Dominici, F. (2020). Air pollution and COVID-19 mortality in the United States: strengths and limitations of an ecological regression analysis. *Science Adv.* 6, 49. doi: 10.1126/sciadv.abd4049
- Yeoh, E. K., Chong, K. C., Chiew, C. J., Lee, V. J., Ng, C. W., Hashimoto, H., et al. (2021). Assessing the impact of non-pharmaceutical interventions on the transmissibility and severity of COVID-19 during the first five months in the Western Pacific Region. *One Health* 12, 100213. doi: 10.1016/j.onehlt.2021.100213
- Yousefzadeh, M., Hasanpour, M., Zolghadri, M., Salimi, F., Yektaein Vaziri, A., Mahmoudi Aqeel Abadi, A., et al. (2022). Deep learning framework for prediction of infection severity of COVID-19. *Front. Med.* 9, 960. doi: 10.3389/fmed.2022.940960
- Zhang, Y., Luo, W., Li, Q., Wang, X., Chen, J., Song, Q., et al. (2022). Risk factors for death among the first 80 543 coronavirus disease 2019 (COVID-19) Cases in China: relationships between age, underlying disease, case severity, and region. *Clinic. Infect. Dis.* 74, 630–638. doi: 10.1093/cid/ciab493
- Zhao, Z., Anand, R., and Wang, M. (2019). “Maximum relevance and minimum redundancy feature selection methods for a marketing machine learning platform,” in *2019 IEEE International Conference on Data Science and Advanced Analytics (DSAA)*.
- Zimmerman, R. S., and Frohlich, E. D. (1990). Stress and hypertension. *J. Hypertens. Supplement* 8, S103–S107.
- Zou, H., and Hastie, T. (2005). Regularization and variable selection via the elastic net. *J. Royal Statistic. Soc. Series B (Statistical Methodology)* 67, 301–320. doi: 10.1111/j.1467-9868.2005.00503.x